Spacecraft Environmental Interactions Technology 1983

NASA

National Aeronautics
and Space Administration

Scientific and Technical
Information Office

1985

PREFACE

The Spacecraft Environmental Interactions Technology Conference was held at the U.S. Air Force Academy, Colorado Springs, Colorado, from October 4 to 6, 1983. The fourth in a series of conferences jointly sponsored by NASA and the Air Force, it summarized technology investigations concerning interactions between space systems and their orbital environments and presented information for use by designers of such systems. The series forms a part of the joint NASA/Air Force technology programs and provides a forum for researchers, technologists, and engineers to exchange results and ideas.

The conference was planned to provide an overview of both spaceflight and ground technology investigations directed toward understanding and controlling interactions of space systems with orbital environments. It focus included interactions between orbital environments and large, high-power space systems, including the shuttle, and astronaut extravehicular activity, as well as the geosynchronous spacecraft charging technology that was the main focus of the earlier conferences in this series (in 1976, 1978, and 1980). This shift and expansion of focus reflects the changing areas of emphasis in the NASA/Air Force technology programs in the shuttle era.

We wish to thank Mr. R.E. Smylie, NASA Headquarters, and Col. B. Bolton, Air Force Space Technology Center, for their keynote addresses, and the members of the Conference Program Committee, R.M. Broussard, H.B. Garrett, A. Muelenberg, R.C. Sagalyn, N.J. Stevens, and R.,W. Bercaw, for their assistance. Thanks are also due Ms. Gwen Brewer, Directorate of Plans and Programs, Air Force Academy, who provided outstanding support at the conference, including accommodations, transportation, meals, and facilities arrangements.

Carolyn K. Purvis
NASA Lewis Research Center

Charles P. Pike
U.S. Air Force Geophysics Laboratory

CONTENTS

Session IV - Spacecraft Charging

Session VI - Future Programs and Directions

SPACE STATION TECHNOLOGY PLANNING

R. E. Smylie
NASA Headquarters
Washington, D.C. 20546

I am certainly pleased and honored by the opportunity to come back and speak again to a group that has been working together for so many years with great benefit to spacecraft technology and to the organizations represented. Many of you were here in 1976 at the first conference. Colonel Brooke and I spend a great deal of energy in those days trying to generate cooperative programs between NASA and the Air Force Laboratory structure. This group is one of the many shining examples of success in that area.

We both are proud of what we were able to set in motion in those years. There already was a great deal of interchange at the individual level, but it did not extend as far as it should have to give the maximum benefit to both organizations. We have tried to establish not just cooperative programs but a spirit of cooperation among the people involved in technology programs all along the management chain.

I am going to speak for a few minutes about space station technology and what NASA is pursuing in terms of a space station program. It has long been my belief that a manned space station in Earth orbit is almost an imperative. Now it is not a matter of "if," but a matter of "when" and "what kind" the initial station will be.

First, a few words about the Space Station Technology Steering Committee, of which I am Chair. I joined this organization just a few months ago. It had been chaired by Walt Olstad, who had been the Acting Associate Administrator of OAST for quite some time. He moved over to be the Associate Administrator for Management. Walt made some major contributions to the committee, and I am pleased to follow in his footsteps.

We have in the committee a tremendous process by which to generate ideas and plans for the technology we should be pursuing in order to most benefit a space station program once it is begun. Each discipline area has a working group that addresses the particular technology from that discipline that would enhance a space station program, either through greater system performance or through lower life-cycle costs in a program that would extend over many, many years. Once we begin a space station program we expect it to continue indefinitely. It may evolve - in fact it will evolve - over time, but it will not necessarily have a defined endpoint such as many of our programs, including the Apollo Program and the Skylab Program, have had. A space station program is something that will continue into the foreseeable future.

The Centers have assigned their most innovative and competent people to these working groups, so we get very good reports from them. Our problem becomes one of sorting out, from all of the good ideas, the ones that should have the highest priority - the ones we should enact first in a space station program - and trying to combine them into something manageable within a budget we might expect to receive for this project. The work of the Steering Committee, then, is to interact with the working groups and try to prioritize and package the technology programs so that we can pursue them within our allotted resources. We also must generate the data that will allow us to advocate these programs through the management, OMB, and Congressional chains in order to acquire the resources to do this important work.

In this project there are some great technological opportunities to benefit not only an evolutionary space station, but also an initial space station. Usually you think of new technology as something that gives you greater performance. In a space station program, once you have defined your requirements, you want to meet those requirements at the lowest life-cycle cost.

Some people argue that we really do not need new technology to build a space station. They say that we have, in effect, created the equivalent of a space station in Skylab and we have the technology from the shuttle program that will allow us to build a space station with what we have today. And that is true. We could do that. But it would be a shame if we did precisely that. If we are able to bring some areas of technology, particularly power and thermal to a state of readiness to apply to the first space station, that first station will actually be less expensive, both in initial cost and in life-cycle cost. We must verbalize this message and convey it in such a way that it is believed and we can go ahead with it.

We will most likely pursue the space station program by using a modular approach (fig. 1). We believe that the space shuttle will be the basis for putting a manned base in orbit; therefore the station will be built of modules put into orbit by the shuttle and docked to form a core. Other modules will be added as the station evolves. There may also be platforms of various sorts, either in polar or in low-inclination orbit - probably both. These would be tended by the space station. Some kind of transfer vehicle will be used to move payloads from the station to other orbits. A smaller device, called a maneuvering system, will allow servicing of co-orbital platforms.

Figure 2 shows the types of equipment that may eventually be part of the space station. The initial station would be a core consisting of a power system with a few modules attached to it for experimentation in Earth orbit: a co-orbiting platform for experiments that require very good stability; some sort of maneuvering system that could tend the platform; and possibly a polar-orbiting platform. The core station would evolve into something larger and more capable over approximately 10 to 15 years, so a station after this model might be possible about the year 2000.

We are being careful not to produce a particular design before we have had a chance to do a significant amount of concept development and Phase B studies. So this is really an artist's vision of what might be, not any particular design that NASA is advocating. We try to define program requirements and let those requirements drive the technology, rather than the other way around. We think that we should be involved in many programs at once but that there should always be at least one program that is sort of a "technology push." Within a

year or so we would like to go into Phase B studies toward the start of the station in a few years. Therefore we need to pin down the requirements for the station and define the technology to be pursued.

The first requirement is that it be a permanent system, one that you put up and expect to use for a long time. Thus we want it to be able to grow in an evolutionary manner. New technology will come along or requirements will change from those set in the first years. It is essential that it can be relatively easily added to, or changed, to incorporate products of the new technology. You want operational flexibility, because you really do not know right at the beginning all of the things you are going to use it for. The structure should be as flexible as possible in its operation; it should be multiple-use.

Most of the purposes that the space station might be designed to serve require high power across the board. No concept of a space station that I have seen involves other than relatively high power, in the 50- to 75-kW range. That in itself leads to a consideration of higher voltages than we have been accustomed to using in space. The thermal loads will be large because of the high power, and they will vary over an extremely wide margin. With a human presence, and the intention of using the station for many years, we will most likely want to go to closed loop. Extravehicular activity is going to be very important; we are finding this to be more and more true as time goes on.

All automated operations, the data system and the communication system, must be very flexible and adaptive. We will probably want distributed control throughout the station so that we do not get locked into just one way of doing things. Propulsion and fluid management, particularly cryogenic fluid management, will be important drivers in the space station design.

At OAST, the Aeronautics and Space Technology Program has always had what we choose to call a generic technology program. It is sort of a "technology push" program where you do things because the state of the technology indicates that you are able to make certain advances. That program has existed in OAST and is still there. They have identified a certain part of that program that is contributory to the kinds of things that a space station might need. Beyond that, the next step is to define, from the generic program, a focused technology program that would be very specifically oriented toward advancing technology for space station requirements.

I have emphasized in the Steering Committee that the program should have as its output things that can specifically benefit a space station program in its Phase B as well as its Phase C and D activities. That technology is not just hardware. It can be analysis and simulation; it can be results of laboratory tests, results of activity in test beds, and even experimental flight test programs.

The technology flows from this focused program into a number of areas, and the products that come out, again, are not just hardware. In fact hardware is probably the least important thing that comes out of the technology program. Those things that people and organizations are going to need to do this job are what is important. And they need to happen on a schedule that will fit into the overall plan. So we must move forward quickly.

Figure 3 is a flow chart of how technology might develop from the requirements of the space station through the focused program. There are other approaches. One way is to cut through disciplines and say that you will make progress in power, or in thermal, or on attitude control, etc. Another is to look at something like energy management, which is a combination of thermal and power and can affect nearly all of the other technological areas. This can even be extended to structural technology, and to the attitude control system, which becomes important with very large arrays.

We need to integrate all of these activities so that we pay attention to the most important parts of the technology involved (fig. 4). The structures people alone, for example, without understanding what the power people need, may not produce the technology that best coincides with what is needed in the power area. So one activity of the Steering Committee is to encourage this type of integration.

All of these ideas flow into a sort of "bus" of technology (fig. 5) that can then go into all areas of the development of the space station - including a very important area, the evolution of the station beyond its initial capability, or a flexibility over time. This is one of the problems in a technology program: you can never be exactly sure where the benefits are going to show up. We are trying to focus on the specific products needed for a space station.

Now, just a short discussion of a particular activity that might be of interest to this group. OAST is planning flight research as well as their traditional ground-based research. One element of that is a voltage operating limit test, the VOLT Program, for space testing of photovoltaic concepts. A number of people here know more about this than I do, but I would like to mention it in the context of this conference.

The idea at OAST is to use the shuttle to conduct research in the space environment in a number of areas. In the VOLT series (fig. 6) there will be four in-flight experiments beginning in 1985, two inside the bay and two outside the bay; two are planar arrays and two are concentrator arrays. VOLT-1 and VOLT-3 use applied bias voltages; VOLT-2 and VOLT-4 use self-generated voltages. So the entire structure has some symmetry to it. These experiments are needed to obtain data from high-voltage planar and concentrator arrays, the idea being to produce design guidelines for large high-voltage arrays in low Earth orbit, data on the limits on operating voltage, a validated analytical tool for the final designers of the space station array, and a design evaluation for these array technologies.

Figure 7 illustrates the technology flow for the specific case of high-voltage array design. Out of generic technology and the focused program come design data for the creation of the flight experiment. Out of the flight experiment come data that benefit the space station, and it feeds back from the space station into the requirements area. One of the beauties of the space shuttle is that as we learn, we can repeat what we have done before and improve on it. This is just one example of how a technology program can flow into flight testing and eventually result in very specific products that improve other programs, in particular the space station program.

I thank you for your attention. Again, thank you for inviting me here.
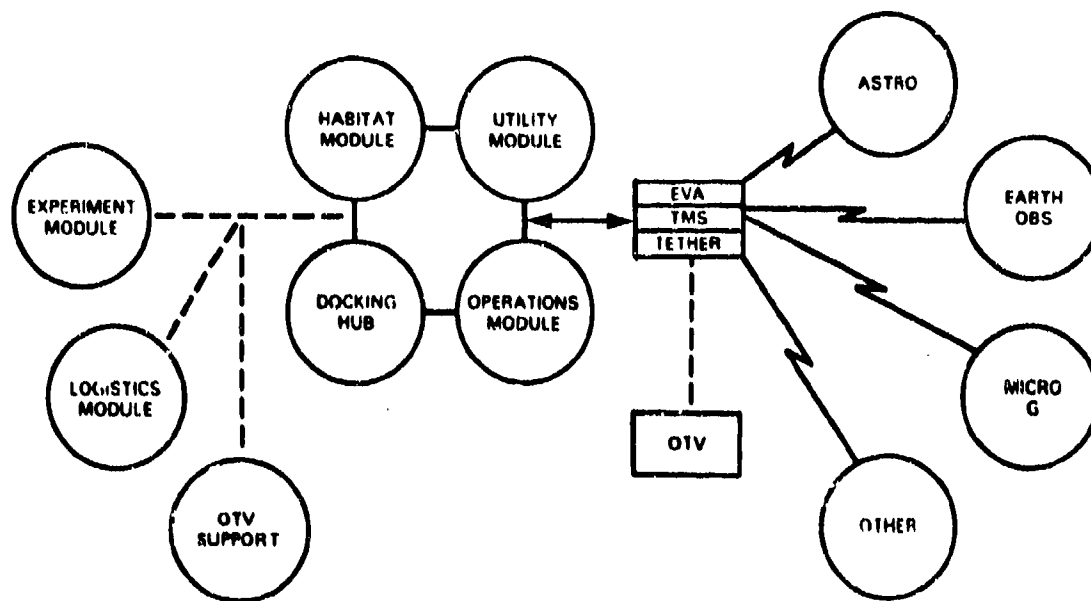
Figure 1. – Space station architecture: a cluster concept.
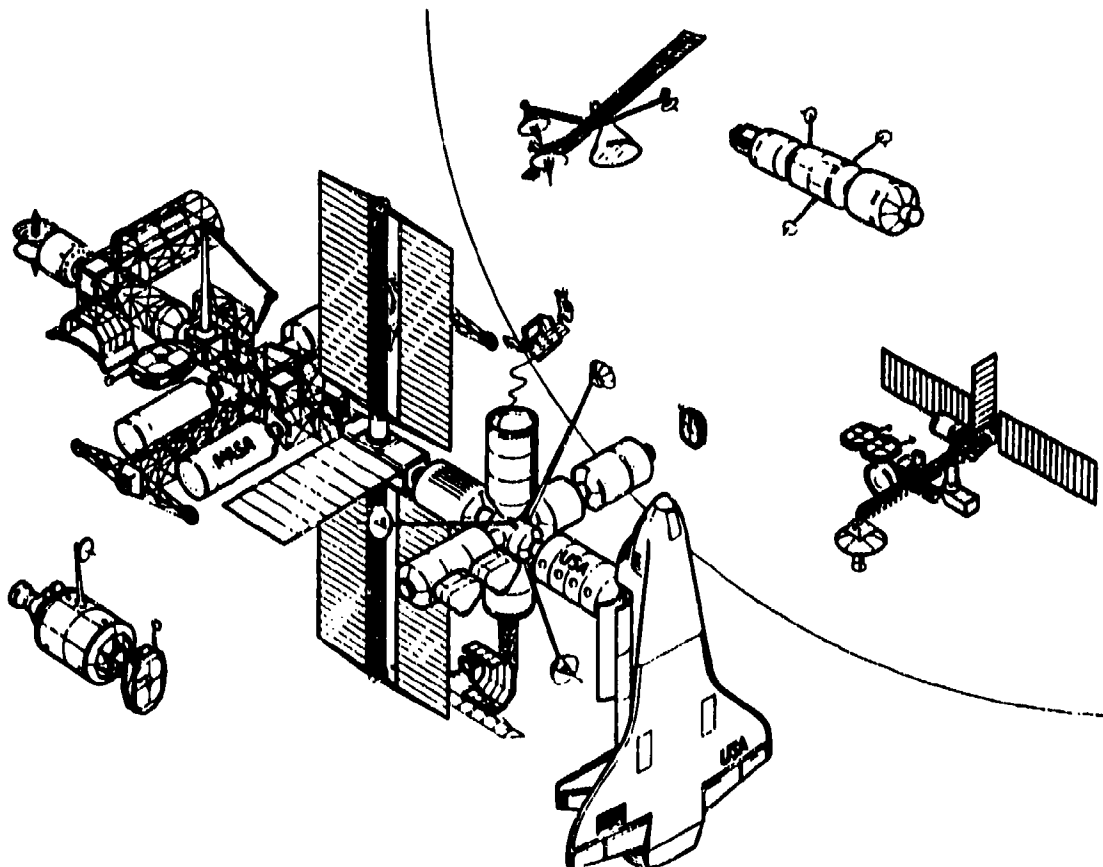
Figure 2. – Artist's concept of a space station.

5
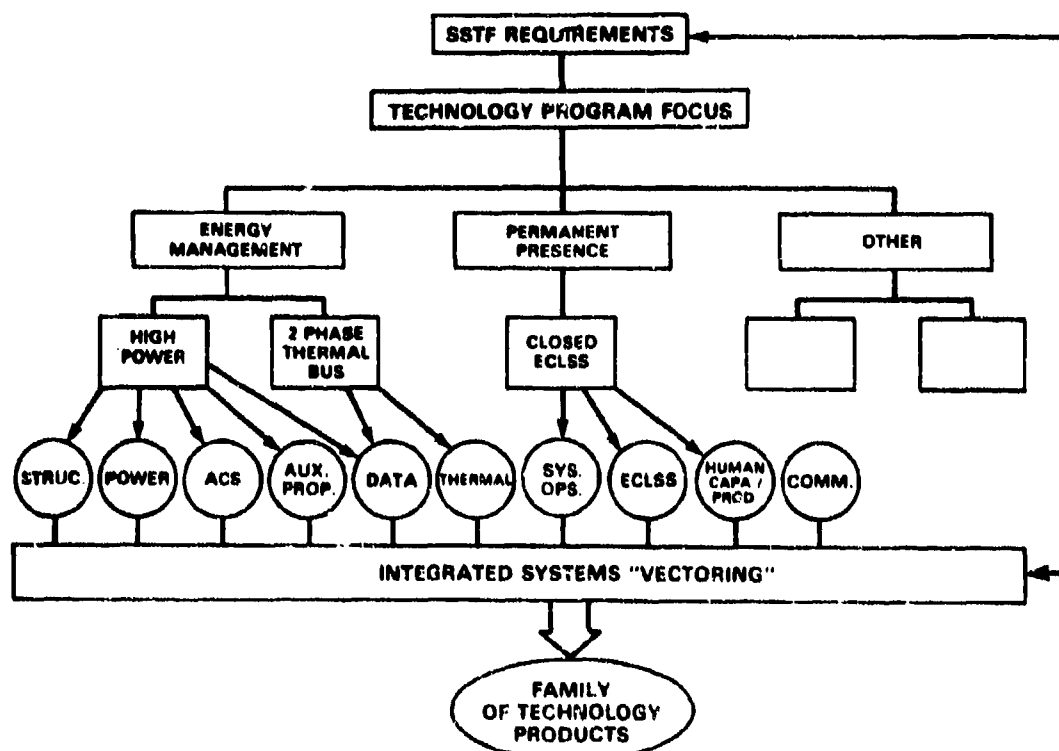
Figure 3. – Integrated activity.
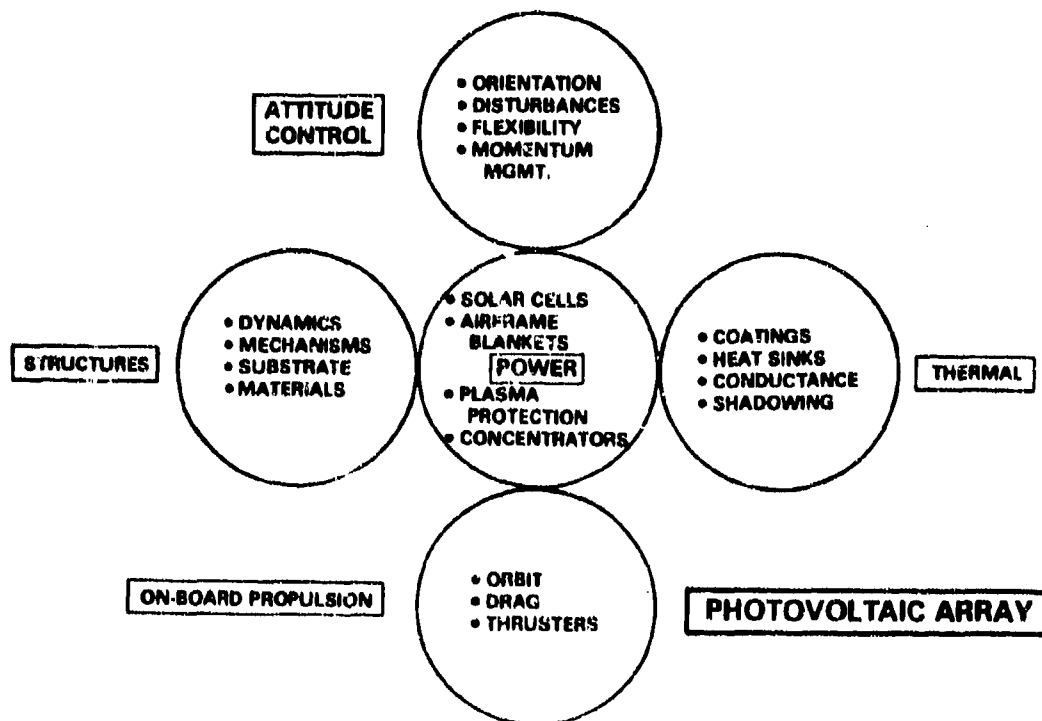
Figure 4. – Subsystem focus to integrate disciplines.
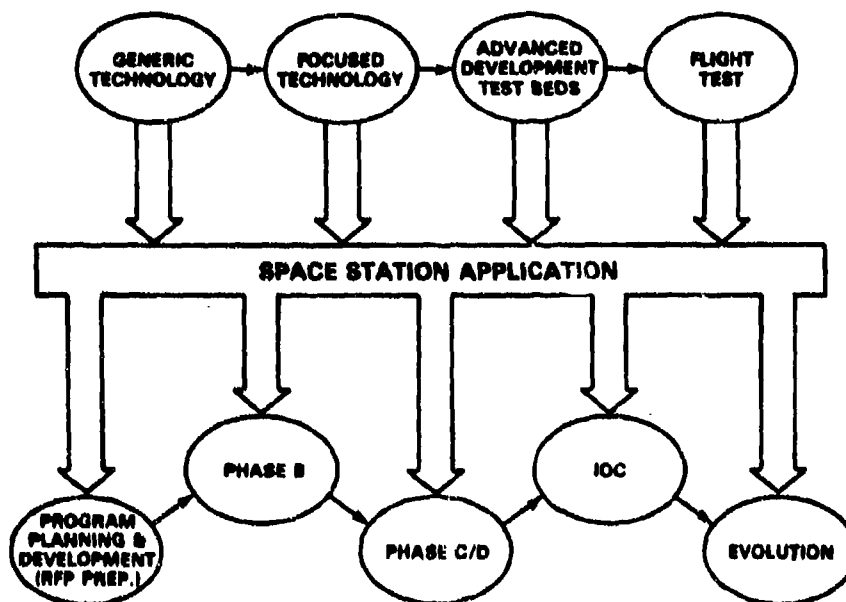
Figure 5. – Technology transfer.

VOLT-1: 1985

• BIASED PLANAR
  ARRAY SEGMENTS
  (± 1000 VOLTS)

VOLT-2: 1987
(EARLY)

• PLANAR ARRAY

• SELF-GENERATED
  VOLTAGES TO
  ~ 500 VOLTS

VOLT-3: 1986

• BIASED
  CONCENTRATOR
  ARRAY SEGMENTS
  (± 1000 VOLTS)

VOLT-4: 1987
(LATE)

• CONCENTRATOR
  ARRAY

• SELF-GENERATED
  HIGHER
  VOLTAGES
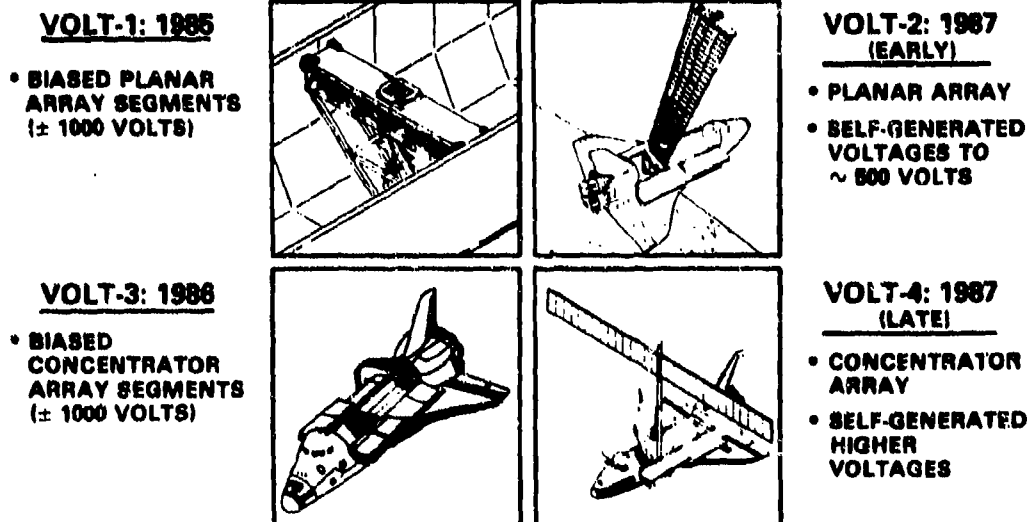
Figure 6. – Voltage operating limit tests.

7
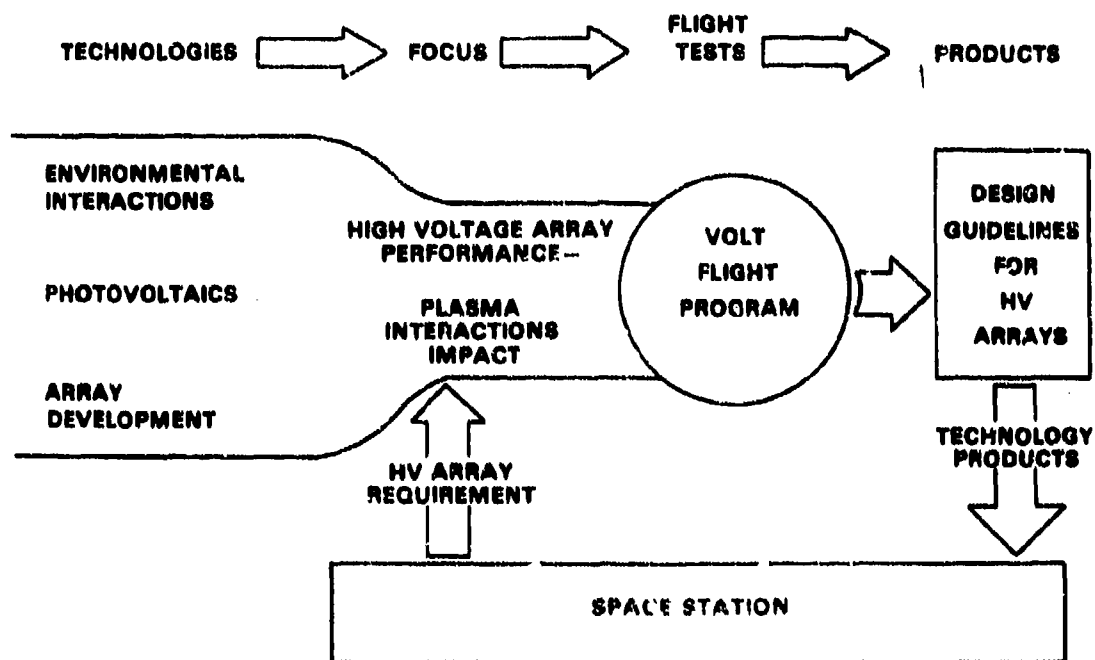
Figure 7. - High-power, high-voltage photovoltaic array for space station.

MILITARY SPACE SYSTEMS' TECHNOLOGY PLAN

Col. B.W. Bolton
Air Force Space Technology Center
Kirtland Air Force Base, New Mexico 87117

I would like to thank the sponsors of this conference for the opportunity to talk to you about the Space Technology Center and the Military Space Systems' technology model and plan. I will speak briefly about where the Space Technology Center fits into the Air Force space business structure and then run quickly through the model to show you how it works.

The Space Technology Center is a relatively new organization, having been in existence just a little more than a year. The Center is a continuation of an Air Force process that brings the Air Force laboratories under the control of specific product divisions. In our case, we are working for Space Division in Los Angeles. Our Commander, Bob Francis, works directly for General McCartney, the Commander of the Space Division, and the Technology Center has a detachment in Los Angeles. We have a Plans Directorate; we have a Technology Directorate that pursues several technology demonstration programs; and our Management Services people keep us all on track.

The Space Technology Center now has control and responsibility for the Geophysics Laboratory, the Weapons Laboratory, and the Rocket Propulsion Laboratory. The Center's mission is to give focus to space technology efforts, to ensure that technology needs are integrated with development efforts, and to plan and execute the non-space-related technology activities of these three laboratories as well. We assess the laboratories in their nonspace activities. We also function as the Space Division Commander's source of technical excellence in the space technology area.

The Plans Directorate is divided into two divisions: Plans and Analysis, the people primarily responsible for the development and evolution of the methodology used in our technology planning, and Development and Applications, a group of technologists who generate technology initiatives. These initiatives are new starts, new technology programs to fill gaps in the technology required to complete specific space missions.

The problem that we face is one that everyone should be familiar with, and that is the extremely long lead time for the development of specific space capabilities. The only consolation is that the Soviets face about the same type of lead time in developing their systems. Small consolation, perhaps, but it still highlights the need for accurate forecasting of technologies. We must ensure that the technology base is available when needed for the development of these specific space systems.

The objective of the technology model is to provide us with a systematic process for joining future technology needs to mission requirements. We stress continuity between space missions and the technology programs we pursue. The

model also acts as a vehicle for communications between the Air Force laboratories and major air commands, operational commands, other government agencies, and NASA. It is also a guide to industry for IR&D. The Technology Center, along with the AIAA, sponsors workshops in which a series of technology panels address all of the technology categories contained within the model. We have recently acquired a NASA field office within the Technology Center; that is staffed by Mr. Wayne Hudson.

We take our guidance from Air Force Headquarters, Space Division, Space Command, and all of the other operational commands that generate requirements and needs for space systems support. Our technical interfaces are with the Space Division program offices, the Air Force laboratories, other DOD agencies, NASA, and industry. All of this goes into the technology model as input, and the output is continually fed back as technology for these systems as we produce our Space Technology Plan. This plan is our technology investment strategy and supports the planning, programming, and budgeting process.

The technology model is divided into six volumes. The first volume is generated primarily by the Plans Office at Space Division. Their input comes from Space Command and the other operational commands. This planning group develops the basic mission requirements, projects needs, and gives priority to missions. From the material they give us, we form a set of preliminary concepts. Since we are talking about operational dates around the turn of the century in many cases, we have to have "strawman" concepts from which we extract technology requirements. These concepts are in volume 2. In volume 3 we project trends in technology so that we might properly assess the technologies of the future. Then in volume 4 we assess and study state-of-the-art technology, the programs that are in force now. In volume 5 we develop a roadmap of how a technology program would continue to develop the technology base required for the specific concepts and missions considered and defined in volumes 1 and 2. Volume 6 will set priorities and present a realistic plan for the development of technologies necessary to support primary space missions as defined in volume 2. These will be our technology investment recommendations.

This analytical product, our prioritized list of technologies, will not be an absolute guide in itself. It will simply be a planning tool for the senior headquarters staff to determine where best to invest their technology dollars. Most likely, other outside considerations will be included, but we feel that the plan is going to be a good starting point and a good yardstick by which to make intelligent decisions.

The technology plan aims to provide in a single document a systematic, logically derived way of investing technology resources. We will look at long-term requirements through our projection of system requirements for turn-of-the-century initial operating capability (IOC) dates for systems. It will provide the rationale and guidance for supporting these programs, thus making the budget process more systematic. The model can be used to support specific requirements for specific technology programs. With the model we also maintain concurrence and synchronization with the Air Force and Systems Command space plans, the Air Force Space Systems' architecture study, and other top-level guidance documentation of that nature.

The technology plan takes the input and runs it through a prioritization process. Then, using a resource review program, we identify the priority technology programs. The plan will tell us something about the availability of the technology base to support certain space missions.

The prioritization methodology is a combination of subjective inputs, a modified Delphi process, some computer modeling, and some analytical work on the different parameters. The plan input is the group of top-level mission requirements that come from Air Force Headquarters guidance. First we develop a set of prioritized missions. We attach importance levels to specific missions and rank them. Then we develop a set of mission requirements that support those particular prioritized missions. These are also computerized; then we sum the priorities of the missions that each of the requirements supports and work them down one more level to the concepts. At this point, we construct these concepts in order to determine what technologies are required to support these specific requirements.

Concepts then go through a review that identifies the mission requirements that each concept supports. At the last level of the plan, which is the technology level, we identify the priorities of the concepts supported by these technology programs to maintain a logical flow throughout this entire scheme, which ultimately links technologies to specific missions. Technologies that support more than one concept, or more than one mission, get appropriate emphasis in the prioritization process.

A major advantage of the model is its ability to incorporate policy changes. If there are changes in the mission rankings, for instance if the space station were to be adopted by the military as a firm requirement, we could alter the mission requirements up front. Another problem we are concerned about is ballistic missile defense. We do not know where to fit that in the model right now because major decisions are yet to be made on the process. But the model process, the model itself, can accommodate these types of change.

Technology breakthroughs are accounted for with the model. We can find potential problem areas in this same process; we can isolate concepts that are affected by technology problems and identify changes in performance and changes in the availability dates of these systems.

The schedule we are working against, the end product, is the publication of volume 6. Earlier volumes are being restudied and a third edition containing new mission requirements is in the process. This project is being developed by Air Staff, Space Command, and Space Division planning staff through the Space Systems architecture study. Volumes 3 and 4 are being updated with support from the laboratories and the AIAA panels. And we are working on the methodology of volume 6.

To conclude, we at the Space Technology Center believe that the model is a very orderly, systematic way of joining technology needs to specific space missions. It supports top-level guidance, the space plan from Air Force and Systems Command. And it is an effective tool for communicating with the Air Staff program element monitors, with the laboratories, and with industry. Volume 6 will be the Air Force Space Technology Center Space Technology Plan. It will be a guide for determining how we invest our technology dollars, and it will give the rationale for supporting programs in the program objective memorandum (POM) process.

SUPRATHERMAL PLASMA OBSERVED ON STS-3 MISSION BY PLASMA DIAGNOSTICS PACKAGE*

W. Paterson, L. A. Frank, H. Owens,
J. S. Pickett, and G. B. Murphy
University of Iowa
Iowa City, Iowa 52242

S. D. Shawhan
NASA Headquarters
Washington, D.C. 20546

Artificially produced electron beams have been used extensively during the past decade as a means of probing the magnetosphere (ref. 1), and more recently as a means of actively controlling spacecraft potential (ref. 2). Experimentation in these areas has proven valuable, yet at times confusing, due to the interaction of the electron beam with the ambient plasma. The OSS-1/STS-3 Mission in March 1982 provided a unique opportunity to study beam-plasma interactions at an altitude of 240 km. On board for this mission was a Fast Pulse Electron Generator (FPEG), which served as part of Utah State University's Vehicle Charging and Potential experiment. Measurements made by the Plasma Diagnostics Package (PDP) while extended on the Orbiter RMS show modifications of the ion and electron energy distributions during electron beam injection.

In this paper, some of the observations made by charged particle detectors are discussed and related to measurements of Orbiter potential. The paper is divided into three sections. A brief description of several of the PDP instruments appears first, followed by a section describing the joint PDP/FPEG experiment. The third section consists of observations made during electron beam injection.

INSTRUMENTATION

The PDP carries a wide range of instruments for the measurement of pressure, waves, fields, and particles. A discussion of these instruments and some of the preliminary results of the mission can be found in Shawhan et al. (ref. 3). Of interest for this discussion are the charged particle detectors, and to a lesser extent, instruments used to measure electric potential and the geomagnetic field in the vicinity of the Orbiter.

The Low Energy Proton and Electron Differential Energy Analyzer (LEPEDEA) is a curved plate detector capable of detecting ions and electrons with energies between 2 eV and 36 keV. It is nearly identical to instruments flown on ISEE-1 and ISEE-2. The energy resolution of LEPEDEA is $\Delta E/E = 0.16$, and 1.6 sec. is required for a complete energy scan. The LEPEDEA fields of view are shown in figure 1. The seven detectors are sampled simultaneously and together have a field of view of 6 degrees by 162 degrees.

An electron fluxmeter is also included in the PDP for detection of electrons. This instrument samples the electron flux independent of energy ten times per second. The fluxmeter is directed opposite to the LEPEDEA. It has a wide field of view with low angular resolution.

Electric fields were measured by two 20 cm spherical probes separated by 1.6m. The average potential between these spheres was measured relative to Orbiter ground with a range of ±8.2v. When the PDP was extended on the RMS, this potential was a measure of the plasma potential in the vicinity of the PDP.

A triaxial fluxgate magnetometer was used to measure magnetic fields. The magnetometer sampled the magnetic field 10 times each second, along each of its 3 axes with a resolution of ±12 mgauss.

THE JOINT PDP/FPEG EXPERIMENT

Joint operations between the PDP and the FPEG were conducted while the Orbiter was in a nose-to-sun attitude with a roll rate of twice per orbit (see figure 2). For the experiment discussed in this paper, the FPEG emitted a 50-mA, 1-keV, unmodulated electron beam. A total of eleven emissions occurred under both daytime and nighttime conditions and at various injection pitch angles with each emission approximately fifteen minutes in duration. During these injections, the PDP was deployed on the Orbiter RMS and moved about the Orbiter in an effort to locate the beam.

The primary instrument for location of the beam was an electron fluxmeter located on the opposite side of the PDP from the LEPEDEA. During the search for the beam, the fluxmeter was pointed downward toward the FPEG aperture in the Orbiter bay which left the LEPEDEA looking away from the electron beam. Because of this orientation, the LEPEDEA did not detect primary beam electrons. At times, however, the PDP was rotated through 90 degrees about its spin axis (see figure 1) which allowed the LEPEDEA to view a range of particle pitch angles including primary particles.

OBSERVATIONS

Because of changing Orbiter attitude (twice per orbit roll rate) and variations in the geomagnetic field over the course of an orbit, a wide range of injection pitch angles were observed. Calculations by J. Sojka of Utah State University show that for injection pitch angles greater than about 60 degrees (depending on the precise beam-orbiter orientation), the beam intercepted the Orbiter surface. At angles less than this the beam escaped. Qualitative analysis of charged particle and potential measurements made by the PDP support this analysis.

Ambient electrons (photoelectrons) were detected with energies up to about 80 eV during the day and 10 eV at night, while ions were seen at energies principally below 10 eV during both day and night. During beam injection at angles less than 30 degrees, intense fluxes of electrons were detected at energies up to the primary beam energy of 1 keV. Virtually no ions were seen at these times. Enhanced electron fluxes were observed at all points accessible to the PDP. However, due to the limited reach of the RMS, no measurements were made at distances greater

than 7m from the beam. For beam injection, at angles greater than 60 degrees, the measured ion and electron fluxes often resembled the flux seen with the beam off.

Measurements of Orbiter potential during small angle injection also differed from the ambient case. When the beam was off, the Orbiter potential relative to the nearby plasma remained $< \pm 8.2v$ consistent with $V \times B \cdot L$ (ref. 3). When the beam was injected at less than 30 degrees, the potential was offscale and positive, and dropped below the maximum measurable value of 8.2v only at the maximum distance from the beam of 7m. Potentials during large angle injections were generally nearer to those measured with the beam off.

The observations tend to support the claim that the beam did escape from the near vicinity of the Orbiter for small angle injection, but did not at larger angles. The enhanced electron flux and elevated potential associated with small angle injection may be due to escape of the beam. If this is so, the large angle conditions which were so similar to ambient conditions could be due to the electron beam impacting the Orbiter rather than escaping. In this case, almost all of the beam current is collected so that the disturbance is localized and the Orbiter does not need to charge.

Figure 3 shows the measured flux during one of these rotations which took place at a distance of 7m from the center of the beam. Since this distance is roughly twice the gyroradius of a 1 keV electron travelling perpendicular to the magnetic field, these measurements must be of electrons outside of the primary beam. The angles shown in figure 3 are the pitch angles of electrons as they were detected by the LEPEDEA. Angles greater than 90 degrees correspond to electrons travelling down the field lines from the direction in which the beam was injected. Angles less than 90 degrees indicate electrons moving up the field in the same direction as the outgoing beam. Although pitch angles less than 30 degrees and greater than 140 degrees were not sampled, this figure seems to show a net return of electrons along the field lines from the direction in which the beam was injected indicating that more current returns from the upper hemisphere during upwards injection than from the lower.

Based on this preliminary analysis of measurements made during electron beam emission, it appears that the electron beam did escape from the Orbiter. These escapes induced positive Orbiter potentials, and were associated with enhanced fluxes of electrons. During escape of the beam, there is evidence that there was a net flow of electrons along the magnetic field from the direction in which the beam was injected.

REFERENCES

1. Winckler, J. R.: The Applications of Artificial Electron Beams to Magnetospheric Research. Rev. Geophys. Space Phys., 18, 659, 1980.

2. Pedersen, A.: Plasma Diagnostics by Electron Guns and Electric Field Probes on ISEE-1. Artificial Particle Beams in Space Plasma Studies, (B. Grandal, ed.), Plenum Press, New York.

3. Shawhan, S. D.; Murphy, G. B.; and Pickett, J. S.: Plasma Diagnostics Package Initial Assessment of the Shuttle Orbiter Plasma Environment. Accepted J. of Spacecraft and Rockets, 1983.
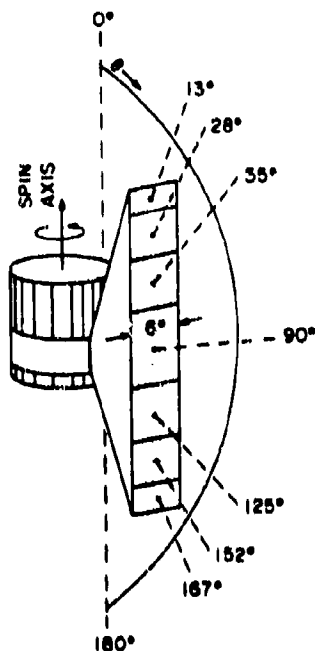
Figure 1. - LEPEDEA fields of view.
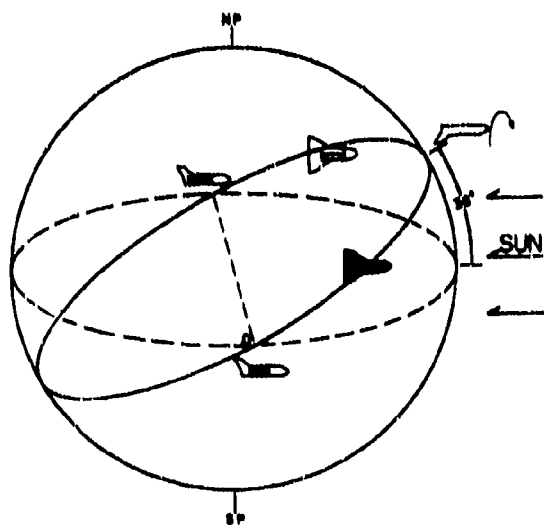
Figure 2. - STS-3 orbit attitude, March 24, 1982 - nose to Sun with twice per orbit roll rate.

16
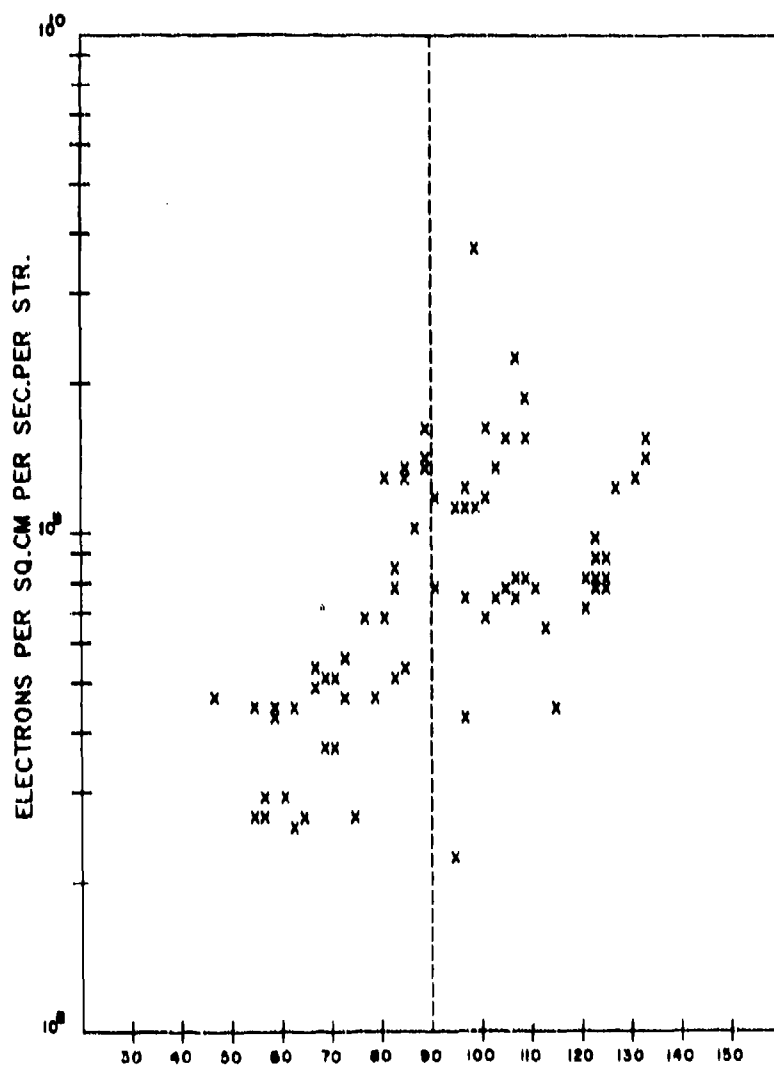
Figure 3. - Electron flux 7 m from beam (2 eV < E < 36 keV).

17

VEHICLE CHARGING ON STS-3 MISSION*

P. R. Williamson, P. M. Banks, and L. R. O. Storey
Stanford University
Stanford, California 95305

W. J. Raitt
Utah State University
Logan, Utah 84322

In the Vehicle Charging and Potential experiment on the STS-3 mission, a pulsed electron gun was used to eject known charges and currents from the Shuttle Orbiter, and the resulting perturbations of the surface charge and current densities were studied with appropriate instruments. An ejected current of 100 mA, if maintained for a time sufficiently long for equilibrium to be established, could change the vehicle potential by 50 V or more when the ambient plasma density was low. In general, the observed perturbations could be ordered qualitatively in terms of the plasma density and of the attitude of the shuttle relative to its orbital velocity vector.

1. INTRODUCTION

The Vehicle Charging and Potential (VCAP) experiment flown on the STS-3 mission was designed to study the electrical interaction of the shuttle orbiter with the low earth orbit environment. The interaction of a large, orbiting body with the low earth space environment is not well known. With the initiation of an operational era in space, it is necessary that we understand (1) the perturbations produced by the orbiter as it moves through the near earth environment, (2) the environment as provided to instrumentation operating in the payload bay of the orbiter and (3) the effects that the environment exerts upon the orbiter itself. Future missions which depend upon knowledge of the electrical interaction of the orbiter with the space environment include those with high power charged particle beam experiments and others with long antennas operating at high voltages in the VLF frequency range. Also, when operations begin with orbit inclinations above about 50 degrees, large fluxes of energetic electrons (and protons) will bombard the orbiter when the vehicle is at high magnetic latitudes. In the past, satellites have

been adversely affected by electrical discharges induced by energetic particle bombardment and these problems present similar concerns for the dielectric-covered orbiter. The VCAP experiment on STS-3 was designed to study the interactions between the orbiter and the environment which are of importance to understanding these problems.

2. INSTRUMENTATION

An electron gun with fast pulse capability was used in the VCAP experiment to actively perturb the vehicle potential in order to study dielectric charging, return current mechanisms and the techniques required to manage the electrical charging of the orbiter. Return currents and charging of the dielectrics were measured during electron beam emission, and plasma characteristics in the payload bay were determined in the absence of electron beam emission.

The VCAP instrumentation as flown on the OSS-1 pallet during STS-3 includes five separate pieces of hardware:

1. Fast Pulse Electron Generator (FPEG) - The FPEG consists of two independent electron guns which are of the diode configuration with a directly heated tungsten filament and a tantalum anode. The two guns, designated as FPEG 1 and FPEG 2, emit electrons with an energy of 1000 eV at currents of 100 mA and 50 mA respectively. The electron beams are collimated to a beam width of about 5 degrees by focus coils mounted just beyond the anodes. Each gun is controlled by a 37-bit serial command word which selects the gun to be used, controls filament and high voltage power supplies, and determines the on time, off time and number of pulses of the beam. The times are controllable in 32 logarithmic steps from 600 nanoseconds to 107 seconds and the number of pulses is controllable in powers of two from 1 to 32,768. The rise and fall times for the electron beam are 100 nanoseconds so that very short pulses (and therefore small increments of charge) can be emitted.

2. Charge Current Probes (CCP1 and CCP2) - Each Charge Current Probe (CCP) consists of two adjacent sensors — one metallic and one dielectric — as shown in figure 1. The current flowing to the metallic sensor is used as an indication of the return current to exposed metal surfaces on the orbiter. The dielectric sensor provides a measurement of the charge accumulation on the dielectric-covered surfaces of the orbiter; the material used for the charge probe dielectric is from the same batch of Flexible Reusable Surface Insulation (FRSI) that was used on the Columbia (OV-102) and covers the payload bay doors and upper wing surfaces (fig. 2). Both of the CCP sensors respond rapidly to changes in the orbiter potential. Measurement rates were set at 50 samples per second but peak hold measurements of both current and charge were made which allowed spikes longer than 100 nanoseconds to be captured.
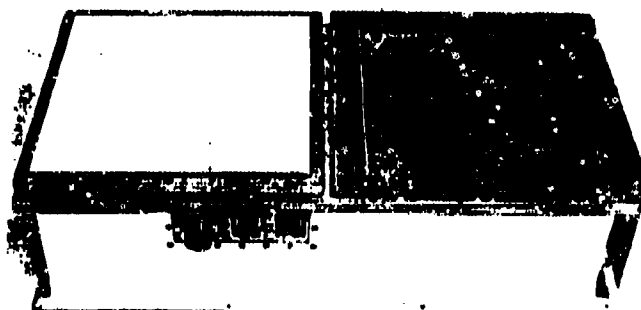
Figure 1. VCAP charge probe (left) and current probe (right). The experiment involved two such units, one on each side of the payload bay.
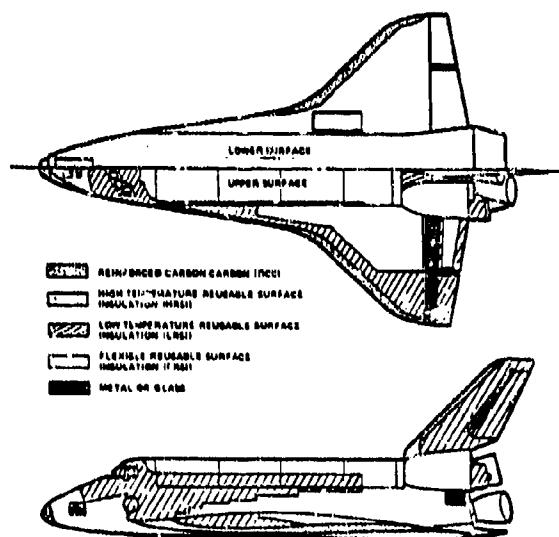
Insulation	Temperature limits	Area, m² (ft²)	Weight, kg (lb)
Flexible reusable surface insulation	Below 644 K (371° C or 700° F)	319 (3 436)	499 (1 029)
Low-temperature reusable surface insulation	644 to 922 K (371° to 649° C or 700° to 1200° F)	268 (2 881)	917 (2 022)
High-temperature reusable surface insulation	922 to 978 K (649° to 704° C or 1200° to 1300° F)	477 (5 134)	3826 (8 434)
Reinforced carbon-carbon	Above 1533 K (1260° C or 2300° F)	38 (409)	1371 (3 023)
Miscellaneous			632 (1 394)
Total		1102 (11 860)	7245 (15 972)

Figure 2. - Distribution of insulating material over the outer surface of the Orbiter.

21

ORBITER FRSI
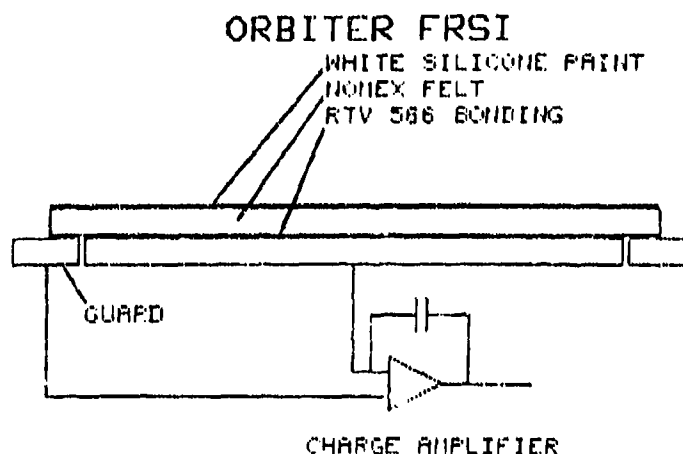
Figure 3. - Schematic of charge probe.

The Charge Probe measures directly the charging of a metal plate covered by a piece of FRSI. Since this is the same material as covers the payload bay doors and upper wing surfaces, we assume that measurements made on the FRSI in the payload bay are indicative of the behavior of this same material on the orbiter. The metal plate is connected to the input of a charge amplifier (fig. 3). When the vehicle potential changes, so does the charge induced on the metal plate: the charge increment is equal to the change in potential multiplied by the capacity between the plate and the ambient plasma. The charge amplifier converts this increment to a voltage. Assuming a theoretical value for the capacity, the change in vehicle potential can be calculated by scaling the output voltage appropriately. This is shown from the CCP measurement of vehicle potential. However two reservations should be made with regard to these data: firstly, the probe can only measure changes in the vehicle potential, and not its absolute value; secondly, the actual capacity of the probe depends on the state of the ambient plasma so it may depart significantly from the assumed value. Hence, although the charge increments are measured precisely, the inferred changes in vehicle potential are only approximate, and may differ for two Charge Probes mounted at different places on the same spacecraft.

On STS-3, two sets of the CCP (designated CCP1 and CCP2) were used with CCP1 mounted adjacent to the FPEG and CCP2 mounted on the opposite corner of the pallet as far away from the FPEG as possible. These probes provide measurements of vehicle potential changes and return currents induced by operation of the FPEG with high time resolution at voltages up to 1000 volts and currents up to 4 mA.

3. Spherical Retarding Potential Analyzer (SRPA) - The Spherical Retarding Potential Analyzer measures the density and energy of ions and provides an absolute value for the vehicle potential as well as a measurement of the plasma environment in the payload bay. The SRPA has a 19 cm diameter spherical collector surrounded

by a 20 cm diameter spherical grid. The biasing voltages applied to these electrodes result in the collection of positive ions by the collector. In the frame of reference of the orbiter the dominant ambient ion O^+ will have a drift energy of approximately 5 eV. This energy is related to the orbiter velocity, which is well known, so any deviation of the O^+ drift energy from the expected value gives a measure of the electrical potential of the orbiter structure relative to the ionosphere. A Langmuir probe is attached to the SRPA. This probe is a small, spherical probe which measures the density and temperature of electrons and provides a cross check on the vehicle potential. The SRPA/Langmuir probe instrument is mounted on a corner of the pallet as far from other surfaces as possible to give the best opportunity to acquire data uncontaminated by wake effects.

4. Digital Control Interface Unit (DCIU) - The Digital Control Interface Unit provided all signal, command and power interfaces between the VCAP instrument and the pallet. Power switching and command decoding were done in the DCIU. Three microprocessors (1802 type) were used in the DCIU. The control microprocessor stored sequences of time-tagged serial commands in both ROM and RAM. These sequences of commands could be initiated in response to a single command sent from a source external to the DCIU and perform a series of operations such as FPEG pulsing, gain changing and resets. A second microprocessor was used to control the offset of the SRPA sweep voltage. The third microprocessor was used to monitor temperatures, voltages and currents and to set out of limit flags passed as bi-level signals to the orbiter GPC for display and alarm signaling.

3. MEASUREMENTS

Passive and active operations were performed during OSS-1. The SRPA and CCP's were operating throughout the mission and data obtained when the electron gun was not being operated determine the characteristics of the orbiter and the payload bay environment in the absence of perturbations from active experiments.

The electromagnetic interference (emi) levels during the mission were the lowest experienced during the project and were unmeasurably low on orbit. The thrusters produced disturbances which were variable in character and magnitude. Strong ram/wake effects were seen in the ion densities in the payload bay. Measurements of the vehicle potential offset indicate that the main engine nozzles provide a reference potential to the ionospheric plasma surrounding the vehicle. Because the orbiter is 97% covered with dielectric materials, the main engine nozzles provide the primary contact between the orbiter metallic structure and the plasma. Vehicle potentials were variable with respect to the plasma and depended upon location on the vehicle relative to
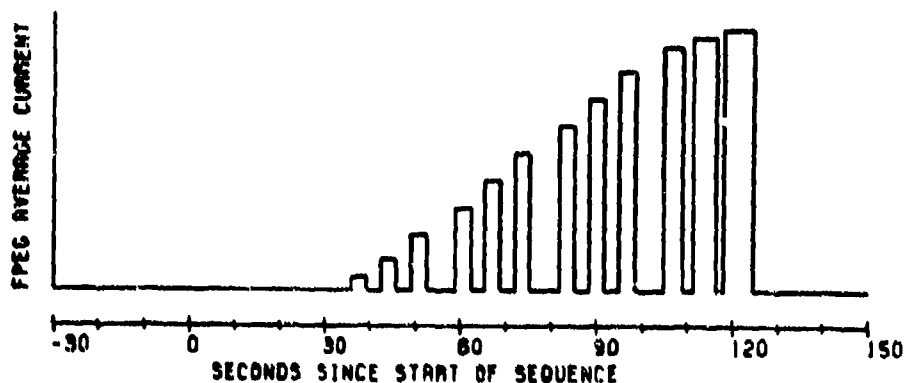
Figure 4. - Sequence of electron current pulses emitted by the Fast Pulse Electron Generator.

the main engine nozzles, the vehicle attitude and the direction of the geomagnetic field; their variations are consistent with the expected effects of the $V \times B$ electric field.

Active experiments were performed by emitting a series of electron beam pulses, as illustrated in figure 4 for instance. Inside each of the positive-going pulses shown in this figure there are 16 narrower rectangular pulses of 100 mA peak current, increasing in width from each group of 16 to the next. Thus the amplitude of the wider pulses, which is equal to the average of the current over the repetition period of the narrower pulses, increases throughout the sequence. The wider pulses are arranged in groups of three, and between each group and the next the Charge Probes are reset to zero so as to eliminate long-term drift.

Data taken during one such sequence, designed to study vehicle charging and return current mechanisms and labeled Charge Current (CC), are shown in figure 5; see table 1 for the meanings of the symbols. The sequence begins with one microsecond pulses (which show no measurable perturbation). When the pulse widths are increased to more than a millisecond in duration, significant charging of the orbiter occurs with induced potentials of tens of volts. The potentials measured close to the FPEG are higher than those on the far side of the pallet and may indicate that a sheath developed around the vehicle. The currents at the two locations (CCP1 and CCP2) are also different, with the larger current near the electron gun as might be expected since the beam produces locally enhanced ionization levels.

24

CHARGE CURRENT SEQUENCE
BEGINNING AT 84/1132:16

VCAP
OSS-1/STS-3
LAUNCH MARCH 22, 1982

SECONDS SINCE START OF SEQUENCE
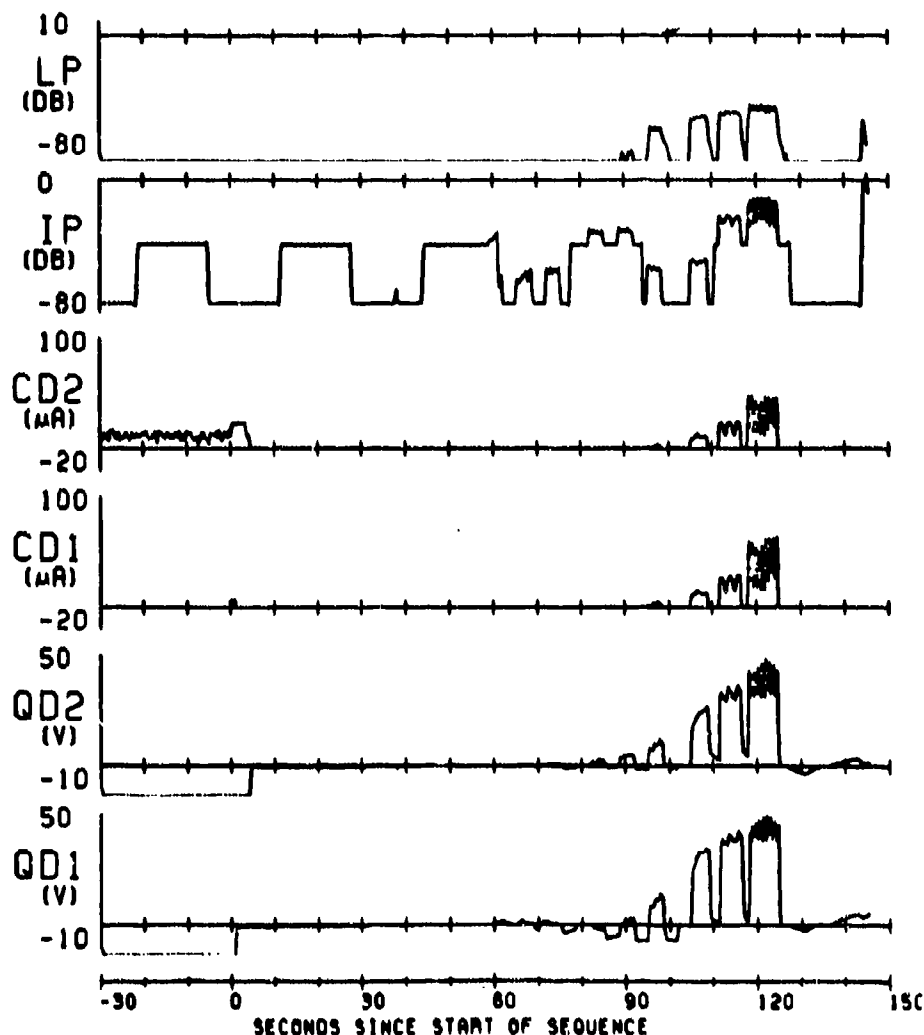
Figure 5. – Representative charge current sequence (1132 GMT on 25 March 1982). In data from SRPA (graph labeled IP), no ion current is observed until about 34 s after start of pulse sequence: rectangular waveform seen at earlier times is due to automatic sw. ching of electronics between two ranges with dif'erent sensitivities.

In a higher time resolution plot of a portion of the same CC sequence (not shown) it appears that the measured currents recover to their normal non-emission levels in the short time between pulses, but the charge on the dielectric is retained and decays much more slowly. Time constants for the vehicle potential (or dielectric charging) to return to non-emission levels vary from less than one second up to minutes. Thus, in the two lowermost graphs of fig. 5, more marked fluctuations appear on the later groups

25

of pulses than on the earlier groups; this difference is probably due to the reduction in the time constant as the vehicle potential increases.

One of the most distinctive features of the STS-3 flight results is the variety in the measurements of charging and return current. Virtually any combination of results can be found in the 52 Charge Current sequences that were performed during this mission. In some cases the charging is negligible, in other cases charging is significant and more than 50 volts for the same sequence. Return currents can be small or large and either the same on both probes or with either one large and the other negligible. In the following series of figures we show examples of this panoply of measurements.

Figure 6 shows some data taken during local daytime, with the nose of the shuttle pointing towards the sun and with the instruments looking into the wake. The latter circumstance explains the low charging currents and also the failure of the Langmuir probe to measure an electron current. The fact that the SRPA nevertheless measured a substantial ion current is unexplained. On this occasion, operation of the electron gun led to large positive excursions of the vehicle potential.

The data shown in figure 7 were also acquired in the daytime, with the shuttle in the same attitude relative to the sun but in a different attitude relative to the orbital velocity vector. The instruments, though still somewhat in the wake, were less well shielded from the plasma than on the occasion represented in figure 6. The attitude was such that the main engine nozzles were pointed more or less along the orbit, i.e., in the ram direction. Hence, the vehicle was in better electrical contact with the plasma, which explains why its potential was relatively unaffected by the gun operations.

In the data of figure 8, the electron and ion currents are comparable with those noted in figure 7. No attitude data are available for this case at the time of writing, but since the vehicle potential did not vary much, again there must have been good contact with the plasma. Even during the most intense FPEG emissions, neither of the current probes registers much current, which means that the return current must have been flowing elsewhere.

Figure 9, like figure 7, presents data acquired during the day with the shuttle in the nose-to-sun attitude and with the instruments partly in the wake. The electron and ion densities are greater this time, however. The changes in vehicle potential are even less than in the case of figure 8, but contrariwise the current probes both register large currents; their data are unusual in that the probe further from the FPEG collects the larger current.

The data of the final figure 10 show large electron and ion densitities, with the output from the ion probe even going off scale. The sizeable current on CD2 during the period

from -30 s to 0 s suggests that this current probe was then facing towards the ram direction; the drop in current at 0 s may be due to the probe having been taken out of this orientation by vehicle roll. The FPEG pulse sequence had almost no effect on any of the six instruments in the VCAP package.

Figures 6-10 have been presented in the order of increasing ambient plasma density, at least as indicated by the Langmuir probe and the SRPA. Qualitatively, increased density leads to greater stability of the vehicle potential, as one would expect.

Although, as mentioned earlier, the 52 recorded Charge Current sequences show a wide variety of behavior, this proves to be reproducible if the sequences are ordered in terms of two parameters, namely the plasma density and the attitude of the shuttle relative to its orbital velocity vector. For a given density and attitude, qualitatively similar behavior has been observed on different occasions. Other parameters, such as the attitude relative to the earth's magnetic field and the presence or absence of sunlight, are less influential but not neglible.

4. CONCLUSIONS

The VCAP experiment on STS-3 has shown that active, controlled experiments on shuttle charging can be successfully performed from the payload bay of the orbiter. Electron beams have been used to perform a series of experiments to study the electrical interaction of the orbiter with the surrounding environment and the environment provided to the payload. A preliminary analysis of the data has shown that, qualitatively, they are reproducible and understandable, which strengthens our confidence that it will be possible to model them quantitatively in the long run.

Table 1

In each of the figures 6-10, the following quantities are plotted as the ordinates of the six graphs (from top to bottom):

LP	Langmuir Probe. Current on a logarithmic scale.
IP	Ion Probe (Spherical Retarding Potential Analyzer). Current on a logarithmic scale.
CD2	Current Probe on the starboard side of the payload bay. Current (µA) on a linear scale. Increased current corresponds to increased electron collection.
CD1	Current Probe on the port side of the payload bay. Current (µA) on a linear scale.
QD2	Charge Probe on the starboard side. Voltage on a linear scale. Increased voltage corresponds to the vehicle becoming more positive with respect to the plasma.
QD1	Charge Probe on the port side. Voltage on a linear scale.

Note: The instruments on the port side of the payload are close to the Fast Pulse Electron Generator

27
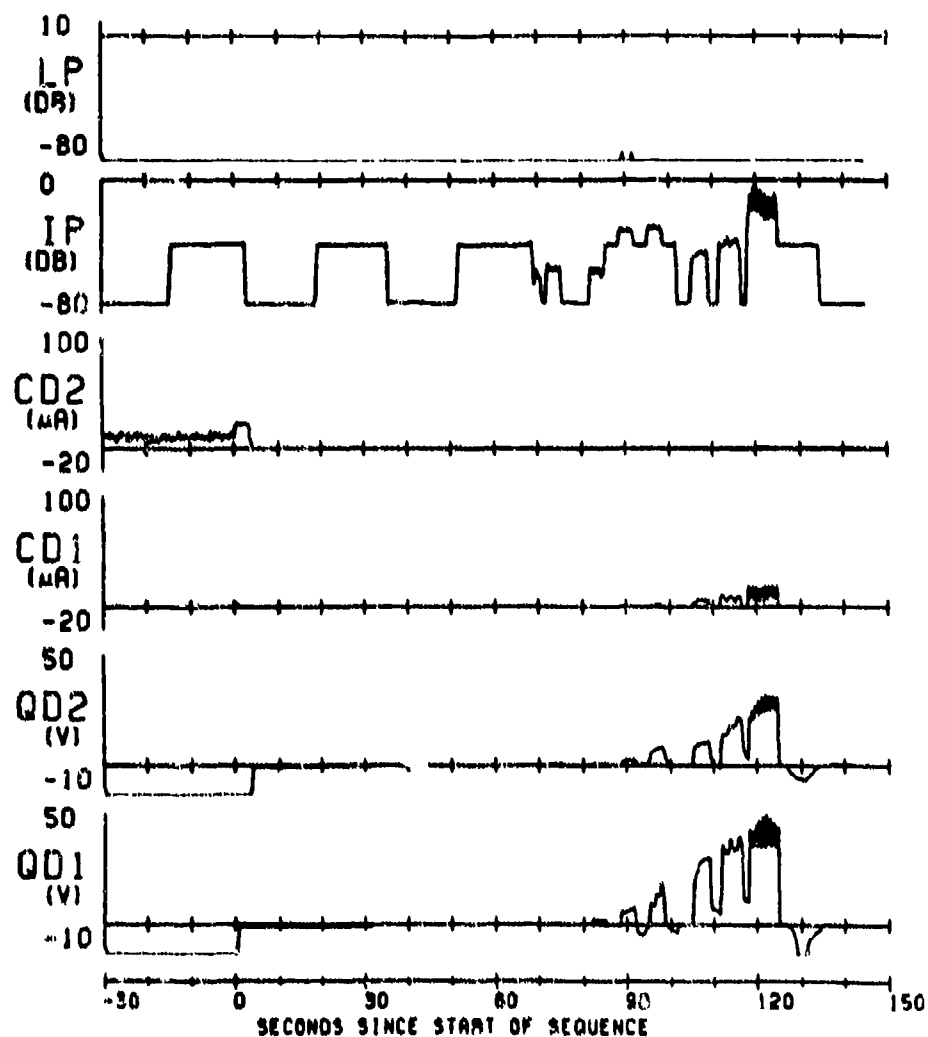
Figure 6. – Charge current sequence (0707 GMT on 26 March 1982).

28

VCAP
OSS-1/STS-3
LAUNCH MARCH 22, 1982
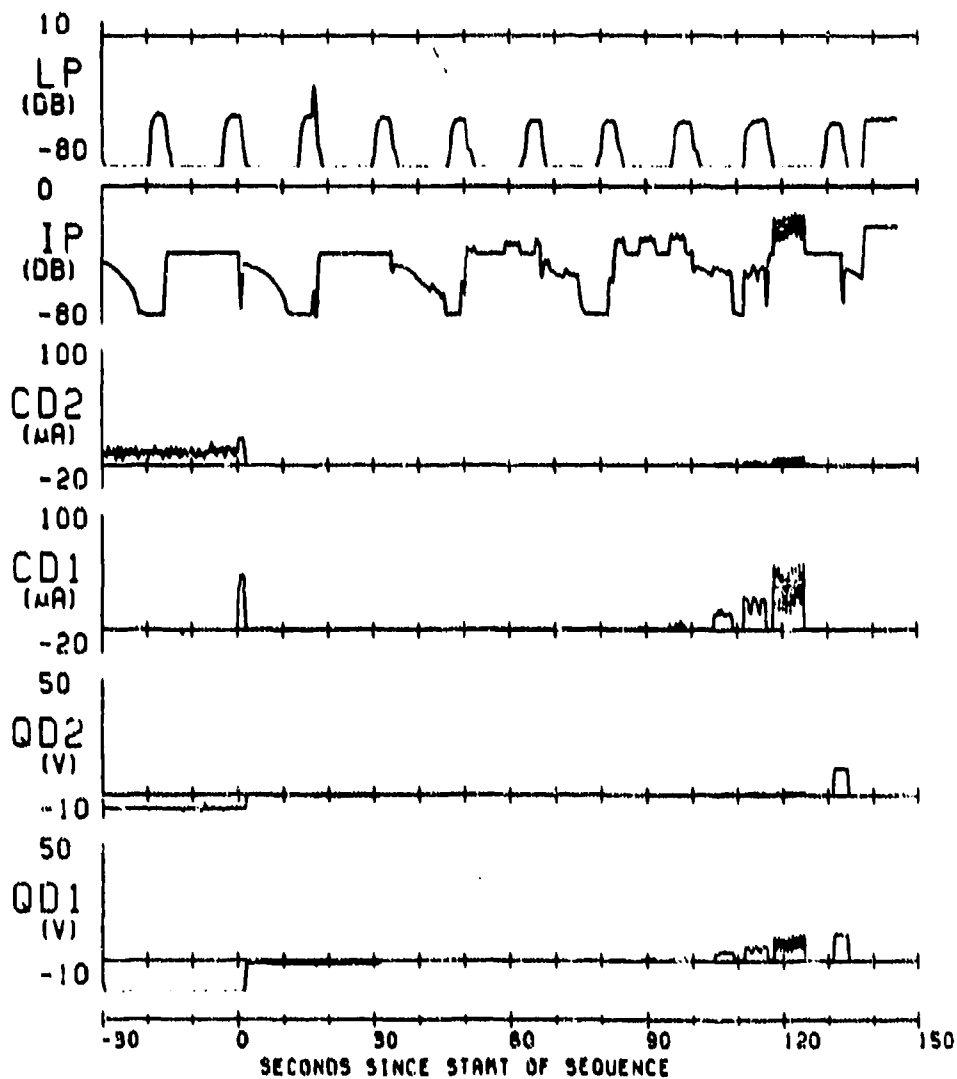
Figure 7. — Charge current sequence (0527 GMT on 25 March 1982).
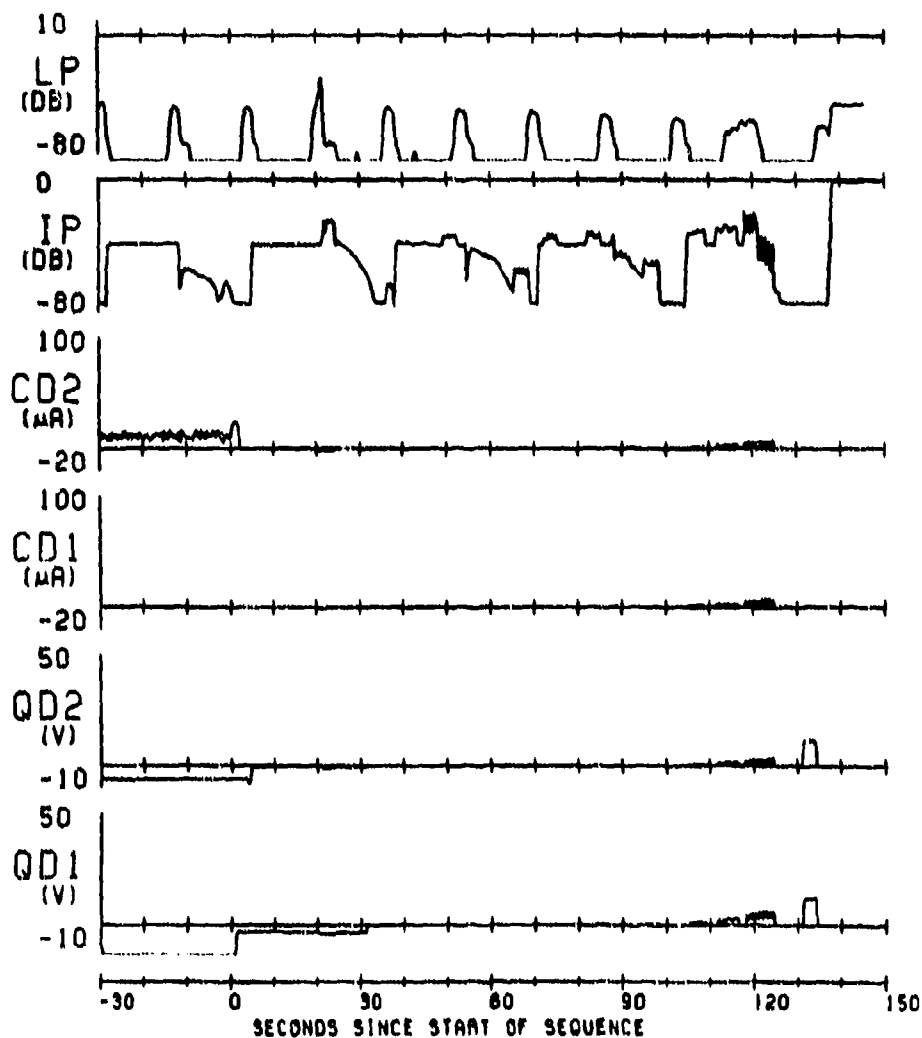
Figure 8. – Charge current sequence (0107 GMT on 26 March 1982).

30
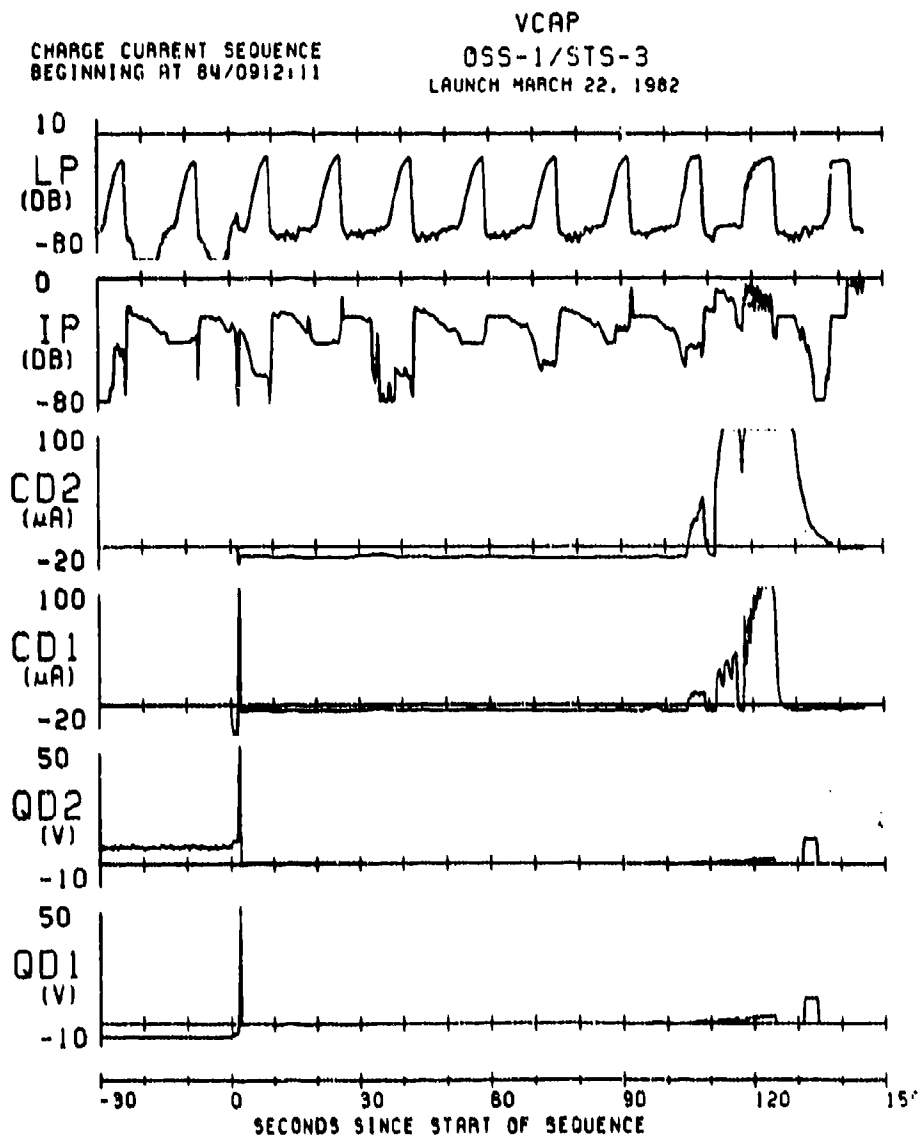
Figure 9. – Charge current sequence (0912 GMT on 25 March 1982).

31
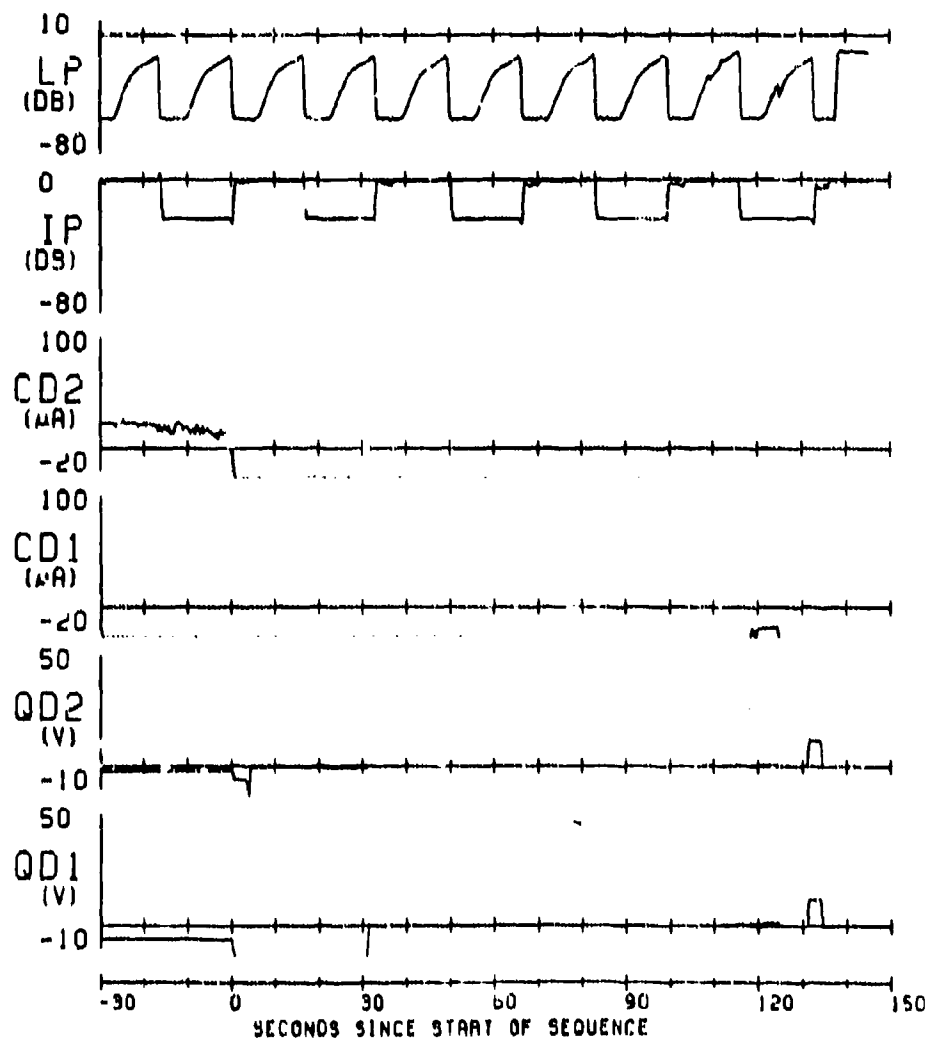
Figure 10. — Charge current sequence (0609 GMT on 27 March 1982).

ELECTRON AND ION DENSITY DEPLETIONS MEASURED IN THE STS-3 ORBITER WAKE*

G. B. Murphy and J. S. Pickett
University of Iowa
Iowa City, Iowa 52242

W. S. Raitt
Utah State University
Logan, Utah 84322

S. D. Shawhan
NASA Headquarters
Washington, D.C. 20546

The third Space Shuttle flight on Columbia carried instrumentation to measure thermal plasma density and temperature. Two separate investigations, the Plasma Diagnostics Package (PDP) and the Vehicle Charging and Potential Experiment (VCAP), carried a Langmuir Probe, and the VCAP also included a Spherical Retarding Potential Analyzer (SRPA). The Langmuir Probe on the PDP made measurements while the PDP was attached to the pallet in the Orbiter bay and while the PDP was articulated by the RMS. Only those measurements made while the PDP is in the payload bay are discussed here since the VCAP instrumentation remains in the payload bay at all times and the two measurements are compared.

Figure 1 illustrates the location of the PDP and VCAP instrumentation on the science payload pallet.

The principle thrust of this paper is to discuss the wake behind a large structure (in this case the Space Shuttle Orbiter) flying through the ionospheric plasma. Much theoretical work has been done regarding plasma wakes (ref. 1) and to a certain extent laboratory plasmas have provided an experimental and measurement basis set for this theory. The instrumentation on this mission gives the first data taken with a large vehicle in the ionospheric laboratory.

First, the PDP Langmuir Probe and its data set will be presented, then the VCAP Langmuir Probe and SRPA with associated data. A discussion of agreement between the two data sets is then followed by some other PDP data which infers an even lower wake density.

Lastly, conclusions, caveats and a description of future work which will further advance the measurement techniques and data set are put forth.

PDP LANGMUIR PROBE RESULTS

The PDP Langmuir Probe is a 6 cm diameter gold-plated sphere which is operated in two modes, the $\Delta N/N$ mode and the swept mode. The swept mode which is of concern
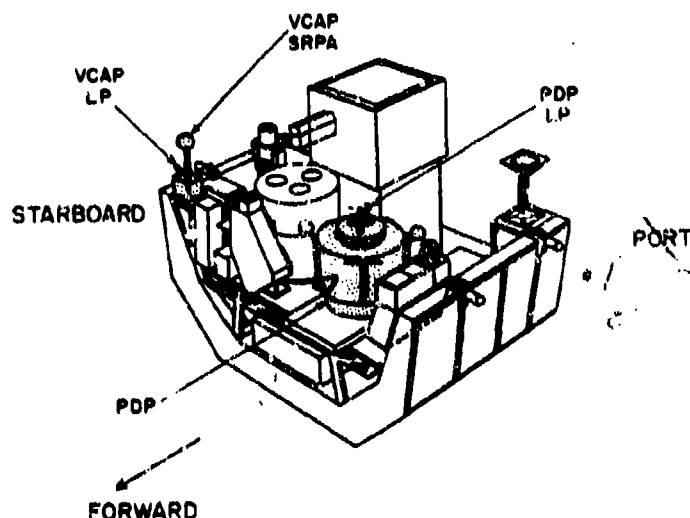
Figure 1. - Science pallet configuration on STS-3 showing location of instru-
mentation.

here is a 120 step voltage sweep which lasts 1.2 seconds and is executed 5 times
per minute. The nominal density range of the probe is approximately 5×10^2 to
$5 \times 10^6 /cm^3$, the precise sensitivity depending on temperature. Operating in this
mode, the Langmuir Probe has a current voltage characteristic whose slope is pro-
portional to $1/T_e$ and which has a "knee" in the curve proportional to N_e.

There are two limitations to the PDP Langmuir Probe measurements. The first
occurs when the plasma is too dense to really see the entire knee of the curve re-
sulting in instrument saturation and an underestimate of density. The second oc-
curs when the plasma temperature is too high and density too low to get a reliable
slope resulting in only an upper bound on density and lower bound on temperature.

Figure 2 illustrates the electron density and temperature for one orbit as a
function of vehicle attitude. (The data is repeated for a second orbit to provide
clarity for the graph and illustrate a periodicity which is real). The vehicle
attitude is described by θ_1 and θ_2 which are illustrated at the top of the figure.
Maximum wake occurs when the vehicle flies tail first with the plasma ramming into
the Orbiter belly (e.g. GMT 83:20:48). At this point in time, the vehicle is
flying a nose-to-sun attitude with a 2 times orbit roll. (See figure 2 in the pa-
per "Suprathermal Plasma Observed on the STS-3 Mission by the Plasma Diagnostics
Package, by Paterson et al. (ref. 2) in this issue for a description of this
attitude.) This results in a once per orbit ram/wake cycle which is evident in
figure 2 by the e^- density and neutral density (pressure) measurements.

Several important observations summarize figure 2:

1. Although density is near ambient while the paylaod bay is neither pointing
   directly into the velocity vector or into the wake, there is evidence that
   the density may be 2 to 10 times ambient when the bay points close to the
   velocity vector. The probe saturates making reliable measurement above
   2×10^6 difficult. The region cross hatched in figure 2 is where this
   higher density regime is encountered.

34

2. Density decreases rapidly as the Orbiter rolls into wake condition.

3. The minimum reliable measurement of density with the PDP probe is approximately 5×10^2 /cm^3. At least another order of magnitude decrease is required to pull the sweep totally offscale which is subsequently observed to happen. The sweep remains offscale for approximately 25 minutes centered around 83:20:48.

4. During all non-wake conditions, the temperature remains relatively constant at about 1000° (±30%).

5. Temperature rises rapidly as density decreases.

6. The highest reliable temperatures occur at 6000°K. However, the trend continues suggesting temperatures in excess of 7000°K in the deep wake.

It is also worthwhile to note that in near ram condition the neutral density (pressure) was almost two orders of magnitude above ambient ionospheric conditions and fell below 10^{-7} torr (the instrument sensitivity limit) during wake conditions.

THE VCAP LANGMUIR PROBE AND SRPA

Data on the characteristics of the ambient thermal plasma are extracted from the probes using a technique similar to that described by Raitt et al. (ref. 3). This AC technique employed for the probes enables direct measurement of the second derivative of the SRPA current-voltage characteristic and the first derivative of the LP current-voltage characteristic.

The SRPA signal is obtained by adding two sinusoidal AC signals (at 8.5 kHz and 10.7 kHz) to a sawtooth sweep voltage. The probe current is passed through a narrow band amplifier that selects the difference freqency of 2.2 kHz, which is a measure of the non-linearity of the probe current-voltage characteristic, and results in a signal proportional to the second derivative of the current-voltage characteristic. Two ac current ranges are available: one from -76 dB to -24 dB and the other from -40 dB to 0 dB relative to 10^{-7} amp rms. Each successive sweep of the probe alternates between the two ranges. Since the sweep period is 17 seconds the complete dynamic range is covered each 34 seconds.

The LP has only one AC signal (at 3.2 kHz) added to the sweep voltage. The amplitude of the alternating component of the probe current derived by using a narrow band amplifier tuned to 3.2 kHz enables the first derivative of the current voltage characteristic to be measured directly. A single dynamic current range, from -80 dB to +10 dB relative to 10^{-6} amp rms, is used for all sweeps. The range of the sawtooth voltage is from -2 V to +3 V, the period and phase of the sweep being synchronized to the SRPA sweep.

Figure 3 illustrates data taken under similar conditions as that taken by the PDP, although at a different time. In this case the vehicle attitude is different, but the same angles are used to characterize the direction of the velocity vector. The addition of the dark bar on this figure serves to show when day and night occur during the orbit.

35
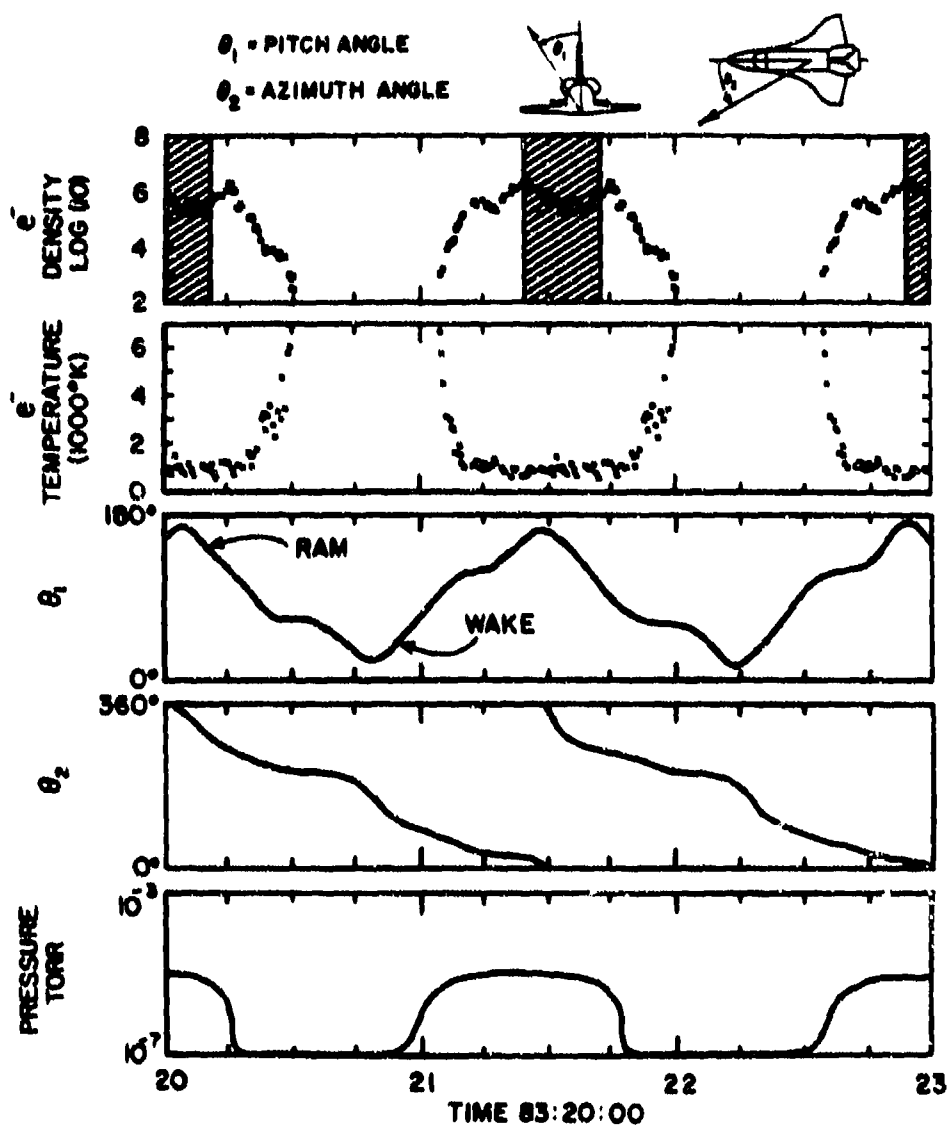
Figure 2. – Summary of PDP Langmuir probe electron density and temperature as function of vehicle attitude. Neutral pressure measurements are included for reference. Cross-hatched areas are where probe sweep saturates and routine used to calculate N_e underestimates density by as much as an order of magnitude.

The results of the Langmuir Probe (dotted line) and SRPA (solid line) generally confirm results of the PDP Langmuir Probe. VCAP Langmuir Probe temperatures are not plotted, but the following results are notable:

1. Close to ambient (1000°K) ionospheric temperatures are measured during non-wake condition.

2. As the Orbiter rolls into wake, a turbulence at all frequencies adds noise to the 3.2 kHz LP first derivative, but measurements indicate an increase in temperature to beyond 4000°K.

VCAP LP densities indicate the following:

1. An upper bound of electron density when the paylaod bay faces close to the velocity vector is $10^7/cm^3$.

2. Density during wake conditions drops to below the instrument sensitivity of 10^4 e/cm^3.

The SRPA measurements are difficult to interpret since the peak in the second derivative as a function of sweep voltage for the dominant ionospheric O^+ ion is often contaminated by locally produced H_2O^+ and NO^+. When the O^+ peak is clearly observable, several observations prevail:

1. Densities consistent with ambient ionospheric O^+ are observed for most conditions which shall be referred to as non-wake.

2. > 2 orders of magnitude depletion occurs in the near wake.

ADDITIONAL EVIDENCE FOR LARGE DEPLETION

Additional evidence for a many order of magnitude depletion in the electron density in the near wake is provided by what amounts to a sounder experiment. Recall that the VCAP SRPA is excited with a signal at 8.5 and 10.7 kHz. The PDP contains a 16 channel (±15% bandwidth) spectrum analyzer capable of detecting electrostatic or electromagnetic waves over a frequency range from 30 Hz to 178 kHz. The instrument has a saturation of approximately 1 V/m electric field amplitude and a usable dynamic range of about 95 dB.

During most of the orbit, the Spectrum Analyzer output is dominated by broadband orbiter generated electrostatic noise, (ref. 4) thruster firings or other events. Figure 4 illustrates that as the wake boundary is approached, the electrostatic noise disappears in all channels simultaneously and as the payload bay is immersed deeper in the orbiter's wake a signal in the 10 kHz channel grows to a point of dominance in the spectrum. This in fact is the VCAP SRPA signal. As the density drops so that the plasma frequency nears or drops below 10.7 kHz, this signal can propagate to the PDP sensor. Detailed calculations and modeling are being done taking field strengths and sensor separation into account, but preliminary work suggests that although the PDP Langmuir Probe infers densities, < $50/cm^3$, the density probably drops at least another order of magnitude to < $5/cm^3$. This would be approximately six orders of magnitude of plasma depletion in the near wake from that measured under ram condition.
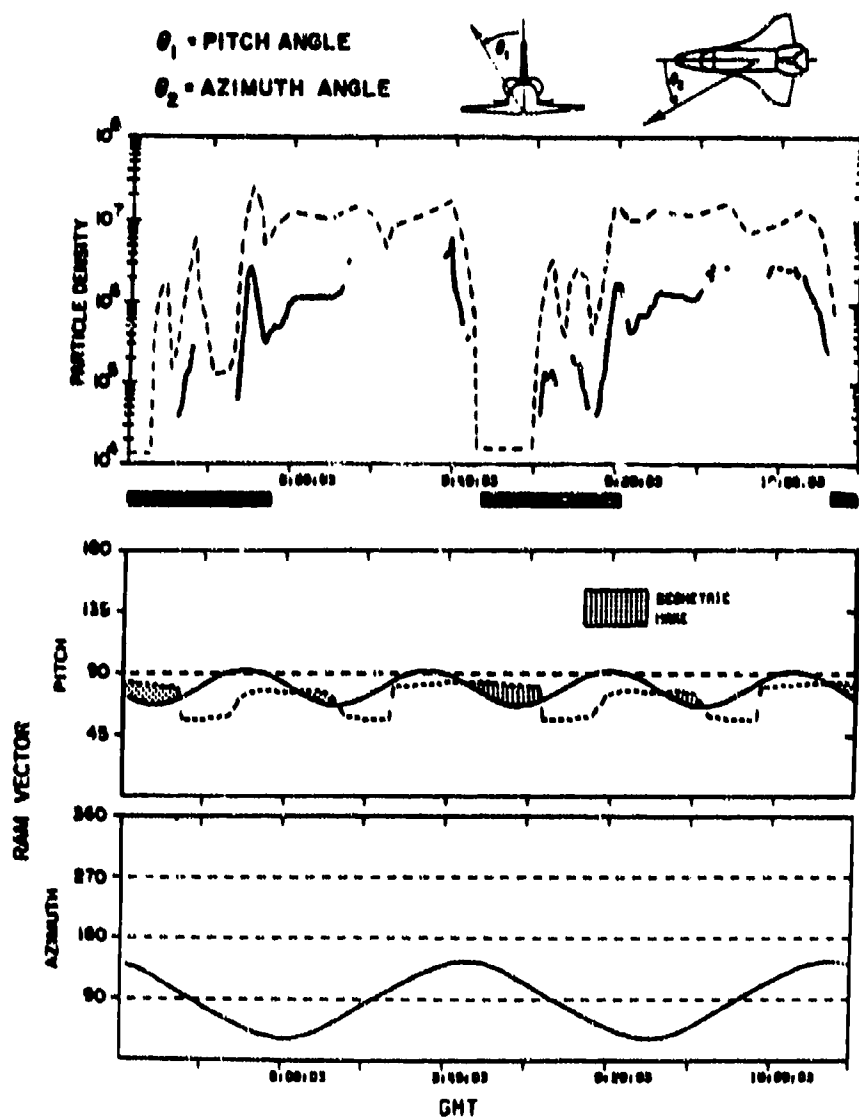
Figure 3. – Summary of VCAP Langmuir probe (dotted line) and SRPA (solid line) results as function of vehicle attitude.
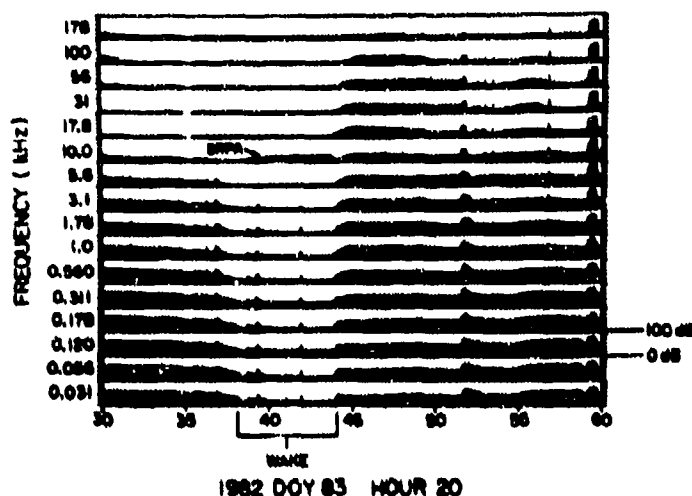
Figure 4. - VLF electric field spectrum showing increasing intensity of received SRPA signal.

SUMMARY

Although measurements are still in a primitive state, several conclusions can be drawn from the STS-3 PDP and VCAP data.

1. Ram conditions seem to result in a higher than expected electron density.

2. Density depletions of at least 4 orders of magnitude in the wake plasma are observed and there is evidence to suggest this depletion may be as high as six orders of magnitude.

3. Effective temperature measured by the thermal plasma probes indicate an increase in electron temperature in the wake to $> 6000°K$.

4. The thermal ions are excluded rapidly as the orbiter bay rolls into wake and only those locally produced H_2O^+ and NO^+ are measurable.

5. Both LP's and the SRPA indicate a degree of plasma density or velocity turbulence which peaks in the transition region between ram and wake.

Several concerns about these measurements are that: first, the VCAP probes' outputs are often contaminated by the turbulence which causes bias in the data; second, the ability of the PDP LP to measure density and temperature reliably beyond a certain limited range is questionable; and third, whether the sounder experiment setup between the VCAP SRPA and PDP Spectrum Analyzer is "calibratable" is still an open question.

39

The first concern is being worked and there is confidence that corrections for the turbulence can be computed. Recall that the PDP LP has a $\Delta N/N$ mode which can provide upper bounds on the turbulence within a given frequency band.

The second concern, which applies to a lesser degree to the VCAP LP, is harder to solve. As the density decreases and temperature increases, the size of the probe in relation to a debye length and thermal electron gyroradius changes drastically. This means that approximations used to derive temperature and density are no longer valid and new formulations must be used. A long-term research effort is underway to better understand the behavior of swept probes in those extreme regimes. (See ref. 5 for a description of the probe theory). Meanwhile, effort has been made to include data in this report derived from regimes where approximations hold. Thus, the densities and temperatures are probably good to a factor of two.

It is encouraging to note that when comparisons are made to measurements made by the DE satellite, which flew through the same altitude and latitude regime within the same day, general agreement is found. The DE data show dayside conditions of $N_e = .9 - 1.1 \times 10^5/cm^3$ and $T_e = 1500° - 2000°$ while the PDP and VCAP data taken dayside out of wake and also out of maximum ram condition indicate $N_e = 2$ to $10 \times 10^5/cm^3$ and $T_e = 1000°$ ($\pm 30\%$).

The third concern is currently being worked and if the "sounder" is calibratable, it should provide valuable input for theory.

The fact that elevated temperatures are observed in the near wake of a spacecraft is not without precedence. Samir et al. (ref. 6) found evidence for elevated electron temperatures in the wake of Explorer 31, a much smaller vehicle than the Shuttle Orbiter.

Additional measurements by the PDP and VCAP instruments will be made on Spacelab-2 where detailed experiments have been designed to study the structure of the wake out to approximately one kilometer from the vehicle.

REFERENCES

1. Samir, U.; Wright, K. H., Jr.; and Stone, N. H.: The Expansion of a Plasma into a Vacuum—Basic Phenomena and Processes and Applications to Space Plasma Physics. Submitted to Reviews of Geophysics and Space Physics Space Science Laboratory, MSFC, Preprint #83-102.

2. Paterson, W.; Frank, L. A.; Owens, H.; Pickett, J. S.; Murphy, G. B.; and Shawhan, S. D.: Suprathermal Plasma Observed on the STS-3 Mission by the Plasma Diagnostics Package. Submitted to Proceedings of the Spacecraft Environmental Interactions Conference, October 4-6, 1983.

3. Raitt, W. J.; Dorling, E. B.; Sheather, P. H.; and Blades, J.: Ionospheric
    Measurements from the ESRO-4 Satellite. Planet Space Sci., 23, 1085-1101,
    1975.

4. Shawhan, S. D.; Murphy, G. B.; and Pickett, J. S.: Plasma Diagnostics Package
    Initital Assessment of the Shuttle Orbiter Plasma Environment. Accepted
    for publication, December 1983, J. Spacecraft and Rockets.

5. Rubinstein, J. and Laframboise, J. G.: Theory of a Spherical Probe in a
    Collisionless Magnetoplasma. Phys. Fluids 25 (7), July 1982, 1174-1182.

6. Samir, U. and Wrenn, G. L.: Experimental Evidence of an Electron Temperature
    Enhancement in the Wake of an Ionospheric Satellite. Planet. Space Sci.,
    1972, Vol. 20, 889-904.

SHUTTLE ELECTRICAL ENVIRONMENT

M. Smiddy, W. P. Sullivan, D. Girouard
Air Force Geophysics Laboratory
Hanscom Air Force Base, Massachusetts 01731

P. B. Anderson
Regis College
Weston, Massachusetts

Part of an AFGL payload flown on the STS-4 mission consisted of experiments
to measure in-situ electric fields, electron densities, and vehicle charging.
During this flight some 11 hours of data were acquired ranging from 5 minute snap-
shots up to continuous half-orbits. These experiments are described and results
presented for such vehicle induced events as a main engine burn, thruster firings
and water dumps in addition to undisturbed periods. The main characteristic of
all the vehicle induced events is shown to be an enhancement in the low frequency
noise (less than 2 KHz), in both the electrostatic and electron irregularity ($\Delta N/N$)
spectra.

The "non-event" results indicate that the electrostatic broadband emissions show
a white noise characteristic in the low frequency range up to 2 KHz at an amplitude
of 10 db above the shuttle design specification limit, falling below that limit
above 10 KHz. The vehicle potential remained within the range of -3 to +1 volt
throughout the flight which exhibits normal behavior for a satellite in a low
equatorial orbit. The measured electron densities and temperatures are compared
with the International Reference Ionosphere showing measured densities somewhat
lower (up to a factor of 10) and temperatures higher (up to 400° K) than the refer-
ence model.

INTRODUCTION

The objective of this experiment is to characterize the electrical interaction
of the shuttle with its environment. This report describes the experiment and
its operation through a shuttle mission during which the instrument functioned
normally and acquired 11.3 hours of data.

DESCRIPTION OF EXPERIMENT

The electric field experiment consists of a 1.575 meter dipole, illustrated
schematically in Figure 1 as sensors A_1 and A_2 mounted along the orbiter X axis.
These sensors are 2 1/4" diameter aluminum spheres mounted on 10" long booms on
the equipment pallet which is mounted 16" above the trunnion fixture on the right
hand (+ y) side of the cargo bay. This puts the sensors at a height of 22.5"
above the edge of the cargo bay door 70" inboard. This geometry is such that when
the shuttle attitude is right wing forward (+ y into velocity vector), then any

roll angle from -18.5° to + 158° will present the sensors with a clear view of positive ion flow.

The spheres are roughened to guarantee good adhesion and are coated with a graphite material, to ensure a uniform surface and constant work function. To obtain the electric field component along the dipole axis, the difference in potential between spheres A_1 and A_2 are measured with circuitry having a much higher input impedance than the resistance between the spheres through the plasma. This potential difference is input to Telemetry at two sensitivity levels, one a factor of five more sensitive than the other. In addition this potential difference is fed to two swept frequency receivers, sweeping simultaneously over the frequency ranges 0 to 66 KHz and 0 to 5 MHz in an eight second period. Details of the different measurements, sensitivies, sampling rates, etc., are given in Table 1. The amplifiers were calibrated by superimposing spikes, at known frequencies, on the signals for one eight second sweep 504 secs after instrument turn-on and at 520 second intervals thereafter. To obtain the required 5 MHz response it was necessary to situate pre-amplifiers as near the sensors as possible which resulted in this circuitry being located inside the sensor supporting booms attached directly to the sensor. Because it was critical that the temperature of these elements not exceed 60°C when operating, a temperature sensor was co-located with this circuitry in one of the booms (A_1) and was closely monitored during the mission.

In order to measure the state of charging of the vehicle with respect to the local plasma the potential of A_1 was also measured with respect to the spacecraft skin (ground), thus giving the spacecraft potential with respect to the plasma at the two points A_1 and A_2 (separated by 1 1/2 meters). Because almost the whole spacecraft is electrically isolated from the surrounding plasma by the thermal tiles, leaving the engine thruster nozzles as the only conducting surface by which the spacecraft potential can anchor itself to the plasma, it would be expected that the spacecraft potential would vary substantially. This was indeed found to be the case on STS-3 (ref. 1). In order to make vehicle potential variations of more than a few volts less likely, another experimenter (NRL-802) provided a "ground plane" of 1/3 square meter area mounted in the shuttle X Z plane approximately 70 cms in the -Y direction from the dipole axis, see Figure 1. This surface is connected to spacecraft ground and is effective in stabilizing the vehicle potential when the ion flow is normal to the surface, i.e., when the vehicle velocity vector is in the spacecraft +Y direction.

The second part of this experiment is the Electron Density sensor which is mounted midway between the electric field sensors (B, Figure 1) and offset inboard from the dipole axis by 10 cms. This sensor consists of a gridded sphere 2 1/4" in diameter with an open/surface ratio of 0.8 mounted concentric with a 1 3/4" diameter collector. The two elements are gold plated to reduce work function potential differences between the surfaces. The inner sphere is biased at +20 volts with respect to the outer sphere, which voltage is sufficient to collect all electrons of energies below 30.625 eV which enter the outer grid and to reject all ions with energies below 20 eV, that is all ions below mass 65AMU moving with the ram velocity (7.7 Km sec^{-1}) which includes the dominant ionospheric ions. Thus, the sensor filters out, and collects the current due to only electrons, which is then input to a logarithmic electrometer measuring in the current range 10^{-9} through 10^{-4} amps. The output is fed to telemetry and to an A.C. amplifier with a gain of 40, then through a bank of eight filters to telemetry giving outputs which measure the electron density irregularities Δ N/N.

The potential on the outer grid of the sensor with respect to ground is programmed to operate 50% of the time as a Langmuir probe where the voltage is varied linearly as a function of time, and 50% in a Irregularity measurement mode where the voltage is kept constant. This programming is depicted in the lower part of Figure 2 where the upper part shows in a block format the signal processing system. To obtain density, temperature and vehicle potential from the Langmuir probe operation it is necessary that the probe be swept through the local plasma potential. To allow for the possibility of the vehicle potential being anywhere in the range of -20 to +4 volts, the + 4 volt sweep was applied with respect to a bias voltage which was stepped at 64 sec intervals through 0, +4, +8 and +16 volts.

This operation was controlled with an internal timer, synchronized to the telemetry frame rate through a 100 Hz clock, and recycled every 256 secs when a timer reset pulse was transmitted to telemetry.

EXPERIMENT PERFORMANCE

Table 2 summarizes the vehicle history and the amount of data acquired in each vehicle attitude. The experiment was commanded on and off by command sequences that were capable of operating for roughly 24 hours before they required updating. This system worked quite well but had the disadvantage that last minute changes in the astronauts schedule caused planned events to be missed. For example, it was important to obtain background EMI data with the payload bay doors closed, thus shutting out the environmental noise. This event was missed completely because of difficulties encountered on the first closure attempt.

Much of the data was acquired in 5 minute "snapshots", longer operating periods were more desirable of course, and were obtained mostly in the gravity gradient and bay-to-earth attitudes. The two longest periods were of 45 minute duration in the bay-to-earth attitude.

In Figure 3a and 3b are shown the temperatures of the electronics package (A452) and the E-field sensor boom A1 (T808) respectively, on 3a is also indicated the vehicle attitude. The payload by doors were opened at Mission Elapsed Time (MET) = 7,305 secs which was 94 minutes prior to the first data acquisition at Revolution (Orbit) number 3.6 when the electronics package and boom were at approximately room temperature of 20°C. Thereafter the electronics cooled to near zero by REV #9.5 where it remained for the rest of the mission. The excursions up to 11°C and 17°C can be seen to coincide with the two Bay-to-Sun (- ZSI) periods. In general, the electronics package temperature increased, as expected, as a function of "on" time except from MET = 170,000 through 200,000 where the pallet was cooling faster than the electronics warmed up. On the other hand, in Figure 3b, the booms being thermally isolated from the pallet experienced wider temperature oscillations ranging from + 30°C in Bay-to-Sun periods down to -40°C at night when the cargo bay faced away from the earth. Thus, the temperature seen on the booms depends solely on the sun/shadow situations.

45

Vehicle charging for the entire mission will be discussed, then typical AC electric field values will be compared to shuttle specifications for broadband emissions. Finally, electron densities and temperatures for a 45 minute period will be compared to an ionospheric model.

Vehicle Charging

Figure 4 shows the result of plotting 64 second averages of vehicle potential for almost all (the period from MET = 13,000 through 90,000 secs was accidently omitted) the periods when the instrument was operational during the mission. It can be seen that the general level in between -3 and +1 volts, which values are tyical for a satellite in a low equatorial orbit where the average electron energy is of the order of 0.16 eV.

Comparing figure 4 with the vehicle attitudes shown on Figure 3a it can be readily seen that the high value of +1.0 volts at MET ≈ 163,000 secs coincides with the bay-to-sun attitude (-ZSI) where photo-electron emissions from the instrument pallet (but not the reference plane, which is edge-on to the sun) drives the vehicle positive with respect to the reference plane. The three data sets near MET = 260,000 secs, where the vehicle potential approaches -4 volts were taken in a bottom-to-sun attitude (+ ZSI) during night-time conditions.

The more extreme variations, seen on the lower panel of Figure 4 (MET > 310,000 secs) ranging from -3.2 volts to + 1.8 volts were all taken during tail-to-sun attitude (- XSI). The positive values around MET = 317,000 secs and at MET = 352,000 secs are identified with the tail pointing into the velocity vector where the ram ion flow coupled with with a low photo-electron emission produces a net positive charge. The low potentials on the other hand, e.g., near MET = 440,000 secs, are identified with periods when the sensors e d cargo bay are in the ion flow wake region.

Broad Band EMI

In Figure 5 we show a typical electric field power spectrum showing the amplitude in db μV/m MHz as a function of frequency on a logarithmic scale. The data from the low frequency sweep (0 - 60 KHz) is represented by squares and that from the high frequency sweep (0 - 5 MHz) as triangles, the lower limits for these measurements are 122 db and 107 db respectively. Shown also on this figure are the maximum shuttle-produced broad band noise limit (Design spec max) and the payload design specification, this latter is a specification for payload design whose limit is only given above 10 KHz whereas the former is based on ground shuttle measurements made by SAIL. It can be seen that below 10 KHz the measured broadband noise exceeds the design limit by a maximum of 12db in the frequency range of 1 to 2 KHz. This is due to electrostatic waves produced by the shuttle body moving through the environment. Taking the ambient oxygen temperature to be 1000° K gives a most probable oxygen speed (random thermal speed) of 1.019 Km/sec, thus a vehicle Mach Number of 7.5.

Other features to note on this figure are the line emissions at 37.5 KHz and the noise enhancements in the frequency range of 200 KHz to 5 MHz. The former is probably due to a DC/DC converter on the pallet which line was also seen on ground integration tests, the latter are probably genuine plasma emissions

46

since they occur in the frequency range of the plasma frequency (900 KHz - 9 MHz) and the electron gyro frequency (840 KHz).

Model Comparison

Comparison of measured electron densities and electron temperature with the International Reference Ionosphere (IRI) are shown in Figure 6 comprising of some 45 minutes of data taken on Rev #24.6. The IRI model is shown as solid lines and the measured data as points with vertical error bars. These data result from analysis of the Langmuir probe mode of operation of the electrons sensor where each 8 second interval results in two points, one from the upsweep (-4 to +4 volts) and one four seconds later from the downsweep (+4 to -4 volts). Because of a well-known hysteresis effect, where electrons accumulate on the outer grid giving an effective grid potential offset from the applied potential, the deduced densities and temperatures differ slightly. In each successive 256 second period only the first 128 seconds gave usable Langmuir probe data, the +8 and +16 volt biases applied at 128 and 196 seconds, respectively produced near-saturation currents.

Comparing the model and measured densities in Figure 6a it is seen that the measured values are lower by up to a factor of 10. On the other hand, the measured temperatures in Figure 6b are in general higher than the model. These differences are explained by the fact that the electron sensor is located in the cargo bay, hence, embedded in the vehicle sheath. If the balance of the sheath has only a net negative charge with respect to the ambient plasma of only a few hundreths of a volt, then a fraction of the lowest energy ambient electrons will be unable to reach the sensor location thus giving the low observed densities and high observed temperatures.

VEHICLE INDUCED EFFECTS

The following three sections describe the effects of a main engine burn, vernier thruster firings and a water dump.

OMS-4 Burn

Figure 7 represent data taken during the fourth burn of the OMS motor, ignition occurred at MET = 18,852.4 secs for a 30 sec burn durations. On the time scale of Figure 7a the burn starts at 169 seconds and ends at 199 seconds. On the upper panel is shown the plasma potential with respect to the vehicle that is, the potential of the A1 sensor on a scale of -9 to +9 volts. The vehicle potential (with respect to the plasma) is the measured quantity with reversed sign thus it can be seen that prior to 170 seconds the vehicle potential is -0.7 volts. The second panel shows the potential difference between the electric field sensors on a scale of -2 to +2 volts, and the third panel is the same quantity on a ten times larger scale. The electric field is obtained by dividing this voltage by 1.575 (dipole separation distance in meters) and gives the component in the -x (nose-to-tail) direction. Thus, it can be seen that the electric field varies from 160 mV/m at time 0 seconds to zero at 256 seconds. A small electric field component along the Shuttle X-axis is expected here because the vehicle is flying in an "aeroplane" attitude (zero pitch and zero yaw) to increase the orbital altitude during the motor burn. The dominant

electric field is due to the vehicle motion through the geomagnetic field, V x B, contributing no field component along the velocity vector in this vehicle attitude.

The lower panel shows on a logarithmic scale the current measured by the electron sensor ranging from 10^{-9} amps to 10^{-3} amps. In section 2 it was pointed out that a bias potential was applied to the sensor with respect to the vehicle and stepped at 64 second intervals through 0, 4, 8 and 16 volts. The effect of this can clearly be seen on this panel where only the constant voltage mode data are shown occurring at even 8 second intervals.

In the time period up to 64 seconds the current is very low where the electrons are being retarded, at 64 seconds when the bias is stepped from zero to +4 volts the current increases over four orders of magnitude because we have now shifted to a voltage where the electrons are accelerated to the sensor. Reading the vehicle potential from the top panel as - 0.7 volts it can be seen that we have moved the sensor potential from - 0.7 volts to + 3.3 volts with respect to the plasma at 64 seconds. At 128 seconds the sensor potential is stepped up another 4 volts to + 7.3 volts with respect to the plasma and the amplifier saturation current of 1.363×10^{-4} amps is almost reached. The final step to 16 volts bias at 196 seconds now saturates the amplifier.

Turning now to the effects of the motor burn. At motor ignition the vehicle potential initially swings negative by almost 2 volts (A1 increases) at 169 seconds, returns to its pre-ignition value of - 0.7 volts in 0.2 seconds and then decreases linearly through the 30 second burn period to - 1.0 volt at 199 seconds. This vehicle potential fluctuation is consistent in sign with the electron current observed on the lower panel in Figure 7a and on an expanded time scale on the lower panel of Figure 7b, where the negative excursion of sensor potential causes a current reduction of 3 orders of magnitude, i.e., apparently takes the sensor potential to zero or slightly below plasma potential. Since the sensor potential prior to motor ignition is + 7.3 volts an excursion of some - 7.5 volts would be necessary to reduce the sensor current to the observed 10^{-7} amps. An alternative explanation is that motor ignition causes a sudden increase in pressure in the local environment which changes the electrical vehicle sheath condition. This hiatus interrupts the flow of electrons to the sensor and could also possibly explain the apparent positive excursion of vehicle potential, seen as a negative excursion of approximately 1.5 volts on A1 at 169 seconds.

Looking at the electric field response on Figure 7a, A1-A2, we see no change in the D.C. electric field but a very apparent increase in noise from 0.2 volts to 0.5 volts peak to peak amplitude throughout the 30 second burn period. This increase in "noise" can be seen by comparing the upper two panels in Figures 7b and 7c, where the spectra are shown for two succesive frequency scans 7c before motor ignition and 7b during and following ignition. Ignition occurs at 1.2 seconds on 7b the vertical scale is proportional to the log of E^2 measured in v^2/m^2Hz and the spectra show the receiver frequency being swept linearly as a function of time. Comparing the amplitude at 5 KHz on either side of the 0 KHz pedestal it is seen that ignition produces a noise value an order of magnitude higher than the subsequent burn noise, which is again an order of magnitude higher than the noise prior to burn. By comparing the 0 KHz peaks it is seen that this noise is at a low (< 1 KHz) frequency. Again, a probable explanation for this increased electrostatic noise is a large local pressure increase, with the additional possibility that the electrostatic noise and the $\Delta N/N$ enhancements are due to the propagation of a sound wave through the plasma.

48

Thruster Firings

Of the 44 thrusters that make up the Reaction Control System (RCS), 38 are primary (PRCS) and six are vernier thrusters (VRCS). This latter system is the one employed for attitude control for the major part of this mission and are the ones which we will discuss. Two are situated in the nose and four, two left and two right, on the engine pod just above the trailing edges of the wings. Of these six vernier thrusters those in front produced no discernable effects, those on the left small perturbations and those on the right large effects with the thruster firing down producing larger fluctuations than the one thrusting to the right. The reason for this difference is probably that the right aileron could, if left in a horizontal position deflect part of the thruster plume upwards towards the starboard cargo bay area where the instruments were located.

The thruster firing effects are shown in Figure 8 with a time history of firings shown in table 3. During this acquisiton period the vehicle was in a bay-to-sun attitude with the right wing (+Y) pointing into the velocity vector (approximately eastward). The local time is near midnight thus the cargo bay is facing the earth and again the measured component of the $\vec{V} \times \vec{B}$ electric field is small (A1 - A2), on Figure 8a. The total thruster firing period of 12.88 seconds commencing at 184.58 seconds is shown in the upper panel of Figures 8a, b, and c. It can be seen that the effects are barely discernible on either vehicle potential (A1) or D.C. electric field (A1 - A2),. but produce a factor of ten decrease in the electron current. This current response cuts off at 192 seconds due to the sensor switching into the Langmuir probe mode of operation, we will return to this later.

The outputs from the eight $\Delta N/N$ filters are shown in Figures 8b and 8c on the same time scale as 8a with again the thruster firing indicator in the top panel. The vertical scale is logarithmic extending from -0.1 to +4.9 with 0 being equivalent to 0% value of $\Delta N/N$ and 5 corresponding to 186% $\Delta N/N$. The large oscillations up to 64 seconds, the smaller oscillations up to 128 seconds and the large negative going vertical spikes thereafter are due to switching in and out of the Langmuir probe mode of operation. An explanation of the positive spikes discernible on all the filter outputs at a time interval of 5 seconds, which come and go throughout the mission has not been found. It is perhaps a cycling time of another experiment or a payload switching operation, this is being investigated. The general signal level is the quantity to note. It can also be seen that the signal level is depressed for frequencies greater than 100 Hz in the first 64 seconds. This is due to the roll-off in frequency response of the logarithmic amplifier above 100 Hz at the lowest current level of 10^{-9} amps, which is the current level indicated on the lower panel of Figure 8 a. The thruster firing effect can be seen starting at 184.6 seconds and extending through 194 seconds, coinciding exactly with the right thruster firing times listed in table 4. No effects are discernible either from the front left firings nor at termination of the front right operation at 197.5 seconds. The right thruster produces an increase in $\Delta N/N$ from 0.5% to 1.6% at 30 Hz, decreasing to zero effect at 500 Hz where $\Delta N/N = 1.6\%$, changing to a suppression with increasing frequency to a maximum of a depression in $\Delta N/N$ from 5% to 0.5%.

An even more dramatic effect of the decrease in noise due to thruster operation can be seen in the Figure 8d through 8g which shows a series of four consecutive spectra from the A.C. electric field outputs. The panel format is the same as in Figure 8 (b and c). These figures show in the third panel the current decrease

49

at the firing start in 8e at 0.2 seconds and then return to its initial value at 1.7 seconds in 8f coincident with the right thruster firing end. Note the almost complete suppression of all frequencies greater than 12 KHz in the top two panels of Figure 8e as compared with 8d, f or g, the reduction in electrostatic noise above 3 KHz and the small increase at frequencies below 2 KHz. These effects are very similar to those observed by the Plasma Diagnostic Package[1] on STS-3, and offer a possible explanation in terms of a local pressure increase caused by gases emitted from the starboard thruster.

Water Dump

A water dump occurred on Rev #33.6 commencing at MET = 175864.84 seconds the effects of which are shown in Figure 9. At this time the vehicle was in a tail-to-sun attitude and was just crossing the terminator from day to night which puts the shuttle in an "aeroplane" attitude with the cargo bay facing away from the earth and the electric field dipole aligned with the velocity vector hence a zero $V \times B$ electric field component.

The water dump start is shown in the upper panel of Figure 9a at 181.4 seconds and continuing through 256 seconds. The vehicle potential decreases by a very small amount -0.2 volts (A1 increases), the D.C. electric field (A1-A2) remains unchanged but the noise increases from 0.1 volts peak to peak to 0.15 volts and the electron density which has been steadily decreasing, increases at the start of the dump by some 10% but sustains the same rate of decrease during the water dump as before.

Looking at the $\Delta N/N$ data in Figures 9b and 9c we see a progressive enhancement of $\Delta N/N$ from 30 Hz up to 503 Hz during the water dump which then decreases back to zero effect at the highest frequency of 7.830 KHz. Figures 9d and 9e show the electrostatic frequency spectra before and after the water dump start the only difference to be noted in the slight filling in around 0 KHz on the low frequency spectrum on 9e compared to 9d. This indicates that the increase in noise on (A1-A2) in Figure 9a occurs at frequencies less than 2 KHz. The explanation for these measurements is probably the presence of eater droplets charged by triboelectric effects and a local increase in pressure.

CONCLUSIONS

1. There exist electrostatic noise at frequencies below 10 KHz generated by body motion at about 135 db V/m MHz amplitude which propagate to the sensor location in the cargo bay.

2. At OMS ignition a large pressure wave is generated for 3/10 second which shields the cargo bay area from the environment.

3. The OMS burn and thruster firings produce acoustic noise detected by its electric field and $\Delta N/N$ effects in addition the local pressure increase produced by starboard thruster reduce the electron density by a factor of 10.

4. Ambient plasma measurements of electron density, irregularities, temperature and electrostatic waves are possible in the cargo bay provided that the shuttle attitude is correct and that appropriate exposure factor corrections are made.

5. Measured vehicle potentials were typical of a satellite in low earth orbit ranging in value from -3 to +1 volts with typical values of around -1 volt.

REFERENCE

1. Shawhan and Murphy, "Plasma Diagnostics Package Assessment of the STS-3 Orbiter Enviornment and Systems for Science", (1982).

TABLE I INSTRUMENTATION AND MEASUREMENTS

1. Electric Field Sensor

DIPOLE LENGTH = 1.575 meters

Measurement	Range	Sensitivity	Sample Rate
a) Probe Potential (A1)	-8.156 to +8.494 volts	± 33 mV	25/sec
b) E-Field LO (DC)	-1.059 to +1.104 V/m	± 7 mV/m	25/sec
c) E-Field HI (DC)	-1061 to -628 mV/m	± 1mV/m	25/sec
d) E-Field LO (AC)	0 to 66 KHz 209 Hz/sample	$10^{-11.587}$ to $10^{-4.196}$ $v^2/m^2/Hz$	50/sec
e) E-Field HI	0 to 4.991 MHz 14.680 KHz/sample	$10^{-14.664}$ to $10^{-7.678}$ $v^2/m^2/Hz$	50/sec

2. Electron Density Sensor

COLLECTION AREA = 1.026 x 10^{-2} m^2

Measurement	Range	Sensitivity	Sample Rate
a) Electron Density	15 to 2 x 10^6 cm^{-3}	± 2%	25/sec
b) Electron Temperature	100 to 100,000 °K	± 2%	
c) Vehicle Potential	-20 to +4 v	± 80mV	
d) Δ N/N	0 to 186% 30, 60, 115, 503, 968, 1939, 3900 AND 7830 Hz	± 0.05%	10/sec (each filter)

3. Housekeeping

    a. Electronics Package Temperature   -80°C to 150°C

    b. Boom 1 Temperature   -80°C to 150°C

    c. Timer Reset Indicator   1 sample/sec

51

TABLE 2

REV #		Mission Elapsed Time (Secs)		Vehicle Attitude†	Data Acquired (Mins)
From	to	from	to		
3	3	12,952	13,552	-ZLV, XPOP, 12° roll	10.0
4	4	18,683	18,983	OMS-4 Burn	5.0
5	6	22,787	29,864	GG	28.167
8	12	36,400	60,068	+ZSI	23.333
13	16	65,158	85,025	-ZSI	40.0
18	21	92,454	109,781	GG	93.333
22	29	113,182	152,527	-ZLV, XPOP, 12° roll	110.0
29	32	154,504	170,063	-ZSI (IECM*)	55.0
33	37	174,052	197,215	-XSI (IECM*)	47.0
38	52	202,171	279,577	+ZSI	112.333
59	59	313,450	313,750	PTC	5.0
59	94	317,084	506,268	-XSI	147.9
				TOTAL	677.066
					= 11.284hrs

* This is the period over which the NASA Induced environment contamination monitor was operating.

† Description of attitude terms:

-ZLV, XPOP, 12° roll = bay (-Z) to earth, X perpendicular to orbital plane, 12° roll cants right wing out of velocity vector.

GG = gravity gradient, approximately nose to earth, right wing into velocity vector such that a stable attitude is achieved.

+ZSI = Bottom to sun

-ZSI = Top (Cargo bay) to Sun

-XSI = tail to Sun

PTC = "Rotisserie" mode, X perpendicular to earth-sun line with a slow roll

TABLE 3. — THRUSTER OPERATION

Thruster	Start (MET)secs	Stop (MET)secs	Start (Fig 7)secs	Stop (Fig 7)secs
FRONT RIGHT	274633.38	274646.26	184.58	197.46
RIGHT RIGHT	274633.38	274642.74	184.58	193.94
FRONT LEFT	274633.38	274634.34	184.58	185.54
FRONT LEFT	274636.26	274636.74	187.46	187.94
FRONT LEFT	274638.66	274639.14	189.86	190.34
FRONT LEFT	274641.06	274641.64	192.26	192.74
FRONT LEFT	274642.74	274646.26	193.94	197.46
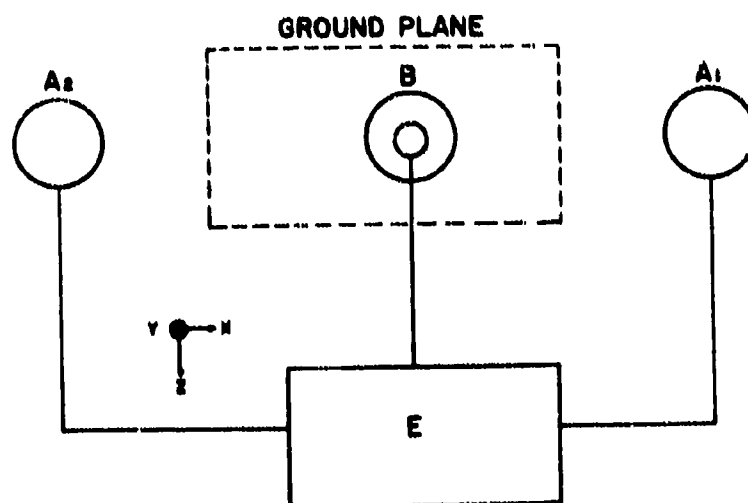
Figure 1. - Schematic layout of electric field dipole (A₁, A₂) and electron sensor (B) with shuttle coordinate area.
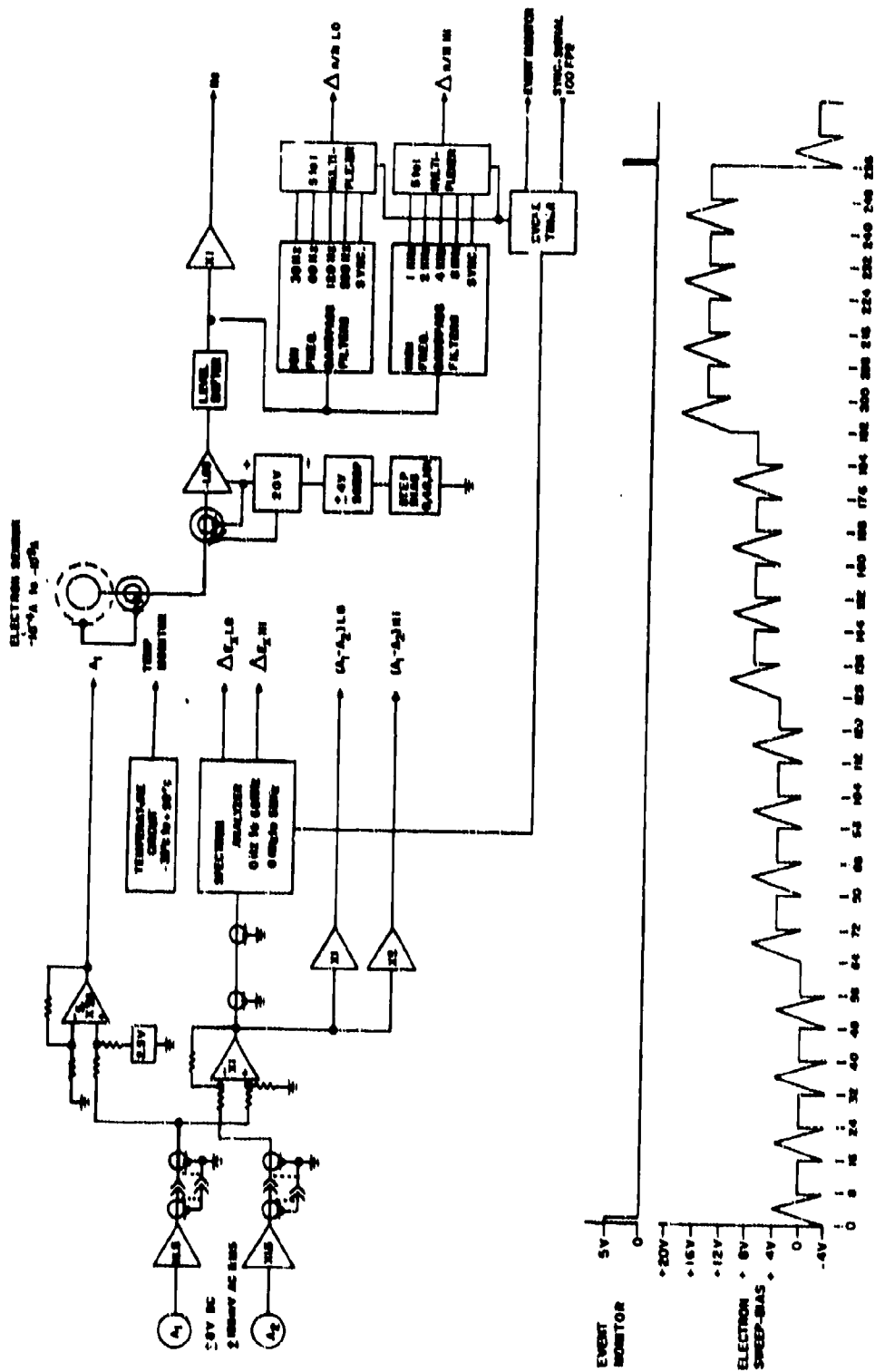
Figure 2. - Signal processing system and electron sensor voltage program.
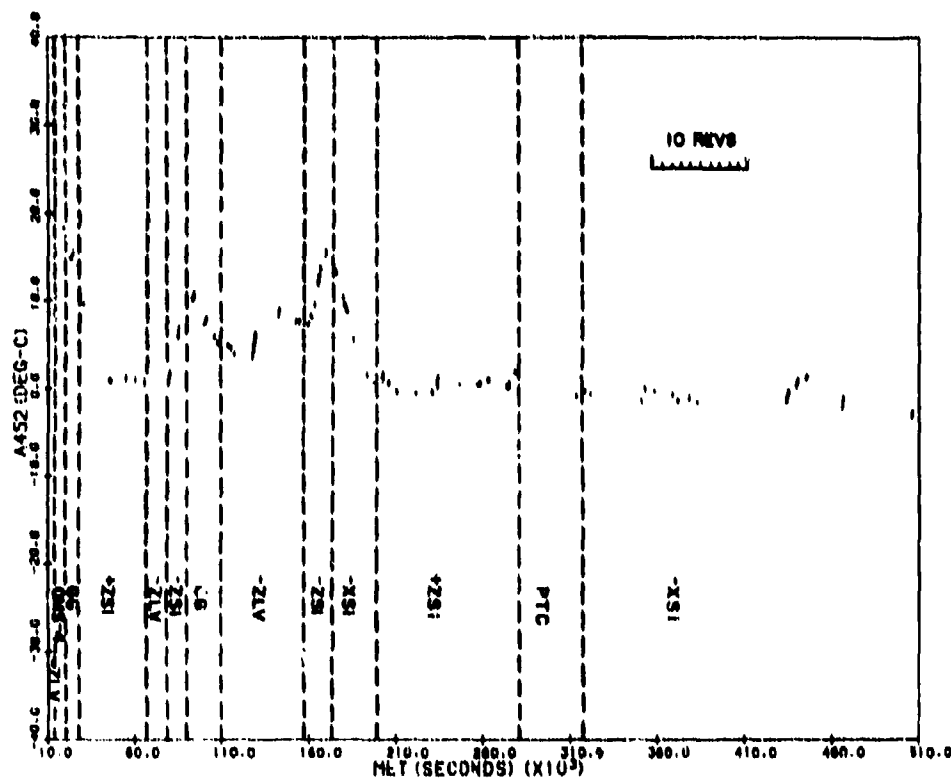
(a) 804C temperature A452.

Figure 3. – Electronics unit temperature (A452) with vehicle attitude and boom A₁ temperature (A808) versus mission elapsed time.
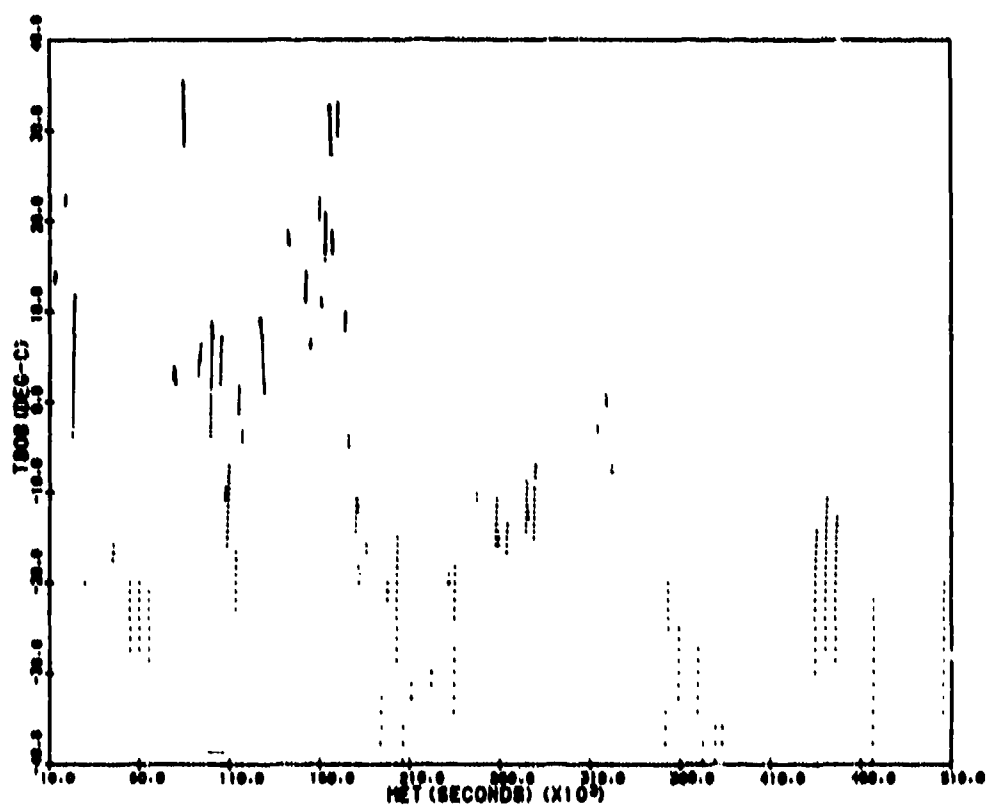
(b)　804C temperature 1808.

Figure 3. - Concluded.
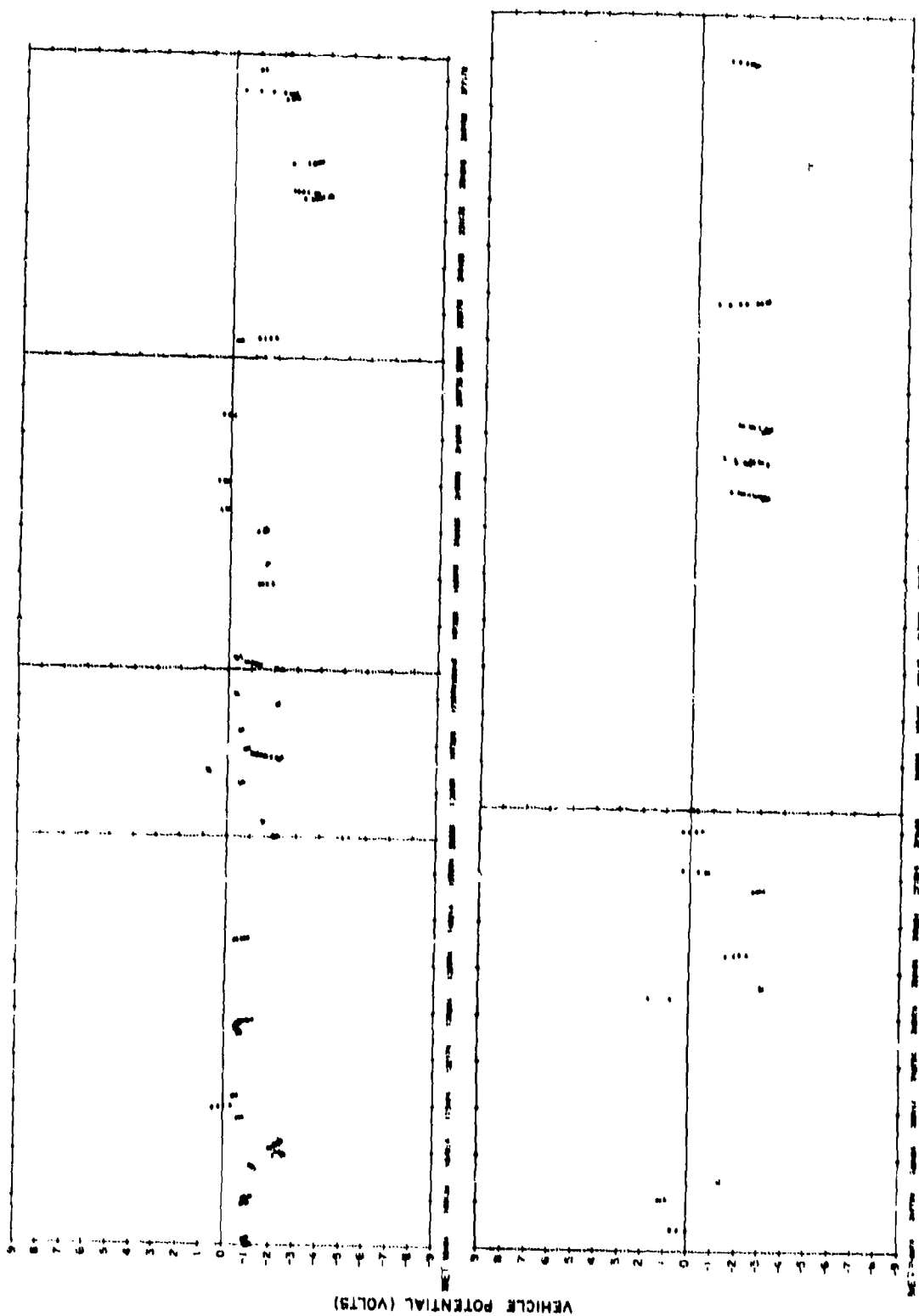
Figure 4. - Vehicle potential for all data collection periods for orbit 18.2 (MET = 92 454 sec) through orbit 34.3 (MET = 505 362 sec).

VEHICLE POTENTIAL (VOLTS)

57
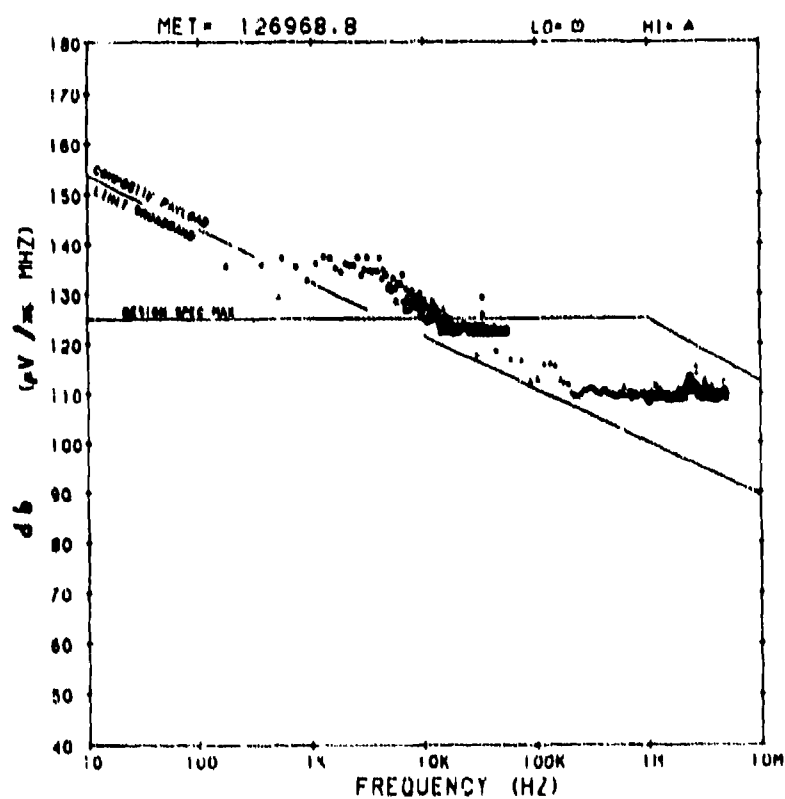
Figure 5. - Typical power spectrum of electrostatic noise.

(a)   Electron density.

MET •   126960.0 127216.0 127472.0 127728.0 127984.0 128240.0 128496.0 128752.0 129008.0 129264.0
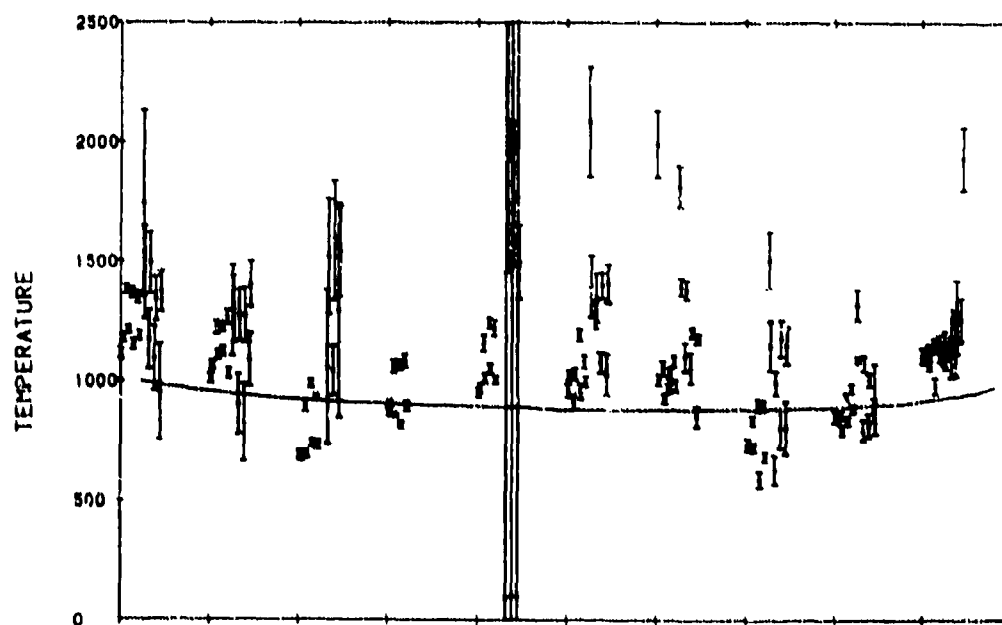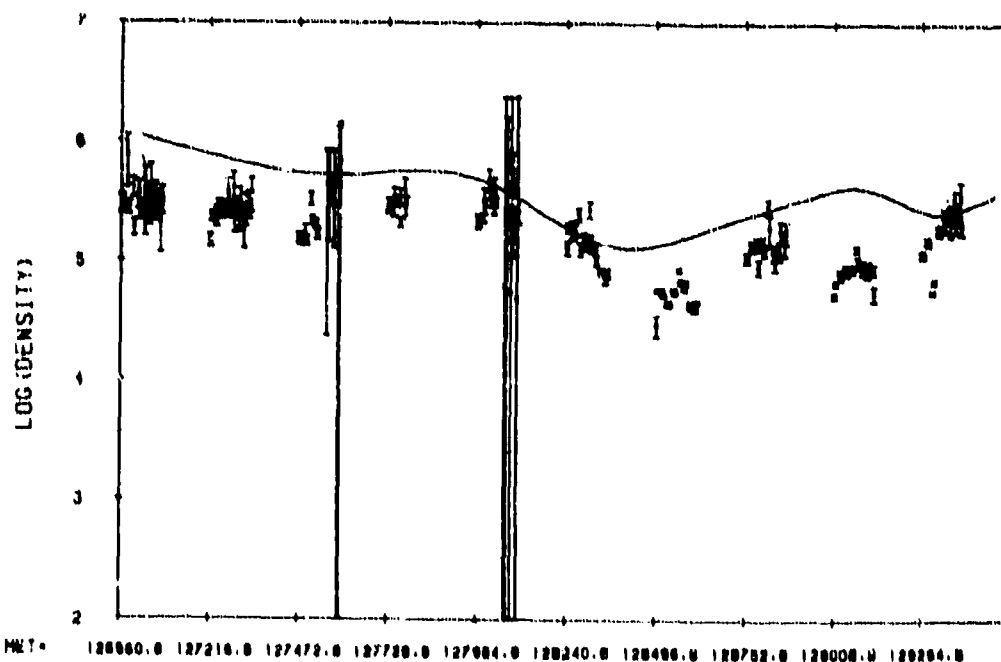
(b)   Electron density.

Figure 6. – Comparison of electron density and electron temperature (points with error bars) against International Reference Ionospheric model (solid line) versus time.
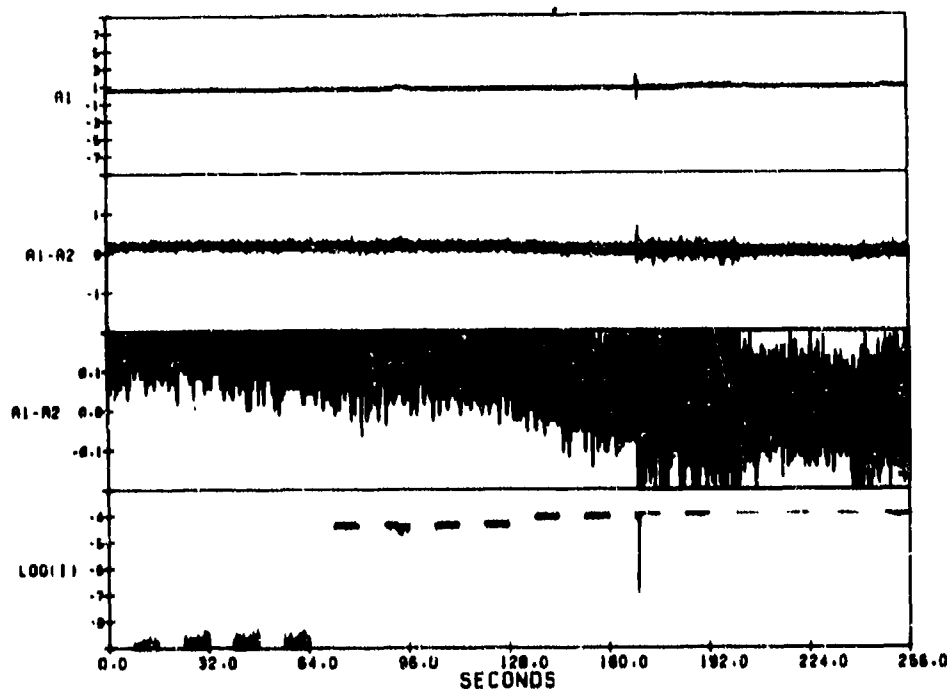
(a) Vehicle potential, electric field, and electron current versus time
MET 18 683.4 sec.
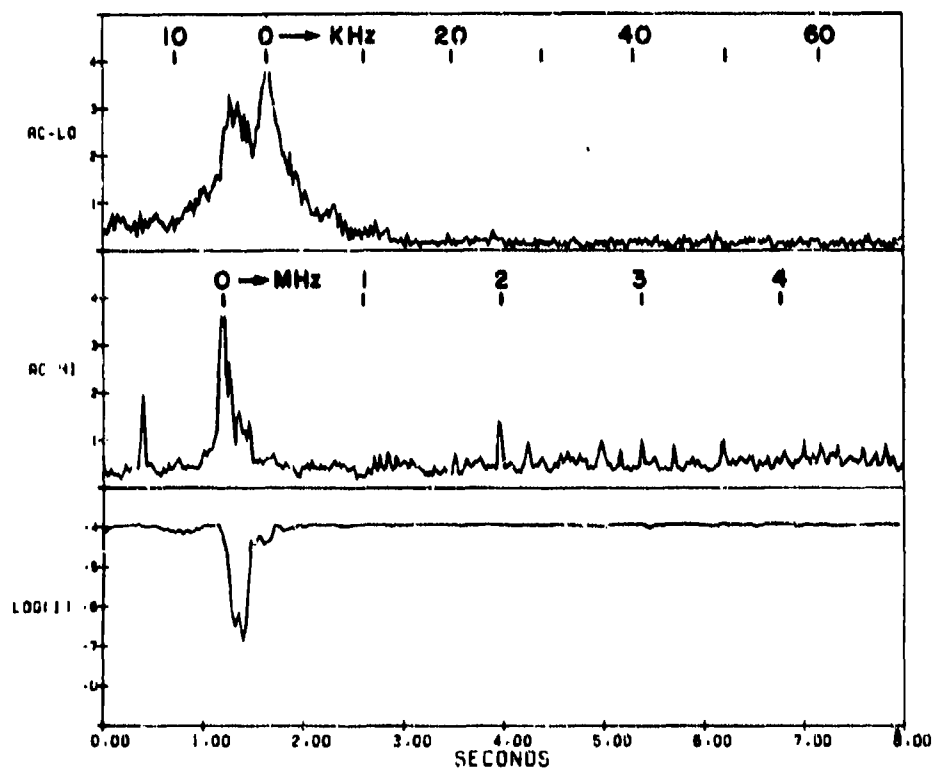
(b) Electrosatic spectra over low- and high-frequency ranges and electron
current versus time. MET, 18 851.4 sec; inteval 22.

Figure 7. - OMS-4 burn.

60
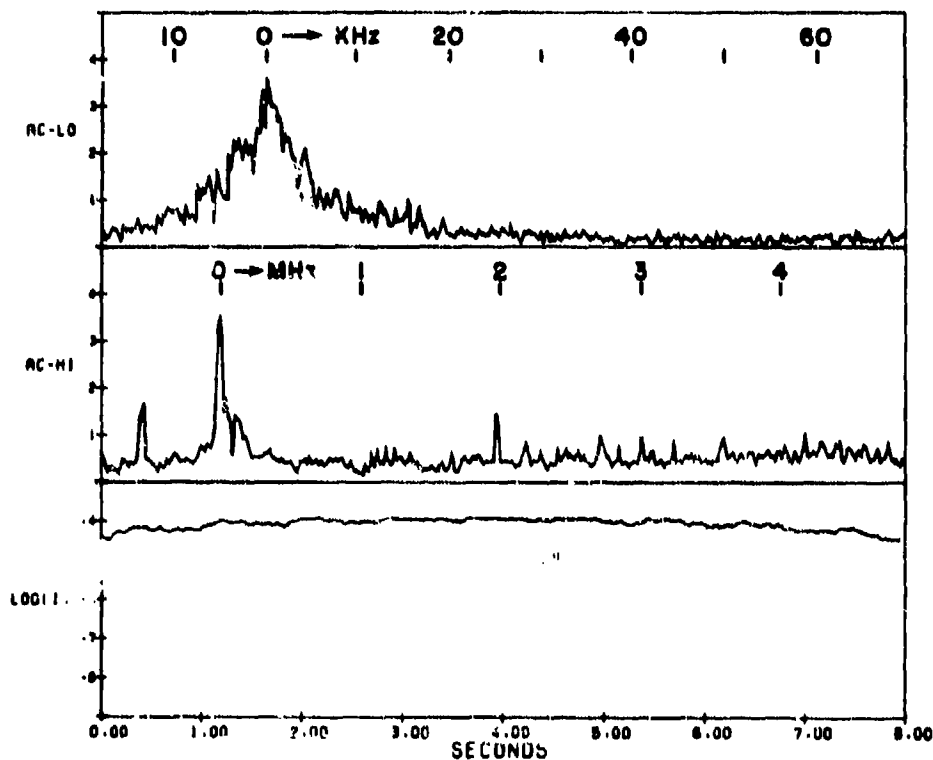
(c) Electrostatic spectra over low- and high-frequency ranges and electron current versus time. MET, 18 843.4 sec; interval 21.

Figure 7. - Concluded.
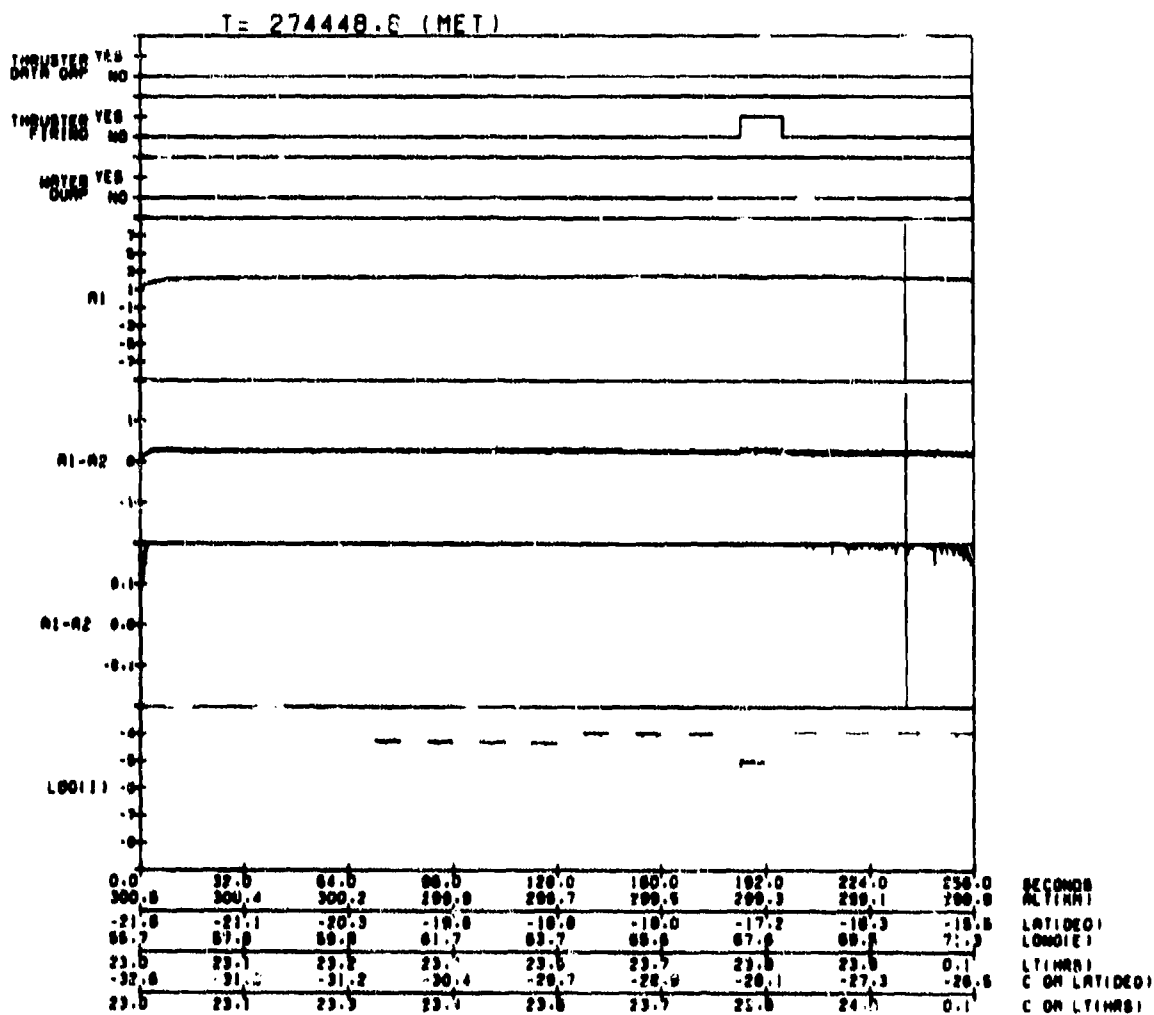
(a) Thruster firing indicator, vehicle potential, electric field and electron current versus time and orbital position.

Figure 8. -- VRCS firings.
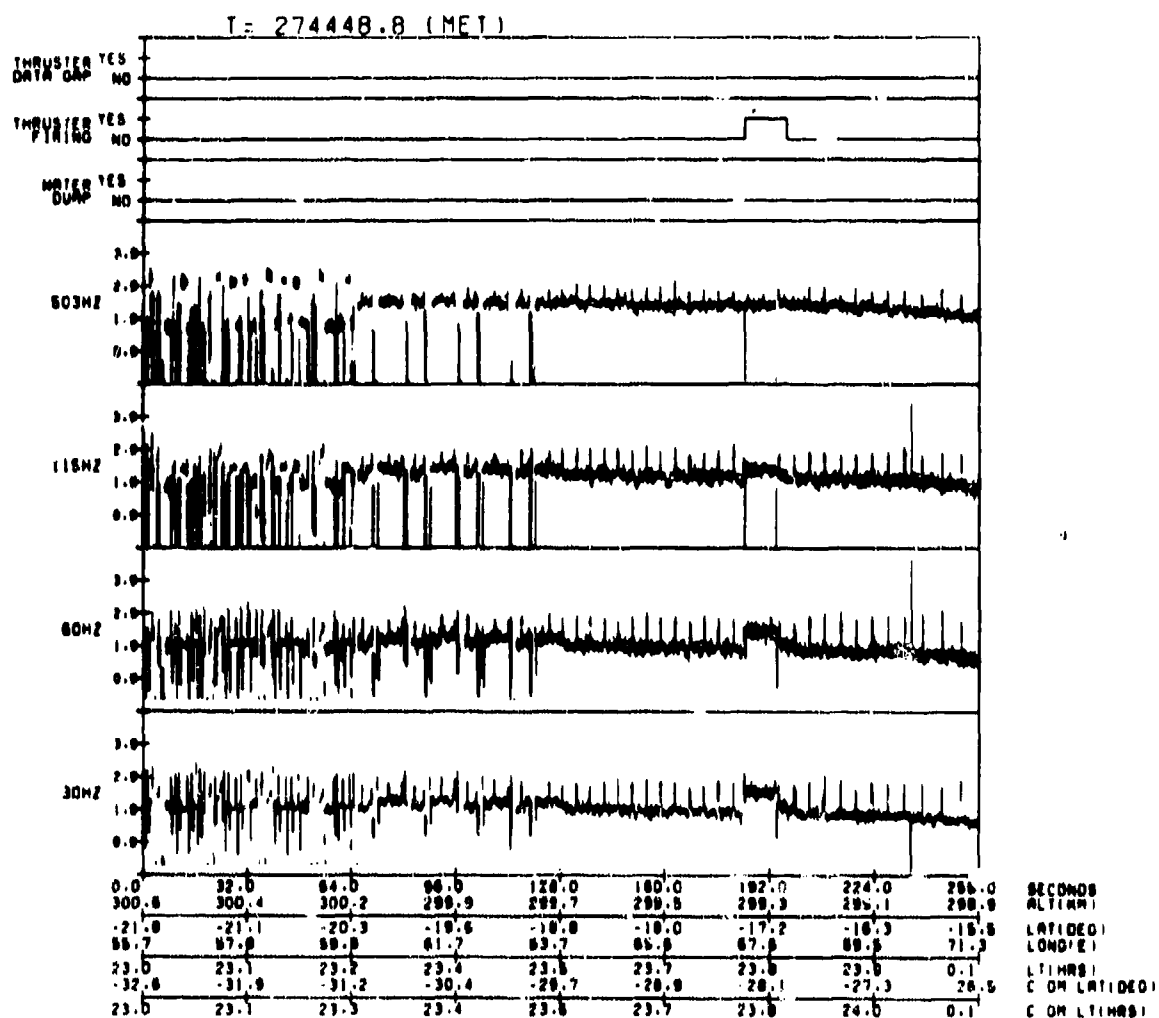
(b) Thruster indicator ΔN/N filter outputs versus time and orbital position.
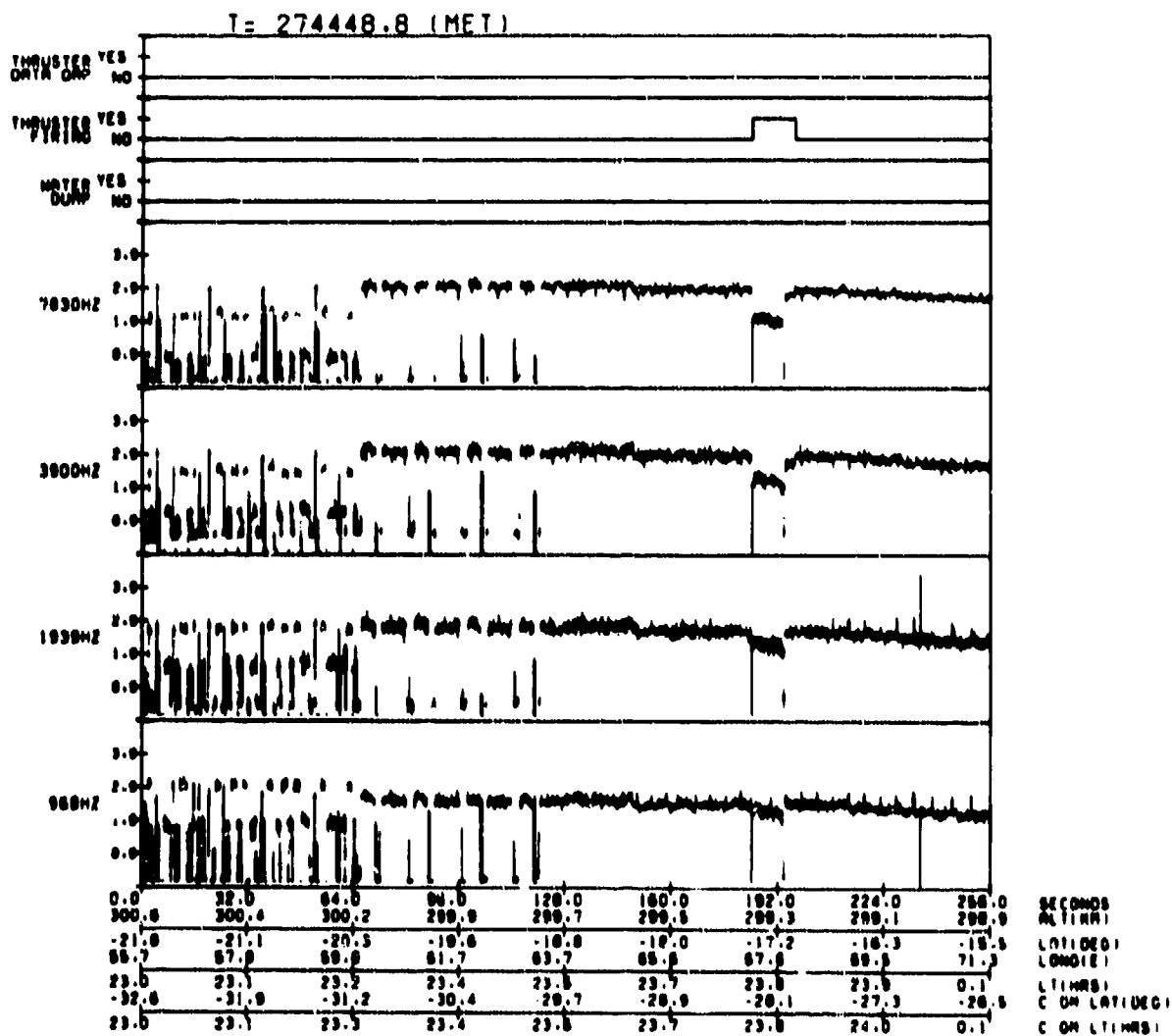
Figure 8. - Continued.

(c) Thruster indicator ΔN/M filter outputs versus time and orbital position.
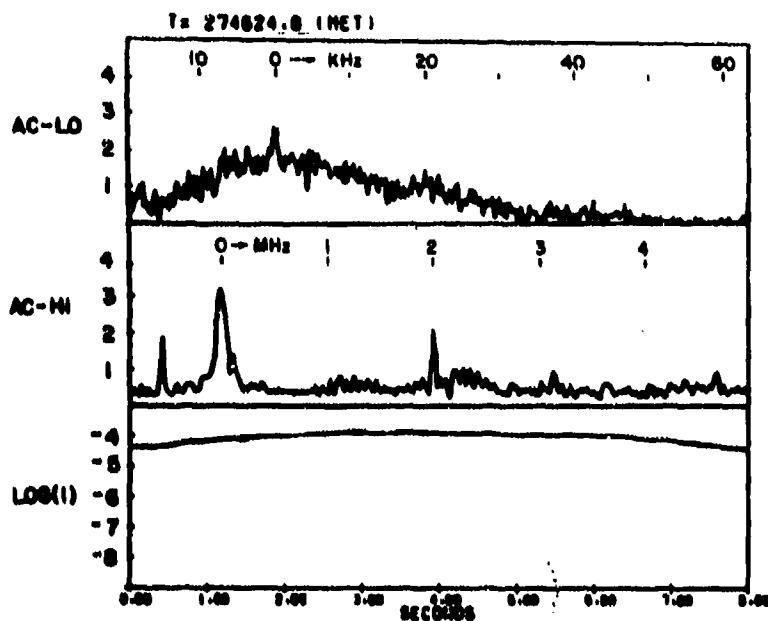
Figure 8. - Continued.

(d) Electrostatic spectra over low- and high-frequency ranges and electron current versus time. Interval 23.
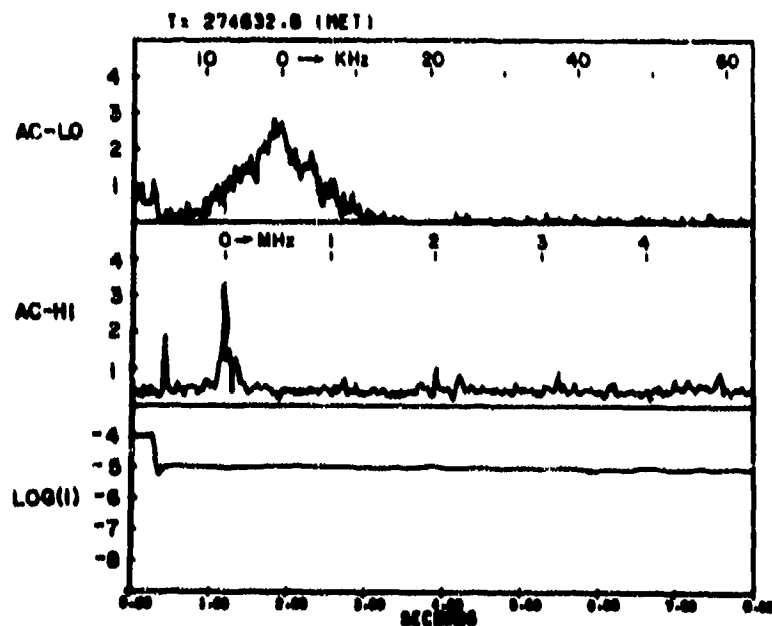
(e) Electrostatic spectra over low- and high-frequency ranges and electron current versus time. Interval 24.

Figure 8. - Continued.

65
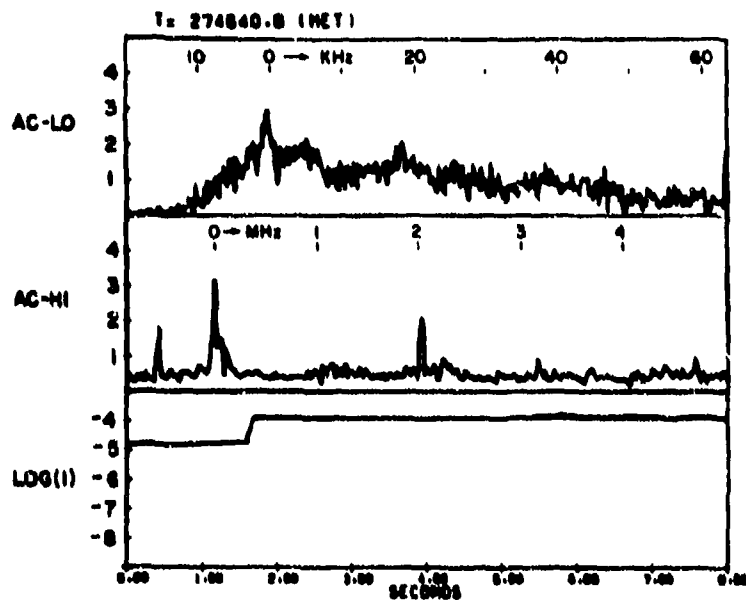
(f) Electrostatic spectra over low- and high-frequency ranges and electron current versus time. Interval 25.
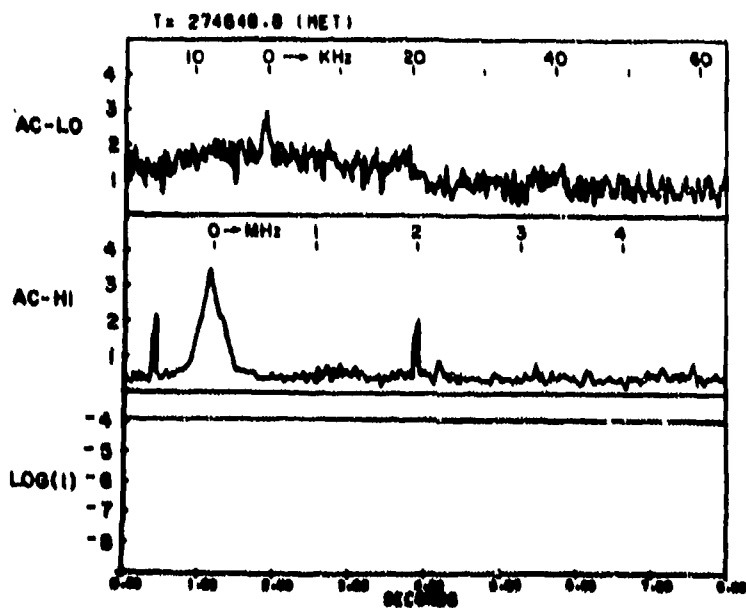
(g) Electrostatic spectra over low- and high frequency ranges and electron current versus time. Interval 26.

Figure 8. - Concluded.
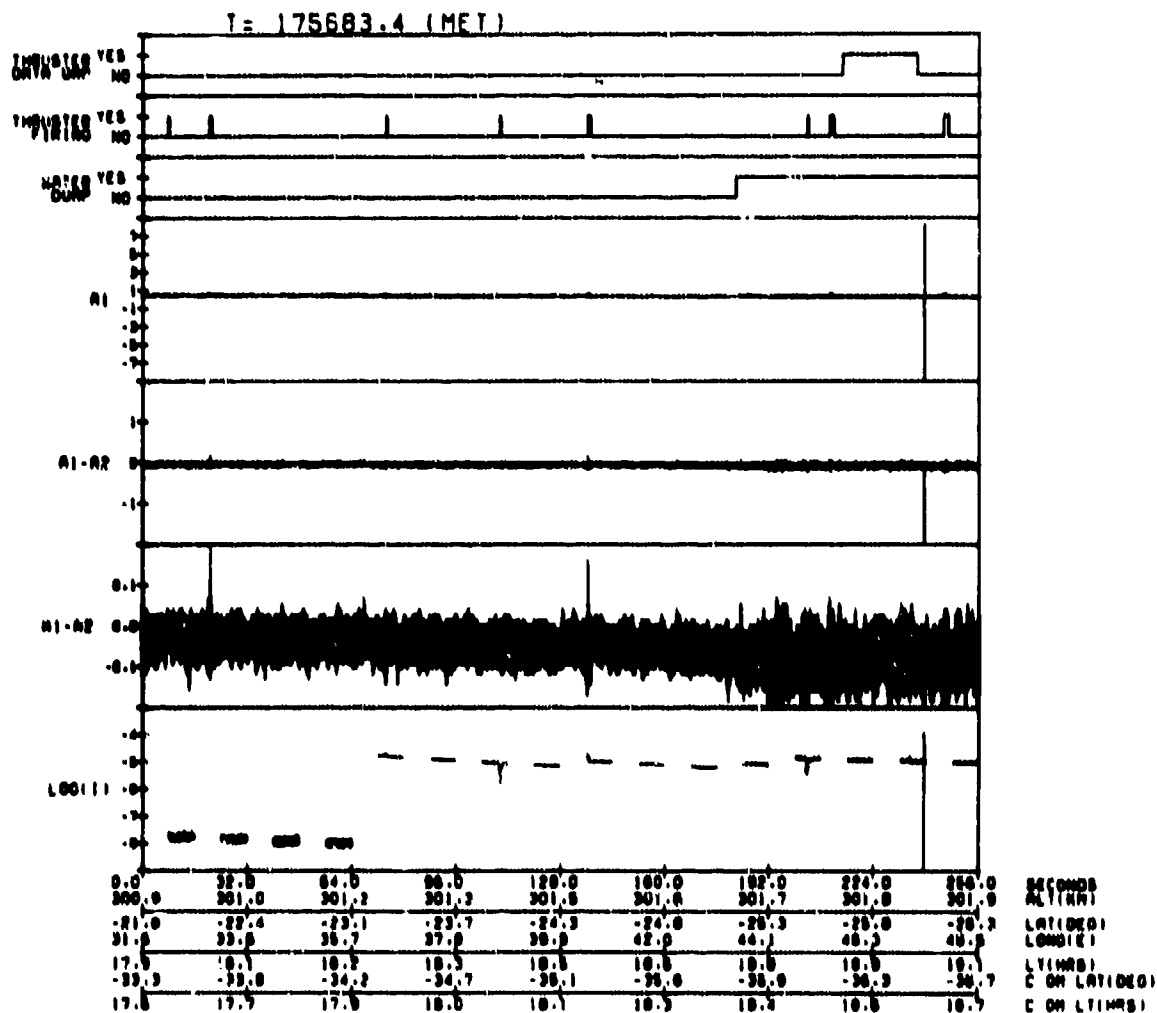
(a) Dump indicator, vehicle potential, electric field, and electron current versus time and orbital position.

Figure ° - Water dump.
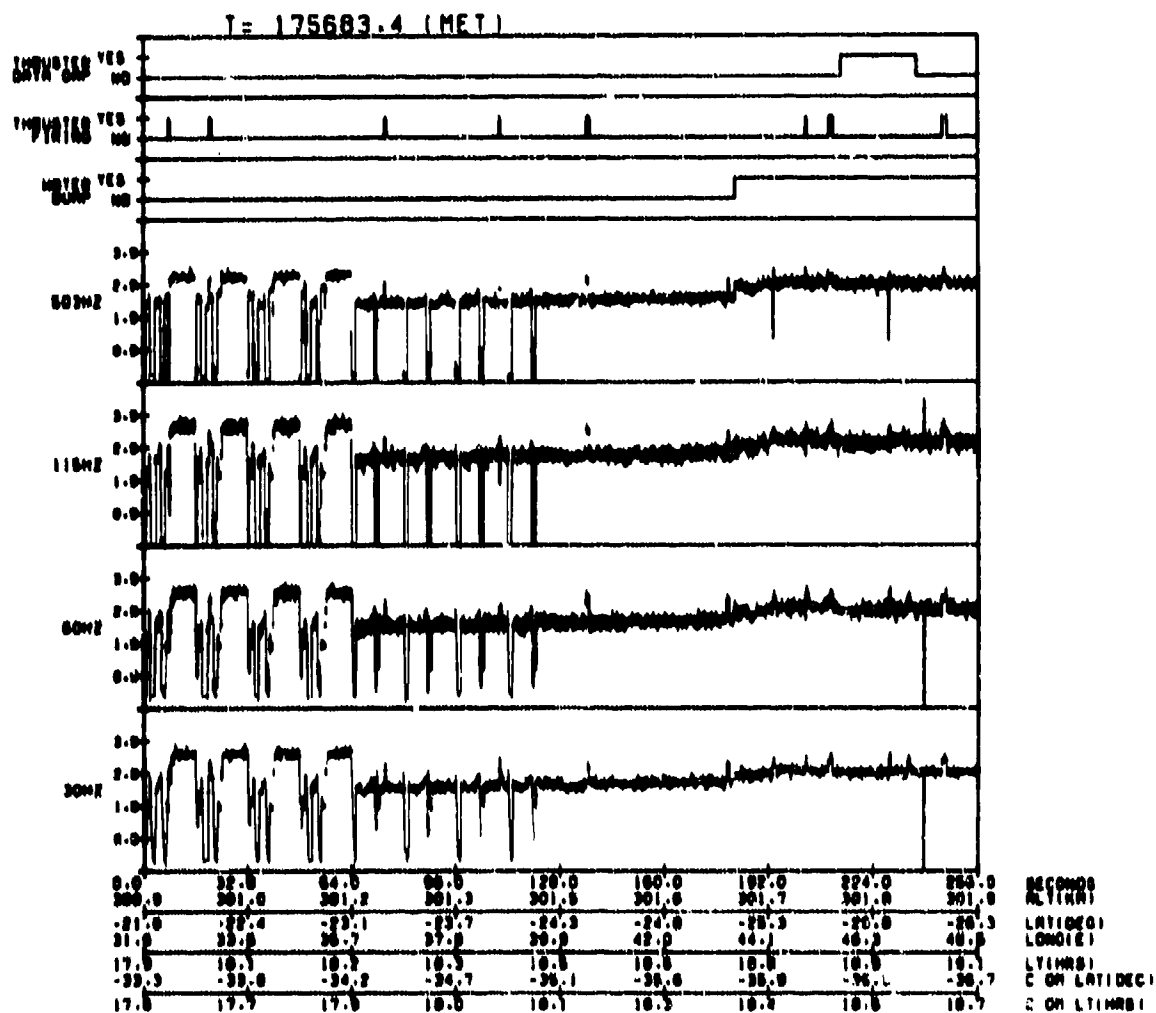
(b) Dump indicator and ΔN/N filter outputs versus time and orbital position.
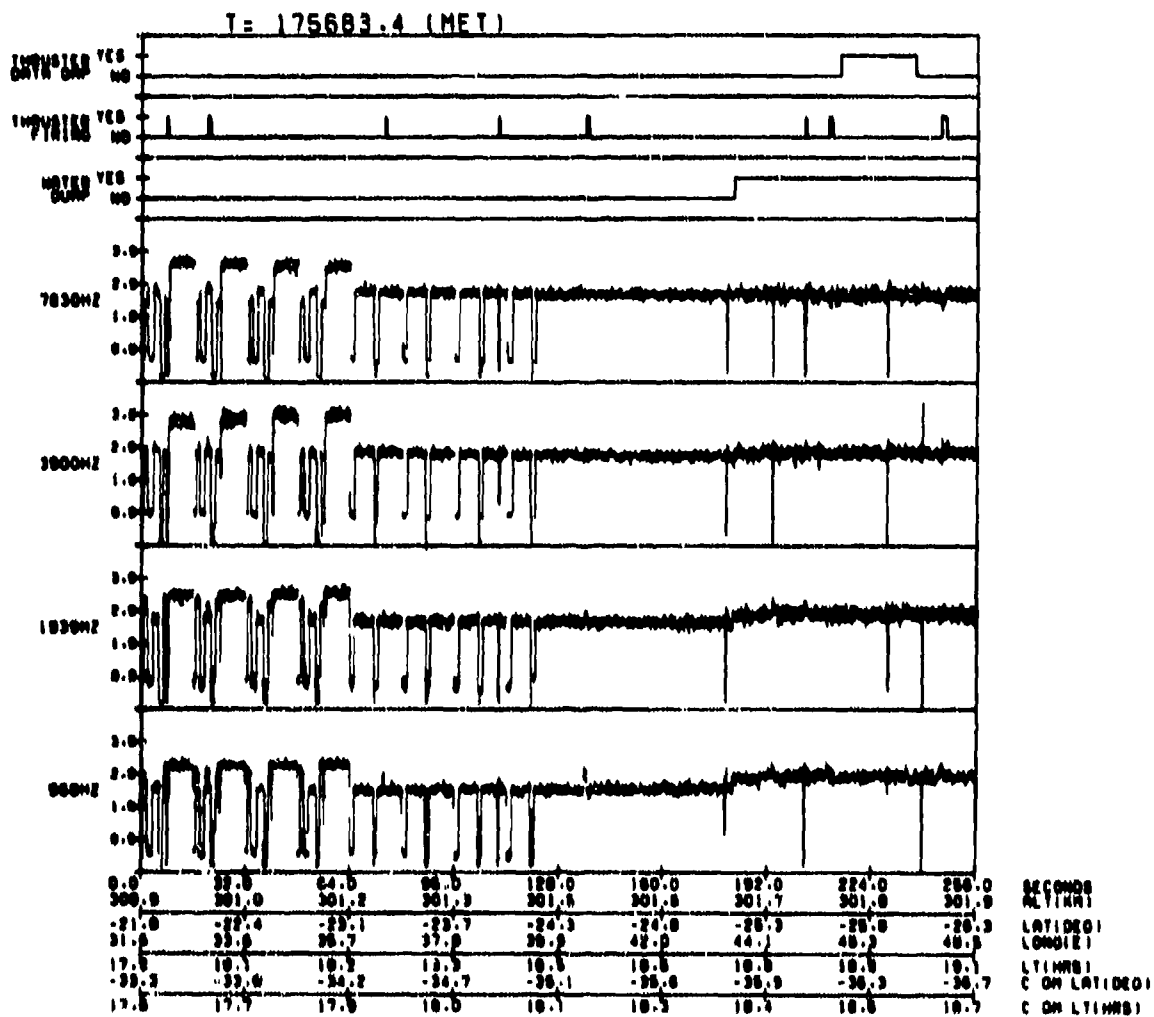
Figure 9. - Continued.

(c) Dump indicator and ΔN/N filter outputs versus time and orbital position.
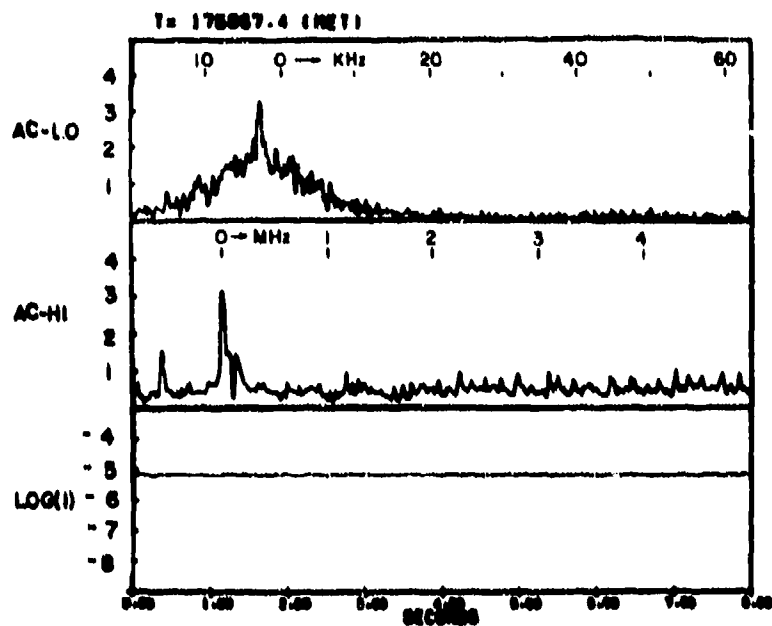
Figure 9. – Continued.

(d) Electrostatic spectra before dump versus time. Interval 22.
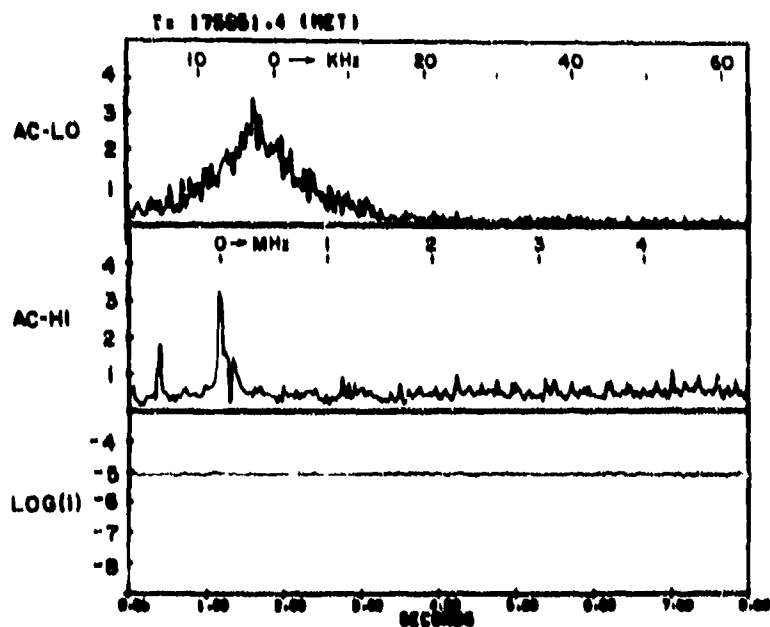
(e) Electrostatic spectra during dump versus time.

Figure 9. - Concluded.

MEASURED ELECTRON CONTRIBUTION TO SHUTTLE PLASMA ENVIRONMENT: ABBREVIATED UPDATE

W. McMahon and R. Salter
Air Force Geophysics Laboratory
Hanscom Air Foce Base. Massachusetts 01731

R. Hills
Tri-Con Associates, Inc.
Cambridge, Massachusetts 02138

D. Delorey
Boston College
Chestnut Hill, Massachusetts 02167

The differential energy spectra of electrons between 1 and 100 eV were measured by an electron spectrometer flown on an early shuttle. This energy range was scanned in 64 incremental steps with a resolution of 7%. The most striking feature that was observed throughout these spectra was a relatively flat distribution of the higher energy electrons out to 100 eV. This is in contrast to normal ambient spectra which consistently show a rapid decline in quantitative flux beyond 50-55 eV. The lower energy (1-2 eV) end of these spectra showed steep thermal trails comparable to normal ambient spectral structure. In general, daytime fluxes were significantly higher than those obtained during nighttime measurements. Quantitative flux excursions which may possibly be associated with thruster firing were frequently observed. Spectral structure suggestive of the N_2 vibrational excitation energy loss mechanism was also seen in the data from some measurement periods. Examples of these spectra are shown and possible correlations are discussed.

INTRODUCTION

The purpose of this experiment was to examine the role of low energy electrons in the interaction between large vehicles and the space environment, and to assess the extent of contamination presented by these electrons. For this purpose, an electron spectrometer was flown on an early shuttle. This instrument was a 127° cylindrical electrostatic deflection analyzer essentially identical to that described in reference 1. Differential energy spectra between 1 and 100 eV were obtained by applying the analyzer voltage in 64 incremental steps. The analyzer resolution was 7% and the stepping increments were set at 7% to match this and thus avoid gaps in the spectral data. Dwell time per step was set at 1.0 sec, thereby requiring 64 secs to scan a full spectrum; this was found to be an undesirably long time period, as will be later discussed. The instrument was mounted near the rear of the shuttle bay with a look direction out over the right wing, along the -Y axis and tilted 12° upward from it.

Before showing the shuttle data it will be useful to first show, by way of contrast, what the ambient or relatively uncontaminated spectra look like. The examples shown in figure 1 are spectra of ambient daytime photoelectrons which were obtained on a rocket flight using an instrument identical to that used on the shuttle. The highest altitude shown, however, is about 80 km below shuttle altitude. These are typical of many hundreds of spectra obtained during several rocket flights

and show four chief characteristics: There is first a steep thermal tail at very low energies (<2eV), only the lower parts of which are seen in these particular spectra. Second is the valley-like structure between 2-5 eV caused by energy loss due to resonant vibrational excitation of N_2 by electron impact -- the so-called nitrogen bite-out. It should be noted, for later reference, that this feature diminishes in the ambient spectra as altitude increases toward 200 km and disappears above this, well below shuttle altitude. Third, in the 20-30 eV region for daytime spectra only, there are several closely spaced peaks due to photoionization of N_2 and O by the intense solar He II line at 304A; this structure is shown here as combined by the limited analyzer resolution to form one broadened peak. And fourth, there is a rapid quantitative decrease in photoelectrons above about 55 eV due to a pronounced decrease in the solar euv flux at higher energies (wavelengths less than about 170A).

MEASUREMENTS

The shuttle spectra showed departures from the ambient characteristics noted above, some of which were expected and some of which were not. Figure 2 shows a typical spectrum which is actually the average of all spectra obtained during this particular data acquisition period. In common with ambient spectra, a thermal tail below 2 eV is seen, as was expected. There is no apparent structure in the 2-5 or 20-30 eV regions which was not unexpected. What was quite unexpected, however, is the continued relatively flat distribution of electrons having energies greater than 50 eV, out to the highest energy measured (100 eV). This was the most striking characteristic of these measurements; it was present in every spectrum taken during the flight. The source of these higher energy electrons is, as yet, unexplained. But it clearly indicates the need for one experimental change for the next flight: that is to extend the energy range coverage out to 500 or 1000 eV to see where, or if, the expected shoulder can be found. Figure 3 shows three individual spectra obtained in this same measurement period during which the vehicle went from daylight to darkness. As shown, the quantitative electron flux decreases significantly at night, clearly suggesting that locally generated solar photoelectrons contribute in large measure to the daytime electron environment of the shuttle. Two of these spectra also show considerable scatter or data point excursions. In an attempt to correlate this scatter with other vehicle events, periods of thruster firing are shown, although this cannot be considered a direct source of electrons in the energy range shown here. It should be noted that thruster firings mentioned herein refer to all cases to the verniers. There was very little firing of the primary thrusters during any of these data acquisition periods, and what little there was appeared to have no effect on the data. Thruster operation involves a hypergolic reaction between monomethylhydrazine (MMH) and nitrogen tetroxide (N_2O_4) and while this generates what might be called a hot plasma, it cannot directly contribute electrons having energies much greater than about 2 eV. Some subsequent accelerating mechanism would clearly be required if thruster activity is to be associated with these flux excursions.

Thruster firings occur for a minimum of 80 msec, although in many cases one or more were active for considerably longer periods of time. But this points up another way in which the experiment should be changed for a subsequent flight: The present scan timing sequence (1sec/step, 64sec/scan) is simply too long to observe, over the better part of a spectrum, any short term phenomenon which may have occurred. Very short term phenomenon could therefore appear as the excursion of a

single data point, or a few consecutive points, which may account for the apparent scatter effect. For the present data to be associated with thruster firing, however, requires that some sort of delayed reaction or response time be inferred -a seemingly plausible concept. But the apparent response time involved is not manifested in any constant manner. The topmost spectrum of figure 3, for example, shows a sharp drop in flux levels approximately 2 seconds after thruster firing ceased while the middle spectrum shows a delay of 13-14 seconds before a similar response is observed. Additional illustration of this is seen in figure 4 which shows three individual spectra taken during a common nighttime period. The lowest spectrum shown (C) was completely free of thruster firing during its measurement and for a period of 15 minutes prior to that. The topmost spectrum (A) was taken following a period of moderate thruster activity and in one during which there was nearly continuous firing of all six vernier thrusters. The middle spectrum (B) was taken immediately following this but represents a largely thruster-free measurement; firing occurred during the very early (low energy) segment of this spectrum and then ceased for all data points taken above 3.4 eV. This spectrum seems to indicate a tendency to return to the normal lower nighttime flux levels, but has not reached this point some 50 seconds after thruster firing ceased. These apparent variations in response time, therefore, tend to obscure the possible association of thruster firings with data perturbations.

An enhanced view of the steep thermal tail below 2 eV is seen in the spectrum of figure 5. This suggests that the generally negative (1-3 volts) vehicle potential had decreased or gone positive at this time, allowing more of the very low energy electrons to enter the analyzer, thus allowing more of this tail to be observed. This is supported by independent measurements from a companion experiment (ref. 2), the data from which indicates a vehicle potential of about +0.8 volts at the time this spectrum was taken.

That thruster firings may contribute to higher flux levels is consistent with the data shown next in figure 6. This relates to a 35 second orbital maneuvering system (OMS) burn which occurred during this period. The OMS employs the same hypergolic reaction as described for the thrusters except that each of the two engines in this system generates 6000 pounds of thrust as compared to only 24 pounds for each of the vernier thrusters. This figure shows two typical individual spectra, the lower of which was taken prior to the OMS burn, and the upper taken during and immediately after the burn. Only a little over two minutes separated these individual spectra in time and yet a difference of an order of magnitude or more is seen in the flux levels.

A substantial number of spectra were obtained while the shuttle was in a bottomto-the-sun attitude and while these were almost exclusively daytime data, their flux levels were among the lowest of the flight. Typically, these spectra were indistinguishable from nighttime measurements. It seems likely that the term "bottom-to-the-sun" can explain these low fluxes: There was almost certainly large numbers of solar photoelectrons being generated at the sunlit bottom surfaces of the wings and fuselage during these periods. The subsequent trajectories of these electrons would largely be governed, exclusive of collision processes, by the geomagnetic field lines. And no matter what the orientation of these lines, it seem unlikely that many of these electrons could migrate into the shuttle bay area and enter the acceptance cone of the analyzer.

There was little or no thruster activity during all measurements of this mode and there was very little variation between individual spectra obtained during these periods; this is again consistent with the possible correlation data perturbations and thruster firing. There was a passage from day to night in the 10 minute bottom-to-the-sun run illustrated in figure 7 which did not appear to have any effect on spectra except at very low energies. This is an averaged spectrum but it very closely represents all those obtained, both day and night, except for the 1-3 eV region where an enhanced view of the thermal tail again appears. The maximum data point for this tail was a factor of 2 or more higher than shown in this averaged spectrum, and was fairly constant in the daytime spectra. Following eclipse, this dropped immediately by a factor of 8 to 10 and remained quite constant in all of the night spectra. This again suggests a diminished vehicle potential and, again, this was supported by the independent measurements of reference 2. It also indicates the influence of daytime solar photoelectrons on the low energy (1-3 eV) region of these spectra but not elsewhere which, in turn, indicates the influence of collision processes since most of these electrons must have come from the sunlit side. Note also that the data points in the extreme low energy region of this spectrum are seen to be reduced substantially below the maximum point, an effect observed in all the spectra of this run. This was due, almost certainly, to geomagnetic shadowing. The orientatin of the geomagnetic field lines throughout the run was toward the aft quarter and downward with respect to the vehicle, or to the right and downward with respect to the analyzer look direction. This means that some electrons spiraling about field lines in trajectories that would normally bring them within the acceptance cone of the analyzer could, in some cases, be intercepted by vehicle or payload components and thus be lost to collection. The lower energy electrons are most vulnerable to such shadowing effects because of their shorter Larmor radii. In the case of the high termal tail seen earlier in which no such effect was observed, the field lines were oriented to the left, or forward, and above, where no vehicle or payload components existed to obstruct the electron paths.

Figure 8 shows a spectrum typical of all those obtained during two of these bottom-to-the-sun periods. These were daytime measurements during which there were no thruster firings and virtually no difference between individual spectra. Note the valley-like structure in the 2-4 eV region. This feature was present in all spectra of these two consecutive runs and is strongly suggestive of the N_2 vibrational excitation energy loss mechanism (the nitrogen bite-out) mentioned earlier as a characteristic of ambient spectra below 200 km. This would not be expected to appear in ambient spectra at the shuttle altitude (300 km). But if sufficient N_2 were present, the mechanism that produces this structural feature should prevail. Residual N_2 from the MMH/N_2O_4 thruster reaction might possibly have provided this. The question of why this feature was seen only in these data, but seen consistently throughout them, has no immediate answer.

SUMMARY/CONCLUSIONS

Undoubtedly, the most remarkable feature of these measurements is the relatively flat spectral distribution of higher energy electrons which was consistently observed but remains essentially unexplained. And while the data associating quantitative electron flux excursions with thruster and OMS firings can be considered pursuasive, it cannot be considered conclusive based on these data alone. The data do seem conclusive in indicating that locally generated solar

photoelectrons contribute substantially to the daytime electron environment of the shuttle. Other observed departures from the general characteristics of these spectra also lend themselves to explanations as, for example, geomagnetic shadowing or the N_2 bite-out mechanism. And the occasional enhanced observations of the steep thermal tail is probably explained by departures in vehical potential levels. Many questions remain, however. A reflight of this experiment, modified as earlier described, should provide very useful additional data and, possibly, some answers.

REFERENCES

1. McMahon, W.J. and Heroux, L., Rocket Measurement of Thermospheric Photoelectron Energy Spectra, J. Geophys. Res., 83, 1390 (1978).
2. Smiddy, M; Sullivan, W.P. Girouard, D.; and Anderson, P.B., Shuttle Electrical Environment, Proceedings of Spacecraft Environmental Interactions Conference, Paper I-4, NASA Lewis Research Center, (1983).

Fig. 2 Electron energy spectrum typical of all shuttle measurements. The paramount feature is the relatively flat distribution for energies greater than 50 eV out to the highest measured. The coordinates of all figures showing shuttle spectra are common to facilitate comparisons between them.

Fig. 1 Examples of typical ambient electron spectra, obtained under conditions of minimal contamination, for comparison with shuttle measurements.

76

Fig. 4 Additional comparison of individual nighttime spectra with thruster firing periods.

Fig. 3 Individual spectra from day-night measurement period showing daytime fluxes considerably higher than those of nighttime spectra. Data point excursions and their possible correlation with thruster firings are discussed in the text.

77

ORBIT 4.6

BCGNT/NIGHT

END OF 35 SEC.
OMS BURN

POST-BURN

PRE-BURN

RELATIVE FLUX (ELECTRONS/SEC-CM**2-SR-EV)

ENERGY (EV)

Fig. 6 Before and after spectra related to short
OMS burn. The apparent delayed response
of flux levels to the burn is seen. These
spectra were obtained about two minutes
apart.

ORBIT 16.8

CBGG/NIGHT - MET= B4553

MIN. THRUSTERS

$V_{gs} = +0.8$

RELATIVE FLUX (ELECTRONS/SEC-CM**2-SR-EV)

ENERGY (EV)

Fig. 5 Enhanced view of thermal tail, apparent-
ly due to varying vehicle potential.
This potential had departed from its
usual slightly negative value to about
+0.8 volts at the time this spectrum
was taken.
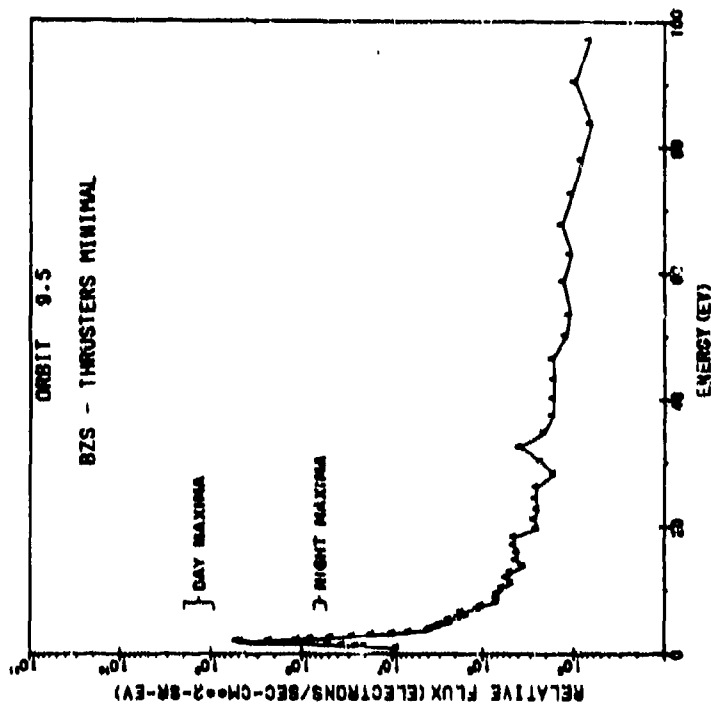
Fig. 7 Bottom-to-sum spectrum representative of those obtained during day-to-night measurement period. Beyond about 3 eV there was no day/night difference in any of these spectra. A diminished but constant vehicle potential coincided with an enhanced view of the thermal tail, the maximum point of which was seen to drop rapidly following eclipse. The effect of geomagnetic shadowing is also seen in the extreme low energy region.
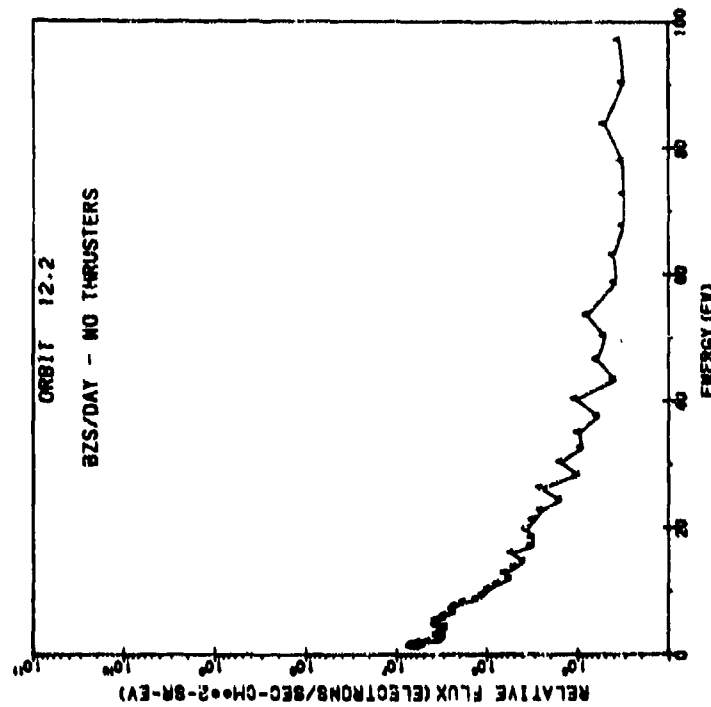
Fig. 8 2-4 eV spectral structure suggestive of the N_2 vibrational excitation energy loss mechanism.

LABORATORY STUDIES OF KAPTON DEGRADATION IN AN OXYGEN ION BEAM

Dale C. Ferguson
National Aeronautics and Space Administration
Lewis Research Center
Cleveland, Ohio 44135

Results are presented from a preliminary laboratory investigation of the degradation of the widely used polyimide Kapton under oxygen ion bombardment. Recent space shuttle flights have shown that Kapton and some other materials exposed to the apparent "ram" flow of residual atmosphere (at orbital velocity in low Earth orbit) lose mass and change their optical properties. It has been hypothesized that these changes are caused by chemical interaction with atomic oxygen, aided by the 5-eV impact energy of atmospheric oxygen atoms in the ram.

In the laboratory investigation the atomic oxygen flow was simulated by a flow of oxygen ions. The ions were generated by a discharge in a microwave resonant cavity, accelerated and decelerated electrostatically, and impacted on Kapton targets in a high vacuum. Tests were also performed using a non-reactive gas, argon, in place of the reactive oxygen. Oxygen-bombarded samples showed a loss of material and a change in optical properties very similar to those of samples returned by the space shuttle. Scanning electron microscope photographs of the oxygen-ion-bombarded samples also showed structures strongly resembling those of samples from the shuttle. Argon-bombarded samples showed no significant material loss or change of optical properties or surface struc-ture under SEM.

All bombarded samples showed changes in surface composition when examined by low-energy windowless energy difference X-ray analysis (EDAX) and Auger spectroscopy. Oxygen-bombarded samples showed an apparent decrease in surface carbon as compared with pristine samples, whereas argon-bombarded samples showed a variable increase in surface carbon, depending on where the samples were located in the argon ion beam. These changes are attributed to sputtering.

The reaction rate under O+ bombardment seemed to be independent of inci-dent energy over a wide range of energies. Although the flux of thermal ions in this experiment was much greater than the accelerated flux, the observed Kapton degradation was limited to the beam area and ram flow direction. This is consistent with an activation energy above the thermal energies but well below the beam energies.

The results reproduce well the material loss, optical changes, SEM surface structure, and "ram" directionality of the samples returned by the shuttle. These factors, along with the lack of degradation under argon ion bombardment, are convincing evidence for ram flow oxidation as the mechanism of degradation.

INTRODUCTION

Kapton and other materials (such as carbon coatings and paints) undergo weight loss and surface degradation in low Earth orbit (ref. 1). Kapton, a polyimide with wide applications in spacecraft technology, experiences surface roughening on micrometer length scales, a change in surface appearance from a glossy transparency to a milky translucence, a loss in weight, and changes in its optical properties. These changes, first noted on the early space shuttle flights (ref. 1), have important implications for conducting extended operations using Kapton in low Earth orbit. Kapton has been used for thermal control coatings and electrical insulation and has been proposed as a flexible substrate for large solar arrays because of its excellent temperature stability, extremely low surface conductivity, and flexible strength. It is important to know the mechanism for deterioration in low Earth orbit so that Kapton can be modified, coated, or replaced with other materials in critical applications.

It has been suggested that interaction with the residual atomic oxygen atmosphere is the mechanism of degradation (ref. 1). The major atmospheric constituent at shuttle altitudes is atomic oxygen. Each atom of oxygen impacts an orbiting vehicle with an energy of about 8×10^{-19} J (5 eV), equivalent to the impact energy of thermal atoms at about 60 000 K. High-temperature oxidation, about which little is known, may then be the reaction leading to mass loss, change of surface properties, etc.

Although oxidation is a likely hypothesis as the mechanism of degradation, other possibilities exist. The mass loss might be due to low-energy sputtering, for example. It is well known that sputtering thresholds for metals seem to be higher than the impact energies of atoms and molecules in low Earth orbit but such thresholds have never been measured for complex organic materials. Also, chemical reactions with other species abundant in low Earth orbit, such as molecular nitrogen, could not be excluded out of hand.

GOALS AND APPROACH

It is desirable to understand the mechanism of the orbital interaction of Kapton and other materials with atomic oxygen, to see whether the interaction is chemical or sputtering in nature, to determine reaction rates and temperature and energy dependences, to investigate the possibility of interfering with the interaction through the use of protective coatings or other materials, and to develop techniques for testing materials before flight. At Lewis Research Center it was decided to attempt the simulation of conditions in low Earth orbit in order to investigate these matters. Since it is difficult to accelerate neutral atomic species to orbital energies, it was decided to use accelerated ions in the Lewis simulation. It is clear from work on sputtering (ref. 2) that charge exchange with the surface can occur long before the momentum exchange, so that by the time the reaction energy is imparted by the incoming ions, they may be identical to neutral atoms for chemical purposes.

Thus an attempt was made to simulate the impact conditions in low Earth orbit by acceleration and impact of oxygen and other ions. Then the exposed specimens were analyzed and the results compared with those reported from shuttle flight experiments and other laboratory simulations. Reaction rates

and surface compositions were found. Finally an attempt was made to understand the laboratory results and to see what light they might shed on the flight results and on the reaction mechanism in order to simulate, understand, and suggest ways to control the reaction in low Earth orbit.

EXPERIMENTAL PROCEDURE

For the preliminary results reported herein, a tunable microwave resonant cavity (fig. 1) was used to dissociate and ionize technical grade (99.5 percent) oxygen gas. The gas was leaked into a glass container within the microwave cavity and, after ionization, was accelerated electrostatically to impact samples of Kapton. The experiment was done in vacuum tank 8 of the Electric Propulsion Laboratory at Lewis. Tank 8 is a horizontal circular cylinder about 1 meter in radius and 4 meters in length. Tank pressures were maintained by diffusion pumps at about 1.3×10^{-2} Pa (10^{-4} torr) during beam operation and at about 1.3×10^{-4} Pa (10^{-6} torr) with the beam off. The help of Shigeo Nakanishi of Lewis was invaluable in obtaining the experimental results reported herein.

The microwave cavity used a maximum of 100 W of radiation at a frequency of 2450 MHz. The cavity was electrically biased at a voltage of approximately 800 V, and the accelerating grid (made of molybdenum that was glass coated on one side) was biased to approximately -200 V. The ion beam produced was about 5 cm in diameter and diverged as it traversed the space between source and samples. A typical oxygen flow rate into the microwave cavity was about 4.2×10^{-7} m^3/s (25 standard cm^3/min).

The Kapton samples were supported by a strip heater with attached thermocouples. Source-to-sample distance was 10 cm for some trials and 23 cm for others. The samples were within 5 cm of the axial beam center. The plasma mean free path in all cases was longer than the source-to-sample distance. The beam was decelerated for some samples by biasing the aluminum backing to retarding potentials of up to 1000 V. The heater strip was insulated from the samples by two layers of 2.5×10^{-3}-cm-thick (1-mil) Kapton tape and from the tank wall by a fiberglass mounting beam. All wires in the cavity were covered with Teflon tubing to reduce glow discharges in the tenuous gas.

A retarding potential analyzer (RPA) that could be swung into and out of the beam was used to determine the beam current density. Typical RPA currents were 185 µA, which when divided by the RPA area of 13.4 cm^2 gives an average central beam current density of about 14 µA/cm^2. The beam was spectroscopically analyzed with a 0.5-m Jarrell-Ash spectrometer with 0.01-nm resolution. The spectrum shows that most of the beam consisted of singly ionized atomic oxygen, although lines of neutral atomic oxygen were prominent near the sample distance because of their greater radiative lifetimes. Equilibrium floating potentials on the heater strip while the beam was in operation were measured on the thermocouple wires to be in the range 400 to 500 V.

While the oxygen beam was operating, a faint white glow extended about 5 mm in front of impacted surfaces. Behind the sample holder a distinct greenish tinge could be seen in the diffuse glow of the beam. The white glow can be attributed to continuum radiation from oxygen recombination at the surface. The green glow appears spectroscopically (ref. 3) to be from the

first negative bands of O_2^+, which one suspects are caused by ionization the recombined oxygen by the impinging ion beam.

Table I gives the parameters of the Lewis preliminary feasibility studies. Fluxes were calculated from RPA currents and estimated beam divergence and total fluence was calculated from fluxes and exposure times. In each case, the expected thermal flux of neutral oxygen was greater than the ion flux in the beam, and yet degradation occurred only in areas where the beam actually struck the samples. Thus the impact energy must be important to the degradation.

RESULTS AND ANALYSIS

Visual inspection of the bombarded surfaces showed that where the oxygen beam had struck, the smooth, yellow transparent surface of the Kapton had changed to a milky yellow translucence. Argon-bombarded samples at the same low fluence showed no such change, only a thin transparent metallic film that EDAX showed to be molybdenum sputtered from the uncoated side of the accelera-tor grid. Under oxygen bombardment, shadowed regions of the Kapton tape sur-rounding the sample holder showed no degradation, nor did areas outside the beam. In one case (11/24/82) the Kapton tape in the center of the beam showed a total loss of Kapton, with only the sticky silicone adhesive remaining. The aluminum back sides of argon-bombarded sample strips were scorched and black-ened near the edges. EDAX later showed this to be a thin molybdenum coating, again presumed to be sputtered from the accelerator grid.

Under the scanning electron microscope the oxygen-bombarded samples had a carpetlike texture, with structures about 1 μm and smaller. They looked quite similar to samples returned by STS flights (fig. 2 from ref. 4). In contrast, pristine samples and argon-bombarded samples of Kapton were smooth at all magnifications.

Also, under a scanning electron microscope, an indication was obtained that the surface conductivity of Kapton was changed by ion bombardment. Both oxygen- and argon-bombarded samples retained their surface charge (as made visible by changes in magnification) for much shorter times than did the pri-stine control sample. It is not clear whether the change in surface conduc-tivity was due to the presence of sputtered contaminants or in part to changes in surface composition.

Low-energy EDAX analysis of the samples was undertaken with the valued assistance of Paul Aron of Lewis. The instrument used had a windowless detector, which allowed very low-energy electrons to be used. Although EDAX at high energies (2.4×10^{-15} J, or 15 keV) showed the presence of aluminum, silicon, and molybdenum in the bombarded samples (presumably sputtered from the accelerator grid and tank wall fixtures) and their absence in the pristine samples, this was of limited usefulness in analyzing the change in surface com-position of the Kapton. Pristine Kapton, being an extremely good insulator, will acquire a charge through loss of secondary electrons for incident electron energies above about 2.4×10^{-16} J (1.5 keV). Thus the pristine standard would see EDAX electrons of a different energy than those seen by the more conductive ion-bombarded samples.

Furthermore, electrons of 2.4×10^{-15} J (15 keV) energy have a mean free path in Kapton of about 6.4×10^{-4} cm (0.25 mil), which makes bulk composition and geometrical effects (due to the texture of the oxygen-bombarded surface) important in the analysis. For these reasons EDAX at incident energies of 1.6×10^{-16} J (1.0 keV) was undertaken. At this energy the mean free path of electrons in Kapton should be about 7.6×10^{-5} cm (0.03 mil). This would insure that the true surface composition would be measured, allowing only for shadowing on the X-ray counts from textured surfaces.

By taking mass attenuation coefficients and fluorescence yields from Robinson (ref. 5) and assuming a 3 percent metallic mass fraction from sputtered metals, the relative carbon, nitrogen, and oxygen abundances at the surface could be determined. Table II summarizes of the present results on samples at different EDAX electron energies. The composition measured with the 1.0-keV energy was significantly different from the pristine Kapton used as a calibration for both oxygen- and argon-bombarded samples.

These results are insensitive to errors in the total count rate, electron penetration depth, and percentage of metals assumed, largely because the penetration depth is so small that there is less than 20 percent absorption for X-rays from any species. The composition obtained from the EDAX analysis can be compared with that which would occur if pristine Kapton lost 40 percent of its carbon atoms (normalizing to C, N, and O only): 59.4 percent C, 10.1 percent N, and 30.5 percent O. This suggests that the major change in composition of the surface was a severe loss of carbon. Since the electron penetration depths at energies of 4 and 15 keV were so much larger, a loss of carbon only near the surface was also consistent with the measurements made at those energies.

An Auger analysis of other samples done by J. Gordon and R. Hoffman of Case Western Reserve University and communicated to us has confirmed these results for oxygen bombardment (severe loss of carbon) but was quite variable for argon bombardment. It may be concluded that the surfaces of the oxygen-bombarded samples suffered a severe carbon loss, but for the argon-bombarded samples the situation is more complicated. For argon bombardment, composition changes may be due to selective sputtering (ref. 6); for oxygen bombardment, beam deceleration may have made sputtering unlikely. Since chemical interaction was indicated at any rate as the source of surface damage in oxygen bombardment, the major chemical change appeared to be oxidation of carbon on the surface, which then evolved as gaseous carbon monoxide or dioxide, leaving a carbon-depleted surface. This hypothesis is consistent with the reported rapid loss of pure carbon coatings in low Earth orbit (ref. 7).

The surface of the oxygen-bombarded samples became quite soft (easily scratched); abraded sections lost their milky translucence and became yellow and transparent, much like the pristine samples. Because no visible amount of material was left on the scratching implement, the change of optical properties was probably indicative only of a change in surface structure.

The indices of refraction of the samples were measured by ellipsometry. The ellipsometer used a He-Ne laser of wavelength 632.8 nm and had a resolution of ~0.1° in polarizer and analyzer angle. Despite some difficulty in keeping the samples flat, repeatable measurements were obtained, with the following results: although the pristine samples were very similar in optical properties

to their aluminum backing (which proved to be coated by a thin film itself), the ion-bombarded samples were significantly different from their aluminum backing. The real and imaginary parts of the index of refraction are given in table III.

The variation with position on the argon-bombarded sample can be ascribed to variations in the amount of sputtered molybdenum on the surface at different points. Position 2 closely resembled the apparent optical properties of the pristine sample.

Although the samples were aluminum backed, optical measurements were probably not heavily influenced by the aluminum backing because the surfaces of the oxygen-bombarded samples, and in particular of sample 2, were quite opaque. These optical values are probably not intrinsic to oxidized Kapton itself but are indicative of the values as changed by the surface structure, as discussed by Fenstermaker and McCrackin (ref. 8).

At the laser wavelength (632.8 nm) and angle of incidence (70°) used, no specular reflection was observed for sample 2. The observed change in reflectance of the oxidized Kapton may be due to the peculiar surface structure shown in the SEM photographs, which, when disturbed by scratching, reverted to the optical properties of smooth Kapton.

An attempt to calibrate the beam intensity by the changed optical properties of argon-bombarded samples, as described in Mirtich and Sovey (ref. 9), failed because of the thin, sputtered molybdenum film deposited in the present experiment.

Mass loss from the Kapton films was evident from the complete loss of material in the beam center in one trial. An estimate, from the depth of material removed and the measured beam fluxes, of the mass loss rate from two trials is given in table IV. The apparent mass loss rates were much higher than those (~3.72x10^{-24} g/O atom) from shuttle experiments (ref. 10). This may be due to reactions in the tank with thermal oxygen atoms and molecules, which had a much greater flux against the sample than did the ion beam. The absence of reactions outside the beam area can be explained if the activation energy for the reactions is assumed to be supplied only by the energetic ions in the beam. Table V gives calculated reaction rates per thermal collision in the tank, assuming the ideal-gas law and pure oxygen at the tank pressure. These rates are consistent with those found on the shuttle and lend further credence to the hypothesis that the laboratory reaction is the same as that occurring in orbit.

SUMMARY AND INTERPRETATION OF RESULTS

The following aspects of the shuttle-returned samples were reproduced in the Lewis ion beam experiments:

(1) Visual appearance
(2) SEM surface structure
(3) Change from specular to diffuse reflection
(4) Directionality (ram dependence)

In addition, the mass loss would have been consistent with rates seen in orbit if ambient thermal gas in the experiment could share in the activation energy supplied by the beam.

The following findings were new to this experiment and suggest further tests on the shuttle samples:

(1) Reduced scratch resistance of surface
(2) Loss of carbon from surfaces
(3) Enhanced surface conductivity
(4) Confirmation that chemistry is involved in surface structure changes

The structures seen on O^+-bombarded Kapton surfaces seemed to be responsible for the change in specular reflectivity. In addition, the loss of carbon suggested that these surface structures may have been produced by oxygen preferentially attacking certain bonds in the polymer. The bonds that are probably attacked most readily are the C-N bond (E = 3.2 eV), the C-O bond (E = 3.7 eV), and the C-C bond (E = 3.8 eV) (ref. 11), all with energies below the apparent impact energy of atomic oxygen in low Earth orbit. Breaking the C-N and C-O bonds breaks the polymer chain, weakening the material and allowing penetration of succeeding oxygen atoms deeper into the plastic. Furthermore, succeeding breaks of the C-C bonds can allow oxidation of the dangling carbon, leading to a volatile product and mass loss.

CONCLUSIONS

It is encouraging that this simulation of low-Earth-orbit conditions using O^+ ion beams succeeded in qualitatively reproducing all of the observed characteristics of the interaction of Kapton with the Earth's atmosphere in space shuttle flights. Oxidation is undoubtedly responsible, as opposed to sputtering or reaction with other species, since simulation with O^+ was successful and high-energy impact by an inert gas did not produce the observed characteristics of samples returned from orbit. It may be possible to test a variety of materials for reactivity and quantitative mass loss rates by using O^+ ion beams in the laboratory.

Regardless of the specific chemical reaction involved, it has already been found that other materials are minimally reactive or nonreactive. It may be possible to retain the desirable characteristics (radiation resistance, electrical resistance, strength, flexibility, and high-temperature stability) of Kapton for use as a substrate by coating it with less reactive films. Oxygen ion beam bombardment is a feasible method of testing such new materials before using them in space. Much work remains to be done at Lewis and elsewhere in testing materials and clarifying the reactions that take place.

REFERENCES

1. Leger, L. J.: Oxygen Atom Reaction with Shuttle Materials at Orbital Altitudes. NASA TM-58246, 1982.

2. Hagstrum, Homer D.: Low Energy De-Excitation and Neutralization Processes Near Surfaces. Inelastic Ion-Surface Collisions, N. H. Tolk, J. C. Tully, and W. Heiland, eds., Academic Press, 1977, pp. 1-25.

3. Pearse, R. W. B.; and Gaydon, A. G.: The Identification of Molecular Spectra. Third ed. Chapman and Hall, 1963. Plate 7.

4. Leger, L. J., et al.: Space Shuttle Preliminary Contamination Assessment from STS-1 and STS-2. 12th Space Simulation Conference. NASA CP-2229, pp. 281-302.

5. Robinson, J. W., ed.: Handbook of Spectroscopy. Vol. 1. CRC Press, 1974, pp. 28-229.

6. Banks, Bruce A.: Ion Beam Applications Research - a 1981 Summary of Lewis Research Center Programs. NASA TM-81721, 1981.

7. Leger, L.: Oxygen Atom Reaction with Shuttle Materials at Orbital Altitudes - Data and Experiment Status. AIAA Paper 83-0073, Jan. 1983.

8. Fenstermaker, C. A.; and McCrackin, F. L.: Errors Arising from Surface Roughness in Ellipsometric Measurement of the Refractive Index of a Surface. Recent Developments in Ellipsometry, N.M. Bashara; A.B. Buckman, and A.C. Hall, eds., North Holland, 1969, pp. 85-96.

9. Mirtich, Michael J.; and Sovey, James S.: Optical and Electrical Properties of Ion-Beam-Textured Kapton and Teflon. J. Vac. Sci. Technol., vol. 15, no. 2, Mar./Apr. 1978, pp. 697-701.

10. Leger, L. J.: JSC STS-5 Experiments Results. Presented at the NASA Meeting on Evaluation of Oxygen Interaction with Materials (Washington, D.C.), Mar. 14-15, 1983.

11. Billmeyer, Fred W.: Textbook of Polymer Science. Second ed. Wiley-Interscience, 1971, p. 16.

TABLE I. - PARAMETERS OF PRELIMINARY FEASIBILITY STUDIES

Date	Thickness, mils	Material	Ion	Flux $cm^{-2}s^{-1}$	Fluence, cm^{-2}	Impact energy		Sample temperature		Pressure	
						J	eV	K	°F	Pa	torr
11/24/82	1	Kapton tape	O+	$(6-12)\times10^{14}$	1.3×10^{18}	$(0-1300)\times10^{-19}$	0-800	450-500	350-440	1.7×10^{-2}	1.3×10^{-4}
12/08/82	1/2, 1, 3, and 5	Al-backed Kapton	O+	$(2-3)\times10^{13}$	2.1×10^{17}	$(0-80)\times10^{-19}$	0-50	304-309	88-96	1.2×10^{-2}	9.2×10^{-5}
12/09/82	1/2, 1, 3, and 5	Al-backed Kapton	O+	$(2-3)\times10^{13}$	2.4×10^{17}	$(<50)\times10^{-19}$	<30	344	160	1.6×10^{-2}	1.2×10^{-4}
12/22/82	1/2, 1, 3, and 5	Al-backed Kapton	Ar+	$(3-4)\times10^{13}$	5.2×10^{17}	$(1704)\times10^{-19}$	1065	311-347	100-165	5.6×10^{-3}	4.2×10^{-5}

TABLE II. – PERCENTAGE BY WEIGHT OF ELEMENTS C, N, AND O

[Assumes 3 percent metals, normalized to C + N + O = 100.0.]

(a) Argon bombardment (E = 1.6x10^{-16} J, or 1000 eV)

Electron energy		Element	Element content, wt %	Pure Kapton content, wt %
J	keV			
1.6x10^{-16}	1.0	C N O	58.1 8.5 33.4	71.1 7.2 21.6
6.4x10^{-16}	4.0	C N O	66.9 6.5 26.5	71.1 7.2 21.6
2.4x10^{-15}	15.0	C N O	72.8 6.6 20.6	71.1 7.2 21.6

(b) Oxygen bombardment (E $\leq$ 4.8x10^{-18} J, or 30 eV)

1.6x10^{-16}	1.0	C N O	61.2 7.0 31.8	71.1 7.2 21.6
6.4x10^{-16}	4.0	C N O	70.4 7.1 22.4	71.1 7.2 21.6
2.4x10^{-15}	15.0	C N O	66.8 8.6 24.6	71.1 7.2 21.6

TABLE III. – COMPLEX INDICES OF REFRACTION FROM ELLIPSOMETRY

Ion	Sample	n (real)	K (imaginary)
O$^+$	1	1.16	^{a}-0.22
O$^+$	2	2.72	-0.34
Ar$^+$	1(position 1)	2.4±0.4	-0.8±0.6
Ar$^+$	1(position 2)	1.0±0.3	2.2±0.1
Pristine		0.5±0.2	1.9±0.1

^{a}Errors for the oxygen-bombarded samples are <0.1 in both parts of the index of refraction.

TABLE IV. – DERIVED RATES OF REACTION ASSUMING ONLY OXYGEN ION BEAM REACTION

Date	O$^+$ fluence, cm^{-2}	Rate, g/O$^+$ ion	Method
11/24/82	1.3x10^{18}	>2.8x10^{-22}	Total loss of 1-mil layer
12/09/82	2.4x10^{17}	≥5x10^{-22}	SEM photographs

TABLE V. – DERIVED REACTION RATES ASSUMING AMBIENT OXYGEN REACTIONS

Date	Thermal fluence	Reaction rate, g/collision
11/24/82	~1.9x10^{21}	>2x10^{-25}
12/09/82	~9.4x10^{20}	≥1x10^{-25}
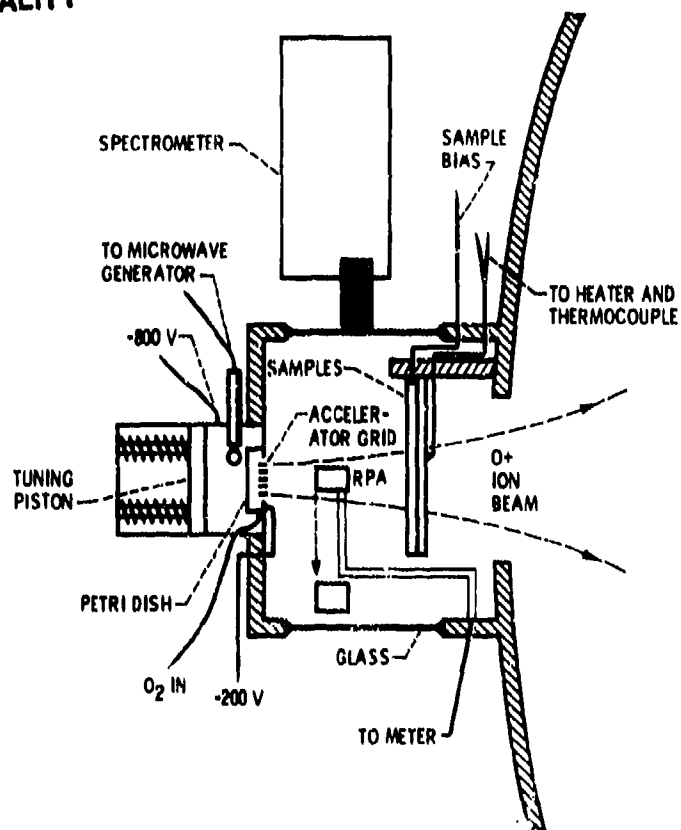
Figure 1. - The experimental setup.

(a) Lewis Research Center O+ beam exposure.
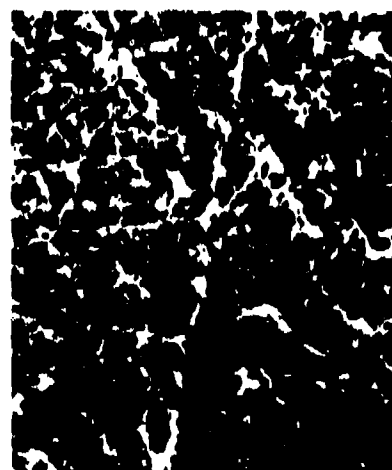
(b) STS-2 orbital exposure.

Figure 2. - Surface structure of exposed samples. SEM magnification 10,000X.

ELECTRON BEAM CHARGING OF SPACE SHUTTLE THERMAL PROTECTION SYSTEM TILES

John V. Staskus
National Aeronautics and Space Administration
Lewis Research Center
Cleveland, Ohio 44135

Six space shuttle reusable surface insulation tiles were tested in the NASA
Lewis Research Center's electron bombardment test facility. The 30-cm-square
specimens were assembled by using the same materials and techniques used to
apply the tiles to the space shuttle and were composed of 15-cm- and 20-cm-
square tiles and pieces on 0.6-cm-thick aluminum substrates. There were two
specimens of each of three thicknesses. One specimen of each thickness had
gaps of less than 0.1 cm between tiles, and the other had gaps of approximately
0.15 cm. The specimens were exposed to monoenergetic electron beams (2 to
25 keV) with nominal fluxes of 0.1 and 1 nA/cm^2. Tests were conducted with
both grounded and floating substrates. The data presented include charging
rates, equilibrium potentials, and substrate currents. There is evidence that
discharging occurred.

INTRODUCTION

The advent of polar orbit space shuttle missions has raised new concerns
about spacecraft charging - concerns formerly associated with high-altitude
(i.e., geosynchronous) satellites. Charging of dielectric materials by multi-
kilovolt-energy electrons can cause arc discharging, which may result in rf
noise that can interfere with communications and may induce voltage transients
in the electrical system that can upset or damage low-level electronic circuit-
ry. At the request of the Air Force Geophysics Laboratory and with specimens
supplied by the NASA Johnson Space Center low-keV electron beam charging tests
were conducted in the electron bombardment test facility at the NASA Lewis
Research Center.

Tests conducted previously at the Rome Air Development Center investigated
the response of shuttle tile materials to electron beams with energies from
10 keV to 1 MeV (ref. 1). In that work discharges were detected as current
pulses to a substrate. This work investigated the charging behavior of surface
insulation tiles from the shuttle's thermal protection system (described in
refs. 2 to 4) when subjected to monoenergetic electron beams with energies of
2 to 25 keV.

TEST SPECIMENS

The test specimens provided by Johnson consisted of 0.6-cm-thick by 30-cm-
square aluminum plates with shuttle tile pieces attached. The materials and
techniques used were the same as those used to apply the tiles to the space
shuttle. There were two specimens of each of three thicknesses (1-1/4 cm,

2-1/2 cm, and 5 cm). The thinnest tiles (20 cm square) were white and the others (15 cm square) were black. One specimen of each thickness had gaps of less than 0.1 cm between tile pieces and the other had gaps of approximately 0.15 cm. Each specimen contained at least one full uncut tile. Most of the tile pieces had 3x5 dot matrix identification code characters stenciled on them - black on the white tiles and yellow on the black tiles. The 5-cm-thick specimen with large gaps had a filler material that appeared to be folded glass fabric in the gaps, with the fold at the exposed surface. Figures 1 to 9 show edges and faces of the six specimens. Capacitances measured from a conductive sheet placed on the tiles to the aluminum substrate were approximately 75 pF for the 1-1/4-cm-thick tile specimens, 50 pF for the 2-1/2-cm-thick specimens, and 30 pF for the 5-cm-thick specimens.

CONFIGURATION AND TESTS

The specimens were tested individually in the 2-m-long by 2-m-diameter electron bombardment test facility (ref. 5). They were mounted approximately 1.2 m from the electron source with the specimen's face normal to the source-target axis. The substrate was supported on Lucite posts so that tests could be conducted with the substrate floating as well as grounded. In the grounded substrate configuration an electrometer was used to monitor substrate current collection. The edges and rear of the substrate, which were not covered with shuttle tiles, were covered with Kapton to minimize the substrate's collection of particles other than the beam electrons intercepted by the irradiated surface.

The capacitance measured between the substrate and its vacuum chamber environment was approximately 20 pF. This would also be an upper limit to the capacitance expected between the exposed tile face and the chamber environment in parallel with the 30- to 75-pF capacitance across the tile to the substrate.

Noncontacting electrostatic voltage probes were used to measure potentials across the tile surface and on the substrate when it was floating. For early tests a single probe was available and was swept across the tile surface at a separation of approximately 0.2 cm. When the substrate was floating, a small patch of metal connected to the substrate was placed in the path of the probe in order to monitor the substrate's potential. The patch was shielded from direct interception of beam electrons, but the substrate was less well isolated from other particles in its environment. For later tests a second probe continuously monitored the substrate from behind.

The tests consisted of exposing the specimens to monoenergetic electron beams of 2-,5-,10-,15-,20-, and 25-keV energy with nominal fluxes of 0.1 and 1 nA/cm^2. The data presented herein consist of current to the specimen substrate read with an electrometer, potential profiles across the sample obtained by periodically sweeping a noncontacting voltage probe across the specimen's face, and time-exposure photographs of the irradiated surface made with a camera located outside one of the vacuum chamber windows.

RESULTS

A typical test began with exposure of the specimen to the electron beam while the voltage probe was sweeping across the tile surface. This gave an

indication of the charging rate of the uncharged surface during the initial seconds of exposure. A single point on the surface could not be monitored continuously as the presence of the voltage probe would shield that point from charging by the electron beam. Generally the tile surface was charged to nearly its equilibrium potential in less than 1 min from the time of initial exposure. Figure 10 illustrates the charging behavior. It shows the charging of one of the thinnest, highest capacitance specimens for two electron beams with order-of-magnitude different fluxes. As would be expected, there is approximately an order-of-magnitude difference in the time taken to reach a given potential in the two beams. Figure 11 presents the equilibrium surface potentials as a function of beam energy for the six specimens. The range of potentials observed across a specimen's surface is indicated by symbols joined with a vertical line. The charging of the tile surfaces to within 2 kV of the beam accelerating potential suggests that the secondary electron emission coefficient's second crossing of unity occurs at approximately 2 kV (ref. 6). Table I presents the substrate currents for the six specimens at the ends of the tests.

An interesting observation made in some of the tests was that the potential of the dot matrix characters on the tile was sometimes greater than the beam accelerating potential. This could conceivably occur if the secondary electron coefficient of the character paint were sufficiently less than that of the surrounding tile. The characters would rapidly charge negative relative to the surrounding tile. Then if the charging rate of the surrounding tile were rapid enough, the potential difference between the characters and tile could be maintained, carrying the characters to potentials greater than the beam accelerating potential. This kind of behavior has been observed in the charging of dielectrics on metallic substrates that were initially grounded and then permitted to float (ref. 7).

Figure 12, a 15-min time-exposure photograph for a 25-keV, 1-nA/cm^2 irradiation, shows the optical evidence of discharging that takes place on the tile surfaces with the substrate grounded. The activity was not visible to the eye and was not apparent in the substrate current being monitored. The fuzzy illumination along the gaps between tiles was barely evident in the photograph made at 15 keV and 1 nA/cm^2 but became brighter with increasing beam energy. Fifteen-minute time exposures made with the electron flux at 0.1 nA/cm^2 do not show the discharging along the gaps. Photographs with an order-of-magnitude longer exposure were not attempted since the discharging activity was not the only source of light in the chamber: the electron gun, though designed to minimize it, produced a low level of illumination. The activity along the tile gaps could be reduced by inserting a dielectric barrier in the gap, as was done with the 1-1/4-cm-thick specimen having the wide gaps between tiles. Figure 13 shows the locations of the barrier materials as well as time-exposure photographs made before and after addition of the barriers.

Results from tests with the substrate floating seem to indicate that the discharging was dependent on the potential difference across the tile from its exposed face to its substrate. In all of those tests, the one specimen that did not exhibit the optical evidence of discharging was the one for which that potential difference never exceeded 3 kV. The other five specimens produced evidence of discharging in the 15- to 25-keV beam energy range, where the surface-to-substrate potential difference usually exceeded 10 kV. Some photographs showed discharging taking place along the outer edges of the specimens as well as along the gaps between tiles. None of the photographs indicated

anything taking place away from the edges near the center of any uncracked tile or segment of tile. Figure 14 shows the potentials as a function of beam energy for the six specimens tested with their substrates floating.

An experiment was conducted in which an edge of one of the thickest specimens was irradiated. One-half of the edge had the hard borosilicate glass skin of the finished edge of a tile and the other half had the exposed low-density silica fiber bulk tile material of a tile that had been cut. The specimen was positioned so that the voltage probe swept across both materials as far as 3 cm away from the grounded substrate. Figure 15 presents the surface potentials observed as a function of beam energy. The borosilicate material charged to potentials observed in the earlier testing. The silica fiber material charged to no more than 13 percent of the beam accelerating potential for any test and is probably the result of high secondary electron emission (ref. 1). Figure 16, a time-exposure photograph, shows glowing silica fiber material and discharging in or across the nylon fiber strain isolation pad (SIP) located between the tiles and the grounded aluminum substrate.

When the substrate was permitted to float, the borosilicate surface charged to the same potentials as before. The silica fiber material became somewhat more negative than when the substrate was grounded but was now positive with respect to the substrate - the substrate being nearly as negative as the borosilicate surface. Figure 17 shows the potentials as a function of beam energy, and figure 18 is a time-exposure photograph showing little discharging in or across the SIP. Time-exposure photographs made immediately following the 25-keV exposure gave no indication of continuing activity after the electron beam was turned off. However, in the tests with the substrate grounded the electrometer sensitivity was increased after the electron beam was turned off, and a non-exponential-decaying positive current was detected as well as positive current spikes whose frequency of occurrence decreased with time. The current read immediately after electron beam turnoff was approximately 0.4 nA, decaying to 0.04 nA at 160 s and to 0.004 nA at 925 s.

CONCLUDING REMARKS

When subjected to monoenergetic electron beams, the space shuttle thermal protection system tiles rapidly charged to potentials about 2 kV less in magnitude than the beam accelerating voltage. This is indicative of a secondary electron emission coefficient second-crossover potential of approximately 2 kV. Optical evidence of surface discharge activity was produced for beam energies of 15 keV and greater and is concentrated along gaps between tiles and cracks in the glass skin. The intensity of the activity appeared to be dependent on the potential difference between the exposed tile surface and the tile's substrate. Evidence of discharging was not seen when that potential difference was 3 kV or less. Placing a barrier of high-voltage-insulating material such as Kapton or Teflon in the gaps between tiles reduced the discharging along the gaps. The potentials achieved on the bulk tile material during tile edge irradiation were quite low and suggest that the silica fiber material has a high secondary electron emission yield in contrast to the highly insulating glass skin. In addition, discharge activity was detected to occur at a decaying rate after the electron irradiation source was turned off.

1. Frederickson, A. R.; and Chesley, A. L.: Charging/Discharging of Space Shuttle Tile Material Under Irradiation. IEEE Trans. Nucl. Sci., vol. 30, no. 6, Dec. 1983, pp. 4296-4301.

2. Dotts, Robert L.; Smith, James A.; and Tillian, Donald J.: Space Shuttle Orbiter Reusable Surface Insulation Flight Results. Shuttle Performance: Lessons Learned, J. P. Arrington and J. J. Jones, eds., NASA CP-2283, Part 2, 1983, pp. 949-966.

3. Banas, Ronald P., et al.: Lessons Learned from the Development and Manufacture of Ceramic Reusable Surface Insulation Materials for the Space Shuttle Orbiters. Shuttle Performance: Lessons Learned, J. P. Arrington and J. J. Jones, eds., NASA CP-2283, Part 2, 1983, pp. 967-1008.

4. Cooper, Paul A.; and Sawyer, James Wayne: Life Considerations of the Shuttle Orbiter Densified-Tile Thermal Protection System. Shuttle Performance: Lessons Learned, J. P. Arrington and J. J. Jones, eds., NASA CP-2283, Part 2, 1983, pp. 1009-1024.

5. Borkopec, F. P.; Stevens, N. J.; and Sturman, J. C.: The Lewis Research Center Geomagnetic Substorm Simulation Facility. Proceedings of the Spacecraft Charging Technology Conference, C. P. Pike and R. R. Lovell, eds., NASA TM-73537 and AFGL TR-77-0051, 1977, pp. 423-430.

6. Jenkins, Ronald Osmond; and Trodden, W. G.: Electron and Ion Emission from Solids. Dover Publications, Inc., 1965.

7. Purvis, C. K., et al.: Charging Rates of Metal-Dielectric Structures. Spacecraft Charging Technology - 1978, Robert C. Finke and Charles P. Pike, eds., NASA CP-2071 and AFGL TR-79-0082, 1979, pp. 507-523.

TABLE 1. - EQUILIBRIUM SUBSTRATE CURRENTS

Beam energy, keV	1-1/4-cm-thick tiles				2-1/2-cm-thick tiles				5-cm-thick tiles			
	Minimum gap		Wider gap		Minimum gap		Wider gap		Minimum gap		Wider gap	
	Flux, nA/cm²	Equilibrium substrate current, nA	Flux, nA/cm²	Equilibrium substrate current, nA	Flux, nA/cm²	Equilibrium substrate current, nA	Flux, nA/cm²	Equilibrium substrate current, nA	Flux, nA/cm²	Equilibrium substrate current, nA	Flux, nA/cm²	Equilibrium substrate current, nA
2	-0.145	-0.026	-0.132	-0.09	-0.107	0.07	-0.102	-0.016	-0.075	0.028	-0.1	0.076
	-1.19	-.226	-1.28	-.1	-.61	.03	-1.16	-.128	-1.01	.064	-.64	.083
5	-0.17	-3.5	-0.082	-2.6	-0.088	-0.7	-0.144	-6	-0.09	-0.5	-0.1	-0.57
	-2.59	-17	-1	-1.8	-1	-2	-.6	-41.7	-1.03	-4.5	-1.04	-.22
10	-0.166	-.9	-0.092	-7	-0.09	-6	-0.101	-7	-0.094	-7.4	-0.088	-2
	-1.88	-82.4	-.72	-73	-.82	-55.8	-1.16	-79	-.92	-109	-1.29	-8
15	-0.126	-9	-0.104	-7.5	-0.09	-6	-0.106	-8	-0.085	-10	-0.106	-2.2
	-1.054	-73.7	-.855	-111.3	-.95	-75.8	-1.05	<-79	-.95	-107	-.66	10
20	-0.145	-4.6	-0.103	-9	-0.095	-4.9	-0.117	-8.8	-0.085	-9.3	-0.1	-7.2
	-1.19	-74.3	-.94	-98	-1.00	-70	-1.130	<-85.6	-.94	-99	-.96	-50
25	-.35	-10.6	-0.136	-10	-0.09	-5	-0.127	-8.1	-0.093	-7	-0.1	-8
	-1.305	-87.8	-.94	-76.7	-.995	-51.5	-1.12	<-71.3	-1.05	-94	-.814	-68

Figure 1. – Edge view of 1-1/4-cm-thick tile specimens A and B.
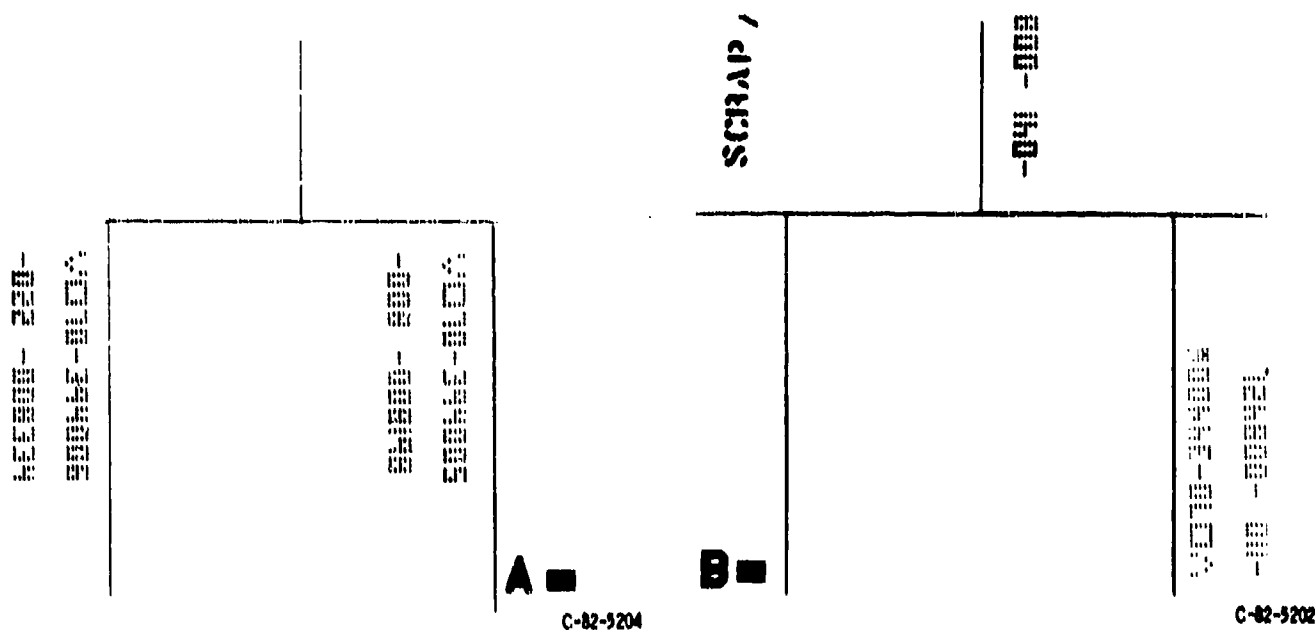
C-82-5204

Figure 2. – Face of 1-1/4-cm-thick tile specimen A.

C-82-5202

Figure 3. – Face of 1-1/4-cm-thick tile specimen B.
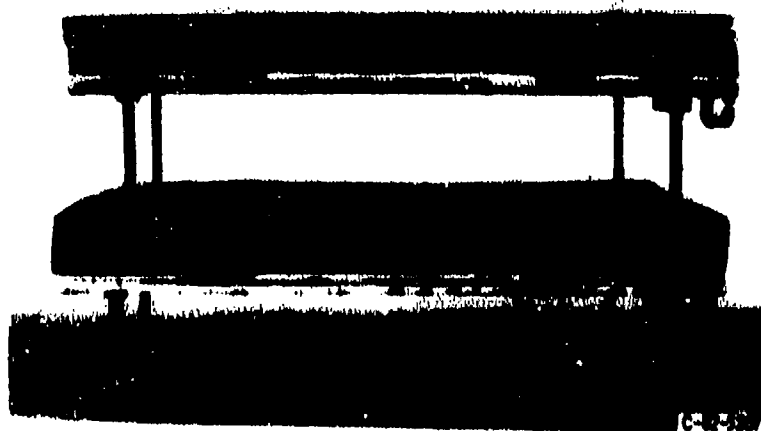
Figure 4. – Edge view of 2-1/2-cm-thick tile specimens C and D.

96
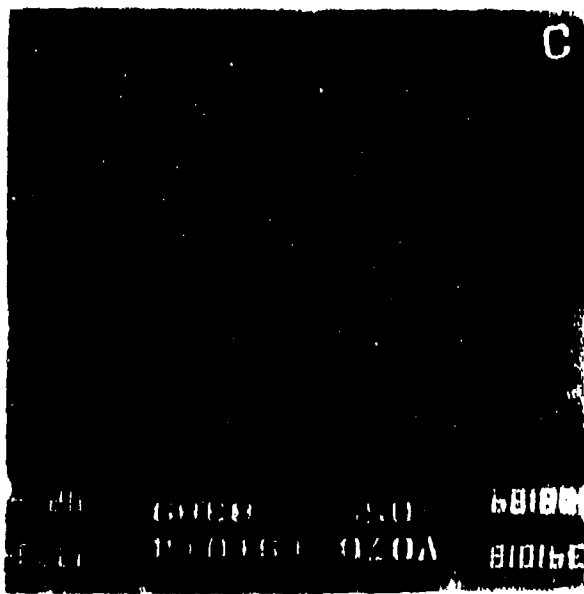
Figure 5. - Face of 2-1/2-cm-thick tile specimen C.
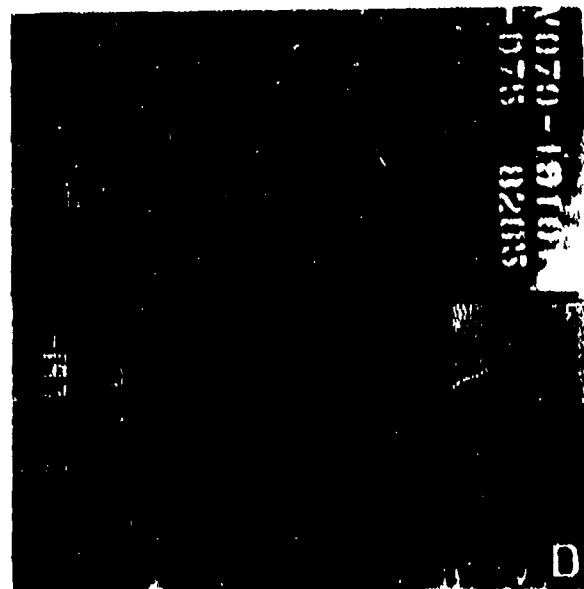
Figure 6. - Face of 2-1/2-cm-thick tile specimen D.
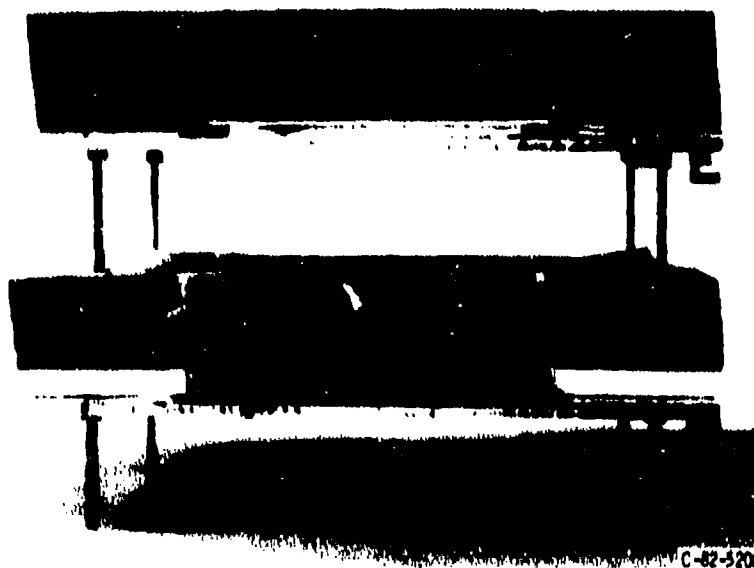
Figure 7. - Edge view of 5-cm-thick tile specimens E and H.

97
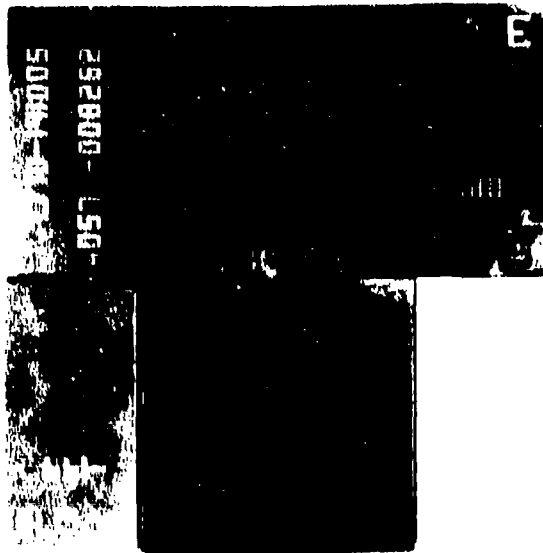
Figure 8. - Face of 5-cm-thick tile specimen E.

C-82-5200
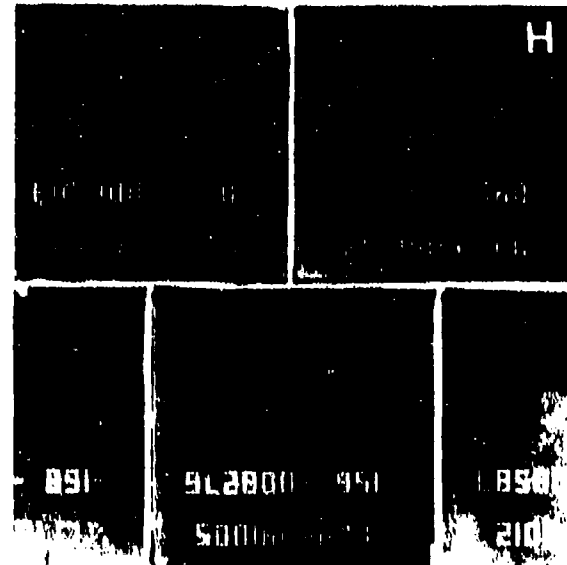
Figure 9. - Face of 5-cm-thick tile specimen H.

C-82-5199
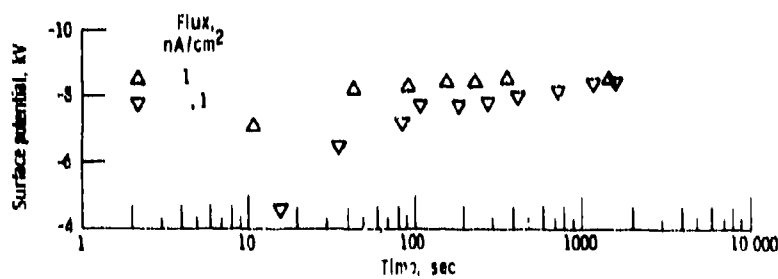
Figure 10. - Electron beam charging of 1-1/4-cm-thick shuttle tile specimens - 10-keV beams.

98
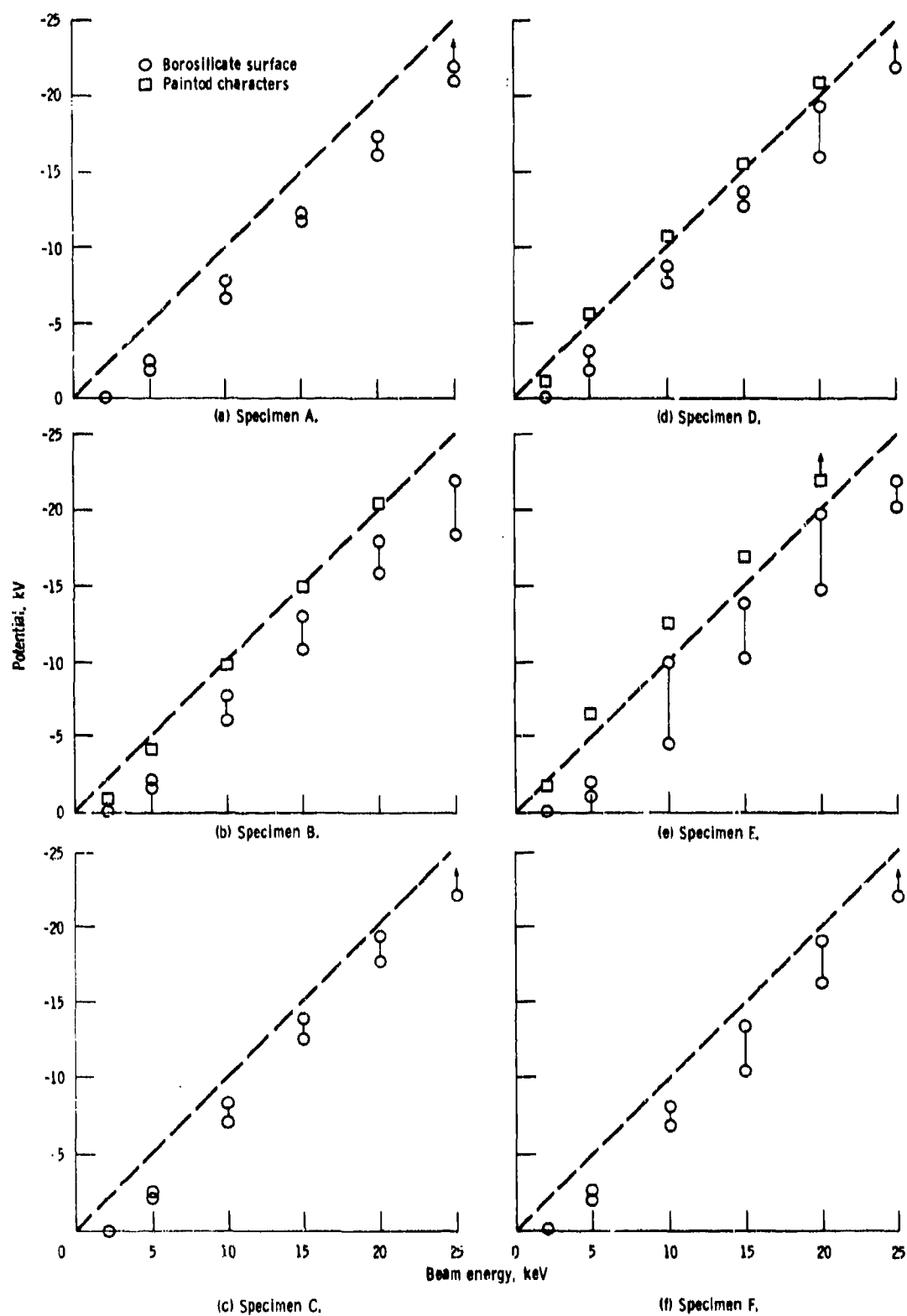
Figure 11. – Potential as a function of beam energy. Flux, 1 nA/cm².

99

Figure 12. - Time exposure of discharging along shuttle tile gaps.
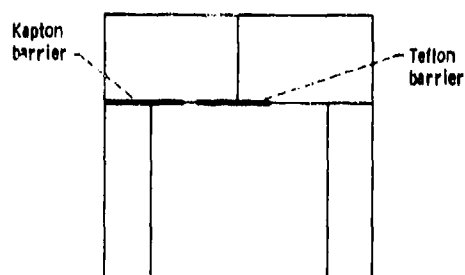
(a) Location of Kapton and Teflon gap barrier strips.

(b) Discharging before instal-
lation of dielectric gap fillers.

(c) Discharging after instal-
lation of dielectric gap fillers.

Figure 13. - Barrier strips.

100
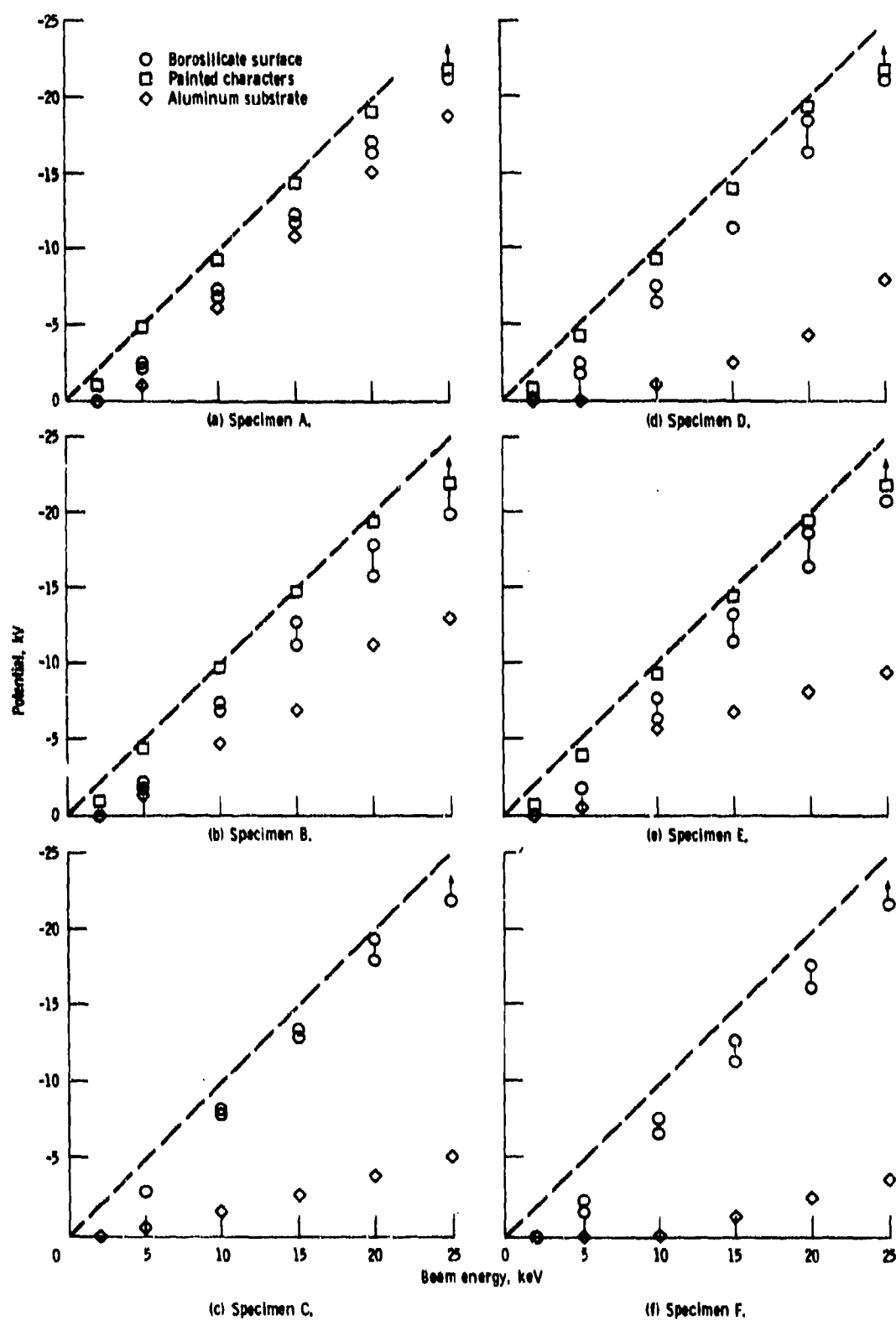
Figure 14. – Potential as a function of beam energy – floating substrate.
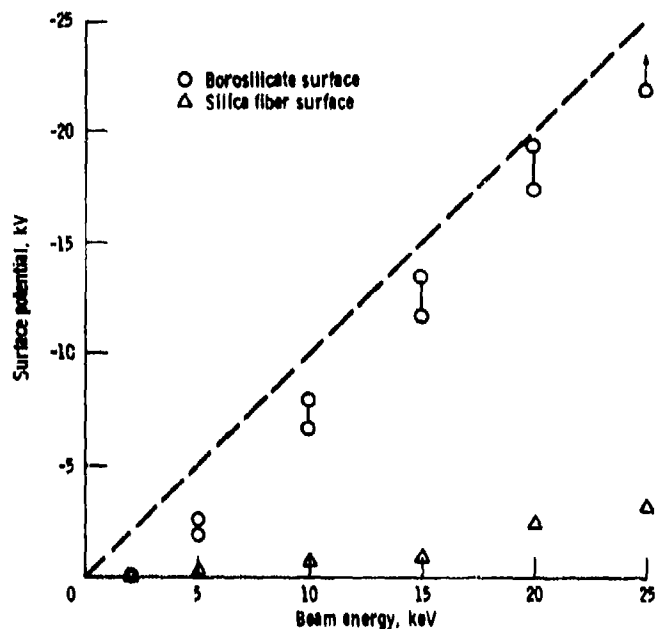
Figure 15. - Surface potential as a function of beam energy - substrate grounded.

Figure 16. - 15-Minute time exposure of edge-irradiated specimen - substrate grounded. Beam energy, 25 keV; flux, 1 nA/cm².
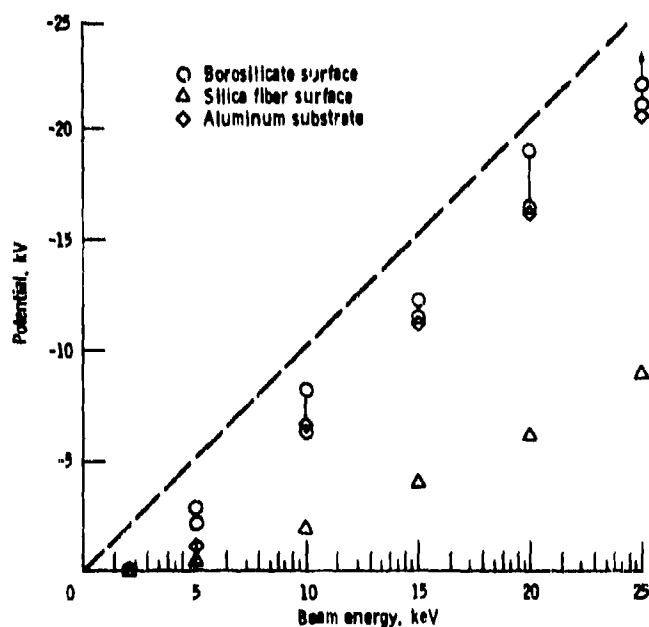
Figure 17. - Potential as a function of beam energy - substrate floating.

Figure 18. - 15-Minute time exposure of edge-irradiated specimen - substrate floating. Beam energy, 25 keV; flux, 1 nA/cm².

102

SPACECRAFT-ENVIRONMENT INTERACTION - THE ENVIRONMENTAL PLASMA ASPECT

Uri Samir*
University of Michigan
Ann Arbor, Michigan 48109
and Tel-Aviv University, Israel

The knowledge and understanding of the interactions between an "obstacle" and a space plasma are fundamental to space plasma physics and are essential to space plasma diagnostics, in-situ data interpretation, and spacecraft charging. The obstacle can be a natural body moving in the solar system (i.e., a planet or a moon) or an artificial obstacle (i.e., a spacecraft orbiting the Earth or any other planet or moon). Artificial obstacles consist of rockets, satellites, space shuttle, space station, etc.

The effects involved in the interaction between an obstacle and a space plasma can be divided into

(1) Effects on the obstacle itself (i.e., its charging)

(2) Effects on the environmental plasma due to the motion of the obstacle (i.e., the creation of shocks ahead of the obstacle and complicated wakes behind the obstacle). In the wake (or antisolar direction), plasma oscillations are excited and instabilities, wave-particle interactions, turbulence, etc., are believed to take place.

The effects on the obstacle and on the environmental space plasma are coupled. Hence, simultaneous solutions to the Vlasov (or Boltzmann) and Poisson equations are sought. To obtain realistic solutions of practical use, three-dimensional and time-dependent models of the interaction are needed. Achieving the latter is indeed not simple.

The point should be made that experimental and theoretical work of practical interest (e.g., in low Earth orbit) can serve as model-experiments of a wider scope of interest and importance in space plasma physics and in astrophysics (e.g., Falthammar (1974), Samir and Stone (1980), and Podgorny and Andrijanov (1978)). This will, of course, require the use of qualitative scaling (Falthammar (1974) and Samir and Stone (1980)).

EXPERIMENTAL AND THEORETICAL THERMAL PLASMA RESULTS - STATUS REPORT

In-situ experimental results regarding the distribution of low-energy ions and electrons around ionospheric satellites in the altitude range $250<H<3000$ km are available in the open literature. For recent brief review papers on this

---

subject we cite Samir (1981) and Samir and Stone (1980). Unfortunately, most of these results are limited to the very near vicinity of the satellite since most of the relevant measurements were made by probes flush mounted on the surface of the satellite. Although significant results were obtained which enhanced our knowledge and understanding of the interaction, more extensive spatial regions ahead and behind the satellite have to be researched.

In-situ results were compared with the theoretical models of Gurevich et al. (1970), Parker (1976), and Call (1969). Results of such comparisons are given in Samir and Fontheim (1981), Samir (1981), and Samir and Stone (1980). It is our understanding that studies along similar lines are now being performed by the S-CUBED group (Parks et al. (1983)). The main conclusion from these studies is that except for specific cases there is no quantitative agreement between theory and experiment for unmanned, low-altitude, small ionospheric satellites. The recent results from the space shuttle mission STS-3/Columbia known to the author have not, unfortunately, yielded thermal plasma information which can be used in a meaningful theory-experiment comparison. It is possible that the wave data (Shawhan and Murphy (1983)) may yield new relevant information.

More recently the distribution of H^+ and He^+ ions around the DE-A magnetospheric satellite at $H \approx (1, 4-3)R_E$ (R_E = radius of the Earth) have been examined (Samir, Comfort, and Chappell (1983)). This study extends the range of plasma parameters vis-a-vis earlier studies and is expected to be useful in magnetospheric physics and astrophysics. The wake of an auroral sounding rocket in the altitude range 120 to 320 km was studied by Bering (1983). The comments made in this paper should be of interest and direct relevance to the interpretation of parallel electric field measurements at low altitudes.

Effects involved in the charging aspect of the interaction were studied extensively in situ and in the laboratory. A large effort was also devoted to theoretical modeling. Recent review papers regarding this aspect of the interaction were published by Whipple (1981) and Garrett (1981) and will not be further discussed here. One point should, however, be made, namely, that in order to get realistic solutions for ϕ from $EI = 0$, the distribution of charge around a spacecraft has to be reliably known. This includes time-dependent effects, wave-particle interactions, instabilities, and turbulence.

To overcome the limitation mentioned above, where measurements are restricted to the very near vicinity of the spacecraft, multibody systems or multiprobe systems are needed. Mother-daughter concepts as well as shuttle-tether systems are applicable (Samir and Stone (1980) and Williamson et al. (1982)). The first time a multibody system was used to perform wake measurements was in the Gemini-Agena 10 mission (Troy et al. (1970)). The recent measurements of the thermal plasma environment of the STS-3/Columbia shuttle mission (Raitt et al. (1983)) yielded initial results some of which are in general accord with measurements and predictions obtained earlier from unmanned ionospheric satellites. Raitt et al. (1983) concludes that "thermal plasma probes mounted on the space shuttle orbiter are not a very good arrangement to obtain measurements of the ambient ionospheric thermal plasma." This conclusion is not surprising and indicates that, in order to study the interaction of a spacecraft with its environment, multibody systems are needed.

In addition to in-situ data, there are laboratory measurements which are directly relevant to spacecraft-environment interaction. In Stone (1981a,b) and Stone and Samir (1981), available results for thermal plasmas are reviewed. In Intriligator and Steele (1982, 1983), similar studies were performed for high-energy beams and an attempt was made to apply them to the Venusian wake. Other relevant comments are given in Eselevich (1983).

EXPANSION OF A PLASMA INTO A VACUUM

In a recent review paper (Samir et al. (1983)) the interaction between an obstacle and a rarefied space plasma was examined versus the phenomena and physical processes involved in the expansion of a plasma into a vacuum. This is a new approach based on theoretical and experimental work done in fusion research. Briefly, the basic processes involved in the expansion are (1) the propagation of a rarefaction wave into the unperturbed or ambient plasma and the existence of jump discontinuities (Gurevich and Meshcherkin (1981a)) at the front of the rarefaction wave, (2) the acceleration of ions to high veloc-ities (i.e., to velocities reaching the order of the electron thermal speed in the ambient plasma) by the transfer of energy from the infinite reservoir of ambient thermal electrons, (3) the existence of an ion front, and (4) the excitation of plasma oscillations and instabilities over several spatial loca-tions in the vacuum region. The intensity of these processes depends on the specific ionic constituents and their relative concentrations in the ambient plasma (Gurevich et al. (1973) and Singh and Schunk (1982, 1983)), as well as on the ambient electron temperature, the normalized characteristics length, and the nature of the density gradient at the plasma-vacuum interface. Theoretical results showing the distribution of ions, electrons, and electric fields in the vacuum region are given in Gurevich and Pitaevsky (1975), Gurevich and Meshcherkin (1981b)), and Singh and Schunk (1982, 1983).

The point to be made is that the wake behind an obstacle can be approxi-mated by a vacuum region into which the ambient plasma expands. Intriligator (1983) suggests that structural patterns similar to those predicted in the plasma-expansion (Samir et al. (1983)) may exist in the Venusian wake.

REMARKS AND CONCLUSIONS

(1) Despite the fact that the interaction between a spacecraft and its environmental plasma is of fundamental interest and importance to science and technology alike, relatively few experimental results are available at the present time. This is particularly so for the angular distribution of charge and potential around a spacecraft orbiting the Earth.

(2) Reliable phenomenological knowledge and in-depth physical understand-ing of the structure of the close and far regions surrounding a spacecraft are needed in order to test models describing the entire interaction.

(3) To achieve the above objective, well-conceived in-situ and laboratory experiments are needed. Such experiments cannot be byproducts of geophysical measurements only.

(4) Future in-situ measurements can best be performed by using multibody and multiprobe systems. The space shuttle with its capability of ejecting and capturing small satellites is a suitable space platform for such investigations. Another facility adequate for performing relevant experiments is the shuttle-tether system. Numerous combinations exist by which very meaningful scientific and technological experiments can be performed by using the space shuttle (or any other large space platform) and ejectable multiprobe systems.

(5) By adopting a wider scientific viewpoint and considering the phenomena involved in the expansion of a plasma into a vacuum, an attempt can be made to preceed toward a UNIFIED perception of the interaction between an obstacle and a space plasma.

REFERENCES

Bering, E. A. (1983), _J. Geophys. Res._, 88, 961.

Call, S. M. (1969), Report No. 46, Plasma Laboratory, Columbia Univ., N.Y.

Eselevich, V. G. (1983), _Plan. Space Sci._, 31, 615.

Falthammar, C. G. (1974), _Space Science Rev._, 15, 803.

Garrett, H. B. (1981), _Rev. Geophysics and Space Physics_, 19(4), 577.

Gurevich, A. V., L. P. Pitaevsky and V. V. Smirnova (1970), _Soviet Physics/ Uspekhi_, 99, 595.

Gurevich, A. V. and L. P. Pitaevsky (1975), _Prog. Aerospace Sci._, 16, 227.

Gurevich, A. V. and A. P. Meshcherkin (1981a), _Soviet Physics, J.E.T.P._, 53, 937.

Gurevich, A. V. and A. P. Meshcherkin (1981b), _Soviet Physics, J.E.T.P._, 53, 688.

Intriligator, D. S. and G. R. Steele (1982), _J. Geophys. Res._, 87, 6053.

Intriligator, D. S. (1983), Private Communication.

Parker, L. W. (1975), NASA CR-144159.

Parks, D. E. (1983), Private Communication.

Podgorny and Andrijanov (1978), _Plan. Space Sci._, 26, 99.

Raitt, J. W., D. E. Siskind, P. M. Banks and P. R. Williamson (1983), submitted for publication.

Samir, U. and N. H. Stone (1980), _Acta Astronautica_, 7, 1091.

Samir, U. (1981), _Advances in Space Res._, 1, 373.

Samir, U. and E. G. Fontheim (1981), <u>Plan. Space Sci.</u>, <u>29</u>, 975.

Samir, U., K. H. Wright and N. H. Stone (1983), <u>Rev. Geophysics and Space Physics</u>. In press.

Samir, U., H. Comfort and R. Chappell (1983), In preparation.

Shawhan, S. D. and G. Murphy (1983), Private Communication.

Singh, N. and R. W. Schunk (1982), <u>J. Geophys. Res.</u>, <u>87</u>, 9154.

Singh, N. and R. W. Schunk (1983), <u>Physics of Fluids</u>, <u>26</u>, 1123.

Stone, N. H. and U. Samir (1981), <u>Advances in Space Res.</u>

Stone, N. H. (1981a), <u>J. Plasma Phys.</u>, <u>25</u>, 351.

Stone, N. H. (1981b), <u>J. Plasma Phys.</u>, <u>26</u>, 385.

Troy, B. E., D. B. Medved and U. Samir (1970), <u>J. Astronautical Sci.</u>, <u>18</u>(3), 173.

Whipple, E. C. (1981), <u>Reports on Progress in Physics</u>, <u>44</u>, 1197.

Williamson, P. R., W. F. Denig, P. M. Banks and J. W. Raitt (1982), <u>Artificial Particle Beams in Space Plasma Studies</u>, (ed., B. Grandal), 645.

DIRECT MEASUREMENTS OF SEVERE SPACECRAFT CHARGING IN AURORAL IONOSPHERE

W. J. Burke, D. A. Hardy, F. J. Rich, and A. G. Rubin
Air Force Geophysics Laboratory
Hanscom Air Force Base, Massachusetts 01731

M. F. Tautz
Radex Inc.
Carlisle, Massachusetts 01741

N. A. Saflekos* and H. C. Yeh
Boston College
Chestnut Hill, Massachusetts 02167

Due to limitations of methods commonly used to detect particles and plasmas few
examples of spacecraft in the ionosphere charging beyond a few volts appear in the
literature. This impasse has been overcome with the launch of the DMSP/F6 satellite.
It was equipped with up-looking detectors to measure 20 point spectra of precipitat-
ing ions and electrons with energies between 30 eV and 30 KeV, once per second. A
generous geometric factor for the ion detector allows the application of a technique
regularly used to identify the degree of charging for satellites at geostationary
orbit. The Liouville Theorem can be used to show that a spacecraft charged, to say,
-100 V, will measure no positive ions in energy channels < 100 eV. Because of the
acceleration of cold, ionospheric ions by the spacecraft potential a large count
rate should be seen in an energy channel centered near 100 V. A preliminary search
of early DMSP measurements shows that such charging peaks frequently appear in the
vicinity of intense inverted-V structures. An example that closely approximates the
"worst case" charging environments derived from previous DMSP missions, with only
electron measurements available has been examined. In this case, with the satellite
in darkness, peak electron fluxes occurred at energies of 10 keV and charging peaks
were observed in ion energy channels up to ~65 eV. The fact that the spacecraft
was charged was verified using the SSIE thermal plasma probe on the same vehicle.
Calculations indicate that dielectric surfaces in the wake side of the vehicle charge
to many times this number.

* Present address: Southwest Research Institute, Space Physics Section, San Antonio,
  TX 78284.

PRECEDING PAGE BLANK NOT FILMED

INTRODUCTION

In this symposium we are addressing questions concerning how large space structures in polar orbit will interact with auroral environments. Because spacecraft charging at ionospheric attitudes does not seriously threaten the operation of today's relatively small polar satellites the subject of environment interactions has not received the widespread attention given to it at geostationary altitude. As a matter of economics it is desireable for us to apply as much as possible of what we have learned about spacecraft interactions at geostationary orbit to low earth orbits. Economics, however, must not blind us to real differences between the two problems.

The environment at auroral latitudes in the ionosphere differs from that encountered at geostationary altitude in at least two major aspects.

(1) There is a large reservoir of high-density, cold plasma which tends to mitigate charging effects by providing a large source of charged particles from which neutralizing currents maybe drawn. However, since Debye lengths in the ionosphere are measured in centimeters as opposed to hundreds of meters at geostationary altitude effective current collecting areas may be severely limited. Significant wake effects behind large structures will introduce new problems with differential charging.

(2) Between the magnetic equator and the ionosphere, auroral electrons frequently undergo field-aligned accelerations of several kilovolts (ref. 1). The degree to which auroral, as opposed to plasma sheet, electrons deviate from isotropy is a complex function of the electron's energy and the potential distribution along magnetic field lines (ref. 2). In such environments, fluxes of energetic protons are usually below the levels of instrumentation sensitivity (refs. 3 and 4).

It is anticipated that polar-orbiting shuttles will encounter the most severe charging environments in the vicinity of westward travelling surges and near inverted-V structures. Westward travelling surges occur in the midnight sector during the expansion phases of substorms. Substorm onsets are frequently marked by the sudden brightening of the equatorward-most arc (ref. 5). This is followed by a bulging and rapid poleward expansion of active arcs in the midnight sector (ref. 6). For observers on the ground in the evening sector the bulge appears on the eastward end of arcs and moves quickly toward the western horizon. Using DMSP satellite imagery and electron flux measurements Meng and coworkers (ref. 7) constructed a composite morphology of westward travelling surges shown in Figure 1. Bright arcs emanate to the west (A) and to the east from the equatorward and poleward edges of the bulge region, respectively. A myriad of arc-like structures are embedded in the bulge region (C), while nonuniform diffuse auroral precipitation (D) is found to the east of the bulge and equatorward of the B arc.

Differential spectra typical of downcoming electrons in the vicinity of surges are shown on the left side of Figure 1. In region A, to the west (evening side) of the bulge, spectra are similar to those measured over quiet-time arcs. However, the "monoenergetic beams" shift to higher than quiet-time values. This indicates that stronger field-aligned potentials occur during substorm periods. In the region of the poleward arc (region B) two spectral types are measured. One has a shape similar to that found in the diffuse aurora (D) but with lower mean energy. The second spectral type is characterized by electrons with energies of 100 eV and differential flux levels of $10^{11}/cm^2$ sec sr keV. The spectral shapes indicate that field-aligned accelerations in regions B and D are not significant. Within region C electron spectra are relatively flat, sometimes out to the high-energy, measuring limit of

DMSP spectrometers. If, as suggested by the "worst-case" study of SCATHA's environ ment,(ref. 8), severe charging most strongly correlates with fluxes of electrons with energies in the several tens-of-keV regime, then region C electrons may present the most severe charging environment for polar-orbiting shuttles.

Hazards due to spacecraft charging of large space structures should also occur in "inverted-V" events. The term inverted-V was first used to describe structures that appear in energy-time spectrograms from polar orbiting satellites (ref. 3). In these structures the mean energy of precipitating electrons rises from a few hundred eV to several keV then returns to a few hundred eV. Often the electrons have Maxwellian distributions characterized by a mean thermal energy E_0 that have been accelerated through a field-aligned potential drop ϕ_0 (ref. 9). In traversing the inverted-V, ϕ_0 increases to some maximum value then decreases. In the evening sector ϕ_0 can rise to over 10 kV. The danger posed by inverted-V precipitation is more ubiquitous than westward travelling surges. Lin and Hoffman (ref. 2) showed that inverted-V events occur in all MLT sectors except in the dayside auroral gap (ref. 10).

To date, all investigations of inverted-V structures report no measurable fluxes of precipitating protons. This limitation more likely reflects on the sensitivity of proton detectors rather than on a real absence of proton fluxes. In the plasma sheet protons have mean thermal energies that are about five times those of electrons. Some protons in the high energy tail of these distriutions should be sufficiently energetic to overcome the ϕ_0 potential barrier and reach the ionosphere.

Herein lies a serious verification problem for modelers of low-earth orbit space-craft charging. It is rather easy to specify the "worst charging environment" (ref. 11). However, the relatively small geometric factors on positive ion detectors flown to date on polar satellites have not allowed us to use the straight-forward methods used at geostationary altitudes (ref. 8) for measuring satellite potentials in excess of a few volts. In only one case, as INJUN-5 passed through an intense inverted-V, has a large satellite potential been measured (ref. 12). In this case only an upper bound of -28V could be directly assigned.

The purpose of this report is to provide information for interaction-modelers on the capabilities of a new generation of charged particle spectrometers now flown on DMSP (Defense Meteorological Satellite Program) satellites. These detectors, which are sensitive to downcoming, positive ions with energies greater than 30 eV, allow the direct measurements of satellite potentials less than -30V. The following section describes the plasma and particle instrumentation on the recently launched DMSP/F6 satellite. We then present a detailed analysis of measurements taken as the satellite passed through an intense, inverted-V structure in the midnight sector on 10 January 1983. The discussion section compares observational measurements of the satellite potential with the predictions of a small-satellite charging model.

INSTRUMENTATION

DMSP satellites are three axis stabilized and fly in sun-synchronous, circular polar orbit at an altitude of 840 km. Their orbital periods and inclinations are are 101 minutes and 98.75°, respectively. DMSP/F6 was launched in late December 1982 into an orbit near the dawn-dusk meridian with an ascending mode of 0612 LT. The two sets of detectors of interest here were designed to monitor variations in the topside thermal plasma and in the flux of precipitating charged particles.

The thermal plasma detector (ref. 13, 14), known as the Special Sensor for Ions and Electrons (SSIE) consists of a spherical Langmuir probe and a planar, retarding potential analyzer (RPA). The Langmuir probe consists of a 1.75" diameter collector surrounded by a concentric, wire-mesh grid of 2.25" diameter. It is mounted at the end of a 2.5' rigid boom. The sensor operates in 2 modes. In the first mode the grid bias is held at a fixed level determined by ground command. In the second mode the voltage of the grid with respect to satellite ground is swept to determine the thermal electron density and temperature. The mode 2 voltage sweep occurs every 64 s and lasts for 10 s. To ensure that all electrons passing through the grid are collected the collector is always held at a potential of 20 V above that of the grid. During Mode 1 operations on 10 January 1983 the grid-bias was fixed at +7.8 V with respect to the spacecraft frame potential.

The thermal ion detector is a retarding potential analyzer (RPA) that consists of a collector, a supressor grid, a swept grid and an aperture grid. The aperture grid is circular with a diameter of 1.0". This sensor is mounted 3/4 of the way up the 2.5' boom with an outward surface normal facing in the direction of the satellite velocity. The RPA also operates in two modes. In Mode 1 the retarding grid is fixed at satellite potential plus a bias potential of 6.3V. In Mode 2 the retarding grid is swept from -5 V to 12 V, every 64 s. From the shapes of the current-voltage characteristics obtained during Mode 2 sweeps it is possible to determine the ion densities, temperatures and relative mass concentrations. Complete descriptions of the SSIE instruments and the methods of data reduction and analysis have been written by Smiddy and co-workers (ref. 13) and by Rich and co-workers (ref. 14).

The energetic particle detector on DMSP/F6 are designed to measure the flux of downcoming electrons and positive ions in 20 energy channels, logrithmically spaced between 30 eV and 30 keV. Both the electron and ion detectors consist of two curved plate electrostatic analyzers. The aperatures of the analyzers always face toward local vertical. Thus, at auroral and polar-cap latitudes they detect precipitating rather than backscattered or trapped particles. One set of analyzers covers the energy range 30 eV to 1 keV has a geometric factor of 4×10^{-4} cm^2-sr for electrons and 2×10^{-2} for ions. In both cases $\Delta E/E$ is 13% The other set of analyzers measures the flux levels over the 1 to 30 keV range. The geometric factor for these electron and ion detectors is 10^{-3} cm^2-sr with $\Delta E/E = 10\%$. These large geometric factors ensure statistically significant count rates in the auroral oval.

OBSERVATIONS

During the period of interest on 10 January 1983, DMSP was in darkness crossing the midnight sector of the northern auroral oval from dawn to dusk. Simultaneous measurements from the imager on F6 and ground magnetograms are not available at this time. In general, however, the period may be characterized as one of magnetic quieting. Although Kp was 2^+ at the time of the overpass, 10 January was the most disturbed day of the month with Σ Kp = 39.

Measurements from the energetic electron and ion spectrometers are presented in Figures 2 and 3, respectively. The format for data presentation is the same in both figures. Plotted as functions of UT, geomagnetic latitude, and magnetic local time are the particle's average energies (top panel), the directional energy fluxes (middle panel) and number fluxes (bottom panel). Attention is directed toward the one minute interval following 2045 (74700) UT. Beginning at 2045 UT the number flux (JTOT) rises from 10^9 to 4×10^9 electrons/cm^2 sec sr at 2045:22 UT. In the next 20 sec

112

it decreased to 10^7 electrons/cm^2 sec sr. The average energy of the pre-
cipitating electrons increased from 800 eV to 7.5 keV then returned to 800 eV,
the classic signature of an inverted-V structure. The flux of ions reaching the
detector also increased to a sharp maximum at 2045:22 UT. However, the average
energy of the ions was lowest at this time. This signature is similar to that
obtained when spacecraft at geosynchronous orbit undergo charging.

Figures 4, 5 and 6 give three examples of measurements from the energetic electron
and ion sensors at 2045:17, :22 and :24 UT, respectively. Data represented as elec-
tron and ion phase space densities are plotted as functions of energy from 30 eV to
30 keV. The insets give expanded plots of ion distribution functions in the energy
range 30 to 200 eV. In all three cases the electron distributions show low-energy
or suprathermal components. The fact that the energetic components of the electron
distributions are not monotonically decreasing in energy is consistent with the
primary electrons having been electrostatically accelerated in some attitude range
above the satellite. Electrons with energies below the peak in the distribution
functions are energy-degraded primaries that are trapped below the electrostatic
barrier. The primary-electron distributions are non-Maxwellian, containing high
energy tails.

The ion distribution functions also contain both energetic and suprathermal com-
ponents. In the case of the ion measurement at 2045:22 UT the energetic component
has a Maxwellian distribution out to 30 keV. Using the Liouville theorem and assum-
ing an isotropic distribution function in the magnetosphere we find that for charge
neutrality to prevail in the parent populations, the field-aligned potential drop
above the auroral ionosphere is ~ 8 kV. We note that this is consistent with the
measured distribution where the actual peak must lie between the energy channels
centered at 6.46 and 9.48 keV.

At 20:45:22 and :24 UT the suprathermal ions have non-monotonic distributions. The
peaks in the energy channels centered at 65 and 44 eV suggest that ions measured in
these channels are ionospheric particles that have been accelerated by satellite
potentials of -65 and -44 V, respectively. The fact that ion counts are recorded in
energy channels less than at the peak in the distribution is consistent with the
finite spread in the energy-acceptance of the sensor's energy channels. Recall that
to assure high count rates the geometric factor of the low-energy ion detector was
made large. The only other possible source of ions in these energy ranges at DMSP's
altitude are the so-called ion conics (ref. 15). These are thermal ions that are
accelerated perpendicular to magnetic field lines through resonant interactions with
lower-hybrid or ion-cyclotron electrostatic waves. Such cannot be the case here since
the ion detector is looking almost along, rather than across, the magnetic field.
Note that the negative potentials of several tens of volts represent the potentials
of the dielectric surfaces in the vicinity of the ion-detector's aperture rather
than the potential of the satellite's frame.

Further information concerning the environment in which the charging of DMSP/F6
occurred can be gained from thermal probe measurements. Figure 7 gives the
"densities" of thermal electrons and ions measured during Mode 1 operations. In
this representation data taken while sensor grids were being swept in voltage (Mode 2)
are suppressed. The grid on the spherical Langmuir probe was biased at 7.8 V with
respect to the satellite frame. Thus, in Mode 1 the electron sensor is operating
in the accelerating mode. This leads to overestimates of the ambient electron densi-
ties. In regions where both sensors vary in the same sense the measurements accurate-
ly measure relative density fluctuations. In regions where the measurements vary in

113

opposite senses the variations are mostly due to satellite potential fluctuations. Absolute values of the plasma density are obtained through analyses of Mode 2 current -voltage sweeps. Figure 7 shows that in the period following 2045 UT the current reaching the thermal electron probe decreased by more than four orders of magnitude, consistent with a strongly negative vehicle potential. The thermal ion current increased by a factor of 2.

In the immediate vicinity of the charging event Mode 2 sweeps cannot be used to determine the plasma temperature and composition. The last Mode 2 sweep, taken equatorward of the event and before vehicle potential fluctuations make results of Langmuire probe analysis questionable, occurred at 2043:26 UT. This sweep showed a total plasma density of $\sim 10^4 \text{cm}^{-3}$. The ion composition was mostly O^+. The ion and electron temperatures were $\sim 1200°$ and $4000°K$, respectively. The following sweep, beginning at 2044:30 UT showed signs of a significant light ion contribution. It should be noted that other measurements in the diffuse auroral region show large, even dominant light ion mixtures. The light ion that best fit the measured current-voltage characteristics was He^+. Close to the event the current character-istics also showed signs of a light-ion component. However, rapid fluctuations of the satellite potential do not allow quantitification of this observation.

DISCUSSION

In modelling the DMSP charging event described in the previous section two con-ditions should be kept in mind. First, the event occurred while the satellite was in darkness. Thus, photoemission currents from the vehicle can be ignored. Second, the surfaces of DMSP satellites are almost entirely made up of dielectric materials. The potential drop V_s experienced by positive ions reaching the electrostatic analyzer should be that required for local current balance near that sensor's aperture. For the sake of simplicity we model the satellite as a sphere whose surface material is kapton. The satellite moves at a speed of 7.4 km/s through the combined ionospheric and auroral plasmas.

The local current balance condition can be written in the form:

$$I(V) = -J_{eM} + J_{iM} + J_{e2} + J_{eB} + J_{ei} + J_{iI} = 0$$

The terms J_{eM} and J_{iM} represent currents due to energetic electrons and ions of magnetospheric origin, respectively. The energetic electrons include both primaries and energy degraded primaries. The terms J_{e2}, J_{eB}, and J_{ei} refer to currents generated by: (1) secondary electrons resulting from energetic electrons impacting the satellite, (2) backscattered energetic electrons, and (3) secondary electrons due to impacting ions, respectively. Currents resulting from impacting ionospheric ions are represented by J_{iI}.

If we assume that the auroral electrons are well approximated by an isotropic distribution function $f_{eM}(E)$ then the total currents to the satellite directly attributable to energetic electrons has the form

$$\text{(2)} \qquad J_e = J_{eo} \, e^{-qV_s/kT_e}$$

where $J_{eo} = -J_{eM} + J_{e2} + J_{eB}$; V_s is the satellite potential and q is the elementary (negative) unit of charge and $kT_e = 2/3 \langle E \rangle$. Here $\langle E \rangle$, the mean thermal energy of the energetic electrons is 5.45 keV. Finally,

114

(3) $$J_{eo} = \frac{4\pi^2 q}{m^2} \int_0^\infty \int_0^{\pi/2} E f_{eM}(E) [1 - \Delta_2(E, \psi) - \Delta_B(E, \psi)]$$

$$\cdot \cos\psi \sin\psi \, d\psi \, dE$$

is the total current due to energetic electrons if the satellite were at plasma potential. The functions of energy and angle ψ from normal incidence, for secondary $[\Delta_2(E, \psi)]$ and backscattered $[\Delta_B(E, \psi)]$ electrons are given by Laframboise and co-workers (ref 16).

The current due to impacting ions can be represented in the form

(4) $$J_i = J_{io}(1 + \frac{eV_s}{kT_i})$$

where kT_i is the mean thermal energy of the magnetospheric ions. J_{io} represents the sum of $J_{iM} + J_{ei}$ if the satellite were at plasma potential

(5) $$J_{io} = \frac{4\pi^2 e}{M_i} \int_0^\infty \int_0^{\pi/2} E f_{iM}(E) [1 + \Delta_{ei}(E, \psi)]$$

$$\cos\psi \sin\psi \, d\psi$$

$f_{iM}(E)$ is the distribution function of magnetospheric ions in the vicinity of the satellite. $\Delta_{ei}(E, \psi)$ is the secondary electron conversion factor (ref 16).

Values of J_{eo} and J_{io} in equations (3) and (5) were solved by numerical integration using the energetic electron and ion distribution functions measured at 2045: 22 UT. Setting V_s equal to -65 V in equations (2) and (4) and adding we calculate that in the vicinity of the ion sensor there is a current of 6.33 $\mu A/m^2$ flowing away from the satellite. From equation (1) we see that this must be balanced by the thermal ion current J_{iI} to the vehicle.

The current to the satellite due to ionospheric ions is given by a sum, over ion species α

(6) $$J_{iI} = N_o e U_{sat} \sum_\alpha \Gamma_\alpha(b_\alpha, \Theta)$$

where N_o is the total ion density, U_{sat} is the satellite speed, Θ is the angle with respect to the ram direction, b_α is the Mach number of the α species $[1/2 M_\alpha V_s/kT_e]^{1/2}$. Based on satellite measurements in the ionosphere, Gurevich and co-workers (ref. 17) derived an expression for the angular term

(7) $$\Gamma_\alpha(b_\alpha, \theta) = \frac{N_\alpha}{N_o} [\frac{1 + erf(b_\alpha \cos\phi_0 \cos\theta}{1 + erf(b_\alpha \cos\phi_0)}]$$

where erf (x) represents the standard error function. ϕ_0 is the complement of

the Mach angle. With U_{sat} = 7.4 km/s and T_e = 4000° K we calculate values of ϕ_0 = 71° for an O^+ plasma and 55° for an He^+ plasma. Note that for Θ = 0° $\sum_\alpha \Gamma_\alpha$ = 1 and the current $N_0 e\, U_{sat}$ is the ram current. For a plasma density N_0 of $10^4\, cm^{-3}$ the ram current is 11.8 $\mu A/m^2$. Thus, to balance a current of 6.33 $\mu A/m^2$, $\sum_\alpha \Gamma_\alpha$ (90°) must equal 0.536.

Figure 8 is a plot of $\sum_\alpha \Gamma_\alpha$ (90°) plotted as a function of the fraction of He^+ present in the ionospheric plasma. The horizontal line at 0.536 represents the value of $\sum_\alpha \Gamma_\alpha$ (90°) required to balance the auroral current with V_s = -65 V on the top surface of the satellite. The solutions are not unique. As expected the ϕ_0 = 55° condition is satisfied only for a pure He^+ plasma. Higher values of ϕ_0 require less He^+.

It is interesting to now use this model to estimate the surface potential in the wake region of a small satellite like DMSP. To do this we first choose a value of ϕ_0 which gives a solution to V_s = - 65V at Θ = 90°. This is equivalent to some mixture of He^+ and O^+. With this we next solve equation (6) for the ionospheric ion current at any location on the satellite. The final step is to solve equations (2) and (4) for the potential V_s that gives an I(V) = 0 solution to equation (1).

Figure 9 demonstrates the results of this procedure. Here we have chosen the value ϕ_0 = 60°. From Figure 8 we see that this corresponds to a case with N_{He}^+/N_0 = 0.63. On the ram side of the vehicle the potential is slightly positive. As we go away from 90° into the wake direction the model predicts that the surface potential rises quickly and saturates at a value of $\sim$ 1 kV. We have examined the model predictions for other values of ϕ_0 in the range 55° to 70° and found that within a few percent the results are insensitive to these variations.

REFERENCES

1. Mozer, F.S., Cattell, C.A., Hudson, M.K., Lysak, R.L., Temerin, M., and Torbert, R.B. (1980) Satellite measurements and theories of low altitude auroral particle acceleration, Sp. Sci. Rev. 27: 155.

2. Lin, C.S. and Hoffman, R.A. (1979) Characteristics of the inverted-V event, J. Geophys. Res. 84: 1514.

3. Frank, L.A. and Ackerson, K.L. (1971) Observation of charged particle precipitation into the auroral zone, J. Geophys. Res. 76: 3612.

4. Frank, L.A., and Ackerson, K.L., (1972) Local time survey of plasma at low altitudes over the auroral zone, J. Geophys. Res. 77: 4116.

5. Akasofu, S.-I. (1964) The development of the auroral substorm, Planet. Sp. Sci. 12: 273.

6. Akasofu, S.-I., Kimball, D.S. and Meng, C.-I. (1965) The dynamics of the aurora, II, Westward travelling surges, J. Atmos. Terr. Phys. 27: 173.

7. Meng, C.-I., Synder, A.L. and Kroehl, H.W. (1978) Observations of auroral westward travelling surges and electron precipitations, J. Geophys. Res. 83: 575.

8. Mullen, E.G., and Gussenhoven, M.S. (1982) High-level spacecraft charging environments near geosynchronous orbit, AFGL-TR-82-0063 Hanscom AFB, MA 01731.

9. Burch, J.L., Fields, S.A., Hanson, W.B., Heelis, R.A., Hoffman, R.A. and Janetzke, R.W. (1976), Characteristics of auroral acceleration regions observed by Atmosphere Explorer C., J. Geophys. Res. 81: 2223.

10. Dandekar, B.S., and Pike, C.P. (1978) The midday, discrete auroral gap, J. Geophys. Res., 83: 4227.

11. Hardy, D.A. (1983) The worst case, charging environment, in Proceeding of AFGL Workshop on Natural Charging of Large Space-Structures In Near-Earth Polar Orbit: Sept 14-15, 1982, ed by R. C. Sagalyn, D.E. Donatelli and I. Michael AFGL-TR - 83-0046, Hanscom AFB, MA, 01731.

12. Burke, W. J. (1983) Environmental interactions of polar orbiting satellites, in Proceedings of AFGL Workshop on Natural Charging of Large Space-Structures in Near-Earth Polar Orbit: Sept. 14-15, 1982, ed. by R. C. Sagalyn, D. E. Donatelli and I. Michael, AFGL-TR-83-0046, Hanscom AFB, MA 01731.

13. Smiddy, M., Sagalyn, R.C., Sullivan, W. P., Wildman, P. J. L., Anderson, P. and Rich, F. (1978) The topside ionosphere plasma monitor (SSIE) for the Block 5D/Flight 2 DMSP satellite, AFGL-TR-78-0071, Hanscom AFB, MA 01731.

14. Rich, F.J., Smiddy, M., Sagalyn, R.C., Burke, W.J., Anderson, P., Bredesen, S. and Sullivan, W. P. (1980). In-flight characteristics of the topside ionospheric monitor (SSIE) on the DMSP satellite Flight 2 and Flight 4, AFGL-TR-80-0152, Hanscom AFB, MA 01731.

15. Gorney, D.J., Clarke, A., Croley, D., Fennell, J. Luhmann, J. and Mizera, P. (1981). The distribution of ion beams and conics below 8000 km, J. Geophys. Res. 86: 83.

16. Laframboise, J.G., Godard, R., Kamitsuma, M. (1982) Multiple floating potentials, "threshold temperature" effects, and "barrier" effects in high-voltage charging of exposed surfaces on a spacecraft" in Proceedings of International Symposium on Spacecraft Materials in Space Environment, Toulouse France, 8-11 June 1982, Publications Branch ESD, Noordwijk, The Netherlands.

17. Gurevich, A.V., Pitaevskii, L.P. and Smirnova, V.V. (1969) Ionospheric aerodynamics Space Sci. Rev. 9: 805.
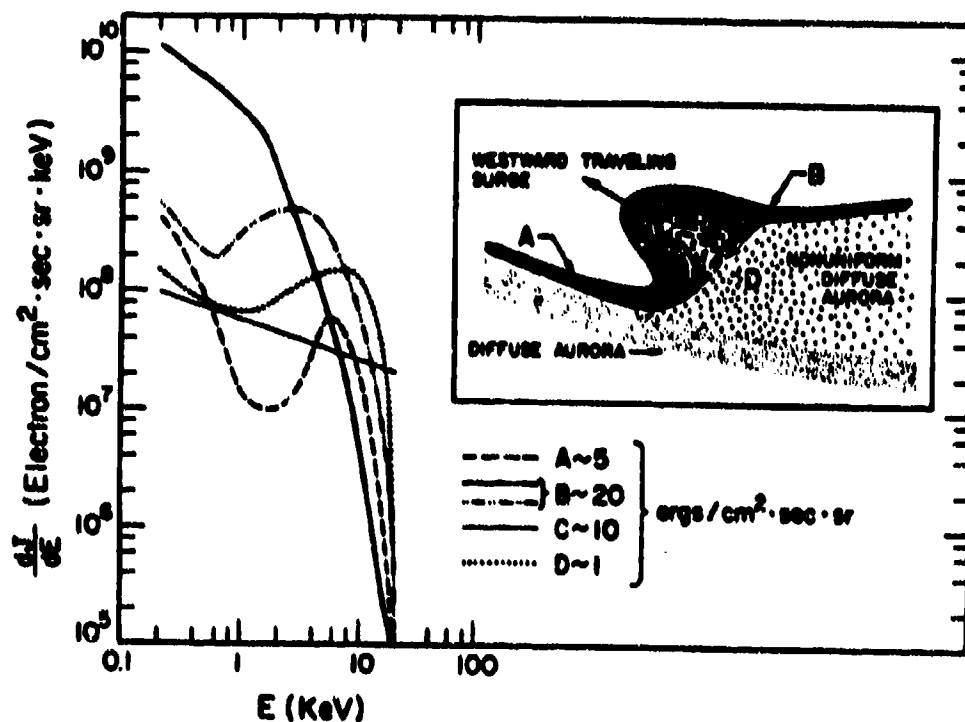
1. The morphology of auroral luminosity and precipitating electron spectra in
the vicinity of westward travelling surges.

118
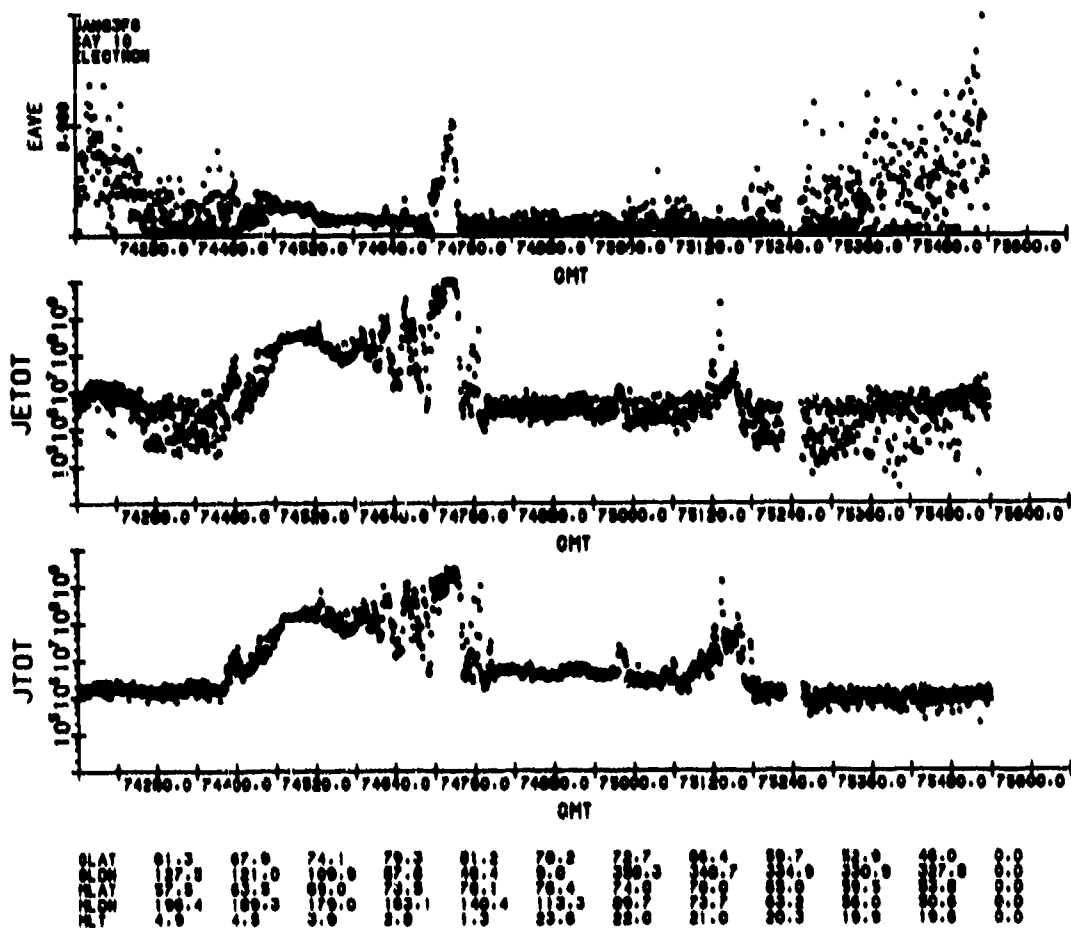
2. Average energy, directional energy flux and directional number flux of pricipitating electrons measured during DMSP/F6 northern auroral pass of 10 January 1983.

3. Average energy, directional energy flux and directional number flux of downcoming ions measured during DMSP/F6 northern auroral pass of 10 January 1983.
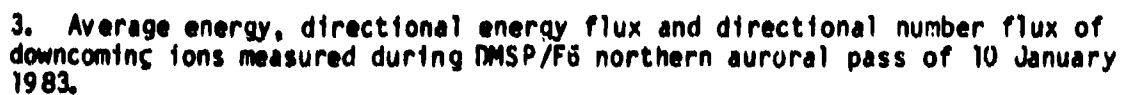
DMSP F6 JAN 10
UT 20:45:17
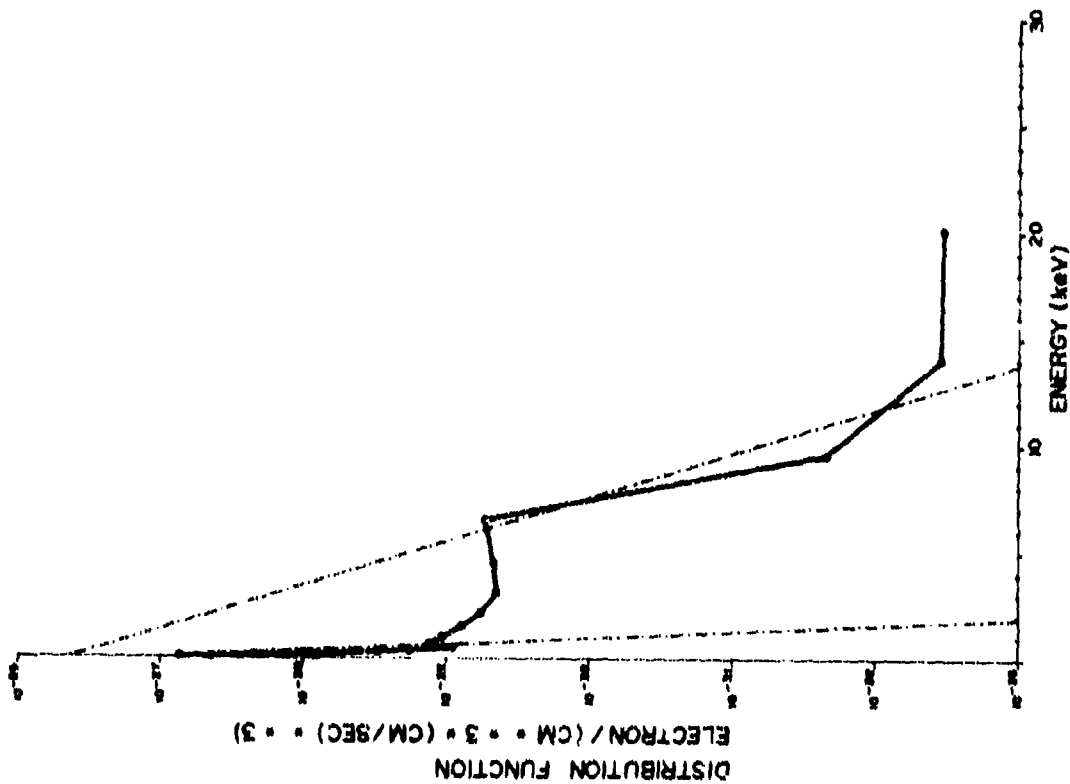
DMSP F6 JAN 10
UT 20:45:17
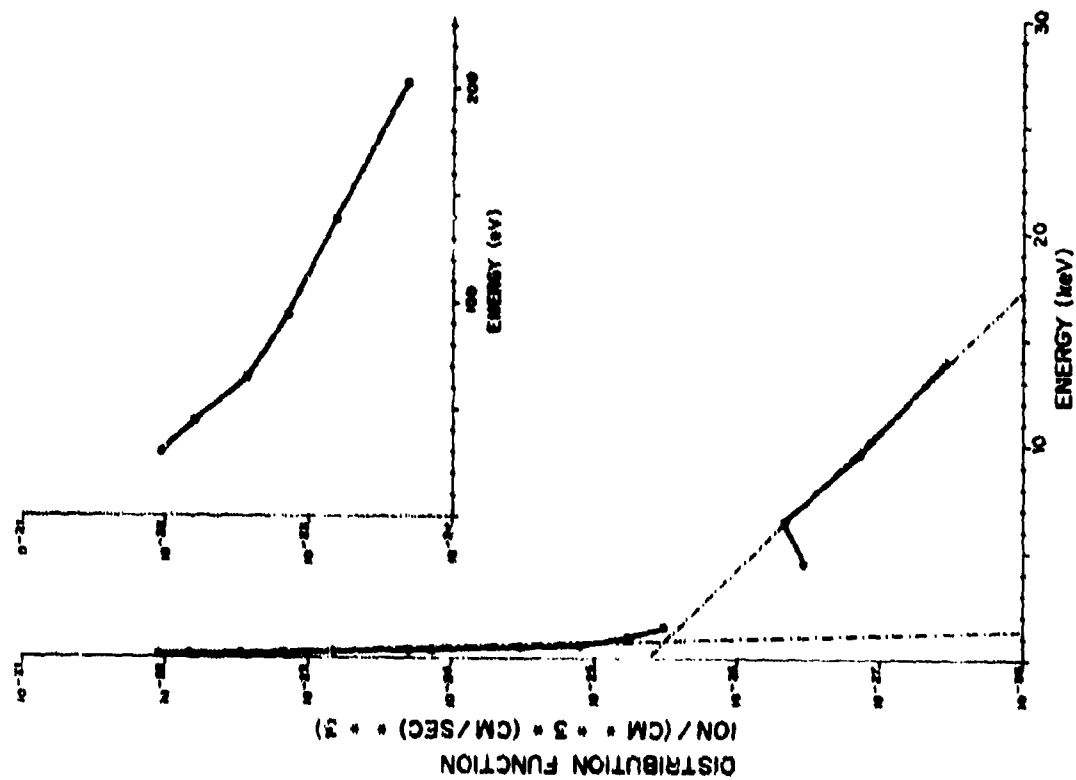
4. Distribution functions of downcoming electrons and ions with energies between 30eV and 30 KeV detected at 2045:17 UT of 10 January 1983.

121
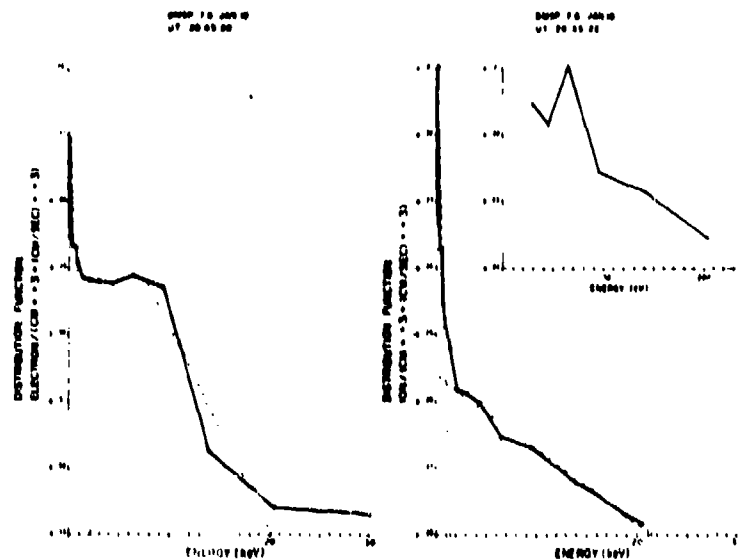
5. Distribution functions at 2045:22 UT in same format as Figure 4. The inset expansion of the low energy portion of ion distribution function shows a charging peak at 65 eV.
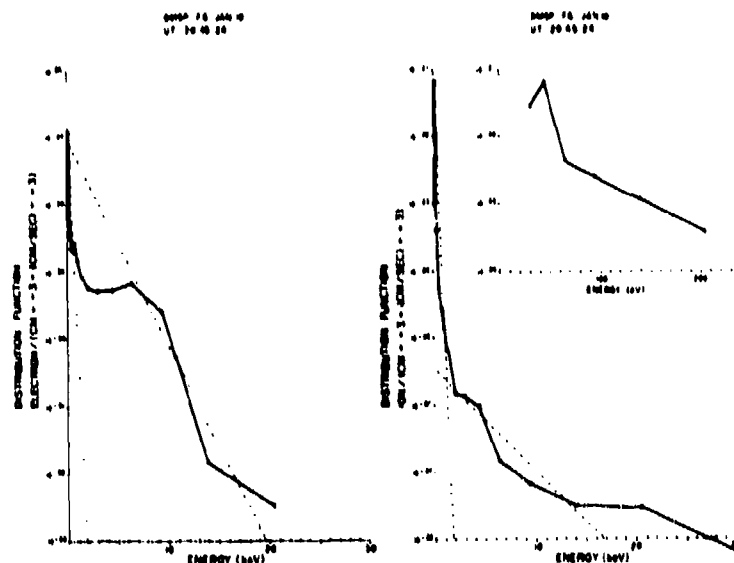
6. Distribution functions at 2045:24 UT, in same format as Figure 4. Here the charging peak is at 44 eV.

10 JANUARY 1983
DMSP THERMAL PLASMA
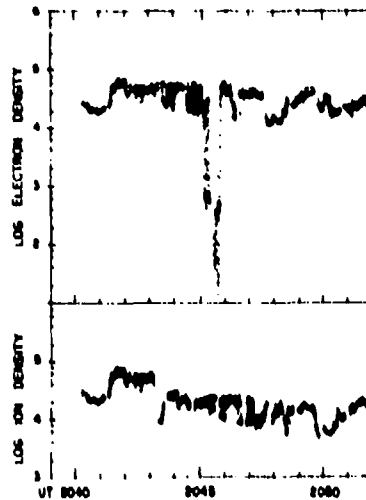
7. Mode 1 currents to the thermal electron and ion sensors during the northern auroral pass of 10 January. The "densities" calculated from these currents assume that the grids are at plasma potential and are overestimates in both cases.
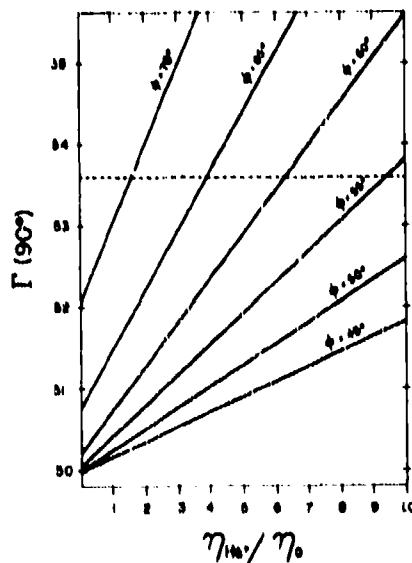
8. Plot of Γ, with Θ set equal to $90°$, as a function of $N_{H_e^+}/N_0$. for several values of ϕ_0. The line at 0.536 represents the value of Γ required for current balance with $V_S = -65$ V on the top surface of DMSP.
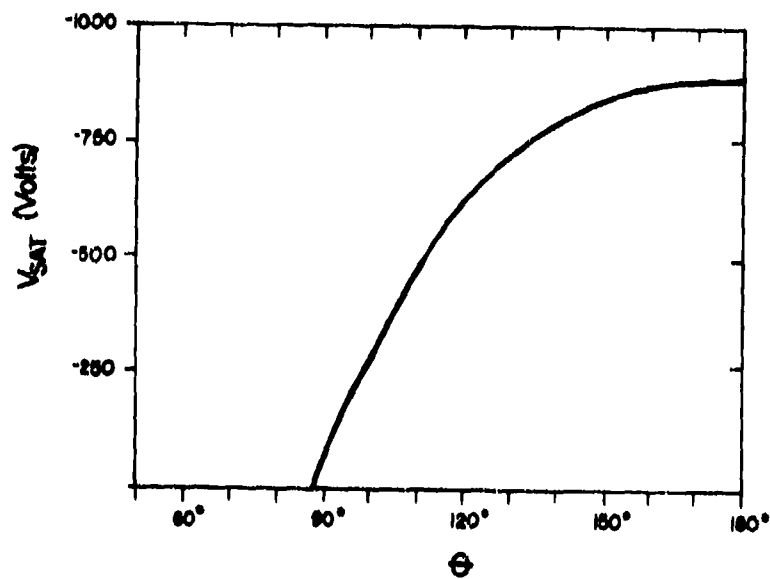
9. Surface potential as a function of Θ for $\phi_0 = 60°$.

CHARGING OF DMSP/F6 SPACECRAFT IN AURORA ON 10 JANUARY 1983

Arthur L. Besse, Allen G. Rubin, and David A. Hardy
Air Force Geophysics Laboratory
Hanscom Air Force Base, Massachusetts 01731

Two independent instruments on the spacecraft showed charging to a
moderate (44 volts) negative potential. The electron spectrometer
showed a flux of 2×10^9 electrons ($cm^{-2} sec^{-1} ster^{-1}$) peaked at 9.5 keV.
This was marginally sufficient to overcome the flux of cold ambient
ions. Charging calculations are presented showing where simplications
are justified and where serious uncertainties exist. More serious charging
is predicted for the Shuttle in polar orbit.

INTRODUCTION

Spacecraft charging has been widely observed in geosynchronous orbit
on the ATS-5 and ATS-6 pair and on the SCATHA spacecraft (ref 1 & 2).
An adequate theory for explaining the observations exist. Neither the
data or theory can be exported to low polar orbit and its drastically
different environment. This paper gives evidence of charging on the DMSP
F6 spacecraft (see ref 3 for instrumentation). A simple model is set up
explaining the observations.

BRIEF THEORY OF SPACECRAFT IN THE AURORA

The cold ambient electrons can charge a spacecraft to a few volts
negative at most. More severe charging occurs in the earth's shadow when
the energetic (over a kilovolt) precipitating electron current exceeds
the ram ion current. Charging continues until an increase in ram ion
current and/or a decrease in precipitating electron current produces a
zero net current.

In the absence of plasma shielding, the ram ion current increases
rapidly with increasingly negative potentials. This typically limits
charging to tens of volts negative. In the presence of intense plasma
shielding (electrostatic or magnetic) the ram ion current does not respond
to negative potentials. Charging then proceeds to much higher negative
potentials until a slowly decreasing precipitating electron current brings
about a current balance. Calculations indicate possible potentials of
several kilovolts. Below some size plasma shielding is negligible and
above some size it dominates. There exists no commonly accepted way of
calculating these sizes.

A knowledge of the relative velocities and densities of the various

particles is essential to the understanding of auroral charging. Typical values arranged in order of increasing velocity are:

Ambient oxygen ion: $v = 1.5 \times 10^5$ cm/sec; $N = 1 \times 10^4$ cm^{-3}

Spacecraft: $v = 8 \times 10^5$ cm/sec

Ambient electron: $v = 3 \times 10^7$ cm/sec; $N = 1 \times 10^4$ cm^{-3}

Precipitating electrons: $v = 6 \times 10^9$ cm/sec; $N = 1$ cm^{-3}

Also essential is a knowledge of the various time scales involved.

Typical values arranged in order of increasing time are.

Charging response:	0.01 Seconds
Aurora, fine structure:	0.1 Seconds
Instrument response:	1 Seconds
Aurora, coarse structure:	10 Seconds

The value for charging response applies to the main frame. Thin dielectric coatings may charge differentially with very much longer response times. The aurora time scale is in the spacecraft's frame of reference and is due primarily to spatial variations in the aurora.

DETECTION OF SPACECRAFT CHARGING

Charging was detected by an ion spectrometer sensing acceleration of the ram ions to 30 volts or more and by a probe sensing the deceleration of ambient electrons. Charging to negative potentials less than 30 volts was detected by the probe alone.

The accelerated ions appeared as an intense narrow band never occupying more than one energy channel. This is as predicted by theory. However, the spectrum was not void below the intense band as predicted by theory and observed on geosynchronous spacecraft.

THE CHARGING EPISODE

The probe indicated charging starting at 74701 seconds UT and ending at 74737 UT, with a very brief drop out at 74705. The start, drop out, and end of charging accompanied large abrupt changes in electron flux, particularly in the 4.4 keV channel. The ion spectrometer indicated charging to potentials of 30 to 65 volts negative for a portion of this period, namely from 74721 UT to 74731 UT. The evidence that charging to these levels actually occurred appears to be conclusive.

126

Five representative time intervals, each lasting from three to five seconds, were chosen for study. Within each time period the spectra remained relatively constant. The electron spectra were averaged over each interval. The average spacecraft potential was determined by probe and ion spectrometer data. When the charging was insufficient to show up on the ion spectrometer but showed strongly on the probe, a value of 10 volts was assigned. The five spectra are shown in figure 1. The starting times from A to E were respectively: 74697, 74708, 74712, 74722, and 74729. Durations were respectively 4, 3, 5, 4 and 3 seconds. Average fluxes and potentials are given in the figure. The fluxes include only five channels from 3.0 to 13.9 kilovolts for reasons to be discussed later.

The figure shows both broad spectra and narrow "inverted V" spectra. The actual shape of the "inverted V" spectrum is unresolved, it could be much narrower and more intense than shown. The electron spectrometer is not designed for accurate flux measurements when the spectrum is very narrow, therefore, the flux indicated in the figure for the "inverted V" may be in error.

We authors postulate an accelerating electric field that is sometimes high above the spacecraft and sometimes close above the spacecraft. In the former case, but not in the latter, there should be strong collisional broadening of both the energy and the pitch angle distribution.

CHARGING CALCULATIONS

Five first order approximations will be made. They are:

1) A spherical spacecraft with a conducting and hence equipotential surface.

2) Zero ambient electron temperature. The energy of these particles in either the plasma frame of reference or in the spacecraft frame of reference was much smaller than the measured potentials.

3) Infinite precipitation electron temperature. The energy of these particles was very large compared to the measured potentials.

4) Precipitating electron flux equal to that measured in the 3 to 14 keV energy range. Fluxes at higher energies were very low. Fluxes at lower energies were small and were largely offset by secondary electrons. Secondaries were not included in the calculations. The flux is treated as isotropic within some field aligned solid angle and zero elsewhere.

5) Ambient ion temperature equal to the drift energy of an ion in the spacecraft frame of reference. This energy is large compared to the thermal energy. Probe theory assumes that the total particle energy (kinetic plus potential) is independent of position. This assumption is valid in and only in the spacecraft frame of reference. The ambient ions are predominantly singly ionized atomic oxygen.

127

The first four approximations simplify calculation of the electron current to the negatively charged spacecraft. The "zero temperature" ambient electrons are repelled and do not reach the spacecraft. The "infinite temperature" precipitating electron current is independent of the spacecraft potential. Secondary electrons are adequately allowed for by discarding the low end of the spectrum and need not appear explicitly in the calculations. With these considerations, the electron current to the spacecraft becomes

$$I_e = -e \; J \; S \; (\pi R^2) \tag{1}$$

where I_e = electron current
   e = elemental charge
   J = precipitating electron flux per steradian in 3 to 14 keV channels
   S = solid angle of precipitating electrons
   R = spacecraft radius
   (πR^2) = spacecraft electron collision cross section.

The first and fifth approximations simplify calculation of the ion current to the spacecraft. Spherical probe theory gives the ion current in the long Debye length limit as:

$$I_i = e \; v \; N \; [(\pi R^2)\left(1 + \frac{-eV}{T}\right)] \equiv evNA; \; -eV \underline{>} 0 \tag{2}$$

where I_i = ion current
   v = ion drift velocity
   N = ion density = 1×10^4 cm^{-3}
   V = spacecraft potential
   T = temperature associated with ion drift velocity = 5ev
   A = spacecraft ion collision cross section.

When the Debye length is not long compared to the probe radius, a sheath containing a net positive charge forms around the probe. The charge in the sheath shields ambient ions outside the sheath from the probe's electric field, thereby reducing the number attracted to the probe. The shielding effect may be incorporated in equation (2) by multiplying the potential by a shielding factor K less than unity. This factor is a function of potential and generally does not appear explicitly in probe theories. It may also be a function of the ion angular distribution (in this case almost mono-directional in the spacecraft frame of reference).

At equilibrium potential the absolute values of electron and ion currents are equal. This leads to the equilibrium equation

$$JS = v \cdot N \cdot (1 + k \frac{-eV}{T}); \; eV \underline{\leq} 0, \; k \underline{\leq} 1 \tag{3}$$

where k = shielding factor.

The unknowns in this equation are the electron solid angle S and the ion shielding factor k. These unknowns were evaluated from the data in figure (1) and from other measurements. The solid angle is determined from equation (3) using the threshold flux required for charging. The data consistently yields a narrower solid angle for inverted "V" spectra than for broad spectra. The shielding factor was determined by the electron

flux associated with a potential of -44 volts. This flux was approximately four times greater than the threshold flux. The results of the evaluations were

$S = \pi$, inverted "V" spectra
$S = 2\pi$, broad spectra
$k = 1/2$.

These results should be regarded with caution. The data is not conclusive due in part to an environment whose rate of change is fast compared to the sampling rate of the instruments - probably fast compared to any practical sampling rate.

The value given above for the shielding factor is substantially less than unity. If true, this has serious implications. It means that the DMSP spacecraft are already of a size where space charge in the sheath acts to increase the magnitude of charging potentials and that any larger spacecraft such as the Shuttle, will charge to higher potentials, other factors being equal.

REFERENCES

1) Olsen, R.C., and Purvis, C.K., Observations of Charging Dynamics, J. Geophys. Res., 88, 5657, 1983.

2) Mullen, E.G., Gussenhoven, M.S., and Garrett, H.B., A worst case spacecraft environment as observed by SCATHA on 24 April 1979, Rep. AFGL-TR-81-0231, Air Force Geophys. Lab., Hanscom AFB, MA 1979; ADA 108680.

3) Hardy, D.A., Gussenhoven, M.S., and Huber, A., The precipitating electron detectors (SSJ/3) for the block 5K/flights 2-5 DMSP satellites: Calibration and data presentation, Rep, AFGL-TR-79-0210, Air Force Geophys., Lab., Hanscom AFB, MA., 1979; ADA 083136
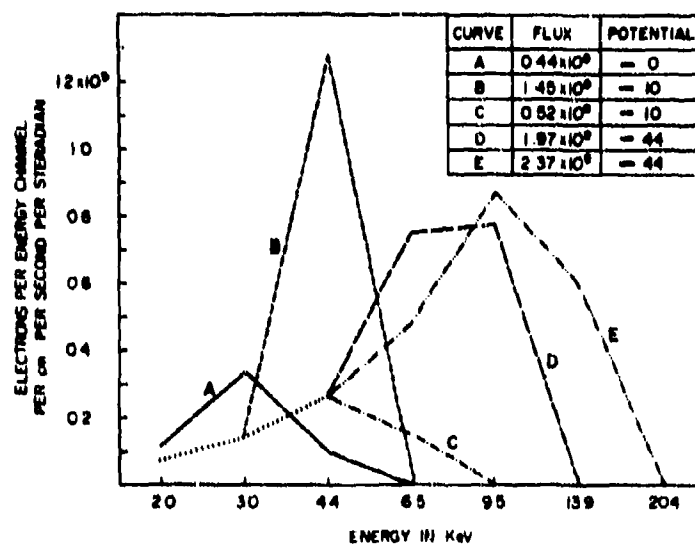
Figure 1. – Five precipitating electron spectra. (The flux associated with each spectra is listed in the upper right corner along with the corresponding spacecraft potential.)

130

AVERAGE AND WORST-CASE SPECIFICATIONS OF PRECIPITATING
AURORAL ELECTRON ENVIRONMENT

David A. Hardy, William J. Burke, and M. S. Gussenhoven
Air Force Geophysics Laboratory
Hanscom Air Force Base, Massachusetts 01731

E. Holeman
Emmanuel College
Boston, Massachusetts 02115

H. C. Yeh
Boston College
Chestnut Hill, Massachusetts 02167

The precipitating electrons in the auroral environment are highly variable in their energy and intensity in both space and time. As such they are a source of potential hazard to the operation of the Space Shuttle and other large spacecraft operating in polar orbit. In order to assess these hazards both the average and extreme states of the precipitating electrons must be determined. In this paper we present work aimed at such a specification. In the first half of the paper we present results of a global study of the average characteristics. In this study the high latitude region was divided into spatial elements in magnetic local time and corrected geomagnetic latitude. The average electron spectrum was then determined in each spatial element for seven different levels of activity as measured by K_p using an extremely large data set of auroral observations. In the second half of the paper we present a case study of an extreme auroral electron environment in which the electrons are accelerated through a field aligned potential as high as 30,000 volts and in which the spacecraft is seen to charge negatively to a potential approaching .5 kilovolts.

INSTRUMENTATION

The data used for this analysis were from the SSJ/3 detectors on the F2 and F4 satellites and the SSJ/4 detector on the F6 satellite of the Defense Meteorological Satellite Program as well as the CRL-251 experiment on the P78-1 satellite of the Space Test Program. The SSJ/3 detectors consisted of a set of two curved plate electrostatic analyzers capable of measuring the flux of precipitating electrons in 16 energy channels between 50eV and 20,000 eV. The SSJ/4 detector consists of a set of four curved plate electrostatic analyzers that measure both electrons and ions in 20 energy channels each,

in the energy range from 30 eV to 30000 eV. Both the SSJ/3 and SSJ/4 detectors return a full spectrum over all energy channels once per second and all detectors are oriented on the spacecraft such that they look towards the local zenith. The CRL 251 experiment consists of two SSJ/3 detectors mounted at right angles with their look directions in the spin plane of the satellite. Each detector returns 4, 16 point spectra each second. The satellite has a spin rate of approximately 11 RPM with the spin plane in the orbit plane of the satellite.

All the satellites were launched into circular sun synchronous orbits. The F2 satellite's orbit plane was initially in the dawn-dusk meridian but precessed towards the 0830-2030 MLT meridian during the satellite's lifetime. The period for which data are available, the altitude of the orbit, and the orbital plane are listed in Table 1.

The DMSP sensors are operated continuously and approximately 80% of the data were available for this study. For the P78-1 approximately 1000 polar passes were available from 1979. For the determination of the average character-istics, the F2, F4, and P78-1 data were used. The worst case study was performed using the F6 data since these data cover a wider range in energy.

AVERAGE CHARACTERISTICS

Historically, there have been two approaches to global specification of the average characteristics of auroral precipitation. In the first of these the researcher builds up a global or local time picture using a set of indi-vidual passes each studied in detail (ref 1 & 2). The advantage of such an approach is that all the details of each pass are considered in creating an overall picture. The major disadvantage in such studies is that in order to keep both the analysis and data presentation manageable the researcher must restrict the total number of passes studied either by spacing them widely in magnetic local time or in activity. In the second approach the researcher builds up his global picture by dividing the region of interest into zones in magnetic local time, geomagnetic latitude and activity he then uses very large data sets to determine the average value of the quantity of interest in each zone (ref 3 through 9). This approach has the advantage of providing real global maps. It's major disadvantage is that in the averaging process all small spatial and temporal variations are smoothed out, of necessity. The number of such studies done in the past has additionally been restricted by the fact that they require very large data sets (millions of samples) and they require significant amounts of computer time.

In this study we have taken the second of these two approaches using the data set from identical electrostatic analyzers flown on three Air Force sat-ellites. We divided the high latitude region into zones in magnetic local time and corrected geomagnetic latitude. In MLT the divisions were 48 one half hour sections. In latitude there were 30 divisions at 2^0 increment between 50 and 60 degrees, 1^0 increments between 60 and 80 degrees, and 2^0 increments from 80 to 90 degrees. Seven such matrices were created, one for the Kp = 0, 0+ cases, one for Kp = 1-, 1, 1+ cases and so on up to Kp = 5-, 5, 5+. The last matrix included all cases greater than Kp = 6-. Fifteen months of data were used from the F-2 and F-4 satellites. The fifteen months were chosen to give an even distribution of the data over the seasons of the year and to provide sufficient coverage at high activity. Altogether the 15 months

of data provided 13.6 million spectra. All orbits of the P78-1 satellite in the interval from February 1979 to January 1980 were used. This comprised approximately .52 million additional spectra. The 14.1 million spectra were divided among the 7 levels of Kp as follows; Kp = 0, 7.85%; Kp = 1, 23.82; Kp=2, 26.9%, Kp = 3, 21.9%; Kp = 4, 10.5%; Kp = 5, 5.3%; Kp > 6-, 3.6%. In each zone the average and standard deviation of the differential number flux for each of the 16 energy channels of the detector was calculated using all spectra that fell within that zone. The final product is therefore the average spectrum in each zone at each level of activity.

From the average spectra we calculated integral quantities over the entire energy range of the average energy spectrum. The three quantities calculated were the integral number flux in units of e/cm^2-sec-ster defined as:

$$JTOT = j(E_1) (E_2 - E_1) + \sum_{i=2}^{15} j(E_i)\frac{(E_{i+1} - E_{i-1})}{2} + j (E_{16}) (E_{16} - E_{15})$$

The integral energy flux in units of keV/cm^2-sec-ster defined as:

$$JETOT = E_1 \, j(E_1) (E_2 - E_1) + \sum_{i=2}^{15} j(E_i) \, j(E_i)\frac{(E_{i+1}) - E_{i-1})}{2} +$$

$$E_{16} j (E_{16}) (E_{16} - E_{15})$$

and the average energy

$$EAVE = JETOT/JTOT$$

where

$j(E_i)$ = the average differential flux in the ith energy channel

E_i = the central energy of the ith channel

These three quantities are displayed as isocontour maps in Figures 1a-d, 2a-d, and 3a-d where we have plotted the Kp = 0, 2, 4, and 6 cases. The discussion of these maps is in two sub-sections; the first dealing with the characteristics of the relatively hot electron (EAVE > 600 eV) and the second dealing with the characteristics of the colder electrons. Such a division is made based on a comparison of the maps of integral flux and average energy. Such a comparison shows that the high latitude region separates naturally into two regions based upon the average energy of the electrons. The hotter plasma is confined to a roughly annular region whose low latitude edge is the equatorward edge of the auroral zone while the colder plasma fill the remaining area between the poleward edge of the annulus and the geomagnetic pole. The colder electron region is composed of a band of relatively intense precipitation bounding the poleward edge of the hot plasma and a region of lower intensity precipitation in the rest of the area up to the pole.

HOT ELECTRON REGION

For the hot electrons we note the following:

1) The average energy of the precipitating electron varies greatly in magnetic local time. In general the peak average energies are highest on the morning side of the oval. Within the morning side region there are two maxima in the average energy; one between midnight and 0600 MLT and the second typically two hours pre-noon. In tables 2a and 2b the location and electron characteristics for the two maxima are listed for all seven Kp zones.

One notes that the average energy of the post midnight maximum is between 3 and 5 keV in a latitude range between 63 and 67°. The local time of these maxima varies over 6 hours and the trend is for the energy flux to increase with increasing Kp. The lack of a post midnight maximum for the Kp=5 case we attribute to the relatively limited sampling provided by the P78-1 satellite in this region and at this level of activity. The pre-noon maximum is more fixed in magnetic local time and more ordered by Kp. Except for Kp=0 case this maxima is always found between 0930 and 1100 MLT and at a geomagnetic latitude that smoothly decreases with increasing Kp. The average energy increases from Kp=0 to Kp=3 but then decreases for all higher Kp reaching a value for the highest activity case a factor of two below that of the Kp=0 ease. In a similar manner the energy flux increases from Kp=0 to Kp=3 but then is approximately stable for all higher activities.

2. At energies above 1 keV the region of hot plasma is not continuous about the oval. For Kp=0 the average energy does not reach 1keV at any latitude in the MLT range from ~ 1800 to 2200. For the Kp=1 and 2 cases there is a minimum within the region of hot plasma at approximately 1800 hour MLT. For the four remaining cases there is a clear minimum between noon and 1800 hours MLT. The average energy of this minimum falls below 1 keV. For the four highest activity cases the location of the minimum appears to move to earlier local times with increasing activity. Part of this effect appears to result from a change with activity in the magnetic local time past noon to which hot electrons drifting around on the morning side are able to penetrate. These electrons are seen at the latest MLT for Kp=0 and penetrate to progressively earlier MLTs with increasing activity. For the Kp >6- case there are few regions to the dayside of the dawn-dusk meridian in which the average energies reaches 1.5 keV.

3. The majority of the energy flux of particles into the high latitude region is carried by the hot electrons. Typically for any MLT zone on the nightside of the oval the latitude of the maximum in energy flux is near or coincides with the maximum in average energy. At all activity levels above Kp=0 the isocontours of energy flux within the hot electron region have a C or horseshoe shape that is roughly symmetric about a meridian one to two hours post midnight and post-noon. The maximum energy flux occurs slightly before midnight for Kp=0 and 1 but is clearly post midnight for all higher activity cases.

4. The energy flux into the nightside oval and up to approximately 1000 MLT on the dayside increases with increasing activity as the oval expands. By contrast the energy flux carried by hot electrons at noon reaches a maximum

at Kp=2 and then decreases for higher activity. This is shown in Table 3 where we have listed the maximum energy flux and it's latitude for the 0000 to 0030 MLT zone and for the peak in average energy for the hot electrons in the 1130 to 1200 MLT zone.

The latitude for both cases decreases for increasing activity as would be expected from the overall movement of the oval equatorward. The energy flux at midnight increases by more than an order of magnitude from Kp=0 to Kp >6- while the energy flux at noon reaches a maximum value of 7.79×10^7 keV/ cm^2-sec-ster for Kp=2 and then decreases for increasing Kp above this point, reaching a value for the Kp≥6- case approximately a factor of two lower than the Kp=0 case. The ratio of the energy flux at midnight to that at noon increases with increasing Kp except for the Kp=5 case. The 7 values from Kp=0 to Kp≥6- are 2.7, 4.1, 4.7, 12.0, 21.5, 18, 72.5.

COLD ELECTRON REGION

For the cold electrons (EAVE < 600 eV) we note the following:

1. The highest number flux of cold electrons is found within the dayside portion of the overall region of electron precipitation. At the first five activity levels there is a clear crescent shaped region of cold electrons roughly symmetric about noon or slightly skewed towards prenoon. The crescent shaped region is most clearly evident in the Kp=0 and Kp=1 cases where at a level of above 5×10^7 electrons/cm^2-sec-ster it extends in magnetic local time over the entire dayside region and one to several hours into the nightside region. The region extends closer to midnight on the morning side than the evening side. The same behavior is maintained for the next three levels of activity but is obscured in the isocontour plots by the increasing integral flux on the night side from the hot electrons. For the two highest activity cases there is still an extended region of low energy precipitation on the dayside but it is not as well organized as for the lower activity cases.

2. The intensity of the integral number flux within the dayside region shows little if any increase with increasing activity. Except for the Kp ≥ 6- case the integral number flux is typically between 5×10^7 and 2×10^8 electrons /cm^2-sec-ster. Although the level of flux within the region is relatively constant the total flux of electrons into the region is increasing with increasing activity. For the 7 levels of activity the total downcoming flux over the entire dayside with energies between 50 eV and 660eV are 7.65×10^{24}, 8.89×10^{24}, 1.0×10^{25}, 1.21×10^{25}, 1.56×10^{25}, 1.97×10^{25} and 3.78×10^2electrons/ -sec-ster. These numbers were obtained by determining the integral flux for electrons with energies between 50 eV and 660 eV in each spatial element on the dayside multiplying these by the area of the spatial element and summing. For all but the Kp≥ 6- case this trend is well fit by the equation,

$$I = 7.8 \times 10^{24} e^{.2Kp} \text{ electrons/sec-ster}$$

3. Within the dayside region of cold electron precipitation there is, in all but the Kp≥ 6- case, a clear prenoon maximum. In Table 4 the parameters for these maxima are listed.

One notes that the maximum's location in MLT is relatively constant while the latitude decreases with increasing activity as the oval expands. The integral number flux increases only from 3.05 to 4.1 x 10^8 from the Kp=0 to the Kp> 6- case. Both the integral energy flux and average energy are similarly within a narrow range except at the two highest activities. These increases at higher activity are attributable to an increase in the spatial variability of the oval such that some hot electron spectra have been used to determine the average spectrum from which the energy flux and average energy were calculated If at all activity levels the values listed in Table 3 are recalculated using only the portion of the spectrum between 50eV and 660eV the values for the Kp=0 to Kp=3 cases vary by less than 10% for all three quantities. For Kp=4 and 5 cases, however, the energy flux drops to values below 10^8 keV/cm^2-sec-ster and the average energy to values below 200 eV.

4. In the dayside region of cold electrons there is a clear minimum in average energy. The location and electron characteristics at the minimum are listed in Table 5.

The location in latitude shows a total variation of 5^0 with activity and except at high activity is found between 1100-1200 MLT. Again the electron characteristics are quite stable with increasing activity. The integral number flux ranges between 3 and 10 electrons/cm^2-sec-ster except for the KP > 6- case. The integral energy flux value falls in a similar narrow range and the average energy shows a slight decrease with increasing activity. These average energy minima sit near the poleward edge of the cresent shaped region of cold electron precipitation.

WORST CASE ENVIRONMENT

The concept of a worst case environment for large space structures in near-earth, polar orbit involves an extrapolation of experience with small satellites near geostationary altitude. The need for extrapolation derived from our historical situation which presents many well-documented examples of severe charging at geostationary altitude, a few cases of small-satellite changing at ionospheric altitudes, and as yet no experience with large structures, such as Shuttle, in polar orbit. At geostationary altitude the worst charging occurs when satellites are in the shadow of the earth during some substorm injection events. In this situation the occurrence of charging is unambiguously determined by the location in energy of the so-called "charging peaks" in the positive ion spectrum. If a satellite charges to - 5kV, low-energy ions in the vicinity of the satellite are accelerated through this potential. Typically, a large flux of ions would he measured in the energy channel centered nearest 5KeV while few if any ions would be detected in energies channels below this value. Mullen and Gussenhoven (ref 10) (1982) found that the most severe charging occurs during those substorm injection events that are characterized by strong fluxes of electrons with energies above 10 keV. Impacting electrons with energies above (below) this value produce less (more) than one secondary electron per particles for typical spacecraft materials (ref 11) With this criterion in mind Hardy (ref 12) surveyed more than 10,000 passes of DMSP/F2 over the auroral zone to identify conditions under which the flux of electrons with energy > 1 keV exceeded 10^{10} electrons/cm^2-sec-ster. Although these energetic electron observations are useful for modelers who require realistic, worst-case fluxes it provides no empirical guidelines as to what degree the satellites actually charge.

With the launch of DMSP/F6 in December 1982 it has become possible to specify the degree to which charging occurs in "worst case" auroral environments. This satellite carried detectors capable of measuring the fluxes of downcoming electrons and positive ions with energies between 30 eV and 30 keV. The satellite also carried detectors to measure the densities and temperatures of thermal ions and electrons. Because the geometric factor of the energetic ion detector greatly exceeds that of any previously flown, it is possible for the first time, to look for ion "charging peaks" as indicators of spacecraft charging in the ionosphere. The detector systems as well as the methods for data presentation and identifying severe charging events are described in a companion paper (ref 13) and will not be repeated here.

Figures 4 and 5 give the average energies (top panels), directional energy flux (middle panels) and directional number flux of electrons and positive ions measured during a northern, high-latitude pass of DMSP on 12 January 1983. The data are presented as a function of UT in seconds of the day, geographic latitude and longitude; magnetic latitude, longitude and local time. Attention is directed to the two minute interval between 35820 (0957) and 35940 (0959) UT. The electron flux rose sharply from typical polar rain values of 2×10^6/cm^2-sec-ster, starting at 35860 UT to a maximum value of 10^{10}/cm^2-sec-ster at 35878 UT. The flux level then decreased to a nearly steady value of 5×10^8 for the following minute. The average energy profile suggests that the satellite either passed through two closely spaced inverted-V structures or through a single, complex inverted V with a very intense substructure at its poleward boundary. During the subinterval 35860-35880 UT, the ion flux increased by three orders of magnitude with no easily recognized increase in average ion energy. An intense flux of high-energy electrons accompanied by an increased flux of low-energy ions is often an indicator of spacecraft charging at geostationary altitudes (ref 14). An analysis of individual distribution functions for ions and electrons, presented below, shows that this can also be regarded as a signature of charging at ionospheric altitudes. Before examining individual spectral measurements two additional comments related to Figures 4 and 5 should be made. First, during the interval 35880 to 35940 as the satellite passed through the equatorward (portion of the) inverted V the flux of ions remained constant at $\sim 10^6$ /cm^2-sec-ster and their average energy increased to several kilovolts. As demonstrated below no measurable charging occurred during this interval. Second, the electron flux levels of 10^{10}/cm^2-sec-ster near 35875 UT represent lower bounds on the actual flux. The integrations are performed only over the finite energy range (30 eV - 30 keV) of the sensor.

Figures 6 a-f give six examples of phase space densities for electrons and ions with energies between 30 eV and 30 KeV as measured by DMSP/F6 in crossing the inverted V structure(s). Before examining the measurements it should be recalled that both the electron and ion detectors consist of two analyzers. The low (high) energy analyzer covers the range 30 eV to 1 keV (1 to 30 keV) in 10 logarithmically spaced steps. Each of the analyzers steps from high to low in energy. Thus, the 1 keV sample of the low-energy analyzer occurs almost a full second before the 1 keV sample of the high energy analyzer. In rapidly varying environments the 1 keV measurements of the two analyzers can be quite different. In smoothly varying regions measured fluxes agree within normal, statistical fluctuations. The different values of electron distribution functions at 1 keV, in the examples given in Figure 6 reflect rapid spatial-temporal variations in the environment rather than a calibration deficiency in the instrument.

137

The electron and ion distribution functions in Figure 6 were chosen to illustrate conditions leading to weak (a,f), moderate (c,e) and strong (b,d) spacecraft charging. To help identify the degree of charging expanded plots of the low energy portions of ion distributions appear as insets. At 0957:48 UT as the satellite entered the inverted V the ion distribution decreases monotonically indicating that the satellite potential was greater than or equal to - 30 V. One second later the electron distribution hardened considerably and the low-energy portion of the ion distribution shows a peak at 300 eV indicating a vehicle potential of -300 V (ref. 13). The rapidity with which the vehicle potential fluctuates is shown in examples c (0957:56) d (0957:58) and e (0957:59) where the charging peak is seen at 100 eV, 440 eV and 44 eV, respectively. We note that, at 0957:58 UT in the energy range 9 to 30 keV, the electron distribution function is monotonically increasing. If we assume that the auroral electrons have undergone a field-aligned acceleration between the magnetosphere and ionosphere, then the detected electrons are secondary and degraded primaries. The potential drop above the ionosphere is at least 30 kV. The primary electron beam has an energy greater than 30 keV; beyond the energy sensitivity of the DMSP/F6 detection range. The final example at 0958:06 UT comes from the equatorward inverted-V. Although the primary electron beam has been accelerated through a potential of 14 kV, the ions have a monotonically decreasing distribution. Potentials > - 30 V are typical of this equatorward inverted-V encounter.

The control of spacecraft charging exerted by energetic electrons is illustrated in Figure 7. The top panel gives the directional flux of electrons with energies > 5 keV (dashed line) and > 10 keV (solid line). As just mentioned the flux measured at 0957:58 (35878) UT is lower bound on the actual flux. The satellite potentials inferred from the measured ion distribution functions appear in the bottom panel. We see that there are one for one variations in the energetic electron flux and the satellite potential. The degree of charging achieved at geostationary altitude in a given energetic particle environment exceeds that expected for satellites in the ionosphere. In the ionosphere severe charging effects should be mitigated due to currents carried by relatively dense, cold ions. Simultaneous measurements from the thermal plasma probes in the vicinity of the inverted-V event(s) are presented in Figure 8. Data are presented as densities of thermal electrons (top panel) and ions (bottom panel) determined while the detectors operated in the constant bias Mode 1 (ref 13). A positive bias on the outer grid of the electron sensor is responsible for the factor of two greater electron than ion density prior to 0957 and after 0959 UT. Note that between 0956 and 0957 UT the electron and ion densities decreased by a full order of magnitude. This density decreased occurred prior to the first encounter with the inverted V. Beginning at 0957:30 the current to the electron sensor decreased by more than another order of magnitude. Because the ions show the opposite response we attribute the thermal electron current suppression as due to the increase satellite charging encountered at this time.

In the companion paper, Burke and coworkers (ref 13) presented another example of severe charging by DMSP. In this event the satellite potential only reached -65V. The present case differs in two significant ways. First, although the inverted V electron flux levels were comparable, the average energies were significantly larger in the present case. Second, the thermal plasma density was an order of magnitude higher in the case presented by

138

Burke and coworkers. This means that there is roughly an order of magnitude less ion current available to neutralize the current due to energetic electrons. It would appear that both energetic electrons and a cold plasma depletion are required for satellites at ionospheric altitude to acquire the high degree of charging observed by DMSP on January 12, 1983.

REFERENCES

1. Winningham, J.D., F. Yasuhara, S.-I. Akasofu and W.J. Heikkila, (1975), The Latitudinal Morphology of 10eV to 10 keV Electron Fluxes during Magnetically Quiet and Distrubed Times in the 2100 - 0300 MLT Sector, JGR, 80, 3148.

2. Lui, A.T.Y., D. Venkatesan, C.D. Anger, S. -I. Akasofu, W.J.Heikkila, J.D. Winningham and J.R. Burrows, (1977), Simultaneous Observations of Particle Precipitation and Auroral Emissions by the ISIS 2 Satellite in the 1900 - 2400 MLT, Sector, JGR, 82, 1977.

3. Feldstein, Y.I., (1966), Peculiarities in the Auroral Distribution and Magnetic Disturbances Distribution in High Latitudes Caused by the Asymmetrical Form of the Magnetosphere, Planet. Space Sci, 14, 121.

4. Sharp, R.D. and R.G. Johnson, (1968), Some Average Properties of Auroral Electron Precipitation as Determined from Satellite Observations, JGR, 73, 970.

5. Eather, R.H. and S.B. Mende, (1971), Airborne Observations of Auroral Precipitation Patterns, JGR, 76, 1746.

6. Starkev, G.V. and Y.I. Feldstein, (1971), Substorm in Auroras, Geomagn. Aeron., 11, 478.

7. McDiarmid, I.B., J.R. Burrows and E.E. Budzinski, (1975), Average Characteristics of Magnetospheric Electrons (15 eV to 200 keV) at 1400 km, JGR, 80, 73.

8. Walis, D.D. and E.E. Pudzinski, (1981), Empirical Models of Height Integrated Conductivities, JGR, 86, 125.

9. Spiro, R.W., P.H. Reiff and L.J. Maher, Jr., (1982), Precipitating Electron Energy Flux and Auroral Zone Conductances - An Empirical Model, JGR, 87, 8215.

10. Mullen, E. G., and Gussenhoven, M. S. (1982) High-Level spacecraft charging environments near geosynchronous orbit, AFGL-TR-82-0063 Hanscom AFB, MA 01731.

11. Lamframboise, J. G., Godard, R., Kamitsuma, M. (1982) Multiple floating potentials, "threshold temperature" effects, and "barrier" effects in high-voltage charging of exposed surfaces on a spacecraft" in Proceedings of International Symposium on Spacecraft Materials in Space Environment, Toulouse France, 8-11 June 1982, Publications Branch ESD, Noordwijk, The Netherlands.

12. Hardy, D. A. (1983) The worst case, charging environment, in Proceeding of AFGL Workshop on Natural Charging of Large Space-Structures in Near-Earth Polar Orbit: Sept 14-15, 1982, ed by R. C. Sagalyn, D. E. Donatelli and I. Michael, AFGL-TR-83-0046, Hanscom AFB, MA 01731.

13. Burke, W. J., Hardy, D. A., Rich, F. J., Rubin A. G., Tautz, M. F. Saflekos, N. A. and Yeh, H. C., (1984), Direct measurements of severe spacecraft charging in the auroral ionosphere, Proceedings of Spacecraft Environment Interactions Conference (this volume).

14. DeForest, S. E., (1972) Spacecraft Charging at Synchronous Orbit, JGR, 77, 651-659.

Table 1

Satellite	Orbital Plane	Altitude	Data Availability
F2	0600 - 1800	840 Km	9/77 - 2/80
F4	1030 - 2230	840 Km	6/79 - 8/80
P78-1	0000 - 1200	600 Km	3/79 - present
F6	0600 - 1800	840 Km	12/82 - present

Table 2a
Post Midnight Maximum

Kp	Average Energy	Energy Flux	Magnetic Latitude	MLT
0	3.41 KeV	8.27×10^7 KeV/cm^2-sec-ster	67°	0400-0430
1	4.71 "	7.65×10^7 "	66°	0530-0600
2	3.78 "	3.90×10^8 "	65°	0130-0200
3	3.93 "	6.98×10^8 "	65°	0130-0200
4	3.46 "	7.10×10^8 "	66°	0000-0030
5	---	---	---	---
>6-	5.87 "	1.67×10^9 "	63°	0230-0300

Table 2b
Pre Noon Maximum

Kp	Average Energy	Energy Flux	Magnetic Latitude	MLT
0	2.97 KeV	2.16×10^7 KeV/cm^2-sec-ster	71°	1400-1430
1	3.90 "	6.34×10^7 "	70°	0930-1000
2	5.68 "	1.07×10^8 "	70°	1030-1100
3	6.40 "	1.38×10^8 "	69°	1000-1030
4	5.02 "	9.42×10^7 "	67°	1000-1030
5	4.81 "	1.33×10^8 "	66°	0930-1000
>6-	1.80 "	1.06×10^8 "	65°	0930-1000

141

Table 3

Kp	0000 - 0030 MLT Max. Energy Flux	C.G. Latitude	1130 -1200 MLT Energy Flux	C.G. Latitude
0	1.04×10^8 KeV/cm^2-sec-ster	69°	3.75×10^7 KeV/cm^2-sec-ster	72°
1	1.90×10^8 "	68°	4.55×10^7 "	71°
2	3.69×10^8 "	66°	7.79×10^7 "	71°
3	6.64×10^8 "	66°	5.50×10^7 "	69°
4	7.75×10^8 "	66°	3.51×10^7 "	67°
5	4.67×10^8 "	62°	2.61×10^7 "	66°
>6	1.37×10^9 "	62°	1.92×10^7 "	64°

Table 4

Prenoon Integral Number Flux Maximum

Kp	Latitude	MLT	Integral Number Flux	Integral Energy Flux	Average Energy
0	79°	0800-0830	3.05×10^8 e/cm^2-sec-ster	7.04×10^7 e/cm^2-sec-ster	232eV
1	78°	0800-0830	3.22×10^8 "	8.45×10^7 "	273eV
2	78°	0930-1000	3.32×10^8 "	8.43×10^7 "	256eV
3	77°	1100-1130	3.80×10^8 "	7.03×10^7 "	187eV
4	74°	0830-0900	3.61×10^8 "	1.95×10^8 "	552eV
5	73°	0830-0900	4.10×10^8 "	1.66×10^8 "	465eV

Table 5

Average Energy Minimum

Kp	Latitude	MLT	Integral Energy Flux	Average Energy
0	81°	1100-1130	4.57×10^7 KeV/cm^2-sec-ster	199 eV
1	81°	1130-1200	4.88×10^7 "	183 eV
2	81°	1130-1200	3.83×10^7 "	168 eV
3	79°	1100-1130	4.44×10^7 "	165 eV
4	78°	1130-1200	3.96×10^7 "	162 eV
5	78°	1230-1300	3.18×10^7 "	147 eV
> 6-	76°	1200-1230	7.29×10^7 "	184 eV

142
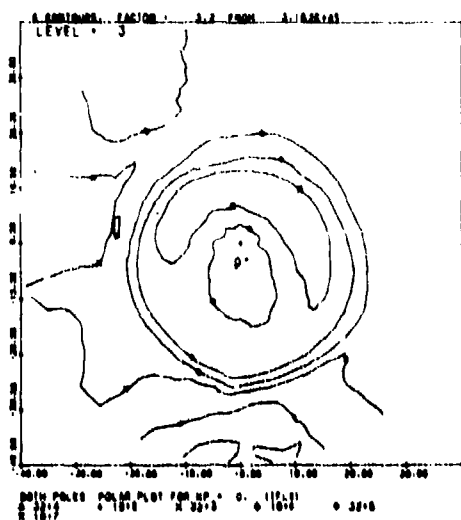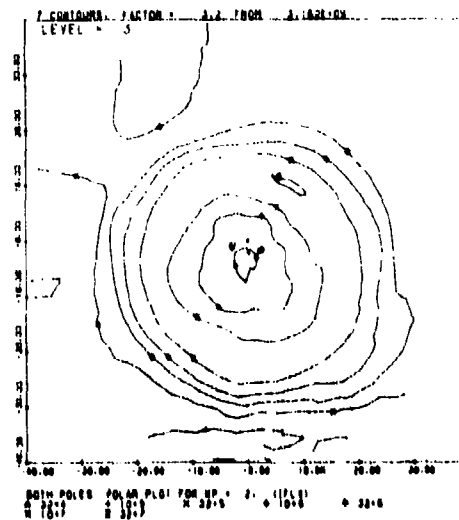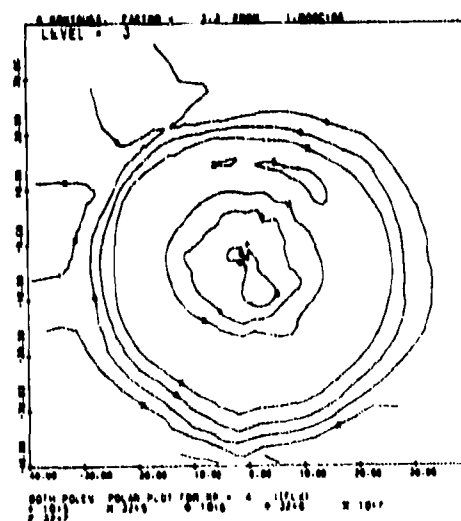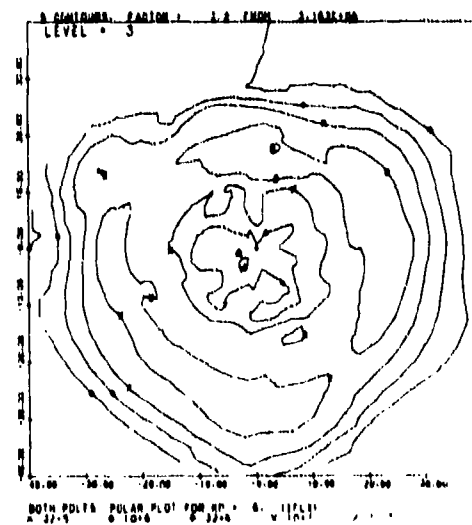
Figure 1. - Isocontour maps of the integral number flux (IFLX) of precipitating electrons in units of electrons/cm^2 sec sr for the four activity levels K_p=0, 2, 4, and $\geq$6-. The plots are in a corrected geomagnetic latitude - magnetic local time coordinate system. The geomagnetic pole is marked by a cross (+). Midnight magnetic local time is centered at the bottom of each figure, noon at the top.
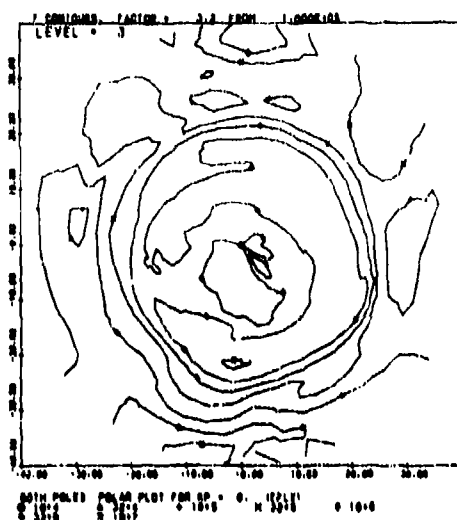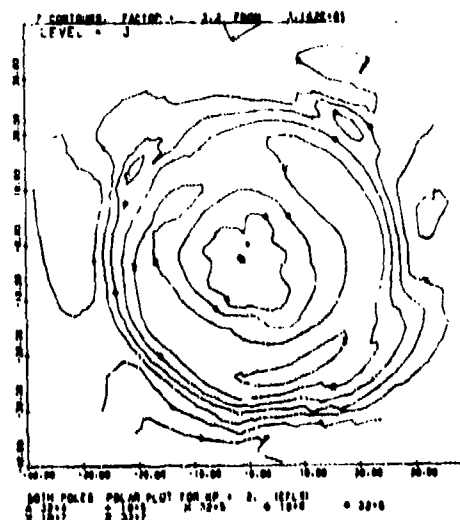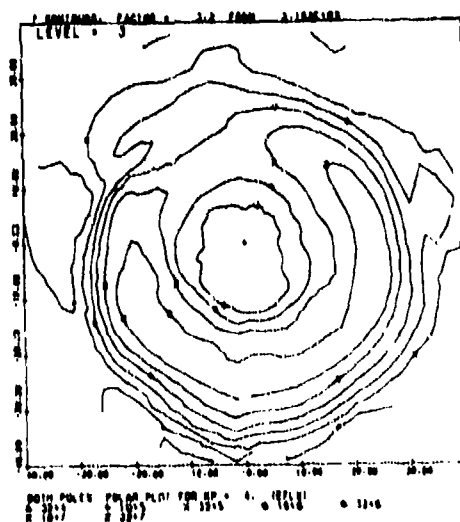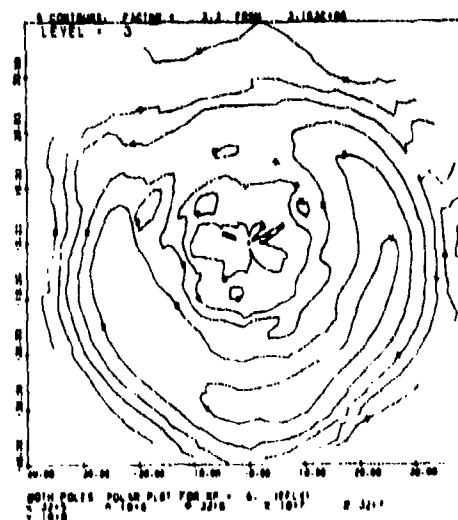
Figure 2. - Isocontour maps as in figure 1 for the integral energy flux (EFLX) of precipitating electrons in units of keV/cm² sec sr.
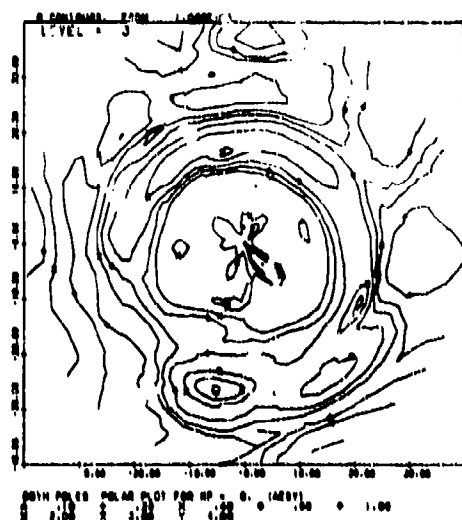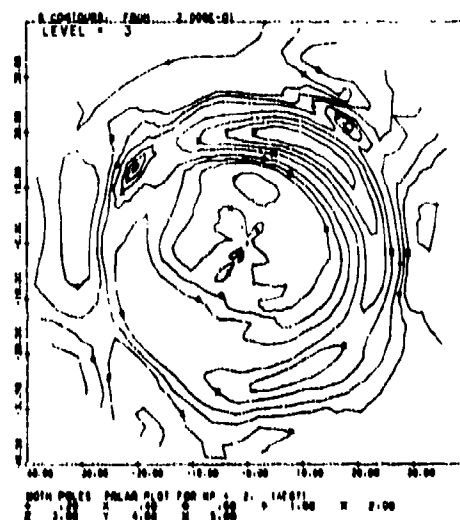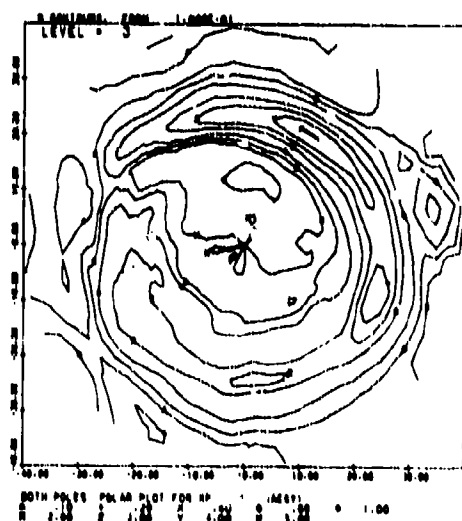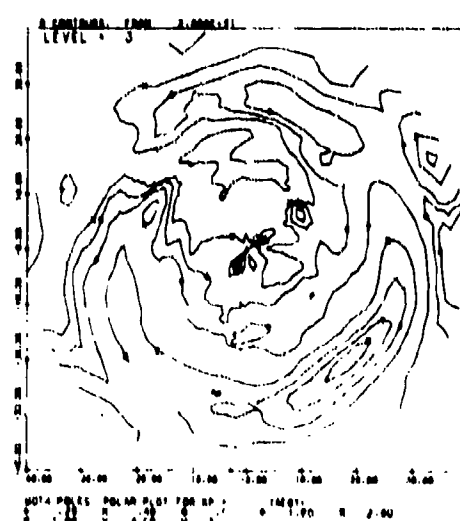
Figure 3. – Isocontour maps as in figure 1 for the average energy (AEGY) of precipitating electrons in units of keV.
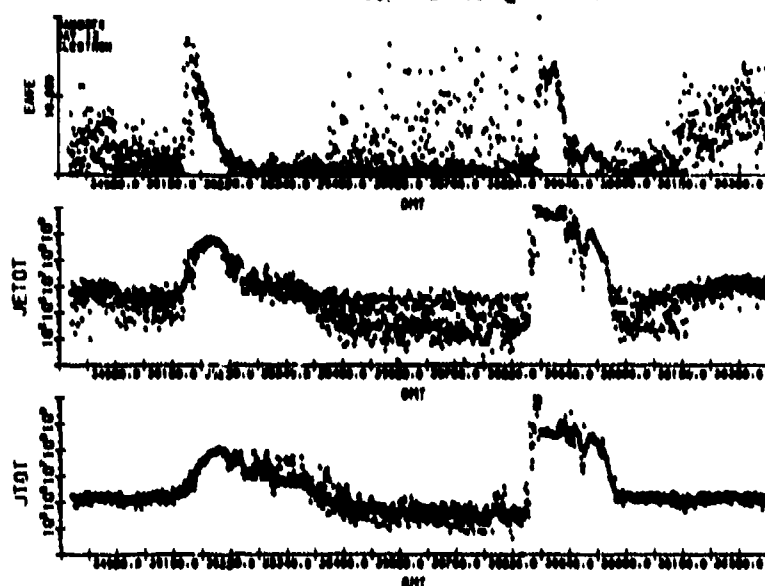
Figure 4. - Average energy, directional energy flux, and directional number flux of downcoming electrons with energies between 30 eV and 30 keV.
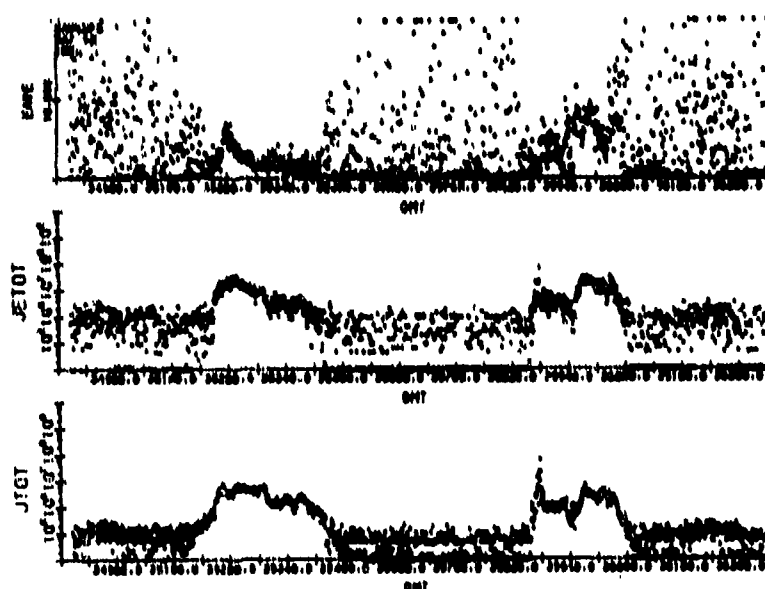
Figure 5. - Average energy, directional energy flux, and directional number flux of downcoming ions with energies between 30 eV and 30 keV.

146
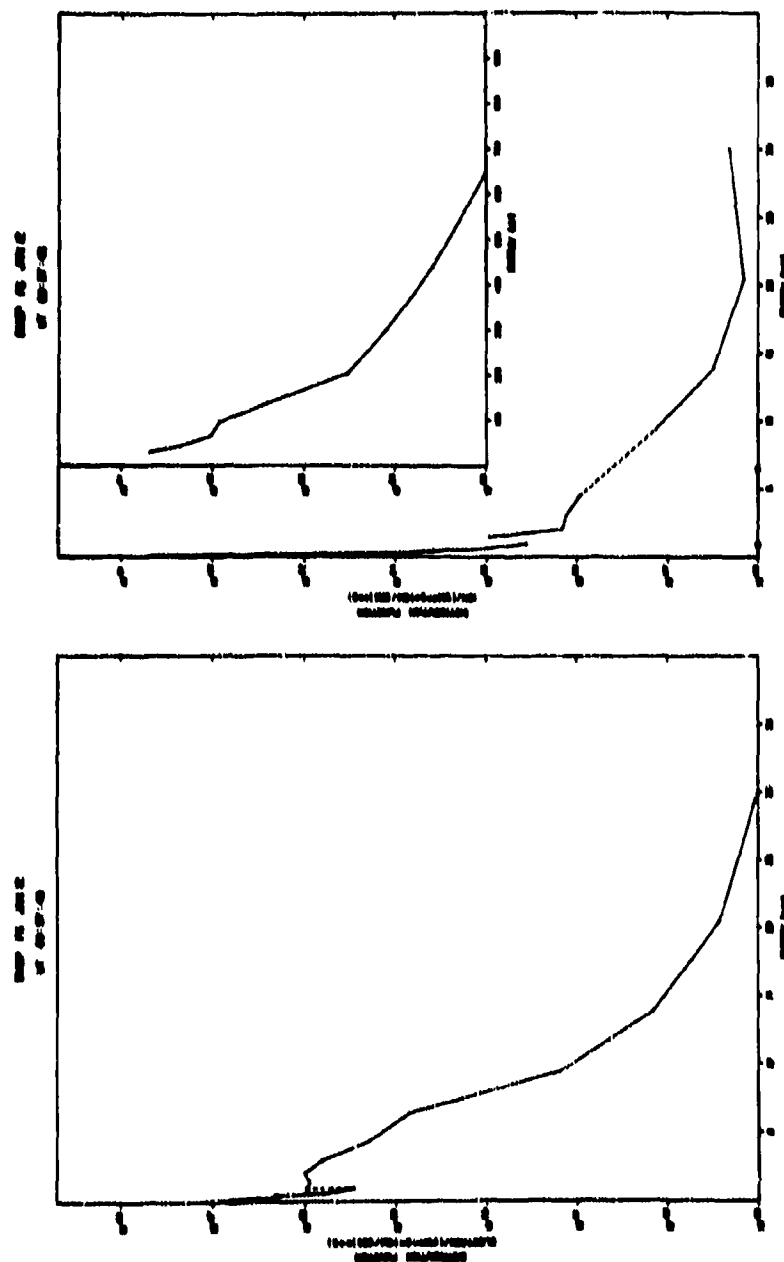
(a) At 09:57:48 UT.

Figure 5. - Distribution functions of electrons and ions with energies between 30 eV and 30 keV as measured on 12 January 1983 by DMSP/F6.
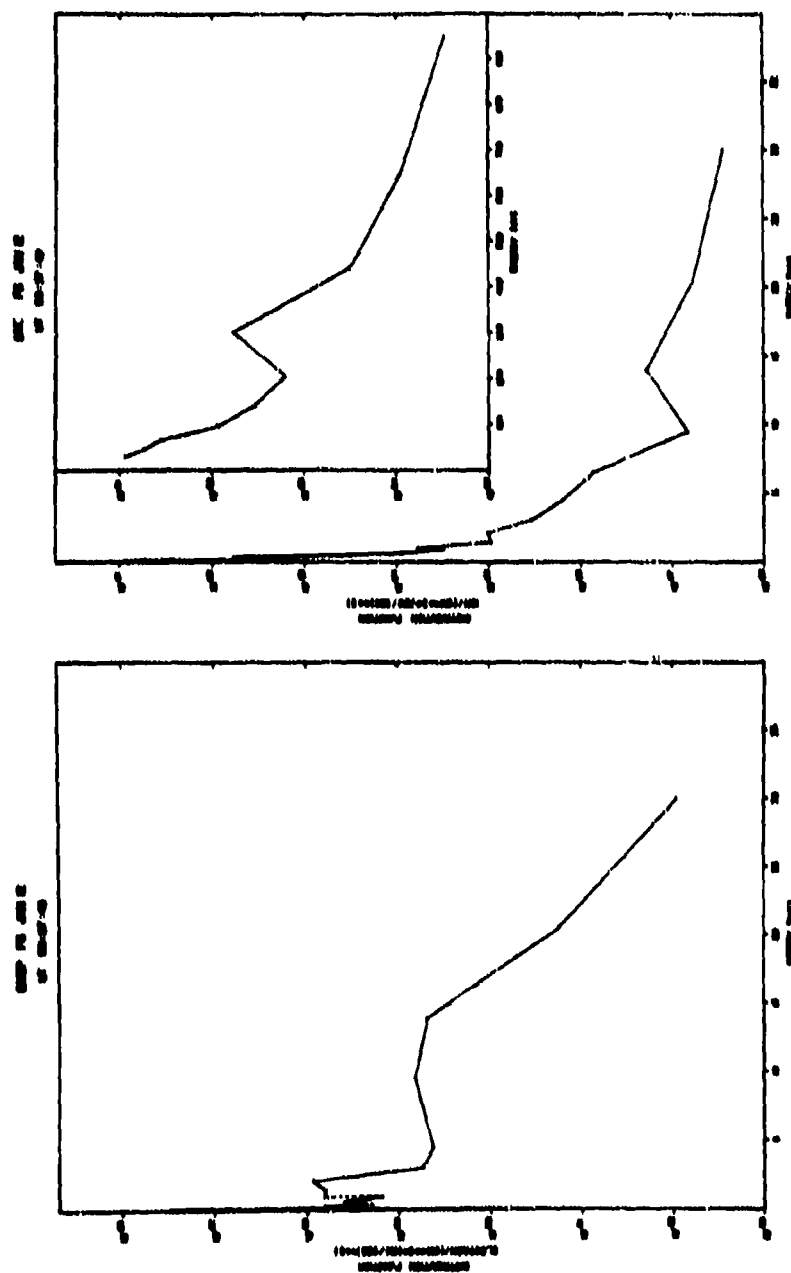
(b) At 09:57:49 UT.

Figure 6. — Continued.
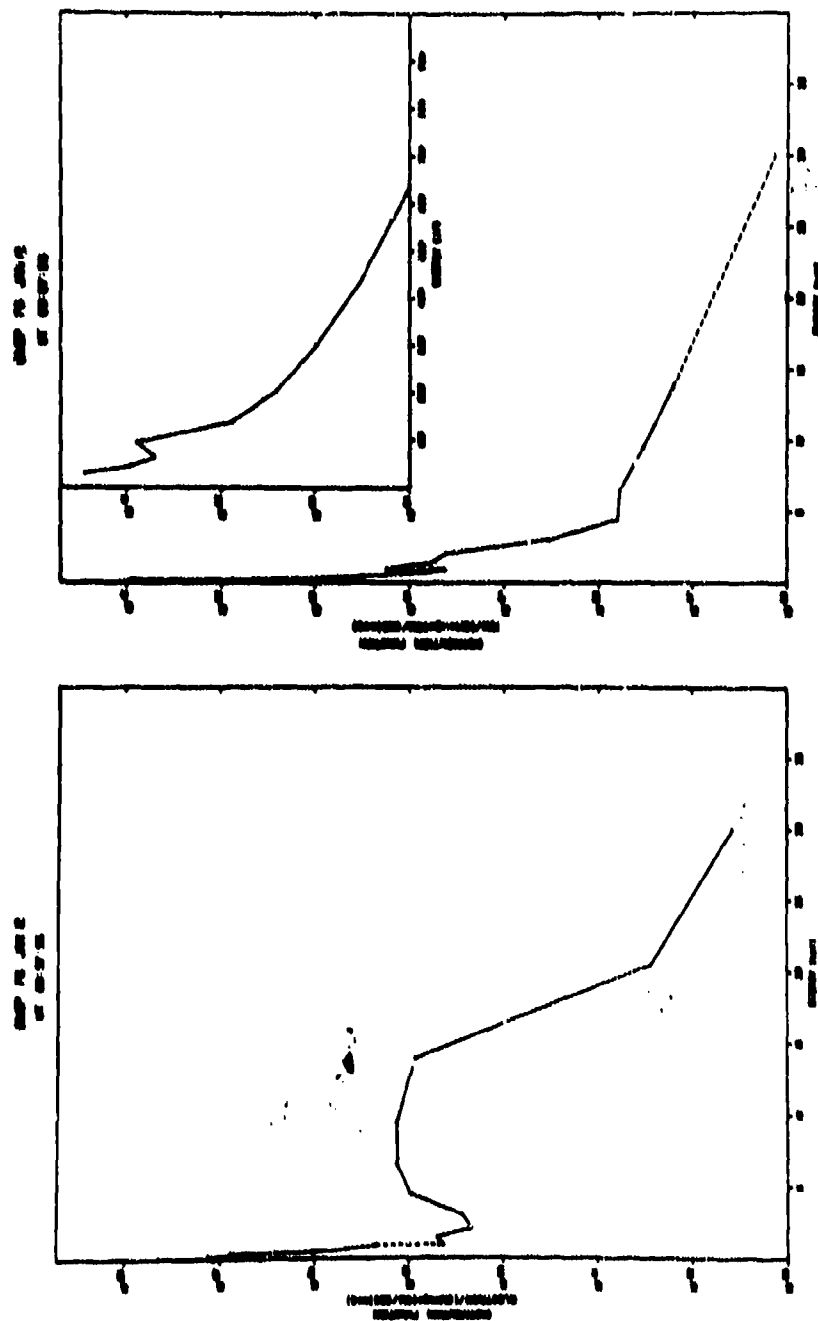
(c) At 09:57:56 UT.

Figure 6. – Continued.
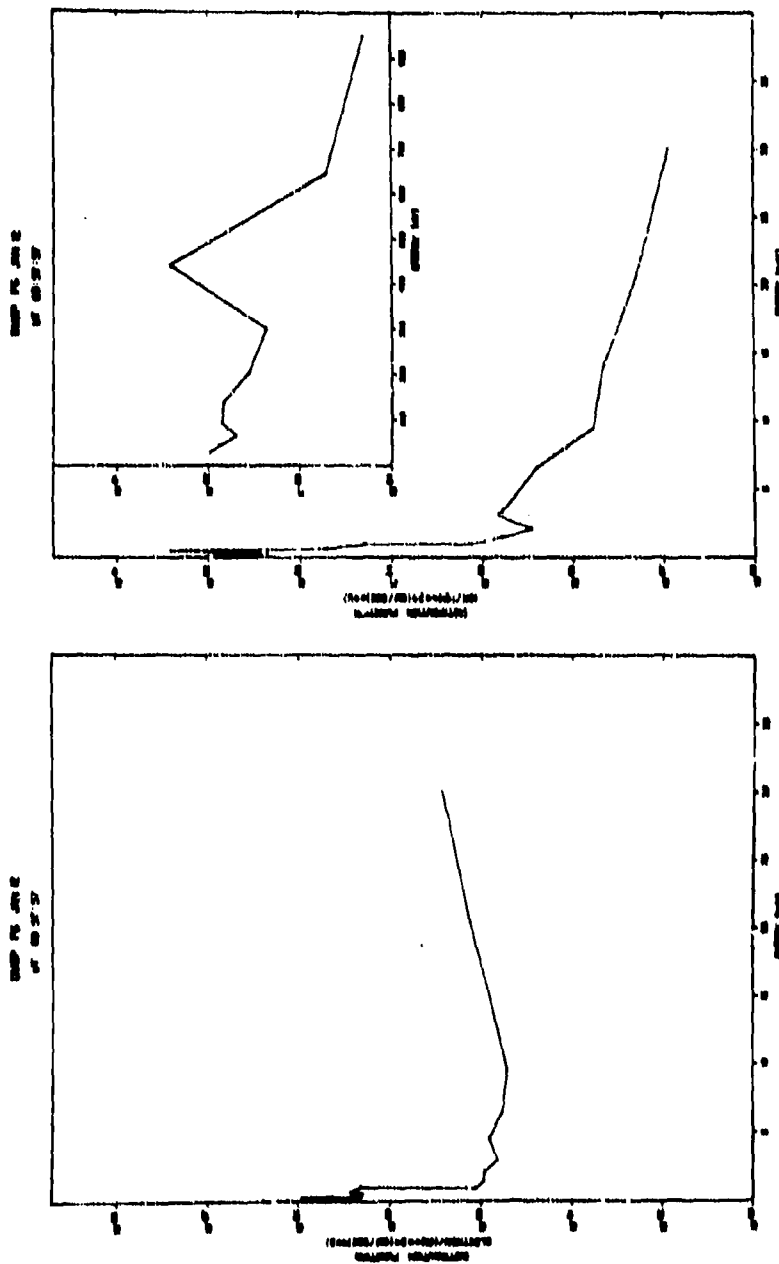
(d) At 09:57:57 UT.

Figure 6. – Continued.
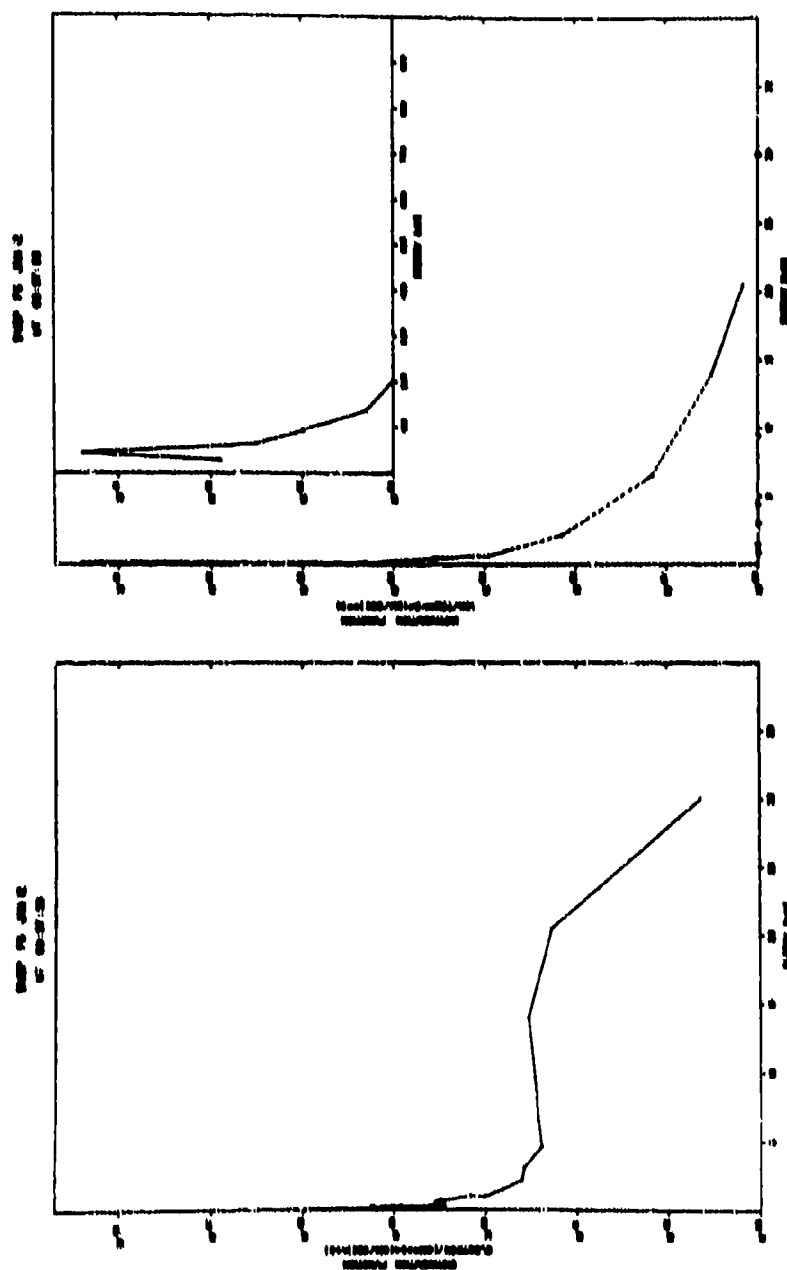
(e) At 09:57:58 UT.

Figure 6. — Continued.

(f) At 09:56:06 UT.

Figure 6. — Concluded.

12 JANUARY 1983

DMSP THERMAL PLASMA

LOG ELECTRON DENSITY

LOG ION DENSITY
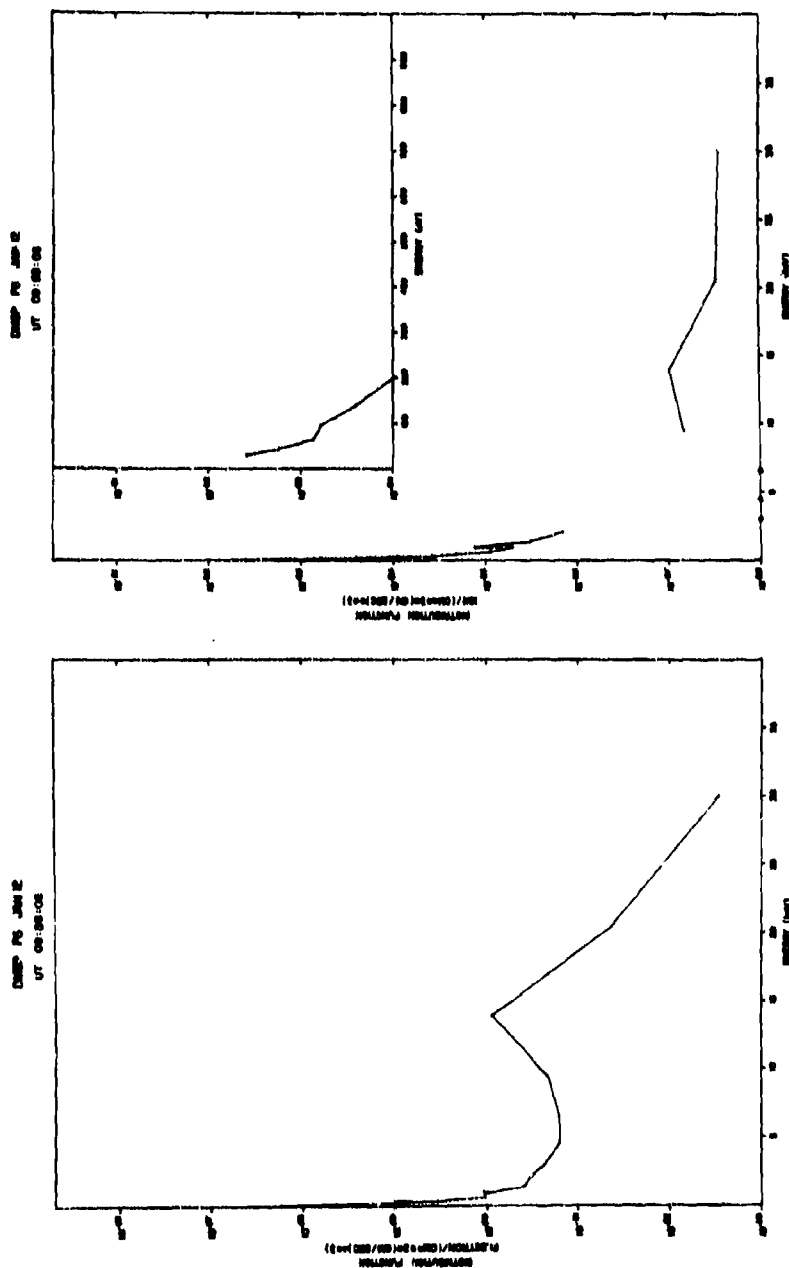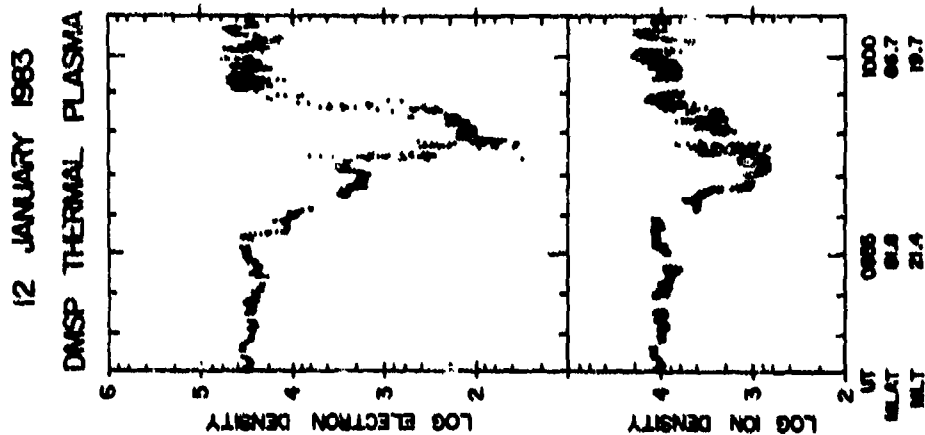
Figure 8. – Densities of thermal electrons and ions measured by DMSP/F6 in the vicinity of the inverted-V structure, in which large spacecraft potentials were detected.

12 January 1983

E > 5 keV
E > 10 keV

J(E)electrons/cm²-s-sr

V$_{SAT}$ (Volts)

UT
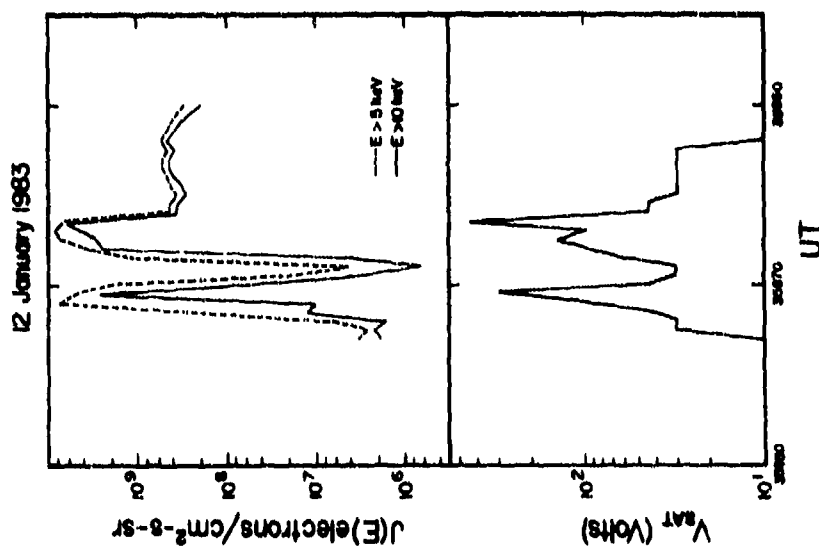
Figure 7. – Integral flux of electrons with energies >5 keV and >10 keV in the poleward inverted-V structure. The bottom panel gives the measured satellite potential as determined from charging peaks in the ion distribution functions at 1-sec intervals.

153

POLAR PLASMAS AS OBSERVED BY DYNAMICS EXPLORERS 1 AND 2*

J. Barfield, J. Burch, C. Gurgiolo, C. Lin, D. Winningham, and N. Saflekos
Southwest Research Institute
San Antonio, Texas 78284

Plasma measurements from the Dynamics Explorer 1 and 2 satellites have been used
to characterize the polar cap environment. Analysis of numerous polar-cap passes have
indicated that, in general, three major regimes of plasma exist:

    (1) polar rain--electrons with magnetosheath-like energy
                spectra but much lower densities, most
                intense near the cusp and weakening
                toward the central polar cap;

    (2) polar wind--low energy upward flowing ions with both
                field-aligned and conical distributions;

    (3) acceleration events--sporadic events consistent with the
                acceleration of electrons and positive
                ions by parallel electric fields.

(1)-(3) have been observed at high altitudes by Dynamics Explorer 1, while (1) and (3)
have been observed at low altitudes by Dynamics Explorer 2. The plasma parameters
associated with these plasma regimes are presented and discussed in terms of source
and acceleration mechanisms.

INTRODUCTION

    The polar cap is a region threaded by magnetic field lines which intersect the
earth poleward of the auroral oval. The magnetic field lines of the polar cap are
generally accepted as either being open or closed at such large distances from the
earth that they are effectively open. This linkage between the polar cap ionosphere
and the interplanetary medium makes the polar caps extremely important in the study of
the interaction between the solar wind and the high-latitude ionosphere. Since the
polar caps are not directly connected to those closed-line regions of the magneto-
sphere where plasma and energy are stored, electric fields, currents, and particle
precipitation in the polar caps respond quickly to changes in solar wind conditions.
Many authors have studied the relationships between the solar wind conditions and the
polar-cap environment. However, much remains unknown at present concerning the char-
acteristics of polar cap plasmas.

PRECEDING PAGE BLANK NOT FILMED

Examination of the DE-1 and DE-2 data has provided new information on three major polar-cap plasma regimes:

(1) polar rain--electrons with magnetosheath-like energy spectra but much lower densities, most intense near the cusp and weakening toward the central polar cap;

(2) accelerated polar wind--low energy upward flowing ions with both field-aligned and conical distributions;

(3) acceleration events--sporadic events consistent with the acceleration of electrons and positive ions by parallel electric fields.

The Dynamics Explorer satellites, launched in 1981, have afforded new and unique opportunities to probe polar cap plasmas. (Details of the satellites, their orbits, and instrumentation may be found in Space Science Instrumentation, Vol. 5, No. 4, 1981--special issue.) The combined high-altitude polar orbit of Dynamics Explorer 1 (DE-1) and the low-altitude polar orbit of Dynamics Explorer 2 (DE-2) have been used to observe the polar cap plasma environment on a large number of passes.

The next section briefly describes the instrumentation used for the observations. Following that, the next three sections present observations.

INSTRUMENTATION

The DE-1 satellite was launched on August 3, 1981, into an elliptical polar orbit with an apogee of 4.6 R_E geocentric and a perigee of 650 km altitude. The DE-1 High Altitude Plasma Instrument (HAPI) consists of five electrostatic analyzers mounted in a fan-shaped angular array at angles of 45°, 78°, 90°, 102°, and 135° with respect to the spacecraft spin axis. Each analyzer makes differential measurements of positive ions and electrons over an energy per charge range of 5 eV/e to 32 keV/e. The energy stepping rate may be commanded over a range up to 64 sec^{-1}, producing three-dimensional plasma distributions at the six-second spin period of DE-1 (see ref. 1 for details).

The DE-2 satellite, launched with DE-1 on August 3, 198 has an elliptical polar orbit at approximately 300 x 1000 km altitude. DE-2 is three-axis stabilized, with one axis in the zenith, another perpendicular to the orbit plane, and the last completing a right-hand triad. The DE-2 Low Altitude Plasma Instrument (LAPI) consists of 15 ion and 15 electron energy/unit charge analyzers mounted on an external scan platform (ref. 2). The detector array can be held approximately fixed (<1°) with respect to the local magnetic field vector. The plane of the sensors is in the orbital plane and thus in the local magnetic meridian plane. Two pairs of out-of-plane detectors allow for sampling near 0° and 180° pitch-angle when the magnetic field vector deviates significantly from the plane of the detector array.

OBSERVATIONS

Polar Rain

Winningham and Heikkila (ref. 3) first described polar rain, using data from the

ISIS 1 satellite. Polar rain is the most common type of particle precipitation over the polar caps. This broad and relatively structureless electron precipitation can often fill the entire polar cap. The precipitating electrons typically have thermal energies on the order of 100 eV and are isotropic over the downcoming hemisphere. The energy flux carried by the particles is of the order of 10^{-3} to 10^{-2} erg cm^{-2}sec^{-1} (ref. 4). The spectral distribution of the polar rain electrons has the same shape as that of cusp electrons, but is lower in intensity, suggesting that polar rain originates in the magnetosheath and travels to the polar ionosphere via the lobes of the magnetotail.

Figures 1a and 1b show differential energy flux from the LAPI instrument aboard DE-2 for a portion of a polar pass on day 295 (22 October) of 1981. The top panel shows data for 8° pitch angle electrons, and the bottom panel shows 45° pitch angle ion data. The upper center panel shows 90° and 0° pitch angle electron data from the GM tube. The data are coded according to the color bars at the right. Satellite ephemeris is shown at the bottom. In this particular pass, DE-2 passed through the northern polar cusp at approximately 1306-1307 UT and into the polar cap. The polar rain can be seen clearly as a bright band in the electron panel over the energy range ≈60-600 eV. The electron flux intensity remained fairly constant in intensity until just after 1309 UT when it abruptly decreased. Notice the lack of ion fluxes over the polar cap.

Figure 2 shows line plots of the average energy, energy flux, and density of the downcoming electrons for 1306-1311 UT. These parameters are obtained by integrating distribution functions over energy from 5 eV to 20 keV. During the entire interval, the average electron energy and density remained roughly constant. The average energy was about 100 eV and the density of downcoming electrons was in the range of 1-5 cm^{-3}. These values of energy and density are representative of the polar rain. After exit from the cusp at about 1307 UT, the energy flux increased very slightly toward the pole until just after 1309 UT when it decreased by approximately 50%.

Figure 3 shows a DE-1 high-altitude polar pass approximately three hours after the DE-2 pass shown in Figure 1. During the interval 1617-1619 UT, DE-1 traversed the magnetic local time and invariant latitude corresponding to those of DE-2 just poleward of the cusp in Figure 1a. The format is the same as for Figure 1, except for the absence of GM tube data. The polar rain may be seen as a band in the spectrogram over the energy range ≈100-600 eV. Bracketing the polar rain are counter-streaming energetic (E>600 eV) electron beams at 0° and 180° pitch angle and upward-moving low-energy (E<100 eV) electron beams. The source of the energetic counter-streaming electrons is open to question and presently under study by Gurgiolo and Burch (unpublished). Two possibilities for the source would be reflection by a potential barrier at the magnetopause (ref. 6) or direct access of solar electrons. Upstreaming ion conics may be seen in the lower panel.

Comparing Figure 1 and Figure 3, it is interesting to note that the polar rain is of the same spectral nature at both altitudes, suggesting the absence of any significant acceleration between the two satellite locations. To demonstrate further the similarity between the electrons at the two satellites, Figure 4 shows number density, energy flux, and average energy at DE-1 for the period 1614-1619 UT. The average energy was ≈100 eV, density was ≈1 cm^{-3} and the energy flux was 0.8 ergs cm^{-2}s^{-1}. The corresponding values at lower altitudes were ≈100 eV, ≈2 cm^{-3}, and ≈0.8 ergs cm^{-2}s^{-1}.

A detailed look at the near-field-aligned electron populations at the two satellite locations is provided in Figure 5. Shown are three data sets - two single energy sweeps from LAPI, one just at the poleward edge of the cusp and one approximately 10° poleward of the cusp, and a single energy sweep from HAPI at a location which maps to near the location of the first LAPI spectrum. From Figure 3, we first can see that above photoelectron energies the LAPI population can be represented by a Maxwellian, allowing the temperatures to be estimated. Near the cusp a least squares fit gives a temperature of 92 eV, while farther poleward the temperature is 99 eV. The HAPI spectrum appears well-fitted by two Maxwellians above photoelectron energies. The low-energy population has a least-squares fit temperature of 65 eV, while the higher energy population has a temperature of 141 eV.

Accelerated Polar Wind

The polar wind refers to the continual escape of ionospheric plasma from the polar ionosphere along open magnetic field lines. This escape of particles has consistently been observed to lead to a depletion of light ionospheric ions (ref. 7) and electrons in the upper polar ionosphere. Until recently, observations of the polar wind in the literature were limited to the low-altitude observations of Hoffman and Dodson (ref. 7). They reported a continual upward flow of H^+ and He^+ over the polar caps in the range 1-5 km/sec and 1-3 km/sec, respectively. The low energy of these particles precluded most instruments from directly obtaining a distribution function. However, as pointed out by Gurgiolo and Burch (ref. 5), polar-wind models predict that the particle velocity should increase with altitude (ref. 8). Thus, the high altitude satellite DE-1 is an ideal platform from which to study the polar wind.

Plasma data from DE-1 polar passes indicate that ions with peak differential energy fluxes in the 5 to 100 eV range are continually flowing out of the dayside cusp and polar cap. The flows have both a field-aligned and a conic component. The field-aligned component is unmistakably the polar wind. Gurgiolo and Burch (ref. 5) concluded that the conics observed in conjunction with the polar wind are polar-wind ions that have been perpendicularly heated.

The polar-wind observations to be discussed were made during a polar pass on day 272 (September 29) of 1981. Figure 6 consists of 3 sets of particle spectrograms on the same format as Figure 3. Each spectrogram displays the differential energy flux for the particle detectors which lie closest to the plane containing the local magnetic field vector.

Figure 6 shows a continuous band of upward flowing ions (near 180° pitch angle). The satellite was inside the cusp during the interval covered in Figure 6a. At 1411 UT, the satellite passed through the poleward cusp boundary. The upward ions showed a gradual increase in energy throughout and slightly poleward of the cusp, then they begin to decrease steadily, the peak in the differential energy flux eventually dropping below the lowest energy channel of HAPI. Within the cusp, the conic and field-aligned ions appear as "tuning forks" in the spectrograms. In the polar cap the conics become less and less apparent, as the energy and angular separation of the conic and field-aligned ions decrease. In the polar cap, there also is a shift in the field-aligned ions from ~130° pitch angle to ~105°, indicating an antisunward flow.

Figure 7 shows a detailed view of the field aligned ion population. Two data sets are shown, each of which was averaged over four satellite revolutions to improve counting statistics. Each of the distributions was transformed to the rest frame of

the plasma prior to averaging (except for S/C charging which was about 20V). The two
data sets were taken beginning 1434:05 UT (solid circles) and 1434:54 UT (open
circles). In Figure 7 Maxwellian distributions are straight lines, with the slope
being proportional to the plasma temperature and the intercept with the distribution
axis being proportional to the plasma density.

From Figure 7 we can see that the field-aligned ion component observed in the
polar regions is comprised of two ion populations--a low energy component with tem-
perature below .5 eV and a high energy tail with temperature above 1.5 eV. Both ion
populations would appear to be well represented by a Maxwellian distribution, allow-
ing the estimates of the temperatures to be made. A least squares fit to the low-
energy population of Figure 7 gives a temperature of .29±.16 eV (3200°K±1800K). The
corresponding temperature of the high energy plasma population in Figure 7 is found
to be 2.7±.7 eV. The peak at about 1 eV may be due to an ion heavier than H^+.

There is little doubt that the lower energy, field-aligned ions constitute the
"classical" polar wind. The high energy tail, however, is not a feature predicted by
polar-wind models. It is likely that this hotter plasma is the result of a perpen-
dicular heating of polar-wind ions. Assuming that all ions in the polar wind are of
equal temperature, Figure 7 gives heating on the order of 4 to 10.

We envision a scenario as shown in Figure 8 occurring during the polar wind
escape along magnetic field lines. At low altitudes the generation of the polar wind
occurs and ionospheric ions begin to escape along the open polar cap and cusp field
lines (Figure 8a). The presence of ion perpendicular heating along the open field
lines produces the characteristic conic signature (Figure 8b). The distribution
above the heating region can be considered a two-component plasma consisting of un-
heated and heated polar-wind particles. The unheated polar wind is still field
aligned, while the heated ions have large velocities in the direction perpendicular
to B. As the distribution travels upward, the perpendicular arms of the distribution
will begin to collapse toward the magnetic field direction in accordance with the
first adiabatic invariant, and a field-aligned high energy tail to the polar wind
should develop (Figure 8c). Figure 8d shows contours of a typical conic/polar-wind
population measured in the cusp on day 272.

Ion conics have been reported by numerous people (Refs. 9 and 10). Theories as
to the production of the conic ion distribution have favored a perpendicular heating
by electrostatic ion-cyclotron waves (ref. 9, refs. 11 and 12), although recently
(ref. 13) it has been proposed that a heating by lower hybrid waves may also be a
viable conic generation mechanism. The problem is, however, that most of these theo-
ries are applicable only at low altitudes in the auroral zone. Adaptations of the
theories to the environment of the polar cap must be made to explain these observa-
tions.

Using the observed conic pitch angle distribution, the altitude of the observa-
tion and an assumed value for the initial conic pitch angle, it is possible through
the first adiabatic invariant to estimate the altitude of the conic generation. In
general the initial conic pitch angle for such computations is assumed to be 90°;
however, if the source plasma already has a significant $V_\parallel$, as the polar wind does,
then the initial conic pitch angle is expected to shift to lower values. Using a di-
polar magnetic field approximation and estimating the values of the initial conic
pitch angle through energy conservation arguments (which assume that $V_\parallel$ does not

change between the observation height and the conic height) we estimate the heating to occur at an altitude of about 12,000 km--constant throughout both the cusp and polar cap. By using an initial conic pitch angle of 90° we can place a lower limit to the heating altitude at 8000 km.

Acceleration Events

The electrical coupling between the high-altitude and low-altitude regimes of the polar cap is an important aspect of magnetosphere-ionosphere interactions. The unique placement of the Dynamics Explorer orbits with respect to each other has afforded an excellent opportunity to investigate this coupling between the two regimes. Frequently, DE-1 and DE-2 observe signatures of field-aligned acceleration of ions and electrons above the polar cap. In this section, we briefly present observations made on October 17, 1981 (day 81290) above a "theta aurora" signature.

Figure 9 shows a spectrogram of 180° ions and 0° pitch angle electrons from HAPI. The satellite crossed the polar-cap arc field lines during the interval 1630-1650 UT. Two intervals of intense electron fluxes below 1 keV were seen: ~1631:30-1633:15 UT and ~1642-1649 UT. Figure 10 shows contour plots of the log of the distribution functions of ions (Figure 10a) and electrons (Figure 10b) for the interval 1632:45-1632:57 UT. The ions showed a strong upgoing beam at approximately 100 eV. The electron fluxes were isotropic except for a loss cone. Thus, the combined electron and ion observations indicated that an approximately 100 eV potential drop lay below the satellite altitude.

Figure 11 shows contours in the same format as Figure 10, for the interval 1646:30 to 1646:36 UT. By this time the ions had become isotropic, while the electrons showed a downcoming beam of ~100 eV. Thus, the acceleration region appears now to be above the satellite altitude (17313 km) while remaining at ~100 eV.

The plasma characteristics described above are very similar to those observed by DE-1 in the high altitude (>15,000 km) nightside auroral zone, except that the energy of the polar cap acceleration events is lower. Correlation studies by Hardy et al. (ref. 14) have already noted that the plasma signatures of polar cap acceleration events at low altitudes are similar to those of evening discrete arcs. The parallel electric field responsible for the polar-cap acceleration could be produced by the same process as the evening auroral arcs.

Satellite observations of convection and electron precipitation at low altitudes (<1000 km) have indicated that convective electric fields point toward the region of polar-cap acceleration (∇·E<0) (ref. 15). The polar cap acceleration region is therefore a region of negative space charge. Burke et al. (ref. 16) used the simultaneous electric field, magnetic field and electron flux measurements of the S3-2 satellite to demonstrate that upward Birkeland currents were embedded in regions of polar cap acceleration. These observations suggest that field-aligned potentials develop as a result of imperfect mapping of magnetospheric convective electric fields to the ionosphere (ref. 14; ref. 16).

SUMMARY AND CONCLUSIONS

Plasma measurements made on the Dynamics Explorer 1 and 2 spacecraft are providing new information on the altitude dependence of polar-cap plasma populations, their sources, and the acceleration processes they undergo. In this study we have found that the polar-rain electron population apparently exhibits no significant altitude dependence between altitudes of a few hundred to ~20,000 km. This result was expected from the magnetosheath-like energy spectrum of the low-altitude polar rain.

In the case of the polar wind, a significant velocity increase was theoretically predicted to occur between the two spacecraft altitudes, and this effect has been confirmed by the DE-1 plasma measurements. A major result of our study of the accelerated polar wind is its significant conic component, which indicates that the ions are heated perpendicularly as they emerge from the polar-cap ionosphere. The gradual decrease in polar-wind energy that is observed to occur from the cusp across to the nightside polar cap suggests that the perpendicular heating process, probably in cyclotron waves, is most intense near the cusp region.

Significant altitude effects are also observed in the plasmas that occupy magnetic flux tubes connected to polar-cap auroral arcs (or theta auroras). At DE-2, typical low-energy (~100 eV) inverted-V electron distributions are observed. At DE-1 the electron and positive-ion distribution functions are consistent with electrostatic potential drops that are at times below the typical DE-1 altitude of 15,000 to 20,000 km and at times above these altitudes. Thus, compared to auroral-oval acceleration regions those in the polar cap appear to be weaker and at significantly higher altitudes.

REFERENCES

1. Burch, J. L., J. D. Winningham, V. A. Blevins, N. Raker, W. C. Gibson, and R. A. Hoffman: High-Altitude Plasma Instrument for Dynamics Explorer-A, Space Sci. Instr., 5, 455, 1981.

2. Winningham, J. D., J. L. Burch, N. Baker, V. A. Blevins, and R. A. Hoffman: The Low Altitude Plasma Instrument (LAPI), Space Sci. Instr., 5, 465, 1981.

3. Winningham, J. D. and W. J. Heikkila: Polar Cap Electron Fluxes Observed with ISIS-1, J. Geophys. Res. 79, 949, 1974.

4. Burke, W. J.: Magnetosphere-Ionosphere Coupling: Contributions from IMS Satellite Observations, Rev. Geophys. Space Phys., 20, 685, 1982.

5. Gurgiolo, C. and J. L. Burch: DE-1 Observations of the Polar Wind--A Heated and an Unheated Component, Geophys. Res. Lett. 9, 945, 1982.

6. Foster, J. C. and J. R. Burrows: Electron Fluxes over the Polar Cap 1. Intense keV Fluxes During Poststorm Quieting, J. Geophys. Res., 81, 6016, 1976.

7. Hoffman, J. H. and W. H. Dodson: Light Ion Concentrations and Fluxes in the Polar Regions during Magnetically Quiet Times, J. Geophys. Res., 85, 626, 1980.

8. Schunk, R. D. and D. S. Watkins: Proton Temperature Anisotropy in the Polar Wind, J. Geophys. Res., 87, 171, 1982.

9. Ungstrup, E., D. M. Klumpar, and W. J. Heikkila: Heating of Ions to Superthermal Energies in the Topside Ionosphere by Electrostatic Ion Cyclotron Waves, J. Geophys. Res., 84, 4289, 1979.

10. Gorney, D. J., A. Clarke, D. R. Croley, J. F. Fennell, J. Luhman, and P. Mizera, The Distributions of Ion Beams and Conics below 8000 km, J. Geophys. Res., 86, 83, 1981.

11. Dusenbery, P. B., and L. R. Lyons, Generation of Ion-Conic Distribution by Upgoing Ionospheric Electrons, J. Geophys. Res., 86, 7627, 1981.

12. Lysak, R. L., M. K. Hudson and M. Temerin: Ion Heating by Strong Electrostatic Ion Cyclotron Turbulence, J. Geophys. Res., 85, 678, 1980.

13. Chang, T. and Coppi, B.: Lower Hybrid Acceleration and Ion Evolution in the Supraauroral Region, Geophys. Res. Lett., 18, 1253, 1981.

14. Hardy, D. A., W. J. Burke, and M. S. Gussenhoven: DMSP Optical and Electron Measurements in the Vicinity of Polar Cap Arcs, J. Geophys. Res., 87, 2413, 1982.

15. Burch, J. L., S. A. Fields, and R. A. Heelis: Polar Cap Electron Acceleration Regions, J. Geophys. Res., 84, 5863, 1979.

16. Burke, W. J., M. S. Gussenhoven, M. C. Kelley, D. A. Hardy, and F. J. Rich: Electric and Magnetic Field Characteristics of Discrete Arcs in the Polar Cap, J. Geophys. Res., 87, 2431, 1982.
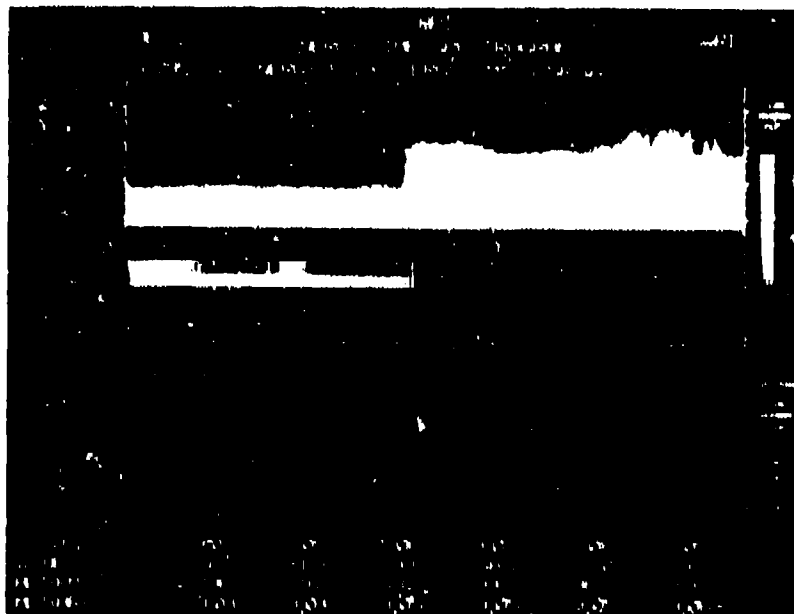
(a)   13:04 to 13:09 UT.
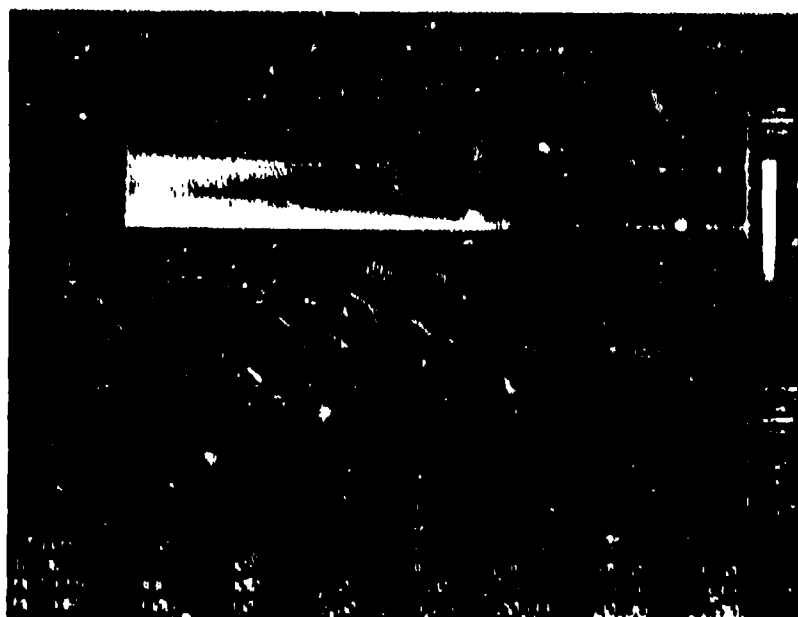
(b)   13:10 to 13:16 UT.

Figure 1. - LAPI energy-time spectrogram for DE-2, day 295 of 1981.
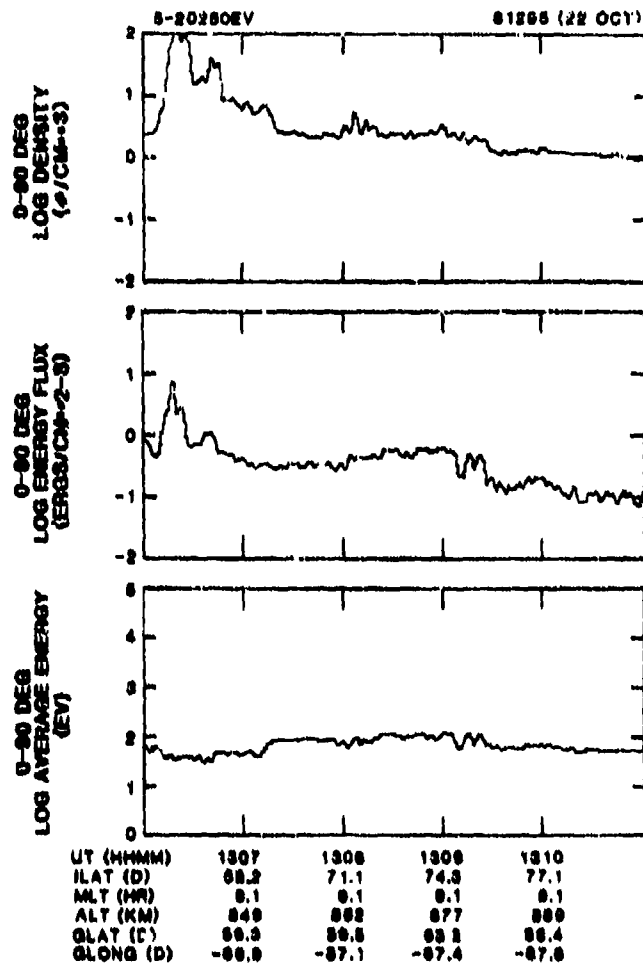
Figure 2. - DE-2 electrons, day 295 of 1981.
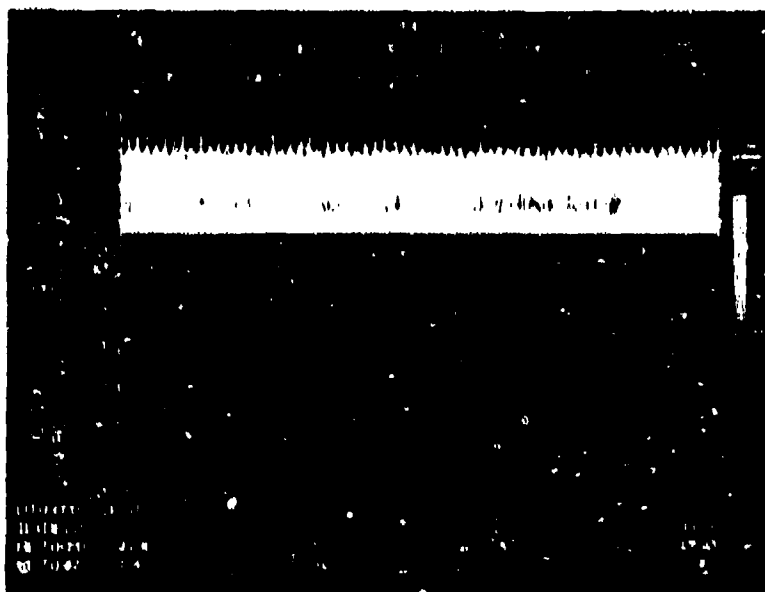
Figure 3. - HAPI energy-time spectrogram for DE-1, day 295 of 1981.
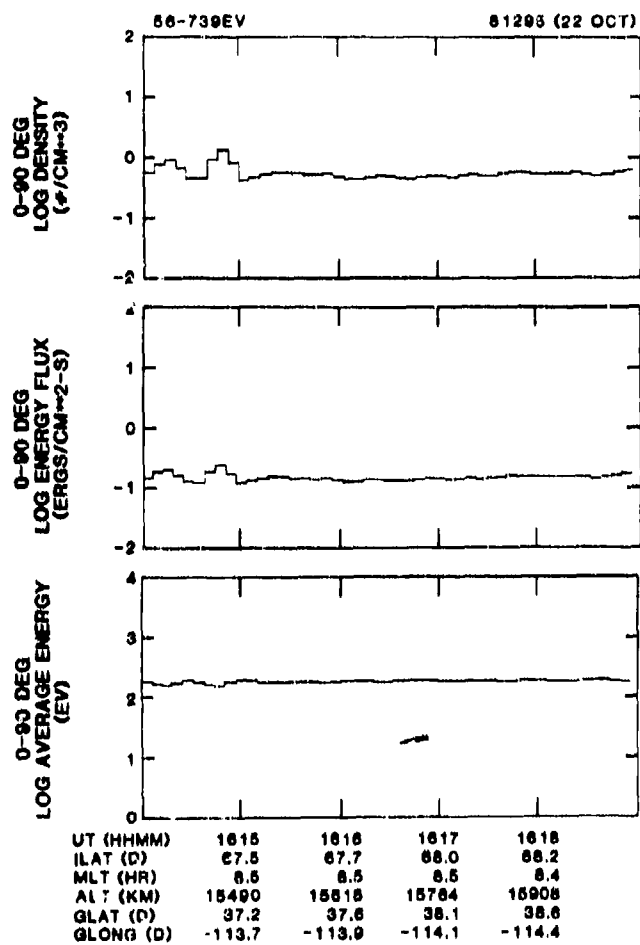
Figure 4. - DE-1 electrons, day 295 of 1981.
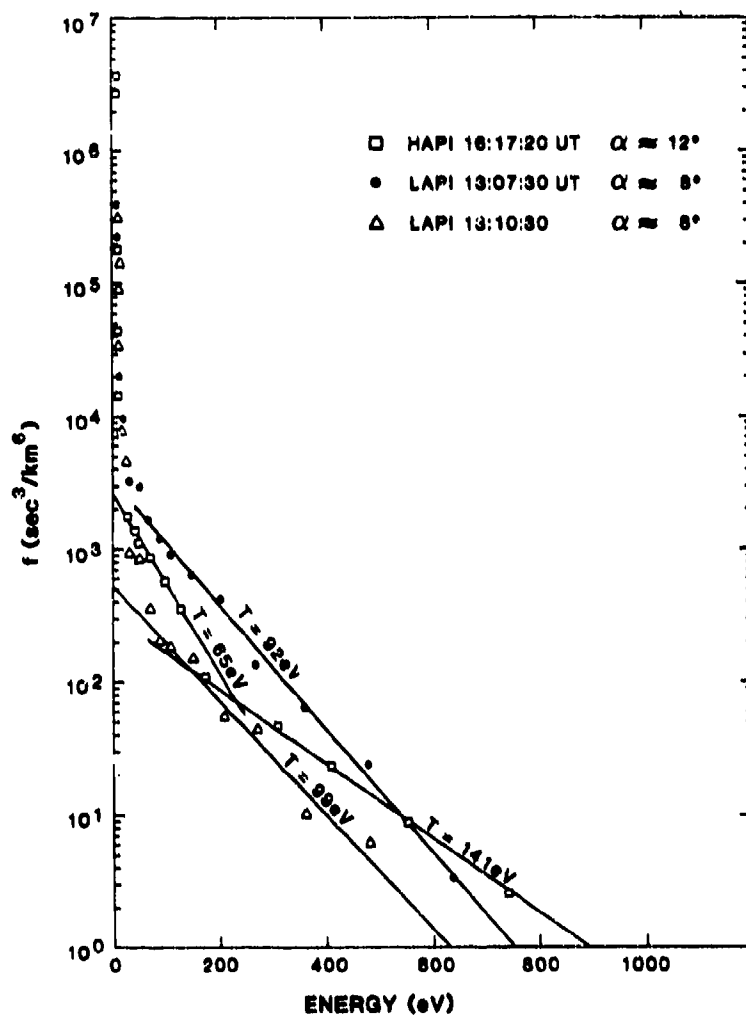
Figure 5. – Near-field-aligned electron populations.
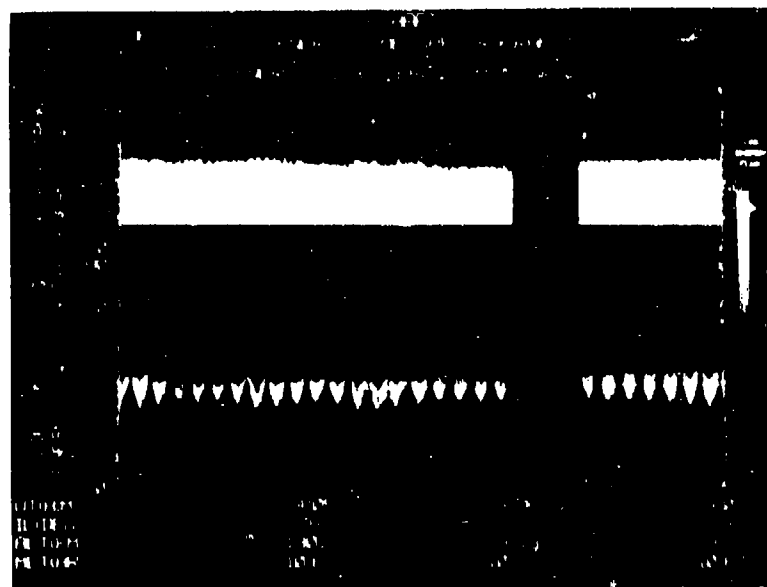
(a)   14:04 to 14:07 UT.
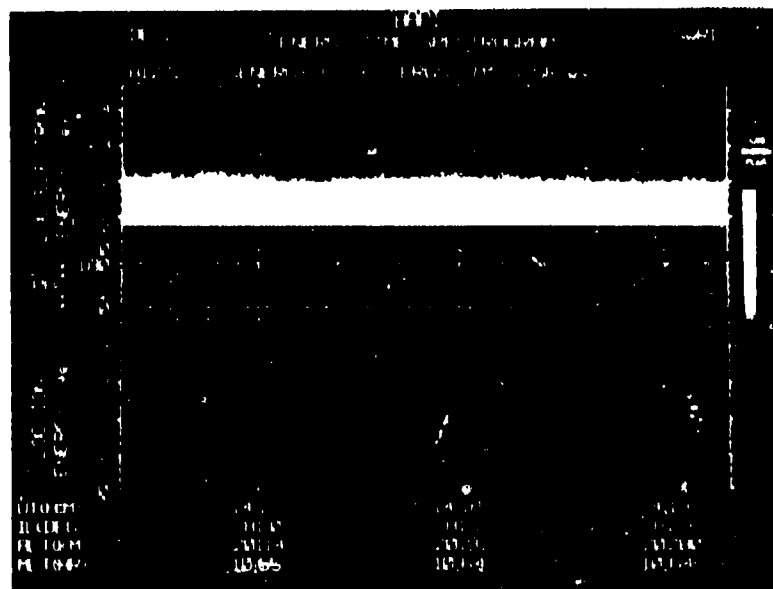
(b)   14:16 to 14:19 UT.

Figure 6. - HAPI energy-time spectrogram of DE-1, day 272 of 1981.
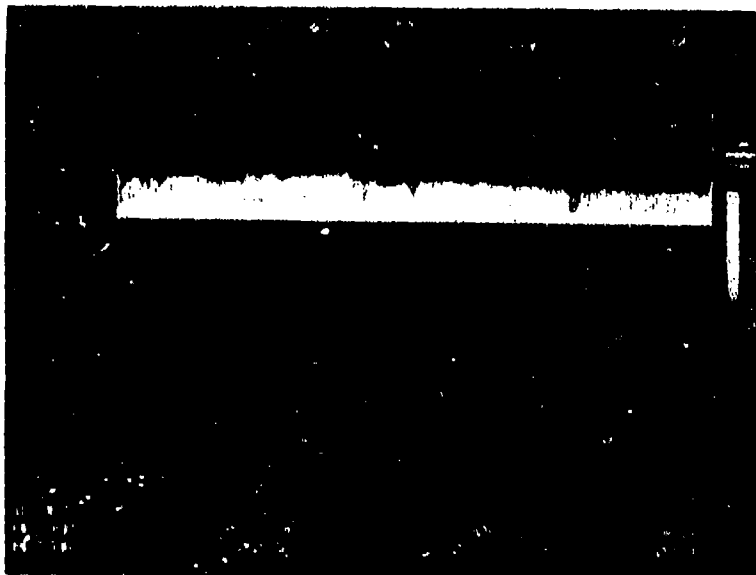
(c)   14:31 to 14:34 UT.

Figure 6. - Concluded.
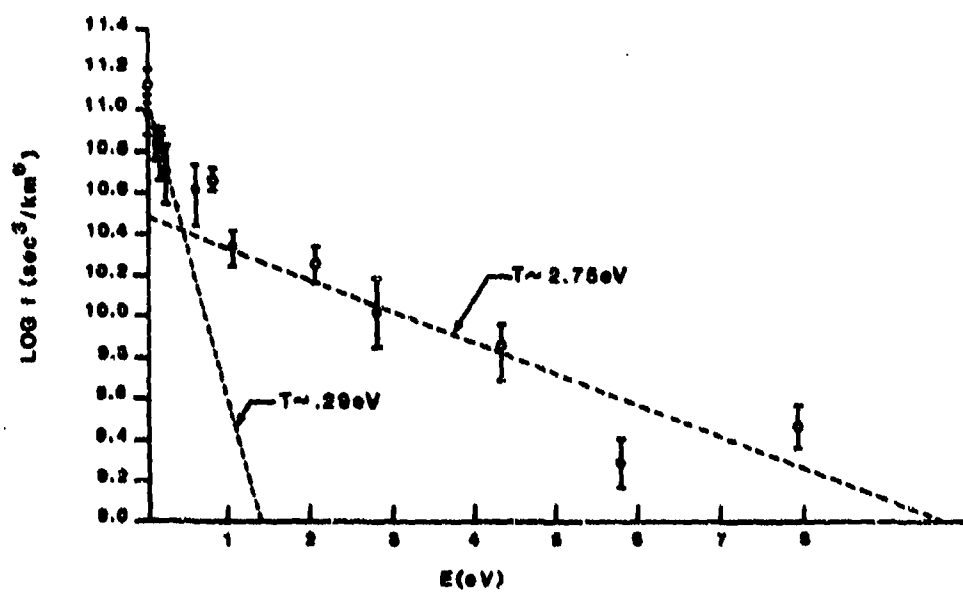
Figure 7. - HAPI velocity space spectrum.
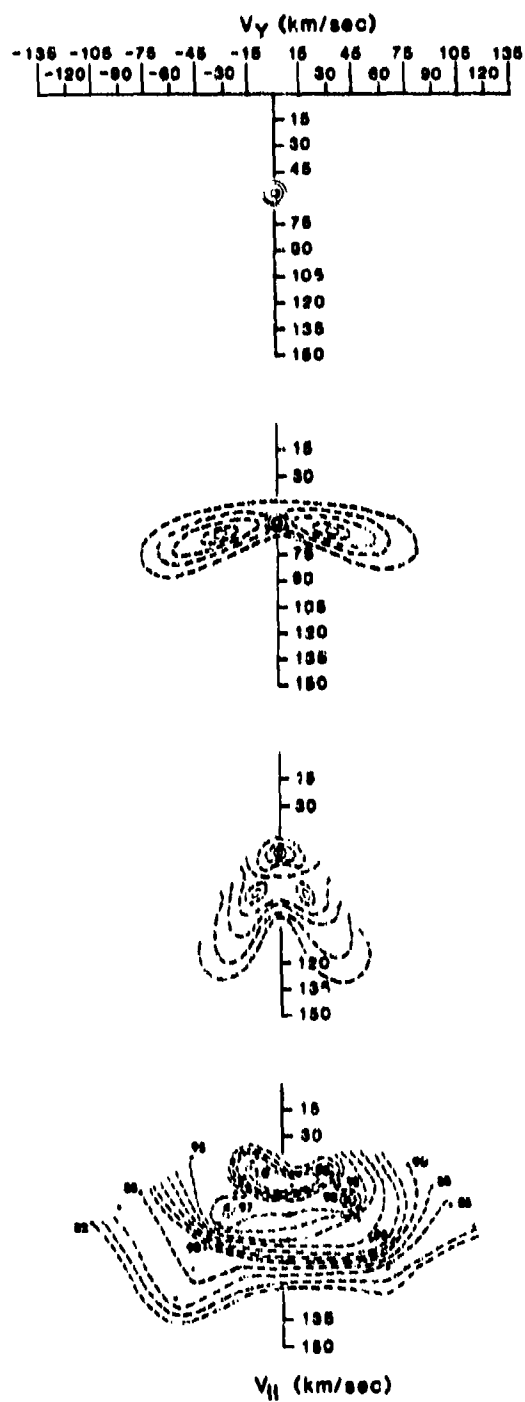
Figure 8. - Evolution of polar wind.
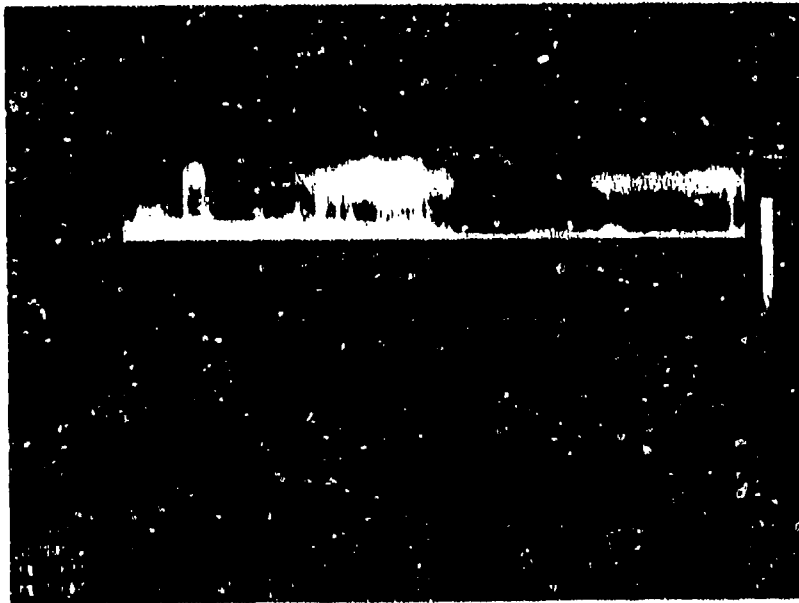
Figure 9. - HAPI energy-time spectrogram of DE-1, day 290 of 1981.

(a) Ions.

Figure 10. - HAPI contour plots for DE-1, day 290 of 1981, 16:32:45.1 to 16:32:57.1 UT.
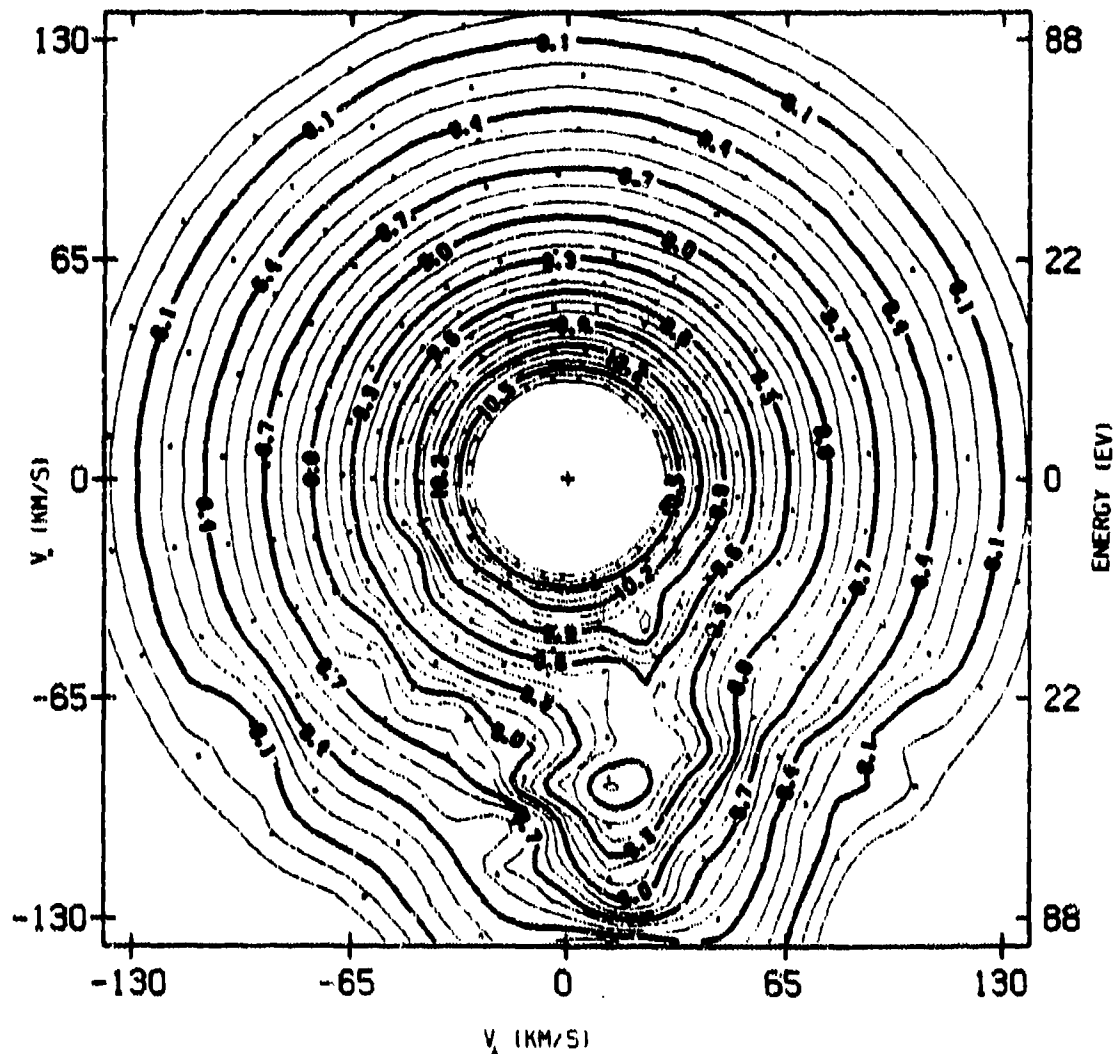
173

DISTRIBUTION CONTOURS LOG F (SEC³/KM⁶)
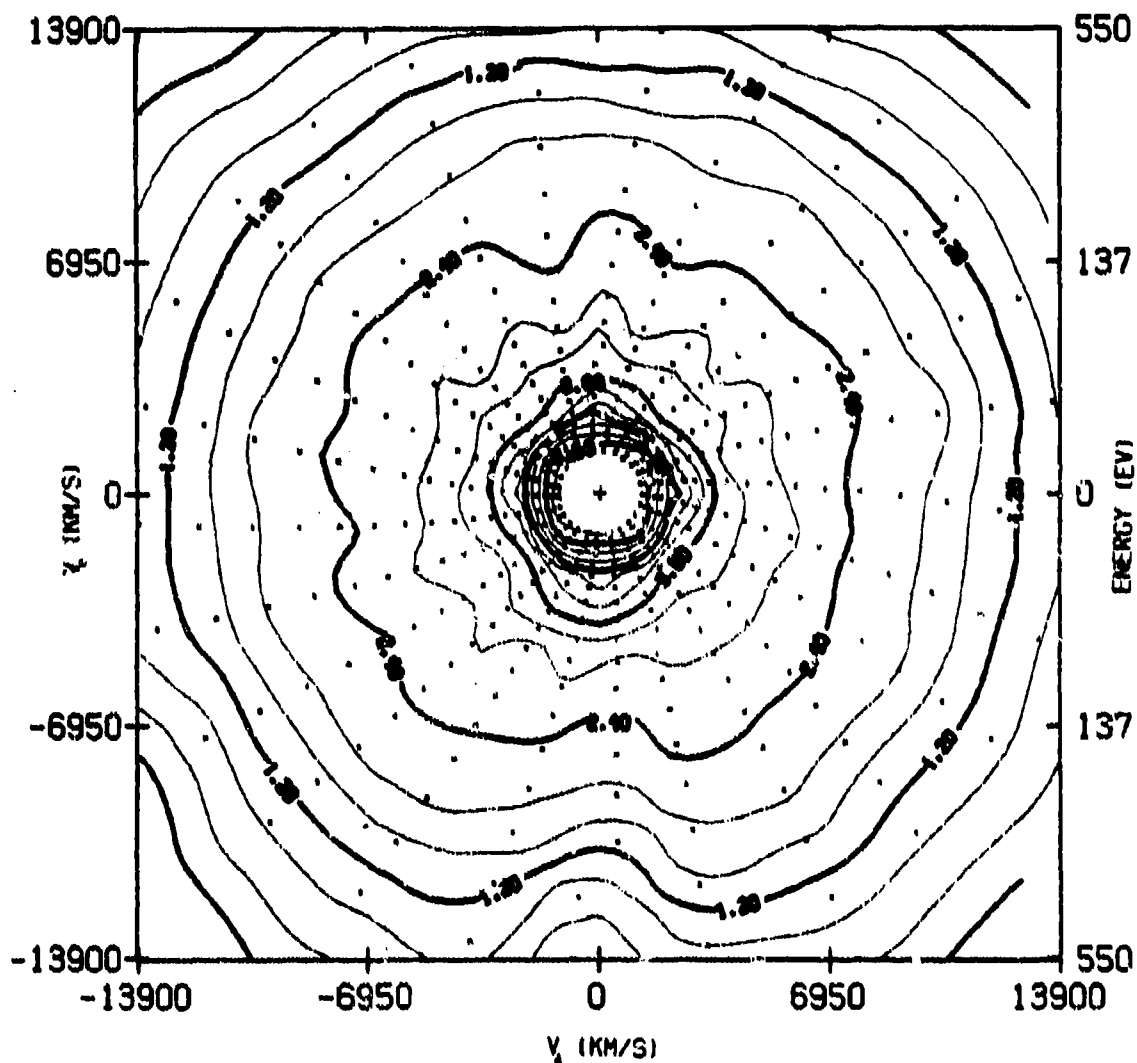
ILAT (D) 70.0
MLT (HR) 22.0
ALT (KM) 10010
GLAT (D) 70.0
GLONG (D) 60.3

MIN EV	MAX EV	AV. EV.	MMPS/M²
0.	730.	1.00E+01	-1.47E-07

FLUX (/CM²S)	DEN (/CM³)	EROS/CM²S
0 - 90	0 - 90	0 - 90
4.02E+09	2.04E+01	2.04E-01

VPAR (KM/S)	PC (MHOS)	HC (MHOS)
-2.24E+01	N/A	N/A

(b) Electrons.

Figure 10. - Concluded.

174

(a) Ions.

Figure 11. - HAPI contour plots for DE-1, day 290 of 1981, 16:45:30.0 to 16:46:35.7 UT.

175

(b) Electrons.

Figure 11. - Concluded.

AURORAL/POLAR CAP ENVIRONMENT AND ITS IMPACT ON
SPACECRAFT PLASMA INTERACTIONS*

Henry B. Garrett
Jet Propulsion Laboratory
California Institute of Technology
Pasadena, California 91109

As space systems become more complex, they have demonstrated an
increasing sensitivity to the space environment. Although the shuttle will
not in general be in orbit long enough to suffer severe radiation exposure
nor normally experience the "hot" particle fluxes responsible for
geosynchronous spacecraft charging, deleterious environmental effects are
anticipated at shuttle altitudes. The high density of the plasma at
shuttle altitudes is, for example, likely to increase greatly the
possibility of arcing and shorting of exposed high voltage surfaces. For
military missions over the polar caps and through the auroral zones, the
added hazards of high energy auroral particle fluxes or solar flares will
further increase the hazard to shuttle, its crew, and its mission. The
purpose of this presentation is to review the role that the auroral and
polar cap environment play in causing these interactions. A simple, though
comprehensive attempt at modelling the shuttle environment at 400 km will
be described that can be used to evaluate the importance of the
interactions. The results of this evaluation are then used to define areas
where adequate environmental measurements will be necessary if a true
spacecraft interactions technology is to be developed for the shuttle.

INTRODUCTION

As the pace of space activities increases with the advent of the
"shuttle era", the concern of engineering and scientific communities over
possible adverse interactions between the space environment and spacecraft
systems has grown proportionally. In particular, with the desire for
large, high voltage structures, cost, complexity, and sensitivity of
spacecraft have increased greatly. The necessity for long (10 years or
more) mission durations in order to recoup expensive development costs has
further intensified the concern for "endurable" or "survivable" spacecraft.
Although much experience has been gained in these matters over the last 25
years, the fact is that there are still major gaps in our knowledge of how
systems affect and are affected by the environment. After the
geosynchronous environment, which has been studied extensively over the
last decade, the earth's polar and auroral environments at shuttle
altitudes pose the greatest risks to future space systems. The objective
of this study is to review the capabilities that currently exist to predict
the shuttle auroral/polar environments and to compare these predictions

with similar ones for the equatorial environment. In order to limit the analysis, this study will only consider the environment at 400 km over the northern hemisphere during winter. Even with this limitation, the amount of information covered is still enormous. As a result, we have further restricted the study to periods of high solar (sunspot number, R, of 100) and geomagnetic activity (geomagnetic activity level, Kp, of 6_0). The emphasis will not be on the accuracy, but rather on the models necessary to adequately specify the shuttle environment. Listings of the actual models, data for other locations and conditions, and references to models not covered in the report can be obtained directly from the author.

The secondary object of the study is to determine the relative importance and sensitivity of different types of environmental interactions as a function of the environment. To accomplish this, where possible, the modelled environments have been used to predict the level of the anticipated interaction. Although this has proven to be a valuable output from the study, the interactions models employed were by necessity quite simplistic so that the absolute levels predicted are not intended to be accurate. Rather, the results demonstrate potential parameter sensitivities and areas where the environmental models need to be improved.

The report is organized into 4 sections dependent on the environment being considered. In this study, only the natural atmosphere, geomagnetic field, ionosphere, and auroral environment at shuttle altitudes were considered. Models of the cosmic ray flux, radiation level, solar electromagnetic flux, ambient electric field, gravity field, and debris environment will be presented at a later time. For each of the environments studied, an interaction is modelled. For the neutral environment, the drag is computed. For the geomagnetic field, the induced vxB electric field is estimated. For the ionosphere and auroral environments, the vehicle to space potential is estimated. The results of this analysis demonstrate, as would be anticipated, that there are indeed major differences in the environment between the equatorial and auroral/polar environments that are reflected in the interactions.

THE NEUTRAL ATMOSPHERE

By far the major environmental factor at shuttle altitudes is the earth's ambient neutral atmosphere. Whether it be through drag or the recently discovered interactions with atomic oxygen, the effect of the neutral atmosphere (predominately the neutral atomic oxygen) on spacecraft dynamics and surfaces greatly exceeds any of the other effects that will be considered in this report. Currently there exist a number of models of the earth's neutral atmosphere. These models are based on differing ratios of data and theory. The 3 main sources of data at shuttle altitudes have been neutral mass spectrometers, accelerometers, and orbital drag calculations. Without going into detail, most models attempt to fit the observations with some form of an algorithm that includes the exponential fall off of the neutral density, the effects of increasing solar activity (particularly in the ultraviolet), the local time, and geomagnetic activity. Of these, the large variations associated with increasing geomagnetic activity (and subsequent heating of the atmosphere) have eluded adequate modelling by this fitting process. Unfortunately, it is clear from many sources (see,

for example, ref. 1) that these variations, particularly in density, over the auroral zone often dominate the neutral environment and that to date no adequate method of including these effects in the models has been devised (some recent very sophisticated theoretical computer models do hold promise, however).

With the preceding caveat in mind, 2 models were used to compute the variations in drag due to the neutral atmosphere at 400 km. These are the Jacchia 1972 model (ref. 2) and the MS$^-$S model (refs. 3 and 4). These models are readily available in computer format and have been well developed over the last decade. For the purposes of this study, the Jacchia 1972 model results are presented (the MSIS model results deviate by about 20% from the Jacchia values on the average—a relatively small value given the much larger average uncertainties in the models themselves). Figure 1 illustrates the type of output that can be obtained. As stated earlier, the results are for the northern hemisphere (the reader is looking down on the north pole with the projection in terms of equal latitude intervals) and 400 km. The geomagnetic conditions for the model are for $F10.7 = 2.2 \times 10^{-20}$ W-m^2-Hz^{-1} (the solar radio flux at 10.7 cm; believed to be proportional to the extreme ultraviolet flux) and $Kp=6_0$. These give an exospheric temperature of about 1500 $^\circ$K.

Several features are apparent in the figure. First is the two-fold increase in density from midnight to noon. Further, there is the pronounced shift by 2 hours of the peak in the density and temperature maxima away from local noon. This well know phenomena results from the rotation of the earth and causes the peak in atmospheric heating to occur after local noon. The figure shows no clear feature associated with the auroral zone. This is directly due to the averaging techniques used in deriving models of this type which smooth out the density waves actually observed over the auroral zone. Even so, the model results are useful in estimating the levels of atmospheric drag and, when the processes are better known, the levels of shuttle "glow" and surface degradation.

The major effects of the neutral atmosphere at 400 km result from the impact of neutral particles on spacecraft surfaces. This causes drag and surface damage. The standard expression for the drag force is:

$$F(drag) = 1/2 \, pV^2 \, CD \, A =$$
$$= \sim(300 - 5000) \text{ dynes} \tag{1}$$

where:

p = 10^{-16} g/cm^3 at 400 km
CD = drag coefficient = 2.2 - 4.0
A = cross-sectional area of spacecraft
= $\sim$50 m^2 (Frontal) for shuttle
= $\sim$400 m^2 (Base) for shuttle
V = spacecraft velocity
= 7.6 km/s

Comparing these values with Figure 1, it is evident that uncertainties in the orientation of the shuttle and lack of knowledge in the drag coefficient are equal to or greater than variations in the neutral environment at these altitudes. Given, however, the very real uncertainty

in the effects of auroral heating, it is also apparent that these variations, if they are greater than a factor of 10 (which they can be), will be the major contributor to uncertainties in neutral drag calculations.

MAGNETIC FIELD

Aside from the gravitational field of the earth, the geomagnetic field at shuttle altitudes is the most accurately known. It can be crudely modelled in terms of a tilted (~11° from geographic north) magnetic dipole of magnitude 8×10^{25} G-cm^3. Numerous accurate models of this field exist. Here we have used the POGO model (refs. 5 and 6) as it is the basis of the International Reference Ionosphere (IRI) model employed in the next section. This model is a straight forward expansion of fits to the earth's magnetic field in terms of spherical harmonics. The total magnetic field magnitude at 400 km according to this model is presented in Figure 2. The surface field is seen to vary from a minimum of 0.25 G near the equator to 0.5 G over the polar caps. The existence of 2 peaks in the magnitude is real and reflects the true complexity of the magnetic field in the auroral/polar cap regions (note: if vector components had been included in this figure, it would have been obvious that the maximum at 270° east longitude is the true "dip" magnetic pole). Geomagnetic storm variations are typically less that .01 G so that even during a severe geomagnetic storm, magnetic fluctuations would be small compared to the average field—a marked contrast with the atmospheric and ionospheric environment. Even so, the great complexity of the magnetic field over the poles makes it difficult to use magnetic guidance systems in these regions—a fact long known to navigators.

Besides magnetic torques (which are very system dependent), the earth's magnetic field can induce an electric field in a large body by the vxB effect:

$$E = 0.1 \ (vxB) \ V/m = 0.3 \ V/m \hspace{3cm} (2)$$

where:

v = spacecraft velocty =
  = 7.6 km/s
B = 0.3 G

Since the shuttle is roughly 15 m x 24 m x 33m, potentials of 10 V could be induced by this effect. As systems grow to km or large dimensions, the induced fields will grow accordingly.

In Figure 2, the induced electric field for a vehicle of ~90° inclination has been calculated. As would be anticipated, the largest electric fields are seen over the polar caps. The ambient environment can also produce strong electric fields in the auroral/polar regions. Although not shown here, these fields can reach values of nearly 100 mV/m (see ref. 7)—a sizable fraction of the induced field. These fields are also comparable to the fields necessary to deflect charged particles in this

environment as the particles have ambient energies of typically 0.1 eV (ram energies for the ions like oxygen can reach several eV, however) and thus must be taken into account when studying ionospheric fluxes.

IONOSPHERE

Given the importance of the ionosphere to radio and radar propagation, it is surprising to find that relatively few models are available for the ionosphere. Less surprising is the fact that most of these models only predict electron densities—the most readily measureable quantity by ground means and the most important to radio propagation. The principle ionospheric model available based on observations is the International Reference Ionosphere (ref. 8). This is the only readily available computer model that gives the electron and ion composition and temperature as a function of longitude, latitude, altitude (65 to 1000 km), solar activity (by means of the sunspot number, R), and time (year and local). Although the model is obviously limited (it is confined to R values of 100 or less whereas R values of 200 or greater may occur during solar maximum), it nonetheless is the "best" available comprehensive model of the ionosphere.

In Figures 3 and 4, for the northern hemisphere, are presented several examples of the output from the IRI model. Figure 3 presents the electron number density and temperature at 400 km for R=100 in December. Unlike the neutral temperature, the electron temperature increases by a factor of 2 in going from the equator to the pole. Like the neutral density, however, the peak in the electron density again is shifted by about 2 hours from local noon.

At 400 km, the ionosphere, primarily because of the corresponding high level of neutral oxygen, is dominated by oxygen ions (45% near local midnight and below 30° latitude to 97% over the pole). Values for oxygen are presented in Figure 4. The temperature is assumed to be the same for all ion species in this model (i.e., for O^+, H^+, He^+, O_2^+, and NO^+) and can not for physical reasons ever exceed the electron temperature. Unfortunately, at 400 km for R=100 or larger, the IRI model will occasionally predict ion temperatures far in excess of the electron temperature. This reflects the fact that the model is based on a limited set of data (R<100) and needs improvement. Theoretical models exist that avoid this problem but these models are still too cumbersome to be usable on all but the largest computers.

In Figure 5, using a simple 1-dimensional, "thin sheath" ram model for ion collection (described in ref. 9), potentials for the case of no secondary emission and no photoelectron current were calculated based on Figures 3 and 4. The spacecraft to space potential varied from -0.2 V at the equator to -0.7 V at the pole—in rough agreement with observations (ref. 9). Thus, based on the IRI model environment alone, spacecraft charging should not be a concern (note: the high plasma density will, however, encourage plasma interactions with exposed high potential surfaces as discussed elsewhere in this book).

The most dramatic changes in the earth's environment at shuttle altitudes are brought about by geomagnetic substorms. These changes are reflected in visible auroral displays and in intense particle and field variations in the auroral region at shuttle altitudes. In this section, a simple auroral flux model based on data provided by the Air Force Geophysics Laboratory (courtesy M. Smiddy and D. Hardy; see papers by Smiddy and Hardy, this volume) is presented in order to estimate these effects. The data were provided in the form of 7 sets of color contour plots of the electron number flux and energy flux in intervals of Kp from 0 to 6. The plots were crudely approximated by a simple analytic function in geomagnetic local time and latitude and the geomagnetic Kp index. Although, the AFGL data were for about 800 km, no attempt has been made to correct for altitude in this model.

The crude model developed from the AFGL data was used to estimate the auroral/polar cap electron temperature and number densities. These results for the northern winter hemisphere and a Kp of 6_0 are shown in Figure 6. They imply that there is a peak in the density of the auroral electron flux of about 1000 cm^{-3} in the noon sector while the auroral electron temperature is 1 keV in the post-midnight sector. Although the validity of this crude result will need to be compared with the actual AFGL data when they become available, the range of values should at least be indicative of the characteristics of the average auroral fluxes (comparisons with other data sources bear this out).

The results in Figure 6 can be used in conjunction with the IRI data at 400 km to estimate the expected variations in spacecraft potential in the auroral zone and over the polar caps (note: the auroral ion fluxes should not contribute significantly to the ambient ion current so that their exclusion should not seriously alter the results). When this calculation was carried out, there was little or no change from the results in Figure 5. This is not surprising as it is generally believed that the average auroral flux levels seldom exceed the ambient ion and electron ionospheric fluxes.

In order to estimate what auroral flux levels are in fact necessary to bring about significant increases in the spacecraft potential in the auroral/polar cap regions, the electron density and temperature in Figure 6 were increased by varying factors. Changes of a factor of 10 in either the temperature or density had little effect on the potential. A factor of 10 in both the electron density and temperature did, however, bring about a significant increase in the potential—raising it from a few tenths of a volt negative to several thousands of volts in the early afternoon sector. These results are illustrated in Figure 7. Such a large increase in the auroral flux may seem unrealistic but a careful review of auroral data does imply that occasionally intense fluxes 10 to 100 times that of the average flux may indeed occur over narrow regions in the auroral zone (see, for example, Burke, this conference).

In carrying out the potential analysis, it was found that the details
of the assumed charging model greatly affected the results. Specifically,
if a 1-dimensional, thin sheath model was assumed, the auroral potentials
could reach -8000 V when the ion return current was equated to the cold
ambient ion current. If the ion return current was assumed to be the ram
current, as was done here, the potential was about -1200 V maximum (this is
probably the more "realistic" assumption). If on the other hand the ion
return current in the charging model was assumed to be for the thick
sheath, orbit-limited case such as normally assumed at geosynchronous
orbit, the potential was only -1 to -2 V! This sensitivity to the details
of the amount of return current is to be expected given the simplicity of
the charging model and its resolution will need to await the development of
more accurate charging models for the conditions at shuttle altitudes.

CONCLUSIONS

This paper has brought together most of the elements needed to form a
complete model of the ambient shuttle environment for the purpose of
studying spacecraft interactions. Emphasis has been on modelling the
interactions in the auroral/polar cap regions where it was demonstrated
that, although models of the average ambient environment (neutral
particles, fields, ionospheric particles, and auroral/polar cap fluxes) are
probably satisfactory for many interaction study purposes, the intense
variations in the auroral zone are not adequately modelled. These
variations are known from in-situ observations to exist and to result in
several orders of magnitude increase in the charged particle fluxes and
atmospheric heating which can similarly alter the neutral composition. It
is only relatively recently that long term statistical studies and examples
of extreme cases have become available. It is to be anticipated that, in
the near future, models of the environment will become increasingly
sophisticated and capable of being used in modelling effects such as
spacecraft charging much more accurtely than presented here. Even so, the
results presented should assist current interaction studies in better
assessing average levels of effects in the auroral/polar regions and in
comparing equatorial and auroral/polar environments. The process of
presenting the models has also clearly indicated where improvements need to
be made in the existing models. This is particularly true in the case of
the auroral model due to the varying sensitivity of the principle
interaction to changes in the ambient environment (i.e., spacecraft
potential calculations).

P. McConnell, M. Harel, and J. Slavin of JPL assisted in the
collection and development of many of the models listed in this report.
Any information on listings may be obtained through them or the author
directly.

REFERENCES

1.   Straus, J. M.: Dynamics of the Thermosphere at High Latitudes. Rev.
Geophys., 16 1978, pp. 183-194.

2.   Jacchia, L. G.: Atmospheric Models in the Region from 110 and 2000 km.
CIRA 1972, Akademie-Verlag, Berlin, 1972, pp. 227-338.

3.   Hadin, A. E., Jr.; Salah, J. E.; Evans, J. V.; Reber, C. A.; Newton, G. P.; Spencer, N. W.; Kayser, D. C.; Alcayde, D.; Bauer P.; Cogger, L.; and McClure, J. P.: A Global Thermospheric Model based on Mass Spectrometer and Incoherent Scatter Data, MSIS 1, N2 Density and Temperature, *J. Geophys. Res.*, 82 2139-2147, 1977a.

4.   Hadin, A. E, Jr.; Reber, C. A.; Newton, G. P.; Spencer, N. W.; Brinton, H. C.; Mayr, H. G.; and Potter, W. E.: A Global Thermospheric Model based on Mass Spectrometer and Incoherent Scatter Data, MSIS 2, Composition, *J. Geophys.Res.*,82 2148-2156, 1977b.

5.   Knecht, D. J.: The Geomagnetic Field. *Air Force Surveys in Geophysics, No. 246,* AFCRL-72-0570, 26 September 1972.

6.   Cain, J. C.; and Langel, R. A.: The Geomagnetic Survey by the Polar Orbiting Geophysical Observations Ogo-2 and Ogo-4, 1965-1967, *GSFC Rep.X-612-68-502*, Greenbelt, Maryland, 1968.

7.   Foster, J. C.: An Empirical Electric Field Model derived from Chatanika Radar Data. *J. Geophys. Res.*, 88 1983, pp. 981-987.

8.   Rawer, K. (Chairman): International Reference Ionosphere - IRI 79 (edited by J. V. Lincoln and R. O. Conkright). World Data Center A, *Rpt. UAG-82,*November 1981.

9.   Garrett, H. B.: The Charging of Spacecraft Surfaces. *Rev. Geophys.,* 19 1981, pp. 577-616.
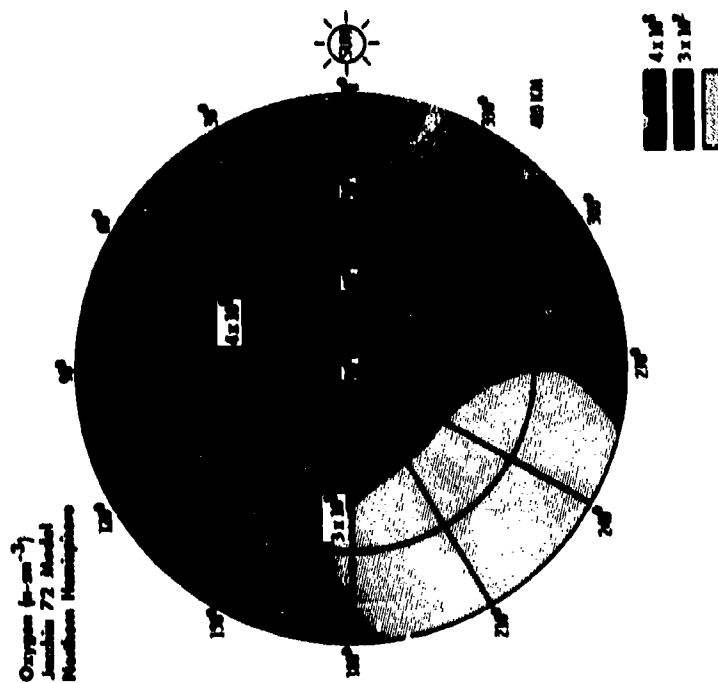
(c) Number density of oxygen.

Figure 1. – Concluded.
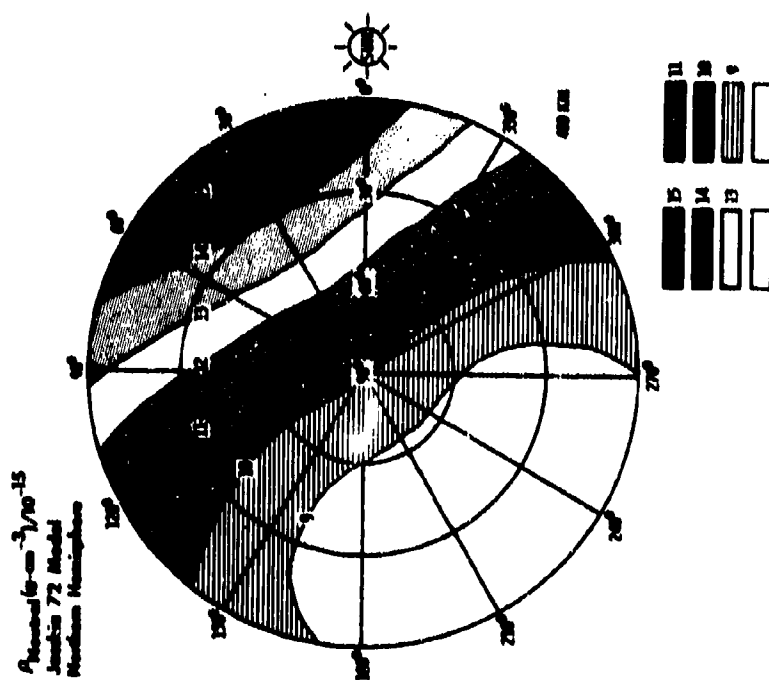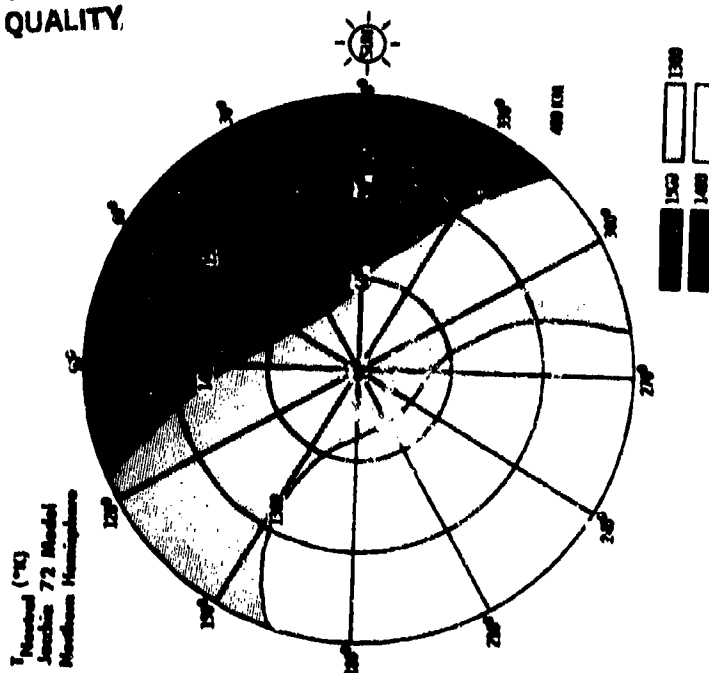
(b) Neutral temperature.

(a) Neutral density.

Figure 1. - Polar view of Northern Hemisphere. Polar coordinates are employed such that radial distance is in intervals of equal latitude (0° is the equator) while angular coordinate is east longitude. Neutral atmosphere conditions for $K_p=6_0$, F10.7=220, day 357.5, and altitude of 400 km as computed by the Jacchia 1972 model are shown.
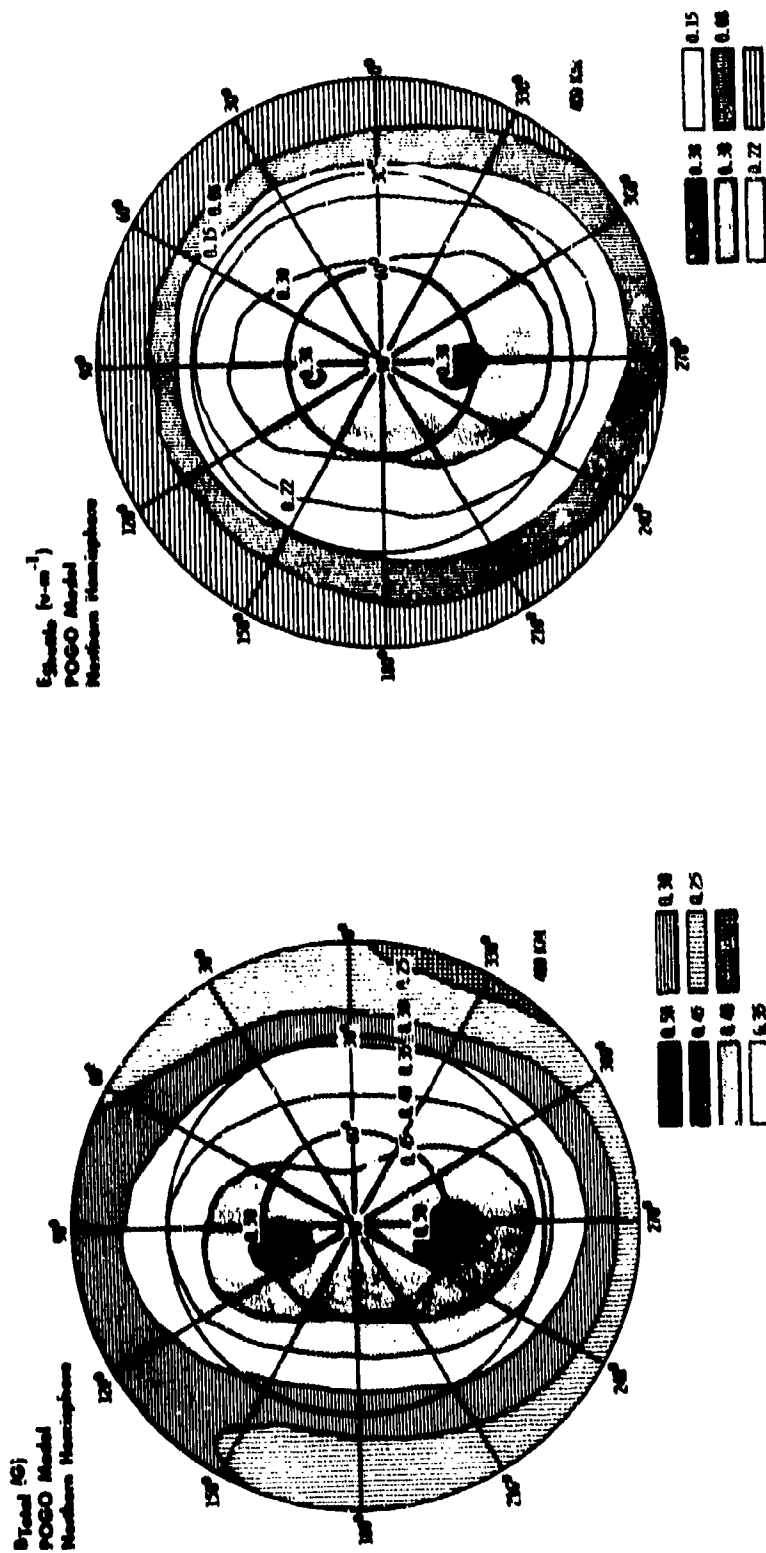
(a) Total magnetic field at 400 km.

(b) Absolute value of vxB electric field induced on a body in a 90° inclination orbit for POGO model.

Figure 2. – Polar view as in figure 1 for POGO magnetic field model.

187
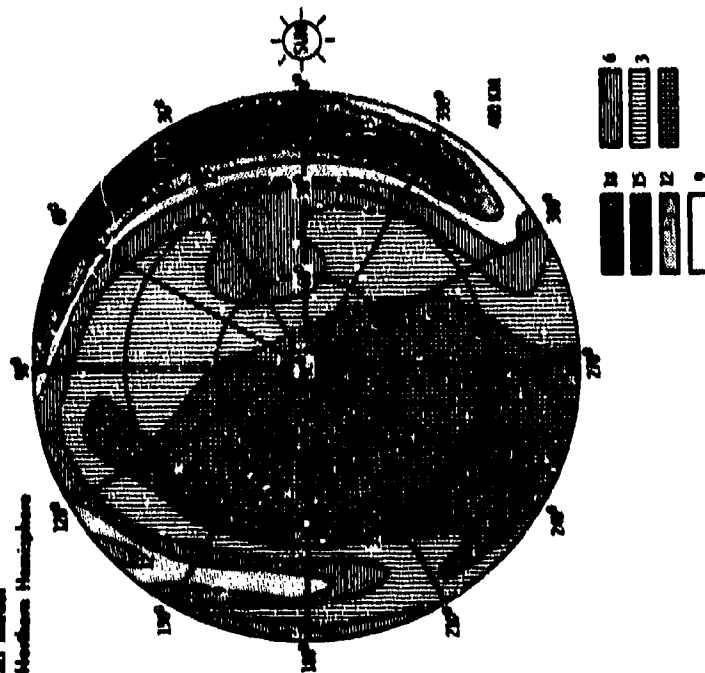
(a) Electron density at 400 km.
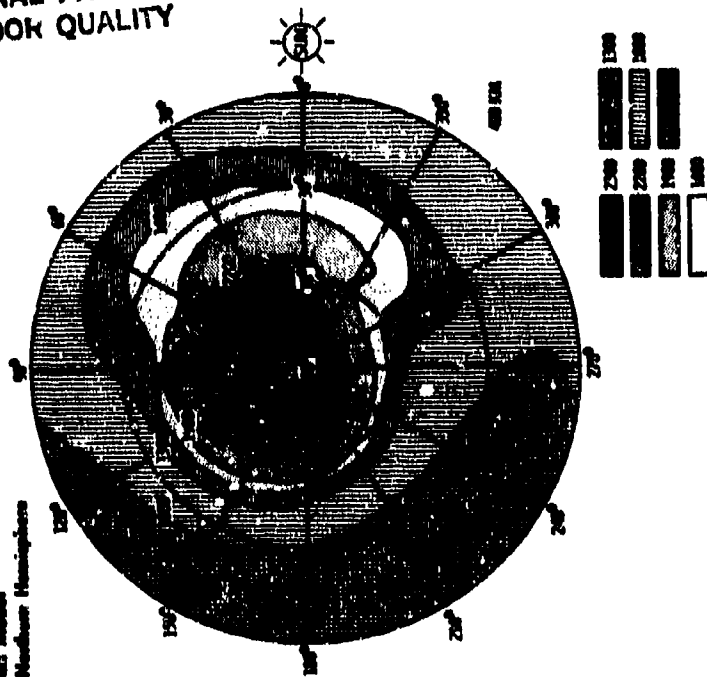
(b) Electron temperature at 400 km.

Figure 3. – Polar view of electron environment as in figure 1 for IRI model. Conditions are the same as in figure 1 with the additional constraint that R=100.
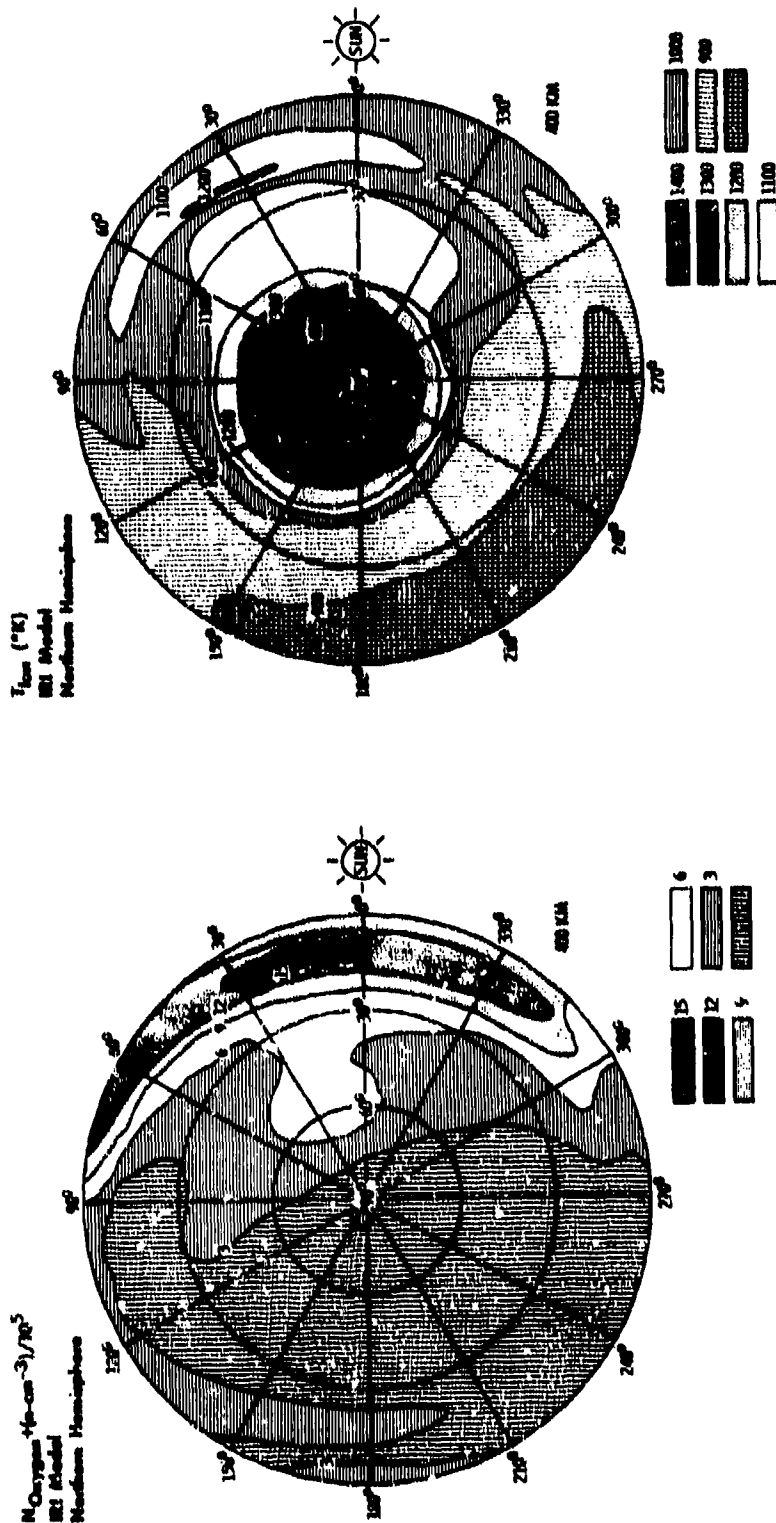
(a) Oxygen ion density at 400 km.

(b) Oxygen ion temperature at 400 km.

Figure 4. - Polar view of oxygen ion environment as in figure 1 for IRI model. Conditions are the same as in figure 1 with the additional constraint that R=100.

SPACECRAFT POTENTIAL (V)
IRI MODEL
R = 100
DAY = 357.5
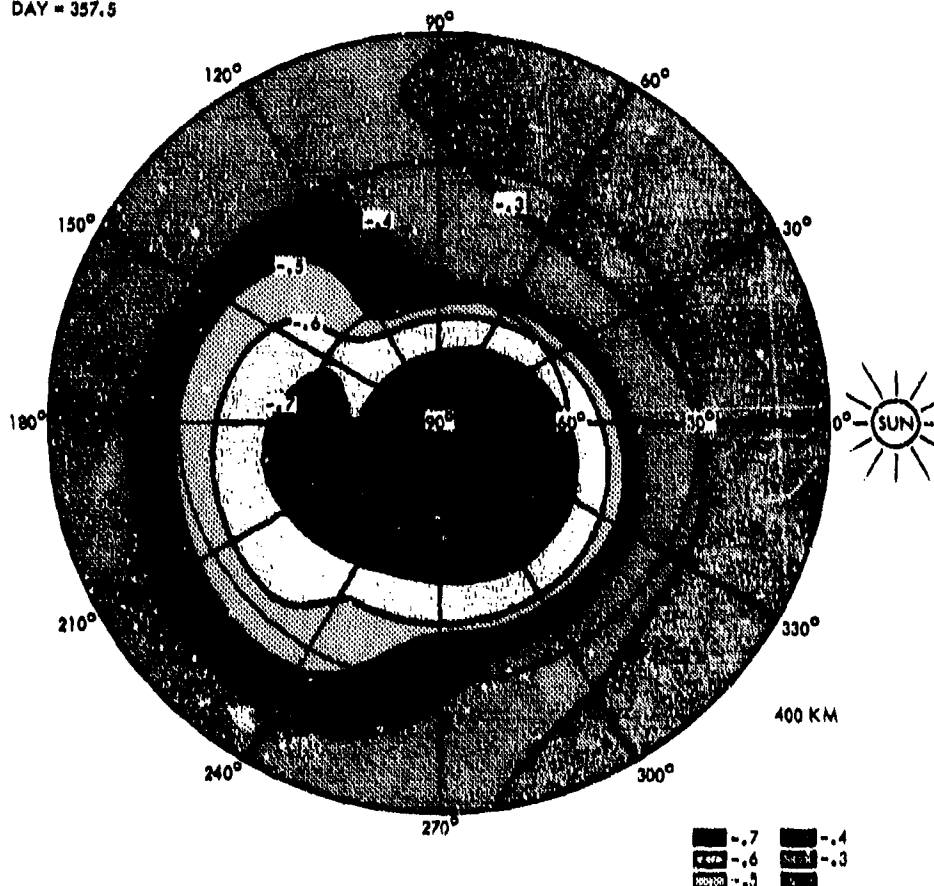
Figure 5. - Polar view as in figure 1 of spacecraft-to-space potentials pre-
dicted for IRI model. Potentials were computed assuming that the ion current
was proportional to the ion ram flux (see text) and that there were no sec-
ondary or photoelectron currents.

190
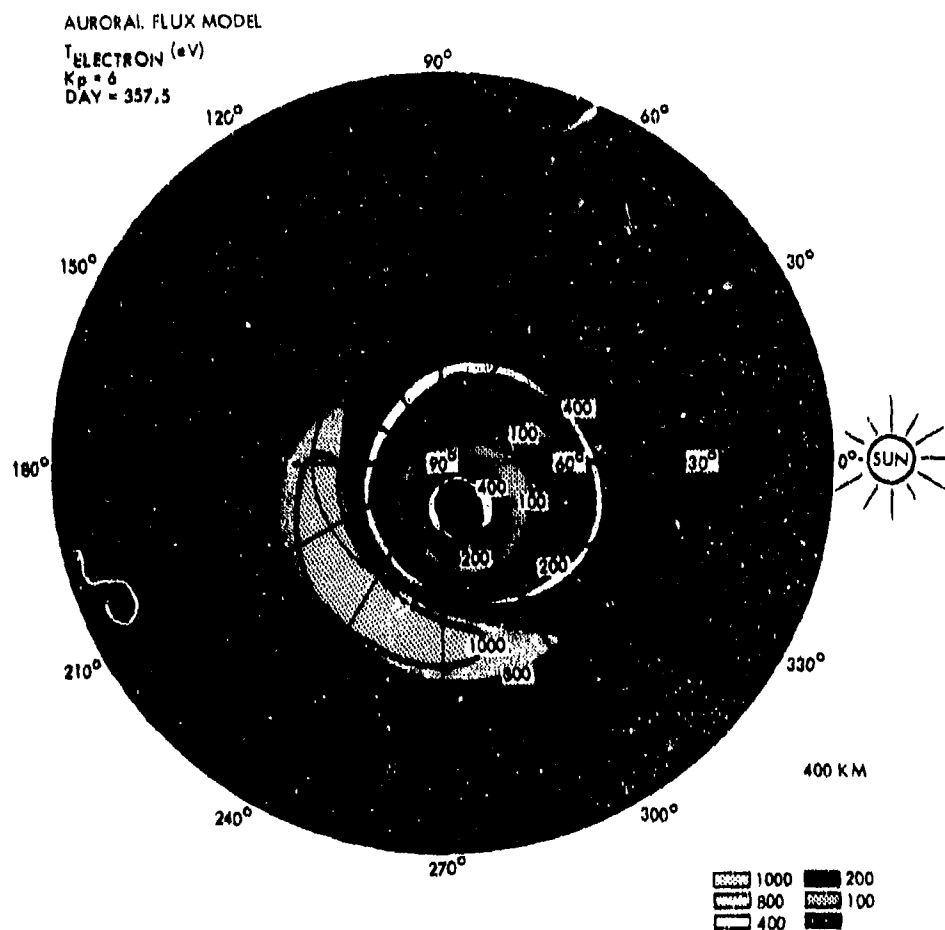
(a) Density of auroral electron flux at 400 km.

Figure 6. - Polar view as in figure 1 of auroral flux model adapted from AFGL observations. Conditions correspond to $K_p = 6_0$ and for day 357.5.

191
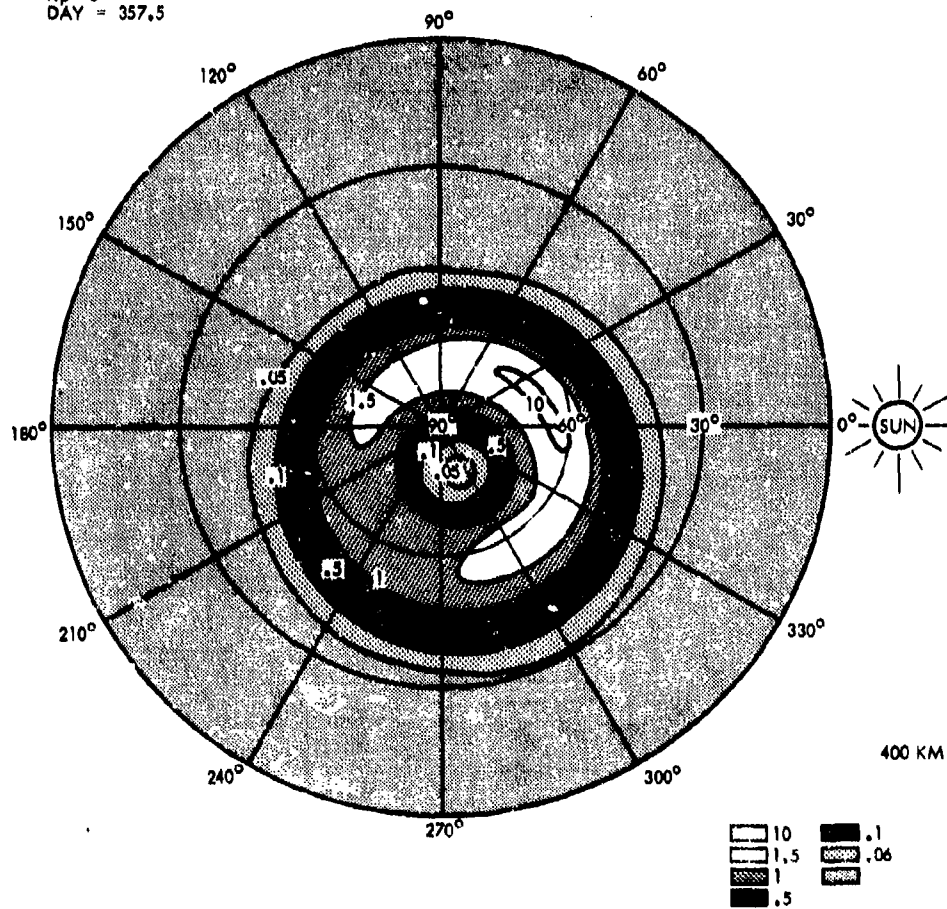
(b)   Temperature of the auroral electron flux at 400 km.   Units are °K.

Figure 6. – Concluded.

SPACECRAFT POTENTIAL
IRI MODEL + 10 *(AURORAL MODEL)
R = 100
Kp = 6
DAY = 357.5
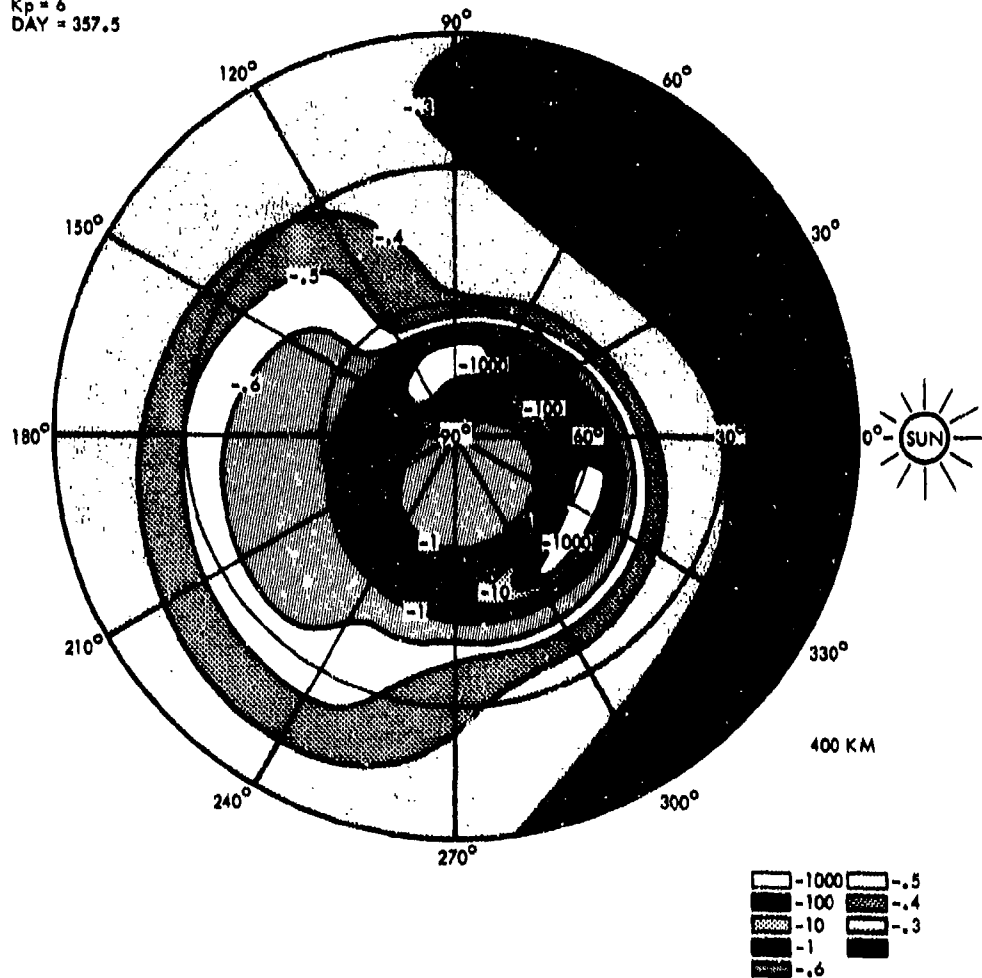
Figure 7. — Polar view as in figure 1 of spacecraft-to-space potentials predicted for combination of IRI and auroral models. Potentials were computed as in figure 5 except that the auroral density and temperature from figure 6 have both been multiplied by 10.

ELECTRIC FIELD EFFECTS ON ION CURRENTS IN SATELLITE WAKES*

D. E. Parks and I. Katz
S-CUBED
La Jolla, California 92038

Small currents associated with satellite spin, dielectric conduction, or trace concentrations of H^+, can have a substantial effect on the potential of a satellite and the particle currents reaching its surface. The importance of such small currents at altitudes below about 300 km stems from the extremely small O^+ currents impinging on the wake-side of the spacecraft.

The focus of the present study is the particle current on the downstream side of the AE-C satellite. Theoretical estimates based on a newly described constant of the motion of a particle indicate that accounting for small concentrations of H^+ remove a major discrepancy between calculated and measured currents.

1. INTRODUCTION

Many studies, both theoretical and experimental, have been made of the interaction between a satellite and the near earth plasma (refs. 1-11). The present study concerns charged particle current on the wake-side surface of a spacecraft in the earth's ionosphere, where the vehicle is mesothermal; its speed V_0 exceeds the thermal velocity of plasma ions but is much less than the thermal velocity of the ambient electrons.

In our analysis calculated currents are compared with those that have been observed by Samir et al. (ref. 10) on the Atmosphere Explorer C (AE-C). The AE-C experiments are well suited to our purpose, since its rate of spin, as well as the plasma densities, constituents and temperatures were known. Moreover, measurements were conducted at night, thus avoiding complications associated with active solar arrays.

Measured satellite voltages were in the range $V \sim 9-10\Theta$, where the electron temperature Θ is in electron volts. These results exceeded theoretical estimates based on balance between ion and electron current on a conducting surface by a factor $\sim 2.0-2.5$. Theoretical surface potentials were also substantially less than expected from ion-O^+ current balance at each point of a dielectric surface. In a previous work it was shown that accounting for either rotating currents of charge embedded in the dielectric or small concentrations of H^+ suffice to bring theory and experiment into conformance (ref. 12). The calculated voltages reported in Reference 12 will be used in the calculations of current given in Section 3.

The reported charged particle densities in the ambient plasma encountered by AE-C are in the range 10^4-10^6 cm^3, with equal electron and ion temperatures $\Theta \sim 0.1$ eV, corresponding to ambient Debye lengths $\lambda_D \leq 3$ cm. The ionic components of the plasma are the singly charged species of atomic oxygen, O^+, and atomic hydrogen H^+. Our primary focus will be in the altitude regime below about 300 km where O^+ is the dominant ion in the ambient ionosphere and in the far wake trailing the satellite. In the highly evacuated wake region near the surface of the satellite, however, H^+ may be the dominant ion (ref. 13).

Particle densities and currents, especially in the rarefied wake downstream of the satellite, are the most difficult to determine. Indeed the question of wake structure is the most intensively studied aspect of interactions between a spacecraft and the ionosphere (refs. 4-11). In the quiescent environment of the equatorial ionosphere, where satellites can develop potentials of several times Θ, ion currents to the satellite surfaces facing upstream are little affected by electric and magnetic fields and may be calculated in the neutral approximation (ref. 1), as if particles moved in straight lines with constant speed. The manner of estimating current to surface elements on the wake-side of a high Mach number vehicle is much less clear. One might suppose, for example, that electrical forces may attract substantially greater currents than estimated on the basis of straight line orbits. In Section 2, we will invoke constants of the motion in an axi-symmetric potential field to determine that O^+ number and current densities at the wake-side pole of a non-emitting sphere at an altitude of a few hundred kilometers are several orders of magnitude above neutral approximation densities. The wake-side O^+ currents remain small, however, relative to H^+ currents, and calculations presented below show that electric fields suffice to increase the H^+ currents by orders of magnitude to the observed level.

Two of the dynamical constants used in the calculation are the energy and the axial component of angular momentum; the third is a less well known constant of the motion which applies for potentials of the form $V_0(r) = f(\theta)/r^2$ where θ is the polar angle and r the distance in a spherical co-ordinate system. It reduces to the total angular momentum in the limit of spherically symmetric potentials.

The general physical assumptions underlying the model developed in the subsequent sections of this paper are that

1. The plasma is collisionless and quiescent.

2. The geomagnetic field has a negligible effect on particle motion in the spacecraft sheath.

3. In the plasma rest frame, the unperturbed ions have Maxwellian velocity distributions with finite, equal temperatures.

4. Ions are neutralized on impact with a surface.

5. The spatial dependence of its electron density distribution is related to the space potential V, through the Boltzmann factor $\exp(eV/\Theta)$.

Discussion of further simplifying approximations of a more special character occurs at the point in the text where they are introduced.

2. ION CURRENTS

The normal component of ion current density at a surface element located at $\vec{r}_s$ on the body is given by

$$j = -e \int_{\vec{v}\cdot n < 0} \vec{v}\cdot\vec{n}\; f(\vec{r}_s,\vec{v})\; d^3\vec{v} \tag{1}$$

where $\vec{n}$ is the outward normal at $\vec{r}_s$. The distribution function $f(\vec{r},v)$ at the phase space point $\vec{r}$, $\vec{v}$, satisfies, in general, the Vlasov-Poisson system of equations. For a perfectly absorbing body f satisfies the boundary condition $f(\vec{r}_s,\vec{v}) = 0$ for $\vec{v}\cdot\vec{n} > 0$.

Calculations of current to a satellite surface often use the assumption that ion currents to the satellite are given by the neutral approximation, which neglects the influence of electric fields. This assumption is quite good at the front (upstream) surface where ions reaching the satellite have energies (~ 5 eV for O^+) substantially larger than electrical potential energies. The situation is less clear on the wake-side where electric fields may substantially enhance particle and current densities over the neutral approximation values. In the following paragraphs, this problem is addressed by formulating bounds on $j(\vec{r}_s)$ and $n(\vec{r}_s)$, and applying these bounds for an assumed, non-self-consistent model potential.

The normal current density at a point r_s on the surface where the potential is $V(\vec{r}_s)$ can be written ($m_i = e = 1$)

$$j(\vec{r}_0) = \int \mu_0\; f(\vec{r}_s,\vec{v}_0)\; v_0^3\; dv_0\; d\vec{\Omega}_0$$

$$= \int \mu_0\; f_0(\vec{v})\left(\frac{1}{2}v^2 - V(\vec{r}_s)\right) dv^2 \left|\frac{d\vec{\Omega}_0}{d\vec{\Omega}}\right| d\vec{\Omega} \tag{2}$$

Here $\vec{v}_0 = (v_0,\vec{\Omega}_0)$ is the velocity of a particle at $\vec{r}_s$, $\mu_0 = -\vec{\Omega}_0\cdot\vec{n}(\vec{r}_s)$ ($1 \geq \mu_0 \geq 0$), and $\vec{v} = (v,\vec{\Omega})$ the velocity at $r = \infty$ on the trajectory that connects to the phase space point $(\vec{v}_0, \vec{r}_s)$. If

$$|d\Omega_0 / d\Omega| < 1 \tag{3}$$

then

$$j \leq j_b = 2\int f_0(\vec{v})\left(\frac{1}{2}v^2 - V(\vec{r}_s)\right) v\; dv\; d\vec{\Omega} \;, \tag{4}$$

that is, j_b is an upper bound on the normal ion current density at $\vec{r}_s$. Similarly the particle density satisfies

$$n < n_b = \sqrt{2}\int f_0(\vec{v})\left[\frac{1}{2}v^2 - V(r_s)\right]^{1/2} v\; dv\; d\vec{\Omega} \tag{5}$$

197

The bounds established here require the inequality (3); that is, in terms of inside-out trajectories, neighboring orbits emanating from r_0 with a given energy must diverge more at $r = \infty$ than at their point of origin. Although the inequality (3) appears to be a reasonable assumption for attractive potentials, the general conditions under which it applies have not been established.

For the following considerations, we take a spherical satellite in the potential $V(r,\theta)$ where r and θ are spherical polar coordinates with polar axis in the direction of $\vec{V}_0$. We consider model potentials of the form

$$V = -r^{-2} f(\theta) + V_0(r) \tag{6}$$

where $V_0(r)$ is a spherically symmetric potential. The asymptotic, far wake potential has in fact this form with (ref. 1)

$$V_0(r) = 0$$

$$f(\theta) \sim M^2 a^2 \cos^{-2}\theta \exp(-M^2 \tan^2\theta) \tag{7}$$

where a is the radius of the satellite. For the discussion below the particular form of $f(\theta)$ is arbitrary, however, and may be chosen to fit potentials near the satellite.

The utility of the potential of the form in equation (6) is that a particle moving in it possesses three constants of motion. In addition to energy and the component of angular momentum about the polar axis the quantity

$$C = \frac{L^2}{2} - f(\theta) \quad , \tag{8}$$

where L is the magnitude of the angular momentum about $r = 0$, is conserved along a particle trajectory. This follows readily upon taking the scalar product of $\vec{L} = \vec{r} \times \vec{V}$ with both sides of the torque equation ($m_i = e = 1$)

$$\frac{d\vec{L}}{dt} = -\vec{r} \times \nabla V \tag{9}$$

taking account of equation (6) for V. There are fewer constants of motion than for $V = V(r)$, since in the latter case the direction of L as well as its magnitude is constant. The dynamical constant C of equation (8) is a rigorous constant for potentials of the form (6), and should not be confused with the invariants used by Samir and Jew (ref. 14) and criticized by Laframboise and Whipple (ref. 15).

The effective potential for radial motion of a particle is now given by

$$V_{eff}(r) = V_0(r) + \frac{C}{r^2}. \tag{10}$$

With this V_{eff} we can solve for the orbits and evaluate the bounds on ion current and particle densities at the satellite surface. The orbit equations are particularly tractable for the interesting case of particles which reach the poles of the sphere, especially the wake-side pole. For these particles the axial component of angular momentum is zero, the orbits are planar, and the solution of the equations of motion is reducible to quadratures.

From

$$E = \frac{1}{2} v^2 = \frac{1}{2} \dot{r}^2 + \frac{C}{r^2} + V_0(r) = \frac{1}{2} v_0^2 + V_0(a) - \frac{f(\theta_0)}{a^2} \tag{11}$$

$$C = \frac{1}{2} a^2 v_0^2 (1 - \mu_0^2) - f(\theta_0) = \frac{1}{2} r^4 \dot{\theta}^2 - f(\theta) \tag{12}$$

we obtain

$$\int_{\theta_0}^{\theta} \frac{d\theta'}{[C + f(\theta')]^{1/2}} = \pm \int_a^\infty \frac{dr}{r[Er^2 - C - r^2 V_0(r)]^{1/2}} \tag{13}$$

for the final direction θ of a particle launched from $r = a$, $\theta = \pi$ in the direction μ_0 with speed v_0. Here μ_0 is the cosine of the angle between $\vec{v}_0$ and $\vec{r}_0$.

Consider now a positive energy particle with initial coordinate $\theta_0 = \pi$. For attractive potentials, the orbits will appear as indicated in figure 1.
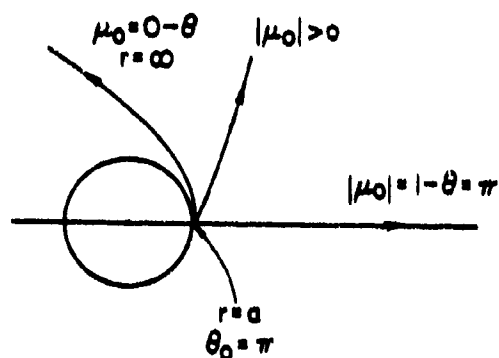
Figure 1. Schematic diagram of inside-out orbits starting on the sphere $r = a$ at $\theta_0 = \pi$.

The range of θ integration for calculating the bounds of equations (4) and (5) is generated by variations of μ_0^2 between 0 and 1. Here we have assumed that the particles are not attracted back to the surface. This affect however can only decrease the particle flux at the point of interest, and therefore does not influence the nature of equations (4) and (5) as upper bounds.

To proceed further, we now specialize to potentials of the form

$$V_0(r) = 0$$

$$\frac{f(\theta)}{a^2} = \frac{4}{3\pi^2} |V(\pi)| \left(\theta^2 - \frac{\pi^2}{4} \right), \qquad \frac{\pi}{2} \le \theta \le \pi \qquad (14)$$

$$= 0 \qquad\qquad\qquad 0 \le \theta \le \frac{\pi}{2}$$

which approximates the surface potentials given by Parks and Katz (ref. 12). The final angle at $r = \infty$ on the inside-out trajectory corresponding to $\mu_0 = 0$ is given by

$$\theta_\ell = \frac{\pi}{2} \left| \frac{3E}{V(\pi)} \right|^{1/2} \ell n \frac{\left(1 + \left| \frac{V(\pi)}{E} \right| \right)^{1/2} + 2 \left| \frac{V(\pi)}{3E} \right|^{1/2}}{1 + \left| \frac{V(\pi)}{3E} \right|^{1/2}} \qquad (15)$$

and the limiting angle for the outside-in orbit is

$$\alpha = \pi - \theta_\ell \qquad (16)$$

When the velocity distribution remote from the spacecraft is Maxwellian, j_b and n_b are given by

$$j_b = \frac{\sqrt{2}}{\pi^{1/2}} \frac{N_0}{V_0 V_T} \int_0^\infty e^{-\frac{V_0^2 + v^2}{2v_T^2}} \left(\frac{1}{2} v^2 + |V(\pi)| \right) g(v) \, dv \qquad (17)$$

$$n_b = \frac{1}{\pi^{1/2}} \frac{N_0}{V_0 V_T} \int_0^\infty e^{-\frac{V_0^2 + v^2}{2v_T^2}} \left(\frac{1}{2} v^2 + |V(\pi)| \right)^{1/2} g(v) \, dv \qquad (18)$$

where

$$g(v) = \exp[vV_o \cos\alpha(v)/v_T^2] - \exp[-vV_o/v_T^2] \qquad (19)$$

3. RESULTS

Numerical integration for the case $M = V_o/v_T = 8$, $|V(\pi)| = 15\ v_T^2$ gives for O^+ ions

$$\frac{J_b}{N_o e v_T} = 1.55 \times 10^{-10}$$

$$\frac{n_b}{N_o} = 2.64 \times 10^{-11}$$

The last ratio is to be compared with the density ratio

$$\frac{n}{N_o} = 6.22 \times 10^{-16}$$

for the case of zero electric field. Thus, although the effect of electric field may be to yield densities several orders of magnitude larger than those obtained in the neutral approximation, they remain extremely small in comparison with ambient ion densities, amounting to about $1\ m^{-3}$ for $N_o \sim 10^{11}\ m^{-3}$. By way of further contrast, the ion density ratio is also small compared with the electron density ratio

$$\frac{n_e}{N_o} \approx e^{-15} = 3.06 \times 10^{-7} .$$

Let us now calculate the effect of electric fields on the density of hydrogen ion current striking the wake side of the satellite at $\theta = \pi$. The result of this calculation is intended to throw some light upon the issue raised by Samir and Fontheim (ref. 16) in their comparison between measured current ratios $I(\phi)/I(90°)$ and those calculated from Parker's model (refs. 17,18). Parker's model is based on solutions of the Poisson equation in which ion densities are determined by particle tracking techniques. Only one species of ion is treated, however, and its mass is the mean mass of ions in the plasma. Samir and Fontheim contend that the two-to-three-order of magnitude discrepancy between measured and calculated current ratios might be removed (1) by properly treating the separate ionic components of the plasma, or (2) by considering the non-steady nature of the plasma environment. The results of our calculations, summarized in Table 1 below, indicate that proper treatment of the hydrogen component of the plasma suffices to remove the discrepancy between theory and experiment.

Several observations are in order. First, Table 1 shows that both the measured ratio r and the estimated upper bound on the ratio exceed the ratio estimated from the neutral approximation, which one may reasonably expect to be a lower bound on r. Second, the measurement at 160° should give a somewhat greater ratio than would be observed at 180°; the neutral approximation

Table 1. Comparison of Measured and Calculated Current Ratios[a]

Case[b,c]	2	3	5	6
$N(H^+)/N(0^+)$ [d]	1.28(-3)	1.07(-3)	1.40(-3)	4(-2)
$[J(180)/J(J(90)]_{N.A.}$ [e]	8.8(-6)	7.4(-6)	2.8(-6)	2.8(-4)
$Jb(180)/J(90)$ [f]	1.5(-2)	1.3(-2)	1.7(-2)	0.48
$[J(160)/J(90)]_{EXPT.}$ [g]	1.49(-2)	2(-2)	5.8(-3)	4(-2)

(a) Numbers in parentheses give power of 10 by which adjacent entries are multiplied.
(b) Case identification is the same as that in Table 2 of Reference 15.
(c) Case 1 is not considered because no value for hydrogen density was reported in Ref. 10. Case 4 is not considered because of the order uf the magnitude difference between ion densities reported in Tables 2 and 3 of Reference 10.
(d) Hydrogen ion to oxygen ion ratios are taken from the Bims measurements given in Table 3 of Reference 10.
(e) The ratio of H^+ and 0^+ currents at $180°$ and $90°$, respectively, calculated in the neutral approximation.
(f) The ratio of H^+ and 0^+ currents at $180°$ and $90°$, respectively, where jb is the bound on H^+ current calculated from equation (17) using a $V_0/V_T(H) = 2.83$.
(g) The ratio of measured currents at $160°$ and $90°$.

determines that the former would be only about 20 percent greater than the latter. Third, the measured current is well below the estimated upper bound in cases 5 and 6, slightly below it in case 2, and slightly above it in case 3.

That the measurements yield a value slightly in excess of the estimated upper bound could be attributed to the approximate nature of the potential used in the calculations, to the fact that the current probe was at a distance of about 0.5 R_0 from the surface, to uncertainties in the in situ H^+ density, or possibly to other factors. We believe nevertheless that the results in Table 1 are a strong indication that accounting for H^+, while ignoring the non-steady character of the plasma, suffices to remove the major discrepancies between measured and calculated currents incident on the wake side of the AE-C satellite.

4. SUMMARY

To determine the effect of electric fields on the wake-side ion currents, we have developed an expression for the upper bound on the current density normal to an element of surface. To be a rigorous upper bound it is required that the Jacobian $|d\Omega_0/d\Omega|$ be less than unity. Utilizing the bounding expressions it is shown for a non-self-consistent model potential that the particle and current densities of 0^+ ions at $\theta = \pi$, though substantially enhanced by electric fields over neutral approximation values, still constitute an effect that is small in comparison with the effect of spin for the case of AE-C. Finally, accounting for the effects of electric fields on the small concentrations of H^+ in the ambient plasma appear sufficient to remove the major discrepancies between measured and calculated currents on the wake side of the satellite.

The effect of a magnetic field in the absence of electric fields can only be to reduce ion currents incident on a surface, and therefore cannot account for the vehicle ground potentials observed on AE-C (ref. 12). The

combined effect of electron and magnetic fields is not considered in this paper.

For different ionospheric satellites in different environments, for example, in polar environments, the relative importance of the various physical effects may differ from that found for AE-C in the conditions we investigated. Thus for satellites subjected to fluxes of energetic auroral electrons, field enhancement of wake-side collection could be a substantial effect.

REFERENCES

1.   Al'pert, Ya. L., A. V. Gurevich and L. P. Pitaveskii: Space Physics with Artificial Satellites. Consultants Bureau, New York, 1965, pp. 186-210.

2.   Whipple, E. C.: Potentials on Surfaces in Space. Reports Progress in Physics, 44, 1981, pp. 1197-1250.

3.   Whipple, E. C.: The Equilibrium Electric Potential of a Body in the Upper Atmosphere and in Interplanetary Space. Goddard Space Flight Center Report X-615-65-296, 1965.

4.   Liu, V. C.: Ionospheric Gas Dynamics of Satellites and Diagnostic Probes. Space Science Reviews, 9, 1969, pp. 423-490.

5.   Grabowski, R. and T. Fischer: Theoretical Density Distribution of Plasma Streaming Around a Cylinder. Planetary Space Sciences, 23, 1975, pp. 287-304.

6.   Taylor, J. C.: Disturbance of a Rarefied Plasma by a Supersonic Body on the Basis of the Poisson-Vlasov Equations-I, The Heuristic Method. Planetary Space Science, 15, 1967, pp. 155-187.

7.   Parker, L. W.: Differential Charging and Sheath Asymmetry of Nonconducting Spacecraft Due to Plasma Flows. Journal of Geophys. Res., 83, 1978, pp. 4873-4876.

8.   Samir, U., M. First, E. J. Maier and B. Troy: A Comparison of the Gurevich et al. and the Liu-Jew Wake Models for Ion Flux Around a Satellite. Jour. Atmos. Terr. Phys., 37, 1975, pp. 577-586.

9.   Samir, U. and D. Widjaja: On the Significance of Including the Thermal Motion of Ions in Determining the Ion Distribution Behind a Satellite. Journal of Geophys. Res., 86, 1981, pp. 4807-4810.

10.   Samir, U., R. Gordon, L. Brace and R. Theis: The Near-Wake Structure of the Atmosphere Explorer C (AE-C) Satellite: A Parametric Investigation. Journal of Geophys. Res., 84, 1979, pp. 513-525.

11.   Samir, U., P. J. Wildman, F. Rich, H. C. Brinton and R. C. Sagalyn: About the Parametric Interplay Between Ionic Mach Number, Body-Size, and Satellite Potential in Determining the Ion Depletion in the Wake of the S3-2 Satellite. Journal of Geophys. Res., 86, 1981, pp. 11, 161-11, 166.

203

12. Parks, D. E. and I. Katz: Mechanisms That Limit Potentials On Ionospheric Satellites. To be published in J. Geophys. Res.

13. Gurevich, A. V., L. P. Pitaevskii and V. V. Smirnova: Ionospheric Aerodynamics. Space Sci. Rev., 9, 1969, p. 805.

14. Samir, U. and H. Jew: Comparison of Theory with Experiment for Electron Density Distribution in the Near Wake of an Ionospheric Satellite. J. Geophys. Res., 77, 1972, p. 6819.

15. Laframboise, J. G. and E. C. Whipple, Jr.: Comments on Paper by Uri Samir and H. Jew, 'Comparison of Theory with Experiment for Electron Density Distribution in the Near Wake of an Ionospheric Satellite.' J. Geophys. Res., 78, 1973, p. 6827.

16. Samir, U. and E. G. Fontheim: Comparison of Theory and In Situ Observations for Electron and Ion Distribution in the Near Wake of the Explorer 31 and AE-C Satellites. Planet. Space Sci., 29, 1981, p. 975.

17. Parker, L. W.: Computation of Collisionless Steady-state Plasma Flow Past a Charged Disc. NASA CR-144159, February 1976.

18. Parker, L. W.: Calculation of Sheath and Wake Structure About a Pillbox-shaped Spacecraft in a Flowing Plasma. Proc. Spacecraft Charging Technology Conference (edited by C. P. Pike and R. R. Lovell), Joint Air Force-NASA Report, AFGL-TR-77-0051 and NASA TMX-73537, p. 331, February 1977.

THREE-DIMENSIONAL CALCULATION OF SHUTTLE CHARGING IN POLAR ORBIT*

D. L. Cooke, I. Katz, M. J. Mandell, J. R. Lilley, Jr.
S-CUBED
La Jolla, California 92038

A. J. Rubin
Air Force Geophysics Laboratory
Hanscom Air Force Base, Massachusetts 01731

The charged particle environment in polar orbit can be of sufficient intensity to cause spacecraft charging. In order to gain a quantatative understanding of such effects, the Air Force is developing POLAR, a computer code which simulates in three dimensions the electrical interaction of large space vehicles with the polar ionospheric plasma. It models the physical processes of wake generation, ambient ion collection, precipitating auroral electron fluxes, and surface interactions, including secondary electron generation and backscattering, which lead to vehicle charging. These processes may be followed dynamically on a subsecond timescale so that the rapid passage through intense auroral arcs can be simulated. POLAR models the ambient plasma as isotropic Maxwellian electrons and ions (O^+, H^+), and allows for simultaneous precipitation of power-law, energetic Maxwellian, and accelerated Gaussian distributions of electrons. Magnetic field effects will be modeled in POLAR but are currently ignored.

The theoretical models and approximations employed in POLAR are discussed, including an effective process for stabilizing the Poisson-Vlasov iteration process in the short Debye length extreme. A preliminary POLAR calculation is presented which predicts the effects of measured auroral fluxes on the shuttle orbiter, and demonstrates the combination of conditions required for substantial differential charging of the orbiter.

INTRODUCTION

The charging of the space shuttle orbiter in the polar (auroral) ionosphere has been investigated by Katz and Parks (ref. 1). In that paper, the authors argue that observed precipitating electron fluxes can exceed the ram ion flux (~ 120 $\mu A/m^2$ for $n = 10^5$ cm^{-3}, $V = 8$ km/sec). This implies a possible overall current balance at a negative potential to enhance ion collection and retard electron fluxes. Both theoretical and experimental (refs. 2, 3, 4) studies have shown that as object dimensions become large with respect to the local Debye length, space charge effects will severely reduce the ion current collection compared to orbit limited theory. This leads to a "size-effect" for the potential buildup on objects subjected to auroral electron fluxes. Katz and Parks (ref. 1) have calculated, for a conducting

sphere, the equilibrium potential as a function of K, the ratio of secondary electron corrected precipitating electron flux to the secondary corrected ram ion flux. For a beam energy of 5 KeV and K = 3, a sphere radius to Debye length ratio of 10 leads to a potential of -100 volts, whereas a size ratio of 100 leads to a potential of -1300 volts.

The space shuttle is many times larger than any vehicle that has been previously flown through auroral regions. Consequently, the predicted size-effect on vehicle charging suggests that past experience will not be adequate for predicting and understanding the interactions of large objects with the auroral ionosphere.

An understanding of the charging dynamics of a real spacecraft requires more than a good probe theory. Differential charging depends on the often complex interplay of differing materials and their spatial relationships. The sunlight charging of ATS-6 (ref. 5) provides an example of how a charging surface can create electrostatic barriers that will bootstrap the entire vehicle to a highly charged state.

Thus, for a little more than a year, S-CUBED has been developing the computer code, POLAR, with the following design criteria:

- Three-dimensional
- Quasistatic
- Flexible plasma parameters including flow
- Magnetic field effects
- Complex geometries, electrical model
- Material effects
- Wake model
- Self-consistent inclusion of space charge effects
- Small (core storage)
- Fast

The preliminary version of POLAR is nearly complete. This paper will outline physical models and computational techniques, review the current program status, and present preliminary calculations of auroral charging.

POLAR

Why a three-dimensional code? Results from a 3-D code can be compared directly to satellite data during validation without the interpretational uncertainties that spring from reduced dimensional models. This benefit will ultimately carry over as POLAR becomes a design tool for structures with limited symmetry. Also, arbitrary arrangements of vehicle velocity, magnetic field, sun angle, and vehicle orientation, can only be properly modeled in three-dimensions. It can be argued that solving problems in 3-D within reasonable machine limits can compromise the accuracy of the physics, and/or result in an impractical program. With this in mind, the POLAR design philosophy dictates the limited use of particle tracking methods in favor of coordinated approximations and analytic models.

POLAR is a quasistatic code. That is, it employs implicit timestepping to follow surface charging where timescales, τ, are determined by incident currents and vehicle capacitances (10^{-3} sec $< \tau < 10^2$ sec), but assumes that the plasma environment is always in steady state. In the future, we may find

206

it necessary to include wave effects and turbulent phenomena by the use of time averaged models, diffusion rates, heating, etc.

The lower auroral ionospheric environment is summarized in Table 1. The values given in the table are considered typical, but none are fixed in POLAR where these and other parameters (such as the oxygen to hydrogen ion ratio) are variable over wide ranges. The energetic electron spectrum is currently modeled as a sum of power law, hot Maxwellian, and Gaussian distributions.

POLAR presently ignores the magnetic field; however, its inclusion is a current effort. Some of the methods under study for including magnetic effects are:

Place $\vec{v} \times \vec{B}$ potential gradient on the vehicle.
Include $\vec{B}$ in ion trajectories interior to sheaths.
Pitch angle conics for the energetic electrons (presently, isotropy is assumed).
Modification of secondary and photoelectron emission where $\vec{B}$ parallels a surface.
Modification of secondary and photoelectron surface conductivities in directions perpendicular to $\vec{B}$.

We now outline the methods used in POLAR to perform charging calculations. A calculation is broken in to the major steps listed below:

Vehicle definition.
Environment specification and computational grid construction.
Presheath and wake ion density calculation.
Initial surface charging using flux estimates.
*   Poisson and electron charge density calculation.
*   Sheath determination and particle (ions) tracking to determine:
        sheath ion densities
        ion surface currents
*   Surface charging.

After all of the above modules have been executed once, the * items are iterated upon to produce a final solution. At this stage in the development of POLAR, only negative surface potentials are allowed. Although slightly positive potentials could occur under natural charging conditions due to secondary or photoelectron emission, the ambient electrons should limit positive potentials to a few kT at most. With this constraint, electrons are considered to be repelled with densities given by the Boltzmann expression, $n_e = n_0 \exp(-qV/kT)$. The methods used to calculate the attracted ion densities are described later in this paper.

Positive potentials may also be achieved by the emission of electrons (ref. 6). The physics of electron collection in the lower ionosphere appears more complex than the collection of ions due to turbulent processes in both the emitted beams and in the ambient plasma (refs. 7, 8). Thus, spacecraft generated high positive potentials are not now considered in POLAR but will be addressed in future work.

OBJECT DEFINITION

POLAR objects are built from the same set of blocks used in NASCAP (ref. 9) with the addition of slanted thin plates and the exclusion of booms. These blocks are illustrated in figure 1. These blocks can be easily combined to construct complex objects as illustrated by our model of the shuttle orbiter, shown in figure 2. Objects are defined on a variably sized object grid

of cubic volume elements. Since POLAR must model objects moving at high ion Mach numbers, the extended ion wake is included in the computation by embedding the object space in a sliced, staggered computational grid. Figure 3 illustrates the arrangement of object, object grid, Mach vector, and computational grid. All data arrays are sliced into individual NX*NY pages at every Z mesh point, and stored on disk. During computation, POLAR will page into core only the required set of slices. Using the potential array as an example, the Poisson solver will need only two slices at a time; the sheath location algorithm, four slices; and the trajectory tracker, two slices.

Since the data structure is sliced along the $\hat{Z}$ axis, the Mach vector is constrained to have a dominant $\hat{Z}$ component. When other arrangements of Mach vector and object orientation are to be modeled, POLAR can rotate the object and Mach vector to meet this constraint, thus avoiding a redefinition of the object.

PRESHEATH AND WAKE ION DENSITIES

POLAR utilizes a sharp edged sheath approximation to divide space into presheath and sheath regions. The sheath region contains all of the significant space charge, while the presheath is a quasineutral region. The wake region is divided by the sheath edge, with the extended wake assumed to be essentially quasineutral and included with the presheath. The sheath edge is considered to be an absorption surface from which no attracted particles escape.

In the presheath-wake region, and initially for all space, the ion densities are determined by a "neutral ion approximation". This refers to the assumption of straight line trajectories as if following neutral particles. This means that the ion density in this region is calculated taking fully into account ion thermal velocities but ignoring bending of trajectories by electric or magnetic fields. This can be expressed by the following equation:

$$f_i(\vec{x}, \vec{v}) = g(\vec{x}, \hat{\Omega}) \, f_{io}(\vec{v})$$

where $f_i(\vec{x}, \vec{v})$ is the ion distribution function at a point x in space for a velocity $\vec{v}$ and $f_{io}(\vec{v})$ is the unperturbed velocity distribution function for a drifting Maxwellian (the assumed condition at an infinite distance from the vehicle). The function $g(\vec{x}, \hat{\Omega})$ has value zero if a ray starting from $\vec{x}$ going in the direction $\hat{\Omega}$ would strike the vehicle, it has value 1 otherwise. This function takes into account particles which cannot contribute to the local charge density because they run into the vehicle. The ion density is obtained by integration over velocities:

$$n_i(\vec{x}) = \int f(\vec{x}, \vec{v}) dv = \int_{\Omega} g(\vec{x}, \hat{\Omega}) \int_0^{\infty} f_{io}(\vec{v}) v^2 dv \, d\vec{\Omega}$$

208

This "neutral ion" approximation to the density is particularly simple to calculate for two reasons. First, the straight line orbits allow trajectories to be "traced" instantly, and second, the orbits, and thus shadowing factors, are independent of particle kinetic energy. For every point in space the basic algorithm finds the perimeter of each object surface in solid angle space and eliminates all orbits within the perimeter from contributing to the local phase space density. While using only discrete directions this technique has been proven fast and reasonably accurate. The major numerical approximations are the discretization of the angles and the interpolation in solid angle space of the surface perimeters. Typically the solid angle space is gridded 36 x 180 and a few extra points are added along each surface edge in order to minimize interpolation errors. Since the potential varies logarithmically with density in the quasineutral region, a factor of 2 error in this density will lead to less than kT/e error in the local potential; thus the approximation is not expected to be a source of any large error. Figure 4 is a contour plot of the neutral ion densities calculated for the shuttle orbiter with Mach velocity, $M = 6$ in an oxygen plasma. Figure 5 shows the same calculation for our favorite test object, the quasisphere.

A new "experimental" feature for POLAR is an algorithm that provides a "first order" correction for the focusing of ion trajectories by the weak presheath electric fields. This correction is based on a study by Gurevich and Pitaevskii (ref. 10) of the flow of a hypersonic plasma over a semi-infinite wall where they include electric fields in calculating the ion densities in the rarefied region (wake) behind the wall. Neutral gas densities may also be obtained analytically for this same problem. The ratio of the plasma to neutral densities, from the wall problem, is used as a correction factor to the neutral ion approximation densities calculated by POLAR.

In figure 6, we present a comparison of the corrected neutral ion density, calculated by POLAR, with electron density measurements by Murphy et al. (ref. 11). These measurements were made on STS-3 by the PDP Langmuir probe. For STS-3, the estimated range of Mach numbers was 5-8, and the estimated uncertainty in the absolute scale of electron densities was 2-5. POLAR densities were calculated at Mach numbers of 6 and 7 using the shuttle model presented in this paper. A comparison between electron and ion densities is strictly valid only when the plasma is quasineutral and the actual degree to which the wake plasma is quasineutral cannot be determined without a complete analysis; however, the deviations from quasineutrality are probably within the experimental error and numerical uncertainties. The emphasis of this comparison is placed upon the horizontal agreement which demonstrates POLAR's ability to model the wake edge using actual orientation data.

As a calculation proceeds, POLAR locates (by inspection of potentials) those regions where quasineutrality does not hold, defines the sheath to include such regions, and recalculates the ion density there by tracking particles inwards from the sheath. Once these sheath ion densities are available, they replace the neutral-ion densities in the Poisson calculation. This replacement process is currently being implemented in POLAR; the calculations presented here used only the neutral ion densities.

SURFACE CHARGING

The POLAR surface cells are the exposed squares, rectangles, and triangles that border the filled space of each individual volume element containing a piece of the object (sub units of the building blocks used in object definition).

POLAR models the accumulation and transport of charge on the vehicle using a lumped element circuit analogy. In this equivalent circuit, each surface cell and conductor represents a node of the circuit. Surface voltages are updated by implicitly timestepping a differenced approximation to the equation

$$I = C \frac{d}{dt} V(t) - \sigma V(t) \quad ,$$

where I and V are current and voltage vectors with each surface and conductor contributing a component, C is the capacitance matrix, and σ the conductance. The current vector is composed as

$$I = I_i + I_{is} + I_{ae} + I_{aes} + I_{aeb} + I_{ph}$$

where we have the current due to ions, ion impact secondary electrons, auroral electrons, auroral electron secondary and backscatter electrons, and photoelectrons. The auroral electron currents and their secondary and backscatter electron currents are determined each timestep by assuming them to be dependent only on the individual surface voltage, then integrating the model distributions with and without secondary and backscatter yield functions. The ion and ion secondary currents are updated only when the sheath module is called. Note that the ambient electrons are absent from this last equation. Because of their low temperature, they will not contribute significant current to any surface more negative than a few kT/e. When a surface charges positive, it is assumed to be because of their omission and the surface is held near zero until it again shows negative charging behavior. This technique prevents the oscillations that could occur with a combination of large timestep and an extremely voltage sensitive current source.

As mentioned previously, POLAR models the flux, ϕ, of the energetic auroral electrons as a combination of power law, hot Maxwellian and Gaussian distributions (ref. 12) given by the following expression:

$$\Phi(K) = AK(K + qV)^{-(\alpha+1)} + F \pi^{-1}(kT)^{-2} K \exp(-(K+qV)/kT)$$

$$+ BK \exp(-(K-K_0)^2/\delta^2)$$

where K is kinetic energy, V is the surface potential, $F = n \cdot \sqrt{kT/2\pi m}$, and A, α, T, B, E_0 and δ are the parameters used to fit spectra. This expression has been fitted to a spectrum observed by the DMSP-F2 satellite (ref. 13),

which is shown in figure 7, along with the POLAR fit. This analytic form can be quickly integrated to find the contributed surface current.

At the start of a ... culation, before any sheath calculations have been performed, a vehicle ... be started at a uniform voltage, or precharged by using the thermal and ram ion currents to surfaces at zero voltage for the ion currents. For this precharging, the auroral electron currents are cal- culated and the charging equations solved as described to produce an initial estimate for the surface potentials.

THE CHARGE STABILIZED POISSON ITERATION

The Poisson equation can be written as

$$-\nabla^2 \phi = \lambda^{-2}(n_i - n_e) \tag{1}$$

where $\phi = eV/kT$, $\lambda^2 = \epsilon_0 kT/N_0 e^2$, N_0 is the ambient density, and $n_i = N_i/N_0$, $n_e = N_e/N_0$. POLAR solves this equation on its dis- crete mesh using a finite element method (refs. 14, 15). It is not practical to develop it here, but we will present a few of its pertinent features.

POLAR's finite element formulation assumes a trilinear interpolation function for the potential in spaces so that the influence of each node goes to zero in one mesh unit. This allows for the development of a matrix to ap- proximate $-\nabla^2$ for each element. The finite difference approximation to the equation (1) would be

$$\left(\sum_e \underset{\sim}{w}^e\right) \phi = \lambda^{-2} (\underset{\sim}{n}_e - \underset{\sim}{n}_i) \quad h^3 \tag{2}$$

where h^3 is the volume of element e. However, rather than summing the indi- vidual matrices into one large matrix, matrix solvers can be taught to work just as efficiently on the individual element matrices. This produces many advantages. One such advantage is core storage. For a problem with 20,000 grid points, the complete matrix would require 4×10^8 words of storage if no compression methods were used, whereas, there are only a limited number of element types (six so far) requiring less than 1000 words of storage for their matrices. Another advantage is that this method very naturally allows us to solve for potentials with only one slice of elements (two slices of nodes) in core.

The traditional approach to the solution of equation (2) has been an explicit iteration of the form

$$-\nabla^2 \phi^\nu = \lambda^{-2}[n_i(\phi^{\nu-1}) - n_e(\phi^{\nu-1})] \tag{3}$$

where ν is the iteration index, and the charge density is determined using the potentials of the previous iteration. This method can be shown to be unstable

211

(ref. 16) when the Debye length, λ, becomes small with respect to other scale lengths of the problem. This can be understood by considering that a smooth potential variation over a distance of, say, 1000 λ, would require a smooth $\nabla^2\phi$ (the 'second derivative') which is in turn given everywhere by the charge density. But, maintaining a smooth charge density distribution is difficult when any errors in determining $(n_e - n_i)$ are multiplied by the huge number λ^{-2}. There is one effective remedy to this dilemma (ref. 16) but the process reported here appears to be more efficient in the short Debye length limit. This method involves the combination of two concepts. One uses a partial implicitization of the repelled density $(n_e$, here) (ref. 17). The other simply reduces the charge density to an acceptable level whenever the first method is inadequate.

Suppose a plasma of ambient density N_0 and temperature T consists of Boltzmann electrons, $N_e(\vec{r}) = N_0 \exp(\phi(\vec{r}))$ and ions of known density $N_i(\vec{r}) = N_0\, n_i(\vec{r})$. The normalized charge density is then given by

$$q(\vec{r},\phi^\nu(\vec{r})) = \lambda^{-2} [n_i(\vec{r}) - \exp(\phi^\nu(\vec{r}))] \tag{4}$$

Equation (4) may be linearized about the previous potential iterate

$$q(\phi^\nu) = q(\phi^{\nu-1}) + q'(\phi^{\nu-1}) * (\phi^\nu - \phi^{\nu-1})$$

where $q' = \partial q/\partial\phi$, and the $\vec{r}$ dependence has been dropped for clarity. With this expression we may write the implicit Poisson iteration scheme

$$-\nabla^2\phi^\nu - q'(\phi^{\nu-1}) * \phi^\nu = q(\phi^{\nu-1}) - q'(\phi^{\nu-1}) * \phi^{\nu-1} \tag{5}$$

Though it is not immediately obvious, the implicit character of (5) makes it more stable than scheme (3). This can be understood by realizing that in equation (3) the electron density was treated as an independent variable, whereas in (5) the electron density is determined simultaneously with the potential, both being consistent with the ion density.

The finite element approximation to (5) produces the matrix equation

$$\sum_e (\underset{\sim}{W}^{(e)} - \underset{\sim}{S'}^{(e)} \underset{\sim}{V}^{(e)}) * \phi^\nu = \underset{\sim}{S} - \underset{\sim}{S'} * \phi^{\nu-1} \tag{6}$$

where S is derived from q by the following analysis:

For small h/λ, S is simply the total charge associated with each node, $Q = q\, h^3$. If the elemental volume becomes large compared to λ, then numerical noise and features like a sheath edge which may span only a few λ, becomes incorrectly amplified when the q determined at a point becomes multiplied by all of h^3. When it is not possible to reduce the zone size, stability can be preserved by replacing Q (and Q') with a reduced value S (S')

which is calculated to be the maximum allowable charge for the element. Because of the artificial amplification argument, S is often the more realistic total for an element. Before deriving S, we define the barometric potential $\phi_b = \ln(n_i)$ which is the potential for which $Q = 0$ and note that it is important that $S \to Q$ as $\phi \to \phi_b$ if quasineutral regions are to be modeled correctly. To determine S, consider a capacitor with potential difference $(\phi_b - \phi)$, area h^2, and a separation of h. The charge q_c on this capacitor is given by

$$q_c = C\Delta V = \frac{\epsilon_o h^2}{he} (\phi_b - \phi)kT$$

In the units of our previous Q, q_c becomes

$$Q_M = \alpha h(\phi_b - \phi)$$

which is the maximum allowable charge per element, with the parameter α, adjusted to insure that Q_M is maximized. Thus at each node, we choose for the charge

$$|S| = \min (|Q_M|, |Q|)$$

with

$$S' = \begin{cases} -\alpha h & \text{for } S = Q_M \\ -h^3 \lambda^{-2} \exp\phi & \text{for } S = Q \end{cases}$$

The effect of this algorithm is this: If a problem has been specified where a boundary potential would be screened in less than a zone or two (the limit of any code's resolution), sufficient sheath charge will be redistributed so as to allow the potential to be screened over the minimum number of zones that are consistent with stability. When this occurs it is necessary to have a modified criteria for locating the sheath "edge". Our choice is to place the edge at $\phi_m = \ln(\alpha\lambda^2/h^2)$ (when $\phi_m > kT/e$) which is the potential at which $Q'_n = Q'$. This is the potential contour that marks the region where the most drastic charge reduction occurs.

SHEATH PARTICLE TRACKING

Internal to the sheath boundary, strong electric fields will cause significant bending of ion trajectories and focusing of currents. POLAR models these effects by tracking "particles" inward from the sheath edge to the object surface. This tracking provides both the distribution of surface currents, i.e. currents to surfaces, and the ion density within the sheath. Prior to performing this calculation, we must know the suitable sheath location and the currents from the plasma to the sheath.

The sheath edge can be thought of as an absorption surface where for the attracted species (ions, here) there is only flow in, none out. If this surface were the same for all ion energies, and there was no presheath focusing, we would find that in a non-flowing plasma, the density just outside the sheath edge to be $n_{is} = 1/2\ n_o$. We can next invoke quasineutrality with Boltzmann electrons

$$n_e = n_o\ e^{\phi_s} = n_{is} = n_o/2$$

and find for a sheath edge potential $\phi_s = -\ln 2 = -0.69$. In their treatment of space charge limited probes, Parrot et al. (ref. 18) indicate that in a non-flowing Maxwellian plasma, the sheath edge potential ϕ_s of a spherical probe asymptotically approaches the value -0.49 (-0.86 for a cylinder) as the ratio of surface potential to plasma temperature becomes infinite. For a probe in a flowing plasma, the most distended absorption surface is likely not to be an equipotential. In the ram direction, we would expect $\phi_s \rightarrow 0$, whereas in the wake direction we can conjecture that the sheath edge potential would lie in the range $1/2 > \phi_s > M^2/2$, where M is the Mach number. The degree of importance placed upon accurately locating the sheath edge must consider the resulting effects on the primary issue, surface charging. POLAR currently uses an equipotential chosen as described in the previous section. This numerically defined sheath boundary typically lies in the quasineutral region.

Ions dropped inwards from the sheath boundary are assigned currents according to the calculated presheath current to their points of origin. For the case of a non-flowing plasma, Parrot et al. (ref. 18) have determined the presheath current enhancement to be $J/J_o = 1.45$ for both spherical and cylindrical cases, where $J_o = N_o(kT/2\pi m)^{1/2}$ is the ambient thermal current. To find this enhancement for an arbitrarily specified boundary in a flowing plasma, we make the approximation that in the presheath region currents may be calculated from orbit limited theory, i.e., an outwardly directed hemisphere of trajectories will all connect to infinity if the total trajectory energy is greater than zero. For the case of a 1/r potential distribution in a non-flowing Maxwellian plasma (ref. 19), this approximation would lead to the well-known Langmuir formula

$$J = J_o\ (1 - \phi_s) = 1.49,\ \text{for } \phi_s = -0.49$$

This can be compared to the 1.45 given by Parrot et al. (ref. 18). For our flowing plasma, we assume a $1/r^2$ potential (the most rapidly diminishing for which all energetically allowed trajectories may escape) (ref. 20), and the flowing distribution at infinity

$$f_{i\infty} = N_o(2\pi)^{-3/2}\ \exp\left[-\frac{1}{2}\ (\vec{V}-\vec{M})^2\right]$$

Sheath surface current densities are determined by numerically calculating the first velocity moment of the sheath surface distribution function. Results

214

are presented in figure 8 for three sheath surface potentials. The curves for higher potential in figure 8 are consistent with the orbit limited approximation in the wake-ward direction only. Elsewhere the higher potentials would be screened more rapidly than $1/r^2$.

Return now to the question of sheath boundary placement. The results of figure 8 indicate that the current density enhancement factors are not tremendously sensitive to the sheath boundary potentials for the ram-ward angles. For wake-ward angles, there is a much greater enhancement sensitivity but this may not carry over into a surface charging sensitivity. A lower potential sheath boundary will tend to extend ellipsoidally in the wake direction producing increased sheath surface area. Focusing within the sheath/wake area will collect these lower sheath currents and reduce the sensitivity to sheath boundary placement. Also, all of these wake/sheath currents are small, and may ultimately be negligible when compared to other positive current sources such as the contribution from secondary electrons and the hydrogen component, for which the Mach speed will be a factor of 4 less than for oxygen. The paper by Parks et al. in these same proceedings investigates the effects of a hydrogen component.

In each spatial element, the sheath edge is contoured by triangular plates. From each, two or more (typically four) particles are started. Before these particles are assigned currents, a test particle is ejected outward from each plate across a few elements to probe for objects or potential barriers that would shield presheath currents from that plate. If such obstacles are formed, the particles from that plate are deleted.

Once all particles and currents have been assigned, particles are advanced along their trajectories by a "pusher". This pusher sweeps back and forth along the Z axis, operating on successive single slices of elements (two slices of nodal potentials). Within each slice, trajectories advance in the X and Y directions until they reach the present Z or Z+1 slice boundaries, X, Y boundaries or the vehicle surface. If the pusher is sweeping in the +Z direction, particles exiting at Z+1 are continued in the next push, whereas particles exiting at Z (moving in the -Z direction) are stored on disk and picked up on the return pass of the pusher. The pusher continues sweeping until all trajectories have been concluded.

RESULTS

Two model calculations are presented, the quasisphere and the shuttle. For both problems, the plasma is an O^+ plasma with $kT = 0.1$ eV, $N = 10^4$ cm^{-3} and $\lambda = 2.3$ cm. Both models have the objects moving at an ion Mach speed of 8 (~8 km/sec). Neutral ion density contour plots for these objects have been presented in figures 4 and 5. All of the contour plots are 2-D cuts through the 3-D arrays of potentials or densities. In the quasisphere (Q-S) plots, the cuts go through the center of the object and its wake. For the shuttle, the longitudinal cuts (showing a side profile of the orbiter) run just to the side of center and through one of the engines.

In these calculations, the Q-S is modeled as a grounded conductor covered with 0.1 mm thick kapton and a "quasiradius" of 2.5 m. At $t = 0$, the auroral spectrum of figure 7 is switched on, with all surfaces at zero potential. The Q-S is allowed to charge for a total of 7.8 seconds in 13 intervals

of 0.6 sec each. Ambient electron spacecharge factors and auroral electron surface currents are calculated at each step. All secondary electrons are assumed to escape. Ion surface currents are determined from sheath particle tracking at the 0.6, 2.4, 4.8 and 7.2 sec intervals, while the 0-0.6 sec interval uses the precharge estimates of ion currents. Figure 9 shows a potential contour plot with linearly spaced contours at 2.4 sec, where the maximum surface potential is -130 volts on the wake side of the Q-S. Figure 10 is a contour plot of the same potentials using logarithmically spaced contours, where the sheath contour is chosen to be -0.6 volts and is indicated by the X's. A subset of the sheath ion trajectories are also shown. Figure 11 shows linear potential contours for the Q-S at 4.8 seconds with the new sheath location (-0.6 volts) indicated again by X's; the maximum surface potential is -252 volts. The end point of the calculation is shown in figure 12 at 7.8 seconds where a rough equilibrium has been established and the maximum surface voltage is -447 volts. The apparent discharging of the side surfaces at 7.8 seconds when compared with the Q-S at 4.8 seconds is a plotting illusion due to the same number of contours being spread over a large potential difference. The long charging times reported here are not realistic and are due to the combination of grounded conductor and thin dielectric which produces a high capacitance to ground. This fixed ground has been retained as a developmental convenience and will be allowed to float in the future.

A preliminary model of shuttle orbiter charging is presented in figures 4, 13, 14, and 15. The materials specified for this model are not realistic, and again, the ground was not allowed to float. Starting with the ion densities shown in figure 4, the orbiter is exposed to the same plasma and aurora as was the Q-S with a mesh spacing of 1.16 m/grid unit. The shuttle is allowed to charge for only 3 seconds in three steps. Potential contours at the 3 second point are presented in figure 13 for the same cut as figure 5. The maximum surface potential is -101 volts. The lowest contour is at -20 volts so it is not possible to see lower space potentials in the wake, but one can observe the compression of contours on the underside compared to those in the cargo bay. Figure 14 is a cut through the ion density data at Z - 17 (see figure 13). In figures 14 and 15, the complete projected silhouette is outlined whereas only a portion of the cargo bay floor, wall and doors actually lie in this cut. Since the plasma is flowing predominantly along the length of the orbiter, the ion density wake shown in figure 14 is due to portions of the orbiter upstream of the cut. Figure 15 shows potential contours in the cut at Z - 17, where significant charging can be observed on the outside of the bay doors which lie in the wake of the wings, but not on the inside which was a grounded conductor.

The shuttle model employed 41,175 grid points, but due to POLAR's disk data management and segmented construction, only about 70,000 words of core memory were required. On our UNIVAC 1100/80, the shuttle model calculation required about 3 hours of CPU time.

CONCLUSIONS

The results of these POLAR calculations are quite preliminary and are presented primarily to demonstrate the capabilities of the code. However, we are quite pleased with the close resemblance of the quasisphere model to the DMSP charging events reported in these same proceedings by Burke and Hardy. Perhaps the most significant result of these calculations is that POLAR's

216

design criteria are proving to be realizable, and although more development will be required we anticipate that POLAR will become a useful scientific and engineering tool.

ACKNOWLEDGMENTS

REFERENCES

1. Katz, I. and D. E. Parks: Space Shuttle Orbiter Charging. J. Spacecraft and Rockets, 20, 1983, pp. 22-25.

2. Parker, L. W.: Plasmasheath-Photosheath Theory for Large High-Voltage Space Structures. Progress in Astronautics and Aeronautics, Space Systems and Their Interactions with Earth's Space Environment, 71, AIAA, New York, 1980, pp. 477-522.

3. McCoy, J. E., A. Konradi and O. K. Garriott: Current Leakage for Low Altitude Satellite. Progress in Astronautics and Aeronautics, Space Systems and Their Interactions with Earth's Space Environment, 71, AIAA, New York, 1980, pp. 477-522.

4. Cohen, H. A. et al.: P78-2 Satellite and Payload Responses to Electron Beam Operations on March 30, 1979. USAF/NASA Spacecraft Charging Technology Conference III, NASA CP-2182, AFGL-TR-81-0270, 1980, p. 509.

5. Olsen, R. C. and C. K. Purvis: Observations of Charging Dynamics. J. Geophys. Res., 88, 1983, pp. 5657.

6. Raitt, W. J., P. M. Banks, P. R. Williamson, K. D. Baker, T. Obayaski and J. L. Burch: Early Experiments in Charged Particle Beams From the Space Shuttle. Presented at AIAA 20th Aerospace Sciences Meeting, Orlando, FL, 1982.

7. Linson, L. M.: Current-Voltage Characteristics of an Electron-Emitting Satellite in the Ionosphere. J. Geophys. Res., 74, 1969, p. 2368.

8. Winkler, J. R.: The Application of Artificial Electron Beams to Magnetospheric Research. Rev. Geophys. and Space Physics, 18, 1980, pp. 659-682.

9. Katz, I., M. J. Mandell, G. W. Schnuelle, J. J. Cassidy, P. G. Steen and J. C. Roche: The Capabilities of the NASA Charging Analyzer Program. Spacecraft Charging Technology-1978, NASA CP-2071, AFGL-TR-79-0082, 1979, pp. 123-143.

10. Gurevich, A. W., L. W. Parilskaya and L. P. Pitaevskii: Self-similar Motion of Rarefied Plasma. Soviet Physics, JETP, 22, 1966.

11. Murphy, G. B., S. D. Shawhan, L. A. Frank, J. M. Grebowsky, D. L. Reasoner, N. Stone, N. D'Angelo and D. A. Gurnett: Interaction of the Space Shuttle Orbiter With the Ionospheric Plasma. Presented at 17th ESLAB Symposium, Spacecraft-Plasma Interactions and Their Influence on Field and Particle Measurements, Noordwijk, Netherlands, 1983.

12. Fontheim, E. G., K. Stasiewicz, M. O. Chandler, R. S. B. Ong, E. Gombosi and R. A. Hoffman: Statistical Study of Precipitating Electrons. J. Geophys. Res., 87, A5, 1982.

13. Hardy, D. A.: The Worst Case Charging Environment. Proceedings of Air Force Geophysics Laboratory Workshop on Natural Charging of Large Space Structures in Near Earth Polar Orbit: 14- 15 September 1982, AFGL-TR-83-0046, January 1983.

14. Stannard, P. R., M. J. Mandell and I. Katz: NASCAP Programmers Reference Manual. S-CUBED Report SSS-R-82-5443, March 1982.

15. Strang, G. and G. J. Fix: An Analysis of the Finite Element Method. Prentice-Hall, George Forsythe, ed., 1973.

16. Parker, L. W. and E. C. Sullivan: NASA Report No. NASA TN D-7409, 1974.

17. Parker, L. W.: Calculation of Sheath and Wake Structure About a Pillbox-Shaped Spacecraft in a Flowing Plasma. Proceedings of the Spacecraft Charging Technology Conference, AFGL-TR-77-0051, NASA TMX-73537, 1977.

18. Parrot, M. J. M., L. R. O. Storey, L. W. Parker and J. G. Laframboise: Theory of Cylindrical and Spherical Langmuir Probes in the Limit of Vanishing Debye Number. Phys. Fluids, 25, 1982.

19. Laframboise, J. G. and L. W. Parker: Probe Design for Orbit-Limited Current Collection. Phys. Fluids, 16, 5, pp. 629, 1973.

20. Laframboise, J. G.: Theory of Spherical and Cylindrical Langmuir Probes in a Collisionless, Maxwellian Plasma at Rest. UTIAS Report 100, 1966.

21. Al'pert, Y. L., A. V. Gurevidh and L. P. Pitaevskii: Space Physics with Artificial Satellites. Consultants Bureau, New York, 1965.

TABLE 1. - POLAR/IONOSPHERIC PARAMETERS

Orbit Altitude	150-350 km

Ambient Plasma

Temperature (eV)	0.1-0.3
Ion Density(cm^{-3})	10^4-10^6
Ion Species	O^+, N^+, He^+, H^+
Neutral Density (cm^{-3})	10^8-10^{11}

Ambient Electron Acoustic Speed	$V_{ae} = \sqrt{kT/m} = 133$ km/sec
Ambient O^+ Acoustic Speed	$V_{ao} = 1$ km/sec
Satellite Velocity	8 km/sec, $\vec{M} = \vec{V}/V_{ao} = 8$

Auroral Electrons

Energies	$\approx 10^2$-10^5 eV
Fluxes	$<10^9$/cm^2·sec·str·KeV
Integrated Currents	<100 μA/m^2

Magnetic Parameters

Magnetic Field Strength	5×10^{-5} Tesla (0.5 Gauss)

Particle	Gyroradius	Gyroperiod
Ambient Electrons	(0.1 eV) 2 cm	
Secondary Electrons	(3 eV) 13 cm	7×10^{-7} sec
Auroral Electrons	(10 KeV) 4 m	
Ambient Ions (O^+, 0.1 eV)	3 m	2×10^{-2} sec
(H^+, 0.1 eV)	0.2 m	1.3×10^{-3} sec

Cycloid Spacing Observed At 8 km/sec

Electrons	0.6 cm
H^+	10 m
O^+	160 m

Characteristic Lengths

Ambient Debye Length	$\lambda_D \leq 1$ cm	
Shuttle Orbiter	$L = 37$ m	

	1 kV	5 kV
Sheath Thickness For Potentials		
Around 3 m Radius Sphere †**	6.9 m	11.6 m
Planar Child–Langmuir †	9.32 m	31.2 m

†   Calculated for $\lambda_D = 0.74$ cm, kT = 0.1 eV
** From Figure 72, Al'pert et al. (ref. 21)
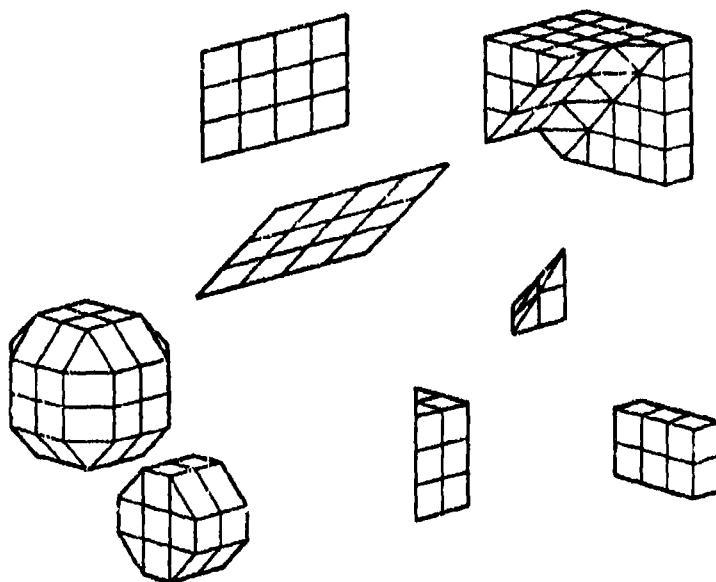
Figure 1. The eight building block types are shown here. From right to left and top to bottom: flat plate, FIL111 smoothing a corner, slanted plate, tetrahedron, quasisphere, wedge, rectangular parallelepided, and octagon right cylinder.
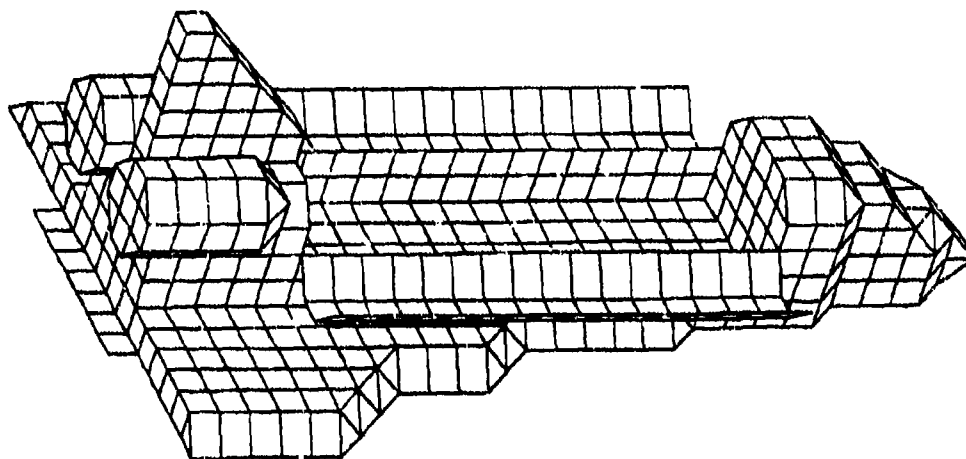
Figure 2. Perspective plot of the POLAR shuttle model used for these calculations, showing individual surface cells.
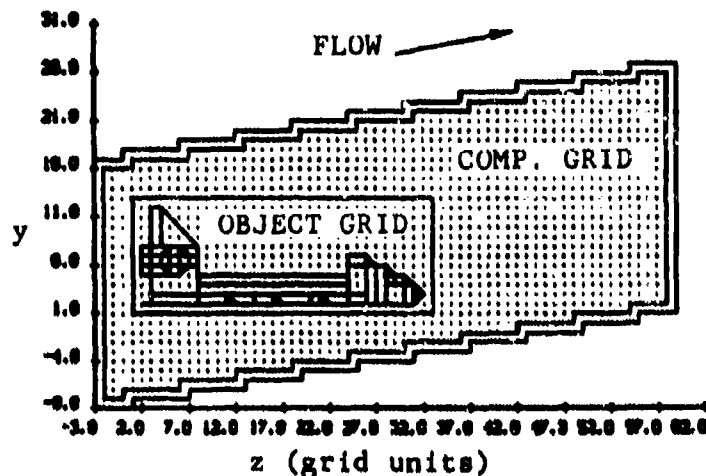
Figure 3. Two-dimensional cross-section of POLAR's computational and object grids. The combination of orthogonal transformations of the object and object grid with staggering in the X·Y node slices allows for any orientation of object and plasma flow.
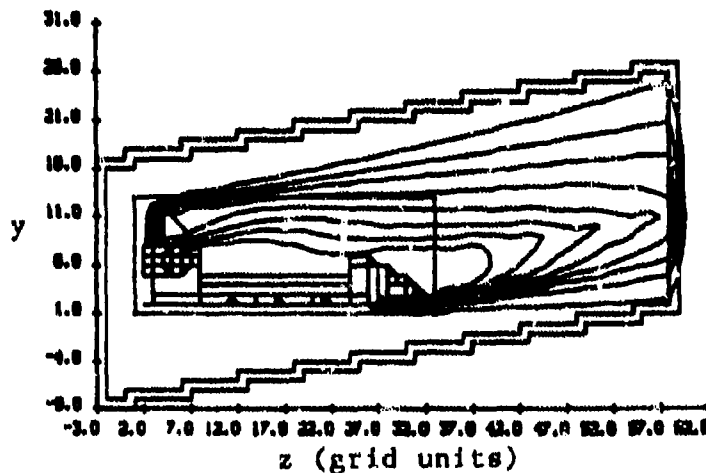
Figure 4. Two-dimensional cross-section of normalized neutral ion densities, for a slice one unit from center, running through an engine. One mesh unit = 1.16 m, ion Mach speed = 8, contour interval = 0.11, $N_0 = 10^4$ cm^{-3}, kT = 0.1 eV.
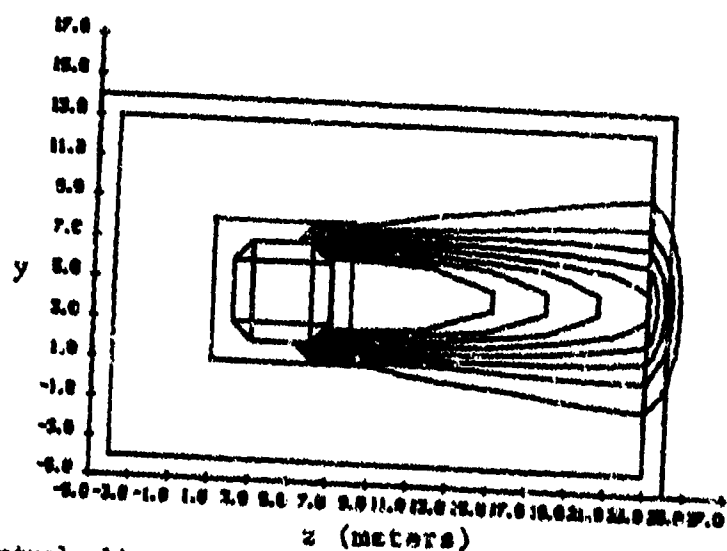
Figure 5. A central slice of ion density contours for a quasisphere. One mesh unit = 1.0 m, ion Mach speed = 8, kT = 0.1 eV, contour interval = 0.11.
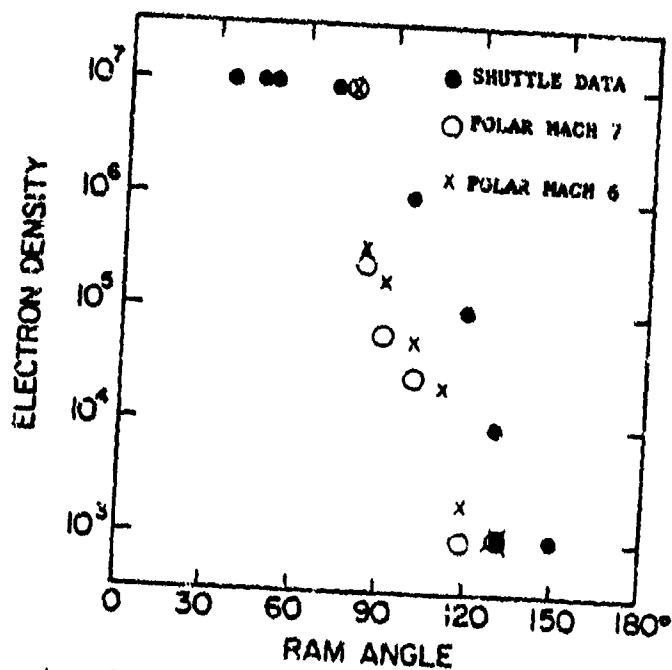
Figure 6. POLAR code calculation of shuttle cargo bay plasma densities compared with measurements made by Murphy et al. (ref. 11).
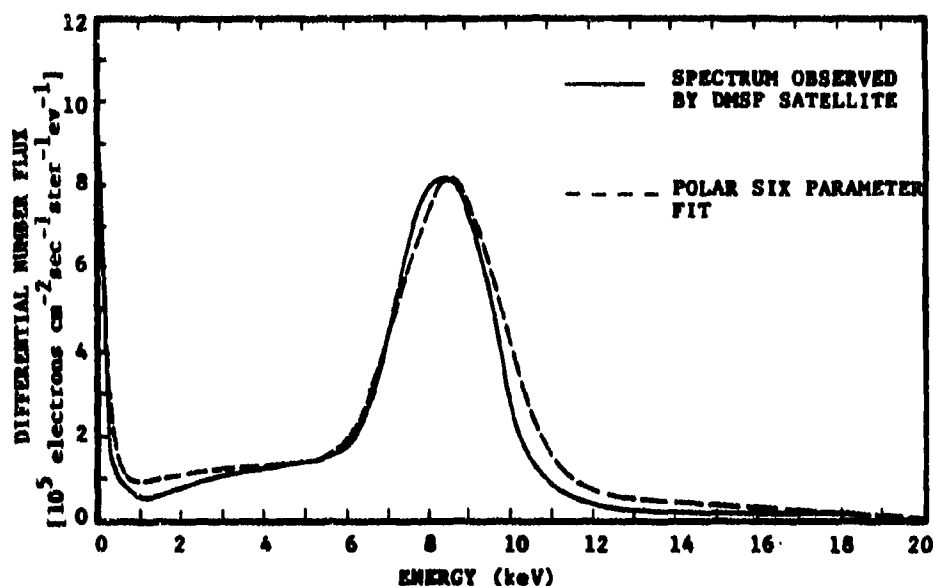
Figure 7. Fit and comparison of POLAR's analytic spectral form to an energetic electron event observed on DMSP-F2 (ref. 13). Assuming isotropy the total current carried by this spectra was 14 μA/m².
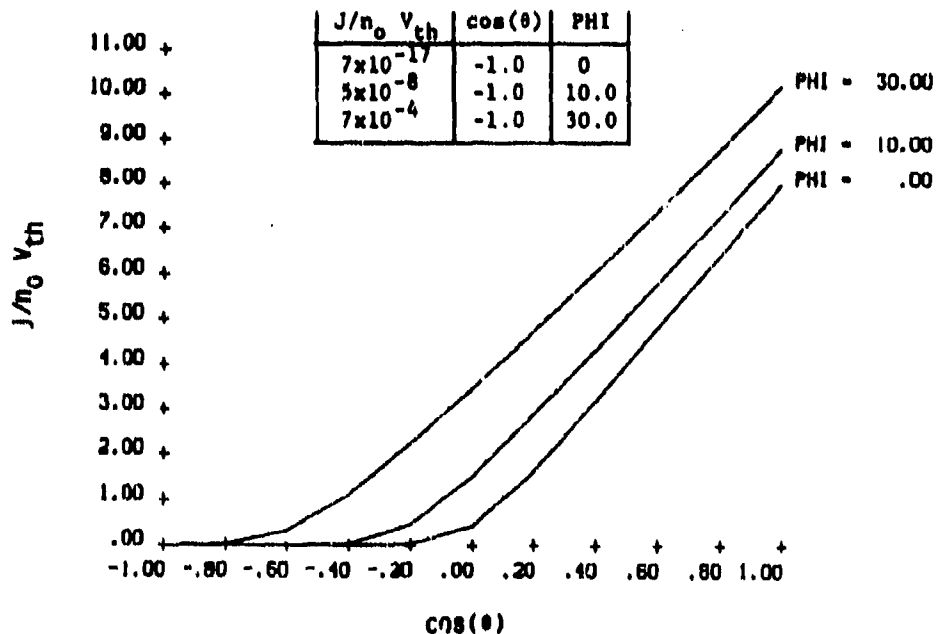
Figure 8. Current density to a sphere of potential PHI = eV/kT in a Mach 8 plasma using orbit limited theory, cos(θ) = 1.0 for ram direction, cos(θ) = -1.0 for wake direction.

223
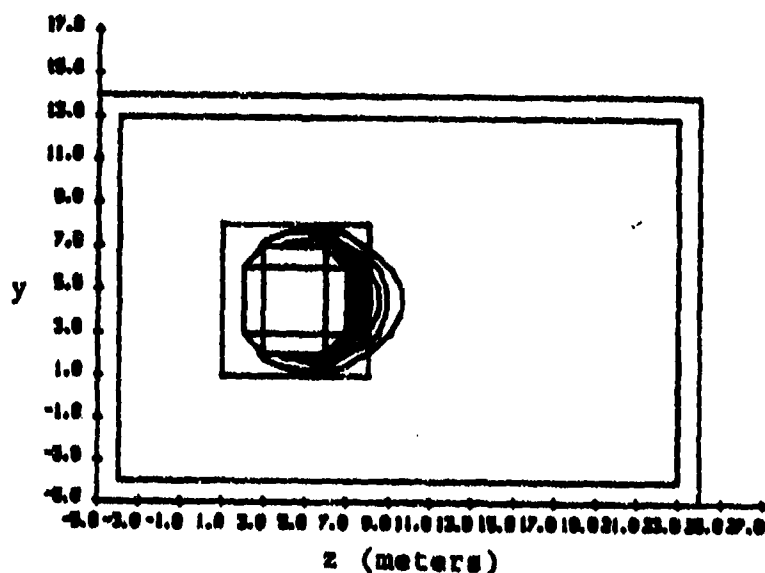
Figure 9. Contour plot of potentials for the quasisphere in the same cross-section as figure 5 after 2.4 seconds of charging. Contour intervals are 14.5 volts, and the maximum surface potential is -130.0 volts. The ambient plasma density is 10^4/cc, kT = 0.1 eV, and λ_D = 2.3 cm.
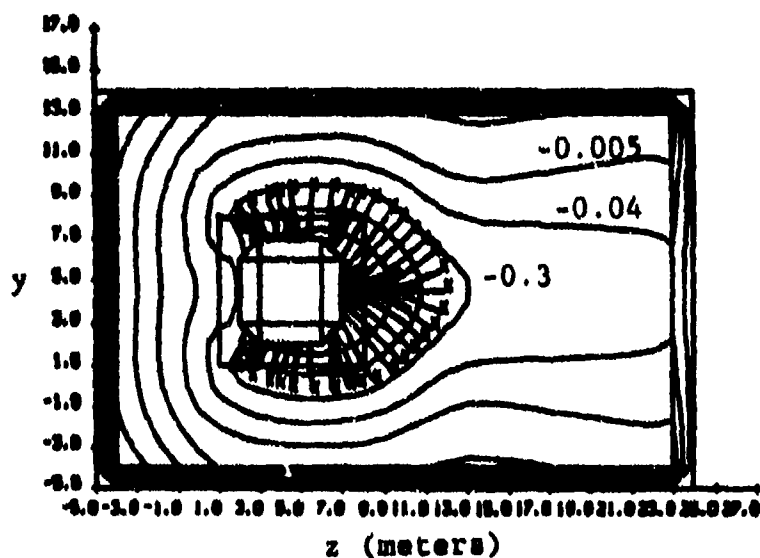
Figure 10. The same potentials and cross-section as figure 9, but with logarithmic contours. The contour interval is $\Delta\log(-V)$ = 0.87, labeled contours are in volts. The lower left tip of the x's mark the sheath location (-0.6 v), where a subset of trajectories illustrate the sheath ion tracking.
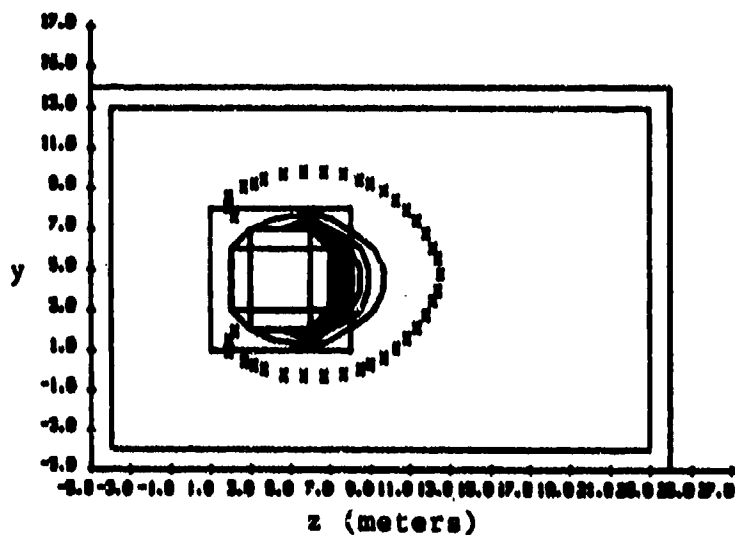
Figure 11.   Quasisphere potential contours after 4.8 secs of charging. The maximum surface potential is -252 volts, and the contour interval is 28 volts. X's again mark the -0.6 volt sheath contour.
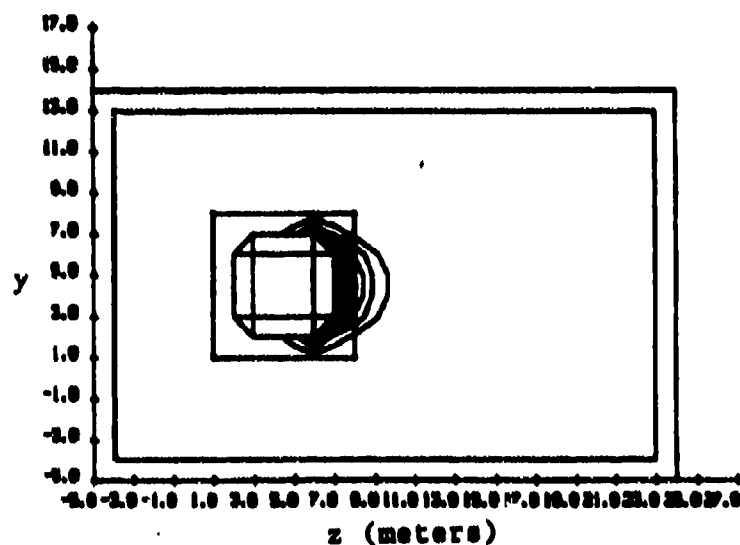
Figure 12.   Quasisphere potential contours after 7.8 secs of charging, where some surfaces have reached equilibrium. The maximum surface potential is -447 volts and the contour interval is -49.7 volts.

y

z (grid units)
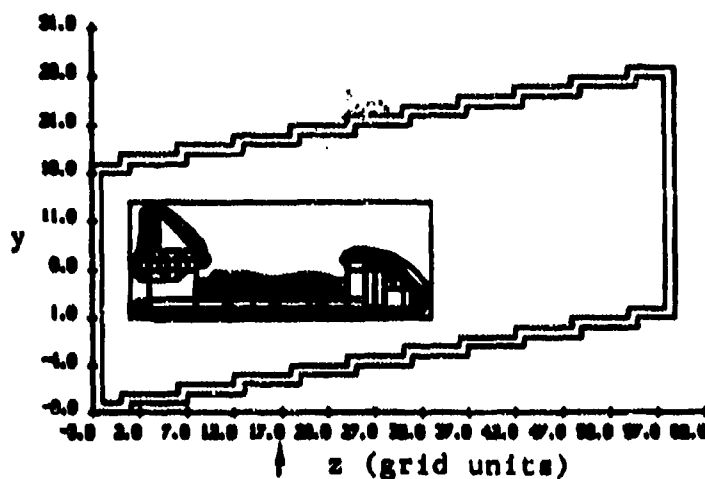
Figure 13.   Contour plot of potentials about the shuttle orbiter in the same cross-section as figure 4. The maximum surface potential in this cross-section is -101 volts, and the contour interval is 20 volts. The arrow at Z = 17 indicates the location of cross-section shown in figures 14 and 15.

y

x (grid units)
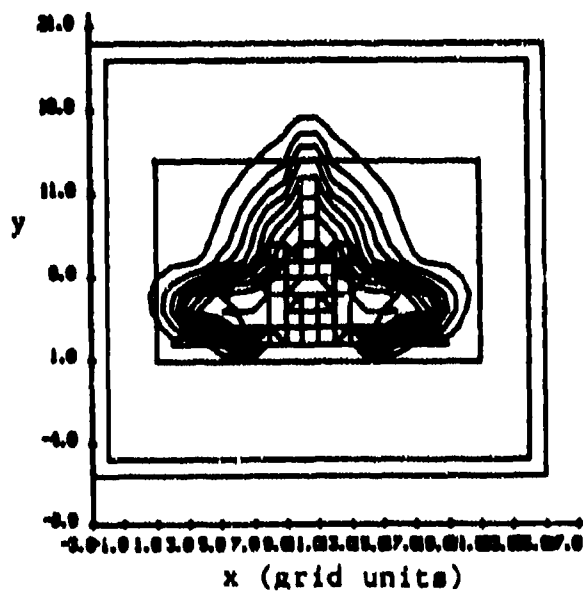
Figure 14.   Ion density contour cross-section at Z = 17 (see figure 13). The full projected sillouhette of the orbiter is shown, although only cargo bay walls, doors, and floor lie in this slice. Ion densities range from 8×10^{-7} to 1.0 in intervals of 0.11.

226
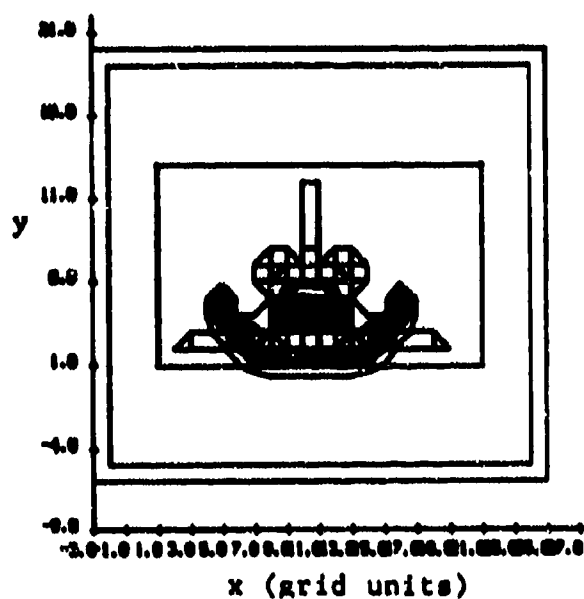
Figure 15. Shuttle potential contours in the cross-section of figure 14. The
maximum surface potential in this slice is -101 volts and the con-
tour level is 11 volts.

227

POLAR ORBIT ELECTROSTATIC CHARGING OF OBJECTS IN SHUTTLE WAKE*

I. Katz, D. E. Parks, D. L. Cooke, and M. J. Mandell
S-CUBED
La Jolla, California 92038

A. J. Rubin
Air Force Geophysics Laboratory
Hanscom Air Force Base, Massachusetts 01731

A recent survey of DMSP data has uncovered several cases where precip-
itating auroral electron fluxes are both sufficiently intense and energetic to
charge spacecraft materials such as teflon to very large potentials in the
absence of ambient ion currents. In this paper we provide analytical bounds
which show that these measured environments can cause surface potentials in
excess of several hundred volts to develop on objects in the orbiter wake for
particular vehicle orientations.

INTRODUCTION

We consider an object in the wake of a spacecraft flying at an altitude
of a few hundred kilometers in low polar earth orbit. We suppose that the
object is charged to large negative voltages with respect to the ambient
plasmas by an intense current, perhaps of order 10^{-8} amps/cm^2, of multi-
kilovolt electrons. Our objective is to estimate upper bounds on the ion cur-
rent attracted by the object, and lower bounds on its electric potential.

We assume that the plasma consists predominantly of O$^+$ at a concentra-
tion of about 10^5/cm^3 and a thermal energy per particle $kT \sim 0.1$ eV. The
speed of the satellite V_O is 8×10^5 cm/sec, corresponding to O$^+$ flow
energy $1/2 \, M_O \, V_O^2 = 5.12$ eV per particle, and a ratio $V_O/\sqrt{2 \, kT/M_O}$
$= 8$. The plasma may also contain H$^+$, again with $kT \sim 0.1$ eV, but with a
smaller Mach number, $V_O/\sqrt{2 \, kT/M_H} = 2$. In the considerations that follow
we assume that the vehicle is in eclipse and that no spacecraft generated
plasmas surround the vehicle.

The estimates are based on orbit limited theory collection by a
shadowed, ion attracting object in a cold flowing plasma. Initially, thermal
effects are not considered; it is anticipated that such neglect is justified
for high Mach number flows, especially if the negative potential on the col-
lecting object is very much larger than kT. Supposing that thermal effects
are negligible, it is then argued that the theory provides an upper bound on
collected ion current, or equivalently, a lower bound on the potential to
which the object becomes charged. Because H$^+$ ion speeds are not very much
less than flow velocities, thermal effects on H$^+$ collection will be further
considered later in the paper.

For ionospheric plasmas with negligible hydrogen concentration, ener-
getic electron currents to the wake side object can be neutralized only by
attracted O$^+$ ions. For a one meter object shadowed by a ten meter shuttle,

PRECEDING PAGE BLANK NOT FILMED

we find that the magnitude of the minimum voltage for attracting O^+ ions is about 500 volts. In contrast, space charge limited collection of O^+ ions through a ten meter radius sheath requires about 4 KeV to neutralize a current of 10^{-8} amp/cm^2 of energetic electrons.

The effect of H^+ is to lower the voltage threshold for orbit limited collection to several tens of volts, but H^+ concentrations much larger than $100/cm^3$ are required to neutralize energetic electron currents as large as 10^{-8} amps/cm^2 if potentials more negative than 100 volts with respect to the ambient plasma are to be avoided.

THEORY

Consider a sphere of radius a at a potential $-V$ shadowed by a disk of radius R_0 at a distance ℓ from the sphere center. The geometry is axisymmetric, with the symmetry axis defined by the line connecting the centers of the sphere and disk parallel to the plasma flow velocity $\vec{V}_0$.
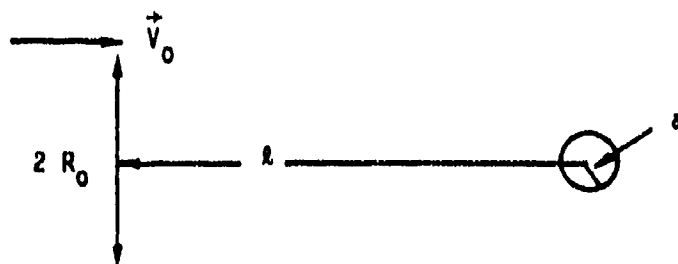
Figure 1. Geometry for ion collection.

To proceed further, we assume that the electrical potential is spherically symmetric about the center of the collecting sphere, and that the potential field is unaffected by the shield. In reality, the configuration of electric potential is much more complex, being strongly shielded by the plasma in the upstream direction and extending over substantial distances into the wake of the shield. Thus, by invoking the assumption of spherical symmetry one overestimates the upstream range of the potential and thereby the collected current.

Given the foregoing assumptions, the maximum ion current drawn by the sphere occurs when the distance between the shield and collector is infinite. Then, in accordance with orbit limited theory, which also overestimates collected currents, the current of ions of a particular species intercepted by the sphere is given by

$$I_i = \pi e \, N_i V_0 \, [b_i^2 - R_0^2] \tag{1}$$

where N_i is the density of the species i in the unperturbed plasma and the maximum impact parameter b_i is determined from

$$V_0 b_i = va \qquad \text{conservation of angular momentum} \tag{2}$$

230

$$\frac{1}{2} M_1 V_0^2 = \frac{1}{2} M_1 v^2 - eV \qquad \text{conservation of energy} \qquad (3)$$

where M_1 is the ion mass, e the electron ion charge, and v the speed of the ion at the collector. Finally the collection current is

$$I_1 = \pi e N_1 V_0 \left[\left(1 + \frac{2}{M_1 V_0^2} \frac{eV}{} \right) a^2 - R_0^2 \right] \qquad (4)$$

with a collection threshold at

$$eV = \frac{1}{2} M_1 V_0^2 \left[\frac{R_0^2}{a^2} - 1 \right] \qquad (5)$$

For a pure 0^+ plasma $(1/2 \ M_1 V_0^2 \sim 5 \ eV)$ and with $R_0/a \simeq 10$, the voltage threshold for the onset of collection occurs at about 500 volts. A current density of 10^{-8} amps/cm^2 corresponds roughly to maximum observed levels of intensity of energetic precipitating electrons (E > 1 KeV) (refs. 1-3). For $N_0 \sim 10^5$ cm^{-3}, the collected ion current is a sufficiently steep function of voltage that neutralization of the electron current of 10^{-8} amps/cm^2 occurs only slightly above the threshold.

The voltage threshold for hydrogen ion collection is $eV_H \sim 30$ volts for $R_0/a = 10$. Below 300 km altitude the H^+ concentrations are <100 cm^{-3}, and would not contribute substantially to the neutralization of electron energetic electron currents as large as 10^{-8} amps/cm^2. Instead at the 500 volt threshold for 0^+ collection, the collected H^+ current is only $I_H \simeq 2 \times 10^{-10}$ amps/cm^2 for $N_H^+ = 100$ cm^{-3}, $R_0/a \sim 10$. Thus for $H^+ \sim 100$ cm^{-3} to effectively control the charging by energetic electrons, it is necessary, but perhaps not sufficient, that the charging currents be less than 2×10^{-10} amps/cm^3. Of course, at higher altitudes where the H^+ concentrations are greater, the effect of H^+ in neutralizing charging is correspondingly greater.

The previous considerations, utilizing orbit limited theory with the shield a long distance from the collector, overestimate the collected ion current. We can also estimate the collected current with the shield at a finite distance from the collector. In this case the current is given by

$$I = \pi N \ eV_0 \left[\left(1 + \frac{2}{M_1 V_0^2} \frac{qV}{} \right) a^2 - R_\infty^2 \right] \qquad (6)$$

where R_∞ is the ambient parameter at infinite distance which causes the ion to intersect the outer edge of the shield located at the distance $R_0 = (R_0^2 + \ell^2)^{1/2}$ from the center of the collector. To relate R_∞ to the collector potential and geometry, we must know the ion's orbit in the potential field. Suppose for this purpose that the potential is given by

231

$$\phi = -V_a/r \tag{7}$$

Solving the orbit equations then leads to the relation

$$\frac{R_\infty}{a} = \frac{1}{2}\left\{ \frac{R_0}{a} + \left[\left(\frac{R_0}{a}\right)^2 + \frac{4}{M}\frac{eV}{V_0^2}\left(1 - \sqrt{1 - \left(\frac{R_0}{r_0}\right)^2}\right) \right]^{1/2} \right\} \tag{8}$$

In Table 1 we compare the voltage thresholds for ion collection for the two extreme cases $\ell = \infty$ ($r_0 = \infty$) and $\ell = 0$ ($r_0 = R_0$), obtained by setting I = 0 in equation (6).

<div align="center">

Table 1. Approximate Voltage Thresholds for Ion Collection,
$R/a = 10$, V_T (volts)

	$\ell = \infty$	$\ell = 0$
O^+	507	2000
H^+	31.7	120

</div>

Potentials decreasing more rapidly than $1/r$ for increasing r would lead to increases in the threshold voltage by even more than the factor of four given in Table 1.

We next ask whether thermal effects on H^+ collection will substantially alter our estimates of minimum potential required for current neutralization. For this purpose we neglect shadowing of the collector by the spacecraft and assume orbit limited collection of H^+ ions. The orbit limited collection by a sphere at potential $-V$ in a warm flowing plasma is given by Kanal's expression (ref. 4)

$$I = \pi a^2 \, N \, eV_0 \left[\left(1 + \frac{2}{M}\frac{kT}{V_0^2} + \frac{2}{M}\frac{eV}{V_0^2}\right) \, \mathrm{erf}\left(\sqrt{\frac{M}{2\,kT}}\, V_0\right) \right.$$

$$\left. + \frac{1}{V_0} \sqrt{\frac{2\,kT}{\pi M}} \, \exp\left(-\frac{M\,V_0^2}{2\,kT}\right) \right] \tag{9}$$

For H^+, $M\,V_0^2/2\,kT \sim 3$ and the collected current does not differ substantially from the cold plasma result

$$\frac{I}{\pi a^2} \simeq N_e \, V_0 \left(1 + \frac{2}{M}\frac{eV}{V_0^2}\right) \tag{10}$$

Thus, for V ~ 500 volts, N ~ 100 cm^{-3},

$$I/\pi a^2 \approx 1.3 \times 10^{-9} \text{ amp/cm}^2 , \tag{11}$$

and this extreme overestimate of collected H$^+$ current is still substantially less than the maximum observed charging currents.

So far, we have estimated upper bounds on selected ion current by invoking orbit limited theory. To ascertain how much the estimated bound might exceed actual current collection, let us consider space charge limited collection of O$^+$ ions by a one meter sphere through a spherically symmetric sheath of ten meter radius, the latter radius representing the radial extent of a wake. The Langmuir-Blodgett theory for space charge limited collection of O$^+$ by a sphere permits the required voltage to be estimated from (ref. 5)

$$j = 1.37 \times 10^{-8} \frac{V^{3/2}}{(\alpha a)^2} \tag{12}$$

For $j = 10^{-8}$ amp/cm^2, a $\approx$ 100 cm, and an outer emission radius of 10^3 cm, equation (12) with $\alpha^2 = 30$ gives

$$V \approx 3.6 \text{ kV} \tag{13}$$

DISCUSSION

Simple theoretical considerations have been invoked to estimate upper bounds on the ion current collected by a shadowed object subjected to intense fluxes of energetic electrons. In the course of these estimates, many complicating factors associated with geometry, vehicle potentials, field asymmetries, and charging properties of materials have been ignored. It is appropriate to ask whether any of the effects that have been neglected may substantially alter the magnitude of current drawn by an object located in the wake of an ionospheric spacecraft.

The effect of secondary emission would be to increase the effective current to the object. While secondary emission may be small for primary electron energies ~10 KeV, it may be substantial for softer components of the precipitating electron spectrum, including those reflected from the dense atmosphere.

The effect of a shuttle potential and field asymmetries is difficult to determine. One might argue that a potential on the shuttle increases its effective size and decreases current to a shadowed object; one might also argue that the fields around the shuttle focus more ions into the near wake where the object is located. The theoretical resolution of these questions will require multidimensional calculations of electric fields and ion trajectories in those fields. The required techniques will be embodied in the POLAR code, now under development at S-CUBED.

REFERENCES

1. Shuman, B. M., R. P. Vancour, M. Smiddy, N. A. Saflekos and F. J. Rich:
    Field-Aligned Current, Convective Electric Field and Auroral Particle
    Measurements During a Magnetic Storm. Jour. Geophys. Res., 86, 1981,
    p. 5561.

2. Parks, D. E. and I. Katz: Charging of a Large Object in Low Polar Earth
    Orbit. USAF/NASA Spacecraft Charging Technology Conference III,
    NASA-CP-2182, AFGL-TR-81-0270, November 1980, p. 979.

3. Katz, I. and D. E. Parks: Space Shuttle Orbiter Charging. Journ.
    Spacecraft and Rockets, 20, 1983, p. 22.

4. Kanal, M.: Theory of Current Collection of Moving Spherical Probes.
    Space Physics Research Laboratory, University of Michigan, Ann Arbor,
    MI, Sci. Rep. No. J5-5, 1962.

5. Langmuir, I. and K. B. Blodgett: Currents Limited by Space Charge
    Between Concentric Spheres. Phys. Rev., 24, 1924, p. 49.

WAKES AND DIFFERENTIAL CHARGING OF LARGE BODIES IN LOW EARTH ORBIT

Lee W. Parker
Lee W. Parker, Inc.
Concord, Massachusetts 01742

Highlights of earlier results by the author and others using the author's Inside-Out WAKE code on wake structures of LEO spacecraft are reviewed. For conducting bodies of radius large compared with the Debye length (large inverse Debye number), a high-Mach-number wake develops a negative potential well. Quasineutrality is violated in the very near wake region, and the wake is relatively "empty" for a distance downstream of about one-half of a "Mach number" of radii. There is also a suggestion of a core of high density along the axis. We report recent work on very large bodies in LEO.

A comparison of rigorous numerical solutions with in-situ wake data from the AE-C satellite suggests that the so-called "neutral approximation" for ions (straight-line trajectories, independent of fields) may be a reasonable approximation except near the center of the near wake. This approximation is adopted here for very large bodies.

In an earlier investigation of differential charging of small nonconducting bodies due to plasma flows, it was found that the scale of the voltage difference between the upstream and downstream surfaces ("front" and "wake" surfaces of a nonconducting body) due to a high-Mach-number plasma flow is governed by the ion drift energy. Hence kilovolt potential differences may occur in the solar wind, for example, between a spacecraft and a piece of insulated material in its near wake.

Recent work has concerned the "wake-point" potential of very large nonconducting bodies such as the Shuttle Orbiter. Using a cylindrical model for bodies of this size or larger in LEO (body radius up to 10^2 Debye lengths), approximate solutions are presented based on the neutral approximation(but with rigorous trajectory calculations for surface current balance). There is a negative potential well if the body is conducting, and no well if the body is nonconducting. In the latter case the wake surface itself becomes highly negative. The wake-point potential is governed by the ion drift energy.

LARGE-BODY WAKE STRUCTURE: CONDUCTING BODIES

Parker's wake-theory computer model for pillbox shapes (Inside-Out Method for warm ions - see refs. 1-3) was applied by the author and others in a number of wake calculations. High-voltage sheaths and wakes of large bodies require special numerical techniques (see refs. 3 and 12 for generalization to 3-D geometries, CLEPH code).

Wake of Moderately-Large Conducting Body in LEO

First we present highlights of earlier results obtained (1976, see refs. 1-2) in a problem involving the wake of a large body in LEO, 100 Debye lengths in radius. The body is in the form of a disk oriented normal to the flow. For two cases (figs. 1a and 1b) the parameter values are:

Case 1		Case 2

Case 1   Case 2

$\phi_0 = -4$ (dimensionless potential in units of kT/e) $\phi_0 = -4$

$\lambda_D^{-1} = 100$ (inverse Debye number = ratio of body $\lambda_D^{-1} = 100$
                                radius to Debye length)

$M = 4$ (ion Mach number) $M = 8$

This size of moving body is larger than had been treated prior to 1976 by trajectory-following, i.e., realistic, calculations. The results show what may be expected for the wake structure of large bodies in general. The problem of a large body requires more effort (computer time and judicious selection of numerical parameters) than that of a smaller body. The solutions shown, therefore, are intended to be illustrative rather than accurate. The Inside-Out Method was used (refs. 1-3).

Poisson-Vlasov iteration was applied (refs. 1,2), starting with the neutral-approximation ion density as an initial guess. A nominal number of trajectories, 512, was used at all grid points. The grid is similar to fig. 2a with z>0.

The profiles of n_i, n_e, and ϕ (dimensionless ion density, electron density and potential) are shown in figure 1a for Case 1. Tabulated values are given in reference 2. The wake is essentially "empty" of both ions and electrons between z=0 and z=1, and begins to fill up between z=2 and z=3, where z denotes the distance downstream in units of the body radius.

Two sets of ion-density profiles are shown on the left side of figure 1a, the unlabeled profiles for the final iteration, and the profiles labeled "A" for the previous iteration. Comparison of the n_e-profiles with the n_i-profiles labeled "A" (to denote that the ϕ-profiles and n_e-profiles in the figure are derived from these) indicates that the quasineutrality assumption is valid everywhere outside a cone-shaped region near the wake surface; the cone height along the axis is between one and two radii. This is in accord with expectation for a large body. Near the wake surface, however, quasineutrality is violated because the effective Debye length is large. The similarity of the n_i-profiles labeled "A" and the n_e-profiles in figure 1a is a consequence of near-quasineutrality.

Despite possible inaccuracies, one may infer certain physical conclusions from figure 1a, namely, (a) the suggestion of a core of high (approximately ambient) density of ions and electrons on the axis, and (b) the occurrence of a potential well in the near wake, defined as a region with ϕ-values below -4. The shading in the two lowest ϕ-profiles denote cross sections of this well. The wake-surface normalized fluxes are 1.1×10^{-8} ("A") and 2.4×10^{-7} (final) for ions, and 4.3×10^{-3} for electrons. The electron current density is less than $\exp(-4)$, as would be expected in the presence of a potential well.

The region of wake disturbance probably extends more than 6 radii downstream, and between 2 and 3 radii in the transverse direction.

Case 2 (fig. 1b) is similar to Case 1 except that the Mach number is increased from M=4 to M=8. The next-to-final and final-order ion densities are labeled "A" and unlabeled, respectively. On comparing these, the convergence seems fairly good at z=0.5 and z=1 radii downstream. Again, the disturbance extends beyond z=5, so that the downstream boundary should be moved further than z=6 radii downstream.

Despite possible inaccuracies, the consistency is such that physical conclusions may be drawn as follows. In this case the wake is seen to remain empty further downstream than in the M=4 case. In addition, the suggestion is much stronger that there is a central core of ambient density for both ions and electrons along the axis. Moreover, the potential well is wider and longer than in the M=4 case, although the depth is about the same. The normalized wake-surface fluxes are 7.4×10^{-30} ("A") and 4.2×10^{-30} (final) for ions, and 3.7×10^{-3} for electrons. The electron flux is slightly less than the M=4 value, and is again less than $\exp(-4)$.

The conical region behind the disk where quasineutrality breaks down is now longer than in the M=4 case, extending to between z=4 and z=5 radii along the axis.

The region of wake disturbance is probably longer than 6 radii downstream, as in the M=4 case, but may not extend beyond about 2 radii in the transverse direction.

Theory-Experiment Comparison for AE-C Satellite

Next, we note that Parker's wake theory computer model has been applied by Samir and Fontheim (ref. 4) in a comparative study of ion and electron distributions in the wakes of ionospheric satellites. From a comparison between the theory and ion measurements on the AE-C satellite, Samir and Fontheim show that theory and experiment agree fairly well in the "angle-of-attack" range between 90° and 135°. (The upstream and downstream directions are defined by 0° and 180°, respectively.) A significant finding is the fact that in that angular range even the "neutral approximation" for ions (straight-line trajectories, independent of electric fields) gives fair agreement with the measurements. (In the near-wake maximum rarefaction zone near 180°, both the neutral approximation and the self-consistent solution underestimate the measured ion densities - inferred from probe currents - by orders of magnitude. Electron data obtained by the Explorer 31 satellite also shows an underestimation near 180° by the Parker wake theory, although less pronounced.)

The largest ratio of body-radius-to-Debye-length (that is, the inverse of the Debye number) treated by Samir and Fontheim (ref. 4) is $R_D=162$, in one of the AE-C cases.

Figures 2a, b (from ref. 4) illustrate the geometry of the AE-C ion measurement, and the ion results for inverse Debye number 162. The locations of the ion current observation points, and of the numerical grid points at which densities were calculated, are shown in figure 2a. The geometry of the theoretical model is that of a pillbox cylinder with its axis parallel to the flow, while the true geometry is that of a pillbox cylinder in a "cross-flow," that is, with its axis perpendicular to the flow. In spite of this, the theory-experiment comparison is deemed by Samir and Fontheim to be meaningful, in view of uncertainties in the calculations and estimated measurement errors. (The depth in the direction of the flow is the same for both the satellite and the model, and the cross sections presented to the flow are nearly the same.) The current probe moves on a circular arc at a radial distance of about 1.5 satellite radii.

In figure 2b, the measured angular profile is shown together with the neutral approximation (zero-th iteration) and the self-consistent solution (15-th iteration). The self-consistent solution is closer to the experimental profile, in the angular range 90° - 147°, than the neutral approximation. Near 180°, the self-consistent solution is 2 to 3 orders of magnitude below the measured data, while the neutral approximation is about 10 orders of magnitude lower.

However, in their overall comparison assessment, Samir and Fontheim state that the neutral approximation describes the observed profiles more and more accurately as the inverse Debye number (ratio of body radius to Debye length) becomes large. This is justified physically based on the expectation that charge separation effects become weaker as the body size increases. This is equivalent to the setting-in of the quasineutrality regime, at sufficiently large inverse Debye numbers.

Wake of Very Large Conducting Body in LEO: Recent Results

We now treat the wake of a much larger conducting body, larger than any treated previously, In this case the self-consistent calculation becomes computationally relatively expensive. However, a reasonable approximation is afforded through the use of the "neutral approximation" for ions. That is, the ion trajectories governing ion space charge density are treated as if the ions were uncharged and unaffected by the field. The electron space charge density is assumed to be given by the "Boltzmann factor", that is, the exponential of the repulsive dimensionless potential. To some extent this approximation is supported by the Samir and Fontheim in-situ comparison discussed above. In any case it is qualitatively valuable and leads to physical insights with a minimum of computational expense. This approximation was used by Kiel et al (ref. 11). (We compute current balance later using rigorous trajectories.)

The potential distribution in the wake of a conducting satellite, in the form of a long cylinder with its axis normal to the flow, assumed to have a dimensionless potential of 3 kT/e, is shown in figures 3a, b and c, for bodies with inverse Debye numbers ranging from 10 to 10^5, and flow Mach numbers 2, 5 and 8. Figure 3a shows how the wake potential profile varies with inverse Debye number, for fixed Mach number = 8. The profiles for inverse Debye numbers 10, 10^2 and 10^3 are similar to results obtained earlier for a sphere by Kiel et al (see fig. 5 of ref. 11). The Kiel et al (ref. 11) results are for inverse Debye numbers up to 10^3. We have extended the solutions to 10^5. The wake potential profile has a negative minimum for inverse Debye numbers greater than about 10. The magnitude of the minimum is about 7, 10, 14 and 19, respectively, for inverse Debye numbers 10^2, 10^3, 10^4 and 10^5. Figure 3b shows how the wake potential profile varies with Mach number, for fixed inverse Debye number = 10^5. The depth of the potential minimum clearly increases with both increasing Mach number and inverse Debye number. Figure 3c shows equipotential contours for Mach number = 8 and inverse Debye number = 10^5.

These results would be applicable to the Shuttle Orbiter (inverse Debye number about 10^4) if it were a conducting body. However, most of its surface (about 97%) is covered with nonconducting tiles. Hence it must be treated as a large nonconducting body in LEO. The differential charging of such bodies is treated in the remainder of this paper.

WAKE STRUCTURES AND DIFFERENTIAL CHARGING OF SMALL AND LARGE NONCONDUCTING BODIES DUE TO PLASMA FLOWS

Differential Charging

Differential spacecraft charging takes place when the spacecraft surface is partly or entirely insulating and the charged-particle fluxes vary from point to point over the surface. In the familiar case of photoelectric emission from a sunlit

insulated area, due to electrons escaping from it the sunlit area tends to become positively charged relative to the surrounding dark areas (refs. 5-7). Another mechanism of differential charging, which is less familiar and appears to have been treated only very recently (ref. 8), is that due to the relative motion between a nonconducting spacecraft and the external plasma (e.g., a spacecraft in the ionosphere or in the solar wind). The fluxes of ambient ions and electrons on the wake surface are not the same as on the front surface. For high velocities of relative motion compared with the mean ion thermal velocity, whether this occurs in the ionosphere (due principally to spacecraft motion) or in the solar wind (due principally to plasma motion), there is a significant differential in the ion fluxes, but a negligible differential for the electrons. Since the net current density must vanish locally at each surface point in the steady state, this plasma-flow effect leads to a larger negative equilibrium potential on the wake surface than on the front surface. If there is photoemission as well on the front surface (as in the solar wind), this differential charging is enhanced. As shown below, this plasma-flow effect can generate differences between the front and wake surface potentials amounting to many kT/e (where T is the temperature, k is Boltzmann's constant, and e is the electron charge), together with a potential barrier for electrons. The potential difference can be expected to be of the order of volts in the ionosphere, and one kilovolt in the solar wind, that is, of the order of the ion drift energy (ref. 8).

Even weak differential charging can interfere with measurements of, say, weak ambient electric fields or low-energy particle spectra, and it can create electron potential barriers which can return emitted photoelectrons or secondary electrons to the surface and lead to erroneous interpretations of the data (ref. 9). This type of electron potential barrier is distinct from, and should not be confused with, the more familiar space-charge potential minimum which can be produced by emitted-electron space charge (ref. 10) and is not due to differential charging. The barrier produced by differential charging effects may be more important than the potential minimum caused by space charge.

The next section results show what may be expected: (a) in the ionosphere for small insulated objects, small meteroids, or small parts of a spacecraft (e.g., a painted antenna) located within the wake region of a moving spacecraft, and (b) in the solar wind for an entire spacecraft, or small natural bodies in the solar system. Following the next section, the wake structure and differential charging of very large nonconducting bodies in Low Earth Orbit will be treated.

Differential Charging of Small Nonconducting Body

In the problem treated next (see fig. 4), we assume the nonconducting spacecraft to have a "pillbox" shape, and to be in a flowing plasma, with the plasma flow along the axis, from the "front" region toward the "wake" region. The plasma is taken to be ionized hydrogen and is assumed to have a velocity of flow 4 times larger than the most probable ion thermal velocity (ion "Mach number" = 4). (In the solar wind, this Mach number would be approximately 10.) Since the unperturbed ion flux to the wake surface is about 9 orders of magnitude smaller than the corresponding ion flux to the front surface, and since the electron fluxes are about the same to the front and wake surfaces, there will be a significant differential between the equilibrium potentials at the front and wake surfaces (see below).

Using the Inside-Out Method, current densities of ions and electrons are evaluated at many points on the spacecraft surface (refs. 7-8). The local surface potentials were varied until current balance was achieved at each point.

Figure 4 shows equipotential contours around the spacecraft, obtained by numerical solution, labeled by numbers representing dimensionless values of the potential (in units of kT/e, where T is the plasma temperature, and assuming $T_i = T_e$). These potentials are obtained from Laplace's equation (space charge negligible for small bodies), where the surface potentials are obtained by the relaxation method discussed by Parker (ref. 8), under the requirement of zero net current density at all surface points. The errors in the solution shown are estimated to be under 10 percent, based on several runs giving similar answers starting from different initial guesses.

There are three regions of characteristic behavior of the potential: the "wake", the "side", and the "front". Near the "wake point," the potentials are of the order of -10 kT/e. This large negative value is associated with the reduction in ion flux due to the flow. In the side region the potentials are of the order of -3 kT/e; this is essentially the order of the equilibrium potential when there is no flow ($\sim -(kT/e)\ln(m_i/m_e)^{\frac{1}{2}}$). In the front region the potentials are of the order of -kT/e, i.e., are less negative than those on the side, because of the enhancement of the ion flux due to the flow. (Adding photoemission here would make the front potential still less negative.) The surface points are thus not equipotential. Note that there is a saddle point in the front region, that is, a potential barrier for electrons. This feature is caused by the interaction between the relatively large magnitude wake-point potentials and the relatively low magnitude front potentials. The dashed part of the contour labeled "-3.0" near the side surface indicates that there is more complicated fine structure (variation of potential along the side surface) than is shown in the figure. The potentials along the wake surface fall off toward the corner. The potentials along the front surface first fall with radius and then rise sharply as the corner is approached. This may be a "corner effect."

It is shown by Parker (ref. 7) that when the ion Mach number is large (in the ionosphere and solar wind), the potential difference ΔV generated by the flow should be of the order of $m_i v^2/2e$, or $0.0052 m_i (amu) v^2 (km/s)$ in volts, where $m_i (amu)$ and $v (km/s)$ denote the ion mass in atomic mass units and the flow velocity in kilometers per second, respectively. In the ionosphere, with oxygen ions and orbital velocities of the order of 8 km/s, ΔV is about 5 V. Hence one would expect a relatively small body in the ionosphere, such as a thin antenna or boom painted with nonconducting paint, or a painted or insulated object in the very near wake of a spacecraft (or the spacecraft surface itself if it is a dielectric) to become highly negatively charged to potentials of the order of volts in the ionosphere.

In the solar wind these results could apply to an entire spacecraft, since it is small in comparison with the Debye length. With protons and solar wind velocities of about 400 km/s or higher, ΔV is of the order of 1 kV. This means that one may have kilovolt potential differences between the wake and front surfaces. The electric fields due to this differential charging may significantly disturb measurements of space electric fields, or of low-energy plasma electrons, for example, on the Helios spacecraft (ref. 6). Moreover, because of this solar wind flow effect, small natural bodies in the solar system (i.e., bodies not large in comparison with the Debye length or ion gyroradius) may be expected to become differentially charged with potential differences of the order of 1 kV, independent of whether there is photoemission or not. Candidates for this effect include micrometeroids, dust, asteroids, the planet Pluto, and natural small satellites such as Mars' moon Deimos and Saturn's ring material when they are outside the bow shock (M. Dryer, personal communication, 1978).

For large bodies in flowing plasmas, space charge cannot be neglected. The wakes and differential charging of very large bodies are treated in the following section.

Wake Structure and Differential Charging of Very Large
Nonconducting Bodies in LEO Plasma Flows: Recent Results

There is considerable interest in the charging and electric fields of the Shuttle Orbiter. This is an important example of a very large spacecraft in Low Earth Orbit (inverse Debye number about 10^4) with most of its surface (about 97%) nonconducting. Only the small area in the vicinity of the engines is conducting and electrically grounded to the main frame. Figures 5a and 5b indicate how the Orbiter may be subjected to different types of differential charging depending on its orientation with respect to the plasma-flow direction. In figure 5a, the Orbiter is moving "nose-forward," i.e., heading into the flow. The wake-point potential (location indicated by a cross) occurs essentially in the engine area, and thus defines also the Orbiter's ground potential. The rest of the spacecraft surface is electrically isolated and has in general a different potential distribution. The cargo bay area is a "side" region according to the terminology of the previous section. In figure 5b the Orbiter is moving "belly-forward." With this orientation the wake-point potential occurs in the cargo bay area, which is electrically isolated from the Orbiter ground. The ground is defined by a different potential attained by the engine area. In the shown orientation, the engine area is a "side" region.

Hence, the maximum negative ground potential of the Orbiter would occur when the Orbiter is in the nose-forward orientation, while the cargo-bay potential would be intermediate between this and the plasma potential. With the belly-forward orientation, the roles of ground potential and cargo-bay potential would be reversed, with the cargo bay at maximum negative potential, and Orbiter ground at intermediate potential.

In the present paper the wake structure and the wake-point potential of a very large nonconducting body in LEO such as the Orbiter are calculated using certain approximations. The geometry is modeled by a circular cylinder as illustrated in figure 6. The wake point is the isolated area indicated by a cross in the figure. Again, because of computational expense, we use the neutral approximation, but only for ion space charge. However, the differential charging, e.g. the wake-point potential, is calculated rigorously by current balance using Inside-Out-Method trajectories (refs. 7-8), for both ions and electrons, in the resulting electric field distribution.

For a nonconducting body of any size, current balance at the wake point results in significant negative wake-surface potentials. (Nonconducting bodies were not treated by Kiel et al.) Figures 7a and 7b show results for inverse Debye number 10^5, and Mach numbers 2, 5 and 8. There is no potential minimum. Instead the wake point attains the highest negative potential, resulting in a monotonic rather than non-monotonic potential profile in the wake. Figure 7a shows how the wake-point potential increases with increasing Mach number, for a fixed inverse Debye number $= 10^5$. The wake-point potential magnitude is about 8, 20 and 36 kT/e, respectively, for Mach numbers 2, 5 and 8. Figure 7b shows equipotential contours for Mach number $= 8$ and inverse Debye number $= 10^5$. These contours (nonconducting body) may be compared with those of a large conducting body with the same parameters (fig. 3c).

Table 1 shows how the wake surface potential of a nonconducting large body varies with Mach number and inverse Debye number. Evidently, the wake surface potential is insensitive to inverse Debye number. The table also gives the values of the dimensionless current density (equal of course for ions and electrons) at the wake surface. For comparison, also shown are the ion currents that would result from using the neutral approximation to calculate currents (see ref. 7). These are seen

to be many orders of magnitude smaller than the more realistic currents calculated using ion trajectories affected by the field.

For large nonconducting bodies in high-Mach-number flows, the wake-to-front potential difference generated by the flow is less than but of the order of the potential-equivalent of the ion drift energy. This result is similar to that obtained above for the case of a small nonconducting body.

Finally, we illustrate in figures 8a, 8b and 8c examples of intricate 3-D large-body geometries of aerospace interest (including the Orbiter) for which a wake-modeling capability will be achieved using techniques presently under development at Lee W Parker, Inc.

REFERENCES

1. Parker, L. W.: Calculation of Sheath and Wake Structure About a Pillbox-Shaped Spacecraft in a Flowing Plasma. In Proceedings of the Spacecraft Charging Technology Conference, C. P. Pike and R. R. Lovell, eds., AFGL-TR-77-0051/ NASA TMX-73537, 1977, pp. 331-366.

2. Parker, L. W.: Computation of Collisionless Steady-State Plasma Flow Past a Charged Disk. NASA CR-144159, Lee W. Parker, Inc., Feb. 1976.

3. Parker, L. W.: Contributions to Satellite Sheath and Wake Modeling. In 17th ESLAB Symposium: Spacecraft-Plasma Interactions and Their Influence on Field and Particle Measurements, A Pedersen, ed., European Space Technology Center, Noordwijk, The Netherlands, 1983.

4. Samir, U. and Fontheim, E. G.: Comparison of Theory and In-Situ Observations for Electron and Ion Distributions in the Near Wake of the Explorer 31 and AE-C Satellites. Planet. Space Sci., vol. 29, 1981, pp. 975-987.

5. Grard, R. J. L.; Knott, K.; and Pedersen, A.: The Influence of Photoelectron and Secondary Electron Emission on Electric Field Measurements in the Magnetosphere and Solar Wind. In Photon and Particle Interactions with Surfaces in Space, R. J. L. Grard, ed., D. Reidel, Dordrecht, Netherlands, 1973, pp. 163-189.

6. Rosenbauer, H. R.: Possible Effects of Photoelectron Emission on a Low Energy Electron Experiment. In Photon and Particle Interactions with Surfaces in Space, R. J. L. Grard, ed., D. Reidel, Dordrecht, Netherlands, 1973, pp. 139-151.

7. Parker, L. W.: Potential Barriers and Asymmetric Sheaths Due to Differential Charging of Nonconducting Spacecraft. AFGL-TR-78-0045, Lee W. Parker, Inc., Jan. 1978.

8. Parker, L. W.: Differential Charging and Sheath Asymmetry of Nonconducting Spacecraft Due to Plasma Flows. J. Geophys. Res., vol. 83, 1978, pp. 4873-4876.

9. Fahleson, U.: Plasma-Vehicle Interactions in Space - Some Aspects of Present Knowledge and Future Development. In Photon and Particle Interactions with Surfaces in Space, R. J. L. Grard, ed., D. Reidel, Dordrecht, Netherlands, 1973, pp. 563-569.

10. Guernsey, R. L. and Fu, J. H. M.: Potential Distribution Surrounding a Photo-Emitting Plate in a Dilute Plasma. J. Geophys. Res., vol. 75, 1970, pp. 3193-3199.

11. Kiel, R. E.; Gey, F. C.; and Gustafson, W. A.: Electrostatic Potential Fields of an Ionospheric Satellite. AIAA J., vol. 6, 1968, pp. 690-694.

12. Parker, L. W.; Holeman, E. G.; and McCoy, J. E.: Sheath Shapes: A 3-D Generalization of the Child-Langmuir Sheath Model for Large High-Voltage Space Structures in Dense Plasmas. In Proceedings of the Air Force Geophysics Laboratory Workshop on Natural Charging of Large Space Structures in Near-Earth Polar Orbit: 14-15 September, 1982, R. C. Sagalyn, D. E. Donatelli and I, Michael, eds., AFGL-TR-83-0046, 25 January 1983, pp. 337-389.

TABLE 1. WAKE-POINT POTENTIALS OF LARGE NONCONDUCTING BODIES IN PLASMA FLOWS

ϕ_{sw} = dimensionless potential magnitude on wake surface, in units of kT/e ($\phi_s = 3$ at "side" surface)

M = Mach number

λ_D^{-1} = Inverse Debye number

J_{eo} = electron random thermal current density

J_e = electron current density (in units of J_{eo}). Rigorous trajectory analysis.

J_i = ion current density (in units of J_{eo}). Rigorous trajectory analysis.

J_{in} = neutral-approximation ion current density (in units of J_{eo})

$\sim (m_e/m_i)^{1/2} \exp(-M^2)/2M^2$ (ref. 7)

	M = 2	M = 5	M = 8
λ_D^{-1}	10 to 10^5	10 to 10^5	10 to 10^5
ϕ_{sw}	~8	~20	~40
$J_i = J_e$	~10^{-4}	~10^{-8}	~10^{-16}
J_{in}	~10^{-5}	~10^{-15}	~10^{-32}
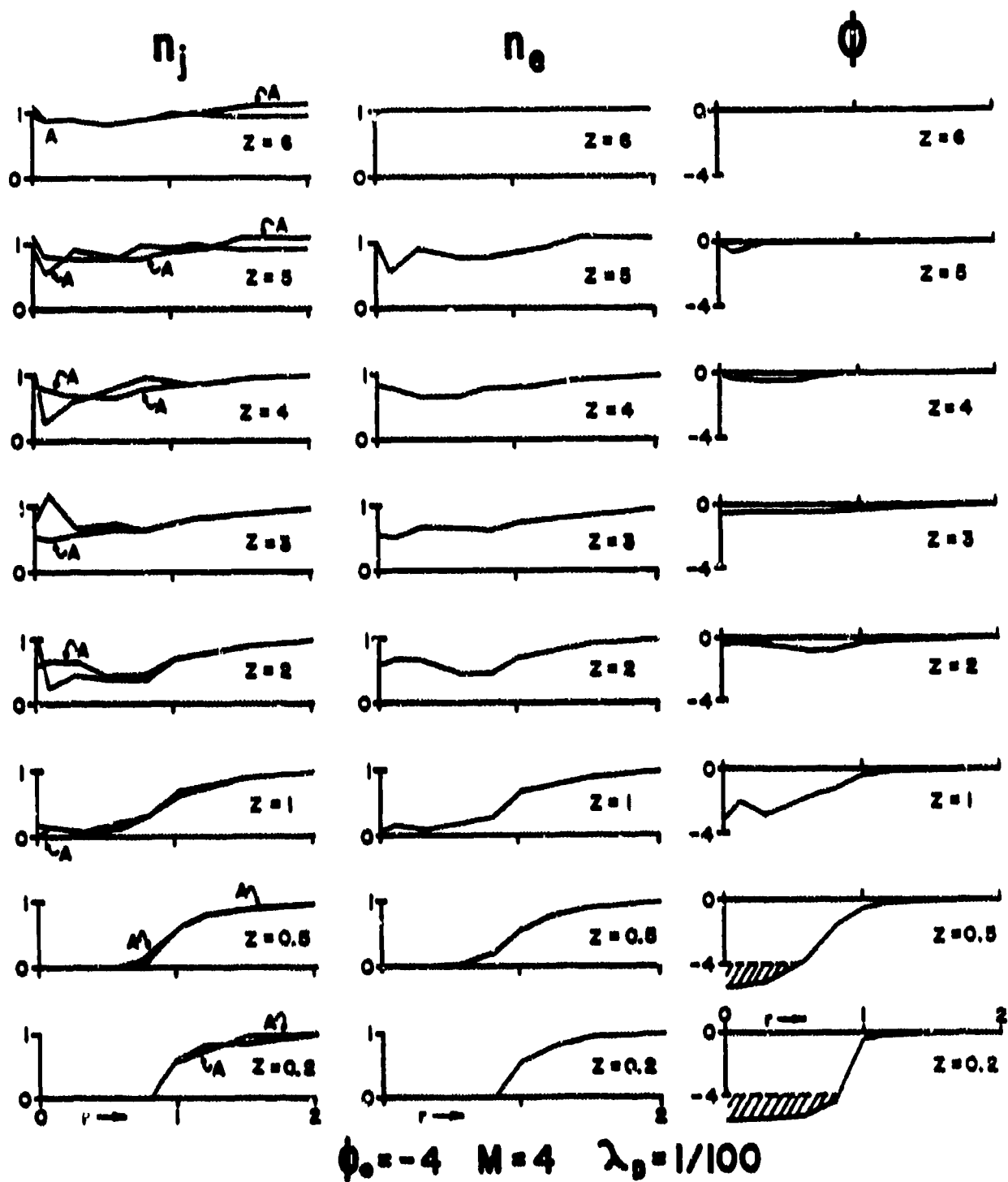
(a) M=4.

Figure 1. – Large-body wake profiles. Conducting disk with 4 kT/e surface potential.
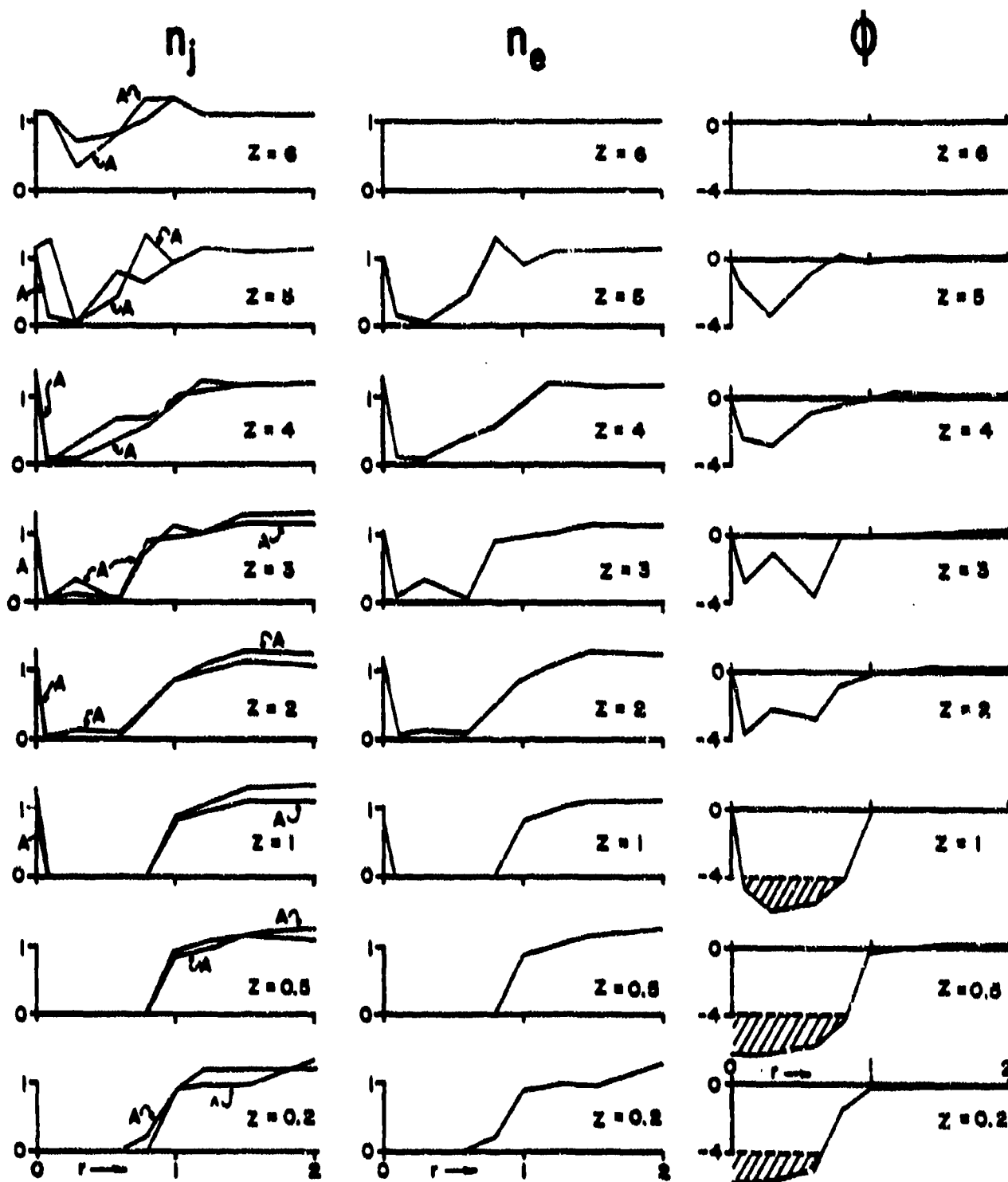
(b) M=8.

Figure 1. – Concluded.

245
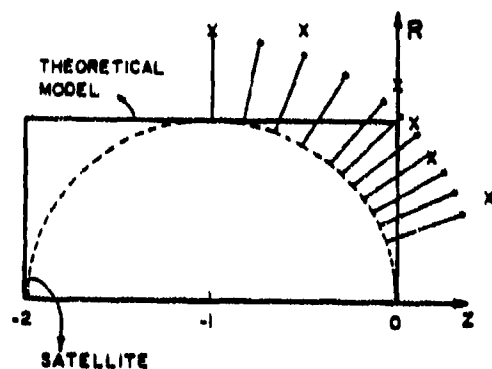
(a) Theoretical model (solid) versus real satellite geometry (dotted). (Dots denote ion current observation points; X's denote numerical grid points at which densities are calculated.)
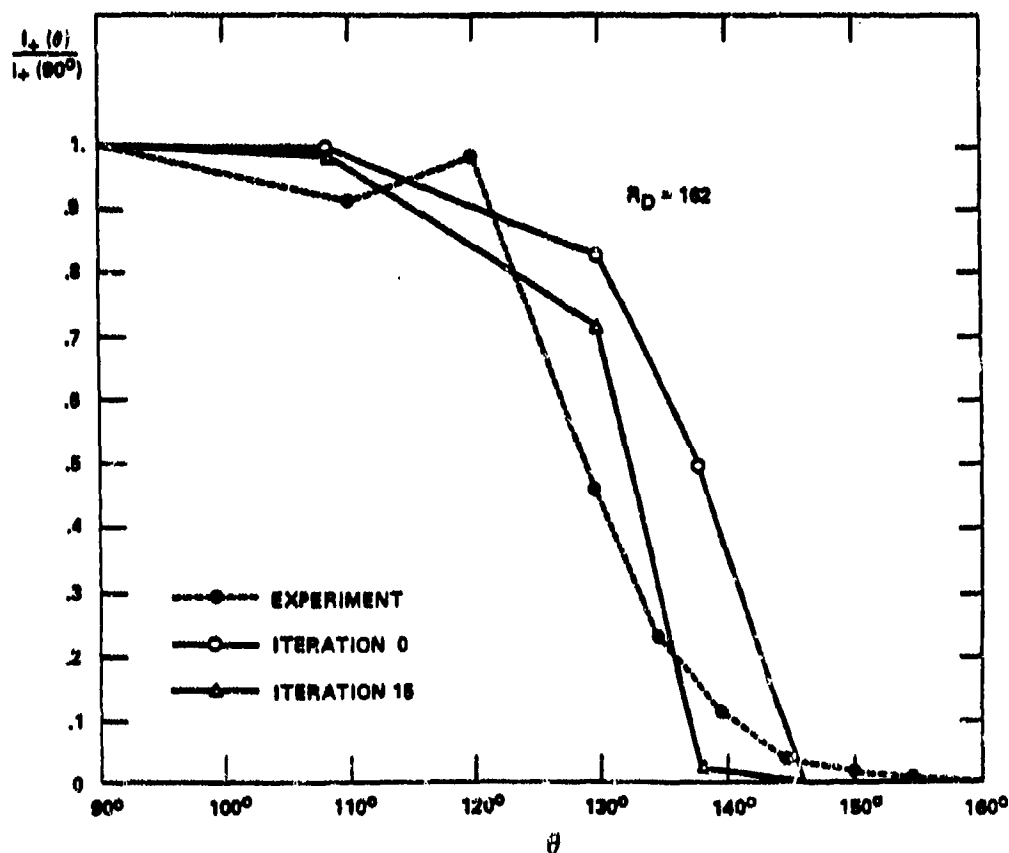
(b) Measured angular profile on AE-C satellite (large body; 162 Debye lengths) compared with neutral-approximation theory (iteration zero) and self-consistent theory (iteration 15).

Figure 2. — Geometry of AE-C ion measurements.
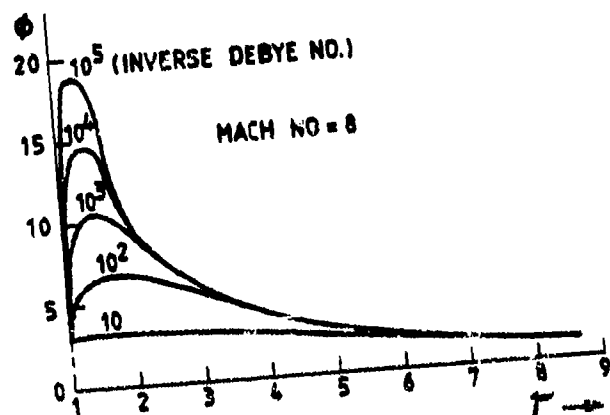
(a) Variation with inverse Debye number at fixed Mach number = 8.
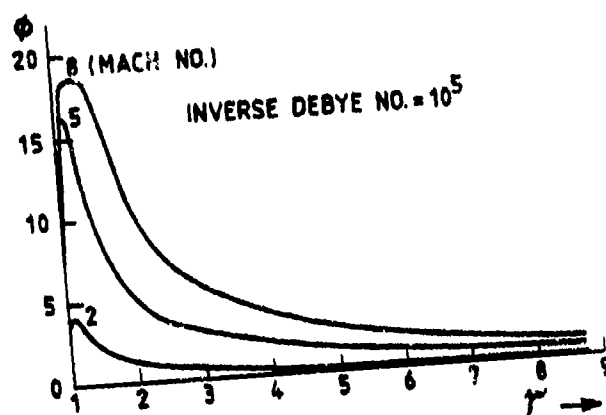
(b) Variation with Mach number, at fixed inverse Debye number = 10^5.
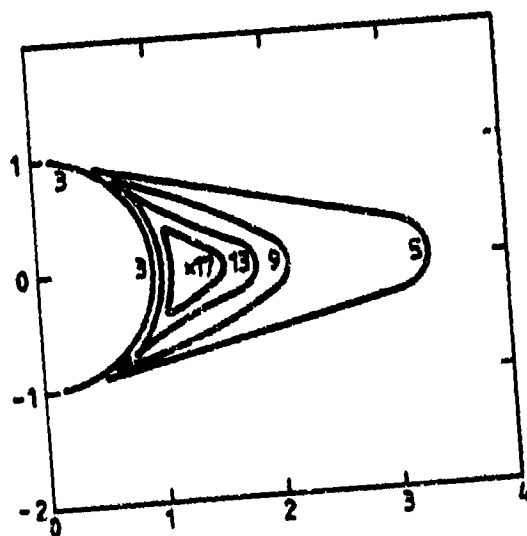
(c) Equipotential contours. Mach number = 8. Inverse Debye number = 10^5. (The point marked "x" is the position of peak potential = 19; dimensions in units of spacecraft radius.)

Figure 3. - Wake potential profiles (dimensionless potential) and equipotential contours in wake of conducting cylinder with 3 kT/e surface potential. ϕ = potential in units of kT/e; r = downstream distance in units of spacecraft radius.

247
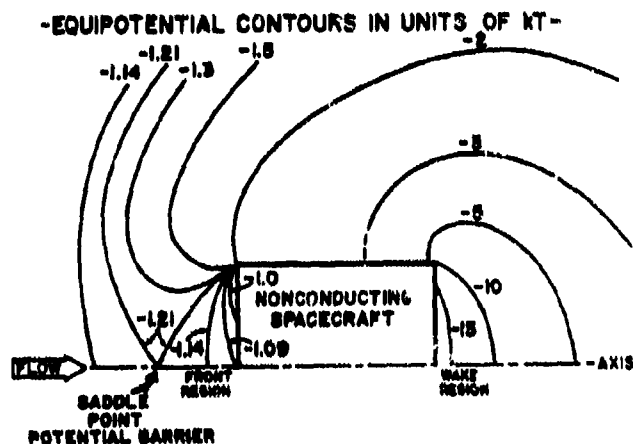
Figure 4. – Differential charging of nonconducting spacecraft in plasma flow at Mach 4. No space charge.
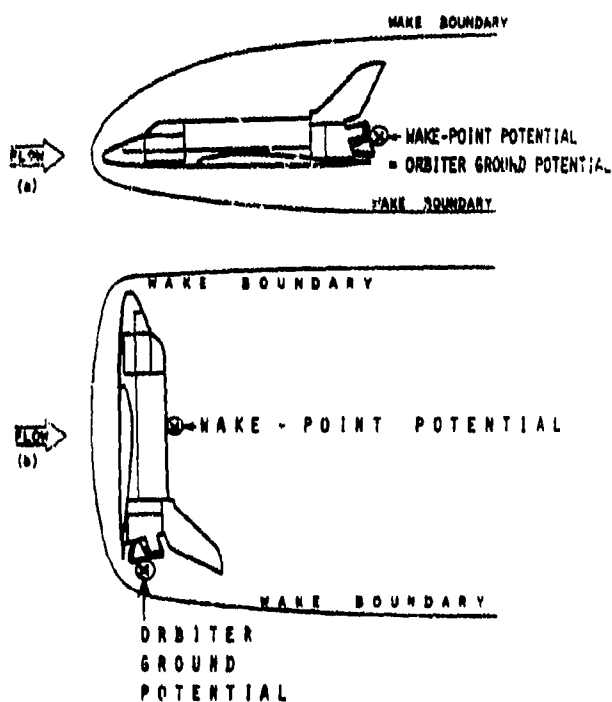
(a) Nose-forward orientation.

(b) Belly-forward orientation.

Figure 5. – Shuttle orbiter in LEO plasma flow, indicating wake points and orbiter ground potential points. Very large nonconducting body.
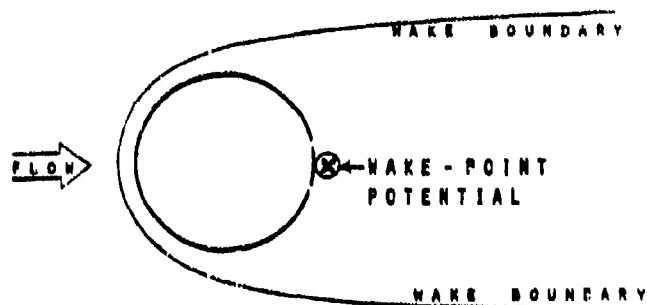
Figure 6. - Very large nonconducting cylinder model of shuttle orbiter in LEO plasma flow, indicating wake point.
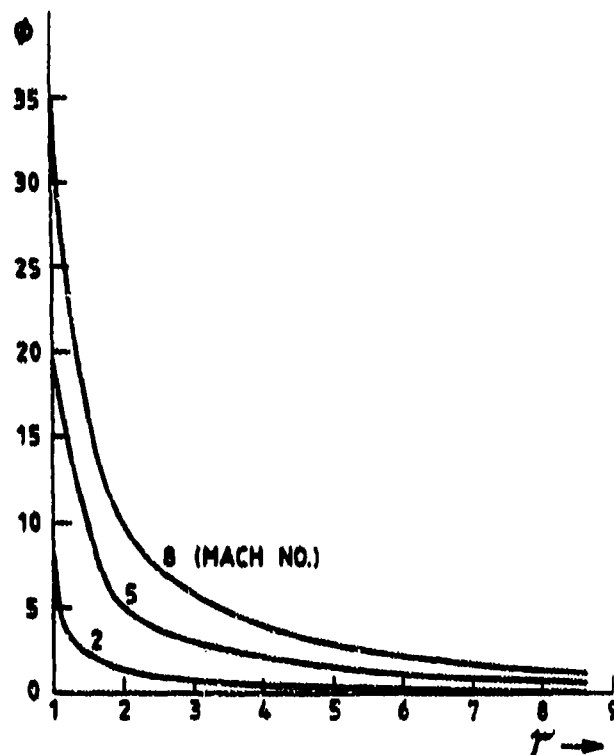
(a) Variation with Mach number at fixed inverse Debye number of 10^5.
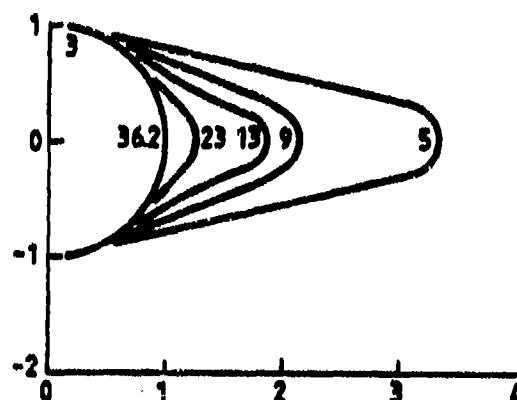
(b) Equipotential contours (dimensionless potential) in wake of nonconducting cylinder. Surface potential distribution from 3 to 36.2, in units of kT/e, determined by pointwise current balance. Mach number = 8. Inverse Debye number = 10^5. (Dimensions in units of spacecraft radius).

Figure 7. — Wake potential profiles (dimensionless potential and equipotential contours in wake of nonconducting cylinder. ϕ = potential in units of kT/e; r = downstream distance in units of spacecraft radius.
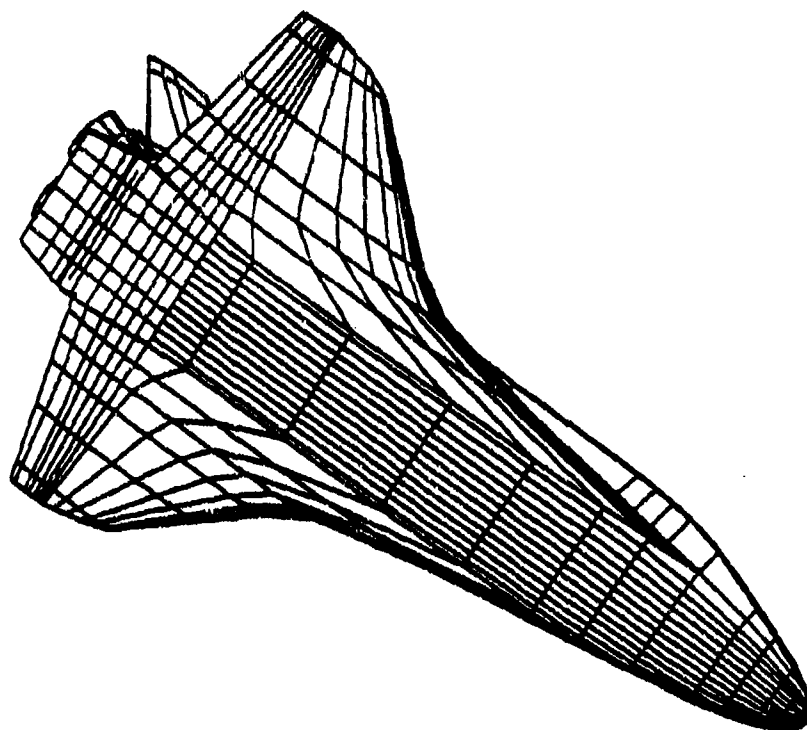
(a) Shuttle-orbiter model.
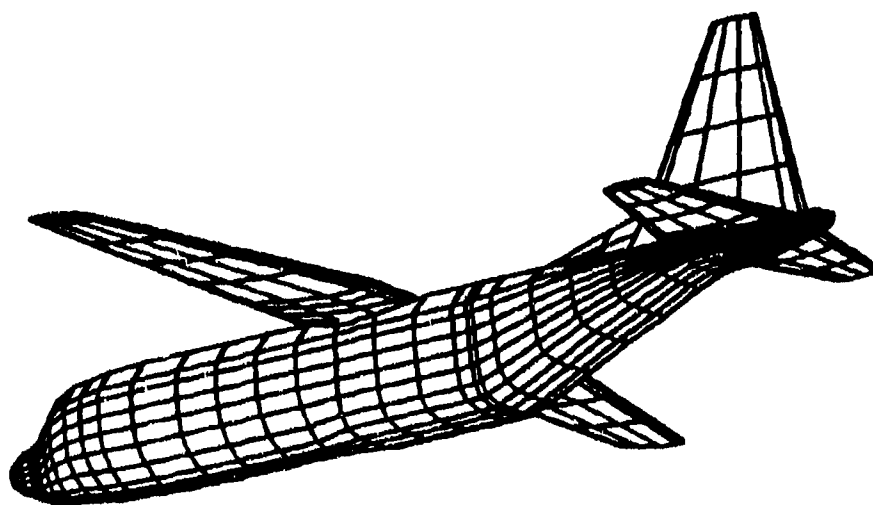
(b) C-130 Hercules aircraft model.

Figure 8. – Three-dimensional computer models constructed of quadrilateral patches.
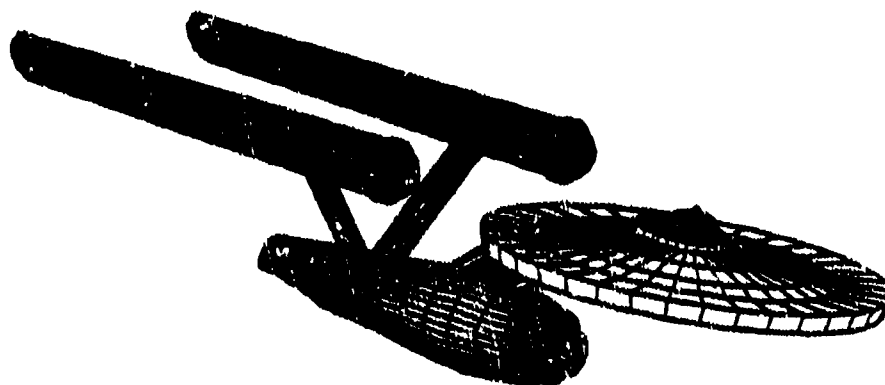
(c) Starship Enterprise model.

Figure 8. - Concluded.

SHEATH IONIZATION MODEL OF BEAM EMISSIONS FROM LARGE SPACECRAFT

S. T. Lai and H. A. Cohen
Air Force Geophysics Laboratory
Hanscom Air Force Base, Massachusetts 01731

K. H. Bhavnani and M. Tautz
Radex, Inc.
Carlisle, Massachusetts

An analytical model of the charging of a spacecraft emitting electron and
ion beams has been applied to the case of large spacecraft. In this model,
ionization occurs in the sheath due to the return current. Charge neutraliza-
tion of spherical space charge flow is examined by solving analytical equations
numerically. Parametric studies of potential of large spacecraft are performed.
As in the case of small spacecraft, the ions created in the sheath by the
returning current play a large role in determining spacecraft potential.

INTRODUCTION

The potential difference created between spacecraft ground and the ambient
plasma during the ejection of a beam of electrons from a sounding rocket pay-
load in the ionosphere (ref. 1) has been found to be much less than had origi-
nally been theoretically predicted (ref. 2). To determine the reasons for
this limited potential difference, large-vacuum-chamber tests were conducted
in which electron and ion currents were ejected from a payload into a simulated
ionosphere.

As a plausible explanation to the observed current voltage behavior,
sheath ionization models (refs. 3,4) for small spacecraft have been studied.
When an electron beam is emitted from a spacecraft, ambient electrons are
attracted by the charged spacecraft (ref. 5). They collide with the neutral
atmospheric molecules in their paths and may be energetic enough to ionize the
neutrals to form new electrons and ions (ref. 6). These newly created charges
alter the space charge current arriving at the spacecraft and shift the poten-
tial to a lower value. The beam electrons are assumed to be energetic enough
to leave the spacecraft completely and to play a negligible role in the ioniza-
tion. This mechanism is capable of explaining the nonmonotonic current-voltage
behavior observed.

In this paper, we apply the sheath ionization model to large spacecraft
in the ionosphere. In particular, it is important to find out whether the
nonmonotonic current-voltage behavior during electron beam emissions would
still be present for large spacecraft. Details of the method are given and
followed by a discussion of results.

e   electron charge

E   electric field

I_b beam current

m_e mass of electron

m_i mass of ion

n_e density of ambient electrons

n^+ density of ionization ions

n^- density of ionization electrons

P   probability of ionization

R   radius of spacecraft

r   radial position measured from center of spacecraft

r'   radial position used as integration variable

r_0 radius of sheath measured from center of spacecraft

v_e velocity of an electron in sheath

v_{th} thermal velocity of ambient electron

v_s sweep velocity

ϵ_0 permittivity of space

λ mean free path of electron neutral collision

ρ space charge density

ϕ electric potential

MATHEMATICAL FORMULATION

The method of approach used is to study an analytical "plasma probe" model (refs. 3,4,7,8), with space charge flow of electrons accelerating through the sheath surrounding a spherical "probe," which represents a spacecraft in an ionizable plasma environment. Magnetic field effect is ignored in this model.

The beam is assumed to be energetic enough to leave the spacecraft completely and is not stopped by its own space charge at all. As the beam electrons leave, the spacecraft becomes charged oppositely. A polarization region (sheath) is formed in the vicinity of the spacecraft. In our model, ions are assumed to be depleted due to charge repulsion inside the sheath (fig. 1).

The depletion radius r_0 will be defined by the balance of the outgoing beam current with the incoming ambient current. For a beam current I_b, the depletion radius r_0 is determined by

$$I_b = 4\pi r_0^2 n_e e v_{th} \tag{1}$$

where v_{th} is the thermal velocity and n_e is the number density of ambient electrons. Some typical values of sheath radius as calculated by means of equation (1) are shown in figure 2.

254

The potential ϕ at any point inside the sheath is governed by Poisson's equation:

$$\nabla^2 \phi = - \frac{\rho}{\epsilon_0} \tag{2}$$

where ρ is the space charge density and ϵ_0 is the permittivity of empty space.

Spherical Symmetric System

To simplify the geometry, we assume spherical symmetry in the spacecraft and sheath system. Equation (2) becomes simply a radial equation:

$$\frac{1}{r^2} \frac{\partial}{\partial r} \left(r^2 \frac{\phi(r)}{\partial r} \right) = - \frac{\rho(r)}{\epsilon_0} \tag{3}$$

where the gradient of the potential ϕ gives the electric field E:

$$\frac{\partial \phi(r)}{\partial r} = - E(r) \tag{4}$$

Taking into account the electron and ion pairs created as a result of ionization, the charge density ρ at any point r in the sheath is given by the sum of charge densities (fig. 3):

$$\rho(r) = e \left[n^+(r) - n^-(r) - n_e(r) \right] \tag{5}$$

where n_e is the return current (primary) electron density and n^+ and n^- are the ionization ion and electron densities, respectively, due to return current electron collisions with neutrals.

The ionization electron density $n^-(r)$ is due to all ionizations that occur outward of r, and the density $n^+(r)$ of ions at r is due to all ionizations that occur inward of r. Thus

$$n^-(r) = \frac{1}{r^2} \int_r^{r_0} \frac{\left[\frac{dn}{dt}\right]_{r'} r'^2 \, dr'}{\left[2e|\phi(r) - \phi(r')|/m_e \right]^{1/2}} \tag{6}$$

and

$$n^+(r) = \frac{1}{r^2} \int_R^r \frac{\left[\frac{dn}{dt}\right]_{r'} r'^2 \, dr'}{\left[2e|\phi(r) - \phi(r')|/m_i \right]^{1/2}} \tag{7}$$

255

where

$$\left[\frac{dn}{dt}\right]_{r'} = \lambda^{-1} P[v_e(r')] n_e(r') v_e(r') \tag{8}$$

Numerical Method

To solve the system of equations (3) to (8), one divides the space of the sheath into N concentric shells and sets up N equations for the N unknowns ϕ_i (fig. 4). In view of the complexity of the ionization terms in equations (6) and (7), it is impossible to solve these equations exactly. Instead, one seeks the approximate solutions that minimize a function F, the mean square of f_i, constructed from the radial Poisson equation (eq. (3)) for the ith cell, where $i = 1, ..., N$.

$$f_i(E_1, ..., E_N) = (r^2 E)_{i+1} - (r^2 E)_i - \frac{1}{\epsilon_0} \left[r^2 \rho(E_1, ..., E_N) \right]_i \Delta r \tag{9}$$

where the electric field E (eq. (4)) is constructed in a finite difference scheme:

$$\phi_i - \phi_{i+1} = \frac{\Delta r(E_i + 2E_{i+1} + E_{i+2})}{4} \tag{10}$$

The numerical method used to solve equations (8) to (10) is the standard Newton-Raphson method of iteration:

$$E_i^{(j+1)} = E_i^{(j)} - \frac{f_i\left[E_1^{(j)}, ..., E_N^{(j)} \right]}{\partial f_i\left[E_1^{(j)}, ..., E_N^{(j)} \right]/\partial E_i} \tag{11}$$

A set of trial solutions is used to start in the Newton-Raphson iteration process, and a convergent set of solutions is sought for each set of input parameters such as beam current, ambient electron density, ambient electron temperature, mean free path, and spacecraft radius.

RESULTS AND DISCUSSION

Figure 5 shows the computed results of spacecraft potential as a function of electron beam current for various electron densities, electron temperatures, and mean free paths. The nonmonotonic behavior of potential current curves shows up. At low currents, the potential increases with beam current. When the current increases further, ionization occurs inside the sheath. The potential then turns around as the current of the electron beam increases.

The ion and electron charges created by ionization alter the behavior of the space charge flow, originally governed by the single charged Poisson equation. The potential turns to a lower value and stays approximately constant as current further increases.

At this stage, the potential profile as a function of radial distance shows locally flat gradient. This is due to ions created inside the sheath not being able to move out quickly because of their heavy masses. If a local ion charge buildup forms a potential hump, ion motion would be two ways, and the theory would then break down.

To overcome this difficulty, a sweep velocity v_s is added to the ions. Equation (7) becomes

$$n^+(r) = \frac{1}{r^2} \int_R^r \frac{\left[\frac{dn}{dt}\right]_{r'} r'^2 \, dr'}{[2e|\phi(r) - \phi(r')|/m_i + v_s^2]^{1/2}} \tag{12}$$

It is argued that the motion of a spacecraft relative to its plasma environment can provide such a sweep velocity v_s (eq. (12)). The value of v_s is of the order of spacecraft velocity and is an arbitrary input to the computation. However, at a higher current, a potential hump again shows up, and the computation fails to converge. The technique breaks down. It is conjectured that two-way space charge flows should be accommodated when a potential hump appears.

For increasing spacecraft radii, the nonmonotonic current-voltage behavior still persists (fig. 6). However, increased spacecraft radius lowers the maximum spacecraft potential induced by beam emission. Also, the amplitude of the difference between the maximum potential and the minimum (beyond the turnaround) diminishes. Figure 7 shows a plot of the envelope of maximum and minimum potentials for various spacecraft radii.

For a given beam current I_b (eq. (1)), the sheath surface area remains constant and is unaffected by the increase in spacecraft radius. The sheath thickness (defined as the sheath radius minus the spacecraft radius), however, diminishes. As a result, a lower spacecraft potential is sufficient to attract ambient electrons, through the sheath, for the compensation of electron beam current leaving the spacecraft.

Beyond the turnaround point in a current-potential curve, the minimum potential is limited by the minimum energy required to ionize a neutral molecule in the atmosphere. Since such a minimum energy is generally of the order of 20 eV (ref. 6), the minimum potential in a current-potential curve is expected to approach about 20 eV asymptotically, depending on the model of ionization used. For the same reason, if the maximum potential induced by beam emissions is below about 20 eV, no nonmonotonic behavior is expected.

Figure 7 shows the calculated envelopes of the maximum and minimum (beyond turnaround) potentials for various spacecraft radii in a given ambient environment. The amount of ionization becomes very small as the sheath potential approaches the minimum ionization potential. The amplitude of the potential drop beyond the turnaround also approaches the value of minimum ionization energy.

There is another critical beam current, which manifests itself for large spacecraft, but not for small ones. This current is determined by equating the sheath radius to the spacecraft radius. If the sheath radius is too small,

257

the spacecraft will receive enough ambient electrons to compensate beam emissions without being charged so the potential of the spacecraft is that of natural charging, in this case. Beyond this critical current, the beam emission is able to swing the spacecraft to an opposite potential and hence control the charging of the spacecraft. This phenomenon shows up in the calculations (fig. 6).

In the model studied, as the radius of a spacecraft increases, three regimes of physical behavior can be identified. Figure 8 shows these regimes clearly. The potential-versus-spacecraft-radius curve is relatively flat in the small-radius regime. This is the regime in which saturated ionization occurs (i.e., this is the regime beyond the minimum potential in a current-voltage curve). The second regime is characterized by the presence of the potential maximum, which is the main feature of nonmonotonic behavior. The third regime occurs when the spacecraft is so large that its radius exceeds the sheath radius (measured from the spacecraft center) for a given current. The beam loses its control of the spacecraft potential and natural charging dominates.

REFERENCES

1. O'Neil, R. R.; Bien, F.; Burt, D.; Sandock, J. A.; and Stair, A. T., Jr.,: Summarized Results of the Artificial Auroral Experiment PRECEDE. J. Geophys. Res., vol. 83, no. A7, p. 3273, 1978.

2. Parker, L. W.; and Murphy, B. L.: Potential Buildup on an Electron-Emitting Ionospheric Satellite. J. Geophys. Res., vol. 72, p. 1631, 1967.

3. Leadon, R. E.; Woods, A. J.; Wenaas, E. P.; and Klein, H. H.: Analytical Investigation of Emitting Probes in an Ionized Plasma. AFGL-TR-81-0138. 1981. (ADA104166).

4. Cohen, H. A.; Lai, S. T.; McNeil, W. J.; Wenaas, E. P.; and Leadon R. E.: Spacecraft Charging with Beam Emissions in an Ionizable Environment. EOS, vol. 64, no. 18, p. 301, 1983.

5. Beard, D. B.; and Johnson, F. S.: Ionospheric Limitations on Attainable Satellite Potential. J. Geophys. Res., vol. 66, pp. 4113-4122, 1961.

6. Rapp, D.; and Englander-Golden, P.: Total Cross-Sections for Ionization and Attachment by Electron Impact in Gases. J. Chem. Phys., vol. 43, p. 1464, 1965.

7. Chen, F. F.: Electric Probes. Plasma Diagnostic Techniques, R. H. Huddleston and S. L. Leonard, eds., Academic Press, 1965.

8. Lam, S. H.: Unified Theory of the Langmuir Probe in a Collisionless Plasma. Phys. Fluids, vol. 8, no. 1, p. 73, 1965.
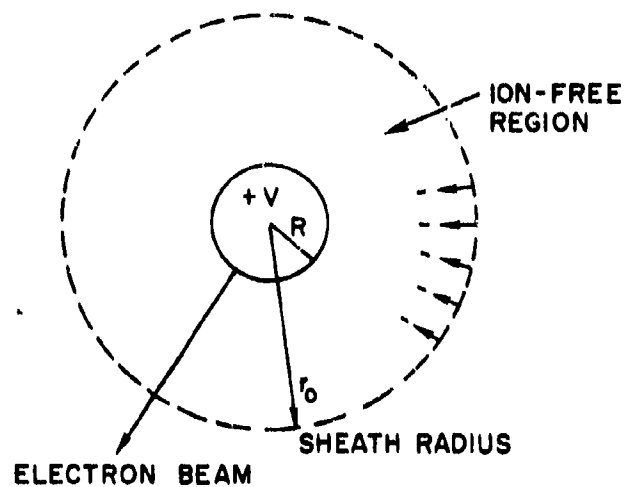
Figure 1. – Sheath formation during beam emission.

ELECTRON TEMPERATURE = 0.1 eV
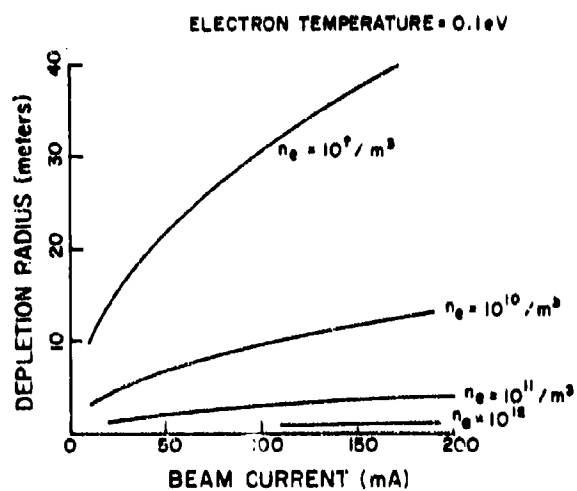
Figure 2. – Parametric dependence of sheath size.
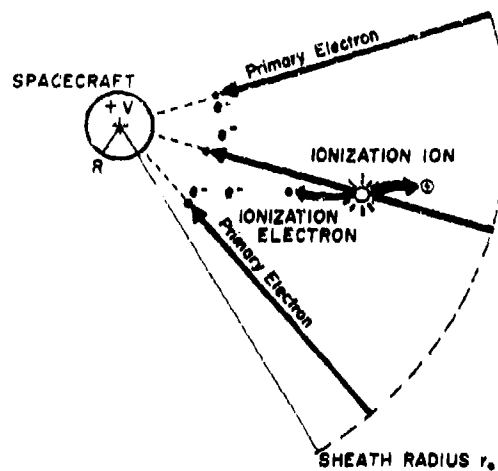
Figure 3. — Ionization pair — creation in sheath.
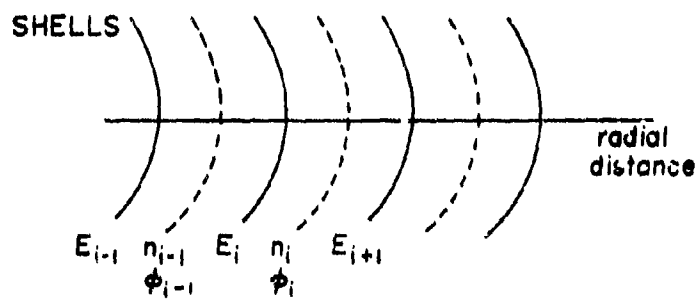
Figure 4. — Decomposition of sheath into shells.

POTENTIAL PROFILE   I-V CURVE
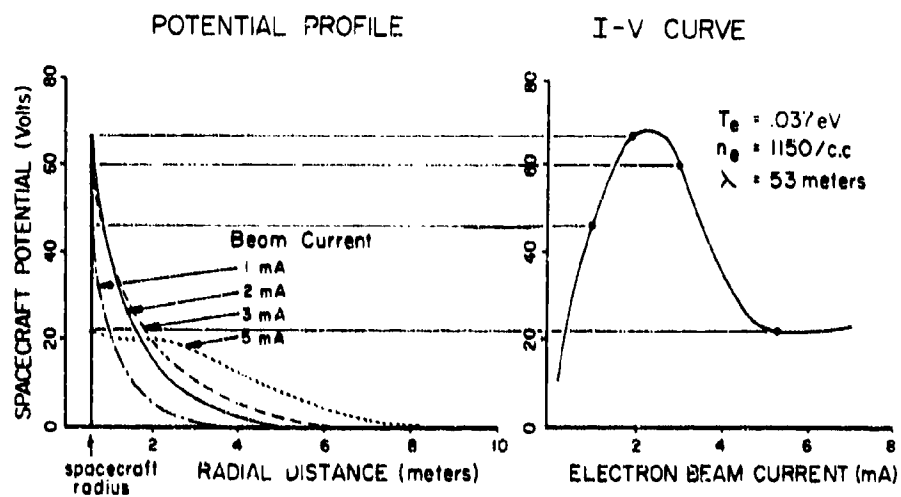
Figure 5. — Relation between potential profile and I-V behavior.
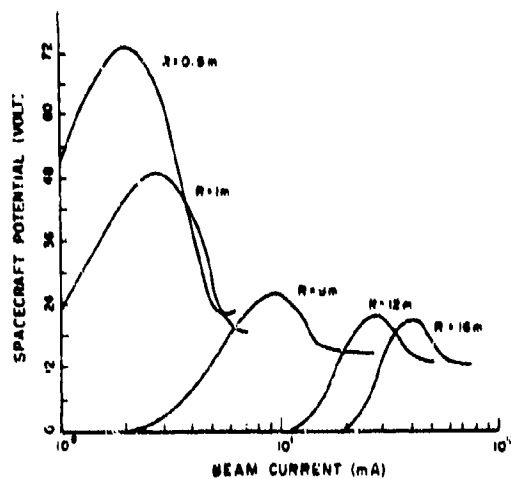
Figure 6. — Persistence of nonmonotonic I-V behavior. Parametric conditions
are as in fig. 7.
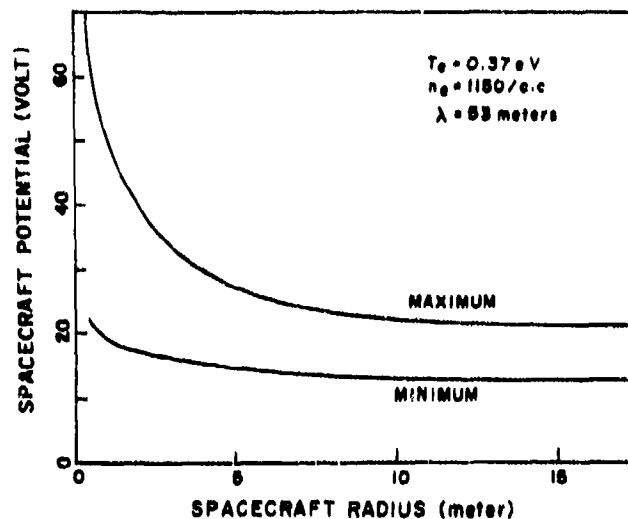
Figure 7. - Envelope of potential extrema in fig. 6.
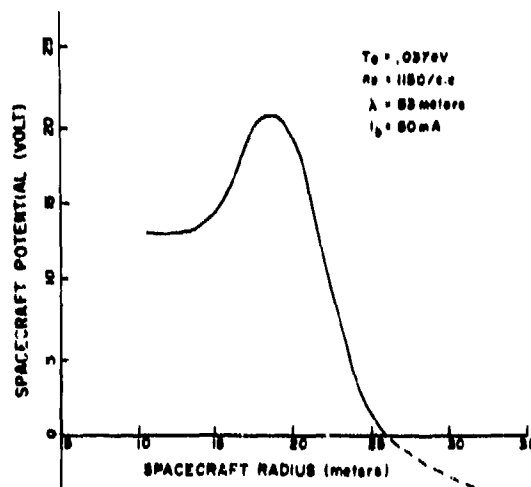
Figure 8. - Nonmonotonic behavior of spacecraft potential as a function of spacecraft radius, for a given electron beam current.

INTERACTIONS BETWEEN LARGE SPACE POWER SYSTEMS AND LOW-EARTH-ORBIT PLASMAS

N. John Stevens
Hughes Aircraft Company
El Segundo, California

There is a growing tendency to plan space missions that will incorporate very large space power systems. These space power systems must function in the space plasma environment, which can impose operational limitations. As the power output increases, the operating voltage also must increase and this voltage, exposed at solar array interconnects, interacts with the local plasma. The implications of such interactions are considered herein. The available laboratory data for biased-array segment tests are reviewed to demonstrate the basic interactions considered. A data set for a floating high-voltage array test was used to generate approximate relationships for positive and negative current collection from plasmas. These relationships were applied to a hypothetical 100-kW power system operating in a 400-km, near-equatorial orbit. It was found that discharges from the negative regions of the array are the most probable limiting factor in array operation.

INTRODUCTION

For the past several years NASA has been conducting mission-planning studies calling for extremely large satellites to be placed in low Earth orbits by the space shuttle.[1-4] Because the planners were freed from the constraints imposed by expendable launch vehicle shrouds, satellite dimensions grew to tens of meters and power generation requirements rose to hundreds of kilowatts.

Now that the Space Transportation System (i.e., shuttle) is operational, there is an effort under way to place such a large structure in orbit in the near future. The projected system could be a manned space platform capable of conducting Earth-oriented studies, space science investigations, or space manufacturing experiments. Although the mission is not finalized, it could involve an expandable platform -- initially a simplified station that can be expanded in the future. The platform would probably be placed in an orbit similar to Skylab's (400 to 500 km) so that it could be serviced by the shuttle and yet be high enough to minimize reboost cost and have an adequate mission life. Array power requirements are postulated as being between 50 and 100 kW.

The generation of large power levels requires very large solar arrays since the nominal power density is of the order of 100 W/m^2. Hence a 50-kW array would require an area of 500 m^2. This area implies long cabling to bring power to the user. If the system were operated at a nominal voltage of 30 to 60 V, currents of the order of 1000 A would be required. Currents of this magnitude can produce either significant cable harness losses (I^2R) or unacceptable increases in weight if the cable loss is reduced by using thicker cross-sectional areas.[5] In addition, large currents flowing in the array can generate magnetic fields that can interact with the Earth's. This increases

both the drag on the system and reboost cost. The alternative is to increase the operating voltages and thereby reduce currents. However, to date, the largest operating voltage used in space was the 100 V used for relatively short periods in Skylab.[6] For this new space platform, operating voltages of 200 to 1000 V are being considered. The operation of power systems at high voltages can give rise to interactions with the space plasma environment that must be considered in designing these systems.

The interactions of concern are illustrated in the high-voltage space power system shown in Figure 1. This system consists of two large solar array wings surrounding a central body or spacecraft. The solar arrays are assumed to be assembled by standard construction techniques. This means that the cover slides do not completely shield the metallic interconnects from the environment. These cell interconnects are at various voltages depending on their location in the array circuits. Hence the interconnects can act as plasma probes and attract or repell charged particles. At some location on the array the generated voltages will be equal to the space plasma potential. Since the electrons are more mobile than the ions, the array will float at voltages that are mostly negative with respect to space plasma potential. Cell interconnects at voltages above this space plasma potential will collect electrons; those at voltages below this space plasma potential will collect ions. The voltage distribution in the interconnects relative to the space plasma potential must be such that these electron and ion currents are equal (i.e., the net current collected is zero).[7]

This flow of particles can be considered to be a current loop through space that is in parallel with the operational system and hence is a power loss. In addition, the cover glass used on the solar cells must also have a zero net current collection. This interaction with the space plasma forces the cover glass to a small negative potential and can produce large voltage gradients in the gap region between solar cells. This can give rise to arcing conditions or transient breakdowns to space.

The severity of these plasma interactions depends on the array operating voltages and the charged-particle environments. The operating voltage will be determined from power system studies but will probably be less than 1000 V. The charged-particle environment is determined by the orbital altitude (Fig. 2). At the projected operating voltages only the low-energy or thermal plasma environment should be of concern since the array voltage is too low to influence the higher energy environmental particles. This plasma environment has particles with temperatures of about 1 eV and densities that vary from a maximum of about 3×10^6 cm-3 at 300 km to between 1 and 10 cm-3 at geosynchronous altitudes. Hence plasma interactions should be more severe at the lower altitudes than at synchronous altitude.

These possible interactions between space power systems and plasma environments have been discussed elsewhere in general terms. In this paper the basic phenomena are reviewed and application to a space power system is discussed.

REVIEW OF BIASED-ARRAY TESTS

Tests of small segments of solar arrays biased by laboratory power supplies while exposed to simulated plasmas in vacuum facilities have been conducted over the past 10 years.[8-16] A test of a similar nature has been conducted in space.[17] Regardless of the size of the array segment (from 100-cm^2 to 13 600-cm^2 areas have been tested) the results are quite similar. In this section the test procedure and the pertinent results are summarized.

Such plasma interaction tests are typically conducted in an experimental arrangement shown schematically in Figure 3(a). The vacuum chamber is capable of pumping to background pressures of 10^{-6} torr or less. The plasma environment is created by ionizing a gas (e.g., nitrogen, argon, or helium). The plasma parameters (plasma number density and particle temperature) are usually determined with either cylindrical or spherical Langmuir probes. The solar array segment (Fig. 3(b)) is mounted in the chamber and is electrically isolated from the tank ground. A high-voltage power supply is connected to one or both ends of the array through an isolated feedthrough in the tank wall. A current-sensing instrument is placed between the power supply and the test sample to measure any coupling current between the segment and the tank ground through the plasma environment. This lead is shielded to minimize extraneous currents. A surface voltage probe (such as that manufactured by TREK) is used to sense the voltage on the array during the test. Hence a surface voltage profile and a leakage current measurement are obtained as functions of applied positive or negative voltage for a given plasma environment. It should be pointed out that the tank ground is not the plasma potential. This plasma potential is determined from the probe readings and must be added to, or subtracted from, the applied bias voltage in order to interpret the test data. It is very important to make this correction at low bias voltages since the plasma potential can be in the range ±20 V.

Typical results for a 100-cm^2 solar array segment biased positively and negatively are shown in Figures 4(a) and (b).[14] In the positive bias voltage case (Fig. 4(a)) the current collection starts at relatively low current values and increases slowly until a bias of about 100 V is reached. At this point there is a marked increase in current collection (by orders of magnitude). Above about 250 V the current tends to increase linearly with voltage. The surface voltage probe traces give an indication as to why this behavior occurs: At the low applied biases the voltage is confined to the gap region between the cells. The cover glass maintains its required zero current balance with the plasma by a slightly negative surface voltage. The superposition of the fields resulting from these voltages shields the bias voltage from the plasma. At biases greater than 100 V, the shielding appears to break down. The bias field now is stronger and starts to encompass the cover glass. This accelerates electrons from the plasma into the cover glass and creates secondary-emitted electrons. The surface voltage must now change to maintain a zero current balance at the glass surface. This surface voltage assumes a value that is about 50 V less than the bias voltage. Hence at this transition, called "snapover,"[18] the collecting area is increased to the full segment area, and this increase changes the coupling currents. The data can be modeled empirically as cylindrical probe collection at positive bias voltages up to 100 V and as spherical probe collection (with the bias reduced by 100 V) at positive voltages greater than 100 V.[16]

For negative bias voltages (Fig. 4(b)) the data indicate that the coupling current increases slowly and then transits into an arc or breakdown, which is signified by a rapid rise in current that trips off the laboratory power supply. Since the supply is also used to bias metallic probes without breakdowns, it must be assumed that the arcing results from the interaction between the negatively biased conductor (cell interconnects), the dielectrics (cover slides), and the plasma environment. The surface voltage probe traces indicate that the gap region between cells is the probable cause for the breakdown. As the bias voltage is made more and more negative, the fields resulting from the cover glass voltage confine the bias field to this limited area. It is known that a negative conductor confined by a less negative dielectric is prone to breakdown and this appears to be happening here.

Both the positive and negative bias voltage effects described above are plasma-density-dependent phenomena. For the positive bias voltage cases both the low- and high-voltage collection changes in direct proportion to the density.[11,14] However, the transition remains at about 100 V. The only condition that seems to influence the transition appears to be the relative areas of the segment and its dielectric and conductive boundaries. The data obtained in support of the PIX flight seemed to indicate a higher transition voltage[17] probably because of the use of a small segment mounted on a large plate. The negative bias breakdown thresholds as a function of plasma density are shown in Figure 5. At the peak space plasma density environment (about 300-km altitude), this breakdown value is uncomfortably low (about 300 V negative relative to the space plasma potential).

The phenomena described above seem to occur independently of the interconnect configuration and array size. Both the standard interconnect configuration and wraparound configurations have been tested. Array sizes of 100 to 13 600 cm^2 gave similar results. The higher positive bias voltage results for the larger panels can be questioned, however, since the tank walls can interact with bias voltage sheaths and distort the results.

REVIEW OF FLOATING-ARRAY TESTS

Although the phenomena of plasma interactions with high-voltage solar arrays can be studied on small segments with bias voltages provided by external power supplies, tests must be run with self-generated voltages in order to validate the concepts developed. Unfortunately there have been relatively few such tests primarily because of the large array required to generate the high voltages needed and the subsequent large facility (with large solar simulators) required to obtain interaction data without wall effects. Even the small amount of data available is incomplete.

A nine-panel array is shown in Figure 6. This array was made up of surplus flight solar array panels with no attempt to match panel characteristics. Seven panels (1400 cm^2 each) were originally assembled in the late 1960's for the Space Electric Rocket Test (SERT-2) project, and two panels (1950 cm^2 each) were assembled in the early 1970's for the Space Plasma High-Voltage Interaction Experiment (SPHINX) project. This nine-panel array was used in a series of tests conducted at both the Johnson Space Center and the Lewis Research Center to evaluate the influence of facilities on plasma interactions.[19] Johnson also did a series of floating tests using the solar simulator.

For this paper the results obtained with the nine-solar-panel array in the Johnson Space Center facility[19] are used to provide a basis for predicting performance of large space power systems in a space environment. Since the panels were not matched and the solar simulator did not uniformly illuminate all nine panels, the results must be viewed as an approximation to the desired test data. Furthermore not all of the plasma properties were reported, so the particle energies and the plasma potential in the chamber had to be approximated.

The test was run with the array in an open-circuit condition but with the capability of measuring each panel voltage and the current between panels. The plasma density was 2×10^4 cm^{-3}. The distribution of open-circuit voltages per panel after correcting for the assumed value of the plasma potential (10 V) is shown in Figure 7. The slope of the voltage is not the same for each panel because of the nonuniformity of the panels. In this configuration the array open-circuit voltage was about 248 V or slightly less than the 260 V obtained without the plasma. This is either due to a fluctuation in the solar simulator or, more probably, a slight loading of the array by leakage through the plasma. As shown in Figure 7 the array floats slightly positive and predominantly negative. This distribution was expected because the electrons are more mobile than the ions. It is interesting to note that the average value of the positive voltage panel is about 10 percent of the overall voltage. This is the assumption usually made in computing power system interactions with plasma environments.

The following empirical approximations for current collection[16] were used to compute the coupling currents:

$$I_- = J_{eo} A_{int} \sqrt{1 + \frac{V_+}{E_e}}$$

$$I_+ = J_{io} A_{int} \left(1 + \frac{V_-}{E_i}\right)$$

where

J_{eo}, J_{io} thermal electron and ion current densities, A/cm^2

A_{int} interconnect area, cm^2

V_+, V_- positive and negative average panel voltage (relative to plasma potential), V

E_e, E_i electron and ion energies (normalized to electronic charge), eV

The relationships were iterated until the electron coupling current was approximately equal to the ion current. The results are shown in Figure 8 along with the measured values. The agreement is reasonable.

The agreement obtained here may be fortuitous in view of the many approximations made. If the behavior of high-voltage solar array systems is to be understood, it is mandatory that a well-conceived, complete set of experiments be conducted. These experiments must include bias voltage tests and self-generated voltage tests with the capability of achieving positive voltages above the snapover condition. This would answer questions on the negative voltage breakdown phenomena as well.

APPLICATION TO SPACE POWER SYSTEMS

To illustrate the effect of plasma interactions on a large, high-voltage space power system, consider a 100-kW generator, made up of 10 modules of 10 kW each, operating in a 400-km, near-equatorial Earth orbit (Fig. 9). It is assumed that the modules are connected electrically in parallel to avoid a single-point failure that could occur with a series connection. Each of the modules is assumed to operate at a load voltage V_L and a load current I_L. The 100-kW power output of the system would then be available to the loads at a voltage V_L and current 10 I_L.

Furthermore each of the modules is assumed to be built up from ten 1-kW solar array blocks connected in series. Each block would then generate a current I_L at an average voltage of 0.1 V_L. Approximately one block would be at a positive potential relative to the space plasma potential; the other nine would be negative (Fig. 9).

The plasma environmental parameters for the 400-km orbit are given in Table I.[18] The implications that could arise from the environmental measurements made on the third shuttle flight are discussed later in this section.

The plasma coupling or drainage current can be computed for the 10-kW module operating at an average V_L of 500 V and producing an I_L of 20 A. Each block would generate 1 kW of power at an average voltage of 50 V. The relationships derived in the previous section are used to compute the positive and negative coupling currents for this module, which is assumed to be typical for the system. The results are summarized in Table II. These results indicate that the currents do not balance and that another iteration should be made. But the average loss, of the order of 15 mA, represents a possible power loss of about 0.1 percent. This is such a negligible loss that refining the computations is considered to be unwarranted. This is true only when the positive voltage stays below snapover conditions (i.e., <100 V).

What is a concern is whether the blocks that are at negative voltages relative to the space plasma potential approach the breakdown threshold. This can have more serious consequences than the coupling current losses - a block discharging to space can disrupt the whole power system output.

From discharge photographs obtained in ground tests on small biased solar array segments,[16,18] it appears that the whole segment area is not involved in a given discharge. Hence only a finite area of a large solar array may be involved in any single discharge. The location of this finite area within the power system 1-kW block then becomes critical to evaluating the effect of discharges on system performance. If discharges occur at parallel paths within the block, thus allowing the module to continue to be a power generator, one would expect a ripple impressed on the dc voltage (Fig. 10). Since the breakdown threshold is not an absolute value and since there are 10 modules in this power system, there should be considerable randomness in the breakdowns and the resulting overall ripple.

The worst case would be when the discharge occurs in the series portion of the block and thus interrupts the block power output. If the output of a whole block is involved, the module output will also have a transient behavior since all blocks are in series. If a module power output is involved, then

the whole array output could temporarily collapse (Fig. 10). Random oscilla-
tions in the power output could be caused by the breakdowns in each mode and
by the, as yet unknown, lifetime influence on breakdown threshold.

Environmental measurements on the third shuttle flight[20,21] compound the
difficulties imposed by possible plasma interactions. It has been found that
because of photoemission from the surface the plasma environment around the
shuttle in sunlight is approximately 10 times denser than previous measurements
would indicate. Furthermore this dense environment seemed to stay with the
shuttle for the 8 days of the mission. If this phenomenon holds true for all
altitudes and for extended periods of time, the plasma surrounding a large
power system could also be denser than previously considered. A factor of 10
increase in plasma density would increase the coupling current losses to about
1 percent, which may still be unimportant. However, the discharge threshold
would be reduced significantly by such an increase and more blocks would be
involved in discharge transients. This is a much more serious interaction
problem.

These considerations apply to cases where the environment is assumed to be
isotropic. Such conditions do not always exist in low Earth orbits and there
can be significant changes during the orbit (Fig. 11). At certain times the
active area of the array faces the orbital velocity direction ("ram"). Under
such conditions the ion currents are increased (ram velocity is greater than
ion thermal velocities), and this causes the array to float more positively
relative to the space plasma potential. The result is higher coupling currents
and lower discharge tendency. When the active area faces away from the orbital
velocity direction ("wake"), the resulting deficiency of ions causes the system
to float more negatively and thus the discharge probability to be greater.
Finally the system will enter eclipse each orbit. This eclipse period is long
enough to allow the array to cool significantly. Upon reentry to sunlight the
cold solar array system could generate up to twice its normal voltage until the
temperature returns to normal. Unfortunately the system would be entering the
ram condition upon leaving eclipse, and so for a short time both power losses
and discharges could be a concern.

The conditions described apply to a large space power system operating in
a 400-km, near-equatorial Earth orbit. If the system were placed at a lower
altitude (~300 km), the higher plasma density would increase the coupling
losses and the discharge probability. At a higher altitude high-energy parti-
cle damage to solar arrays must be considered. Operating in a polar orbital
environment brings in a variable plasma environment along with possible auro-
ral flux interactions. Yet a plasma environment is not prohibitive to opera-
tions of space power systems provided that the possible interactions are
considered and accounted for in system designs. The alternative of lower volt-
age operations is not necessarily safe nor conducive to power system growth.

CONCLUDING REMARKS

Plans for future NASA missions call for large space platforms operating in
low Earth orbits. These platforms require large space power systems capable of
generating a few hundred kilowatts of power. At these levels the operating
voltage must be greater than voltages commonly used in present power systems.
However, the higher voltage can result in interactions with the space plasma
environment that can influence the operating characteristics of the power
system.

Tests in ground simulation facilities in which small solar array segments were biased to positive and negative voltages in a plasma environment have shown that interactions can be detrimental. When positive voltages are applied, electron currents can be collected that become proportional to the panel area at voltages greater than 100 V. Under negative bias voltages arcing or breakdown can occur. This arcing threshold depends on the plasma density and can be as low as -300 V in simulated 300-km-orbit plasma environments.

Relatively few tests have been conducted in which an array capable of generating high voltages under solar simulation conditions was operated in a plasma environment. One such test of a nine-block, 13 600-cm^2 array has shown that the array would float electrically such that one block would have an average positive voltage that would be 10 percent of the overall voltage, with the other eight blocks progressively more negative. This test indicated that array behavior could be approximated by considering the interaction with separate blocks at an average voltage.

This approach was applied to a 10-kW array that was considered to be part of a 100-kW space power system operating at 500 V. Ten 10-kW arrays, each in parallel, made up this system. It was found that, under normal quiescent conditions, the power drain due to the electron coupling current would be negligible. However, the arcing in the negative-voltage regions could seriously disrupt system operations either by introducing a ripple on the output or by terminating operations depending on the severity and location of the breakdowns. The orbital oscillations ranging through ram, wake, and eclipse conditions generally tend to make the situation worse. Finally the evidence from the shuttle experiments that indicate that large space structures could create their own plasma environment tends to make plasma interactions even more critical.

For the past 12 years the advantages and disadvantages of large space power system operations at high bus voltages have been argued and discussed. There are obvious advantages to using high voltages in space. Possible hazards to such operations with standard array technology have been addressed herein. These interactions are not insurmountable but can be overcome given adequate understanding of the phenomena. What is needed is a systematic investigation to determine why discharges occur and how to prevent them. This would require test programs involving large arrays with self-generated voltages and finally a flight experiment to prove that all of the interactions can be minimized.

REFERENCES

1. "Outlook for Space," NASA SP-386, 1976.

2. Johnson, R. D. and Holbrow, C., eds., "Space Settlements, A Design Study," NASA SP-413, 1977.

3. Bekey, I., "Big COMSATS for Big Jobs at Low User Cost," Astronautics and Aeronautics, Vol. 17, No. 2, Feb. 1979, pp. 42-56.

4. Snoddy, W. C., "Space Platforms for Science and Applications," Astronautics and Aeronautics, Vol. 19, No. 4, Apr. 1981, pp. 28-36.

5. Stevens, N. J., "Interactions Between Spacecraft and the Charged-Particle Environment," Spacecraft Charging Technology - 1978, NASA CP-2071/ AFGL-TR-79-0082, 1979, pp. 268-294.

6. Woosley, A. P., Smith, O. B. and Nassen, H. W., "Skylab Technology Electrical Power System," AAS Paper 74-129, Aug. 1974.

7. Chen, F. F., "Electric Probes," Plasma Diagnostic Techniques, edited by R. H. Huddlestone and S. L. Leonard - Pure Applied Physics, Vol. 21, Academic Press, New York, 1965, pp. 113-200.

8. Cole, R. K., Ogawa, H. S. and Sellen, J. M., Jr., "Operation of Solar Cell Arrays in Dilute Streaming Plasmas," TRW Systems, Redondo Beach, CA, TRW-09357-6006-R000, Mar. 1968. (NASA CR-72376.)

9. Knauer, W., Bayless, J. R., Todd, G. T. and Ward, J. W., "High Voltage Solar Array Study," NASA CR-72675, 1970.

10. Herron, B. G., Bayless, J. R. and Worden, J. D., "High Voltage Solar Array Technology," AIAA Paper 72-443, Apr. 1972.

11. Kennerud, K. L., "High Voltage Solar Array Experiments," NASA CR-121280, 1974.

12. Stevens, N. J., "Solar Array Experiments on the SPHINX Satellite," NASA TM X-71458, 1973.

13. Domitz, S. and Grier, N. T., "The Interaction of Spacecraft High Voltage Power Systems with the Space Plasma Environment," Power Electronics Specialists Conference, IEEE, New York, 1974, pp. 62-69.

14. Stevens, N. J., Berkopec, F. D., Purvis, C. K., Grier, N. T. and Staskus, J. V., "Investigation of High Voltage Spacecraft System Interactions with Plasma Environments," AIAA Paper 78-672, Apr. 1978.

15. McCoy, J. E. and Konradi, A., "Sheath Effects Observed On A 10-Meter High Voltage Panel in Simulated Low Earth Orbit Plasmas," Spacecraft Charging Technology - 1978, NASA CP-2071, 1979, pp. 315-340.

16. Stevens, N. J., "Review of Biased Solar Array-Plasma Interaction Studies," NASA TM-83693, Apr. 1981.

17. Grier, N. T. and Stevens, N. J., "Plasma Interaction Experiment (PIX) Flight Results," Spacecraft Charging Technology-1978, NASA CP-2071/AFGL-TR-79-0082, 1979, pp. 295-314.

18. Purvis, C. K., Stevens, N. J. and Berkopec, F. D., "Interaction of Large, High Power Systems with Operational Orbit Charged-Particle Environments," NASA TM X-73867, 1977.

19. Grier, N. T., "Experimental Results on Plasma Interactions with Large Surfaces at High Voltages," NASA TM-81423, 1980.

20. Banks, P. M., Williamson, P. R. and Raitt, W. J., "Results from the Charged Particle Beam Experiments on the Space Shuttle," AIAA Paper 83-0307, Jan. 1983.

21. Shawhan, S. D., Anderson, R. R., D'Angelo, N., Frank, L. A., Gurnett, D. A., Murphy, G. B., Owens, H. D., Reasoner, D., Stone, N., Brinton, H. and Fortna, D., "Beam-Plasma Interactions and Orbiter Environment Measurements with PDP on STS-3," AIAA Paper 83-0308, Jan. 1983.

TABLE I. - ENVIRONMENT AT 400-km ORBIT

Plasma characteristics:
  Electrons:
    n_e, m^{-3} . . . . 2×10^{11}
    E_e, eV 0.22

  Ions (O_{16}^+):

    n_i, m^{-3} . . . . 2×10^{11}
    E_i, eV 0.09

Spacecraft orbital velocity, km/sec 77

Plasma current densities, A/m^2:
  Isotropic:
    Electron, J_{eo} . . . . 2.4×10^{-3}
    Ion, J_{io} . . . . 9.4×10^{-6}
  Ram (Ion): J_{ic} . . . . 2.6×10^{-4}

TABLE II. - SUMMARY OF PLASMA COUPLING CURRENTS

[Assumed operating conditions for module: V_{op} = 500 V and I_{op} = 20 A; for block: V_{op} = 50 V and I_{op} = 20 A.]

Block	Average potential (relative to space), V	Plasma coupling current, mA
1	50	-10 } -10.4 mA
2	0	-.4
3	-50	.6
4	-100	1.1
5	-150	1.7
6	-200	2.3 } 20.4 mA
7	-250	2.8
8	-300	3.4
9	-350	4.0
10	-400	4.5

C-4
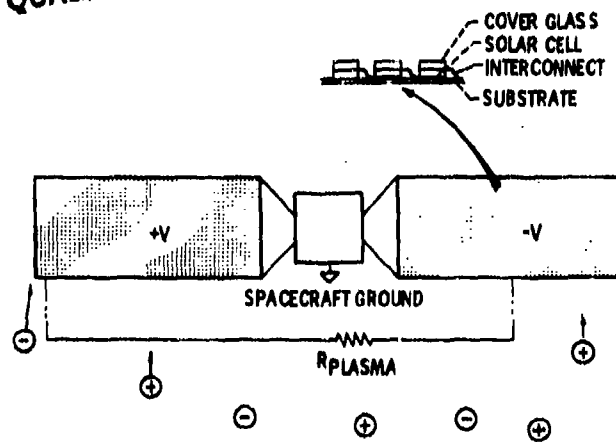
Figure 1. - Spacecraft high-voltage system - environment interactions.
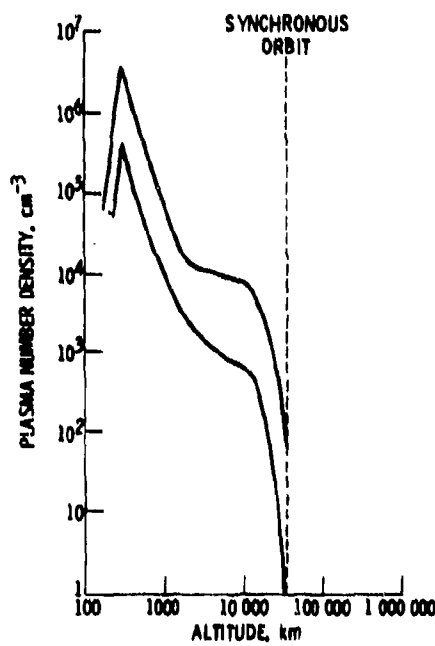
Figure 2. - Plasma number density versus altitude in equatorial orbit.
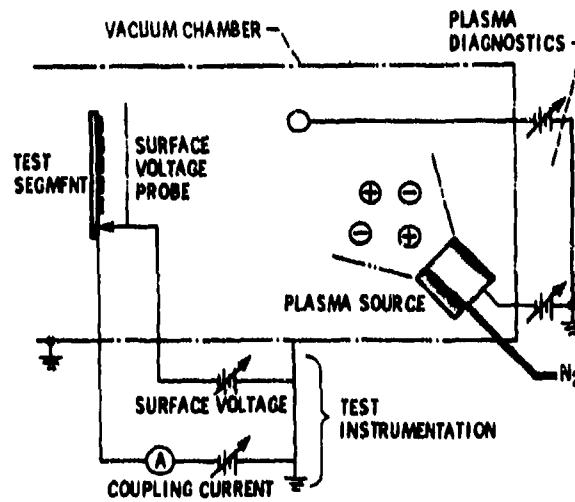
(a) Schematic diagram of test arrangement.
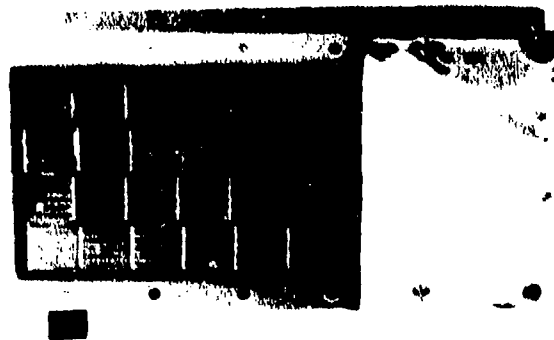
(b) Solar array segment.

Figure 3. - Ground simulation tests.
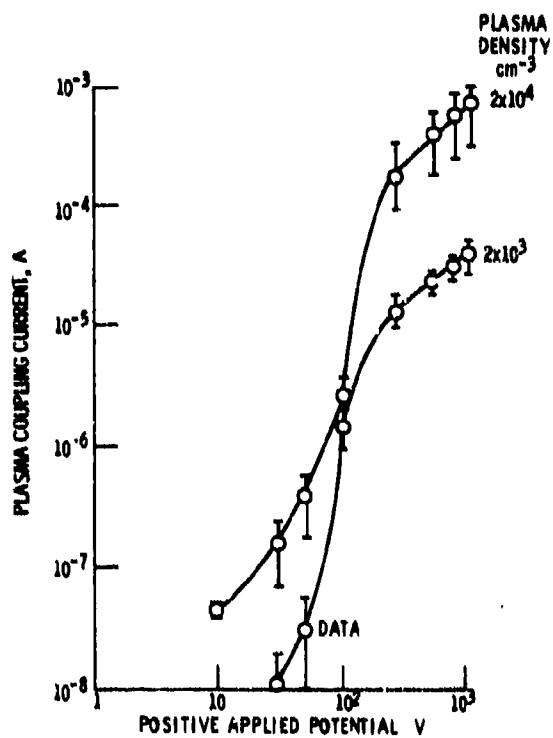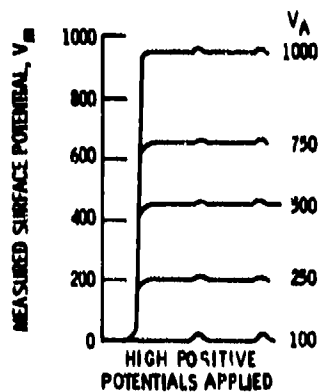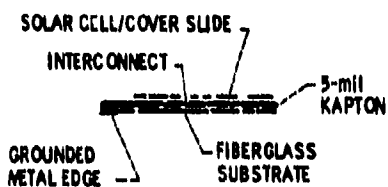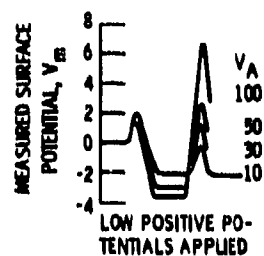
(a) Positive applied potentials.

Figure 4. - Solar array surface voltage profiles and coupling currents.

274

LOW NEGATIVE PO-
TENTIALS APPLIED

SOLAR CELL/COVER SLIDE
INTERCONNECT
5-mil KAPTON
GROUNDED METAL EDGE
FIBERGLASS SUBSTRATE
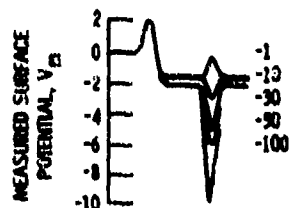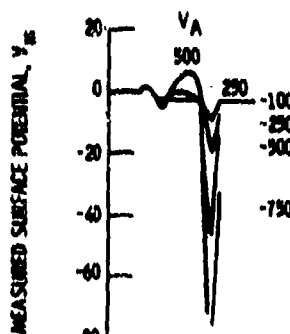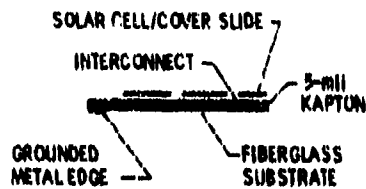
HIGH NEGATIVE PO-
TENTIALS APPLIED
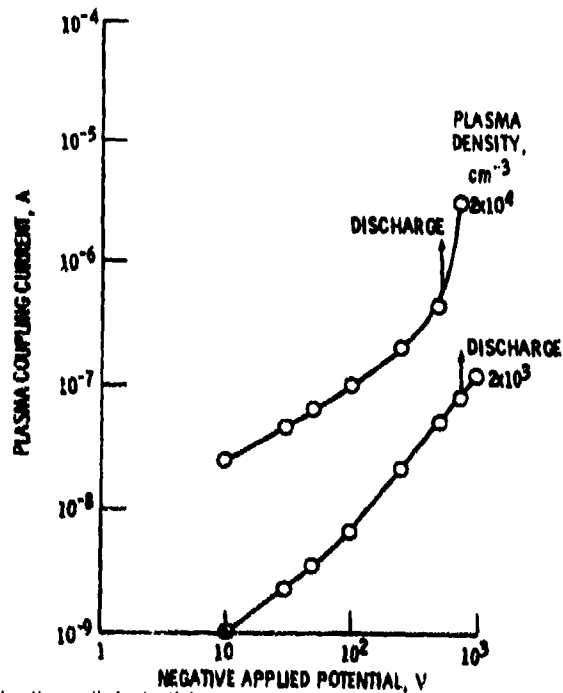
(b) Negative applied potentials.

Figure 4. - Concluded.
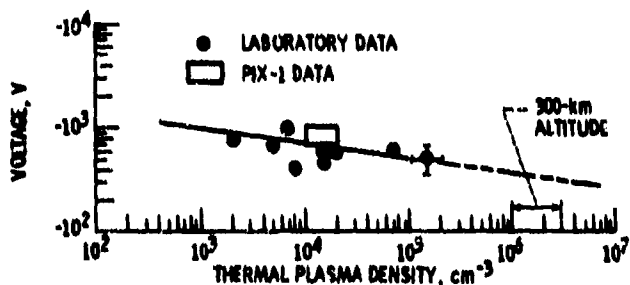
Figure 5. - Voltage threshold for breakdown.
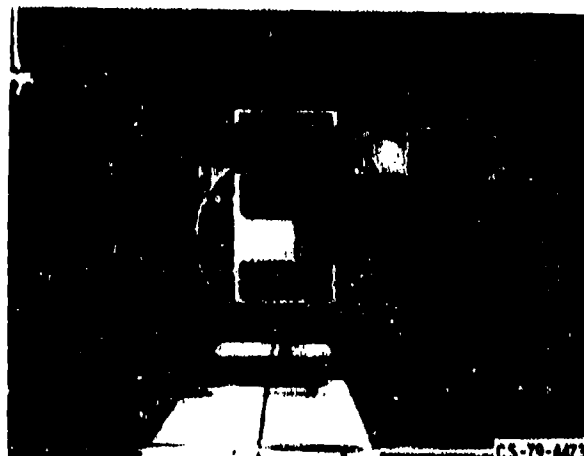
Figure 6. - Large solar array panel test.

275
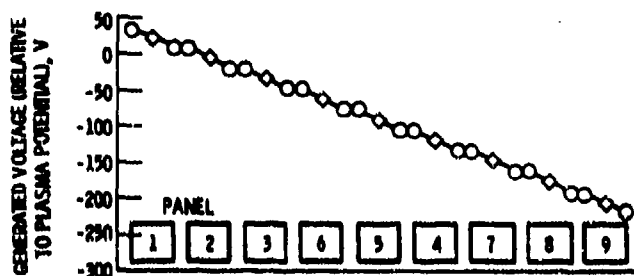
Figure 7. - Generated voltage distribution for nine-panel array.

(a) Measured plasma coupling currents.

(b) Predicted plasma coupling currents.
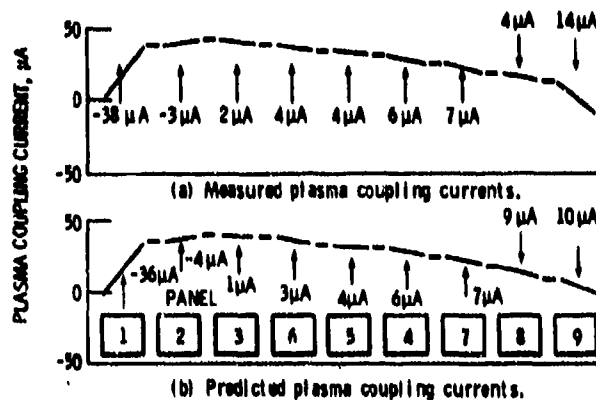
Figure 8. - Comparison of measured and predicted plasma coupling currents for nine-panel array.

TEN-BLOCK MODULE - SERIES CONNECTION (500 V AT 20A)

AVERAGE BLOCK POTENTIAL (RELATIVE TO PLASMA POTENTIAL)

TEN-MODULE ARRAY - PARALLEL CONNECTION
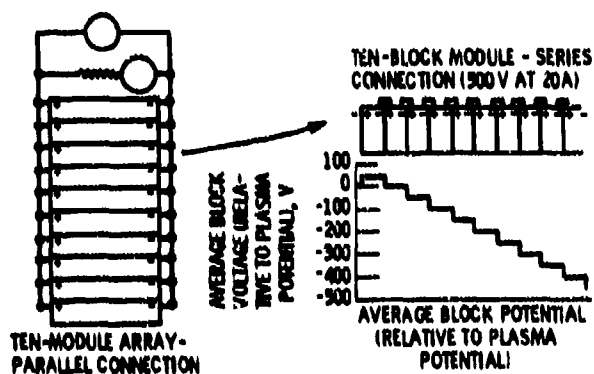
Figure 9. - Space power system concept (100 kW generated at 500 V).

(a) Design distribution.

(b) Minor breakdown (one block).

(c) Major breakdown (one block).

Figure 10. - Influence of breakdowns on solar array behavior.

Figure 11. - Orbital variations in operating conditions - 400-km orbit.

CALCULATION OF SECONDARY-ELECTRON ESCAPE CURRENTS FROM INCLINED SPACECRAFT SURFACES IN A MAGNETIC FIELD*

J. G. Laframboise
York University
Toronto, Canada M3J 1P3

In low Earth orbit, the geomagnetic field $\vec{B}$ is strong enough that secondary electrons emitted from spacecraft surfaces have an average gyroradius much smaller than typical dimensions of large spacecraft. This implies that escape of secondaries will be strongly inhibited on surfaces which are nearly parallel to $\vec{B}$, even if a repelling electric field exists outside them. This effect is likely to make an important contribution to the current balance and hence the equilibrium potential of such surfaces, making high-voltage charging of them more likely. We present numerically-calculated escaping secondary electron fluxes for these conditions. For use in numerical spacecraft-charging simulations, we also present an analytic curve-fit to these results, accurate to within 3% of the emitted current.

1. INTRODUCTION

The prediction of high-voltage charging or other environmental effects on a spacecraft in low Earth orbit appears likely to be more complicated than in geostationary orbit, for at least three reasons.

These reasons are: (a) space charge effects (on sheath and wake potentials) are more important, because space-charge densities are much higher (the Debye length is no longer >> typical spacecraft dimensions) (b) ion flow effects are more important, because spacecraft orbital speed $\gtrsim$ ion thermal speeds (c) the geomagnetic field $\vec{B}$ is likely to have an important influence on charged-particle motions because $\vec{B}$ is now much larger, and not all of the average particle gyroradii of importance are any longer >> typical spacecraft dimensions.

We wish to investigate an important consequence of (c), which concerns the escape of secondary electrons emitted from spacecraft surfaces. Our discussion will also apply, with minor modifications, to photoelectron or backscattered-electron escape. In low Earth orbit, in the auroral-zone geomagnetic field ($|\vec{B}| = 0.44$ gauss = 4.4×10^{-5}T), the gyroradius of a "typical" 3eV secondary electron and a 10 keV auroral electron are 13 cm and 8 m, respectively. The average gyroradius of "cold" ionospheric electrons (temperature T = 0.1 eV) in the same $\vec{B}$ is even smaller (2 cm), but this is not an important parameter in most cases because these electrons are repelled if the spacecraft potential is negative, and their density is then well-approximated by a Boltzmann factor, which is unaltered by $\vec{B}$ effects.

The reason why $\vec{B}$ affects secondary-electron escape is shown in Fig. 1. In Fig. 1(a), the spacecraft surface is perpendicular to $\vec{B}$, and the emitted electrons, which

experience an electric force $-e\vec{E}$ directed away from the surface, all escape, helping to discharge it. In Fig. 1(b), the spacecraft surface is nearly parallel to $\vec{B}$, and almost all of the emitted electrons return to it, even though they still experience an electric force directed away from it. These electrons therefore are unable to help discharge it, so a surface nearly parallel to $\vec{B}$ is more likely to charge to a large negative voltage. Note that the component of $\vec{E}$ which is perpendicular to $\vec{B}$ results only in an $\vec{E} \times \vec{B}$ drift parallel to the surface.

For any object much larger than 13 cm, the escape of secondary electrons will be strongly affected by this process. For example, most surfaces on the Shuttle are effectively "infinite planes" by this criterion. On the other hand, the average gyroradius of high-energy auroral electrons is comparable to Shuttle dimensions, so the deposition of these electrons onto Shuttle surfaces is likely to be only moderately inhibited.

For a larger object (size >> 8 m), deposition of auroral electrons will also become strongly orientation-dependent, with both collection and escape of electrons now being inhibited on surfaces nearly parallel to $\vec{B}$. This suggests that high-voltage charging of such surfaces may be more likely on objects of intermediate size than on either larger or smaller ones. In the calculation of Parks and Katz[1], Katz and Parks[2], the tendency toward high-voltage charging increased with spacecraft size because in their model, ion collection increased less rapidly with spacecraft size than did electron collection. To determine which of these two effects predominates will require more detailed calculations than have been done so far.

As already mentioned, strong ion flow effects also are generally present in low orbit; the ion speed ratios (flow speed/most probable ion thermal speed) for H^+ at 1 keV, H^+ at 0.1 eV, and O^+ at 0.1 eV are 0.02, 1.8, and 7.3, respectively. Whenever the latter is the predominant ion species, ion collection on downstream surfaces will therefore be strongly inhibited. If a surface is simultaneously downstream and nearly parallel to $\vec{B}$, as is likely to be the case in the auroral zones, then the tendency for high-voltage charging to occur on it will be greatly increased (Fig. 2).

To "straightforwardly" include $\vec{B}$ effects on secondary electron emission in a large two or three dimensional simulation program would involve the numerical integration of very large numbers of secondary-electron orbits. The resulting computing costs usually would be formidable, especially since these orbits would have relatively large curvatures. A desirable alternative is to "parameterize" the situation by treating in advance a simplified but still sufficiently realistic model problem. In order to do this, we make the approximations described in the next Section.

2. THEORY FOR $\vec{E}$ NORMAL TO SURFACE

We assume that the spacecraft surface is an infinite plane, and the electric and magnetic fields $\vec{E}$ and $\vec{B}$ outside it are uniform. In the work presented here, we also assume that the electric force $-e\vec{E}$ on electrons is directed along the outward normal to the surface; here e is the magnitude of the elementary charge. This assumption is to be relaxed in a later paper (J.G. Laframboise, to be published) in order to permit variations of potential along the surface to be taken into account. We assume that the secondary electrons are emitted with a Maxwellian distribution corresponding to a temperature T. The ratio $i = I/I_0$ of escaping to emitted flux is then a function of two parameters: the angle θ between the surface normal and the direction of $\vec{B}$ (Fig.3), and a parameter describing the strength of $\vec{E}$. A convenient choice for this parameter is the difference in potential across a mean secondary-electron gyroradius $\bar{a} = (1/eB)(\pi mkT/2)^{\frac{1}{2}}$, divided by kT/e, where m is electron mass and k is Boltzmann's constant.

This quotient is:

$$\varepsilon \equiv \frac{E}{B} \sqrt{\frac{\pi m}{2kT}} \qquad (2.1)$$

where $E \equiv |\vec{E}|$ and $B \equiv |\vec{B}|$.

This quantity also has an alternative, more useful interpretation: it is the ratio of the magnitude $|\vec{E} \times \vec{B}|/B^2$ of the $\vec{E} \times \vec{B}$ drift speed, to one-half the mean thermal speed $(8kT/\pi m)^{\frac{1}{2}}$ of the emitted electrons. It is useful to estimate the value of ε for a high-voltage spacecraft sheath in low-orbit conditions. To do this, we use the sheath solution of Al'pert et al (Ref. 3, Table XXIV and Fig. 72). For a 1 kV and a 5 kV sheath around a sphere of radius 3m in a collisionless plasma having an ambient ion temperature of 0.1V, number density of 3×10^5 cm^{-3}, and resultant (ion) Debye length of 0.43 cm, their results give, respectively, sheath thicknesses of 2.6 and 6.1 m, and surface electric fields $E = 0.86$ and 2.9 kV/m. Using $B = 4.4 \times 10^{-5}$T and $T = 3$ eV for secondary electrons, we then obtain $\varepsilon = 33.9$ and 114.2. Both of these are relatively large values, whose significance can be understood if we consider what would happen if ε were infinite.

In this limit, it is easy to show that secondary electrons would all escape unless $\vec{B}$ were exactly parallel to the surface (θ were 90°). This can be shown as follows. In this limit, secondary electrons would have no "thermal" motion. The (y,z) projection of their motion would then be similar to that shown in Fig. 4. This motion would be the sum of: (i) an $\vec{E} \times \vec{B}$ drift in the y direction (ii) a uniform acceleration along $\vec{B}$, whose projection in the (y,z) plane would be upward (iii) just enough gyromotion to produce a cycloidal path when combined with (i), so that in the absence of (ii), the electron would (just) return to the surface at the end of each gyroperiod. In the presence of (ii), these "return points" are displaced upward by progressively increasing amounts (Fig. 4), so the electron can never return to the surface, unless $\vec{B}$ is exactly parallel to the surface, so that the upward component of $-e\vec{E}$ along $\vec{B}$ vanishes.

This result suggests that for large finite values of ε (including the values calculated above), electron escape is likely to be almost complete except for θ very near 90°, where it should drop to zero very steeply. The occurrence of high-voltage charging in marginal circumstances may therefore depend very strongly on the precise orientation of a surface.

The escaping secondary-electron flux is given by:

$$I = \iiint f(\vec{v}_0) H(\vec{v}_0) v_{0z} \, d^3\vec{v}_0$$
$$= \int_{-\infty}^{\infty} dv_{ox} \int_{-\infty}^{\infty} dv_{oy} \int_0^{\infty} n \left(\frac{m}{2\pi kT}\right)^{3/2} \exp\left(-\frac{m v_o^2}{2kT}\right) H(v_{ox}, v_{oy}, v_{oz}) v_{oz} \, dv_{oz} \qquad (2.2)$$

where: $\vec{v}_0$ is the initial velocity of an emitted electron, $f(\vec{v}_0) \equiv d^3 n/d^3\vec{v}_0$ is the velocity distribution of emitted electrons, n is a reference number density, and $H(\vec{v}_0)$ is equal to 1 for escaping electrons and 0 for those which return to the surface. The emitted flux is:

$$I_o = n(kT/2\pi m)^{\frac{1}{2}}. \qquad (2.3)$$

We also introduce the dimensionless velocity:

$$\vec{u} = \vec{v}(m/2kT)^{\frac{1}{2}}. \qquad (2.4)$$

Equation (2.2) then becomes:

$$\frac{I}{I_0} = \frac{2}{\pi} \int\!\!\int_{-\infty}^{\infty} du_{ox} du_{oy} e^{-u_{ox}^2 - u_{oy}^2} \int_0^{\infty} du_{oz}\, u_{oz}\, e^{-u_{oz}^2}\, H(u_{ox}, u_{oy}, u_{oz})$$

$$= \frac{1}{\pi} \int\!\!\int_{-\infty}^{\infty} du_{ox}\, du_{oy} \exp(-u_{ox}^2 - u_{oy}^2) \sum_{k=1}^{k_{max}(u_{ox}, u_{oy})} (-1)^{k+1} \exp\left[-u_{lim,k}^2(u_{ox}, u_{oy})\right]$$

$$\approx \frac{1}{\pi} \sum_i \sum_j \Delta u_{ox} \Delta u_{oy} \exp(-u_{ox,i}^2 - u_{oy,j}^2) \sum_{k=1}^{(k_{max})_{i,j}} (-1)^{k+1} \exp\left[\left(-u_{lim,k}^2\right)_{i,j}\right] \quad (2.5)$$

which is in a form suitable for numerical summation. The quantities $u_{lim,1}, u_{lim,2}$, ..., $u_{lim,k_{max}}$ are the values of u_{oz} for which H changes between 0 and 1 for each u_{ox} and u_{oy}. These values must be found by numerically determining which particle orbits reimpact the surface. These orbits can, however, be determined in analytic form, with time as a parameter. To do this, we use the coordinate system shown in Fig. 3, together with a y-axis (not shown) directed into the plane of the Figure. The equation of motion for an electron is:

$$\dot{\vec{v}} = -\frac{e}{m}(\vec{E} + \vec{v} \times \vec{B}). \quad (2.6)$$

We solve this with the initial conditions $\xi = y = \eta = 0$, $v_\xi = v_{o\xi}$, $v_y = v_{oy}$, and $v_\eta = v_{on}$. We introduce the dimensionless variables:

$$\epsilon_x = \frac{E_x}{B}\sqrt{\frac{\pi m}{2kT}}, \quad \epsilon_y = \frac{E_y}{B}\sqrt{\frac{\pi m}{2kT}}, \quad etc;$$

$$\tilde{x} = x/\bar{x}, \quad \tilde{y} = y/\bar{x}, \quad etc;$$

$$\tau = \omega_0 t = (eB/m)t. \quad (2.7)$$

In the present work, ϵ_x and ϵ_y are both zero, but for future use, we have retained these quantities in the formulas below. We obtain:

$$u_{o\xi} = u_{ox} \sin\theta + u_{oz} \cos\theta;$$

$$u_{on} = -u_{ox} \cos\theta + u_{oz} \sin\theta;$$

$$\tilde{\xi} = -\frac{1}{\pi}\epsilon_\xi \tau^2 + \frac{2}{\sqrt{\pi}} u_{o\xi}\tau;$$

$$\tilde{y} = \left(\frac{2}{\sqrt{\pi}} u_{oy} - \frac{2}{\pi}\epsilon_\eta\right)\sin\tau + \left(\frac{2}{\sqrt{\pi}}u_{o\xi} + \frac{2}{\pi}\epsilon_y\right)(\cos\tau - 1) + \frac{2}{\pi}\epsilon_\eta\tau;$$

$$\tilde{\eta} = \left(\frac{2}{\sqrt{\pi}}u_{on} + \frac{2}{\pi}\epsilon_y\right)\sin\tau + \left(\frac{2}{\sqrt{\pi}}u_{oy} - \frac{2}{\pi}\epsilon_\eta\right)(1 - \cos\tau) - \frac{2}{\pi}\epsilon_y\tau; \quad (2.8)$$

$$\tilde{z} = \tilde{\xi}\cos\theta + \tilde{\eta}\sin\theta.$$

Equations (2.8) can also be differentiated to find $d\tilde{z}/d\tau$. The numerical procedure for finding the quantities $u_{lim,k}$ in Eq. (2.5) then involves calculating $\tilde{z}$ and $d\tilde{z}/d\tau$ at a succession of points along an orbit (the electron will reimpact during the first gyroperiod $0 < \tau \le 2\pi$ if at all, so this interval always suffices), and making the appropriate tests on these quantities to find out whether the orbit reimpacts or escapes. For each $u_{ox,i}$ and $u_{oy,j}$, this is done for a succession of values of u_{oz}. These tests also yield the local minimum of $\tilde{z}(\tau)$ if one exists. Whenever a change occurs between no escape and escape from one such value of u_{oz} to the next, an interpolation using these minima can be used to provide the corresponding value of

$u_{lim,k}$. In cases where they are unavailable, the arithmetic mean of the two successive u_{oz} values is used. This completes the definition of the procedure used for calculating the ratio I/I_o of escaping to emitted flux.

3.   RESULTS AND DISCUSSION

Escaping secondary-electron current densities, computed as described in Sec. 2, are shown in Table 1 and Fig. 5. Each value of $i = I/I_o$ was calculated using 191808 orbits, evenly spaced in the intervals $-4.5 \leq u_{ox} \leq 4.5$, $-4.5 \leq u_{oy} \leq 4.5$, and $0 \leq u_{oz} \leq 4.5$, with points on the orbits calculated at intervals $\Delta\tau = \pi/45$. For 8 values each of ϵ and θ, the resulting calculation took 83 hr total on a Hewlett-Packard 1000F minicomputer with Vector Instruction Set. The results are accurate to within about 0.5% or better. The result for $\epsilon = 0$ is just the analytic result $i = \cos\theta$. To see why this is so, we consider the electron orbit shown in Fig. 6, which has been fictitiously extended so as to pass through the surface and re-emerge from it. In the absence of an electric field ($\epsilon = 0$), this orbit has the same speed at the re-emergence point C as at the emission point A. Since we have also assumed that the emitted velocity distribution is isotropic, and therefore a function of speed only, the real orbit, for which C is the emission point, must carry the same population as would the fictitious re-emerged orbit. The flux crossing the reference surface DE, which is $\perp \vec{B}$, is therefore the same as if such passages and re-emergences actually occurred, and is the same as if another reference surface FG, also $\perp \vec{B}$, were emitting electrons having the same velocity distribution. However, in reality, the electrons come from the real surface HJ, which is not $\perp \vec{B}$, and all the electron-orbit guiding centers which are inside any given magnetic-flux tube through DE will also be inside the projection of the same flux tube onto HJ, and the ratio of the intersection areas of this tube with HJ and DE is just $\sec\theta$. The ratio of escaping to emitted flux must therefore be the reciprocal of this, or $\cos\theta$, as stated above.

Also evident in Fig. 5 is the fact, mentioned in Sec. 2, that when ϵ is large enough, electron escape becomes essentially complete except when θ is very nearly 90°. In a real situation, $\vec{E}$ would not be uniform, but would decrease with distance from the surface, contrary to our assumptions. Our results can therefore be expected to overestimate electron escape. This would probably not be a large effect, but this presumption remains to be verified. An approximate compensation for it can be made by calculating ϵ using an electric field value which is averaged over the first mean gyroradius distance from the surface.

The results in Table 1 are approximated to within 2.5% of I_o by the empirical formula:

$$a = 1 + 1.35\epsilon^{1.1394} \exp\left[0.083725 \left\{1 + \tanh\left[1.9732 \ln\left(\frac{\epsilon}{1.13}\right)\right]\right\}\right.$$
$$\left. - 0.07825 \ln\left[1 + (\epsilon/8.5)^{1.78148}\right]\right],$$

$$b = 0.38033\epsilon^{0.95892} \exp\left[2.0988 \left\{1 + \tanh\left[1.49 \ln\left(\frac{\epsilon}{3.26}\right)\right]\right\}\right],$$

$$c = \ln(90°/\theta), \tag{3.1}$$

$$i = \cos\left[90° \exp(-ac - bc^2)\right].$$

This formula also has the correct limiting behavior when $\epsilon \to 0$ or ∞, or $\theta \to 0°$ or 90°.

An approximation formula for the emitted flux is also available [Eqs. (5) and

(6) of Laframboise et al, Ref. 4, and Laframboise and Kamitsuma, Ref. 5].

4. CALCULATION OF SECONDARY-ELECTRON DENSITIES

Once the secondary-electron escape fluxes are known (Sec. 3), a simple, inexpensive, approximate calculation of their space-charge density distribution can be set up. The proposed method is as follows: (1) ignore the gyromotion of the secondary electrons once they have escaped. Their motion then involves: (a) an acceleration along magnetic field lines, of amount $-(e/m)\vec{E}\cdot\vec{B}/B$ (b) a drift motion of velocity $\vec{E}\times\vec{B}/B^2$ across magnetic field lines. (2) Integrate enough of the trajectories defined by this motion (i.e. their guiding-center trajectories) to define trajectory tubes whose cross-section at any point can be calculated with sufficient accuracy; the method described by Laframboise et al (Ref. 6, Sec. 7), can be used to calculate the area of a trajectory tube without reference to neighbouring trajectories. (3) Calculate their space-charge density $n(\vec{r})$ at any point by (a) ignoring the "thermal" spread of their velocities (b) then invoking the fact that their density × their velocity [as given by the orbit integration mentioned in (2)], × the cross-sectional area $A(\vec{r})$ of the trajectory tube (which must be calculated in a plane ⊥ the trajectory) at the point $\vec{r}$ in question, = a constant (whose value is given by the initial conditions at the point on the spacecraft where the trajectory originates) (c) finding their velocity at the point in question by using energy conservation, together with the values of electric potential $\phi(\vec{r})$ and ϕ_0 at that point and the emission point, and their assumed velocity v_0 at the emission point. The result is:

$$n(\vec{r}) = n_0 v_0 A_0 / \left\{ A(\vec{r}) \sqrt{ v_0^2 + (2e/m)\left[\phi(\vec{r}) - \phi_0 \right] } \right\} \tag{4.1}$$

where $n_0 v_0$ is the escaping flux calculated in Sec. 3. At most positions, $n(\vec{r})$ will be insensitive to the precise value assumed for v_0^2; assuming that $v_0 =$ the one-sided thermal speed $(2kT/\pi m)^{\frac{1}{2}}$ will suffice for most purposes.

REFERENCES

1. Parks, D.E., and Katz, I. (1981) Charging of a large object in low polar Earth orbit. In: Spacecraft Charging Technology 1980, NASA Conference Publication 2182/Report No. AFGL-TR-81-0270, Air Force Geophysics Laboratory, Massachusetts, pp. 979-989.

2. Katz, I., and Parks, D.E. (1983) Space shuttle orbiter charging. J. Spacecraft and Rockets 20, 22-25.

3. Al'pert, Ya.L., Gurevich, A.V., and Pitaevskii, L.P. (1965) Space Physics with Artificial Satellites, Consultants Bureau, New York.

4. Laframboise, J.G., Kamitsuma, M., and Godard, R. (1982) Multiple floating potentials, "threshold-temperature" effects, and "barrier" effects in high-voltage charging of exposed surfaces on spacecraft. In: Proc. Internat. Symp. on Spacecraft Materials in Space Environment, June 1982, Toulouse, France, European Space Agency, Paris, Publication No. ESA SP-178, pp. 269-275.

5. Laframboise, J.G., Kamitsuma, M. (1983) The threshold temperature effect in high-voltage spacecraft charging. In: Proc. Air Force Geophys. Lab. Workshop on Natural Charging of Large Space Structures in Near Earth Pol. Orbit, edited by R.C. Sagalyn, D.E. Donatelli, and I. Michael, Report No. AFGL-TR-83-0046/ Environmental Research Paper No. 825, Air Force Geophysics Laboratory, Massachusetts, pp. 293-308.

6. Laframboise, J.G., Kamitsuma, M., Prokopenko, S.M.L., Chang, Jen-Shih, and Godard, R. (1982) Numerical Simulation of spacecraft charging phenomena at high altitude, Final Report on Grant AFOSR-76-2962, York University.

THETA EPS	15.00	30.00	45.00	60.00	75.00	80.00	85.00	89.00
0.00	.945	.865	.707	.500	.258	.174	.087	.017
.20	.991	.931	.796	.585	.311	.209	.105	.030
.50	.995	.978	.892	.704	.397	.271	.137	.027
1.00	.999	.997	.971	.857	.545	.384	.198	.039
2.00	.999	1.000	.999	.982	.802	.617	.342	.070
5.00	.999	1.000	1.000	1.000	.998	.968	.723	.172
10.00	.999	1.000	1.000	.999	1.000	1.000	.971	.338
20.00	.999	1.000	1.000	.999	1.000	1.000	1.000	.617

TABLE 1

Values of the ratio $i = I/I_0$ of escaping to emitted flux, for various values of θ, the angle (in degrees) between the surface normal and the magnetic field direction, and ϵ, the nondimensional repelling electric field strength. These two quantities appear in the table as THETA and EPS, respectively. These results are accurate to within about 0.5% or better; thus the differences between .999 and 1.000 in the Table are not significant. For $\theta = 0^\circ$, $i = 1$ for all values of ϵ.
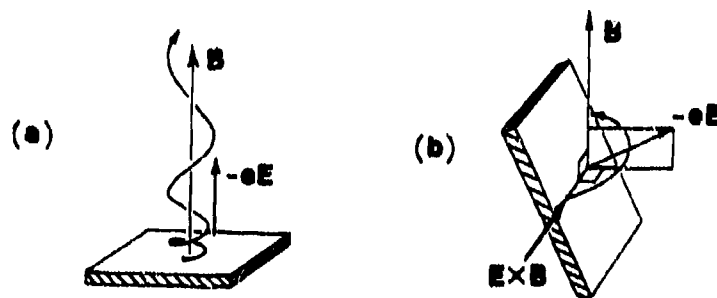
Figure 1. Effect of surface orientation on escape of emitted electrons. In (a), the spacecraft surface is perpendicular to the magnetic field $\vec{B}$, and the emitted electrons, which experience an electric force $-e\vec{E}$ directed away from the surface, all escape. In (b), the spacecraft surface is nearly parallel to $\vec{B}$, and almost all of the emitted electrons return to the surface, even though they still experience an electric force directed away from it. Note that the component of $\vec{E}$ perpendicular to $\vec{B}$ results only in an $\vec{E} \times \vec{B}$ drift parallel to the surface.
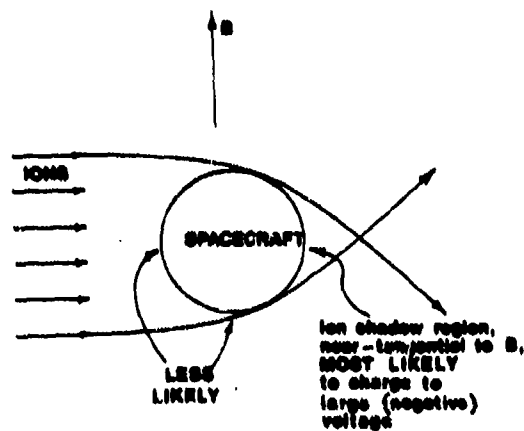
Figure 2. Spacecraft simultaneously in a collisionless ion flow and a magnetic field $\vec{B}$.
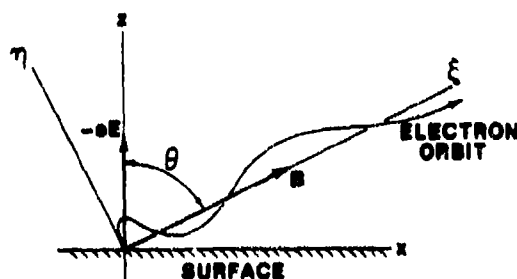
Figure 3. Coordinate system for calculating electron escape fluxes. The y-coordinate (not shown) is directed into the plane of the Figure.
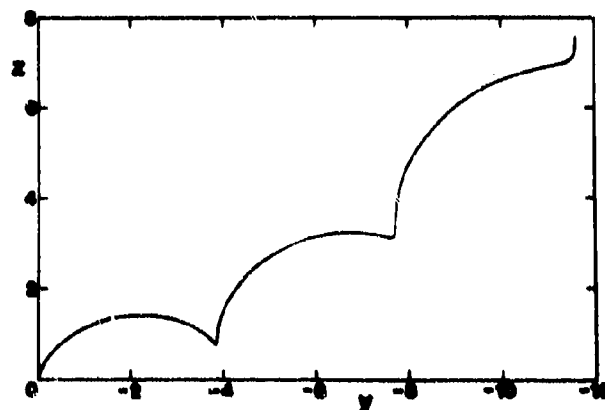
Figure 4. Example of an electron orbit having zero initial velocity. The magnetic field $\vec{B}$ is parallel to the (x,z) plane, and makes an angle $\theta = 75°$ with the z axis. $\varepsilon = 1$. Three gyroperiods of the orbit ($0 \leq \tau \leq 6\pi$) are shown.
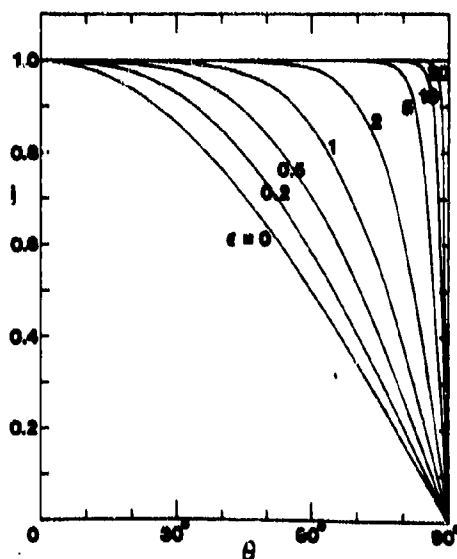
Figure 5. Ratio $i = I/I_0$ of escaping to emitted secondary-electron flux, as a function of the angle θ between the surface normal and the magnetic field direction, for various values of the repelling electric field strength parameter $\varepsilon = (E/B)(\pi m/2kT)^{\frac{1}{2}}$. The result for $\varepsilon = 0$ is given by $i = \cos\theta$.

285
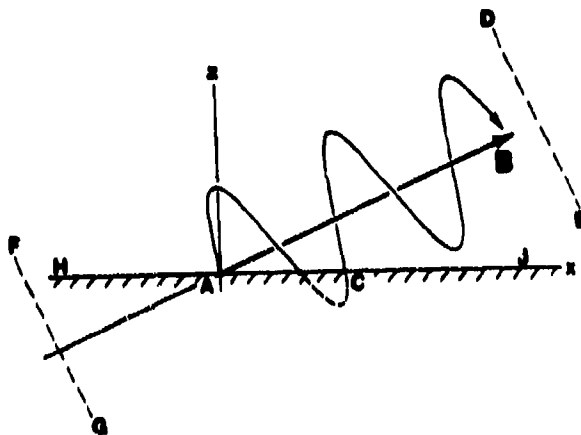
Figure 6. Electron orbit for $\epsilon = 0$, fictitiously extended so as to pass through the surface and re-emerge from it.

SELF-CONSISTENT SIMULATION OF PLASMA INTERACTIONS WITH
SECONDARY-EMITTING INSULATORS

S. T. Brandon, R. L. Rusk, T. P. Armstrong, and J. Enoch
University of Kansas
Lawrence, Kansas 66045

A cylindrical particle-in-cell (PIC) plasma simulation code applicable to plasma densities encountered in low earth orbit (LEO) is nearing completion. The simulated geometries include that of a plain disk and a disk surrounded by a dielectric. Both configurations are mounted upon a ground plate in contact with a plasma environment. Techniques allowing simulation of dielectric charging using PIC time scales are discussed. Current versus voltage characteristic curves are calculated and the results are compared to experimental data.

INTRODUCTION

The plasma densities present in LEO (10^4 - 10^6 /cm^3) may cause the collection of large plasma coupling currents for spacecraft operating at high voltages. In particular, large high-voltage solar cell arrays exposed to the LEO environment could collect enough parasitic current from the ambient plasma to degrade their performance. Additionally, exposed dielectric material can develop large differential potentials. Punctures in insulators over conductors have been seen to collect currents much larger than would be expected based on the area of the exposed conductor (ref. 1).

In this paper, a status report of the results of a continuing effort to develop a self-consistent numerical simulation to explore more thoroughly the interactions of an ambient plasma with a conducting disk, which may be partially covered with a dielectric material, is presented. The disk surrounded by dielectric material represents a hole in an insulator covering a conductor. The background plasma parameters are chosen to resemble conditions of LEO. Since all particle trajectories are known, any process which can be modeled statistically for a single plasma particle can be included by the simulation code. Plasma interactions currently considered include the effects of charge collection on the dielectric and secondary electron emission. The simulation region includes a ground plate on which the disk or disk and dielectric are mounted. The resulting configuration closely matches the experiments (ref. 2).

This combination of geometry and plasma parameters incorporates the basic physics of the interactions which would be present between a high voltage solar cell array and the plasma environment. Yet, unlike the solar array, the geometry is simple enough to be handled by a particle-pushing code. Although a ratio of ion to electron mass of 1:1 is commonly used, mass ratios of 100:1 or higher can be handled. This allows the simulation of

negative voltages present upon the central conductor. Thus, information gained from an analysis of the disk and dielectric configuration will be directly applicable to the design of large-scale, high-voltage solar cell arrays meant to be placed in low earth orbit.

REVIEW OF THE SIMULATION MODEL

The plasma simulation code is a further development of the 2-1/2 dimensional program described previously (refs. 3 to 6). The cylindrical simulation region is divided into a numerical grid which is used to calculate the potentials and fields of the problem. The calculational grid is shown in figure 1. Each cell represents a ring of space due to rotational symmetry about the Z-axis (boundary region 1). Boundary regions 2 and 3 represent the outer boundaries of the calculation. The outer boundaries are assumed to be removed far enough from the conducting disk so that potentials imposed upon the disk do not affect the boundaries. Thus, the plasma is maxwellian at the outer boundaries and the potential is set to zero. Particles are added to the simulation along boundaries 3 and 4 according to the value of the random thermal current. Particles are lost to the simulation whenever their orbits cross one of these two boundaries. Boundary region 4 represents the ground plate. The potential on boundary region 4 is set to zero and all particles intersecting this boundary are absorbed. The surface of the dielectric covering part of the conductor is represented by boundary region 5 (may have zero length). All particles striking boundary region 5 are absorbed. Electrons striking the dielectric may emit secondaries with their number distribution given by fits to experimental data presented by Haffner (ref. 7). The potential on the surface of the dielectric is determined by the following equation:

$$\phi(\delta) = \frac{\delta}{\varepsilon} \left[4\pi\sigma + \frac{\varepsilon}{\delta}\phi(0) \right] + \delta\phi(\Delta Z) \tag{1}$$

where δ is the thickness of the dielectric, ε is the dielectric constant, σ is the charge per unit area, and $\phi(0)$ is the potential of the conducting disk. This is just an infinite capacitor approximation which may not be valid near the edges of the dielectric surface. Boundary region 6 represents the exposed portion of the conducting disk which can be set at a desired potential with respect to the potential of the plasma exterior to the simulation region (zero). Particles which enter boundary region 6 are absorbed and form the current drawn by the conductor from the plasma.

The simulation code is based upon standard PIC simulation techniques whenever possible. An overview of the program is shown in figure 2. The initial particles are randomly added to the simulated space with velocities chosen from a maxwellian distribution. This represents a nonequilibrium situation unless a potential of zero is specified on the conductor. The equations of motion are integrated using a second-order leap-frog method. To avoid the singularity present in the cylindrical equations of motion as r approaches zero, cartesian coordinates are used to compute particle movement. The coordinates are converted back into the cylindrical form when

the move is completed. The particle mover advances particles through the simulation in increments of the time step value. The time step value is set such that the fastest particles move less than 1 grid cell per time step (about 10^{-9} sec). Particles are added at the outer boundaries from the surrounding undisturbed plasma (assumed to have a maxwellian velocity distribution, usually of 10,000 deg K, about 1 eV). All particles present which have entered any of the sink regions are discarded. The remaining particle charges are spread over the grid using volume weighting over the nearest grid cells. Successive over-relaxation with odd-even stepping is used to solve Poisson's equation - yielding a self-consistent calculation of the electrostatic potential. The electric field can then be calculated by differentiating the potential.

The total number of time steps simulated may range from about 4000 time steps for the plain disk configuration to 20,000 time steps for the disk and dielectric configuration. The average age of particles within the simulations for the 20x20 grid is about 100 time steps. This implies a complete cycling of particles in the simulation space occurring about 200 times for a 20,000 time step simulation. Hence, plasma parameters such as temperature and density are determined by the additions of particles on the outside boundaries, not by the initial particle distribution. It is important to ensure that the program can maintain a constant density and temperature for a free plasma over many time steps. Simulation of a free plasma is accomplished by setting the radius of the conductor to zero (extending boundary region 4 over the entire lower boundary) and reflecting any particles which cross boundary region 4. The potential on boundary region 4 is set to zero. A plot of the total number of particles present in the simulation region versus time step number is shown in figure 3. The initial number of particles (2000 per species) remains constant within statistical fluctuations for the entire 8000 time steps computed using a 20x20 calculational grid size. The average kinetic energy per particle remains constant as shown in figure 4. Thus the simulation code has been shown to be able to simulate a free plasma for a large number of time steps without undergoing any nonphysical instabilities.

This simulation program is applicable when the plasma Debye length is of about the same order of magnitude as the disk radius. Large plasma densities would cause large fluctuations in the collected current, since this calculation makes use of a small number of particles. The PIC assumptions made also imply that the Debye length is larger than one grid cell. With these restrictions and probe sizes ranging from 1.75 cm to 10.0 cm in radius and with electron and ion temperatures of about 1 eV, plasma densities are then about 10,000 particles per cubic centimeter. This corresponds to environments encountered in the upper ionosphere or low earth orbit. The Debye length under these conditions is about 5 cm.

PLAIN DISK CALCULATIONS

Approach to Equilibrium

The plain disk or electrostatic probe configuration is the simplest configuration simulated. The rapid approach to equilibrium is demonstrated in figure 5. Voltage versus current density curves drawn by the disk are shown for simulation runs of various durations. The value for the current can be

seen to achieve an equilibrium state after 2000 time steps of the simulation have been completed. Since only two or three thousand time steps need be taken, a large number of runs may be made for the disk only case using a relatively small amount of computer time (1 minute on the CRAY I, and 36 minutes for the VAX 11/750 with a 4000 time step run). Thus the plain disk simulations can be used to explore a wide range of plasma parameters and establish areas of applicability for the more complex disk and dielectric simulations.

Comparison with Experiment

The comparison with experiment (ref. 2) is displayed by figure 6. The experimental current-voltage curve is shown for a plasma density of 20,000 particles per cubic centimeter and a disk radius of 1.75 cm. The only modification to the experimental curve has been the correction of -8 volts so that voltages in both the simulation and the experiment will be referenced to the plasma potential, and not to the vacuum chamber wall. In spite of experimental uncertainties in the plasma parameters and statistical errors present in the simulations, the experiment and calculated values of the collected current versus voltage are in good agreement.

The calculated curve was constructed as a hybrid of three separate series of computer runs. The voltage points between 20 and 200 volts were obtained using a 10x10 grid simulation running for 3200 time steps on a VAX 11/750 computer. The lower voltage points were also calculated with a 10x10 grid simulation, but 16,000 time steps were necessary to reduce the statistical fluctuations. The higher voltages were simulated with a 20x20 grid utilizing the same spacial resolution as the other 10x10 grid calculations. Both the lower and higher voltage points were computed on a CRAY I machine.

The negative voltage experimental curve can also be compared to the positive voltage simulation results. The current collected by the positive voltage simulations is scaled by the square root of the mass ratio (for a nitrogen plasma the scale factor is 160) to produce the expected results of a negative voltage run. This comparison is shown in figure 7. The agreement between simulation and experiment is not as good as for the positive voltages. The simulation collects about 1/2 of the current of the experiment throughout the voltage range. This is within the experimental uncertainties and simulation statistical error. However, unlike the positive voltage case, the mean values of the collected current do not agree. This indicates that current scaling by the square root of the mass ratio for negative voltages (large ion to electron mass ratios) is only approximate.

Simulation of Large Mass Ratios

For the disk only configuration, the current collected by the positive voltage calculation can be scaled to the expected current that would be seen in a negative voltage simulation. For the disk and dielectric configuration the current scaling to negative voltages is inappropriate due to the presence of a dielectric surface which will charge differently in the two voltage ranges. The charging of the dielectric will also depend upon the ratio between the ion and electron mass. With the normal 1:1 mass ratio, the dielectric surface, when exposed to the plasma, will not charge, in spite of

the fact that the increased mobility of the electrons should charge the surface of the dielectric negatively. In order to be able to realistically simulate dielectric charging effects and negative voltages for the disk and dielectric configuration, it is necessary to relax the PIC requirement of 1:1 mass ratios.

The disk only configuration provides an excellent test of the methods developed to handle larger mass ratios. This configuration is simple and gives simulation results with a minimum of CPU time. The expected collected current for each mass ratio can be found by simply scaling the positive voltage result to the negative voltage simulation value. The diagnostics furnished are excellent.

The usual way to handle larger mass ratios is to simply give the ions a larger mass value. This method has several disadvantages. Since the simulation procedure is not affected, it takes the same CPU time per time step to simulate larger mass ratios as it would to simulate a 1:1 mass ratio. The distance each ion would move per time step decreases with the increasing value of the mass ratio. Thus, for reasonable mass ratios (hydrogen plasma, 1836:1), the simulation would have to be run many times longer (at the same relative speed) to come to equilibrium. Also the ion motion per time step might become so small as to be dominated by roundoff error. This generally limits PIC simulations to various small values of the mass ratio. From these results, speculations are made as to the effect of realistic mass ratios.

Another method to simulate large mass ratios can be developed. The relatively slow movement of the ions per time step indicates that it is a wasted effort to move them every time step. Instead, ions can be moved once every n time steps. In this case n is chosen to be large enough so the ions move about the same average distances every n time steps as they would in a simulation run with a mass ratio of 1:1 for each time step. Thus ion and electron particle movement are restored to a relative parity at the expense of the additional assumption that the electric fields remain constant (at least in the average) for n time steps. The constant electric field assumption is clearly invalid at the beginning of a run. However, once a simulation reaches an equilibrium state, the assumption of a constant electric field should be justified. Once again it is postulated that if the simulation is run until an equilibrium state is reached, details about the approach to the equilibrium are lost - implying the equilibrium state is unique.

The remaining problem is to determine n for a given mass ratio in such a manner that the least amount of extra computing is required. The particle's energy should remain constant as the mass ratio is varied. Therefore, the ion velocity is proportional to the square root of the inverse of its mass ratio. The time period over which the ions are moved then is just proportional to the square root of their mass ratio. The simulated mass ratio should be chosen such that its square root is an integer.

The above algorithm can be implemented with the PIC code by the following simple procedure. The form of the equations of motion describing the R coordinate which are solved by the particle mover are:

$$m(V_{r,new} - V_{r,old}) = \Delta t \left(\frac{l^2}{mr^3} + qE_r \right) \tag{2}$$

$$r_{new} = r_{old} + \Delta t V_{r,new} \tag{3}$$

Since the energies of particles with differing mass ratios are constant at each point along the trajectory, the angular momentum term, l^2/mr^3, remains constant under variations of the ion mass ratio. The combined effects of substituting $m'=n^2 m$ and $\Delta t'=n\Delta t$ just cancel in the equations of motion. A similar behavior is found for the equations of motion describing the Z coordinate. Thus, mass ratios of $n^2:1$ can be simulated simply by moving the ions only once every n time steps.

Results obtained by using the direct and indirect methods to simulate large mass ratios have no effect on the current collected by the disk for positive voltages. The collected current is dominated by electrons; any difference in the ion mass is not seen. The best test of the larger mass ratio simulation methods is the simulation of negative voltages on the conductor. In this case the ions dominate the current and the electrons are excluded from the conductor. Results of simulations using several different mass ratios by both methods are shown in figure 8. The expected current which would be collected by the conductor decreases with increasing mass ratios. The general shape of the current-voltage curve remains intact for both approximations down to mass ratios of 4:1. For mass ratios of 100:1, the straightforward method of computing mass ratio effects using a larger mass value begins to collect more current than the simulations which move the ions once per every 10 time steps. When a mass ratio of 1849:1 is attempted, by moving the ions once per 43 time steps, the current-voltage curve begins to bend over. This could be caused by a lack of statistics (30,000 time steps result in only 700 ion movements) or possibly the assumption of constant electric fields over the 100 time step interval is beginning to break down.

THE DISK AND DIELECTRIC CONFIGURATION

The Approach to Equilibrium

The final equilibrium situation of the disk and dielectric is much harder to identify than that of the plain disk. The capacitance inherent in the dielectric causes the response time for charging to be large compared with the plasma frequency. Typically the dielectric may slowly charge or discharge during the simulation run, imitating an equilibrium situation in the steadiness of the current values obtained. It is important to take a detailed look at the available history information to determine whether a run reached an equilibrium state. For quick inspections, the value of the total charge collected by the dielectric is usually the most sensitive indicator of equilibrium. In practice it has been difficult to run current-voltage points long enough to arrive at an equilibrium value. Techniques have been developed to make the calculation come into an equilibrium state in a reasonable number of time steps.

One way to reach equilibrium is simply to run the simulation long enough (many plasma periods) until the equilibrium state is found. This method was tried for the 10x10 grid with 500 particles per species. A time history plot of the total charge on the dielectric obtained from a 20,000 time step run made at 10 volts is shown in figure 9. Beginning with an uncharged dielectric, charge accumulates rapidly for about the first 15,000 time steps. Due to the uniformly decreasing value of the slope of the curve, it is difficult to determine the onset of the equilibrium situation.

The first method implemented to speed the approach to equilibrium is based upon the observation that the dielectric generally charges until its potential decreases to zero (the voltage is lower than the first crossover point for secondary emission). If most of the charge needed to reach zero potential is added during the initialization, less time will be spent collecting charge during the run. Effects of loading the dielectric with different amounts of charge are also shown in figure 9. All runs come to the same equilibrium, which suggests that the equilibrium is unique. This method of decreasing the time to reach equilibrium proves to be ineffective at higher voltages. The dielectric must collect more particles to charge to an equilibrium value than are added at the boundaries during the 20,000 time steps of the calculation.

The relationship which causes the simulation to approach equilibrium slowly is contained in the boundary condition imposed upon the dielectric (equation 1). The leading factor of the thickness of the dielectric over the dielectric constant is usually small (in the previous runs we have used a value of 1/28 as opposed to the experimental value of 1/280 in order to keep this ratio large enough to be somewhat manageable). The small value of δ/ε means that a large amount of simulation time will be used to accumulate this charge. The second method implemented to speed up the approach to equilibrium was the introduction of artificially high values for δ/ε. The physical effects of increasing δ/ε can be thought of in one of several ways:

1. a decrease in the capacitance associated with the dielectric
2. an introduction of an artificial dielectric thickness
3. artificially increasing the charge collected by the dielectric

The result of a 10 volt run with a 10x10 grid of 500 particles per species is shown in figure 10. The time history graph of the total charge collected by the dielectric shows that equilibrium is reached after about 500 time steps for a value of $(\delta/\varepsilon)^*$ set to 1.

The artificial value of $(\delta/\varepsilon)^*$ must be chosen with care. If the value is too small, equilibrium still will not be reached. If the value is too large, the potential on the dielectric will vary dramatically with the collection of only small numbers of particles (one). Assuming a constant charging rate proportional to the thermal current leads to the following expression:

$$\left(\frac{\delta}{\varepsilon}\right)^* = C \frac{V}{(\Delta t)(n)(T)^{1/2}} \tag{4}$$

where V is the voltage on the conductor, Δt is the time step value, η is the electron density, T is the electron temperature, and C is the proportionality

293

constant. Substituting values of the other variables for the above 10 volt run determines C (.4824).

The artificial value of $(\delta/\varepsilon)^*$ computed with the above equation assumes the number of particles present is large enough so that non physical effects associated with the granularity of charge collected on the dielectric do not occur. In practice, the value of $(\delta/\varepsilon)^*$ must be kept small enough that the change in the potential on the dielectric surface per particle impact is only a small fraction of the potential applied to the conductor (1%). The upper limit of the value of $(\delta/\varepsilon)^*$ is then given as follows:

$$\left(\frac{\delta}{\varepsilon}\right)^* = \frac{0.0075(dr)V}{q} \tag{5}$$

where dr is the length of a grid cell and q is the charge per macroparticle.

Comparison with Experiment

The resulting current-voltage curves for the disk and dielectric configuration are shown in figure 11 for a disk radius of 1.75 cm and a dielectric radius of 8.75 cm. The simulation with a mass ratio of 1:1 collects the same amount of current as the plain disk (the size of the exposed conductor is the same) for low voltages. As the voltage on the conductor is raised, a point is reached where the current collected by the disk surrounded with dielectric material increases compared to that of the plain disk. This increase in collected current is due to the presence of the dielectric and occurs when the dielectric begins to come to an equilibrium with positive potentials near the conducting disk. The dielectric will charge to positive values when the average number of secondaries released by the impacting primary electrons is greater than one. The point at which this occurs is determined by details of the secondary emission yield curve for the dielectric and by the energy spectrum of the primary particles. The calculated current-voltage characteristic curve shows a current enhancement beginning at a lower voltage than that found in the experiment.

Also shown in figure 11 are calculated current-voltage curves for mass ratios of 4:1 and 100:1. The larger mass ratios allow the surface to charge negatively for low voltages. The negative voltages present on the dielectric reduce the collection of electrons by the conductor for low voltages. As the voltage on the conductor is increased, the surface of the dielectric begins to become positive, as in the 1:1 mass ratio case. From this point on, the current remains almost unaffected by the ion mass ratio. These current-voltage curves show qualitatively correct behavior using the correct boundary conditions.

Variations of the Secondary Electron Emission Yield Parameter

The effect of variations in σ_m, the maximum number of electrons scattered from the dielectric surface per incoming primary electron, upon the current voltage curves is shown in figure 12. The voltage of the onset of

294

the increase in collected current with reference to the plain disk decreases
with increasing σ_m. The increase in σ_m lowers the energy of the first
crossover for secondary emission. Also, the number of secondaries released
for energies larger than the first crossover point increases. Both effects
create more secondary emission at lower voltages than would normally be
found. The sensitivity of the calculation to the secondary electron
production might be sufficient to allow the measurement of the yield curve
parameters for low voltages by fitting the response to experimental data.

A detailed examination of the potential present along the top of the
dielectric during a simulation run which collected more current than that of
the plain disk reveals what is happening. The initial condition shown in
figure 13 for time step zero is a fully charged dielectric; the potential on
the dielectric surface is zero. This would be realistic if the voltage on
the conductor were increased slowly from a value low enough that the
dielectric surface became fully charged. As the simulation proceeds, the
potential upon the dielectric remains unstable, but positive for the first
6,000 time steps. After the equilibrium situation is reached, the potential
remains constant to the termination of the run after 20,000 time steps. The
equilibrium potential over the dielectric is uniformly positive and
decreasing in value from the voltage on the exposed conductor to near zero at
the outside edge of the dielectric. The potentials behave as if they have
"snapped over" from their normal near zero level. This resembles the
snapover phenomenon observed in experiments with solar cell arrays (ref. 2).
The potential upon the cover slips for the array increased from values near
zero below 100 volts to values about 50 volts less than that of the
interconnects for voltages greater than about 200 volts.

CONCLUDING REMARKS

A cylindrical particle-in-cell plasma simulation code applicable to
plasma densities encountered in low earth orbit is nearing completion.
Results of the calculation of plasma coupling current for the plain disk are
in agreement with experiment for positive voltages. Any deficiencies in the
simulation of the disk and dielectric configuration are due solely to the
interactions of the dielectric. Techniques have been developed which allow
dielectric charging to occur at PIC time scales. The current-voltage
characteristic curves are in qualitative agreement with experiment,
indicating that for these voltage ranges charge sticking and secondary
emission probably adequately describe the dielectric interactions with the
ambient plasma. The amount of secondary emission from the dielectric at low
voltages during the simulations needs to be reduced to match the experimental
current-voltage characteristic curve. Calculations using large ion to
electron mass ratios are made possible by restricting both the grid size and
particle number and simulating the mass ratio effects by moving the ions once
for every n time steps. The square root of the desired ion to electron mass
ratio determines the value of n. Further computational effort is required to
extend the range of the disk and dielectric simulations to higher voltages
and larger mass ratios.

REFERENCES

1. Domitz, Stanley and Norman T. Grier, "The interaction of spacecraft high voltage power systems with the space plasma environment.", NASA TM X-71554, 1974.

2. Stevens, N. J., F. D. Berkopec, C. K. Purvis, N. Grier, and J. Staskus, "Investigation of high voltage spacecraft interactions with plasma environments.", AIAA/DGLR 13th International Electric Propulsion Conference Paper 78-672, 1978

3. Nonnast, J. H., "Numerical simulation of a disk-shaped electron accelerating electrostatic probe.", J. Appl. Phys. 54-2, 1983, pp. 621-631.

4. Chaky, R. C., J. H. Nonnast, and J. Enoch, "Numerical simulation of sheath structure and current-voltage characteristics of a conductor-dielectric in a plasma.", J. Appl. Phys. 52-12, 1981, pp. 7092-7098.

5. Nonnast, J. H., R. C. Chaky, T. P. Armstrong, J. Enoch, and C. G. Wiseman, "Numerical simulation of plasma-insulator interactions in space, Part I: The self-consistent calculation.", Spacecraft Charging Technology - 1980, NASA CP-2182, 1981.

6. Chaky, R. C., J. H. Nonnast, T. P. Armstrong, J. Enoch, and G. C. Wiseman, "Numerical simulation of plasma-insulator interactions in space, Part II: Dielectric effects.", Spacecraft Charging Technology - 1980, NASA CP-2182, 1981.

7. Haffner, J. W., "Secondary electron effects on spacecraft charging.", Spacecraft Charging Technology Conference, NASA CP-2071, 1978.
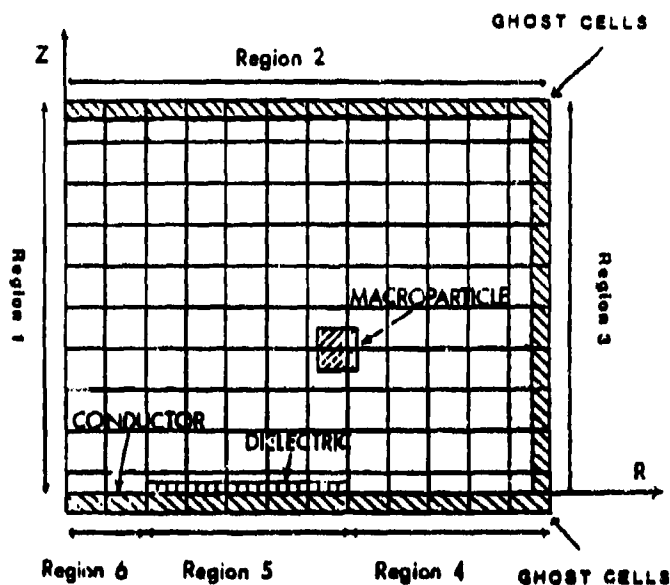
Figure 1. - Simulation grid.

INIT — Sets initial particle locations and velocities, calculates Potential and Electric fields

MOVER —
$$m\ddot{r} = \frac{\ell^2}{mr^3} - \frac{\partial V}{\partial r}$$
"leapfrog" difference equation approximations

BOUNDR — Particles from surrounding plasma inserted with Maxwellian distribution

CHKPRT — Checks if particles have crossed any boundaries

SETCRG — Charge per particle spread over neighboring grid cells using volume weighting

ESPOT — SOR solves a difference equation approximation to POISSON's equation:
$$\Phi_{new}(r,z) = \Phi_{old}(r,z) + \omega R(r,z)$$
Boundary condition over dielectric:
$$\Phi(\delta) = \frac{\xi}{\delta}\left[4\pi\sigma + \frac{\delta}{\xi}\overline{\Phi}(0)\right] + \delta\overline{\Phi}(\Delta z)$$

EFLD — Differentiates Potential to find Electric Fields

Figure 2. - Overview of simulation code.
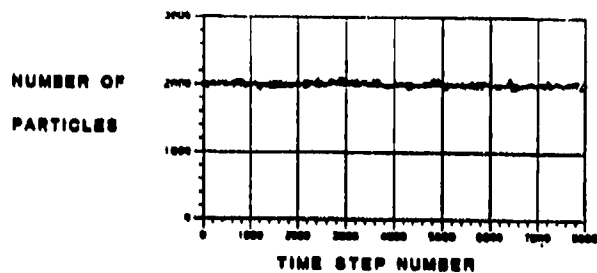
Figure 3. – Simulation of a free plasma – number of particles.
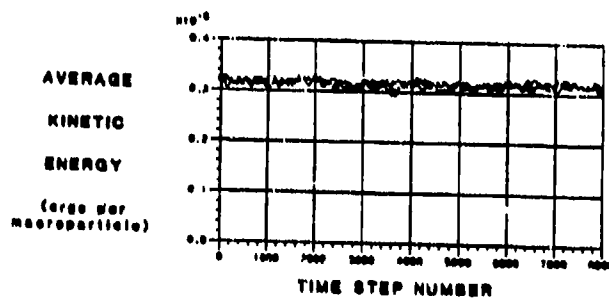
Figure 4. – Simulation of a free plasma – average kinetic energy.

299
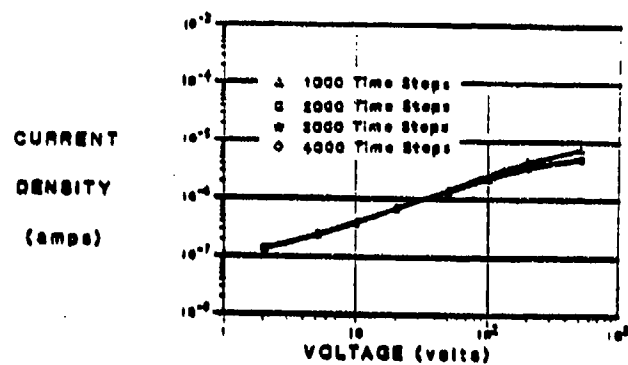
Figure 5. — Approach to equilibrium — plain disk.
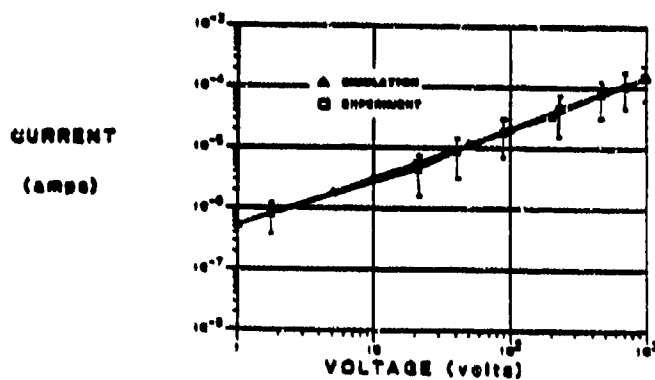
Figure 6. — Comparison with experiment — positive voltage.
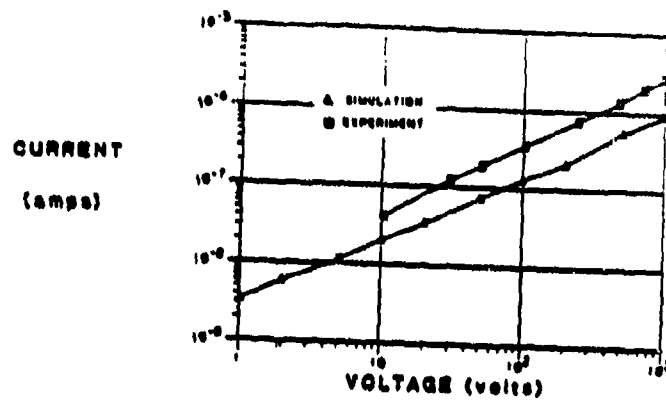
Figure 7. – Comparison with experiment – negative voltage.
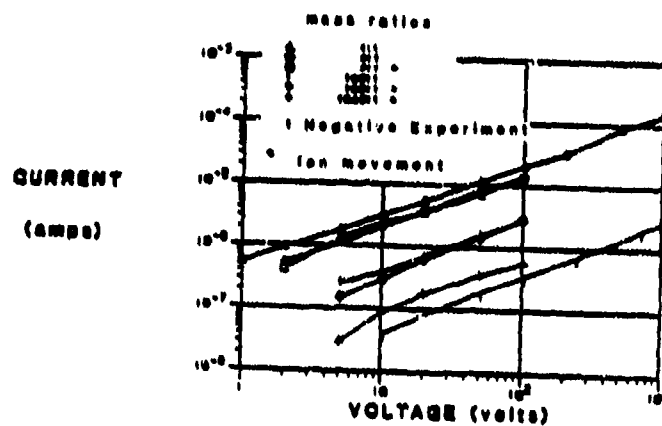
Figure 8.– Large mass ratio calculations.
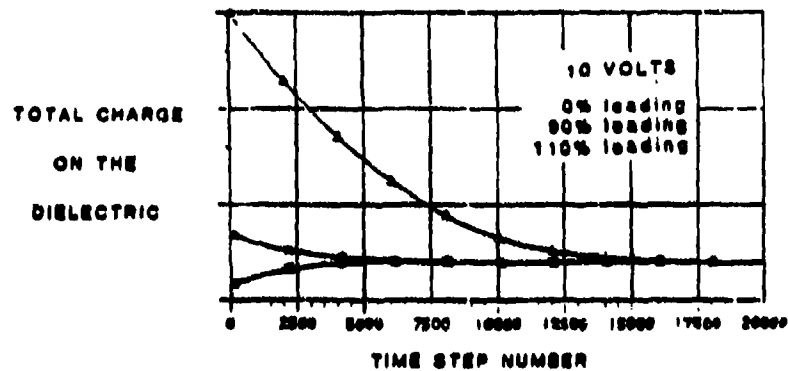
Figure 9. – Approach to equilibrium – effects of loading dielectric with different amounts of charge.
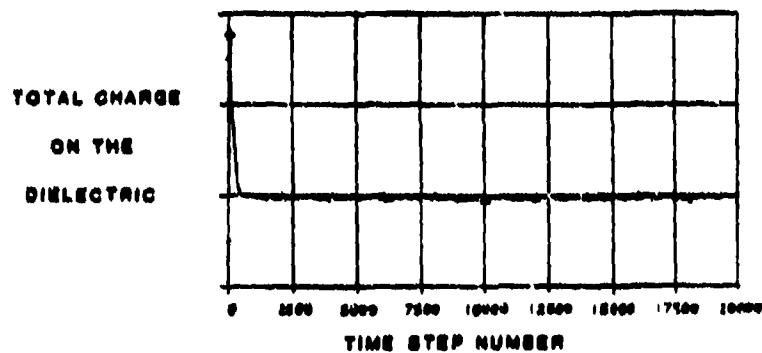
Figure 10. – Approach to equilibrium – effects of increasing δ/ϵ.

301
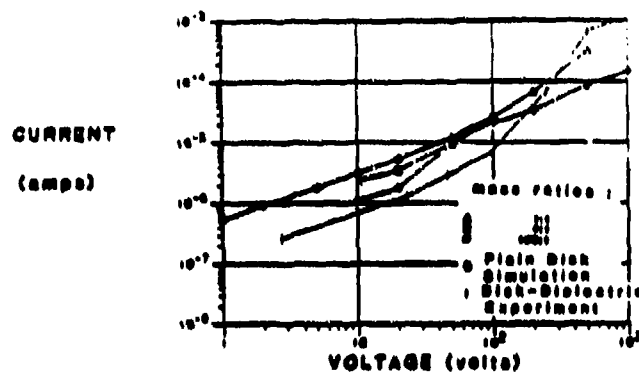
Figure 11. – Disk and dielectric results.
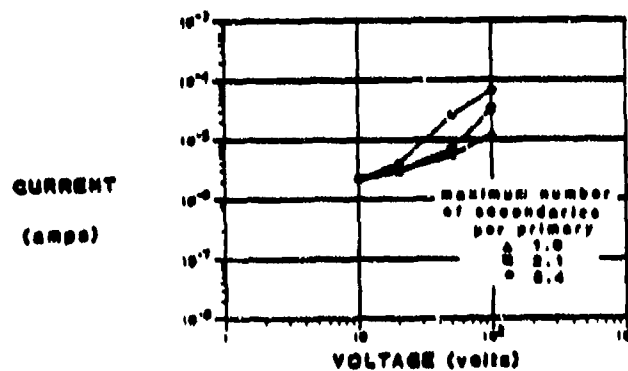
Figure 12. – Variations in secondary emission yields.
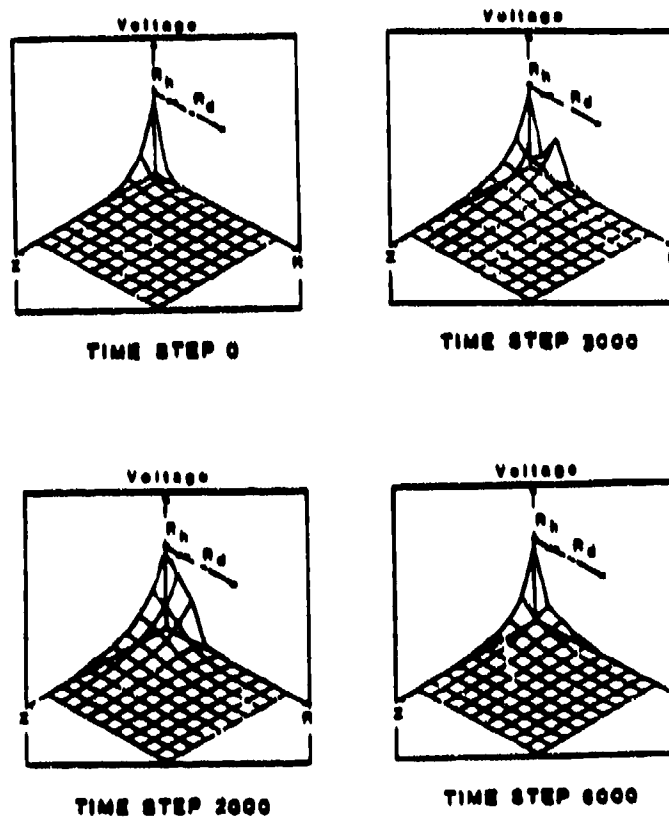
Figure 13. — Snapover effect (potential snapshots).

SURFACE INTERACTIONS AND HIGH-VOLTAGE CURRENT COLLECTION*

M. J. Mandell and I. Katz
S-CUBED
La Jolla, California 92038

Spacecraft of the future will be larger and have higher power requirements than any flown to date. For several reasons, it is desirable to operate a high-power system at high voltage. While the optimal voltages for many future missions are in the range 500-5000 volts, the highest voltage yet flown is ~100 volts. (For a proposed solar power satellite, voltages as high as 40 kV have been mentioned.)

S-CUBED, under contract to NASA/Lewis Research Center, is developing the NASCAP/LEO (ref. 1) code to embody the phenomenology needed to model the environmental interactions of high voltage spacecraft. In this paper we will discuss some aspects of the interaction between a high voltage spacecraft and its plasma environment. We will also describe the treatment of the surface conductivity associated with emitted electrons. Finally, we will excerpt some simulations by NASCAP/LEO of ground-based high-voltage interaction experiments.

PLASMA INTERACTIONS

Table 1 shows two representative low-orbit environments compared with a typical geosynchronous plasma. The low orbit plasma is far colder and denser, resulting in a short (~1 cm) Debye length. The short Debye length is deceptive, however, as a high voltage spacecraft will expel plasma from its vicinity. A better estimate (refs. 2-4) of the collection distance is provided by the Child-Langmuir length

$$D_{CL} = (4\epsilon_0/9)^{1/2} (4\pi/e\theta)^{1/4} n^{-1/2} |\phi|^{3/4}$$

where θ is the plasma temperature (eV), ϕ the surface potential, and n the plasma density. This expression is derived by equating the plasma thermal electron current to the current collected by a space-charge-limited planar diode operating at the surface voltage, and solving for the plate separation. As shown in Table 1, this distance can easily be many meters for a kilovolt bias. It follows that the "sheath surface", which divides the high voltage region from relatively unperturbed plasma, will not be within a few Debye lengths of the

spacecraft surface (thin sheath approximation), nor will it be far distant from the spacecraft (orbit-limited approximation), but it will be in an intermediate regime such that the full spacecraft geometry must be taken into account.

TABLE 1.-TYPICAL PLASMA PARAMETERS FOR LEO AND GEO

	GEO (Typical)	LEO (Low Density)	LEO (High Density)
Density (m^{-3})	10^6	10^{10}	10^{12}
Temperature (eV)	10^3	0.3	0.1
Debye Length (m)	235	0.04	0.002
Electron Thermal Current (A/m^2)	10^6	10^{-4}	10^{-2}
Ram Ion Current (A/m^2)	5×10^{-10}	10^{-5}	10^{-3}
Ion (O^+) Mach Number	0.04	6.0	10.0
Current Collection D_{CL}	Orbit Limited	Space-Charge Limited 22 m at 1 kV	Space-Charge Limited 3 m at 1 kV

Currents to a large spacecraft are indicated schematically in figure 1. The primary current to the negative surfaces consists of ram ions, while the positive surfaces collect thermal electrons. As the ram ion current is only about one-tenth the electron thermal current, the spacecraft will float about 90 percent negative. However, for high bias the ion current will be enhanced by ion-generated secondary electrons. An additional source current to negative surfaces is charge blowoff from arc discharges. As discussed elsewhere in this volume (refs. 5-7), discharges on solar arrays have been observed for negative biases as low as ~250 V.
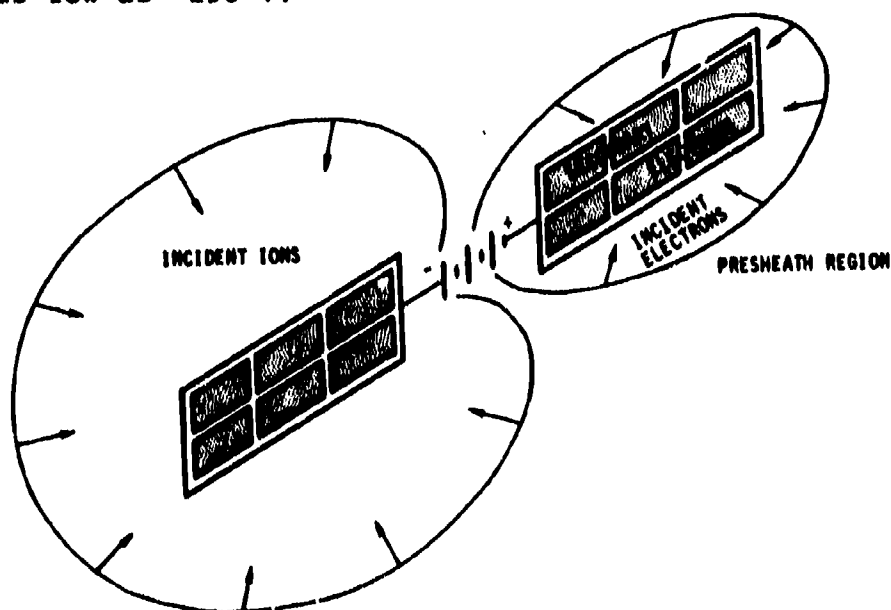
Figure 1.   A high-voltage spacecraft collects ions and electrons from a plasma.

Positive surfaces attract plasma electrons, and the resultant secondary electrons form a conductive layer over the surface, as discussed below. Due to smoothing of voltage gradients provided by this effect, positively biased array surfaces are much less likely to arc than negatively biased surfaces.

The plasma currents collected by array surfaces constitute a parasitic current through the array. The effects of this parasitic current on array operation were discussed at the 1978 Spacecraft Charging Technology Conference by Domitz and Kolecki (ref. 8). As shown in figure 2a, solar cells maintain a nearly constant voltage up to a maximum current. When this current is exceeded the voltage drops sharply to zero. Clearly, it is advantageous to operate as closely as possible to the solar cell's power peak (figure 2b). Figure 3a illustrates that plasma current is collected in a distributed fashion over the array. The parasitic current at any point of the array is the integral of the plasma current density. Figure 3b shows a case in which a relatively small parasitic current, when added to the load current, shorts out the central portion of the array.

THE NASCAP/LEO CODE

NASCAP/LEO is being developed to predict self-consistently surface potentials, collected currents, and spatial electric fields for high voltage spacecraft in dense plasmas. While much of the code's algorithmic structure is adapted from the widely used NASCAP code (ref. 9), NASCAP/LEO also contains several noteworthy features necessary for modeling the intended physical regimes.

NASCAP/LEO has NASCAP-like object definition routines. Like NASCAP, the object is contained in a primary grid (figure 4), which may be surrounded by one or more outer grids with successively doubled mesh spacing. Enhancements include the ability to put mirror planes coincident with one or more of the inner grid boundary planes, and to include subdivided regions in the primary grid in order to resolve small but important object features.

Space charge, which is typically ignored in NASCAP, is treated by NASCAP/LEO as a local, nonlinear function of potential. Presently the function is taken to be

$$\rho = -(\varepsilon_o \phi / \lambda_D)^2 \ [1 + \sqrt{4\pi} \ (\phi/\theta)^{3/2}]^{-1}$$

A particularly important enhancement in NASCAP/LEO is the ability to apply either potential or normal-electric-field boundary conditions to each surface cell. The field condition is used for cells whose potential is governed by emission of low energy electrons (see below).

To calculate plasma currents, NASCAP/LEO defines the sheath surface as a specified equipotential, and tracks representative particles inward. The current represented by each particle is determined taking into account ram effects as well as the local plasma density and temperature. Care is taken not to generate sheath particles in regions from which plasma is excluded by high fields or by nearby object surfaces. Thus NASCAP/LEO determines the ion and electron currents to an

307
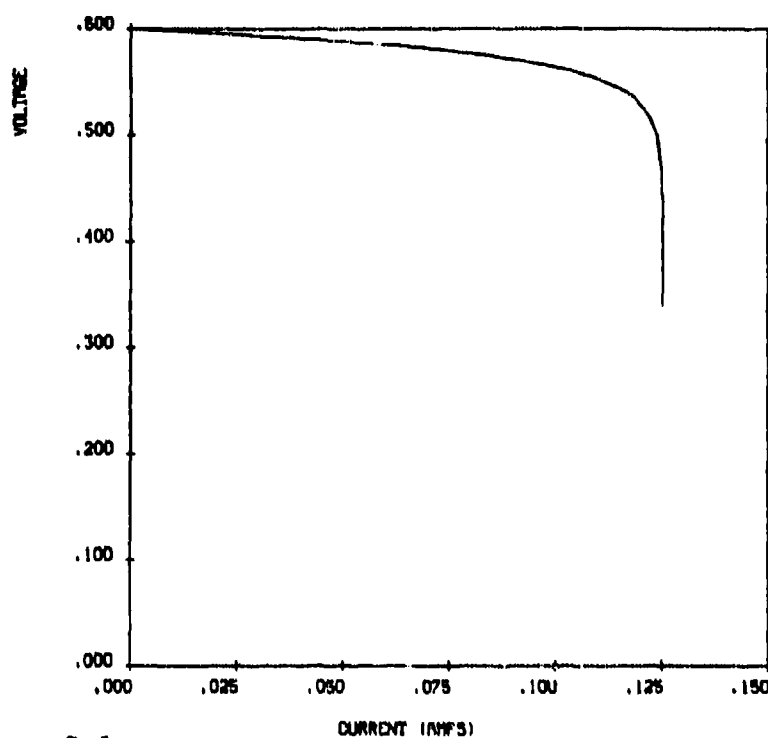
Figure 2a.   Solar cell voltage versus current, according to
Domitz and Kolecki (ref. 8).
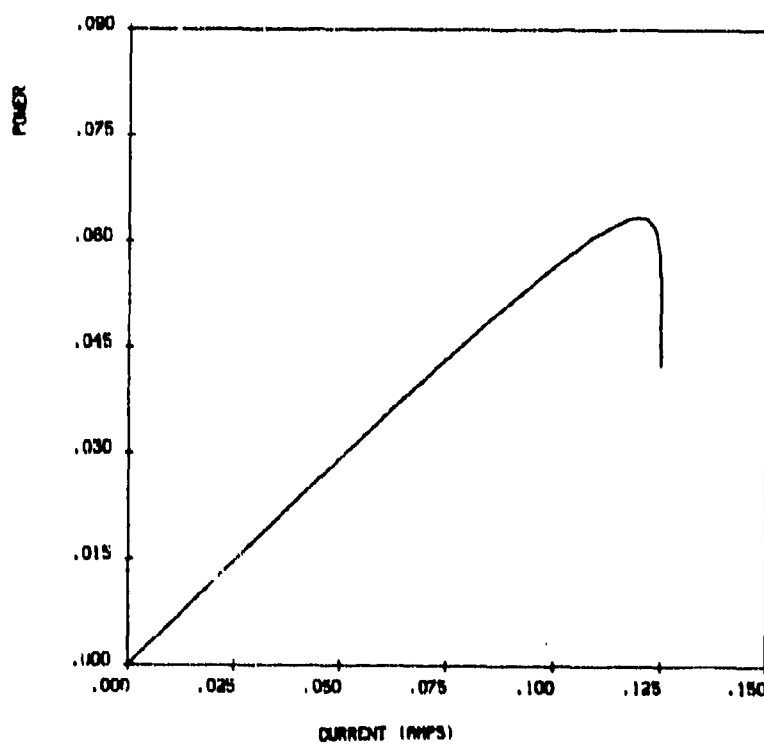
Figure 2b.   Solar cell power delivered to load versus
current, according to Domitz and Kolecki (ref. 8).

308
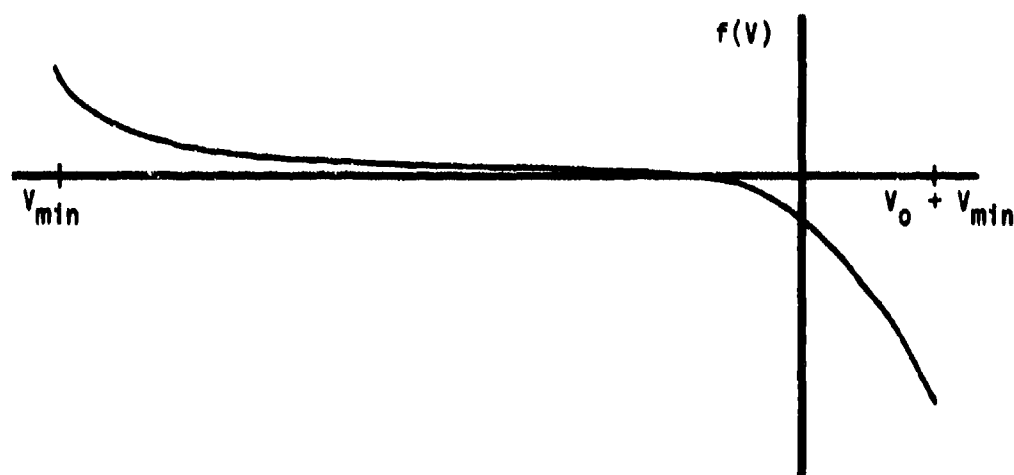
Figure 3a. Plasma current density, f(V), to a solar array (schematic).
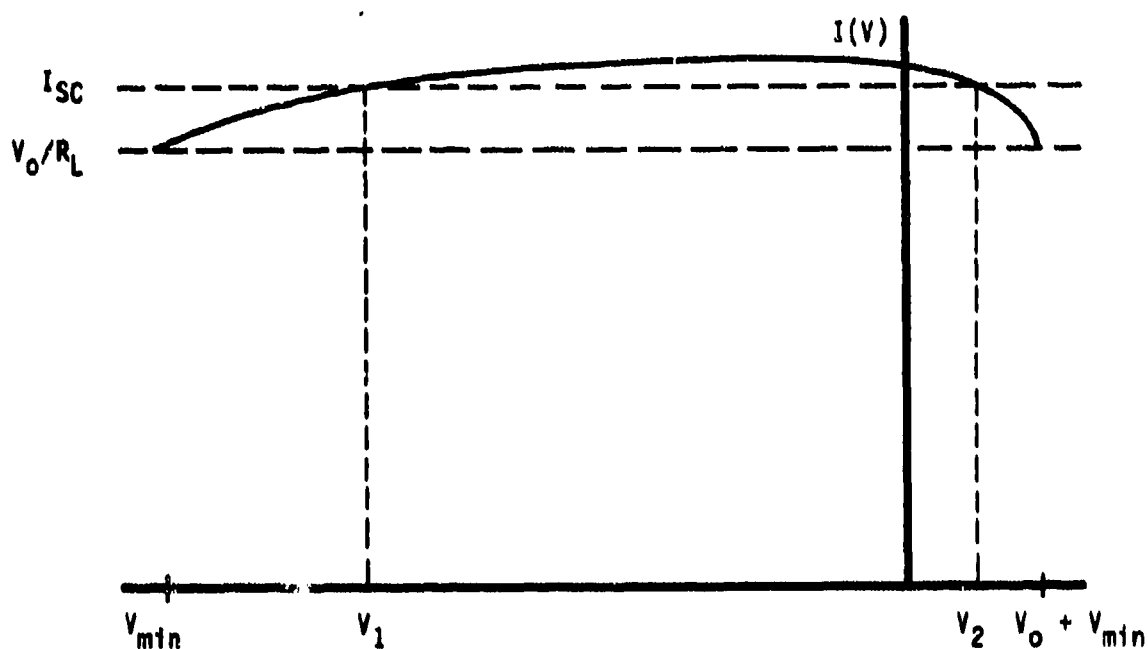
Figure 3b. Total array current as a function of voltage (solid line; schematic), consists of load current, V_0/R_L, plus parasitic current. For this case, a substantial part of the array will be shorted out.
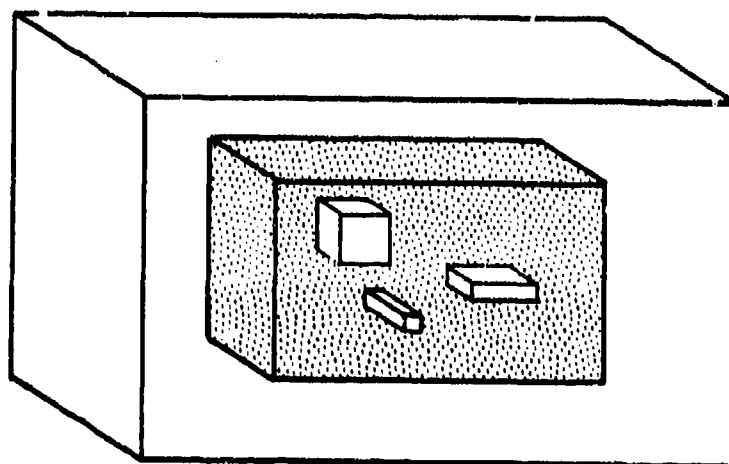
Figure 4. NASCAP/LEO grid structure, showing primary grid (shaded), outer grid, and locally subdivided regions.

object, as well as the distribution of current over the object.

ELECTRIC FIELD BOUNDARY CONDITIONS

For electron attracting insulating surfaces dominated by secondary electron emission, NASCAP/LEO sets an electric field boundary condition such that the incident electron current is balanced by a net outflow of secondaries to neighboring surfaces. The derivation of electron hopping conductivity has been presented elsewhere (refs. 10-11), but we repeat it here for completeness, then proceed to derive the electric field boundary condition.

Assume a surface has an electron-attracting (positive) surface-normal component of electric field, $E_\perp$, and emits a low energy electron current $-J_e(A/m^2)$. These electrons travel in parabolic orbits, with "flight time", τ, given by

$$\tau = 2 \ [2m\langle\epsilon\rangle/e \ E_\perp^2]^{1/2}$$

where m is the electron mass and $\langle\epsilon\rangle$ is the (appropriately averaged) electron energy. These electrons form a charge density (coul/m^2) given by $-J_e\tau$. This surface charge layer will be accelerated by any transverse electric field, $E_\parallel$, to a mean velocity of $-e \ E_\parallel\tau/2m$, and thus constitutes a surface current, K (A/m) given by

$$K = (-J_e\tau^2/2)(-e \ E_\parallel/m) = 4 \ J_e \ E_\parallel\langle\epsilon\rangle/E_\perp^2 = \sigma_\parallel E_\parallel$$

The last relation defines the transverse conductivity, $\sigma_\parallel$ (ohms^{-1}).

To derive the electric field boundary condition, we further assume that the emitted current is proportional to the incident current, J_{in}:

$$J_e = -Y \ J_{in}$$

310

Current balance requires that

$$J_{in} = \nabla \cdot (\sigma_\parallel E_\parallel) .$$

Since the previous derivation assumed uniform fields, it is no further approximation to remove $\sigma_\parallel$ from the divergence, giving

$$J_{in} = [4(-Y J_{in}) <\epsilon>/E_\perp^2] (\nabla \cdot E_\parallel) .$$

The incident current cancels from the above equation, which may then be solved for the desired condition:

$$E_\perp = [-4 Y<\epsilon> (\nabla \cdot E_\parallel)]^{1/2} .$$

ILLUSTRATIVE CALCULATIONS

To illustrate the type of information obtainable from the NASCAP/ LEO code we present results from three previously published simulations of laboratory experiments. For more details we refer the reader to the original publications (refs. 1, 2, 12).

Early NASCAP/LEO calculations were restricted to potentials about, and current collection by, surfaces of known potential. McCoy and Konradi (ref. 3) reported at the 1978 Spacecraft Charging Technology Conference experiments on a biasable metal strip, about 10 meters long, mounted on insulating plastic. Figure 5 shows sheath trajectories for cases in which the metal strip was linearly biased. The four cases are 0-600 V, 0-1200 V, 0-2400 V, and 0-4800 V. The shape of the sheath, as indicated by the plotted trajectories, is in agreement with observations by low-light-level television. Also, the calculated and measured currents are in good agreement.

NASCAP/LEO was later improved to predict the spread of high voltages onto insulating surfaces. N. John Stevens (ref. 13) reported experiments in which a 3.5 cm diameter biased metal disk (figure 6) was surrounded by either grounded metal or by kapton, and the collected current was measured. For the "plain disk" case (figure 7) agreement was excellent. The Disk-on-Kapton case (figure 8) is far more diffi- cult, as the kapton enhances collected current at high bias voltage, and suppresses it at low voltage. While the simulation results were in fair agreement at high bias, both for collected current and insula- tor surface voltage (figure 9) they did not predict the low voltage current suppression. This was because the charging algorithm at the time was unable to predict negative charging of the kapton surfaces.

A similar experiment was reported by S. Gabriel et al. (ref. 15), who used an emissive probe to measure the electrostatic potential in the plasma over a biased "pinhole". The computer model (figure 10) made use of the NASCAP/LEO subdivision capability to get good spatial resolution in the neighborhood of the pinhole. For negative bias (figure 11) agreement was excellent. Fairly good agreement was also obtained for positive bias (figure 12), although the experiment showed more distinction between two different plasmas than the calculations predicted. Good agreement was achieved as well for the collected currents. This latter calculation showed the utility of the
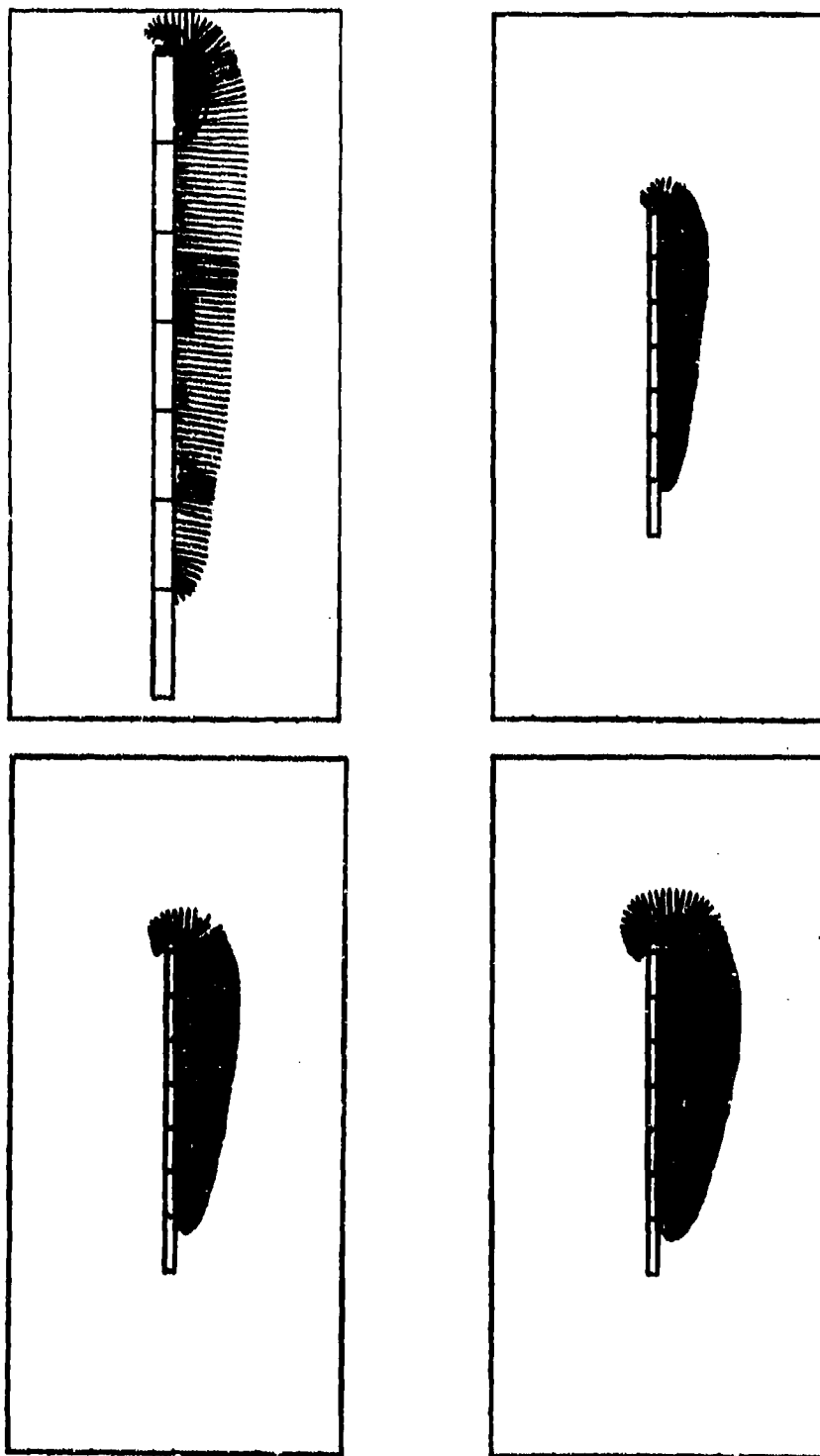
Figure 5. Sheath particle trajectories for an array linearly biased 0-600 volts (upper left; twice scale); 0-1200 volts (upper right); 0-2400 volts (lower left); and 0-4800 volts (lower right).

KAPTON OR GROUNDED METAL

GROUNDED METAL

BIASED DISK

|← 3.5 cm →|

|← 20 cm →|
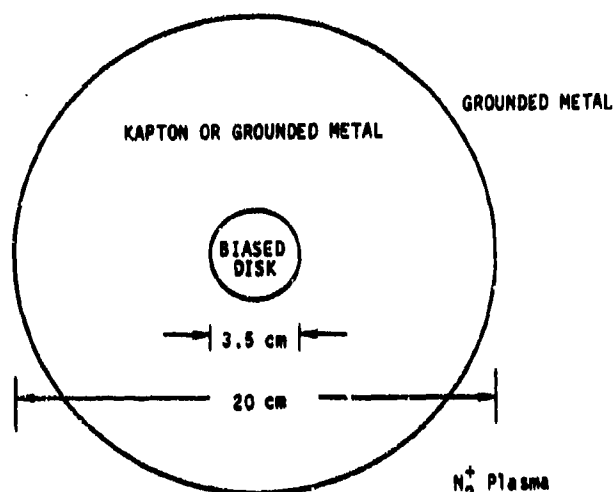
N_2^+ Plasma

$\rho = 2 \times 10^4$ cm^{-3}

$\theta = 1$ eV

Figure 6. Plain disk experiment - tests treatment of external potentials and currents; disk-on-kapton experiment - tests treatment of insulator charging (from ref. 13).
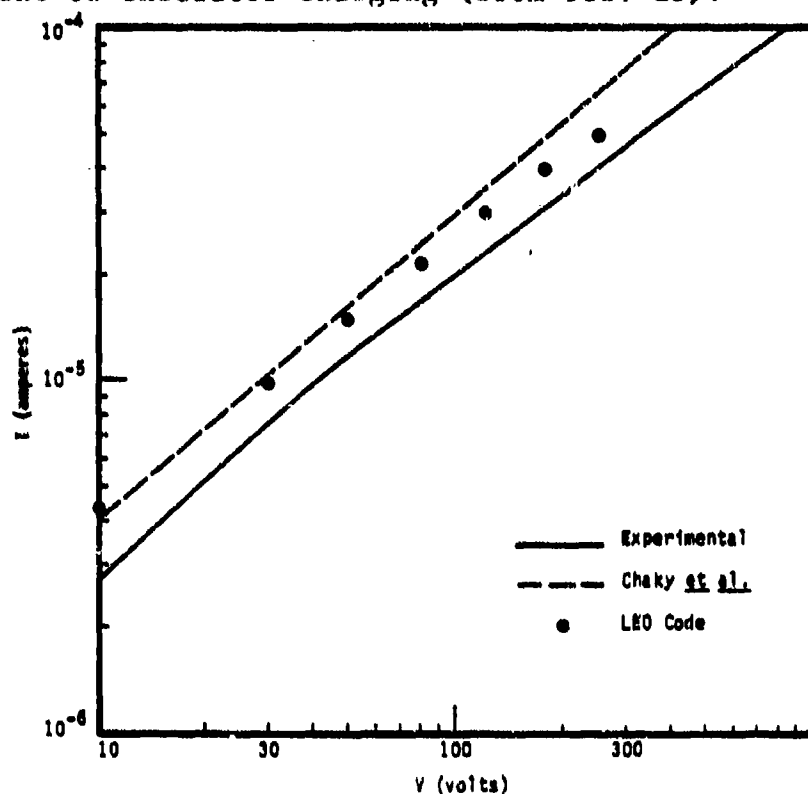
Figure 7. Current collected by a biased disk surrounded by grounded metal. The dashed curve is a prediction by a two-dimensional particle-in-cell code (ref. 14).

313
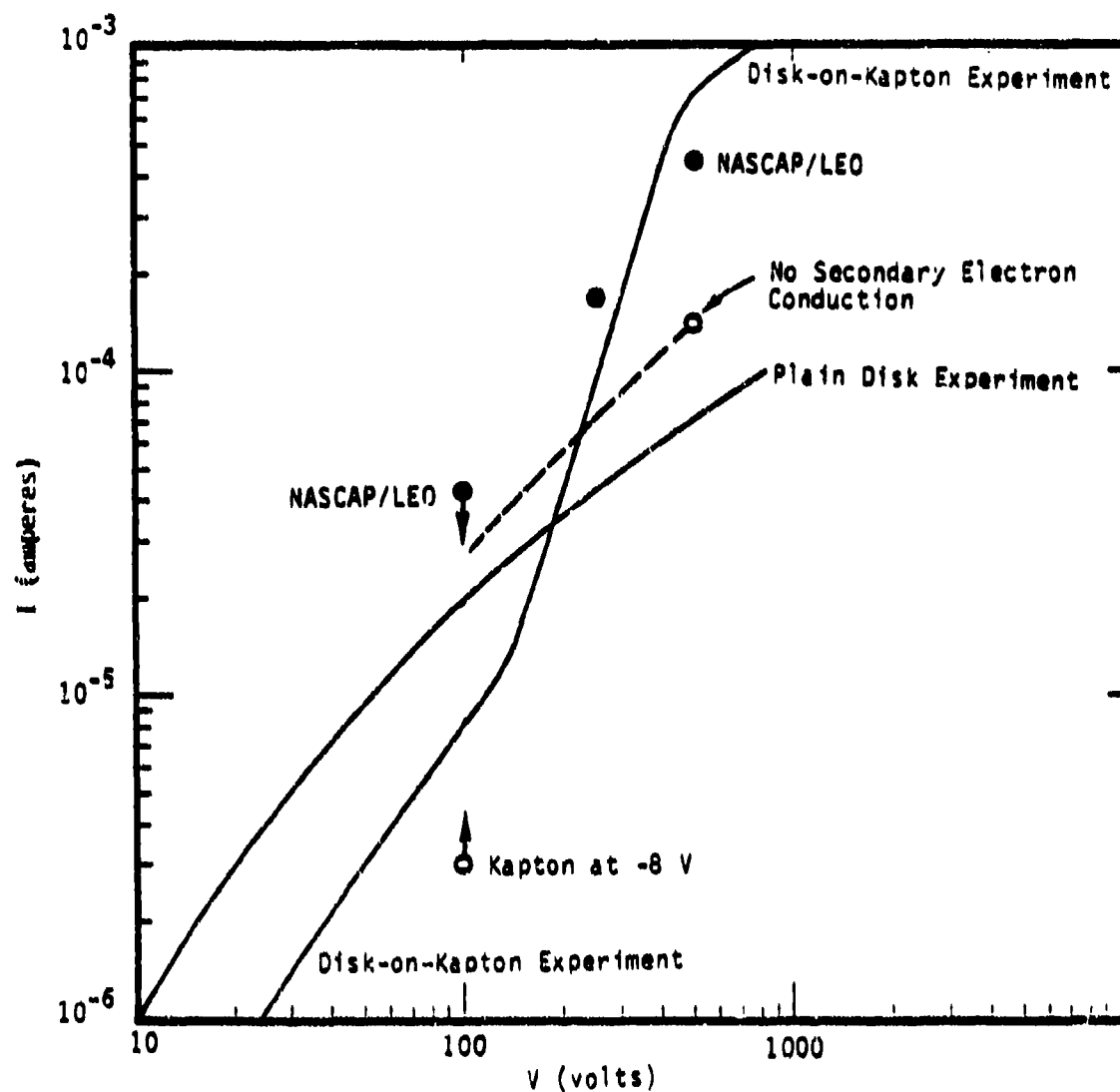
Figure 8. Current collected by a biased disk surrounded by kapton. For high bias, NASCAP/LEO correctly predicts current enhancement (relative to the plain disk). For low bias current is suppressed due to accumulation of negative charge on the kapton. At the time of the calculation the NASCAP/LEO charging algorithm did not predict negative floating potential for insulators.
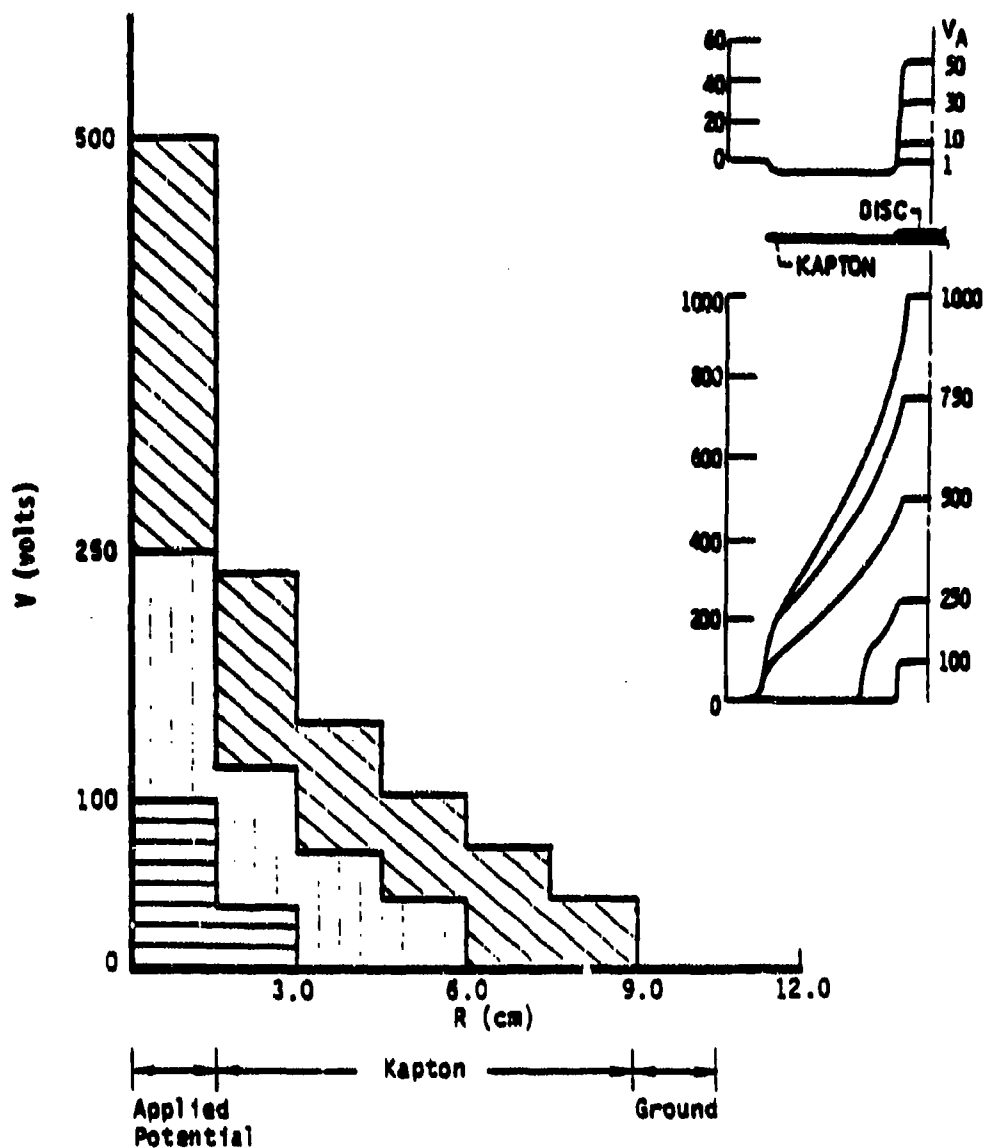
Figure 9. For high bias, NASCAP/LEO is in good agreement with
experiment (inset) concerning the spread of high
voltage onto the insulator.
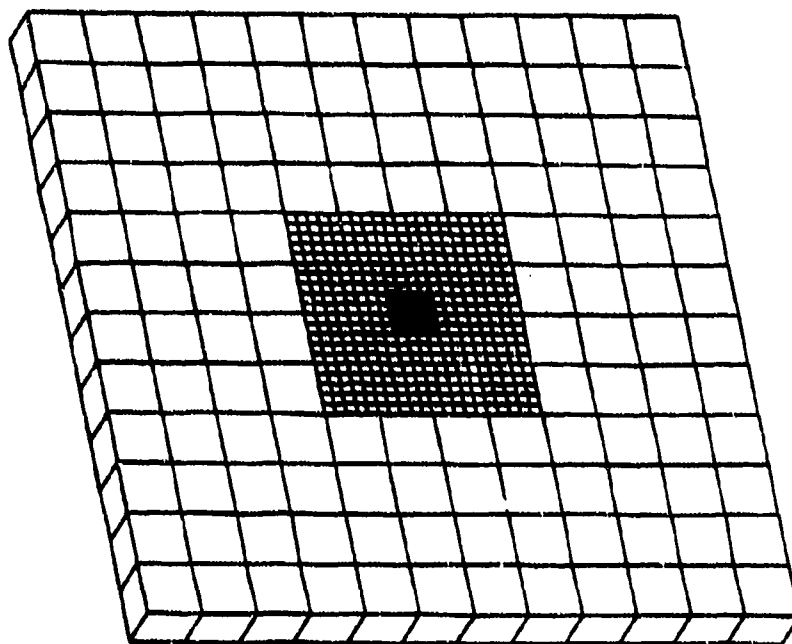
Figure 10.   NASCAP model of biased pinhole experiment, showing sub-
grid resolution of insulator surrounding 1.27 cm pinhole
(central black area).   The major grid resolution is
1.46 cm, and the subdivided region resolution is 0.29 cm.
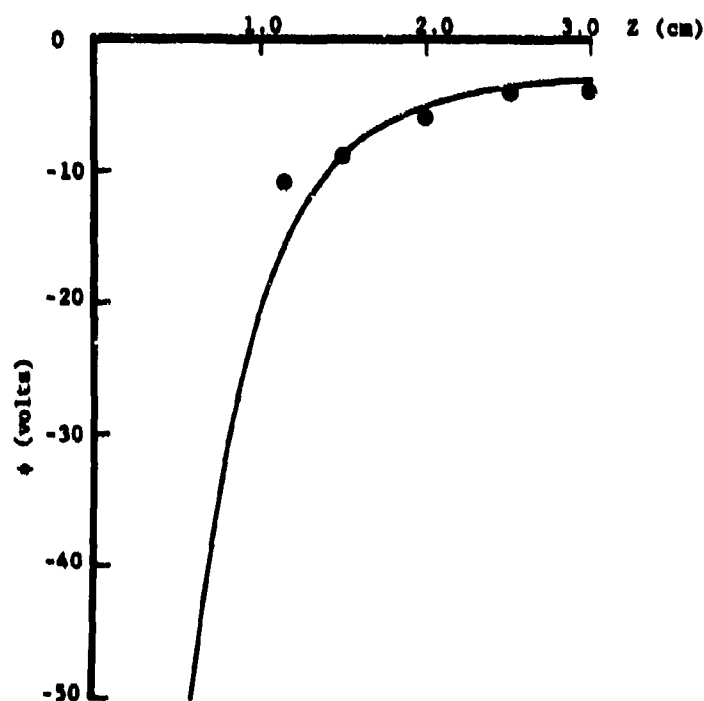
Figure 11.   Potentials on axis for 0.64 cm diameter pinhole at
-452 V.   Solid line: Calculated with kapton at 0 volts;
Points: Experiment.
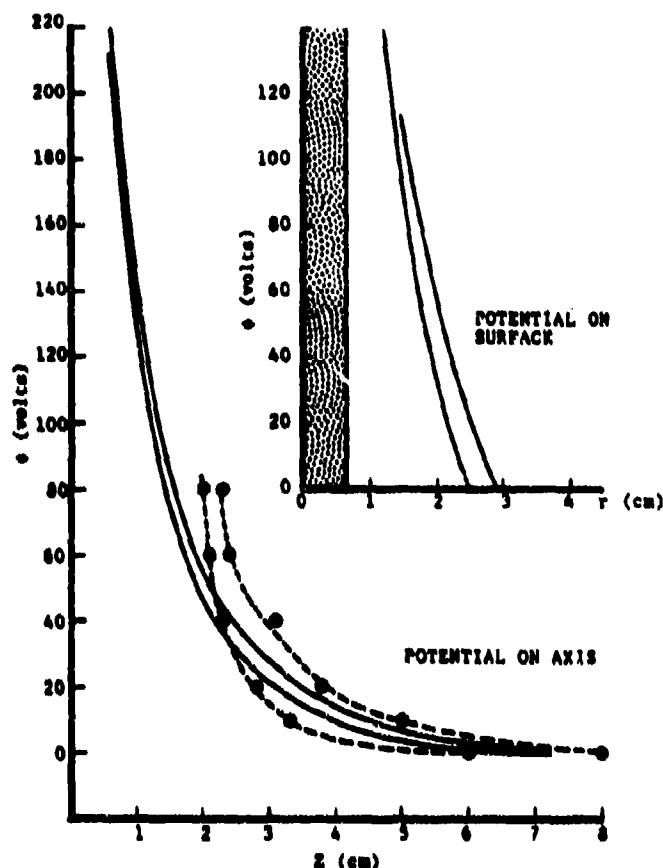
Figure 12. Potentials for 1.27 cm diameter pinhole.
Solid curves: Calculation.
Dashed curves: Experiment.
Upper curves: $n_e = 2.5 \times 10^4$ cm^{-3}, $\theta = 5.3$ eV.
Lower curves: $n_e = 5.8 \times 10^4$ cm^{-3}, $\theta = 4.0$ eV.

subdivision capability, and validated our electric field boundary condition model for the secondary electron layer.

FUTURE DEVELOPMENT

We plan to develop NASCAP/LEO for use as a reliable design tool. Among the planned improvements are prediction of spacecraft floating potential, treatment of sheath ionization, improved ram-wake model, generalization to full NASCAP geometry, and self-consistent power system representation. Validation/improvement cycles will continue at each stage, aided by both ground-based and space-based experiments.

REFERENCES

1. Katz, I.; Mandell, M. J.; Schnuelle, G. W.; Parks, D. E.; and Steen, P. G.: Plasma Collection by High-Voltage Spacecraft at Low Earth Orbit. J. Spacecraft and Rockets, 18, 1981, p. 79.

317

2. Mandell, M.J.; Katz, I.; and Cooke, D. L.: Potentials on Large Spacecraft in LEO. IEEE Transactions on Nuclear Science, NS-29, December 1982, pp. 1584-1586.

3. McCoy, J. E.; and Konradi, A.: Sheath Effects Observed on a 10 meter High Voltage Panel in Simulated Low Earth Orbit Plasma. Spacecraft Charging Technology-1978, NASA CP-2071, AFGL-TR-79-0082, 1978.

4. Cooke, D. L.; Parker, L. W.; and McCoy, J. E.: Three-Dimensional Space Charge Model for Large High-Voltage Satellites. Spacecraft Charging Technology-1980, NASA CP-2181, AFGL-TR-81-0270, 1981.

5. Grier, N. T.: Plasma Interaction Experiment II: Laboratory and Flight Results. Spacecraft Environment Interactions Technology Conference, Colorado Springs, CO, October 4-6, 1983.

6. Miller, W. L.: An Investigation of Arc Discharging on Negatively-Biased Dielectric-Conductor Samples in a Plasma. Spacecraft Environment Interactions Technology Conference, Colorado Springs, CO, October 4-6, 1983.

7. Snyder, D.: The Time Dependence of Discharges from a Biased Solar Array. Spacecraft Environment Interactions Technology Conference, Colorado Springs, CO, October 4-6, 1983.

8. Domitz, S.; and Kolecki, J. C.: Effect of Parasitic Plasma Currents on Solar Array Power Output. Spacecraft Charging Technology-1978, NASA CP-2071, AFGL-TR-79-0082, 1979.

9. Katz, I.; Cassidy, J. C.; Mandell, M. J.; Schnuelle, G. W.; Steen, P. G.; and Roche, J. C.: The Capabilities of the NASA Charging Analyzer Program. Spacecraft Charging Technology-1978, NASA CP-2071, AFGL-TR-79-0082, 1979.

10. Mandell, M. J.; Katz, I.; and Schnuelle, G. W.: Photoelectron Charge Density and Transport Near Differentially Charged Space-craft. IEEE Transactions on Nuclear Science, NS-26, 1979, p. 5107.

11. Pelizzari, M. A.; and Criswell, D. R.: Differential Photoelectric Charging of Nonconducting Surfaces in Space. Journal of Geophysical Research, 83, 1978, p. 5233.

12. Mandell, M. J.; Katz, I.: Potentials in a Plasma Over a Biased Pinhole. Presented at 1983 IEEE 20th Annual Conference on Nuclear and Space Radiation Effects, Gatlinburg, TN, July 18-21, 1983; to be published in IEEE Transactions on Nuclear Science, NS-30, December 1983.

13. Stevens, N. J.; Berkopec, F. D.; Purvis, C. K.; Grier, N.; and Staskus, J.: Investigation of High Voltage Spacecraft System Interactions with Plasma Environments. AIAA/DGLR Electric Propulsion Conference, AIAA Paper No. 78-672, 1978.

14. Chaky, R. C.; Nonnast, J. H.; and Enoch, J.: A Numerical Simulation of Plasma-Insulator Interactions in the Spacecraft Environment. Journal of Applied Physics, 52, 1981, p. 7092.

15. Gabriel, S. B.; Garner, C. E.; and Kitamura, S.: Experimental Measurements of the Plasma Sheath Around Pinhole Defects in a Simulated High-Voltage Solar Array. AIAA Paper No. 83-0311, AIAA 21st Aerospace Sciences Meeting, Reno, NV, January 10-13, 1983.

THE PIX-II EXPERIMENT: AN OVERVIEW

Carolyn K. Purvis
National Aeronautics and Space Administration
Lewis Research Center
Cleveland, Ohio 44135

The second Plasma Interactions Experiment (PIX-II) was launched in January 1983 as a piggyback on the second stage of the Delta launch vehicle that carried IRAS into orbit. Placed in a 870-km circular polar orbit, it returned 18 hr of data on the plasma current collection and arcing behavior of solar array segments biased to ±1000 V in steps. The four 500-cm^2 solar array segments were biased singly and in combinations. In addition to the array segments PIX-II carried a sun sensor, a Langmuir probe to measure electron currents, and a hot-wire filament electron emitter to control vehicle potential during positive array bias sequences. Like its predecessor, PIX-I, PIX-II was designed, built, and tested at the NASA Lewis Research Center. This paper provides an overview of the PIX-II experiment from program and operational perspectives.

INTRODUCTION

Most U.S. spacecraft to date have used low-voltage solar arrays, generating power at ~30 V. The highest voltage array flown by NASA was on Skylab, which had an array voltage of 70 to 115 V and generated 16 kW of power. Space stations and other large future systems will require increasing power generation capability. As power levels increase, the weight and I^2R power loss penalties for maintaining low solar array voltages increase dramatically (refs. 1 to 3). Power systems generating hundreds of kilowatts are required for such missions as the space station. At these power levels, voltages of at least a few hundred volts are required to reduce internal resistive losses within the array and to reduce the wiring harness mass required to transport the power. This need to operate at higher voltages has spurred evaluation of high-voltage solar array operation in space.

Solar array systems consist of strings of solar cells with metallic interconnects between them. These interconnects are at voltages that depend on their positions in the array circuit and are usually exposed to the environment. When these systems are placed in orbit, they will interact with the naturally occurring space plasma. Two types of potentially hazardous interactions to an isolated solar array in orbit are presently recognized: power loss from parasitic currents through the plasma, and arcing. Both of these interactions are plasma density dependent and present greater hazards at higher densities. The low temperature ionospheric plasma has a peak density (of ~10^6 particles/cm^3) at about 300-km altitude (ref. 4). High-voltage system - plasma interactions will therefore be most severe in low Earth orbits.

The PIX-II experiment was conducted to provide flight data on high-voltage solar array - plasma interactions. These data are being analyzed to calibrate ground simulation results and to guide and validate modeling efforts. This paper presents the background, describes the experiment, and summarizes the

operational sequences that characterize the data set. The following papers describe some results of the data analysis.

BACKGROUND

Investigation of interactions between high-voltage systems and thermal plasmas was begun in the late 1960's. Experimental work using small segments of solar arrays and insulated electrodes with pinholes indicated that the presence of the insulators caused plasma current collection phenomena that departed dramatically from the predictions of Langmuir probe theory. Experiments indicated greatly enhanced electron collection at voltages in excess of about +150 V and arcing on solar array segments biased several hundred volts negative with respect to plasma ground. Concern for the implications of these results for high-voltage systems in orbit prompted the development of the SPHINX (Space Plasma High Voltage Interactions Experiment) satellite (ref. 5). SPHINX was launched in early 1974 but failed to attain orbit due to a launch vehicle malfunction.

After the loss of SPHINX, the attention of the environmental interactions community was for several years focused on investigating spacecraft charging, an interaction that had been found to be hazardous for geosynchronous spacecraft and was intensively studied by NASA and the Air Force. In the late 1970's, interest in high-voltage interactions again intensified, and their study was resumed under the auspices of the joint NASA/USAF Environmental Interactions Technology Investigation (ref. 6). The ground technology program utilizes the experimental facilities at NASA and USAF centers and builds on the modeling capabilities developed during the spacecraft charging investigation, as well as using the earlier high-voltage-study results (refs. 7 to 12). The goal is to develop guidelines and analytical tools to guide the design of large high-voltage systems in Earth orbit. The approach is to perform experiments and develop models in an interactive program in which experimental results are used both to guide and validate the models.

The ground technology programs require complementary flight experiment data to calibrate the ground-based testing, to guide and validate the models, and to investigate experimental conditions not obtainable in ground facilities. The first such data were obtained by the Plasma Interaction eXperiment-I (PIX-I) which flew in March 1978 as a piggyback on a second-stage Delta launch vehicle. It remained with the Delta stage, operating in a 900-km circular near-polar orbit for 4 hr. About 2 hr of data were returned by real-time telemetry. The mission time was limited by the lifetime of the second-stage Delta's telemetry battery; data return was limited by the real-time recovery requirement. The PIX-I results verified that the electron collection enhancement and arcing phenomena observed in ground tests also occur in space (ref. 13).

THE PIX-II EXPERIMENT

Objectives and Approach

The basic objectives of the PIX-II experiment were to acquire flight data for use in calibrating the ground simulation facilities and in developing and validating models. Because the orbital environment cannot be duplicated on the ground, flight data are required to evaluate the effect of simulation inadequacies on the plasma collection and arcing response of solar arrays. Of

particular concern for PIX-II were the current collection and arc threshold behavior of array segments in proximity to one another.

The approach chosen was to divide the experimental array into four independently biasable segments, each of area about 500 cm². These were biased in a preprogrammed sequence in various combinations, in voltage steps to ±1000 V. Currents collected by each of the array segments were measured by electrometers. A hot wire filament electron emitter was included to avoid large negative potential excursions of the vehicle during high positive bias conditions on the arrays. A spherical Langmuir probe and a sun sensor were included to provide plasma diagnostic and orientation information. The package was designed as a piggyback experiment to remain with the second stage of a Delta launch vehicle.

Experiment System

The PIX-II experiment was designed and built at Lewis. The design was based on that of PIX-I, with a number of changes incorporated to improve the quality and quantity of data obtained.

PIX-II consisted of two major subassemblies: the electronics enclosure box and the experiment plate. These were located 180° from each other around the Delta's circumference (fig. 1).

The experiment plate (fig. 2) was 91.4 cm (36 in) in diameter, truncated to 81.3 cm (32 in) at the top to fit the launch vehicle. The four-segment solar array, 48.3 by 40.6 cm (19 by 16 in), was located on the front center of the plate. The 134° acceptance angle sun sensor was located 5.7 cm (2.25 in) above the solar array and 7.0 cm (2.75 in) to the left of center.

For thermal control the space-facing side of the experiment plate, except for the arrays, was covered with a single layer of 2.5×10^{-3} cm (1 mil) aluminized Kapton coated with a black conductive paint (Sheldahl G113600), black side out. This sheet was attached to the plate with Kapton tape and stainless steel screws, the latter providing electrical grounding for the black coating.

The solar cells used on the PIX-II program were flight-qualified cells identical to those used on other flight programs. The cells were 2- by 2-cm silicon solar cells 0.03 cm (0.012 in) thick with a bulk resistivity of 10 ohm-cm. The coverslides were type 7940 silica 0.05 cm (0.020 in) thick. The cells were configured in segments, each consisting of 19 series-connected submodules. Each submodule consisted of six parallel-connected solar cells. There were 114 solar cells per segment, so the the total number of cells flown was 456. For comparison, 24 cells were flown on PIX-I. The peak power capability of the solar panel was 25 W, but no power was drawn from the cells since each segment was shorted from one end to the other.

Each segment was mounted on a fiberglass sheet. All four segments were bonded with polyurethane adhesive to a 0.013-cm (5-mil) thick, 40.6- by 53.3-cm (16- by 21-in) Kapton sheet to achieve good electrical isolation. The Kapton sheet was bonded with polyurethane adhesive to a 0.95-cm (0.375-in) thick aluminum substrate of the same dimensions as the sheet. This assembly was bolted to the experiment plate.

The sun sensor, used to indicate the test array orientation relative to the sun was a vertical multijunction solar cell. It worked into a fixed resistor to provide a 0- to 4-V signal whenever the Sun was within its 134° field of view. Its location on the experiment plate is shown in figure 2.

The electronics enclosure box (fig. 3) was a rectangular structure 58.4 by 54.6 by 30.5 cm (23 by 21.5 by 12 in). It housed the experiment electronics and battery and supported the deployable Langmuir probe and the hot-wire filament electron emitter probe. The outside surfaces of the box were covered with a multilayer insulation (MLI) blanket of 0.00254 cm (1 mil) aluminized Kapton. The outer-facing layer was 0.00254-cm (1-mil) aluminized Kapton covered with an electrically conductive black coating of Sheldahl G113600, black side out. The MLI blanket and black coating were electrically grounded with straps connected to the structure.

The interior of the enclosure box consisted of three stiffened trays of shelves to which the various electronics boxes and the experiment battery were attached.

The high-voltage power supply provided a programmable voltage to the PIX-II solar array experiments via the electrometer package. It was programmable to provide 32 voltage steps from 0 to 1 kV. It accepted 24 to 32 V dc input to a maximum power of 110 W and outputted 0- to 1-kV positive voltages at 80-mA maximum current and 0- to 1-kV negative voltages at 4-mA maximum current.

The PIX-II electrometer provided four independent channels, one for each array segment. The electrometer floated at the high-voltage supply potential and measured electron currents in the range 1 µA to 80 mA (positive voltages) and ion currents of 0.01 µA to 1.0 mA (negative voltages). In addition to measuring collected plasma currents, the electrometer box incorporated the high-voltage-array switching function.

The experiment command sequencer and data multiplexer unit (SEQ/MULT) controlled the operational configuration of the experiment while collecting and compiling data from the remaining electronics subsystems. The command sequencer was a read-only-memory-based controller that was preprogrammed to the desired flight sequence before launch. After executing the preprogrammed sequence (8 hr, 53 min, 20 s after turnon), the sequencer cycled to the start and repeated it. The data multiplexer collected and compiled experiment information and formatted it into a serial stream for use by the Delta transmitter. The SEQ/MULT box also housed the data storage unit, a solid-state memory that was included to ensure full-orbit data coverage.

The power control unit (PCU) provided power conditioning, control, and distribution for PIX-II and interfaced to the Delta. It served as the single-point ground reference for the experiment and provided power returns to each component. The PCU box also housed the electronics associated with the hot-filament emitter.

The battery provided power to the entire flight experiment. It contained 18 silver-zinc cells rated at 15-Ah capacity in a sealed case.

The Langmuir electronics unit operated the Langmuir probe to provide a measurement of plasma density. The probe voltage could vary from -20 to

324

+110 V in steps, and currents in the range 10^{-8} to 10^{-4} A could be recorded. The probe voltage stepped through its range (in 5- and 10-V steps) during probe sweeps. When not sweeping, the probe voltage was held at +50 V. The Langmuir probe was located on one side of the electronics enclosure box (figs. 1 and 3). It was stowed during launch and deployed 90° to the side of the box after the Delta's depletion burn. Overall length of the assembly was 71.1 cm (28 in). The probe itself was a 1.9-cm (3/4-in) diameter aluminum sphere.

Like the Langmuir probe the hot-filament emitter was attached to the electronics box and deployable by using an identical release mechanism. It deployed 90° from the face of the electronics box (approximately radially outward from the Delta vehicle). The filament's purpose was to emit electrons to neutralize the charge collected when the solar arrays were at high positive bias in order to minimize charging of the Delta vehicle under these conditions.

The flight hardware underwent thermal-vacuum, vibration, shock, and plasma testing and a functional electrical checkout before launch.

The Flight

PIX-II was launched with IRAS on Delta launch 166 on January 25, 1983, at 9:17 p.m. e.s.t. (01-26-83, 03:17 G.m.t.). PIX-II was activated at 03:23:20 G.m.t. on January 26, after release of IRAS. Its orbit was 870 km circular, 100° inclination. PIX-II was near the terminator and experienced eclipse conditions for about 8 min per 103-min orbit, near the north pole. Experiment duration was limited by the lifetime of the Delta telemetry battery and the experiment battery. Design life was 10 hr. In fact, PIX-II returned about 18 hr of data as both real-time data and memory dumps. The experiment operated nominally except that full deployment of the Langmuir probe was uncertain. The probe was released from its stowed position, but the signal indicating latching into the fully deployed position was not received. The attitude of the Delta vehicle was variable since there was no active attitude control.

Data Obtained

Figure 4 summarizes the PIX-II experimental arrangement from the "science" point of view. The four array segments were biased independently in various combinations to ±1 kV in steps and the collected currents measured in a preprogrammed sequence. Langmuir probe sweeps were done periodically as part of the sequence. The emitter was activated during most positive-voltage scans, although some were done with the emitter off to evaluate its effectiveness. Electron currents of 10^{-7} to 10^{-2} A (positive voltages) and ion currents of 10^{-8} to 10^{-3} A (negative voltages) were recorded.

The voltage bias levels used were 0, ±30, ±60, ±95, ±125, ±190, ±250, ±350, ±500, ±700, and ±1000 V. These were stepped through sequentially (e.g., 0, +30, +60, etc.). Each voltage was held for 16 s for most voltage scans, although a few used 32-s steps. Currents in each electrometer were read at 2-s intervals.

Table I summarizes the array bias scans and Langmuir probe operations conducted during one full program sequence, over a period of 8 hr 53 min 20 s. Two full program sequences and one partial sequence were completed during the flight. For clarity of presentation the array segments have been numbered 1

to 4, from left to right in the view depicted in figure 2. The first column identifies which segments were being biased. Segments not biased in a given scan were electrically floating. Thus an entry of "1" signifies array segment 1 biased and segments 2, 3, and 4 floating; an entry of "1 + 4" signifies segments 1 and 4 biased and segments 2 and 3 floating, and so forth. The entry "Gradient" refers to a special mode in which a constant 100-V bias difference was maintained between adjacent array segments during a scan. In this case $V_1 > V_2 > V_3 > V_4$ and $V_i - V_j = 100$ V, $(i,j) = (1,2)$ or $(2,3)$ or $(3,4)$, where the subscripts refer to segment numbers. All four arrays were biased in the gradient mode. The number of scans during which the hot-wire-filament emitter was activated is a subset of the total number of positive scans, so a table entry of "12 (10)" signifies 12 positive bias scans of which 10 were done with the emitter on.

Langmuir probe scans were done during the sequence at 1/2- and 1-hr intervals, for a total of 11 scans in the full sequence. During scans the voltage was stepped from -20 V to +20 V in 5-V increments and then from +20 V to +110 V in 10-V increments. Each voltage up to 50 V was held for 4 s; the 60-V level was held for 1 s; and the remaining voltages for 2 s each. Current was measured at 1-s intervals. The array segments were held at 0 V during most probe scans, and at 30 V for a few. When the probe was not scanning, it was held at +50 V and its current was monitored at 2-s intervals.

At high negative voltages arcing of the array segments was anticipated. In view of this the high-voltage power supply was shut off when an "overload" current of 1 mA of ions was reached. The original design intended the power supply to recycle back to voltage in 2 s. Last-minute addition of a capacitor resulted in the system's being unable to recycle properly at high negative voltages. Thus, when an arc resulted in shutdown of the power supply, the supply generally could not recycle until the beginning of the next voltage scan. For example, if an arc resulted in shutdown at -500 V in a given scan, no data were obtained at -700 or -1000 V for that scan. This has resulted in some loss of data for the negative-voltage scans.

Data Analysis

Results of data analysis activities to date are summarized in papers by Grier (ref. 14), Ferguson (ref. 15), and Roche and Mandell (ref. 16). Interpretation of the data has been complicated by the variable and uncertain Delta attitude, and by ram/wake effects, which make it difficult to assess local plasma conditions on the array.

Data analysis efforts to date have focused on laboratory-flight comparisons (ref. 14) and ram/wake effects (ref. 15). Findings include evidence for a tank wall effect in ground testing; less effect from emitter operation in space than on the ground; lower than expected arc threshold voltages; confirmation that arc threshold depends on plasma density; and the strong influence of ram/wake effects.

Comparing the flight data with predictions of the NASCAP/LEO code (ref. 16) indicated a need for code refinements. Efforts to analyze and interpret the PIX-II data and to compare them with ground test results and model predictions are continuing.

SUMMARY

The PIX-II experiment was conducted to provide flight data on the interactions between high-voltage solar arrays and space plasmas. Understanding these interactions is critical to the design of high-voltage photovoltaic power systems for low-Earth-orbit applications. Flight data are required to calibrate ground simulations and to guide and validate interaction modeling efforts. The PIX-I experiment flown in 1978 returned data that established that the current collection and arcing phenomena observed in ground tests do occur in orbit. Like its predecessor, PIX-II was designed, built, and tested at the NASA Lewis Research Center and flown as a piggyback on a second-stage Delta. The data set recovered is far more extensive than that from PIX-I (18 hr of data with full orbit coverage as compared with 1 hr of real-time data) and focused on the crucial solar array interactions. Analysis and interpretation of the data have been complicated by the lack of well-defined attitude information and the influence of ram/wake effects. Several significant results have been obtained. These include evidence for lower arc thresholds in space than are observed on the ground; confirmation of the arc threshold voltage dependence on plasma density; and evidence for tank wall effects at high positive voltages. Much remains to be done to evaluate fully the information contained in the data base that PIX-II's successful flight has provided. Data analysis and interpretation are continuing along several lines.

REFERENCES

1. Stevens, N.J.: Interactions Between Spacecraft and the Charged-Particle Environment. Spacecraft Charging Technology - 1978, NASA CP-2071, 1979, p. 268.

2. Finke, R.C.; Myers, I.T.; Terdan, F.F.; and Stevens, N.J.: Power Management and Control for Space Systems. Future Orbital Power Systems Technology Requirements, NASA CP-2058, 1978, p. 195.

3. Renz, D., et al.: Design Considerations for Large Space Electric Power Systems. NASA TM-83064, 1983.

4. Smith, R.E.; and West, G.C., compilers: Space and Planetary Environment Criteria Guidelines for Use in Space Vehicle Development, 1982 Revision (Vol. 1), NASA TM-82478, 1983.

5. Stevens, N.J.: Solar Array Experiments on the SPHINX Satellite. NASA TM X-71458, 1973.

6. Pike, C.P.; and Stevens, N.J.: Agreement for NASA/OAST-USAF/AFSC Space Interdependency on Spacecraft-Environment Interaction. Spacecraft Charging Technology - 1980, NASA CP-2182, 1981, p. 912.

7. Kennerud, K.L.: High Voltage Solar Array Experiments. NASA CR-121280, 1974.

8. McCoy, J.E.; and Konradi, A.: Sheath Effects Observed on a 10-Meter-High Voltage Panel in Simulated Low Earth Orbit Plasmas. Spacecraft Charging Technology - 1978, NASA CP-2071, 1979, p. 315.

9. McCoy, J.E.; and Matucci, D.T.: Experimental Plasma Leakage Currents to Insulated and Uninsulated 10 m^2 High-Voltage Panels. Spacecraft Charging Technology - 1980, NASA CP-2182, 1981, p. 931.

10. Katz, I.; et al.: Additional Application of the NASCAP Code. NASA CR-165349, 1981.

11. Nonnast, J.H.; et al.: Numerical Simulation of Plasma-Insulator Interactions in Space, Part I: The Self-Consistent Calculation. Spacecraft Charging Technology - 1980, NASA CP-2182, 1981, p. 932.

12. Chaky, R.C.; et al.: Numerical Simulation of Plasma-Insulator Interactions in Space, Part II: Dielectric Effects. Spacecraft Charging Technology - 1980, NASA CP-2182, 1981, p. 946.

13. Grier, N.T.; and Stevens, N.J.: Plasma Interaction Experiment (PIX) Flight Results. Spacecraft Charging Technology - 1978, NASA CP-2071, 1979, p. 295.

14. Grier, N.T.: Plasma Interaction Experiment II (PIX-II): Laboratory and Flight Results. This volume.

15. Ferguson, D.C.: Ram/Wake Effects on Plasma Current Collection of the PIX-II Langmuir Probe. This volume.

16. Roche, J.C.; and Mandell, M.J.: NASCAP Simulation of PIX-II Experiments. This volume.

TABLE I. - PIX-II EXPERIMENT

[One full program sequence.]

(a) Array bias scans (0 to ±1000 V)

Segment	Number of positive voltage scans[a]	Number of negative voltage scans
1	12 (10)	8
2		9
2+3		8
1+4		9
1+2+3		8
1+2+3+4		10
Gradient	3 (3)	3

(b) Langmuir probe scans

- -20 to +110 V (11 per sequence)
- Held at +50 V when not scanning

[a]Number in parentheses denotes number of scans during which hot-wire-filament emitter was activated.

329

Figure 1 - PIX II/Panel. (Dimensions are in inches.)
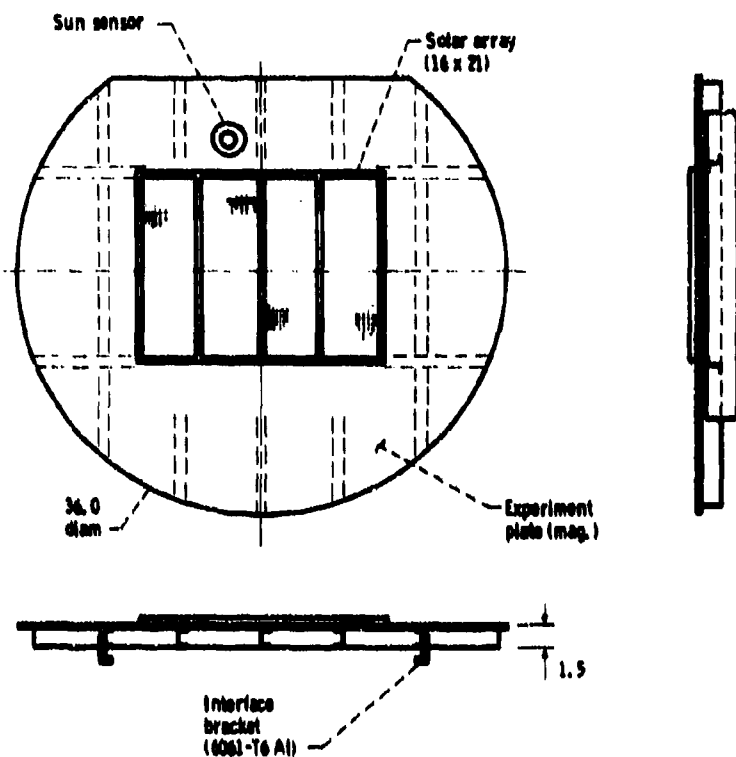
Figure 2. - Experiment plate assembly. (Dimensions are in inches.)
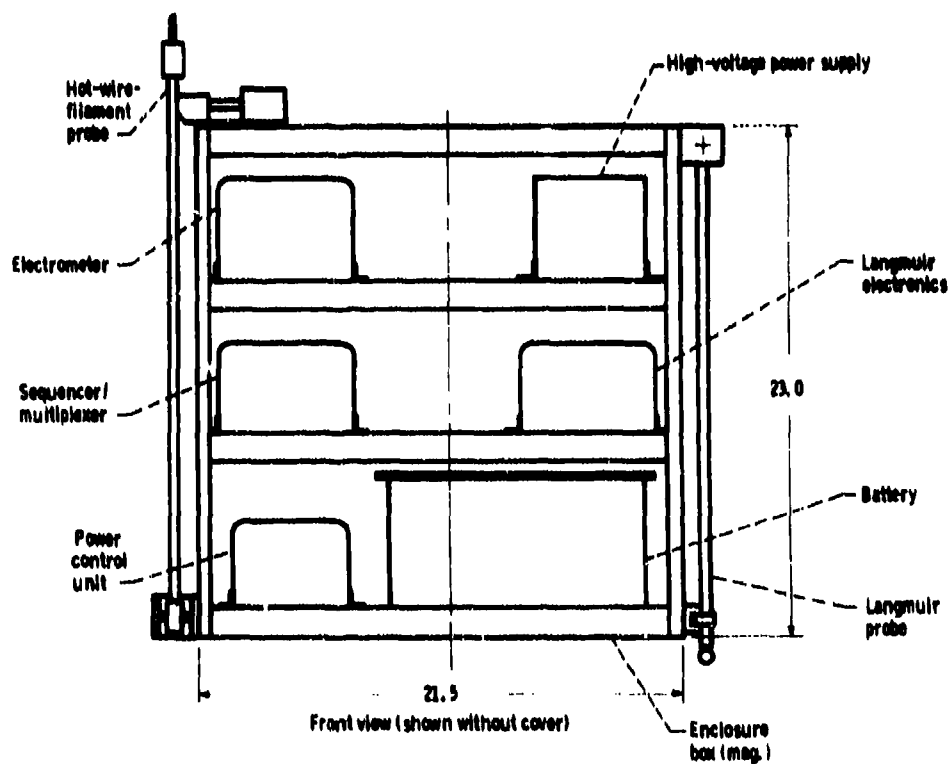
Figure 3. - Enclosure box assembly. (Dimensions are in inches.)

331
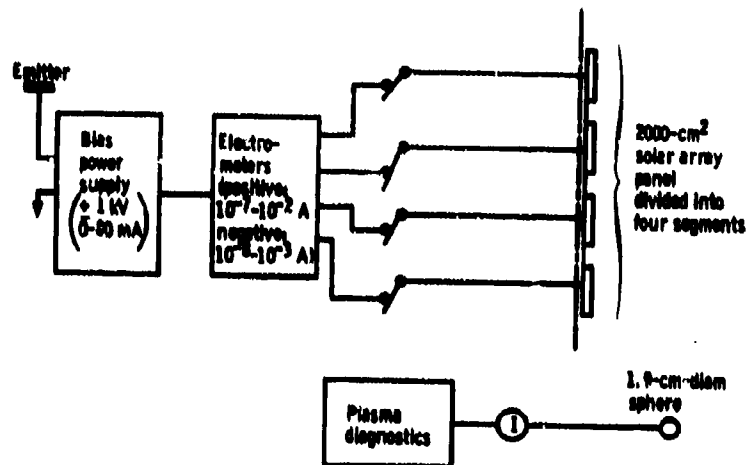
Figure 4. - PIX II electrical arrangement.

PLASMA INTERACTION EXPERIMENT II (PIX II): LABORATORY AND FLIGHT RESULTS

Norman T. Grier
National Aeronautics and Space Administration
Lewis Research Center
Cleveland, Ohio 44135

The Plasma Interaction Experiments I and II (PIX I and II) were designed as first steps toward understanding interactions between high-voltage solar arrays and the surrounding plasma. PIX II consisted of an approximately 2000-cm^2 array divided into four equal segments. Each of the segments could be biased independently and the current measured separately. PIX II was tested in the laboratory and in space.

PIX II was launched on January 25, 1983, into a nearly circular polar orbit and attained an altitude of approximately 900 km. It was launched as a piggyback experiment on the IRAS spacecraft launch. It remained with the Delta rocket second stage and used the Delta's telemetry system. Approximately 18 hr of data were received: this was the life of the Delta's telemetry battery.

In addition to the solar array segments, PIX II had a hot-wire-filament electron emitter and a spherical Langmuir probe. The emitter was operated when the array segments were biased positively above 125 V. Thermal electrons from the emitter aided in balancing the electron currents collected by the array.

This paper presents laboratory and flight results of PIX II. At high positive voltages on the solar array segments, the flight currents were approximately an order of magnitude larger than the ground test currents. This is attributed to the tank walls in the laboratory interfering with the electron currents to the array segments. From previous tests it is known that the tank walls limit the electron currents at high voltages. This was the first verification of the extent of the laboratory "tank effect" on the plasma coupling current.

INTRODUCTION

The Plasma Interaction Experiments (PIX I and II) are part of a broad investigation by the Lewis Research Center to develop design guidelines, materials, devices, and test methods for controlling detrimental interactions between high-voltage systems and the space environment. Systems of interest include solar arrays, power systems, conductors and insulators, and other exposed components. Surface-plasma interactions include current drains, charge buildup on insulators, and discharges to or through the space plasma.

Future satellites, including space stations, will require operating power from tens of kilowatts to megawatts. In the near future most, if not all, of this power will be generated by arrays of solar cells. To keep the weight of the power distribution and conditioning components to a minimum, the arrays

will have to operate at much higher voltages than the 100 V or less of present arrays. Previous investigations (refs. 1 to 7) have shown that solar arrays biased at voltages greater than approximately 150 V positive and operating in a plasma like that of the lower ionosphere attract large currents of electrons from the plasma environment. That is, the electron currents are enhanced at these voltages. These electron currents are balanced by ion currents attracted to other portions of the spacecraft that are negative with respect to space potential. Thus circuits are created through the plasma for parasitic currents. Because these parasitic currents are in parallel with the load current, they represent power losses.

On a spacecraft operating with a negative-grounded, high-voltage solar array, large portions of the spacecraft surface will be negative with respect to space plasma potential. This is caused by the difference in the electron and ion mobilities and the requirement that electron currents to the spacecraft be balanced with ion currents (i.e., the net current to the spacecraft must be zero). Even though there will be surfaces at relatively high negative voltages, the ion current to these surfaces will be low and therefore will not be a problem. However, there are other adverse effects. On laboratory test arrays biased negatively more than approximately -250 V, blowoff arcing discharges have been observed. PIX I (ref. 1), which was launched in March 1978, verified that both the current enhancement for positive bias and the arcing for negative bias occur in flight. The present paper presents results from the second plasma interaction experiment (PIX II).

The objective of the PIX II flight experiment was to obtain flight data on plasma - solar array interaction phenomena by using a much larger solar array (2000 cm^2) than the one flown on PIX I (100 cm^2). These interactions include plasma coupling currents and negative bias arcing. The data obtained can also be used to calibrate ground test facilities. The experiment consisted of four identical array segments of about 500 cm^2 each. Various combinations of these segments were biased over a range of voltages from -1 to 1 kV. A spherical Langmuir probe was used to measure local plasma densities. As expected, a range of densities was encountered during each orbit. An emitter was activated at high positive voltages to prevent the whole spacecraft from being driven greatly negative by the large electron currents collected at such voltages. The solar arrays were voltage biased in a preprogrammed step sequence.

The PIX II flight package consisted of the 2000-cm^2 solar array panel mounted on a 91.4-cm-diameter plate that was truncated to 81.3 cm on one side, an electronics enclosure box housing all of the electronics hardware, the emitter, and the spherical Langmuir probe. On the Delta, the electronics enclosure box was mounted 180° around the perimeter from the solar array panel.

EXPERIMENT AND PROCEDURE

The experimental setup is shown in figure 1. For positive bias each electrometer could measure currents from 10^{-7} to 10^{-2} A; for negative bias the range was 10^{-8} to 10^{-3} A. The power supply was capable of an output of 80 mA at 1000 V and was programmed for output voltages of 0, ±30, ±60, ±95, ±125, ±190, ±250, ±350, ±500, ±700, and ±1000 V. Even though the solar array segments were operated individually and in combinations, the current to each segment was always measured individually.

The PIX II telemetry systems operated in real time. However, full real-time telemetry ground coverage was not possible with the limited number of ground receiving stations available. So PIX II was given the capability of storing data for 68 min. After 68 min from PIX II turnon, the old data were overwritten continuously at a rate of 64 bits/sec. The stored data were also read continuously at a rate of 512 bits/sec. Both the stored and the real-time data were transmitted continuously. With this system, almost full orbit coverage of PIX II data was possible. As a precaution against a failure of the data storage unit, the sequence was preprogrammed to sweep each of the solar array segments at least once positive and once negative in view of a ground telemetry-receiving station.

The emitter was a loop of 0.025-cm-diameter tungsten wire connected at one end to spacecraft ground. It was activated for positively biased solar array voltages greater than 125 V. To see the effect of the emitter on the results, some voltage cycles were operated with the emitter off. The emitter was mounted such that, when deployed, it extended 71 cm on a boom fastened along an edge and perpendicular to the face of the electronics enclosure box (fig. 2). The emitter operated with no accelerating grid as a passive thermonic emitter of electrons. The positive potential of the plasma relative to the spacecraft served to draw the electrons from the spacecraft.

The Langmuir probe was used to determine ambient plasma densities. The probe, a 1.9-cm-diameter aluminum sphere, was deployed on a 71-cm boom. It was mounted on an edge of the enclosure box such that when deployed it was tangent to the Delta (fig. 2). (The emitter extended radially outward from the Delta from an edge of the enclosure box far from the Langmuir probe.) During a Langmuir scan the probe's voltage was stepped from -20 to 110 V. The voltage was stepped in 5-V increments from -20 to 20 V and in 10-V increments from 20 to 110 V. When not being scanned, the Langmuir probe was held at 50 V and its collection current monitored.

GROUND TESTS

The complete flight package was ground tested in a plasma environment before the flight (fig. 3). The tests were performed in a 9-m-long by 4-m-diameter vacuum chamber. The solar panel and the electronics enclosure box were mounted back to back in the center of the chamber perpendicular to its centerline. The solar panel faced opposite to the deployed emitter probe. The plasma was generated by four plasma sources: two mounted at least 2.3 m from the solar array and two mounted at least 2.3 m from the electronics enclosure box.

RESULTS AND DISCUSSION

All activities on PIX II were preprogrammed to occur at particular program counts in a sequence. Each program count was held for 16 sec. The program count timer was activated at PIX II turnon. After program count 2047 (9 hr, 5 min, 52 sec) the sequence returned or "rolled over" to program count 0 and the sequence was repeated. Data were obtained on PIX II until program count 248 after the second rollover. There were some gaps in the data after the first rollover because of less ground coverage than earlier orbit passes.

Langmuir Probe

Typical Langmuir probe current-voltage curves are shown in figure 4. The program counts shown on the figure are for the beginning of each sweep. Each voltage step between -20 and 50 V was held for 4 sec, the 60-V level was held for 1 sec, and all others were held for 2 sec each. The maximum current the Langmuir electrometer could measure was 1×10^{-4} A. This limit caused the leveling off of the current shown for program count 1343 in figure 4.

The electron plasma densities were determined from the electron saturation region of the curve (fig. 5). As expected, the current varied quite linearly with voltage above 30 V. This behavior was typical of all of the Langmuir sweeps.

In the saturation region of the spherical Langmuir probe characteristic, the equation for the current (ref. 8) is

$$I = neA \left(\frac{kT}{2\pi m}\right)^{1/2} \left(1 + \frac{eV}{kT}\right) \tag{1}$$

where V is the voltage measured with respect to the plasma potential, e the electronic charge, k Boltzmanns's constant, m the mass of the electron, T the temperature, and A the area of the probe. Taking the derivative with respect to voltage allows the density to be written in terms of the slope as

$$n = \frac{(2\pi mkT)^{1/2}}{Ae^2} \frac{dI}{dV} \tag{2}$$

where dI/dV is the slope. The electron saturation region data for each scan of the PIX II probe were plotted as in figure 5 and the slopes determined graphically. Twenty-three Langmuir scans were made during the life of PIX II.

To find the density at times when the Langmuir probe was not being scanned, the Langmuir probe current at a voltage of 50 V and the density at program count 878 were used as references. It was assumed that the Langmuir probe current at 50 V varied in proportion to the density. The density at any program count was found from

$$n = I \, (n/I)_{PC878;50V}$$

where n and I are the density and Langmuir probe current at 50 V, respectively. In using this equation, care was exercised that the spacecraft ground voltage remained constant. This was achieved by limiting the use of this equation to program counts where the applied voltage to the solar array was less than 60 V. It was felt that voltages in this range were low enough that the currents collected by all of the exposed grounded metallic surfaces on the Delta would be enough to balance the currents collected by the solar array without driving the Delta's ground potential negative. This method was used to estimate the ambient plasma densities for the flight results presented herein.

Plasma density varied as much as two orders of magnitude during an orbit (fig. 6). Revolution 8 (fig. 6(b)) had the most uniform density. Even here the variation was more than an order of magnitude. Although large variations over the poles were expected, the density elsewhere was expected to be more uniform. Some of the nonuniformity was caused by the Langmuir probe being in the ram or wake of the Delta, as shown in reference 9.

Emitter Operation

The emitter was operated for positive biases of 125 V and higher on the solar array segments. Since there were no accelerating grids on the emitter, it emitted electrons only when the spacecraft ground potential became negative with respect to plasma potential.

The emitter operation was first tested in the laboratory. The PIX II flight package was mounted so as to float electrically in the vacuum chamber. As in flight the PIX II was operated in a plasma environment. The emitter-on currents (fig. 7(a)) were approximately an order of magnitude larger than those for emitter-off operation. The results shown for the emitter-on operations compare very closely to those obtained when the PIX II structure was grounded to the tank walls. From this it was concluded that the emitter kept the PIX II flight package near tank ground potential.

In flight (fig. 7(b)) the emitter-on current was approximately five to six times larger than the emitter-off current. This difference is smaller than that observed in laboratory tests. In flight the solar array segments were operated at different times in different locations. Thus the smaller effect observed in flight as compared with ground tests may have been caused by the difference in the densities during operation of the segments.

The Langmuir probe current was very sensitive to emitter operation both in the laboratory and in flight (fig. 8). The voltage on the Langmuir probe was 50 V. With the emitter off, the Langmuir probe collected ions with a bias of 200 V or greater on the solar array in the laboratory tests and 350 V or greater in flight. This implies that the spacecraft floated at least 50 V negative in this voltage range. Even with the emitter on, the Langmuir probe dropped about an order of magnitude when the voltage on the array was increased to 1000 V.

For the emitter to operate properly, the spacecraft must float negatively with respect to plasma ground. The floating potential (fig. 9) was found from the following procedure:

(1) The Langmuir probe current-voltage characteristic curve was determined with the solar array segments at zero voltage.

(2) The corresponding voltage was found by using the Langmuir probe current reading when the solar array segments were at the applied voltage and the Langmuir probe current-voltage characteristic curve from step 1.

(3) This voltage minus 50 V was assumed to be the floating potential.

337

The floating potential is a function of the ambient density and the applied voltage to the solar array segments. Since each set of segments was operated in different parts of the flight, each had a different density environment. The sets of segments therefore could not be compared directly. However, the trend is obvious from figure 9, namely, higher positive solar array voltages produce higher negative floating potentials on the spacecraft. In general, the floating potential increased almost linearly with applied solar array voltage after snapover.

Solar Array Positively Biased

Since the laboratory and flight plasmas for solar array segments positively biased to 1000 V had different densities and temperatures, corrections were made to the flight results for direct comparison with the laboratory results (fig. 10). If we assume that the currents to the solar array segments vary linearly with V, eV/kT >> 1, and if I_0, T_0, and n_0 are known current, electron temperature, and density, respectively, at one plasma condition, the current I at any other temperature T and density n can be found by using the spherical probe equation (1).

$$I = I_0 \frac{n}{n_0} \sqrt{\frac{T_0}{T}} \qquad (4)$$

Equation (4) was used to compute the flight values in figure 10 by using the laboratory values of kT = 1.8 eV, n = 3.4×10^3 cm^{-3}, and flight values of $n_0 = 3.0 \times 10^3 \sqrt{kT}$ for solar array segments 2 and 3 and $n_0 = 5.5 \times 10^3 \sqrt{kT_0}$ for solar array segments 1 to 4. The n_0 is the flight result determined from the Langmuir probe readings. So the two flight curves in figure 10 are the values the flight data would have had if the flight ratio $n/\sqrt{kT}$ had had its laboratory value.

In figure 10 it appears that the laboratory currents are truncated above 200 V. This is caused by the tank wall interfering with the current collection. The calculated sheath at a voltage of 200 V at these plasma conditions extends approximately 1.6 m from the solar array. This is beyond the tank wall. Thus this verifies the hypothesis that sheath-wall interactions occur during laboratory tests at high voltages and limit the current collection.

The flight data for solar array segments 2 and 3 (fig. 10) show that current increased slightly less than linearly with voltage for voltages greater than approximately 350 V. This was as expected since for an infinite flat plate the current would be a constant and for a plane small compared with the Debye length it would vary linearly. This array was between these sizes. The current for all four segments varied even more slowly. This is also in agreement with rough expectations.

Another set of curves for the total current collected by one, two, and four array segments (fig. 11) also shows that the current increased almost linearly with voltage above about 350 V. It is tempting to compute an area effect from this figure. However, it is not known whether the array was in the ram, the wake, or neither when each of these sets of array segments was activated. Also it is not known whether the ambient densities were the same

338

during these times. The density can vary by over two orders of magnitude over an orbit (fig. 6). These facts prevent a definite determination of the area effect.

Solar Array Negatively Biased

The maximum total steady current measured for negative biases on any of the sets of array segments was approximately 5 μA. This level of current does not pose a problem for operation of high-voltage solar arrays in space. The problem associated with negative bias is the probability of arcing. During arcing, there are high surges of current through the array. These surges reach levels of milliamperes and higher. In both ground and flight tests, once arcing begins, it continues through the higher (more negative) voltage levels. In fact, the arcing becomes more frequent and intense at the higher voltage levels.

Most of the arcs were initiated between -500 and -1000 V (table I). There was one initiation at -255 V. On closely examining the data, it was noticed that the arcing inception voltage tended to increase with time. That is, fewer arcs occurred at -350 and -500 V near the end of PIX II life. Out of the 106 times the segments were activated negatively, the solar array segments reached -1000 V, without arcing, 12 times.

SUMMARY

PIX II consisted of four 500-cm^2 solar array segments, a spherical Langmuir probe, an emitter, and associated electronics. The Langmuir probe data indicated densities that varied over two orders of magnitude over an orbit and large differences from orbit to orbit. Some of these density variations are thought to be attributable to the Langmuir probe being in the ram or wake of the spacecraft. Since the attitude of the spacecraft was not known, separation of the ram/wake effect from the ambient density variation is very complex and has not been attempted in this work.

Spherical probe theory fitted the Langmuir probe data very well. This suggests that the densities determined from the Langmuir probe were the actual densities surrounding the probe. However, the solar array segments were mounted on the opposite side of the Delta from the Langmuir probe. So the densities surrounding the solar array were not necessarily those of the probe.

Different combinations of the solar array segments were activated by using a preprogrammed sequence throughout the life of PIX II. The sequence was chosen to maximize the information received by the limited real-time ground coverage in case the data storage/playback unit failed to operate. As it turned out, all units on PIX II operated as designed and data were obtained through program count 247 after two rollovers of the sequencer (two full and one partial sequence, approximately 19 hr).

For positive bias on the solar array segments, the data showed current enhancement for voltages greater than approximately 200 V. This current enhancement was larger than that predicted by ground tests. The difference is attributed to suppression in the ground test currents by the interaction of the

sheath with the walls of the vacuum chamber. Suppression in the ground test currents was observed for all of the solar array segments whether run singly or in combinations. This implies that only relatively small solar arrays can be completely plasma tested in present ground facilities.

For negative bias on the solar array segments, arcing occurred. In both ground and flight tests the current sometimes increased from microamperes to milliamperes and higher during arcing. In flight, arcing was observed for voltages as low as -255 V. The arcing inception voltages tended to increase negatively with time. There were fewer arcs observed at -500 V and lower near the end of PIX II life than in the beginning. This suggests that preconditioning high-voltage solar arrays by operating them at high negative voltages in a plasma environment on the ground may help to drive the arc inception voltage in flight more negative.

The emitter was a passive hot-wire filament and was activated for positive biases on the solar arrays of 125 V or greater during part of the experiment sequence. This was necessary since the second stage of the Delta had very little exposed bare metal surface to collect ions for balancing the electrons collected by the array. The largest negative potential observed on PIX II with the emitter operating was approximately -50 V, as compared with voltages greater than -200 V without the emitter. Thus the emitter was able to keep the spacecraft within reasonable proximity of the space plasma ground.

CONCLUSIONS

Four 500-cm^2 solar array panel segments were biased positively and negatively in steps to ±1000 V on a spacecraft in a polar orbit at an altitude of approximately 900 km. Various combinations of the four array segments were activated during the flight. At each voltage level the current collected by each solar array segment was measured. When the array was biased positively to 125 V or higher, an electron emitter was activated to aid in keeping the spacecraft near plasma potential. A spherical Langmuir probe was used to determine the plasma density throughout the flight.

The following conclusions were drawn from the data for positive bias on the array segments:

1. Even the large laboratory plasma simulation facilities at Lewis are too small to correctly estimate the plasma coupling current at high positive voltages to solar arrays that are 2000 cm^2 or larger in area.

2. If the negative terminal of a spacecraft array is connected to spacecraft ground, the spacecraft will float far negatively with respect to space plasma potential if large bare metallic areas are not provided for ion current collection, which is necessary to balance the electron current collected by the solar array.

3. The plasma coupling current may vary over an order of magnitude between ram and wake conditions.

The following conclusions were drawn for negative bias on the array segments:

1. Arcing is the most serious detrimental effect.

2. The arcing inception voltage may be as low as -255 V on conventionally constructed solar arrays.

3. Arcing may occur at densities as low as 10^3 electrons/cm^3.

TABLE I. - PIX II ARCING INCIDENCE RESULTS FOR NEGATIVE BIAS

(Arcing occurred at -350 V with densities of 10^3/cm^3. Arcing inception voltage tended to increase with time.)

Array segments active	Applied voltage for arc initiation, V					Number of arcs[a]	Total
	-255	-350	-500	-700	-1000		
1	----	2	2	5	6	1	16
2	----	1	3	5	5	5	19
2,3	----	1	3	3	5	3	15
1,4	----	---	9	5	4	----	18
1,2,3	----	1	4	6	3	1	15
1,2,3,4	1	1	6	6	7	2	23
Total observations	1	6	27	30	30	12	106
Incidence, percent of total	0.9	5.7	25.5	28.3	28.3	11.3	---
Cumulative incidence, percent	0.9	6.5	32.1	60.4	88.7	100	---

[a]Combined total of arcs initiated after being at voltage level a few seconds plus arcs that occurred on first reaching this level from the previous nonarcing one.
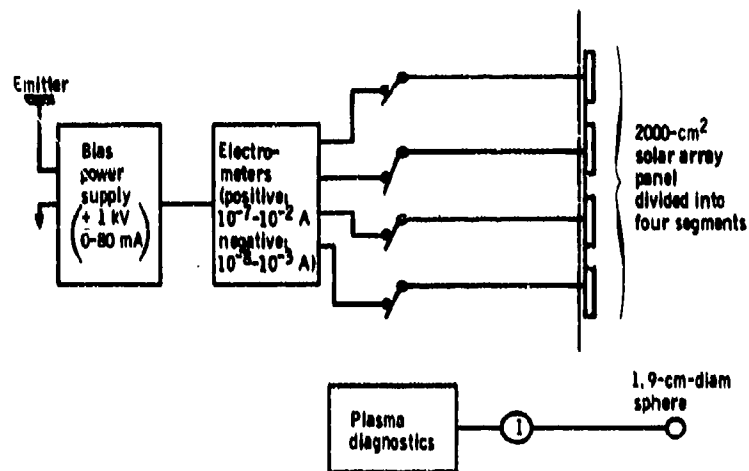
Figure 1. - PIX II electrical arrangement.
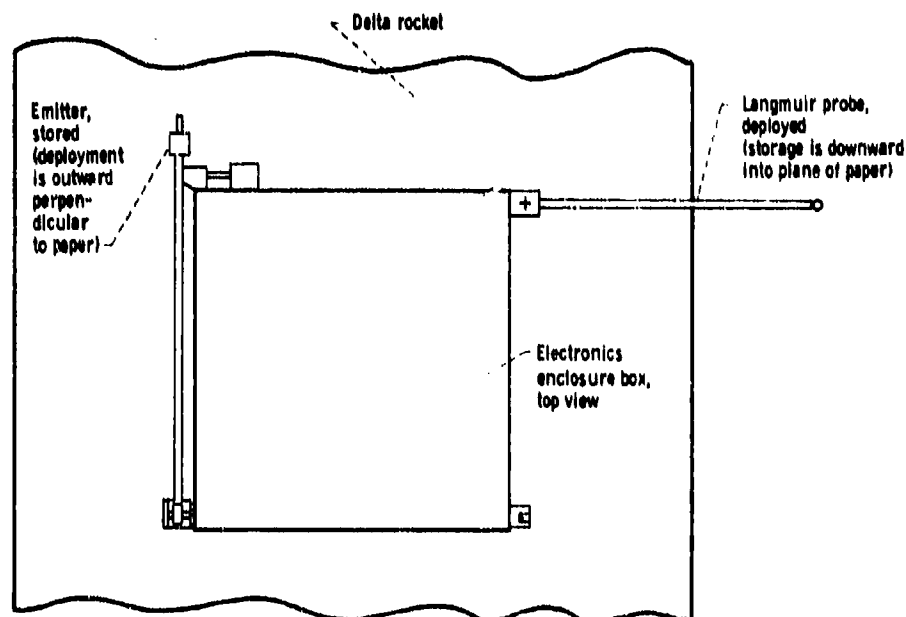
Figure 2. - Electronics enclosure box showing emitter and Langmuir probe positions.

Figure 3. - PIX II setup in large vacuum facility for ground testing.
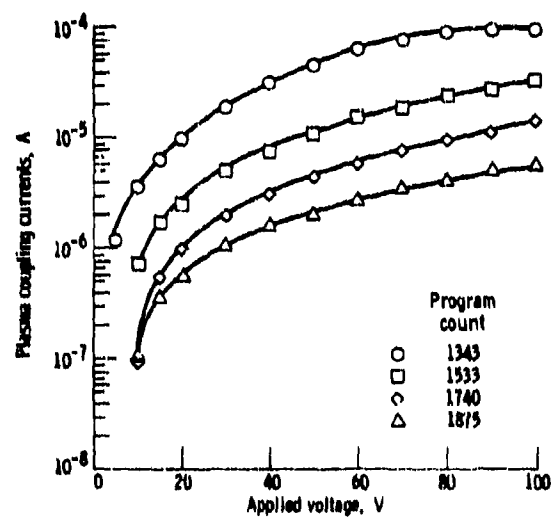
Figure 4. - Typical sweeps of Langmuir probe during flight.
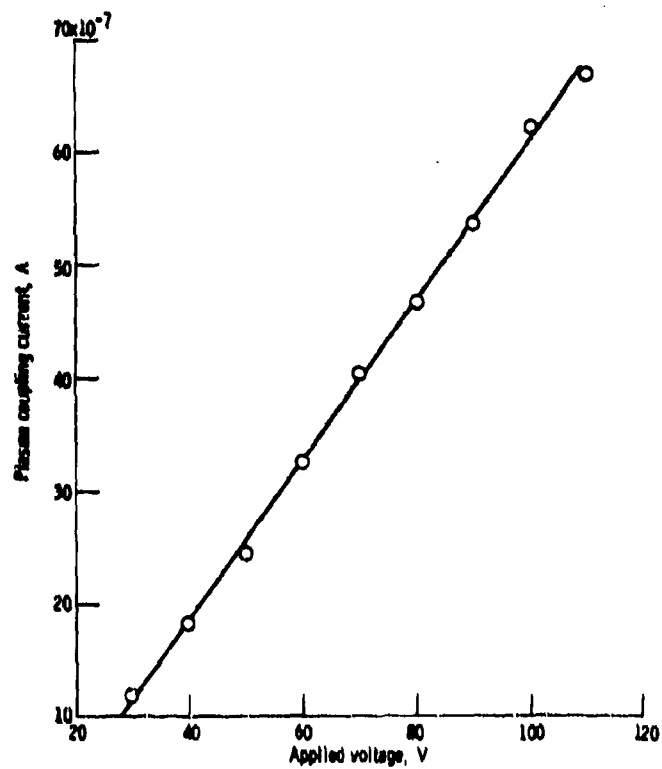
Figure 5. – Typical sweep of Langmuir probe in electron saturation region, showing linear behavior. Program count, 878.

(a) First orbit. Program counts 116 to 499.

(b) Program counts, 751 (RO) to 1133 (RO).
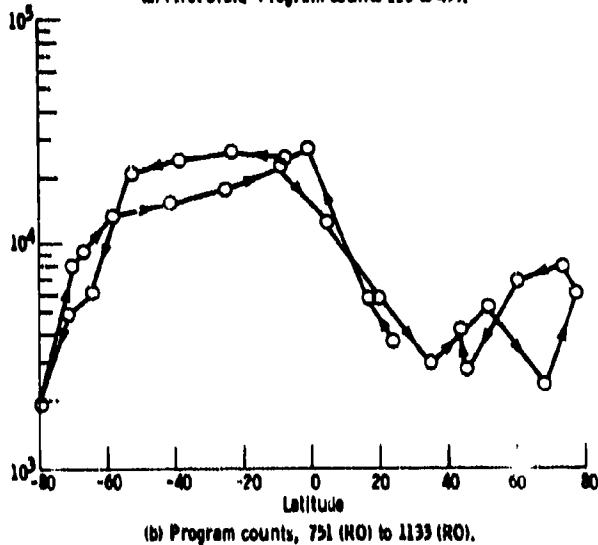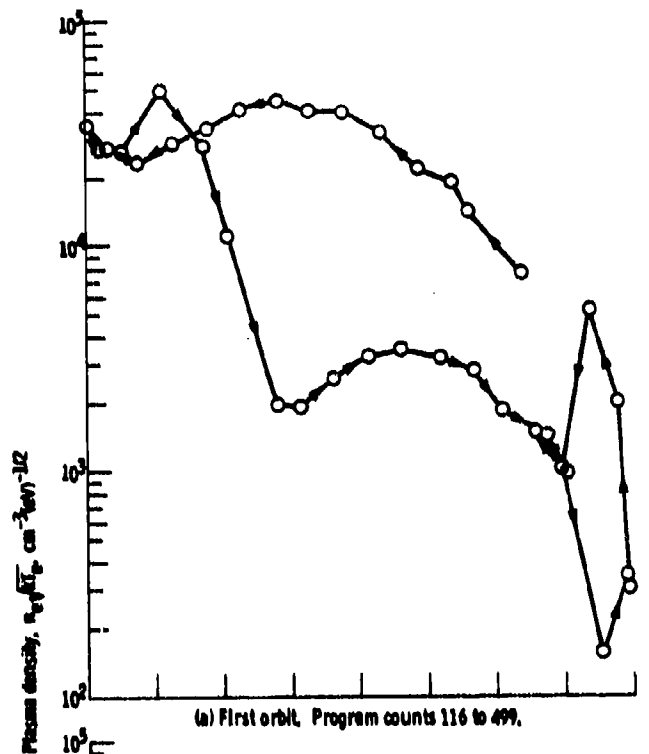
Figure 6. - Electron plasma density divided by square root of electron temperature as function of latitude. (Arrows denote direction of spacecraft travel.)

(a) Ground tests.

(b) In flight.
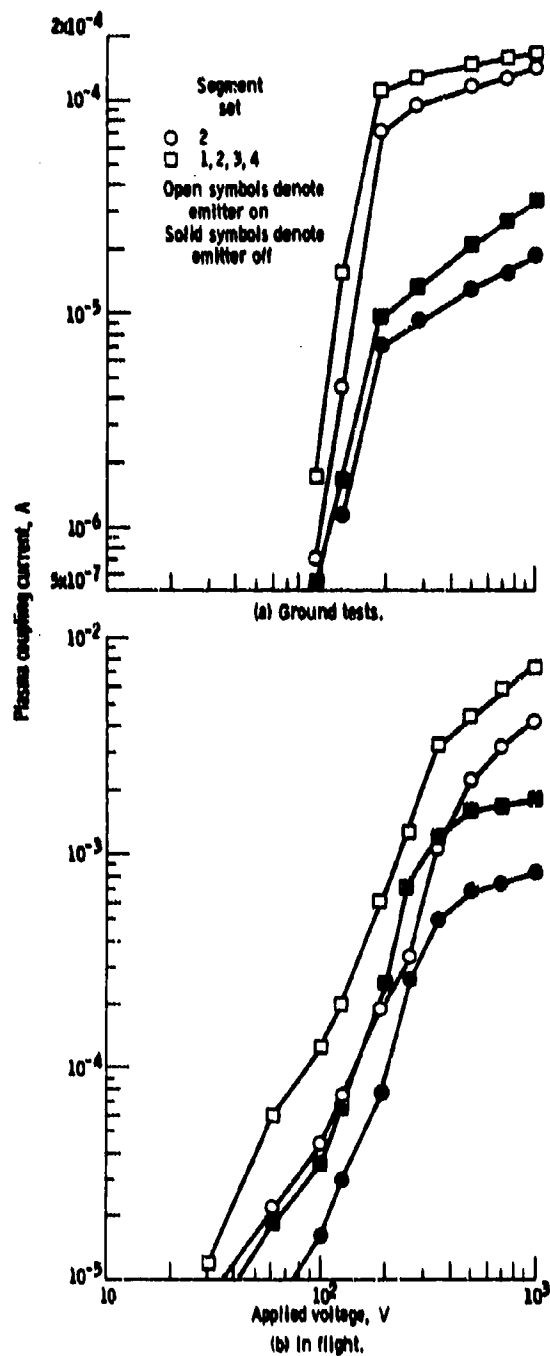
Figure 7. - Emitter on/off operation on total plasma coupling current for solar array segment 2 and combination (1, 2, 3, 4) as function of applied voltage.
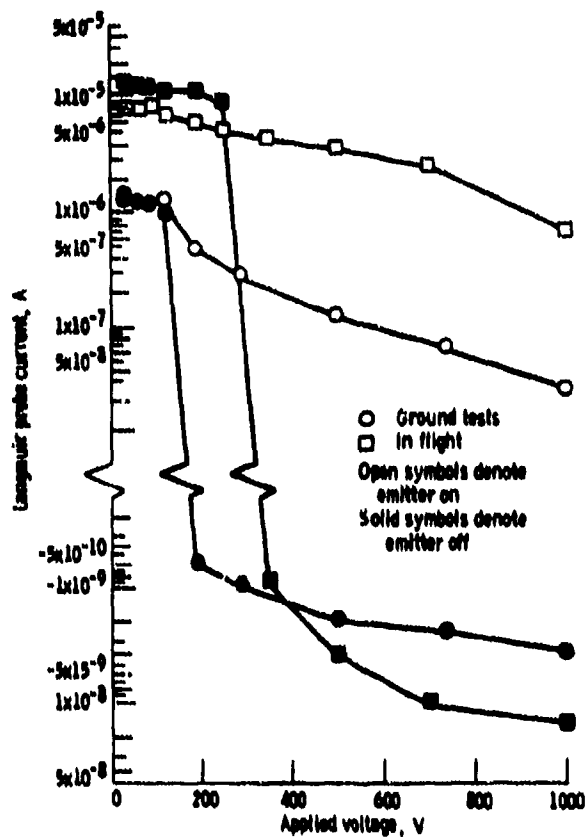
Figure 8. - Emitter on/off operation on Langmuir probe current as function of applied voltage to solar array segments for ground and flight operations.
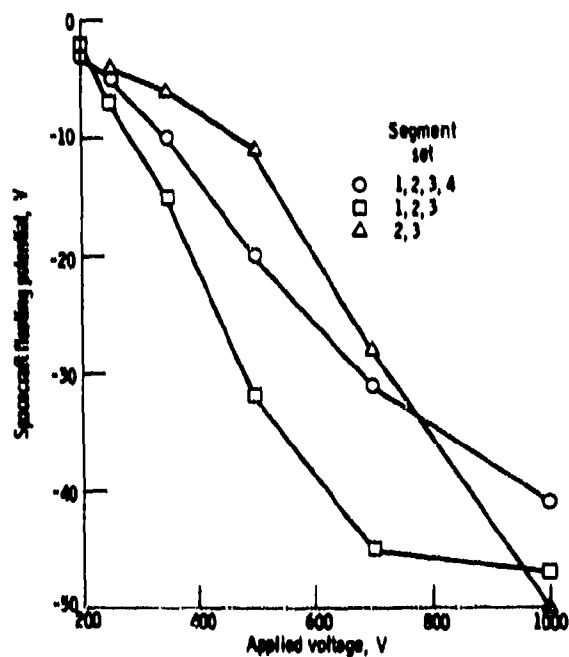
Figure 9. - Spacecraft floating potential as function of applied voltage to solar array segment sets (2, 3), (1, 2, 3), and (1, 2, 3, 4). Emitter on.
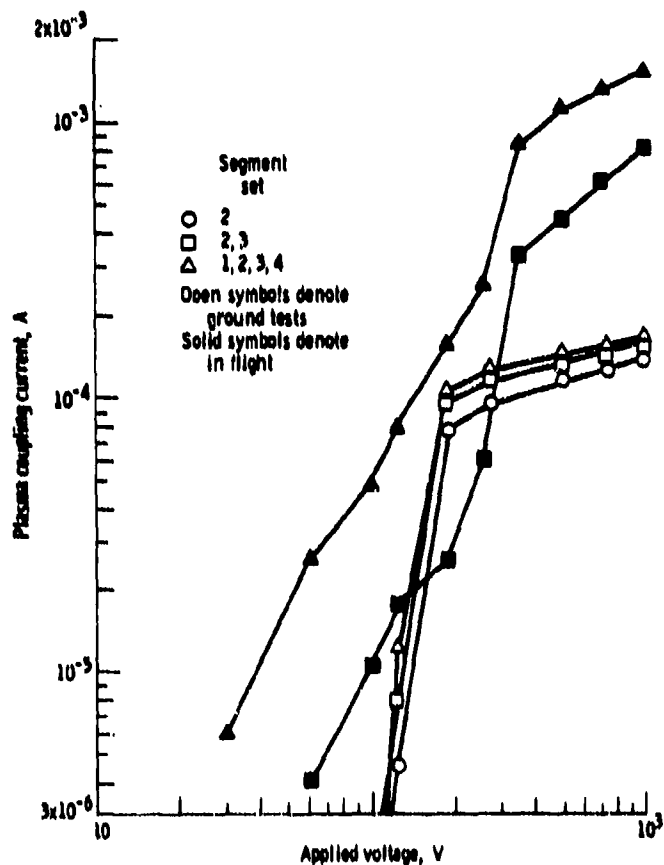
Figure 10. - Total currents to different combinations of solar array segments for flight and ground testing. Emitter on.

346
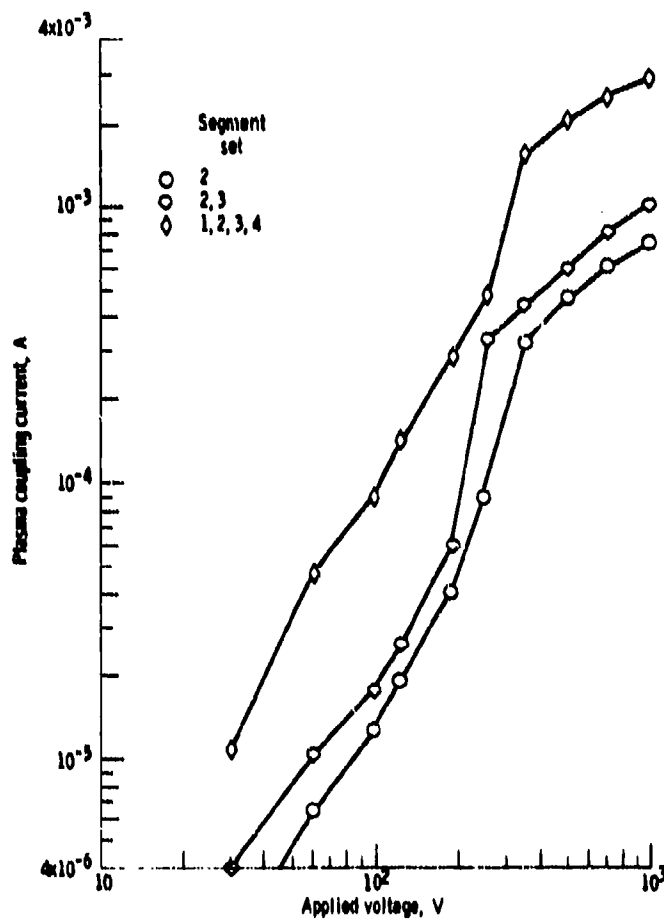
Figure 11. - Typical flight total current to combination of solar array segments as function of applied voltage. Emitter on.

RAM/WAKE EFFECTS ON PLASMA CURRENT COLLECTION OF THE PIX II LANGMUIR PROBE

Dale C. Ferguson
National Aeronautics and Space Administration
Lewis Research Center
Cleveland, Ohio 44135

Data returned from the NASA PIX II flight of January 1983 were analyzed and the results are presented herein. The PIX II experiment carried a Langmuir probe, an electron emitter, biasable solar array segments, a Sun sensor, temperature sensors, and other instruments. Its approximately 900-km polar orbit allowed measurements of the currents collected from the magnetospheric plasma in polar and equatorial regions.

PIX II Langmuir probe readings of the same polar magnetospheric regions taken on consecutive orbits showed occasional apparent densities as much as 10 times lower than the average, although each pass clearly showed density structures related to the day/night boundary. At other points in the orbit, Langmuir probe currents varied by as much as a factor of 20 on a time scale of minutes.

The hypothesis is advanced that these apparent inconsistencies in Langmuir probe current are the results of the probe's orientation relative to the body of the spacecraft and the velocity vector. Theoretical studies predict a possible depletion in collected electron current by a factor of 100 in the wake of an orbiting spacecraft of the velocity and dimensions of the PIX II Delta upper stage. Experimental results from other spacecraft indicate that a wake electron depletion by a factor of 10 or so is realistic. This amount of depletion is consistent with the PIX II data if the spacecraft was rotating. Both the Sun sensor and temperature sensor data on PIX II show a complex variation consistent with rotation of the Langmuir probe into and out of the spacecraft wake on a time scale of minutes. Furthermore, Langmuir probe data taken when the Sun sensor indicated that the probe was not in the spacecraft wake are consistent from orbit to orbit. This supports the interpretation that ram/wake effects may be the source of apparent discrepancies at other orientations.

Analyses of variations in the Sun sensor and temperature sensor data are in progress that in combination with limited information obtainable about the spacecraft orientation may allow the attitude to be modeled to determine the ram/wake orientation at any time. Empirical corrections can then be made to the Langmuir probe data and to the solar array plasma current collection data. The amount of the corrections and the corrected data themselves contribute to our knowledge of the electrical interaction of spacecraft with the orbital environment.

INTRODUCTION

The PIX II satellite was launched into a polar orbit on January 25, 1983, to investigate interactions between high-voltage solar arrays and the orbital plasma environment. During analysis of the PIX II data it has become evident

that the plasma density as indicated by currents collected by the PIX II Langmuir probe varied in a way inconsistent with real ambient plasma density variations. In this paper the nature of the problem is discussed, and the hypothesis is presented that the currents measured while the Langmuir probe was in the spacecraft wake were much smaller than would be measured by a probe outside the wake. The amount and kind of corrections that must be applied to the readings to derive true plasma densities from straightforward probe theory provide information about large spacecraft wakes.

THE NATURE OF THE PROBLEM

The current collected by a spherical probe of radius r and positive voltage V in a plasma of electron number density n_e and temperature T is, according to probe theory (ref. 1),

$$I = \frac{n_e \sqrt{\frac{2kT}{m_e}}\, 4\pi r^2}{2\sqrt{\pi}} \left(1 + \frac{Ve}{kT}\right)$$

for a probe whose radius is small compared with the plasma sheath. Here k is Boltzmann's constant, e is the electron charge, and m_e is the electron mass. The Langmuir probe on the PIX II satellite was about 1 cm in radius and nominally extended about 0.6 m from the spacecraft on a boom. At the nominal 900-km PIX II orbital altitude and 50-V applied potential, the Langmuir probe was in the thick sheath limit and $Ve >> kT$, so that

$$I \propto n/\sqrt{T}$$

if the influence of the spacecraft can be neglected.

There are indications that for the PIX II Langmuir probe, the influence of the spacecraft cannot be neglected. Being in a polar orbit, PIX II traversed regions near the north and south poles where consecutive orbital paths intersected as seen from the rotating Earth. Figure 1 shows the orbital paths near the north geomagnetic pole for several orbits. The convention used here for orbit numbering is that orbit 1 begins at the first south polar passage after launch. Thus orbit 2 begins at approximately program count 267. Each orbit is about 384 16-sec program counts long. In the conference paper by N. T. Grier the start of revolution 1 coincides with the Langmuir probe deployment at program count 116. Thus orbit 1 here starts 233 program counts before revolution 1 of Grier. Figure 2 shows the PIX II Langmuir probe current readings for the two consecutive orbits near the north pole labeled orbits 2 and 3 in figure 1. Although the behaviors of the current with time before and after the night/day crossing were similar for the two orbits, the absolute levels differed by about 1 on the $\log_{10}$ scale, or about a factor of 10. Quantitatively, the correlation coefficient between the logs of the currents for these passes with the times of the night/day crossing aligned is 0.78 (for a confidence level of greater than 99 percent), but the difference in <log> is 0.939. Similar effects are shown for other orbits. Unless the magnetospheric electron densities or temperatures can vary uniformly over the polar cap by a factor of 10 in less than 100 min, we must infer that the Langmuir probe currents are sometimes much higher or lower than the electron densities would necessitate in naive probe theory.

Another indicator of the reliability of the Langmuir probe currents as density and temperature indicators can be obtained by comparing them with readings from other satellites. Fortunately, the Defense Meteorological Satellite Program satellite DMSP/F6 was simultaneously taking data in an orbit nearly identical in inclination to the PIX II orbit at an altitude of 833 km (not too different from the ~890-km PIX II altitude). The data obtained by this satellite (and kindly supplied by Frederick Rich of the Air Force Geophysics Laboratory) were compared with the PIX II data for orbits corresponding most closely in day/night orientation and geomagnetic longitude and latitude. The calculated DMSP ion densities (to be used because there was a negative bias on the DMSP satellite) were compared with the PIX II Langmuir probe electron collection currents for consecutive equatorial passes of the two satellites (fig. 3). The qualitative behaviors were quite similar and the correlation coefficients were quite high for these data, an indication that changes in electron/ion density were followed by both satellites. However, again the multiplicative factor relating the two measured currents was quite different from orbit to orbit, varying by as much as a factor of 6.5 from orbit 2 to orbit 3. Again, the PIX II currents seemed to be uniformly lower in orbit 3 by a large factor for the same regions of the magnetosphere as measured by DMSP/F6. Note that all of the PIX II Langmuir probe currents used in this analysis were made with the solar panels biased at voltages more negative than 30 V to eliminate any effects of vehicle charging.

A logarithmic plot (fig. 4) was made of the PIX II Langmuir probe current versus the DMSP/F6 ion density for a large sample of closely corresponding magnetospheric data points. Here, points where the DMSP/F6 ion density was a rapidly varying function of time or geomagnetic latitude have been thrown out. Although the correlation is high (0.78) and significant (at the >>99 percent level), the 50 data points seem to show a well-defined narrow upper range, with a downward trail of a few Langmuir probe currents to a factor of about 10 lower than the upper limit. It is significant, and consistent with the picture obtained in figures 2 and 3, that the Langmuir probe current on PIX II was occasionally depressed by as much as a factor of 10 from that expected from the true electron density and simple probe theory.

Although the PIX II Langmuir probe current was highly correlated with that of the DMSP/F6 sensors, neither was well correlated with a calculated model ionosphere supplied by H. B. Garrett of JPL. Evidently the Langmuir probe on PIX II and the ion sensor on DMSP/F6 both measured highly correlated physical quantities, but occasionally the Langmuir probe's readings were abnormally low. It is desirable to understand the discrepancy fully.

THE RAM/WAKE HYPOTHESIS

A rapidly moving body traveling through a plasma will leave a wake disturbance. This is easily seen to be true for ions when the velocity of the body exceeds the ion thermal velocity. It is also true that the electrons will feel a wake influence because of the predominantly negative space charge built up in the wake by the partial ion evacuation there. The shape of the wake region for a moving sphere is a trailing cone with a half-angle θ given by (ref. 1)

$$\tan \theta = \frac{\sqrt{2kT_i/m_i}}{v} \tag{1}$$

where m_i and T_i are the ion mass and temperature and v is the velocity of the moving body. The potential in the wake cone may be more negative than that of the body by an amount (ref. 1)

$$V_- = - \frac{2kT}{e} \ln \frac{R}{\sqrt{\epsilon_0 kT/n_i e^2}} \tag{2}$$

where ϵ_0 is the permittivity of free space, n_i is the ion density, and R is the body radius. For a neutral body this limits the thermal electrons that might collect on the trailing edge of the body to those able to surmount this negative potential barrier. Calling the density of such electrons n_b, one has

$$\frac{n_b}{n} = e^{-2\ln R/\sqrt{\epsilon_0 kT/n_i e^2}} = \frac{\epsilon_0 kT}{n_i e^2 R^2} \tag{3}$$

Taking the radius of the PIX II Delta upper stage ($R = 0.76$ m) and putting in $n_i = 10^{10}$ m^{-3} and $T = 2900$ K (extrema from Garrett's model) yield

$$V_- = - 1.5 \text{ V}$$

$$\frac{n_b}{n} \leq 2.4 \times 10^{-3}$$

for PIX II. If it is further assumed that only these electrons could be attracted by a positively charged Langmuir probe in the vehicle wake, the collection current of the Langmuir probe could go down by a factor of 400 in the wake of a neutral spherical body with the Delta's radius.

The extent of the Delta wake can be estimated from equation (1). The distance d of the tip of the wake cone from the surface of the Delta upper stage is

$$d = R \left(\frac{1}{\sin \theta} - 1 \right) = R \left(\sqrt{1 + \frac{1}{\tan^2 \theta}} - 1 \right) \tag{4}$$

which, assuming equation (1) and spherical geometry, is

$$d = R \left(\sqrt{1 + \frac{v^2 m_i}{2kT}} - 1 \right) \tag{5}$$

Since the spacecraft environment contains ions of different species, which is indicated in parentheses after d, each ion will have a wake region of different extent. Putting in $v = 7.4$ km/sec, $T = 2000$ K, and $R = 0.76$ m results in

$$d(O^+) = 3.23 \text{ m}$$

$$d(H^+) = 0.48 \text{ m}$$

$$d(He^+) = 1.34 \text{ m}$$

The boom on the Delta on which the Langmuir probe is deployed extends it to about 0.6 m from the Delta surface. Thus the Langmuir probe is never in the hydrogen ion wake but can be in the oxygen and helium ion wakes. From the model data of Garrett the lowest percentage by number of hydrogen ions is about 36 percent. If the wake potential barrier is then lessened by the presence of H^+ ions at the Langmuir probe location, the total reduction in collection current is expected to be substantially less than calculated earlier.

More realistic estimates of the wake effect on electron current collection can be obtained by examining data from other satellites. Figure 2 of Samir and Stone (ref. 3) shows that the Ariel I, Explorer 3, and AE satellite data are consistent with a maximum reduction of wake electron collection current by a factor of about 10 at a 900-km altitude. Thus the occasional factor-of-10 reduction in PIX II Langmuir probe current is consistent with the hypothesis that the probe is in the O^+ and He^+ wake when the reduction occurs.

There is evidence that during the flight the PIX II satellite was in a complex rotation that allowed the Langmuir probe to be carried into the space-craft wake. Both the Sun sensor (a photocell mounted on the solar array panel) and the array temperature sensor showed readings that varied in a manner con-sistent with rotation or precession with respect to the Sun. In addition, data returned by Delta launch telemetry and kindly provided by Elizabeth Beyer of Goddard Space Flight Center (private communication) indicate that in the early stages of the flight the Delta upper stage was precessing and rotating with at least one period near 100 min. Unfortunately, the time span over which the data were taken was too short to allow an adequate determination of the geometry and frequency of rotation and precession.

Further analysis of all available Sun sensor, temperature, and telemetry data is needed with the goal of modeling the PIX II attitude to allow determi-nation of the ram/wake orientation at all times in the flight.

EVIDENCE FOR THE RAM/WAKE HYPOTHESIS

Although the absolute orientation of the PIX II satellite at all times in the flight has not been determined, there are some rough indications of the attitude at certain times. For instance, the Sun sensor can indicate times when the Sun is high on the solar array. Since the Sun was at a very high angle to the orbital plane and the array was roughly opposite the Langmuir probe on PIX II, a condition of high Sun on the array implied that the Langmuir probe was probably not in the vehicle wake. A map constructed of Langmuir probe currents for the high-Sun condition showed no discrepancies between adjacent orbits of more than a factor of 3, consistent with most points in figure 4 (presumed not to be in the wake).

Perhaps the best test of whether the Langmuir probe currents were at times not indicative of the true plasma density is to show that a real physical effect follows not the Langmuir probe current but another indicator of the plasma density. N. J. Stevens (ref. 4) has shown that for solar arrays in the laboratory, the negative breakdown voltage decreases with increasing plasma density. Such an effect should also be seen in orbit if the indicator of plasma density used is reliable and the biased array is not in the vehicle wake. To insure this, the PIX II data were searched for breakdowns that occurred when the Langmuir probe (LP) current was much lower than the DMSP/F6 satellite current. Such an occurrence was taken to mean that the Langmuir probe was in the vehicle wake, so that the solar array opposite was not in the vehicle wake. The voltage at which the solar arrays arced versus the corresponding DMSP/F6 ion density was plotted (fig. 5) for all breakdowns occurring when

$$\log_{10} \text{ (LP current)} \leq \log_{10} \text{ (DMSP ion density)} - 9.90$$

For these points there is a relation between breakdown voltage and ion density in the same sense as Stevens found. Quantitatively, $\log_{10} V_{arc}$ is correlated with $\log_{10}$ (DMSP ion density) with a correlation coefficient of -0.73, significant at more than the 99.9 percent level for these 20 data points.

$$\log_{10} V_{arc} = -0.34 \log_{10} \text{ (DMSP ion density)} + 4.26$$

The same breakdown voltage was plotted versus the Langmuir probe current presumed to have been read in the spacecraft wake (fig. 6). This diagram has a correlation coefficient of -0.68, which is lower than the correlation with the density found by another satellite. Also, most of the correlation was due to one data point of very low current. The least-squares fit here is

$$\log_{10} V_{arc} = -0.20 \log_{10} \text{ (LP current)} + 1.59$$

Thus for these data the LP current is a worse indicator of the PIX II plasma density than the readings of the DMSP/F6 satellite. Furthermore, although these data were selected in a way that should have produced a correlation between $\log_{10}$ (LP current) and $\log_{10}$ (DMSP ion density) even for originally uncorrelated data, the correlation for these points was only 0.27, not significant at the 80 percent confidence level and consistent with a large degree of randomness. It may be concluded that when the Langmuir probe currents were abnormally low they were no longer a valid indicator of the plasma density at the solar array.

The Langmuir probe currents (fig. 4) can sometimes be as much as 10 times lower than normal, so that a maximum correction factor of 10 may be appropriate for plasma densities derived from LP currents when the probe is deepest in the vehicle wake.

CONCLUSIONS AND IMPLICATIONS

The ram/wake hypothesis seems to satisfactorily explain the variations in Langmuir probe current from orbit to orbit on the PIX II satellite. The time scale for vehicle rotation or precession may be short enough to place the Langmuir probe in the vehicle wake in one orbit and outside the wake on the succeeding orbit. Theoretical considerations make the amount of the variation

plausible, and comparisons with ion densities found by a satellite in a similar orbit show the same range of discrepancy. Furthermore, when the probe might have been in the wake, probe currents were poorly correlated with the array breakdown voltage, as compared with the correlation of other plasma density indicators.

The importance of these results can be summarized in the following way: first, the PIX II Langmuir probe data must be used with caution if simple probe theory is used to infer plasma densities. Second, when the probe is in the wake, correction factors of up to 10, depending on the geometrical circumstances, must be applied to the Langmuir probe currents to derive plasma densities simply. Third, wake effects can be significant for collection currents on large spacecraft and may be a consideration in the geometrical design of large solar arrays. Whenever possible, for instance, an array should perhaps be fitted with "blinders" on each side or other devices to put the array in a plasma wake and to minimize leakage currents while maximizing breakdown voltages. Finally, the amount of diminution of the PIX II Langmuir probe current when the probe is in the vehicle wake may be important to understanding vehicle/plasma interactions.

The PIX II data analysis should be continued in order to model the vehicle orientation. It may be possible to find the correction factor necessary for any angle of attack with respect to the vehicle velocity vector. This would make PIX II a laboratory for studying not only collection currents and breakdowns but also the dynamic interaction between a large space vehicle and its stationary plasma environment.

REFERENCES

1. Whipple, E. C.: The Equilibrium Electric Potential of Bodies in the Upper Atmosphere and in Interplanetary Space. Ph.D. Thesis, George Washington Univ., 1965. (NASA TM X-55368.)

2. Grier, N. T.: Plasma Interaction Experiment II: Laboratory and Flight. Paper in this CP.

3. Samir, U.; and Stone, N. H.: Shuttle-Era Experiments in the Area of Plasma Flow Interactions with Bodies in Space. Acta Astronaut., vol. 7., no. 10, Oct. 1980, pp. 1091-1141.

4. Stevens, N. J.: Interactions Between Large Space Systems and Low Earth Orbit Plasmas. AIAA-83-0310, Jan. 1983.
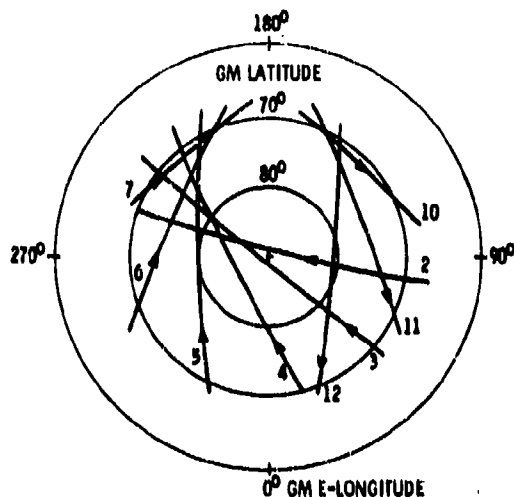
Figure 1. - Orbital paths near north geomagnetic pole.
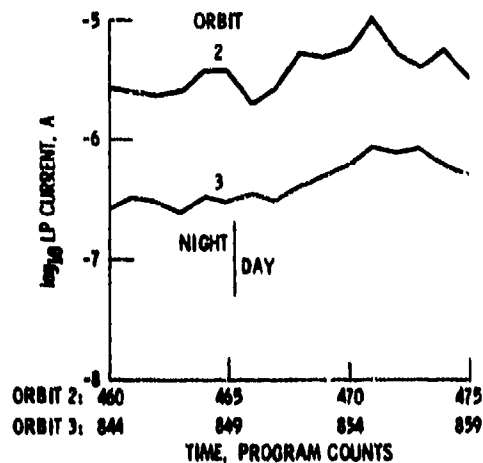
Figure 2. - PIX II Langmuir probe current readings for two consecutive polar passes. (Corresponding points are never more than 9° apart in geomagnetic latitude nor 9° apart in geomagnetic longitude. Geomagnetic latitude, >68°.)
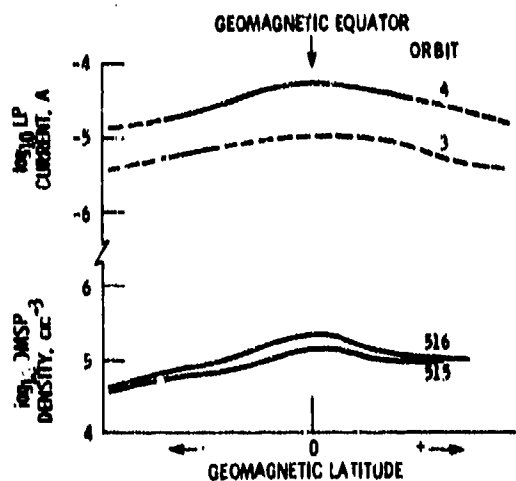
Figure 3. - PIX II orbits and corresponding DMSP/F6 orbits.
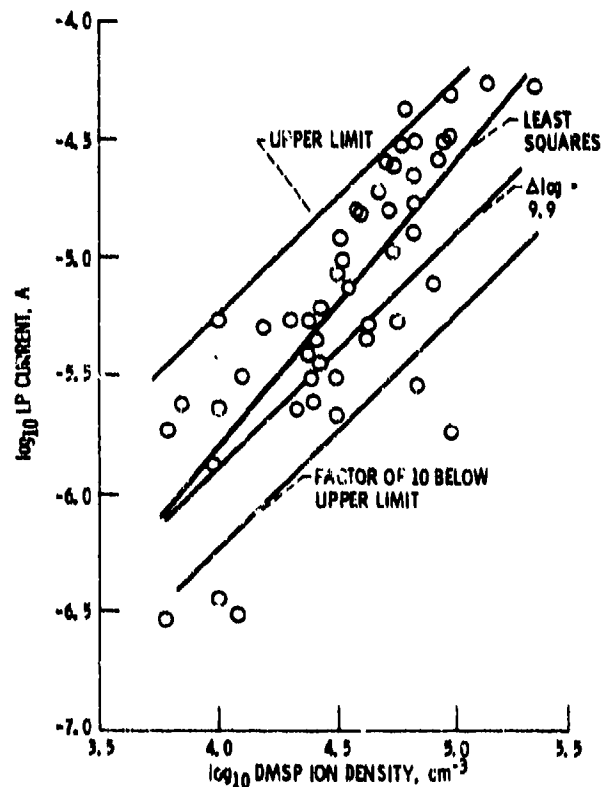
Figure 4. - Langmuir probe current versus ion density.
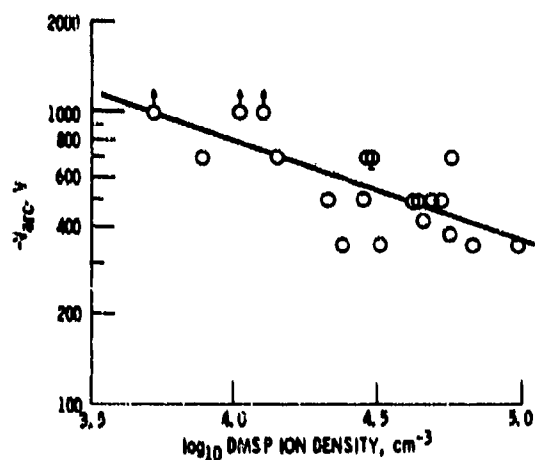
Figure 5. – Array arcing voltage versus ion density – array not in wake.
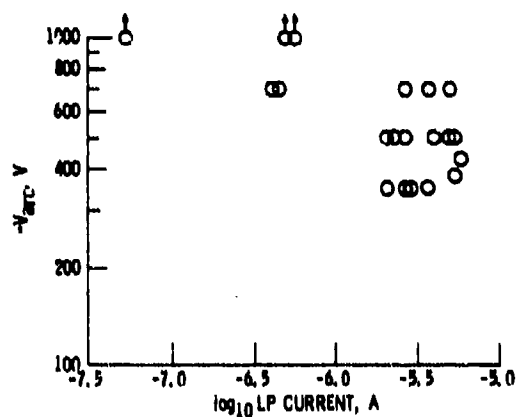
Figure 6. – Array arcing voltage versus Langmuir probe current – Langmuir probe presumed in wake.

357

NASCAP SIMULATION OF PIX II EXPERIMENTS

James C. Roche
National Aeronautics and Space Administration
Lewis Research Center
Cleveland, Ohio 44135

and

Myron J. Mandell
S-CUBED
San Diego, California 92121

The second Plasma Interaction Experiment (PIX II) consisted of a set of four short-circuited solar array modules mounted on the side of a Delta launch vehicle. The modules were independently biased over a range of positive and negative voltages relative to the Delta ground structure. The experiment was launched into low Earth orbit on 25 January 1983, and data were gathered for 18 hr on the currents collected by the modules from the space plasma. In this presentation the latest version of the NASCAP/LEO digital computer code was used to simulate the PIX II experiment. NASCAP is a finite-element code and previous versions have been restricted to a single fixed mesh size. As a consequence the resolution was dictated by the largest physical dimension to be modeled. The latest version of NASCAP/LEO can subdivide selected regions. This permitted the modeling of the overall Delta launch vehicle in the primary computational grid at a coarse resolution, with subdivided regions at finer resolution being used to pick up the details of the experiment module configuration. Langmuir probe data from the flight were used to estimate the space plasma density and temperature and the Delta ground potential relative to the space plasma. This information is needed for input to NASCAP. Because of the uncertainty or variability in the values of these parameters, it was necessary to explore a range around the nominal value in order to determine the variation in current collection. The flight data from PIX II were also compared with the results of the NASCAP simulation.

OBJECT DEFINITION

<u>GEOMETRY</u>
- RECTANGLES ONLY
- MAIN GRID MESH: 0.25 m
- SUBDIVISION FACTOR: 9
- 1194 SURFACE CELLS
    - 708 MAIN GRID
    - 486 SUBDIVIDED GRID

<u>SURFACE MATERIALS</u>
- 751 INSULATING CELLS:
    - WHITE PAINT, CELL, AND KAPTON
- 443 CONDUCTING CELLS:
    - BLACK PAINT, STAINLESS STEEL, THERMAL CONTROL MATERIAL, AND SOLAR CELL INTERCONNECTS
- PHYSICAL PROPERTIES DEFAULTED

<u>COMPUTER TIME</u>: 2.5 min TOTAL

RUN PARAMETERS

<u>STANDARD CONDITIONS</u>
- TEMPERATURE: 0.15 eV
- DENSITY: 10^{10} IONS/m^3 (14.3 amu)
- DEBYE LENGTH: 0.0288 m
- SPACECRAFT GROUND POTENTIAL: 0 V
- INITIAL POTENTIAL ON WHITE PAINT: -0.9 V
- ALL FOUR MODULES SAME BIAS: +30, +50, +100, +125, +190, +255, +350, +500, +700, AND +1000 V

<u>VARIATIONS</u>
- TEMPERATURE: 0.10 eV (0.0235 m)
- DENSITY: 10^9 IONS/m^3 (0.0910 m)
- SPACECRAFT GROUND POTENTIAL: -30 V

<u>COMPUTER TIME</u>: 26 min/RUN (AVERAGE)

DELTA ROCKET (ELECTRONICS BOX SIDE)
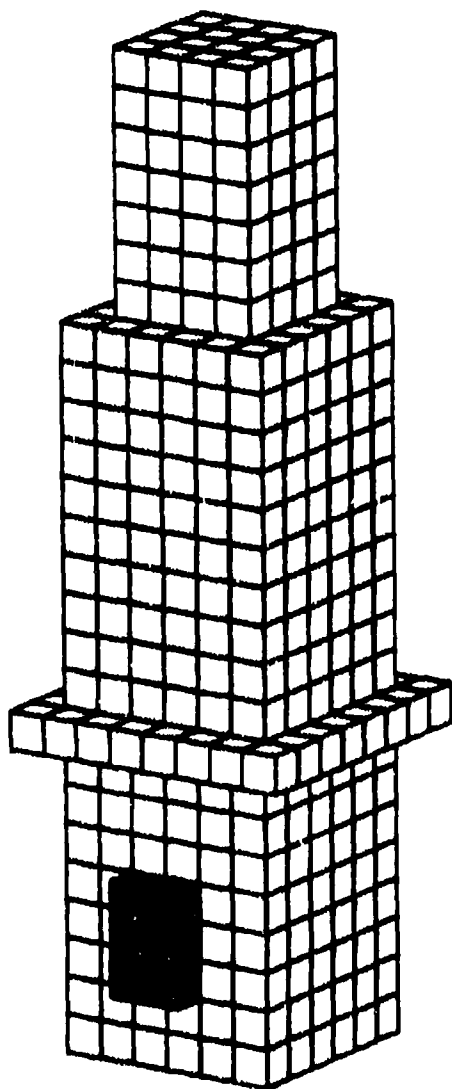
DELTA ROCKET (EXPERIMENT PLATE SIDE)

PIX II EXPERIMENT PLATE

KAPTON

SOLAR CELL INTERCONNECT

SOLAR CELL

BLACK PAINT
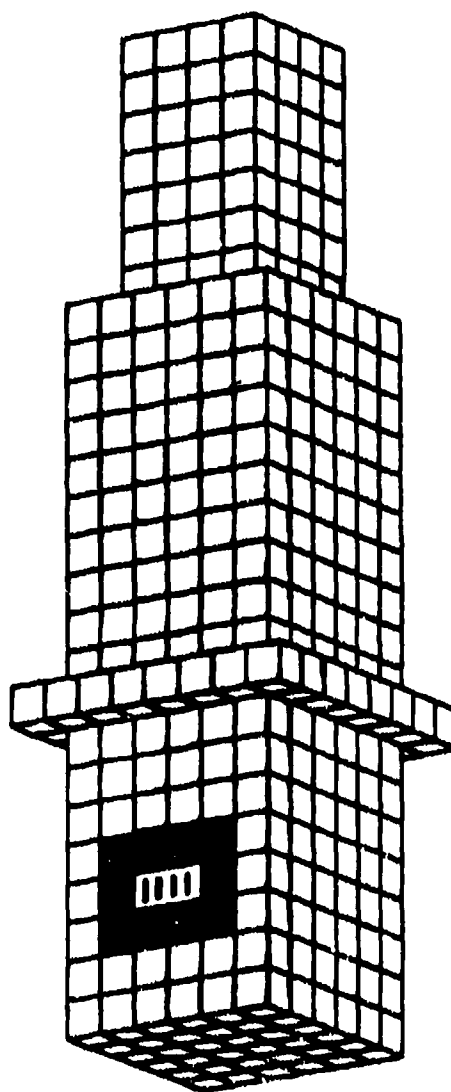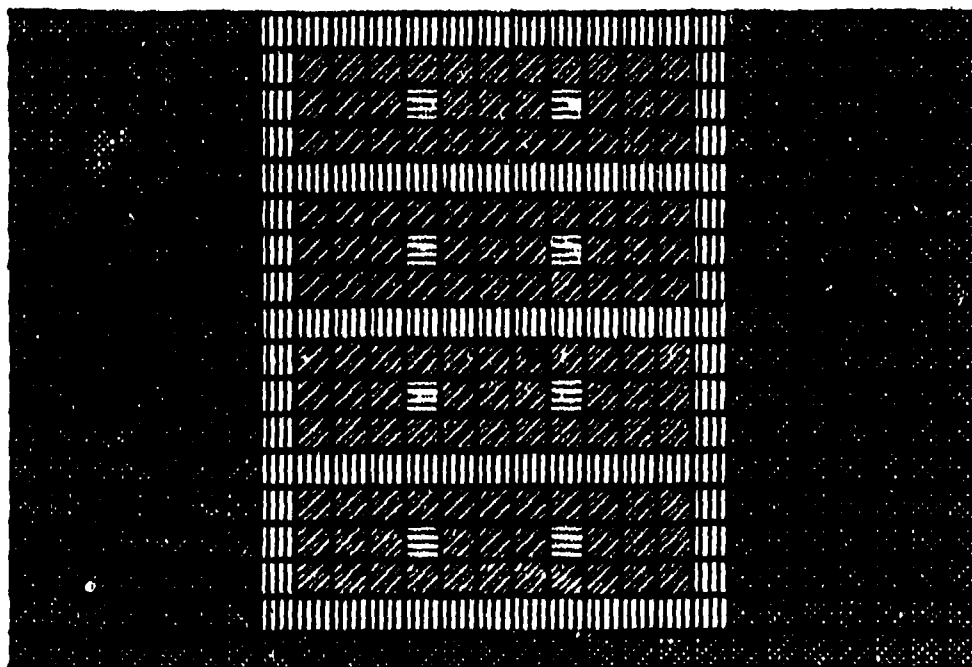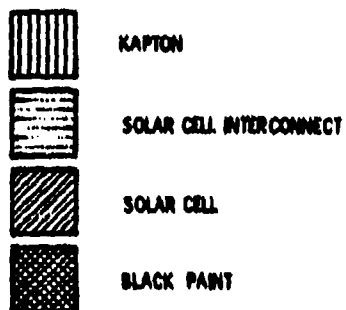
POTENTIAL CONTOURS AT X = 6 FOR BIAS OF +30 V

CONTOUR LEVELS, -11.7 TO 20.3 V WITH POTENTIAL
INCREMENTS OF 2 V

Z-AXIS, MESH UNITS

Y-AXIS, MESH UNITS
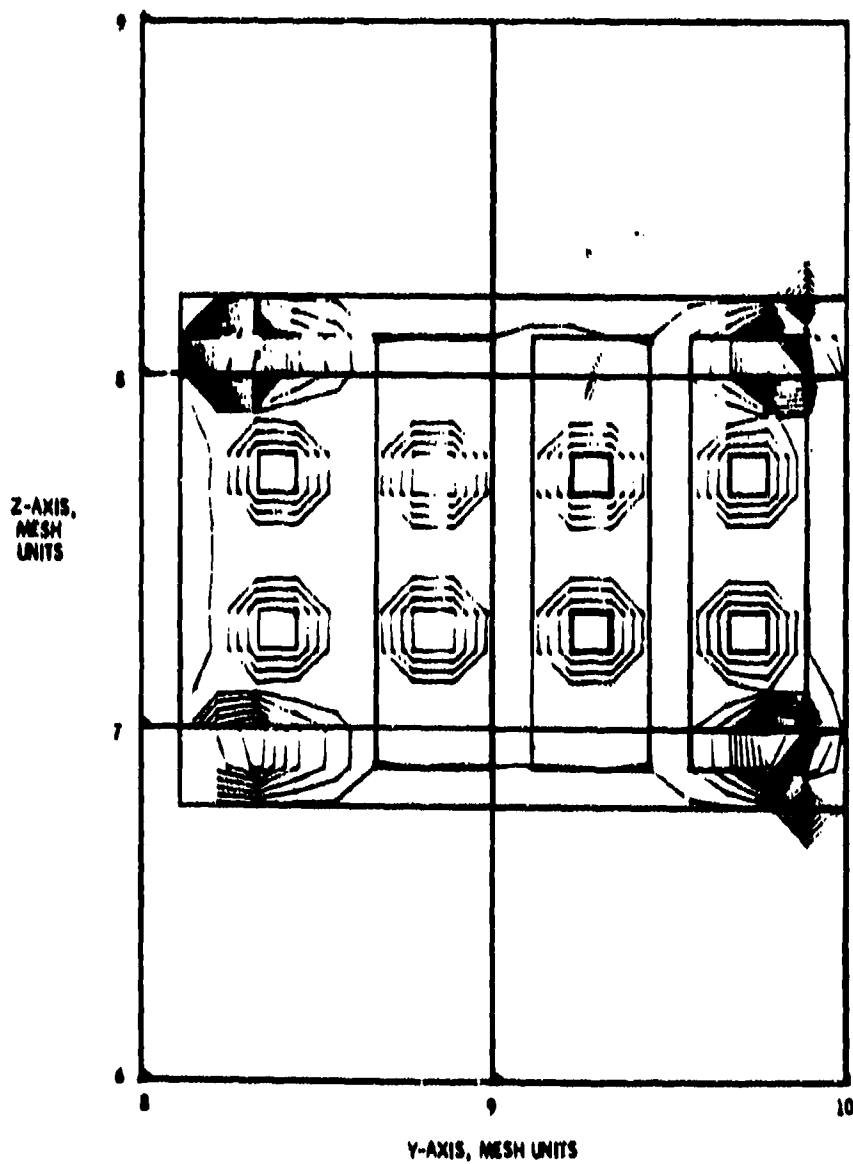
POTENTIAL CONTOURS AT X = 6 FOR BIAS OF +1000 V

CONTOUR LEVELS, -0.9 TO 819 V WITH POTENTIAL
INCREMENTS OF 50 V

Z-AXIS,
MESH
UNITS

Y-AXIS, MESH UNITS
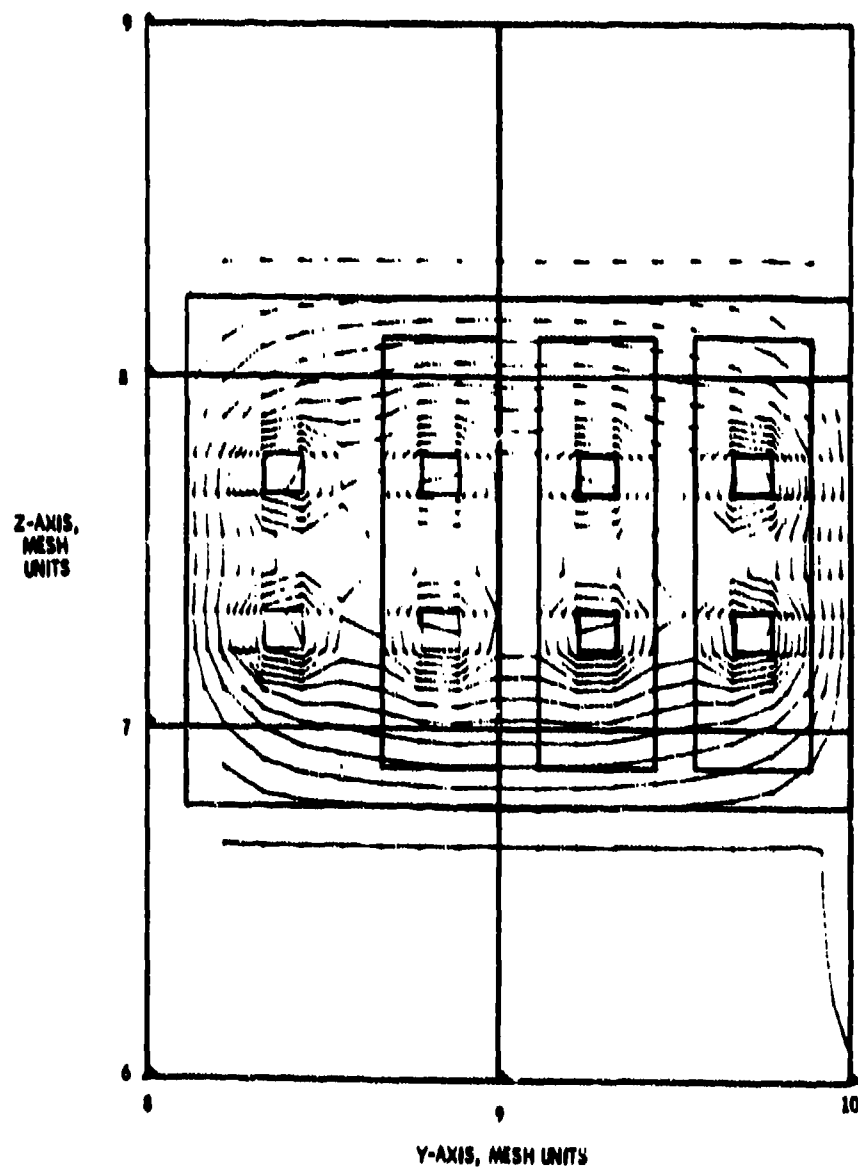
POTENTIAL CONTOURS AT Z = -7.28 FOR BIAS OF +1000 V

CONTOUR LEVELS, 0 TO 342 V WITH POTENTIAL INCREMENTS OF 20 V

Y-AXIS, MESH LIMITS

X-AXIS, MESH LIMITS
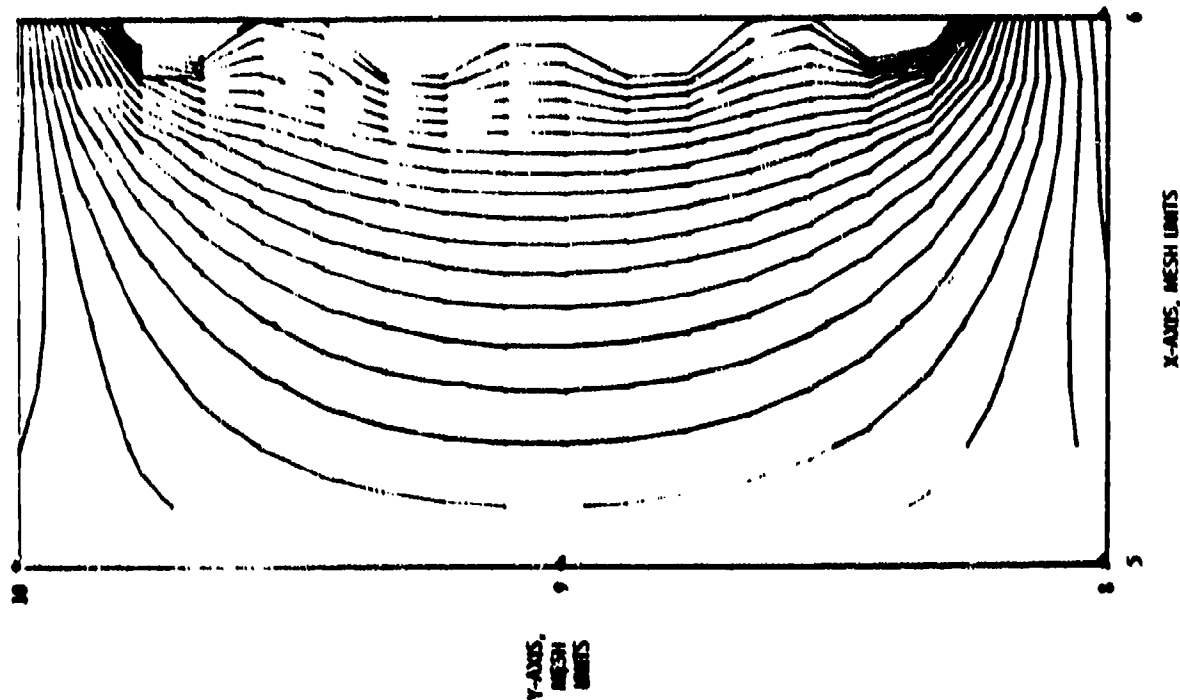
POTENTIAL CONTOURS AT Z = -7.28 FOR BIAS OF +30 V

CONTOUR LEVELS, -0.185 TO 2.96 V WITH POTENTIAL INCREMENTS OF 0.2 V

Y-AXIS, MESH LIMITS

X-AXIS, MESH LIMITS
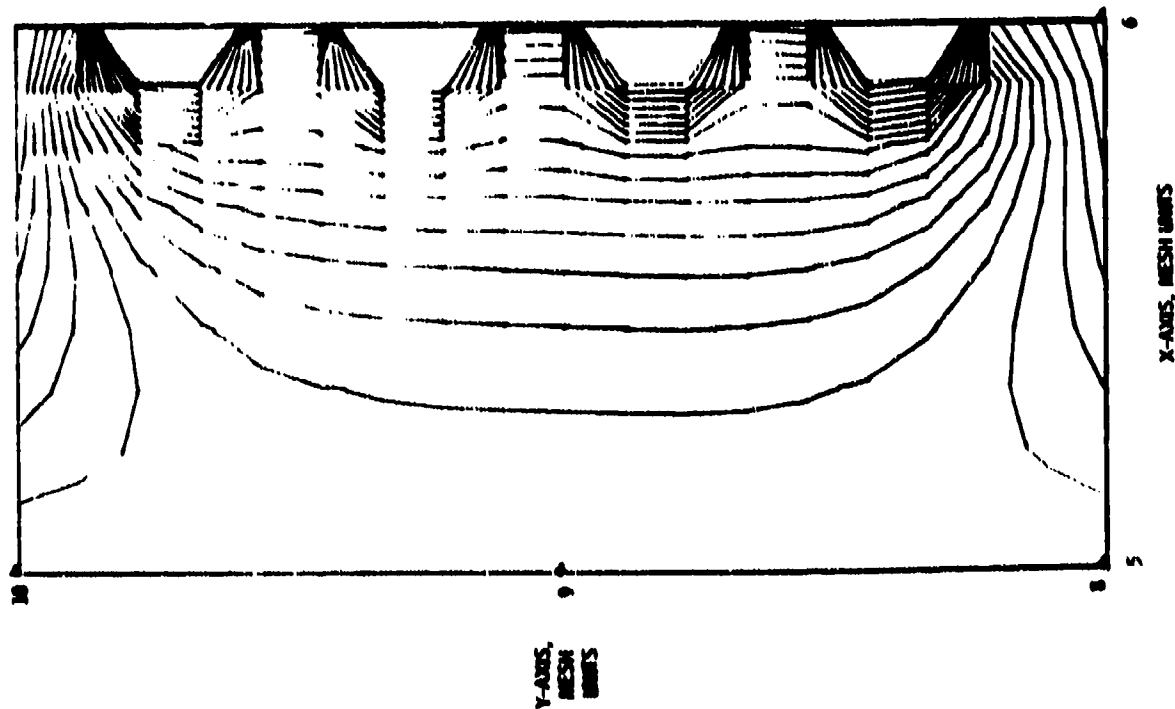
COMPARISON OF NASCAP WITH PIX II DATA

ALL SOLAR ARRAY MODULES HAVE SAME POTENTIAL
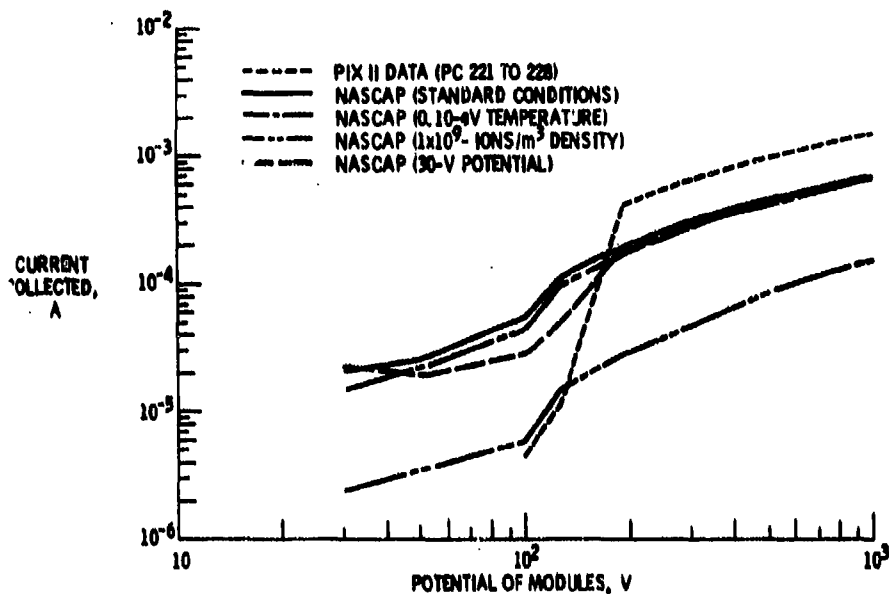
PIX-II FLOATING POTENTIAL
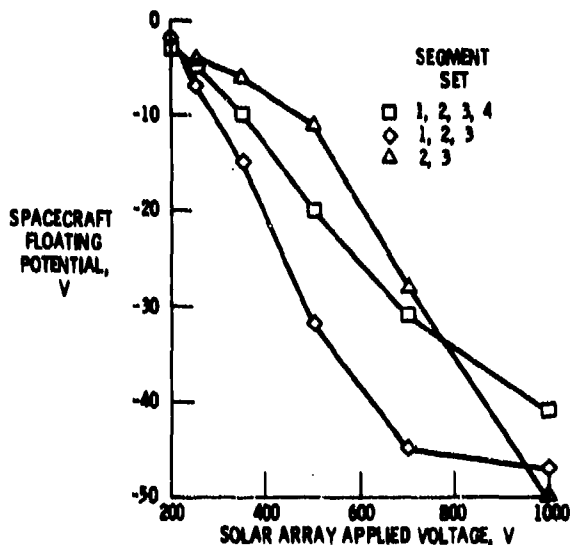
SUMMARY OF RESULTS

LEO MODEL CONSTRUCTED
- 10-INCH RESOLUTION ON VEHICLE
- 1.1-INCH RESOLUTION ON EXPERIMENT

POSITIVE BIAS MODELED
- TEMPERATURE
- DENSITY
- SPACECRAFT POTENTIAL

RESULTS
- SLOPE GOOD ABOVE 200 V
- CURRENT ENHANCEMENT TOO SMALL
- UNKNOWN DENSITY AND SPACECRAFT POTENTIAL COMPLICATE INTERPRETATION

FUTURE WORK
- REFINE DENSITY AND SPACECRAFT POTENTIAL
- RAM/WAKE
- GRADIENT MODE

LEO ENHANCEMENTS
- SELF-CONSISTENT DETERMINATION OF CONDUCTOR POTENTIAL
- BETTER GEOMETRY
- RAM/WAKE DENSITY MODEL

C-5

AN INVESTIGATION OF ARC DISCHARGING ON NEGATIVELY BIASED DIELECTRIC-
CONDUCTOR SAMPLES IN A PLASMA*

William L. Miller
National Aeronautics and Space Administration
Lewis Research Center
Cleveland, Ohio 44135

Proposals are now being developed for the construction of high-power photovoltaic systems for operation in low Earth orbit, where the plasma number density is about 10^3 to 10^6 per cm^3. Existing data indicate that interactions between the plasma and high-voltage surfaces of an orbiting power system will occur. In ground tests, where the applied voltage is increased negatively from ground, the array current collection shows an approximately linear rise until it terminates in arcing at greater than several hundred volts negative. This arcing may reduce the power generation efficiency and could possibly affect the low-level logic circuits of the spacecraft. Therefore it is important that the arcing phenomenon be well understood. This study is a survey of the behavior of different dielectric-conductor samples, including a solar cell module, that were biased negatively in a low-density plasma environment with the intent of defining arc discharge conditions and characteristics. Procedures and results are discussed.

INTRODUCTION

Recent proposals for the construction of large spacecraft to operate in low Earth orbit envision much greater power requirements than those of presently operating spacecraft. The employment of very large solar arrays has been suggested as a means of generating such power. These arrays may operate at higher voltages than have been previously used in order to reduce the mass of conductive materials.

Conventional solar array design exposes cell interconnects to the plasma environment of low Earth orbit, which can be as dense as 10^6 per cm^3. Ground and flight tests have shown the existence of interactions between array surfaces at high voltage and the surrounding plasma. For positive applied bias voltage a nonlinear current collection phenomenon known as "snapover" has been documented (ref. 1). For negative applied bias voltage, to be considered herein, recorded observations of solar arrays (e.g., ref. 2) include current transients and visible flashes of light, both referred to as "arcing." Although no effort to characterize these arcs in detail appears in the literature to date, there is agreement that arcs seem to occur on or near exposed metal surfaces of a solar cell array at bias voltages of -300 V or more (in this paper, "more" implies an increasing magnitude of negative voltage). If violent enough, these

arcs could conceivably disrupt efficient power generation and low-level electronic circuit operation, as well as cause physical damage to the solar cells of an orbiting system. Therefore a thorough understanding of the arc phenomenon is vital for the successful design of large-scale photovoltaic power-generating systems.

In this investigation, dielectric-conductor samples of various configurations, including a solar cell module, were biased negatively in a plasma of known density. The test facility was a small vacuum chamber, equipped with an argon plasma source. Arcing behavior and its dependence on sample configuration, bias voltage, and plasma density were studied.

TEST FACILITY

Figure 1 shows the electrical circuit and a typical experiment configuration. The test chamber was a 46-cm-diameter by 81-cm-high steel bell jar evacuated with mechanical and oil diffusion pumps. Plasma was obtained by flowing argon gas past a hot tungsten-filament cathode located in an anode cylinder immersed in a magentic field. The source was mounted about 40 cm above the test samples and produced densities of 10^3 to 10^5 per cm^3. A 1.3-cm baffle at the exit aperture of the source diffused the emerging particles and prevented filament electrons and other particles in the source chamber from striking the samples directly. With the plasma source on, chamber pressures during testing ranged from $5x10^{-6}$ to $3x10^{-5}$ torr.

The test samples were mounted on electrically insulating rods. They were biased using two external, continuously variable voltage sources connected in series, giving an output of zero to -1000 V. Plasma characteristics data were obtained with a 1.91-cm-diameter spherical Langmuir probe connected to an automated data system. Surface potential profiles were made by using a noncontacting electrostatic potential probe. This probe senses a voltage by nulling the electric field between itself and a small area of test sample surface. The probe was mounted on a movable arm and its sensing surface was swept in a plane 2 to 5 mm above the test sample surfaces.

In the high-voltage electrical line from the voltage source, 21.1-MΩ series resistance was shunted by 0.0117-uF capacitance. Although some tests were run without the series resistance, it served to isolate the discharge process from the characteristics of the voltage source, as well as limit the current flow from the voltage source during arcing to protect the equipment. Collection current was monitored with a digital electrometer and an analog panel ammeter. A current pulse transformer detected transients in the high-voltage line between the capacitors and the sample. The transformer's output was fed to a waveform recorder, connected in turn to an oscilloscope, where the traces were photographed. Surface voltage profiles, test-sample applied bias voltage, and Langmuir probe current were recorded on a strip chart.

PROCEDURE

After the plasma source was allowed to stabilize and the plasma data were obtained, voltage was applied to a sample in 50- to 100-V increments, with a 3- to 10-min waiting period at each voltage. One to 2 min were generally required for collection current stabilization, although completely stable conditions

were not reached in some solar cell array tests. Tests were also conducted by setting the bias voltage at a fixed value for an extended period of time. The longest test duration at a constant applied bias voltage with constant test conditions was 8 hr.

TEST SAMPLES

The samples tested are illustrated in figure 2. The disk/pinhole sample (fig. 2(a)) was a 10-cm-diameter fiberglass disk with a centered 5-cm-diameter electrode. The disk and electrode were completely covered with 0.0127-mm-thick Kapton insulation, except for a 0.8-mm-diameter "pinhole" in the center exposing the electrode. Tests were also conducted with wire strands inserted between the Kapton and the electrode and extending 5 to 10 mm beyond the disk's surface.

A four-solar-cell module (fig. 2(b)) of 2-cm by 4-cm cells was tested with the array output leads shorted together. Two separate tests were conducted with Kapton tape masking all but a small section of the cells and exposed interconnects.

Also examined was a 0.4-mm-base-diameter tapered tungsten pin protruding from a 10-cm-diameter fiberglass disk (fig. 2(c)). The disk covered a 5-cm-diameter, centered, concave electrode. The pin, attached to the electrode, extended through a 0.7-mm-diameter hole in the fiberglass to about 0.8 mm above the disk's surface. Thus metal touched dielectric only on the underside of the fiberglass at the edges of the concave electrode. The back side of the sample was covered with Kapton tape to prevent current collection on the rear surface. The same sample was also tested with a 3-cm by 2-cm piece of Kapton tape on the fiberglass surface. The tape was pierced by the pin so that the pin was in contact with the tape.

Finally, a 5-mm-diameter coaxial cable (RG 58B/U) was cut (fig. 2(d)) with the ground shielding stripped 1.5 cm away from the exposed surface to expose the copper center-conductor and surrounding insulation.

DISCUSSION AND RESULTS FOR INDIVIDUAL SAMPLES

Disk/Pinhole

Current collection rose linearly with voltage but rarely terminated in arcing for the plain pinhole sample. The few arcs that did occur were attributed to dust particles inside the hole. With the wire strands in place, arcs occurred regularly at an applied bias of about -500 V or more and were seen near or in the pinhole but not at the strand tips. The observations might suggest that sharp or discontinuous surfaces and close proximity of dielectric are requirements for arc discharging.

Solar Cell Array

In tests of the fully exposed (unmasked) solar array, arcing occurred at -300 V or more, and arcs were seen on all interconnects, although they tended to occur more frequently toward the outer edges of the array. The exposed area of the second masking test, located on an edge of the array, arced more

369

often than the first, although the exposed metal area was roughly the same (fig. 2(b)).

During long constant-applied-bias-voltage tests, the discharge rate of the fully exposed array segment decreased with time (fig. 3). Perhaps arcs were blunting metal edges, rendering them less likely sites for future arcing. The arc rate appeared to reach some nonzero equilibrium value. However, longer tests are needed to determine this conclusively. The rapid decrease and subsequent rise in arc rate from about 20 to 75 min (fig. 3) may be the result of varying plasma characteristics early in the test.

Visible damage to the solar cell array as a result of arcing (fig. 4) appeared to be limited to a roughening of interconnect surfaces, mostly concentrated in spots near interconnect edges and protrusions. In addition, coloration of the interconnect surfaces occurred along the length of several interconnects. The coloration may be the result of vacuum pump oil contamination, although this is not certain. It is not known to what extent a film of oil might affect the test results.

With the 21.1-MΩ current-limiting series resistance removed, arcs were much brighter, exhibited larger peak currents, and were longer in duration. Damage to the interconnect surfaces was much more extensive and included regions where metal appeared to have melted and then resolidified (fig. 5). Coloration occurred and was also more pronounced and extensive than after tests with the large resistance in place.

Tungsten Pin/Disk

No arcing was observed with the plain pin/disk sample. However, with the Kapton in place, energetic discharges occurred at applied bias of -800 V or more. The difference in behavior with and without the Kapton (arcing versus no arcing) could be due to the differing dielectric properties of fiberglass and Kapton. Yet, based on aforementioned observations of the disk/pinhole sample, it is more likely that the dielectric must be very close to or actually touching an exposed conductor for arcing to occur. The intensity of the arcs and the high threshold voltage for the pin/disk, relative to those of the other samples tested, suggest that the sample configuration and the type of conductive material used play some role in the discharge mechanism.

Cable End

The cable end arced at applied bias of -400 V or more. Since the total insulation area was much less on this sample than on others, it can be deduced that a large dielectric area is not a requirement for arc discharging. Further exploration is needed to determine the nature of dielectric area dependence.

GENERAL ARC CHARACTERISTICS

Some general statements can be made concerning the discharge phenomena observed on all of the samples that arced when tested.

Arc Events

The observed discharges appeared to be blue point flashes that seemed to occur individually. The time between arc events was measured to be as short as 1 sec or less. Often, current collection appeared to be stable right up to the point of discharge, with stable collection resuming shortly afterward. This was excepted in certain cases of a high arcing rate (of the order of 1 arc/sec) when the steady-state collection current was not well defined.

There was an approximately linear increase in collection current as the bias voltage was increased negatively, and discharges began to occur at some definite threshold voltage. As shown in figure 6, steady-state collection was measurable and continued to rise linearly at applied bias voltages greater than or equal to the arcing threshold voltage. The difference in the slopes of the masked solar cell array and pin/disk curves represents the difference in available collection area (exposed metal area) of the two samples.

Threshold Voltage

Each sample that arced did so at a slightly different initial threshold voltage, ranging from -300 V for the fully exposed solar cell array to -800 V for the tungsten pin/disk sample. In all cases the threshold voltage became more negative as the total arcing experience accumulated. For example, a sample with an initial threshold for arcing of -500-V applied bias, which was biased at -800 V for some time, would later exhibit arcs rarely, if at all, at -500 V. The data were not conclusive as to the effect of plasma density on threshold voltage, in part because of this variance in threshold voltage with accumulation of arcing.

Duration and Peak Current

Oscilloscope traces of current pulses were recorded during arc events on various samples. The traces (fig. 7) represent negative charge leaving the capacitors in the electrical system during an arc event. The arc duration was about 10 to 30 μsec with the 21.1-MΩ resistance in series, and greater than 1 msec without the resistance. Arc peak current was generally 0.5 to 2 A with the resistance, and about 40 A or more without it. The fact that arc peak current decreased with series resistance may indicate a cutoff point at which the available current would not be enough to sustain arcing.

Arc Rate

The arc rate increased with applied voltage and plasma density for the fully exposed solar array (fig. 8). This behavior was characteristic of all of the samples that arced. The arc rate decreased with time during long tests of the fully exposed solar cell module (fig. 3). This trend was also indicated during shorter tests of other samples. As stated earlier, longer tests are needed to determine conclusively whether the arc rate does indeed reach some nonzero equilibrium value.

Surface Voltage Profiles

Strip-chart records of typical surface potential profiles were obtained by sweeping the electrostatic probe (fig. 9). Characteristics of these profiles include large voltage readings over exposed metal regions and lower potential readings over dielectric areas. During the electrostatic probe's sweep, discharges would often occur as the probe moved over an exposed metal region. This behavior suggests that the probe could have induced some discharges. It is thought that localized solar cell arcs affect the surface potentials of the rest of an array (ref. 3). The potential profiles made in this investigation indicate that the test-sample response time to an arc event was probably shorter than the response times of the electrostatic probe and the strip chart.

In addition, the results show that arcs can occur not only on solar cell arrays, but also on other surfaces with exposed metal that are biased at high voltages in a plasma.

SUGGESTIONS FOR FURTHER STUDY

More data are needed to clarify the relationships of arc rate and threshold voltage to bias voltage and plasma density. Surface potentials and plasma behavior should be examined more closely. It must be discovered to what extent arcs physically affect the dielectric-conductor surfaces and current-voltage characteristics of a given test sample. A metal plate placed some distance above a test sample surface might show if and how much metal or dielectric is vaporized. Finally, since arcing is an optical as well as electrical phenomenon, spectral analysis of the discharges could provide valuable insights into arc mechanism and composition.

Of major concern is the comparative validity of results obtained by using a test rig containing shorted solar cell arrays that are biased with an external power supply rather than by using self-generated voltages. The difficulties that arise here are the introduction of the effects of the external supply's characteristics and the lack of the ability to examine the actual electronic behavior of the solar cells during arcing. Also, the test chamber's limited size (and the subsequent introduction of boundaries) probably affects the plasma behavior (e.g., wave propagation). However, this test setup does allow for visual and spectroscopic observation of arcs, which would probably not be possible during a simulated sunlight test because of the great intensity of ambient light in the test chamber.

CONCLUSIONS

This study confirms the results of previous studies that found that visible arcs occur on, or very near, the interconnects of solar cell arrays biased several hundred volts negative. The results show that arcing is not solely a solar array phenomenon, but that arcs can occur on other dielectric-conductor configurations as well. There are indications of geometrical, material, plasma density, and applied bias voltage dependence of the discharges. In addition, the arc behavior of a sample can be categorized by parameters that include arc rate, threshold voltage, duration, arc current, and optical intensity. Moreover, further study is required before the arc phenomenon will be

adequately understood, and hence, before the limiting factors of arcing in the
design of large high-power photovoltaic systems can be thoroughly assessed.

REFERENCES

1. Stevens, N. J.: Space Environmental Interactions with Biased Spacecraft
    Surfaces. Space Systems and Their Interactions with Earth's Space
    Environment, Henry B. Garrett and Charles P. Pike, eds., AIAA, 1980,
    pp. 455-476.

2. Grier, N. T.: Experimental Results on Plasma Interactions with Large
    Surfaces at High Voltages. NASA TM-81423, 1980.

3. Snyder, D. B.: Discharges on a Negatively Biased Solar Array in a Charged
    Particle Environment. NASA TM-83644, 1983.
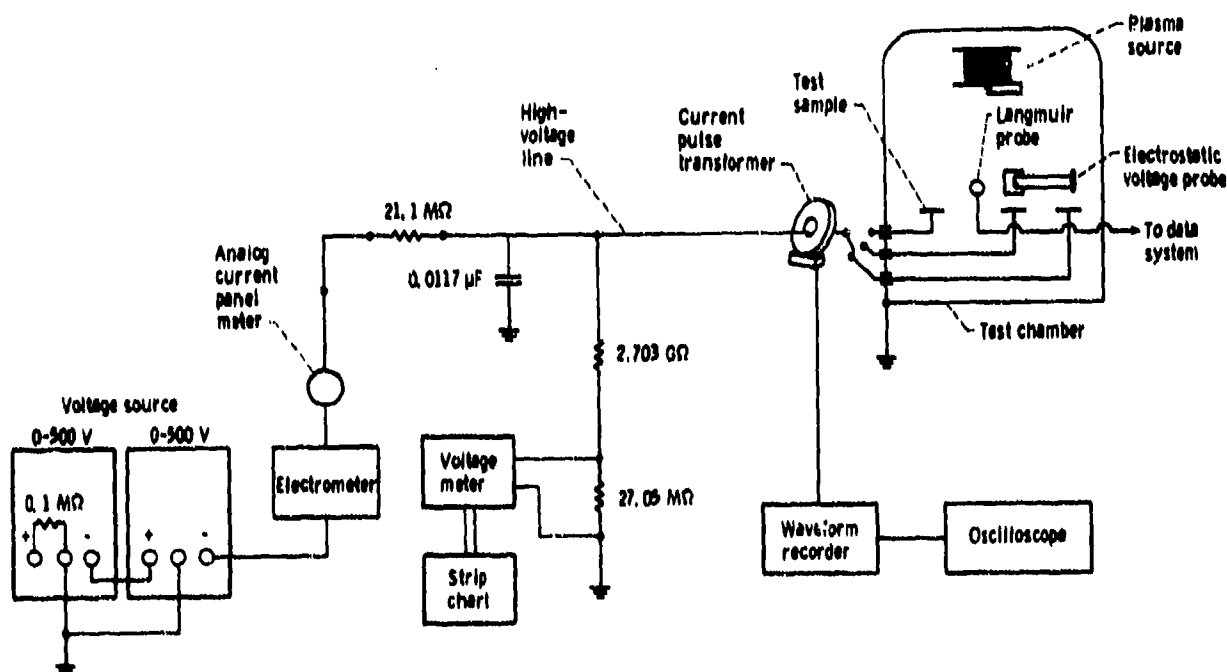
(a) Circuitry.
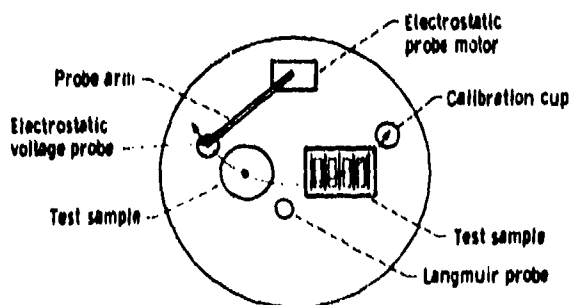
(b) Configuration and electrostatic probe path.

Figure 1. - Typical experiment circuitry and configuration.

(a) Disk/pinhole.

(b) Solar cell module.

(c) Tungsten pin/disk.

(d) Cable end.

Figure 2. - Test samples.

374
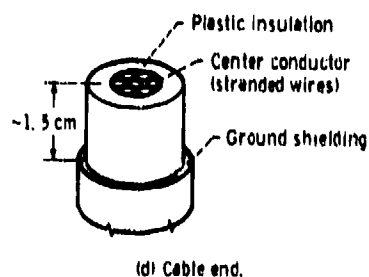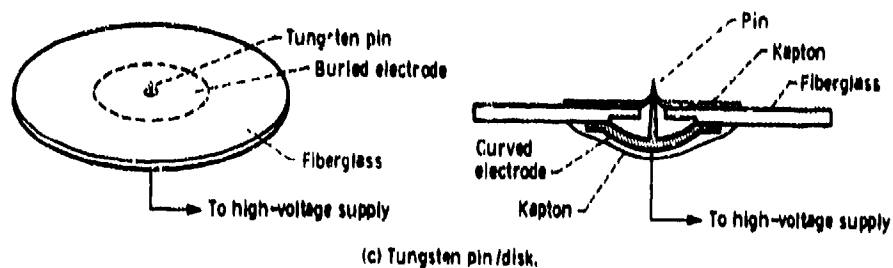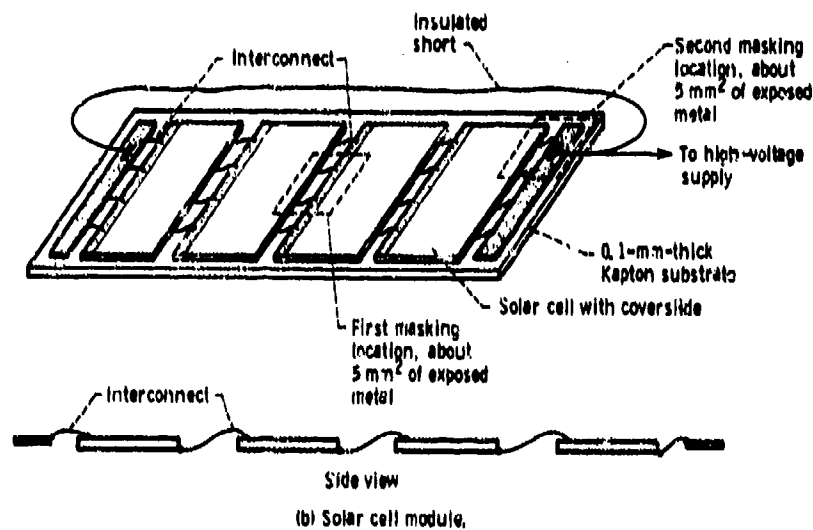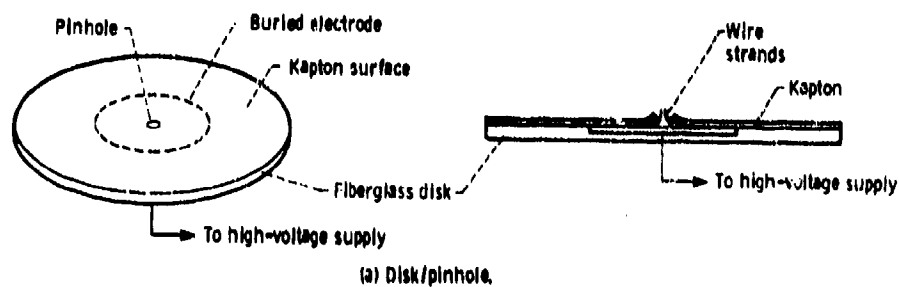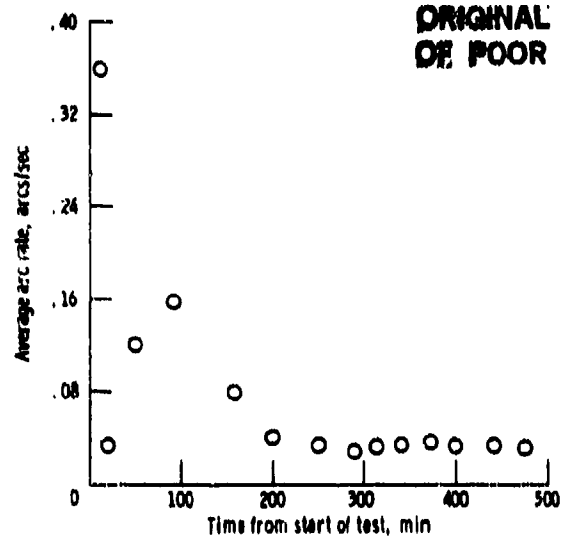
Figure 3. - Arc rate decrease during long constant-
voltage test. Fully exposed solar cell module; applied
bias voltage, -700 V; plasma number density,
$N_e = 1.8 \times 10^5$ electrons/cm^3.
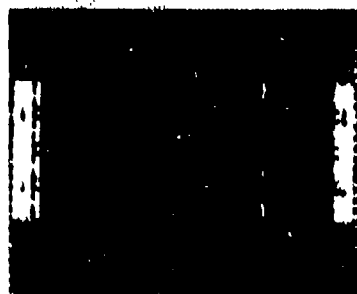
(a) Untested specimen.
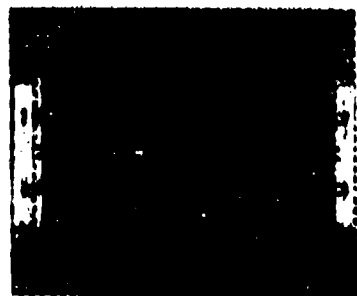
(b) Tested specimen.

Figure 4. - Comparison of untested solar cell
module and one that underwent extensive
arcing tests without current-limiting
resistance.
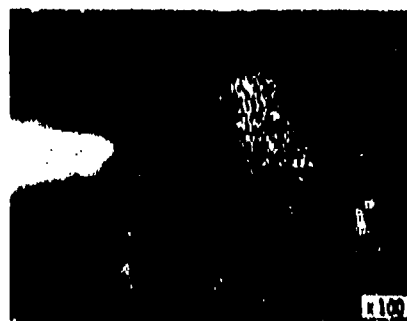
Figure 5. - Damage at two separate interconnect
locations on fully exposed solar cell module after
tests without current-limiting resistance.

375
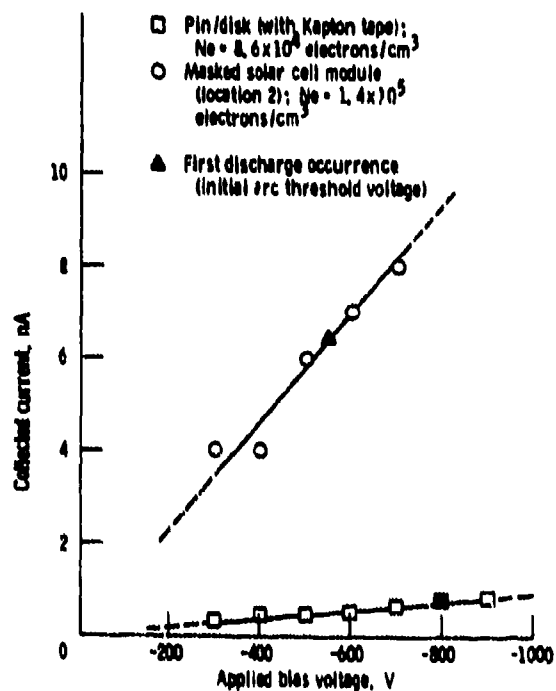
Figure 6. - Linear rise of collected current with applied bias. Voltage thresholds (initial arcs) are indicated.
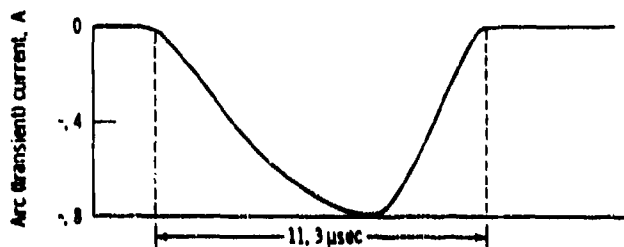
(a) Fully exposed solar module. Applied voltage, -600 V; capacitance, 0.01 μF.
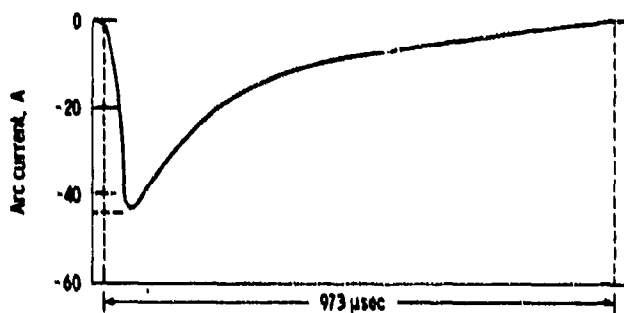
(b) Fully exposed solar cell module. Series resistance removed; applied voltage, -775 V.
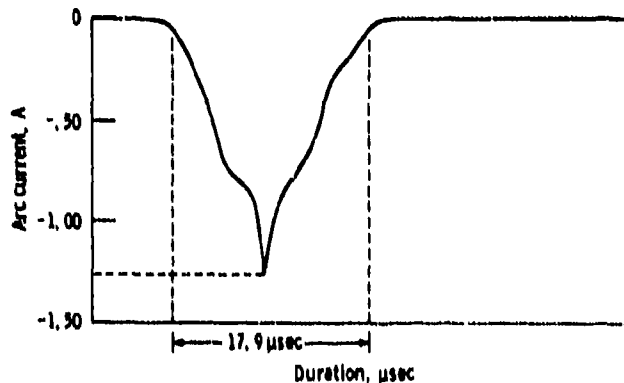
(c) Tungsten pin/disk with Kapton tape. Applied voltage, -800 V, capacitance, 0.01 μF.

Figure 7. - Illustrations of oscilloscope traces recorded during arc events, showing peak current and duration of arcs.

(a) With applied bias voltage.
$Ne = 1.64 \times 10^5$ electrons/cm³.

(b) With plasma density. Constant applied bias voltage, –600 V.
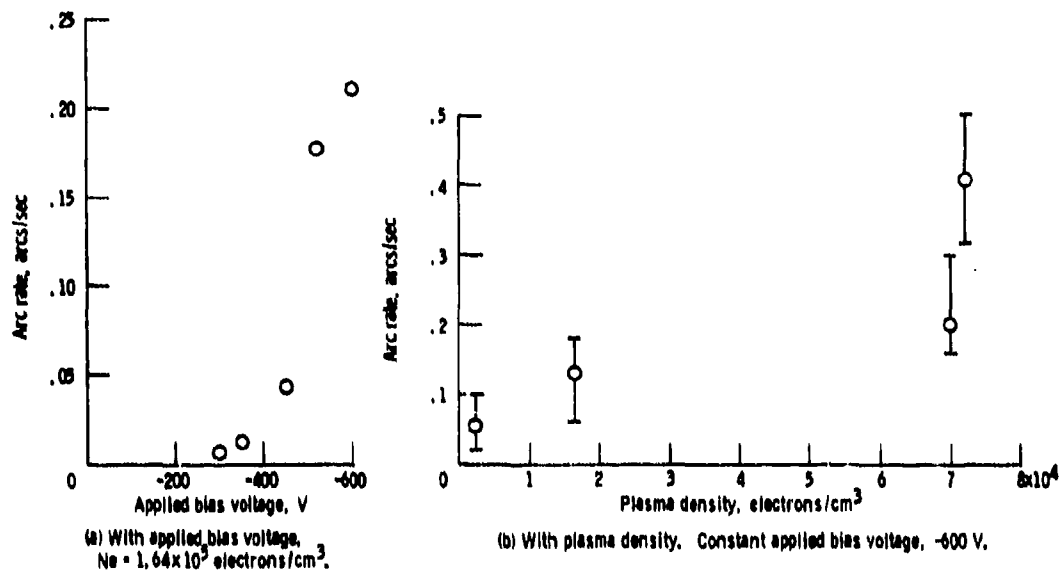
Figure 8. – Arc rate increase for fully exposed solar cell module.

(a) Fully exposed solar cell (five interconnects and four cells).

(b) Pin/disk with Kapton tape.
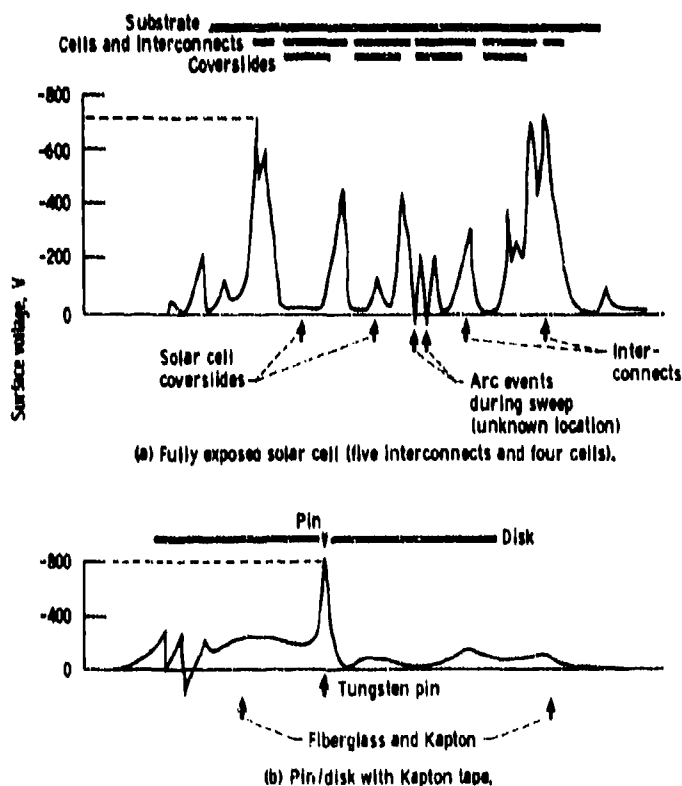
Figure 9. – Surface voltage profiles made with sweeping electrostatic probe.
Exposed metal regions at high voltages; dielectric at lower potentials.

377

DISCHARGES ON A NEGATIVELY BIASED SOLAR CELL ARRAY
IN A CHARGED-PARTICLE ENVIRONMENT

David B. Snyder
National Aeronautics and Space Administration
Lewis Research Center
Cleveland, Ohio 44135

The charging behavior of a negatively biased solar cell array when subjected to a charged-particle environment was studied in the ion density range 200 to 12 000 ions/cm^3 with the applied bias range -500 to -1400 V. The profile of the surface potentials across the array was related to the presence of discharges.

At the low end of the ion density range the solar cell coverslides charged to 0 to 5 V independent of the applied voltage. No discharges were seen at bias voltages as large as -1400 V. At the higher ion densities the coverslide potential began to fluctuate and became significantly negative. Under these conditions discharges can occur. The threshold bias voltage for discharges decreased with increasing ion density. A condition for discharges emerging from the experimental observations was that the average coverslide potential must be more negative than -4 V. The observations presented suggest that the plasma potential near the array becomes negative before a discharge occurs. This suggests that discharges are driven by an instability in the plasma.

INTRODUCTION

It is well known that if an unilluminated, shorted solar cell array is biased sufficiently negative in the presence of a plasma, it will exhibit arc discharges (refs. 1 to 3). The trigger mechanism for these discharges is not yet understood. This work studied this effect. The current working hypothesis (ref. 3) is that when the electrical field strength between the solar cell coverslides and the interconnects becomes too great, a discharge can occur. The electric fields will be roughly proportional to the potential difference between the interconnects and adjacent coverslides and the distance over which most of the change in potential occurs.

As an alternative hypothesis, I assumed that the gradient of the potential causes the attracted positive ions to be focused on the interconnects and that the size of the region over which the potential changes can vary, changing the efficiency with which ions are collected at the interconnects. Eventually, over microseconds, this current might become great enough to overload the power supply and result in an apparent discharge.

In this study, both of these hypotheses were examined, taking into account the potentials observed on the biased solar array. A shorted, biased solar array was subjected to a plasma where the ion density was low enough that the

379

profile of the potential along the surface of the array changed on a time scale of seconds to minutes. The profile of the potential along a portion of the array was monitored by sweeping an electrostatic voltage probe across the array at 5-min intervals. Discharges were detected by a probe that was capacitively coupled to the back of the array. With this apparatus the conditions under which discharges do and do not occur was investigated. The charging behavior of the coverslides is discussed with respect to these discharges.

The observations reported herein do not support either of the preliminary hypotheses, which assume that a discharge arises from the electric fields on the array. Instead the plasma itself may be responsible for the discharge.

EXPERIMENT

This work was undertaken to measure the profile of the potential across a biased solar array and to determine its response to a plasma environment. Of special interest is the behavior under conditions where discharges occur. The experimental apparatus (fig. 1) consisted essentially of a plasma source, a solar array, plates to monitor the environment, and an electrostatic probe to read the potential along the surface of the array. The vacuum chamber was 1 m in diameter by 2 m long. It used ion pumps and a turbopump to reach a base pressure of under 10^{-6} torr. During these experiments, with the plasma source on, the pressure was in the range 4×10^{-6} to 10×10^{-6} torr, the lower pressure corresponding to lower ion densities.

An electron bombardment ionizer was the plasma source. It used a hot filament to generate electrons. The electrons were accelerated to about 50 V to ionize nitrogen gas as it flowed into the vacuum system. Current through a coil concentric with the ionization chamber generated a magnetic field to increase the effective path length of the electrons in the gas and thus increase the plasma density.

Limited plasma measurements were obtained during the experiments. To improve confidence, plasma characteristics under similar conditions were obtained later by using a 1200-cm^2 plate as a Langmuir probe. The electron temperatures were about 1 eV; the plasma potentials were about 10 V; and the ion densities ranged from 200 to 12 000 cm^{-3}. These parameters should be regarded as order-of-magnitude estimates.

The array segment (fig. 2) used in this work was originally constructed for the SPHINX satellite. It has been used for studies of electron-beam-stimulated discharges (refs. 4 and 5). It was constructed from twenty-four 2-cm by 2-cm solar cells connected in series and forming a 6x4 array. The interconnects were 1-mm-wide silver strips running along the edge of each cell and had four flat wires forming the connections to the following cell. The gaps between cells for these connections were 0.2 to 0.5 mm wide. The surfaces of the cells were protected by fused silica coverslides, 0.15 to 0.25 mm thick. The coverslides did not extend over the main metal strip. The base for the array was a fiberglass printed circuit board. A sheet of Kapton separated the array and base. On the back of the base, a 2.5-cm-radius copper disk had been etched and covered with Kapton. This back plate served as a probe capacitively coupled to the array and measured changes in the array's potential. The bias

voltage was applied to the interconnects with a Spellman RHR-20PN60/RVC power supply. This power supply can provide voltages to 20 kV and current to 3.3 mA (ref. 6).

During a typical run data were taken for 1920 sec and stored at 0.5-sec intervals by a MINC-23 computer with an analog/digital converter. At 300-sec intervals the noncontacting Trek electrostatic voltage probe was swept across the array. This probe reads a voltage by nulling the electric field between itself and area being investigated. It was close enough to the array, about 0.75 mm, to average the potential over an area of about 1.6 mm^2. The probe took 120 sec to sweep down the array, during which time its position and voltage were recorded. During the following 180 sec, until the next probe sweep, the pressure was monitored. The electrostatic probe returned to its base position over a ground reference plate during the first 60 sec of this period.

Discharge transients were detected by using the back-plate probe. The capacitance of the back plate to the solar array was 65 pf, and to ground it was 616 pf. A fast test pulse was used to determine the characteristics of the system. This caused the cable to ring at 15 to 20 MHz, consistent with the 4.4-m cable length from back plate to a Biomation 610B transient recorder. But the transient recorder had an internal high-frequency limit of 2.5 MHz. The 50-ohm cable was terminated with 50 ohms at the transient recorder but was open at the back plate. This arrangement measured rate of change of the average voltage on the array. During discharges the arc current exceeded the current limit of the power supply, and the power supply did not succeed in maintaining the bias voltage at the discharge site on the solar array. The signal shown in figure 3 is characteristic of discharges that appear as arcs on the array. The time of appearance of this signal was used as the time of discharging. The discharge times were recorded and the waveforms of the discharges (i.e., the current to the back plate) were recorded by the transient recorder.

RESULTS

Three sets of data were obtained: one for low ion density (pressure of 4×10^{-6} torr; ion density of about 200 cm^{-3}), one for a medium density (pressure of 6×10^{-6} torr; ion density of about 8000 cm^{-3}), and one for a high ion density (pressure of 8×10^{-6} torr; ion density of about 12 000 cm^{-3}). The data obtained are summarized in table I.

At low ion densities, bias voltages of -600 to -1400 V were applied. No discharges occurred. A typical electrostatic voltage profile across the array is shown in figure 4. Figure 4(a) illustrates the profile across the array at various times; figure 4(b) shows the behavior of two particular cells. When the biasing voltage was first applied, both the interconnects and the coverslides went to the applied potential (i.e., the coverslides had no net charge). The coverslides then slowly accumulated positive charge and approached a slightly positive potential. The potential of the surrounding Kapton changed relatively rapidly because of its lower capacitance to the interconnects. On the array itself the central coverslides charged rapidly, with those coverslides closest to the plasma source charging most rapidly. This effect was probably related to the array's vertical orientation in the tank. When the array was vertical, the door of the tank was about 1 m in front of it and the center charged most rapidly. In a horizontal orientation, the edges of the array charged most rapidly, with the wall of the tank being about 0.4 to 0.5 m

381

above the array. This behavior was apparently a consequence of the relevant characteristic lengths of the plasma being of the same order of magnitude as the dimensions of the tank. This particular charging feature is not expected in space.

The coverslides tended to charge to a slightly positive potential, 4 to 10 V. They simply charged to the plasma potential. At high bias voltages fluctuations in potential across the array appeared and tended to get more pronounced at higher biases, as shown in table I. These fluctuations suggest that the local plasma potentials near the array are becoming nonuniform.

At higher ion densities the behavior of the coverslide potential was substantially different (fig. 5). Initially the coverslides charged rapidly to a slightly positive potential (the plasma potential). But the coverslides then slowly became negative, and the potential across the array began to fluctuate. At higher negative biases and higher ion densities, the average coverslide potential was more negative, and the fluctuations became more substantial. This is demonstrated in table I, where the high standard deviations indicate significant variations in potential across the array. Under these conditions discharges can occur.

The fluctuations in potential across the array can be used to identify sites associated with discharges. The potentials of the two coverslides at 1 and 3 cm (fig. 5(a)) became increasingly negative between 300 and 900 sec. After a discharge at 1189 sec this feature disappeared, an indication that the discharge occurred near this region of the array.

In several cases discharges occurred while the electrostatic probe was measuring the surface potential. From these cases (fig. 6) it is apparent that the coverslides attained nearly the interconnect potential at the time of the discharge and then recharged to ground. Since not all of the features in the potential profile were changed, the discharge was apparently a local effect.

DISCUSSION

The shapes of the potential profile near an interconnect are shown under conditions that do not (fig. 7) and do (fig. 8) cause discharges. Figure 7 shows the measured voltage profile at an interconnect at low ion density for biases of both -800 and -1400 V (i.e., conditions where no discharges were detected). The spatial resolution of the electrostatic probe is poor compared with the size of an interconnect, and the distances between positions where the potentials are read were long compared with the width of the interconnects. However, data from separate probe sweeps were consistent with each other. Data from separate sweeps could be aligned by calculating the position of the negative peak from the curvature at the three most negative points. When aligned in this way, the data constructed a consistent view of the potential in the region of the interconnect. In fact, there were no measurable differences between the two profiles when the -800-V profile was normalized to the -1400-V profile by using an appropriate scaling factor of 14/8.

Figure 8(a) shows the profile at an interconnect biased to -1000 V under conditions where discharges were detected. The primary difference between profiles obtained at different times was that the average potential of the

coverslides shifted. In figure 8(b) the data points for this case are super-
imposed on and compared with the profile when no discharges were seen (-800 V).
The difference between these two sets of data was primarily due to the cover-
slide potentials.

The hypothesis proposed by Stevens et al. (ref. 4) that discharges are
related to the potential gradient between the coverslides and the interconnects
is not supported by this work. At low ion densities no discharges were seen
even though the coverslide potentials reached ground and the bias was very neg-
ative. In contrast, under discharge-prone conditions, discharges were more
likely to occur when the coverslides were at a substantially negative potential
rather than when their potentials were near ground or slightly positive. The
electric fields did not appear to change significantly. The spatial resolution
of the measurement was millimeters, so this observation was not conclusive.
In fact, these measurements show that the electric field was above 10^6 V/m.
But because the coverslides were more negative, and the change in voltage less
under conditions where discharges occurred than when they did not, the hypoth-
esis was not supported.

Similar conclusions were drawn with respect to the other hypothesis ad-
vanced here, that focusing of the attracted ions near the interconnect is im-
portant to the discharge mechanism. Changes in the surface potentials near
the interconnects would permit the ion-focusing characteristics of the inter-
connect to change. At low ion densities the profile of the potential near the
interconnects did not change with bias voltage, within the resolution of the
experiment.

In cases where discharges occurred (fig. 8), the behavior was less con-
clusive. The shape obviously changed, yet the variations were primarily due
to shifts in the coverslide potential. The width of the interconnect region
did not change significantly. If the potential profile did change, it was
only over distances as small as, or smaller than, the interconnect width.
Therefore the size of the region over which focusing could change was small.
This work produced no evidence that ion focusing near an interconnect is im-
portant to discharging.

These data do indicate that discharges occurred when the average cover-
slide potential was more negative than -4 V, regardless of bias voltage.
Figure 9 shows the average coverslide potential as well as its standard devia-
tion at various interconnect biases, for different plasma conditions. In
addition the number of discharges in a half-hour run is shown for those cases
where discharges occurred. This average was determined by the ion density and
the bias voltage. Except for the single case of a discharge at -600 V, all
discharges occurred when some coverslides were negative.

The charged-particle environment near the array became negative under con-
ditions where discharges can occur. The current to the grounded sensor became
negative, and the coverslide potential became negative by several tens of volts
locally. Two reasons are suggested for this behavior: the increase in nega-
tive charge density could be due to secondary electron emission from ion colli-
sions with the array, or it could indicate that interconnects at high negative
biases have more of an influence on the shape of the sheath near the array at
high densities that at low densities and that the shape of the sheath has an
important role in the occurrence of discharges.

The second suggestion seems to be the more likely of the two. The electron emission could not be from the coverslides, since they approached a roughly equilibrium potential. This emission could occur only near the interconnects, and this would limit the amount of emission available for a discharge. Also since the secondary electron yields for ions on metals are low, ion collection should not induce significant electron emission. An instability in the plasma, however, might be able to access the large amounts of charge from the plasma used in a discharge.

CONCLUSIONS

The data collected in this work have been examined in an effort to identify the mechanism initiating discharges on biased solar arrays in a plasma. The evidence submitted does not support either of the two hypotheses examined. The potential gradient near an interconnect was not directly responsible for the discharges. At very low plasma densities, biases as large as -1400 V did not result in discharges even though the coverslides charged slightly positive. With a resolution of the order of millimeters, the distance over which the potential changed with no discharges resulting was no different than the distance for cases that resulted in discharges. In addition, the electric field near the interconnects was greater when no discharges were seen than when they were seen.

Focusing of attracted ions probably does not play an important role in the initiation of discharges. Again, the shape of the potential profile near the interconnect did not change appreciably, on a scale of millimeters, between conditions that produced discharges and those that did not.

Both the plasma and dielectric surfaces seemed to play important roles in the initiation of discharges. Before discharges occurred, the coverslides on the array became negative. This indicated that changes in the plasma sheath were taking place, which in turn suggested that the plasma itself was playing an important role in the appearance of discharges on high-voltage arrays. The plasma was not simply supplying charge to the process but might have been driving the discharges.

Further work needs to be done to verify these observations. First, the work should be carried out under better controlled and monitored conditions. The fluctuations in the coverslide potentials should be observable at lower bias voltages at higher plasma densities. In addition, theoretical work should be done to discover if plasma instabilities can exist under these conditions.

REFERENCES

1. Stevens, N. John: Review of Biased Solar Array - Plasma Interaction Studies. NASA TM-82693, 1981.

2. Grier, Norman T.; and Stevens, N. John: Plasma Interaction Experiment (PIX) Flight Results. Spacecraft Charging Technology, 1978. NASA CP-2071, AFGL-TR-79-0082, 1979, pp. 295-314.

384

3. Grier, Norman T.: Experimental Results on Plasma Interactions with Large Surfaces at High Voltages. NASA TM-81423, 1980.

4. Stevens, N. John; Mills, Hilton E.; and Orange, Lisa: Voltage Gradients in Solar Array Cavities as Possible Breakdown Sites in Spacecraft-Charging-Induced Discharges. IEEE Trans. Nucl. Sci., vol. 28, no. 6, Dec. 1981, pp. 4558-4562.

5. Snyder, D. B.: Environmentally Induced Discharges in a Solar Array, IEEE Trans. Nucl. Sci., vol. 29, no. 6, Dec. 1982, pp. 1607-1609.

6. Instruction Manual: Model RHR20PN60/RVC High Voltage Power Supply, Serial No. SPC-1878-3, Date Produced - Aug. 82. Spellman High Voltage Electronics Corp., 1982, pp. 1-2, 1-16.

TABLE I. - DATA OBTAINED

Bias voltage, V	Pressure, torr	Coverslide, voltage, V	Number of discharges
Low ion density (about 200 cm^{-3})			
-600	3.70x10^{-6}	2.5±0.9	0
-800	3.30	3.0±1.2	
-1000	4.40	4.5±1.6	
-1200	3.90	3.7±1.2	
-1400	4.10	2.3±5.4	
Medium ion density (about 8000 cm^{-3})			
-600	6.15x10^{-6}	18.2±4	1
-800	6.45	10.0±6	0
-900	6.15	3.6±6	0
-1000	5.00	-3.1±11	0
-1100	5.65	-6.0±15	1
High ion density (about 12 000 cm^{-3})			
-500	8.05x10^{-6}	8.3±11	0
-600	8.00	6.3±16	0
-700	7.40	-4.5±19	0
-800	8.35	-17.8±20	2
-900	7.90	-16.4±25	4
-1000	8.00	-31.4±28	4
-1100	7.70	-3.3±14	2
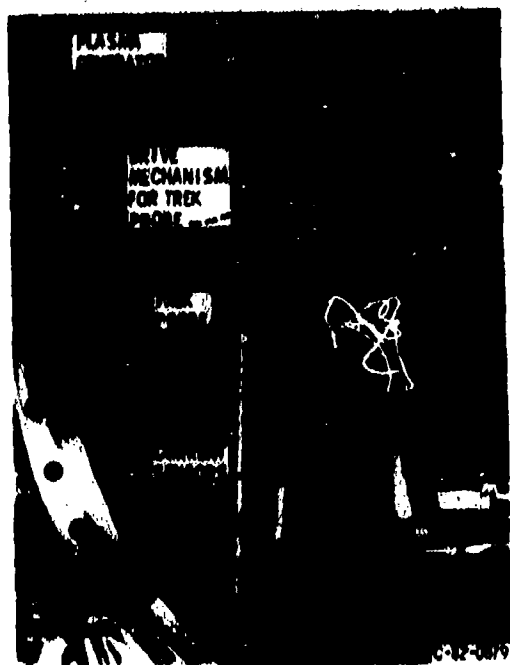
Figure 1. - Tank arrangement.

ROW SWEPT
BY TREK PROBE
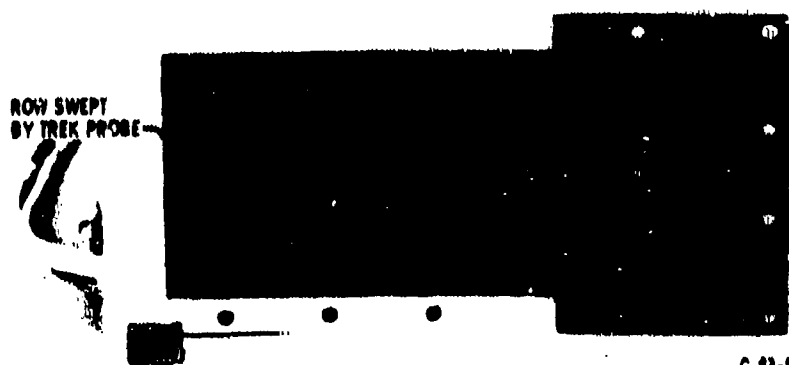
C-83-5902

Figure 2. - Solar array.
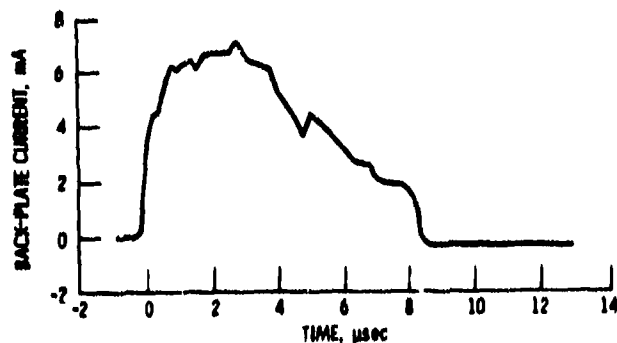
Figure 3. - Back-plate response to a discharge. Bias, -800 V; ion
density, 12 000 cm^{-3}.
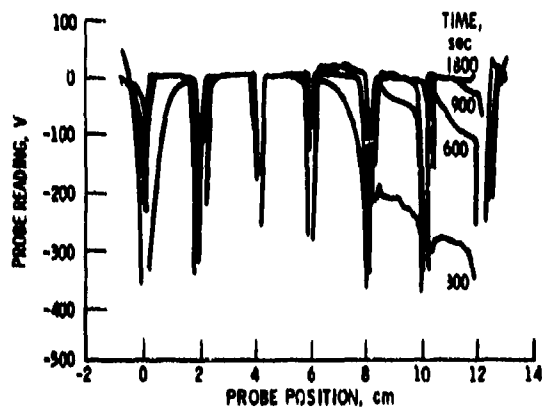
(a) Voltage profile of array.
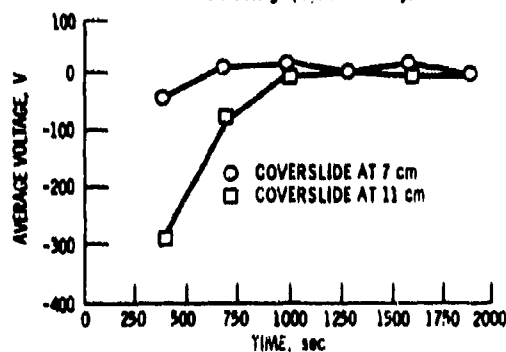
(b) Average voltage of individual coverslides as function of time.

Figure 4. - Coverslide behavior at low ion density. Bias, 1400 V; ion density, 200 cm^{-3}.
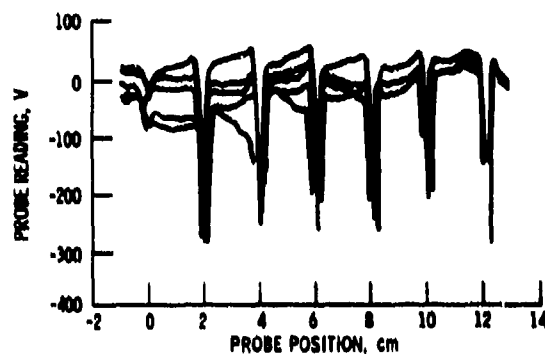
(a) Voltage profile of array.
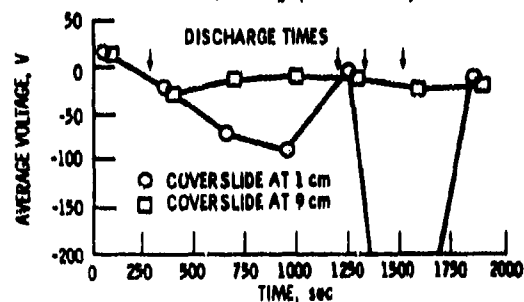
(b) Average voltage of individual coverslides as function of time.

Figure 5. - Coverslide behavior under conditions that allow discharges. Bias, -1000 V; ion density, 12 000 cm^{-3}.

(a) Bias, -800 V.

(b) Bias, -1000 V.
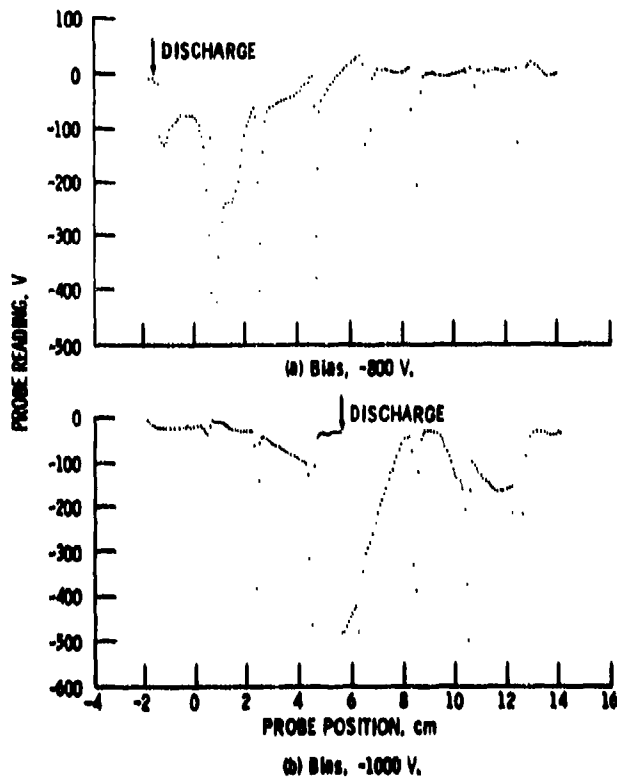
Figure 6. - Coverslide behavior during a discharge. Density, 12 000 cm⁻³; 0.5 sec per point.

(a) Bias, -1000 V; ion density, 12 000 cm⁻³.

(b) 800-V reading scaled by 10/8.
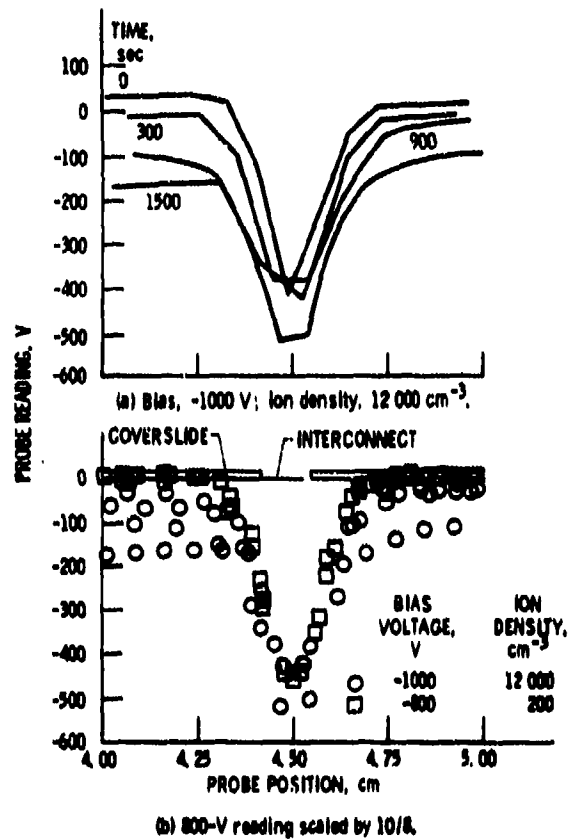
Figure 8. - Profile of potential near an interconnect under conditions where discharges can occur.
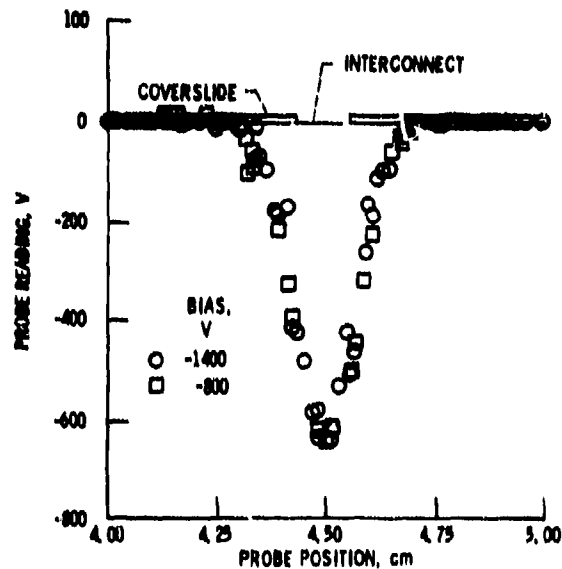
Figure 7. - Profile of potential near an interconnect under conditions where discharges cannot occur. Ion density, 200 cm⁻³; 800-V reading scaled by 14/8.
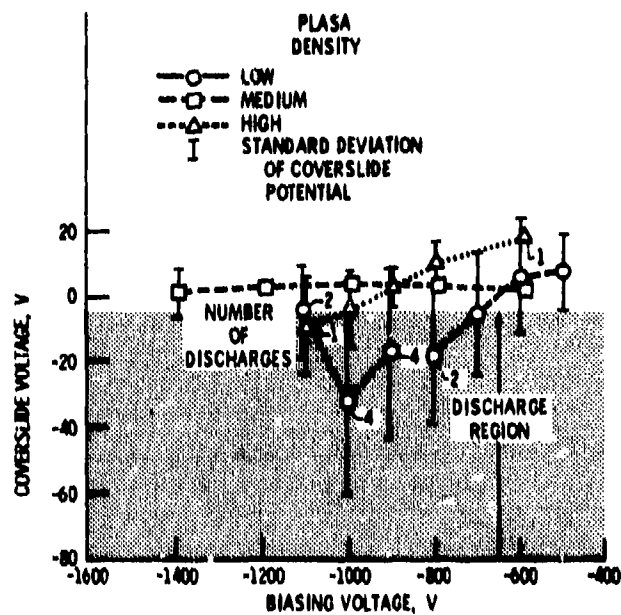
Figure 9. - Summary of average coverslide potentials.

383

DESIGN GUIDELINES FOR ASSESSING AND CONTROLLING SPACECRAFT CHARGING EFFECTS

Carolyn K. Purvis
National Aeronautics and Space Administration
Lewis Research Center
Cleveland, Ohio 44135

H. B. Garrett and A. Whittlesey
California Institute of Technology
Jet Propulsion Laboratory
Pasadena, California 91109

N. John Stevens
Hughes Aircraft Company
El Segundo, California

Experience has indicated a need for uniform criteria, or guidelines, to be used in all phases of spacecraft design. Accordingly, guidelines have been developed for the control of absolute and differential charging of spacecraft surfaces by the lower energy (less than approximately 50 keV) space charged-particle environment. Interior charging due to higher energy particles was not considered. The guidelines have been compiled into a NASA Technical Paper entitled "Design Guidelines for Assessing and Controlling Spacecraft Charging Effects," NASA TP-2361.

The document is divided into five sections: (1) spacecraft charging concepts of importance to the designer, (2) the modeling techniques to be used to assess whether the design is adequate for environmental immunity, (3) specific guidelines for protecting systems and subsystems, (4) test procedures for demonstrating system immunity, and (5) active charge control and monitoring techniques. Appendixes present illustrative examples and the bibliography lists other documents for those desiring further information on specific topics.

The design guidelines document is to be regarded as a guide to good practices for assessing and controlling charging effects. It is not a NASA or Air Force mandatory requirement unless specifically included in project specifications. It is expected, however, that this document, revised as experience may indicate, will provide uniform design practices for all space vehicles. Copies can be obtained by contacting Carolyn K. Purvis.

AEROSPACE SPACECRAFT-CHARGING GUIDELINES DOCUMENT

J. F. Fennell, D. F. Hall, H. C. Koons,
P. F. Mizera, and A. L. Vampola
The Aerospace Corporation
Los Angeles, California 90009

A short summary document on spacecraft charging has been prepared for use by engineers in the various Aerospace Corporation program offices that support Air Force Space Division programs. The document outlines the magnetospheric charging environment at near-geosynchronous altitudes, discusses the mechanisms of charging and discharging, and presents statistical results from the P78-2 (SCATHA) satellite engineering experiments. The document is intended to be a layman's source for charging information and for design guidance and criteria.

EMI CHARACTERISTICS OF A POTENTIAL CONTROL SYSTEM*

D. E. Donatelli
Boston College
Chestnut Hill, Massachusetts 02167

H. A. Cohen and W. J. Burke
Air Force Geophysics Laboratory
Hanscom Air Force Base, Massachusetts 01731

H. C. Koons
The Aerospace Corporation
Los Angeles, California 90009

With the development and use of charged particle sources for controlling space-
craft potentials there is a need to better understand the effects of these systems
on spacecraft operations. The emission of charged particles perturbs the spacecraft
environment and signals are generated which may interfere with other vehicle functions.
In particular, the generated signals are apt to interfere with detectors for observing
waves that exist naturally in the space environment. Examples of this type of inter-
ference are presented from the SCATHA satellite during a period when the vehicle was
highly charged. A plasma source on board the spacecraft succeeded in discharging
the vehicle with each of four different operating modes. The VLF broadband receiver
on SCATHA detected interference over the entire 0-5 kHz range of both the electric
and magnetic field detectors during these charged particle emissions. This frequency
range includes the 2 kHz electron gyrofrequency but is below the 9 kHz electron plasma
frequency. The observations suggest that interference occurs through introduction
of anomalous signals, and through suppression of background field measurements.

INTRODUCTION

The development of active means for controlling spacecraft potentials is moti-
vated from both engineering and scientific considerations. Large spacecraft potentials
may be responsible for operational anomalies (ref. 1 and references therein) and may
interfere with measurements of the characteristics of the cold plasma embedded in
the plasma sheet. The cold plasma plays a significant role in providing neutralizing
currents to spacecraft (ref. 1). It also acts as a catalyst for the generation of
wave turbulence in the plasma sheet (ref. 2 and 3). The waves cause energetic
electrons to diffuse in pitch angle (ref.4 and 5). The lifetime of the charging
environment should then be controlled by the diffusion rate of these electrons.
Thus, exact measurements of the low density, cold plasma component in the plasma
sheet is required both for specifying severe charging environments and for modelling
their dynamics. Unfortunately, the densities and temperatures of the cold electron
and ion populations can only be measured if the satellite potential is maintained at
low values relative to the plasma.

Charge ejection systems have been proposed for satellite missions to facilitate measurement of cold plasma fluxes by actively maintaining the entire satellite close to plasma potential. Purvis and Bartlett (ref. 6) have pointed out that during a 92-hour period of continuous charged particle ejection by ATS-6, no spacecraft charging events were detected, although several plasma injection events were encountered. Experience with similiar injection events suggests that if the charge ejection system had not been operating, severe charging would have occurred.

Electron beam and plasma beam systems were put on the SCATHA satellite to study the discharging of satellites near geostationary orbit. During the satellite-eclipse period of 24 April 1979, SCATHA encountered such an environment and satellite potentials as low as -8 kV were measured (ref. 7). Attempts were made to discharge the vehicle using both beam systems. The electron beam system was able to raise the vehicle potential to -1 kV, but not bring about complete discharge. During periods of plasma-beam emissions the vehicle was completely discharged.

Few, if any, direct measurements of electromagnetic interference (EMI) generated during plasma beam operations have been published in the technical literature. The purpose of this report is to consider the impact of EMI generated by the emitted plasma on the operation of wave experiments. Since SCATHA is equipped with a plasma beam system and a VLF experiment capable of monitoring beam-induced waves, it provides a unique set of measurements for an EMI impact assessment. Even though there are major differences between the plasma-beam system flown on SCATHA and the charge ejection systems proposed for vehicle potential control, these measurements should have relevance for a satellite that will spend a significant fraction of its life in plasma sheet environments similiar to those encountered by SCATHA.

In the following section the plasma beam and VLF instruments on SCATHA are described. The observations soction examines VLF measurements taken during the eclipse period of 24 April (day 114) 1979. In a fifteen-minute period of intermittent plasma-beam emissions, four different modes of plasma emissions successfully discharged the vehicle.

INSTRUMENTATION

SCATHA was launched in January, 1979, into a near-geosynchronous (23 hour, 35-minute), near equatorial orbit with a 7.9 degree inclination. The satellite is cylindrical in shape, spin-stabilized, with a period of rotation of about 58 seconds. The spin axis is in the orbital plane and is maintained normal to the earth-sun line within ± 5 degrees. The satellite orbit has apogee of 7.8 R_E (earth radii) and perigee of 5.3 R_E. During the spring and fall the satellite enters an eclipse season, a period in which a portion of each orbit intersects the earth's shadow. The maximum eclipse duration per orbit is 71 minutes.

The SC4-2 instrument on the SCATHA satellite was developed to eject currents of positive and negative charge either separately or together. The major elements of the system are a xenon gas storage reservoir, a feed line from the reservoir to a hollow cathode, a discharge chamber, ion optics, a filament neutralizer, and support-ing electronics. A functional block diagram of the SC4-2 payload is shown in Figure 1. On command, gas from the reservoir is fed through the hollow cathode and into the discharge chamber. Ions are produced in the discharge chamber by the impact of electrons from the heated cathode with neutral xenon atoms. The ion energy is deter-mined by both the anode-cathode potential difference and the chamber (screen) potential

relative to spacecraft ground. The ions could be ejected from the SC4-2 with low (eV), as well as high (keV), energies. The neutralizer could be independently commanded to be heated, biased with respect to spacecraft ground, or both. Wide dynamic-range electrometers permit measurements of the ion current from the beam power supply, the electron current from the neutralizer emission, and the net emitted current.

The SC1 instrument on SCATHA includes a very-low-frequency (VLF) wave analyzer capable of taking broadband measurements of electrostatic and electromagnetic emissions from 0-6 kHz. A 100 meter tip-to-tip dipole antenna (SC10) detects the electric field component (E), and an air-core loop detects the magnetic field component (B) of the waves. The SC10 antenna consists of two 50 meter, 1/4 inch diameter antennas extending from the spacecraft. The sensitivity of the electric field receiver is 5×10^{-7} V/m Hz$^{1/2}$ at 1.3 kHz. The air-core loop is electrostatically shielded and has an effective area of 575 m^2 at 1.3 kHz. It is constructed of 1530 turns of 36 AWG copper wire on a form 50 cm in diameter. The antenna is boom-mounted two meters from the central portion of the spacecraft. The sensitivity of the magnetic field receiver is 3×10^{-6} γ/Hz$^{1/2}$ at 1.3 kHz. Prior to flight laboratory tests were conducted to insure that the instruments were shielded so there would be no internally generated signals detected by the E and B antennas. During periods of SC1 operations presented here the wave environment was sampled alternately for periods of 16 seconds duration with the E and B antennas. Data are presented in a frequency versus time format. A grey scale indicates relative intensities at a given time. The maximum amplitude is measured by the detector's automatic gain control (AGC) system four times per second in unequal intervals. The AGC measurements, plotted in field strength versus time, are given with each data sample. In the frequency-time spectrograms information about wave fields more than 20 db below the frequency of maximum amplitude is supressed.

OBSERVATIONS

During the period between 0747:34 and 0801:45 UT on 24 April 1979 the SC4-2 system on SCATHA operated intermittently in the plasma-beam mode. Throughout this period the satellite was at an altitude of ~ 6.7 R$_E$ in the plasma sheet and in the earth's shadow. Figure 2 contains plots of the emitted ion current (top panel) and the satellite frame potential (bottom panel) for the twelve minutes following 0750:10 UT. Note that when the plasma-beam was not operating the satellite potential ranged between -2 and -3 kV. This potential was discharged during four distinct plasma-beam operating modes. The ion and electron current and energy levels connected with the four plasma beam modes are listed in Table 1. Also listed in Table 1 is the range of maximum amplitudes measured by the electric and magnetic antennas during both background and beam operation intervals. These ranges were determined from the gain states of the AGC. Throughout this paper the word "background" denotes waves detected while the discharge system was not operating.

To help distinguish beam-induced EMI effects from background emissions it is useful to consider VLF measurements from the E and B antennas prior to beam turn-on. The bottom portions of Figures 3a and 3b provide examples of the E and B background measurements, respectively. The curves in the top panels of these figures give the AGC levels of maximum signal intensities. These measurements correspond to the darkest portions of the 0-6 kHz spectrograms. They are given in db V and μV/m for E$_{max}$ and db γ and mγ for B$_{max}$. The background signals consist of narrow bands, approximately 200 Hz in width centered near 0.6 and 1.2 kHz. The signal near 1.2 kHz is

the most intense. The harmonic bands near 1.7 and 2.2 kHz are believed
to be artifacts of ground station instrumentation.

Examples of VLF signals as well as E_{max} and B_{max} as measured during each of
the four modes of plasma beam emissions, are presented in Figures 4-7. For ease in
comparing intensities of fields measured during beam operations with background
measurements E_{max} and B_{max} from Figure 3 are plotted, represented by the symbol 0,
with the appropriate beam mode (1, 2, 3, 4). Note that AGC measurements taken
immediately after the receiver switches to the electric antenna do not provide reliable
values of the electric fields. During these intervals the AGC is searching for the
appropriate gain state. Often the appropriate state is considerably lower for the
elecric than the magnetic antenna. This is because the reference voltage is 1.0 V
for the electric receiver and only 300 µV for the magnetic receiver. The system is
designed such that the receivers center on chorus emissions and permit the detection
of waves within ± 30 db of chorus fields.

The mode 1 beam emissions, from 0753:12 to 0754:08 and from 0800:07 to 0801:45,
generated the largest amounts of EMI. In this mode ions were emitted with energies
of 1 keV and currents between 1.1 and 1.7 mA. Electrons were emitted from a heated
filament biased at -10V with respect to the satellite. Figures 4a and 4b contain
examples of B and E signals as well as B_{max} and E_{max} measured during mode 1
operations. The magnetic signal consists of a band extending from 0.5 to 5.0 kHz
that has maximum intensities near 1.3 and 3.5 kHz. Since the antenna response maximizes
at 1.3 kHz, the greater intensity of that signal band near that frequency is partly
an artifact of of the system. However, the null in the noise band near 3 kHz implies
that the double-banded structure is real. Values of B_{max} range from 40 to 100
mγ and are consistantly stronger than the background emissions. The electric
signal contains narrow bands centered near 1, 2 and 3 kHz with E_{max} in the 20 to
100 µV/m range. The bands that appear between seconds 6 through 8 of Figure 4
are harmonics of the background, double band spectrum. In other mode 1 measurements
(not shown) even small-scale rising tone features are exactly replicated in each of
the bands. These multiple bands sometimes span the entire 0-6 kHz bandwidth of the
detector. The values of E_{max} for the multiple bands lie between 100 and 400 µ V/m.
Although E_{max} approaches background values during these periods it is, in general,
less than the background E_{max}.

In the second plasma-beam mode (0754:08 - 0756:19 UT) ions were again emitted
with 1 keV energy but at current strengths that varied between 0.75 and 0.9 mA.
Electrons were emitted with the same filament bias of -10 V with currents slightly
more than 1.0 mA. Magnetic and electric signals characteristic of mode 2 operations
are shown in Figures 5a and c, and 5b and d, respectively. Again the magnetic signal
covers the entire 0.5 to 5 kHz band. However, B_{max} which ranges from 10 to 100
mγ may be either less than or greater than background values. Note that the noise
level is reduced and the background signal intensified in the second sample, Figure
5c, compared to the first which is taken at the beginning of the mode. The electric
signal is consistently weaker than the background level. The stronger values of
E_{max} (40 - 200 µV/m) occur when background frequency signals are visible in
the spectrogram. The weaker values of E_{max} occur during periods of 0-1 kHz broadband
noise. Note the stronger signals in the second sample, Figure 5d, which is taken in
the latter portion of the mode operation. The significance of these changes will be
discussed below.

The third plasma-beam mode (0756:19 - 0758:09 UT) was characterized by ion
currents of 0.04 mA at energies less than 40 eV. The electron current was 0.45 mA
with the filament biased at -10 V. VLF data representative of this beam mode are

presented in Figure 6. The magnetic signal appears as a band, decreasing in intensity with increasing frequency, covering the 0.5 to 4 kHz range. The most intense signal is near 1.2 kHz with B_{max} between 10 and 20 mγ. This is lower in intensity than the background signals of Figure 3. Some narrow band signals are barely discernible near 2.8, 3 and 5 kHz between seconds 0 to 2 and 8 to 13. The electric signal is more complex. It includes a persistent narrow band at the background frequency of 1.2 kHz and intermittent signals at 0.6, 2.2 and 5 kHz. Note also the presence of a multiple band near 3 kHz. The portion of this spectrogram between 4 and 6 seconds and 9 and 11 seconds shows that the signal near 2.8 kHz can exceed the 1.2 kHz signal in intensity. These periods are also marked by the presence of narrow bands near 0.1 kHz. Throughout this plasma-beam operation E_{max} was between 40 and 200 μV/m, again less than the intensity of background signals.

The fourth beam mode started at 0759:10 UT as a discharge in the ion source chamber that lasted until 0800:07 UT. The current electrometer measured a net <u>positive</u> current of 0.01 mA. The energy of the ejected positive charge was < 40 eV. During this interval the satellite frame discharged from -2.7 kV to within 100 V of plasma potential. Corresponding B and E signals are presented in Figure 7. The magnetic signal appears as a band of variable intensity, from 0.5 to 5 kHz, with B_{max} in the 10-30 mγ range near 1.2 kHz. This is similiar to but stronger in intensity than signals detected during mode 3 operations. A comparison of AGC levels with the spectrogram shows that in mode 4 B_{max} is usually less than the background level. Narrow-band signals near 5 kHz are visible when B_{max} is weakest. The electric signals also have characteristics similiar to those of mode 3 operations. The mode 4 electric signals, however, contain numerous bursts that cross the entire band. E_{max} varies betwen 40 and 200 μV/m. The background signal at 1.2 kHz was dominant during periods of strongest signals. During periods of weaker signals (seconds 5 to 7 and 12.5 to 14.5) the 0.6 kHz band and 0 to .5 kHz noise was dominant.

SUMMARY AND DISCUSSION

To provide a context for interpreting the VLF measurements presented above it is useful to summarize the plasma and magnetic field environment of SCATHA. During the period of interest the SCATHA dc magnetometer measured magnetic fields in the 75-80 nT range. Thus, the electron gyrofrequency, f_e, was ~ 2 kHz. There were no measurements of the cold plasma (< 10 eV) by SCATHA Instruments. The Rapid Scan Particle Detector (SC5) measurements of electrons and ions with energies between 50 eV and 1 MeV have been discussed in reference 7. During the period of spacecraft charging the density of plasma sheet electrons in the energy range of detectability was between 0.5 and 1 cm^{-3}. Corresponding plasma frequencies and upper hybrid frequencies, which lie in the 6.3 to 10 kHz range, cannot be detected by the SCATHA VLF receiver. It is interesting to note that the charging period corresponded to an injection of high energy (30 - 335 keV) electrons whose combined fluxes strongly correlated with the satellite potential. Electrons in this energy range were highly anisotropic with maximum fluxes perpendicular to the magnetic field.

The background signals shown in Figure 3 consist of a double band that appears in both the electric and magnetic field spectrograms. Thus, they are electromagnetic rather than electrostatic phenomena. The frequencies are centered at 0.6 and 1.1 kHz with a null near 0.5 f_e. There is a weaker double band with a similar structure with frequencies centered at 1.7 and 2.2 kHz and a null near f_e that is considered to be an artifact of the ground station instrumentation.

The double-banded electromagnetic emissions with a null near 0.5 f_e are a form of magnetospheric chorus that has been discussed extensively in the literature (refs. 8-14). There is general agreement that chorus emissions result from a Doppler-shifted, cyclotron resonance between anisotropically distributed, energetic electrons and generally present background, electromagnetic noise. The energy of resonant electrons, derived in reference 4, is:

$$E_R = \frac{B^2}{8\pi} \left(\frac{f_e}{f}\right) \left(1 - \frac{f}{f_e}\right)^3$$

With the observed magnetic field 75-80 nT and electron densities 0.5 - 1.0 cm^{-3} the magnetic energy density per particle lies between 14 and 32 keV. Setting $f = .5\ f_e$ we estimate a band of resonant energies extending from 3.5 to 8 keV. Electron measurements from this period reported in reference 7, show that anisotropic electrons in this energy range were present in abundance. To the best of our knowledge, there is no generally accepted explanation for the missing emission band near 0.5 f_e.

Examples of the effects of plasma beam emissions on the detection of electric and magnetic signals at VLF frequencies have been presented in Figures 4-7. Before the plasma beams were ejected, between beam emissions and after beam turn-off, the vehicle was charged several kilovolts and discrete, narrow-band emissions were detected by the electric and magnetic receivers. As shown in Table 1 the values of E_{max} and B_{max}, with no beam emissions were in the ranges 200-600 $\mu V/m$ and 20-60 mγ, respectively. To varying degrees the detection of background electric and magnetic VLF signals was compromised during four distinct modes of plasma-beam operations that discharged the satellite. During beam operations magnetic spectrograms were characterized by broad bands extending from 0.5 to 5 kHz that make visual identification of background signals difficult. The intensity of B_{max} varied with the strength and duration of the emitted current. The electric field spectrograms more readily provide information about background signals. The narrowband, background signal near 1.2 kHz is nearly always present. However, there are electric field signals at other than "background" frequencies. The AGC measurements, summarized in Table 1 show that E_{max} was consistently lower with the beam on than during beam-off periods.

Before considering the wave measurements during beam operations, it is useful to attempt a description of the zero-order effects of the plasma beam in the immediate vicinity of the satellite and the VLF sensors. There is evidence from the active potential control experiments on ATS-5, ATS-6 and SCATHA that plasma beams are successful in discharging differentially charged surfaces as well as the conducting frame of the satellite (refs. 6 and 15). From an analysis of SCATHA experimental data, in reference 15 it is shown that different physical processes must be responsible in each case. To begin with, the plasma beam must be dispersed such that a cloud eventually envelopes the whole satellite. To discharge the negatively charged satellite frame most beam electrons must escape to infinity. The discharge of dielectric surfaces requires that positive ions from the emitted beam impact these surfaces in sufficient numbers to neutralize negative charges deposited from the magnetospheric plasma. Secondary electrons from the impacting beam ions and magnetospheric electrons probably play crucial roles in this discharging procedure. Whatever the details of the discharging process may be, two things are clearly required. First, the sheath in the immediate vicinity of the satellite is transformed from a depleted plasma to an enhanced plasma. The extent of the enhancement sheath is not known. Second, the near satellite enhancement

region is characterized by multiple, complex current loops that couple dielectric surfaces with the magnetospheric plasma and the satellite frame. Recall that the air core loop is located 2 m from the satellite while the active element of the electric field antenna extends from 20 to 50 m from the satellite. If the scale size of the plasma-enhanced region is less than 50 m very different affects on the two systems may be anticipated.

The magnetic spectrograms are dominated by wide bands that extend from 0.5 to 5 kHz. The apparent low frequency cut off is an instrumental effect. At frequencies less than 1 kHz the frequency response of the magnetic VLF receiver decreases rapidly with decreasing frequency (cf Figure 2 of ref. 14). The presence of an enhanced plasma in the immediate vicinity of the satellite should of itself, have no effect on the performance of the low impedance loop antenna (ref. 16). Rather, the data suggest that the air core loop is embedded in a dense region of fluctuating currents inherent to the satellite discharge process. These bands may have harmonic structure (figures 4a and 5a) with intensity exceeding that of the background signals. The signal strength intensifies just below the first and second harmonics of the electron gyrofrequency; i.e., 2 kHz and 4 kHz, respectively. One possible explanation comes from Ohnuma, et al., (ref. 17). They have shown that in a high density, hot plasma, electromagnetic waves may be generated at these harmonics. These waves are back-scattered at some critical low density which implies they would be confined to the enhanced sheath region around the satellite.

Structured emissions are detectable, to varying degrees during all beam operations but are more easily perceived in the electric field spectrograms. These emissions have five different kinds of signatures: (1) chorus emissions centered at .6, and 1.2 kHz, (2) chorus harmonic bands,(3) narrow bands near 3 and 5 kHz, (4) multiple bands near 3 kHz, and (5) 0 to .5 kHz ELF bands. The background chorus signals centered at 1.1 kHz were present a large fraction of the time while those at 0.6 kHz were less frequently detectable. Intensities of chorus signals were usually well below those measured when the beam system was off. The diminished and sometimes totally suppressed chorus seems to be related to the beam emission process rather than to variations in the emitting plasma. This is evidenced by the relative constancy of (1) E_{max} and B_{max} when the beam was off and (2) the flux levels and pitch angle distributions of electrons in the resonant energy range of 5 to 10 keV. A possible mechanism for reducing chorus intensity measurements is discussed below.

Multiple harmonics of chorus emissions are occasionally detected during mode 1 operations, and are most visible on the electric field spectrograms (figure 4b). The fact that multiple harmonics only appear during a specific mode of operation and have never been detected outside beam operations suggests that they are artifacts of the beam emission process. How they are produced is not understood at this time. It may be that the beam emission which is highly anisotropic occurring at pitch angles of 70°-140°, or the vehicle discharging process, create sufficiently energetic, anisotropic electrons to produce cyclotron harmonic resonances as discussed in references 4 and 18, which in turn may produce harmonics of chorus emissions. In the near vicinity of the satellite, the high current emissions are shown to intensify the 1.2 kHz signal (figures 4a and 5a).

At sometime during all four modes of plasm-beam operations narrow bands near 3 kHz are visible in the spectrograms. A similar band at 5 kHz is detectable intermittantly during modes 3 and 4. These signals are present in both the electric and magnetic spectrograms. They appear to be electron cyclotron harmonic (ECH) waves. Wave modes of these types propagate nearly perpendicular to the magnetic field between harmonics of the electron gyrofrequency and may be associated

392

with positive slopes in the electron distribution function ($\partial f/\partial v_\perp > 0$).
However, the responsible electrons have energies considerably lower than those responsible
for chorus waves (ref. 2). We note that on several occasions the appearance
of ECH waves coincided with the complete suppression of the 1.2 kHz chorus band.

The observation of a magnetic component is contrary to other observations in
space (ref. 3) and is not yet understood. The ECH waves are assumed to have
long wavelengths, much greater than the 50 cm diameter of the magnetic loop antenna.
Therefore, there should be no coupling of the wave electric fields to this antenna.
It may be, however, that these waves generate local current oscillations in the
satellite sheath in which the magnetic antenna is imbedded. These oscillations
would occur at the same frequency as those of the naturally occurring ECH waves.

During the entire mode 3 and seconds 11 to 16 of mode 4, multiple bands are
detected near 3/2 f_g. Similar multiple bands have been reported by Koons and
Fennell, (ref. 20). They are usually associated with electrons at energies of a
few keV whose distribution functions have relative minima at pitch angles of 90°.
We have examined particle measurements and found that at the times of modes 3 and
4, electrons with energies of ~1 keV had trapped pitch angle distributions but
with a local minimum at 90°. Electrons in all other energy channels have normally
trapped distributions.

Sporadic emissions of signals in the 0 to .5 kHz range were detected during
all four beam modes on the electric field spectrograms. Similar ELF bursts have
been detected (ref. private communication, 1982) during beam-off periods. Again we
note that several of these bursts (Figures 5 and 7) coincide with periods in which
the 1.2 kHz signal is completely suppressed.

Since the ECH and ELF emissions naturally occur in plasma sheet environments
this is probably true in the present case as well. Their appearances during beam
operations frequently coincide with low amplitudes or absences in the chorus bands.
This suggests that when the beam system is not operating the ECH and ELF waves are
more than 20 db below background chorus intensities. Only when the level of detected
chorus signals is diminished or supressed does the AGC react to the presence of
these waves. The question of beam related EMI thus becomes, how does the beam emission
process lead to diminished chorus measurements by the antenna systems. Two possible
mechanisms come to mind: (1) diminshed antenna coupling between the antenna and the
medium, and (2) interactions between the chorus and the plasma cloud around the
satellite.

The first alternative, diminished antenna coupling with the medium applies only
to the electric antenna and does not seem to be correct for two reasons. First,
during beam emission periods the density of particles in the sheath around the antenna
should be increased. This leads to a decreased sheath impedance (ref. 16) and
better coupling to the medium (ref. 21). Second, there is no reason for the antenna
to be coupled efficiently to the medium at 0.0 to 0.5 kHz and at 3 kHz and inefficiently
coupled at 1.2 kHz.

The vehicle discharging process results in the emission of secondary electrons
from dielectric surfaces. In reference 15 it is shown that these surfaces discharge
at different rates based on surface material and location. Independent of material,
a surface which was readily accessible to beam ions would discharge more rapidly
than one that was in a less accessible location on the satellite. The discharging
of the satellite frame was almost instantaneous whereas the rate for each sample
varied such that discharging occurred over a period on the order of minutes. This

indicates that secondary electrons are emitted over this entire period with varied
and decreasing energies depending on the particular surface from which they were
emitted, its location and rate of discharge. These electrons would produce a cloud
of varied length and diameter that decreased in time. This is indicated by comparing
the two samples of mode 2. The first sample shows considerable suppression of the
background signal on the E and B spectrograms even with a reduced noise level on the
B spectrogram. The second sample indicates a greater variability in the plasma
cloud permitting more of the background signal to penetrate on the E spectrogram and
intensification of the 1.2 kHz signal on the B spectrogram.

The direction of wave propagation for chorus and ECH waves combined with an
assymetry of the local plasma could could lead to a selective diminution of
chorus. Chorus waves usually propagate in directions close to that of the magnetic
field while ECH waves propagate mostly normal to the magnetic field. Because
particles in the plasma cloud emitted during beam operations are relatively free to
move along but not across the magnetic field the cloud could have a relatively
large extent along the magnetic field. Waves propagating along the magnetic field
could see an "optically thick" medium while those propagating across the magnetic
field an "optically thin" medium.

Chorus waves amplify due to the presence of free energy contained in the
anisotropic pitch angle distributions of resonant, energetic electrons. They are
also subject to Landau damping processes. Waves grow in regions where the free
energy available exceeds the rate at which Landau heating of the plasma occurs.
The introduction of large quantities of low-energy electrons in the plasma cloud
greatly increases the negative slope of the total electron distribution function
and consequently the rate of Landau damping. The length and diameter of the plasma
cloud along the magnetic field would then modulate the admittance of chorus waves
to the satellite. The diameter of the cloud should be limited to a few electron
gyroradii. For emitted 10 eV electrons this is of the order of a few hundred
meters; for 2-3 keV secondary electrons this is of the order of kilometers. Since
the Debye length in the plasma sheet is several kilometers such a cloud should have
little effect on perpendicularly propagating waves.

CONCLUSIONS

The combination of plasma beam emissions and the discharging process has been
shown to have three distinct affects on the detection of VLF waves. First, the
magnetic loop antenna detects intense signals during high current emissions, modes 1
and 2, that are apparently localized to the near vicinity of the satellite. They
are assumed to be generated and/or amplified within the plasma that envelopes the
satellite upon beam emission. These signals span the 0.5 to 5 kHz band, may be
double-banded, and often saturate the magnetic receiver, thus obscuring the detection
of signals that do not lie within 20 dB of this signal amplitude. Second, on the
electric antenna during mode 1, the highest current emitting mode, occasionally
multiple bands of chorus emissions are detected. These are assumed to be generated
by the large anisotropic fluxes of beam electrons. Third, the fields of the chorus
emissions are often suppressed. This suppression permits observations of much weaker
wave fields. It is suggested that electrons emitted by the beam and during the
discharge process create an irregular plasma cloud along the field lines which becomes
an optically thick screen for parallel propagating waves.

401

REFERENCES

1. Garrett, H.B., The charging of spacecraft surfaces, <u>Rev. Geophys and Sp. Phys.</u>, <u>19</u>, 577, 1981.

2. Young, T.S.T., Electrostatic waves at half electron gyrofrequency, <u>J. Geophys. Res.</u>, <u>79</u>, 1985, 1974.,

3. Ashour-Abdalla, M. and R.M. Thorne, Towards a unified view of diffuse auroral precipitation, <u>J. Geophys. Res.</u>, <u>83</u>, 4755, 1978.

4. Kennel, C.F. and H.E. Petschek, Limit on stably trapped particle fluxes, <u>J. Geophys. Res.</u>, <u>71</u>, 1, 1966.

5. Lyons, L.R. Electron diffusion driven by magnetospheric electrostatic waves, <u>J. Geophys. Res.</u>, <u>79</u>, 575, 1974.

6. Purvis, C.K., and R.O. Bartlett, Active control of spacecraft charging, in <u>Space Systems and Their Interactions with Earth's Space Environment</u>, <u>Prog. Astronaut. Aeronaut.</u>, vol. 71, edited by H.B. Garrett and C.D. Pike, pp. 299-317, American Institute of Aeronautics and Astronautics, New York, 1980.

7. Gussenhoven, M.S. and E.G. Mullen, Geosynchronous environment for severe spacecraft charging, <u>J. Spacecraft and Rockets</u>, <u>20</u>, 26, 1983.

8. Burtis, W.J. and R.A. Helliwell, Banded chorus--A new type of VLF radiation observed in the magnetosphere by OGO 1 and OGO 3, <u>J. Geophys. Res.</u>, <u>74</u>, 3002, 1969.

9. Burton, R.K., C.T. Russell, and C.R. Chappell, The Alfven velocity in the magnetosphere and its relationship to ELF emissions, <u>J. Geophys. Res.</u>, <u>75</u>, 5582, 1970.

10. Burton, R.K., and R.E. Holzer, the origin and propagation of chorus in the outer magnetosphere, <u>J. Geophys. Res.</u>, <u>79</u>, 1014, 1974.

11. Tsurutani, B.T. and E.J. Smith, Postmidnight chorus: a substorm phenomenon, <u>J. Geophys. Res.</u>, <u>79</u>, 118, 1974.

12. Tsurutani, B.T. and E.J. Smith, Two types of ELF chorus and their substorm dependences, <u>J. Geophys. Res.</u>, <u>82</u>, 5112, 1977.

13. Anderson, R.R., and K. Maeda, VLF emissions associated with enhanced magnetospheric electrons, <u>J. Geophys. Res.</u>, <u>82</u>, 135, 1977.

14. Koons, H.C. and J.F. Fennell, Fine structure in electrostatic emission bands between electron gyrofrequency harmonics, <u>EOS</u>,<u>63</u>, 1074, 1982.

15. Cohen, H.C. and S.T. Lai, Discharging the P78-2 satellite using ions and electrons, Proceedings of AIAA 13th Aerospace Science Conference, Orlando, Florida, January, 1982.

16. Koons, H.C. D.A. McPherson, and W.B. Harbridge, Dependence of Very-LowFrequency electric field antenna impedance on magnetopheric plasma density, J. Geophys. Res., 75, 2490, 1970.

17. Ohnuma, T. and T. Watanabe, Wave fronts of electromagnetic cyclotron harmonic waves, Phys. Fluids, 25, 1217, 1982.

18. Lyons, L.R., R.M. Thorne and C.F. Kennel, Pitch-angle diffusion of radiation belt electrons within the plasmaphere, J. Geophys. Res., 77, 3455, 1972.

19. Young, T.S.T., J.D. Cullen and J.E. McCune, High frequency electrostatic waves in the magnetosphere, J. Geophys. Res., 78, 1082, 1973.

20. Koons, H.C., The role of hiss in magnetospheric chorus emissions, J. Geophys. Res., 86, 6745, 1981.

21. Fahleson, U., Theory of electric field measurements conducted in the magnetosphere with electric probles, Space Sci. Rev., 7, 238, 1967.

TABLE I. - CONDITIONS DURING PLASMA BEAM MODES

Plasma Mode	Ion Current (mA)	Ion Energy (keV)	Electron Current (mA)	Electron Energy (keV)	Maximum Field Strength Electric (µ V/m)	Magnetic (m γ)
0	0	0	0	0	200-600	20-60
1	1.1 - 1.7	1.0	2.1 - 2.4	0.01	20-400	40-100
2	0.75 - 0.9	1.0	1.0	0.01	10-200	20-100
3	0.04	0.04	0.45	0.01	40-200	10-20
4	0.01	0.04	0.0	0.0	40-200	10-30
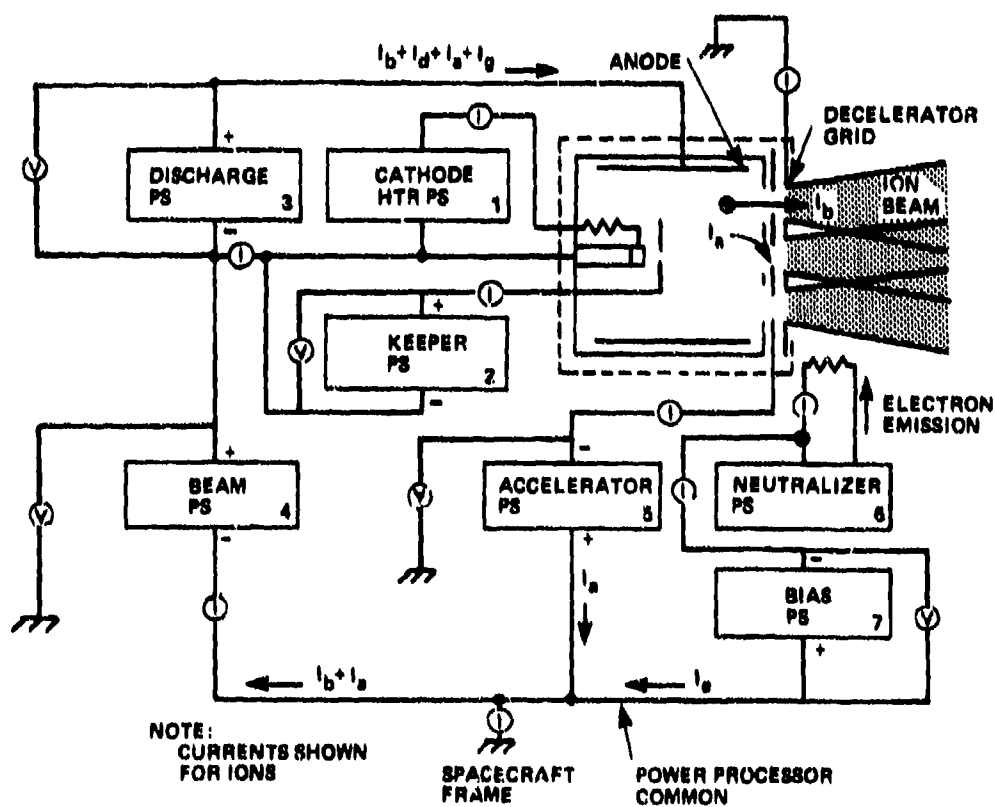
Figure 1. - Functional block diagram of ion source and power processor for SC-4.
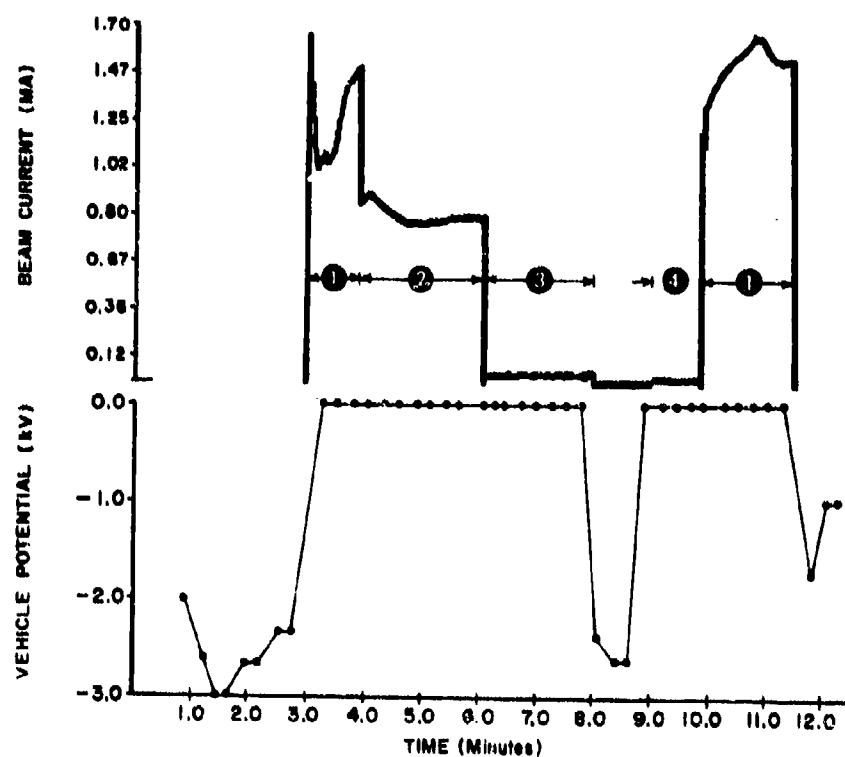
Figure 2. – Ion beam current and vehicle potential during the four modes of plasma beam operations. (Note the response of the vehicle potential to the beam emission.) $T_0 = 07:50:10$.

Figure 3. - Background wave fields detected by VLF broadband receiver. (Relative intensity of wave fields is indicated by grey scale with darkest being most intense portion. In this case it is chorus band just above 1 kHz. This intensity is plotted above recorded field signals as 0-curve, given in dBγ intensity is plotted above recorded field signals as 0-curve, given in dBγ and mγ for magnetic field and dBV and μV/m for electric field.)

(a) Magnetic loop antenna. T_0 = 07:46:27.75.

(b) Electric dipole antenna. T_0 = 07:46:11.75.
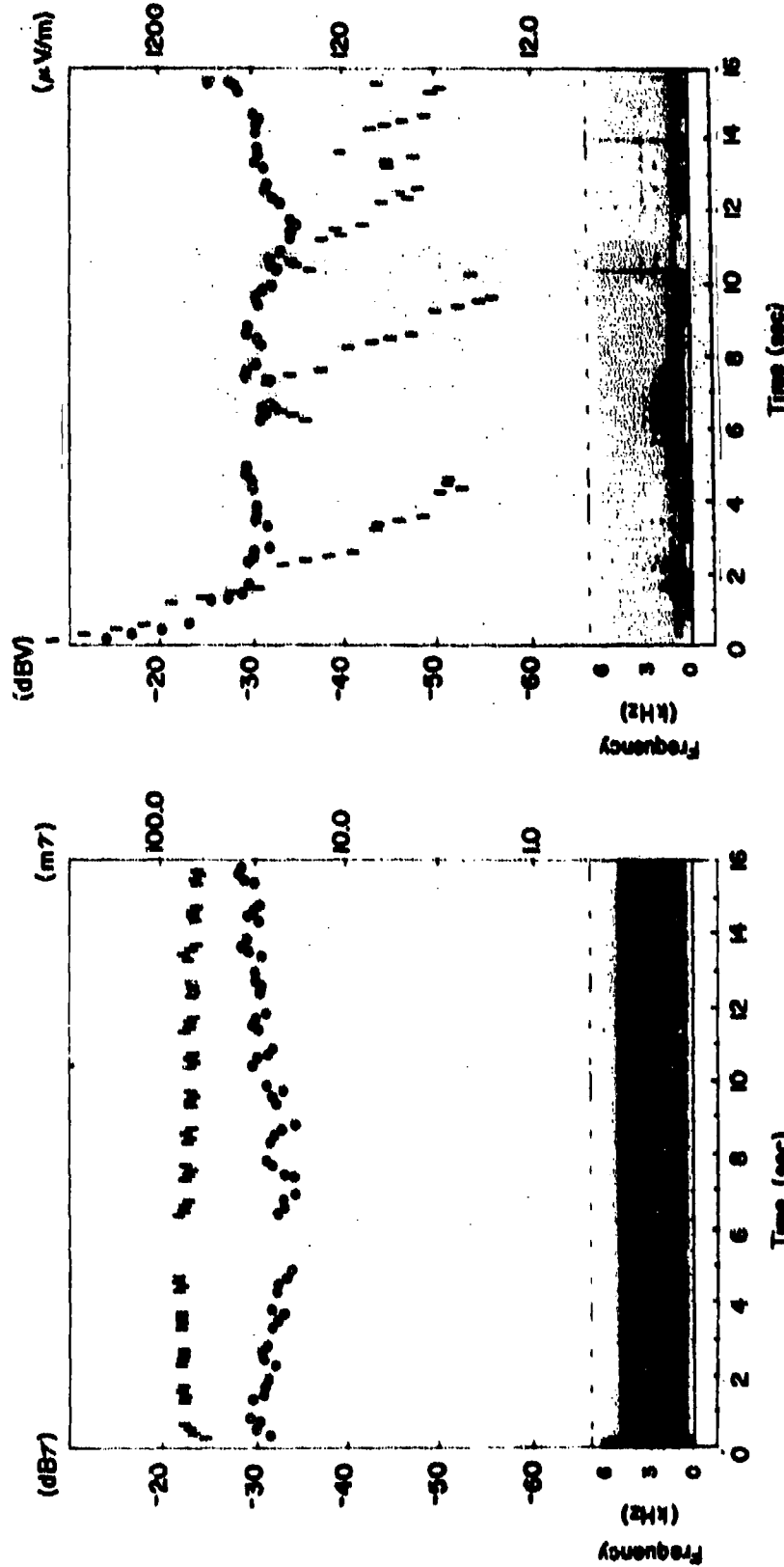
Figure 4. – Signals detected during mode 1 plasma beam operations with ion
beam current of 1.1 to 1.7 mA. (The curve of maximum background field
intensity from fig. 3 (0-curve) is replotted here for comparison with signal
intensity during beam operations (1-curve). Note the double–banded structure
of the magnetic field signal band and the complex multiband structures in the
electric field signal that vary with maximum field intensity.)

(a) Magnetic loop antenna. $T_0 = 08{:}00{:}19.75$.

(b) Electric dipole antenna. $T_0 = 08{:}00{:}35.75$.
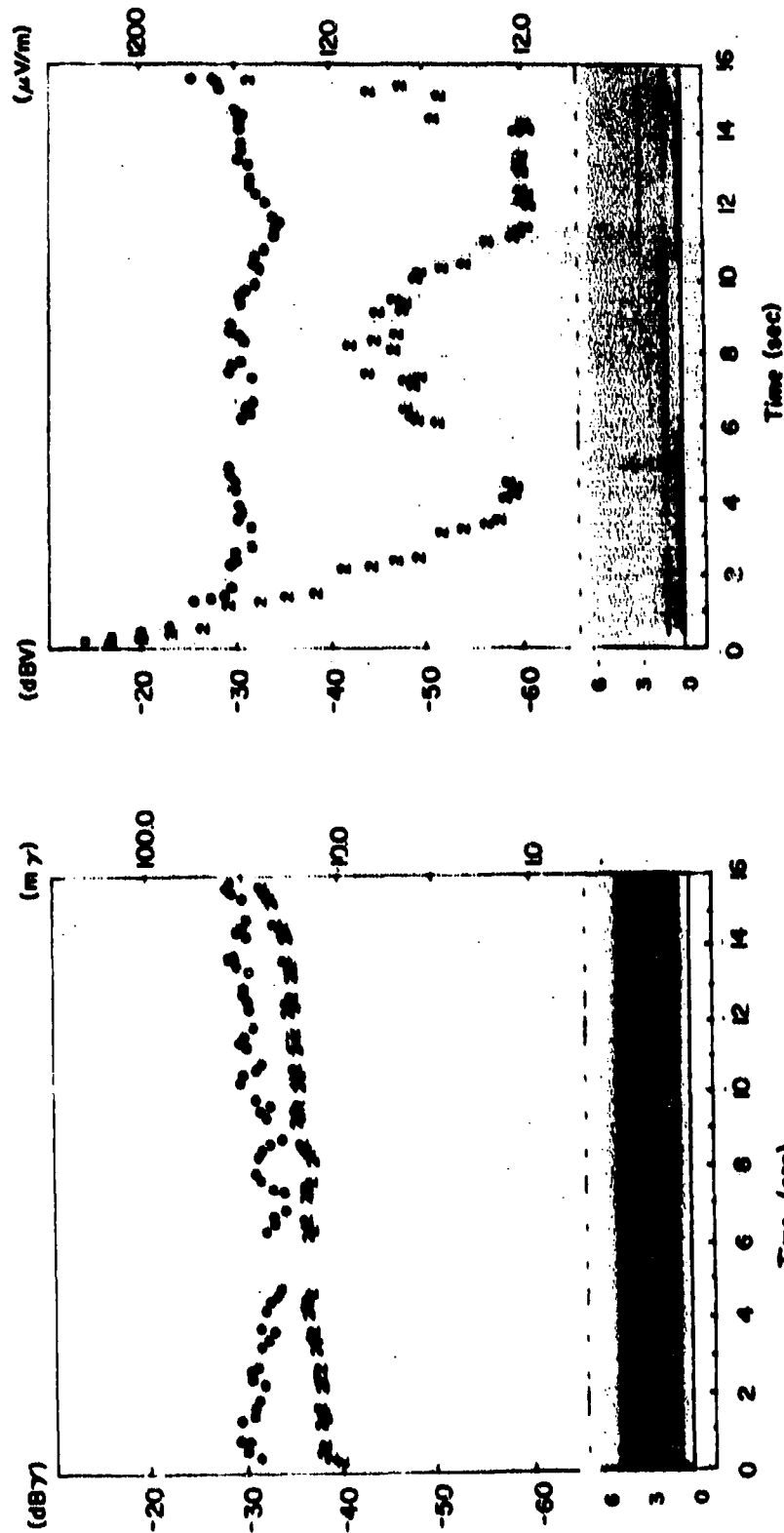
(a) Magnetic loop antenna. $T_0 = 07:54:27.75$.

(b) Electric dipole antenna. $T_0 = 07:54:43.75$.

Figure 5. — Signals detected during mode 2 plasma beam operations with ion current of 0.7 to 0.9 mA. (Double-banded structure is still apparent in magnetic field data.) Electric field data are less structured although maximum field intensity (2-curve) is still quite variable.)
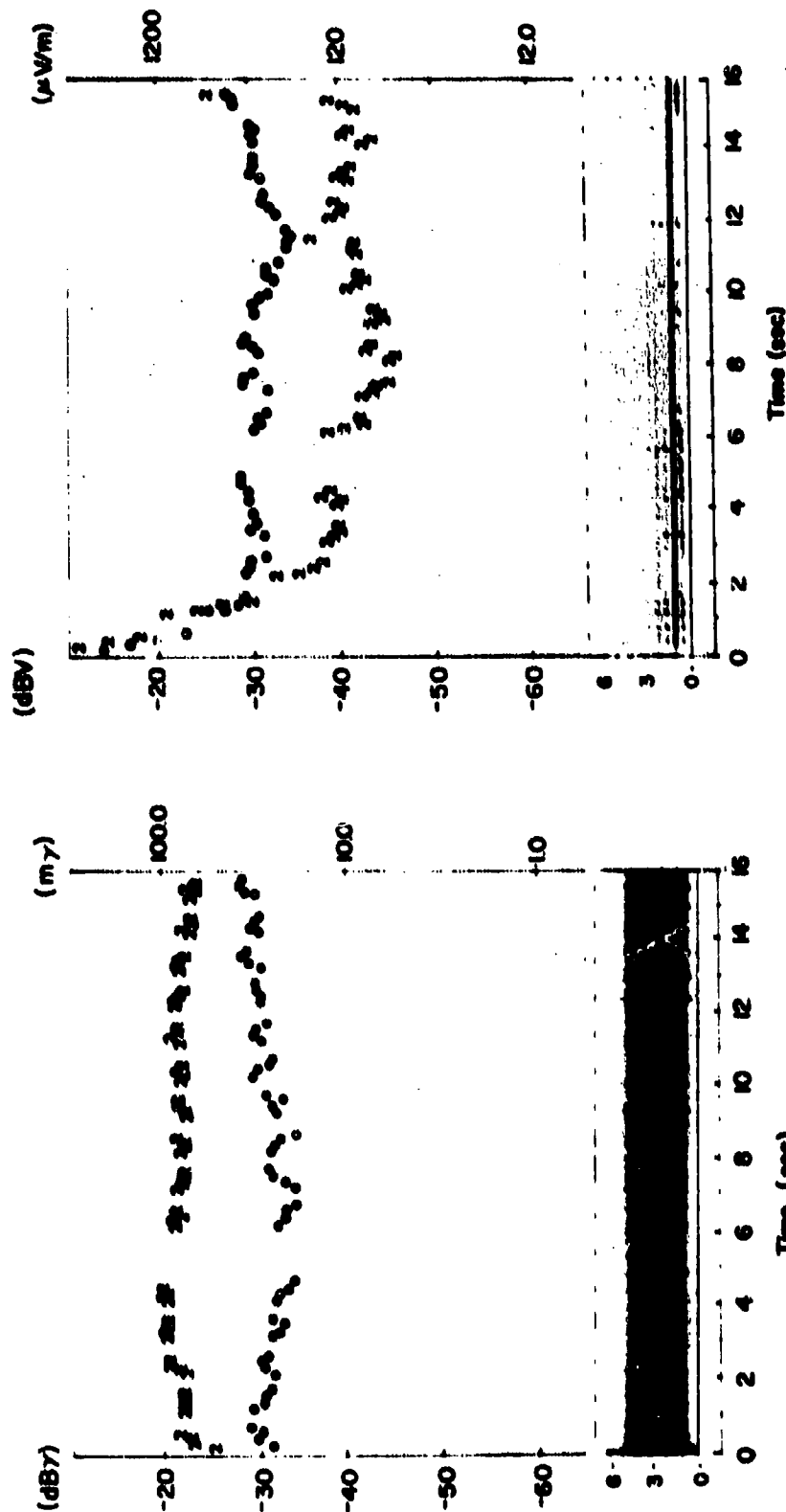
(a) Magnetic loop antenna. T_0 = 07:55:31.75.

(b) Electric dipole antenna. T_0 = 07:55:47.75.

Figure 5. – Concluded. (Here change in signal with duration of plasma beam emission is apparent. Both electric and magnetic field signals are stronger and more nearly resemble background structure of fig. 3, although signal strengths (2-curves) are quite different.)

409
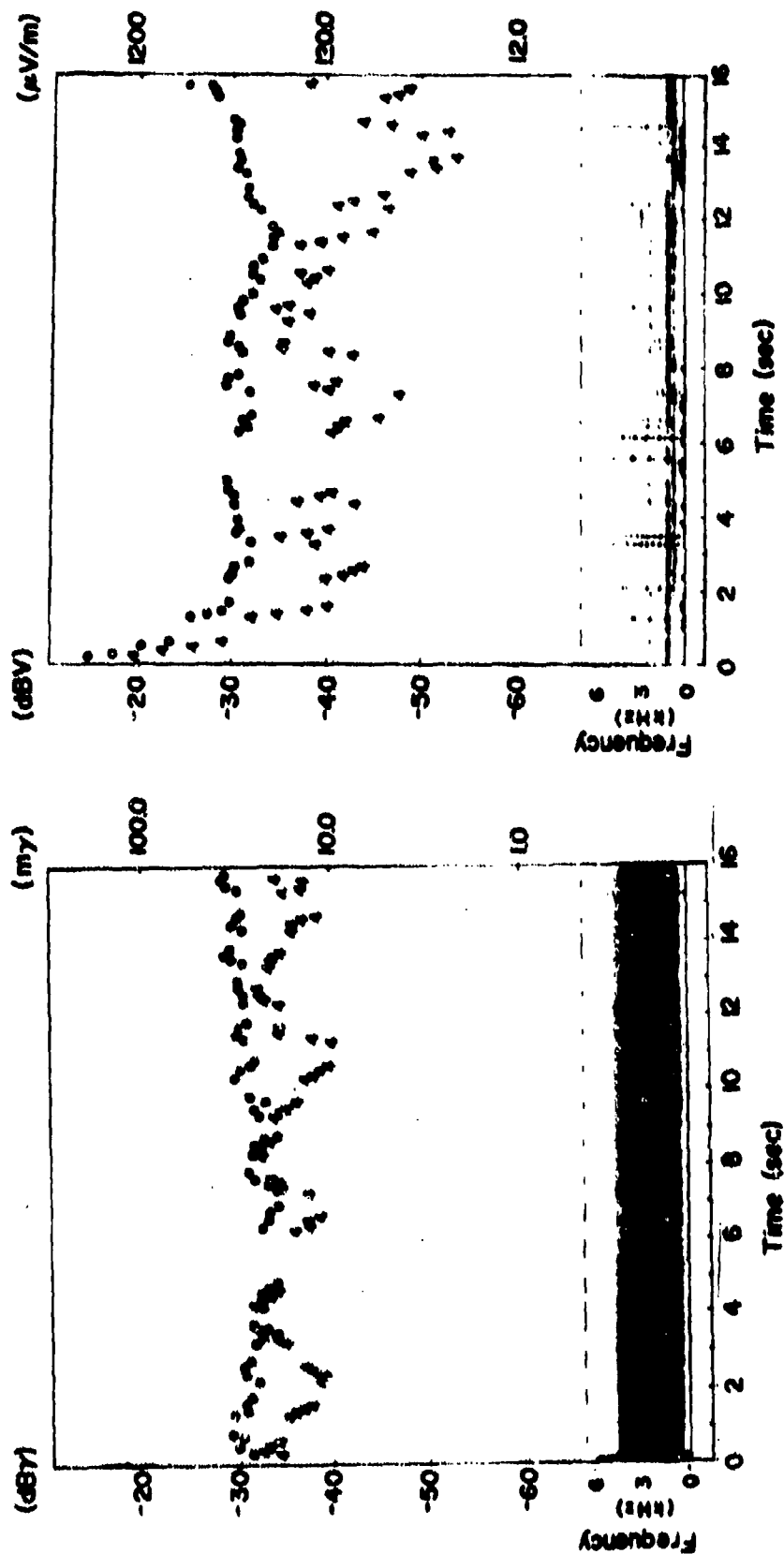
Figure 7. – Signals detected during mode 4 plasma beam operations with ion beam current of about 10 mA. (Maximum signal intensity (4-curve) is variable in both fields as is signal structure.)

(a) Magnetic loop antenna. T_0 = 07:59:15.75.

(b) Electric dipole antenna. T_0 = 07:59:31.15.

410
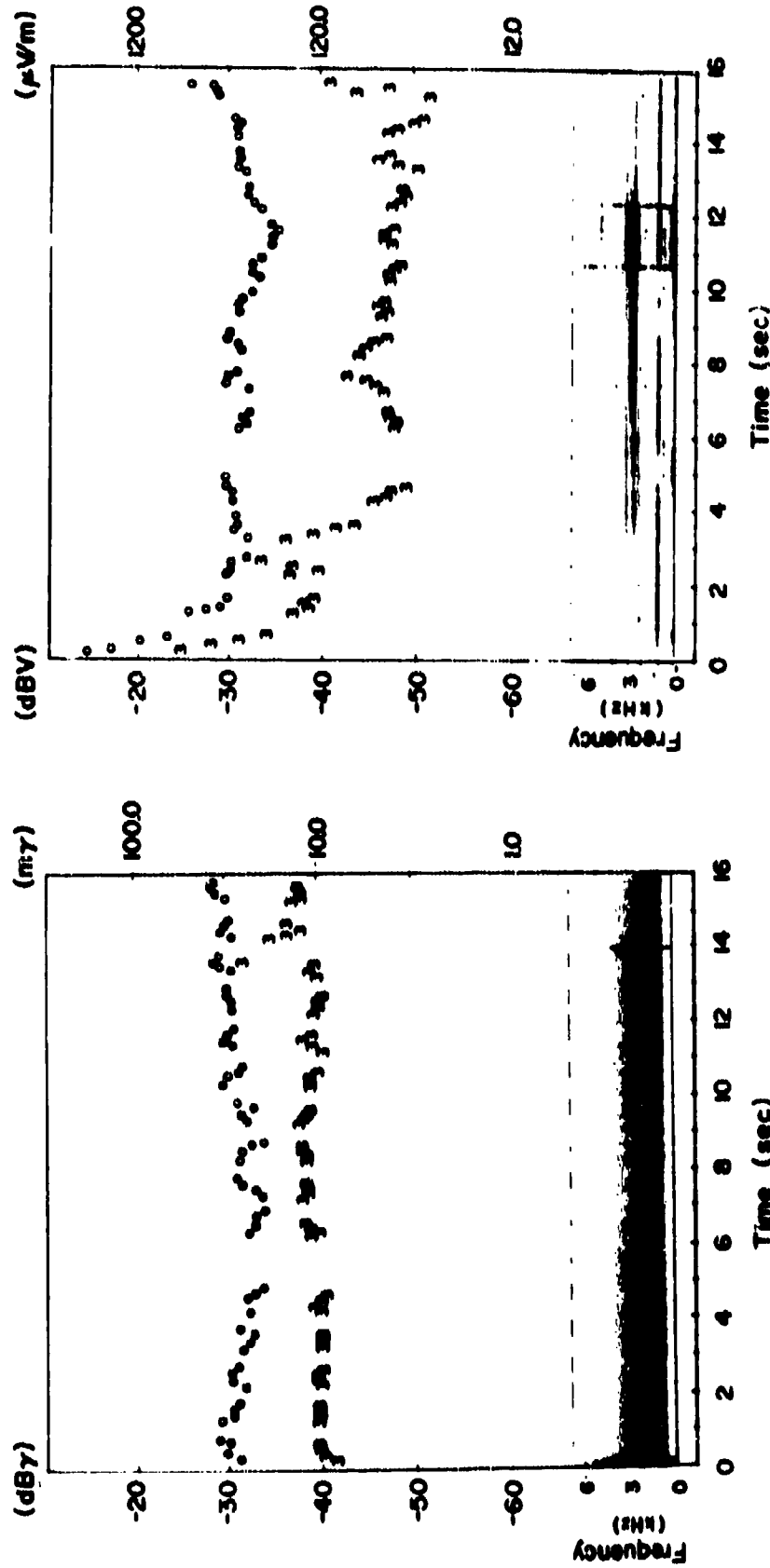
Figure 6.— Signals detected during mode 3 plasma beam operations with ion
beam current of about 40 μA. (Both magnetic and electric field signals are
weak. Traces of signal bands are just barely visible in magnetic field data;
electric field data are quite structured.)

(a) Magnetic loop antenna. T_0 = 07:57:07.75.

(b) Electric dipole antenna. T_0 = 07:56:51.75.

411

ANOMALOUSLY HIGH POTENTIALS OBSERVED ON ISEE*

E. C. Whipple, I. S. Krinsky, and R. B. Torbert
University of California at San Diego
La Jolla, California 92093

R. C. Olsen
University of Alabama
Huntsville, Alabama 35899

Data from the two electric field experiments and from the plasma composition experiment on ISEE-1 show that the spacecraft charged to close to -70 V in sunlight at about 0700 UT on March 17, 1978. Data from the electron spectrometer experiment show that there was a potential barrier of some -10 to -20 V about the spacecraft during this event. The potential barrier was effective in turning back emitted photoelectrons to the spacecraft. Potential barriers can be formed because of differential charging on the spacecraft or because of the presence of space charge. The stringent electrostatic cleanliness specifications imposed on ISEE make the presence of differential charging unlikely, if these precautions were effective. Modeling of this event is required to determine if the barrier was produced by the presence of space charge.

INTRODUCTION

The International Sun Earth Explorer (ISEE) project involves three spacecraft which were designed to study the magnetospheric plasma under the auspices of the International Magnetospheric Study program. ISEE-1 and ISEE-2 were launched on October 22, 1977, into almost identical orbits but with a variable separation distance in order to be able to separate temporal and spatial variations of the environment. Their apogee was at 23 earth radii, and their period was approximately 57 h. ISEE-3 was launched into a "halo orbit" about the libration point at about 240 earth radii towards the sun from the earth. Further information on the ISEE mission can be found in References 1 through 3.

The ISEE spacecraft were built according to a set of electrostatic cleanliness specifications which were intended to make the exteriors of the spacecraft be equipotential surfaces and to prevent the buildup of asymmetric potentials which could interfere with low energy particle and electric field measurements. The specifications required that no exposed spacecraft component (with some exceptions) charge to potentials in excess of 1 volt with respect to the spacecraft potential. This requirement demanded that all spacecraft components that were exposed to the plasma environment be "sufficiently conducting," and be connected to the spacecraft ground through low impedance paths. These specifications which were also used in the construction of the GEOS spacecraft, appear to have been relatively effective; the most negative potential reached by GEOS 2 was -1500 volts in eclipse which is

much less than potentials reached by other magnetospheric spacecraft such as ATS-5, ATS-6 and SCATHA (References 4 through 6).

In spite of these electrostatic cleanliness requirements, there have been indications of significant charging events on ISEE-1, with the spacecraft going at times to a negative potential on the order of -100 volts in sunlight. These indications came from ion data obtained by the plasma composition experiment (Ref. 7) which showed that low energy (thermal) ions had been accelerated to kinetic energies on the order of 100 eV before they were detected by the instrument. It is important to understand such charging events, if they are indeed real, in order to be able to evaluate the effectiveness of the electrostatic cleanliness specifications. For example, the charging of electrostatically "dirty" spacecraft such as ATS-5, ATS-6 and SCATHA has been shown to be very dependent on differential charging effects (Ref. 8 and 9). Differential charging on a spacecraft can produce a potential barrier which prevents low energy photoelectrons from escaping, and can thus lead to much larger negative potentials in sunlight than would otherwise be expected. The purpose of this paper is to examine in detail such a sunlight charging event on ISEE-1.

DATA THAT INDICATE CHARGING

Several experiments on ISEE-1 are capable of giving information on the potential of the spacecraft. In this section we present evidence from the two electric field experiments and from the plasma composition experiment which indicate that between 0600 and 0800 UT on March 17, 1978 (Day 76), the ISEE-1 spacecraft charged to about -70 volts in sunlight. At that time the vehicle was near synchronous orbit, at 7.7 earth radii, and at 0300 local time. In addition, we present data from a synchronous altitude spacecraft, ATS-5, on the same date but at about 0400 UT and at midnight local time, which show that ATS-5 charged to about -6 kV in eclipse. Thus the plasma environment during this period of time was sufficiently hot to provide significant charging.

The spherical double probe electric field experiment on ISEE-1 (Ref. 10) measures the potential difference between the probes, which are two 4 cm radius spheres at the ends of wire booms separated by 73.5 m in the spin plane of the spacecraft. In addition, the experiment monitors the potential difference between each of the probes and the spacecraft. The potential of the spheres with respect to the plasma is adjusted to be near zero by introducing bias currents to the spheres based on current/voltage sweeps which are made during a quarter-second interval every 128 sec.

Figure 1 shows the quantity V2S which is the potential difference between sphere #2 and the spacecraft during the interval from 0500 to 0800 UT on March 17, 1978. The spacecraft potential with respect to the sphere (which was near ambient plasma potential) is the negative of V2S. The figure shows that the spacecraft was near zero volts at 0600 and that it gradually charged to a more negative potential, going off-scale at -50 volts at about 0715 UT. The potential came back on scale briefly at 0745. During the period from 0700 to 0800 the vehicle potential was close to or more negative than -50 volts. Since the sphere bias current is negative at this time (i.e., electrons are being pushed onto the sphere), the fact that the spacecraft is more negative than the sphere implies that the sphere and the spacecraft are responding differently to the environment. For example, there may be

414

more secondary electrons emitted from the sphere, or there may be potential barrier
effects around the spacecraft that are not around the sphere.
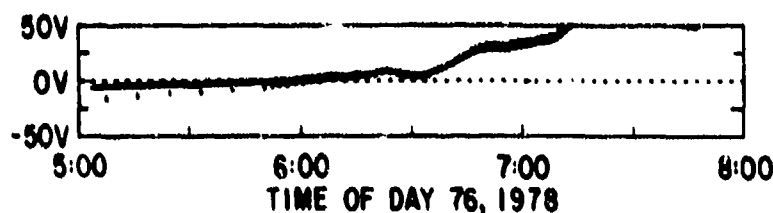
Figure 1. Probe data from Mozer's electric field
experiment showing the probe-to-spacecraft
potential (V2S) from 0500 to 0800 UT on
March 17, 1978.

Figure 2 shows similar data from the Goddard electric field experiment on ISEE-1
(Ref. 11). The active probes in this experiment are 36 m uninsulated tip sections
of two wires independently deployed to lengths of 106.7 m. This gives an effective
baseline between the two active elements of 179 m. The figure shows the potential
difference between one of these
elements and the spacecraft
during two periods of time: at
0600 and at 0645 UT. The
potentials of the active elements
in this experiment are floating
with respect to the ambient
plasma. That is, the potential
of the elements is determined by
a current balance between
collected plasma ions and
electrons and emitted secondary
electrons and photoelectrons.
The floating potential is
modulated by the spin of the
spacecraft. The potential is
most positive when the wire
elements are perpendicular to the
direction of the sun since this
is the orientation where the
photoemission current is a
maximum.

The floating potential of the
active wire elements with respect
to the local plasma is not
directly measured in this
experiment, but it is expected to
be on the order of a few volts
positive when the wires are
perpendicular to the sun
direction. The two spherical
probes in the other electric
field experiment floated at
approximately +5 V during this
period of time, as determined from current/voltage sweeps when the bias current was
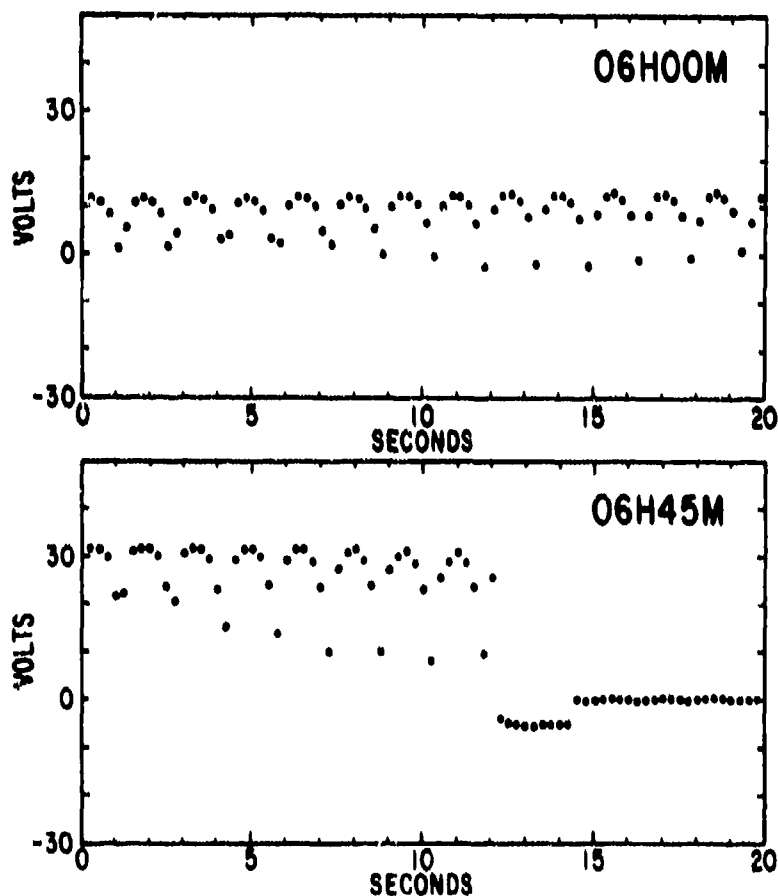
Figure 2. Probe data from Heppner's electric
field experiment showing the probe-to-spacecraft
potential at 0600 and 0645 UT on March 17, 1978.

415

zero. If the wire element is also floating at about +5 volts during this time, then the spacecraft potential has changed from near zero to about -25 V between 0600 and 0645. These values are in reasonable agreement with the data shown in Figure 1.

The plasma composition experiment is described in Ref. 7. It consists of two identical mass spectrometers which can be operated independently. The ions enter a collimator and then go through a three-grid retarding potential analyzer (RPA). The retarding grid is programmable between 60 mV and 100 V in 32 steps with approximately equal logarithmic intervals. After passing through the third grid, the ions are accelerated through a potential difference of approximately -2950 V before they pass through a cylindrical electrostatic analyzer. Due to the pre-acceleration, the lowest energy step of the electrostatic analyzer passes all ions with external energies between zero (i.e., those cold ions which can reach the spacecraft) and approximately 100 eV.

Figure 3 shows results from the plasma composition experiment between 0600 and 0800 UT on March 17, 1978. The four panels show ion counts during the four half-hour intervals, where the data has been accumulated as a function of spacecraft spin angle and RPA retarding potential. The count rate is indicated by the gray scale, with dark signifying high count rates, and light signifying low count rates. The retarding potential at which the count rates are sharply reduced is a measure of the (negative) spacecraft potential. In this mode of operation, the instrument is passing all species of ions, but it is known from the other modes of operation that the ions are predominantly hydrogen but with a significant oxygen component. It can be seen that this cut-off potential increases during this period of time from about 10 V at the beginning to somewhat under 100 V at the end.

DAY 76, 1978

06:00-06:30   06:30-07:00

07:00-07:30   07:30-08:00

ENERGY (eV)

Figure 3. Ion data from the plasma composition experiment from 0600 to 0800 UT on March 17, 1978. Dark indicates high ion counting rates and light indicates low rates. The energy at which the counting rate decreases abruptly is an indication of the spacecraft potential.

Individual RPA scans were examined during part of this period of time, and the spacecraft potential was estimated for scans when the experiment was most nearly looking at ions coming in the ram direction. Individual scans were obtained approximately every three minutes, although there were some gaps in the data. The results are shown in Figure 4. Again, the data show that the

potential of the spacecraft increased in the negative direction from near -5 V at about 0630 UT to a value more negative than -60 V after 0710 UT.
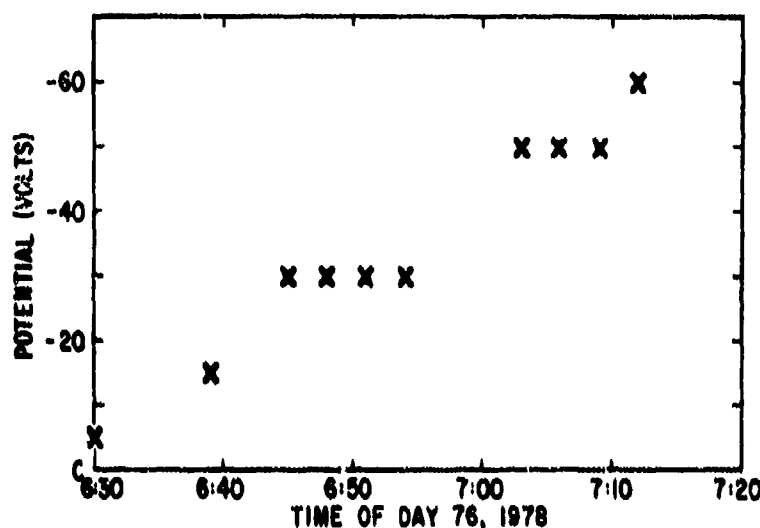
Figure 4. ISEE spacecraft potentials on March 17, 1978, inferred from the plasma composition experiment.

Figure 5 shows a spectrogram from the UCSD particle detector on the ATS-5 satellite between 0410 and 0510 UT on the same day. Data is only available during the time when the spacecraft was entering and within the earth's shadow. This was a period when special operations of the ATS-5 ion engine and neutralizer were being carried out to test the capability of these devices to discharge the spacecraft (Ref. 12). The spacecraft entered eclipse at 0411; the neutralizer was turned on at 0418 and off at 0433. The neutralizer consisted merely of a heated filament which could emit electrons independently of operation of the ion engine. During the neutralizer operation, the spacecraft potential was held to about -2 kV but when it was turned off the potential went to about -6 kV. The ion spectrum during this period of time as measured by the UCSD detector is in good agreement with the ion spectrum obtained by the LEPEDEA experiment (Ref.13) on ISEE-1 at 0700 UT. Thus it appears that the plasma near geosynchronous
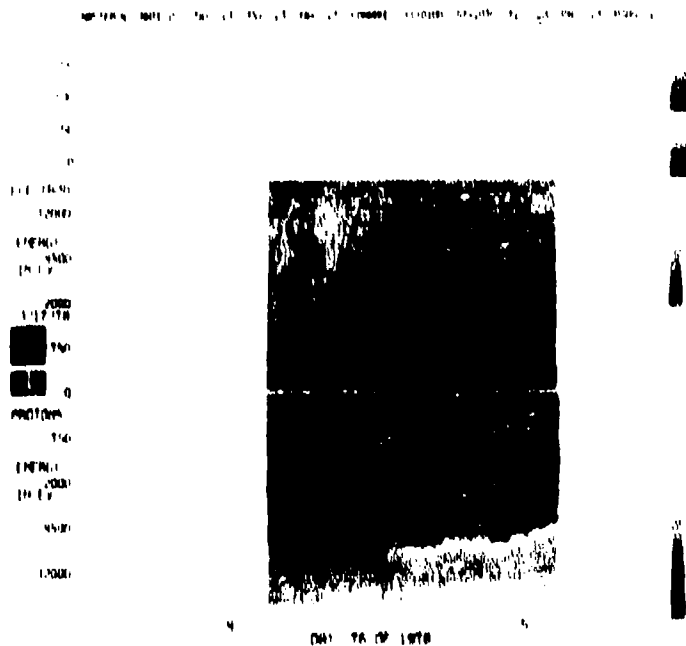
Figure 5. A spectrogram from the UCSD particle detector on the ATS-5 spacecraft showing charging to about -6 kV in eclipse on March 17, 1978. The dark regions indicate low count rates.

417

orbit during the morning of March 17, 1978, was sufficiently hot to charge "dirty" spacecraft such as ATS-5 to several kilovolts negative in shadow, and "clean" spacecraft such as ISEE-1 to approximately -100 V in sunlight.

EVIDENCE FOR A POTENTIAL BARRIER

Figures 6 and 7 show electron data from the Electron Spectrometer experiment on ISEE-1 (Ref. 14). The electron distribution function on a logarithmic scale is shown against electron energy at 0600 UT (Fig. 6) and at 0700 UT (Fig. 7). At 0600 the spacecraft potential was near zero whereas at 0700 the potential was on the order of -40 V, as we showed in Section 2 (See Figure 4). At low energies, both Figures 6 and 7 show a steepening of the electron spectrum characteristic of photoelectrons and/or secondary electrons.

The straight line in Figure 6 which goes through the lower energy electrons indicates that these electrons are characterized by a density of about 20 cm^{-3} and a temperature near 2 eV. These values are very reasonable for photoelectrons emitted from typical spacecraft surfaces at the earth's distance from the sun. The actual value of the photoelectron density would of course depend on the material and on the orientation of the emitting surface with respect to the solar direction. The fact that photoelectrons with energies as high as 20 eV are seen returning to the spacecraft indicates that there must be a significant electric field which turns back the emitted photoelectrons. In other words, there must be a potential barrier around the spacecraft. This behavior of the electron spectrum was seen at all orientations of the spacecraft during its spin, although the magnitude of the inferred photoelectron density was somewhat modulated by the spin.
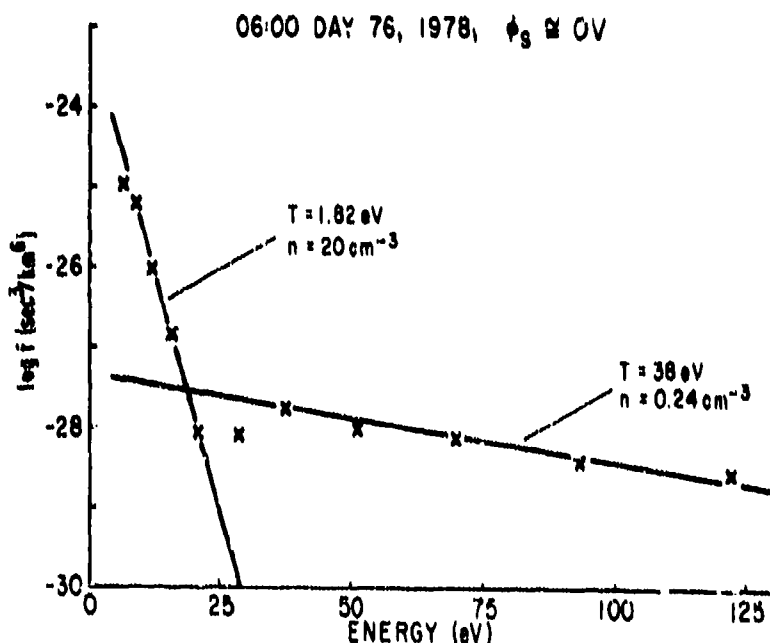
Figure 6. Electron distribution function from the ISEE electron spectrometer at 0600 UT on March 17, 1978.

The behavior of the electron spectrum in Figure 7 is similar to that in Figure 6. The low energy part of the spectrum is fitted well by a Maxwellian distribution with a temperature of 3.4 eV and a density of about 9 cm^{-3} if these low energy electrons are photoelectrons coming from the spacecraft. If these low energy electrons were ambient plasma electrons reaching a negatively charged spacecraft at -40 V, they would have to have a density of almost 10^6 cm^{-3} in the undisturbed plasma. This is completely unreasonable for the plasma at this location near geosynchronous orbit in the earth's magnetosphere. We conclude, therefore, that there must still be a potential barrier around the spacecraft at 0700 UT in spite of the negative spacecraft potential.

The higher energy parts of the distributions in both Figures 6 and 7 give reasonable values for the plasma electron temperatures and densities for this location in the magnetosphere. Measurements of the electron spectrum at higher energies by this instrument and also by the quadrispherical LEPEDEA instrument (Ref. 13) show a significant increase of energetic (keV) electrons over this time period (not shown). The ISEE-1 plasma wave experiment and radio propagation experiment (Ref. 15 and 16) both indicate that the plasma electron density during this period of time was about 1 cm^{-3}.

The existence of a negative potential barrier when the spacecraft is either uncharged or at a negative potential requires a mechanism for its formation. There are two possibilities for a mechanism: one is that there is differential charging of the spacecraft surfaces. This can lead to a potential distribution which has a potential barrier more negative than the spacecraft body if there were some isolated

07:00 DAY 76, 1978; $\phi_s \cong$ -40V

T = 3.44 eV
n = 8.8 cm^{-3} if photoelectrons
n = 8.8 x 10^5 cm^{-3} if ambient electrons

T = 38 eV
n = 0.48 cm^{-3}
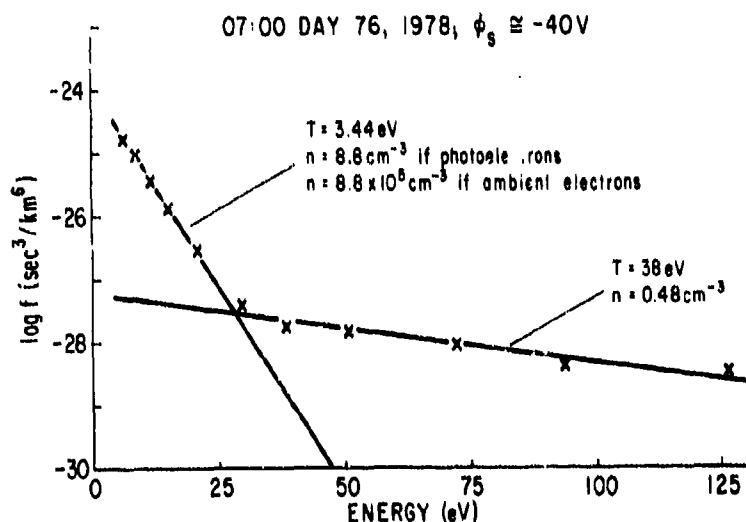
Figure 7. Electron distribution function from the ISEE electron spectrometer at 0700 UT on March 17, 1978.

surface such as a dielectric also at a more negative potential than the main body. The second possibility is that there is sufficient negative space charge in the vicinity of the spacecraft, produced by the emitted photoelectrons and by the ambient plasma, that a negative potential barrier is formed (Ref. 17 and 18).

419

The situation here on ISEE is somewhat similar to that on ATS-6 where photoelectrons and secondary electrons were observed to be reflected from a potential barrier about the spacecraft when the spacecraft was charged to a negative potential (Ref. 19). In the case of ATS-6, it was shown that the observed potential barriers were too large to be attributed to the effects of space charge (Ref. 20). It was inferred that the barriers must be caused by differential charging. This was later confirmed by detailed calculations (Ref. 8).

It appears unlikely that differential charging can be the mechanism responsible for the creation of the potential barrier around the ISEE spacecraft. The stringent cleanliness specifications that were imposed should have prevented potential differences of more than 1 V between portions of the spacecraft surfaces. The precise magnitude of the potential barrier about ISEE during this event is not known, since the returning photoelectrons were observed at oblique rather than normal angles to the spacecraft surface. However, since photoelectrons were observed to return at energies up to abut 20 eV, it is likely that the magnitude of the potential barrier was at least 10 V. This is too large to be attributed to differential charging if the cleanliness specifications were effective in keeping differential potentials to less than 1 V. Hence we conclude that the most likely mechanism causing the formation of the potential barrier is the presence of space charge.

In the solar wind and in the quiet magnetosphere, the spacecraft potential is usually positive so that low energy photoelectrons would return to the spacecraft anyway, without the necessity for the creation of a potential barrier. The fact that the electric field probes are floating at about +5 V while the spacecraft is at about -70 V during this period does not necessarily imply an inconsistency. If the current balance is between collected plasma electrons and escaping photoelectrons and secondary electrons, then it is possible to have more than one potential at which the net current vanishes (Ref. 21). If the potential barrier has been formed because of the presence of space charge, it is not surprising that barriers have not been formed around the electric field probes which are quite small compared to either the photoelectron or ambient plasma Debye lengths (a few meters and a few tens of meters respectively).

CONCLUSIONS

(1) We have shown that on March 17, 1978, the ISEE-1 spacecraft charged to a negative potential on the order of -70 V in sunlight. Evidence for the charging were presented from the two electric field experiments on the spacecraft and from the plasma composition experiment. In addition, we showed that the ATS-5 spacecraft charged to a potential of about -6 kV in eclipse about three hours earlier on the same day but in what appeared to be the same plasma environment.

(2) We have shown from the electron spectrometer experiment on ISEE-1 that there appeared to be a potential barrier about the spacecraft during this event. The potential barrier was on the order of 10 to 20 V negative with respect to the spacecraft body, and was effective in returning emitted photoelectrons to the spacecraft.

(3) It is likely that the potential barrier was produced by the effects of space charge rather than by differential charging of the spacecraft surfaces if the

electrostatic cleanliness precautions were indeed effective. Verification of the mechanism responsible for the creation of the potential barrier requires detailed modeling of this event. The modeling should use photoemission and secondary electron yields appropriate for the ISEE-1 surface materials.

REFERENCES

1. Farquhar, R. W., D. P. Muhonen and D. L. Richardson, "Mission Design for a Halo Orbiter of the Earth," _J. Spacecraft and Rockets, 14,_ 170, 1977.

2. Ogilvie, K. W., A. C. Durney, and T. von Rosenvinge, "Descriptions of Experimental Investigations and Instruments for the ISEE Spacecraft", _IEEE Trans. on Geosc. El., GE-16,_ 151, 1978.

3. Knott, K., A. Durney and K. Ogilvie (editors), "_Advances in Magnetospheric Physics with GEOS-1 and ISEE_", D. Reidel, Dordrecht, 1979.

4. Wrenn, G. L., "Spacecraft Charging", _Nature, 277,_ 11, 1979.

5. Wrenn, G. L., A. D. Johnstone and J. F. E. Johnson, "Spacecraft Charging Studies in Europe", _AFOSR Final Rep._, Grant No. AFOSR-78-3713, 1979.

6. Whipple, E. C., "Potentials of Surfaces in Space", _Rpts. Progr. Phys., 44,_ 1197, 1981.

7. Shelley, E. G., R. D. Sharp, KR. G. Johnson, J. Geiss, P. Eberhardt, H. Balsiger, G. Haerendel, and H. Rosenbauer, "Plasma Composition Experiment on ISEE-A", _IEEE Trans. on Geosc. El., GE-16,_ 266, 1978.

8. Olsen, R. C., C. E. McIlwain and E. C. Whipple, "Observations of Differential Charging Effects on ATS 6", _J. Geophys. Res., 86,_ 6809, 1981.

9. Olsen, R. C., and C. K. Purvis, "Observations of Charging Dynamics", _J. Geophys. Res., 88,_ 5657, 1983.

10. Mozer, F. S., R. B. Torbert, U. V. Fahleson, C. G. Falthammar, A. Gonfalone and A. Pedersen, "Measurement of Quasi-Static and Low-Frequency Electric Fields with Spherical Double Probes on the ISEE-1 Spacecraft", _IEEE Trans. Geosc. El., GE-16,_ 258, 1978.

11. Heppner, J.P., E.A. Bielecki, T.L. Aggson and N.C. Maynard, "Instrumentation for DC and Low-Frequency Electric-Field Measurements on ISEE-A", _IEEE Trans. Geosc. El., GE-16,_ 253, 1978.

12. Olsen, R. C., and E. C. Whipple, "Active Experiments in Modifying Spacecraft Potential: Results from ATS-5 and ATS-6", UCSD Final Report on NASA Contract NAS 5-23481, 1979.

13. Frank, L. A., D. M. Yeager, H. D. Owens, K. L. Ackerson, and M. R. English, "Quadrispherical LEPEDEAS for ISEE's-1 and -2 Plasma Measurements", IEEE Trans. Geosc. El., GE-16, 221, 1978.

14. Ogilvie, K. W., J. D. Scudder and H. Doong, "The Electron Spectrometer Experiment on ISEE-1", IEEE Trans. Geosc. El., GE-16, 261, 1978.

15. Gurnett, D. A., F. L. Scarf, R. W. Fredricks and E. J. Smith, "The ISEE-1 and ISEE-2 Plasma Wave Investigation", IEEE Trans. Geosc. El., GE-16, 225, 1978.

16. Harvey, C. C., J. Etchato, Y. De Javel, R. Manning and M. Petit, "The ISEE Electron Density Experiment", IEEE Trans. Geosc. El., GE-16, 231, 1978.

17. Guernsey, R. L., and J. H. M. Fu, "Potential distribution surrounding a photo-emitting diode in a dilute plasma", J. Geophys. Res., 75, 3193, 1970.

18. Fu, J. H. M., "Surface potential of a photoemitting plate", J. Geophys. Res., 76, 2506, 1971.

19. Whipple, E. C., "Observation of Photoelectrons and Secondary Electrons Reflected From a Potential Barrier in the Vicinity of ATS 6", J. Geophys. Res., 81, 715, 1976.

20. Whipple, E. C., "Theory of the Spherically Symmetric Photoelectron Sheath: A Thick Sheath Approximation and Comparison with the ATS 6 Observation of a Potential Barrier", J. Geophys. Res., 81, 601, 1976.

21. Laframboise, J. G., R. Godard and M. Kamitsuma, "Multiple Floating Potentials, "Threshold-Temperature "Effects, and "Barrier" Effects in High-Voltage Charging of Exposed Surfaces on Spacecraft", Proc. Internat. Symp. on Spacecraft Materials in Space Environment, Toulouse, France, June, 1982; ESA Rpt. SP-178, pg. 269, European Space Agency, Noordwijk, The Netherlands.

GALILEO INTERNAL ELECTROSTATIC DISCHARGE PROGRAM*

Philip L. Leung, Gregory H. Plamp, and Paul A. Robinson, Jr.
Jet Propulsion Laboratory
California Institute of Technology
Pasadena, California 91109

The Galileo spacecraft which will orbit Jupiter in 1988 will encounter a very harsh environment of energetic electrons. These electrons will have sufficient energy to penetrate the spacecraft shielding, consequently depositing charges in the dielectric insulating materials or ungrounded conductors. The resulting electric field could exceed the breakdown strength of the insulating materials, producing discharges. The transients produced from these Internal Electrostatic Discharges (IESD) could, depending on their relative location, be coupled to nearby cables and circuits. These transients could change the state of logic circuits or degrade or even damage spacecraft components, consequently disrupting the operation of subsystems and systems of the Galileo spacecraft during its expected mission life. An extensive testing program was initiated for the purpose of understanding the potential threats associated with these IESD events. Data obtained from these tests were used to define design guidelines.

INTRODUCTION

The Galileo spacecraft will be launched in late 1986. Galileo is to perform a far more intensive and comprehensive investigation of the Jupiter system than was possible with Voyager. Its design has benefited from the experience of the Voyager spacecrafts. The Voyager 1 spacecraft, as it entered Jupiter's magnetosphere, experienced a number of Power on Resets (POR). An extensive study was carried out to determine the cause of PORs. A study of the environment was performed. The environment consists of low energy (<100 keV) plasma and intense high energy (>100 keV) electrons. Our investigation showed that the time for the occurrence of PORs did not correlate with the severity of the plasma environment. The plasma instrument onboard the spacecraft also confirmed that significant surface charging did not occur. An investigation of the radiation electron environment indicated that the PORs occurred during the time that the flux of radiation electrons was at its peak. Consequently, internal discharges induced by the penetrating electrons were proposed as a possible cause of PORs (Ref.1).

In order to prevent the occurrence of PORs during the Galileo mission, a test program was initiated to investigate the effect of penetrating electrons on

electronic circuits. The program consists of two phases. In the initial phase, the phenomena of IESD were investigated through analysis and testing. This was done with contractor support from General Electric and JAYCOR. Analysis and tests during this phase demonstrated that some of the dielectric insulation of spacecraft components did discharge when they were irradiated by an electron beam with a flux level corresponding to the levels they would experience in the Jovian environment. To ensure that IESD related anomalies will not occur during Galileo's encounter with Jupiter, the second phase of this program was to acquire the necessary data to generate the required design guidelines for the Galileo spacecraft. The design guidelines are on the material selection, grounding criterion, transient characteristics and coupling of discharge energy into circuits.

This paper discusses the test configuration, the test results, and the application of test results for design guideline generation.

GENERAL TEST PROGRAM

The tests were performed in the dynamitron facility of the Jet Propulsion Laboratory. The dynamitron is capable of delivering an electron beam in the energy range of 0.8-2.5 Mev. To simulate the environment that the dielectrics would experience in space, it was decided that a high vacuum system would be required. This system uses a standard diffusion pump with a cold trap provided to control oil contamination (Figure 1). The dynamitron electron beam enters the test chamber through a 75 µm stainless steel diaphragm. The sample holder is located inside the vacuum chamber and is situated perpendicular to the electron beam. A Faraday cup is mounted in the plane of the sample specimen so that the flux levels at the test sample could be accurately monitored. Pressures of 2×10^{-5} torr or less are required before initiating the test.

The occurrence of discharges are monitored by current transformers placed along the possible paths of discharge currents. Another diagnostic for the discharge is a plasma current detector, which is a thin sheet (50 µm thick) of aluminium with a diameter slightly smaller that of the chamber. This plasma current detector is placed right in front of the test sample and hence it detects the presence of charged particles generated during discharges. In some of the tests, the test items (such as cables and circuit traces) were used as detectors for the occurrence of discharges. The transient signals induced on these detectors are transmitted outside the vacuum chamber through coaxial cables. These signals are displayed on storage scopes or transient digitizers. The length of coaxial cable used in our experiments are about 10 m. The effect of long cables on the transient signals was investigated by applying a pulse on one end of the cable and receiving the pulse at the other end. No significant amplitude loss or waveform distortion was observed.

The flux level used in our experiment was determined by the expected inflight deposited flux levels at the samples. The expected inflight deposited flux level as well as the dynamitron deposited flux levels were both determined by Monte Carlo computer calculations. The test fluence for our test is usually chosen as Jupiter Orbit Insertion (JOI) plus 5 orbit fluence. This selection is based on the fact that JOI+5 orbits are the minimum required for a successful mission. Due to the constraint of time and cost, the flux level used to achieve this fluence was usually at least a factor of three higher than the anticipated worst-case level.

The test items chosen for this test program were parts of the Galileo spacecraft. They were either components with dielectric insulation or components with floating conductors. The criteria for test sample selection are based on: (1) the intensity of the expected deposited flux level, and (2) the proximity of the components to sensitive circuits. Initial tests were performed to determine if breakdown was possible. If breakdown did occur, then tests were performed to determine the transient parameters. The transient parameters of importance are rise time, pulse width, and peak voltage. The electron beam had previously been charted inside the chamber to determine its uniformity. The results indicated that the beam was uniform over the surface of the sample holder (36-cm diameter). Before any radiation tests were initiated in the chamber, a dry run was performed at a very high flux level. This was done in order to determine if there existed any dielectric in the chamber that might break down producing unwanted data. The results of the tests were negative.

Table 1 presents the test samples and the results of radiation tests performed on these items. This table does not include the results on circuit boards and cables; the results on these two items are presented in more detail in the next section. This table provides information on the electron beam energy and the flux level. If discharges occurred, the associated worst-case IESD parameters are also presented. Note that the flux levels used in testing the connectors were far greater than the anticipated environment. We were interested in acquiring as much information on the transient parameters and, therefore, it was decided to greatly increase the flux level.

DESIGN GUIDELINE TEST

It was determined that the greatest hazard existing to the subsystems and systems of Galileo originated from the circuit boards (Ref. 2) and flight cabling. Extensive testing was performed on these items to determine the effects of discharge on nearby circuitry.

Different circuit board designs were fabricated to determine the effects of electron radiation on floating circuit traces of various area, spacing, and length. The boards were fabricated out of FR4 material. Circuit board A (Fig. 2a) was designed to determine the effects of the floating trace area on the characteristics of discharges. The areas varied from 5×5 cm (25 cm^2) to a plated-through hole (elements 1 to 5). In addition, the effects of spacing between the nearest grounded conductor was investigated using elements 6, 7, and 8 on board A. Board B (Fig. 2b) was designed to determine the effects of spacing and length variation on IESD events.

During each test, only one element of a circuit was left floating while the other elements were connected to strips which were grounded through 50-ohm resistors. Two grounded strips on each board were monitored for signs of an IESD event. The discharge current collector was used to monitor the blowoff electrons resulting from discharges. The boards above were tested under two different configurations. In the first configuration the board was bare, and in the second configuration it was coated with Solithane (a conformal coating).

Tests were also designed to characterize the transient signals generated by discharge of the cables. The cabling employed on Galileo uses two different types of insulation, Kapton and Teflon. Previous results obtained from the irradiation of Kapton (Refs. 3, 4, and 6) and Teflon (Refs. 4 and 5) materials indicate that they will break down under Jupiter's anticipated flux level. The concern raised was the voltage and energy levels associated with the transient induced on the center conductors. Typical flight-like cabling of both Kapton and Teflon material were obtained for testing. The length of the Kapton and Teflon cables varied from 15 to 300 cm. The center conductors were terminated with an impedance of 50 ohms, and they were also used as discharge detectors.

In some of the cables that we have tested, some conductors were accidentally left floating. The transient characteristics generated by cables with floating conductors were found to be vastly different from cables with all conductors grounded. The cables with floating conductors included cables inside a Teflon bundle cable and cables from the Data Management Subsystem (DMS) of the Galileo spacecraft. The wires associated with the DMS cable were nonshielded single conductors. The length of the wires tested were approximately 30 cm.

The electron beam employed in testing the circuit boards ranged from 0.85 to 1.75 MeV. The current density of the beam varied from 4 to 26 pA/cm^2. The position of the circuit traces was perpendicular to the incoming beam. The Faraday cup was positioned at the sample level of the circuit board such that the appropriate current density could be maintained.

The Kapton and Teflon cables were coiled on the surface of the sample holder around the Faraday cup. In this way the cable surface was perpendicular to the incoming electrons. The DMS cable, due to its limited length, was positioned along the length of the sample holder. The beam energy used in testing the cables ranged from 1.45 to 1.65 MeV. The current density of the electron beam varied from 160 to 320 pA/cm^2 for the Kapton and Teflon cable bundles. The current density used in the case of the DMS cable was 16 pA/cm^2.

DESIGN GUIDELINE TEST RESULTS

Several types of discharges were observed in the circuit board tests. Small discharges were usually observed at the beginning of irradiation of a "fresh" circuit board. This could have been due to the occurrence of discharges within the imperfections of the circuit board. The transient voltage coupled to the nearby grounded conductor was usually very small (<1 V) and was of narrow pulse width (<20 ns). Large amplitude (>5 V) signals were usually not observed until the circuit board had been irradiated for a period of 2-4 hours. Therefore, the magnitude of transients depends on the time history of the irradiation. Consequently, there was a great deal of variation in the transient characteristics associated with the discharges of each circuit trace. Table 2 displays the worst-case transient parameters observed during the irradiation of the A board. In the case of element A4 (Table 2), the small voltage of 0.8 V was observed at the beginning of the electron beam irradiation; if we had rerun the test again at a later period we would expect the observed voltage to be much higher than 0.8 V. The average rise time of the pulses observed ranged from 5-10 ns.

426

The signals coupled to nearby grounded conductors during big discharges indicated that there were two different discharge processes. In one process, a negative spike with a narrow pulse width (40 ns) was induced on a nearby grounded conductor (Fig. 3). The negative signal was probably due to the flow of electrons from the floating trace to the grounded trace. In another process, the transient signal coupled to a nearby conductor consisted of two distinct parts. The first part was the negative narrow pulse width signal (Fig. 4a) with characteristics similar to the previously mentioned signal. The second part of the signal consists of a positive signal with a wide pulse width (400 ns). The negative portion of this signal was again due to the floating circuit trace discharge. However, this discharge also caused the expulsion of electrons stored in the circuit board material. These blowoff electrons, which were many times greater in number than the electrons stored in the floating circuit trace, were collected by the plasma detector. This process was confirmed by the negative wide pulse width signal on the plasma current collector (Fig. 4b). The positive signal detected by the grounded trace was due to the return current of the electrons stored in the circuit board.

Experiments with conformal coated circuit board A indicated the maximum energy and voltage of the transient was reduce by a factor of 2 or more. The reduction is due to the fact that the conformal coating reduces the efficiency of coupling by eliminating the direct couple path.

After performing a variety of tests on Kapton and Teflon flight cabling, it became obvious that the danger lay not in the dielectrics of the cabling but the problems associated with floating conductors that may exist in the cabling. Induced transients with voltages of 4-6 V were observed when the dielectric insulation of the cable discharged. However, due to engineering changes or undetermined plans, wires within the cable bundle may end up not being used. These wires would exist as floating conductors inside the bundle during the Galileo mission. Once in the Jovian environment the bundle would be exposed to penetrating radiation. The wires could then be charged to high enough potentials to breakdown the insulation of the wires or the connectors. Typical discharge signals associated with grounded and floating conductors inside cable bundles are shown in Figs. 5a and 5b. This signal was detected by a grounded (through 50 ohm) conductor in the cable bundle. Notice the difference in magnitudes of transient signals between the two cases.

It was found that when one varied the impedance of the monitored wire the effect was to alter the pulse width of the induced transient. The amplitude of the transient remained at basically the same level. This seems to indicate that the governing impedance of the detection system actually depends on the source impedance of the discharge itself.

DESIGN GUIDELINE DISCUSSION

From the measured waveforms, the energy that can be coupled to a load of impedance R is given by the following equation:

$$E = \frac{V_{pp}^2}{4R} T$$

Where V_{pp} is the peak voltage, R is the impedance, and T is the pulse width. Since most of the observed waveforms resemble a damped sine wave, to add some conservatism in the energy calculation T is the e-folding pulse width. This method was applied to calculate the energy of all transient pulses observed.

In the discharge of each circuit trace, pulses of different magnitudes were observed. As an engineering approach, only the pulses with the highest magnitude (Table 2) were used for the correlation study. The energy and voltage data are plotted in Figs. 6a and 6b. In both plots, the data obtained from circuit trace element #4 were omitted. Figures 6a and 6b do indicate a trend, i.e. the voltage and energy that can couple to a load increases with the area of the circuit traces.

The results obtained for elements 6-8 on the noncoated A circuit board did not display any consistency in terms of floating trace spacing and the resulting transient parameters. Tests performed on circuit board B indicated that the transient parameters did not show any correlation with either the spacing or the length of the circuit traces. With additional statistics it may be possible to determine some relationships.

As mentioned in the previous section, the cable tests indicated that the breakdown of cable insulation would induce a 4-6 V transient on the conductors of the cables. This low voltage level is acceptable to Galileo spacecraft subsystems since all the circuits are designed to withstand a 10-V transient voltage. However, the breakdown of cables with floating conductors can induce voltage in excess of 10 V into circuitry; therefore, a design requirement is needed for cables with floating conductors. In order to derive this requirement, the results from the Teflon cable bundle test and the DMS cable test were used. Figures 7a and 7b display the voltage and energy that were coupled to a 50-ohm load, respectively. The upper data point is for the Teflon cable bundle. There were several floating conductors in both the Teflon and the DMS cable bundles. Because of the wide pulse width of the observed discharges, the discharges were most likley caused by more than one floating conductor. The error bars in Figs. 7a and 7b indicate the uncertainties in the total length of floating conductor involved in the observed discharges.

Steps were taken to define design guidelines based on the information derived from the tests. The raw data provided a margin of one. However, for engineering purposes a safety factor of two was incorporated into the design guidelines. These design guidelines had their origin in the assumption that an IC would not be damaged by a transient having a voltage of 20 V and an energy of 4 μJ. The two design guidelines derived are:

(1) All individual wires exceeding 25 cm in length within subsystem wire harnesses, Orbiter system wire harnesses, and assembly-to-system interface cabling shall have a conductive path to ground with 1×10^6 ohm resistance when measured in air or 1×10^{12} ohm resistance when measured in vacuum.

(2) All radiation shields, circuit traces, and conductor with a surface area greater than 3.2 cm^2 shall be electrically grounded unless one of the following conditions can be verified:

(a) The conductive element and circuit is identical to Voyager and is approved by the Environmental Requirements Engineer and Orbiter Manager to be an acceptable risk.

428

(b) The conductive element is verified by test or analysis to have
$<1 \times 10^8$ ohm resistance to ground in air or 1×10^{12} ohm
resistance in vacuum.

REFERENCES

1. Leung, P.; Whittlesey, A.; Garrett, H. B.; and Robinson, P. A. Jr.: "Environment-Induced Electrostatic Discharges as the Cause of Voyager 1 Power on Resets," to be published in the Journal of Spacecraft and Rockets, 1983.

2. Private communications with M. Treadaway at JAYCOR, La Jolla, CA.

3. Treadaway, M.; Denson, R.; and Wenaas, E.: "Dielectric Discharge Characteristics in a Two-Electron Simulation Environment," Spacecraft Charging Technology 1980, NASA Conference Publication 2182, AFGL-TR-81-0270, Nov. 1980, pp. 4-16.

4. Hazelton, R. C.; Yadlowsky, E. J.; and Churchill, R. J.: "Experimental Validation of a Numerical Model Predicting the Charging Characteristics of Teflon and Kapton Under Electron Beam Irradiation," Spacecraft Charging Technology 1980, NASA Conference Publication 2182, AFGL-TR-81-0270, Nov. 1980, pp. 65-73.

5. Beers, Brian L. and Pine, V. W.: "Electron-Beam-Charged Dielectrics-Internal Charge Distribution," Spacecraft Charging Technology 1980, NASA Conference Publication 2182, AFGL-TR-81-0270, Nov. 1980, pp. 17-32.

6. Leung, P. and Plamp, G.: "Characteristics of RF resulting from Dielectric Discharges," IEEE Transactions on Nuclear Science, Vol. NS-29, No. 6, Dec. 1982, pp. 1610-1614.

TABLE 1. – RESULTS OF ELECTRON IRRADIATION TESTS FOR VARIOUS GALILEO SPACECRAFT COMPONENTS

TEST ITEM	ELECTRON BEAM ENERGY (MeV)	FLUX (pA/cm²)	WORST-CASE IESD TRANSIENT PARAMETERS				COMMENTS
			VOLTAGE (V)	RISE TIME (ns)	PULSE WIDTH (ns)	ENERGY (J)	
SIGNAL AND TOROIDAL POWER TRANSFORMERS	2.50	29	—	—	—	—	TRANSIENT NOT OBSERVED
SYNTACTIC FOAMS	1.45 - 2.50	16 - 80	—	—	—	—	TRANSIENT NOT OBSERVED
ANTENNA MATERIAL	1.45	64	0.3	5	200	3.6×10^{-10}	TRANSIENT SIZE AREA DEPENDENT
BOOM MATERIAL	1.85 - 2.50	53 - 106	1.6	—	6000	3.6×10^{-7}	TRANSIENT SIZE LENGTH AND ANGLE OF INCIDENT DEPENDENT
COAX CABLE (RG 142/U)	1.00 - 1.25	80 - 160	8	10	1000	3.2×10^{-7}	MEASURED ACROSS 50 Ω
STANDARD DENSITY CONNECTOR DS 313-22-55	1.60 - 2.50	640	5.8	5	50	8.4×10^{-9}	MEASURED ACROSS 50 Ω
HIGH DENSITY CONNECTOR ST-11949-12-35	1.60 - 2.50	640	5.3	5	30	4.2×10^{-9}	MEASURED ACROSS 50 Ω
FLEX PRINT CONNECTOR ST-11493-50	1.60 - 2.50	160 - 640	28	10	70	2.7×10^{-7}	MEASURED ACROSS 50 Ω

TABLE 2. – TRANSIENT PARAMETERS OBSERVED DURING DISCHARGE OF ELEMENTS OF NONCOATED BOARD A

ELEMENT NO.	WORST-CASE IESD TRANSIENT PARAMETERS		
	VOLTAGE (V_{pp})	PULSE WIDTH (ns)	ENERGY (J)
1	60	339	6.1×10^{-6}
2	25	510	1.6×10^{-4}
3	18	375	6.1×10^{-7}
4	0.8	10	3.2×10^{-11}
5	6	52	9.4×10^{-9}
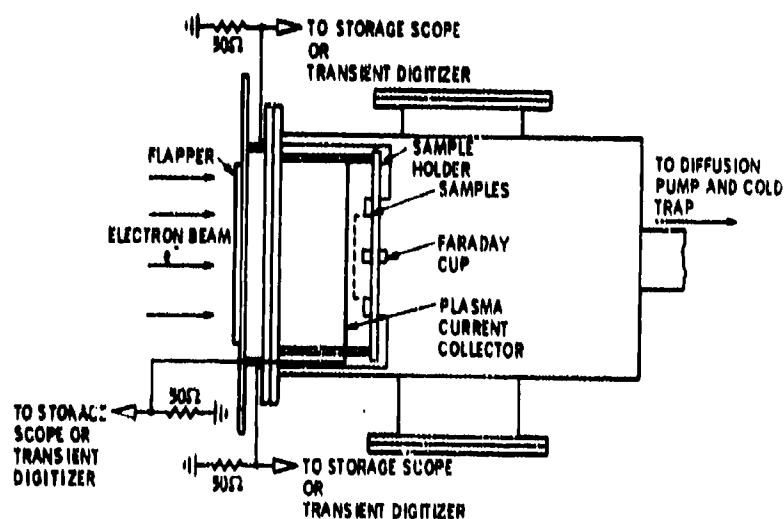
Figure 1. - Target chamber and fixtures.
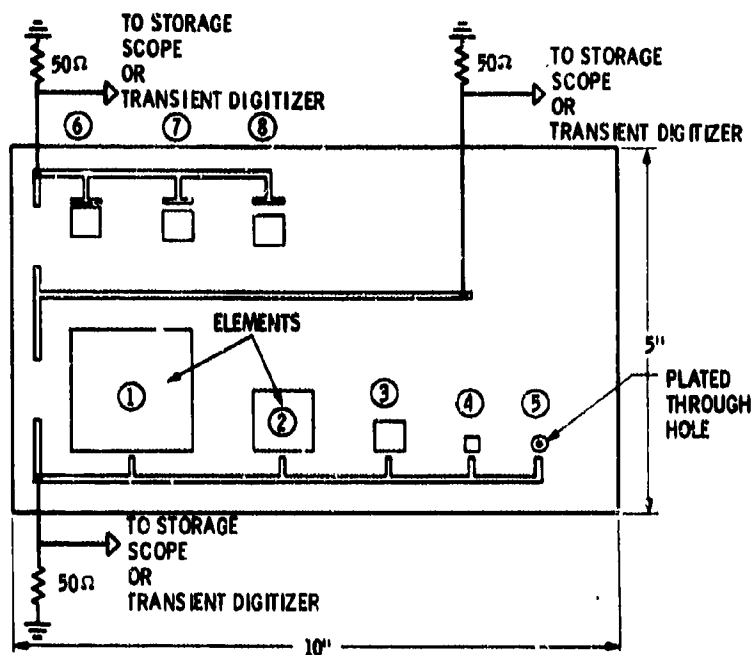
(a) Board A.
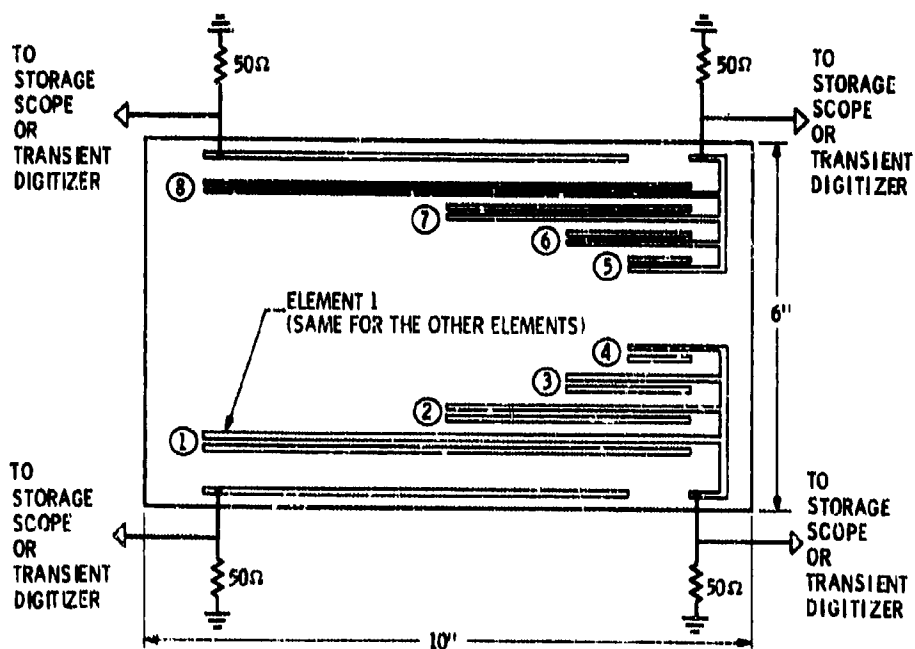
(b) Board B.

Figure 2. - Trace length and spacing variation.

432
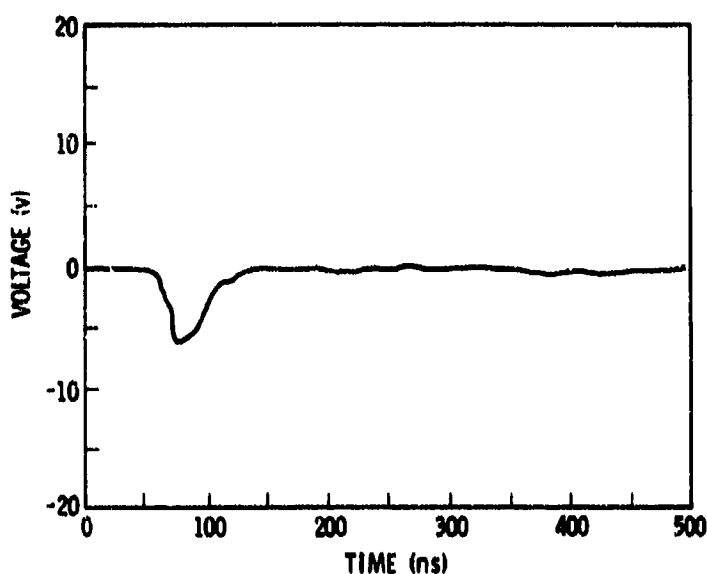
Figure 3. – An intermediate discharge pulse observed during electron beam irradiation of circuit boards with floating circuit trace. Detector is a nearby grounded trace.
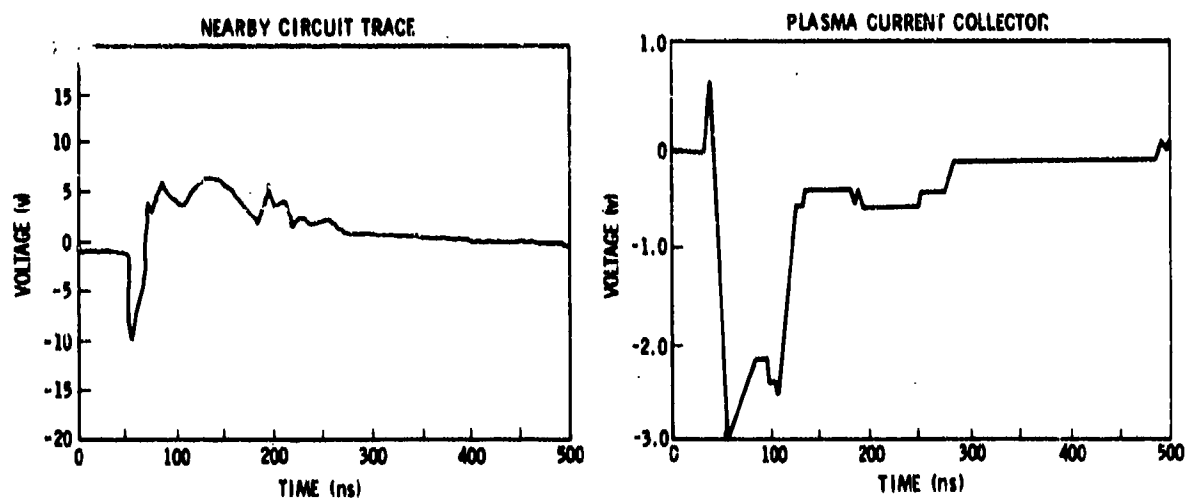
(a) Detector, nearby grounded trace.

(b) Detector, plasma current detector.

Figure 4. – Large discharge pulse observed during electron beam irradiation of circuit board with floating traces.

433
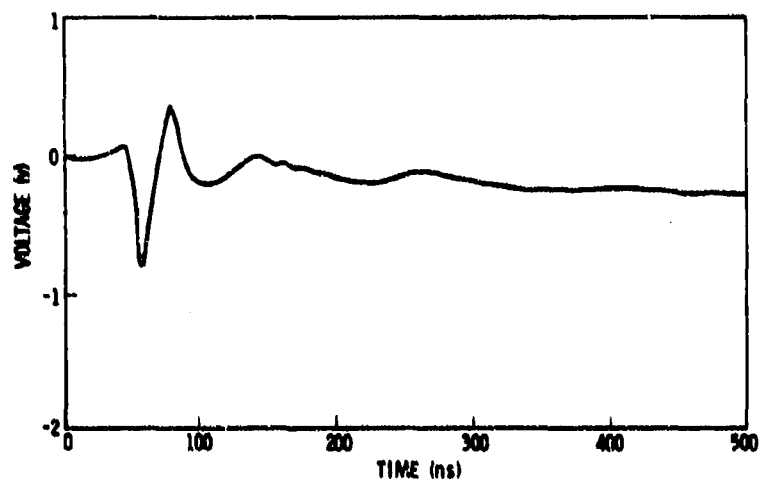
(a) Grounded conductors.
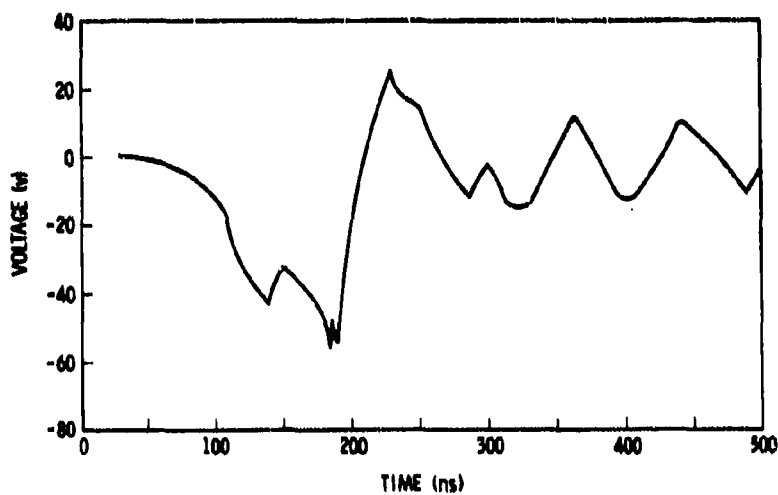
(b) Floating conductors.

Figure 5. – Discharge pulses observed during electron beam irradiation of
Teflon cable bundle. Detector in both cases was a grounded conductor within
cable bundle.

434
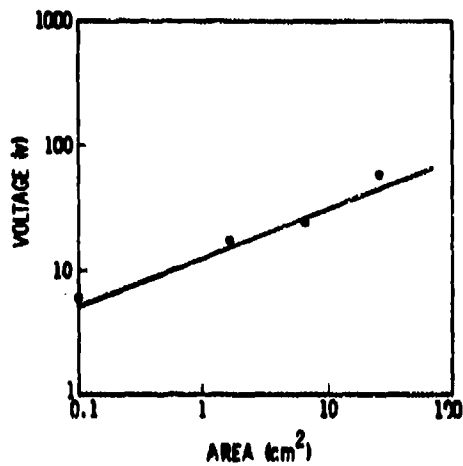
(a) Voltage versus area. (b) Energy versus area.
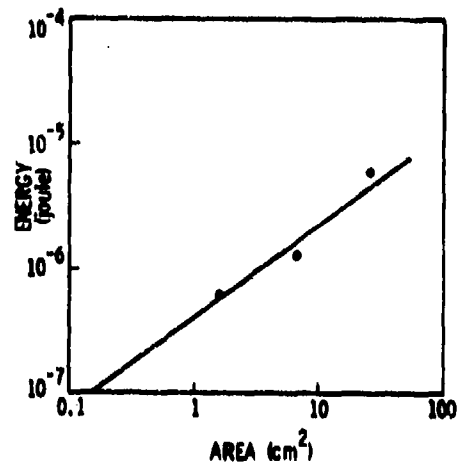
Figure 6. - Dependence of transient parameters on circuit trace area.
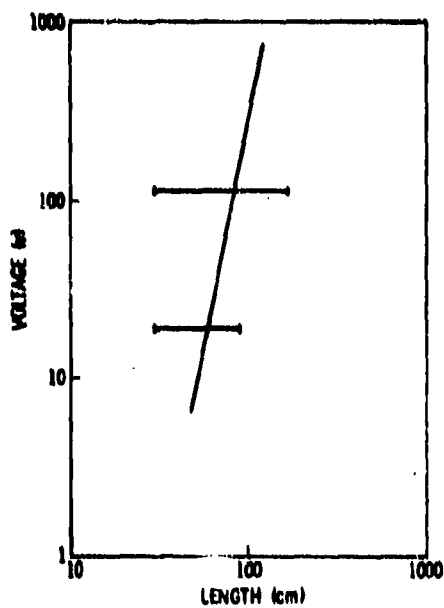
(a) Voltage versus length. (b) Energy versus length.
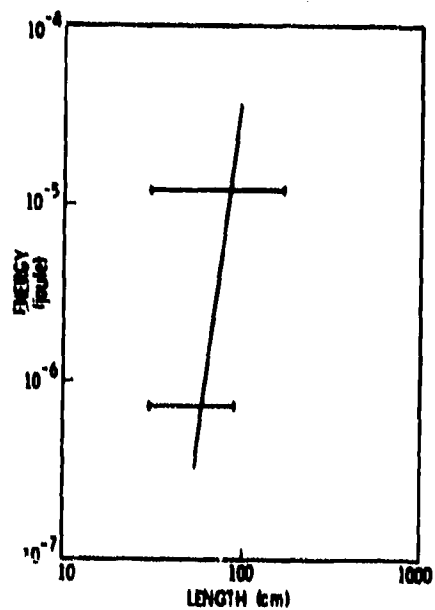
Figure 7. - Dependence of transient parameters on floating conductor length.

CHARACTERISTICS OF EMI GENERATED BY NEGATIVE METAL/POSITIVE DIELECTRIC
VOLTAGE STRESSES DUE TO SPACECRAFT CHARGING

R. C. Chaky and G. T. Inouye
TRW Space and Technology Group
Redondo Beach, California 90278

Charging of spacecraft surfaces by the environmental plasma can result in differential potentials between metallic structure and adjacent dielectric surfaces in which the relative polarity of the voltage stress is either negative dielectric/positive metal or negative metal/positive dielectric. The first stress polarity, negative dielectric/positive metal, has been studied extensively in prior work in which dielectric targets were bombarded with electrons. The second polarity, negative metal/positive dielectric, has not had much research attention, although this stress condition may arise if relatively large areas of spacecraft surface metals are shadowed from solar UV and/or if the UV intensity is reduced as in the situation in which the spacecraft is entering into or leaving eclipse. In this paper we present results of experimental studies of negative metal/positive dielectric systems.

NASCAP charging analyses and SCATHA data have shown that differential stresses greater than 3-6 kV of either polarity are not easily generated on spacecraft exposed to the geosynchronous orbit environment. Measurements by many workers have shown that negative dielectric/positive metal electrostatic discharge (ESD) thresholds are in the 10-20 kV range. Negative metal/positive dielectric discharge thresholds are in the 1-3 kV range, and are therefore much more likely to be the source of in-orbit electromagnetic interference (EMI). Prior studies (1, 2, 3) have identified this more viable arc discharge mode in a qualitative sense. Figure 1 illustrates some of the features of the phenomena associated with the negative metal/positive dielectric configuration. Figure 1 is a strip chart record obtained with a solar cell test sample biased negatively by a power supply through a 10 kilomegohm series resistor. The positive dielectric (cover glass) potential is generated by photoemission induced by UV irradiation. The setup is shown in Figure 2. The voltage-divided substrate voltage, V, provides the input for the strip chart recorder. With the bias voltage applied, turning on the UV reduces the substrate voltage by the normal photoemission current IR drop, i.e., the sample voltage V_s drops from 7.1 kilovolts to 6.9 kilovolts. Shortly after the lamps are turned on arc discharges, blowoff of electrons, are seen as momentary pulses raising the substrate voltage towards zero volts. About a minute later the substrate voltage settles below ~1 kV, a steady-state condition of enhanced electron emission. The noisiness of the enhanced emission current should be noted. At 7.32 minutes the UV lamps are turned off, but the enhanced electron emission (e^3) continues. This condition may

continue for tens of minutes or may abruptly or gradually "wear out" and return to a normal photoemission level with the UV lamps on, and only arc discharge, or may revert to the e^3 state. The phenomena associated with the negative metal/positive dielectric configuration are summarized below:

o Arc discharges at low voltages (1-3 kV)

o Enhanced electron emission (e^3)

o Corona-like noise associated with e^3

Figure 3 shows the surface and structure potentials relative to the far plasma calculated as a function of the solar UV intensity for a three-axis stabilized spacecraft. In full sunlight, sunlit dielectric surfaces as well as structure are a few volts positive, mainly because of the predominance of photoemission currents over the incident negative currents due to the substorm electrons. Dark dielectric surfaces, surfaces shadowed by other parts of the spacecraft, are 2-3 kV negative because these surfaces are not photoemitting. As the UV intensity is decreased, the structure potential drops towards -3 kV first because its exposed surfaces are both sunlit and shadowed. The sunlit dielectric surfaces eventually also drop to -3 kV at about 20% of full sunlight. At zero UV intensity, complete eclipse, all potentials are nearly equal at about -3 kV.

Figure 4 shows the differential voltages relative to structure computed from the data for Figure 3. The positive dielectric voltages, the sunlit surfaces, peak at about plus 2.8 kV at about 20% of full sunlight, a photoemission current density, J_{uv}, of above 0.5 na/cm^2. This, then, is the regime in which the low voltage reversed polarity arc discharges may be expected to occur most readily. Figure 5, from the paper by H. C. Koons (4), shows arc discharges observed on the P78-2 (SCATHA) satellite as it goes into and out of eclipse during a substorm.

Arc discharge blowoff current magnitudes and those of the associated replacement currents depend on the capacitance of the spacecraft to space. This capacitance to space is directly proportional to the linear dimensions of the spacecraft, and hence the hazard due to blowoff will increase as spacecraft become larger in future designs. Structural replacement currents are collected over all spacecraft surfaces and flow back towards the arcing source. They become more and more concentrated near the source, but the possibility exists for coupling unwanted EMI into victim circuits remote from the source. The flashover component of a positive dielectric discharge increases with the source dimension, but its effects are confined to localized electrostatic and magnetic coupling. The peak voltage associated with these discharges was found to be that of the negative metal potential prior to the discharge, a positive-going step in 0.5 to 1.5 microseconds. The recovery time to re-adjust to the original negative potential was the RC recharge time constant, on the order of a fraction of a millisecond.

Another facet of the EMI generated by the negative metal/positive dielectric configuration arises if it results in the enhanced steady-state corona-like electron emission condition. The emission currents exhibit an impulsive noise characteristic which increases in amplitude and frequency of occurrence with the level of emission current. We interpret this noise

characteristic as being due to the burn-up of localized sharply pointed high field emission sources. Peak noise voltages of 1.5 kV and currents of 4 microamps have been observed on a strip chart recorder (0-10 Hz bandwidth). On a wide band oscilloscope the amplitude and risetimes may approach those of the individual discharges discussed earlier.

TEST CONFIGURATION

Test were performed in a 2' x 4' vacuum chamber at pressures between 10^{-5} and 10^{-6} Torr. Negative sample substrate potentials were obtained with a high voltage power supply, and the more positive but still negative dielectric surface potentials were obtained by irradiation with mercury UV lamps. The test setup for EMI characterization is shown in Figure 6. Earlier tests by Inouye and Sellen (1) applied the negative bias with an electron beam from a gun located at the opposite end of the vacuum chamber to more nearly simulate the in-orbit situation. The adjustable (0 to 20 kV) power supply with selectable series resistor, R_1 (80 Meg to 10 kMeg), provides a more easily controlled and defined source of negative bias.

The 25 kMeg - 1 Meg resistive divider tied to the point between R_1 and the sample performs two important functions. First, it provides a convenient measure of sample voltage, and because of the IR_1 voltage drop, the sample emission current. The strip chart record of Figure 1 was obtained at this test point. Even more important, the 25 kMeg, in parallel with R_1, isolates the sample from the vacuum system ground and allows the sample potential to more nearly simulate equilibration as it would occur in orbit. Short duration arc discharge voltage swings and associated currents will also be more closely simulated than in test configurations in which low impedance (power supply output impedance, 50 ohm cable terminations) were used.

The strip chart record provides a low frequency (0-10 Hz) measure of the sample voltage and current which is fine as an indication of equilibration currents, but is only a qualitative measure of the total electromagnetic interference (EMI) situation. The additional circuitry shown in Figure 6 provides the necessary diagnostics to define the higher frequency EMI components. The test sample is further isolated with a 15 Meg resistor, and C_1/C_2 is a capacitive voltage divider, just outside the vacuum chamber, which provides a measure of sample voltage. The 1 ohm resistor at the bottom of C_2 provides a direct measure of the sample current. C_1, 25 pf to 0.1 µf, represents the spacecraft capacitance to space. These two capacitance values, for a spherical spacecraft, represent spacecraft radii of 0.5 m and 1 km respectively, and will be demonstrated that the spacecraft dimension has a critical effect on the character of arc discharges.

The sample voltages and currents measured by C_1, C_2 and the 1 ohm resistor and the strip chart record provide a measure only of emitted or blowout currents. Another component, the flashover currents which flow from the front of the dielectric directly to the substrate, cannot be detected at the 1 ohm resistor. That this component exists and that a uniform wipeoff of the initial charge occurs has been demonstrated by scanning the dielectric surface potential with an electrostatic voltage probe (not shown in Figure 6) before and after a discharge. A loop antenna with its axis parallel to the

439

plane of the dielectric has been installed to attempt to obtain a measure of the flashover currents. Since the direction of surface current flow is random, only a qualitative indication is to be expected. The blowout component may also couple magnetic flux into this horizontal loop. Its time history, however, is known from the 1 ohm resistor, and therefore the loop may provide data on the flashover component.

Two stainless steel wire meshes are located in front of the test sample between the sample and the UV lamps. They have a transparency of 80 to 90 percent and hence do not materially affect the UV intensity at the sample. These meshes were installed to detect separately the electrons and the positive ion components of the blowoff current. The first grid is grounded through 50 ohms, and the second is biased negatively, after filtering, from the power supply. The first grid at ground potential is necessary to permit photoelectrons to leave the dielectric surface, thus biasing that surface positively relative to the metallic substrate.

TEST RESULTS

The majority of test samples in the tests reported here were solar cells mounted in the configuration shown in Figure 7. Table 1 lists the eight various combinations of coverglass material, interconnect type and insulation (or not) from the aluminum substrate. Samples 9 and 10 were duplicates of Sample 1 and 2. One objective of the tests was to determine which type of sample exhibited enhanced electron emission and which did not. Only a few samples exhibited e^3, and not all arc discharged. Table 2 summarizes the results.

The following results on detailed EMI characteristics were obtained on a solar cell sample with the normal interconnects, fused silica coverglass and Kapton insulation, Sample No. 1 on Table 1. Figure 8 is a plot of the steady-state e^3 current versus sample voltage. It shows that e^3 currents become significant above 200 volts and increase monotonically with increasing sample voltage. Figure 9 is a plot of peak noise currents as seen on the strip chart record (0-10 Hz) as a function of the dc e^3 current. Peak noise voltages of 1.5 kV and 4 microamperes in amplitude have been observed. On a wideband oscilloscope these peaks can be as high as the individual arc discharges which are discussed next. The main point here is that the steady-state e^3 condition is best described as being corona-like and is very noisy. One other important aspect of enhanced electron emission is its very localized nature. By covering successively smaller halves of the test sample surface with 5 mil Kapton, nearly the entire emisson current was found to be emitted from less than 1/128 of the total sample area. This small exposed area, of course, included some metal and some dielectric. Thus, e^3 currents are emitted from a extremely localized source, and should not be considered as a per unit area phenomenon such as the charging process.

Arc discharges due to negative metal-positive dielectric charges were investigated at the diagnostic points shown in Figure 6 using a wideband oscilloscope and Polaroid camera. Most of the oscilloscope waveform records were taken with C_1 equal to 100 pf (a 1 meter radius spacecraft), and C_2 equal to .05 uf, a 500:1 voltage division ratio. Figure 10a is the substrate voltage waveform showing a rise from the predischarge potential (-3 kV) to

zero volts in about 1.2 μs. The voltage falls back to the predischarge level in about 5 μs, a time defined by the spacecraft capacitance and the chargeup current defined by the series resistor, R_1, in our test setup. Figure 10b is the rate-of-change of current as measured by the loop antenna. Figure 10c is the substrate voltage when C_1 is made to be 0.1 μf and C_2 is replaced with a 50 ohm resistor. The voltage risetime is 6 μs, and the total pulsewidth is about 20 μs. Figure 10d is the voltage waveform at the first grid or mesh in front of the test sample, with C_1 equal to 100 pf. The mesh is collecting blowoff electrons most of the time except for a positive pip at the end due to ions. Figure 10e is the same mesh current when C_1 is 25 pf. The collected current is ionic for most of the time except for a short electronic pip at the beginning. For values of C_1 greater than 100 pf, the waveform is always negative. Figure 10f is the waveform at the second grid when it is biased negatively. Positive ions are collected after the first microsecond with a risetime of about 6 μs. The ionic current pulse lasts for about 6 ms. These waveforms demonstrate that the discharges are not purely electronic, but that ions are intimately involved in the discharge process.

DISCUSSION AND CONCLUSIONS

The test results reported here characterizing the EMI generated by negative metal/positive dielectric voltage stresses are not all-encompassing nor complete. However, important data has been obtained:

o Enchanced electron emission I-V curves

o e^3 corona noise vs e^3 steady-state current

o Localized nature of e^3 and negative metal arc discharge currents

o Negative metal arc discharges at stress thresholds below
   1 kilovolt

o Negative metal arc discharge characteristics

o Dependence of blowoff arc discharge current on spacecraft capacitance
   to space (linear dimension)

o Damage to second surface mirrors due to negative metal arcs

Among the arc discharge parameters of interest are the relatively slow risetimes on the order of 1 μs for approximately 200 cm^2 sample sizes. A quick-look analysis of the phenomenology of a negative metal discharge as compared to that of a brushfire model developed for the opposite stress polarity, positive metal/negative dielectric, leads to many dissimilarities in the physical situations. For example, field emission of electrons is possible from a negative metal but not from a positive metal. The empirical data shows that risetimes are too slow for purely electronic processes, and the detection of an ionic component in the blowoff current indicates that many aspects of the brushfire model may yet be applicable. The slow risetime as compared to

discharges of the opposite polarity may have to do with the reduced breakdown voltage threshold rather than any fundamental difference in the on-going physical processes.

A significant aspect of the blowoff current is that it increases in magnitude as the spacecraft capacitance to space, C_1 in our test, increases. Figure 11 shows the linear rise of peak discharge current vs C_1 obtained in our tests. Our test data also indicate that, unlike the prediction of the brushfire theory for discharges of the opposite polarity, the blowoff current source is localized rather than moving over the surface at the head of the brushfire wavefront. The cracking of second surface mirrors, not observed with the positive metal polarity, is a further indication of this aspect of negative metal discharges.

Much more work needs to be done in understanding the phenomenology of negative metal/positive dielectrics discharges, and in characterizing the various associated EMI parameters. For example, the dependence of discharge characteristics on sample area, sample thickness and sample material have not been determined, and a basic phenomenological model has not been developed which is completely consistent with our physical intuition and the observational data. The authors acknowledge the skillful assistance of J. R. Valles in obtaining the laboratory test data.

REFERENCES

1. G. T. Inouye and M. J. Sellen Jr., "TDRSS Solar Array Arc Discharge Tests", Spacecraft Charging Technology-1978, NASA CP 2071, AFGL-TR-79-0082, 1979.

2. N. J. Stevens, H. E. Mills and L. Orange, "Voltage Gradients in Solar Array Cavities as Possible Breakdown Sites in Spacecraft-Charging-Induced Discharges", IEEE Transactions on Nuclear Science, Volume NS-28, No. 6, December 1981.

3. G. T. Inouye and R. C. Chaky, "Enhanced Electron Emission from Positive Dielectric/Negative Metal Configurations on Spacecraft", IEEE Transactions on Nuclear Science, Volume NS-29, No. 6, December 1982.

4. H. C. Koons, "Summary of Environmentally Induced Electrical Discharges on the P78-2 (SCATHA) Satellite", AIAA 20th Aerospace Sciences Meeting, January 1982.

5. G. T. Inouye, "Brushfire Arc Discharge Model", Spacecraft Charging Technology-1980, NASA CP 2182, AFGL-TR-81-0270.

TABLE 1. - CHARACTERISTICS OF INDIVIDUAL SOLAR CELL SAMPLES. (Samples 1, 2, 9, and 10 are most nearly flight-like.)

SAMPLE NUMBER	COVER GLASS MATERIAL	INTERCONNECTS USED	KAPTON USED AS INSULATION
1	FUSED SILICA	STANDARD	YES
2	CERIA GLASS	STANDARD	YES
3	FUSED SILICA	IN-PLANE	YES
4	CERIA GLASS	IN-PLANE	YES
5	FUSED SILICA	NONE	YES
6	CERIA GLASS	NONE	YES
7	FUSED SILICA	NONE	NO
8	CERIA GLASS	NONE	NO
9	FUSED SILICA	STANDARD	YES
10	CERIA GLASS	STANDARD	YES

TABLE 2. - SOLAR CELL TEST SUMMARY

SAMPLE NUMBER	PHOTOEMISSION CURRENT (NA)	ARCING	ENHANCED ELECTRON EMISSION
1	4.0	YES	YES
2	4.1	YES	NO*
3	4.0	YES	NO
4	3.4	YES	NO
5	0.7	YES	NO
6	0.042	YES	NO
7	29.0	YES	YES
8	20.6	YES	NO*
9	3.6	YES	NO*
10	5.5	NO	NO*

*WE HAVE OBSERVED E^3 PREVIOUSLY FOR THIS CONFIGURATION, BUT NOT THIS SAMPLE
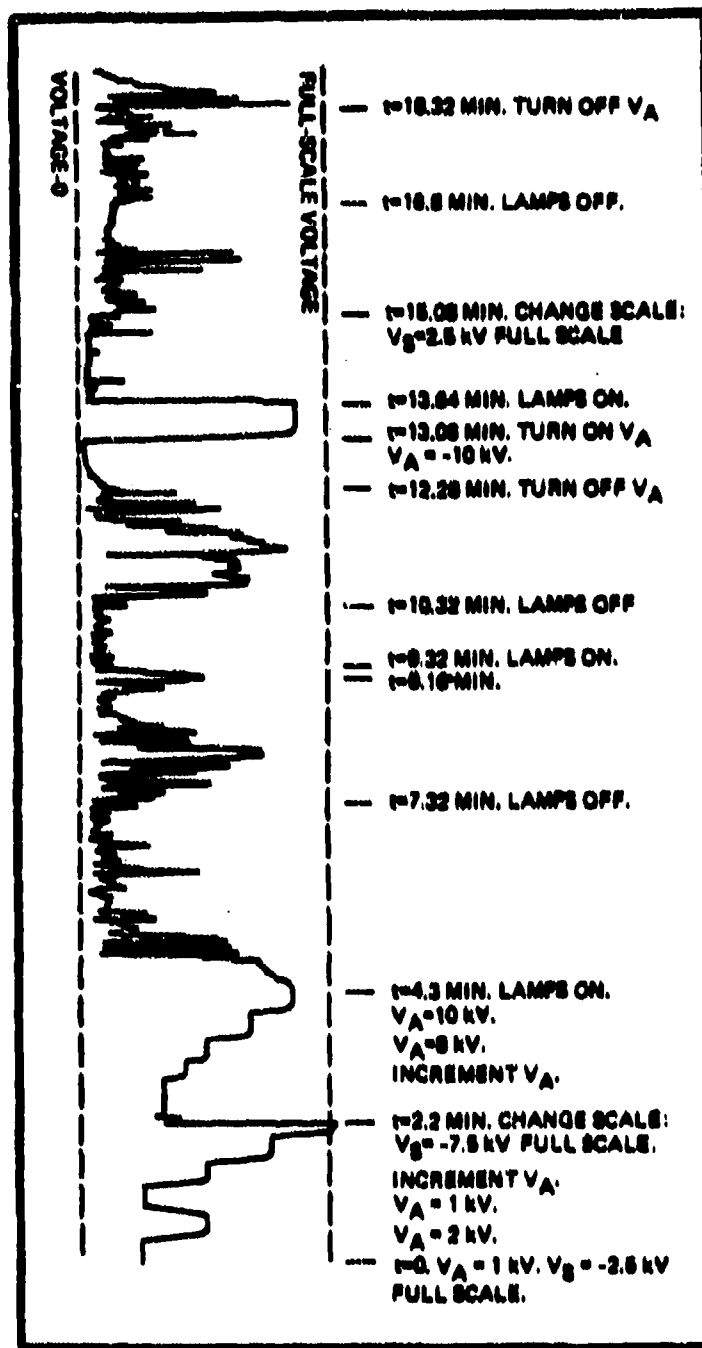
Figure 1. – Strip chart record of voltage variation in time, for solar cell sample. (This illustrates noisy voltage characteristic of enhanced electron emission.)

444
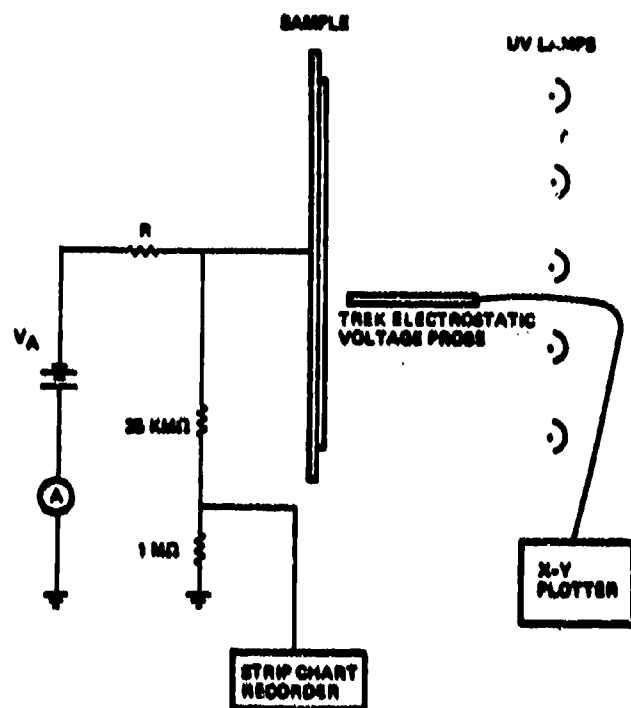
Figure 2. – Schematic of test setup using negative applied voltage and UV lamps.
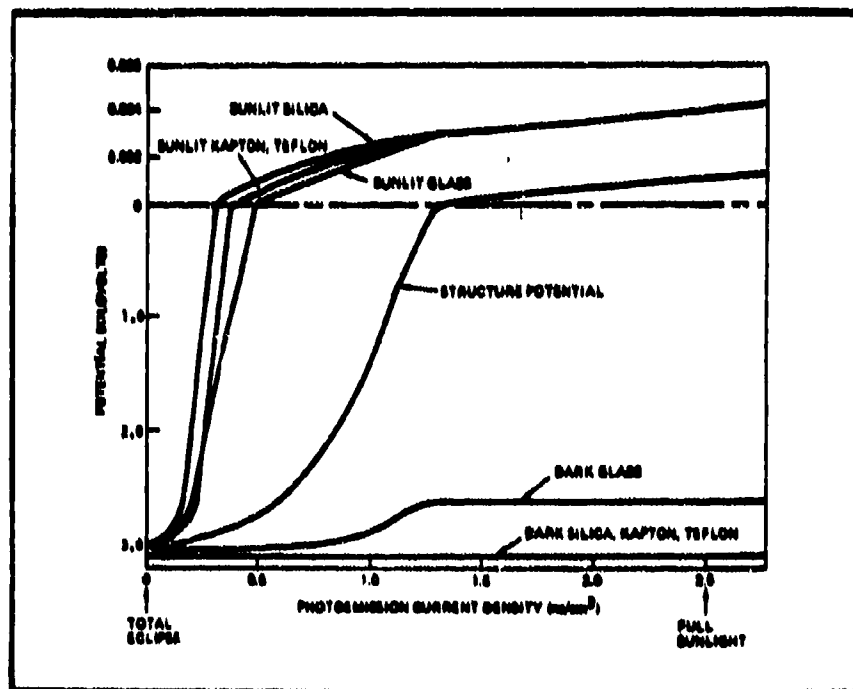
Figure 3. – Spacecraft surface potentials for NASA severe environment as function of photoemission current density, computed using TSCAT (TRW spacecraft charging technique).

445
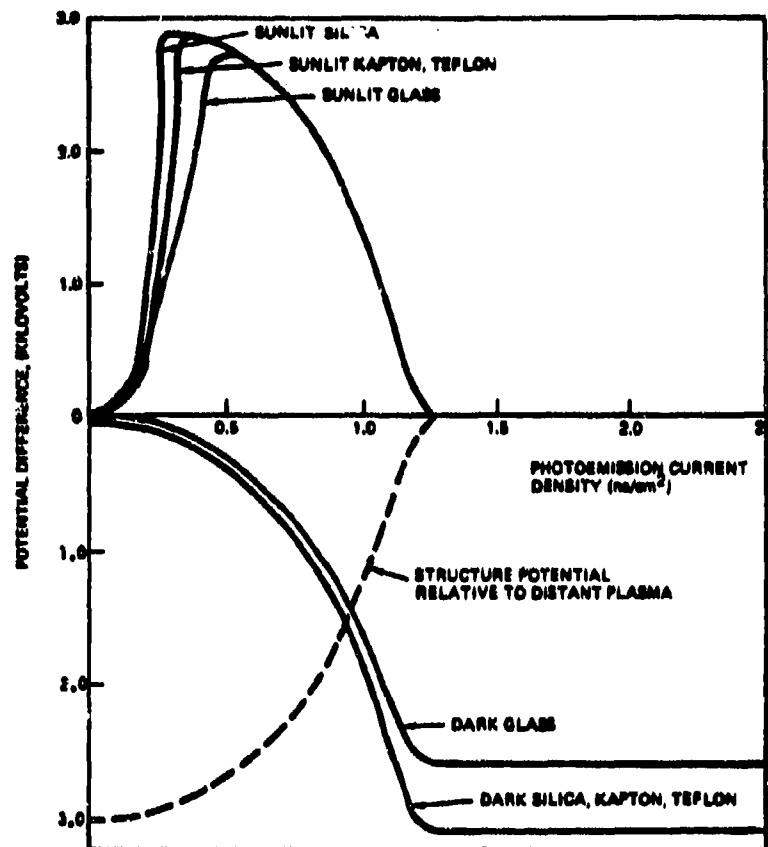
Figure 4. - Differential surface voltages corresponding to figure 3.
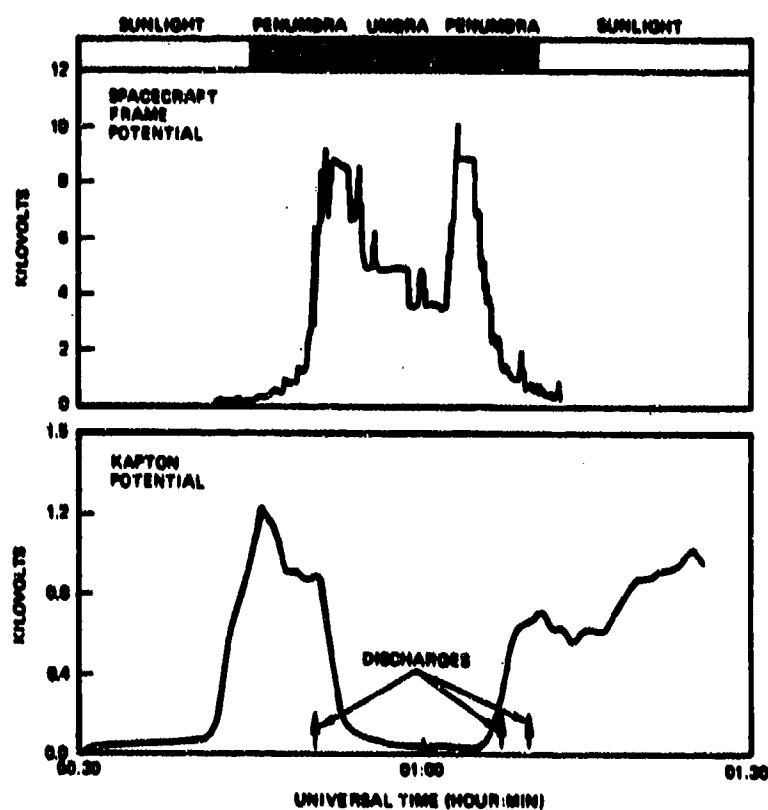
Figure 5. – Correlation of occurrence of arc discharges in SCATHA P78-2 spacecraft with reduced sunlight intensity with entrance and exit for eclipse (Coincides with peak in differential surface voltages from figure 4.).

447

Figure 6. – Test setup to characterize negative metal EMI characteristics.

Figure 8. – Steady-state enhanced electron emission current versus sample voltage.

Figure 7. – Solar cell sample configuration.

449
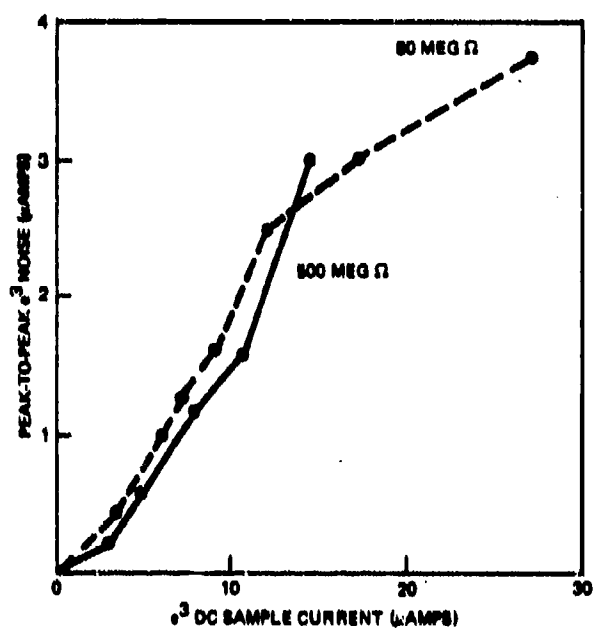
Figure 9. – Peak-to-peak enhanced electron emission (e³) noise current versus dc e³ current. (0–10 Hz).
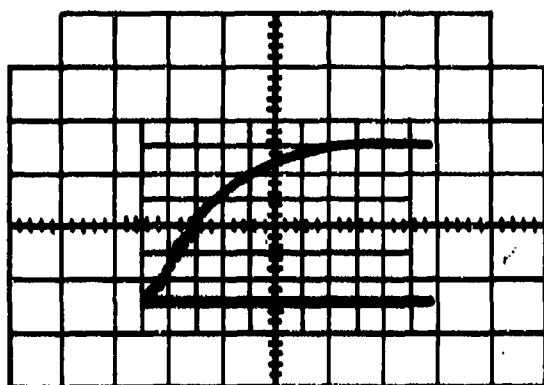
(a) Substrate voltage: $C_1 = 100$ pF; voltage from -3 kV to ground in 0.8 μsec.
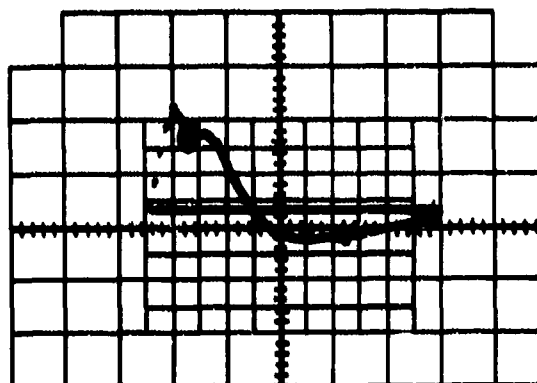
(b) Substrate replacement current: $C_1 = 100$ pF; peak = 0.5 A; rise-time = 0.4 μsec; width = 1.5 μsec.
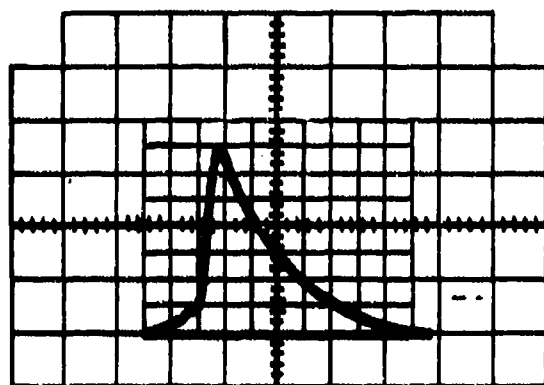
(c) Substrate voltage: $C_1 = 0.1$ μF; R = 50 Ω; risetime = 6 μsec; width = 20 μsec.
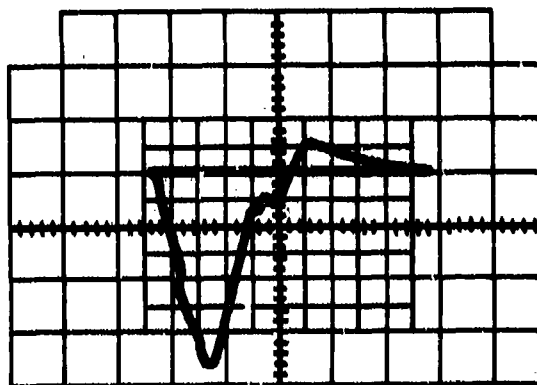
(d) First grid blowoff current: C = 100 pF; 1 μsec to negative peak (electrons).
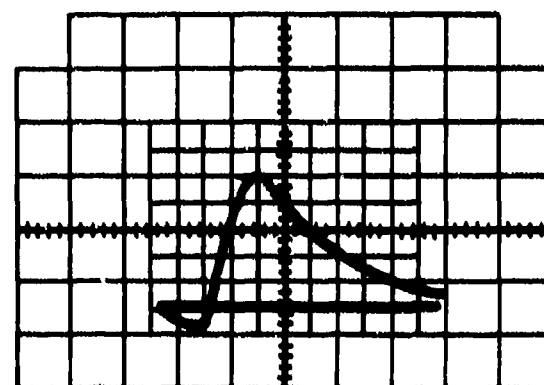
(e) First grid blowoff current: $C_1 = 25$ pF; 1 μsec to positive peak (ions).
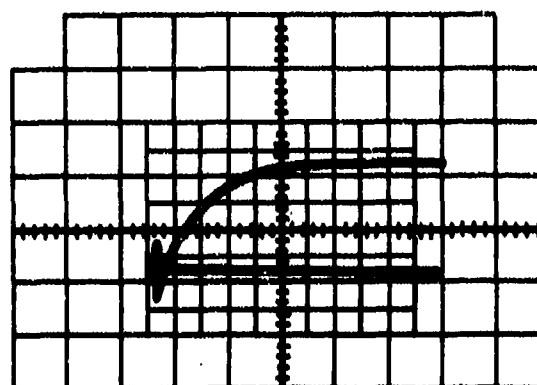
(f) Second grid blowoff current: Shows ion collection; risetime = 6 μsec.

Figure 10. - Negative metal arc discharge waveforms.

451
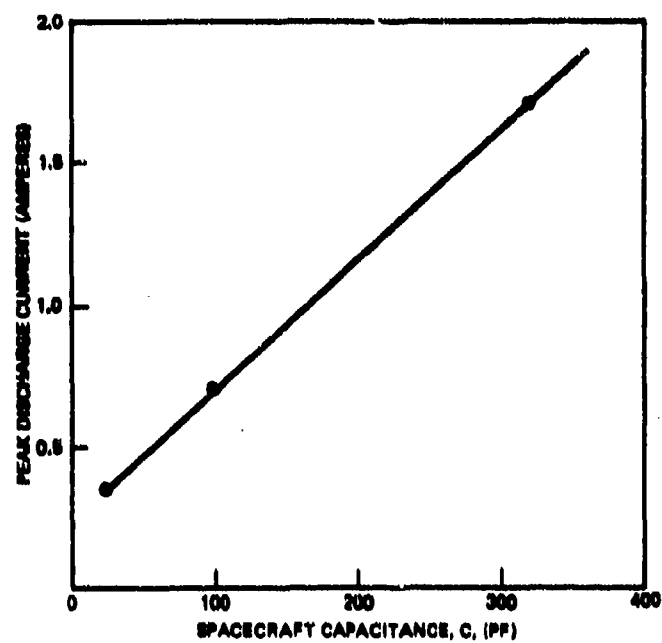
Figure 11. - Peak discharge current versus spacecraft capacitance.

LABORATORY STUDIES OF SPACECRAFT RESPONSE TO TRANSIENT DISCHARGE PULSES*

J. E. Nanevicz and R. C. Adamo
SRI International
Menlo Park, California 94025

A set of preliminary laboratory experiments was conducted to investigate
several basic issues in connection with the in-orbit measurement of spacecraft
discharge properties. These include design and fabrication of appropriate sensors
and effects of spacecraft electromagnetic responses on the interpretation of the
discharge data. Electric field sensors especially designed to respond to high-speed
transient signals were installed on a mock-up of a satellite. The simple mock-up
was basically a sheet of aluminum rolled to form a cylinder. A movable spark-dis-
charge noise source designed to be electromagnetically isolated from its power
supply system was used to induce transient signals at various locations on the
"spacecraft's" outer surface. These measurements and their results and implications
are described herein. It is concluded that practical orbital measurements to define
discharge noise source properties should be possible, and that simple mock-ups of
the type described below are useful in sensor system design and data interpretation.

INTRODUCTION

It was recognized about ten years ago that spacecraft charging occurs
(ref. 1)** and constitutes a potential electromagnetic hazard to operational
satellites (ref. 2). In spite of this awareness, surprisingly little orbital
information has been generated to date regarding the electromagnetic properties of
the discharge source (refs. 3,4). Such information is essential to the proper
specification, design, and ground testing of satellites.

In designing an instrumentation system for the in-orbit measurement of
discharge properties, it is necessary to recognize and take into account the effects
of both the sensor and spacecraft in modifying the signal radiated by the
discharge. In particular, since the sensor antennas and the spacecraft itself
exhibit electromagnetic resonances, the received signal will not exactly

duplicate the signal at the source. To investigate the problems associated with orbital measurements, a rudimentary laboratory mock-up of a spacecraft was assembled and equipped with sensors and transient-measuring instrumentation. This work extended earlier laboratory measurements conducted to investigate the electromagnetic properties of discharges on spacecraft thermal-control materials (refs. 2,5,6). Provisions were made to excite the mock-up with an isolated spark source and to record the sensor responses to record simulated vacuum arc.

Tests on the mock-up indicate that, with proper sensor design and placement, it is possible to minimize the effects of sensor and vehicle resonances in masking important characteristics of the signals generated by the discharges. Furthermore, the tests indicate that the same simple instrumentation can be used in orbit to define certain important characteristics of arc discharges and to infer where on the spacecraft discharges are occurring.

SENSOR DESIGN

It is important to recognize that a discharge caused by spacecraft charging is a very brief transient phenomenon, and that excessive distortion of the measured data by successive reflections from the ends of the sensing antenna (ringing) must be prevented. Two possible solutions to this problem are illustrated in figure 1. First, the sensor element may be made long so that the interesting portion of the transient signal has been recorded before the reflection from the end of the sensor returns (fig. 1a). To minimize reflections, the far end of the sensor may be made lossy and terminated in its characteristic impedance. Alternatively, the dimensions of the sensor may be made electrically small so that the first sensor resonance occurs above the highest frequency of interest (fig. 1b). In this design, either the source spectrum does not contain appreciable energy at the ringing frequency or the measuring system bandwidth is too narrow to permit the ringing to be recorded. Although large antennas have been considered for the ground-based study of transient signals, electrically small sensors are the only ones practical for in-flight measurements.

The electrically small field sensor provides an output proportional to the electric or magnetic field or its derivative at the sensor's location. Equivalent circuits for the small electric dipole, evolved during the development of low-frequency avionic systems (refs. 7, 8) are shown in figure 2. The open-circuit voltage of the electric dipole is directly proportional to the local electric field (fig. 2a) while the short-circuit current is proportional to the derivative of the electric field (fig 2b). The short-circuit current can be measured using a broadband current transformer. With modern high-impedance FET-input amplifiers, it is possible to measure the open-circuit voltage over a wide range of frequencies. The experimenter is therefore free to choose between measuring E or D. In the laboratory experiment of refs. 5 and 6, a small dipole with a built-in FET preamplifier was used.

Equivalent circuits for the magnetic dipole are shown in figure 3. The open-circuit voltage of the magnetic dipole is proportional to the derivative of the magnetic field (fig. 3a) and the short-circuit current is proportional to the magnetic field (fig. 3b). To measure the short-circuit current, the measuring apparatus must have an insertion impedance that is small compared with $j\omega L$, the inductive reactance of the sensor, throughout the frequency range of interest. For a given antenna inductance, L, and system input impedance, R, this implies that:

$$\omega > \frac{R}{L} \tag{1}$$

Thus, to measure I_{sc} at low frequencies, the loop inductance should be high. Unfortunately, simply increasing the loop inductance lowers the resonant frequency of the loop and reduces the effective sensitivity of the dipole. A modern current tranformer (such as the Tektronix CT-2) may have an insertion impedance of 0.04 Ω in parallel with 5 μH, thus allowing the design of loops responding directly to the tangential magnetic field intensity, H, over a bandwidth ranging from several kilohertz through HF.

If the loop inductance is reduced to extend the high-frequency response to VHF, the inductive reactance becomes small compared to the insertion impedance of available current probes over much of the frequency range of interest. Therefore, with magnetic field sensors intended for high-frequency studies, the open circuit voltage is usually measured, and so the response is proportional to $\dot{B}$.

At the surface of a good conductor, the magnitude of the surface current density, J, is equal to the magnitude of the tangential magnetic field intensity, H. Thus, a skin current density sensor may be either a magnetic dipole (small half-loop) or a current dipole (small slot). The loop antenna responds to the magnetic field at the surface of the conducting plane based on the elementary flux linkage concept (figure 4a). The loop may also be considered to respond to the current induced in the plane by the magnetic field. In the dynamic field case, the current in the ground plane and the surface magnetic field are inseparable. A slot interrupts the uniform current density, J, that would normally flow on the surface, forcing part of this current to flow through the short-circuited slot terminals (fig. 4b). The slot current is:

$$I = J\ell_e = H\ell_e \tag{2}$$

where ℓ_e is the effective height of the antenna.

The impedance of the small slot is primarily inductive reactance. Hence, the open-circuit voltage at the slot terminal is:

$$V = \ell_e L \frac{dJ}{dt} = \ell_e L \frac{dH}{dt} \tag{3}$$

The short-circuit current and open-circuit voltage of a small loop antenna are, respectively:

$$I = \frac{\mu A}{L} J \quad \text{and} \quad V = \mu A \frac{dJ}{dt} \tag{4}$$

where A is the area of the loop, $\mu = 4\pi \times 10^{-7}$ H/m, J is the surface current density, and L is the loop inductance.

Shielding is necessary to make the loop insensitive to the electric field. Conventional shielded loop design can be used for this purpose. Although loops are more sensitive than slots of comparable size, they protrude from the skin and may lead to mechanical interference problems. Since slots are flush with the skin, they may be installed anywhere a break in the skin can be allowed.

455

As indicated earlier, measuring the short-circuit current requ: the m   :r-
ing apparatus to have an insertion impedance that is small compared   the
inductive reactance, jωL, throughout the frequency range of interest.   ..cause ω is
small for a small half-loop and even smaller for a small slot, it is difficult to
measure the late-time, short-circuit current directly. Therefore, the open-circuit
voltage is usually measured in transient electromagnetic studies. Measurement of
magnetic fields in the laboratory experiments of refs. 5 and 6 was implemented by
using a series of slot antennas installed in the ground plane of the test set up.

The problem of developing and optimizing sensors for transient electromagnetic
field measurements has been of great concern to the EMP community. Techniques for
extending the performance of the basic sensors discussed above have been developed
by Baum and others and have been published in the Sensor and Simulation Notes edited
and authored by Baum (ref. 9). Portions of this work applicable to lightning
measurement are contained in reference 10. Many of these sensors and sensor
concepts can be adapted for spacecraft applications.

In addition to electromagnetic field measuremonts, the spacecraft experimenter
is often interested in the currents and voltages induced in internal wiring. A
variety of commercial current transformers are available covering the frequency
range of interest. These transformers are well shielded and designed to minimize
response to electric fields. Thus, current measurements are simple and straightfor-
ward to instrument.

Voltage measurements--particularly differential voltage measurements--may be
more difficult to carry out. To measure the voltage between a particular wire and
the frame, the probe must have adequate bandwidth, impedance, and dynamic range.
Measuring the differential voltage between a pair of wires is more difficult. Not
only must the probe be able to cover the dynamic range and bandwidth of interest, it
must function in the presence of common-mode signals substantially larger than the
desired signal. The present state of spacecraft charging research is such that
differential voltage measurements are probably best deferred to the future.

SENSOR PLACEMENT (AIRFRAME EFFECTS)

An electromagnetic field sensor provides information about the electromagnetic
fields at its location; unless special precautions are taken, the vehicle itself
acts as an integral part of the sensor. At frequencies corresponding to the vehicle
resonances, the antenna/spacecraft system can exhibit complex interactions. At VHF
and above, the antenna/spacecraft system has the characteristics of the antenna
element mounted on a large, complex ground plane. These problems have been studied
in substantial detail for aircraft and rockets in connection with antenna design and
investigation of EMP susceptibility (ref. 11). In particular, for the case of a
slender cylinder, it is possible to derive a formula for the time domain response to
a unit-step driving pulse. The results of such a calculation, shown in
Figure 5, demonstrate several interesting affects: the ringing of the system at a
frequency determined by the length of the cylinder is clearly evident. Also, it
should be noted that the current is maximum at the center of the cylinder (u = 0)
and decreases as one moves toward the ends (u = 1/4). Thus, in the case of a slim
cylinder such as an aircraft or rocket, a substantial degree of decoupling from the
airframe resonances can be achieved by locating the magnetic sensor at the end of a
structural member (e.g., at the nose of the fuselage) where the current is zero.

Conversely, since the electric field is maximum at the ends of a conductor, E-field sensors are most strongly affected at the extremities.

SATELLITE MOCK-UP EXPERIMENTS

Although the time waveforms in Figure 5 indicate that substantial ringing can occur when a body is excited by a transient impulse, it must be recognized that the data in the figure are valid for a _slender_ cylinder. In general, electromagnetic theory indicates that, for fatter bodies, the ringing dies out much more rapidly (i.e., fat bodies have a lower Q). Thus, it was possible that the signals excited on a satellite by a transient discharge might be much less complicated than one would infer from figure 5. To investigate the electromagnetic properties of a body resembling a satellite, and to gain insight into the feasibility of discharge source characterization, the laboratory "satellite" mock-up shown in figures 6 and 7 was assembled. Figure 6 shows the general size and form of the mock-up, which is simply a hollow uncapped cylinder made of sheet aluminum. It is approximately 1.8 m in diameter and 1.2 m high and stands upright on a 0.75-m high non-conductive, large-area wooden table. For the initial tests, two small electric-dipole sensors (equipped with high input impedance preamplifiers so that they respond directly to the local E field as was discussed earlier) were mounted 180° apart on the outside curved surface along the circumferential center line of the cylinder. The sensor cables were routed to the inside of the cylinder through small holes near the sensors. The signals from the two sensors were recorded simultaneously using a 400-MHz bandwidth dual-beam oscilloscope which was mounted inside the conductive cylinder where it was well shielded from external fields.

Transient electromagnetic fields were generated on the exterior of the mock-up using a dc spark-gap formed by positioning a 10-cm-diameter hollow copper sphere on an insulating support at a distance of approximately 3 mm from the outer cylinder surface at selected simuated arc locations. To prevent measurement errors resulting from transients radiated from, or field perturbations caused by the presence of the high-voltage cables, the copper sphere was connected to a 20-kV power supply located 4 m away, using special "electromagnetically-transparent," high-resistance wire as shown in figure 7. The required dc return path between the cylinder and the high-voltage supply was provided in this same way. Thus, electromagnetically, at RF the spark source appeared to be a completely isolated sphere charged to a high voltage. The spark source produces a unidirectional current pulse with an amplitude of roughly 400 A, and total duration of the order of 2 ns. It should be noted from figure 6 that the mock-up experiments were conducted in the middle of a laboratory area with no effort to shield the setup from ambient noise.

Some of the results of the satellite mock-up experiments are shown in figure 8. For the experiments illustrated, the spark source was moved to various positions along the equator of the "satellite" and the signals induced in the two sensors were recorded. When the spark source is near sensor #1 (as in fig. 8a), substantial signal is induced in this sensor, and a barely perceptible response is induced in sensor #2.

It should be noted that the initial pulse in sensor #1 is clearly defined, and that it is uncontaminated by the reflected pulses arriving late in time. This behavior is vastly different from the pronounced ringing illustrated in figure 5, when a slender cylinder is excited by a transient. Thus, the laboratory experiments

457

indicate that satellite electromagnetic characteristics are such that flight experiments intended to characterize discharge noise source characteristics in orbit should not be unduly plagued by satellite and sensor responses, provided the system is properly designed and configured.

In figure 8b, the spark noise source was positioned roughly equidistant from the two sensors, and signals of roughly equal amplitude are induced in the two systems. Again, it should be noted that the direct signal from the source is clearly defined, and not contaminated by ringing and reflections from discontinuities on the satellite.

In the course of these preliminary experiments, the satellite configuration was changed to include a boom, and the sensors and noise source were moved to a number of different positions. The resulting responses differed from those presented here, but were all explainable by electromagnetic considerations.

CONCLUSIONS

By applying proper electromagnetic principles to sensor design, it is possible to develop systems capable of responding to fast transients of the sort expected from spacecraft charging. The form many of practical satellites is such that they will not unduly contaminate the signals radiated by spark discharges. Accordingly, it should be possible to design flight systems for the study of spacecraft discharge characteristics. Finally, a simple satellite mock-up such as that used in the present experiments is easy to assemble, inexpensive, and adequate to provide important guidance during system design and for data interpretation.

REFERENCES

1. Deforest, S. E.: "Spacecraft Charging at Synchronous Orbits," Vol. 77, Journal of Geophysical Research, February 1972, pp. 651-659.

2. Nanevicz, J. E. and Adamo, R.C.: "Occurrence of Arcing and Its Effects on Space Systems," Space Systems and Their Interactions With Earth's Space Environment, Editors: Henry B. Garrett, Charles P. Pike, Martin Summerfield Series Editor, Vol. 71, Progress in Astronautics and Aeronautics, Pub. American Inst. of Aeronautics and Astronautics, New York, New York, 1980.

3. Koons, Harry C.: "Aspects Dependence and Frequency Spectrum of Electrical Discharges on the P78-2 (SCATHA) Satellite 2192," NASA Conference Publication AFGL-TR-81-0270, U.S. Air Force Academy Colorado Springs, Colorado, November 12-14, 1980.

4. Damron, S. A.; Adamo, R. C.; and Nanevicz, J. E.: "Preliminary Analysis of Data from SRI International Transient Pulse Monitor on Board P78-2 SCATHA Satellite," AIAA 20th Aerospace Sciences Meeting, Orlando, Florida, January 11-14, 1982.

5. Nanevicz, J. E. and Adamo, R. C.; SRI International; Beers, B. L.; Science Applications, Inc.: "Characterization of Electromagnetic Signals Generated by

Electrical Breakdown of Spacecraft Insulating Material," NASA Conference Publication 2071 AFGL-TR-79-0082, U.S. Air Force Academy Colorddo Springs, Colorado, October 31–November 2, 1978.

6. Nanevicz, J. E.: "Electromagnetic Fields Produced By Simulated Spacecraft Discharges," Spacecraft Charging Technology, U.S. Air Force Academy Colorado Springs, November 12–14, 1980.

7. Granger. J. V. N. and Bolljahn, J. T.: "Aircraft Antennas," Vol. 43, No. 43, Proceedings of the IRE, May 1955.

8. Bolljahn, J. T.: "Antennas for Airborne ADF Systems," Stanford Research Institute, Menlo Park, California, July 1954.

9. Baum, Carl E.: "Electromagnetic Sensor and Simulation Notes," EMP 1-12, Vol. 12, Notes 137-147, Air Force Weapons Laboratory, Kirtland Air Force Base, New Mexico, May 1973.

10. Baum, Carl E.; Breen, Edward L; and et al.: "Electromagnetic Sensors for General Lightning Application," NASA Conference Publication 21-28, FAA-RD-80-30, NASA Langley Research Center, Hampton, Virginia, Proceedings April 22-24, 1980.

11. Lee, K.S.H. Editor: "EMP Interaction: Principles, Techniques and Reference Data," Contract #F29601-79-C-0149, Dikewood Industries Inc., 1009 Bradbury Drive, S.E., Albuquerque, New Mexico 87106, December 1980.

C-6
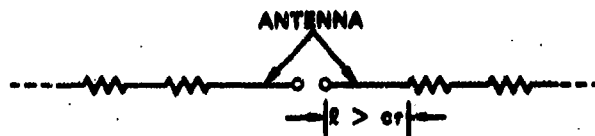
where   c = velocity of light
        τ = transient duration

(a) USE OF LONG ANTENNA TERMINATED IN LOSSY
    MATERIAL TO INHIBIT REFLECTIONS
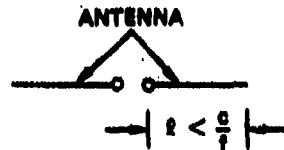
where   c = velocity of light
        f = upper frequency limit
          of recording system

(b) USE OF SHORT ANTENNA SYSTEM--RINGING
    OCCURS ABOVE HIGHEST FREQUENCY RECORDED

Figure 1. - Approaches to transient field sensor design.
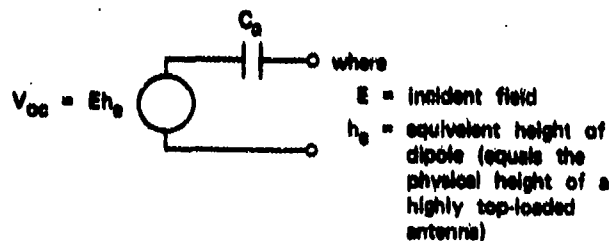
where

E = incident field

h_e = equivalent height of dipole (equals the physical height of a highly top-loaded antenna)

$V_{oc} = Eh_e$

(a) THEVENIN EQUIVALENT CIRCUIT
    OF ELECTRIC DIPOLE

where

$\dot{D} = \frac{\partial}{\partial t} D_{incident}$

a = induction area of antenna -- related to equivalent height by $\epsilon_o a = h_e C_a$

$I_{sc} = a\dot{D}$
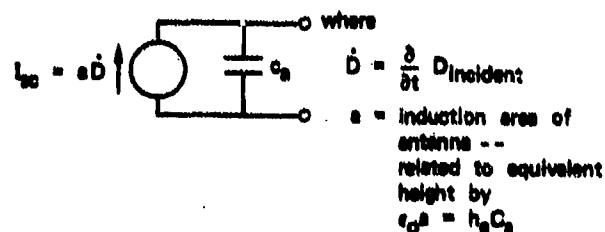
(b) NORTON EQUIVALENT CIRCUIT
    OF ELECTRIC DIPOLE

Figure 2. - Equivalent circuits of small electric dipole.
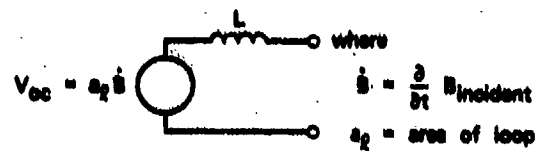
(a) THEVENIN EQUIVALENT CIRCUIT
OF MAGNETIC DIPOLE

where

$\dot{B} = \frac{\partial}{\partial t} B_{incident}$

a_ℓ = area of loop

$V_{oc} = a_\ell \dot{B}$

(b) NORTON EQUIVALENT CIRCUIT
OF MAGNETIC DIPOLE

where

H = incident field

ℓ_e = effective length
of antenna --
regulated to loop
area by
$\mu a_\ell = \ell_e L$

$I_{sc} = \ell_e H$
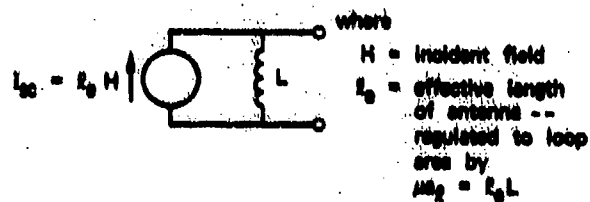
Figure 3. - Equivalent circuits of small magnetic dipole.
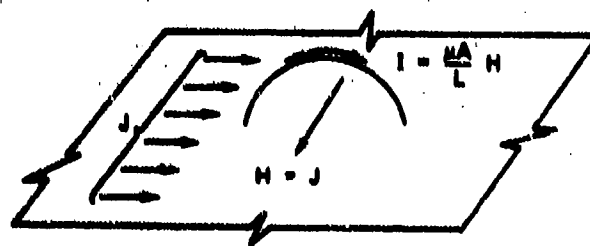
(a) HALF-LOOP OVER GROUND PLANE

$I = \frac{\mu A}{L} H$

H = J

J
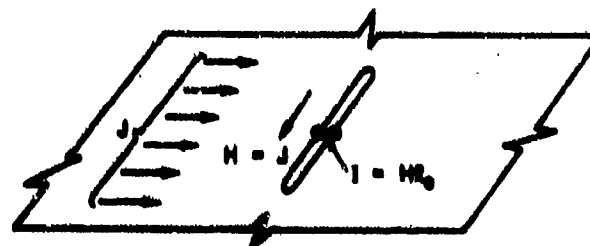
(b) SLOT IN GROUND PLANE

H = J

$I = H\ell_e$

J

Figure 4. - Field, current density, and short circuit current relations for loop and slot antennas.
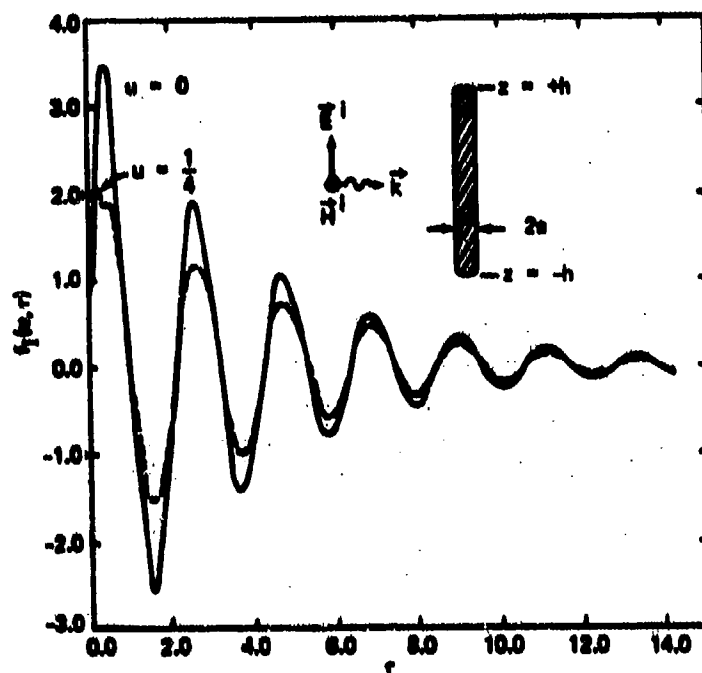
Figure 5. - Normalized axial current at two positions along a cylinder for a unit-step incident pulse ($u = z/L$, $\tau = ct/L$, $L = 2h$).
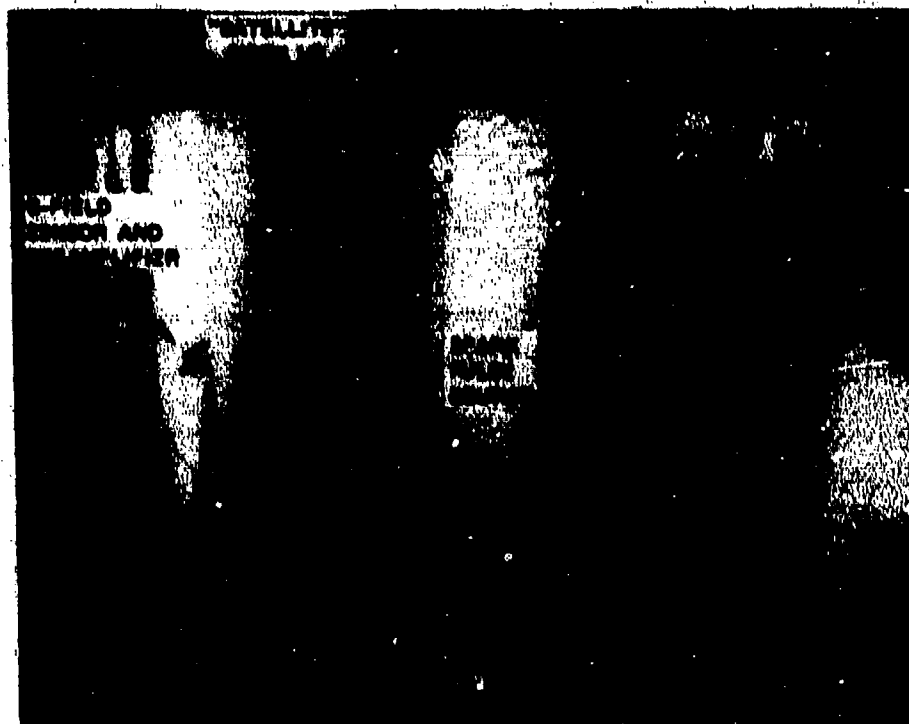
Figure 6. - Satellite mock-up.

462
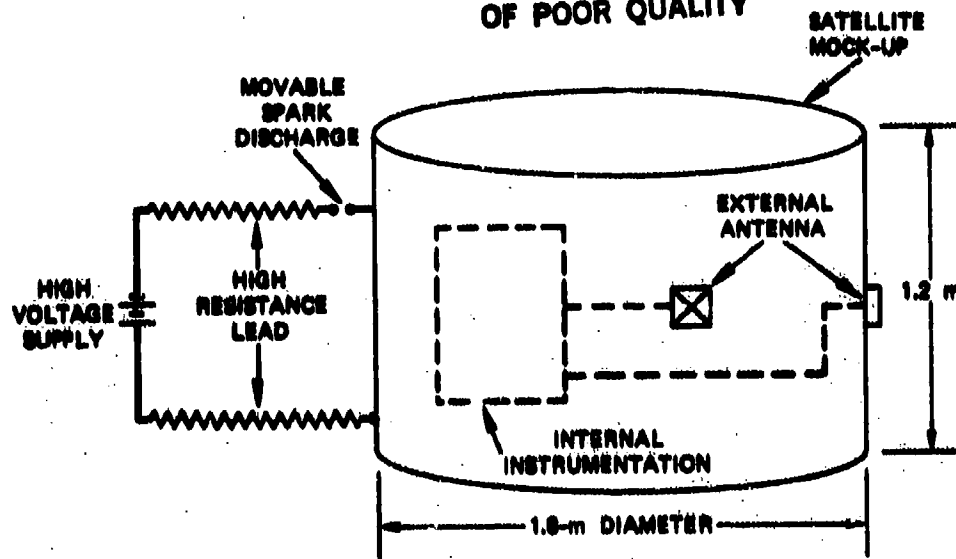
Figure 7. - SRI laboratory test of discharge localization technique.
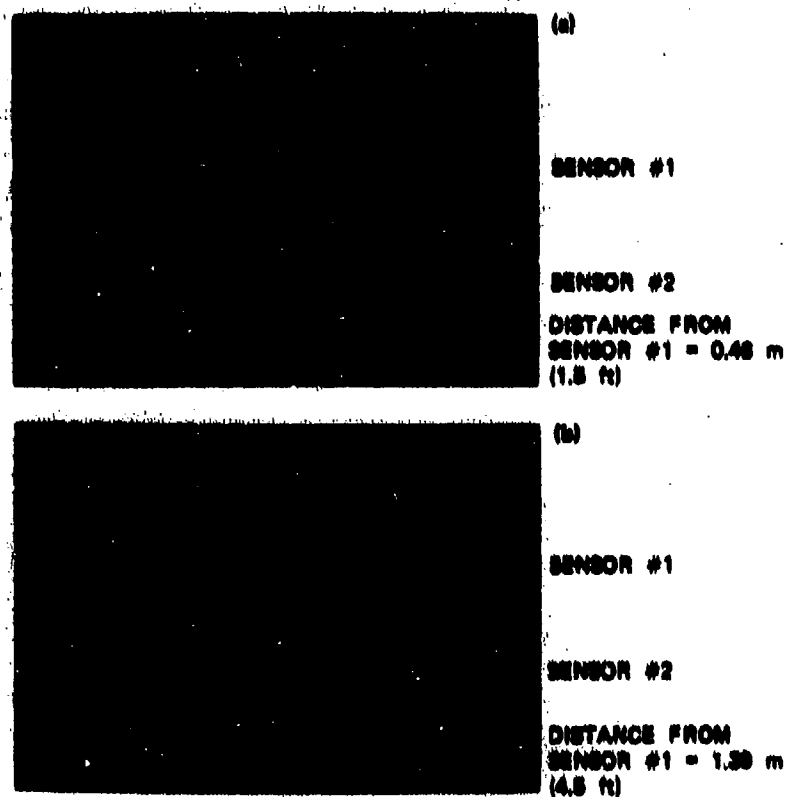
Figure 8. - Sensor responses.

DEVELOPMENT OF A CONTINUOUS BROAD-ENERGY-SPECTRUM ELECTRON SOURCE*

R. C. Adamo and J. E. Nanevicz
SRI International
Menlo Park, California 94025

The primary accomplishment of the laboratory research program described herein has been the development of a practical prototype, large-area, continuous-spectrum, multienergy electron source to simulate the lower energy (≈ 1 to 30 keV) portion of the geosynchronous orbit electron environment. The results of future materials-charging tests using this multienergy source should significantly improve our under-standing of actual in-orbit charging processes and should help to resolve some of the descrepancies between predicted and observed spacecraft materials performance.

BACKGROUND

Complex interactions between a spacecraft and the surrounding space environment can cause the deposition and redistribution of significant amounts of electrical charge on the exterior of conducting and insulating surfaces and within exposed dielectric materials (ref. 1).

This naturally occurring phenomenon, known as spacecraft charging, can ad-versely affect normal system performance in a number of ways. For example, the resulting local external static fields can interfere with the operation of electric-field-sensitive instruments and cause the reattraction and deposition of contami-nants on critical thermal control, solar array, and other optical surfaces. More serious effects can occur if the electric fields between adjacent surfaces or within dielectric materials become large enough to produce electrical breakdowns (ref. 2). The electric currents produced by these rapid changes in charge distribution can cause local physical damage to external thermo-optical surfaces and radiate electromagnetic signals of sufficient amplitude to upset or possibly damage onboard electronic systems.

Over the past decade, a substantial effort has been made to increase the avail-able knowledge relating to the causes and effects of spacecraft charging, and the results of numerous theoretical studies, laboratory tests, computer simulations, and limited in-orbit measurements have been published. Unfortunately, the combination of interactions between actual operational spacecraft and the real space environment is too complex to predict accurately or explain many observed or suspected in-orbit spacecraft responses, with confidence, using presently available techniques.

To date, laboratory simulations of the charging and electrical-breakdown characteristics of typical spacecraft materials have been performed, by most agencies, using conventional monoenergetic, thermionic (hot-filament) electron sources to simulate the lower-energy (less than 40 keV), geosynchronous-orbit electron environment.

Although thermionic sources are ideal for many applications, in general they exhibit several practical disadvantages for spacecraft charging studies, including:

- Cathode contamination--Most thermionic cathodes are readily contaminated by outgassing products from realistic spacecraft material test samples.

- Poor beam uniformity--Achieving a large diameter beam with uniform current density is difficult.

- Limited beam diameter at close range--Expanding the beam from most thermionic sources to cover a large area sample at close range is also difficult.

- Interdependent beam characteristics--In particular, in a simple system, changing the beam current density or profile requires a complex electrostatic lens system and a readjustment of lens and grid voltages.

- Filament illumination--In some experiments, undesirable optical radiation from the heated cathode can alter the responses of the test-sample materials.

Several years ago, SRI International developed an alternative type of electron source, based on the multipactor phenomenon, for use in spacecraft charging studies (ref. 3,4). Although this basic source, shown schematically in Figure 1, also produces a monoenergic electron beam, it eliminated many of the disadvantages of conventional thermionic systems.

Many independent studies of the charging and discharging properties of spacecraft materials have been performed using monoenergetic electron sources. Although the results of these independent laboratory tests have agreed reasonably well, a number of discrepancies appeared between the test results and actual in-orbit observations of electrical charging and discharge occurrences on operational spacecraft. For example, SRI International discharge detection instrumentation on a DSP satellite and on the P78-2 (SCATHA) satellite (along with a full complement of other spacecraft-charging instruments), has indicated that electrical discharges (and, in some cases, resulting spacecraft anomalies) occur at times when they would not be expected according to the results of laboratory tests. This is not altogether surprising, however, since the theory of dielectric charging predicts that the exact profiles of the internal charge distributions and, therefore, the magnitudes of the internal electric fields are determined by the details of the incident electron energy distribution (ref. 5).

Material charging tests performed using two separate monoenergetic electron guns at different energies have confirmed that, with just two discrete energies, the test results differ significantly from those obtained using a single-energy source (ref. 6,7).

The primary objective of the laboratory research program discussed herein has been to develop a practical prototype, continuous-spectrum, multienergy electron source to simulate more precisely a significant portion of the lower-energy in-orbit electron environment. The results of this work are described below.

BASIC MULTIENERGY ELECTRON SOURCE CONCEPT

If a beam of electrons having an energy of a few tens of keV strikes a thick metal target, a portion of the beam (≈10-20%) will be backscattered. The remaining electrons will penetrate to various distances within the material before being stopped. If instead, the target is a sufficiently thin foil, some of the electrons will pass completely through the foil and emerge with reduced energies. This phenomenon has been used to modify the monoenergetic multipactor electron gun to produce a continuous multienergy beam.

Many theoretical and experimental studies have been made of the transmission of electrons through thin metal films (e.g., ref. 8-14). Figure 2 shows typical energy distributions of electrons transmitted through various thicknesses of aluminum and gold films with an incident electron beam energy of approximately 20 keV. For the illustrated range of film thicknesses, each of the transmitted electrons is likely to have lost some of its energy within the film through numerous scattering events. As expected, for a given material, the total energy loss per electron, as well as the percentage of incident electrons totally lost within the film, increases in thicker films as a result of a statistically greater number of scattering events.

Results similar to those in Figure 2 were obtained in a series of tests at SRI. In these tests, small samples of 0.75-, 1- and 2-μm thick aluminum films were mounted across a 50-mm-diameter aperture in a large aluminum plate which replaced the outer accelerating grid of the monoenergetic multipactor source. A simple standard type of retarding potential analyzer consisting of three wire-mesh grids within a cylindrical Faraday cup was used to measure the electron energy spectra.

Figure 3 shows a few examples of "typical" electron energy distributions measured under various conditions in geosynchronous orbit (ref. 15). The top curve in this figure is the expected maximum. In these examples, the in-orbit electron current density decreases monotonically and quite rapidly with increasing energy. In contrast, the electron currents of Figure 2, produced by scattering through foils of uniform thickness, increase to a maximum at an energy somewhat below the incident beam energy (E_o) and then decrease more rapidly to an immeasureably low level at or below E_o.

Fortunately, this difference in spectral form can be overcome, to a large extent, by using a specially prepared composite foil as illustrated in Figure 4. The first composite foils of this type were prepared in steps by vapor deposition of gold through appropriate masks onto commercially available aluminum film substrates.

The foil illustrated in Figure 4, though not drawn to scale, combined with the spectra in Figure 2, can be used to explain qualitatively the basic composite-foil concept as follows. The portion of a 20-keV incident beam that passes through the substrate alone will emerge with an energy distribution as shown in the 0.74-μm spectrum in Figure 2a. The portion that passes through only one gold layer will enter the substrate with approximately the 0.28-μm spectrum in Figure 2b and will emerge with its electron energies further reduced, thus "filling-in" a lower energy range in the total composite spectrum. Electrons passing through both gold layers as well as the substrate will obviously emerge with even lower energies.

It is, in this way, possible to "tailor" the overall character of the output energy spectrum through an appropriate choice of patterns and thicknesses of additional metal layers on the composite foil. Since the transmitted current density is

significantly lower through the thicker metal layers, the production of a relatively flat or monotonically decreasing output energy spectrum requires that the thicker metalized layers cover a larger relative percentage of the total foil area.

A major advantage of the multienergy beam production technique described above is that the composite foil is a totally passive device, and therefore, no major modifications of the monoenergetic electron source, other than mounting the foil accross the exit aperture, are required for multienergy operation. In addition, the energy spectrum of the source can be readily changed by physically interchanging foils, and, within a certain range, the energy of the overall spectrum can be shifted up or down by changing the energy of the incident beam. The source can also easily be converted for single-energy operation simply by replacing the composite foil assembly with a standard wire-mesh accelerating grid.

The successful results obtained in initial, small-scale tests of the composite foil concept formed a promising basis for the development, on this program, of a more practical, larger-beam-area, multienergy electron gun system. To accomplish this effort, however, it was necessary to devise new techniques for fabricating and mounting the composite foils.

For example, to produce a broad output energy spectrum, a significant fraction of the input beam energy must be absorbed by the foil. Since metal films are relatively poor thermal radiators, the resulting heat is removed mainly by conduction to the mounting plate at the foil edges.

In initial tests with a 20-keV incident beam energy, composite foils mounted across a 50-mm-diameter aperture performed satisfactorily with output current densities of 10 nA/cm^2 but were readily damaged by excessive heating with current densities 2 to 3 times higher. This problem was subsequently solved by mounting the composite foils between pairs of 0.06-in.-thick perforated aluminum plates that act as heat-sinks for the absorbed power. The holes in these plates are small enough (0.19-in.-diameter) to allow sufficient heat conduction from the unsupported foil areas, and numerous enough (0.25 in. between centers) to provide a 53% exposed foil area when properly aligned. With this mounting arrangement, it became possible to increase the overall transmitted current density by at least a factor of five, with no detectable foil damage. In addition, the protection and support provided by these mounting plates makes handling and installation of the foils considerably easier.

It was originally planned that larger area aluminum foils of this same thickness (0.75 μm) would be used as the basic composite foil substrate. However, upon careful examination, each of the available unused 50- and 75-mm-square foils was found to contain a number of small pinholes. Subsequent discussions with the manufacturer of these foils, and with another foil supplier, indicated that it is not practical to produce such "large-area" foils of this thickness that are pinhole-free. These pinholes, if not covered by the mounting plates, would allow some uncontrollable, small portion of the incident beam to pass through the foil with little or no reduction in current density or energy.

As a result of this discovery, the electron transmission properties of several alternative thin-film materials, known to be available in larger-area sheets, were measured in an attempt to identify a more suitable pinhole-free substrate material. These measurements were made using a scanning electron microscope (SEM) with incident beam energies ranging from 20 to 40 keV. With this instrument it was possible both to measure total electron transmission ratios and to examine the material samples

for pinholes. It was quickly determined that the available pure metal foils that were thick enough to be pinhole-free were too thick to transmit the required electron currents. However, the materials tested also included several thicknesses of Kapton, Teflon, and Mylar films with thin aluminum, gold, or silver coatings on one or both sides. Several of these materials, normally manufactured for use as thermal-control surfaces on spacecraft, were found to transmit a reasonable fraction of the incident beam current. In addition, these materials are available in large sheets and are considerably less expensive and easier to handle than the previously employed thin metal foils.

The transmission measurements obtained with polymer samples having metallization on one side only were not as repeatable as those obtained with similar samples metallized on both sides. This effect is most probably due to variations in the internal and external electric fields produced by the buildup of charge on and within the exposed dielectric surface. Further tests were therefore confined to polymer films with both sides metallized, since both of the outer metal layers can then be electrically grounded to eliminate external electric fields. It is also likely that the additional thermally conductive path provided by the second metallized surface increases the foil's power-handling ability.

Of the materials tested, Teflon was found to be the most susceptible to thermal damage. Mylar films performed somewhat better, with transmission efficiencies of up to 70% in a 30-keV incident beam, but suffered increasing thermal degradation during relatively short periods of operation with input current densities of a few $\mu A/cm^2$

The candidate substrate materials also included 7.5-μm- thick aluminum-coated and 12.7-μm- thick gold-coated Kapton foils. The metal layer on each side of these foils was approximately 100 nm thick. In a 31-keV beam, these materials transmitted 50% and 25%, respectively, of the 20-$\mu A/cm^2$ incident beam current with no noticeable damage.

Doubly aluminized 7.5-μm Kapton film was selected as the most appropriate composite-foil substrate material for the final tests on this program, due both to its higher electron transmission efficiency and because it is less expensive and more readily available than gold-coated Kapton film.

The final composite-foil configuration developed on this program is illustrated in Figure 5. This figure (not drawn to scale) shows the pair of polished aluminum mounting plates that serve as a heat sink for the beam power absorbed by the foil.

The actual metallization pattern, which differs from the pattern in Figure 5, was formed by depositing pairs of almost completely overlapping 10-mm-wide, 0.2-μm - thick silver stripes on a 12-cm-square aluminized Kapton substrate, with approximately 1-mm gaps between each pair of overlapping stripes. This pattern results in 0.4-μm and 0.2-μm silver layers covering approximately 75% and 17%, respectively, of the total foil area, thus leaving approximately 8% of the aluminized substrate exposed.

The measured electron energy spectrum produced by this particular composite foil is shown in Figure 6. A "typical" electron energy spectrum measured during a geomagnetic substorm by the ATS-5 spacecraft in synchronous orbit (ref. 16) is also shown in this figure, for comparison. Since, with an incident electron beam energy of 33 keV, the overall transmission efficiency of this composite foil is approximately 4%, an input current density of 250 nA/cm^2 is required to produce a total output current density of 10 nA/cm^2.

The largest substrate foil size that could be conveniently processed in the vapor deposition system available for use on this program was a 12-cm square. As a result, the maximum exit diameter of the multienergy beam was limited to approximately 10 cm. The aluminized Kapton film used as the substrate, however, is routinely manufactured in 100-ft rolls, with widths of up-to-3 ft. For most practical applications, the multienergy beam diameter is therefore limited mainly by the size and total current capacity of the input current source (35-cm diameter in the present system) and by the maximum usable dimensions of the metal deposition system used to fabricate the composite foil.

CONCLUSION

The simulation of the medium energy ($\approx$1 to 40 keV) portion of the geosynchronous orbit electron environment for material and spacecraft testing requires a relatively large-area, uniform electron beam with a total current density, at the test object, of 10 nA/cm^2 or less and, if possible, a realistic distribution of electron energies. This program has resulted in the design and construction of an electron source that meets these requirements.

When operated in a monoenergetic mode, this source produces exit current densities of up to 20 μA/cm^2 at beam energies up to 40 keV. A control grid permits adjustment of the beam current density over a range from 20 μA/cm^2 to less than 0.1 nA/cm^2 .

In comparison with other types of electron sources used for spacecraft charging studies, the multipactor source is physically simple and easy to fabricate, produces minimal external electric fields, and is less susceptible to cathode contamination.

In addition, the basic monoenergetic multipactor source produces a large-area electron beam directly, without complex electrostatic lenses, so that the beam characteristics are relatively independent of accelerating voltage.

The major achievement of this program is the further development of the composite scattering foil technique for converting a monoenergetic electron beam to one containing a continuous, broad range of electron energies.

The electron energy spectrum in Figure 6 is just one example of a wide range of spectra that could be obtained using other foil configurations. The illustrated spectrum was produced with an incident 33-keV monoenergetic beam. For a given foil, the overall output energy range can, to some extent, be shifted up or down by changing the input beam energy.

The total output beam current density (i.e., integrated over the entire energy spectrum) is determined by the foil characteristics and by the energy and current density of the input beam. Since a large percentage of the incident beam power is absorbed by the foil, the maximum practical output current density is limited by the ability of the foil and its mounting to dissipate heat. With the present foil-mounting configuration, continuous operation for several hours with an output current density of 40 nA/cm^2 produced no noticeable foil damage.

The basic monoenergetic multipactor source is ideally suited for conversion to multienergy operation, since the composite-foil assembly can be mounted directly across the large-area exit aperture, thus forming a single compact unit. In prin-

470

ciple, however, the composite-foil technique could be used with a conventional thermionic electron source by mounting the foil assembly at an appropriate distance from the source in the diverging monoenergetic beam.

SUGGESTED APPLICATIONS AND FURTHER DEVELOPMENT

The basic monoenergetic multipactor electron source can be used in place of a conventional thermionic source in single-energy, material-charging studies and in support of simplified analytical and modeling efforts. The large-area, collimated electron beam produced at the exit aperture makes it possible to irradiate relatively large targets at short range in a small vacuum chamber test facility.

Although the present source produces a beam of circular cross-section for special applications, it is possible to change the shape of the output beam by placing a mask over the exit aperture or by fabricating a similar system with a noncylindrical geometry. Because of the overall mechanical and electrical simplicity of the multipactor electron source concept, many design configurations are possible and can be fabricated using readily available, basic shop materials.

Earlier experiments at SRI indicate that, with some simple modifications, it should be possible to convert the basic multipactor system from an electron source to an ion source. In these experiments, nitrogen gas was injected at a low rate into the multipactor region between the cathode plates. The gas was thereby ionized by multiple collisions with the oscillating electron cloud, and the resulting positive ions were extracted by reversing the polarity of the high-voltage accelerating power supply. Although few quantitative measurements were made in these early tests, it appears that, with some further development, the basic multipactor system could serve as a practical source of both ions and electrons. In addition to its usefulness in spacecraft charging studies, the multipactor electron or ion source may have applications in a variety of material-processing applications.

The development of the continuous multienergy electron beam generation technique is a major advance in our ability to simulate more realistically the lower-energy, in-orbit electron environment. The results of future materials-charging tests using this multienergy source should significantly improve our understanding of actual in-orbit charging processes and should resolve some of the discrepancies between predicted and observed spacecraft materials performance.

REFERENCES

1. H. B. Garrett, "Spacecraft Charging: A Review," in Space Systems and Their Interactions with Earth's Space Environment, H. B. Garrett and C. P. Pike, eds., Vol. 71, pp. 167-226 (American Institute of Aeronautics and Astronautics, 1980).

2. J. E. Nanevicz and R. C. Adamo, "Occurrence of Arcing and Its Effects on Space Systems," in Space Systems and Their Interactions with Earth's Space Environment, H. B. Garrett and C. P. Pike, eds., Vol. 71, pp. 252-275 (American Institute of Aeronautics and Astronautics, 1980).

3. J. E. Nanevicz and R. C. Adamo, "A Rugged Electron/Ion Source for Spacecraft Charging Experiments," in Proceedings of the Spacecraft Charging Technology Conference, pp. 549-555, (Air Force Geophysics Laboratory, Hanscom AFB, 24 February 1977).

4. J. E. Nanevicz and R. C. Adamo, "Further Development of the Multipactor," in Spacecraft Charging Technology, NASA Conference Publication 2071, pp. 881-886 (1978).

5. B. L. Beers and V. W. Pine, "Electron-Beam-Charged Dielectrics--Internal Charge Distribution," in Spacecraft Charging Technology, pp. 17-32 (1980).

6. M. S. Leung, M. B. Tueling, and E. R. Schnauss, "Effects of Secondary Electron Emission on Charging," in Spacecraft Charging Technology, NASA Conference Publication 2182, pp. 163-178 (1980).

7. M. Treadaway et al., "Dielectric Discharge Characteristics in a Two-Electron Simulation Environment," in Spacecraft Charging Technology, NASA Conference Publication 2182, pp. 4-16 (1980).

8. R. Shimizu et al., "Energy Distribution Measurement of Transmitted Electrons and Monte Carlo Simulation for Kilovolt Electron," pp. 820-828, J. Phys. D: Appl. Phys., Vol. 8 (1975).

9. T. Matsukawa, R. Shimizu, K. Harada, T. Kato, "Investigation of Kilovolt Electron Energy Dissipation in Solids," J. Appl. Phys., Vol. 45, No. 2, pp. 733-740 (Febraury 1974).

10. I. Adesida, R. Shimizu, and T. E. Everhart, "A Study of Electron Penetration in Solids Using a Direct Monte Carlo Approach," J. Appl. Phys., Vol. 51, No. 11, pp. 5962-5969 (November 1980).

11. A. Y. Vyatskin and A. N. Pilyankevich, "Some Energy Characteristics of Electron Passage through a Solid," Soviet Physics--Solid State, Vol. 5, No. 8, pp. 1662-1667 (Febraury 1964).

12. R. Shimizu et al., "A Monte Carlo Approach to the Direct Simulation of Electron Penetration in Solids," J. Phys. D: Appl. Phys., Vol. 9, pp. 101-114 (1976).

13. V. E. Cosslett and R. N. Thomas, "Multiple Scattering of 5-30 keV Electrons in Evaporated Metal Films," Brit. J. Appl. Phys., Vol. 15, pp. 883-907 (1964).

14. L. Reimer, K. Brockman, and U. Rhein, "Energy Losses of 20-40 keV Electrons in 150-650 μg cm^2 Metal Films," J. Phys. D: Appl. Phys., Vol. 11, pp. 2151-2155 (1978).

15. J. B. Reagan et al., "Role of Energetic Particles in Charging/Discharging of Spacecraft Dielectrics," in Spacecraft Charging Technology, NASA Conference Publication 2182, pp. 74-85 (1980).

16. N. L. Sanders and G. T. Inouye, "NASCAP Charging Calculations for a Synchronous Orbit Satellite," in Spacecraft Charging Technology, NASA Conference Publication 2182, pp. 684-708 (1980).
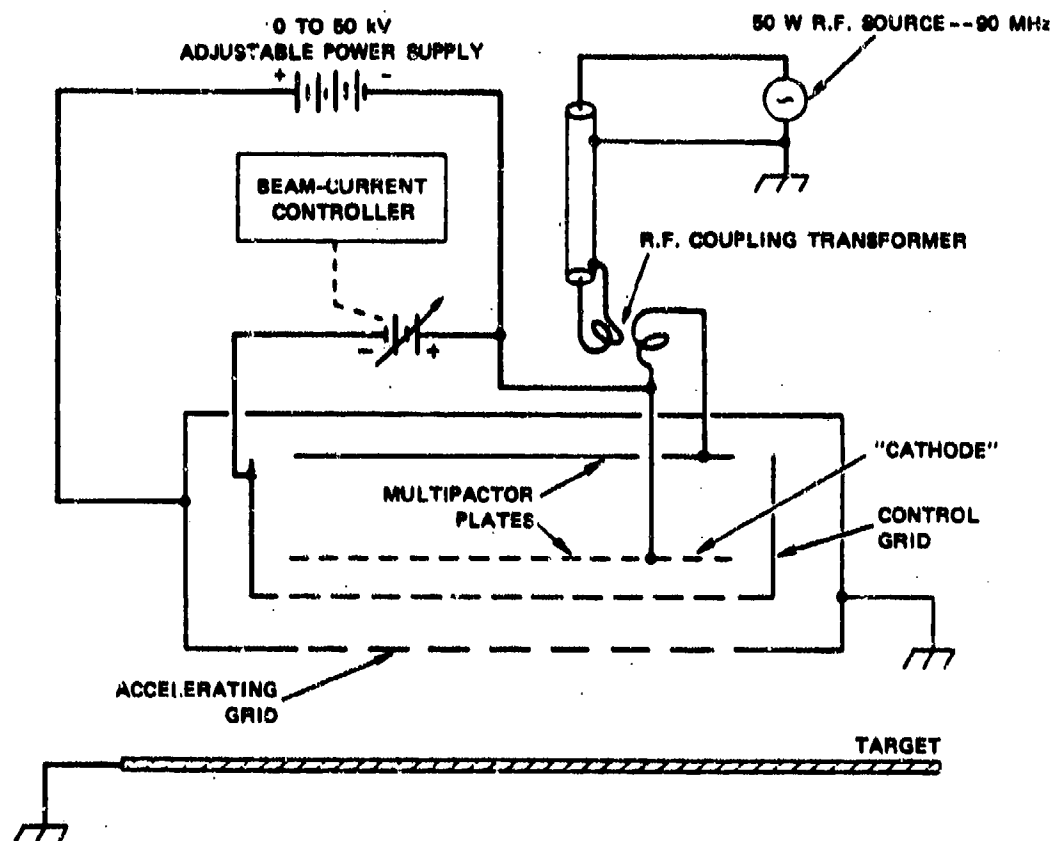
Figure 1. - Present multipactor electron source (schematic).
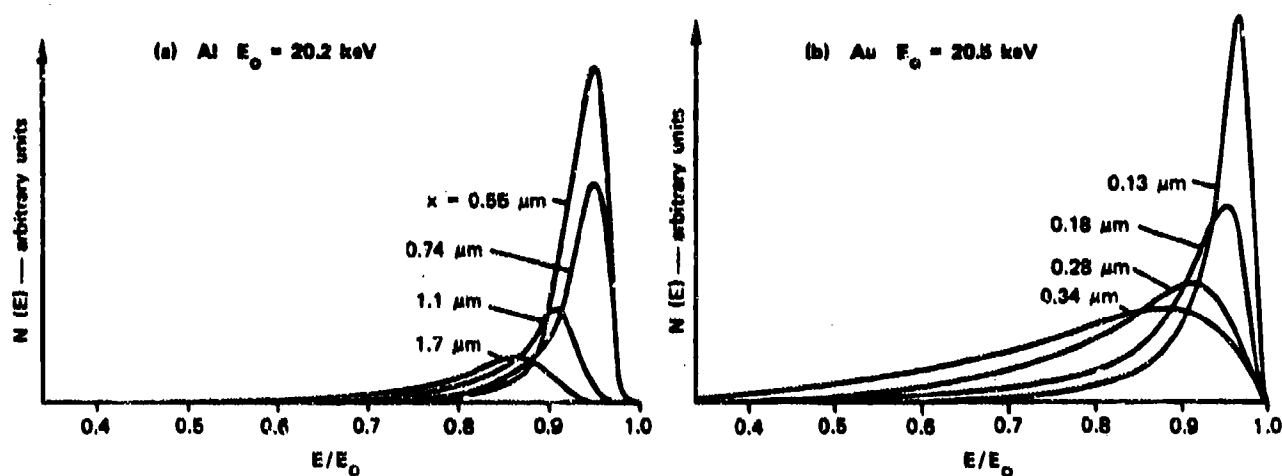
Figure 2. - Energy distributions of electrons transmitted through thin metal films.

473

28 MARCH 1978
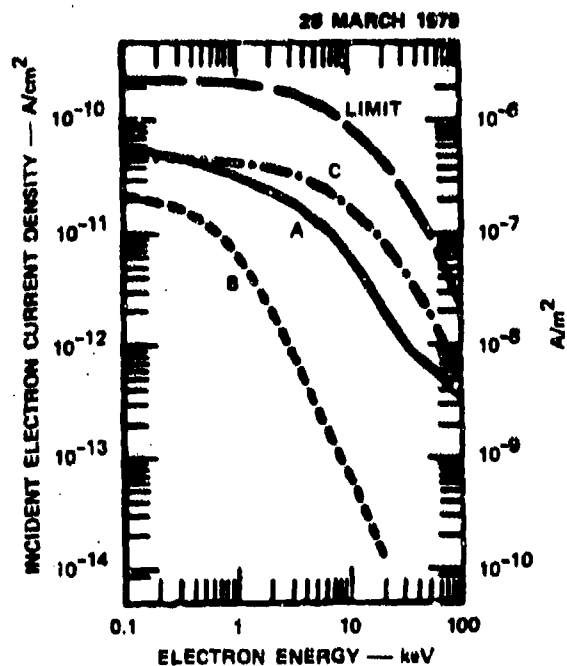
Figure 3. – Typical geosynchronous electron current densities.

MONO-ENERGETIC BEAM IN

ADDITIONAL METAL LAYERS
(e.g., 0.25 μm Au)

SUBSTRATE
(e.g., 0.75 μm Al)

MULTI-ENERGY BEAM OUT
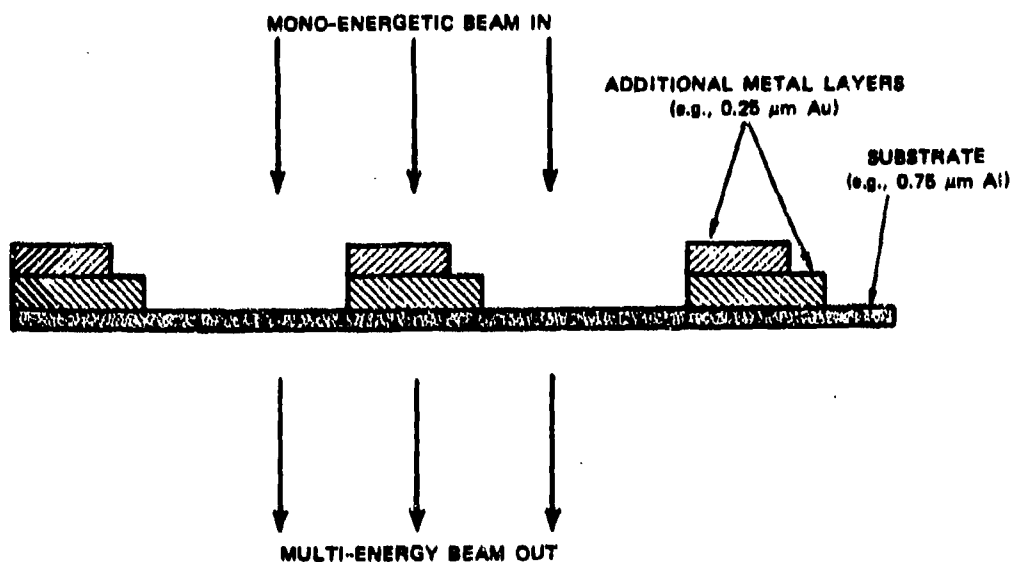
Figure 4. – Composite-foil concept.
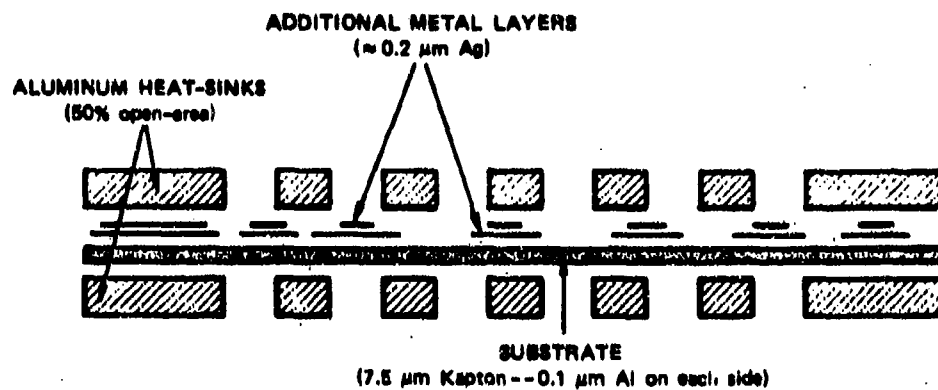
Figure 5. – Multiple-layer composite film.
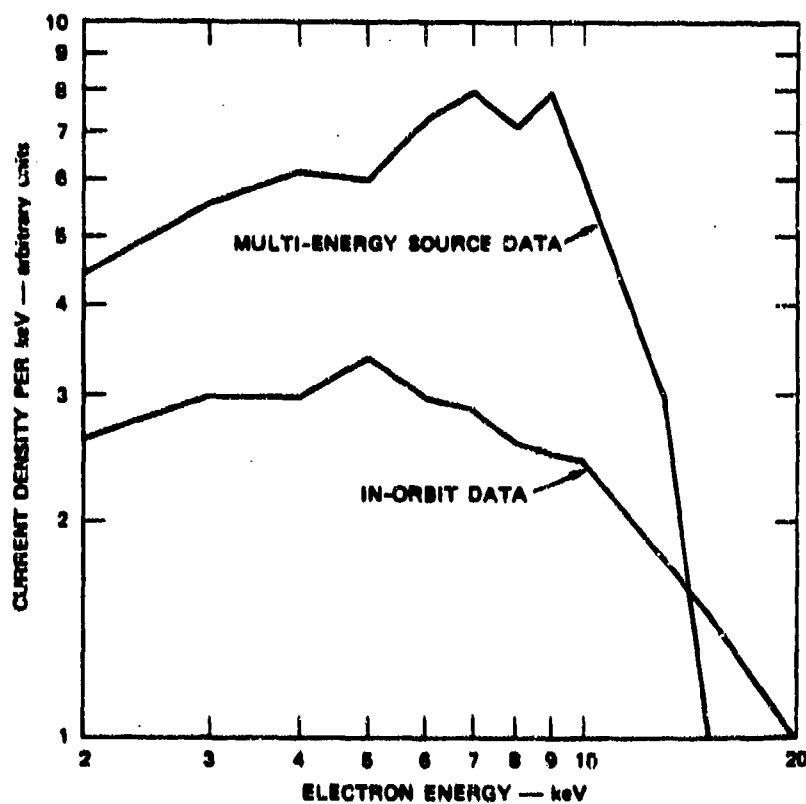
Figure 6. – In-orbit and simulated electron spectra.

AUTOMATIC CHARGE CONTROL SYSTEM FOR SATELLITES

B. M. Shuman and H. A. Cohen
Air Force Geophysics Laboratory
Hanscom Air Force Base, Massachusetts 01731

SCATHA as well as the ATS-5 and -6 spacecraft have provided some answers and insights to the problem of spacecraft charging at geosynchronous altitudes. In particular they have indicated the approach to reducing the levels of both absolute and differential charging -- namely, by the emission of low energy neutral plasma. It is now appropriate to complete the transition from experimental results to the development of a system that will sense the state-of-charge of a spacecraft, and, when a predetermined threshold is reached, will respond automatically to reduce it. The Air Force is embarking on such a development program, utilizing sensors comparable to the proton electrostatic analyzer, the surface potential monitor, and the transient pulse monitor that flew in SCATHA, and combining these outputs through a microprocessor controller to operate a rapid-start, low energy plasma source. A flight-ready system should be available for spacecraft integration by 1988.

INTRODUCTION

This paper is by way of announcing the Air Force's intent to carry out the technology transition from SCATHA to the next logical phase -- namely, the development of an automatic charge control system for spacecraft. The problem of spacecraft charging as a potential hazard for Air Force satellites operating in deep space has been recognized now for just over a decade. The buildup of spacecraft charge and its subsequent discharge, particularly at geosynchronous orbit, can limit the performance and operational lifetime of satellites. The arcs generated in this fashion can couple into the command and data lines of the spacecraft causing spurious signals, triggering erratic commands, and destroying solid-state electr ics. The SCATHA satellite, which was dedicated solely to this problem, was launched to near geosynchronous orbit with a full range of sensors (ref. 1) to determine the spacecraft state-of-charge as well as the background conditions in space when the charging occurred. Also on board were the AFGL active experiments, the electron gun and the SPIBS positive ion gun, which could be used to swing the potential of the satellite either positive or negative on command. One of the alternate operating modes of the SPIBS ion gun was as a neutral plasma source, and that proved to be the safest and most effective method of reducing both absolute and differential charging on the satellite (ref. 2). These SCATHA results, as well as those from the NASA ATS-6 satellite using a cesium plasma bridge neutralizer (ref.3), have shown that a charged spacecraft, and the dielectric surfaces on it, could be safely discharged by emitting a very low energy ($<$ 50 eV) neutral plasma -- in effect "shorting" the spacecraft to the ambient plasma before dangerous charging levels could be reached. This technique forms the basis for our Flight Model Discharge System (FMDS), which is to be an active charge control system for satellites that will operate automatically in space.

Much of the development of the FMDS, particularly with regard to the state-of-charge sensors, follows directly from the SCATHA technology. A block diagram of the system is shown in figure 1. The heart of the system is the low energy plasma source. The major change from its SCATHA predecessor is that it must be capable of a simple and rapid start-up -- responding within ten seconds. The microprocessor controller will be the "brains" of the system, interpreting the three different charging sensor outputs, and "deciding" when to turn on the plasma source. The electrostatic analyzer (ESA) will detect incoming protons in different energy channels to provide a measure of the absolute charging of the spacecraft. Since a negatively charged satellite will accelerate ambient protons up to its potential, the lowest energy channel at which sizeable fluxes of protons are detected would correspond to the absolute charging level of the spacecraft (i.e. relative to the ambient plasma in space). The surface potential monitor will measure the differential spacecraft charging (i.e. the potential developed on insulating surfaces relative to spacecraft frame ground). Essentially, the back surface voltage of a dielectric sample (i.e. kapton, teflon, etc.) is measured with an electric field sensor, and that in turn is translated into a front surface potential by means of a prior vacuum chamber calibration. The transient pulse monitor will detect arc discharges occurring on the external surfaces of the
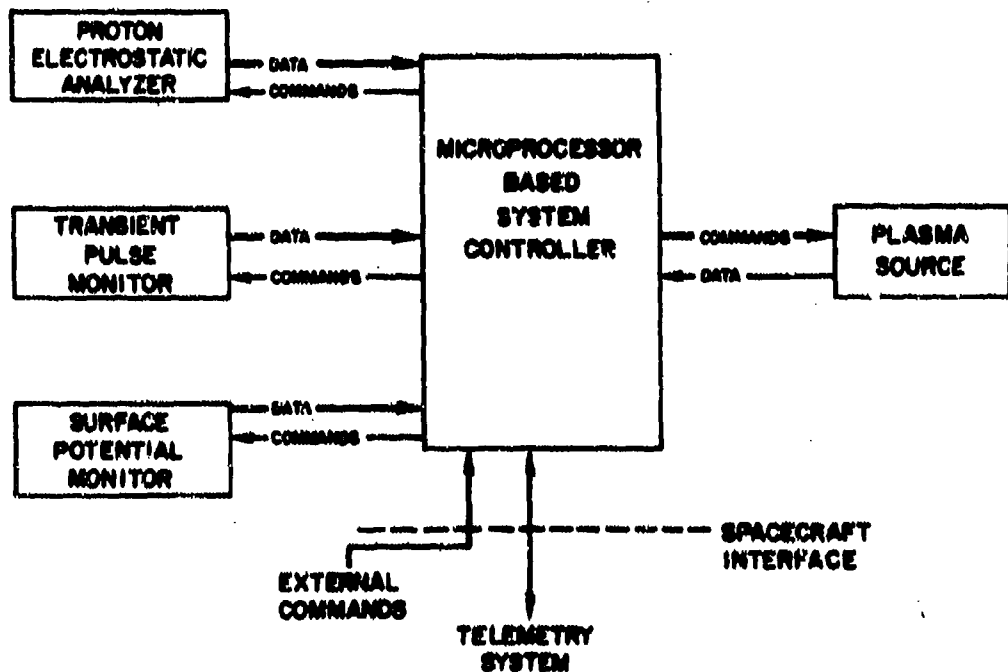
Figure 1. - Flight model discharge system.

spacecraft by measuring the radiated electomagnetic noise pulses. The pulse
characteristics should provide the means of discriminating between arc discharges
and spacecraft-generated noise. The combination of these three different sensors
should provide a good indication of the state of spacecraft charging, but any
one alone (by exceeding a preset threshold level) will be able, via the controller,
to activate the plasma source and reduce the charging.

Considering each of the components in somewhat more detail, we come back to
the plasma source. This will produce a low energy (<50 eV) neutral plasma where
the ions are derived from a noble gas. Xenon was chosen as the active source for
the SPIBS experiment on SCATHA, and would be a likely choice here as well. The ion
current levels would be selectable by remote command -- 10 μ A, 100 μ A, or 1mA.
On SCATHA, SPIBS discharged the vehicle from a potential of -3kV using as little as
6 μ A of current. The plasma source will be simpler than SPIBS in that neither
multi-energetic positive ion beams nor electron beams will be required. However,
the activation process must be far simpler and quicker than for SPIBS since it will
be turned on automatically by the controller, and must be capable of responding
within ten seconds. The plasma source will have the capability for 1200 hours of
operation in space, with at least 1000 on-off cycles. This is expected to be more
than enough to operate for three years, with a large safety factor besides. There
will be monitor outputs to telemetry for plasma current flow, remaining gas
supply, command status, and other diagnostics. Provisions will be made, as was
the case for SPIBS, for a vacuum enclosure around the plasma source to allow for
operation during spacecraft integration checks. The weight of the plasma source
will be less than 10 pounds, and the power required for operation will be less than
10 watts.

The proton electrostatic analyzer will measure the incident proton spectra in
the energy range from less than 100 eV to 20 KeV. It will be simpler than the ESAs
used on SCATHA since it will require, as a minimum, only eight incremental energy
channels, with maximum channel energies (i.e. upper edge of full width at half maxi-
mum [FWHM]) nominally set at 100 eV, 200 eV, 500 eV, 1 KeV, 2 KeV, 5 KeV, 10 KeV,
and 20 KeV. The energy channels will be adjacent, and with a minimum of overlap at
FWHM -- not more than 2% of the channel central energy. The algorithms developed by
Spiegel (ref. 4) to allow for automated interpretation of the ESA data depend criti-
cally on the energy channels being sharply defined. The sweep period for the ESA
to sample all channels, which determines the time-scale for the detection of space-
craft charging, will be selectable by external command -- 1 second, 5 seconds, or
10 seconds. The ESA will include a sun sensor to reduce electron multiplier gain
when the instrument looks toward the sun, and also a control grid to prevent the
low energy (< 50eV) ions from the on-board plasma source from being counted. There
will also be available, by external command, the possibility of changing the bias
voltage of the electron multiplier detector in order to offset the effects of de-
gradation, and to extend its operating lifetime in space. The weight of the ESA
will be less than 5 pounds, and the power requirement will be less than 1 watt.

The surface potential monitor will measure the back surface voltage of a
dielectric sample as in the SCATHA SC-1 experiment. The surface potential and
polarity will be determined once per second, and will include the range 100 volts
to 20 kilovolts. The instrument will use two different dielectric samples in
flight. These will be chosen prior to flight from a previously-calibrated selection
of at least six different samples of "typical satellite dielectric surfaces" such

as aluminized kapton, silvered teflon, fused silica cover glass, etc. Weight and power for the instrument should be less than 3 pounds and 2 watts, respectively.

The transient pulse monitor (TPM) will detect arc discharges occurring on the external surfaces of the spacecraft by measuring the radiated electromagnetic noise pulses with an externally mounted dipole sensor. Similarly to the SRI instrument on SCATHA, it will record the number of pulses counted over each one-second interval; also the maximum pulse amplitude (both positive and negative) occurring over that interval, and the integral of the signal (both positive and negative) over the interval. It will determine pulse width, with the capability of detecting pulses from 10 nanoseconds to 10 microseconds. It will also accomodate amplitudes of electric field strength from 10 kilovolts/meter down to 10 volts/meter. Multiple threshold levels, selectable by external command, will be provided to determine the minimum signal level above which pulses will be recorded. Multiple attenuator levels, to determine the overall gain of the system, will also be selectable by external command. Protection will be provided against ringing by incorporating a dead time that will limit pulse counts to once per millisecond. One phase of the calibration of the transient pulse monitor will include the detection of simulated spacecraft arc discharges -- such as may be induced in a vacuum chamber by bombarding a typical spacecraft thermal control material with energetic electrons. The weight and power requirements for this instrument should be less than 3 pounds and 3 watts, respectively.

The controller will be the nerve center and coordinator of autonomous operation of the charge control system. It will accept inputs from the state-of-charge sensors (i.e. the proton ESA, the surface potential monitor, and the transient pulse monitor), interpret the sensor data based on previously stored algorithms, determine when pre-established threshold levels of charging have been met and then activate the plasma source, and finally, turn off the plasma source when the spacecraft has been discharged. Once activated by the controller, the plasma source will remain operating for a fixed time period. That time period will be selectable by remote command, and will include the nominal intervals of 5, 10, 30, and 60 minutes. The threshold levels at which the plasma source will be activated will also be selectable by external command, and will include at least the (absolute and differential) potential levels 200, 500, 1000, and 2000 volts. Indications of spacecraft arcing, as determined by the TPM will also cause the plasma source to be activated. The algorithm for determining the occurrence of spacecraft arcing from the TPM data will have the capability of being modified in-flight by external command so that it will not respond to the normal background level of electromagnetic noise from the spacecraft itself. As a safety measure, the controller will also incorporate the capability for external-command override of the operation of the plasma source -- for turn-on, turn-off, and current level settings. Finally, the controller will contain sufficient excess capacity to accomodate an additional sensor input, if that should turn out to be desirable at some future date. Allotting approximately 5 pounds and 3 watts for the controller brings the system totals for weight and operating power (with the plasma source on) to 26 pounds and 19 watts. System power requirements with the plasma source not operating will be 9 watts.

We expect the development, fabrication, and test of the charge control system to take approximately four years, so that it would be available for spacecraft integration in 1988. Our present plan is to test-fly the system on a polar-

orbiting Space Shuttle, along with other AFGL-sponsored experiments. The ultimate test of the system will require a flight at geosynchronous orbit, which is the regime this system is primarily designed for and where it will be of most value.

REFERENCES

1. Stevens, J.R., and A.L. Vampola: Description of the Space Test Program P78-2 Spacecraft and Payloads, SAMSO TR-78-24, 1978.

2. Cohen, H.A., and S. Lai: Discharging the P78-2 Satellite Using Ions and Electrons, Paper No. AIAA-82-0266, presented at the AIAA 20th Aerospace Sciences Meeting, Orlando, Florida, January, 1982.

3. Purvis, C.K., and R.O. Bartlett: Active Control of Spacecraft Charging, Progress in Astronautics and Aeronautics: Space Systems and Their Interactions with Earth's Space Environment, Vol. 71, edited by H.B. Garrett and C.P. Pike, AIAA New York, 1980, pp. 299-317.

4. Spiegel, S.L., R.J. Raistrick, N.A. Saflekos, M.S. Gussenhoven, and H.A. Cohen: Real Time, Automatic Vehicle Potential Determination from ESA Measurements, Part I: The Count Ratio Algorithm, Paper No. AIAA-82-0267, presented at the AIAA 20th Aerospace Sciences Meeting, Orlando, Florida, January, 1982.

DISCHARGE PULSE PHENOMENOLOGY

Arthur R. Frederickson
Rome Air Development Center
Hanscom Air Force Base, Massachusetts 01731

A model is developed which places all of the published radiation induced discharge pulse results into a unified conceptual framework. Only two phenomena are required to interpret all space and laboratory results:

  a) Radiation produces large electrostatic fields inside insulators via the trapping of a net space charge density, and

  b) The electrostatic fields initiate discharge streamer plasmas similar to those investigated in high voltage electrical insulation materials; these streamer plasmas generate the pulsing phenomena which have been seen by many workers.

The apparent variability and diversity of results seen to date in space and laboratory experiments is an inherent feature of the plasma streamer mechanism acting in the electric fields which were created by irradiation of the dielectrics. The implications of the model are extensive and lead to constraints over what can be done about spacecraft pulsing.

INTRODUCTION

At first look one is struck by the diversity of pulsing results reported on spacecraft and ground testing of irradiated dielectrics. A new vocabulary has been developed in this community (blowoff, bulk pulsing, punchthrough, surface discharge, brushfire, bi-layer, charged-surface, floating-conductors, breakdown-potential) which may be responsible for unnecessarily increasing the diversity of results. Until recently, experimenters were hindered by the facts that the field of investigation was still young and that apparently new observables kept appearing. One experimenter would observe flashes of light, another would see a potential drop, another measured pulses of current, still others observed microdamage after the irradiation emission of ions, emission of energetic electrons, area-charge scaling, lack of pulsing under certain spectra, cessation of pulsing under continued irradiation, pulses of opposite sign, etc., etc.

For the past decade I have been correlating the occurrence of pulses with radiation generated electric fields in the bulk of irradiated insulators. Electrical insulation breakdown and prebreakdown events are usually (ref 1,2) related to an applied electric field strength. We find that irradiated polymers begin pulsing when the estimated radiation induced electric field exceeds 100 kV/cm (ref 3). In the process of reviewing (ref 4) the spacecraft charging literature I concluded that whenever pulses were observed, the irradiation had produced internal space charge densities large enough to create fields in excess of 10^5 V/cm within the dielectric.

Researchers in the field of electrical insulation have consistently divided
the phenomenon of breakdown into two parts: Prebreakdown and Breakdown (full permanent
failure). So far it appears to me that we see only the prebreakdown phenomena in our
space radiation situation. If one applies an electric field in excess of 10^5 V/cm
to a solid dielectric, then random and very small current pulses are observed which
are called prebreakdown events. These pulses are associated with flashes of light
and very small discharge streamers which last on the order of nanoseconds or less.
The insulator does not fail even after the occurrence of thousands of prebreakdown
pulses. Such pulses are sometimes thought to be due to the failure of very small
weak spots or the discharge of microvoids within the solid. I am not aware of one
complete reference to this phenomenon but there are many papers dealing with various
aspects of it in the electrical insulation literature. Reference 2, the IEEE
Transactions on Electrical Insulation, and the annual proceedings of the Conference
on Electrical Insulation and Dielectric Phenomena (IEEE sponsored) are good starting
points. Prebreakdown phenomena is a rapidly growing research field which contains,
in my opinion, some exciting solid state physics problems.

In this paper we show how all the spacecraft charging results, both ground and
space results, can be explained by the mechanism of electric field generated pre-
breakdown streamer channel formation. The electric fields are due to either applied
voltages in dielectrics, or to radiation generated space charge electric fields, or
to a combination of the two. The streamer formation is a quantum mechanical many-
body process which is only recently being attacked with appropriate tools; its
existence is observed but not understood. These processes "explain" all spacecraft
effects including: area scaling, pulse height, pulse width, pulsing frequency,
radiation spectrum dependencies, microwave emission, surface discharging, bulk
pulse characteristics, fibrous material discharging, correlations (or lack of)
with surface potential, light flashes, edge effects, emission of ions and electrons,
etc.

RADIATION GENERATED E FIELDS

Estimates of radiation generated electric fields in dielectrics are available
(ref 3,5-8) but only a few good measurements have been made. The measurements are
difficult and actually measure charge density (ref 9,10) not electric field. The
electric fields are obtained from the charge density by use of Poisson's equation.
One excellent review (ref 11) is available which surveys most of the existing
charge density work and is a good introduction to the literature. The literature
on this topic is extensive but does not answer the critical engineering question
"Given a particular dielectric device under various broad radiation spectra what
electric fields are generated?" Most of the cases that have been discussed involve
monoenergetic electron beams and short total irradiation times ($<10^8$ rads total
dose). A few cases address the question of broad spectra but then simplify the
modeling to assume no electronic conduction occurs in the electric field.

Photon irradiations simulate the broad energy spectrum situation because
photon spectra themselves, as well as the excited electrons generated by each
monoenergetic portion of the photon spectrum, are often broadly distributed in
energy. Calculations indicate that photons from 10 KeV to 2 MeV produce electric
fields of nearly 10^6 V/cm, (ref 7,12) in most practical geometries. Only for the
case of slabs surrounded by very thick layers (>1 electron range) of identical atomic
number material do we find field strengths below 10^4 V/cm in photon irradiated
solid insulators. Photon beams produce a net charge deposition somewhere in irradi-

ated solids by a number of processes depending on photon energy but one process always occurs; the attenuation of the photon beam results in a concentration gradient of highly excited electrons which then diffuse and "pile up" in the more weakly irradiated regions, and this process will generate 10^3 V/cm fields in most good solid insulators. Other processes produce much larger fields in photon irradiated solids.

It is possible to conceive of an irradiated solid which does not develop net spatial charging. A radioactively doped insulator with uniform doping profile would not charge. But such a device would not be practical in electrical application since electrodes or surfaces remove the uniform doping constraint and create large fields near the electrodes or near the surfaces. I have not encountered a practical dielectric device which will not charge with strong E fields. The E fields are usually strongest near electrodes or near surfaces and edges and are produced partly by the divergence of the high energy electron currents (or by their flux gradients) near the surfaces and electrodes.

In practical devices only conduction processes will prevent the accumulation of excess charge to levels where E exceeds 10^5 V/CM. Basically, all highly excited (≳ 10 eV above conduction band) electrons are stopped in solids with more than 10^5 V/cm stopping power and in the absence of conduction, this process of stopping electrons is the field limiting factor: if the electric field exceeds the stopping power of the solid, then the excited electrons would be accelerated out of the solid until the resulting field strength decreased to the stopping power. In reality, for the exposure rates expected in space ($< 10^3$ roentgens/second) it is the radiation induced conductivity and the dark conductivities which are the parameters which most strongly control the electric field strengths.

One can make changes in the incident radiation spectrum until one is "blue in the face" and only insignificant changes in peak E field will result. In the highly insulating dielectrics (low conductivity) one cannot prevent fields from exceeding 10^5 V/cm, however some faulty models have been invoked to predict such impossible lower field cases by, for example, the use of so called "penetrating" radiations.

It turns out that for the best dielectrics and for nearly any radiation spectrum and any geometry the field strength will exceed 10^5 V/cm somewhere in the solid and in some special cases can reach 10^7 V/cm. To avoid this high field strength one needs only to increase the conductivity. Based on ten years experience, I find that equation 1 is a good guide to the field strength dependence on conduction processes at low dose rates ($< 10^3$ rads/second). Geometry and spectrum changes will not produce more than an order of magnitude correction to equation 1 predictions.

$$(E \text{ Peak}) \approx 10^{-12}/k(1+\sigma/kD) \tag{1}$$

where: 10^{-12} has units of $(sec \cdot V)/(cm^2 \cdot ohm \cdot rad)$,
  k is the coefficient of radiation induced
  conductivity in units of $(sec/ohm \cdot cm \cdot rad)$,
  σ is the dark conductivity in units $(ohm \cdot cm)^{-1}$,
  D is the average dose rate in the volume of
  interest in units of rads/sec.

For the best dielectrics k is typically 10^{-18} (seconds/ohm·cm·rad) resulting in peak fields of 10^6 V/cm. Of course k is dependent on many things including D, so one must evaluate k at the dose rate of interest, D, using eq 2.

485

where RIC is empirically determined for the dielectric material in question. References 3-8, 12 and 13 have examples of electric field strength profiles in irradiated dielectrics. Reference 3 compares the occurrence of pulses with the electric field strength in irradiated dielectrics.

ELECTRICAL INSULATION BREAKDOWN PHENOMENA

Background

While surveying the breakdown literature I learned that there are apparently many failure modes for electrical insulation. In most of the modes a very large current flows for long enough times to blow a fuse or kill a power supply. However, in most of the spacecraft tests to date we only see rapid pulses without permanent failure and without continued pulsing.

In the insulator industry this kind of pulsing is known as high voltage DC prebreakdown phenomena. If one applies an electric field of order 10^5 to 5×10^5 V/cm to a good dielectric, small pulses may occur as depicted in figure 1 for a period of an hour or so and may even reoccur for a short time again many days later but usually the short pulses have stopped unless one changes polarity or increases the field strength. These pulses are called prebreakdown events and usually do not lead to full breakdown. However, if one applies sufficient field strength a rapid burst of prebreakdown pulses will be immediately followed by full breakdown of the insulation.

In the case of space radiation it is unlikely that total breakdown occurs because there is no "stiff" power source which can continue to provide significant current to the system. Even though peak currents approaching 10^3 amperes have been seen during short pulses, the dielectric was not destroyed as an insulator by one pulse. With maximum differential potentials of 10^4 volts and incident currents of 10^{-9} A/cm^2 we find that space radiation cannot produce a d.c. power flux exceeding 10 μ Watts/cm^2. It is unlikely that such low power flux will permanently change an insulator into a conductor. Thin oxide electronic device insulations, however, are hurt by the transient pulses.

The most common dielectric experiment is shown in figure 2. A current is measured between two electrodes while the dielectric is irradiated and/or biased. Any currents or current pulses, including the motion of irradiation driven charged particles (usually electrons), will register on the meter according to the equation in figure 2. If one measures I throughout the irradiation and independently knows the dose-depth and charge-depth distributions for the radiation then one can calculate the E fields internal to the dielectric (ref 3,7). Pulses will also show up on the meter according to the equation. The experiment in figure 2 is the most generally useful arrangement.

A common embodiment of figure 2 is to have most of the space between X=0 and X=A in vacuum and thin layer of solid dielectric of thickness d from X=A-d to X=A. Again, electric fields build-up in both the vacuum and the dielectric but space-charge accumulates only in the dielectric. Because space-charge cannot accumulate in the vacuum, charge current flowing in the vacuum must be a constant across the vacuum

space (in the quasi-static approximation which is valid for this spacecraft problem) although it can vary in time.

Consider an idealized current pulse of arbitrary magnitude J_p. Let $d \ll A$. Then if J_p occurs in the vacuum region, it must be constant across the vacuum and

$$I = \frac{1}{A} \int_0^{A-d} J_p \cdot dx \approx J_p$$

But if J_p is confined to the dielectric then

$$I = \frac{1}{A} \int_{A-d}^{A} J_p \cdot dx < \frac{d}{A} J_p \qquad (3)$$

To date, most experiments were designed such that $\frac{A}{d} \approx 5000$.

Thus pulses confined to the dielectric will be detected much more weakly on the ammeter I than similarly sized pulses in the vacuum will be detected. Therefore an ammeter set to a scale to detect pulses in the vacuum will not detect similar pulses in the dielectric.

The Basic Phenomenon

All of the observed pulsing phenomena reported by spacecraft charging investigators can be explained as normal derivatives of the streamer phenomenon described in reference 2 and reported extensively in the prebreakdown electrical insulation community. It is found that solid dielectrics subjected to electrical stresses greater than 10^5 V/cm (and in some instances as low as 10^4 V/cm) spontaneously develop streamers of gas/plasma phase matter which start at a point but rapidly expand along a line roughly parallel to the local electric field vector. The streamers tend to form tubes whose diameters are in the range 0.1 to 10 microns (typically 1 micron) but can become much larger where many streamers join together, and appear to have no limit to their maximum length. Streamers continue to propagate as long as sufficient E field exists at the tip of the streamer.

Figure 3 is a pictorial streamer. Stop action photographs indicate that streamers are usually brightest at their tip but emit light throughout their length. The insulation industry reports a wide range of propagation velocities from 10^3 to 10^6 m/sec but for conditions of electron irradiation Balmain et al. report (ref 14) velocities of 10^5 to 10^6 m/sec. In Balmain's case streamers propagate at or just beneath the surface and surface effects may play a role in the propagation velocity so it might be instructive to do similar tests for the deeper penetration case.** Under electron irradiation it appears that streamers originate at a surface (where the field strength is maximum) and propagate to or a little beyond the average

---

**footnote: deeper penetration will not be obtained by raising the energy because the surface potential rises to slow the incident electrons to roughly 2 keV incident energy. Most of the irradiation in Balmain's experiments was by 2 keV electrons. Instead, one should ground the surface with UV photons or low energy protons (ref 13).

trapped electron depth whence they turn at right angles and spread out at this
depth; the right angle turn is made because the plasma filled streamer has almost
eliminated the potential difference between the tip of the streamer and the dielec-
tric surface so that the E field vector at the tip is now perpendicular to the
original field direction and pointing towards the centroid of the spacecharge
electrons (ref 15).

Streamers have been seen to occur in many materials (liquid, crystals, glasses,
polymers) used for insulating purposes. In all these materials streamers similar
to those reported by Balmain (ref 15), by Gross (ref 16), and by the many people
using irradiation to create lichtenberg trees, are occuring in dielectrics which
are under electrical bias stress alone.

It appears that the basic streamer forms as a highly ionized plasma tube. The
plasma is extremely dense and under high pressure so that when it approaches a
surface it "explodes" from the surface allowing plasma subsequently formed at the
streamer tip to escape through the tube. At the cessation of the discharge propaga-
tion one finds the remains of the discharge to be a tree or bush shaped network of
hollow tunnels. Reference 17 reports on measurements of this highly ionized plasma
debris which escapes the solid. In the case of applied electric bias experiments,
the plasma may be confined to the dielectric by the electrodes so that hollow
tunnels do not occur and the plasma resolidifies in place. However, if the plasma
tube propagates between electrodes entirely across the dielectric, it becomes a
conductive tunnel effectively shorting out the insulator for as long as the power
supply can maintain sufficient plasma arc power to continue the plasma between the
electrodes.

Although streamers have been seen to develop at 10^4 V/cm applied bias, they may
have actually occurred at localized high field regions due to space charge which was
developed by conduction process. I would quess that at least 10^5 V/cm is required
to initiate streamers but that once formed they can continue to propagate in lower
field regions, perhaps in regions of field strength as low as 10^4 V/cm or less.

The streamer obtains its energy from the electric field, not from the space charge
itself. For typical geometries the spacecharge density developed under irradiation
is in the range 10^0 to 10^4 coulombs/meter ^{3}. Thus a one micron diameter tunnel
intersects from 5 to 5×10^4 excess trapped charges (electrons, holes, ions) per
centimeter of propagation. Assuming that a reasonable fraction of the atoms within
the tube are ionized by the streamer propagation/formation process there are of
order 10^{10} ions and free electrons per centimeter of 1 micron diamter tube. Thus the
excess spacecharge contributes very little to the plasma density.

I don't know of any physics which can predict the occurrence of these streamers.
Electric field strengths of 10^6 V/cm probably cannot accelerate an internal free
electron much beyond 10 eV kinetic energy because at higher kinetic energies the
stopping power on the free electron in, for example, polyethylene exceeds 10^6 V/cm
(ref 18). Thus one free electron cannot avalanche because it takes more than 10 eV
on average (probably from 20 to 30 eV) to create a secondary free electron. Perhaps,
in a region of high field, occasionally it happens that sufficient local random
ionization occurs to significantly alter the band structure and the dielectric
constants so that the stopping power is significantly reduced and free electrons
can accelerate to avalanche levels. Assume that 50 eV is necessary for free electron
avalanching: then at 10^6 V/cm E field we require a thickness of order 0.5 microns

to generate this kinetic energy. A lower limit may exist on the thickness of
material required to initiate a streamer and this effect is partly responsible for
the increased breakdown strength of very thin film insulators. In addition, the
statistics of streamer initiation are such that rare atomic level events may be the
initiating mechanism; application 10^6 V/cm does not cause streamers automatically
everywhere, they happen rarely and far apart relative to their size.

Empirical knowledge of the streamers allows us to explain the spacecraft charging
results even though we don't understand streamer physics. Streamer propagation
velocity, total streamer volume, streamer tube diameter, ionization density inside
the streamer and the empty tunnel which remains, along with electric field strength,
are sufficient parameters to explain the spacecraft charging phenomena. Using this
empirical data and applying standard electromagnetic analysis, the rest of the
paper explains the observed pulsing results. In addition, the modeling predicts
results which have yet to be investigated. However, this modeling has not been
tested and it would be wise to do so: for example, one should make measurements of
the externally measured pulse current and relate it to the specific streamer tunnel
which produced the pulse.

Electric Fields and Streamers in Spacecraft Dielectrics

The most common spacecraft charging laboratory experiment has been irradiation of
thin polymer or glass sheets by approximately 20 keV electron beams in vacuum. The
irradiated side (front) of the sheet can float to any potential but the other side
(rear) of the sheet is attached to a grounded electrode. Experimenters have
monitored current to the electrode, discharge current to the electrode, discharge
current pulses to the electrode, potential of the front surface, light flashes,
discharges associated surface trees, and electron, ion, and neutral particle
emission from the front surface. Figure 4 is an estimate of the electric fields
in a 1 millimeter thick mylar sample bombarded by 20 keV electrons (ref 13). These
electric fields are crucial to an understanding of the results of the experiments.

Referring to figure 4, at 36 seconds the front surface attained a potential of -18
kV and therefore it was being bombarded by 2 keV electrons. Because of secondary
electron emission the front surface will remain at this -18 kV potential as long as
it continues to be bombarded by 2 keV electrons. However, the internal fields
continue to evolve as shown in figure 4. The field profile at 1036 seconds is
essentially a final equilibrium value as change will occur only very slowly beyond
this time under continued irradiation. Reasonably similar curves would occur for
teflon or polystyrene or other highly insulating solid. Notice that the 10^5 V/cm
electric field strength is sufficient to initiate streamers with either polarity.

Figure 5 shows the electric field calculation for a 25 micron mylar sheet where the
front surface is held at ground potential during the 20 keV electron beam irradia-
tion. In this case even larger electric field strength occurs (exceeding 10^6 V/cm)
near the front surface. If one changes the sheet thickness to any value in excess
of 10 microns it turns out that only minor changes in the equilibrium electric field
would occur at the front surface for either fig. 4 or fig. 5 conditions. However,
the equilibrium field strength at the rear surface is roughly proportional to the
inverse thickness of the sheet.

The electric field profiles in figures 4 and 5 are crucial to understanding space-
craft charging phenomena to be described below. The field profiles between the
front surface and the charge centroid (where E = 0) are key to understanding the

phenomena because a discharging or pulsing sample under irradiation is, in the sense, hopping between the two extreme cases shown in figs. 4 and 5.

In the case of an insulator with both surfaces grounded, pulses have been correlated with the theoretical electric field strength (ref 3). The pulses occur only under field strength exceeding 10^5 V/cm. Also, the pulses had the polarity consistent with the polarity of the electric field which had exceeded the minimum field strength required for pulses in the individual sample.

EXPERIMENTAL SCENARIOS

There are several specific experiments reported in the literature. Each experiment can be explained by the streamer hypothesis as follows.

Floating Front Surface Potential

Consider the experiment of figure 6 where a dielectric in vacuum is irradiated and its irradiated surface is allowed to float to any potential. If the dielectric is thicker than the penetration depth of the monoenergetic electrons, then the front surface fields will be approximately as shown in figure 4 for any choice of beam energy above one keV. As the irradiation progresses from its inception, the potential of the surface "rises" and slows the incoming electrons until the quasi-equilibrium occurs where the secondary electron current cancels the incoming primary beam current. The quasi-equilibrium will occur when the primary electrons bombard the surface at the "secondary electron second cross-over energy" (ref.19), typically from 1 to 3 keV. The continued irradiation by 1 to 3 kev electrons produces further field strength enhancement at the front surface. At long times the sample will have lost the field contributed at early times by the deeply penetrating higher energy electrons because of compensating conduction currents.

Assuming that:

E_0 is the initial electron kinetic energy in eV,

ϕ_2 is the second crossover energy in eV

ϕ_e is the quasi-equilibrium surface potential

E_d is the electric field magnitude in most of the bulk of the dielectric

E_v is the electric field magnitude in the vacuum in front of the dielectric

ℓ is the dielectric thickness

a is the distance from the front surface to the ground plane on the other side of the vacuum;

R is the penetration range of initial E_0 electron beam

then $E_0 - \phi_e = \phi_2$ typically 2 keV,   (4)

and $E_v = \phi_e/a \approx E_0/a$ for $E_0 \gg \phi_2$,   (5)

and $E_d = \phi_e/\ell \approx E_0/\ell$ for $\ell > R$,   (6)

490

but the E field near the front surface will remain as shown in figure 4 for any choice of E_0, A, or ℓ greater than R.

If one monitors the potential of the front surface during an irradiation, the result is often as shown in figure 7. The front surface potential rises roughly to the "second cross over" level. After some irradiation time (which is very variable) a pulse occurs discharging the front surface. The second pulse may occur with a shorter elapsed time and at a lower surface potential than the first pulse. Subsequent pulses may occur at even lower surface potential and sometimes at very close time intervals. Finally all pulsing ceases and the surface reaches the "second cross over" level permanently.

The experimental results such as shown in figure 7 can be explained in the following way. Electric field strengths of 10^5 V/cm or greater (fig 4) cause a discharge streamer to form near the front surface and the resulting plasma erupts from the surface. The negative plasma components then accelerate across the vacuum space to the vacuum chamber walls effectively "grounding out" the surface potential. The positive components return to the surface of the dielectric spread out over most of the surface. The plasma particles actually spread out in the vacuum due to a combination of effects including pressure waves, diffusion and electric forces and then, from everywhere in the vacuum, they flow to the appropriately biased surface. The streamer channels resulting from this process are hollow, having ejected all their mass into the vacuum and producing sufficient charged particle quantities to discharge large areas; as much as 10^{-2} coulombs has been seen and a great deal more charge is probably available judging from the largest lichtenberg trees that I've seen.

The polarity of the current pulse seen in the rear electrode current monitor is such that a net electron flow occurs from the dielectric through the vacuum to the chamber walls. The surface is not discharged by streamers flowing through the dielectric to the rear electrode for a fundamental reason: If a streamer were to cross through the dielectric from the rear electrode to the the front surface, it would make a shorting contact with only a small portion of the front surface but would then burst from the front surface at high pressure spilling plasma into the vacuum. The major discharge would then proceed in the vacuum region as discussed in the preceeding paragraph. However, for reasons to be published in the near future, I believe that, due to radiaton alone, a streamer will not propagate entirely through a dielectric but will reach only one surface; in otherwords, for the experimental conditions published to date the so called "punchthrough" discharge is an impossibility.

The surface potential discharge measurements are discussed in references 20 through 26. The return current to the rear electrode is discussed in references 15, 20 through 26. The emission of particles into the vacuum is discussed in refs 17 and 22 and elsewhere in this conference proceedings.

So far during the irradiation we have described the first pulse which then discharges the surface. The discharged surface now changes the field profile within the dielectric increasing the field strength immediately below the surface. The incident electrons go back to their initial value of energy, say 10 or 20 keV and begin the surface charging process over again. But the electrons are, at least for a while, penetrating more deeply within the dielectric and attempting to produce field profiles as described in figure 5. Larger E fields are produced to deeper depths than figure 4 shows, but only after the first pulse occurs. It is these larger and

deeper fields which then produce more pulsing in shorter time increments. As the pulsing progresses, field strengths vary between the extremes shown in figures 4 and 5 and the depth dependence varies between these extremes. Finally, in analogy to the well known capacitor prebreakdown phenomena, all the "weak spots" between the surface and full electron penetration depth are "pulsed" and further pulsing ceases until the radiation spectra change significantly. Exact calculation of the field profiles during a series of breakdowns has not been performed so this description is only qualitative. It is well known that the streamers create physical damage but that this damage does not increase the probability for future streamer occurrence and that under d.c. stress, pulsing usually ceases after a time depending usually on the field strength.

An interesting result is predicted by the above phenomena. The field profile in figure 4 is such that a surface pulse is not likely because the field strength at the surface is not exceptional and involves very little depth. The note to figure 4 indicates that the basic concepts used to derive the figure are known to be faulty in such a way that as time under irradiation continues, electrons will drift deeper and deeper into the dielectric so that the field profile will very slowly move towards that shown by figure 5. As this drift occurs, the probability that a "weak spot" near the surface finds itself in a high field region slowly increases. Once this weak spot is found by the drifting field front, a discharge occurs and almost instantly the field strength is significantly increased in the dielectric to deeper depths and perhaps many new weak spots are found resulting in a flurry of pulses. Finally all the weak spots near the surface are discharged and pulsing ceases. This effect has not been reported formally but K. Balmain has indicated to me that the initial pulse takes a long time to occur in electron beam experiments but once it happens the remaining pulsing happens relatively soon.

If one evaluates eq. 6 for most of the published experiments it turns out that the electric field in the bulk of the dielectric beyond the electron penetration range significantly exceeds 10^5 V/cm. For example, many experiments were performed using 20 keV electrons on approximately 100 micron thick samples; this resulted in field strengths of approximately 2×10^6 V/cm. Reference 13 has calculations of electric fields in thin polymers. You are, I hope, wondering why I have neglected this large electric field which occurs in most of the dielectric. I neglect this big bulk field because it produces only very small electrical pulses (though it produces many pulses) which can not be monitored in this arrangement. The bulk pulses are similar to the pulses discussed under the section "Both Surfaces Grounded" below.

Meter Current, I, Floating Front Surface

The discharge pulse current I flowing in the meter (fig 2) depends on several variables such as front surface potential, surface area, and random fluctuations. Not every pulse causes the front surface potential to go nearly to ground potential (ref. 24). In general one finds that, (ref. 15):

a) discharge pulse time duration $\propto$ (surface area)$^{1/2}$

b) discharge pulse current $\propto$ (surface area)$^{1/2}$

c) total discharge coulombs $\propto$ surface area

These rules are for the conceptually simple cases where all other variables (other than surface area) such as dielectric constant, insulator thickness, and surface voltage, are held constant.

What happens if we change the other parameters? What is the physical process which causes these effects? Again the answers can be found in the streamer propagation process and its resulting plasma. Reference 15 argues that the scaling with the $\sqrt{area}$ result is due to a streamer propagation process because the streamers which propagate at a reasonably constant velocity (ref. 14) have lengths scaling as the linear dimension of the insulator which necessarily scales as the $\sqrt{area}$. In the addition, I argue that the total charge available is limited by the total volume of the streamer tunnels; and if every atom initially in the tunnel is singly ionized when it arrives in the vacuum space, there is a great deal of charge available to "ground" the front surface. Injecting an excess of charge of both signs into the vacuum space does not by itself _fully_ ground the front surface because a great deal of the plasma charge is shielded from the electric fields by the plasma itself. Instead, the injected plasma will spread out in the vacuum in a way which depends on its initial temperature, pressure, velocity, density and vacuum E fields and then scatter off the walls of the vacuum chamber, and the scattered components may also contribute to the "grounding" of the front surface. Injecting an excess of charge however does cause the surface potential to drop with a similar statistical distribution for any surface area and this will often happen because the tunnel volume varies nearly linearly with the surface area (tunnels tend to spread out in a fan shape under the entire surface which has been irradiated).

If one were to vary the sample thickness the concepts proposed here might predict the following relationships:

  d) pulse time duration $\propto$ (sample thickness)$^{-1/2}$

  e) pulse current $\propto$ (sample thickness)$^{-1/2}$

  f) total discharge coulombs $\propto$ (sample thickness)$^{-1}$.

Varying the surface voltage might cause these scaling laws:

  g) pulse time duration $\propto$ (surface voltage)$^{1/2}$ $f(v)$

  h) pulse current $\propto$ (surface voltage)$^{1/2}/f(v)$

  i) total discharge coulombs $\propto$ surface voltage.

And varying the dielectric constant might give us scaling laws like:

  j) pulse time duration $\propto \epsilon^{1/2}$

  k) pulse current $\propto \epsilon^{1/2}$

  l) total pulse charge $\propto \epsilon$

The function $f(V)$ is inserted to indicate that the separation of the positive and negative components of the plasma in the vacuum is strongly dependent on the electric field strength in the vacuum such that the rapidity of grounding of the surface is sensitive to this effect.

The actual meter current, $I(t)$, during the pulse depends directly on the collapse of the vacuum electric fields caused by the separation of the plasma particles. In these experiments no external voltage source is applied, it is only the electrostatic fields due to trapped space charge which force currents to flow; therefore the current flow is purely a displacement current since no real charge flows through a complete circuit. The plasma only responds to and collapses the electric field where the plasma resides; this occurs within the streamer tubes and in the vacuum space. Figure 8 describes the geometry.

Consider the one dimensional case where plasma in the form of uniform sheets of unipolar charge is injected between two grounded electrodes placed "a" meters apart. Let there be one positive sheet and one negative sheet each of the equal charge density, ρ coulombs/m^2, and spaced dx meters apart.

Then the image charge density induced in either electrode by the charge sheets is given by

$$\Delta \sigma = (\rho /a) \, dx. \tag{7}$$

Between the sheets the electric field created by the two sheets is given by

$$\Delta E = \rho / \epsilon \tag{8}$$

and is zero elsewhere.

Eq. 7 then becomes

$$\Delta \sigma = \frac{\epsilon \Delta E}{a} \, dx \tag{9}$$

and the current density required to generate the image charge is

$$\Delta I = \frac{d}{dt} \Delta \sigma = \epsilon \frac{d}{dt} \ (\Delta E \, dx/a) \tag{10}$$

Returning to the problem of excess plasma generated in a vacuum between biased electrodes we can apply eq. 10 by assuming that many sheets are injected throughout the vacuum which changes E everywhere in the vacuum. Linear superposition of electric fields holds in a vacuum so we can generalize eq. 10 to

$$\Sigma \Delta I = I(t) = \frac{\epsilon}{a} \int_0^a \frac{\partial E}{\partial t} dx \tag{11}$$

where $E = E(x,t)$ is a continuous function over space and time.

Let me postulate that the dominant effect in a discharging dielectric with one surface floating is the injection of a net neutral plasma into the vacuum. The plasma spreads out in the vacuum to neutralize the existing vacuum electric fields and the meter current I is given by eq. 11. Because we do not know the dynamics of this plasma injection and spreading we can't a-priori calculate $I(t)$, but we can predict the integral over the pulse duration:

$$Q = A \int I(t)\, dt \tag{12}$$

where A is the surface area of the dielectric. It turns out that in most experiments Q was nearly equal in magnitude and opposite in polarity to the "so called" surface charge residing on the irradiated insulator surface (actually residing in the bulk typically within 5 microns of the surface). This is equivalent to the statement that the plasma fully collapsed the electric field in the vacuum.

The amount of charge injected by streamers will be discussed later; this should be a variable number depending on the total irradiation fluence as well as on geometrical factors.

Pulses in Dielectrics with Both Sides Grounded

An extensive set of experiments (ref 3) have been performed in the geometry of figure 2 where dielectric fills the entire space between the electrodes. In this case only small pulses were seen and negligible charge was removed from the dielectric during the pulsing process. Tunnels are seen in such dielectrics after irradiation and are probably similar to those described above. In this set of experiments thick samples were used (circa 5 mm) under high energy (circa 500 keV) electron bombardment. However, the experimental results can all be explained by the same streamer phenomena as in the floating surface case.

The tree which results from the streamer connects to an electrode at one point and branches out into the bulk of the dielectric. Again the basic principle is that the streamer is a dense plasma which can collapse the electric field in the volume occupied by the plasma. However, the streamer follows tortuous paths and the calculation of outer currents is complicated beyond the simple concepts engendered in eqs 7-12. There can be regions in the dielectric which initially have zero electrostatic field strength but once a streamer has propagated some distance it can introduce significant space charge density into these originally zero field strength regions. In otherwords, a streamer must initiate in a high field region but once it has traveled some distance it can create a high local field strength near its tip in a region which initially had zero electric field. In fact, the bulk of the "tree branches" in radiation induced trees occur in intially low field regions of the dielectric. In the process of forming trees, streamers can produce large current flows in relation to the current which would be required to eliminate the electrostatic fields initially present in the volume of material penetrated by the streamer. Equation 11 cannot be applied alone to this problem.

For the region of the streamer which runs parallel to the electrostatic fields eq. 11 is valid but one must remember that the cross sectional area, A, in eq. 12 is typically a square micron so that the total charge Q is very small.

In the experiments, typical fields were 10^5 V/cm so that eq. 12 provides the following estimate of charge pulse magnitude due to the portion of the square micron streamer parallel to E.

$$Q = A \int I(t)\, dt = (A\, \varepsilon/a) \int_0^a \int_0^t \frac{dE}{dt}\, dx'\, dt \tag{12a}$$

Assuming that the field E is fully collapsed in some short time T, assuming that E is roughly constant and assuming the streamer passes nearly all the way through the sample, we get:

$$Q = A \varepsilon E$$
$$A = 10^{-12} \text{ meter }^2$$
$$\varepsilon = 10^{-11} \text{ farads/meter}$$
$$E = 10^8 \text{ volts/meter}$$
$$Q = 10^{-15} \text{ coulombs}$$

For the region of streamer perpendicular to the initial E field the streamer propagates most commonly because of high charge density and effectively conducts this charge to the electrode. The argument is essentially that the streamer forms the path of a line integral over which every element has nearly zero E field, ie:

$$E(\ell) = 0 \quad \text{everywhere along path } \ell,$$

$$\frac{dE}{d\ell} = 0 = \rho$$

in analogy with Gauss' law. This condition is met when there is no net charge in the streamer tube (tunnel) which implies that the streamer removed the net charge originally along the streamer length.

The net charge injected by irradiation is in the range 10^0 to 10^4 coulombs/m^3 (refs 13,27) so that per cm of tunnel length the following charge is removed:

$$\text{for } 10^0 \text{ Coul/m}^3, \quad Q/cm = 10^{-12} \text{ m}^2 * 10^{-2} m/cm * 10^0 \text{ Coul/m}^3$$

$$= 10^{-14} \text{ coul/cm}$$

$$\text{for } 10^4 \text{ coul/m}^3, \quad Q/cm = 10^{-10} \text{ coul/cm}$$

Of course these estimates again assume a tunnel cross section of a square micron.

One more component of meter current flows in the streamers which are antiparallel to the original static E field. This component is the collapse of the static E field across the streamer. Eqs 11 and 12 provide an estimate of this current contribution. Assume a 0.1 mm thick sample with an E field strength of 10^5 V/cm in the streamer region with 1 square micron streamer 1 cm long. In this case eq. 12 reduces to

$$Q = A \frac{\varepsilon}{a} E \Delta x = 10^{-16} \text{ coulombs/cm tunnel}$$

where $A = 10^{-6} \times 10^{-2}$ m^2, $a = .0001$ m, $\Delta x = 10^{-6}$ m.

The net result of this modeling is that for the kinds of tunnels seen in low dose rate tests (micron diameter, less than a meter total tunnel length) one would expect integrated current pulses to be measured less than a nanocoulomb when shorted electrodes are on both sides of the dielectric. This is in contrast to the floating front surface where the vacuum currents produce measured charge transfers exceeding a microcoulomb. The numbers which result from both the model and the assumptions are in agreement with the range of pulsing results seen in experiments.

The pulsing rates (pulses per unit time or per unit fluence) seen in the open front surface experiments are in rough agreement with the rates seen in fully grounded experiments (ref. 3, 28,29). This is further evidence that in both geometries the pulses have a common origin.

Pulse Energy for Floating Surface Case

Previous calculations have only estimated charge flow. For the radiated EM wave problem one needs an estimate of maximum pulse energy because the collapse of the E field radiates waves directly as well as causing image charge motions. Because the dynamics of the field collapse are not known to me, I cannot address the directly radiated EM wave intensity problem; it is certainly complex containing plasma oscillation components as well as resonant cavity ringing phenomena. But we can estimate the initial electrostatic energy available to be radiated.

Referring to figure 8 and assuming as usual that most of the trapped charge resides near the floating surface we find that most of the electrostatic energy resides in two fields. If V_o is the surface potential, then the energy stored per unit surface area in the dielectric is given by

$$\mathcal{E}_d = \epsilon V_o^2/2a \tag{13}$$

where a is the dielectric thickness, and the energy stored in the vacuum (per unit area) is

$$\mathcal{E}_v = \epsilon V_o^2/2b \tag{14}$$

where b is the distance through the vacuum to ground (or one debye length in the space plasma). Assuming that the sample dielectric constant is similar to vacuum, that the vacuum spacing b is 0.5 m and that the sample thickness is 10^{-4} m we find that

$$\frac{\mathcal{E}_d}{\mathcal{E}_v} = \frac{b}{a} = \frac{.5}{10^{-4}} = 5 \times 10^3 \gg 1. \tag{15}$$

However, the electrostatic energy within the dielectric is not discharged by a propagating streamer. Only the volume occupied by the streamer is discharged. If we let $\mathcal{E}'$ be the discharged electrostatic energy, then in the vacuum the total discharge energy is

$$\mathcal{E}'_v = \epsilon \text{ (Vacuum volume) } V_o^2/2b^2 \tag{16}$$

and for the streamer the total discharge energy is

$$\mathcal{E}'_d = \epsilon \text{ (Streamer volume) } V_o^2/2a^2 \tag{17}$$

Assuming a sample surface area of 10^{-2} m^2, a dielectric constant similar to vacuum, a streamer length of 1 meter with one square micron cross section we find

$$\frac{\mathcal{E}'_d}{\mathcal{E}'_v} = 4 \times 10^{-3} \ll 1. \tag{18}$$

Thus the discharge pulse energy is significantly smaller in the dielectric than in the vacuum for the typical irradiation geometries reported to date. Yet it is the plasma created in the dielectric which causes the relatively large energy dumps in the vacuum region of space.

It has been reported that the space shuttle tiles show no discharge pulses under monoenergetic irradiation but do pulse when irradiated with a broad spectrum (ref 30). This effect will also occur in space and, contrary to popular opinion of the moment, the effect proves that testing with monoenergetic beams is not necessarily a worst case test.

The cause for the effect has not been proven but I postulate the following cause. Early in the irradiation, before pulses begin, the surface comes to its equilibrium potential say 2 keV below the incident monoenergetic electron energy. Figure 4 describes a typical result where surface potential equilibrium occurred in 36 seconds (ref 13). The electric field at the front surface which can produce streamers that eject plasma into the vacuum will not penetrate beyond 0.1 micron. The rest of the dielectric beyond 0.1 micron will produce streamers which connect to the rear electrode, not to the vacuum. Balmain finds that he must wait long times for discharging to begin (ref. 29) even at his much higher dose rates. Such long times probably invalidate fig 4 conclusions because of trapped charged diffusion effects which would bring the high fields near the surface to deeper depths. It may be that 0.1 microns of material is unlikely to produce a streamer, it may require 1.0 microns or more of depth to allow a streamer to propagate. Thus in Balmains experiments he waits until diffusion has moved the charge centroid (where $E = 0$) to some depth perhaps 1 micron or more. At this point in time a streamer initiates and pulsing begins. But with a broad spectrum one doesn't have to wait, the high energy tail rapidly produces the deeper surface field penetration.

Figure 9 describes the quantitative approach for estimating the importance of the tail. The dielectric surface comes to a potential ϕ_e in space typically between 0 and -10 kV. The surface has a backscattered plus secondary electron yield curve (ref. 31) which, when folded with the space electron energy spectrum, produces a specific energy $\mathcal{E}_t$ determined by

$$I = \int_{\phi_e}^{\mathcal{E}_t} N(\mathcal{E}) \left[1 - \delta(\mathcal{E} - \phi_e) \right] d\mathcal{E} = 0 \tag{19}$$

where $N(\mathcal{E})$ is the space electron energy distribution. This is equivalent to saying that the net current to the sample by all electrons below $\mathcal{E}_t$ is zero. $\mathcal{E}_t$ will generally be >1 kV above the second crossover energy for most polymers and at energies above $\mathcal{E}_t$ the backemitted yield (figure 9) is roughly a constant. Typically in space the electron energy spectrum above $\mathcal{E}_t$ can be characterized by a function like

$$N(\mathcal{E} > \mathcal{E}_t) = N_0 \mathcal{E}^{-n}, \qquad n > 1 \tag{20}$$

and we can solve directly for I

$$I = \int_0^\infty N(\mathcal{E}) \left[1 - \delta(\mathcal{E} - \phi_e) \right] d\mathcal{E} = \int_t^\infty N(\mathcal{E}) \left[1 - \delta(\mathcal{E} - \phi_n) \right] d\mathcal{E}$$

$$I = \left[1 - \delta(\mathcal{E}_t) \right] N_0 \Big/ (n-1) \, \mathcal{E}_t^{n-1} \tag{21}$$

If we know the spectrum (such as eq. 20) we can determine $\mathcal{E}_{t}$ from eq 19 and by measuring I we can then determine the total incident current above $\mathcal{E}_{t}$ because all this current must go to the electrode. Now if $I > 10^{-12}$ A/cm^2 it is in principle capable of creating sufficient field strength over sufficient depth to produce streamers at the surface because the tail beyond $\mathcal{E}_{t}$ is depositing charge beyond 0.1 micron depth in sufficient quantities. The above mechanism is postulated to explain the shuttle tile results where monoenergetic electrons do not cause discharge but broad spectra do. The extensive polymer results where monoenergetic electrons cause pulsing but only after inordinate time delays is postulated to be due to slow carrier drift (typically up to 5 microns as reported in the literature) before deep trapping. The basic reason for the difference is, again, postulated to be due to a streamer phenomena ie: there is some minimum dielectric thickness, probably field dependent, required for the generation of these (non thermal type) streamers.

EXPERIMENTAL PREDICTIONS

Several new experimental results can be predicted from this modeling. These experiments could be a check on the model.

Containment of Streamer

The streamers reported by Balmain et. al. are almost surface streamers. At first look they appear similar to the bulk streamers which occur at deeper depths when irradiated by higher energy (100 keV - 10 MeV) electrons in air. However, I think both streamers are produced by electric fields as the driving force. If one were to perform Balmain's irradiations with a very thin (say 500 Å Al) front grounded electrode then the streamers would occur mostly at 5 micron depth and be similar to the trees generated by higher energy irradiations. The resulting tree would burst through the 500 Å electrode leaving a hole.

However, if one were to use a 2 mm thick electrode tightly clamped to the surface and irradiate with say MeV electrons, I predict that streamers still form but do not leave the sample. The streamer will re-solidify in its track. It might be visible as a tree of less crystallinity after the event. One could look at the edge of the sample for the flash of light to be sure that a streamer occurred. In my experiments with heavy electrodes, trees were never seen leaving the dielectric at the electrode, they were only seen at a gap or at the edge of the electrode.

It is often presumed that trees only originate at gaps, edges, or flaws. I feel they can originate elsewhere but of course prefer "high field" or "weak spot" regions associated with gaps, edges, or flaws. The experiment above using 500 Å Al electrodes should demonstrate that streamers also propagate to (or start at) an electrode interface and in this case will blow away the electrode at this point. I have seen this effect with carbon paint electrodes which are admitedly not very smooth and may have had a microcrack at the discharge site.

Experimental Proof of Vacuum Field Collapse Thesis

I propose irradiating a sample in the geometry of figure 8 while holding the irradiated surface at ground potential (either using VUV light to photoemit electrons from the surface or using a thin grounded metalization). This will make all pulses seen by meter I very small. Then one can simulate the floating surface field in the vacuum by biasing the lower electrode in fig. 8 to +10 kV through a very high

impedance. This will cause the pulses to become the large type just as if the front surface had been charged to -10 kV.

In addition I propose biasing the lower electrode with a very low impedance. This will allow one to collect much more of the plasma charge which the streamer injects into the vacuum. Or, at least, it allows more of the charge to be separated and to register as a current on the meter. Thus, in this low impedance case charge collected will not scale with surface area but will scale with streamer volume. In such experiment one must be sure to expose the upper electrode to the vacuum plasma in order to collect the positive plasma charge, otherwise the plasma will just clamp the surface potential to the lower electrode and the charge collected will, again, scale with surface area.

Streamer Volume/Plasma Charge Thesis

One can irradiate a sample in a chamber which also has two extra electrodes near the front of the dielectric. These electrodes can be biased at high voltage and with low impedance so that a fraction of the plasma charge will be collected on the electrodes and appear as a current in a meter connecting the two electrodes (one electrode is biased positive and one negative). The integrated current is then proportional to the amount of plasma injected into the vacuum.

One irradiates until the first pulse occurs and immediately turns off the beam. The total streamer volume is then measured (I'll let you figure out how) and compared to the pulse charge measured. This is repeated using differing dose rates, beam energies and sample sizes until a large distribution in pulse sizes is generated. The streamer volume as measured by the remaining tree volume should scale with the pulse charge. (Of course this pressumes that the plasma charge collection efficiency is a monotonic function of the streamer size.)

This experiment is also a measure of the limit to pulse size. The ultimate pulse current magnitude is limited by the total free charge in the streamer plasma. In the scaling experiments reported to date I think it is true that the streamer injected free charge far exceeding the charge required to drop the insulator surface to ground. In addition, experiments with radiation induced lichtenberg trees indicate that they usually spread out to encompass most of the solid so that the total streamer volume will scale roughly as the total irradiated surface area. It will also scale with the static field strength just prior to streamer formation because the trees are known to put on more branches when the discharge occurs at higher field strength.

Coupling to Biased Spacecraft Elements

It is well known that electromagnetic coupling will occur to other elements on a spacecraft when a discharge occurs. The plasma injected into the vacuum creates another coupling mechanism. Other elements with bias and near the discharge site will interact directly with the plasma. This mechanism could be more important than direct EM coupling. Experiments on this phenomenon are obviously specific to the spacecraft application but they can be a-priori modeled since experiments B and C above provide the basic information for modeling this phenomenon.

Pulse Rate versus Dose Rate

It is often thought that the pulse rate relates to the dose rate. In experimental tests this is roughly true as long as the sample continues pulsing. However, the thought is contradicted by the fact that all pulsing stops after some time (for pure polymers only, fiber filled materials can pulse virtually forever, refs 3, 28, 30).

A better interpretation would be similar to the common high voltage capacitor pre-breakdown pulse explanation. In this case, if one first applies 10^5 V/cm to a dielectric small pulses are seen which eventually stop. Presumably the weakest spots have been relieved. Raising the field to 2 X 10^5 V/cm introduced more pulsing which also stops, presumably relieving more weak spots. In the case of radiation, a higher dose rate simply causes the high field strengths to evolve more rapidly but once equilibrium fields are attained pulsing will soon stop.

Pulses Caused by Changing Spectra

After an irradiation has progressed to electric field equilibrium and pulsing appears to have stopped, further pulsing is only occasional. However, a change in radiation energy spectrum will cause a relatively rapid redistribution of electric field strength. This redistribution can cause new weak spots to find themselves in a high field region and pulsing can begin again. Such an effect has been seen (ref. 28).

Do Punchthrough Breakdowns Occur?

Whenever insulators are irradiated in air (the air ions hold the surface at ground potential) the resulting tree exits from only one surface; no punchthrough occurs. This happens for good reason; the electric field distribution will not propagate a streamer all the way through the insulator. The streamer stops propagating when the field at its tip goes to zero (figs. 4 and 5). Given a constant spectrum it is unlikely that conditions can be created to get a streamer all the way through the insulator by normal streamer propagation mechanisms.

However, if one streamer has been formed and the spectrum changes then a new streamer may occur and intersect the earlier streamer's hollow tunnels. The force of high pressure then may drive the new streamer through the old tunnels and seemingly penetrate through the sample. This occurrence appears to me to be very infrequent.

On the other hand, if one looks at figure 4 it is possible for streamers to occur at the rear electrode and propagate to within 0.1 micron of the front surface. In this event it may be that the pressure in the confined streamer is enough to blow off the 0.1 micron layer at some point and effectively propagate the streamer through the entire insulator. Since I don't know the pressure developed in the streamer nor do I know the dynamics of crater blowoff, I can't discuss the constraints on this process.

REFERENCES

1. J. J. O'Dwyer, The Theory of Electrical Conduction and Breakdown in Solid Dielectrics, Clarendon Press, Oxford, 1973.

501

2. P. Rudenstein, IEEE Trans. Elec. Ins. EI-15, 225 (1980).

3. A. R. Frederickson, IEEE Trans. Elec. Ins. EI-18, 337 (June 1983).

4. A. R. Fredrickson, Proceedings Xth International Symposium on Discharge and Electrical Insulation in Vacuum, 395 (1982), IEEE Catalog #82CH1826-7.

5. B. L. Beers et. al. IEEE Trans. Nuc. Sci. NS-28 (6), 4529 (Dec 81).

6. D. A. Berkley, J. Appl. Phy. 50, 3447 (1979).

7. A. R. Frederickson, IEEE Trans. Nuc. Sci. NS-22, No. 6, 2556 (Dec 1975). Also see: "Radiation Induced Electrical Current and Voltage in Dielectric Structures." AFCRL-TR-74-0582, Nov. 1974. Available from National Technical Information Service.

8. K. Labonte, IEEE Trans. Nuc. Sci. NS-29, 1650 (1982).

9. G. H. Sessler et. al., IEEE Trans. Nuc. Sci. NS-29, 1644 (Dec 82).

10. Bernhard Gross and Kenneth A. Wright, Phys. Rev. 114, No. 3, 725 (May 1, 1959)

11. B. Gross, Topics in Appl. Phys. 33, "Electrets", 217-84.

12. J. Pigneret and H. Stroback, IEEE Trans. Nuc. Sci. NS23, No. 6, 1886 (Dec 76).

13. A. R. Frederickson and S. Woolf, IEEE Trans. Nuc. Sci. NS 29, 2004 (Dec 82).

14. K. G. Balmain, et. al., IEEE Trans. Nuc. Sci. NS 29 1615 (Dec 82).

15. Balmain, K. G. and Dubois, G. R., IEEE Trans. Nuc. Sci. NS26 (No. 6), 5146 (Dec 79).

16. Gross, Bernhard, Phys. Rev. 107 (No. 2), 368 (July 15, 1957).

17. Hazelton R. C., Churchill, R. J., and Yadlowski, E. J., IEEE Trans. Nuc. Sci. NS 26, 5141 (Dec 79).

18. Ashley, J. C., Radiation Research 90, 433 (1982).

19. Whipple, E. C., Reports on Progress in Physics 44, 1197-1250 (1981).

20. Verdin, Derek, "Electrostatic Discharging Behavior of Kapton Irradiated with Electrons", NASA CP-2182, AFGL-TR-81-0270, pg 96 Spacecraft Charging Technology 1980 (NTIS AD/A114426).

21. Passenheim, B. C. et. al., IEEE Trans. Nuc. Sci NS-29, No. 6, 1594 (Dec 82)

22. Yadlowski, E. J., Hazelton, R. C., and Churchill, R. J., IEEE Trans. Nuc. Sci. NS 27, No. 6, 1765 (Dec 80)

23. Flanagan T. M. et. al., IEEE Trans. Nuc. Sci. NS 26, No. 6, 5134 (Dec. 79)

24. Stevens, N. J. et. al., "Testing of Typical Spacecraft Materials in a Simulated Substorm Environment" AFGL-TR-77-0051, NASA TMX-73537, page 431 in Proceedings of the Spacecraft Charging Technology Conference Feb 77. NTIS AD/A045 459

25. Staskus, J. V., and Berkopec, F. D., "Test Results for Electron Beam Charging of Flexible Insulators and Composites" NASA CP-2071, AFGL-TR-79-0082 Spacecraft Charging Technology - 1978, page 457 (1979) NTIS AD/A084626

26. Yadlowsky, E. J., Hazelton, R.C. and Churchill, R. J., ibid, p. 632.

27. Frederickson, A.R., AIAA Progress in Astronautics and Aeronautics 71, 386 (1980).

28. Frederickson, A. R., "Bulk Charging and Breakdown in Electron-Irradiated Polymers", Spacecraft Charging Technology 1980, NASA-CP-2182, AFGL - TR-810270, P. 33 (1981) (NTIS AD/A114426)

29. Balmain, K. G. and Hirt, W., Ibid p. 115.

30. Frederickson, A. R., and Chesley, A. L., IEEE Trans. Nuc. Sci NS-30, (Dec. 1983)

31. Burke, E. A., IEEE Trans. Nuc. Sci. NS 27, 1760 (Dec. 1980)
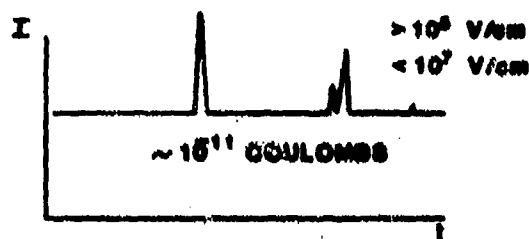
Figure 1. Pictorial of current to the electrodes of a dielectric filled capacitor
under constant dc bias. The non-zero background current is due to dark conduct-
ivity in the dielectric. The pulses are called prebreakdown events and usually
occur at fields of 10^5 V/cm or higher. Pulse sizes vary but are small, commonly
of order picocoulombs.
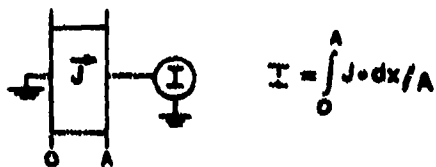
Figure 2. The measured current in a wire connecting two electrodes is the spatial
integral of the currents in the space between the two electrodes. The distance
between the electrodes is "A" in this figure.
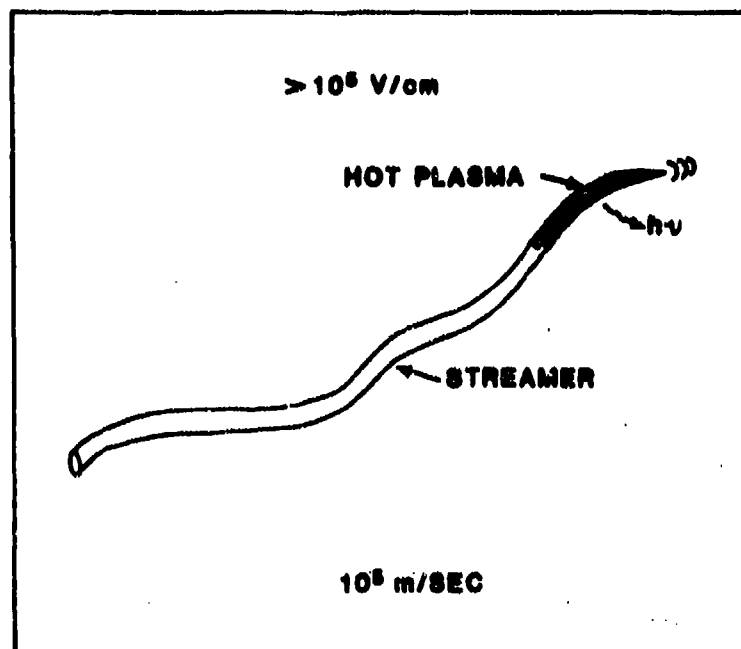
Figure 3. Once a streamer forms in the dielectric the streamer tip propages parallel to the E field at 10^5 m/sec. The streamer probably starts at or near the surface.
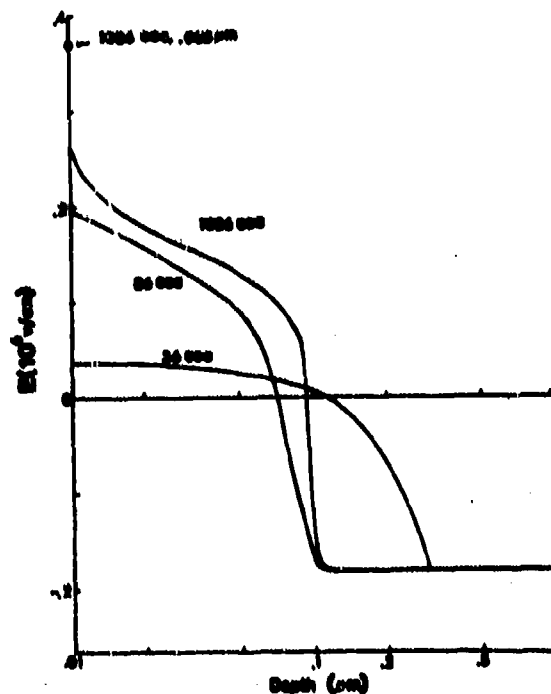
Figure 4. Calculated electric field strengths versus depth from the surface of
mylar irradiated by 10 keV electrons at 10^{-9} A/cm^2. The irradiated front
surface of the 1 mm thick mylar is floating while the rear surface is grounded.
The irradiation begins at 0 seconds. It is important to note that these results
are obtained under the assumption that radiation generated charge carries do
not drift beyond 100 angstroms which is known to be incorrect. However, the
drift rate and the distance travelled before deep trapping is not well known
but 5 micron drifts have been seen in ten minute experiments. Such effects
would cause these E fields to become larger while the depth at which E=0 slowly
drifts to deeper depths, perhaps a few microns.
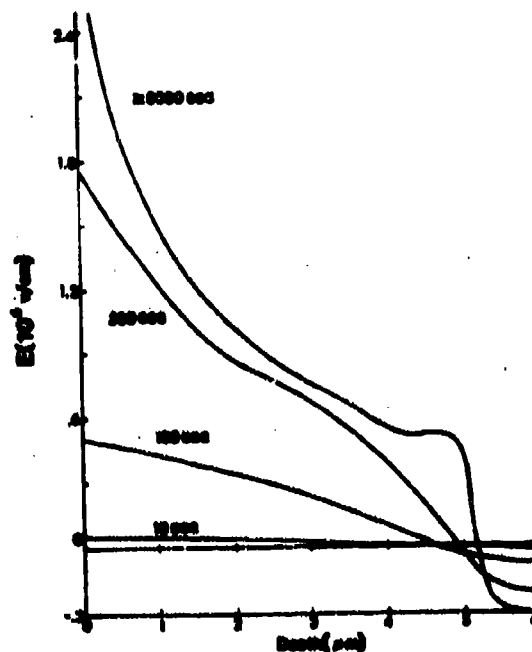
Figure 5. Calculated electric field profile in 25 micron thick mylar with both
surfaces grounded. The front surface (zero depth) is irradiated by 20 keV
electrons beginning at zero seconds. Increasing the thickness of the mylar
would not change the results at depths between 0 and 5 microns.
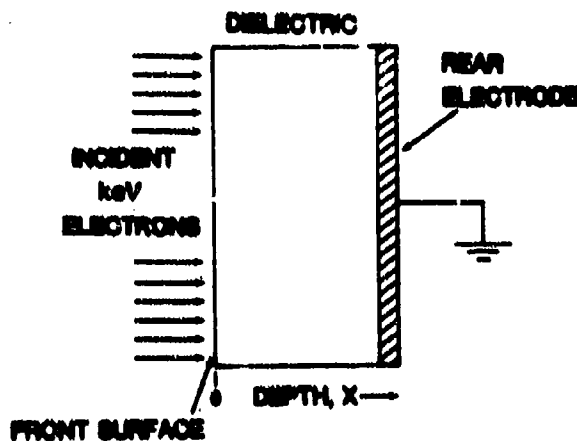
Figure 6. Typical irradiation geometry. This simple structure is inside a metallic
vacuum chamber. The front surface can be left floating or it can be grounded
by application of a very thin conductive coating.
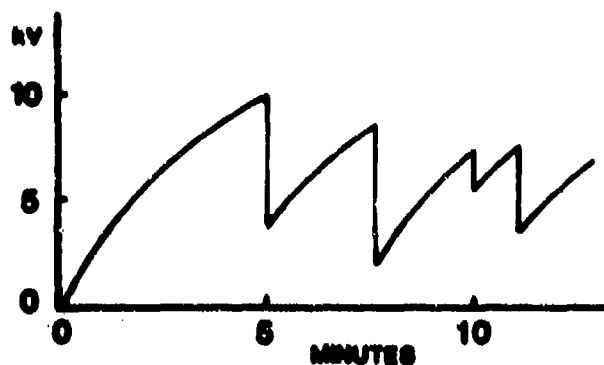
Figure 7. Floating front surface potential as a function of time during irradiation as described in figure 6. The precipitous drops in potential are due to discharges. This is a typical (but not a particular experiment) result but other results have been observed also, including for example no discharges.

$$I \Rightarrow \int \epsilon \frac{\partial E}{\partial t} dV$$

VOLUME
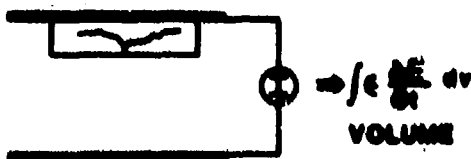
Figure 8. Meter currents resulting from a discharge in which actual charged particles do not reach the electrode. The electric field change is responsible for the metered current. Since we can't know the charged particle trajectories, we must determine I from this displacement current alone. Here, V is volume. We can make an estimate of the total change in E and the volume in which it ocurs even though dE/dt is indeterminate.
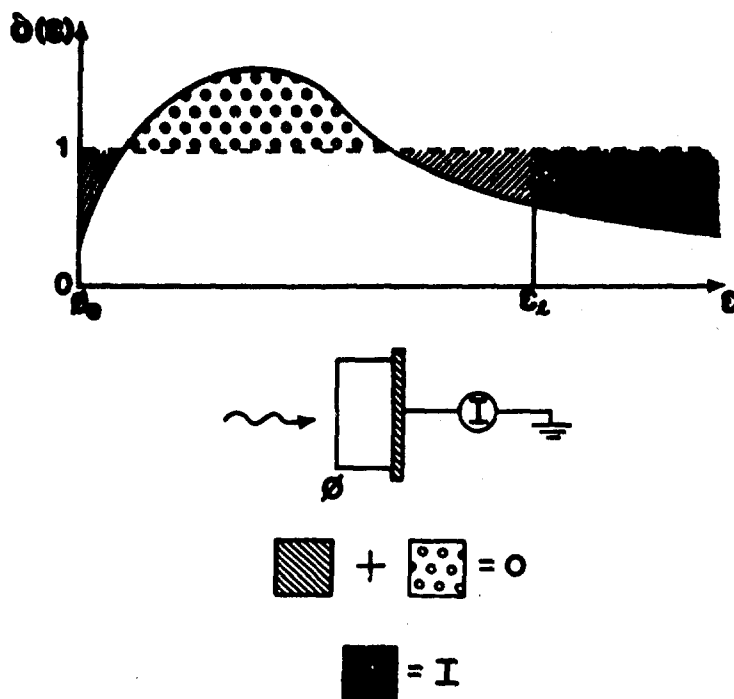
Figure 9. Measured rear electrode current at late times in a long irradiation by a broad energy spectrum. Øe is the equilibrium front surface potential. E_ℓ is the electron energy below which all incoming electrons produce no net meter current due to back emitted electron effects. $\delta(\varepsilon)$ is the back emitted current for a current of incident electrons at initial energy ε. ε_ℓ is usually a few keV above Øe. This figure depicts why the simplified solution in eq. 21 is a good approximation since δ is nearly constant above ε_ℓ.

DISCHARGE CHARACTERISTICS OF DIELECTRIC MATERIALS EXAMINED IN MONO-, DUAL-, AND SPECTRAL ENERGY ELECTRON CHARGING ENVIRONMENTS*

P. Coakley, M. Treadway, N. Wild, and B. Kitterer
Jaycor
San Diego, California 92138

1. INTRODUCTION

In an effort to explain the effects of mid-energy electrons (25 to 100 keV) on the charge and discharge characteristics of spacecraft dielectric materials and expand the data base from which basic discharge models can be formulated, thin dielectric materials were exposed to low- (1 to 25 keV), mid- (25 to 100 keV), combined low- and mid-, and spectral- (1 to 100 keV) energy electron environments. This effort has produced three important results. First, it has determined electron environments that lead to dielectric discharges at potentials less negative than -5 kV. Second, this effort has identified two types of discharges that appear to dominate the kinds of discharges seen: those with peak currents, $I \gg 10$ A and pulse widths, $\tau > 300$ ns, and those with $I < 5$ A and $\tau < 20$ ns. Third, this effort has shown that, for the thin dielectric materials tested, the worst-case discharges observed in the various environments are similar.

Previous laboratory experiments have focused on the effects of monenergetic low-energy electron charging and discharging of various spacecraft dielectric materials (Ref. 1). These experiments showed that, for samples with electrically-grounded substrates, discharges occurred only when surface potentials exceeded -5 kV. The discharges blew off more than 30% of the stored charge (Ref. 2) and the pulse widths of the discharge currents scaled in size as the square root of the sample area (Ref. 3). The discharges brought the sample's surface potential down generally less negative than -5 kV. For samples comparable in area and thickness to the samples that we tested, the pulse amplitudes were much greater than 10 A and the pulse widths equaled or exceeded 300 ns. These laboratory data are in apparent disagreement with satellite data that indicate for satellites in geosynchronous altitude environments, discharges occur when surface potentials are less than -2 kV (Refs. 4 and 5). Furthermore, data from ATS5 and ATS6 indicate that discharges occur in bunches and that as many as 30 discharge events have occurred in a single hour (Ref. 6). This latter observation implies that discharges on satellites may not cleanse the entire surface of stored charge and perhaps occur as small localized events.

This paper discusses the results of our monenergetic, dual-energy and spectrum-energy electron tests performed on seven dielectric samples: Teflon, Optical Solar Reflector (OSR), Alphaquartz, Kapton, perforated Kapton, Mylar, and a "nude" Space Transportation System (STS) tile. Section 2 describes the experimental apparatus and electron simulation environment. Section 3 discusses the general trends found in the data, comparing the samples with each other with emphasis on the four electron environments: monoenergetic low-, monoenergetic mid-, dual-, and spectrum-energy electrons. Finally, in Section 4 we present conclusions.

2. EXPERIMENTAL APPARATUS AND ELECTRON SIMULATION ENVIRONMENT

The experiments were performed in a 1.3-m long, 1.3-m diameter vacuum chamber, shown in Figure 1. Thirty-cm diameter test samples were positioned 20 cm off the door at one end of the chamber, and two Kimball Physics monoenergetic-electron guns pointed toward the samples. Pressures in the test chamber during experimental tests measured in the mid 10^{-7} torr regime. The energy of one of the two guns ranged from 1 to 100 keV, whereas the range of the other gun went from 1 to 25 keV. The maximum current output of the two guns measured 400 µA. For sample exposure tests the beam current density measured in the plane of the test sample was generally held between 0.03 and 3 nA/cm^2. For monoenergetic exposure tests the beam of each gun was rastered over the entire sample end of the chamber using pairs of the Helmholtz coils driven with alternating currents at frequencies of 60 Hz horizontal and 103 Hz vertical. The rastered beams produced a time-averaged flux across the sample, uniform to within ±15% for electrons from the low-energy gun and to within ±7% for electrons from the mid-energy gun.

2.1 SPECTRAL SOURCE

Our electron spectral source used the two Kimball Physics electron guns and two high-voltage biased disc-shaped scattering foils. Each scattering foil consisted of several thicknesses of aluminum sheets, ranging in size from 0.04 mils to 2.0 mils thick, and configured as wedges to a pie. Monoenergetic electrons incident on a thin foil lose energy and intensity as they scatter through the foil, depending on the relative thickness of each aluminum scatterer. The average scattered electron energy $\langle E_s \rangle$ approximately equals the average energy lost, $dE/dx|_{E_0}$, times a foil thickness, ΔX, and subtracted from the incident electron energy E_0,

$$\langle E_s \rangle \approx E_0 - dE/dx|_{E_0} \cdot \Delta X . \tag{1}$$

The average scattered electron energy has nearly a linear dependence on foil thickness and a weak functional dependence on average energy lost [i.e., dE/dX depends weakly on E_0 (Ref. 7)]. The electron transmission intensity has a power series dependence on the foil thickness or incident electron energy. The thinner the foil or the higher the incident electron energy, then the greater the transmitted electron intensity.

By adding a high-voltage bias, V, to the scattering foil, one then has for the average scattered electron energy

$$\langle E_s \rangle \approx (E_0 + V) - (dE/dX|_{E_0+V}) \cdot \Delta X - V \tag{2}$$

or

$$\langle E_s \rangle \approx E_0 - (dE/dX|_{E_0+V}) \cdot \Delta X . \tag{3}$$

Any electrons incident on the scattering foil pick up an energy, V, when they hit the foil. With a total energy of $E_0 + V$ they scatter through the foil. They give up the added potential energy V (the last term in Eq. 2) when they pass close to any grounded surface, e.g., a test sample. Compared with the unbiased foil, the scattered electron energy changes by a small amount since it depends weakly on $dE/dX|_{E_0+V}$, whereas the scattered electron intensity becomes greatly enhanced.

This high-voltage bias technique makes an impact when one tries to produce 1- to 10-keV scattered electrons using an incident 16-keV electron beam and when trying to produce 12- to 30-keV scattered electrons using an incident 85-keV electron beam. Without high-voltage bias, it becomes next to impossible to produce a flux of scattered 1- to 5-keV electrons with an incident electron beam of 10 keV or above, due to the attenuation of the incident beam in the foil. We enhanced the flux by an order of magnitude when exposing a 0.22-mil foil with 16-keV electrons (comparing results with and without a 15-kV foil bias).

Figure 2 shows a graph of Spectrum 1, $dN/dE = const.$, that was produced using the high-voltage biased foil technique. The multiple curves at the bottom of the graph are the scattered electron spectra produced from each given foil thickness and area. There were 16-keV electrons incident on the 0.22-mil, 0.16-mil, 0.12-mil, and 0.06-mil foils (all with a +15-kV bias). The foils formed wedges of a pie through which the beam scattered. The guns generated 30 µA of 16-keV electrons and 40 µA of 85-keV electrons, and the foils scattered the electrons to a spectrum energy of 1 to 85 keV and a current of 3 µA. The resultant spectrum was measured using an electromagnetic electron spectrometer and is indicated by a dashed line on the graph. We generated Spectrum 2, $dN/dE \propto E^{-1}$, and Spectrum 3, $dN/dE \propto E^{-2}$, using this technique with different foil combinations.

Source electron diagnostics consisted of an electromagnetic spectrometer and an array of Faraday cups. The Faraday cups measured 4 cm deep and had an entrance aperture measuring 1.2 cm^2. The Faraday cups were positioned at eight points around the sample. If viewed from the gun end of the chamber the cups were located at 12 o'clock, 3 o'clock, 6 o'clock, and 9 o'clock. At each of the four dialed positions, one cup rested close to the sample and another near the edge of the back blowoff plate (see cross-sectional view in Fig. 1). The spectrometer was used to measure the electron energy distribution during spectral tests. Sample charge diagnostics included an electrostatic voltmeter (ESV; details of which may be found in Ref. 2). Discharge diagnostics consisted of a back blowoff plate, situated between the samples and the chamber door, a blowoff liner spanning the distance between the samples and the electron guns, and a substrate disc clamped to the dielectric samples. Figure 1 shows a side view of the diagnostics and Figure 3 shows a conceptual view. The blowoff liner, back plate, and substrate were electrically connected to ground using numerous resistors connected in parallel to form a low-inductance 1-Ω path to ground (twenty 20-Ω resistors for the blowoff liner, eighty-two 82-Ω resistors for the back blowoff plate and twelve 12-Ω resistors for the substrate). Electrons that blew off the sample produced negative current signals on the two blowoff diagnostics and produced a positive signal on the substrate.

The signals produced on the substrate and liners during a discharge event were monitored using Tektronix 7903 oscilloscopes with 7A19, 50-Ω impedance plug-ins. Data channels were time-tied. All the scopes were triggered simultaneously using a pulse sent from a fiducial generator and fan-out box. The fiducial generator was triggered only when discharge currents, as measured on the substrate, were greater than a preset value (generally selected between 0.02 and 0.5 A). A sample of a time-tied discharge event is shown in Figure 4. All graphs presented in this paper key on the substrate current trace.

3. GENERAL TRENDS IN THE DATA

This section discusses the charge and discharge properties that the dielectric samples as a unit exhibited in the four types of electron tests - monoenergetic low,

monoenergetic mid, dual, and spectrum. It compares the results obtained in each test in terms of sample surface potential, discharge amplitude, and time rate of change of a discharge. The samples consisted of 5 sheet dielectric samples - Teflon (5 mil); OSR (8 mil), Kapton (2 mil), perforated Kapton (5 mil), and Mylar (2 mil); and 2 porous dielectric samples - Alphaquartz and a "nude" STS (Space Transportation Systems) tile. The OSR sample was formed from an array of 20 cells and constituted a segmented dielectric sample and the perforated Kapton sample had a repeating hole pattern in the form of squares spaced every 0.9 cm. The "nude" STS tile had no thermal paint and since electrons of energy 100 keV or less cannot penetrate the thermal paint that exists on actual shuttle tile, the results should not be extrapolated to anticipated space shuttle environments.

3.1 LOW-ENERGY ELECTRON TEST RESULTS

Several interesting results were noted when exposing the seven samples to low-energy electrons. First, none of the samples discharged when exposed to electrons of energy 8 keV or less. Second, the nonporous samples exhibited two distinct types of discharges: (1) small discharges with $I < 5$ A and $\tau_{FWHM} < 20$ ns accompanied by no change in the sample surface potential, and (2) large discharges with $I \gg 10$ A and $\tau_{FWHM} > 300$ ns accompanied by a change in the samples's surface potential equal to or exceeding half the initial potential. Third, the porous samples exhibited only small discharges $I < 5$ A and $\tau_{FWHM} < 50$ ns. Fourth, the porous samples discharged with surface potentials at or less than -1.1 kV and the nonporous samples had to reach surface potentials exceeding -5.5 kV prior to discharge. Finally, all samples displayed a discharge equal to their worst-case discharge current when exposed to 25-keV electrons. Table 1 summarizes the worst-case discharge characteristics of the seven samples. Except for the Kapton sample the worst-case discharge amplitudes agree with results found in previous studies. The Kapton sample produced its few discharges only when exposed to 25-keV electrons at 16 nA/cm^2; otherwise, exposed to an electron flux of 1 nA/cm^2 the Kapton sample produced small discharges $I < 5$ A. All other samples could produce their worst-case discharges when exposed to electrons at fluxes of 1 nA/cm^2 or less.

As noted in the table, the perforated Kapton sample produced a larger discharge than the nonperforated Kapton sample. This result should be alarming; especially since the perforated Kapton sample was developed to ward off discharges better than the nonperforated Kapton sample. Moreover, Mulenberg and Robinson noted this discharge characteristic several years ago (Ref. 8). (These data reaffirm their findings.)

The Kapton samples displayed a general lack of ability to discharge. Published literature pertaining to Kapton testing in the laboratory misleads one into believing that all Kapton samples discharge [Verdin 1980 (Ref. 9), Balmain 1980 (Ref. 10), Balmain 1979 (Ref. 3), Adamo 1980 (Ref. 11)]. Every article speaks of large discharges observed on Kapton samples and only one article [Treadaway, et al., 1977 (Ref. 2)] mentions any difficulty in making a sample discharge. Balmain (Ref. 12) confirms the misrepresentation of the discharging ability of Kapton found in the literature. Balmain has acquired several samples of Kapton that refuse to discharge. Stevens (Ref. 13) has also come across numerous Kapton samples that will not discharge. In fact, in a recent experiment performed by Leung and Plamp (Ref. 14), after they failed to make their sample discharge by electron exposure alone, Leung enlisted the help of Stevens who in turn suggested that a hole be punched through the sample to help it to produce discharges (Ref. 15). The

experience of these researchers shows that there exist batches of Kapton that would make excellent spacecraft insulators because of their ability to ward off discharges.

3.2 MID-ENERGY ELECTRON TEST RESULTS

The general response of the samples was fairly insensitive to the energy of electrons, provided the electrons did not penetrate entirely through the sample (electrons greater than 80 keV could penetrate the 2-mil Kapton and 2-mil Mylar samples). Figures 5, 6, 7, and 8 summarize the discharge amplitude (two figures), I, rate of rise of the pulse, dI/dt, and surface potential prior to discharge, V_i, all as a function of incident-electron energy.

Pulse amplitudes on the OSR, Mylar, Alphaquartz, and STS tile show no dependence on incident-electron energy. Despite the fact that 100-keV electrons (50 keV for Mylar) bury themselves much deeper than 16-keV electrons, the samples produced a similar discharge at both extremes in energy. Even though the perforated Kapton and Teflon samples show a marked decrease in discharge amplitude at 80 keV and 100 keV, they too show little effect on pulse amplitude or shape from 15 keV to 75 keV despite the fact that for Kapton the practical range of 25-keV electrons is 8×10^{-4} cm and for 75-keV electrons it is 5.4×10^{-3} cm (6×10^{-4} cm and 4.4×10^{-3} cm for Teflon)(Ref. 7).

Figure 7 shows that the rate of rise of the pulse, dI/dt, is certainly independent of energy, and appears to be independent of sample. All samples except the Alphaquartz sample had dI/dt $\approx 5 \times 10^8$ A/s. The Alphaquartz sample had dI/dt $\approx 5 \times 10^6$ A/s. Large discharges and small discharges had similar dI/dt. Furthermore, visual observations made of the discharges on Teflon indicate that a bright flash from a localized spot can be associated with both types of discharges (where large discharges have a dimmer and very broad flash that covers the entire sample together with the bright localized arc). These observations may indicate that (1) a similar discharge process initiates both small and large discharges, and (2) the discharge process may be the same sample by sample.

Figure 8 shows the sample surface potential prior to discharge. Note that the predischarge surface potential remains the same or slightly increases for increasing electron energy. One would think that if the bulk electric field determines the potential at breakdown, then the closer the charge is buried to a grounded substrate, the lower the potential required to equal a given field and hence initiate a discharge. The data disagree with this simple model. Despite the difference between the practical range of 16-keV electrons (2.4×10^{-4} cm) and 100-keV electrons (6.4×10^{-3} cm) on the 2.16×10^{-2} cm thick OSR sample, the potential at discharge went from -6.5 kV for 16-keV exposure to -12 kV at 100-keV exposure (instead of something less negative than -6.5 kV). As a further note, the sheet dielectric materials of Mylar, Teflon, and Kapton had breakdown potentials close to 10^6 V/cm breakdown threshold electric field times the sample's thickness. The perforated Kapton and OSR sample produced discharges at potentials approximately one quarter of the bulk field threshold times sample thickness. Finally, the porous samples displayed discharges at very low potentials compared to their thickness and any supposed net threshold field.

3.3 COMBINED LOW- AND MID-ENERGY ELECTRON TEST RESULTS

Figures 6, 7, and 8 also summarize data obtained from combined energy electron exposure tests (see left-hand portions of the graphs).

515

The pulse amplitudes observed in the combined energy tests are smaller than the pulses found in monoenergetic tests. In fact, the small discharges, I < 5 A, observed in the monoenergetic tests appear identical to most discharges seen in the combined energy tests. These discharges have I < 5 A and τ_{FWHM} < 20 ns.

Despite the small pulse amplitude, Figure 7 shows that dI/dt for the combined-energy produced discharges remains near 10^8 A/s. Moreover, the discharges observed in this electron environment occurred when the samples had a much reduced surface potential compared to monoenergetic tests. The Teflon, perforated Kapton and STS tile produced discharges in all combined-energy electron environments, even when their surface potentials were as low as -1 kV (0 kV for the STS tile). The Mylar and OSR samples produced discharges when surface potentials were less negative than -5 kV, but required a structured potential surface with a variation of 1 kV or greater across the plane of the sample. The Teflon and perforated Kapton samples did not require any potential structuring in order to produce discharges. The Kapton and Alphaquartz samples did not discharge in a combined-energy electron environment when their surface potential was kept less negative than -5 kV.

A simple qualitative model can explain the reduced potentials at discharge for combined low- and mid-energy electron exposures compared to the discharge potentials with mid-energy electrons alone. Leung, et al. (Refs. 16 and 17) have demonstrated experimentally that the surface potential of a dielectric sample can be varied over a considerable range by irradiating with electrons of two energies. Moreover, they showed that the surface potential is a strong function of the secondary electron-emission properties of the test dielectric due to the low-energy incident electrons. Where only mid-energy electrons are used, the charge is stopped at some average depth, a fraction of its practical range, R_p, beneath the surface of the sample. An electric field, established between the buried charge and the sample substrate, increases as more charge is deposited. If the breakdown threshold electric field is exceeded at a critical point in the sample (not necessarily the bulk of the material), then a discharge will occur. The surface potential of the sample at such an instance reflects the electric field integrated over a line path from the substrate to the charge layer.

When low-energy electrons are combined with the mid-energy electrons, the trajectories of the mid-energy electrons will not be affected significantly so they will again be deposited at a depth R_p into the sample. However, as the surface potential increases due to the trapped electrons, the low-energy electrons will reach the second crossover for secondary electron emission from the surface. Thereafter, the low-energy electrons will emit more than one electron per incident electron and the surface of the sample will become positively charged. The electric field inside the dielectric will then consist of a positive field from the substrate to the trapped mid-energy electrons and a negative field from those trapped electrons to the sample surface. The surface potential will then be the line integral of these two fields. A discharge could occur if either of the two fields exceeds the threshold field at some critical point.

3.4 SPECTRAL-ENERGY TEST RESULTS

Figures 6, 7, and 8 also summarize spectral test discharge characteristics of the four samples tested (Teflon, OSR, Alphaquartz, and Kapton), this time on the right-hand side of the graph. Several important trends are noted in the figures.

a. The worst-case discharges observed in the spectral tests, particularly the dN/dE = const. (Spectrum 1), equals the worst-case discharges seen in monoenergetic tests.

b. The OSR and Teflon samples produced predominantly two types of discharges: large discharges with $I \gg 10$ A and $\tau_{FWHM} > 300$ ns, and small discharges with $I < 5$ A and $\tau_{FWHM} < 20$ ns.

c. A rarely seen mid-size discharge was observed and after close scrutiny of the monoenergetic test results we have concluded two things: (1) the mid-size discharges appeared in monoenergetic tests as well, and (2) the mid-size discharge is accompanied by a structured surface potential before discharge. For the Teflon sample, the mid-size discharge has a mid-size amplitude 5 A $< I < 100$ A and mid-size pulse width 20 ns $< \tau_{FWHM} < 300$ ns. Figures 9 and 10 summarize these data for the Teflon sample. Note that most discharges on Teflon are large or small, but that there are only a few discharges with pulse amplitudes between 5 and 100 A.

It is also interesting to note that Balmain's discharge area scaling laws (Ref. 18) may be applied here in order to infer the area of a discharge site. Balmain found three laws: $I \propto A^{1/2}$, $\tau_{FWHM} \propto A^{1/2}$, and $I/\tau_{FWHM} \propto$ const. (where A was the area of the sample and in this case represents the area of the discharge site). Assuming that the pulse duration is determined by the propagation time of an arc across the sample, i.e., $A = \pi(\tau V)^2$ where $V = \sqrt{I}/\tau$ is the discharge propagation velocity, Balmain found $V \sim 3 \times 10^7$ cm/s. Balmain's measured value for I/τ was 2.8×10^8 A/s. From the dashed line in Figure 10, values for I/τ are seen to span the range 7×10^7 to 7×10^8 A/s. This yields an average propagation speed of 3.5×10^7 cm/s. Thus, a 5-ns wide pulse would have an implied discharge site area of 0.1 cm^2. The rarely observed mid-size discharges would have discharge areas covering up to one half the sample's area, and the large discharge pulses, with $\tau_{FWHM} \sim 300$ ns, appear to cover nearly the entire surface area.

d. The substorm-like spectral tests, Spectrum 3 tests, produced discharges only on the Teflon sample. However, it kept all samples from charging more negatively than -5 kV. Thus, the effect of secondary electron emission is important in determining the sample's potential.

e. The Alphaquartz and Kapton samples exhibited the charge and discharge characteristics that they exhibited in all their monoenergetic tests. Both samples charged to only a few kV when exposed to electrons at fluxes less than 1 nA/cm^2, and both samples warded off any large discharges. If a material selection were based on these tests alone, the Kapton and Alphaquartz samples would make excellent spacecraft charge and discharge control materials.

4. CONCLUSIONS

a. For worst-case testing of satellite dielectrics, monoenergetic 25-keV electron beams should be sufficient to bound the amplitude and pulse width of discharges anticipated in both enhanced and natural space environments without significant over or understress.

b. Dual-energy and spectral-energy electron environments can generate sample discharges while maintaining low surface potentials. Low-energy electrons can cause enough secondary emission to keep the surface potential low while the mid-energy electrons deposit enough charge to produce discharges. This result should help

explain why and how low surface potentials can be measured at the time of discharge on operational satellites.

c. Two distinct types of discharges are noted: small discharges with small amplitude and pulse width ($I < 5$ A and $\tau < 20$ ns), and large discharges with large pulse widths ($I \gg 10$ A and $\tau > 300$ ns). The large discharges have been well characterized in previous studies. These discharges are accompanied with large changes in surface potential and act to cleanse the sample of stored charge. The small discharges have gone relatively unmentioned in previous work and appear to not change the sample's surface potential nor release much of the stored charge (much less than 0.1%). The small discharges may give way to the large discharges when the appropriate environmental conditions are met (namely surface potentials exceeding negative 5 kV).

d. For the thin dielectric samples that were tested, the Alphaquartz and nonperforated Kapton samples appear to be best suited to ward off large discharges. The samples produced only small narrow discharges when exposed to realistic fluxes (less than 0.3 nA/cm^2). A well documented data base found in the literature supports our observation that Alphquartz does not produce any charge-cleansing large discharges. The open literature, however, reports that Kapton produces large discharges. Under reexamination, though, many researchers confirm that it is sometimes impossible to produce large discharges on selected Kapton samples.

REFERENCES

1. For a review of the literature, see Spacecraft Charging Technology, 1977, 1978, and 1980, NASA Conference Publication, NASA TMX-73537, 2071, 2181, respectively. Also see December issue (No. 6) of the IEEE Trans. Nucl. Sci. for the last several years.

2. M. J. Treadaway, et al. "Effects of Laboratory Simulation Parameters on Spacecraft Dielectric Discharges," JAYCOR Report J200-79-155, July 1979.

3. K. G. Balmain and G. R. Dubois, "Surface Discharges on Teflon, Mylar, and Kapton," IEEE Trans. Nucl. Sci., NS-26, No. 6, December 1976, p. 5146.

4. P. Mizera, et al., "Spacecraft Charging in the Spring of 1981," Aerospace Report TDR-0081 (6508-05)-01, Sept. 30, 1981.

5. N. J. Stevens, "Analytical Modeling of Satellites in Geosynchronous Environment," Spacecraft Charging Technology, 1980, NASA Pub. 2182.

6. R. Shaw, et al., "Observations of Electrical Discharges Caused by Differential Satellite-Charging," Spacecraft Charging by Magnetospheric Plasmas, Alan Rosen, Ed., MIT Press, Mass., 1976., p. 61.

7. M. J. Berger and S. M. Seltzer, "Tables of Energy Loss and Ranges of Electrons and Positrons," NASA Report NASA-SP-3021, 1964.

8. A. Mulenberg and P. A. Robinson, Jr., "Conduction through Punctures in Metal-Backed Dielectrics," Spacecraft Charging Technology, AFGL-TR-81-0270, p. 342.

9. D. Verdin, "Electrostatic Discharging Behavior of Kapton Irradiated with Electrons," Spacecraft Charging Technology - 1980, AFGL-TR-81-0270, p. 96.

10. K. G. Balmain and W. Hirts, "Dielectric Surface Discharges: Effects of Combined Low-Energy and High-Energy Incident Electrons," Spacecraft Charging Technology - 1980, AFGL-TR-81-0270, p. 115.

11. R. C. Adamo and J. E. Nanevicz, "Preliminary Comparison of Material Charging Properties Using Single-Energy and Multienergy Electron Beams," Spacecraft Charging Technology - 1980, AFGL-TR-81-0270, p. 129.

12. K. Balmain, private communication, 1983.

13. N. J. Stevens, private communication, 1983.

14. P. Leung and G. Plamp, "Characteristics of RF Resulting from Dielectric Discharges," IEEE Trans. Nucl. Sci., NS-29, No. 6, December 1982, p. 1610.

15. P. Leung and G. Plamp, private communication, 1983.

16. M. S. Leung, et al., "Effects of Secondary Electron Emisssion of Charging," Spacecraft Charging Technology - 1980, NASA Pub. 2182.

17. P. F. Mizera, M. S. Leung, and H. K. A. Kan, Laboratory and Space Results from the SSPM Experiment, Aerospace Report No. TOR-0081 (6505-02)-3, July 15, 1981.

18. K. G. Balmain, "Scaling Laws and Edge Effects for Polymer Surface Discharges," Spacecraft Charging Technology - 1978, AFGL-TR-79-0082, p. 646.

Table 1. Characteristics of worst-case discharges

		OSR #04	Teflon #653	Perforated Kapton #638	Kapton #136	Mylar #139	Alphaquartz #904	STS tile #988
V_i(kV)	Potential prior to discharge	10.5	20	6.1	15	13.7	5.2	0
V_f(kV)	Potential following discharge	2	3.3	0.9	--	1.4	5.2	0
$\langle\Delta V\rangle$ (kV)	(V_i-V_f) average change in surface potential	8.5	16.7	5.2	--	12.3	0	--
I_{sub}(A)	Peak discharge current	70	300	100	12.5	425	0.3	0.35
τ_{FWHM}(ms)	Full-width at half-max. of I_{sub} vs. time	300	280	200	800	700	100	20
dI_{sub}/dt (A/s)	Peak change in current measured with respect to time	3.6×10^8	1×10^9	1×10^9	5×10^8	1.2×10^9	5×10^6	4×10^8
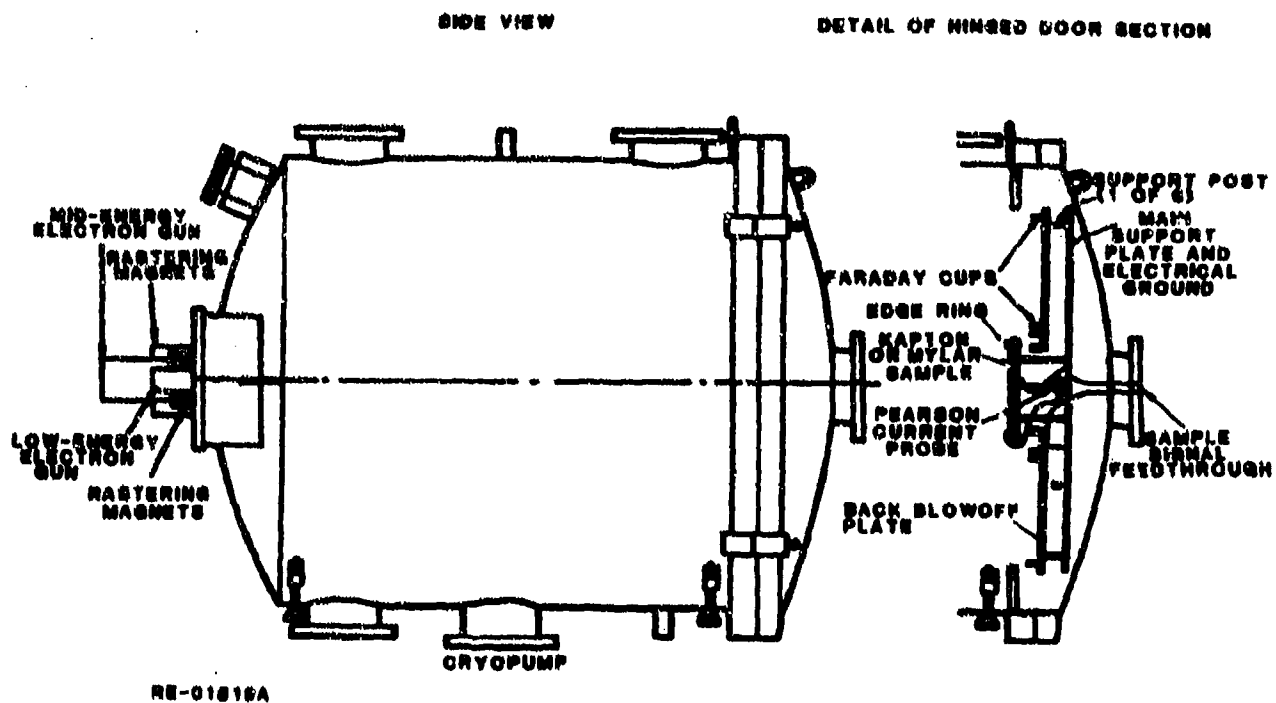
Figure 1. Diagram of the test configuration
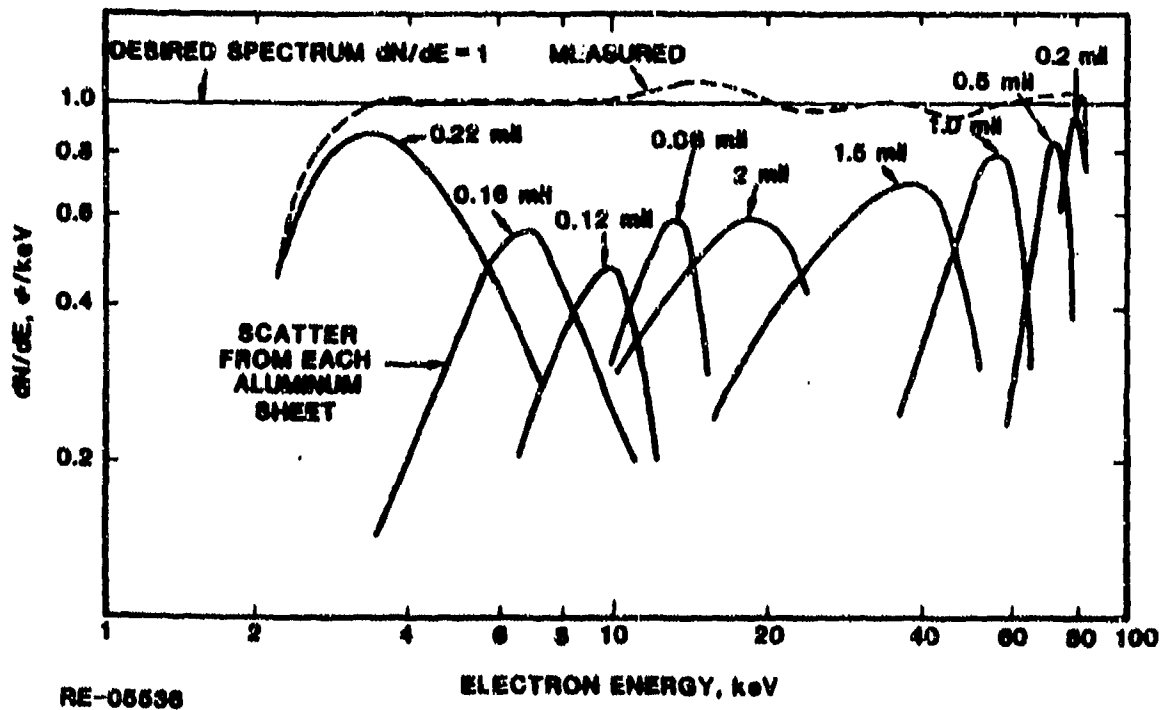
Figure 2. Energetic electron spectrum from 1 to 100 keV
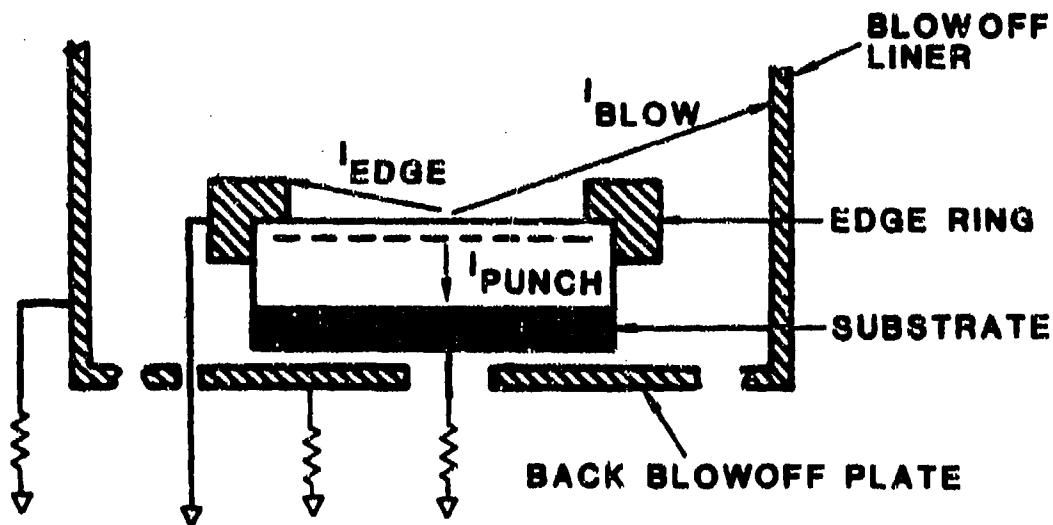
RE-02529B

Figure 3. Diagram of charge motion and discharge diagnostics

SUBSTRATE
500 A/DIV
200 ns/DIV

BACK BLOW-
OFF PLATE
500 A/DIV
200 ns/DIV

BLOWOFF LINER
20 A/DIV
200 ns/DIV

EDGE RING
100 A/DIV
200 ns/DIV

MYLAR SAMPLE SHOT 215
100 keV at 0.09 nA/cm^2
and 25 keV at 3.0 nA/cm^2

PEAK CURRENT SIGNAL OCCURRED
500 - 800 ns AFTER THE SCOPES
TRIGGERED
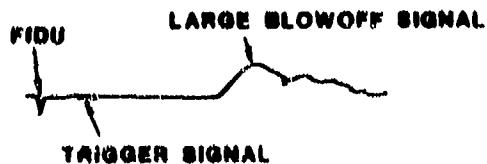
RE-04691

Figure 4. Time-tied discharge event on Mylar in combined-energy environment

WORST-CASE DISCHARGES
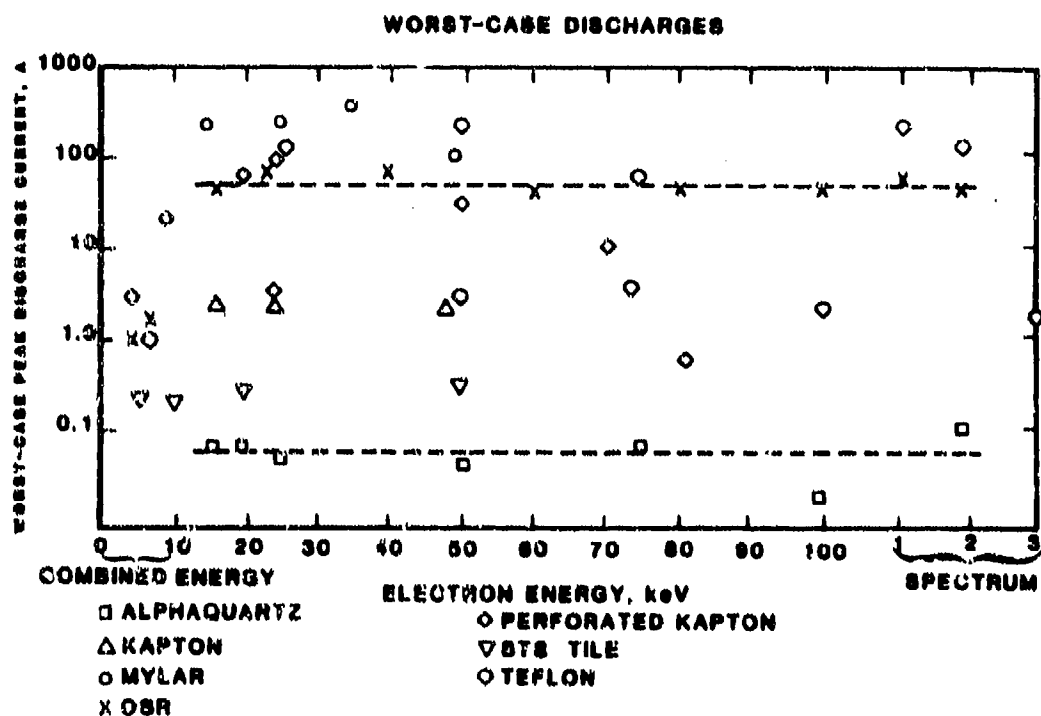
RE-05939

Figure 5. Worst-case discharges observed in the four testing environments
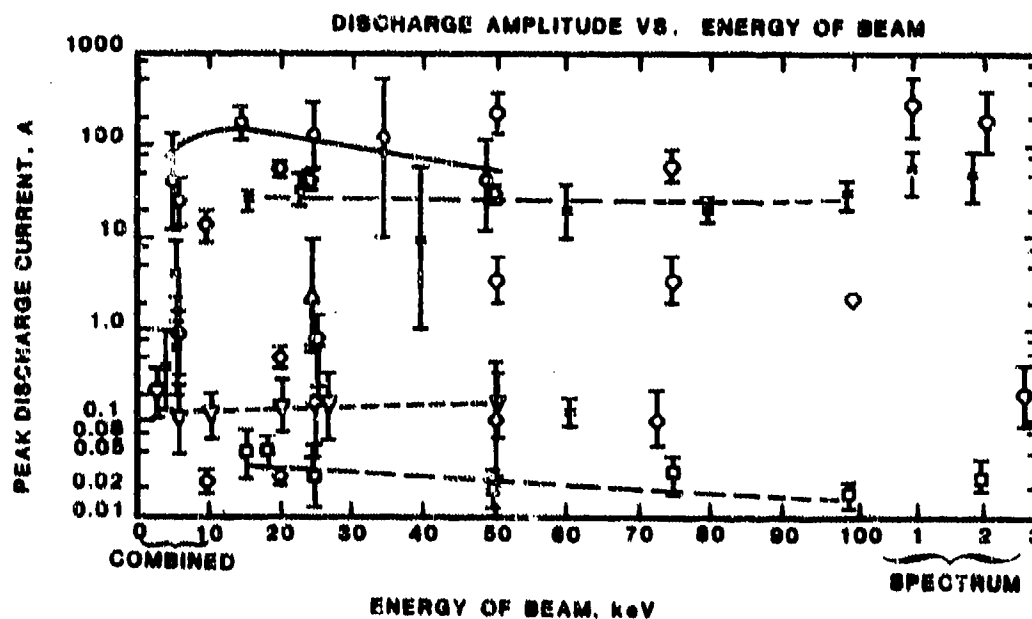
RE-04978A

Figure 6. Compilation of all data: peak discharge currents vs. electron energy
(same symbol legend as Figure 5)
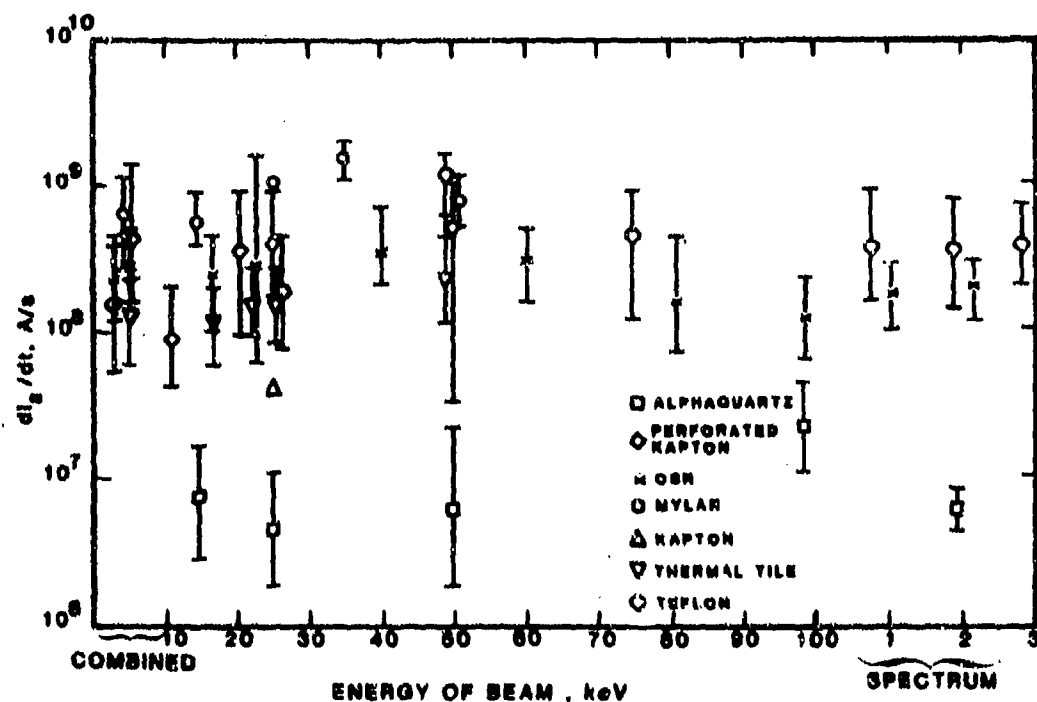
RE-04874A

**Figure 7. Compilation of all data: dI/dt vs. electron energy
(same symbol legend as Figure 5)**
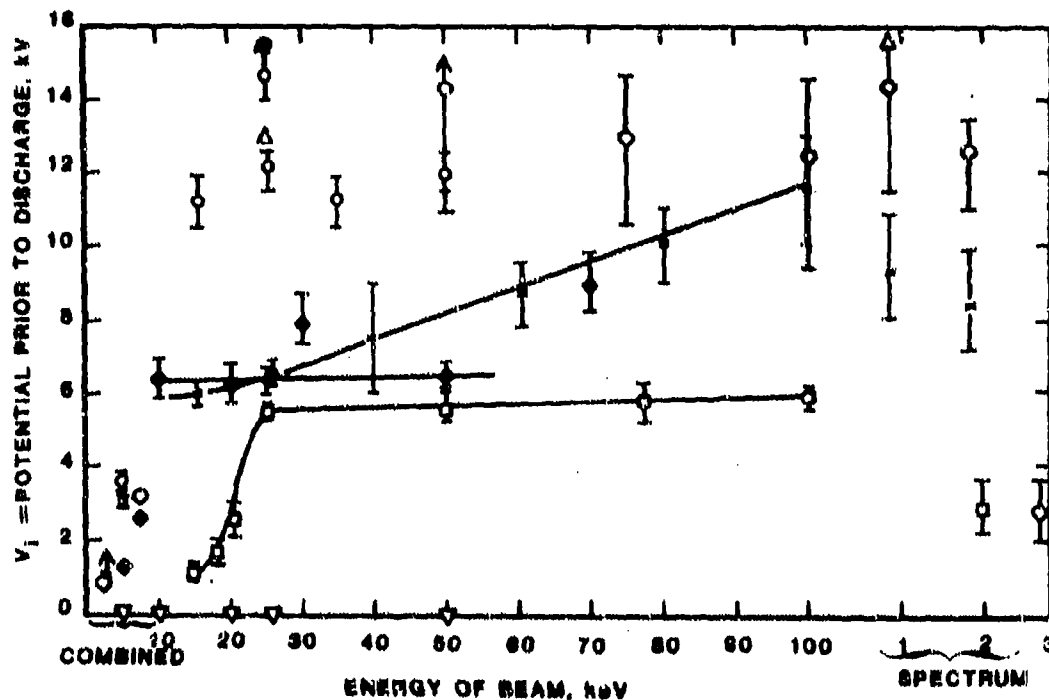
RE-04876A

**Figure 8. Compilation of all data: potential of sample prior to discharge
vs. electron energy (same symbol legend as in Figure 5)**

523

TEFLON SAMPLE 5 mil
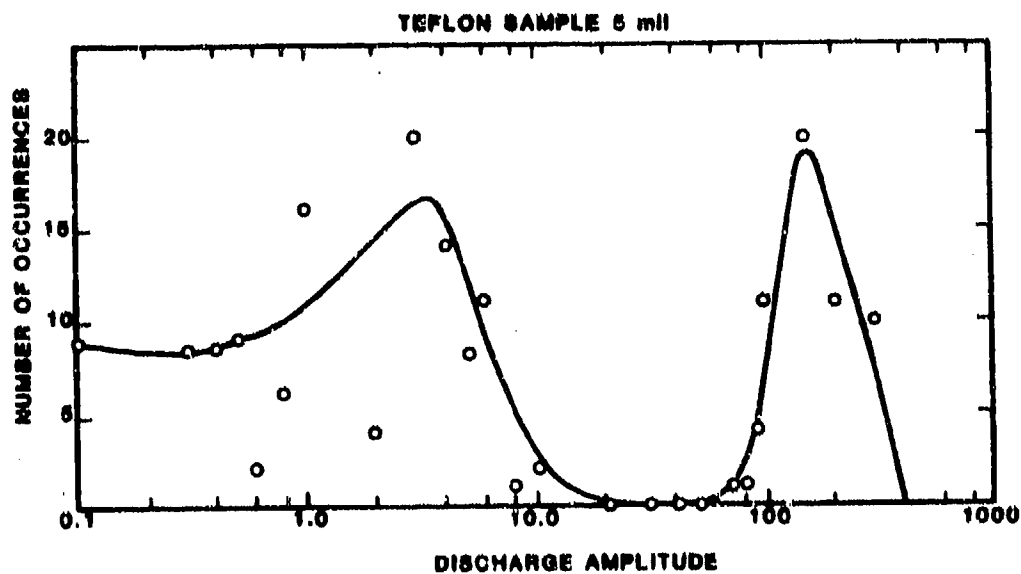
RE-05037

Figure 9. Number of discharge occurrences at a specific amplitude: depicts void of 10 to 100 A discharges

TEFLON SAMPLE 5 mil

RE-05036
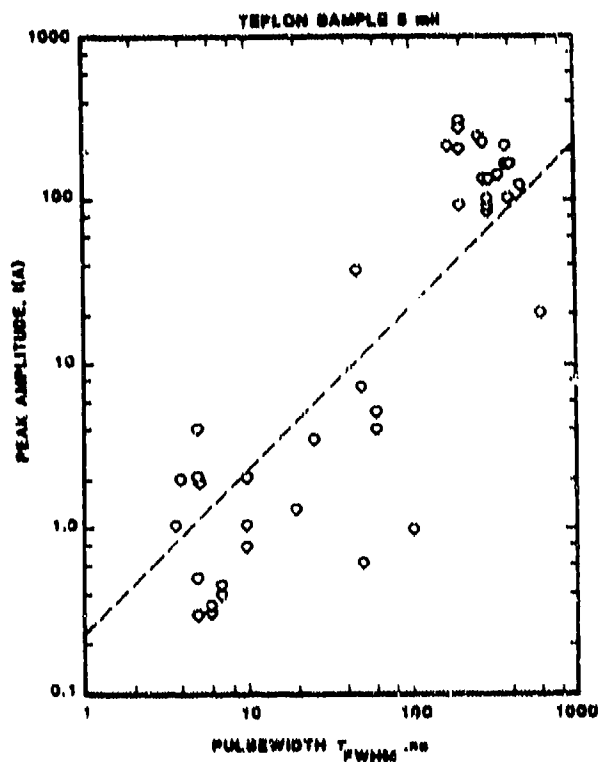
Figure 10. Plot of discharge pulse amplitude vs. pulse width showing a lack of 60 to 200 ns pulse widths

MASS SPECTRA OF NEUTRAL PARTICLES RELEASED DURING ELECTRICAL BREAKDOWN OF THIN POLYMER FILMS*

B. R. F. Kendall
The Pennsylvania State University
University Park, Pennsylvania 16802

Little is known of the composition of the neutral particle flux released during the electrical breakdown of polymer films. Mass spectrometric analysis of the particles is unusually difficult because of the transient nature of the event, the unpredictability of its exact position and timing, and the very large amount of information generated in a period as short as one microsecond. A special type of time-of-flight mass spectrometer triggered from the breakdown event has been developed to study this problem. Charge is fed onto a metal-backed polymer surface by a movable smooth platinum contact. A slowly increasing potential from a high-impedance source is applied to the contact until break- down occurs. The breakdown characteristics can be made similar to those pro- duced by an electron beam charging system operating at similar potentials. With this apparatus it has been shown that intense instantaneous fluxes of neutral particles are released from the sites of breakdown events. For Teflon FEP films of 50 and 75 microns thickness the material released consists almost entirely of fluorocarbon fragments, some of them having masses greater than 350 amu (atomic mass units), while the material released from a 50 micron Kapton film consists mainly of light hydrocarbons with masses at or below 44 amu, with additional carbon monoxide and carbon dioxide. The apparatus is being modified to allow electron beam charging of the samples.

INTRODUCTION

Because of the scarcity of data on the composition of the neutral and ion fluxes from dielectric breakdown events on spacecraft, mass spectrometric anal- yses of these fluxes are particularly important.

Mass analysis of particles from an electrical breakdown involves a partic- ularly difficult set of constraints. The event occurs essentially at a point in space and at an instant in time. The exact position and timing of the event are not known in advance. The event produces a swarm of neutral molecules, molecular clusters and ions of different masses which radiate from the breakdown site over a wide range of speeds and directions. At a distance greater than a few cm from the breakdown site the particle number density is likely to be quite low and falling rapidly because of both speed variations and angular dispersion. The expanding gas and ion burst will pass any given point in a time much shorter than the time taken for any conventional mass spectrometer to scan once through its mass range.

The difficult experimental conditions listed above make it essential to use a mass spectrometer in which a maximum amount of output data can be obtained in the shortest possible time. This effectively limits the choice of spectrometer types to those in which all of the ions leaving the ion source become part of a recorded output signal. It was decided that a specially designed time-of-flight mass spectrometer offered the most cost-effective solution.

MASS SPECTROMETER

The time-of-flight mass spectrometer and the vacuum chamber used for its development are shown in Figure 1. The pulsed two-field ion source (ref. 1) is on the left. Incoming molecules are ionized by an electron beam inside the ion source and the resulting ions are accelerated in approximately monoenergetic bunches into the flight tube. The ions therefore reach the ion detector in ascending order of mass, according to the formula

$$t = s(m/2eV)^{1/2}$$

where t is the flight time through the flight tube, s is the length of the flight tube, m is the ion mass, e is the ion charge, and V is the potential difference through which the ions fall inside the source. With a 115cm flight tube and 300V accelerating potential, the flight time of an ion of mass 100 amu is approximately 47μsec.

A segmented cylindrical lens focuses the ion beam and centers it on the input of the ion detector. The flight tube is operated at ground potential, rather than at high potentials as in most time-of-flight mass spectrometers, in order to minimize electrostatic interactions with the sample charging apparatus. An electron multiplier ion detector is used for high sensitivity and fast response.

It follows from the equation for the flight time of an ion that the electrical signals leaving the ion detector represent a series of complete mass spectra, each one having the corresponding source pulse at its t=0 point. Any number of successive spectra can be displayed, from a single spectrum up to as many as 100 spectra per millisecond. A typical mass spectrum of residual gases in the vacuum chamber is shown in Figure 2. Special techniques are needed for operation at repetition intervals faster than the ion flight times (ref. 2) and for displaying the rapidly-changing spectra (refs. 3, 4).

This mass spectrometer was originally intended for remote operation inside a N.A.S.A. space simulation chamber which already contained the necessary electron beam charging and sample monitoring equipment. These plans had to be changed when it was discovered that the operational lifetime of the sensitive electron multiplier ion detector was unacceptably short in this chamber, apparently because of oil contamination traceable to the early history of its diffusion-pumped vacuum system.

A partial redesign was made to allow electrical breakdown experiments to be done in the turbo- molecular-pumped chamber which had been used for the original development of the mass spectrometer (fig. 3). This solved the oil contamination problem but imposed other difficulties because of the small volume and pumping

capacity. The first experiments have been done with a simple contact device feeding charge onto the insulating surface. At the same time a miniaturized electron beam charging system is being developed.

DIRECT-CONTACT EXPERIMENTS

Figure 4 shows the charging apparatus. Electrons are fed onto the insulating surfaces from a smooth platinum contact. A slowly increasing negative potential from a high-impedance, low-capacitance source is applied to the contact until breakdown occurs. The sample is held in place on a perforated, rotatable 9cm disc by a circumferential retaining ring.

The discharge current waveforms, peak currents, and surface damage characteristics obtained with this apparatus can be made similar to those produced by a high-voltage electron beam charging system by choosing a suitable length (about 45 cm) of coaxial cable as an energy storage line. A useful feature is that, by progressively rotating the sample beneath the contact, the observed gas bursts can be correlated with actual discharge sites left behind on the sample, which can then be removed and observed under an optical or electron microscope. Discharges normally occur within about 4mm of the contact. Few occur directly beneath the contact. Breakdown voltages are similar to those obtained with a monoenergetic electron beam charging system.

The samples tested in the direct-contact experiments were Teflon FEP and Kapton H films of 50 and 75 micron thicknesses. They were metallized on one side with silver overlaid by an Inconel protective coating. No adhesive backing was used.

The first tests with Teflon samples showed that an intense burst of neutral fragments was being released from each discharge. A large number of peaks representing Teflon fragments of the form $C_xF_y^+$ could be seen in each mass spectrum.

The variation with time of the number density of these Teflon fragments was obtained by using the mass peak amplitude signals to intensify a cathode-ray oscilloscope trace, producing an array of dots. By deflecting this display downwards, a semiquantitative indication of the various changes in number densities was obtained. Such a display is shown in Figure 5 with the major peaks identified. A background spectrum is included for comparison.

Close examination of these and other similar records showed that release of neutral particles often began just before breakdown with production of hydrocarbons, followed by a burst of fluorocarbons during the actual breakdown. Hydrocarbons are visible in the lower left photograph in Figure 5. Both hydrocarbon and fluorocarbon concentrations then fall with a time constant of about 120 msec, determined by the volume and pumping speed of the vacuum system. The hydrocarbon peaks are probably caused by adsorbed surface impurities. Further work is required to establish their origins.

The most intense fluorocarbon peak corresponds to CF_3^+ but ions up to and beyond $C_5F_9^+$ are present. Switching off the ionizing electron beam in the mass spectrometer ion source causes these peaks to disappear, showing that they are ionization products of even larger neutral fragments and not ions released directly

from the   discharge. Far more of these heavy ions were observed than are present
in the mass spectrum of the heaviest fluorocarbons for which published data are
available (C_6F_{14}), suggesting that very large neutral fragments, of mass much
greater than 350 amu, were leaving the Teflon surface during the discharge.

After completion of the Teflon tests, a 50 micron Kapton film with metal
backing was installed in the apparatus and a new series of breakdown measurements
was begun. Results were very different. The Kapton produced only light frag-
ments, giving rise to mass spectra containing mainly masses 44,28, and 15, as
shown in the intensity-modulated spectrum of Figure 6. It appears that the mass
44 peak represents CO_2^+ and $C_3H_8^+$; mass 28 is CO^+ and $C_2H_4^+$, and mass 15 is CH_3^+ .
It should be noted that Kapton contains a substantial amount of oxygen.

In general breakdown voltages were higher for a given thickness of Kapton
than with Teflon.

Figure 7 shows the chemical structure of Teflon and Kapton. The origins of
many of the observed fragment ions (formed in the mass spectrometer ion source
by electron bombardment of even larger polymer fragments released by the dis-
charge) are obvious.

HIGH SPEED RECORDING

High resolution mass spectra are generated at such a rate in this experiment
(up to 10^5/sec.) that even modern digital recorders are barely adequate for
following complex events. Photographic techniques have been used almost exclu-
sively to date. Examples are the intensity-modulated displays of Figures 5 and
6. When quantitative measurements of peak heights are desired an offset raster
display is used as in Figures 8 and 9. Here successive conventional mass spectra
(in this case 16 per group) are superimposed upon one another, after which the
oscilloscope trace moves upwards and to the right for display of the next group.
Figure 8 shows the background gases in the absence of breakdown, and Figure 9
shows the burst of light gases and polymer fragments from the breakdown of a 50
micron Kapton film.

ADDITIONAL RESULTS

Items (1) — (3) of Figure 10 summarize the results of the experiments
described above. The figure also shows five additional phenomena which have been
identified and studied.

Secondary discharges were seen on several occasions. Electrical breakdowns
were triggered at distances up to 15cm from the site of a Teflon film breakdown.
In some cases the metallic electrodes between which the secondary discharge
occurred were operating at less than 65% of their normal breakdown potential
difference. Triggering is presumably caused by the burst of neutral and ionized
material from the polymer breakdown site. The effect probably occurs also with
Kapton, but this has not been checked. This phenomenon has been seen with both
electron beam and direct charging of the sample.

Direct transfer of Teflon fragments is obviously likely because of the large fragments observed in the mass spectrum. It has been confirmed by the formation of insulating layers near the breakdown site and by instantaneous changes in the secondary electron emission coefficient of surfaces up to 100cm away. Partial recovery occurs over a period of several days. The effect does not appear to occur with Kapton, but this point needs further study.

Indirect transfer of Teflon has similar effects. It appears to be the result of Teflon fragments striking an intervening surface and then being almost instantaneously re-emitted into areas which are not on a direct line of sight from the discharge.

Removal of metal from the backing film was detected with Kapton samples. In some cases the Kapton film remained intact above the damage site. The effect is originally observable only under magnification but after several months in air the holes are easily visible with the naked eye because of local discoloration of the Kapton.

Photon-induced desorption and electron-induced desorption of adsorbed gases from surfaces near discharge sites are to be expected and have been observed. The effect is not directly linked with the presence of a polymer film, since any spark could supply the necessary photons and electrons. The effect is about one order of magnitude smaller than the direct gas evolution from polymer film breakdowns.

CONCLUSIONS

Many of the phenomena listed in Figure 10 could have significant effects on spacecraft surfaces. Jets of heavy polymer fragments from Teflon discharge sites could form insulating layers on adjacent electrodes, could act as triggers for gas discharges, and could change the secondary electron emission properties of distant surfaces. The much lighter fragments from Kapton may also be capable of triggering remote discharges. The ejection of material from the conducting backing of polymer films may result in metallic contamination of nearby insulation. Photon-induced and electron-induced desorption of gas from surfaces adjacent to a discharge site also occurs and adds to the intensity of the observed neutral-particle pulses.

REFERENCES

1. Wiley, W. C. and McLaren, I. H. : Time-of-Flight Mass Spectrometer with Improved Resolution, Rev. Sci. Instrum. 26, pp 1150-1157 (1955).

2. Kendall, B. R. F. : Automatic Data Processing for a Sensitive Time-of-Flight Mass Spectrometer, Jour. Sci Instrum. 39, pp 267-272 (1962).

3. Meyer, R. T. : Fast Recording Techniques for Time-Resolved Mass Spectrometry; in "Time-of-Flight Mass Spectrometry" (ed. D. Price and J. E. Williams), Pergamon Press, London, 1969, pp 61-87.

4. Lincoln, K. A. : Data Acquisition Techniques for Exploiting the Uniqueness of the Time-of-Flight Mass Spectrometer: Application to Sampling Pulsed Gas Systems; in "Dynamic Mass Spectrometry" (ed. D. Price and J. F. J. Todd), Heyden and Son, London, 1981, pp 111-119.
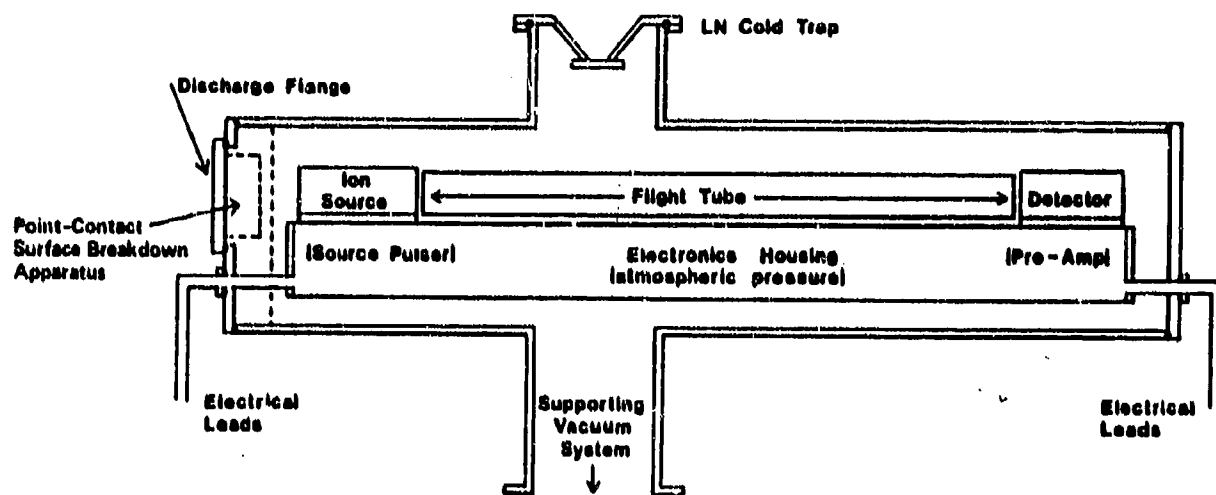
Figure 1. – Physical layout of TOFM's.

21 OCT 82 BK
BG Spm 7 x 10⁻⁸ Torr
Linear
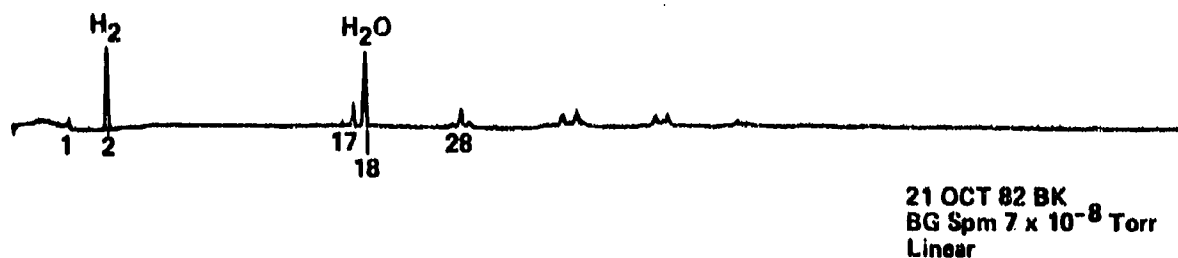
Figure 2. – Mass spectrum of background gases in vacuum chamber.
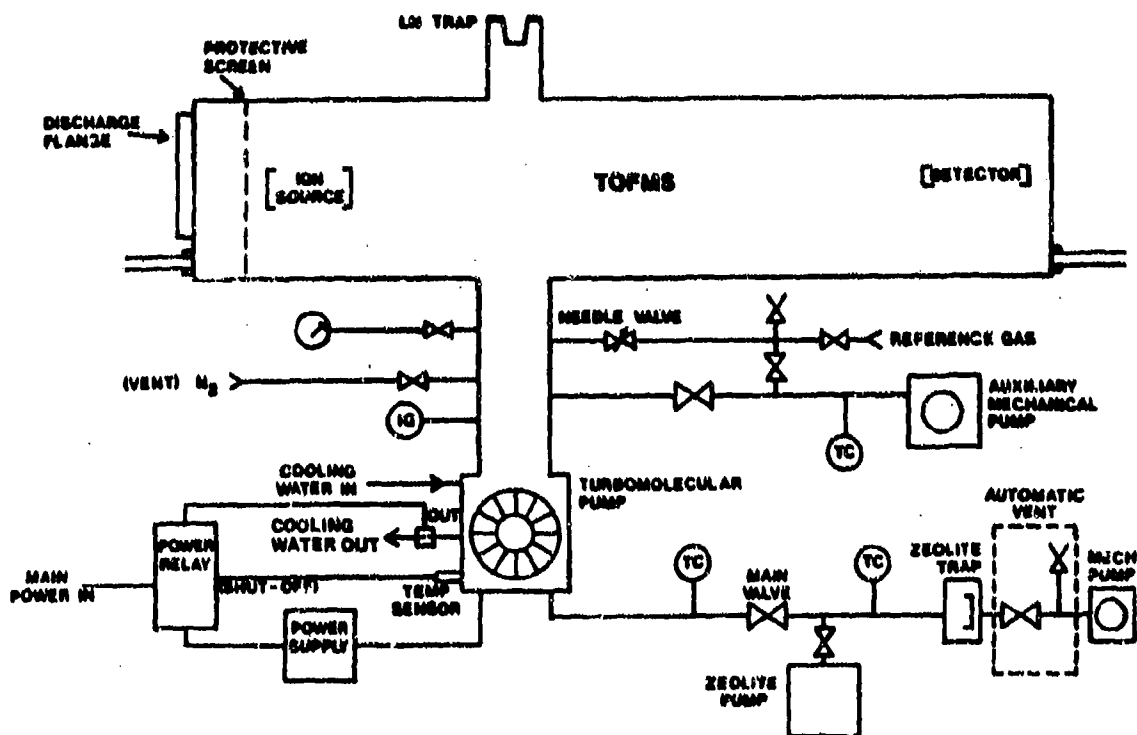
Figure 3. – General layout of vacuum system.
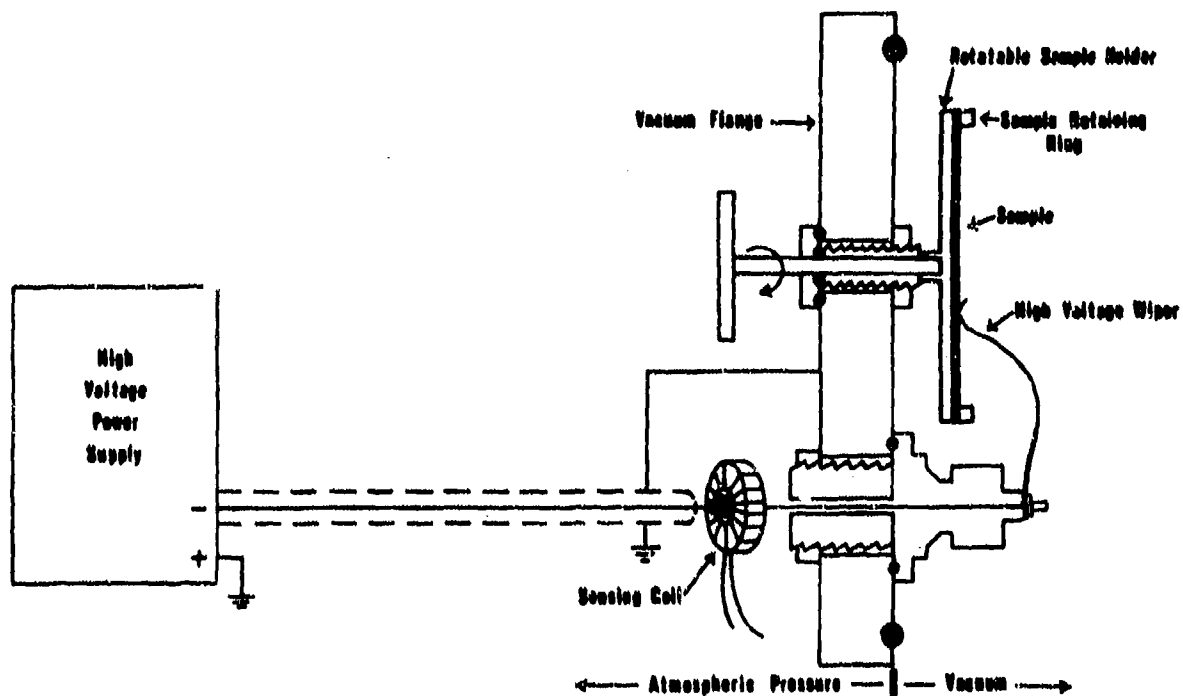
Figure 4. – Point-contact surface breakdown apparatus.

531
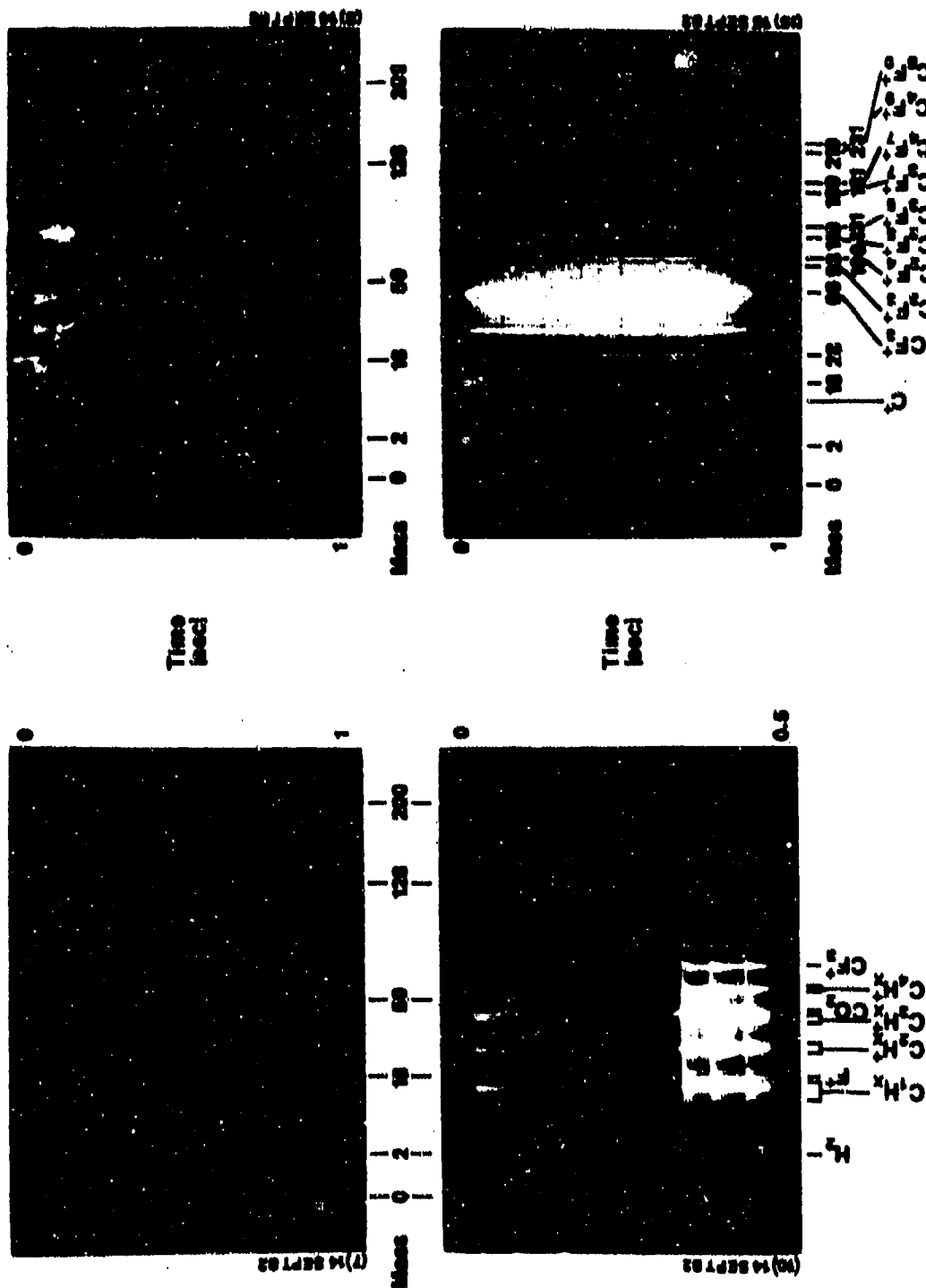
Figure 5. – Variations with time of intensity-modulated mass spectrum associated with point-contact breakdown of 50μ Teflon layer.

Upper Left: Background spectrum, no breakdown. 9x10^{-8} Torr.
Upper Right: Breakdown at 13 kV. Approx. 0.01 J.
Lower Left: Breakdown at 16 kV. Multiple strike.
Lower Right: Continuous discharge through spark-damaged area of surface at 12-13 kV.
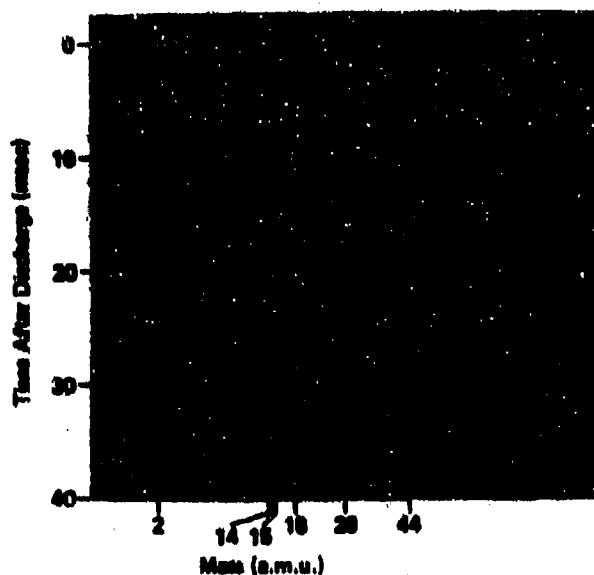
Figure 6. – Intensity-modulated raster display for breakdown of 50 micron Kapton film at 18 kV. Main peaks 44 (CO_2^+, $C_3H_8^+$), 28 (CO^+, $C_2H_4^+$), 15 (CH_3^+).
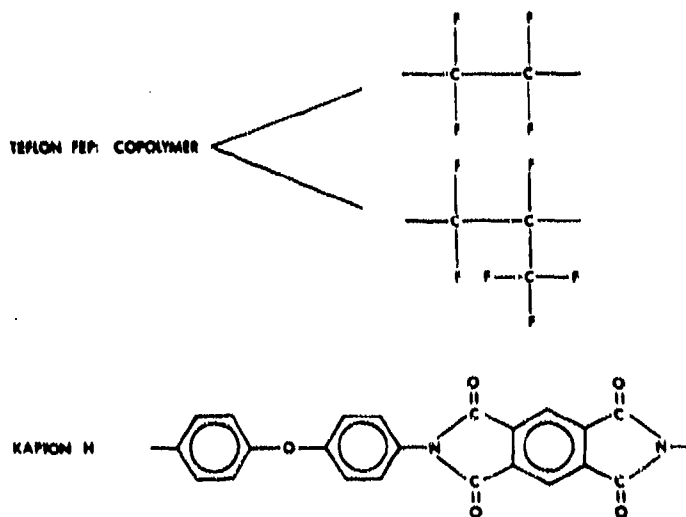
Figure 7. – Polymer structures. Hydrogen bonds omitted in Kapton structure for clarity.
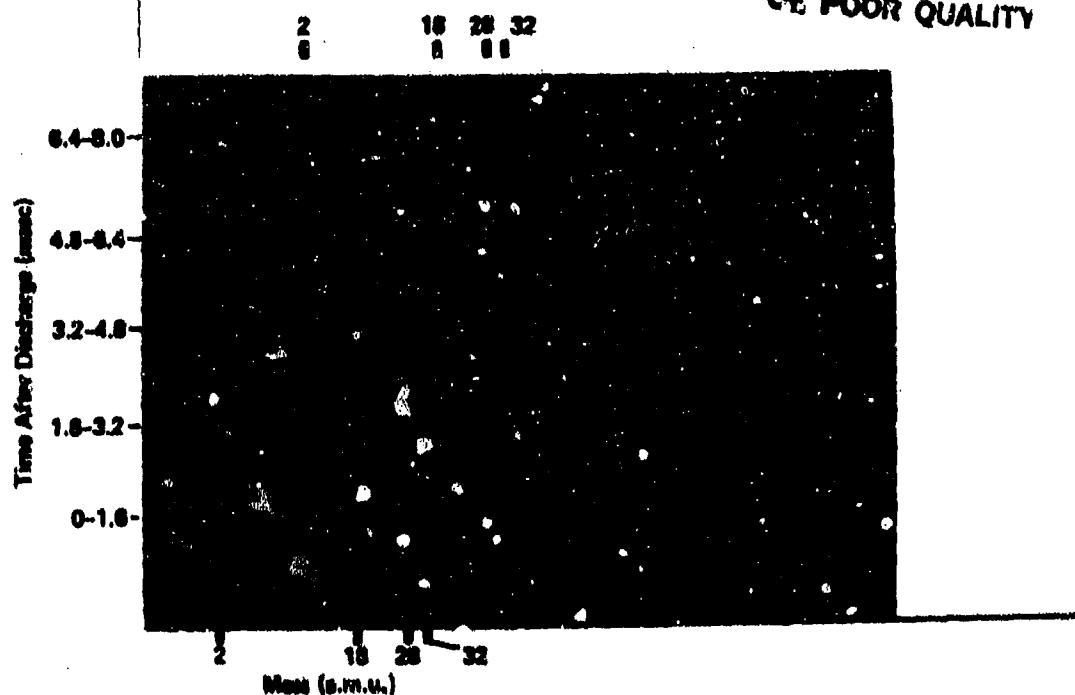
Figure 8. – Background gas spectrum (no discharge). Offset multitrace raster display, 16 spectra per trace.
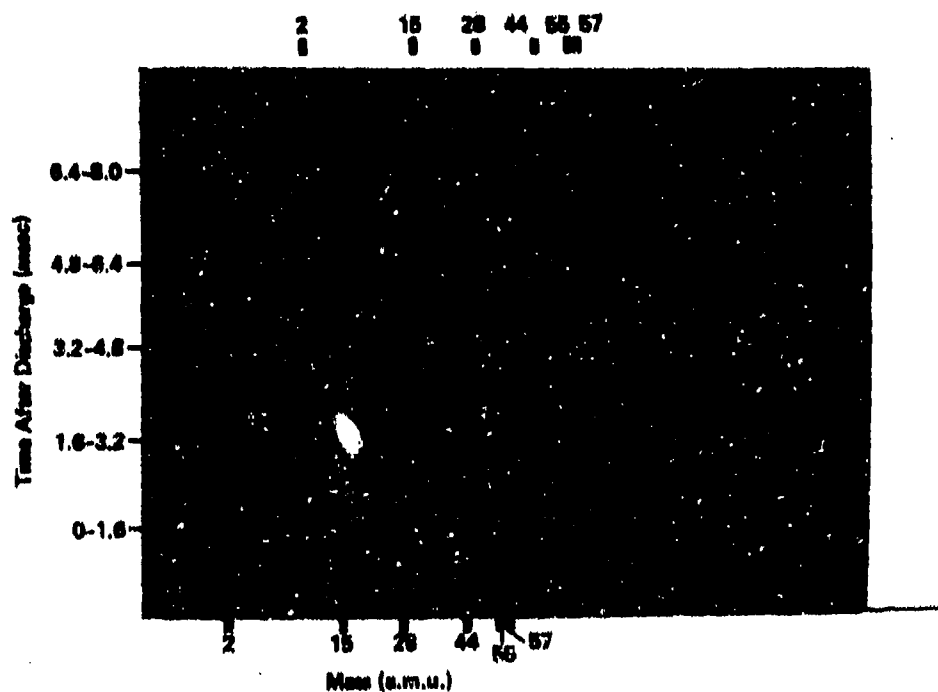
Figure 9. – Contact discharge through 50μ Kapton film at 16 kV. Offset multi-trace raster display, 16 spectra per trace.
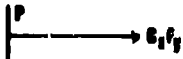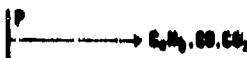
PHENOMENON	POLYMER	SYMBOLIC REPRESENTATION	COMMENTS
1. Intense neutral-particle pulse	Teflon Kapton		Easily detectable by fast ion gauge.
2. Emission of heavy fragments	Teflon	C_2F_3	> 300 amu
3. Emission of light fragments	Kapton	C_2H_2, CO, CO_2	< 44 amu
4. Secondary discharge	Teflon		Gases emitted from electrode surfaces.
5. Direct material transfer	Teflon		Change in secondary emission characteristics.
6. Indirect material transfer	Teflon		As for (5).
7. Removal of metal backing	Kapton		
8. Photon-induced desorption / Electron-induced desorption	—		CO_2, CO, H_2, H_2O, CH_4

Figure 10. —Neutral-particle phenomena observed during electrical breakdown of polymer films (contact charging). Insulating side of metal-backed polymer films indicated by (P).

ELECTRON YIELDS FROM SPACECRAFT MATERIALS*

K. Yang, W. L. Gordon, and R. W. Hoffman
Case Western Reserve University
Cleveland, Ohio 44106

Photoyields and secondary electron emission (SEE) characteristics have been determined under UHV conditions for a group of insulating materials used in spacecraft applications. The SEE studies were carried out with a pulsed primary beam while photoyields were obtained with a chopped photon beam from a Kr resonance source with major emission at 123.6 nm. This provides a photon flux close to that of the Lyman α in the space environment. Yields per incident photon are obtained relative to those from a freshly evaporated and air oxidized Al surface. Samson's value of $\sim 2.4\%$ is taken for the Al yield. Results are presented for Kapton, FEP Teflon, the borosilicate glass covering of a shuttle tile, and spacesuit outer fabric.

INTRODUCTION

In the use of NASCAP (ref. 1), a computer code which simulates charging of a three-dimensional object in space, it is important to have data on electron yields from the various materials comprising the spacecraft surface. In an on-going program (ref. 2) pulsed primary electron beam methods have been developed to avoid charging effects in yield measurements from insulating surfaces. These studies are carried out in an ultra high vacuum system employing a commercial double pass CMA which permits sequential Auger analysis of the surface and target current measurements of electron yield data as a function of the primary energy, EP. This pulsed beam technique has been extended to permit vacuum ultraviolet (VUV) photoyield measurements of these insulating surfaces: Kapton, Teflon, the borosilicate glass surface of shuttle tile, and the outer fabric of spacesuit material.

EXPERIMENTAL TECHNIQUES

Target current measurements of secondary yield by pulsed electron beam methods, introduced in a study of insulating materials, have already been discussed in reference 2. We describe here the adaptation of this approach to obtain photoyields. The spectral range of interest is restricted to the VUV because of the photoemission threshold of most materials. We have chosen to carry out these preliminary experiments with an Opthos VUV krypton source powered by a Kiva Model MPG 4 microwave generator producing resonance lines at 116.6 and 123.6 nm with a relative intensity of approximately 1 to 7 respectively (or 1 to 15 after transmission through the MgF_2 windows). This provides a reasonable approximation to the relevant portion of the solar spectrum with its intense Lyman H_α line.

537

As illustrated in figure 1, the Kr source is mounted on the end of a cylindrical housing containing a camera shutter to permit chopping of the light beam. The beam travels in an argon atmosphere to avoid air absorption and enters the UHV system through a MgF$_2$ window. The incident beam intensity is determined by irradiating a freshly evaporated and air oxidized Al film of $\sim$ 150 nm thickness deposited on a glass substrate and using Samson's value (ref. 3) of 2.4% yield per incident photon at the Lyman H$_\alpha$. The yield from freshly evaporated samples is typically 50% greater than that from samples exposed to air for about 10 minutes, which corresponds to an essentially saturated value. It is this result which we assume corresponds to Samson's yield but have not placed this on an absolute basis as yet. Samples to be studied and the Al detector are mounted on the faces of the six-sided rotatable carousel.

A cylindrical cup collector electrode was mounted facing and surrounding the sample on the target as shown in figure 1. The collimated UV beam irradiates the sample by passing through an aperture on the axis of the collector. Our usual procedure was to measure collector current with the collector biased + 22.5 V relative to the grounded target. Typical currents ranged from 0.5 nA for relatively high yield materials down to 5 to 10 pA for the lowest yields. Although the shutter is capable of 1 millisecond pulse lengths, we have been able to avoid charging with pulses as long as 1 second. This has permitted use of a fast response chart recorder to obtain a plateau value for the collector current during each pulse.

MATERIALS

Only insulating materials were studied in this investigation and all samples were obtained from NASA LeRC. Table I summarizes the materials studied and includes the preparation of rear surfaces since good electrical contact to the target is important. Approximately 2 cm x 2 cm samples were used in the photoyield studies with approximately 1 cm x 1 cm sizes employed in electron yield work. Dust particles were removed by blowing dry nitrogen across the surface but no other cleaning steps were used.

Square samples were cut from the $\sim$ .5 mm thick borosilicate glass surface coating of the shuttle tile with a thin rotating disk. The silica fiber backing material was brushed away to permit good contact with indium foil in which the sample was embedded. An Al backing was evaporated on the rear surface of the outer fabric of the spacesuit later to provide better electrical contact with the target. As discussed later, this fabric and to a lesser extent the shuttle tile surface material, exhibited qualitatively stronger charging effects than did the Kapton and Teflon sheet. The greater average "thickness" of the cloth ($\sim$ 1 mm) means a reduced capacitance and thus an increased charging rate, per current pulse.

RESULTS AND DISCUSSION

Photoyields

Results, expressed as yields per incident photon, are summarized in table II with uncertainties based on the scatter of repeated measurements. Systematic uncertainties, such as the assumption that Samson's value of 2.4% yield applies to a

freshly evaporated and air oxidized Al surface or the effects of surface contamination, if present, are not included. Light pulses used in obtaining these results were generally 1 second in duration. A test for charge accumulation was done by repeated irradiation in the same location on the sample. Here we discovered that for the intensities employed, several (up to 10) pulses could be delivered to Kapton before the yield would begin to drop - such a drop is taken as our operational definition of charging. For the white shuttle tile, however, charging began after only one or two pulses and for the spacesuit fabric on the first pulse.

We experienced some difficulties in measuring the highly insulating materials having relatively low photoyields. This is due, in part, to low current values corresponding to the small yields such that the values are comparable to the noise. In the low yield insulating materials we also found a trend towards even lower values when we chose a modification of figure 1 consisting of grounding the collector, biasing the target - 22.5 V relative to ground and measuring the target current. This effect has not been explored in any detail as yet and may be spurious since it did not appear for the higher yield materials. We conclude that the results for both Teflon and the spacesuit fabric are preliminary and will require further study.

Secondary Electron Yields

Results, using target current measurements with pulse beam methods as described in reference 2, were obtained for the materials in table I and are presented in figures 2 through 8 where only the total SEE coefficient, σ, is displayed. The primary electron beam was slightly defocussed to $\sim$ 2 mm diameter and was moved to various locations on the sample during a series of measurements to reduce surface charging effects. Kapton and Teflon are displayed in figures 2 and 3 respectively. In figure 4, figures 2 and 3 are compared using a normalized scale on which σ/σ_{max} is plotted vs. EP/EP_{max} and it is clear that they are in close agreement. This is in contrast with the early work of Willis and Skinner (ref. 4) in which the Teflon data are well above the Kapton results on a similar normalized plot. Since very different samples were measured in these two investigations and different surface cleaning techniques were employed, we merely note these differences. Figures 5 and 6 present the SEE coefficients for the borosilicate glass shuttle tile surfaces in both as-received and sputtered condition. Some difficulties were experienced with charging of these samples because of their thickness ($\sim$ 0.5 mm) but we feel the results, while preliminary, are representative for reasons discussed later. Results from a sample of microscope cover glass are also included for comparison in figure 7. In each of these cases, sputtering sufficient to remove the nominal surface contamination has reduced the SEE coefficients substantially.

Figure 8 contains preliminary results for the outer fabric of the space suit. As noted earlier, the large sample thickness increased the tendency to charge. SEE results for all materials reported here are summarized in table III to provide a general comparison. EP_I and EP_{II} are the primary beam energies for which the total SEE coefficient is unity.

It is important to note that our usual method of obtaining SEE data for insulating materials appears to reduce charging problems. In biasing the target negatively then positively to obtain both the SEE coefficent, σ and δ, at a given primary energy EP, the surface charge is reduced in the positive biased situation by electrons attracted back to the surface. This is illustrated by the record of multiple pulses (at EP $\simeq$ 500 eV) delivered to the same location in the sample in figure 9. Here, the series of dots, although they show substantial scatter, tend to drop away much less

from the initial σ value than do the series of + points for which the target remained negatively biased. The latter points approach a unity value much more closely, indicating that charging has brought the surface potential close to the EP_{II}, the second cross-over value. The immediate effect of low energy electrons from a flood gun is also illustrated and appear somewhat more clearly in the highly charged case than in the alternating bias mode. One can conclude from these results that, though the data show substantial scatter, alternating the target bias helps to reduce surface charging effects.

CONCLUSIONS

We have demonstrated reasonable results for both electron and photoyields from highly insulating materials where such data are not usually available. Pulsed irradiation methods were used to minimize charging effects.

REFERENCES

1. Katz, K., Cassidy, J.J., Mandell, M.J., Schnuelle, R.W., Steen, P.G., and Roche, J.C.: The Capabilities of the NASA Charging Analyzer Program. Spacecraft Charging Technology - 1978, NASA Conf. Publ. 2071, 1979, p. 101.

2. Krainsky, I., Lundin, W., Gordon, W.L., and Hoffman, R.W.: Secondary Electron Emission Yield, Spacecraft Charging Technology - 1980. NASA Conf. Publ. 2182, 1981, p. 179.

3. Cairns, R.B. and Samson, J.A.R.: Metal Photocathodes as Secondary Standards for Absolute Intensity Measurements in the Vacuum Ultraviolet. J. Opt. Soc. Am. 56, 1966, p. 1568.

3. Willis, R.F. and Skinner, D.K.: Secondary Electron Emission Yield Behavior of Polymers. Sol. St. Comm. 13, 1973, p. 685.

TABLE I - MATERIALS STUDIES

Material	Back Surface
Thermal Blanket	
Kapton, 2 mil	Al
FEP Teflon 2 mil	Ag/Inconel
Shuttle Tile	
White borosilicate glass outer coating	In Foil*
Black borosilicate glass outer coating	In foil
Space Suit Components	
Outer fabric	Evaporated Al
(ST11 G041-01)	layer

*Embedded in 0.5 mm In foil without covering sample surface.

TABLE II - PHOTOYIELDS

Material	Photoyield (%)
Kapton	0.65 ± 0.03
FEP Teflon	0.04 ± 0.03
White Shuttle Tile surface	0.2 ± 0.03
Black Shuttle Tile surface	0.3 ± 0.03
Outer fabric of space suit	0.06 ± 0.03

TABLE III - SUMMARY OF SEE RESULTS

Sample	σ_{max}	EP_{max}(KeV)	E_1(KeV)	E_2(KeV)
Kapton	1.8	0.2	0.05	0.7
FEP Teflon	2.4	0.3	0.05	1.9
Black Space Shuttle Tile	2.3	0.5	0.06	2.7
White Space Shuttle Tile	2.3	0.5	0.06	3.5
Microscope Cover Glass	3.8	0.5	0.05	5.0
ST11 G041-01	2.3	0.3	0.08	3.2
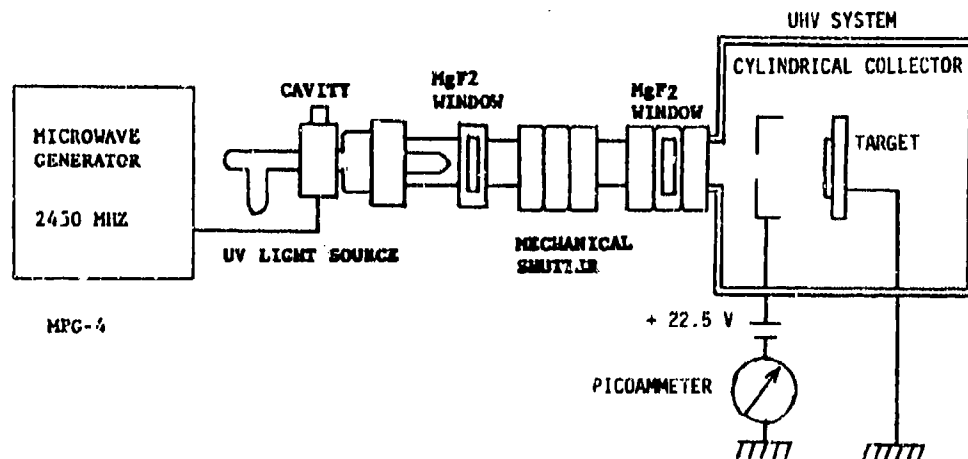
Fig. 1. Schematic diagram of the arrangement for measuring photoyields.
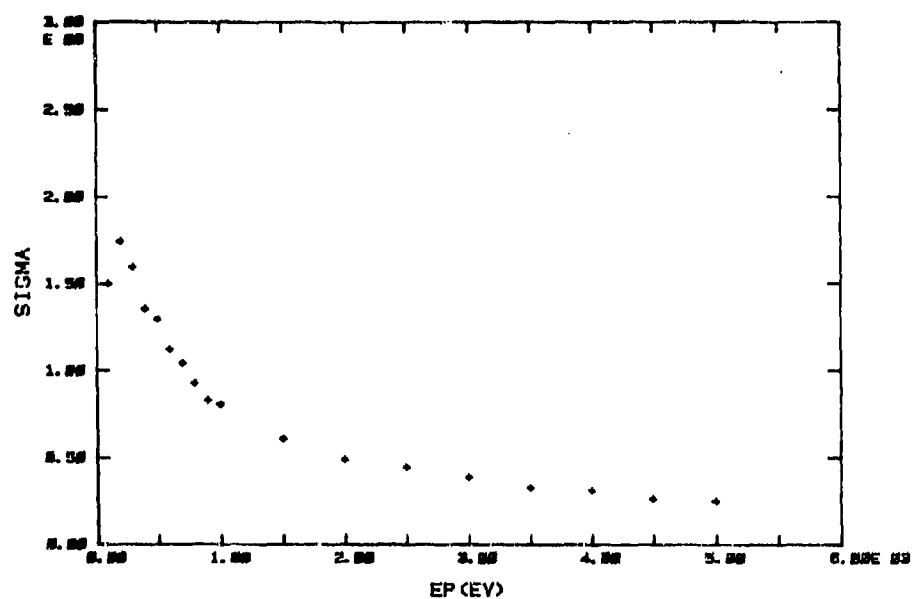
Fig. 2. Total SEE coefficient for Kapton, as-received surface. Single pulse method was used with I_p = 60 nA.
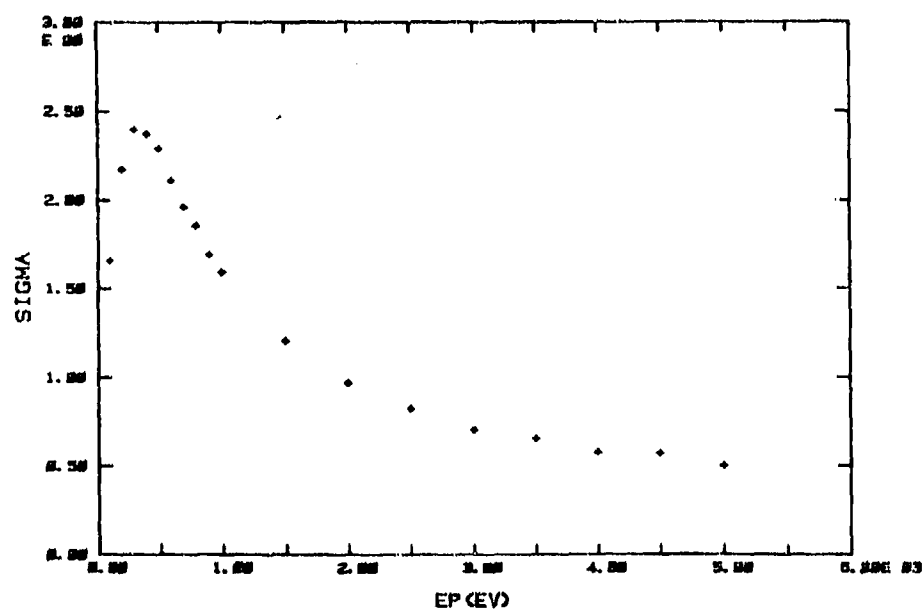
Fig. 3. Total SEE coefficient for FEP Teflon, as-received surface. The single pulse method was used with I_p = 60 nA.
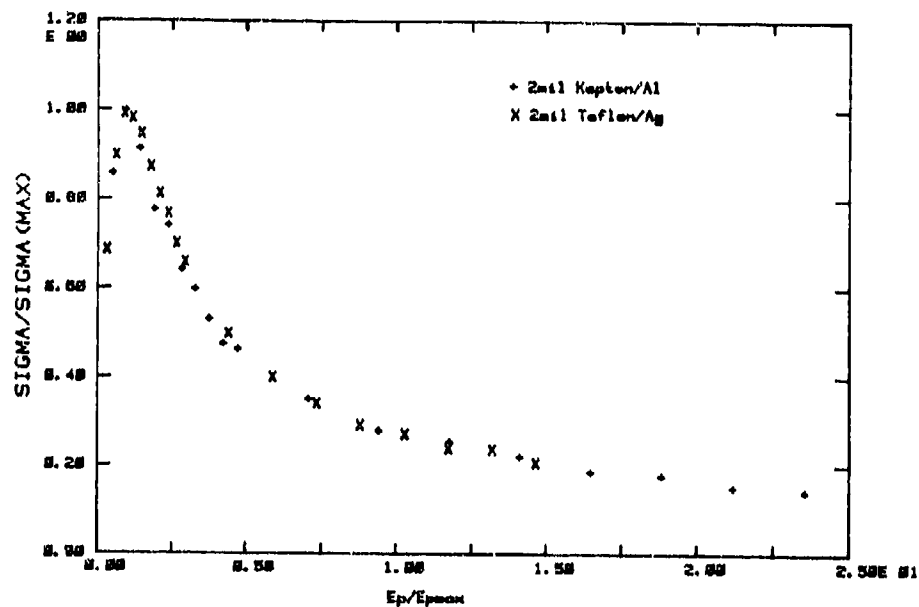
Fig. 4. Normalized total SEE coefficient for Kapton and FEP Teflon compared. Samples and conditions identical to Figs. 2 and 3.
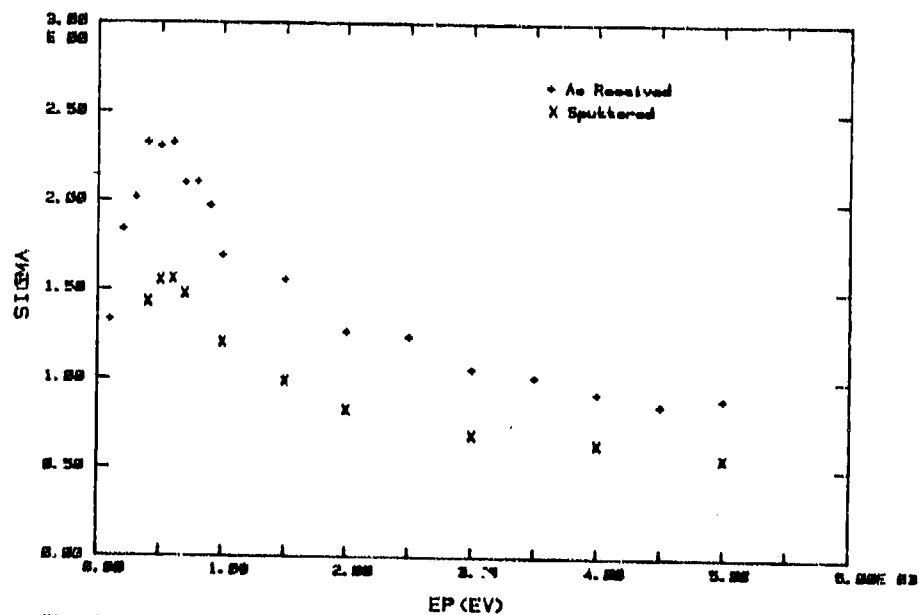
Fig. 5. Total SEE coefficient for the white borosilicate shuttle tile surface. Single pulse method was used with I_p = 60 nA.

543
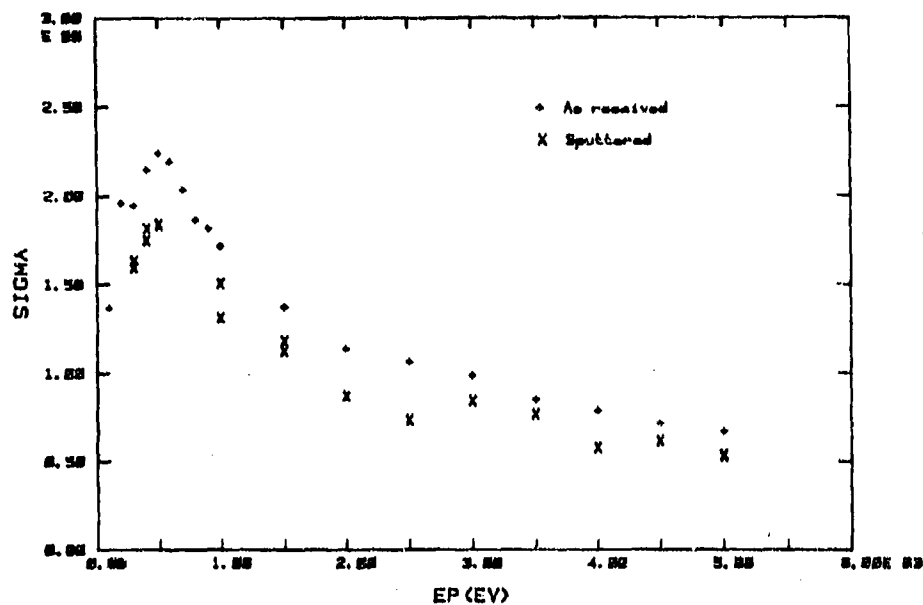
Fig. 6. Total SEE coefficient for black borosilicate surface of the shuttle tile. The single pulse method was used with I_p = 60-70 nA.
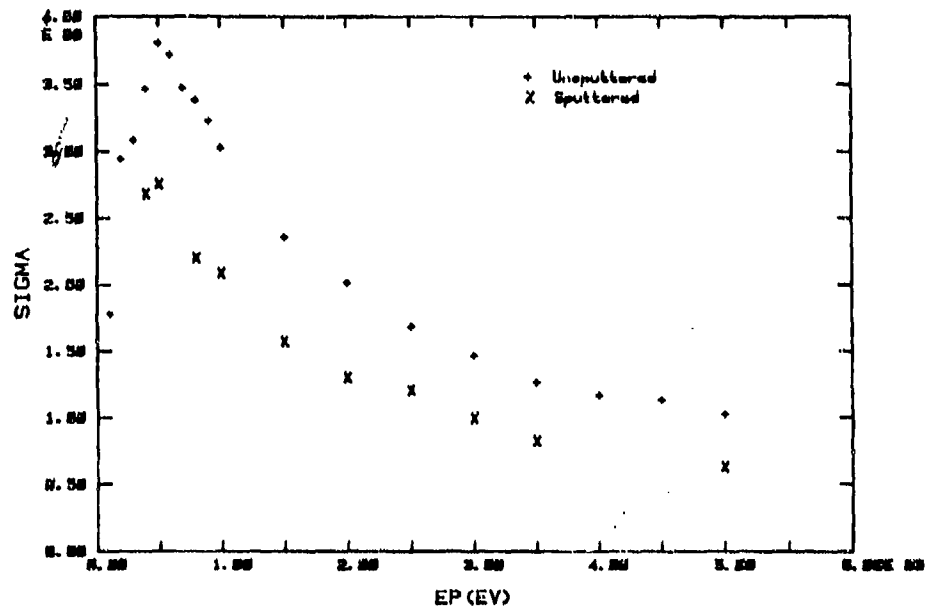
Fig. 7. Total SEE coefficient for microscope slide cover glass, as-received surface. The single pulse method was used with I_p = 70 nA.
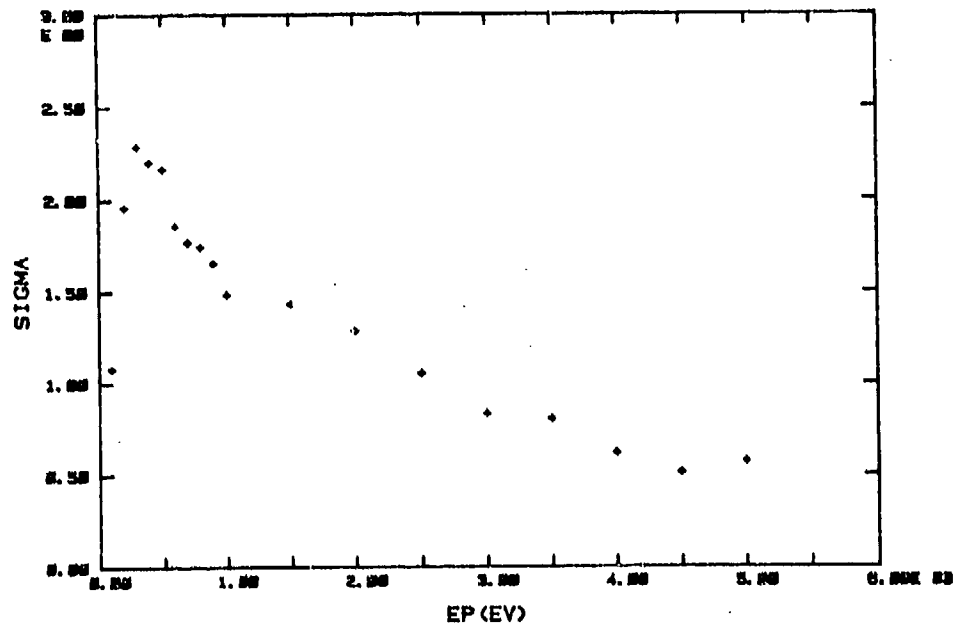
Fig. 8. Total SEE coefficient for the outer fabric of spacesuit material, as-received surface. The single pulse method was used with I_p = 60 nA.
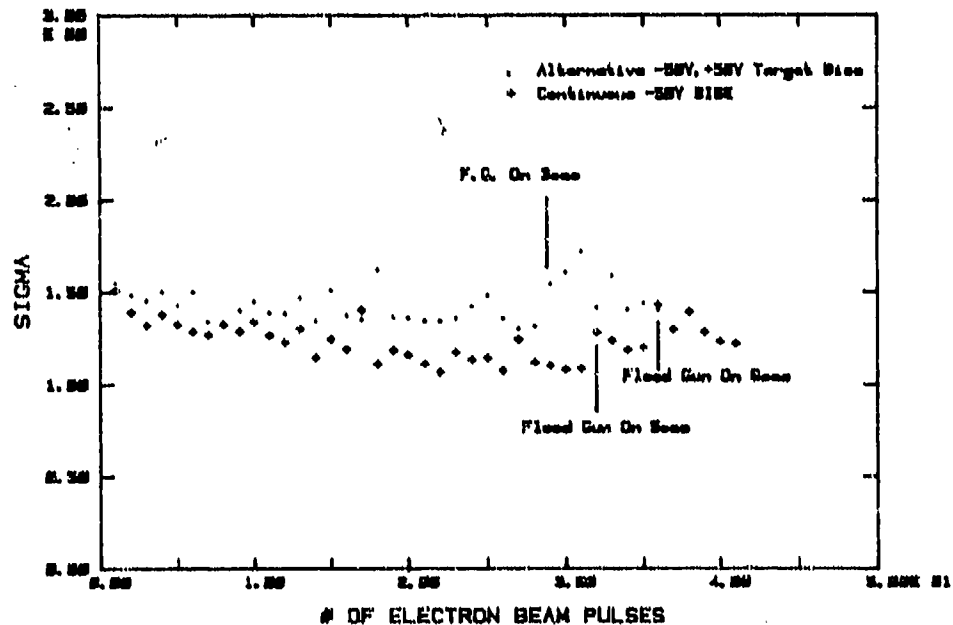
Fig. 9. Changes in total SEE coefficient of the sputtered surface of the white borosilicate glass shuttle tile coating with repeated pulsing to illustrate charging effects in two operating modes. The single pulse method was used with I_p = 40 nA with EP = 500 eV.

545

KAPTON CHARGING CHARACTERISTICS: EFFECTS OF MATERIAL THICKNESS AND ELECTRON-ENERGY DISTRIBUTION

W. S. Williamson, C. R. Dulgeroff, and J. Hymann
Hughes Research Laboratories
Malibu, California 90265

R. Viswanathan
Hughes Space and Communications Group
Los Angeles, California 90009

We report charging characteristics of polyimide (Kapton) of varying thicknesses under irradiation by a very-low-current-density electron beam, with the back surface of the sample grounded. These charging characteristics are in good agreement with a simple analytical model which predicts that in thin samples at low current density, sample surface potential is limited by conduction leakage through the bulk material.

In a second investigation, we measured the charging of Kapton in a low-current-density (3 μAm^{-2}) electron beam in which the beam energy was modulated to simulate Maxwellian and biMaxwellian distribution functions.

INTRODUCTION

The charging characteristics of dielectric thermal-blanket materials in the geosynchronous-earth-orbit (GEO) plasma environment is a subject of considerable importance in spacecraft-charging studies. Polyimide (Kapton) is one of the most commonly used materials in large-area thermal blankets, and this material has been the subject of numerous previous experimental investigations. Many previous studies, however, have employed electron-beam current densities substantially higher than the 3 μAm^{-2} value which we believe represents a reasonable upper bound in the GEO environment.

A second area of concern over ground simulations is that the electron beams that are used are generally monoenergetic, and the charging characteristics that would result in the distributed-energy GEO environment must be inferred from monoenergetic charging data analytically. A model for accomplishing this inference is imbedded in the NASCAP (NASA Charging Analyzer Program) computer code, for example. Since NASCAP is currently being used by spacecraft designers to predict

the spacecraft-charging consequences of their designs, experimental verification of the NASCAP modelling is very timely. A credible distributed-energy electron source is needed to perform these experiments, and we describe a simple means for devising such a source below.

SYMBOLS USED

I_B	electron-beam current density (no sample in place)
I_P	electron-beam current density (incident on charged sample)
ϵ_R	Electron reflux coefficient (including backscatter + secondaries)
σ	bulk conductivity of sample
A	sample area
d	sample thickness
V_S	sample surface potential
eV_B	electron-beam energy
I_R	current of refluxed electrons ($=\epsilon_R I_P$)
k	$=dJ_B \sigma^{-1}$
J_B	electron beam current density
$f_I(V_B)$	electron current distribution function

Only SI units are used in this paper.

KAPTON CHARGING CHARACTERISTICS IN MONOENERGETIC ELECTRON BEAMS

In this section we describe the experimental apparatus and measurements and then present a simple analytical model for comparison with the experimental results.

Experimental Apparatus and Measurements

The experiments were conducted in a 0.6-m-diameter vacuum chamber, which is shown in Figure 1. A divergent-beam electron flood gun, shown in Figure 2, is used to irradiate the sample. This electron gun is built to a design developed at NASA Lewis Research Center. It produces a broad uniform-current-density beam and exhibits excellent stability over a wide range of current densities. The sample is housed in a separate antechamber which can be isolated from the main chamber by a vacuum gate valve. The geometry of the sample and sample holder is shown in Figure 3.

We have measured the charging characteristics of Kapton under conditions which differ significantly from previous practice: we employed an electron-beam current density of 3 μAm^{-2}, and we mounted the sample by wrapping it around the edges of the metal sample-holder and clamping it at the rear. These two innovations are more representative of the electron current

density which exists at GEO, and of the geometry with which thermal-blanket materials are exposed to electron bombardment on GEO spacecraft. We exposed Kapton samples of two thicknesses (25 μm and 127 μm) to irradiation by monoenergetic electron beams with energies up to 14 keV. A typical charging characteristic is shown in Figure 4, where the surface potential of 127-μm-thick Kapton is shown as a function of time, during continuous bombardment by 14-keV electrons. This plot reveals the relatively long time constant involved in charging at these low current densities.

Figure 5 shows the equilibrium surface potential of 127-μm-thick Kapton as a function of incident beam-current energy from 2 keV to 14 keV. The straight-line characteristic intercepts the beam-energy axis at an energy of about 1.6 keV; this energy corresponds to the "second-crossing" energy, i.e., the energy at which the secondary-electron yield of the material is unity. Figure 6 shows the corresponding characteristic of 25-μm-thick Kapton, under the same test conditions. In this curve, the second-crossing intercept is the same, but the surface potential saturates at much lower values than were observed in the 127-μm-thick material. This saturation effect is produced by conduction losses through the bulk Kapton, as evidenced by the fact that the saturation effect disappears when the ground connection on the rear of the sample is removed; the characteristic then remains linear within the limits of our beam-energy capability. We have developed a simple analytical model which successfully predicts the surface potential at which the saturation effect occurs. This model is similar to previous models due to Purvis, et. al. (Reference 1) and Reeves and Balmain (Reference 2), except that it conforms to the specific geometry of the test environment that we used. This model predicts that the saturation surface potential of Kapton depends on the parameter $k=dJ\sigma^{-1}$, where d is the sample thickness, J is the electron-beam current density, and σ is the material conductivity. Material testing with thick (large-d) samples and high current densities (large J) raise the saturation potential beyond usual test limits. This explains why the saturation effect shown in Figure 6 is not often seen in published dielectric-charging results; the saturation is produced by the use of thinner materials and lower electron-beam current densities than are commonly used in material-charging tests.

Analytical Charging Model

In this section we present the simple model of sample charging which we will evaluate by comparison with experimental data. This model is highly simplified and applies to an equilibrium-charge condition (i.e., a condition in which displacement currents and stored charge can be neglected). It also assumes that cylindrical Langmuir-probe theory correctly calculates the reduction in current that is collected by the sample as it charges more and more negative.

549

In equilibrium, the current that is incident on a charged sample is given by

$$I_P = I_R + \frac{\sigma A}{d} V_S \quad , \tag{1}$$

where the first term corresponds to refluxed electrons that are ejected from the surface by backscatter or secondary-electron emission, and the second term corresponds to conduction loss of electrons through the sample to the grounded rear surface. According to cylindrical Langmuir probe theory (Reference 3), the current that is collected by a charged sample is related to the incident current (i.e., current that would be collected by an uncharged sample) by

$$I_F = I_B \frac{V_B - V_S}{V_B} \tag{2}$$

The foregoing expressions can be combined to yield the surface voltage as a function of beam voltage:

$$V_S = \frac{V_B k (1 - \varepsilon_R)}{V_B + k (1 - \varepsilon_R)} \tag{3}$$

Of course, the reflux coefficient ε_R is a function of the impact energy of electrons which strike the surface, $e(V_B - V_S)$; this function, along with the constants contained within k, are in general known only numerically. Equation (3) does not represent a solution for V_S; it can, however, be solved for V_S numerically by a simple iterative procedure.

We have solved Equation (3) numerically, using the Kapton reflux-coefficient and conductivity data that is contained within NASCAP, and values of material thickness and beam current density that are appropriate to our experimental conditions. The results are shown in Figure 7, where we compare the actual equilibrium charging voltages with the values predicted by the model, for several thicknesses of Kapton. The model predictions provide reasonably accurate descriptions of the shape of the charging characteristics and the location of the beam energy at which conduction-induced saturation of the charging voltage begins.

Figure 8 shows the solutions to Equation (3) plotted in a different manner: here the parameter k is used as the independent variable, and electron-beam energy is a parameter. Notice that the curves are spaced evenly in surface voltage V_S for large values of k (i.e., large current density and/or low conductance), and that the surface potential is independent of k in this

region. This case corresponds to the situation in which the impacting electron current is balanced totally by electron reflux. For low values of k, conduction losses become significant, causing the curves to pack together at higher values of V_B. Figure 8 is a convenient tool for estimating Kapton charging; it could be easily reproduced for other dielectrics for which ϵ_R is known by solving Equation (3).

KAPTON CHARGING UNDER
DISTRIBUTED-ENERGY ELECTRON-BEAM IRRADIATION

As described in the Introduction, realistic simulation of spacecraft charging should include the use of a distributed-energy electron source. In principle, of course, multiple experiments can be performed using monoenergetic beams and calculating the expected surface potential using a model such as that given above. This calculation entails solving Equation (3) as before, but using an effective reflux coefficient such as

$$\langle\epsilon_R\rangle(V_S) = \int_{V_S}^{\infty}\epsilon_R(V_B-V_S)f_I(V_B)dV_B \qquad (4)$$

instead of the monoenergetic ϵ_R used above. This approach is hazardous because the effective ϵ_R may differ from that given by Equation (4); that is, the electron reflux which results from the simultaneous presence of two electron-energy species may differ from the sum of the refluxes that would result from each energy species being separately present. Such nonlinearities are well known in the case of sputtering of solids by ion bombardment, but we are unaware of electron-reflux data which would either validate Equation (4) or provide a useful alternative.

In order to provide an empirical foundation for these distributed-energy electron distribution considerations, we have developed a simple and novel means of simulating the broad distribution of electron energies which simultaneously bombard a spacecraft in GEO. We have used this tool to study the charging of 25-μm- and 127-μm-thick Kapton. We find that the thinner material, which is in the conduction-dominated (saturated surface-potential) regime charges to essentially the same surface potential regardless of the electron distribution function. The thicker material, however, experiences more severe charging when exposed to electrons which are distributed in energy corresponding to "moderate" and "severe" charging conditions than it does when exposed to a "quiescent" distribution of electron energies.

Figure 9 illustrates the arrangement of our distributed-energy electron source. The electron source, shown in Figure 2, is a simple hot-cathode source with multiple wire-mesh grids to extract a broad, spatially uniform electron beam. The

e-gun is powered by a programmable high-voltage power supply which operates over the range of 0 to 30 kV. The power supply is programmed by a microcomputer; the microcomputer causes the power supply to generate a repetitive sequence of electron-beam voltages. This repetitive sequence, which is defined in the microcomputer firmware is arranged in such a manner that the time-averaged current produced by the e-gun at a given energy is equal to that which exists in the GEO environment. That is, the system selects an electron-beam energy and causes the power supply to output the corresponding voltage for a time duration that is proportional to the value of the desired current distribution function at that energy. The energies are output in an ascending-energy sequence, but we have found that the same sample charging is produced for descending- or random-energy sequences.

This simulation is reasonable if the time scale within which the electron-beam energy is varied is short compared to the sample charging time. This condition is satisfied in our tests, because the electron-beam energy is varied over a 5-s time period, while the sample typically requires an hour or more to reach equilibrium potential (in cases in which the sample is not grounded at the rear surface, equilibration still requires several minutes). The microcomputer is programmed to generate any of three electron-energy distribution functions (which it selects by reading the position of a front-panel switch); the programs are written in a commercially available integer BASIC and are stored in ROM for convenience.

The three distribution functions we use are a biMaxwellian distribution characteristic of quiescent conditions (Reference 4) and two single-Maxwellian distributions recommended by Stevens (Reference 5) to simulate the moderate and solar-substorm GEO environments. The three distribution functions have identical total currents. These distributions are plotted in Figure 10.

Figure 11 shows the response of both 25-μm- and 127-μm-thick Kapton under irradiation by the multienergetic-beam apparatus. The thicker Kapton charges to substantially higher voltages and evidences a larger difference between the three distribution functions than does the thinner material. It is clear that the single-Maxwellian distribution that simulates "moderate" charging conditions is significantly more severe than the biMaxwellian "quiescent" condition.

REFERENCES

1. C.K. Purvis, N.J. Stevens, and J.C. Oglebay, "Charging Characteristics of Materials: Comparison of Experimental Results with Simple Analytical Models," procedings of the Spacecraft Charging Technology Conference, AFGL-TR-77-0051, NASA TMX-73537, p. 459 (1977).

2. R.D. Reeves and K.G. Balmain, "Two-Dimensional Electron Beam Charging Model for Polymer Films," IEEE Trans. on Nuc. Sci. NS-28, 4547 (1981).

3. F.F. Chen, "Electric Probes," Pure and Applied Physics 21, Plasma Diagnostic Techniques, eds. R. H. Huddlestone and S.L. Leonard. Academic Press, 1965, pp 113-119.

4. H.B. Garrett and S. E. DeForrest, " An Analytical Simulation of the Geosynchronous Plasma Environment," Planet. Space Sci. 27, 1101 (1979).

5. N.J. Stevens, "Design Practices for Controlling Spacecraft Charging Interactions," AIAA Paper No. 82-0115, presented at the AIAA 20th Aerospace Sciences Conference, Orlando, Florida, 11-14 January 1982.
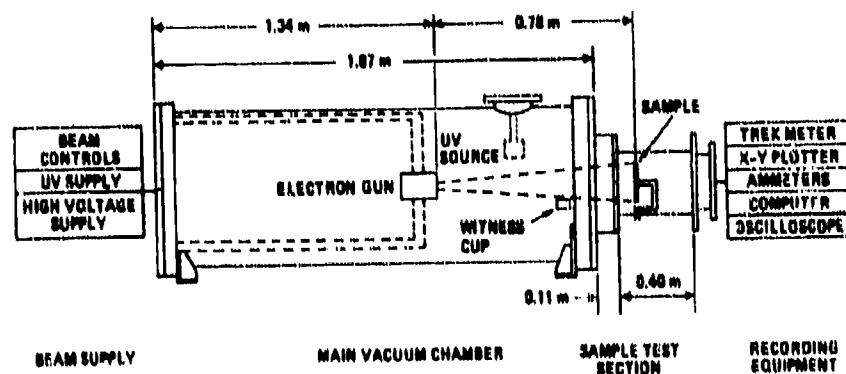
Figure 1. - Hughes spacecraft-charging-simulation facility: overview.
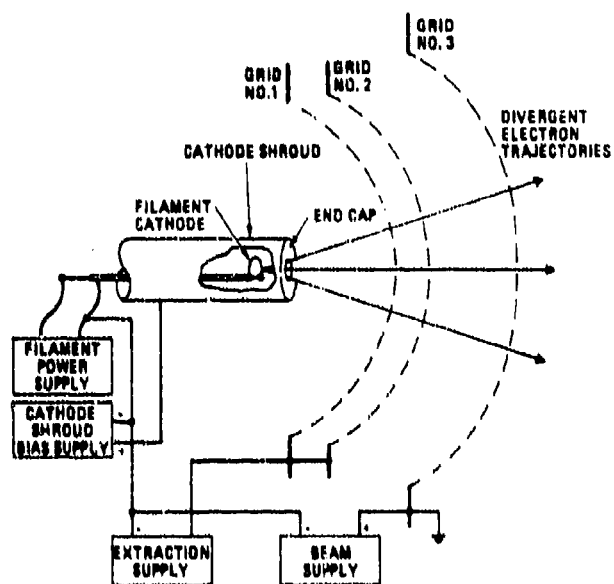
Figure 2. – Electron source (NASA Lewis design).
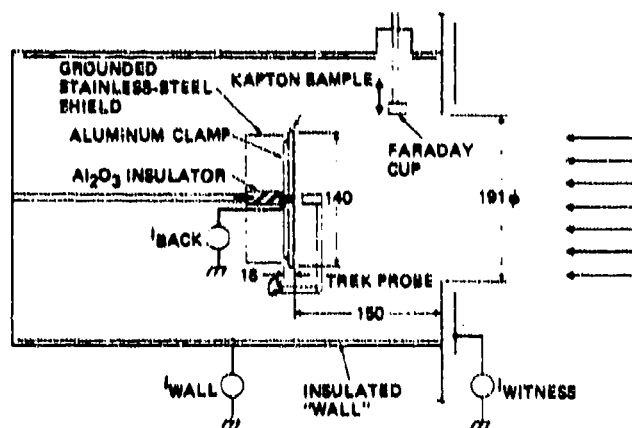
Figure 3. – Hughes spacecraft–charging–simulation facility: sample test
section details. Dimensions are in millimeters.
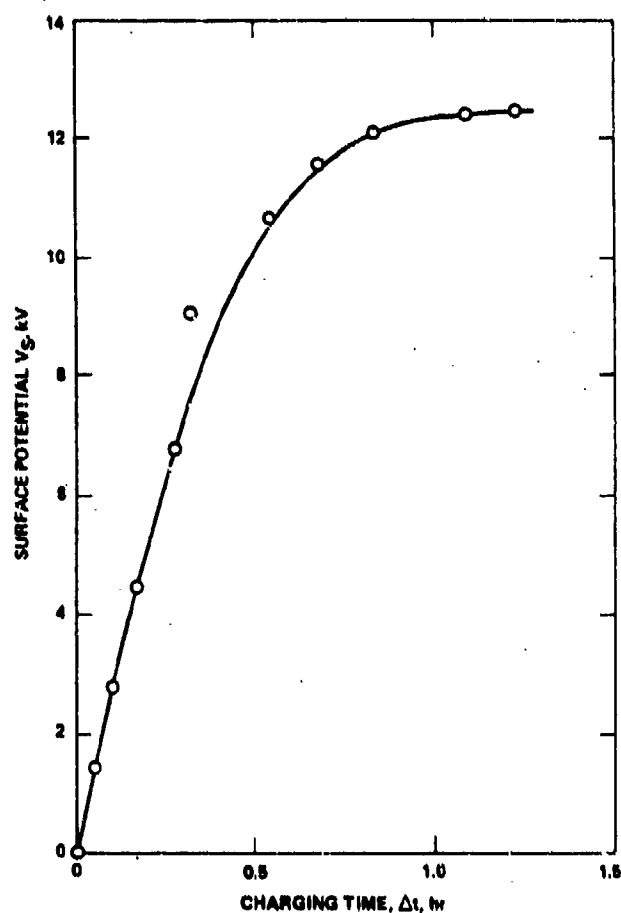
Figure 4. – Surface potential of 127-μm-thick Kapton under irradiation by a 14-keV, 3-μAm^{-2} electron beam.
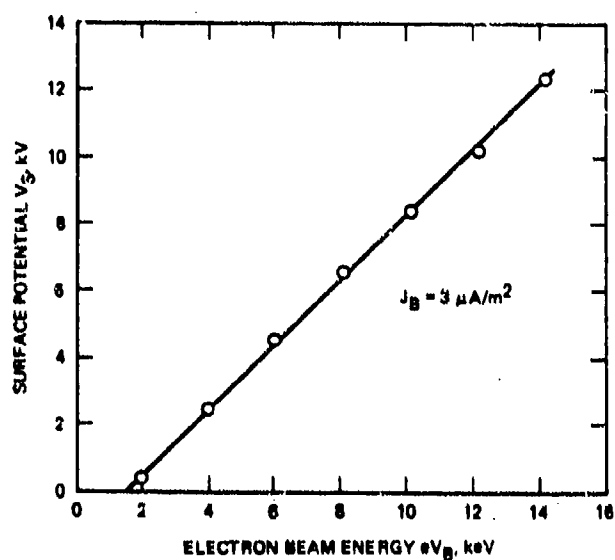
Figure 5. – Equilibrium surface potential of 127-μm-thick Kapton as a function of electron beam energy.

555

C-7
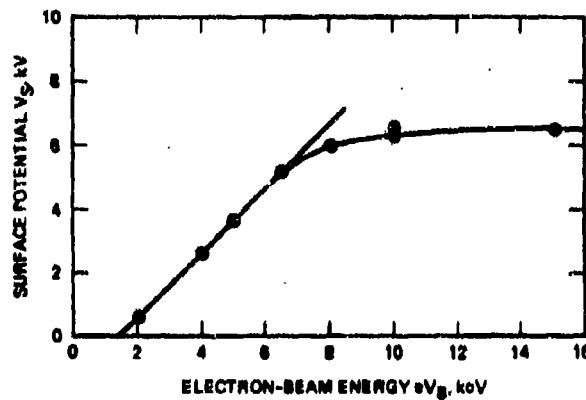
Figure 6. – Surface potential of 25-μm-thick Kapton.
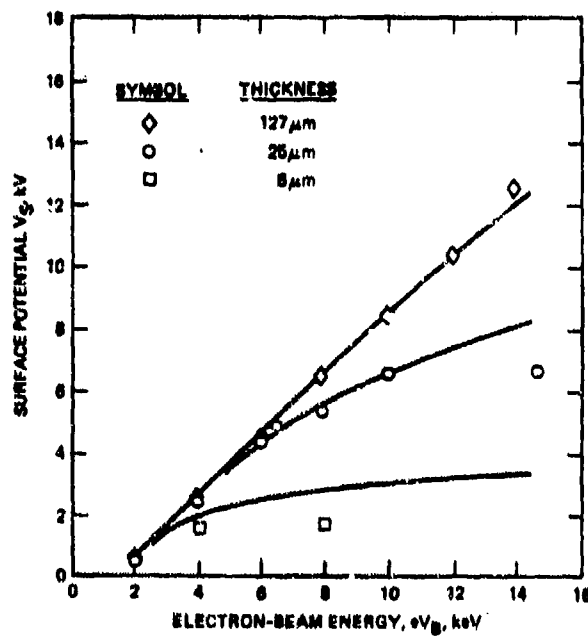
Figure 7. – Comparison of predictions of analytical model with experimental results for charging of Kapton of several thicknesses.
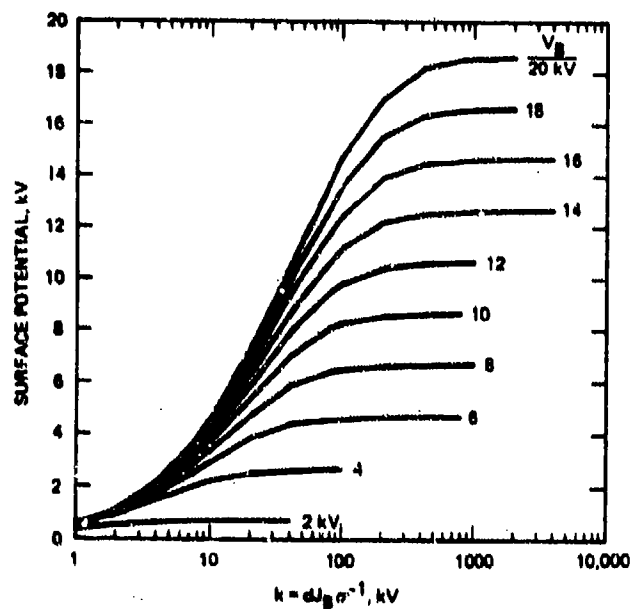
Figure 8.- Analytical charging model for Kapton, showing surface potential as a function of $k = dJ_B \sigma^{-1}$, with beam voltage V_B as a parameter.
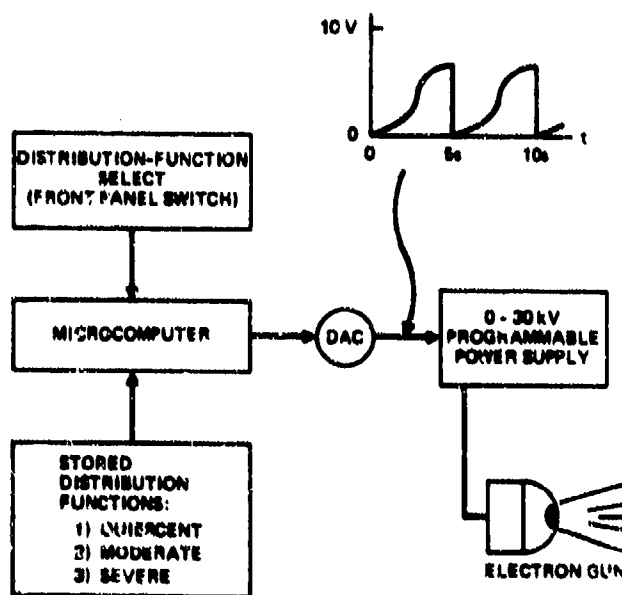
Figure 9. - Block diagram of multienergetic electron beam.
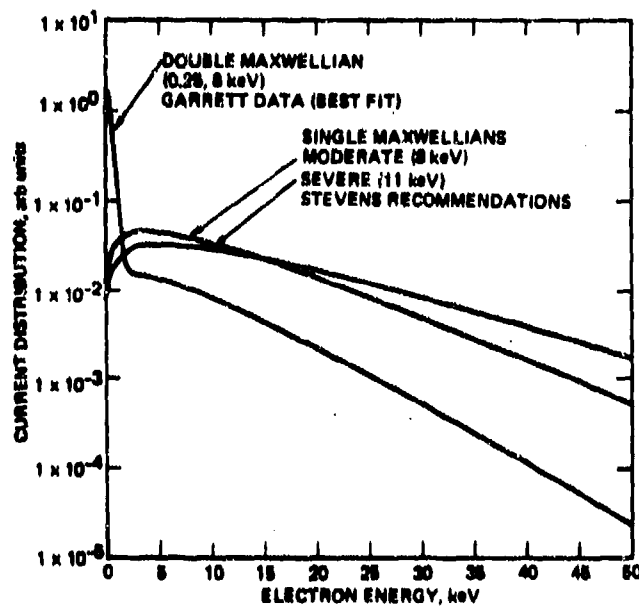
Figure 10. - Electron energy distribution for simulation experiments.
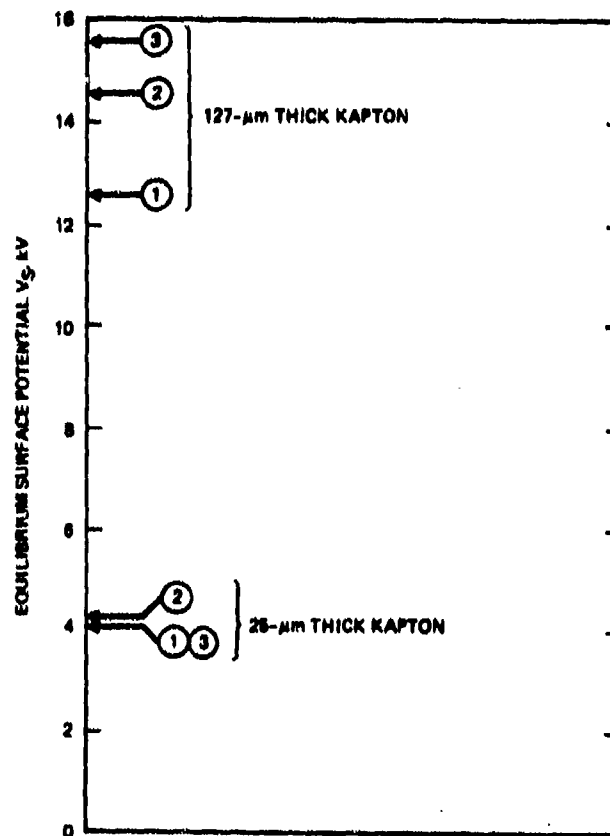
Figure 11. - Equilibrium surface potential of 25- and 127-μm-thick Kapton irradiated by 3-μAm^{-2} multienergetic electron beam: (1) = "quiescent", (2) = "moderate", (3) = "severe" charging environments.

558

ELECTRICAL CONDUCTION IN POLYMER DIELECTRICS*

David B. Cotts
SRI International
Menlo Park, California 94025

The use of polymer dielectrics with moderate resistivities could reduce or eliminate problems associated with spacecraft charging. The processes responsible for conduction and the properties of electroactive polymers are reviewed, and correlations drawn between molecular structure and electrical conductivity. These structure-property relationships have led to the development of several new electroactive polymer compositions and the identification of several systems that have the requisite thermal, mechanical, environmental and electrical properties for use in spacecraft.

INTRODUCTION

One approach to controlling the spacecraft charging phenomena that are the subject of this symposium is the use of moderately conducting dielectrics that would bleed-off accumulated charge before a breakdown or discharge could occur (ref. 1). Despite extensive study, summarized in reference 2, and the recent development of several organic polymers with metallic ($> 10^0$ ohm^{-1}cm^{-1}) conductivities our understanding of this process remains unclear. For example there is considerable debate about the mechanism(s) responsible for charge transport in organic polymers and no means to relate molecular structure to conduction mechanism or to the absolute level of conductivity.

As part of a material-based solution we have reviewed (ref. 3) the electrical and mechanical properties of nearly 250 polymers that are believed to have either the electrical, mechanical, thermal, environmental resistance, or other properties necessary for spacecraft use. Our principle conclusions are two-fold. First there exist materials that could be utilized in near-intermediate-, and long-term experimental tests of the proposed materials-based solution. Second, based on the wide range of properties, conduction mechanisms, and chemical structures encountered in the study a general theory of electrical conductivity in polymers has been formulated. The model succeeds both in explaining the wide range of known properties and structures, and in identifying new polymer compositions that possess unusually high electrical conductivities.

The remainder of this paper is divided into four sections. First the observable, characteristic properties associated with various conduction models are reviewed. Second, the electrical properties of several

---

semiconducting and conducting polymers are examined. By comparing these properties the relative importance of various models can be assessed and inconsistent phenomena identified. Third, the molecular structure of the conducting polymers and their derivatives are considered to illustrate how structure and morphology influence conductivity. Finally, in the fourth section this information is used to identify candidate materials for use in reducing spacecraft charging phenomena. Included are both contemporary materials and new materials, identified on the basis of mechanism and structure-property relationships in sections two and three, that have been found to possess relatively high electrical conductivities.

CHARACTERISTIC FEATURES OF CONDUCTION MECHANISMS FOR ORGANIC POLYMERS

Electrical conduction in polymers is most frequently interpreted according to band gap conduction models as discussed in reference 4. The position of various energy bands is determined by the interaction of atomic and molecular orbitals that are assumed to form long-range periodic arrays. This picture is analogous to taking the repeat unit structure of a polymer and repeating it at regularly spaced intervals in three dimensions indefinitely as if it were the unit cell of a single crystal. With the possible exception of two polymers that are polymerized as single crystals, the validity of this approach is difficult to understand since organic polymers are highly disordered and the crystalline order that is present extends over relatively short distances. In addition, on an absolute scale the length of a polymer molecule is extremely short and macroscopic transport of necessity must be limited by intermolecular charge transport which is not treated by this model.

Experimentally a metallic band gap material can be characterized as having an inverse ($\log \sigma \propto T^{-1}$) temperature dependence due to increased electron scattering at elevated temperature. Since the number of carriers is relatively insensitive to temperature the overall conductivity is determined carrier mobility, which should be in excess of 1 cm^2/V sec for materials to adequately fit a band gap mechanism (ref. 5). Conduction in band gap semiconductors is not mobility limited by scattering but rather by the number of carriers that have been thermally excited into the conduction band. Consequently these systems display a strong thermally activated conductivity (ref. 5).

Because of the inherent high degree of disorder in polymers it is necessary to consider so-called mobility gap mechanisms that successfully describe the electronic properties of amorphous inorganic semiconductors including amorphous silicon and the chalcogenide glasses (ref. 6). In the theoretical description of these materials the band energies are diffuse, sometimes overlapping, and charge transport is mobility limited. Structurally the charge carriers are spatially localized at disordered sites and undergo a variable-range hopping transport. In contrast the mobility gap materials display a weak ($\log \sigma \propto T_0/T^{1/4}$) temperature dependence and mobilities that seldom exceed 1 cm^2/V sec, above cryogenic temperatures. The optical properties are complex and their interpretation is more complicated than that for a simple band edge absorption.

When the mean free path of a charge carrier becomes very low due to extremely tight binding or deep trapping, a nearest neighbor hopping mechanism

characterized by a positive thermally activated process is encountered as discussed in reference 7. In essence carriers are thermally or photolytically pried out of their molecular orbitals into the continum where they undergo an electric field modified transport or recombination. The details of this process can be very complicated but this general type of mechanism is responsible for charge transport in most insulating polymers exposed to ionizing radiation or injected charge.

An intermediate temperature dependence of the conductivity (log $\sigma \propto T_0/T^{1/2}$) is observed for polycrystalline materials composed of conducting regions separated by very thin nonconducting barriers (ref. 8). This could be of particular interest for crystalline polymeric materials since the crystalline regions are extremely small and often distinguised by only a slight shift in molecular orientation.

Finally there exists the possibility of ionic conduction that involves the actual mass transport of ions through the material (ref. 5). These charge carriers may be ionizable pendant groups, inadvertent impurities, or ionized water which is present in small quantities in almost all polymers unless specifically excluded. Because these charge carriers must actually diffuse through and between the polymer molecules ionic conductivity depends strongly on the physical state of the material. Consequently ionic conductivity is inversely dependent on pressure and the temperature dependence can be complicated due to thermal transitions and relaxations in the polymer.

In the following section the properties of some electrically conducting polymers are reviewed in an attempt to understand which conduction mechanisms are involved. Of specific interest is the temperature dependence of the conductivity, in part because only this data is generally available in the literature. While a thorough description requires knowledge about carrier density, mobility, optical properties, etc., these are much less available in the literature and more difficult to measure for polymers.

ELECTRICAL PROPERTIES OF CONDUCTING POLYMERS

In recent years a number of highly conducting polymers have been developed that have stimulated considerable interest conerning the mechanism(s) of conduction and potential applications. The existance of relatively highly conducting materials has facilitated experimental measurements, so there is a large quantity of data in the literature obtained on materials with diverse chemical structures from which general conclusions about polymer conductivity can be drawn.

The most striking example is polythiazyl (SN_x). Needle-like single crystals of polythiazyl can be polymerized directly from single crystals of the cyclic S_2N_2 monomer (ref. 9). Electrical conductivities, which depend strongly on crystal perfection, of from 250 to 1200 (ohm cm)$^{-1}$ have been reported. In single crystalline materials the metallic conductivity shows an inverse temperature dependence characteristic of a band gap mechanism as would be expected from a material with an extremely high degree of long-range order. In even this highly ordered material the importance of intermolecular charge transport is illustrated. It is unlikely that single molecules stretch the entire distance from end to end of a macroscopic single crystal. Even so,

561

above cryogenic temperatures the intrinsic conductivity parallel to the chain axis is only about ten-times that normal to the chain axis indicating extensive charge transport between chains (ref. 10).

A similar high degree of structural order is found in single crystalline polydiacetylenes. These also are prepared through the radical initiated polymerization of single crystals grown from the corresponding monomer. Amorphous films can also be obtained by casting solutions of the polymer in organic solvents. Although the optical properties discussed in reference 11 are characteristic of the long range delocalized π electron orbitals responsible for band gap conduction the extremely low (10^{-10} to 10^{-12} ohm^{-1} cm^{-1}) conductivity and six-fold conduction anisotropy parrallel- and normal-to the chain axis indicate that carrier mobility is strongly limited by the rate of intermolecular charge transport (ref. 12). The absorption of as little as one mole percent of iodine raises the electronic conductivity by several orders of magnitude. Mechanistically the role of iodine is unclear but both pristine and doped materials in reference 13 display T^{-1} conductivities. Since iodine is present as I_3^- it is believed that it locally oxidizes the polymer π electron backbone and may serve as an electronic bridge between molecules.

Unlike most of the conducting polymers studied the polydiacetylenes are soluble organic solvents so their molecular weight can be determined as reported in reference 14. At a fixed dopant level the conductivity increases exponentially with molecular weight and the activation energy decreases linearly to an infinite molecular weight value of 0.4 ev. This illustrates rather clearly that even in the presence of complete electron delocalization along a chain backbone the rate limiting process for carrier transport is intermolecular.

Considerable attention has been focused on polyacetylene because of its potential application to light weight, high power-density batteries. Polyacetylene can be prepared in thin films or as coatings that appear to the eye to be like aluminum foil but microscopically more closely resemble the fibrillar structure of steel wool (ref. 15). The pristine material has a low (10^{-12} ohm^{-1}cm^{-1}) conductivity but this value increases rapidly to 10^1 ohm^{-1} cm^{-1} when it is doped to about 10 mole percent with strong oxidizing agents like I_2 or AsF_5 (ref. 16). Although frequently modeled as an ideal one-dimensional delocalized π electron backbone there is a considerable amount of evidence in reference 17 for structural disorder and a $T^{-1/4}$ dependence of the conductivity on temperature characteristic of variable range hopping in amorphous materials. Yet high ($\sim$60 cm^2/V sec) mobilities are observed and optical studies (ref. 18) indicate that the transition to a metallic conductivity state is not simply a concentration dependent percolation transition of metallic conducting regions.

Similar observations may be made about the doping and electrical conductivity of polypyrrole. It too is prepared as a thin film or coating, becomes conducting at a dopant level of about 25 mole percent, and displays a $T^{-1/4}$ conductivity dependence (ref. 19). Polyphenylene sulfide and polyparaphenylene also become conducting when doped to high (1:1) repeat unit to dopant ratios and possess a $T^{-1/4}$ temperature dependence of the electrical conductivity (ref. 20).

The vast majority of the remaining electroactive polymers show clear thermally activated conduction mechanisms and many examples could be sited with conductivities ranging from 10^{-12} to 10^{-4} ohm^{-1}cm^{-1} (refs. 2-5, 7, 21-22).

Can general conclusions be drawn about the conduction mechanisms operating in organic polymers? The temperature dependence of the conductivity is about the only property that has been determined for enough materials to allow comparisons. More in depth studies have been made on specific materials, but details are frequently regarded as indications of unique material properties, fragmenting an already confused subject.

The long-range periodic order and inverse temperature dependent conductivity characteristic of metallic band gap conduction are only found in polythiazyl. The temperature dependence of the remaining systems clearly indicates hopping transport between inherently localized states. The hop length and the energy barrier to transport will vary according to morphological structure and chemical composition but the inherent rate limiting process is intermolecular charge transport.

The principle objection to this mechanistic interpretation of polymer conductivity is that it does not provide a good explaination for the high mobilities observed in materials like doped polyacetylene. One way around this objection is to postulate a percolation-type transition at which individual localized states begin to interact facilitating long-range transport within a cluster. The rate limiting step to charge transport is still hopping between localized states but fast long range transport occurs within clusters of localized states. With this general model of the conduction process it is possible to relate chemical composition and molecular structure to conductivity in organic polymers.

THE INFLUENCE OF MOLECULAR STRUCTURE ON CONDUCTIVITY

The process of designing a new polymer, or selecting a known material, for use in a specific application with specific performance requirements relies on some set of relationships between molecular structure and physical properties. Some formal relationships exist for polymers but the intelligent design of materials for specific thermal, mechanical, and electrical properties is largely heuristic

The predominance of hopping transport mechanisms indicates that the design of a conducting polymer must include a molecular structure that can exist as a stable radical ion. The less stable the radical ion the more energy will be required to form the ion and the greater the likelihood of trapping or an irreversible chemical degradation. The later is a serious problem with conducting polyacetylene, polypyrrole, and polyphenylene sulfide, which must be protected from atmospheric oxygen and water vapor.

Because the rate limiting step appears to be intermolecular charge transport, not an intramolecular phenomena, it is not necessary for the polymer to possess a delocalized π electron molecular orbital along its entire backbone. The molecular structure of polyphenylene sulfide illustrates this point: its conformation is coil-like and its π electron orbitals are

localized at each individual phenylene sulfide repeat unit.

The optimum size of this localized charge state remains unclear. The molecular weight dependence of the conductivity in the polydiacetylenes, which possess complete π electron delocalization along their rodlike backbone, is only linear, while the addition of a few mole percent of a dopant causes a 10-12 order of magnitude increase in the conductivity at the percolation threshold. Extrapolation of the activation energy for charge transport to infinite molecular weight yields a minimum value of 0.4 eV only one-third the value for an oligomer of 20,000 daltons.

Intermediate between these two extremes of highly extended π orbitals and charge states localized on a single repeat unit lie polyacetylene and polypyrrole. In these systems the localized charge state involves approximately ten and four repeat units, respectively. Whether or not these repeat units are part of the same polymer backbone, or comprise an ordered intermolecular aggregate involving a single dopant, is unknown.

The issue of intermolecular order is an important one since, in the final analysis, it is the intermolecular process that is responsible for macroscopic charge transport. While difficult to quantify, proximity and registry between adjacent localized states is advantageous as is the ability to intercalate oxidizing (or reducing) dopants. Consequently crystallinity, short-range chain stiffness, stereoregularity, and minimal pendant group substitution are believed to be desirable.

These criteria are amply demonstrated in comparisons of the electrical conductivity of polyacetylene or polypyrrole and their derivatives. The addition of pendant groups or copolymerization, which doesn't alter the electronic structure of the backbone appreciably, causes a consistent and often dramatic decrease in conductivity. In other systems containing large fused rings, for example the polyphthalocyanines, pyrolyzed Kapton and polyacrylonitrile, polyvinylcarbazole, and polyacene quinones the influence of intermolecular order between stable charge carriers on conductivity can be seen.

In summary there are a finite set of molecular structural parameters that are responsible for the different degrees of electrical conductivity in organic polymers. They include the electronic structure of the charge bearing state, its size, and the local intermolecular order between states that promotes efficient intermolecular transport. Significantly this model indicates that corrosive dopants (SbF_6, AsF_5, etc.) are not necessary and that processable electrically conducting polymers, unlike the intractable materials currently under study, can be prepared.

A MATERIALS-BASED APPROACH TO THE PROBLEM OF SPACECRAFT CHARGING

A successful theory or model should lead to the identification of new materials or phenomena as well as to explain the properties of known materials or previously observed phenomena. The molecular principles discussed above have in fact identified new polymer compositions that are soluble in organic solvents, stable towards atmospheric exposure and are moderately (10^{-4} ohm^{-1} cm^{-1}) conductivity. The remainder of this section however describes how these

principles can be used to identify or design materials with semiconducting (10^{-12} ohm^{-1}cm^{-1}) electrical properties and the requisite properties for space-based use.

An application like space-based radar requires many square kilometers of a strong polymer film. The material must be stable towards ionizing radiation and temperature extremes for mission lengths of up to five years. These general principles have led to the conclusion that there exist short-, intermediate- and long-term approaches towards identifying the optimum materials.

The short-term approach requires the use of commercially available materials without reformulation or extensive modification. The most promising approach involves the use of a lightly pyrolyzed polyimide film. When commercial aromatic polyimide films are heated under vacuum at temperatures of from 400° to 700°C the polymer molecules condense to form extended, fused-ring structures (ref. 23,24). The conductivity of the films is raised from 10^{-18} ohm^{-1}cm^{-1} to a value, dependent of the pyrolysis temperature, of up to 10^2 ohm^{-1}cm^{-1}. While extensive pyrolysis will embrittle the material only slight changes are necessary to arrive at a value of 10^{-12} ohm^{-1}cm^{-1}. Since the level of conductivity is variable, the same basic feedstock can be tailored, by control of the processing conditions, to fit specific applications.

The major questions that must be answered in evaluating this approach include how does pyrolysis affect the mechanical properties of the polyimide film and is the partially pyrolyzed product stable in a spacecraft environment. Experimental charging data in reference 25 for Kapton samples on the SCATHA mission indicate an exponential decrease in conductivity of nearly two orders of magnitude over a year's time. The resistivity of Kapton can drop by ten orders of magnitude or more in pyrolysis, so if the change in electrical properties observed or SCATHA are due to the moelcular rearrangements observed in pyrolysis the material wil have to be stabilized if a narrow tolerance for electrical propeties is to be maintained.

Polyacrylonitrile undergoes similar electrical changes on pyrolysis described in reference 26. The molecular changes are complex and not well understood, but providential, since the strength retention of elevated temperatures is improved and some intermolecular crosslinking probably occurs. Potential difficulties inherent in the use of pyrolyzed polyacrylonitrile include elevated temperature properties, embrittlement, and stability. Both of these examples are off-the-shelf materials and experimental investigation of the pyrolyzed materials, their electrical and structural properties, could begin immediately.

There exist a wide range of intermediate-term solutions that involve the modification or further investigation of materials that are known, but not commercially available. The object here is to improve the high temperature performance of materials that otherwise have desirable electrical properties or to provide the necessary conductivity to polymers with inherent thermal and mechanical properties.

For example, materials like polyvinylcarbazole (ref. 27) or polyvinylpyridine (ref. 28) possess the necessary electrical conductivity for this application but mechanically can not withstand elevated temperatures.

The introduction of a few pendant ionic groups would convert these polymers into ionomers that contain ionic crosslinks. The conversion of polyethylene into an ionomer raises its softening temperature by 50° to $100^\circ C$ (ref. 29) which would be sufficient to make these two materials candidates for space-based use.

One approach to the problem of long-term stability in pyrolyzed polyimide is the use of blends or molecular composites (ref. 30). The polyimide could be blended, either as a physical mixture or as a copolymer, with one of the high strength/thermally stable organic polymers that have been developed in recent years. The structural component would provide the mechanical integrity while the polyimide pyrolysis product would support charge transport.

Finally, some of the derivatives of polyacetylene (ref. 31) and polypyrrole (ref. 19) could be reinvestigated. Many have the requisite electrical properties but have not been thoroughly characterized with regard to strength, thermal stability, and radiation resistance. Almost all could be reformulated as crosslinkable resins that would possess the requisite strength and thermal stability.

A long-term approach to the development of materials for the reduction of spacecraft charging would require the chemist to go "back to the drawing board" and combine the molecular principles already discussed with those for producing high strength, thermally stable, radiation resistant polymers. The principles for molecular design of conducting polymers are just beginning to evolve. They are about at the point where the design of high strength polymers was ten years ago and there is every reason to believe that, with the proper support, they can evolve into successful commercial technologies.

CONCLUSIONS

Comparison of the limited data available in the literature concerning electrically conducting polymers indicates that hopping transport between localized states is the predominant conduction mechanism. Comparison of the various chemical compositions and morphological structures has allowed the development of a general model for conductivity. The three important material characteristics include the electronic structure of the localized state, its size, and the degree of intermolecular order present. This model has led to the development of new conducting polymers as well as providing a rational explanation for existing materials. Specific materials or modifications have been proposed that would produce polymer dielectrics with the level of conductivity believed necessary to reduce spacecraft charging phenomena and have the requisite thermal, mechanical and environmental properties.

REFERENCES

1. Lehn, W. L.: SCATHA Conductive Spacecraft Materials Development, J. Spacecraft, Vol. 20, No. 2, March 1983, pp. 182-186.

2. Duke, C. B.: Conductive Polymers, Encyclopedia of Chemical Technology, Vol. 18, Third Edition, 1982, J. Wiley and Sons, New York, pp. 755-793.

3. Cotts, D. B., and Reyes, Z.: New Polymeric Materials Expected to Have Superior Properties for Space-Based Uses, Final Report, Contract No. F19628-81-C-0076, August 1983.

4. Goodings, E. D.: Conductivity and Superconductivity in Polymers, J. Chem. Soc. Reviews, Vol. 5, 1976, pp. 95-123.

5. Blythe, A. R.: Electrical Properties of Polymers, Cambridge Solid State Sciece Series, Cambridge, England, 1979, pp. 91-183.

6. Econcmou, E. N., Cohen, M. H., Freed, K. F., and Kirkpatrick, E. S.: Electronic Structure of Disordered Materials, in "Amorphous and Liquid Semiconductors," J. Tauc, ed., Plenum Press, New York, 1974, pp. 101-158.

7. Rembaum, A., Moacanin, J., and Pohl, H. A.: Polymeric Semiconductors, Progress in Dielectrics, Vol. 6, 1965, pp. 41-102.

8. Sheng, P.: Fluctuation-Induced Tunneling Conduction in Disordered Materials, Physical Review B, Vol. 21, No. 6, 1980, pp. 2180-2195.

9. Hsu, C. H., and Labes, M.: Electrical Conductivity of Polysulfur Nitride, J. Chemical Physics, Vol. 61, 1974, pp. 4640-4645.

10. Chiang, C. K., Cohen, M. J., Garito, A. F., Heeger, A. J., M. Kulski, C. M., and MacDiarmid, A. G.: Electrical Conductivity of $(SN)_x$, Solid State Communications, Vol. 18, 1976, pp. 1451-1455.

11. Baughman, R. H., and Chance, R. R.: Comments on the Optical Properties of Fully Conjugated Polymers: Analogy Between Polymers and Polydiacetylenes, Journal of Polymer Science: Polymer Physics Edition, Vol. 14, 1976, pp. 2037-2045.

12. Lochner, K., Reimer, B., and Bassler, H.: Anisotropy of Electrical Properties of a Polydiacetylene Single Crystal, Chemical Physics Letters, Vol. 41, No. 2, 1976, pp. 388-390.

13. Ohnuma, H., Inoue, K., Se, K., and Kotaka, T.: Electrical Conductivity of an Amorphous and Single Crystalline Polydiacetylene Derivitive, Reports on Progress in Polymer Physics in Japan, Vol. 25, 1982, pp. 27-30.

14. Se, K., Ohnuma, H., and Kotaka, T.: Effect of Molecular Weight on Conductive Properties of Polydiacetylene Derivatives, Reports on Progress in Polymer Physics in Japan, Vol. 24, 1981, pp. 409-410.

15. Enkelmann, V., Muller, W. and Wegner, G.: Structure, Morphology and Techniques of Chemical Modification of Polyacetylene, Synthetic Metals, Vol. 1, 1979/1980, pp. 185-192.

16. Park, Y. -W., Heeger, A. J., Druy, M. A., and MacDiarmid, A. G.: Electrical Transport in Doped Polyacetylene, Journal of Chemical Physics, Vol. 73, No. 2, 1980, pp. 946-957.

17. Chiang, C. K., Park, Y. -W., Heeger, A. J., Shirakawa, H., Louis, E. J., and MacDairmid, A. G.: Electrical Conductivity of Halogen-Doped Polyacetylene, Physical Review Letters, Vol. 39, No. 17, 1977, pp. 1098-1106.

18. Feldblum, A., Kaufman, J. H., Etemad, S., Heeger, A. J., Chung, T. C., and MacDiarmid, A. G.: Opto-Electrochemical Spectroscopy of Trans-Polyacetylene, Physical Review B, Vol. 26, 1982, pp. 815-826.

19. Kanazawa, K. K., Diaz, A. F., Gill, W. D., Grant, P. M., Street, G. B., Gardini, G. P., and Kwak, J. F., Polypyrrole: An Electrochemically Synthesized Conducting Polymer, Synthetic Metals, Vol. 1, 1979/1980, pp. 329-336.

20. Rabolt, J. F., Clarke, T. C., Kanazawa, K. K., Reynolds, J. R., and Street, G. B.: Organic Metals: Poly(p-phenylene sulphide) Hexafluoroarsenate, J.C.S. Chem. Comm., 1980, pp. 347-348.

21. Mort, J., Pfister, G.: Electronic Properties of Polymers, Wiley Interscience, New York, 1982.

22. Block H.: Electrically Conducting Polymers, Advances in Polymer Science, Vol. 33, 1979, pp. 33-78.

23. Bruck, S.D.: Thermal Degradation of an Aromatic Polypyromellitimide in Air and Vacuum. III Pyrolytic Conversion into a Semiconductor, Polymer, Vol. 6, 1965, pp. 319-332.

24. Brom, H. B., Tomkiewicz, Y., Avivam, A., Broers, A., and Sunners, B.: On a New Conducting Polymer - Pyrolyzed Kapton, Solid State Communications, Vol. 35, 1980, pp. 135-139.

25. Mizera, P. F. and Boyd, G. M.: A Summary of Spacecraft Charging Results, AIAA-82-0268, AIAA 20th Aerospace Sciences Meeting, Orlando, Fla., January 1982.

26. Teoh, H., Metz, P. D., and Wilhelm, W. G.: Electrical Conductivity of Pyrolyzed Polyacrylonitrile, BNL Report 30141, August 1981.

27. Okamoto, K., Kato, K., Murao, K., Kusabayashi, S., and Mikawa, H.: The Photoconductivity of Polyvinylcarbazole. IV Photoconductivity of Copolymers of N-Vinylcarbazole with Styrene, Vinyl Acetate, and N-Vinylpyrrolidone, Bulletin of The Chemical Society of Japan, Vol. 46, 1973, pp. 2883-2885.

28. Lupinski, J. H., Kopple, K. D. and Hertz, J. J.: New Class of Film-Forming Electrically Conducting Polymers, Journal of Polymer Science: Part C, No. 16, 1967, pp. 1561-1578.

29. Longworth, R.: Thermoplastic Ionic Polymers, Holiday, L., editor. J. Wiley and Sons, New York, 1975, pp. 69-75.

30. Hwang, P. -H., Wiff, D. R., Benner, C. L., and Helminiak, T. E.: Composites on a Molecular Level: Phase Relationships, Processing and

Properties, J. Macromolecular Science - Physics, Vol. B22, No. 2, 1983, pp. 231-257.

31. Hankin, A. G. and North, A. M.: D. C. Conductivity of Some Linear Conjugated Programs, Transactions of the Faraday Society, Vol. 63, 1967, pp. 1525-1536.

INVESTIGATIONS OF RADIATION-INDUCED AND CARRIER-ENHANCED CONDUCTIVITY*

A. Meulenberg, Jr.
COMSAT Laboratories
Clarksburg, Maryland 20734

L. W. Parker
Lee W. Parker Inc.
Concord, Massachusetts 01742

E. J. Yadlowski and R. C. Hazelton
H-Y Tek Corporation
Radford, Virginia 24143

A steady-state carrier computer code, PECK (Parker Enhanced Carrier Kinetics), that predicts the radiation-induced conductivity (RIC) produced in a dielectric by an electron beam was developed. The model, which assumes instantly-trapped holes, was then applied to experimental measurements on thin Kapton samples penetrated by an electron beam. Measurements at high bias were matched in the model by an appropriate choice for the trap-modulated electron mobility ($\mu' = 7 \times 10^{-15}$ m^2/V-s). A fractional split between front and rear currents measured at zero bias is explained on the basis of beam-scattering.

The effects of carrier-enhanced conductivity (CEC) on data obtained for thick, free-surface Kapton samples is described by using an analytical model that incorporates field injection of carriers from the RIC region. The computer code, LWPCHARGE, modified for carrier transport, is also used to predict partial penetration effects associated with CEC in the unirradiated region. Experimental currents and surface voltages, when incorporated in the appropriate models, provide a value for the trap-modulated mobility ($\mu' = 3$-7×10^{-15} m^2/V-s) that is in essential agreement with the RIC results.

I. INTRODUCTION

The theoretical studies reported here were undertaken to establish carrier models for the proper interpretation of experimental data. These studies provide conductivity formulae for thin (ref. 1) and thick Kapton (ref. 1,2) samples in electron beams. ("Thin" here refers to sample thickness smaller than or comparable to the electron range; "thick" refers to sample thickness larger than the electron range.)

The thin-Kapton experiments were designed to evaluate the RIC by subjecting a biased sample with metallized surfaces to a penetrating electron beam and measuring the currents from the front surface (beam side) and rear surface (substrate side). In the thick-Kapton experiments, the front surface was not metallized but was free to float at a surface potential determined by the balance of incident, backscatter,

secondary, and conduction currents. The thick-Kapton experiments were designed to measure secondary yields from the "free" surface and enhanced bulk conductivity, the latter characterizing the nonpenetrated region (comprising most of the sample thickness). The enhancement results from the presence of additional carriers supplied from the irradiated region. The modeling of the CEC and of the RIC is the goal of the present study.

II. RADIATION-INDUCED CONDUCTIVITY

Electron-hole pairs produced by energetic electrons penetrating a dielectric sample sandwiched between metal plates can recombine or separate to become negative and positive free carriers.* These carriers undergo one of three ultimate fates:

a. While free, they can exit the sample by "drifting" under the influence of an electric field (applied plus space charge) or by "diffusing" (random walk) to one of the plates.

b. They can "fall into" (be captured by) a deep trap (localized state) with energy, well below the free electron level. This process effectively immobilizes them, but their presence contributes to the space charge.

c. They can vanish by recombining with an already captured immobile carrier of the opposite sign, also eliminating the trapped carrier.

Fate (b) can be modified by the thermal release ("detrapping") of the trapped carrier. The probability of detrapping depends on temperature, electric field, and trap energy. A free carrier can undergo a series of trapping and detrapping events (more probable with shallow traps than with deep traps) until it is eliminated by fate (a) or fate (b) above. Fate (c) can also include recombination with a free carrier of the opposite sign, but this option is much less probable than recombination with the much more numerous trapped carriers. The notation used in this study is defined as follows:

p, n = concentrations of free holes and free electrons
p_T, n_T = concentrations of trapped holes and electrons
D_p, D_n = diffusion coefficients for free holes and electrons
M, μ = mobilities for free holes and electrons
R_1, R_2 = recombination coefficients (cm^3/s) for free holes with trapped electrons and free electrons with trapped holes
P_T, N_T = concentrations of neutral hole traps and neutral electron traps
E = electric field intensity
$\backslash$ = electric potential
e = magnitude of electron or hole charge
G = production rate of electron-hole pairs (per unit volume) associated with ionization dose rate (G')
H = deposition rate of injected carriers (excess charge assumed here to be electrons only)
ϵ = dielectric permittivity

---

*The terms "hole" or "positive free carrier" used here do not necessarily convey the same meaning as in semiconductor theory. They denote temporally stable positive charge sites; in some dielectrics, this uncompensated positive charge is more likely than a negative charge site to migrate.

τ_p, τ_n = mean lifetimes of free holes and electrons in the conduction band (i.e., time interval between introduction and trapping or "trapping times")

τ_+, τ_- = mean lifetimes of trapped holes and electrons (i.e., time between trapping and release or "detrapping times")

F_p, F_n = fluxes of holes and electrons

J_p, J_n = current densities of holes and electrons ($J = eF$).

The transport and Poisson equations are set up in standard fashion (ref. 3-6) with appropriate boundary conditions and approximations made to help solve the system of differential equations. The complete formulation is given in reference 7.

In our preliminary work on Kapton, we made the following simplifications to more easily understand the carrier kinetics. One simplification is the use of a steady-state solution. We also assume that the holes are instantly trapped (and not released) and that the electrons are not deeply trapped (at most, shallowly trapped and detrapped). Thus, the electrons may be considered quasi-free, but the trapping/detrapping effects inhibit their motion, which is described by replacing the true mobility μ by a much smaller "trap-modulated" effective mobility μ'. This leads to the following system of equations (ref. 7):

$$p = n_T = 0 \quad \text{(no holes or deeply trapped electrons)} \tag{1}$$

$$\frac{\partial f_p}{\partial x} = 0 \quad \text{(no hole migration)} \tag{2}$$

$$p_T = \frac{G}{nR_2} \quad \text{(trapped hole profile)} \tag{3}$$

$$\frac{\partial f_n}{\partial x} = H \quad \text{(electron flux gradient)} \tag{4}$$

$$\frac{d^2V}{dx^2} = -\frac{e}{\varepsilon}(n - p_T) \tag{5}$$

We define $E = -dV/dx$ and arrive at the expression

$$\frac{\mu kT}{e}\frac{d^2n}{dx^2} - \mu E\frac{dn}{dx} + H + \frac{\mu e}{\varepsilon}\left(\frac{G}{R_2} - n^2\right) = 0 \tag{6}$$

The first term is associated with electron diffusion, the second with electron drift, the third with electron deposition, and the fourth with space charge. These equations may be solved by numerical integration, subject to boundary conditions:

$n = 0$ at $x = 0$ and L (diffusion boundary condition)
$V = 0$ at $x = L$ (grounded substrate)
$V = V_A$ at $x = 0$ (applied bias voltage)

If injection occurs, one of the latter two conditions above is replaced by a pre-scribed value of dV/dx at the injection contact.

The method of solving differential equations (5) and (6) used here employs an iterative process. Enforcement of the above boundary conditions is accomplished by starting at $x = 0$ with initial values $n = 0$ and $V = V_A$, and with estimated values of dn/dx and dV/dx. The differential equations are then stepped to $x = L$ with the intention of hitting $n = 0$ and $V = 0$ there as the "target" values. If these targets are not hit, we start again at $x = 0$ with readjusted values for dn/dx and dV/dx. If injection occurs, the initial or target conditions are suitably modified. This pro-cedure is implemented in the computer code PECK. Under most conditions, the task of achieving the "converged" solution is not trivial, since there are two free starting variables. The solutions obtained, however, provide insight into the excess charge and electric fields in an irradiated dielectric.

III. APPLICATION OF THE RIC MODEL TO THE THIN-KAPTON EXPERIMENT

This section presents an implementation of the trapped-hole RIC model, sample solutions, and a comparison of the model with experimental results.

The collected currents in the RIC experiment described below (and in ref. 1) were not symmetric with respect to applied bias. Therefore, the conductivity in-ferred from these data was found to be polarity dependent. Moreover, at zero bias, the rear current was observed to be larger than the front current. (This possibility had been predicted theoretically for sufficiently high-beam energies by Oliveira and Gross (ref. 8), and was seen in experiments on mica by Spear (ref. 9). Oliveira and Gross predicted total current collection at the rear contact when the beam voltage exceeded 35 keV. Aris et al. (ref. 10) considered the Oliveira and Gross theory as well as the Spear experiments, but they did not address the question of why they dif-fer on the rear-front current split. The question is resolved in this study: the current split is associated with the degree of beam-scattering in the sample. The polarity dependence found in the RIC experiment is also explained here, by consider-ing carrier injection, internal fields, and spatially varying conductivities.

A. Experimental Data for Thin Kapton Samples (6.4 μm)

Figures 1 and 2 show variations in the front and rear current densities, J_1 and J_2, with varying net incident beam currents for fixed biases (±196 V and ±45 V) applied to the front surface. Here, J_B' denotes the beam current density, less the backscatter and secondary emission from the front surface. This can also be con-sidered the net beam current entering the sample. The beam energy is 28 keV. Elec-trons moving toward the right are considered positive current. The superscript denotes the sign of the bias that has been applied to the front contact (number 1). Since J_1 and J_2 can exceed J_B', a source of electrons other than the beam must be invoked.

B. Primary Current and Deposition Curves from Theoretical Transport Model

By the use of a Monte Carlo transport code, tabulations were made of the parti-cle and energy fluxes, which were then fitted as analytic functions of depth and net incident energy (ref. 1). The curve shown in figure 3 is the percentage of incident flux P vs depth x. This percentage is normalized to represent the fraction of a

1 nA/cm^2 28-keV incident beam that has penetrated to depth x in the sample. At the surface (x = 0), the value is 0.934, the fraction 0.066 having been lost to back-scatter. (The secondary emission has been ignored here since it is negligible for a high-energy beam.) The primary flux falls off monotonically to 0.023 at 6.4 μm.

Figure 4 shows the dose rate (G') in rads vs depth, obtained from the derivative of the energy flux as a function of x (not shown), and the excess-charge deposition rate (H) obtained from the derivative of the primary flux shown in figure 3. These two functions are similar to those plotted by Matsuoka et al. (ref. 11) in normalized form. The average and peak values of G' are 2,900 and 3,700 rad/s, respectively. The average and peak values of H are 0.14 and 0.21 nA/μm, respectively. (Here, G' denotes dose rate, while G denotes pair production or generation rate.)

C. Parameters of the Model

In the preliminary solutions of equations (5) and (6) that follow, for sim-plicity, constant values of G' and H, 2,900 rad/s and 0.16 nA/μm, respectively, have been assumed. The assumed constant deposition function H corresponds to a pene-trating flux that decreases linearly with depth (extreme scattering), which helps in making analytical approximations. The following parameters were also used to model the experiment in the PECK code:

$$L = \text{thickness} = 6.4 \times 10^{-6} \text{ m} = 6.4 \text{ μm}$$
$$kT/e \text{ at room temperature} = 25 \text{ mV}$$
$$J_B = \text{nominal beam current} = 10^{-5} \text{ A/m}^2 = 1 \text{ nA/cm}^2$$
$$(F_B = \text{flux} = 6.25 \times 10^{13} \text{ electrons/m}^2\text{-s})$$
$$\epsilon = \text{permittivity} = 3.4\epsilon_0 = 3.4 \times 0.804 \times 10^{-11}$$
$$= 3.0 \times 10^{-11} \text{ F/m}$$
$$G = \text{pair generation rate} = 3 \times 10^{21}/\text{m}^3\text{-s}$$
$$= 3 \times 10^{15}/\text{cm}^3\text{-s}$$
$$R_2 = \text{recombination coefficient for free electrons}$$
$$\text{with trapped holes} = 10^{-13} \text{ m}^3/\text{s} = 10^{-7} \text{ cm}^3/\text{s}$$
$$\mu = \text{mobility} = \text{variable (in m}^2/\text{V-s)}.$$

The generation rate is based on our own transport calculations and on values found in the literature. For a 28-keV beam of current density, 1 nA/cm^2, a mean dose rate of 2,900 rad/s in the 6.4-μm Kapton sample was calculated. For a density of 1.43 g/cm^3, this dose rate translates to 2.6×10^{17} eV/cm^3-s. Now, choosing the energy per hole-electron pair (ref. 12) to be 100 eV yields G = 2.6×10^{15} pairs/cm^3-s. Rounding this to 3×10^{15} pairs/cm^3-s yields the value also used by Hughes for a SiO$_2$ photoconduction problem (ref. 4,5). The recombination coefficient is taken to be $R_2 = 10^{-7}$ cm^3/s; hence, $G/R_2 = 3.0 \times 10^{22}/\text{cm}^6 = 3.0 \times 10^{34}/\text{m}^6$.

IV. PRELIMINARY SOLUTIONS FROM THE TRAPPED-HOLE RIC MODEL

A. Zero Bias and Excess Charge Deposition

To gain experience and test the results, the computer model was tested for the simplest cases first. The first set of conditions included the use of constant G and H, no carrier injection from the contacts, and zero bias. Figure 5 illustrates the results under these conditions. The average excess electron concentration, n, exceeds the trapped hole concentration, and a negative potential, V, results inside the dielectric. The symmetry seen in fig. 5 is to be expected with the above conditions.

A series of runs was carried out, varying the value of mobility, μ. For $\mu > 0.88 \times 10^{-8}$ m^2/V-s, the excess electron population drains until a positive potential within the dielectric establishes equilibrium with the incident electron beam. For $\mu < 0.88 \times 10^{-8}$ m^2/V-s, a negative internal potential (fig. 5) develops to push out enough electrons to establish equilibrium with the beam-deposited electrons. As will be seen later, values of μ are much less than 10^{-8} m^2/V-s, so that a significant negative potential is expected within the bulk of a dielectric in an electron beam. This negative internal potential would prevent injection of electrons from the contacts into the dielectric. Our assumption of immobile holes prevents hole injection.

The electron fluxes, F for the primary flux from the beam, F_{DD} for the diffusion + drift flux, and F_{TOT} ($= F + F_{DD}$) provide a 50-50 split in the front and back contact currents $|J_1| = |J_2|$. No change in beam current density J_B or in carrier mobility will alter this balance. However, a change in the shape of G and/or H will affect it. If H shifts, depositing more charge in the rear of the film, the back current, J_2, will increase. If G shifts so that deposited energy, ionization, and conductivity is increased in the front half of the film, the front current, J_1, will increase. Both shifts are necessary to bring the model into closer agreement with the experimental conditions (depicted in fig. 4). Since the results of these shifts are in opposition, the relative importance of G and H are indicated by the experimental data showing $|J_2| > |J_1|$. If a nonlinear (cubic) form for H is used to better approximate the actual value from the 28-keV beam, the resultant distributions (charge, potential, and so on) will be similar in shape and magnitude to the linear case. However, an asymmetry sufficient to cause a 66/34-percent split between the back/front contact currents occurs. (The no-scattering approximation, which assumes no charge deposition except at the end of range, provides for total current collection at the back contact with sufficiently high-beam energies, as described in ref. 8.)

In the zero-bias case, the internal potential established by H is more important than the conductivity created by G, but as bias is applied, the situation changes. The field of an applied bias can exceed that generated by the trapped charge resulting from H. As the externally applied field gets larger, the conductivity provided by G has the greatest effect on the internal potential profiles and, therefore, on the current distribution.

The net current out of a film ($|J_1| + |J_2|$) must equal the total current into the film (J_B) if no bias is applied. The shapes of G and H will alter the relative currents to the two contacts (J_1 and J_2). Only if a bias is applied and injection of carriers from one or both contacts occurs can either J_1 or J_2 exceed J_B.

B. 200-V Bias and Excess Charge Deposition

Experimental results of the penetrating electron beam on a thin Kapton film with a bias voltage (±196 V) applied (fig. 1) showed that all currents exceeded the beam current J_B, and therefore that injection of one form or another must be invoked. A computer fit was made to the experimental data with our simplified model (H and G constant), with high carrier injection from the contacts assumed, and with a +200 V bias applied to the front surface. The beam current deposited into the film was $J_B' = 1$ nA/cm^2; from Figure 1, J_1 and J_2 are -4.4 and 3.4 nA/cm^2, respectively.

The results of the fit are shown in figure 6. The high electron concentration adjacent to the negative contact extends into the bulk of the film and dominates the

beam-deposited charge through much of the dielectric. The effective mobility neces-
sary to fit the model results to experimental results was $\mu' = 7 \times 10^{-15}$ m^2/V-s.
This value must be considered crude because the model did not match the experimental
conditions well; some constants [R_2 and G from eq. (5)] are values for SiO_2; and the
injection represented is an extreme. Despite simplification of the model, some use-
ful predictions can be made. The curvature of the potential within the film reflects
the shape seen in figure 5 for the zero-bias case. At some positive bias, the slope
of this curve is zero (dV/dx = 0) at the back contact; at some negative bias,
dV/dx = 0 at the front contact. As the bias is varied through these critical points,
the potential gradient reverses as does the current at that contact. The symmetry of
the simplifying assumptions predicts a symmetry in the forward and reverse bias re-
sults of the model. However, the experimental results indicate more current flows
when negative bias is applied to the front surface than when a positive bias is
applied. The shape of G and H must therefore be important. The deposited charge and
ionization-induced conductivity are significant relative to the bias-injected charge
under the test conditions. If this is the case, when the bias voltage is reduced,
the effects of G and H, relative to the effects of bias magnitude and polarity,
should increase.

C. ±45-V Bias and Excess Charge Deposition

Experimental data are available for the lower bias situation (fig. 2). When
compared with figure 1, it is seen that at the higher beam currents, one of the
contact currents (J_2') reverses and crosses the J = 0 axis, as predicted by the model
(see above). At even lower bias voltages, J_1' would also be expected to cross over
the J = 0 axis. This crossover results from a deposited charge that establishes
fields which oppose and exceed the field created by the applied bias. Since values
of conductivity are experimentally determined from the measured currents and applied
voltages, care must be taken in dielectrics where internal fields can be reversed
(and maintained) by the presence of excess (or trapped) charge. Assumptions about
uniform fields and conductivities in electron-beam irradiated dielectrics are only
valid under special conditions (e.g., if the beam intensity is low enough, the de-
posited charge will not greatly alter the potential profile compared to the effect of
the bias). In figure 2, the beam current density of 0.65 nA/cm^2 is adequate to
create a field at the back contact equal to that created by the +45-V bias on the
6.4-μm sample (hence, no current flows in this region). If no current is detected
(J_2 = 0) and if uniform fields are assumed, it could appear that the conductivity is
zero. This is obviously not the case. Similarly, under different conditions, inter-
pretation of other effects (such as field and dose dependence) can be incorrect.

This study concludes that measurements of RIC, field-enhanced conductivity, and
dose-dependent effects are unreliable in electron beam experiments without a proper
model that reveals the internal potential profiles. Even irradiation with gamma-rays
is a problem because of the effects of knock-on and back-scattered
electrons (ref. 13).

D. Discussion of RIC Results

Several important facts emerged from the interpretation and modeling of the RIC
experiment. First, injection of carriers from the contacts must be considered, at
least in Kapton with gold contacts (some materials and some contacts might not permit
injection). Second, with so many unknowns in the model, to determine material param-
eters, it is necessary to have as many experiments that vary the independent vari-
ables as there are unknowns to be found. Simplified computer models are very useful

in predicting the types of effects; however, more realistic values for G and H must be inserted to obtain realistic and quantitative values for the material parameters sought.

A brief recapitulation of the important factors in the model and experiment follows.

a. Assumptions about mobile negative charge and deeply trapped positive charge seem to fit the data for Kapton.

b. Depositing negative charge (with low mobility after deposition) means that a negative potential is created in the bulk of the dielectric.

c. With applied bias, injection of negative charge from the negative contact into the dielectric is required to fit the data.

d. The potential profiles in a film depend on the amount of charge deposited from the beam, injection from the contacts, local conductivity, and external bias (fig. 4-6); they are seldom linear.

e. Because of nonlinearities in charge deposition (H), carrier generation from energy deposition (G, which affects conductivity), and internal potentials, V(x), external currents may be dominated by small regions of the dielectric. Material parameters cannot be accurately determined without accounting for these effects.

Two additional factors help explain the experimental data; these are described here more fully.

f. Contact currents J_1 and J_2 can be broken into components $J_{1,2}^V$ and $J_{1,2}^i$, which are composed of charge from the beam and charge injected from one contact or the other. Figure 7 contains two sets of current density components (beam generated and bias generated) for the simplified model. In cases of no applied bias, the beam-generated contact currents $|J_{1,2}^0|$ are equal, since G and H are uniform. In addition, $|J_1^0| + |J_2^0| = J_B$, and no injected component is present. With applied bias V, the beam-generated currents shift so that $|J_1^V| \neq |J_2^V|$, but they still add up to J_B. Injection currents ($J_{1,2}^i$ are the dotted line) flow from the negative contact and $J_1^i = J_2^i$. (The convention used here is that positive currents are described by electrons moving to the right in figure 1, therefore, injected currents have the same sign and the beam-generated currents have opposite signs.) The total contact currents are the sums of the components: $J_1 = J_1^V + J_1^i$; $J_2 = J_2^V + J_2^i$. Figure 7 shows the results of no bias applied and negative bias applied to the front (number 1) contact. Because of the assumptions, the same positive bias applied to the front contact would result in $J_1^+ = -J_2^-$ and $J_2^+ = -J_1^-$.

Figure 8 shows the component currents for a smaller positive bias. The negative values of the current sums $-J_1^+ = -(J_1^i + J_1^i)$ and $-J_2^+ = -(J_2^i + J_-^i)$ are displayed to make comparison with figures 1 and 2 easier. The reason for the $-J_2$ crossover may be easily seen from the summation of its components. Again, reversing the bias polarity provides $J_1^- = J_2^+$ and $J_2^- = J_1^+$ for this simplified model.

The condition $|J_1^V| + |J_2^V| = J_B$ requires that $|J_{1,2}^V| \leq J_B$. Figure 7 illustrates the basis for defining bias-dominated and beam-dominated regions. At a given bias, low-beam currents do not significantly alter the applied fields. However, with high-

beam currents, the deposited charge generates fields greater than those from the applied bias, at which point, charges also flow toward the negative contact and the dielectric becomes beam dominated (fig. 8).

The total current density curves in figures 7 and 8 are symmetric with positive and negative applied bias. Experimental results in figures 1 and 2, however, do not display this symmetry. The asymmetry seen in those figures is a result of nonuniform ionization and charge deposition profiles (G and H in fig. 4). Part of the effect results from the higher back contact current ($|J_2^-| > |J_1^-|$ at zero bias), which will make $|J_2^-| > |J_1^+|$ and $|J_1^-| > |J_2^+|$. However, differences observed in the experimenta data are too great to be explained by this effect alone. An important additional effect involves the field injection of charge into the region of lower ionization near the back contact. To account for the experimental results, more electrons must flow from the irradiated bulk (under negative front bias) than from the metallic contact (under positive front bias). The data base is not adequate to determine if the difference is dominated by different field strengths in the injection region (with bias reversal) or by different charge-release mechanisms (irradiated dielectric vs metal contact).

g. The apparent saturation of injection current (fig. 7 and 8) is attribu ed primarily to a change from an n to an $n^{1/2}$ dependence of conductivity with an in- creasing beam current (ref. 12).

With increasing carrier generation, the principal loss mechanism of electrons changes from shallow traps to recombination with trapped holes (ref. 12). Other effects, which make an actual determination of conductivity dependence-on-dose very difficult, are reduced carrier generation near the rear contact (when the real beam profile is used; see fig. 4) and the injection of carriers into this region from the rear contact or from the bulk of the dielectric. The fact that the observed col- lected currents are higher when a negative voltage is applied to the front contact than when a positive voltage is applied suggests the possibility that injection from an irradiated region of the dielectric is greater than that from a metallic contact.

V. CARRIER-ENHANCED CONDUCTIVITY STUDIES - PARTIAL PENETRATIONS

Carrier-enhanced conductivity (CEC) is almost a tautological phrase, since all conductivity requires carriers and any increase in carrier concentration will enhance conductivity. Radiation-induced conductivity, field-enhanced conductivity, and thermally-stimulated conductivity are all forms of increased conductivity resulting from increased carrier concentrations. However, we reserve the phrase "carrier- enhanced conductivity" for specific cases in which extra carriers are introduced from a contact or from an adjacent irradiated (RIC) region. Because of space charge limitations, we assume that the number of extra carriers injected from a metal con- tact or from a RIC region is not large enough to alter the carrier mobility or to deviate from a shallow-trap controlled dependence (that is, recombination with posi- tive trapped charge can be neglected). The main reason that this small number of carriers may be important is that in high field regions, conductivities may be very low after enough time has elapsed to drain free or easily excited carriers from the dielectric. Unless external charge or ionizing radiation are introduced to provide more carriers, the conductivity of a dielectric in a field can decrease by orders of magnitude in a few hours. In the previous section, we discussed dielectrics with carriers introduced nonuniformly by ionizing radiation. The effects of charge in- jection from contacts or migration of charge from adjacent, heavily ionized regions

were observed in the less heavily ionized regions. Such effects are probably even more important in regions of low free-carrier concentrations (for example, nonirradiated or high field regions).

Two approaches were used to study the CEC problem affecting conduction in the unirradiated region. In one approach, the LWPCHARGE computer program, capable of treating fixed front-surface biases and carrier kinetics, was applied to partial penetrations of thin-Kapton samples and compared with experimental results (ref. 7). In the other approach, an analytical model with field injection from the RIC region was used to determine mobility in the unirradiated region (ref. 14). Additional results from both approaches are discussed below.

A. LWPCHARGE Code Results for Partial Penetrations

Carrier kinetics were included in the code by assuming the conductivity to be $-\mu'\rho$, where μ' is the mobility and ρ is the excess-charge density deposited by the primary beam. Therefore, the drift contribution to the current is determined by multiplying this conductivity by the electric field intensity. Diffusion was neglected (as in ref. 3). The dose and excess charge deposition rates were computed by using the Monte Carlo transport code (ref. 1) as in figure 4.

The following partial penetration results were obtained for the 6.4-μm thin Kapton, using 1 nA/cm^2 beams of energies 5, 10, 15, 20, and 28 keV, with zero bias on the sample. The mobility was assumed to be $\mu' = 10^{-15}$ m^2/V-s.

For each beam energy, table 1 shows the range, substrate current J_2, potential minimum V_m, position X_m of the minimum, and the approximate time scale for the transient. We see that the substrate current becomes significant when the range is greater than about half the sample thickness. (This "threshold effect" is in accord with the literature.) The potential minimum becomes deeper as deeper penetration occurs but starts to weaken after the sample has been penetrated. Its position progresses from zero to the midpoint of the sample with increasing beam energy. The time scale for establishing equilibrium is longest for the low-energy beam (about 20,000 s); the time diminishes as the beam energy (and depth of penetration) increases.

Experimental results of electron beams on 6.4-μm Kapton (normalized to 1 nA/cm^2 incident beam currents, assuming proportional scaling for small differences in beam current) are shown in table 2. (Comparing these results with those of table 1 indicates close agreement of J_2 in the case of penetrating beam (28 keV) and poor agreement in cases of the lower energy beams. However, the choice of $\mu' = 10^{-15}$ m^2/V-s in the computer model is probably low by a factor of three (as seen in the next section) to seven (as seen in Subsection IV B). If mobility is increased by a factor of three, the current J_2 collected at the back contact in the 15-keV case should also increase in magnitude, thereby coming into closer agreement with the experimental value (-0.12 nA/cm^2). The time scales should be reduced by nearly a factor of three (ref. 6), and the resulting ~900- and 300-s theoretical values are in much closer agreement with the 400- and 175-s experimental values for 15- and 28-keV beams, respectively. If the higher value of mobility ($\mu' = 7 \times 10^{-15}$ m^2/V-s) is used, the calculated results are even closer to the experimental results.

The fact that the model (if $\mu' = 3-7 \times 10^{-15}$ m^2/V-s) is in such close agreement with experimental results, even without a diffusion contribution of carriers to the

unirradiated region, indicates that (at least for low beam current densities) diffusion may be unimportant compared to the field-assisted drift of charge from the irradiated region. Before this statement can be confirmed, more comparison with experimental data, a better modeling of the mobile carrier concentration in the RIC region (to include ionization from the beam), and a successful incorporation of a diffusion term into the model must be carried out. However, in contrast to semiconductors (for which diffusion is significant), the diffusion of carriers in dielectrics should be small compared to the drift field injection, since free carrier concentrations and mobility are extremely low in dielectrics. Since field injection dominates diffusion and since diffusion could only have an effect in a charge-depleted region (that is, in a strong field region where field injection is more important), charge diffusion in dielectrics might reasonably be neglected.

B. Analysis of Thick Kapton Samples

In the thin Kapton samples analyzed above, the conduction processes are dominated by radiation-induced conductivity, with space-charge effects playing a lesser role. However, in beam irradiation experiments performed on 127-μm Kapton samples (ref. 2) (which are thick compared to the range of 2 to 18 keV electrons--a few microns), the RIC region is thin compared to the nonirradiated region. In these samples, the properties of the nonirradiated region are expected to control the current voltage characteristics of these materials.

Yadlowsky and Hazelton (ref. 14) have recently analyzed the experimental results of Hazelton et al. (ref. 2) and Adamo et al. (ref. 15) in light of space-charge-limited flow models, a field-enhanced conductivity model (Poole-Frenkel effect), Schottky barrier models, and a combination of Poole-Frenkel conduction and space-charge-limited currents. The classical expression

$$J_s = - \varepsilon\mu \, \frac{9}{8} \, \frac{V^2}{L^3} \tag{7}$$

for the space-charge-limited current through a dielectric sample appears to properly represent the functional dependence observed by Adamo et al. (ref. 15) for current flow between biased electrodes in an unirradiated sample. For an irradiated sample, equation (7) can be made to fit the experimental current-voltage results only if an order of magnitude variation in the value of the mobility is made (ref. 14). Yadlowsky and Hazelton (ref. 14) also found that the current voltage dependence can be represented by the other models mentioned above, but not satisfactorily. For example, in each case, a nonphysical beam energy dependence for the dielectric permittivity, ε, had to be assumed to obtain a functional fit. In addition, the value of the permittivity required to fit the data was five to six times the accepted value in some cases. These results led to the conclusion that these models are unsatisfactory in their usual forms. However, satisfactory results were obtained using a modified version of the space-charge-limited current model (ref. 14).

In the usual form of this model, the field is assumed to be zero at the injection plane. The new model allows the field to have a finite value, E_0, at the virtual injection electrode, which is taken to be the point at which the primary beam current vanishes. Relatively good fits were obtained with a simplified version of this model, emphasizing the importance of including injection electrode effects in the analysis. This model accounts for beam energy dependence effects in a natural way and explains the difference between the Adamo et al. (ref. 15) biased electrode

measurements, for which injection occurs at the metal contact, and the irradiated dielectric studies, for which injection occurs from an ionized region of the dielectric. Measurements and analysis are required to determine whether space-charge effects in the injection region or field-enhanced conductivity in the unirradiated region dominate the charge transport process in the bulk of the dielectric.

Experimental results were used to determine values of the injection fields E_0 (ref. 14). These values, in turn, were used here to calculate values for the trap-modulated mobility μ'. Table 3 displays both sets of values for beam energies of 8, 12, 16, and 18 keV. The values of μ' in table 3 suggest computer input values of μ' in Subsection V B. For consistency, the computer model (with the new value of μ') should also predict the values of E_0 deduced from the experiment results.

C. Discussion of CEC Results

To understand the experimental results of a nonpenetrating electron beam incident on Kapton samples, it is necessary to invoke field-assisted injection of carriers from the irradiated region into the nonirradiated region. An analytical space-charge limited model, with a nonvanishing field at the injection plane (the edge of the irradiated region) has provided results consistent with both experimental data and a preliminary computer carrier model. The conditions under which space-charge limited flow occurs (for example, free carrier density inadequate to neutralize injected carriers) must be investigated. A comparison of other experimental results with the present computer model will provide better material parameters and will indicate where modifications to the model and to the space-charge limited current theory are required. At early times in a charging experiment, free carriers in the dielectric bulk may be too numerous for space-charge limitations to occur. On the other hand, if field injection from an irradiated region (greater than from a metal contact if our RIC results are valid) is high enough, the injected carriers may dominate all other carrier sources.

Comparison of Kapton with different materials such as Teflon (in which field-injected electrons would compete with the more mobile holes) or with ceria-doped-microsheet (in which the high concentration of free carriers resulting from the cerium ions could prevent space-charge limiting) would be very useful in testing the present theory and model.

VI. IMPLICATIONS OF THIS WORK

The use of penetrating beams on a thin, metallized dielectric establishes conditions that are closely analogous to those in the RIC region of a nonpenetrated dielectric. For instance: a 1 nA/cm^2 beam of 28 keV electrons penetrating a 6.4-μm dielectric film deposits nearly 45 mW/cm^3 throughout the sample. On the other hand, a nonpenetrating 1-nA/cm^2 beam incident on a free surface dielectric will charge that surface to within approximately 2 keV of the beam energy (at which point secondary emission balances the incident beam). If most of the 2 keV per electron is deposited in the first 0.2 μm, the deposited power density is 100 mW/cm^3. The dose rate in, and therefore the conductivity of the two regions will be very similar. The deposited excess charge density will be greater in the 0.2-μm layer, but because the distance the excess charge must travel before removal from the layer is less in the thin layer than in the thin film (<0.2 μm vs <3.2 μm), the current densities (and perhaps the potential profiles) should also be similar.

The electric field at the back contact of a thin dielectric with its front contact biased to +45 V and $J_B \approx 0.65$ nA/cm^2 in figure 2 is zero. This back contact corresponds to the zero field region in the RIC volume near the nonirradiated portion of a thick dielectric. This area of the RIC region, then, is equivalent to an electrode in the RIC region. The positively biased front contact of a thin metallized film corresponds to the carrier sink of an irradiated Kapton sample free surface, for which secondary emission removes surface electrons. Changing the bias on this front contact (for a fixed beam current) varies the position of the zero field region. This change permits the RIC region to be probed, allowing a more accurate determination of its material parameters. Other conditions may need to be established for Teflon, in which holes are the majority carrier and for which the irradiated surface (when positive) is therefore an injecting electrode. Materials in which both holes and electrons have comparable mobility or in which conditions are other than those assumed here for Kapton, must be examined in a similar manner to determine the appropriate experiments for establishing material parameters.

Because of nonuniformities in fields and potentials in the RIC region, and because of their strong dependence on changes in beam current density and external applied bias (corresponding to changes in the experimental conditions of a non-penetrating beam experiment), incorrect values for material parameters and even for functional dependence (in both irradiated and nonirradiated regions) are likely to be inferred unless a computer model is used to unravel the problem. Many conclusions from past work are suspect for this reason, or, if correct, they may not pertain to conditions that are applicable to dielectric discharges. Although the data may be good, it must be reevaluated in many cases. Such problems account for many of the deviations observed in experimentally determined parameters (such as dose dependence of conductivity, and so on). Future work must be carried out only after careful study of the conditions to be simulated and after testing of a model to correctly interpret the results.

Once appropriate models are tested and true irradiated material parameters are evaluated, a more valid assessment of breakdown conditions and probability can be made. Variation of material and beam parameters in the computer model can then be used to determine the best means of preventing discharge conditions.

VII. SUMMARY

Although experimental measurements of RIC are available, it is still necessary to use a theoretical model to correctly interpret them. A model for RIC is described here, based on steady-state solutions of general kinetic equations for electrons and holes. An assumption is made that the holes are instantaneously trapped into deep traps, while the electrons hop from shallow trap to shallow trap and are described as quasi-free with a lowered "trap-modulated" effective mobility. This simplifies the description of the system to the Poisson equation plus a single transport equation for the electrons. Parameters required by the model include mobility, pair generation rate, and excess-charge deposition rate.

Raw data on a 6.4-μm sample of Kapton, taken at ±196-V and ±45-V bias penetrated by a 28-keV incident electron beam energy, are considered for interpretation. Of prior concern was the approximately 60-40 split of the rear and front currents observed at zero bias. Moreover, the experimental values inferred for the RIC are polarity dependent. However, the present model can explain the 60-40 split at zero bias, by appropriate choices of dose and excess charge deposition profiles, and by a particular choice of mobility, can match the experimental currents under bias.

Injection at the cathode contact is required to allow matching of the experimental currents. Under conditions of high injection, the shapes of the electron concentration and potential are monotonic and no strong fields are present (fig. 6). The mean value of the RIC turns out to be consistent with values in the literature. The polarity dependence of the experimentally observed currents is explained in terms of spatial variations in charge deposition, internal conductivities, and fields.

The problem of partial penetrations is also considered. The LWPCHARGE code, including carrier kinetics, was used to describe CEC effects. Transient solutions were obtained for partial penetrations of the thin-Kapton sample with beam voltages less than 28 kV. Significant rear currents were predicted when the penetration depth was half the thickness (threshold effects). For low beam voltage, the transient time is very long. As the beam voltage increases, the transient time decreases and the (negative) potential minimum deepens, until full penetration is achieved. The zero-bias, rear-front current split is calculated to be 63-37.

Field extraction of charge from the RIC region is assumed in a space-charge limited current model to interpret experimental results obtained on thick (5-mil) Kapton samples with a free front surface. From our various models, an inferred value of effective mobility ($\mu' = 3-7 \times 10^{-15}$ m^2/V-s), which is consistent with the literature, has been obtained for both RIC and CEC regions.

REFERENCES

1. L. W. Parker et al., "Charging Characteristics and Electrical Parameters of Spacecraft Dielectrics Under Electron Irradiation," Lee W. Parker, Inc., Final Report, INTELSAT Contract INTEL-046, June 1982.

2. R. C. Hazelton et al., "Effect of Material Parameters on the Charging Characteristics of Irradiated Dielectrics," IEEE Transactions on Nuclear Science, NS-28, 1981, pp. 4541-4546.

3. K. Labonte, "Radiation-Induced Charge Dynamics in Dielectrics," IEEE Transactions on Nuclear Science, NS-29, 1982, pp. 1650-1653.

4. R. C. Hughes and R. J. Sokel, "Computation of Photoconductivity in Insulators in the Space Charge and Recombination Regime: Application to PbO Films," Journal of Applied Physics, Vol. 52, 1981, pp. 6743-6746.

5. R. Sokel and R. C. Hughes, "Numerical Analysis of Transient Photoconductivity in Insulators," Journal of Applied Physics, Vol. 53, 1982, pp. 7414-7424.

6. J. M. Churchill, F. E. Holmstrom, and T. W. Collins, "Dynamic Model for e-Beam Irradiation of MOS Capacitors," Journal of Applied Physics, Vol. 50, 1979, pp. 3994-3999.

7. L. W. Parker, "Theoretical Investigations of Radiation-Induced and Carrier-Enhanced Conductivity," Lee W. Parker, Inc., Final Report, INTELSAT Contract INTEL-277, 1983.

8. L. N. Oliveira and B. Gross, "Space Charge Limited Currents in Electron-Irradiated Dielectrics," Journal of Applied Physics, Vol. 46, 1975, pp. 3132-3138.

9. W. E. Spear, "Electron Bombardment Effects in Thin Dielectric Layers," Proc., Physical Society, London B68, 1955, pp. 991-1000,

10. F. C. Aris, P. M. Davies, and T. J. Lewis, "Electron-Beam-Induced Conduction in Dielectrics," Journal Phys. C: Solid State Phys., Vol. 9, 1976, pp. 797-808.

11. S. Matsuoka et al., "Accumula. 1 Charge Profile in Polyethylene During Fast Electron Irradiations," IEEE Transactions on Nuclear Science, NS-23, 1976, pp. 1447-1452.

12. B. Gross, R. M. Faria, and G. F. L. Ferreira, "Radiation-Induced Conductivity in Teflon Irradiated by X-Rays," Journal of Applied Physics, Vol. 52, 1981, pp. 571-577.

13. A. R. Frederickson, "Charge Deposition, Photoconduction, and Replacement Currents in Irradiated Multilayer Structures," IEEE Transactions on Nuclear Science, NS-22, 1975, pp. 2556-2561.

14. E. J. Yadlowsky and R. C. Hazelton, "Conduction Processes in Kapton H Irradiated by an Electron Beam," IEEE Transactions on Nuclear Science, NS-31, December 1983.

15. R. C. Adamo, J. E. Nanevicz, and N. Grier, "Conductivity Effects in High-Voltage Spacecraft Insulating Materials," Proceedings of the Spacecraft Charging Conference, AFGL-TR-77-0051/NASA TMX-73537,669, 1977.

Table 1. Partial Penetrations at Zero Bias

Energy (keV)	Range (µm)	J_2 (nA/cm²)	V_m (V)	X_m (µm)	Time Scale (s)
5	0.4	-6×10^{-5}	-2	0.4	2×10^4
10	1.4	-3×10^{-3}	-11	1.2	3,400
15	2.8	-0.042	-30	2.2	2,500
20	4.4	-0.21	-45	2.8	700
28	>6.4	-0.63	-31	3.0	700

Table 2. Experimental Results for
1 nA/cm² Electron Beams on
6.4 µm Kapton

Beam Energy (keV)	J_2 (nA/cm²)	Time Scale
15	-0.12	400
25	-0.48	
28	-0.61	175

Table 3. Electrical Parameters for
Thick Irradiated Kapton

V_B (keV)	E_0 (V/cm)	μ (m²/V-s)
8	4.7×10^5	3.1×10^{-15}
12	5.2×10^5	2.8×10^{-15}
16	3.7×10^5	4.3×10^{-15}
18	2.8×10^5	1.9×10^{-15}
Average	$4.0 \pm 1.2 \times 10^5$	$3.1 \pm 1.2 \times 10^{-15}$

Figure 2. Collected Currents vs Electron
Beam Current With +45 V Applied Bias

Figure 1. Collected Currents vs Electron
Beam Current Entering a Dielectric
(A +196 V bias applied to front
surface; positive currents are
defined as electrons moving
toward the right; superscripts
indicate polarity of the bias)

Figure 4. Schematic of Experiment: Electron Beam Incident on Biased Front Contact (Number 1), Electrons Scattered and Deposited Within Dielectric (energy and charge deposition rate profiles represented by G and H)

Figure 3. Primary Flux From Monte Carlo Transport Code

Figure 6. Electrical Parameters Determined by Computer Fit to Experimental Data. Assuming Constant G and E (+200 V applied to front contact and high electron injection at back contact)

Figure 5. Electrical Parameters for Dielectric Exposed to an Electron Beam (G and E Constant) With Electric Field E, Potential V, and Drift-Diffusion Flux F_{DD} Resulting From Incident Flux F

Figure 8. Collected Currents $J_{1,2}^+$ vs Electron
Beam Current J_B^+ Modelled With a Positive
Applied Bias, Assuming Constant G and H

Figure 7. Collected Currents $J_{1,2}^-$ vs Electron
Beam Current J_B^- Modelled With a Negative
Applied Bias, Assuming Constant G and H
(constituent parts result from injection
at contacts $J_{1,2}^v$ and from motion
of beam-deposited charge $J_{1,2}^0$)

A SIMPLE MODEL OF ELECTRON BEAM INITIATED DIELECTRIC BREAKDOWN*

B. L. Beers, R. E. Daniell, and T. N. Delmer
Beers Associates, Inc.
Reston, Virginia 22090

We have developed a steady state model which describes the internal charge distribution of a planar dielectric sample exposed to a uniform electron beam. The model includes the effects of charge deposition and ionization of the beam, separate trap-modulated mobilities for electrons and holes, electron-hole recombination, and pair production by drifting thermal electrons. If the incident beam current is greater than a certain critical value (which depends on sample thickness as well as other sample properties), the steady state solution is non-physical. We interpret this to mean that above the critical beam current, the sample breaks down.

INTRODUCTION

This paper describes a simple model of a beam charging experiment. The motivation for the model is the need to understand low voltage breakdown such as that which occurs in dielectric material exposed to the radiation environment of space (ref. 1). Our approach to the problem is motivated by the work of O'Dwyer (ref. 2) on high voltage breakdown.

The model configuration is shown in figure 1, and it is assumed to have reached a steady state. A pair of infinite grounded plates are separated by an infinite, homogeneous dielectric, and a spatially infinite electron beam is incident on the arrangement normally, through one of the plates. The beam causes ionization at one rate, I, and deposits electrons at a second rate, S. The fact that these rates are constant forces the solution to the problem to have symmetry about the centerplane between the plates. All variables are either symmetric ar anti-symmetric about this plane. The problem considered here is simple, but sign conventions must be handled carefully to avoid confusion.

We take current to be positive when it is directed toward the right. Consequently, an electron beam traveling to the right represents <u>negative</u> current which we denote by J_B. Since the beam is losing electrons at the rate S (electrons $cm^{-3}s^{-1}$), the magnitude of J_B is decreasing but

$$\frac{dJ_B}{dx} = eS > 0 \tag{1}$$

where e is the magnitude of the electronic charge. Because of the build up of negative charge, the electric field (E) is positive (i.e., directed toward the

right) in the left half of the dielectric ($0 < x < L/2$), vanishes at the midplane, and is negative in the right half of the dielectric. The electrons and holes produced by the beam drift under the influence of the electric field. We denote the resulting conduction current by J_C. The total current is the sum of the beam current and the conduction current. In steady state, conservation of charge requires

$$\frac{d}{dx} (J_B + J_C) = 0 \tag{2}$$

Since J_C has the same symmetry properties as E, the solution of equations (1) and (2) is

$$J_C = (1 - 2x/L) \, eSL/2 \tag{3}$$

For the geometry as we have defined it, this solution is independent of the ionization rate I, the mobilities of the charged species, and all other parameters except sample thickness and electron deposition rate.

ELECTRON AND HOLE BEHAVIOR

The conduction current is the sum of the electron and hole currents which are defined in the usual manner:

$$j_n = - nev_n = ne\mu_n E \tag{4}$$

$$j_p = pev_p = pe\mu_p E \tag{5}$$

where n and p are the electron and hole densities, v_n and v_p are the electron and hole drift velocities, and μ_n and μ_p are the trap modulated mobilities of electrons and holes. The electron and hole currents have the same symmetry properties as J_C and E. Because of the symmetry of the problem, we will consider only the left half of the dielectric ($0 < x < L/2$). In this case, only J_B, v_n, and ρ (the net charge density) are negative. E, j_n, j_p, n, and p are all positive.

With the use of equations (1) - (5), one variable can be expressed in terms of the others. Solving for p results in

$$p = - \mu_n n/\mu_p + (1 - 2x/L)SL/(2E\mu_p) \geq 0 \tag{6}$$

Transport equations can be written for electrons and holes:

$$\frac{d}{dx}(nv_n) = \gamma n + (I + S) - knp \tag{7}$$

$$\frac{d}{dx}(pv_p) = \gamma n + I - knp \tag{8}$$

where k is the recombination rate and γ is the collision ionization coefficient. Because of equation (6) the equation for holes (eq. 8) is redundant. There is no time derivative because of the assumption of steady state, so the gradient of the electron flux is equal to the three source and sink terms on the right. Note that each unsigned term on the right-hand side of equation (7) is positive: the first term is the avalanche (i.e., collision ionization) term, the second is the beam ionization and charge deposition, and the third is recombination.

The only other equation needed is that for the electric field:

$$dE/dx = \epsilon(p - n)e \tag{9}$$

where ϵ is the dielectric constant of the sample material. The symmetry forces $E(x) = j_n(x) = j_p(x) = 0$ at $x = L/2$ which are the boundary conditions.

Using equations (4) - (7), we obtain the following equation for the behavior of the electron current:

$$
\begin{aligned}
-dj_n/dx = \; & +\gamma j_n/(\mu_n E) + (I + S)e \\
& + [j_n/(e\mu_n E)]^2 \, ek\mu_n/\mu_p \\
& - (1 - 2x/L) \, kSLj_n/(2\mu_n\mu_p E^2)
\end{aligned}
\tag{10}
$$

None of the variables in this equation are negative. Therefore, in the region under consideration, all terms on the right-hand side have the sign explicit in front of them. The last two terms in combination are negative as in equation (6). The equation governing the electric field is equation (9). Equation (6) can again be used to eliminate p and equation (4) to eliminate n with the result that

$$
\begin{aligned}
dE/dx = \; & -[(1 + \mu_p/\mu_n) \, j_n/(\mu_p E) \\
& - (1 - 2x/L) \, eSL/(2\mu_p E)]/\epsilon
\end{aligned}
\tag{11}
$$

We have adopted the form of the collision ionization term given by reference 3:

$$\gamma = a_o\mu_n|E| \exp(\omega_o/|E|) \tag{12}$$

where a_o has units of inverse length.

593

Equations (10) and (11) are a pair of coupled ordinary differential equations for j_n and E. They may be cast into dimensionless form by the use of the dimensionless variables

$$u = 1 - 2x/L \qquad (13a)$$

$$\xi = 2j_n/eSL \qquad (13b)$$

$$\eta = E/aE_o \qquad (13c)$$

and the dimensionless constants

$$a^2 = eSL^2/(4\varepsilon\mu_p E_o^2) \qquad (14a)$$

$$b = \varepsilon k/e\mu_n \qquad (14b)$$

$$\delta = \mu_p/\mu_n \qquad (14c)$$

$$\lambda = \sigma_o L/2 \qquad (14d)$$

$$\sigma = I/S \qquad (14e)$$

The two equations (10) and (11) become

$$d\xi/du = \lambda\xi\exp(-1/a|\eta|)|\eta|/\eta + (1 + \sigma) - b\xi(u - \xi)/\eta^2 \qquad (15)$$

$$d\eta/du = [(1 + \delta)\xi - u]/\eta \qquad (16)$$

The boundary conditions are $\xi(0) = \eta(0) = 0$.

PROPERTIES OF THE SOLUTIONS

Note that $(u - \xi)/\eta$ is the dimensionless hole density while ξ/η is the dimensionless electron density. The requirement that these two densities be non-negative places a constraint on ξ:

$$0 \leq \xi \leq u, \quad \text{for} \quad 0 \leq u \leq 1 \qquad (17)$$

Any solution which fails outside this range is not physically meaningful.

Let us first consider the case for which there is no collision ionization ($\lambda = 0$). Then the two equations (15) and (16) have the solution

$$\xi(u) = cu \tag{18}$$

$$\eta(u) = gu$$

where c is the solution of

$$(1 + \delta - b) c^2 - [(1 + \delta)(1 + \sigma) + 1 - b] c + (1 + \sigma) = 0 \tag{19}$$

and g is defined by

$$g^2 = [(1 + \delta) c - 1] \tag{20}$$

If the solution is to be physically meaningful, then c must be less than unity. For many situations of interest, both δ and b are very small so that $c = 1 - \Delta$ where Δ is much less than unity. To second order in the small quantities δ and b

$$\Delta \approx \delta(1 - \delta - b/\sigma) \tag{21a}$$

$$g^2 \approx \delta b/\sigma \tag{21b}$$

For purposes of illustration, however, it is preferable to use values of order one. In figure 2 we show the solution for $\delta = 0.5$ and $b = \sigma = 1.0$. The solution is independent of a, the dimensionless electron deposition rate. Both the electric field and the two currents (electron and hole) are linear. The electron and hole densities are constant. The quantity ϕ is the dimensionless potential and is defined as

$$\phi(u) = 2V(x)/(aE_0L) = \int_0^u n(u)du - \phi_0 \tag{22}$$

where V(x) is the electrostatic potential with $V(0) = V(L) = 0$, and ϕ_0 is the dimensionless potential at $u = 0$ ($x = L/2$).

In the preceding example the dimensionless electron and hole currents (ξ and $u - \xi$, respectively) as well as the dimensionless electric field (η) are independent of the dimensionless electron deposition rate (a). (Of course, the

dimensional quantities are strongly dependent on the electron deposition rate.) However, when λ is non-zero, the collision ionization term introduces an explicit dependence on a. Because this term is always positive, its presence causes both $d\xi/du$ and $\xi(u)$ to increase. We have solved equations (15) and (16) numerically for the same values of δ, b, and σ as above, but with $\lambda = 0.01$. As expected, the solution is no longer independent of a. Solutions for three values of a are shown in figure 3. Note that for a = 4.58 both the hole current and the hole density vanish at the electrodes. If a is increased beyond 4.58, the solution predicts negative hole densities near the electrode. Since negative hole densities are physically meaningless, this means that there is no steady state solution for a > 4.58. We interpret this to mean that the dielectric will break down.

DISCUSSION

We have presented a simple model of the effects of an electron beam on a dielectric sample. We have assumed that the sample is homogeneous and that the incident beam is spatially uniform. We have also assumed that the beam deposits electrons uniformly throughout the sample. We have found that if the incident beam current (or electron deposition rate) becomes larger than a critical value, there are no steady state solutions, which we interpret to be an indication of breakdown.

We have only begun to explore the properties of this model for realistic values of the model parameters. We anticipate that the simplicity of the model will limit the accuracy with which it represents a real dielectric charging problem. However, we hope that the very simplicity of the model will make it possible to thoroughly study and understand the physical processes leading to breakdown in this idealized case. We feel that this is an important first step in the development of more realistic models which take into account material inhomogeneities (e.g., localized defects).

REFERENCES

1. Stevens, N. J.: Analytic Modeling of Satellites in the Geosynchronous Environment. Spacecraft Charging Technology, NASA CP2181 (AFGL-TR-81-0270), 1980, pp. 717-729.

2. O'Dwyer, J. J.: Theory of High Field Conduction in a Dielectric, J. Appl. Phys., vol. 40, no. 10, Sept. 1969, pp. 3887-3890.

3. Beers, B. L.; Pine, V. W.; and Ives, S. T.: Continued Development of a Detailed Model of Arc Discharge Dynamics. NASA CR-167977, Dec. 1982.
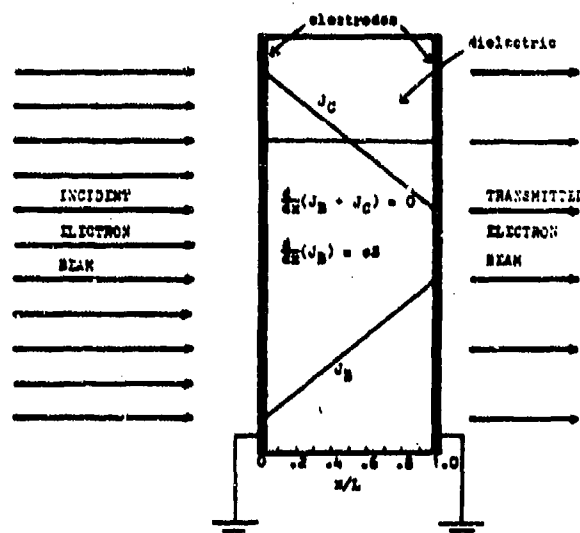
Figure 1. - Model Geometry. Electrons moving to the right produce negative
current. The beam deposits electrons uniformly throughout the sample.
These electrons drift toward the two electrodes where they return to ground.
In steady state the total current flowing to ground is equal to the differ-
ence between the transmitted beam current and the incident beam current.
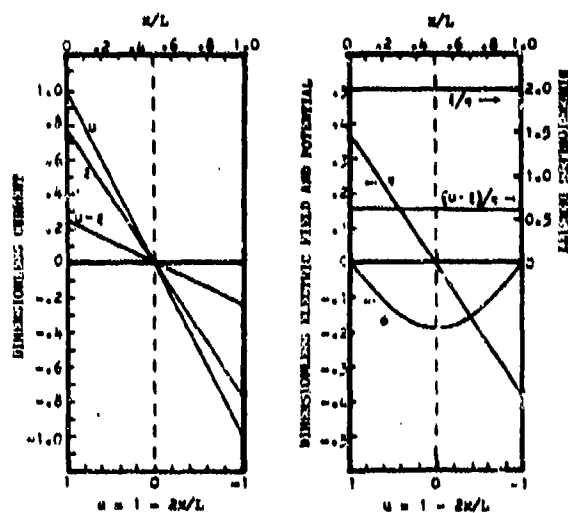
Figure 2. - Solution for no collision ionization ($\lambda = 0$), $\delta = 0.5$, $b = \alpha = 1.0$.
Total conduction current is proportional to u. The electron current (ξ) and
the hole current (u - ξ) are constant fractions of the total conduction
current. The electron and hole densities [ξ/η and (u - ξ)/η] are also
constant. η is the dimensionless electric field, and ϕ is the dimension-
less potential.

597
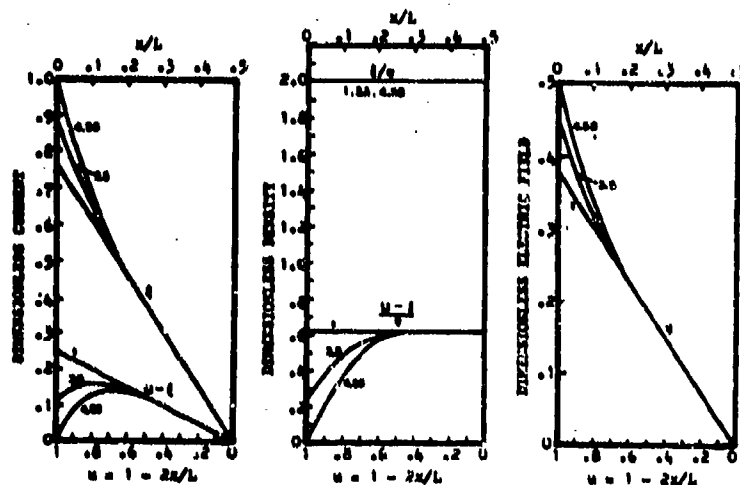
Figure 3. — Solutions for $\lambda = 0.01$, $\delta = 0.5$, $b = \sigma = 1.0$, and $a = 1$, 3.5, and 4.58. When the dimensionless electron deposition rate $a > 4.58$, the solution gives negative hole densities $[(u - \zeta)/n]$ near the electrodes. This implies that there is no physically meaningful steady state solution, i.e., the dielectric breaks down.

SPACECRAFT ENVIRONMENTAL INTERACTIONS: A JOINT AIR FORCE
AND NASA RESEARCH AND TECHNOLOGY PROGRAM

Charles P. Pike
Air Force Geophysics Laboratory
Hanscom Air Force Base, Massachusetts 01731

Carolyn K. Purvis
National Aeronautics and Space Administration
Lewis Research Center
Cleveland, Ohio 44135

Wayne R. Hudson
Office of Aeronautics and Space Technology
NASA Headquarters
Washington, D.C. 20332

A joint Air Force/NASA comprehensive research and technology program on spacecraft environmental interactions is being undertaken to develop technology to control interactions between large spacecraft systems and the charged-particle environment of space. This technology will support NASA/Department of Defense operations of the shuttle/IUS, shuttle/Centaur, and the force application and surveillance and detection missions, planning for transatmospheric vehicles and the NASA space station, and the AFSC military space system technology model. The program consists of combined contractual and in-house efforts aimed at understanding spacecraft environmental interaction phenomena and relating results of ground-based tests to space conditions. A concerted effort is being made to identify project-related environmental interactions of concern. The basic properties of materials are being investigated to develop or modify the materials as needed. A ground simulation investigation is evaluating basic plasma interaction phenomena to provide inputs to the analytical modeling investigation. Systems performance is being evaluated by both ground-based tests and analysis. An environmental impact investigation to determine the effect of future large spacecraft on the charged-particle environment is planned. Finally, spaceflight investigations will verify the results of this technology investigation. The products of this research and technology program are test standards and design guidelines that will summarize the technology, specify test criteria, and provide techniques to minimize or eliminate system interactions with the charged-particle environment. The investigation is coordinated by a Spacecraft Environmental Interaction Program steering committee, which will incorporate into this investigation the requirements of both the Air Force and NASA.

STEERING COMMITTEE

The functions of this committee are to coordinate all phases of the investigation, to review progress, and to direct changes, as required, to satisfy the needs of the Air Force and NASA. The committee will meet annually to

review the program, to resolve pending action items, to form working groups as needed, and to issue required action items. The minutes of these meetings will be issued.

The committee will report to the NASA/Office of Aeronautics and Space Technology, Air Force Space Command/DL, and AFSTC through the Science and Technology Interdependency Group.

The steering committee consists of the following members:

Co-Chairpersons: Charles P. Pike, Air Force Geophysics Laboratory (AFGL); and
Carolyn K. Purvis, NASA Lewis Research Center

Members: Wayne R. Hudson, NASA HQ; Henry B. Garrett, JPL; A. R. Fredrickson, Rome Air Development Center; D. A. Guidice, AFGL; and Lt. R. Cull, Air Force Weapons Laboratory

The steering committee will form working groups as needed to review, plan, and coordinate investigations in specific areas, to recommend new directions as required, and to make periodic progress reports to the steering committee. The working groups will function to keep the various organizations, both those within the formal program and others, coordinated in their various activities. The chairperson of each working group is appointed by the steering committee and is responsible for selecting members of the working group from the technical experts of the government, industrial, and university communities.

JUSTIFICATION

Missions using very large spacecraft are planned for the remainder of the 1980's and the space station is scheduled for operation in the 1990's. The missions are planned to initially use equatorial and low-inclination orbits and then move to polar and geosynchronous orbits. Typical missions are communications platforms and space-based radar. The Air Force/NASA Spacecraft Charging Technology investigation showed that environmental charged-particle fluxes can act on spacecraft surfaces and influence system performance. These new, larger spacecraft can have potentially serious interactions at all altitudes and these interactions must be evaluated. Because the proposed structures have dimensions larger than characteristic plasma lengths, differential surface charging is possible. The motion of such a large structure in the Earth's magnetic field will induce electromagnetic forces on the structure. Since these structures are designed for low-density materials, electromagnetically induced stress can affect the mechanical design.

There is also a trend toward high-power modules for space applications. Plans have been established for 25-kW modules in the late 1980's, expanding to 500-kW modules, possibly nuclear, in the late 1990's. At these power levels the operating voltages will most likely be higher than the present range of 30 to 100 V for greater system efficiency. This elevation of operating voltages means that interactions between the biased surfaces, including thermal radiators for high-power systems, and the plasma environment are more probable.

Laboratory tests on small solar array samples have indicated that possible interactions include the establishment of parasitic current loops through the environment (resulting in power losses), arcing at negative potentials, and

600

disproportionate current collection through holes in insulation to biased surfaces underneath. These effects can adversely influence the operation of space power modules and must be understood before building high-power systems.

There is a growing concern for the influence that the very large structures proposed for future applications can have on the charged-particle environment. This influence may significantly alter the interactions between the structure and the environment.

Testing larger quantities and greater varieties of materials, including prolonged exposure to the space environment, is needed to determine performance reliability for extended-duration missions. As spacecraft become larger and more expensive, the reliability of specialized materials might become the limiting parameter for missions. To improve reliability, the space environment must be well characterized and the material responses to that environment must be determined.

OBJECTIVES

The overall objective of this investigation is to develop the technology for controlling or mitigating spacecraft system interactions with the plasma, particle, and field environment of space. The technology developed in this investigation will support proposed Air Force/NASA space mission concepts into the 1990's.

APPROACH

The initial emphasis in this investigation will be on low-Earth-orbit (LEO) altitudes. The proposed missions will be cataloged, engineering specifications for the charged-particle environment established, and possible interactions identified. The ground technology investigation will concentrate on determining and modeling plasma phenomena and then extrapolating these results to system interactions and performance in space. Applicable techniques available to the participants will be used.

The environmental interactions for large systems operating in altitudes out to geosynchronous conditions will be evaluated after the LEO study. The geosynchronous environmental investigation will use the LEO study results as well as applicable techniques from the Air Force/NASA Spacecraft Charging Technology Investigation. In both the LEO and geosynchronous environmental interactions investigations, the effect of large systems on the environment will be evaluated as well as the effect of the environment on system performance.

Spaceflight experiments will be conducted to verify the results of the ground-based technology investigation of the environmental interactions. These space experiments will be coordinated with the ground-based study.

PRODUCTS

The output of this investigation will be a series of test standards and design guideline documents. These will be issued in a preliminary form early

in the investigation and upgraded as the study continues. The major milestones for this investigation are shown in table I.

TASKS

For each element of this investigation, the approach is summarized and the known tasks identified. The agency or agencies responsible for directing and coordinating the work under each task are given. Although the primary responsibility is assigned to one agency, the expertise of other agencies will be used.

User Requirements

It is necessary to identify those missions or projects that could benefit from the technology that will be developed by this investigation and to incorporate their requirements. This will be done by maintaining close liaison with government funding sources and project offices. Potential applications of the technology have been identified as

(1) Polar shuttle
(2) Space station
(3) Multikilowatt space power systems
(4) Large, high-power communications satellites
(5) Large surveillance satellites
(6) Scientific spacecraft

The primary interactions to be evaluated have been tentatively identified as

(1) Large space system interactions. These interactions involve the possible effects due to the motion of a large body in the space environment and due to material reactions to the charged-particle fluxes.

(2) Biased-system/charged-particle interactions. These interactions include spacecraft systems that generate or use high voltage exposed to space. Communications satellites and spacecraft systems using high-voltage space power modules fall into this category.

(3) Scientific instruments and sensor interactions. The effect of electric fields surrounding a spacecraft on the behavior of scientific instruments and sensors will be evaluated.

(4) Large structure interactions on the environment. The presence of the proposed large structures may affect the environment. Such effects must be evaluated.

(5) Enhanced-particle environment interactions. These interactions involve spacecraft sources of particles that can be ionized and increase the charged-particle environment around the spacecraft. Close coordination will be maintained with the existing Air Force/NASA Spacecraft Contamination Investigation.

(6) High-energy particle interactions. Penetrating radiation effects will be evaluated in this study only insofar as they can influence charging

602

phenomena (e.g., internal spacecraft charging and radiation-enhanced conductivity in materials). Close coordination will be maintained with other groups conducting radiation damage evaluations.

(7) Charging response of spacecraft materials. This response depends on some basic material properties - conduction, prebreakdown streamer formation, photoconduction, and polymer degradation. These and other pertinent material properties will be studied in relation to space environmental interactions.

The specific tasks and responsible agencies are listed here.

Task 1: coordination and overview. - Coordinating user needs and incorporating these needs into the investigation will be the responsibilities of the steering committee.

Task 2: Air Force and NASA contacts. - Each agency will maintain a close relationship with the projects it manages in order to determine user needs and will report those needs to the steering committee for coordination and incorporation into this investigation.

Environment Specifications

The natural environment will be investigated and engineering specifications generated or updated as appropriate. The effect of large spacecraft on the environment will also be investigated and evaluated.

Task 1: Earth environment specification. - The available data for the low-Earth-orbit plasma, particle, and field environment will be reviewed. An engineering specification for this region will be generated and made available to all parties concerned with environmental interactions. This work will be the responsibility of AFGL and JPL.

Task 2: plantary environment specification. - The available data for planetary environments will be reviewed. An engineering specification for these environments will be generated and made available to all parties concerned with environmental interactions. This work will be directed by JPL.

Task 3: enhanced spacecraft environment specification. - The available data on possible outgassing or other sources, including arc discharges on the plasma wake and sheath that can enhance the charged-particle environment, will be reviewed. An engineering specification for this enhanced environment will be generated and made available to all parties concerned with spacecraft environmental interactions. Close coordination will be maintained with the Air Force/NASA Spacecraft Contamination Investigation, which is principally concerned with particulate contamination, and related programs to avoid duplication. This work will be the responsibility of JPL.

Task 4: environmental impact. - Using the environmental specifications and the proposed plans for large spacecraft, the possible alterations to the natural environment due to the presence of the spacecraft will be investigated and evaluated. This work is currently unfunded but is included as it is perceived as a future area of concern to support environmental impact assessments.

603

Materials Investigation

The basic properties of typical spacecraft materials exposed to the space environment will be determined, and new or modified materials will be developed. The specific tasks and responsible agencies are listed here.

Task 1: material property determination. - The classical properties of typical spacecraft materials will be determined as a function of the material parameters and environmental fluxes. The properties to be determined are those that influence the surface potential of the material (e.g., secondary emissions, backscatter, conduction, deposition, and photoemission). Electron, proton, and photon fluxes as determined by the environmental specifications are to be considered. This work will be the responsibility of JPL, Lewis, and RADC.

Task 2: new or modified materials development. - Materials having selective properties will be developed as a means of controlling detrimental effects of spacecraft environmental interactions. The required properties for these materials, including advanced composite materials, will be defined from the interactions studies. The materials will be developed and tested to show that they will meet the requirements. This task will be the responsibility of AFWAL.

Ground Simulation Investigation

Existing facilities will be used to simulate the space plasma environment, and the interactions will be studied experimentally. The specific tasks and responsible agencies are listed here.

Task 1: basic interaction studies. - This task will be divided into several subtasks each devoted to the study of a particular aspect of the interaction phenomena.

(1) Biased-system/charged-particle interactions will be investigated. Here the emphasis is on identifying key parameters (voltage levels, material properties, geometry, plasma temperature and density, and magnetic field strength and direction) affecting the interactions, which include collection of currents from plasmas and arcing in the presence of plasmas. Interactions to be investigated include those between systems and both the natural space environment and the enhanced environment resulting from the presence of large systems. This work will be conducted by Lewis.

(2) Plasma sheath growth will be investigated. Interactions between large structures moving through the environment will be investigated. Plasma wake and ram effects and sheath growth will be evaluated. Responsibility for this work will be assigned as resources become available.

(3) Discharges resulting from environmental interactions will be characterized. Both radiated and conducted characteristics will be determined. This work will be coordinated by JPL.

(4) Penetrating radiation studies will be conducted to evaluate radiation-induced charging interactions. RADC will be the contact point for this work.

Task 2: studies of large, high-voltage power systems. - In this task the
basic interaction study results from section 5.4.1 (table I) will be applied to
the design of large power systems for space applications. The interactions
will be scaled to the size of a typical large power system, the environmental
conditions will be scaled from ground conditions to space, and the effects of
the environment on system performance will be evaluated. Means of controlling
detrimental interactions will be devised. Wherever possible, experiments will
be conducted to demonstrate that the interactions can be controlled. This work
will be conducted by Lewis for NASA missions and by AFWAL for Air Force mis-
sions. AFWAL will also investigate the interaction of various weapons threat
scenarios with the space environment and solar cell power systems. After these
initial studies component hardware will be developed, tested, and integrated
into a complete modular power system. Primary interactions are expected with
the solar cell array and the radiators - both high temperature (>600 K) and
low temperature (300 K). Where necessary, spaceflight experiments will be
developed.

Task 3: mitigation techniques. - The environmental interaction in large,
high-power spacecraft can be mitigated by techniques such as active charge
control devices. Techniques will be evaluated to determine the extent to which
they will alleviate detrimental system performance. This work will be con-
ducted by AFGL.

Analytical Investigation

Models of physical processes and engineering design tools will be devel-
oped. Models of individual interactions will be developed to identify criti-
cal parameters. These will be incorporated into a general engineering analyt-
ical tool (or tools) to aid in designing systems to withstand detrimental
environmental interactions. The specific tasks and responsible agencies are
listed here.

Task 1: basic plasma phenomenological modeling. - The basic plasma phe-
nomena necessary to evaluate environmental interactions with spacecraft systems
will be modeled. These phenomena will include ram/wake velocity effects,
plasma sheath effects, and magnetic field effects. AFGL and Lewis will coor-
dinate the respective efforts.

Task 2: discharge modeling. - Empirical models of discharge phenomena
will be developed. Radiofrequency characterization and discharge modeling as
a function of material and ambient plasma will be carried out. The work will
be coordinated by JPL.

Task 3: system level analytical models. - Analytical models will be de-
veloped to support the design of mission spacecraft for the 1980's and 1990's.
These design tools will incorporate the interaction models developed in
section 5.5.1 (table I) and will be capable of evaluating the effect of envi-
ronmental interactions and of assessing the means of minimizing detrimental
interactions. The following models will be developed:

(1) Large space structures. This model will evaluate the interactions
between large space structures, including the shuttle, and the space environ-
ment. It will be developed by AFGL.

(2) Large, high-voltage power systems. This model will evaluate the interactions that result from the operation of high-voltage systems on spacecraft. It will be developed by Lewis.

Task 4: charging modeling. - Analytical models and empirical data will be developed to determine the level of charging induced in spacecraft materials. The work will be coordinated by RADC.

SPACEFLIGHT EXPERIMENT PLANNING AND EVALUATION

The results of the ground-based technology program must be verified in the actual space environment. To accomplish this, spaceflight experiments have been conducted and are planned. Close liaison will be maintained with the NASA Shuttle Project Office, the NASA Space Station Office, and the DOD Space Test Program Office to maintain cognizance of flight opportunities. At this time it is not possible to completely specify the number and types of experiments that will be required; they will be the logical outgrowth of this technology investigation as it progresses. Space experiments funding is not included in the agreement.

DESIGN GUIDELINES AND TEST STANDARDS

Design guidelines and test standards will be issued and updated as this program develops. These documents will summarize the state of the art of the various interactions being studied. Guidelines to be used in designing systems for space applications and test criteria for verifying conformance will be delineated. All participating agencies will submit their contributions for compilation by the steering committee. Lewis and AFGL will be responsible for issuing the design guidelines and test standards.

ORGANIZATIONAL RESPONSIBILITIES

Steering committee:

(1) Overall planning, coordination, and reporting of the investigation
(2) Incorporation of user requirements into the investigation
(3) Coordination of basic plasma phenomena modeling
(4) Coordination of spaceflight experiment options
(5) Conduct of annual meeting, issuance of minutes, and formation of working groups

AFGL:

(1) Air Force point of contact
(2) Coordination for Air Force
(3) Development of test standards and military standards
(4) Natural environment engineering specifications and basic interaction analytical studies: wake and ram
(5) Techniques for mitigating system-limiting effects
(6) Analytical modeling of large space structures

606

AFWAL:

    (1) Development of new or modified materials
    (2) Studies and development testing of high-voltage, high-power systems

RADC: Study of effects of penetrating radiation and charging on materials

NASA HQ: Ensurance of environmental interactions technology responsible to NASA needs

Lewis:

    (1) NASA point of contact
    (2) Coordination for NASA
    (3) Determination of material properties
    (4) Issuance of design guidelines document
    (5) Conduct of basic interaction experimental studies: biased-system – charged-particle interactions
    (6) Analytical modeling of high-voltage system

JPL:

    (1) Specification of Earth and planetary environments
    (2) Determination of material properties
    (3) Conduct of basic interaction experimental studies: discharges
    (4) Conduct of analytical discharge studies
    (5) Formulation of enhanced spacecraft environment specification

TABLE I. – SPACECRAFT ENVIRONMENTAL INTERACTIONS MILESTONE SCHEDULE
[Fiscal years 1983–91.]

TECHNOLOGY ELEMENT OPR/TITLE	83	84	85	86	87	88	89	90	91
5.2.1/AFGL/Earth Env Spec	Δ		Δ					Δ	
5.2.1/JPL/Earth Env Spec			Δ					Δ	
5.2.2/JPL/Planetary Env Spec									Δ
5.2.2/JPL/Enhanced Env Spec				Δ				Δ	
5.3.1/JPL/Mat Prop Det			Δ		Δ		Δ		Δ
5.3.1/Lewis/Mat Prop Det	Δ		Δ			Δ			
5.3.2/AFWAL/Mat Dev		Δ	Δ Δ	Δ	Δ				
5.4.1/Lewis/Inter Studies	Δ	Δ		Δ			Δ		
5.4.1/JPL/Inter Studies		Δ		Δ		Δ		Δ	
5.4.1/RADC/Inter Studies		Δ	Δ Δ	Δ Δ					
5.4.2/Lewis/Power Sys Study					Δ			Δ	
5.4.2/AFWAL/Power Sys Study		Δ			Δ			Δ	Δ
5.4.3/AFGL/Mitigation Tech			Δ	Δ		Δ			
5.5.2/JPL/Dischg Model			Δ		Δ		Δ		Δ
5.5.3/AFGL/Analytic Tools		Δ	Δ			Δ			
5.5.3/Lewis/Analytic Tools			Δ				Δ		
5.6/AFGL/Spдce Flt Exp Plan & Eval		Δ		Δ		Δ	Δ	Δ	Δ
5.7/Lewis/Des Guidelines					Δ			Δ	
5.7/AFGL/MIL STD-Test Spec			Δ		Δ	Δ		Δ	Δ
CONFERENCES		Δ		Δ		Δ		Δ	Δ

608

INTERACTIONS MEASUREMENT PAYLOAD FOR SHUTTLE

D. A. Guidice and C. P. Pike
Air Force Geophysics Laboratory
Hanscom Air Force Base, Massachusetts 01731

The purpose of the Interactions Measurement Payload for Shuttle (IMPS) is to develop a payload of engineering experiments to determine the effects of the space environment on projected Air Force space systems. Measurements by IMPS on a late-1980s polar-orbit Shuttle flight will lead to detailed knowledge of the interaction of the low-altitude polar-auroral environment on materials, equipment and technologies to be used in future large, high-power space systems. The results from the IMPS measurements will provide direct input to MIL-STD design guidelines and test standards that properly account for space-environment effects.

INTRODUCTION

The adverse effects of the space environment on space systems have caused many operating anomalies in communication and surveillance satellites. These anomalies were mainly associated with energetic-particle radiation or with spacecraft charging at geosynchronous altitudes. For larger space systems operating in low-earth polar orbits, a new set of environment-induced interactions will affect the operation of various equipments and subsystems. These adverse effects may limit the construction or mechanical performance of large structures in space or limit the power levels available for solar-cell sources. Before any new Air Force space systems are built and deployed, we must obtain sufficient environment-interaction information to assure their continued effective operation in space.

The effects of the space environment on large-structure, high-power space systems are unknown. Of particular concern is operation in the polar-auroral region at low to medium altitudes (200 to 2000 km). The physical processes of this regime and the interactions of the environment with materials, subsystems, and technologies characteristic of Air Force space systems of the 1990s must be quantified to assure the reliable operation of projected space systems. IMPS will measure polar-auroral effects on solar-array panels, spacecraft materials, structures, electronic subsystems, and astronaut EVA equipment. It emphasizes application to large, high-power systems and is directed toward technologies identified in the Military Space Systems Technology Model (MSSTM).

SPACE OPERATIONS AND POSSIBLE INTERACTIONS

The first step in deciding what instrumentation should be included in IMPS is to define several Air Force space-operations objectives and determine how the space environment will interact with the equipment or technologies needed to carry out those operations. Since IMPS will fly in polar orbit, polar-auroral environment interactions will be emphasized. The purpose of the IMPS measurements will be to quantify important environmental interactions -- those that will restrict certain kinds of space operation, limit the performance of a particular

system, or prevent (or make impractical) the use of a certain technology. After deciding what kinds of interaction are likely to have serious effects, we must determine what interaction parameters can actually be measured on a polar-orbiting Shuttle flight. In conjunction with the measurements of effects on materials, equipments and technologies, we must characterize the physical properties of the environment causing the interactions. The determination of the required interactions measurements will lead to a definition of IMPS mission objectives.

Some generic Air Force space operations to be addressed by IMPS are:
   a.   Operation of optical systems
   b.   Operation of radar systems
   c.   System deployment or on-orbit repair necessitating astronaut extra-
vehicular activity (EVA).
Operation in the polar-auroral environment is to be stressed.

Possible space-environment effects on optical systems include:

(1)   Effects associated with large heat dissipation resulting from the low efficiency of lasers or cryogenic refrigerators (for cooled infrared detectors).

(2)   Effects of contamination and material property changes on optical surfaces.

(3)   Limitations in power generation due to leakage or arc-discharge in solar arrays.

(4)   Plasma effects on solar-cell material.

(5)   Differential charging of closely-packed small dielectric surfaces (multi-element infrared detectors).

(6)   Effects on large high-precision structures used to support and point complex optical assemblies.

Figure 1 shows a possible configuration for a space-based radar system, from which one can begin to perceive potential environmental interactions. Some possible space-environment effects on radar systems include:

(1)   Limitations in power generation due to leakage or arc-discharge in solar arrays.

(2)   Plasma effects on solar-cell material.

(3)   For power distribution utilizing high voltages: arc-discharges, dielectric breakdowns.

(4)   For power distribution utilizing high currents: structural stresses and torques due to large prime-power current loops and in-orbit varying terrestrial magnetic field.

(5) Electromagnetic interference (EMI) affecting radar receiver performance.

(6) Plasma effects (such as differential charging) on feed structure and reflector materials.

Figure 2 shows astronauts engaged in space-system deployment or in-orbit repair activities requiring EVA. Some possible space-environment effects on this activity include:

(1) Differential charging between the astronaut and his spacecraft or the spacecraft being repaired due to particular environmental conditions in the area.

(2) Interactive effects on the electronics of future EVA-systems due to electromagnetic interference or differential charging.

(3) Effects in the space-plasma environment due to thermal-control water discharge in the astronaut's Life Support System (LSS).

IMPS CONCEPTS

The objective of the Interactions Measurement Payload for Shuttle (IMPS) program is to develop a payload of appropriate engineering experiments to measure the effects of the polar-auroral environment on materials, subsystems, and technologies that will be used in future Air Force space systems. The payload will consist of:

a. A complement of engineering experiments to measure and quantify the different kinds of interactive effects caused by the environment on various parts of projected future space systems.

b. In support of the engineering experiments, a limited set of polar-auroral environment sensors to characterize the environment causing the disruptive interactive effects.

Interactive effects to be investigated by the engineering experiments will include:

(1) Interaction of the auroral plasma and current sheets on high-voltage solar arrays, resulting in power leakage or arc-breakdown.

(2) Interaction of spacecraft electrical currents with polar magnetic fields on large space structures, causing torques or structure deformation (reducing the pointing accuracy of a large antenna, for example).

(3) Interactions that increase electromagnetic interference, reducing the effectiveness of space communications or surveillance systems.

(4) Interactions that degrade the properties or performance of materials or electronic circuitry, resulting in operational anomalies or subsystem failures.

(5) Interactions that pose a threat to the astronaut during polar-orbit EVA (causing a malfunction in the astronaut's Manned Maneuvering Unit, for example).

Figure 3 illustrates the concept of the Interactions Measurement Payload being developed under Project 2822. The IMPS effort is one of three projects in Program Element 63410F, Space Systems Environmental Interactions Technology. PE 63410F is an integral part of the Agreement for NASA/OAST - USAF/AFSC Space Interdependency on Spacecraft-Environment Interaction (May 1980). Under PE 63410F, IMPS is responsible for polar-auroral interactions measurements. IMPS will make substantial use of the space technologies and instrumentation developed by NASA technology centers and Air Force organizations such as Air Force Wright Aeronautical Laboratories (AFWAL).

IMPS PRELIMINARY WORK

Initial Payload Concept Study

In FY82, Jet Propulsion Laboratory (JPL), under the direction of Air Force Geophysics Laboratory (AFGL), carried out a basic shuttle payload concept study. It was through this study that many of the basic concepts for IMPS were first defined. In December 1981, JPL hosted a meeting attended by about 70 experts in a number of key spacecraft interaction areas. Experiment questionnaires were distributed to the meeting's participants; ultimately about 70 were returned. The information from these questionnaires was used by JPL to put together an initial IMPS experiments list which was subsequently reviewed and modified by AFGL. Additional reviews and meetings with AFGL, JPL, and AF Space Division personnel lead to further refinements in the payload concept. Eventually, three sequential payloads were defined, each of the latter payloads adding to the experiments of the previous one.

Payload A consisted of engineering experiments and environmental sensors, but had no "active" engineering experiments (experiments that contribute to the environment causing the interactions). Payload B had, in addition to A's experiments and sensors, two "active" engineering experiments: a Charge Control System (CCS) and a Plasma Interactions Experiment (PIX). Payload C added (to Payload B) an experiment evaluating interactions with astronaut EVA systems. Payload C is shown in Figure 4. AFGL has submitted a Space Flight Request (DD Form 1721) for IMPS utilizing JPL's Payload C to the Space Test Program (STP). IMPS (AFGL-306) now ranks high on the priority list for Shuttle flight under STP.

IMPS Baseline Definition

Before beginning the full-scale development of instrumentation for IMPS, one must first develop a program baseline. For this purpose, Jet Propulsion Laboratory, under AFGL's direction, recently began an IMPS baseline definition effort to include:

a. Determination of what will be required of the IMPS mission to satisfy Air Force space-operations objectives.

b. Preliminary and final recommendations for selection (by AFGL) of engineering experiments and environmental sensors for IMPS through the work of an Engineering/Science Working Group (ESWG).

c. A recommended IMPS implementation plan to serve as a guide for the large-scale future work to develop, test, integrate, and fly IMPS.

d. A cost estimate for the IMPS program (for later trade-off studies).

IMPS FOLLOW-ON WORK

In general, the engineering experiments for IMPS will be obtained through the AF laboratories, NASA technology centers, and other science and engineering organizations that will be developing hardware and technology for future space application. Because these organizations are looking forward to the successful usage or operation of their hardware/technology in space, they have shown a strong interest in the IMPS program as a means of finding out how their hardware/technology will be affected by the space environment. AFGL will provide to these organizations support from the IMPS program to put together engineering experiments involving their internally-developed materials, equipment, or technologies. These experiments will be designed, fabricated, and tested under the direction of the of the particular AF laboratory, NASA technology center, or other S&E organization. In most instances, the detailed work will be carried out through contracts with universities, research organizations, and industrial companies.

Experiment and Sensor Development

Work on IMPS instrument development will include:

a. Selection of required engineering experiments and environmental sensors by AFGL.

b. Design of the individual engineering experiments.

c. Development and fabrication of the experiments and sensors.

d. Testing of individual engineering experiments and environmental sensor packages at the builder's facility to ensure that they fulfill IMPS requirements for making the various measurements. Testing to ensure that they conform to IMPS guidelines regarding command and power distribution, recording and telemetry, etc. Testing to ensure the experiments and sensors meet Shuttle operations and safety standards.

Integration and Shuttle Flight

AFGL will bring together the engineering experiments and environment sensors obtained from the various organizations responsible for their development and deliver them to the Space Test Program for integration. STP will then become responsible for IMPS. Shuttle flight arrangements and scheduling will also be handled by STP.

Data Analysis

During the Shuttle flight of IMPS, there will be a need for real-time monitoring of some of the instruments. Although IMPS operation will be made

essentially automatic, careful monitoring will be required when an "active"
part of an experiment (a plasma source, for example) is turned on. It is also
important that during a significant event (an encounter with an auroral arc,
for example) the data collection rate be increased, so as to permit later high-
time-resolution analysis of important phenomena.

After the flight of IMPS aboard Shuttle, the Space Test Program will provide
AFGL with data for the various engineering experiments and environmental sensors.
Additionally, STP will provide orientation and geographic position of the Shuttle,
position and orientation of any packages moved out of the bay, information on
thruster firings, "housekeeping" data, etc. Under a data utilization plan
developed before the Shuttle flight, AFGL will distribute the data for analysis.
The data will go not only to those responsible for the individual experiments
but also to organizations selected to do comprehensive analyses on various
interaction phenomena. Particular attention will be paid to correlating changes
in the physical properties of the environment with enhanced interactions noted
on particular materials or equipment.

Within the first year following a successful IMPS Shuttle flight, AFGL will
conduct a series of data workshops at which the IMPS data would be made avail-
able so that experimenters can compare their results. Workshops would be con-
fined to key topics such as contamination & materials degradation, or charging
& arc-discharges, or EMI generation, etc. By keying on a particular topic, it
should be possible to generate an authoritative report on that subject as the
output of the workshop. These reports can then be directed toward improving
relevant MIL-STD design guidelines and test standards by providing the proper
environmental interaction input.

CONCLUSIONS

The successful operation of the Interactions Measurement Payload on a late-
1980s Shuttle flight will lead to detailed knowledge of the effects of the polar-
auroral environment on materials, equipment and technologies of future space
systems. The output from IMPS will provide direct input to the development of
MIL-STD design guidelines and test standards for planned military space systems.
The data collected by IMPS can be used to validate computer-aided design (CAD)
tools that properly account for space-environment effects. The utilization of
the information gathered from the IMPS measurements will prevent operational
failures due to unanticipated environmental effects and minimize costly down-
stream redesign of expensive space systems. Risks to spacecraft and crews
will be greatly decreased by the elimination of uncertainties about the disrup-
tive effects of the polar-auroral environment.
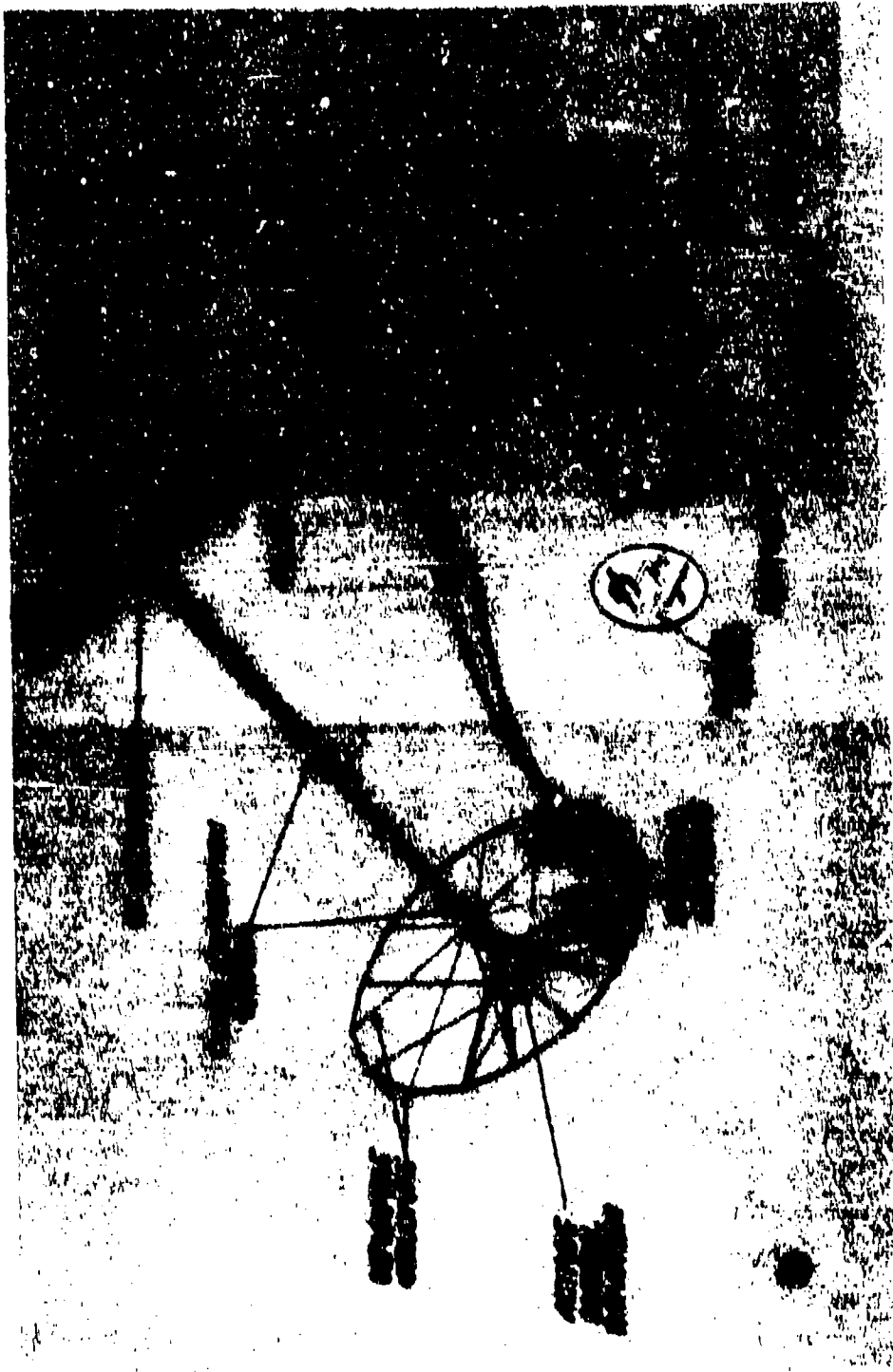
Figure 1. – Space-fed phased array–SBR antenna.
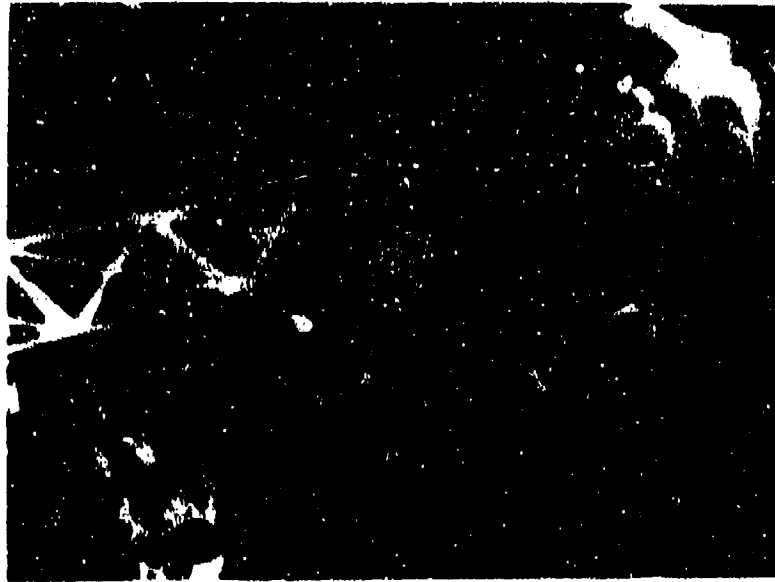
Figure 2. – Extravehicular activity in space.
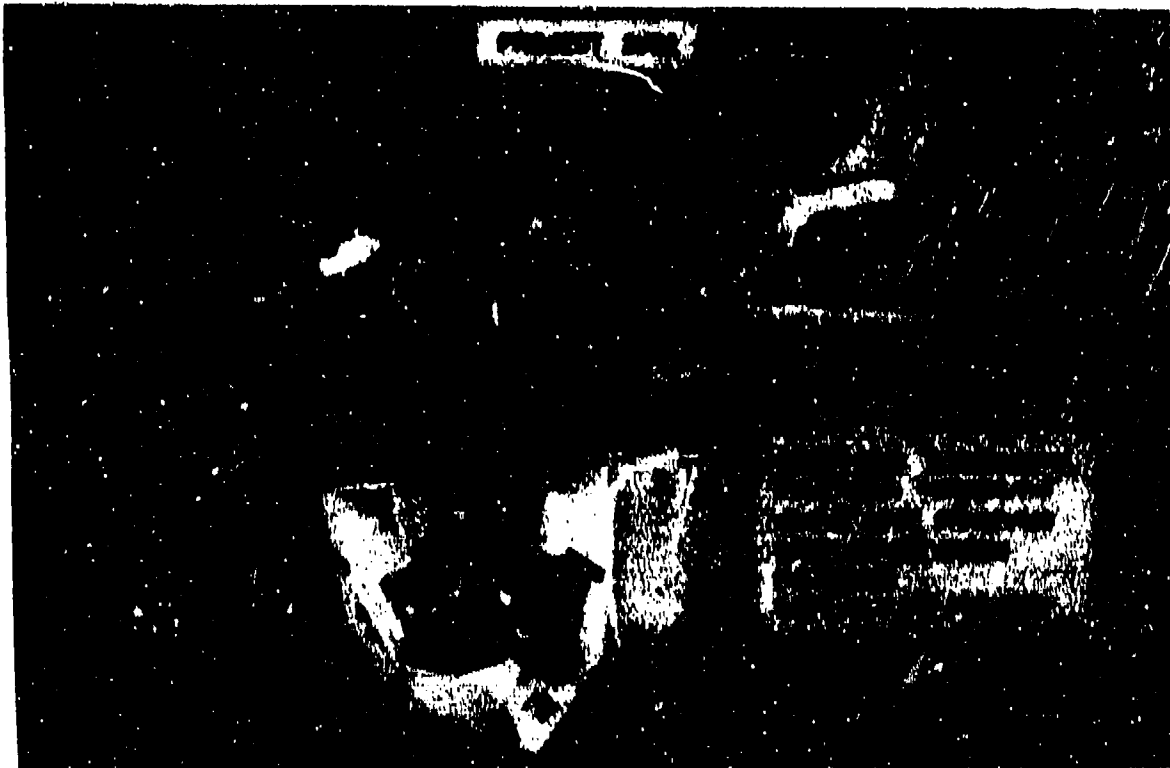
Figure 3. – Interactions measurement payload for Shuttle (IMPS).

ENVIRONMENTAL SENSOR PACKAGE

THERMAL CONTROL QUARTZ CRYSTAL MICRO BALANCE

ELECTRICAL PROP DEGRADATION

FLIGHT DATA SYSTEM

MATL CHARGING & DISCHARGE PULSE MONITOR

PLASMA INTERACTION EXPERIMENTS

SINGLE EVENT UPSET PKG.

CHARGE CONTROL SYSTEM

AURORAL X-RAY IMAGER

POWER DISTRIBUTION ASSEMBLY

ENVIRONMENTAL SENSOR PACKAGE

EVA SYSTEMS EFFECTS EXPERIMENT
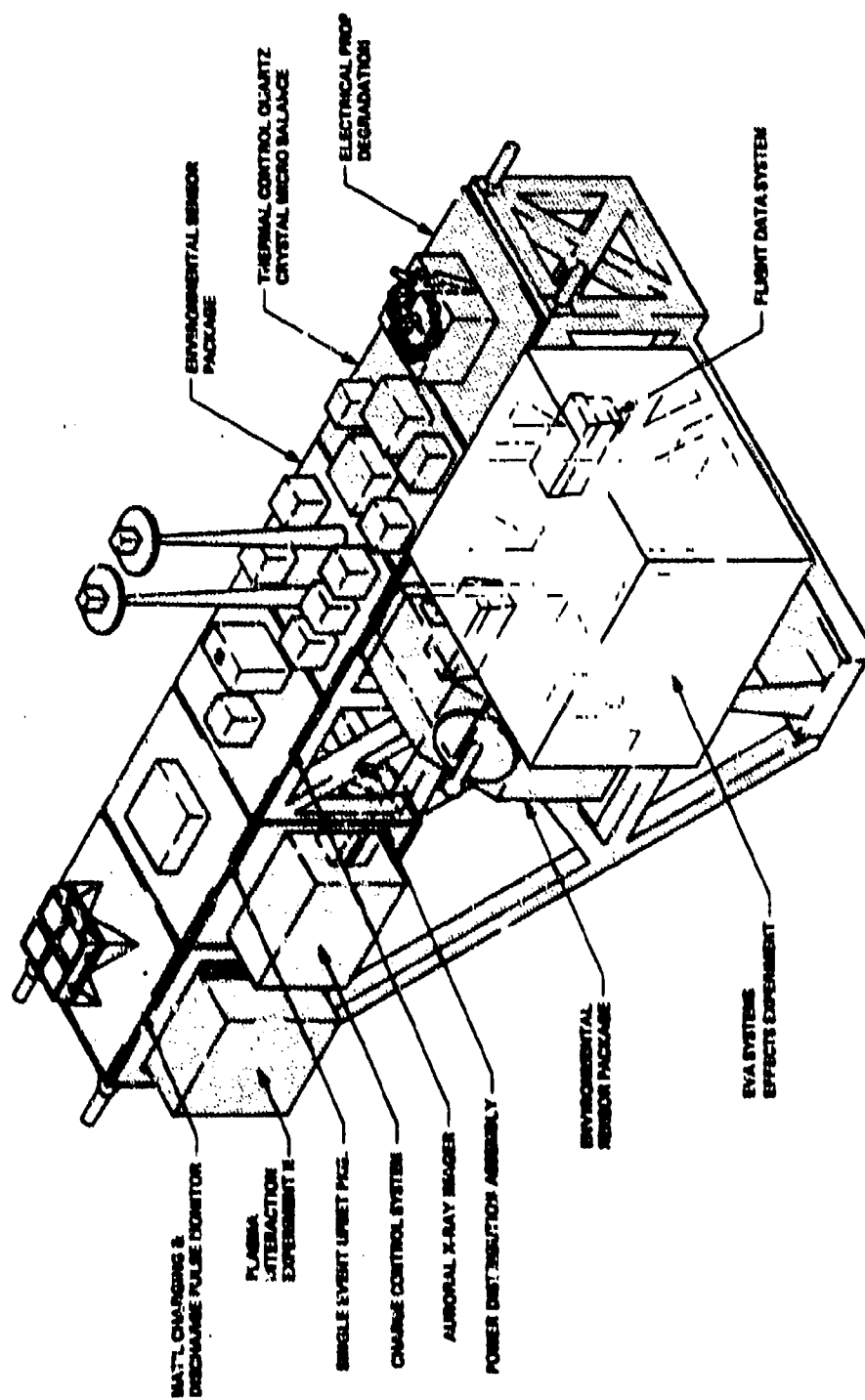
Figure 4. – IMPS payload, mod C.

SPACE TEST PROGRAM OF HIGH-VOLTAGE SOLAR ARRAY/SPACE PLASMA INTERACTIONS

M. R. Carruth, Jr.
National Aeronautics and Space Administration
Marshall Space Flight Center
Huntsville, Alabama

Carolyn K. Purvis
National Aeronautics and Space Administration
Lewis Research Center
Cleveland, Ohio 44135

Future spacecraft, notably the proposed Space Station, will
require power systems much larger than have previously been
flown. Efficiency, cost, mass and array size considerations
demand the solar array operate at a higher voltage than
previous spacecraft. It is recognized that at higher voltages,
and at the relatively high plasma density present at low earth
orbital altitudes, undesirable interactions between the high
voltage solar array and the space plasma will occur. These can
lead to parasitic power loss and/or arcing. Such interactions
are complex and cannot be understood, properly simulated or
evaluated by ground testing and modeling alone. Space
experiments on high voltage solar array space plasma
interactions in low earth orbit are an absolute requirement for
confident design of a higher voltage solar array. Experiments
are presently being identified to provide the necessary space
data for calibration of ground testing, validation of
analytical models, and development of design guidelines
required for confident design of high voltage solar arrays in
space. This paper summarizes one proposed flight experiment
program which is designed to obtain the required data.

INTRODUCTION

Interactions between a spacecraft and its orbital particle and
field environment can have significant impact on the spacecraft
systems' operation and life. Radiation damage and aerodynamic
drag, for example, must be considered in designing any space
system. There are, however, a number of orbital environmental
interactions which become important design considerations only
for large and/or high power systems. Their impact must be
assessed to ensure successful design. In particular,
interactions between higher voltage solar arrays and the space
plasma are of critical concern in designing large orbital power
systems such as are required for a space station.

Most U. S. spacecraft to date have used low voltage solar arrays, generating power near 30 volts. The highest voltage array flown by NASA to date was on Skylab, which had a solar array with a normal operating voltage of 70 volts and generated 16 kW of power. Future large systems will require increasing power generation capability. For example, a solar array providing 35-50 kW of power for a low inclination, low altitude (500 km) space system will need to generate about 100 kW of power when in sunlight. As power levels increase, the mass, I^2R power loss and power distribution system complexity penalties for maintaining low solar array voltages become prohibitive, making higher voltage array designs mandatory (Ref. 1). It is thus necessary to thoroughly understand high voltage solar array operation in the space plasma environment. Unfortunately, no adequate simulation or model calibration can be achieved with ground based experiments alone.

Solar array systems consist of strings of solar cells with metallic interconnects between them. These interconnects are at voltages depending upon their positions in the array circuit and are usually exposed to the space environment. When such systems are placed in orbit, they will interact with the naturally occurring space plasma. Two types of potentially hazardous interactions to a higher voltage solar array in orbit are presently recognized: power loss from parasitic currents through the plasma; and arcing. Both of these interactions are plasma density dependent and present greater hazards at higher densities. The low temperature ionospheric plasma has a peak density (of 10^6 particles/cm^3) at about 300 km altitude. High voltage system-plasma interactions will therefore be most severe in low earth orbits. The power levels envisioned for such spacecraft as the proposed Space Station drive the design toward higher solar array operating voltages. When the spacecraft exits eclipse, this voltage will be even higher until the array warms up. Successful design of higher voltage arrays relies on understanding the limits imposed by plasma interactions.

NASA's Office of Aeronautics and Space Technology (OAST) is pursuing the needed technology development in photovoltaics, energy storage, and power management and distribution to enhance, enable, and ensure the environmental compatibility of high power systems. Technology programs are underway to develop and demonstrate advanced planar and concentrator solar cells and array designs. A joint NASA/U.S. Air Force Spacecraft Environmental Interactions Technology investigation is also underway to evaluate the impact of the plasma and field environments on system performance (Ref. 2). These programs are basically ground technology efforts involving ground experiments and model development. A complementary program of space flight experiments is required for several reasons. First, the ground test environment is necessarily an incomplete

simulation of space conditions. The interactions are dependent on the plasma and neutral background parameters around the solar array. A space environment is therefore required. Because some of the interaction phenomena may extend many meters, there are concerns regarding the effect the chamber walls may introduce in ground testing. Also, most testing has involved applying a voltage bias on solar array segments and evaluating the interaction of such segments with the plasma. From these experiments, estimates of interactions impact on solar array performance have been made. However, the system level interactions can be very complex. Therefore, it is necessary to obtain a direct measure of the performance of a large solar array generating its own voltage and operating in the space environment, including the effects of parameters such as ram/wake which cannot be simulated. Also, it is clear from STS-3 data that the presence of a large body in orbit perturbs the ambient environment in ways which are as yet not fully understood, but which may have significant impact on system-environment interactions. Finally, flight data is absolutely critical to provide "space truth" information for use in calibrating ground simulations, demonstrating operating impacts and validating system level models which must be used to predict interactions impacts for proposed designs. This paper summarizes the interaction concerns for higher voltage arrays in orbit, the ongoing technology investigations, and describes a proposed series of Shuttle experiments designed to obtain the required flight data.

ENVIRONMENTAL INTERACTIONS
BACKGROUND

The attention of the environmental interactions community was for several years focused on the investigation of spacecraft charging, an interaction which had been found to be hazardous for geosynchronous spacecraft and was intensively studied by NASA and the Air Force (Ref. 3). In the late 1970's, interest in high voltage interactions again intensified, and their study was resumed under the auspices of the joint NASA/USAF Spacecraft Environmental Interactions Technology investigation (ref. 2). The ground-technology program uses the experimental facilities at NASA and USAF centers, builds upon the modeling capabilities developed during the spacecraft charging investigation, and uses the earlier high-voltage study results (refs. 4 to 11). Among the goals of the technology program is the development of design guidelines and analytical tools for higher voltage solar arrays for Earth orbital applications.

This requires flight data to ensure that the phenomena observed in ground testing occur in orbit, to examine conditions not obtainable in ground facilities and to validate the models. To

date, two small scale Plasma Interactions Experiments (PIX-I and PIX-II) have been designed, built and flown. Both were piggy-backs on second stage Delta vehicles and in approximately 900 km circular polar orbits. PIX-I, which flew in March 1978, and returned two hours of data, demonstrated that the current collection enhancement and arcing phenomena observed in ground testing of planar array segments also occur in orbit (Ref. 4). The 16 hours of planar array data returned by PIX-II, which flew in January 1983, are still under analysis. Preliminary results indicate that the minimum arcing onset voltage decreases with increasing plasma density and that tank wall effects influence current collection behavior at high positive voltages in ground tests.

No data is available on ram/wake effects, influence of the presence in orbit of a large system, or the effect of interactions on the operational characteristics of a large higher voltage array. Understanding these effects is critical to developing useful design guidelines for such solar arrays.

Solar Array Voltage Positive Relative to Plasma

Figure 1 represents experimental data for a solar array section biased positive with respect to the plasma in which it is immersed (Ref. 11). The left half of the figure illustrates that at voltages greater than 100-150 volts, the electron current collected by the solar array increases dramatically. The right half of the figure illustrates why. Even though the solar array surface is dielectric, the surfaces become highly positive and collect current as though the whole surface were a conductor. The explanation appears to be that as the plasma sheath grows around exposed interconnects or pinholes, the accelerated electrons strike the dielectric and low energy secondary electrons are released which are collected by the exposed metal. This leaves the dielectric cover glass positive, allowing the plasma sheath to grow over the solar cells. Therefore, the solar array collects electron current as though it were a conductor. As the voltage on the array segment and the effective collection area increases, the current collected rises, as indicated in figure 1. This current flow through the plasma is current which is not available to the spacecraft and therefore represents a power loss to this plasma shunt. Depending on the solar array voltage the power loss can be substantial and can seriously impact array performance.

No direct measure of the power loss exists because essentially all data consists of current collected by solar array segments with a potential impressed on them by a power supply. The power loss, which will be experienced in a solar array due to

the collection of current from the plasma, has often been
estimated by multiplying the collected solar array segment
current by the voltage between the solar array segment and the
plasma and summing over the segments. Such an estimation does
not consider the current flow in the solar array. A solar
array which is not in a plasma environment will have only the
load current, I, flowing in it. The current is the same
throughout the array and it can be operated at the maximum
power point. However, a high voltage solar array immersed in a
plasma will collect plasma current which will flow through the
array in addition to the load current. The plasma current
collected at a location on the array is a function of the
potential between that location on the array and space. The
current flowing through a specific point in the array is the
load current and the sum of electron currents collected at
points in the array at higher positive voltages. Therefore,
nonuniform currents will flow within the array. To operate at
the solar array maximum power point, each individual cell will
operate off its individual maximum power point.

In ground tests, a voltage is impressed on test samples and the
current collected from the plasma is measured. Because the
voltage is applied, there is no differential voltage between
the solar cells. However, for a solar array which is
generating its own voltage by having solar cells placed in
series, there will be voltage gradients on the surface of the
cells due to difference in voltage between cells. The
gradients may be quite high if the cells are strung such that
solar cells at considerably different voltages lie next to each
other. The electric field structure in the plasma sheath may
be complex due to solar cell layout. Because such voltage
gradients exist, there is the possibility of currents between
cells due to field emissions and/or secondary electron emission
and/or some other surface current mechanism not identified.
These more localized currents may produce an additional
shunting of portions of the solar array.

A discharge phenomena around the solar array has also been
observed in some ground tests (Ref. 13). In these cases a
bright glow appeared around the solar array and the electron
currents collected by the solar array from the plasma increased
by orders of magnitude. Such an increase in collected current
will substantially affect the power loss in the solar array.

Because of the complex nature of high voltage solar array/
plasma interactions, it is necessary to experimentally
determine the power curve of a solar array operating in a
plasma environment.

Solar Array Voltage Negative Relative to Plasma

Figure 1 illustrates the observed effects of a solar array segment biased positive of the surrounding plasma. Different effects are observed for a solar array segment biased to a negative voltage relative to the plasma. Unlike the positive voltage case, the solar cell cover glass voltage does not rise to the interconnect voltage as the solar cell voltage becomes more negative. A steep voltage gradient exists between the interconnect and other exposed metal parts of the solar cells and the solar cell surface. For impressed voltages of several hundred volts, arcing on the array is observed. Pictures of such arcing events are shown in figure 2 (Ref. 10). The arcing occurs at lower negative voltages for higher plasma densities. Arcing has been observed at voltages of -250 volts on a solar array segment in a plasma with a density of 10^4 electrons/cm^3 (Ref. 13). Ambient plasma densities of up to 10^6 electrons/cm^3 may be encountered in space. Such solar array arcing will introduce large current and voltage transients which may tend to collapse the array voltage. However, the effects of such arcing on the solar array performance is presently uncertain.

Solar Array-Spacecraft-Space Plasma Potentials

A spacecraft in orbit and immersed in the space plasma will come to a potential relative to the plasma such that no net current is collected. The solar array provides an additional complication since ambient charge particles can be collected. There are two solar array voltages to consider. One is the operating voltage generated by the solar cells in series. The other is the potential of the solar array relative to the surrounding space plasma. Some point on the array will be at space potential and the portions of the solar array positive of this point will collect electrons from the plasma while the negative part collects ions. Because of their higher temperature and mobility, electrons are much more easily collected than ions. Therefore, to collect equal electron and ion current, a much larger area at a negative potential relative to the plasma is required. For a spacecraft grounded to the negative side of the solar array, the situation on the right side of figure 3 will result. The spacecraft and negative side of the array will be driven below space potential. For an array of several hundred volts, solar array arcing may result, and since the spacecraft structure will be several hundred volts negative, it will experience a continuous ion bombardment for the spacecraft lifetime which may alter surface thermo-optical properties. Another spacecraft without such a solar array or an untethered astronaut will be near space potential. The resulting potential difference between

624

such a free flyer and the highly negative spacecraft can pose
serious safety concerns. The highly negative spacecraft
potential will also interfere with some science, e.g., particle
and plasma data acquisition.

If an electron gun or plasma source is operated on the
spacecraft, electrons collected by the positive portion of the
solar array will be released back to space. Large negative
potentials will not result, and if electrons are freely
released, the situation on the left in figure 3 will result.

Plasma Perturbation

Many sounding rocket experiments have been flown which
investigated the magnetosphere by releasing electron beams
along the earth's magnetic field lines (Ref. 14). It was
anticipated that the rocket body would charge hundreds to
thousands of volts positive due to the release of a high energy
electron beam. This was not observed to be the case. The
rocket potentials increased to only 30 to 100 volts positive.
Plasma diagnostic devices indicate that the plasma density and
temperature increased when the electron beam was released, and
that a local discharge is created around the rocket either by
electron bombardment ionization or a beam-plasma discharge
(Ref. 14). The plasma is also observed to be perturbed at
large distances from the rocket. An analogous situation can be
expected with a spacecraft powered by a high voltage solar
array. An electron gun or plasma source operation will raise
the spacecraft potential to near space potential and will
therefore drive the high voltage solar array very positive of
the space plasma potential. As previously described, discharge
phenomena for positive solar arrays in a plasma has been
observed in ground tests (Ref. 13). The local discharge and
plasma perturbations observed during rocket experiments can
increase power loss due to parasitic currents and interfere
with science data acquisition.

PROPOSED FLIGHT EXPERIMENTS: VOLTAGE OPERATING LIMIT TESTS

Recently, OAST proposed a new flight initiative, Voltage
Operating Limit Tests (VOLT). The VOLT project is a
comprehensive program composed of a series of four Shuttle
based flight experiments which will provide the data base
required to design successful higher voltage solar arrays for
low earth orbit (LEO) power systems. Two of the experiments,
VOLT-1 and VOLT-3 will utilize biased solar array segments of
planar and concentrator designs, respectively, to scope the
nature of the basic interactions in LEO, determine ram/wake

effects and identify influences of the large ?TS vehicle on
interactions. Results will be used in designing the other two,
more comprehensive, experiments. VOLT-2 and VOLT-4 will test
large area arrays of the planar and concentrator designs,
respectively, to evaluate the impacts of interactions on array
operation directly. VOLT-3 and VOLT-4 are similar in the
plasma interactions portion of these experiments to VOLT-1 and
VOLT-2 except that VOLT-3 and VOLT-4 both use concentrator
solar arrays. Therefore, to prevent repetition, only a
detailed discussion of the VOLT-1 and VOLT-2 plasma interaction
experiments will be presented.

The VOLT-1 experiment, shown mounted in the Shuttle bay in
figure 4, utilises the backup hardware from the PIX-II
experiment, with minor modifications for Shuttle flight
compatibility. The objective of the VOLT-1 experiment is to
evaluate plasma to solar array currents and arc thresholds for
planar solar array segments in the LEO environment. Such data
is like that collected in ground tests and will allow
validation of basic interaction model predictions for the
Shuttle LEO environment. Data will also be acquired in both
ram and wake conditions. Because the experiment is hard
mounted in the bay, the Shuttle attitude will provide ram and
wake conditions for the experiment. The data acquired by
VOLT-1 will allow better prediction of the interactions which
will be expected on VOLT-2.

The VOLT-1 experiment is comprised of an electronics enclosure
and an experiment plate, upon which is attached a 2000 cm solar
array segment. The electronics enclosure houses the
electrometers, power supply, sun and temperature sensor
electronics, a Langmuir probe and associated electronics,
experiment sequence controller and tape recorder. VOLT-1 is
envisioned as being nearly completely self-contained and
automatic, requiring only an electrical ground reference and
experiment initiate signals. During operation positive and
negative voltage biases will be impressed on the array in steps
until potentials of ±1000 volts relative to ground are reached.
Arcing onset and parasitic currents will be measured for both
positive and negative biases.

A reflight of the Solar Array Flight Experiment (SAFE), with
necessary modifications, has been proposed as a high voltage
solar array/space plasma interactions experiment (Ref. 15).
The basic SAFE experiment is a space test of a 12.5 kW size,
lightweight solar array. It is primarily a demonstration of
the solar array's ability to deploy and retract successfully
and to obtain data on the dynamic response of such a large
structure in space. A very small portion of the solar array
consists of active solar cells with the majority of the area
covered by thin aluminum squares to simulate the solar cell
mass. The wing, shown in figure 5 in its fully deployed state,

measures 4m by 32m. Also, a conceptual view of the experiment deployed from the Shuttle bay is shown in figure 6.

The VOLT-2 plasma interactions experiment utilizes the SAFE hardware with three primary modifications. These are: (1) that three solar cell panels, each consisting of two modules, will replace three of the present SAFE panels and will self-generate solar array operating voltages of from near 90 to in excess of 500 volts, (2) that electron release devices will be added to control the solar array potential to space and, (3) plasma diagnostic instruments will be added to determine the ambient and perturbed plasma conditions around the solar array.

The VOLT-2 experiment with retracted solar array, is shown in figure 7. This experiment will allow a direct measure of the solar array's performance by obtaining I-V curves as functions of solar array voltage, solar array-to-space potential, type of charge release device maintaining this potential and ram/wake orientation. It will also determine floating potentials for true distributed voltage solar array, arcing onset voltages and impact of arcing on the solar array. Such data from a functioning solar array will allow validation of system level model predictions of solar array performance.

The three active panels near the end of the solar array wing will provide about 14,500 cm^2 of solar array. Each panel will be composed of two modules. The modules will be placed in various parallel and series configurations to allow testing at solar array voltages from near 90 volts to in excess of 500 volts. Figure 8 indicates the change in module and maximum array voltage as a function of orbital position. When the solar array is floating in the plasma, such that it is collecting equal electron and ion current, 80-90% of it will have to float negative. Tests will be conducted by switching the floating solar array from lower to higher operating voltages and arcing phenomena, floating potential and solar array performance measurements will be obtained.

The high current hollow cathode and plasma source will be operated for tests of the solar array positive relative to space potential. These sources, with possibly the addition of an electron gun generating an energetic electron beam, will, independently, freely emit the solar array collected electrons back to space and will control to solar array to space potential. The majority of the solar array will be positive of the space potential allowing power loss evaluation as well as investigation of local discharge phenomena expected in the solar array vicinity. The array potential will be controlled by the spacecraft automatic active discharge system (SAADS) of which the charge release devices are an integral part. Because of their interest in the results of this experiment, the Air Force Geophysics Laboratory has offered to furnish this

equipment to the VOLT-2 experiment. Some plasma diagnostics
associated with SAADS will be located on the Mission Peculiar
Experiment Support Structure (MPESS).

A minimum complement of three diagnostic instruments will be
mounted on the end of the solar array. These are presently
identified as a neutral density instrument, a Langmuir probe
and a Differential Ion Flux Probe (Ref. 16). These instruments
will allow determination of the ambient conditions in which the
plasma interaction experiment is conducted as well as
evaluation of perturbations to the plasma due to the high
voltage solar array operation.

Figure 9 illustrates the anticipated orbital configuration of
the VOLT-2 experiment. The figure indicates that the solar
array and Shuttle tail will be pointed toward the sun. This
configuration is more advantageous for experiments involving
electron release by electron gun. The beam can be projected
along the magnetic field line and not strike the solar array.
The generated plasmas will also tend to diffuse along magnetic
field lines and away from the solar array.

The orbital velocities of spacecraft for LEO are much greater
than the thermal ion velocity but much less than the thermal
electron velocity. The result is that as a spacecraft moves
through the plasma it sweeps out the ions, leaving much
decreased plasma density in its wake, which is occupied by an
excess of electrons, relative to the ion population. As
observed in figure 10, there will be positions in the orbit
where the wake is on the solar cell side or the backside of the
solar array and where no wake exists (when the spacecraft
velocity vector and sun line are perpendicular). Data
acquisition at these various positions will allow determination
of power loss, arcing and plasma perturbation over the range of
anticipated orbital plasma conditions.

CONCLUDING REMARKS

For a number of years NASA and the USAF have planned space
missions utilizing solar arrays which generate orders of
magnitude more power and operate at a much higher voltage than
has been flown previously. During this same time ground
technology programs have addressed the interactions between
such a high voltage solar array and the ambient space plasma.
These programs have given us a basic understanding of what
interactions to anticipate and under what conditions. Ground
test information has been augmented by flight tests which
verified that the effects observed on the ground are observed
in space. However, it has long been recognized that ground
tests are limited by facility size, facility effects on plasma

and electric field conditions and the capability to accurately
simulate space plasma conditions. It is very important to test
actual solar array performance with a large, self-generated
voltage so that effects of large array area, surface voltage
gradients and varying currents in the solar array can be
evaluated. It is not possible to do this adequately in a
ground test chamber.

The space test program described in this paper is designed to
obtain critical information on solar array-plasma interactions
and their impact on array performance for planar and
concentrator arrays. Data will be obtained under conditions
and at array sizes not obtainable in ground testing. These
data are critical for validating the system level models which
must be used to evaluate candidate large power system designs
and for developing design guidelines for higher voltage arrays.
The data will be obtained with a matrix of variables so that
the maximum information on solar array interactions and
performance in the LEO plasma environment will be collected.
Experiments will be conducted with various applied and
self-generated solar array voltages. These will be performed
with the front of the solar array in plasma ram and wake
conditions and with zero plasma drift normal to the solar cell
face.

Without the crucial information this flight program will
provide, designers of future spacecraft will be forced to be
conservative and operate solar arrays at presently accepted
voltages. This will seriously impact system efficiency and
manageability.

REFERENCES

1. Stevens, N. J.: Interactions Between Spacecraft and the Charged
    Particle Environment. Spacecraft Charging Technology - 1978,
    NASA-CP-2071, 1978.

2. Pike, C. P. and Stevens, N. J.: Agreement for NASA/OAST - USAF/
    AFSC Space Interdependency on Spacecraft - Environmental
    Interaction. Spacecraft Charging Technology - 1980, NASA
    CP-2182.

3. Lovell, R. R., Stevens, N. J., Schober, W., Pike, C. P., and
    Lehn, W.: Spacecraft Charging Investigation: A Joint Research
    and Technology Program. Spacecraft Charging for Magnetospheric
    Plasmas, A. Rosen, ed., Vol. 47, Progress in Astronautics and
    Aeronautics, AIAA, New York, New York, 1976.

4. Kennerud, K. L.: High Voltage Array Experiments. NASA CR-
    121280, 1974.

5. McCoy, J. E.; and Konradi, A.: Sheath Effects Observed on a 10-Meter High Voltage Panel In Simulated Low Earth Orbit Plasmas. Spacecraft Charging Technology - 1978, NASA CP-2071, 1978.

6. McCoy, J. E.; and Martucci, D. T.: Experimental Plasma Leakage Currents to Insulated and Uninsulated 10-m High Voltage Panels. Spacecraft Charging Technology - 1980, NASA CP-2182, 1980.

7. Katz, I.; Cassidy, J. J.; Mandell, M. J.; Parks, D. E.; Schnuelle, G. W.; Stannard, P. R.; and Steen, P. G.: Additional Application of the NASCAP Code. Vol. I: NASCAP Extension. NASA CR-165349, 1981.

8. Nonnast, J. H.; Chaky, R.C.; Armstrong, T. P.; Enoch, J.; and Wiseman, G. G.: Numerical Simulation of Plasma-Insulator Interactions in Space. Part I: The Self-Consistent Calculation. Spacecraft Charging Technology - 1980, NASA CP-2182, 1980.

9. Chaky, R. C.; Nonnast, J. H.; Armstrong, T. P.; Enoch, J.; and Wiseman, G. G.: Numerical Simulation of Plasma-Insulator Interactions in Space, Part II: Dielectric Effects. Spacecraft Charging Technology - 1980, NASA CP-2182, 1980.

10. Stevens, N. J.; Roche, J. C.; and Grier, N. T.: Large Space System: Charged Particle Environment Interaction Technology. NASA TM-79156, 1979. (Also AIAA Paper No. 79-0913.)

11. Stevens, N. J.: Investigation of High Voltage Spacecraft System Interactions with Plasma Environments. AIAA Paper No. 78-672, 1978.

12. Grier, N. T. and Stevens, N. J.: Plasma Interaction Experiment (PIX) Flight Results. Spacecraft Charging Technology - 1978 NASA CP-2071, 1978.

13. Grier, N. T.: Experimental Results on Plasma Interactions with Large Surfaces at High Voltage. NASA TM-81423, 1980.

14. Winckler, J. R.: The Application of Artificial Electron Beam to Magnetospheric Research. Rev. Geophys. and Space Phys., Vol. 18, No. 3, August 1980.

15. Carruth, Jr., M. R., Young, L. E., Purvis, C. K., and Stevens, N. J.: SAFE II-Large Systems Space Plasma Evaluation Experiment. Large Space Antenna System Technology - 1982, NASA CP 2269, Part 2, 1982.

16. Stone, N. H.: Technique for Measuring the Differential Ion Flux Vector. Rev. Sci. Instrum., Vol. 48, No. 11, 1977.
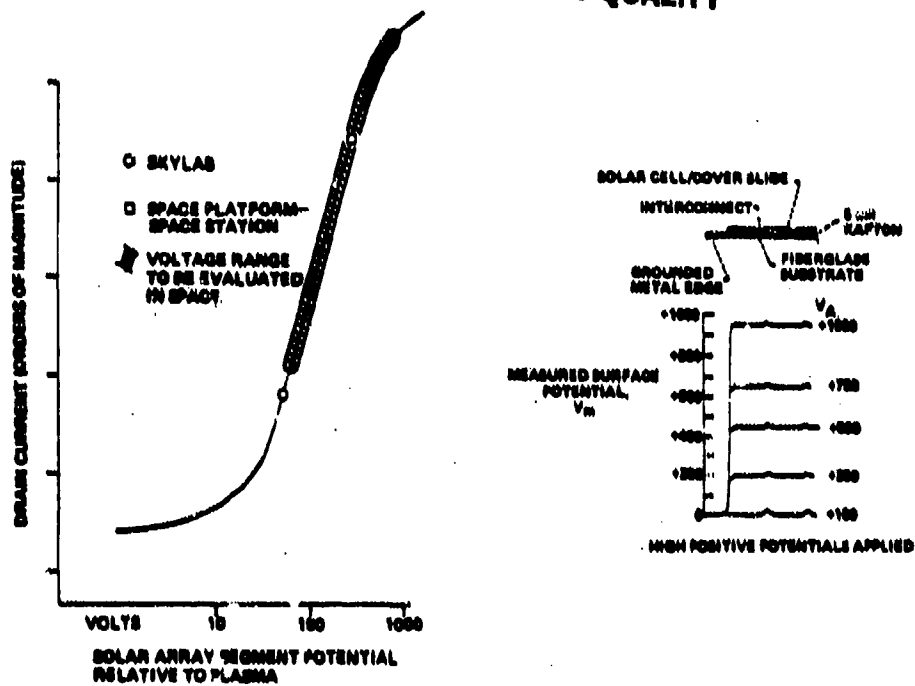
Figure 1. – Solar array positive relative to plasma.
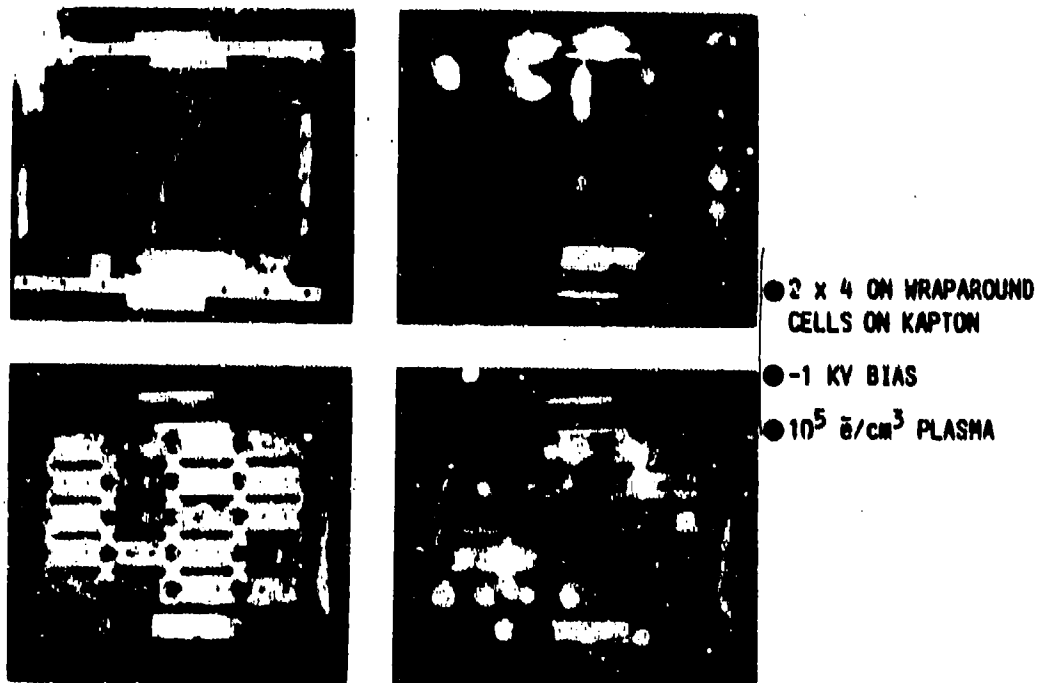
Figure 2. – Arcing on negatively biased solar cells.

631

Figure 3. - Solar array - spacecraft - space plasma potentials.
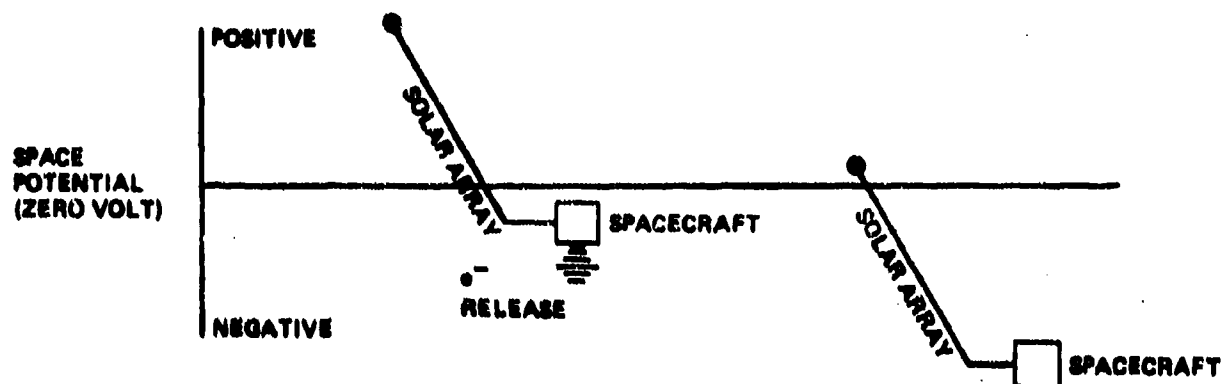
- POWER LOSS
- SCIENCE INTERFERENCE
- BOTH ENHANCED BY POSSIBLE LOCAL DISCHARGE

- ARRAY ARCING
- ION BOMBARDMENT
- DOCKING/EVA SAFETY
- SCIENCE INTERFERENCE
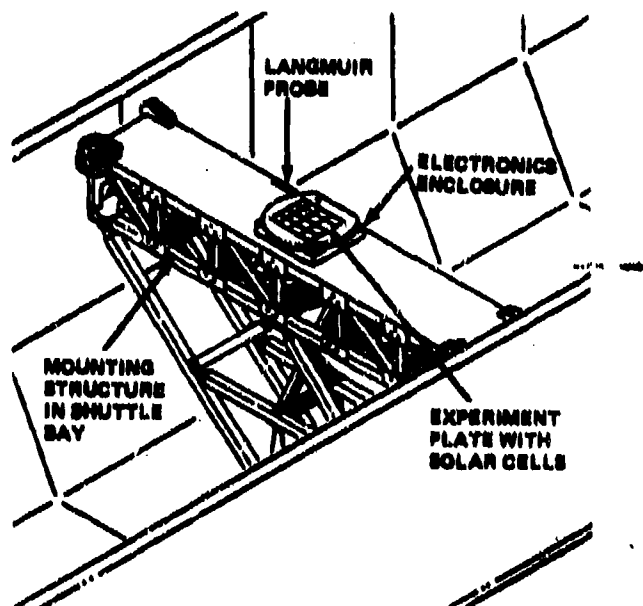
Figure 4. - VOLT-1.
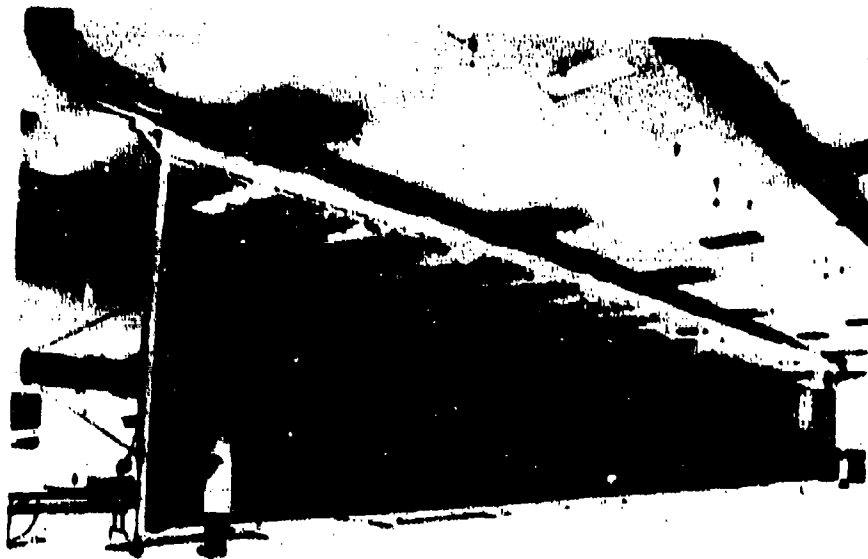
Figure 5. - SAFE wing.
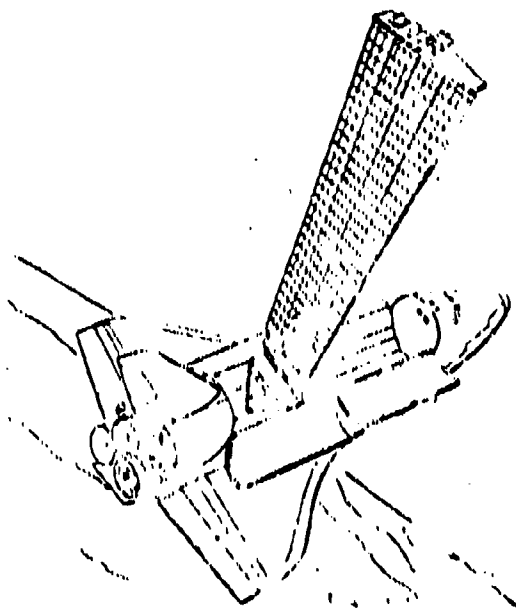
Figure 6. - Conceptual view of SAFE deployed.

633

Figure 7. - VOLT-2.

PERFORMANCE BASED ON

- 2 x 4 WRAPAROUND CELLS (JPL PUB. 79—15 VOLUME XI)
- FLT. EXP. PREDICT'D. ORBIT TEMP.
- 3 PANELS — 2 MODULES/PANEL — 672 CELLS/MODULES — 3 CELLS PARALLEL
- CURRENT AT MAX POWER ≈ 770 MA

Figure 8. - Panel voltage as function of orbit.
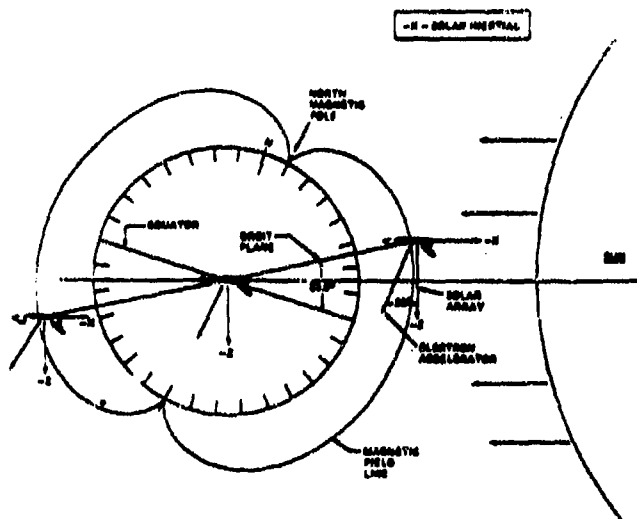
Figure 9. - Orbital configuration.
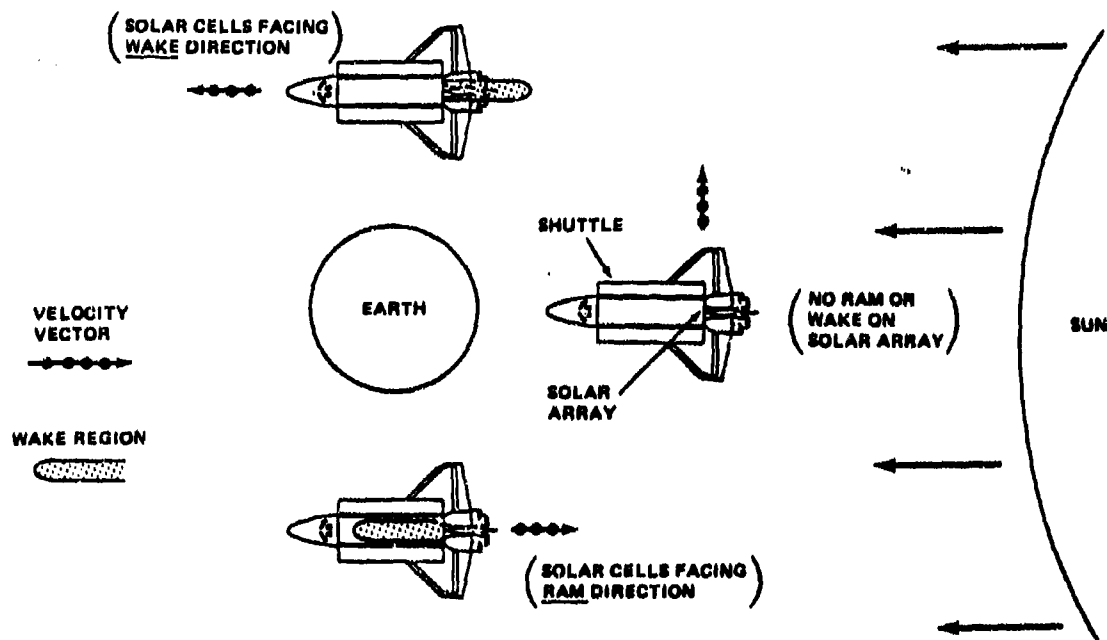
Figure 10. - Ram/wake conditions.

635

PRELIMINARY ASSESSMENT OF POWER-GENERATING TETHERS IN SPACE
AND OF PROPULSION FOR THEIR ORBIT MAINTENANCE

Robert E. English and Patrick M. Finnegan
National Aeronautics and Space Administration
Lewis Research Center
Cleveland, Ohio 44135

The concept of generating power in space by means of a conducting tether
deployed from a spacecraft was studied. Using hydrogen and oxygen as the
rocket propellant to overcome the drag of such a power-generating tether would
yield more benefit than if used in a fuel cell. The mass consumption would be
25 percent less than the reactant consumption of fuel cells. Residual hydrogen
and oxygen in the external tank and in the orbiter could be used very effec-
tively for this purpose. Many other materials (such as waste from life
support) could be used as the propellant. Electric propulsion using tether-
generated power can compensate for the drag of a power-generating tether, half
the power going to the useful load and the rest for electric propulsion. In
addition, the spacecraft's orbital energy is a large energy reservoir that
permits load leveling and a ratio of peak to average power equal to 2. Criti-
cal technologies to be explored before a power-generating tether can be used
in space are delineated.

INTRODUCTION

Tethered spacecraft are a topic of considerable and growing interest
(ref. 1). Among the features they offer is the possibility of power generation
from an electrically conducting tether trailed through the Earth's magnetic
field. Such a tether would be acted on by forces from the gravity gradient,
from aerodynamic drag, and from electrodynamic interaction with the Earth's
magnetic field; the tether would thus trail in a generally radial direction,
either up or down, rather than directly behind the spacecraft as the word
"trail" might indicate.

This paper describes a broad, general study of such power-generating
tethers that explored their potential value and their problems. The following
topics were studied: (1) the conditions of power generation, the drag imposed
on the spacecraft, and the resulting orbit decay; (2) the use of chemical pro-
pulsion to compensate for this drag; and (3) the use of some of the generated
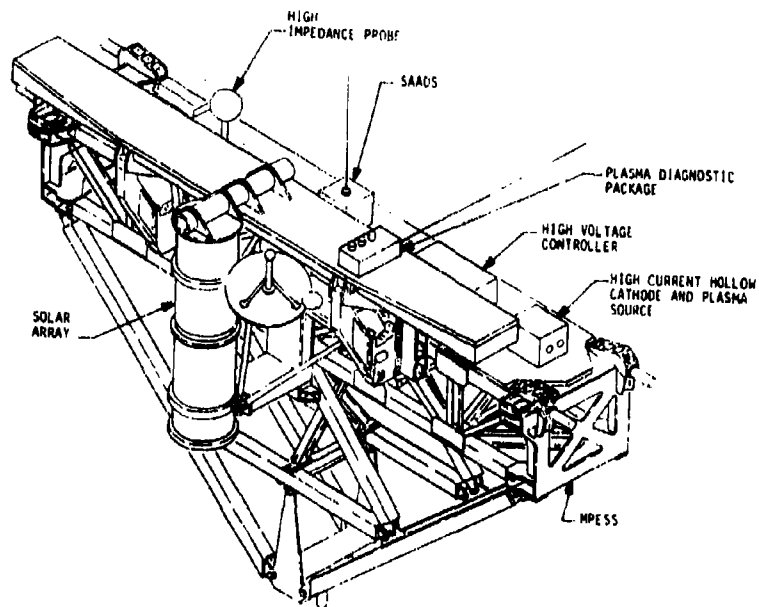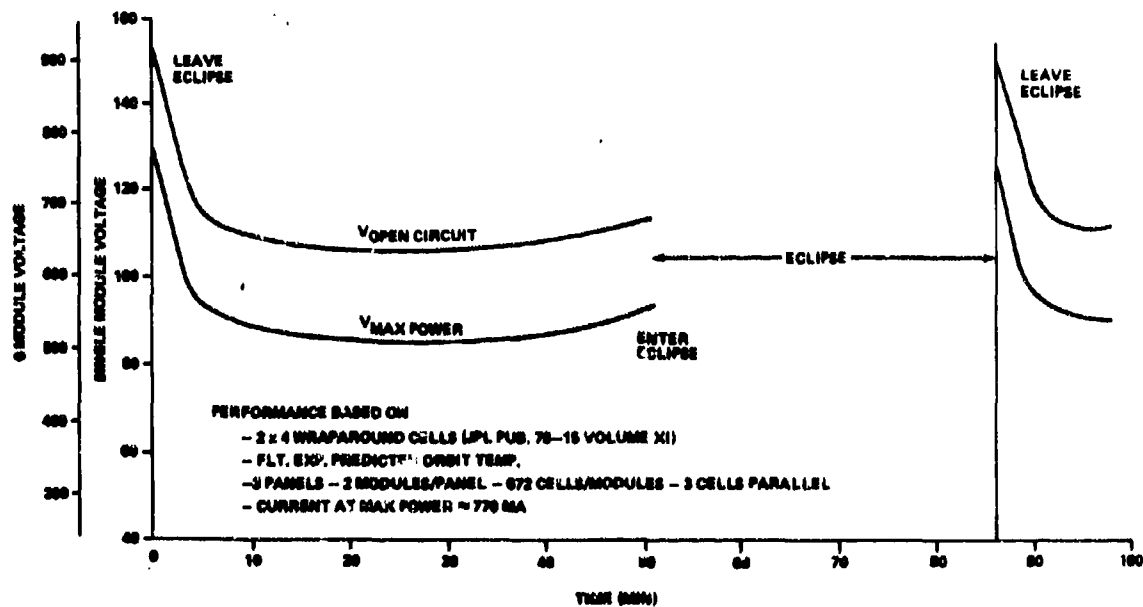power in electric propulsion to compensate for this drag. Finally, questions
of feasibility were considered. These topics define a technology program to
be completed before any application of such power-generating tethers in space.

THE POWER-GENERATING PROCESS

A spacecraft in low Earth orbit that trails an electric conductor that
is, say, 100 km long (fig. 1) will produce an electric potential in that

conductor as a result of its motion through the Earth's magnetic field. The voltage results from the familiar $\underline{v} \times \underline{B}$. For an orbital velocity of 7600 m/s, the potential generated by such a tether might be 15 to 20 kV. For an electric current to flow, electrons must be discharged at one end of the tether. Figure 1 shows an electron gun for this purpose. Electrons, being very mobile, are expected to provide the major flow of current.

For collection of the electrons at the tether's opposite end, an electron collector of large surface area is required. Although figure 1 shows a sphere for the collector, almost any surface would be suitable. Reference 2, for example, suggests a plane surface aligned with the spacecraft's orbit path as a way to decrease the aerodynamic drag from this large area.

Current through the conducting tether will impose a drag on the spacecraft from the familiar $\underline{i} \times \underline{B}$ interaction. Aerodynamic drag on the tether will also extract energy from the spacecraft. Rocket propulsion could compensate for these drags and permit the spacecraft to maintain a stable flightpath.

The useful power output would, of course, be the product of the current flow and the generated voltage. Inasmuch as generated voltages of tens of kilovolts are somewhat of a problem in their own right, the lower voltages produced by shorter tethers might at first appear attractive. For a given power output, however, the voltage reduction must be compensated for by an increase in current flow. At the higher current a larger surface is required for collecting the electrons.

Plasma interactions will also impede electron flow. In a perfect vacuum, the geomagnetic field would force the electrons to move along paths that are roughly helical, that surround given lines of the magnetic field, and that would thereby generally prevent the emitted electrons from reaching the electron-collecting surface. In an actual plasma, collisions of the electrons with ions and neutral particles as well as with other electrons will randomize the electron motions and permit their gradual diffusion toward the electron-collecting surface. Both the plasma impedance from these collisions and the space charge near the electron-collecting surface will restrict the flow of electrons. The regions of space having the highest plasma density may permit high currents of electrons, but these high densities may also impose severe aerodynamic drag. Data to permit optimization of altitude, these conflicting requirements being considered, are not available. Thus the conservative approach at this time requires the assumption of low current flow and, concomitantly, acceptance of the difficulties associated with the high voltages. This will, in turn, require a tether of length sufficient to generate the voltage required. For that reason, the generated voltage in figure 2 was taken as 17.5 kV. The tabulated inputs, outputs, and losses resulted in a projected generator efficiency of 0.73 for the conducting tether, with a useful power output of 70 kW.

The total drag (aerodynamic and electromagnetic) imposed by the tether power generator is about 13 N in this example, with a corresponding energy decay from the tether of 96 kW. In the absence of propulsion to overcome this drag, the orbit altitude would decrease about 20 km each day if the 96 kW were extracted from the orbital energy of a 100-ton space station. Although such

energy extraction would markedly shorten the life of a space station if continued for a long time, this power could be extracted for perhaps a week in an emergency. Spacecraft propulsion could, of course, compensate for this drag and thereby sustain orbit altitude. Both chemical and electric propulsion are likely candidates.

CHEMICAL PROPULSION FOR ORBIT MAINTENANCE

For 70 kW of useful power to be generated by a conducting tether, an average thrust of about 13 N is required to overcome tether drag (fig. 2). In principle, this thrust could be steady or in brief bursts of higher thrust. For a specific impulse of 400 s (already exceeded by hydrogen-oxygen rockets), propellant consumption would average 3 g/s, or 280 kg/day. In turn, propellant consumption would be 0.17 kg/kWh of electric energy. To some in the space-power field, this is a startlingly low value of reactant consumption, for it is only 43 percent of the reactant flow required by hydrogen-oxygen fuel cells. In fact, it is also only 58 percent of the reactant consumption of an ideal fuel cell, operating reversibly. How is this possible? The critical factor is the large amount of kinetic energy possessed by the reactants by virtue of their being in low Earth orbit, about 29 MJ/kg. In contrast, the Gibbs free energy for combining hydrogen and oxygen into water is only 13 MJ/kg, the theoretical limit on fuel-cell output per unit mass of hydrogen and oxygen consumed.

What are the various contributions to energy generation by a chemically propelled space station generating electric power via a conducting tether? A rocket having a specific impulse of 400 s can supply 3923 N-s of impulse to the space station for each kilogram of propellant expelled, corresponding to an exhaust velocity of 3923 m/s. For an orbital velocity of 7612 m/s, the rocket's energy addition to the space station would be 29.86 MJ/kg of propellant. What are the constituents of this energy addition? First, the kinetic energy with which the propellant would be discharged from the space station is 7.69 MJ/kg. The propellant-discharge velocity of 3923 m/s relative to the space station would reduce propellant velocity in Earth-centered coordinates from 7612 to 3689 m/s; in turn, its kinetic energy would be reduced by 22.17 MJ/kg. The sum of these two terms equals the 29.86 MJ/kg added to the space station in the paragraph above. The energy account thus balances.

On theoretical ground, the combination of rocket propulsion and a conducting tether can generate 2.3 times the electric energy that a fuel cell can. Although losses with the tether power generator will decrease this advantage, the gain in performance may still be substantial.

An important problem for a space station is to effectively use the residual propellants from the orbiter and the external tank. Readily recoverable amounts of hydrogen and oxygen might average 1000 and 1400 kg, respectively, for each flight of a fully loaded shuttle. On any given flight however, the recoverable residuals might vary substantially from these values, even for a fully loaded shuttle. For many flights, the shuttle's payload will be limited by volume rather than by a mass constraint, and in that event, the amounts of residual propellants would be substantially greater. For example, if the payload mass were 80 percent of the rate value, the propellant residuals might average 1800 and 5400 kg of hydrogen and oxygen, respectively, totaling over 7000 kg. In either case, the proportion of hydrogen and oxygen would be far

from the stoichiometric proportion of 1/8. A rocket-sustained power-generating tether can make more effective use of such nonstoichiometric residuals than can fuel cells for three reasons:

(1) Inasmuch as the reactant consumption of fuel cells is 200 to 250 percent of that of the power-generating tether, the tether can produce from a given stoichiometric supply of reactants 2 to 2.5 times as much beneficial product (kilowatt-hours of electric energy).

(2) Because the fuel cell requires a stoichiometric proportion of hydrogen and oxygen, any excess of either would be wasted. In contrast with this, a chemical rocket can readily accept imbalances in the proportions of hydrogen and oxygen.

(3) Contaminating gases such as helium in the propellant-grade hydrogen and oxygen will accumulate in fuel cells unless they are frequently purged to vent the contaminants, a factor increasing the reactant consumption above theoretical values.

Scavenging 7000 kg of hydrogen and oxygen from just a single shuttle flight is sufficient to provide 4.7 kW of power from a rocket-sustained power-generating tether for an entire year. The potential of using these residual reactants is thus clear. On the other hand, the long-term potential of the power-generating tether to supply power to a space station is very sensitive to the level of power required, to the frequency of the shuttle flights to the station, and to the mass of residual hydrogen and oxygen recoverable from the orbiter and the external tank. Consider, for example, the 70-kW power source discussed earlier. Even the rocket-sustained power-generating tether would require 100 tons of hydrogen and oxygen a year, or 1000 tons over 10 years. Either a solar or a nuclear power supply would require far less mass in order to provide the same baseload power. For long-term applications the rocket-sustained power-generating tether is utterly dependent on a supply of "free" propellant. This type of power-generating tether is thus an effective competitor only of other reactant-consuming, chemical power systems such as fuel cells, these power systems being generally limited to missions of modest duration.

ELECTRIC PROPULSION FOR ORBIT MAINTENANCE

The high propellant consumption of the rocket-sustained power-generating tether raises the question, Might this propellant consumption be reduced by switching to electric propulsion, which can attain very high specific impulse Because it can use a variety of propellants, electric propulsion also offers a second interesting possibility: perhaps the residual hydrogen and oxygen could be used for other purposes, such as generating power in fuel cells, and then the product water used as propellant for electric propulsion. In fact, the propellant might be almost any supply of material otherwise wasted. The power source for the electric propulsion could be either the conducting tether itself or an independent power supply; both will be considered. The electric propulsion device might be either an electrothermal jet, an arcjet, an electroplasma-dynamic thruster, or an ion thruster (this list being in order of increasing specific impulse). Thus an entire spectrum of specific impulse is available for consideration.

Not all of the concepts to be explored will be found valuable, but at this stage in the study of tethers, some coarse screening of concepts such as this is worthwhile.

Using Tether-Generated Power

Although electric propulsion with its high specific impulse offers the possibility of lower propellant consumption than chemical propulsion, generating power for the electric propulsion itself will impose an added drag on the tether. Concomitantly, this added drag will increase propellant consumption. Let us briefly investigate how these two factors balance, one increasing and the other decreasing propellant consumption.

For the fiducial case of power generation compensated by chemical rocket propulsion,

$$P_0 = \eta_e D_0 V \tag{1}$$

$$-\dot{m}_0 = \frac{F_0}{I_0 g_0} \tag{2}$$

where

P_0 useful power generated
η_e overall efficiency of power generation (0.73)
D_0 drag of tether
V spacecraft velocity (7612 m/s)
$-\dot{m}_0$ propellant flow rate
F_0 propulsive thrust of chemical rocket
g_0 standard gravitational acceleration (9.80665 m/s^2)
I_0 specific impulse of chemical rocket (400 s)

For steady operation, the thrust F_0 must balance the drag D_0, the required propellant flow then being 4.6×10^{-8} kg/J of electric energy.

When electric propulsion is used, the power generated P must be increased by P_f, the power required to produce the thrust, that is,

$$P = P_0 + P_f \tag{3}$$

and

$$P_f = \frac{F I g_0}{2 \eta_f} \tag{4}$$

where

F thrust
I specific impulse
η_f thruster efficiency

As before, the drag D on the tether for this increased power is

$$D = \frac{P}{n_e V} \tag{5}$$

Propellant flow rate $-\dot{m}$ is

$$-\dot{m} = \frac{F}{I g_0} \tag{6}$$

For thrust F balancing drag D, combining equations (1) to (6) yields

$$\frac{\dot{m}}{\dot{m}_0} = \frac{I_0}{I\left(1 - \frac{I g_0}{2 n_e n_f V}\right)} \tag{7}$$

Representative values of propellant flow ratio $\dot{m}/\dot{m}_0$ from equation (7) are given in table I for a thruster efficiency n_f of 0.8 and for various values of specific impulse. In each case, the propellant flow rate $\dot{m}$ or $\dot{m}_0$ is that required to produce the same amount of useful power P_0. As specific impulse approaches 907 s, the propellant flow ratio goes to infinity; that is, all the generated power would be consumed for electric propulsion, and none would be left for the useful load.

The minimum propellant flow rate was determined by equating the derivative of equation (7) to zero:

$$I^* = \frac{n_e n_f V}{g_0} \tag{8}$$

where I^* is the optimum specific impulse. For the nominal conditions assumed herein, this optimum specific impulse is 453 s, the value that for a given useful power P_0 minimizes propellant flow or, for a given propellant flow, maximizes the useful power P_0. For this value of specific impulse, half the generated power is consumed in providing thrust; the remaining half is available to the useful load.

The propellant flow ratio in equation (7) is then 1.76; that is, the propellant flow rate is 76 percent above that for chemical propulsion by a hydrogen-oxygen rocket. From equations (1) to (6), the net useful power P_0 per unit mass flow rate can be expressed as

$$\frac{P_0}{-\dot{m}} = I g_0 n_e V \left(1 - \frac{I g_0}{2 n_e n_f V}\right) \tag{9}$$

Substituting equation (8) into this gives

$$\left(\frac{P_0}{-\dot{m}}\right)^* = \frac{n_e^2 n_f V^2}{2} \tag{10}$$

642

for the optimum specific impulse. The energy generated is then 12.3 MJ/kg of propellant, corresponding to a propellant flow of 0.29 kg/kWh. This value of propellant flow is 25 percent less than that required by hydrogen-oxygen fuel cells. In addition, hydrogen and oxygen are not required, only any material that can be electrically accelerated to 4400 m/s, corresponding to a specific impulse of 453 s.

The amount of useful power that can be generated in this way depends, of course, on the amount of material available as propellant. Some estimates of consumables to be supplied to the space station early in its evolution run as high as 1 kg/h for each astronaut. Using that quantity of propellant could then produce 3.4 kW of useful power per astronaut, or 27 kW for a crew of 8. On the other hand, an alternative use of that same mass of consumables could provide even more power. Consider, for example, a space station having aboard a powerplant of either the solar or the nuclear type. Not only would such powerplants impose less drag than the power-generating tether, but also substantially higher specific impulse would be practical. Thus that same mass of expended consumables could compensate for the drag of a powerplant of much higher power than would be practical with a power-generating tether.

The electrically propelled power-generating tether offers an interesting opportunity for load leveling. If, for example, the tether power generator were capable of delivering 100 kW of total power, the analysis herein suggests that this would normally be divided into two halves: one for the useful load and the other for propulsion. But that need not always be so. At times of high power demand, the entire output of 100 kW could be used by the useful load. During this time the orbit altitude of the spacecraft would decrease, but only slowly if the spacecraft were fairly massive. At times of below-average power demand, the extra power could augment spacecraft propulsion for reboosting the orbit to its nominal altitude. The average power demand must, of course, be low enough for sustaining the orbit altitude or the spacecraft would gradually descend into the Earth's atmosphere. The spacecraft's orbital energy would constitute the reservoir for storage and extraction of energy, and it is quite a large reservoir. For example, if the orbit altitude of a 100-ton spacecraft were to decrease only 10 km, 850 kWh of electric energy would be made available - the power-generating efficiency being taken as 0.73, as before. Without propulsion to compensate for the tether's drag, this reservoir of 850 kWh would sustain the 100 kW of generated power for 8.5 h.

The characteristics of the concept of electrically propelling a power-generating tether can be summarized as follows:

(1) Useful power can be generated in excess of that required for electric propulsion, maximum power for a given propellant flow being generated in low Earth orbit if the specific impulse is about 450 s.

(2) Almost any supply of propellant can be used, provided only that it can be electrically accelerated to about 400 m/s.

(3) The required flow of propellant is 25 percent less than the hydrogen and oxygen consumed by fuel cells producing the same useful power.

(4) The spacecraft's orbital energy is a large reservoir of energy that would permit temporary diversion of power from propulsion to other purposes.

Reversing the current flow through the tether would convert it from a generator into a motor, that is, into a propulsive device. Of course, power from an independent source of, say, the solar or nuclear type would then be required. The voltage and force on the tether would be essentially unchanged from their values for power generation, the force merely changing sign. In this case, no propellant flow would be required, a very favorable condition for long-term missions in low Earth orbit such as that of a space station. Controlling the current flow would control the thrust magnitude. On the other hand, the thrust direction would be aligned with $\underline{i} \times \underline{B}$ and would thus be beyond control.

The overall efficiency of such propulsion by tether would likely be about the same as that for power generation by tether, herein estimated as 0.73. Although this efficiency is lower than already demonstrated values for electric propulsion, the absence of any propellant consumption at all would be a distinct advantage. The reduced propulsive efficiency would, of course, increase the demand for power, and thereby the mass and cost of the powerplant would also increase. This increased demand for power would thus partially offset the advantage of eliminating propellant consumption.

GENERAL DISCUSSION OF TETHERS FOR POWER GENERATION OR PROPULSION

Because essentially no technology exists for power generation or propulsion by means of tethers, there is a variety of questions concerning the overall feasibility of the concepts. On the other hand, the potential benefits of the concepts warrant investigation in a technology program aimed at delineating their true merits. Critical questions center on the interactions of such a conducting tether with the plasma surrounding the Earth. The impedance of this plasma will greatly influence tether design. A highly conductive plasma would permit large currents, a factor producing shorter tethers and lower generated voltages. Although the shorter tether would tend to reduce aerodynamic drag, high plasma conductivity can be achieved only in regions of high particle density, a factor tending to increase aerodynamic drag. The best operational altitude for these conducting tethers is thus an open question that will substantially influence both their design and their potential value.

Plasma impedance will also affect the size of the required electron collector and thus its weight and aerodynamic drag as well. Plasma interactions (chiefly Alfven waves) may add energy to the plasma in regions well beyond the influence of conventional aerodynamics and may thereby increase aerodynamic drag.

In response to the uncertainties concerning interactions of high currents with the Earth's plasma, a prudent program would decrease risk by using low currents and by accepting the long tethers and the high voltages that result. Electric potentials of tens of kilovolts will require not just insulating the tether but also high integrity of this insulation. A pinhole in the insulation would lead to leakage of electrons. Bombardment of the surrounding insulation by these electrons with kinetic energies of, say, 10 keV would chemically decompose that insulation inasmuch as chemical binding energies are only of the order of 1 eV per atom and thus far below the 10 000-eV energy of the

electrons. For that reason, a minute defect in the in tion   en a small
amount of damage from particles in space can lead to pro ssive mage and
failure of the insulation. Extensive testing of the insulation in high-vacuum
chambers here on Earth would aid in delineating the magnitude of the problem
and perhaps point the way to its solution.

Power conditioning for tens of kilovolts is state of the art here on Earth
but has yet to be evolved for space. In particular, the usual power condition-
ing for space accepts low input voltage and increases as well as regulates the
voltage for supply to the useful loads. In using power from a conducting
tether, the power conditioning would be required to reduce voltage for delivery
to the loads, a transformation requiring a new technology. An additional
factor affecting power conditioning is variation in the generated voltage as
the result of variation in $\underline{v} \times \underline{B}$ along the flightpath as well as variation in
the properties of the space plasma.

Using tethers for power generation or propulsion would also encounter
some of the same problems as does every application of tethers in space,
namely, the dynamics and structural problems associated with tether deployment,
orbit maneuvers, and rendezvous with other spacecraft.

SUMMARY OF RESULTS

Power generation in low Earth orbit by means of a conducting tether
trailed off a spacecraft was studied. Analysis of this concept as well as pro-
pulsion (both chemical and electric) to sustain the power-generating tether
produced the following results:

1. Assessment of losses in power generation showed that efficiency of
power generation might be about 0.73.

2. In the absence of propulsion to sustain the spacecraft, the orbit
would slowly decay, the decrease in altitude being 20 km a day if the generated
power were 1 kW/ton of total spacecraft mass. Power might be extracted for
perhaps a week in an emergency, but this would not be a suitable strategy for
any extended mission.

3. If a hydrogen-oxygen rocket were to provide the propulsion to sustain
the low Earth orbit of a spacecraft generating power by means of a conducting
tether, the propellant consumption would be less than half the consumption of
hydrogen and oxygen by fuel cells producing the same power. For missions
beyond perhaps a month, neither concept is weight-competitive with solar or
nuclear powerplants.

4. If residual hydrogen and oxygen from the shuttle's external tank and
orbiter were available to the spacecraft, the rocket-sustained power-generating
tether could make better use of these residues than could a fuel cell because
(a) the proportions will likely not be stoichiometric and (b) the residues may
contain impurities such as helium. Both of these conditions a rocket
tolerates better than do fuel cells.

5. A single lightly loaded shuttle might have propellant residues total-
ing 7 tons. That quantity of hydrogen and oxygen would permit generation of
4.7 kW of power by a rocket-sustained power-generating tether for an entire
year.

6. On the other hand, the rocket propellant to sustain a 70-kW power-
generating tether for 10 years would total 1000 tons, perhaps 100 times the
mass of a solar or nuclear powerplant.

7. A conducting tether could provide useful power plus power for electric
propulsion to compensate for its own drag. The propellant could be any avail-
able supply of material (such as waste from life support) capable of electrical
acceleration to about 4400 m/s (specific impulse of 450 s). The generated
power would be divided equally between the useful load and electric propulsion.
Not only would fuel cells require the specific reactants hydrogen and oxygen in
the stoichiometric proportion but the mass consumption of those reactants would
be about 1/3 higher than the propellant consumption of the self-sustaining
tether. A self-sustaining power-generating tether would by its nature permit
load leveling for peak-to-average powers of 2 to 1, the spacecraft's orbital
energy being the energy reservoir.

8. If early in the evolution of the space station discharges of waste
from life support run as high as 1 kg per astronaut-hour, use of this mass of
waste as propellant in electric propulsion of a self-sustained tether could
continuously provide 3.4 kW per astronaut, or 27 kW for a crew of 8.

9. Several questions concerning the feasibility of the power-generating
tether must be answered by a technology program before such tethers are used
in space. The questions concern the following: plasma impedance in low Earth
orbit, use of low currents and high generated voltages to circumvent high
plasma impedance, aerodynamic drag on the tether, losses in the plasma, the
performance of electrical insulation in space at potentials to tens of kilo-
volts, and power conditioning for these high generated potentials. These
issues are in addition to the usual questions concerning feasibility of tethers
in space, namely, the dynamic and structural problems associated with tether
deployment, orbit maneuvers, and rendezvous with other spacecraft.

REFERENCES

1. Bekey, Ivan: Tethers Open New Space Options. Astronaut. and Aeronaut.,
    vol. 21, no. 4, Apr. 1983, pp. 32-40.

2. Stone, Noble: Summary Presentation of the Electrodynamics Interactions
    Panel. Applications of Tethers in Space, vol. 1, 1983, pp. 4-11 to 4-22.
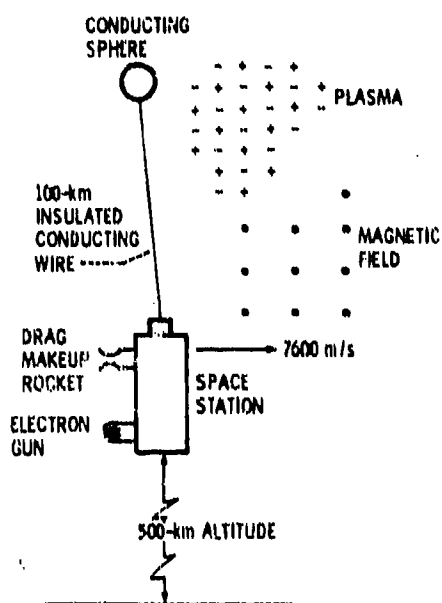
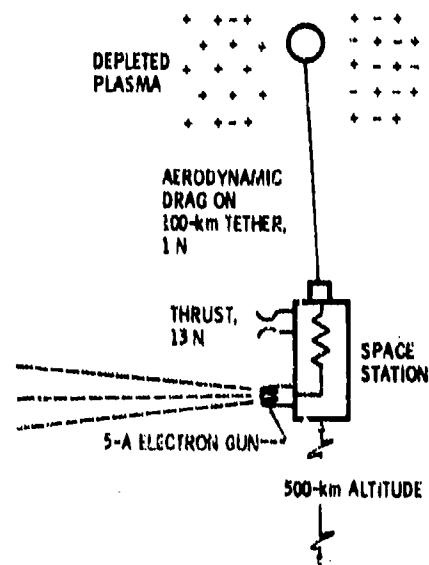Figure 1. - System elements of a power-generating tether.

Figure 2. - Operating characteristics of a representative power-generating tether. EMF, 17 500 V; current, 5 A; power, 88 kW; line loss, 14 kW; power to load, 74 kW; electron gun loss, 4 kW; net to station, 70 kW; aerodynamic drag energy loss, 8 kW; total energy drag on space station, 96 kW; efficiency, 73 percent.

PRELIMINARY INVESTIGATION OF THE ELECTRODYNAMICS OF A CONDUCTING TETHER

W. B. Thompson
University of California at San Diego*
La Jolla, California 92093

An introductory study of the properties of an electrically conducting tether flown from the shuttle is presented. Only a single configuration is considered: a vertical conductor moving normally across the Earth's field, connecting the shuttle to a large conducting balloon that passively extracts electrons from the ionosphere. The rather surprising nature of the distortions in the plasma at maximum current collection are described, as are the local and distant wakes. Numerical values are crude approximations, the emphasis being on the nature of the process, not on engineering values, but it is hoped that this discussion will prove useful.

ELECTRODYNAMIC PROPERTIES OF A CONDUCTING TETHER

There is a developing interest in the possible uses of tethers in space for such purposes as transferring energy and momentum between bodies, effecting rendezvous and probing neighboring parts of space, including regions such as the upper atmosphere otherwise inaccessible to a spacecraft. Tether lengths of up to 100 km have been considered as possible, and major experiments are being designed.

It has been conjectured, perhaps first by Alfven, that if such a tether were made conducting, then since in the neighborhood of the Earth it moves across a magnetic field and hence experiences an emf between the ends, it could draw a current from the surrounding plasma which could provide power for use on a spacecraft (ref. 1). In this paper some aspects of this conjecture are considered in its earliest and perhaps simplest mode: a conducting tether extending up from the shuttle in low Earth orbit to some suitable collector.

Possible Uses of a Conducting Tether (refs. 2, 3)

Power. - In low Earth orbit, h = 200 km, V = 8 km/sec, and the electric field along the tether $E = V \times B = 0.24$ V/m. The exact level of the voltage drop along the wire is $\Delta\Phi = -\Delta L \cdot [(V \pm V_E) \cdot B]$, V_E being the rotational speed speed of the Earth; hence it depends on position and orientation of the tether, field, and velocity: the given figures are representative. If the tether contained an 18-gauge copper wire (0.1-cm diameter, 7.3-kg/km weight, and 20-Ω/km resistance), the maximum current that could be drawn would be ~12 A. Fifteen-gauge wire has half the resistance and double the weight, but would permit a

---

maximum current of 24 A to be drawn. At this current level the power dissi-
pated would be 2.4 kW/km, or 240 kW for a 100-km tether. With 18-gauge wire
about one-quarter of this could be used in the spacecraft; with 15-gauge wire,
about one-half.

The energy, of course, is not free: it is obtained by increasing the drag
on the spacecraft and, if steady operation is required, this drag must be com-
pensated for by using rocket fuel. However, as has been pointed out, there is
an energetic advantage in using fuel this way rather than directly for onboard
power. The energy obtained by using the fuel for thrust includes its poten-
tial, which is comparable to the chemical energy, the only fraction used if it
is burnt for onboard power.

Thrust and drag. - If the tether carries a current I, it experiences a
force I x B/unit length; hence the system (spacecraft + tether + collector)
experiences a total force I x BL_t, where L_t is the vertical length of the
tether. For shuttle heights and a current of 10 A, this is about 0.2 N/km $\approx$
20 N for a 100-km tether. It is essentially a drag, doing work at the rate
I x B · VL_t = $-I\Phi$, although it may be important that there is an out-of-plane
component to the force. Moreover, this component of the drag is readily
controlled simply by modulating the current that is drawn.

The tether may also be used actively. If the collector can also operate
as an electron emitter, a current can be driven through the tether, in which
case a force of I_D x BL_t acts on the shuttle. The potential drop needed to drive
this current is $\Delta\Phi = I_D R + \underline{V} \times \underline{B} \cdot L_t + \Delta\phi$, where $\Delta\phi$ is the potential drop
needed to collect the current from the plasma. The efficiency is then

$$\eta = \frac{I_D \times BL_t \cdot V}{I_D R + V \times B \cdot L_t + \Delta\phi}.$$

Introduce the saturation current

$$I_0 = \frac{V \times B \cdot L_t}{R}$$

and a fictitious "collection current" $\left(\Delta\phi/R = I_C\right)$, which we shall later
show is usually small, then

$$\eta = \frac{1}{1 + \dfrac{I_0 + I_C}{I_D}}$$

Thus although the thrust is small (like most electromagnetically driven thrust-
ers), the efficiency can be quite high. Adequate current collection may cause
problems. Moreover, the thrust need not be in the orbital plane, and depends
on the orientation of the tether. This in turn may be modified by modulating
the current, and many electromechanical games may be played.

Communications. - The tether constitutes a very long antenna immersed in
a magnetoactive plasma; it carries a current that can be passively modulated
just by activating a switch and may be useful for communications at very low

650

frequencies. Because of the peculiar transmission properties of the magnetized plasma, there may be important advantages in using an antenna of this type. Since these transmission properties are so complex, a good deal of theoretical investigation is required before this will have been adequately explored.

Even if the current is not modulated, a significant disturbance is produced by the passage of the tether: the wake it leaves behind in the magnetosphere. The collector also leaves a wake, and these two have rather different and by no means obvious character. Some fraction of the signals produced are attenuated only weakly as the collector-tether system goes by and have characteristics signatures.

Exploration. - Many of the signals that are, or could be, produced by the tether have propagation characteristics that depend in some detail on the nature of the plasma through which they propagate. Hence they may be useful in large-scale synoptic exploration of parts of the magnetosphere. These explorations are of practical importance since they also constitute explorations of possible communications channels.

Questions

Current collection. - The electrodynamic use of a tether requires that it be able to collect the necessary current. It is by no means obvious that this can be done. A small positive probe placed in a plasma collects a current of the order of $ne_{\tilde{v}}/area$, where $\tilde{v} = \sqrt{kT/2m\pi}$. At shuttle heights, where $n \approx 2 \times 10^5/cm^3$ and the temperature is approximately 0.2 eV, this is of the order of 2.5 mA/m^2, and a collector area of approximately 2000 m^2 should be enough to collect about 5 A (refs. 4, 5). On the other hand, it is not clear that the same current can be drawn by a large probe. Suppose the collector has an area $\sim D^2$ and hence a length across the magnetic field of $\sim D$. Then current is collected from any field line for a time D/V, and the number of electrons extracted per unit area is approximately equal to $\tilde{n}v(D/V)$. To collect this, all of the electrons must be removed from a column of length $L_e \propto (\tilde{v}/V) D$. For electrons at 0.2 eV and a collector speed of 8 km/sec, this is $\sim 10 D \approx$ 100 m for a D of 10 m. How does this happen? And how much energy is needed to collect this current?

Wakes. - Some well-known work has been done on the production of Alfven waves (ref. 6) by large structures moving through the magnetosphere. We have instead a structure that draws an electric current, extracting negative charge from one region and ejecting it in another, while seriously modifying the local magnetic field. What is the effect of these modifications on the local and distant properties of the magnetosphere? What happens to the charges? How does the current close? Where does the momentum come from? What is the energy balance?

Communications. - The whole question of low-frequency propagation through the magnetosphere is one that can be answered in principle (i.e., the response function is well known and can easily be written down for a plane wave). How is this connected to the signal produced by a source of a given configuration moving through a nonuniform plasma? (or for that matter, moving through a uniform plasma?) Attempts to deal with these problems require handling the dispersion relation for a warm magnetoplasma, a mathematical object with quite horrendous properties.

Are there significant model experiments that could be carried out on a laboratory scale and would give significant information here? And if so, how should such information be interpreted?

The Present Investigation

To obtain significant results, the present investigation concentrated on two questions for a particular configuration. The two questions were: how is the current collection affected? and what are the most important features of the wake?

The configuration considered is a 100-km tether drawing a saturation current of 5 A from a sphere of radius 25 m, a balloon, with a surface conductivity of a 1-mil layer of copper. The magnetosphere is considered as containing a density of 2×10^5 electrons/cm^3, neutralized by an equal number of singly charged positive O^{16} ions, both at a temperature of 0.2 eV ($\approx 2200°$) (ref. 11).

Current collection. - If the electrons were collected through an inverse Langmuir Childs sheath from a virtual cathode that moved out from the collector to a distance of ~100 m, the required potential drop

$$\phi \sim \frac{kT}{e} \cdot \frac{4}{3} \left(\frac{\lambda}{\lambda_D}\right)^{4/3}$$

would be of order of 10^5 V, and essentially such a current could not be collected. However, this assumes that the positive ions play no role and that the field of the collector is screened by the electrons that it is collecting. We have considered the role of the ions and have come to a much more optimistic conclusion.

Consider the effect near the leading edge of the collector. The parallel electric field that it produces is effectively wiped out by the motion of electrons along the magnetic lines of force ahead of the collector. However, as soon as the collector crosses a line of force, the electrons on that line are drained off, and the electric field begins to appear. As a consequence, the potential on that field line begins to rise. Now, although electrons are confined to magnetic field lines, their gyroradius being ~0.15 cm, this is not true for the much heavier ions that have energies of $1/2 MV^2$ in the collector frame. This is about 6 eV, and until the potential reaches this value, the ions are free to move across the field; however, when this value is exceeded, the ions are reflected. Since the ions have a thermal spread, not all are reflected at this potential; a somewhat higher potential of ~12 eV is needed to reflect most of the ions.

The electrons are accelerated by the parallel electric field and gain a velocity given by $\sqrt{2e\phi/m}$. Since the electron flux remains $\sim n\bar{v}$, the electron density is reduced by a factor of $\sqrt{kT/e\phi} \approx 1/8$. Since both the electron and ion densities are reduced, the electrons by parallel acceleration and the ions by partial reflection, there exists a potential $\phi_0 \approx 12$ eV at which the electron and ion densities are equal. If the collector sits at this potential with respect to the undisturbed plasma, it can collect the saturation current, even though the accelerating fields sit not near the collector, but on a narrow sheath that extends out at an angle $\bar{v}/V$ along the magnetic field and

reaches a distance $L_S \approx \tilde{V}/V \cdot D \sim 150$ m from the collector. The voltage drop needed to collect this current is then only of the order of 12 V, which is equivalent electrically to increasing the tether length by ~50 m. Hence it is negligible for kilometer-length tethers.

Because this extended sheath reflects the ions while it extracts the electrons, everywhere behind the extended sheath the plasma density is very low. As soon as the collector has passed, electrons are no longer extracted and the potential rapidly drops. As it does so, electrons rush out with approximately the thermal speed, leaving only a small negative charge, so that the plasma although at low density is again neutral at a distance of the order of D, the collector width, behind the collector. Behind this, the low-pressure region fills in at a rate given by the ion thermal speed, ~1.5 km/sec. Hence the plasma does not recover its original density for $2L_S$ $(V/v_0^-) \approx 1$ km behind the collector.

The reflected ions have velocity in the plasma frame of 2 V and hence move in gyro orbits with a radius $r_L = 2V/\Omega_+ \approx 90$ m, about a center 90 m below the collector. They produce a net positive charge of the order of $D/4r_L \approx 2.5$ percent of the total ion charge density. This is neutralized by an influx of electrons along the field lines in a distance again of the order of D. The total charge does not disappear but spreads out along the field line, with the electron thermal speed essentially halving in the distance D. After 100 m the charge density is reduced to ~0.1 electrons/cm^2, and its dynamic effect essentially disappears. The excess charge drifts down and across the magnetic field lines and eventually is balanced in the ionosphere.

The wake. - The local effects of the collector are as follows: a volume of height D (≈ 25 m extending out along the field lines a distance $(\tilde{V}/V)$ D (≈ 250 m) on either side of the collector and tapering back to vanish at a distance

$$\frac{V}{V_0^+} \cdot \frac{V_0^-}{V} D = \frac{V_0^-}{V_0^+} D = 5 \text{ km}$$

behind the collector is evacuated of plasma; while a volume of height ~4r$_L$ ≈ 180 m, of width 150 m, and of length ~D acquires a charge of $D/4r_L \approx 3.5$ percent n_ee/unit volume.

The positive current flows out of the collector, with a current density of ~2.5 mA/m^2, carried by the electrons; flows forward and down across the field lines, with a density of 3 mA/m^2, carried by the ions; then flows along the field lines with a density of ~0.3 mA/m^2, carried by the electrons. The associated magnetic perturbations are ~5x10^{-15} g for the first current (a magnetic twist), 3x10^{-6} g for the second (an increase in field strength), and 1.2x10^{-6} g for the third (a further magnetic twist).

The major modification in the background is produced by the magnetic field in the tether. For ~2 cm about the tether this field exceeds the Earth's field and the field lines close about the tether, while beyond this the disturbance falls off as 1/r. It is important to note, however, that the tether bends and compresses the field lines but does not introduce a twist. This is important when we consider the nature of the wakes and is a result of our assumption of a horizontal field.

653

The MHD wake. - The low-frequency disturbances produced by the passing of the tether can be described in the simplest approximation by considering the plasma as an ideally conducting fluid. For our case the velocity of sound is much less than the Alfven speed, $C_S = 2$ km/sec, $C_A = 130$ km/sec, and there are three possible waves (ref. 10): an Alfven wave, which propagates along the magnetic field with the Alfven speed; a channeled sound wave, which again propagates along the magnetic field, but now with the speed of sound; and an isotropic magnetoacoustic wave, which propagates isotropically with the Alfven speed.

Since the Alfven speed is much greater than the speed of the tether (8 km/sec), the magnetoacoustic wake does not appear as a dynamic wave. Instead it is static in the tether frame and is modified slightly by the "Lorentz" contraction $z \rightarrow z \left(\sqrt{1 - V^2/C_A^2} \right)$, which for our case is ~0.1 percent.

The magnetic twists (~2×10^{-4} g) propagate along the magnetic field lines with the Alfven speed but are slowly attenuated as a result of collisions, with a scale length substantially greater than the electron mean free path: in fact of the order of

$$ L \approx \frac{D^2}{d_0^2} \frac{C_A^2}{v_e - V} \frac{L_S}{D} \lambda_f $$

where d_0 is the collisionless screening length, $c/\omega p^- \approx 4$ m for our case and hence $L \approx (C_A/V)^2 \lambda_f \approx 800$ km. If the magnetic field has a vertical component or if the tether is not perpendicular to the field, then a very much larger signal can be propagated as an Alfven wave, and it is here that communications possibilities may exist (frequencies must be substantially less than the ion gyrofrequency, when Doppler shifted, $\Omega_+ \approx 180$, $v \approx 28$ cycles/sec).

The magnetoacoustic mode produces a modification in the magnetic field strength that is almost indistinguishable from the vacuum field. The azimuthal field has the vacuum form, but there is superimposed on this a small radial field

$$ B_r \sim I \frac{V^2}{C^2} \frac{\sin 2\theta}{r} $$

and an associated current density

$$ J = I \frac{V^2}{C^2} \frac{\cos 2\theta}{r^2} $$

This can be quite large near the tether but is only correctly described for values of $r \gg 2$ cm, where nonlinear modifications become unimportant (hence $J \ll I$).

The magnetosonic wave that carries the pressure pulse represents a superposition of the channeled sound wave, and the isotropic magnetoacoustic wave.

654

The pressure pulse propagates along the field line and, as it propagates, produces a pressure disturbance in its neighborhood that falls off as $1/\rho$, where ρ is the perpendicular distance to the field line. The disturbance rapidly becomes small, and in addition, in a more rigorous treatment, is damped.

High-frequency components. - If the plasma is treated by the more rigorous and appropriate method of collisionless kinetic theory, the low-frequency MHD results are reproduced, providing that the conditions $k_\parallel v_e^-/k \cdot V \ll 1$ and $k_\parallel v_e^+/k \cdot V \gg 1$ are satisfied. (Note that this invalidates the slow sound wave, which becomes strongly damped.) There are, however, other modes of oscillation possible, and many of these waves have peculiar transmitting properties.

If we work only to lowest order in the ion gyroradius, using the cold ion approximation, then the tether field gives rise, in addition to the quasi-static response, to an oscillating field whose amplitude depends essentially on the distance along the field line from the point of observation to the tether, and only slowly on the distance along the direction of motion. The frequency, however, varies with this distance and, as a result, a signal modulated in both amplitude and frequency is produced as the tether passes.

The charge density can also excite a narrow band of Langmuir waves, providing that $k \cdot V/k_\parallel v_e^- \gg 1$. These combine again to give a modulated wave as the collector passes. The signal occurs in planes above and below the collector, and this time has a constant amplitude depending only on the distance projected along the field line and is again a slowly modulated sine wave in the region of its appearance.

CONCLUSIONS

This has been an introductory essay on the subject of conducting tethers. We have presented arguments suggesting that current collection can be reasonably efficient even with a fairly simple system, although the local modification in the plasma is both unexpected and dramatic. We have also discussed some features of the wake and have explored several components: the Alfven wave, magnetoacoustics, and high-frequency elements.

This is by no means a complete study; it is suggestive rather than demonstrative. We have not given a complete and consistent theory of the extended sheath (the high field region needs to be analyzed), nor have we discussed its overall stability.

The discussion of the wake is also incomplete. The pressure mode (the slow magnetoacoustic wave) is probably strongly damped, and the connections to the source have not been evaluated in full detail. Some of the results, the lack of Alfven waves from the tether, for example, depend on the orientation chosen and would be modified as the system moved.

The treatment of the high-frequency components is also incomplete. We have used a greatly oversimplified representation of the dielectric response, neglecting the effects of ion thermal motion, including the higher cyclotron resonances.

More importantly, we have restricted the analysis to the static wake. If the current is modulated, new phenomena must be expected, some of which can be analyzed by the methods we have described, but some of which call for more complex investigations.

We have not presented a careful analysis of motion around the tether. This is important since the coupling to the linear waves requires a treatment of the local nonlinear region.

Finally, we have not attempted to consider the possible effect of electro-dynamic forces on the motion of the tether.

Much remains to be done, but at least a start has been made on a detailed and rigorous analysis of the electrodynamics of a tether in space.

REFERENCES

1. Isaacs, J. P., Vine, H. C., Bradner, H., and Backus, G. E., Science 151 682 (1966).

2. Columbo, G., Gaposchkin, E. M., Gross, M. D., and Weiffenbach, G. C., "Shuttle-Borne 'Skyhook', A New Tool for Low Orbital Altitude Research" S.A.O. Reports in GeoAstrophysics (Smithsonian Astrophysical Observatory: Cambridge, Ma., 1974).

3. Wu, S. T., ed., The Uses of a Tethered Satellite System (University of Alabama, Huntsville, Al., 1978).

4. Williamson, P. R., Banks, P. M., and Oyama, K., in Wu (op. cit.) (163).

5. Grossi, M. C. and Columbo, G. in Wu (op. cit.) (p. 177).

6. Drell, S. D., Foley, H. M., and Rudermann, M. A., J. Geophys. Res. 70 3131 (1965).

7. Dobrowolmy, M. G., "Wave and Particle Phenomena Induced by an Electrodynamic Tether" S.A.O. (Report - 388) (1971).

8. Thompson, W. B., An Introduction to Plasma Physics, p. 30 (Pergamon Oxford, 1962).

9. Thompson, op. cit., p. 242.

10. Thompson, op. cit., p. 80.

11. Allen, C. W., Astrophysical Quantities, p. 113, (University of London, 1958).

12. Allen, C. W., op. cit. p. 124.

13. Dobrowolmy, M. G., Columbo, G., and Grossi, M., "Electrodynamics of Long Tethers in the Near-Earth Environment" S.A.O. Reports, No. 3 (1976).

14. O'Neil, T. M., Phys. Fluids, $\underline{8}$ 2255 (1965).

15. Thompson, W. B., op. cit., p. 176.

16. Thompson, W. B., op. cit., p. 196.
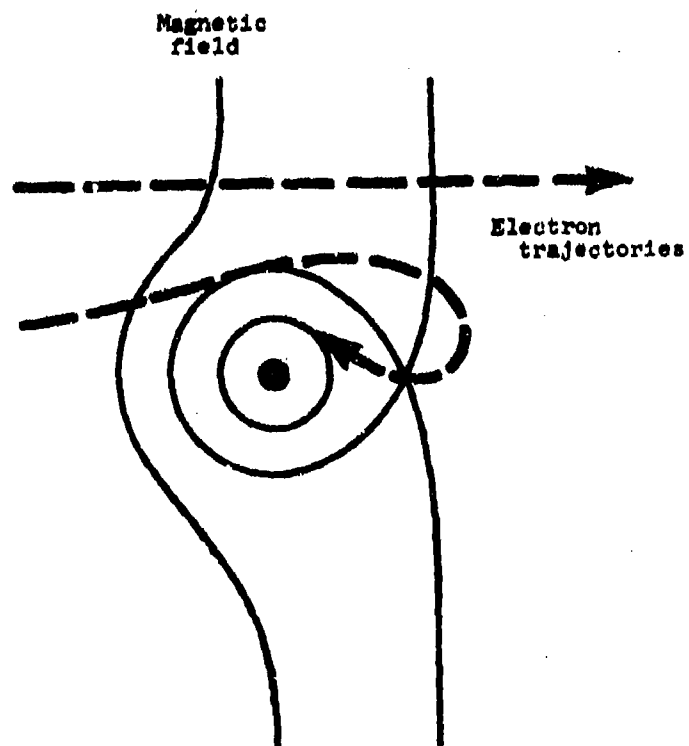
17. Lighthill, M. J., Journal Inst. Math and Appl. $\underline{1}$ 1 (1965).

Figure 1. – Field and motion near tether.
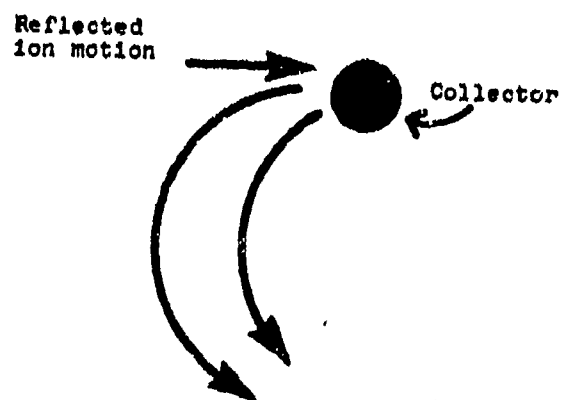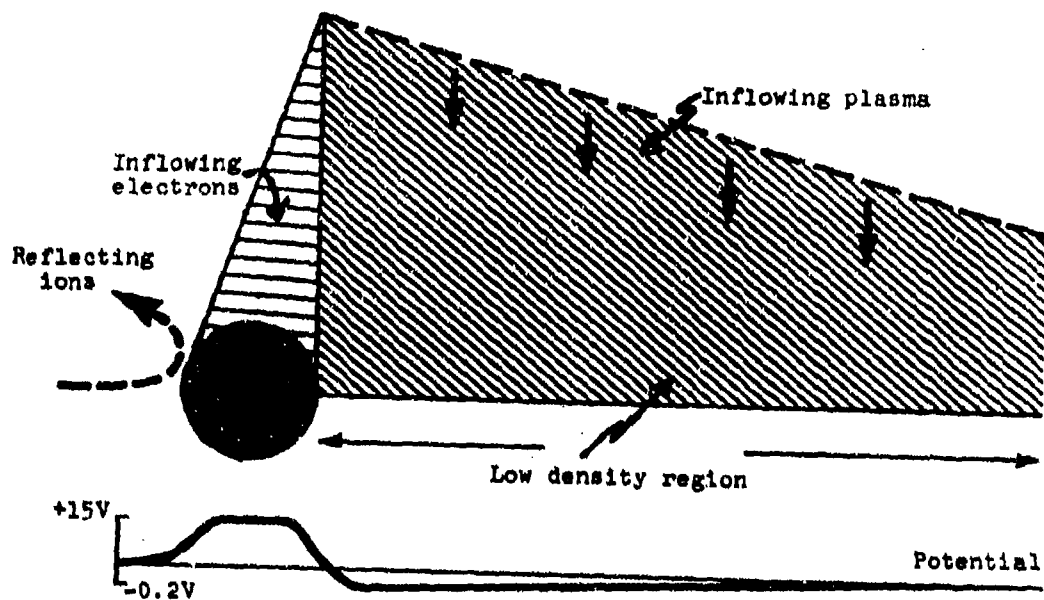
Figure 2. – Current collection – local effects.
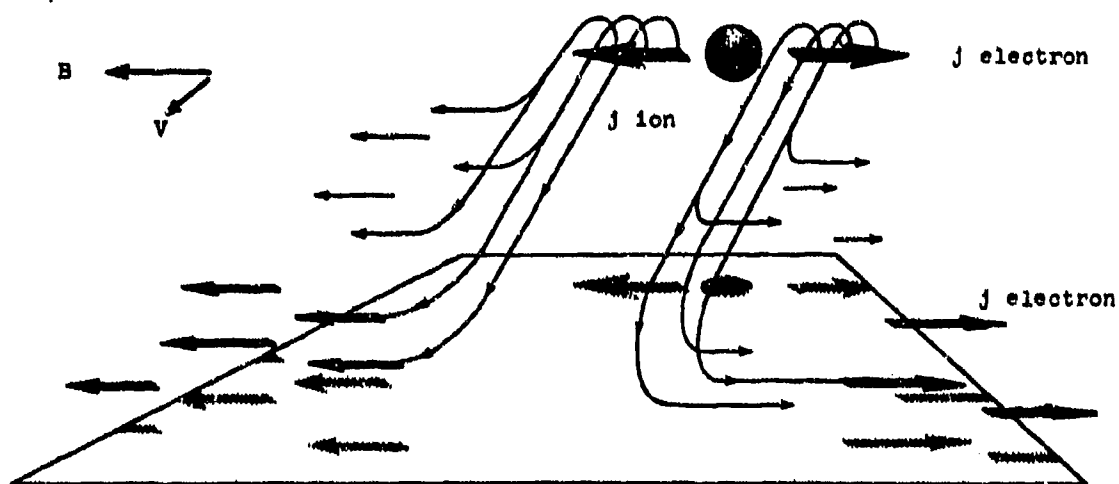
Figure 3. - Current flow near collector.

THE M.H.D. WAKE

Group velocity

Phase velocity

Fast M.S.

Fast magnetosonic

Alfven

B

Alfven   Slow M.S.   Slow

WAKES

B

Alfven

Fast magnetosonic

θ_1

Y

Slow magnetosonic

θ_2

$\tan\theta_1 = \dfrac{V}{C_A}$

$\tan\theta_2 = \dfrac{V}{C_S}$

Figure 4. - Wakes.

661
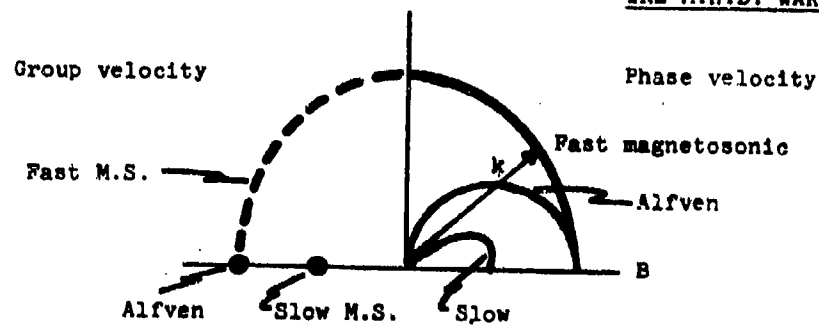
Fast magnetosonic

Figure 5. – Tether wake.

Figure 6. – High-frequency tether wake.

ASTRONAUT HAZARD DURING FREE-FLIGHT POLAR EVA

William N. Hall
Air Force Geophysics Laboratory
Hanscom Air Force Base, Massachusetts 01731

Extravehicular Activity (EVA) during Shuttle flights planned for the late 1980's includes several factors which together may constitute an astronaut hazard. Free-flight EVA is planned whereas prior United States earth orbit EVA has used umbilical tethers carrying communications, coolant, and oxygen. EVA associated with missions like Landsat Retrieval will be in orbits through the auroral oval where charging of spacecraft may occur.
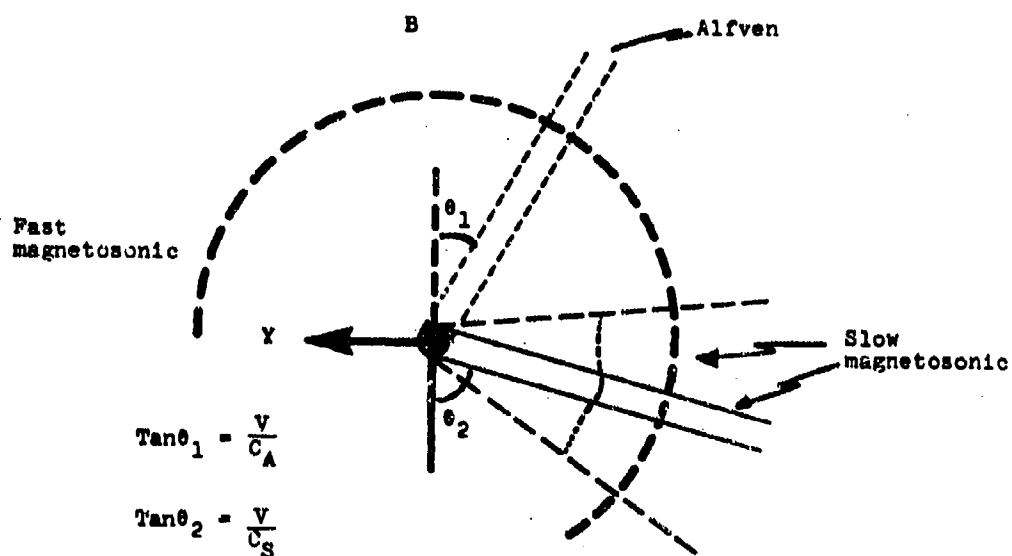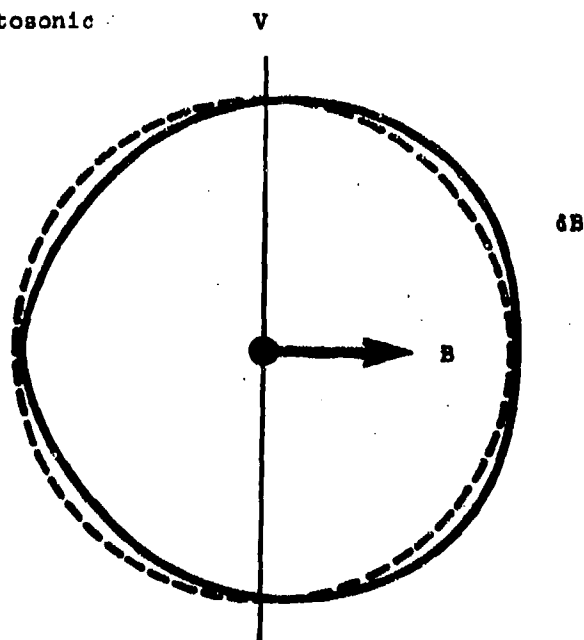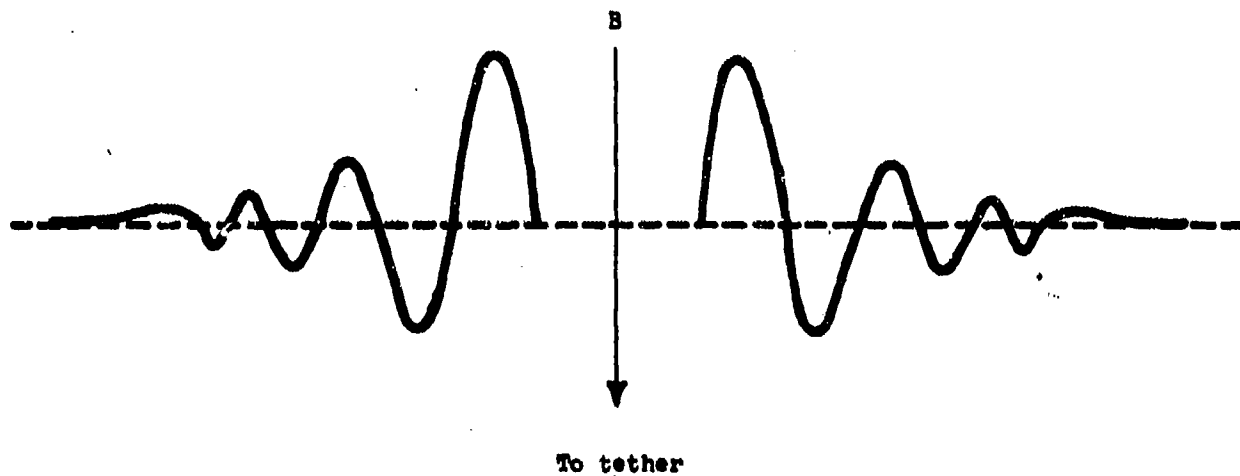
The astronaut performing free flight EVA constitutes an independent spacecraft. The astronaut and the Shuttle make up a system of electrically isolated spacecraft with a wide disparity in size. Unique situations, such as the astronaut being in the wake of the Shuttle while traversing an auroral disturbance, could result in significant astronaut and Shuttle charging. Charging and subsequent arc discharge are important because they have been associated with operating upsets and even satellite failure at geosynchronous orbit. Spacecraft charging theory and experiments are being examined to evaluate charging for Shuttle size spacecraft in the polar ionosphere.

The extensive body of knowledge about auroral phenomena can assist in evaluating the importance of charging. Images recorded by the Defense Meteorological Satellite Program (DMSP) satellites in circular orbits show snapshots of the spatial extent of the optical aurora. Montages of all sky camera images from an aircraft flying a path to remain at constant local midnight show the cyclic behavior and the suddenness of onset of optical aurora. Geophysical conditions measured at the time can be used to evaluate the EVA conducted from Skylab in 1973-74. Skylab, with an orbit inclination of 50 degrees, did encounter the auroral oval when the orbit latitude extremes were at the right longitude and local time. Study of the geophysical conditions and orbits during the Skylab EVAs showed that astronauts on EVA were always at least 5 degrees of latitude equatorward of the auroral oval.

INTRODUCTION

In the process of evaluating space systems environmental interactions (Pike et al, ref. 1), it became apparent that physical interactions between the environment and the astronaut's extravehicular activity (EVA) equipment could be significant. Servicing of satellites after launch is an example of how astronaut free-flight EVA will be used. The EVA equipment now available for use, developed by the National Aeronautics and Space Administration (NASA) at the same time that the Shuttle was being developed, was designed for Shuttle flights at low inclination angles (NASA Johnson Space Center (JSC) Private Communication, 1982). At that time it was not anticipated that polar orbit EVA would involve additional problems.

The special area of concern to Air Force Geophysics Laboratory (AFGL) is with the physical interaction between the environment and the astronaut's EVA equipment, as opposed to the biological interaction between the environment and the astronaut himself. The effort has focused on the interaction of charging and arc discharges (Garrett and Pike, ref. 2) on the Extravehicular Mobility Unit (EMU), the Primary Life Support System (PLSS), and the Manned Maneuvering Unit (MMU). This interaction is important because of the consequences of EVA equipment failure in combination with the great uncertainty involved with charging and arc discharge in the Shuttle environment.

EXTRAVEHICULAR ACTIVITY

The polar orbit EVA to be conducted from Shuttle will encounter conditions differing from those encountered during the NASA successful EVA history during the Gemini, Apollo, and Skylab programs (Furniss, ref. 3). The NASA history of EVA has been one of outstanding success since the first EVA by White on the Gemini 4 flight in 1965. The Gemini program included 9 EVAs at low (several hundred kilometers) altitude and low latitude with the astronauts connected to the spacecraft by an umbilical tether carrying oxygen, coolant, and communications services. Approximately 20 EVAs were conducted during the Apollo program. Most occurred on the lunar surface with 3 in deep space while returning to earth. Although the lunar EVAs were untethered, they were in a deep space environment quite different from the Earth's ionospheric plasma. The 10 EVAs from Skylab were again in the ionospheric plasma with the astronauts connected to Skylab by an umbilical tether. Skylab's 50 degree orbit inclination intersected the auroral oval, the greatest overlap was in the southern hemisphere near Australia. However, the Skylab EVAs were conducted while the orbital latitudinal extremes were in other longitudinal sectors. The geophysical conditions encountered during the Skylab EVAs will be discussed later.

With this successful EVA history as a baseline, what is there about EVA from the Shuttle to cause concern? One significant factor is that at times the astronaut will be untethered and, if simultaneous failures occur, could "float away". Another factor is the development of Vandenberg Air Force Base as a Shuttle launch site. Vandenberg will have the capability of launching the Shuttle into high inclination orbits intersecting the auroral oval 4 times during every orbit. The environment at auroral oval latitudes is markedly different from that at low latitudes and is potentially hostile during geophysical disturbances. NASA is now considering a polar orbit Shuttle flight from Vandenberg to retrieve the Landsat-D satellite. The mission scenario is expected to include EVA and, possibly, free-flight EVA.

Polar Orbit Extravehicular Activity

The polar orbit EVA illustrated in figure 1 depicts the combination of circumstances which make polar free-flight EVA different from other EVAs to date. At the center is a graphical representation of analytical modeling of the Shuttle and an astronaut on EVA in the ambient ionospheric plasma (Cooke et al, ref. 4). The shape of the Shuttle is represented by different sized rectangular and triangular solids. The astronaut is represented as a 2 meter long, 1 meter diameter, dielectric cylinder. The Shuttle is large compared to the size of the astronaut, who will at times be in the wake, where electron and ion densities are decreased. The Shuttle is shown with the negative Z axis in the direction of

motion and the payload bay in the wake. The contours, more distinct in the original color illustration, show the decreased electron and ion density. The innermost contour represents 5% of ambient. Experimental plasma density measurements in the Shuttle payload bay on early flights have shown great differences between the payload bay in the ram direction, where the ionosphere has access to the payload bay, and the payload bay in the wake orientation (Shawhan et al, ref. 5). For some geometrical arrangements during flight through the auroral oval, such as depicted here, the Shuttle and the free-flying astronaut will both be exposed to the incident auroral electron flux. Conditions which support spacecraft charging will occur because of the auroral electron flux combined with the decreased electron density and, more importantly, the reduced thermal positive ion density in the Shuttle wake.

Existing Extravehicular Activity Equipment

Figure 2 identifies some of the surface materials used on the astronaut's EVA equipment (NASA JSC Private Communication, 1982). Many of these materials are similar, or even identical, to materials which were adversely affected on the SCATHA (Spacecraft Charging At High Altitudes) satellite and in laboratory studies of the charging of materials in space. Most of the space suit (EMU) is covered by Orthofabric which has a white surface consisting of expanded teflon. The astronaut's finger tips and shoe soles are silicon rubber. Much of the MMU is covered with the type of Chemglaze paint which has been found to exhibit charging on SCATHA and in other spacecraft charging studies. Some areas have silverized teflon and others have gloss white paint over glass/epoxy or kevlar/epoxy. The astronaut's helmet and the MMU locator light domes are Lexan. A similar material, Plexiglas, which has previously been used for transparent spacecraft components, is known to have been associated with charging. The metal foil decals used for a number of identifying labels, particularly on the MMU, may become involved with charging. Previously, isolated conductive patterns on printed circuit boards have suffered charging and deleterious arc discharges (Leung et al, ref. 6). The decals are an example of a seemingly innocuous item which becomes significant when conditions conducive to charging occur.

Figure 3 shows an astronaut equipped for free-flight EVA. The major equipment systems are the EMU and the PLSS used for all EVAs, along with the MMU used for untethered free-flight EVA. Some problems with EVA equipment can be direct life-threatening hazards to the astronauts. The failure of the PLSS circulating fan motor during the STS-5 flight is an example (Aviation Week, ref. 7). MMU failures are also potentially life threatening. A failure causing an MMU thruster to remain on would cause attitude control problems similar to those encountered by Gemini 8 where a spacecraft control system short circuit caused one thruster to fire continuously. The Gemini astronauts used 75% of their reaction control system fuel before recovering from the malfunction. This forced them to cancel the rest of their mission and return as soon as possible. Operational planning for EVA provides for the Shuttle going after the astronaut if there are multiple failures in the MMU redundant control systems. A MMU thruster malfunction leaving the astronaut spinning rapidly could complicate retrieval by the Shuttle, as well as be a direct danger to the astronaut.

Other EVA equipment problems which would limit EVA operations have just as much significance as life-threatening hazards, from the standpoint of failure to achieve the Shuttle mission objectives. Failure of an EMU astronaut communications

link, while not a threat to the astronaut's life, would cut short a mission such as repair of the Solar Maximum Mission spacecraft. Failures in the helmet television or PLSS Caution and Warning systems also limit operations. EVAs would not be carried out without one of these systems unless, for example, it was necessary for the astronaut to close the payload doors for entry. The presently available EVA equipment uses advanced microelectronics for monitoring status, communications, etc., but not for direct control of life support subsystems. A change to direct microprocessor control of life support functions, proposed for future systems, could make failure even more significant.

Extravehicular Activity Near Solar Array Systems

Figure 4 illustrates another new aspect of EVA in the future, operation near high-power-generating solar array systems, where charging is known to occur and arc discharges have been observed. An example is the 50 KW system NASA is planning for the Space Station. Solar array segments have differences in electrical potential due to the series-parallel interconnection of individual cells. Point to point arc discharges occur when the difference in potential between the most positive and most negative solar cells, or from the solar cells to the ambient plasma, is too large (Stevens, ref. 8). The net effect of the solar array surfaces is to modify the nearby plasma such that a hazard may be created for a free-flying astronaut. A solar array hazard would have a major impact on EVAs anticipated during assembly and operations of a Space Station dependent on solar arrays.

AURORAL OVAL ENVIRONMENT

The concept of the auroral oval was developed by Feldstein and Starkov (ref. 9) but has been most strikingly illustrated by the recordings of auroras made by satellite imaging systems. Originally, the oval was used to describe the location where optical auroras were observed. Later, it has also been found useful in describing other phenomena, including the precipitation of energetic electrons which produce auroras. The oval extends completely around the earth although, in some orientations, observation of optical auroras is masked by sunlight. The auroras are found in a band, somewhat circular in form, with its center displaced towards the night side of the earth. It has a greater latitudinal extent on the dark, or midnight, side. The oval forms a fixed pattern, relative to the sun, which changes in geographical location as the earth rotates beneath (Whalen, ref. 10).

The satellite auroral photos in figure 5 demonstrate how the aurora can have spatial variations, particularly in north-south extent (Pike, ref. 11). Local midnight is at the center of each of the 2 auroral photos. On the right, when the aurora would be described as quiet, the aurora has a narrow latitudinal extent. A spacecraft crossing it at right angles would be exposed to energetic auroral electrons for only a few seconds. As the angle between the orbit and the narrow auroral arc decreases, the time of exposure increases. An orbit tangent to a relatively narrow auroral arc could result in exposure to energetic auroral electrons for tens of seconds, even when the aurora is not disturbed. The left half, from a different orbit of the same satellite, shows that the aurora has a wider latitudinal extent during a geophysical disturbance and, depending on the exact orbit, the spacecraft would encounter the energetic auroral electrons for tens or even hundreds of seconds. A lengthy exposure to energetic electrons is not required in order to have a spacecraft charge to dangerous voltage levels.

A DMSP satellite has been measured to charge to hundreds of volts within seconds (Burke and Hardy, ref. 12). The effect of extended exposure time is to increase the likelihood that the auroral oval would be disturbed during the passage of the spacecraft.

The temporal variation of auroras in the oval is also of interest in evaluating the likelihood of interaction effects on EVA equipment. Auroras are the most variable and the most intense during worldwide magnetic storms following solar flares. Auroral temporal variations are important even at other times. To see this, All Sky Camera (ASCA) pictures taken with a 160 degree field of view fisheye lens from the AFGL Airborne Ionospheric Observatory will be used. The aircraft flew a path with a ground track in geographic coordinates as shown on the left in figure 6 (Krukonis and Whalen, ref. 13). Because the earth rotated as the aircraft flew west, the aircraft remained near local magnetic midnight. The same flight path in the corrected geomagnetic local time and latitude coordinate system is shown on the right. The aircraft flew short north and south tracks, approaching and departing from the magnetic pole. The ASCA field of view covered 4 degrees of magnetic latitude to the north and to the south; therefore, 70 degrees north corrected geomagnetic latitude was always within view.

Each strip of the ASCA montage for this flight, figure 7, shows 30 pictures taken once per minute with a 15 second time exposure. The complete montage represents a continuous 9 hour time history of the temporal variations of the aurora near local magnetic midnight. Each circular image has been rotated during reproduction so that North is to the left and East is at the top. This improves interpretation of the images by removing effects from changes in the heading of the aircraft. At times, the sky was almost clear of auroras with only faint forms not easily seen in these reproductions. At other times, optical auroras covered the field of view from the northern to the southern limits, about 900 kilometers. The energetic electron deposition region producing the optical auroras corresponds closely with the optical aurora. Spacecraft, including a free-flying astronaut, would have been in the area of precipitating particles likely to cause charging for over 100 seconds. It is also important to realize how quickly the upper atmosphere can change from showing only faint traces of aurora to bright auroras covering the ASCA field of view. This can be seen near 0310 UT when the aurora expanded from a narrow feature near the southern horizon to completely fill the field of view within 2 to 3 minutes. This is much too fast for the astronaut to take any action towards protecting himself. Operational planning must consider that the astronaut will find himself immersed in the energetic auroral electron stream. The EVA equipment must not be susceptible to adverse environmental interactions due to energetic auroral electrons.

The values of the Q, AE, and Kp magnetic indices (Mayaud, ref. 14) measured by magnetic observatories during the flight are shown on the right. It is inappropriate to attempt extensive conclusions about the correlation of magnetic index variations with the ASCA montage for this small quantity of data. The magnetic index Q represents the disturbance from quiet day values in a 15 minute period for an auroral oval magnetic observatory, in this case Sodankyla in Sweden. The 2 values are for the first and second half of each row of images. The index Q has been found to be correlated with the location of optical auroras (Feldstein and Starkov, ref. 9). For this data sample, it increased generally as the auroras became brighter and filled more of the ASCA image.

The value for AE represents the hourly aver:ge of the AE index determined for a global network of auroral oval observatories. AE represents the sum of the eastern and western auroral electrojets and increases as the magnitudes of optical auroras increase (Allen et al, ref. 15). In addition to the hourly AE averages, the AE graphical plot showed maxima of 400 gammas at 0330 UT, 425 gammas at 0410 UT, 550 gammas at 0730 UT, and 640 gammas at 1050 UT. These maxima can be associated with brighter image sequences in the figure. In addition, the times which show smaller, fainter auroral images, 05 to 06 UT and 09 to 10 UT, have lower average AE values.

This data sample provides a good example for comparing optical auroral images with the Kp index. The Kp index represents the variation of magnetic activity for low latitude observatories during a 3 hour period. The bright sequence from 0310 UT to 0400 UT and the faint sequence from 0450 UT to 0555 UT are both associated with the 03 to 06 UT value of Kp of 4. This example demonstrates the limitations of using a 3 hour index like Kp to characterize a phenomenon, such as the optical aurora, which can vary greatly within the 3 hours.

GEOPHYSICAL CONDITIONS ENCOUNTERED DURING SKYLAB EXTRAVEHICULAR ACTIVITY

As mentioned previously, Skylab had a 50 degree inclination. Its orbit intersected the auroral oval when the orbital latitude extremes occurred: at longitudes where the magnetic poles are closest to the equator; and, near corrected geomagnetic local midnight when the auroral oval reached its most equatorward extent. The geophysical conditions at the time of the 10 Skylab EVAs have been examined. The closest approach was in the southern hemisphere during the EVA of Garriott and Bean on 22 September 1973, during the Skylab III mission. Partial Skylab ground tracks are shown in figure 8 in the corrected geomagnetic local time and latitude coordinate system. The auroral oval for a Q value of 2 (the value measured at Sodankyla at the same time) is shown. The closest approach was on orbit 2022, where the minimum separation was about 5 degrees of latitude. A 5 degree latitude separation usually means complete absence of the precipitating energetic electrons which are present in the auroral oval. The end of EVA at 1400 UT on orbit 2023 is actually repressurization, meaning that the astronauts were already inside the airlock. This analysis shows that EVA within the aurora is something that the United States has yet to encounter.

SUMMARY

Our preliminary analysis of the special situation of free-flight EVA from the Shuttle while passing through the auroral oval has identified it as a space system environmental interaction deserving of further study. Further investigations by the Air Force and NASA have not resolved this concern. AFGL is continuing to work with NASA scientists to determine if a hazard does exist, how serious it is, and whether it is life-threatening. Discussions have been held with the NASA JSC Crew Equipment Division responsible for developing the astronaut equipment, to bring to their attention that charging and arc discharges may occur on the equipment surfaces. Once the charging hazard has been defined, then the susceptibility of the existing and future systems can be determined by engineering tests. AFGL believes it is prudent and necessary to establish what will happen so that, as shown in figure 9, EVA will continue to be successful as the Shuttle flight envelope expands to orbits through the auroral oval.

REFERENCES

1. Pike, C. P.; Guidice, D. A.; Davis, R. A.; Chesley, A. L.; Hall, W. N.; Shuman, B. M. Space Systems Environmental Interactions Technology Program. Proceedings of the Air Force Geophysics Laboratory Workshop on Natural Charging of Large Space Structures in Near Earth Polar Orbits: 14-15 September 1982. Ed. by Sagalyn, R. C.; Donatelli, D. E.; Michael, I. Report No. AFGL-TR-83-0046. Air Force Geophysics Laboratory, Hanscom AFB, MA 01731, 25 January 1983.

2. Garrett, H. B.; Pike, C. P.: editors. Space Systems and Their Interactions with Earth's Space Environment. American Institute of Aeronautics and Astronautics, New York, 1980.

3. Furniss, T. Manned Spaceflight Log. Jane's Publishing Co., London, 1983.

4. Cooke, D. L.; Katz, I.; Mandell, M. J.; Lilley, J. R., Jr.; Rubin, A. G. Polar Orbit Electrostatic Charging of Objects in the Shuttle Wake. This volume, 1984.

5. Shawhan, S. D.; Murphy, G. B.; Drosselhaus, A.; Pickett, J.; Grebowsky, J.; Reasoner, D. L.; Raitt, W. J. Electron and Ion Density Depletions in the STS-3 Orbiter Wake. This volume, 1984.

6. Leung, P.; Plamp, G. H.; Robinson, P. A. Galileo Internal Electrostatic Discharge Program. This volume, 1984.

7. Aviation Week and Space Technology, 117, No. 22, Nov 29, 1982, p. 70.

8. Stevens, N. J. Summary of High Voltage Solar Array Interactions with Space Plasma Environments. This volume, 1984.

9. Feldstein, Y. I.; Starkov, G. V. Dynamics of Auroral Belt and Polar Geomagnetic Disturbances. Planetary and Space Sciences, 15, 1967, pp. 209-229.

10. Whalen, J. A. Auroral Oval Plotter and Nomograph for Determining Corrected Geomagnetic Local Time, Latitude, and Longitude for High Latitudes in the Northern Hemisphere. Air Force Cambridge Research Laboratories. Environmental Research Papers No. 327, Report No. AFCRL-70-0422, Hanscom AFB, MA 01731, 1970.

11. Pike, C. P. DAPP Satellite Observations of Auroras. EOS - Transactions of the American Geophysical Union, 55, June 1974, pp. 604-605.

12. Burke, W. J.; Hardy, D. A. Direct Measurements of Severe Spacecraft Charging in the Auroral Ionosphere. This volume, 1984.

13. Krukonis, A. P.; Whalen, J. A. Occurrence and Lifetimes of Discrete Auroras Near Midnight. J. Geophysics Research, 85, 1 January 1980, pp. 119-129.

14. Mayaud, P. N. Derivation, Meaning, and Use of Geomagnetic Indices. American Geophysical Union, Washington, D.C., 1980.

15. Allen, J. H.; Abston, C. C.; Morris, L. D. Auroral Electrojet Magnetic
    Activity Indices AE(11) for 1974. Report UAG-59. National Oceanic and
    Atmospheric Administration, Environmental Data Service, Asheville, North
    Carolina, 1976.

Figure 1. - Polar orbit EVA.

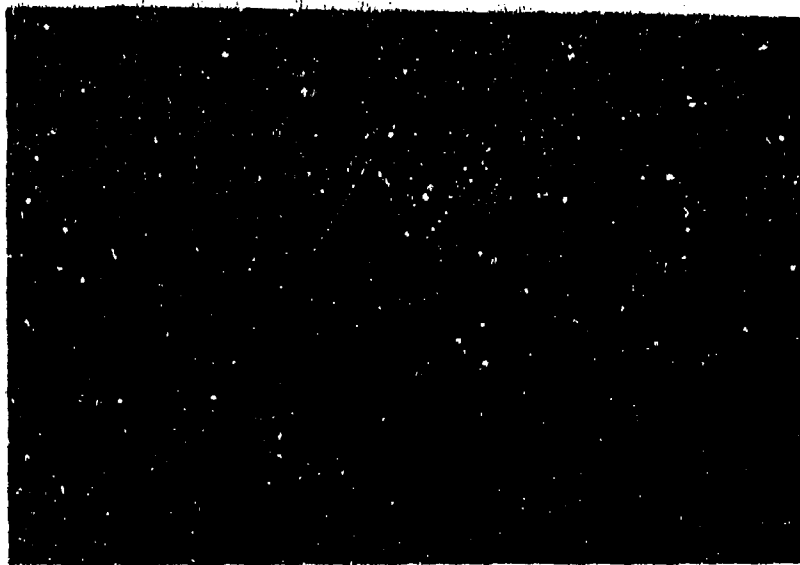Figure 2. - Astronaut equipment materials.
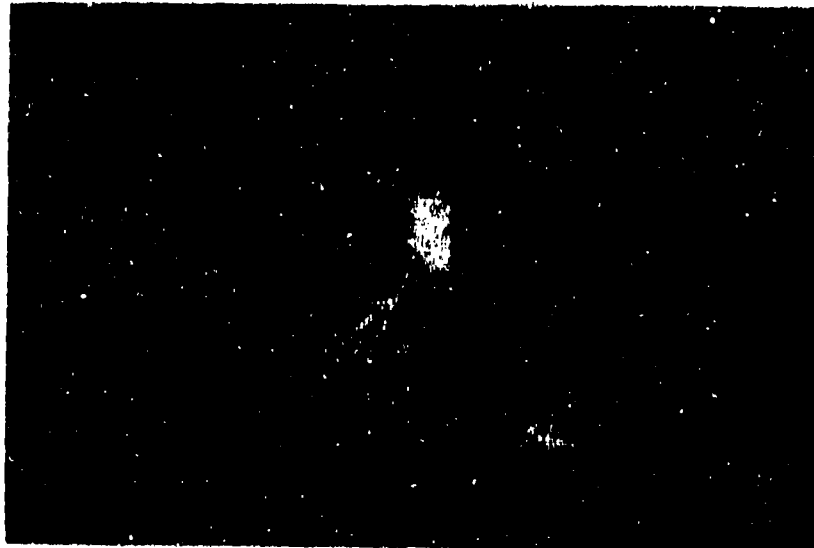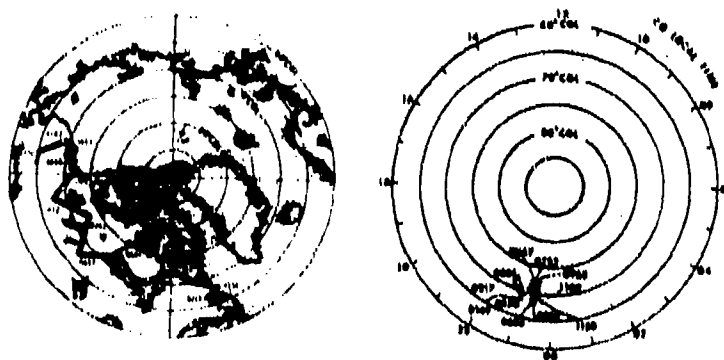
Figure 3. – Astronaut equipment systems.

Figure 4. – Astronaut and solar power systems.

Figure 5. - Aurora.

21 JANUARY 1974

Figure 6. - AFGL Airborne Ionospheric Observatory flight tracks.

Goose AB - Eielson AFB
21 January 1974

Figure 7. – ASCA Montage.

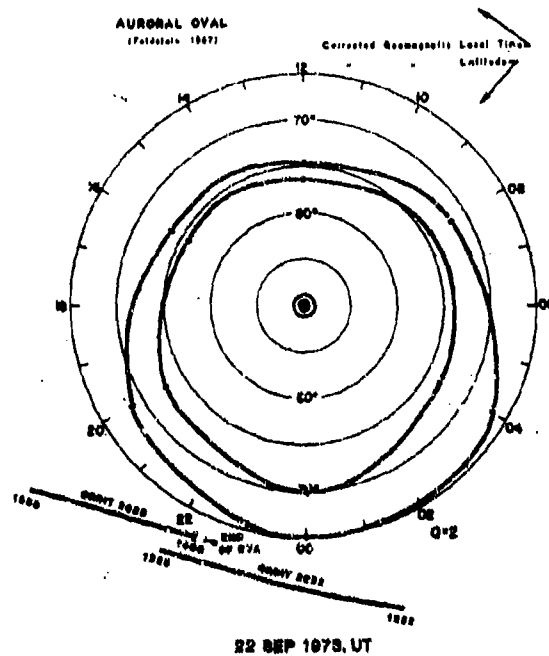AURORAL OVAL
(Feldstein 1967)

22 SEP 1973, UT

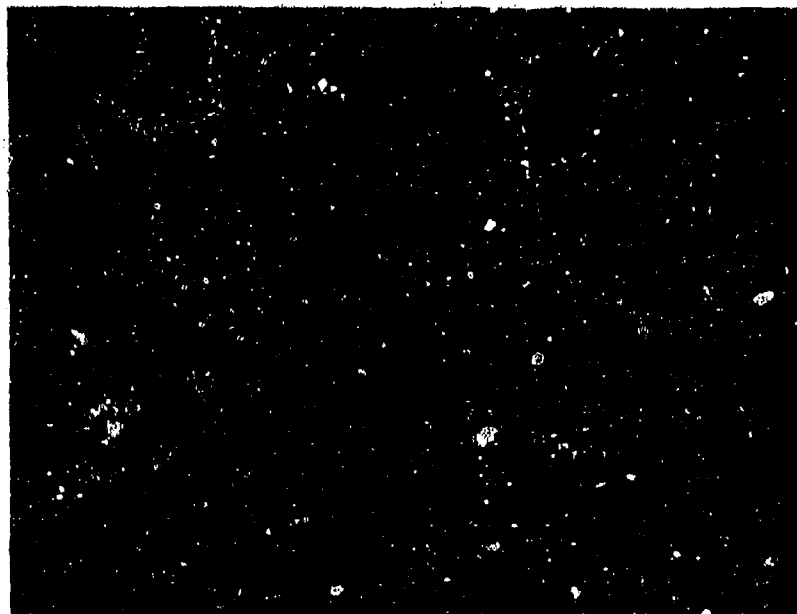Figure 8. - Skylab subsatellite ground tracks.

Figure 9. - Future polar orbit extravehicular activity.

674

ARGON ION POLLUTION OF THE MAGNETOSPHERE

Ramon E. Lopez
Rice University
Houston, Texas 77251

Construction of a Solar Power Satellite (SPS) would require the injection of large quantities of propellant to transport material from Low Earth Orbit (LEO) to the construction site at Geostationary Earth Orbit (GEO). This injection, in the form of $\sim 10^{32}$, 2 KeV argon ions (and associated electrons) per SPS, is comparable to the content of the plasmasphere ($\sim 10^{31}$ ions). In addition to the mass deposited, this represents a considerable injection of energy.

The injection is examined in terms of a simple model for the expansion of the beam plasma. General features of the subsequent magnetospheric convection of the argon are also examined.

INTRODUCTION

In recent years a large scale energy system, the Satellite Power System (SPS), has received considerable attention from the scientific and technical community. The basic concept for SPS is as follows: Large (10 km × 5 km) platforms would be constructed in geostationary earth orbit (GEO) to collect solar energy. This energy would be converted into microwaves and beamed down to Earth, received by a rectifying antenna and fed into the power grid.

In 1978, Rockwell International did a system definition study (ref. 1) in which a 5 GW (at Earth interface) reference system was developed. The transportation component would mandate the construction of several reusable heavy lift launch vehicles (HLLV) to haul material into low Earth orbit (LEO). From LEO the cargo would be shuttled to the construction site GEO in a fleet of electric orbit transfer vehicles (EOTV).

The EOTVs would be solar powered and propelled by argon ion thrusters. Ion thrusters have some advantages over chemical rockets. They can deliver a sustained, steady thrust. Also, the ion thruster propellant velocity is much greater than for chemical thrusters, therefore much less mass need be injected to move an equal amount of cargo from LEO to GEO with ion thrusters.

In spite of the great efficiency of ion propulsion, due to the great mass that must be transported, enormous quantities of energetic argon and the associated (thermal) electrons would be injected into the environment. Such a large scale injection of plasma into the magnetosphere is likey to have a global impact on Earth's magnetospheric morphology and dynamics. In addition, due to the highly anisotropic velocity distribution of the argon, this represents a considerable injection of free energy. Numerous processes should transfer a large portion of the

injection energy to the magnetospheric system.

Ion thruster technology is still developing and so the parameters for the thruster in question are uncertain. The Rockwell reference system described an EOTV propelled by an ion thruster with a grid potential limit of 2 keV, to avoid arcing to the background plasma. It would operate with an ion beam current of 1904 amps, have a radius = 38 cm, and develop 69.7 Nt of thrust. Eighty such thrusters would equip each EOTV, in four groups of 20, with 16 active and 4 spares.

The thruster produces two distinct plasmas: the beam plasma and the thermal plasma produced by charge exchange between the beam plasma and escaping un-ionized argon. The number of charge-exchange ions produced per second is given by Kaufmann (ref. 2) to be:

$$\dot{N} = \frac{2\sigma_{CE} J_B^2 (1 - \eta)}{e^2 V_0 R_B \pi \eta} \quad (Ar^+ \ s^{-1}) \tag{1-1}$$

where σ_{CE} = charge exchange cross section = 2×10^{-19} m^2
J_B = beam current = 1904 A
V_0 = $(8KT/\pi m)^{1/2}$
R = beam radius = .38 m
η = fraction of propellant ionized

Carruth and Brady (ref. 3) state that in experiments with a 900-series, Hughes mercury ion thruster approximately 90% of the propellant is ionized. The remaining 10% escapes through the optics in the form of neutral mercury. Therefore η is assumed to be 0.9 and KT = 10 eV (ref. 4), which gives $\dot{N}$ = 6.07×10^{20} Ar$^+$ s^{-1}. This represents about 5.6% of the beam current.

Parks and Katz (ref. 5), and Carruth and Brady (ref. 3) report that laboratory tests show the charge-exchange plasma near the thruster moves radially outward from the thruster beam. This thermal plasma will be injected into space with essentially the EOTV's orbital velocity. As in the barium release experiments (ref. 6), the plasma is expected to expand until β = 1, at which point the expansion perpendicular to B is stopped by the field.

This thermal argon plasma, apart from the beam plasma, would be in itself a considerable addition to the thermal heavy ion population, especially in the plasmasphere. The remaining un-ionized argon would be subject to charge exchange and photoionization, the latter of which has an e-folding production rate given by Siscoe and Mukherjee (ref. 7) to be 4.5×10^{-4} s^{-1}. This allows many of the fast (charge-exchange) neutrals to escape, while trapping the thermal neutrals in, or near, the plasmasphere.

TABLE I. — SPS PARAMETERS

SPS mass ~ 5×10^7 Kg
EOTV — LEO departure ~ 6.7×10^6 Kg
      Cargo   ~ 5×10^6 Kg
      Propellant ~ 5.5×10^5 Kg
LEO → GEO → LEO trip time = 130 days

The quantities of mass involved in the reference system are given in table I. To build a 5 GW station of a mass $\approx 5 \times 10^7$ Kg, one needs ≈ 10 EOTV flights which would inject 5×10^6 Kg of 2 keV Ar^+ and $\sim 5 \times 10^5$ Kg of thermal Ar^+ (along with the associated electrons) into the magnetosphere. Assuming that two stations are built per year this gives an average injection rate of 5.3×10^{26} Ar^+ s^{-1}. This is comparable to the polar wind injection rate of $\sim 3 \times 10^{26}$ s^{-1} and equal to the plasma sheet loss rate (ref. 8). The average rate of energy injection (in the form of 2 keV Ar^+) is $\sim 10^9$ watts, while an average substorm deposites $10^{11} - 10^{12}$ watts into the ionosphere (ref. 9). This energy will, however, be distributed over a smaller area and so power densities could be similar to auroral power densities.

Needless to say, the scope of the questions involved in such an injection is extensive. This paper will concern itself mainly with two topics: the injection of the energetic ions (beam plasma dynamics) and the subsequent convection of the beam ions in the magnetosphere.

BEAM PLASMA DYNAMICS

The plasma beam that emerges from the thruster is a dense, charge-neutral beam moving perpendicular to $\vec{B}$. The physics of a plasma beam injected into a transverse magnetic field has been studied by many authors, both experimentally and theoretically (refs. 10, 11, 12, 13). Also there have been authors who have considered the problem of ion thrusters in space, some specifically in the SPS context (refs. 4, 14, 15).

Curtis and Grebowsky (ref. 14) argue that the beam polarizes and $\vec{E} = -\vec{V} \times \vec{B}$ cancels the Lorentz force. According to Curtis and Grebowsky (ref. 14) the beam density is always able to support the polarization field. In this case the beam simply passes out of the magnetosphere, depositing a thin non-propagating sheath. While this is correct for a vacuum injection, when the field lines threading the beam are shorted the plasma is stopped (refs. 10, 13). This is exactly the case in the magnetosphere. The beam dynamics paradigm of Chiu et al. (ref. 15) is based on the barium release experiments (refs. 6, 12). In this picture the polarization field accelerates and polarizes the adjacent plasma, which in turn polarizes the plasma adjacent to it. This electric field, which moves along the field line at the Alfven speed, transfers beam momentum to the ambient plasma and magnetosphere. When the Alfven wave reaches the ionosphere it drives dissipative Pedersen currents, and can be partially reflected (ref. 6).

According to this model the plasma velocity decreases like $e^{-t/\tau}$, where τ is the amount of time it takes for the Alfven wave to travel over as much mass per unit area as is causing the disturbance. Therefore, Chiu et al. (ref. 15) give that

$$\tau = \int ds \; \rho_b / 2 V_A \rho_0 \qquad (2-1)$$

where ρ is the mass density (b refers to the beam, 0 to the ambient), V_A is the Alfvén speed, and the integral is along the field line. Calculations using realistic plasmaspheric and magnetic field models, give $\tau \approx 10$ seconds (ref. 16). Thus the beam can travel for distances $\lesssim 1000$ km.

Treumann et al. (ref. 17) have pointed out that as field aligned currents short out the polarization field, electrons cannot $\vec{E} \times \vec{B}$ drift across field lines to neu-

tralize the beam. They postulate that more currents parallel to $\vec{B}$ neutralize the beam head, generating a kinetic Alfvén wave. For the PORCUPINE ion beam (of which more will be said), Treumann et al. (ref. 17) estimate electron drift velocities $\sim V_A$. Due to these high drifts they argue that anomalous heating of electrons energizes them to ~ 20 eV to explain those hot electrons seen in the PORCUPINE experiment (ref. 18).

If we assume that the beam width is on the order of 10 km and the beam length ~ 1000 km then the average neutralizing field-aligned currents (for the EOTV discussed above) must be ~ 15 $\mu A/m^2$. For ambient electron densities of $\leq 10^9$ m^{-3} this results in drift speeds ≥ 100 km s^{-1}. This is still half the thermal speed of a 0.1 eV electron, so ion acoustic waves will be stable, but electrostatic ion-cyclotron waves, with $w = \Omega_i$, are unstable for $V_D \geq 5 \times$ (ion thermal speed) (ref. 19) thus limiting the current. Therefore it is unlikely that the polarization field will be completely shorted out and that the beam ions will be charge-neutralized by a combination of both $\vec{E} \times \vec{B}$ drift of beam electrons across $\vec{B}$ and field-aligned currents.

Haerendal and Sagdeev (ref. 8), writing on behalf of the PORCUPINE experimenters, report on the injection of a 4A, 200 eV, Xe^+, charge-neutralized plasma beam. This beam was injected at $\sim 72°$ to $\vec{B}$ in nine events ranging in altitude from 196 km to 451 km. They report three stages of its beam expansion. The first is free expansion of the beam until the magnetic pressure starts to balance the dynamic pressure. The second phase is one of diffusive expansion, with the polarization field allowing for some motion across $\vec{B}$, although the polarization field is rapidly shorted out by field-aligned currents and the beam is stopped. The third phase is that of single particle motion.

Considerable wave activity was also reported during the injection events (refs. 18, 20, 21). Broadband ion-cyclotron harmonic waves were detected (refs. 18, 21) and it has been argued that the Drummond-Rosenbluth instability (ref. 19) is responsible (ref. 18). Given the much greater scale of the SPS injection it is reasonable to expect intense wave generation which could energize ambient particles. In particular there is experimental evidence for the acceleration of thermal electrons by ion-cyclotron waves. Norris et al. (ref. 22) suggest that these waves in the magnetosphere having $f > f_{He^+}$ accelerate electrons with a clear bias parallel to $\vec{B}_0$, the majority of the electrons heated to 20 eV.

The field-aligned currents produced as a result of this are consistent with the view that such currents will play a central role in the dynamics of the beam, since these currents transfer momentum from the beam and drive Alfvén waves. This is supported by observations of considerably enhanced electron fluxes during the injection of a plasma transverse to $\vec{B}$ as reported by Alexandrov et al. (ref. 23). These authors also suggest that the observed magnetic disturbances are due to field-aligned currents and associated Alfvén waves.

The beam model presented below will deal with only the large-scale dynamics of the beam. It is assumed that the paradigm of Scholer (ref. 6) is essentially correct, so beam velocity decreases as $e^{-t/\tau}$. When the beam emerges from the thruster both nkT and $(1/2)\rho v^2$ are much greater than $B^2/2\mu_0$. Thus the beam will expand radially outward from the beam axis, as if into a vacuum, forming a cone. This phase of the expansion continues until

$$nkT = B^2/2\mu_0 \qquad\qquad (2\text{-}2)$$

after which motion perpendicular to $\vec{V}_B$ and $\vec{B}$ is stopped, while expansion along the field line continues essentially uninhibited (fig. 1). The beam travels in this manner until

$$\frac{1}{2}\rho v^2 = B^2/2\mu_0 \tag{2-3}$$

at which point the geomagnetic field becomes the dominant influence in the argon plasma's motion. The argon's subsequent motion can then be followed by the adiabatic theory.

In the initial phase of the plasma beam we are dealing with a vacuum expansion. It is assumed the beam is charge-neutral and collisionless. In the very early history of the beam it is certainly collisional, the plasma rapidly thermalizing, but by ~100 m downstream the mean free path is of the order of the beam size. We also neglect momentum loss to Alfven waves, assuming $t \ll \tau$ during the first (vacuum) phase of the beam expansion.

To represent the plasma that emerges from the thruster we write

$$f(\vec{X}, \vec{V}, V_z, t = 0) = \frac{n_0 m}{2\pi KT} \delta(V_z - V_B) \exp -\left[\frac{m\vec{V}^2}{2KT} + \frac{\vec{X}^2}{2R^2}\right] \tag{2-4}$$

where
$$\vec{X} = X\hat{i} + Y\hat{j}$$
$$\vec{V} = V_x\hat{i} + V_y\hat{j}$$
$$\vec{V}_B = \text{beam velocity} = V_B\hat{z}$$
$$R = 1/3 \; r_0$$

Liemohn et al. (ref. 4) give $KT = 10$ eV, which for a 2 keV beam gives an effective beam divergence angle ~8°. This same 8° spreading angle is reported by Cybulski et al. (ref. 24) in flight tests of the SERT I ion thruster. To confine the plasma to the thruster at $t = 0$, R is set to one-third the thruster radius, r_0.

We can then write the collisionless, vacuum Boltzman equation

$$\frac{\partial f}{\partial t} + \vec{V} \cdot \nabla f = 0 \tag{2-5}$$

The solution to equation (2-5) is readily found to be

$$f(\vec{X}, \vec{V}, V_z, t) = \frac{n_0 m}{2\pi KT} \delta(V_z - V_B) \exp -\left[\frac{m\vec{V}^2}{2KT} + \frac{(\vec{X} - \vec{V}t)^2}{2R^2}\right] \tag{2-6}$$

The constant, n_0, is given by the normalization condition

$$\int f d^2 v \, d\vec{x} \, V_B t = N = \frac{It}{e} \tag{2-7}$$

where the integral along the beam axis is replaced by multiplication by $V_B t$. From equation (2-7) one finds

$$n_0 = \frac{9I}{2\pi r_0^2 eV_B} \tag{2-8}$$

The density of ions is given by

$$\int f \, d^3v = n(\vec{x}, t) = n_0 \frac{m/KT}{(m/KT) + (t^2/R^2)} \exp\left[-\frac{\vec{x}^2}{2R^2} \frac{m/KT}{(m/KT) + (t^2/R^2)}\right] \quad (2\text{-}9)$$

which for $t \gtrsim 10^{-4}$ s yields, using equation (2-8)

$$n(r, t) = \frac{n}{KT} \frac{1}{2\pi e V_B t^2} \exp\left[-\frac{r^2}{2t^2} \frac{m}{KT}\right] \quad (2\text{-}10)$$

The end of the vacuum expansion phase is given by equation (2-2) using equation (2-10) evaluated at the edge of the beam, which is $r = V_{Th}t$. The time at which this condition is satisfied for the HOTV in question in a dipole field is

$$t_0 = 8.83 \times 10^{-3} L^3 \text{ sec} \quad (2\text{-}11)$$

where L is the magnetic shell parameter. After time t_0 the beam continues to spread along $\vec{B}$ and so the density decreases like $1/t$. But the velocity is also going down as $e^{-t/\tau}$ and so the density must go like $e^{t/\tau}$ to conserve particles. So we may write the central beam density for $t > t_0$ as

$$n(t > t_0) = \frac{t_0 n(r = 0, t = t_0)}{t} e^{-t/\tau} \quad (2\text{-}12)$$

Using this density in equation (2-3) yields an equation for the time of transition from beam motion to adiabatic motion, which is

$$L^5 = 0.216 \, t \, e^{t/\tau} \quad (2\text{-}13)$$

where L is the dipole shell parameter. The fraction of energy the beam ions retain is then $e^{-2t/\tau}$, the rest of the energy being transferred to the magnetosphere and ionosphere. As stated before, $\tau = 10$ sec in the plasmasphere (ref. 15). Figure 2 gives the energy loss as a function of L for $\tau = 10$ sec from $L = 2.5$ to $L = 3.5$.

To estimate the energy density deposited in the ionosphere by the beam we find that at $L = 2$ roughly 3/4 of the beam power is lost to Alfvén waves. From equation (2-11) we find that the beam width ~ few km, and the beam length $\lesssim 1000$ km. This gives an area of $\lesssim 10^4$ km^2, which mapped down to the ionosphere (with a dipole field) results in ionospheric power densities of ~10^{-1} W/m^2 (assuming the bulk of the energy is deposited in the ionosphere). This is considerably larger than auroral power densities of ~10^{-2} W/m^2 (ref. 25), and even if we assume only 10% of the power is absorbed by the ionosphere there would still be power densities equivalent to auroras.

CONVECTION OF THE ARGON PLASMA

Once the argon plasma's transition from beam to individual particle motion is accomplished the subsequent motion is determined by the local magnetic and electric fields. This motion is most easily followed using the guiding center approximation. The two first order drift velocities are the $\vec{E} \times \vec{B}$ and the gradient/curvature drift

velocities. The motion of the plasma is given by

$$\frac{d\vec{x}}{dt} = \frac{\vec{E} \times \vec{B}}{B^2} + \frac{(1/2) \; 'mv^2}{B} (1 + \cos^2 \alpha) \frac{\vec{B} \times \nabla |\vec{B}|}{eB^2} \tag{3-1}$$

Ignoring time dependence, $\vec{E}$ and $\vec{B}$ are functions of $\vec{x}$ and this equation must be solved numerically.

The coordinate system is as follows: x is the antisunward direction, y along the dawn meridian. For a magnetic field the model of Mead (ref. 26) is used with the magnetopause set at r = 10 R_e. In the equatorial plane, $\vec{B}$ just has a z component:

$$B = B_z = \frac{3.11 \times 10^{-5}}{R^3} + 2.515 \times 10^{-9} - 2.104 \times 10^{-9} \; R \cos \theta \tag{3-2}$$

where R is the earth radii, θ is the local time and B in tesla.

There are three components to the electic field: the convection field, the corotation field and the self-electric field of the argon plasma, which will be discussed in more detail below. The convection field is approximated by a constant, dawn to dusk, 0.2 mV/m electric field. This corresponds to a ~ 50 kV cross-polar potential drop mapped out onto a 40 R_e magnetosphere. The corotation field is given by

$$\vec{E}_{cor} = -\vec{v} \times \vec{B} \simeq -\vec{\Omega} \times \vec{r} \times \vec{B}_{Dipole} \tag{3-3}$$

The above model has some obvious shortcomings. The greatest of these is the assumption of a uniform convection field. In addition, there is an inconsistency in making the approximation in equation (3-3), then using it in the drift equation, since the expression for $\vec{B}$ has non-dipole components. The proper way to calculate the corotating field is to calculate $\vec{v} \times \vec{B}$ for the field line in question. This was not done due to the limitations of the Tektronics 4052 minicomputer which was used. However, this rough model should give a somewhat reasonable approximation to the general features of the convection of injected argon.

Chiu et al. (ref. 15) give the time fraction spent from LEO to GEO in figure 3. Using this with the above model one finds that ~3/4 of the injected argon is trapped in the plasmasphere. However, a more complete picture of the argon convection requires the inclusion of the electric field generated by the argon filled flux tube itself. The gradient drift current in the flux tube (or plasma blob) gives rise to Birkeland currents, which close in the ionosphere, if neighboring flux tubes cannot satisfy continuity of current. This current system is illustrated in figure 4.

Assuming that equal amounts of current go to the northern and southern hemispheres current continuity gives

$$\frac{1}{2} \nabla \cdot \vec{J}_{\perp eq} = -J_{\parallel eq} = - \left(\frac{B_{eq}}{B_{ion}}\right) J_{\parallel ion} \tag{3-4}$$

where $J_{\perp eq}$ is the current/length in the equatorial plane, $J_{\parallel eq}$ is the current/unit

area out of the equatorial plane, and $J_{\|ion}$ the current/unit area into the iono-sphere. This current closes in the ionosphere, in which case we can take the divergence of Ohm's Law and, using equation (3-4), obtain

$$\nabla \cdot (\underline{\Sigma} \cdot \nabla V) = \frac{1}{2} \nabla \cdot J_{\perp eq} \left(\frac{B_{ion}}{B_{eq}}\right) \tag{3-5}$$

Assuming $\vec{J}_{ion}$ to be $\perp \hat{B}$, and considering only the Pedersen conductivity, the above becomes

$$\Sigma_p \nabla_h^2 V = \frac{1}{2} \nabla \cdot \vec{J}_{eq} \left(\frac{B_{ion}}{B_{eq}}\right), \quad \nabla_h = \text{horizontal } \nabla \text{ in ionosphere} \tag{3-6}$$

This approach, developed in part by Vasyliunas (ref. 27) and Wolf (ref. 28), allows the calculation of the ionospheric potential set up by the flux tube. This potential can be then mapped out along field lines (assuming they are equipotentials) to give the potential, and electric field, in the equatorial plane.

We assume the argon density to be constant throughout a flux tube of radius a, and zero outside of the flux tube. It is also assumed that there is a uniform, background current density. For this case, in radial coordinates centered on the flux tube, we find

$$\nabla \cdot \vec{J}_{\perp eq} = K \cos \theta \, \delta(r - a) \tag{3-7}$$

where K is a constant. As a further simplification we assume we are dealing with a circle in a locally flat ionosphere, so equation (3-6) becomes

$$\nabla^2 V = \frac{K'}{\Sigma_p} \cos \psi \, \delta(\rho - a') \tag{3-8}$$

where (ρ, ψ) are the ionospheric coordinates whose origin is the field line threading the center of the plasma blob, and K', a' are constants. The solution is obtained in a straightforward fashion to yield, in the ionosphere

$$V = \frac{K'a'}{2\Sigma_p \rho} \cos \psi, \qquad \rho > a'$$

$$= \frac{K'\rho}{2\Sigma_p} \cos \psi, \qquad \rho < a' \tag{3-9}$$

Mapping the resultant electric field out to the equatorial plane along dipole field lines yields

$$\vec{E}_{Blob} = - \frac{K'\hat{\phi}}{2\Sigma_p \lambda^{3/2}} \tag{3-10}$$

where ϕ is local time and λ is the L shell of the center of the argon flux tube. This electric field, for negative K', results in $\vec{E} \times \vec{B}$ motion radially outwards from earth. We also note that the field outside the blob is that of a dipole.

The constant K' is related, by equations (3-6) and (3-7) to the divergence of

the net current, which is

$$\nabla \cdot \vec{J}_{\perp eq} = (|\vec{J}_{BG}| - |\vec{J}_{GC}|) \cos \theta \, \delta(r - a) \tag{3-11}$$

where $|\vec{J}_{GC}|$ is the gradient-curvature current, and $|\vec{J}_{BG}|$ is the background current present in neighboring flux tubes.

We can consider two extreme cases concerning the condition of the argon in the flux tube: very strong pitch angle scattering so that the distribution is isotropic, or very weak scattering so the plasma mirrors at the equator ($\sim$ the state of injection). In the later case

$$\vec{J}_{GC} = N\mu \, \frac{\vec{B} \times \nabla\beta}{B^2} \tag{3-12}$$

where N is the number/area and μ is the magnetic moment. To find μ one can use the beam model of Chapter 2 to obtain the ion's perpendicular energy when they start convective motion. For a dipole field this gives

$$K' = (|\vec{J}_{BG}| - \frac{3M_\perp}{R_e L}) \, (\frac{B_{ion}}{B_{eq}}) \tag{3-13}$$

In the former case the flux tube can be treated as an ideal gas, in which case an adiabatic energy invariant λ can be defined (ref. 29)

$$E_K = \frac{\text{kinetic energy}}{\text{particle}} = \lambda \, (\int ds/B)^{-2/3} \tag{3-14}$$

One can also define a number invariant (ref. 29)

$$n = n \int ds/B = N/B = \#/\text{flux}; \qquad n = \#/m^3 \tag{3-15}$$

then the gradient-curvature drift current is given by (ref. 29)

$$\vec{J}_{GC} = n\lambda\hat{z} \times \nabla_{eq} \, (\int ds/B)^{-2/3} \tag{3-16}$$

Using equations (3-14) and (3-15) the above can be written

$$\vec{J}_{GC} = \epsilon\hat{z} \times \nabla \, (\int ds/B) \tag{3-17}$$

where ϵ is the energy density of the flux tube. This form is convenient since Williams (ref. 30) gives the quiet time energy density to be $\sim 10^{-9}$ Joules/m^3 from $L \sim 2$-5.5, thus we can calculate the background gradient-curvature drift current, $\vec{J}_{BG}$.

To proceed we need to calculate n, λ, $\int ds/B$, and $\nabla(\int ds/B)$. The flux tube volume is given by G.-H. Voigt (personal communication, 1962) to be

$$\int ds/B = \frac{2(L)^{1/2}(L - 1)^{1/2}}{7B_0} [1 + \frac{6}{5} L + \frac{8}{5} L^2 + \frac{16}{5} L^3] R_e \tag{3-18}$$

the gradient of $\int ds/B$ can be obtained by straightforward differentiation of equation

(3-18). In addition, λ may be obtained by using equation (3-14) with the ion kinetic energy given by the beam model in Chapter 2.

The number invariant, η, can be obtained from equation (3-15) if N, the area number density, is known. If I is the ion beam current of the thrusters and V_{EOTV} is the orbital velocity of the vehicle then N is given by

$$N = I/(eV_{EOTV}d_T)$$
(3-19)

where d_T is the extent of the flux tube in the $\vec{V} \times \vec{B}$ direction. The width of the beam is given by $d_B \sim V_{Th}t_0$, where t_0 is given by equation (2-11). This is then the size of the region confining the gyroradii of the ions, therefore

$$d_T = \frac{2mV_{ion}}{eB} + d_B$$
(3-20)

With the above we may now calculate the electric field generated by the argon flux tube's gradient-curvature drift for the two extreme assumptions about the pitch-angle state of the Ar^+. Suprisingly, the difference in the gradient drift velocities, and therefore currents, is only ~10%. It would seem that the total gradient-curvature drift is not overly sensitive to the pitch-angle state of the argon.

Using equations (3-10) to (3-20), equation (3-1) was numerically integrated to produce a plotted trajectory for a model argon filled flux tube. Sample trajectories are plotted in figures 5a and 5b.

In general, the early motion of the model flux tube is dominated by the self-electric field, which results in rapid, radially outward, convection of the argon.

By the time an average flux tube has expanded and cooled to the point where outside fields dominate, it has moved to the plasmapause where a storm can dislodge it. The bulk of the argon should then drift to the magnetopause. The fraction of this argon which is convected back into the tail is of some importance since this Ar^+ could become highly energized (ref. 3). Also of concern is some knowledge of the velocity-space configuration of the Ar^+ when it enters the tail, especially if the triggering mechanism for substorms is related to the ion-tearing mode instability.

Some Ar^+, which is injected at low L can remain trapped, contaminating the plasmasphere (fig. 6). However, the major feature of the convection model is that the bulk of the argon will pass out of the plasmasphere and enter the convective cycle of the magnetosphere. If we assume that ~30% of the Ar^+ comes back up the tail, then the average mass injection rate for the tail is 2.6×10^{24} Ar^+ s^{-1}. If the tail has dimensions of 5 R_e × 40 R_e × 60 R_e, and if we assume that an argon ion is in the plasma sheet on the order of an hour, after which it is lost, then average density would be $\sim 10^4$ m^{-3}. This is smaller than the ambient density by a factor of 10-100 (ref. 9). However, the mass density could go up by as much as a factor of four, cutting the Alfvén speed by 1/2 and thus changing the time scales for dynamic phenomena in the tail.

One more point should be made concerning the motion of the argon flux tube. The electric field of the argon blob is so large that one should ask what the role of inertial drifts is in the motion of the argon. As the flux tubes accelerate

radially outward they produce an inertial drift current oppositely directed to the gradient-curvature drift current. So the flux tubes will accelerate at the rate needed to cancel the gradient-curvature current, thus satisfying continuity, until the velocity of the Ar^+ has reached is that of the $\vec{E} \times \vec{B}$ velocity of the self-electric field, at which point it will not need to accelerate to close the current.

The inertial drift current/length is

$$\vec{J}_I = - \frac{Nm\vec{a} \times \vec{B}}{eB^2} \qquad (3-21)$$

where N is the equatorial area number density and m is the argon mass. Equating this to the gradient drift current and solving for $\vec{a}$, the acceleration, gives (for $B = B_0/L^3$)

$$\vec{a} = \frac{3\mu B_0}{mR_\bullet L^4} \hat{r} \qquad (3-22)$$

For argon injected at L = 2 equation (3-22) yields a ~ 5 km/s² so within a short time $\vec{a}t \sim \vec{E}_{BLOB} \times \vec{B}/B^2$. Thus, except for the first moments of the argon drift, inertial currents need not be self-consistently included. Gravitational and centrifugal drifts may also be neglected.

CONCLUSION

We have seen that the operation of powerful ion thrusters in the SPS context (or for that matter in any space industrial project of such scale) is expected to have a wide variety of effects. Two distinct plasmas are injected: a 2 keV beam plasma and a thermal charge-exchange plasma. The thermal plasma will be a significant addition to the heavy ion content of the plasmasphere. Immediate effects of the beam injection include wideband ion-cyclotron wave generation and field-aligned heating of electrons. Alfvén waves will transfer beam momentum to the ambient plasma and ionosphere. In the ionosphere, power densities will be of the order of, or bigger than natural auroral power densities and so the EOTV will in effect create an artificial aurora on the order of 10^2 km long. These induced aurorae will probably have localized, disruptive effects on communications, and could also affect power transmission lines (ref. 32).

Once the beam ions start to convect, they move radially outward until the argon flux tube energy density is equal to the background energy density. Therefore most of the argon will convect out of the plasmasphere. The field-aligned currents generated could cause further ionospheric disturbances. The argon will then enter the general convective cycle and be distributed throughout much of the magnetosphere. This significant number of heavy ions could substantially alter dynamic quantities like the Alfvén speed. The dispersion relation for waves would also be altered. New cutoffs and resonances should appear along with new wave-particle phenomena. In fact, Chiu et al. (ref. 15) have shown that the presence of Ar^+ damps the instability which precipitates MeV electrons, therefore those levels should rise.

Thus, we see that the operation of an argon-ion propelled orbital transfer system will substantially modify the magnetosphere-ionosphere system. These modifica-

tions, while being substantial, do not seem to be, in and of themselves, so drastic as to rule out this transportation system. Historically, whenever man enters a new environment he modifies his culture, technology, and himself, while in turn altering the environment, both by his activities and to suit his needs. The magnetosphere is no exception, and as man becomes more involved in space in the near future, he will begin to modify it.

REFERENCES

1. Solar Systems Concept Definition Study (Exhibit C). SD 78-AP-0115, National Aeronautics and Space Administration, 1978.

2. Kaufmann, Harold R.: Interaction of a Solar Array with an Ion Thruster Due to the Charge-Exchange Plasma. NASA-CR-135099, Annual Report, October, 1976.

3. Carruth, M. R.; and Brady, M. E.: Production of Charge-Exchange Plasma Produced by an Ion Thruster. AIAA 13th Fluid and Plasma Dynamics Conference, Snowmass, Colorado, July 14-16, 1980.

4. Liemohn, H. B.; Holze, D. H.; Leavens, W. M.; and Copeland, R. L.: Ion Thruster Plasma Dynamics near High Voltage Surfaces on Spacecraft. Part of Space Systems and Their Interactions with Earth's Space Environment, ed. by Henry B. Garrett and Charles P. Pike, American Institute of Aeronautics and Astronautics, 1980, pp. 557-598.

5. Parks, D. E.; and Katz, I.: Spacecraft-Generated Plasma Interaction with High Voltage Solar Array. AIAA/DGLR 13th International Electric Propulsion Conference, San Diego, April 25-27, 1978.

6. Scholer, M.: On the Motion of Artificial Ion Clouds in the Magnetosphere. Planet. Space Sci., 18, 977, 1970.

7. Siscoe, G. L.; and N. R. Mukherjee. Upper Limits on the Lunar Atmosphere Determined from Solar-Wind Measurements. J. Geophys. Res., 77, 6042, 1972.

8. Hill, T. W.: Origin of the Plasma Sheet. Rev. Geophys. Space Phys., 12, 379, 1974.

9. Hill, T. W.; and Wolf, R. A.: Solar Wind Interactions. Part of The Upper Atmosphere and Magnetosphere, Studies in Geophysics, National Academy of Sciences, Washington, D.C., 1977, pp. 25-41.

10. Barney, Gerald O.: Experiments and Observations on Polarized Plasma Injection. Phys. Fluids, 12, 2429, 1979.

11. Sellen, Jr., J. M.; and Bernstein, W.: Interaction of Collisionless Plasma Streams with Transverse Magnetic Fields. Phys. Fluids, 977, 1964.

12. Pillip, W. G.: Expansions of an Ion Cloud in the Earth's Magnetic Field. Planet. Space Sci., 19, 1095, 1971.

13. Wickham, M.; and Robertson, S.: Cross Field Injection and Trapping of a Continuous Plasma Beam in a Magnetic Mirror. Plasma Phys., 25, 103, 1983.

14. Curtis, S. A.; and Grebowsky, J. M.: Changes in the Terrestrial Atmosphere-
    Ionosphere-Magnetosphere System Due to Ion Propulsion for Solar Power
    Satellite Placement. NASA Tech. Memo 79719, Goddard Space Flight Center, J.
    Geophys. Res., 85, 1729, 1980.

15. Chiu, Y. T.; Luhmann, J. G.; Schulz, M.; and Cornwall, J. M.: Magnetospheric
    Effects of Ion and Atom Injections by the Satellite Power System. Space
    Sciences Laboratory Report No. SSL-80(9990)-1, 1980.

16. Chiu, Y. T.: Fate of Argon-Ion Injection in the Magnetosphere. American
    Institute of Aeronautics and Astronautics, Inc., 1980.

17. Treumann, R.; Bauer, O. H.; Haerendal, G.; Häusler, B.: Dynamics of Quasi-
    Neutral Beams. International Symposium on Active Experiments in Space,
    Alpbach, Austria, May 23-28, 1983.

18. Haerendal, G.; and Sagdeev, R. Z.: Artificial Plasma Jet in the Ionosphere.
    Adv. Space Res., 1, 29, 1981.

19. Drummond, William E.; and Rosebluth, Marshall N.: Anomalous Diffusion Arising
    from Microinstabilities in a Plasma. Phys. Fluids, 5, 1507, 1962.

20. Kintner, P. M.; and Kelly, M. C.: Ion Beam Produced Plasma Waves Observed by
    the δn/n Plasma Wave Receivers during the Porcupine Experiment. Adv. Space
    Res., 1, 107, 1981.

21. Jones, Dyfrig: Xe^{+}-Induced Ion-Cyclotron Harmonic Waves. Adv. Space Res., 1,
    103, 1981.

22. Norris, A. J.; Johnson, J. F. E.; Sojka, J. J.; Wrenn, G. L.; Cornilleau-
    Wehrlin, N.; Perraut, S.; and Roux, A.: Experimental Evidence for the Accel-
    eration of Thermal Electrons by Ion Cyclotron Waves in the Magnetosphere. J.
    Geophys. Res., 88, 889, 1983.

23. Alexandrov, V. A.; Babev, A. P.; Gaydukov, V. Y.; Loebsky, A. S.; Popov, G. A.;
    and Romanovsky, Y. A.: Energetic Electron Fluxes Stimulated with Pulsed
    Injection of Plasma in the Ionosphere. Adv. Space. Res., 1, 141, 1981.

24. Cybulski, Ronald J.; Shellhammer, Daniel M.; Lowell, Robert R.; Domino, Edward
    J.; and Kotnik, Joseph T.: Results from SERT I Ion Rocket Flight Test. NASA
    TN D-2718, National Aeronautics and Space Administration, Washington, D.C.,
    March 1965.

25. Spiro, R. W.; Reiff, P. H.; and Maher, Jr., L. J.: Precipitating Electron
    Energy Flux and Auroral Zone Conductances: An Empirical Model. J. Geophys.
    Res., 87, 8215, 1982.

26. Mead, G. D.: Deformation of the Geomagnetic Field by the Solar Wind. J. Geo-
    phys. Res., 69, 1181, 1964.

27. Vasyliunas, V. M.: Concepts of Magnetospheric Convection. Part of The Mag-
    netospheres of Earth and Jupiter, ed. by V. Formisano, D. Reidel Publ. Co.,
    Dordrecht, Holland, 1975, pp. 179-188.

28. Wolf, R. A.: Ionosphere-Magnetosphere Coupling. Space Sci. Rev., 17, 537, 1975.

29. Harel, M.; Wolf, R. A.; Reiff, P. H.; Spiro, R. W.; Burke, W. J.; Rich, F. J.; and Smiddy, M.: Quantitative Simulation of a Magnetospheric Substorm, 1, Model Logic and Overview. J. Geophys. Res., 86, 2217, 1981.

30. Williams, Donald J.: Ring Current Composition and Sources. Part of Dynamics of the magnetosphere, ed. by S.-I. Akasofu, D. Reidel Publ. Co., Dordrecht, Holland, 1979, pp. 407-424.

31. Freeman, J. W.; Hills, H. K.; Hill, T. W.; Reiff, P. H.; and Hardy. D. H.: Heavy Ion Circulation in the Earth's Magnetosphere. Geophys. Res. Lett, 4, 195, 1977.

32. Akasofu, S.-I.; and Aspens, J. O.: Auroral Effects on Power Transmission Line Systems. Nature, 295, 136, 1982.

33. Freeman, J. W.: International Magnetospheric Plasma Flow. ESA SP-148, Proceedings of Magnetospheric Boundary Layers Conference, 1979.
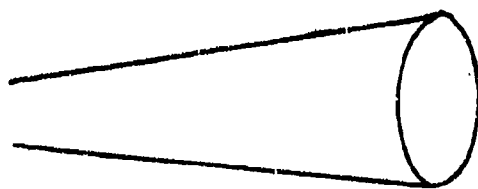
$$MKT \gtrless \frac{B^2}{2\mu_0}$$

(a) Vacuum expansion.

$$\frac{MNV^2}{2} \gtrless \frac{B^2}{2\mu_0}$$
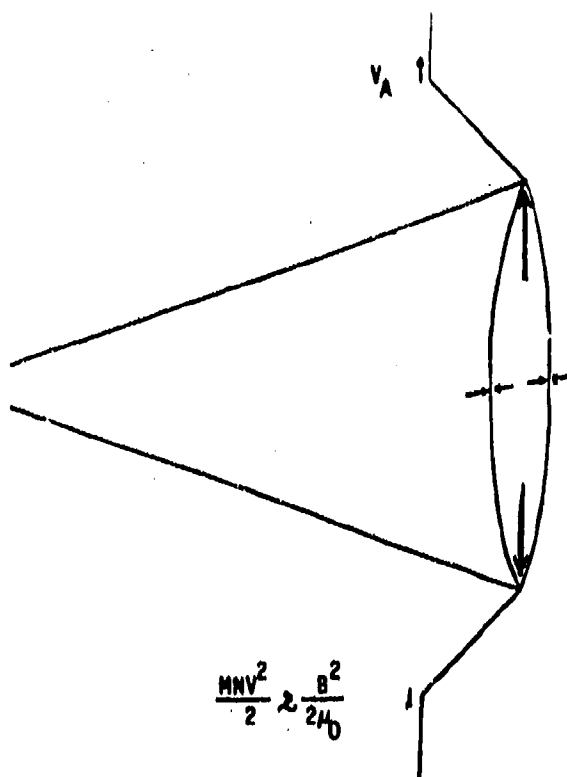
(b) Expansion along $\vec{B}$, also showing Alfven wave propagating down field line.
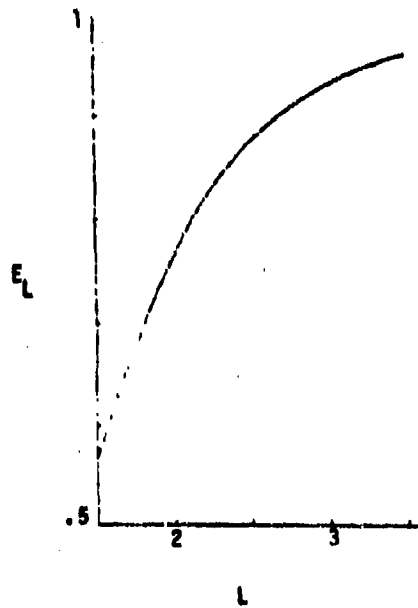
Figure 1. - Two stages of beam expansion.

Figure 2. - Fraction of energy lost to Alfven waves E_L versus magnetic parameter L. It is assumed that e-folding time τ is ~ 10 sec in plasmasphere.
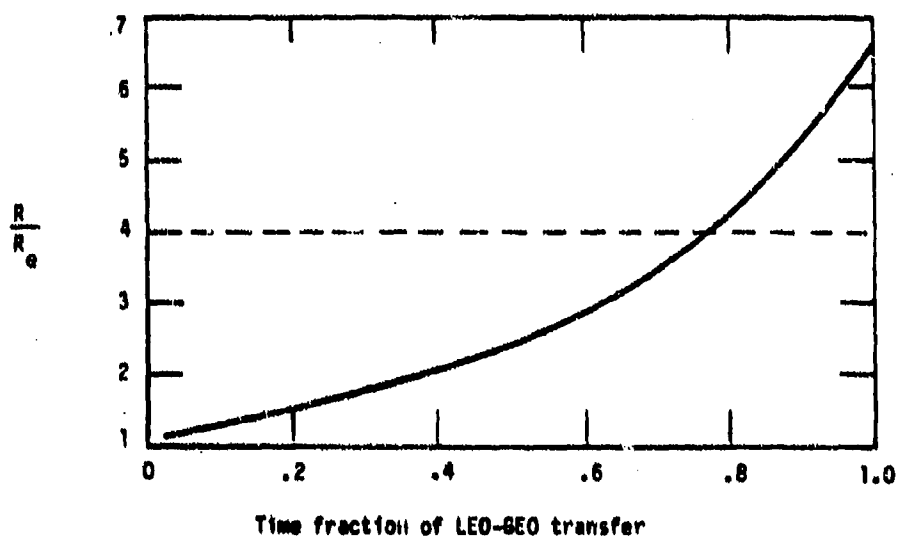

Time fraction of LEO-GEO transfer

Figure 3. - Fraction of total trip time to reach given R/R$_\oplus$. (From Chiu et al. (ref. 15)).
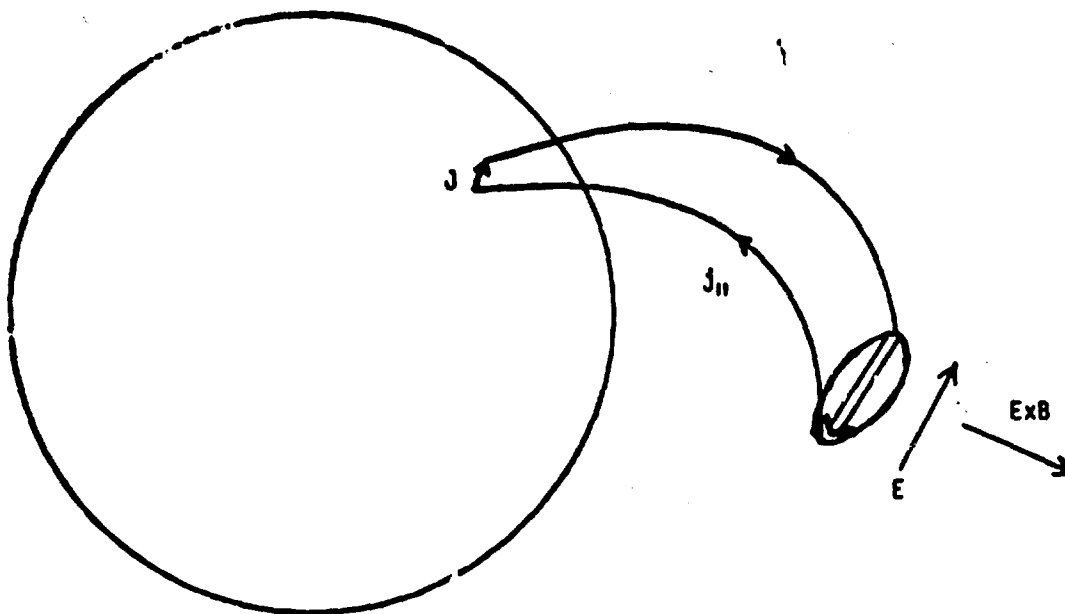
Figure 4. - Birkeland current system for argon flux tube.
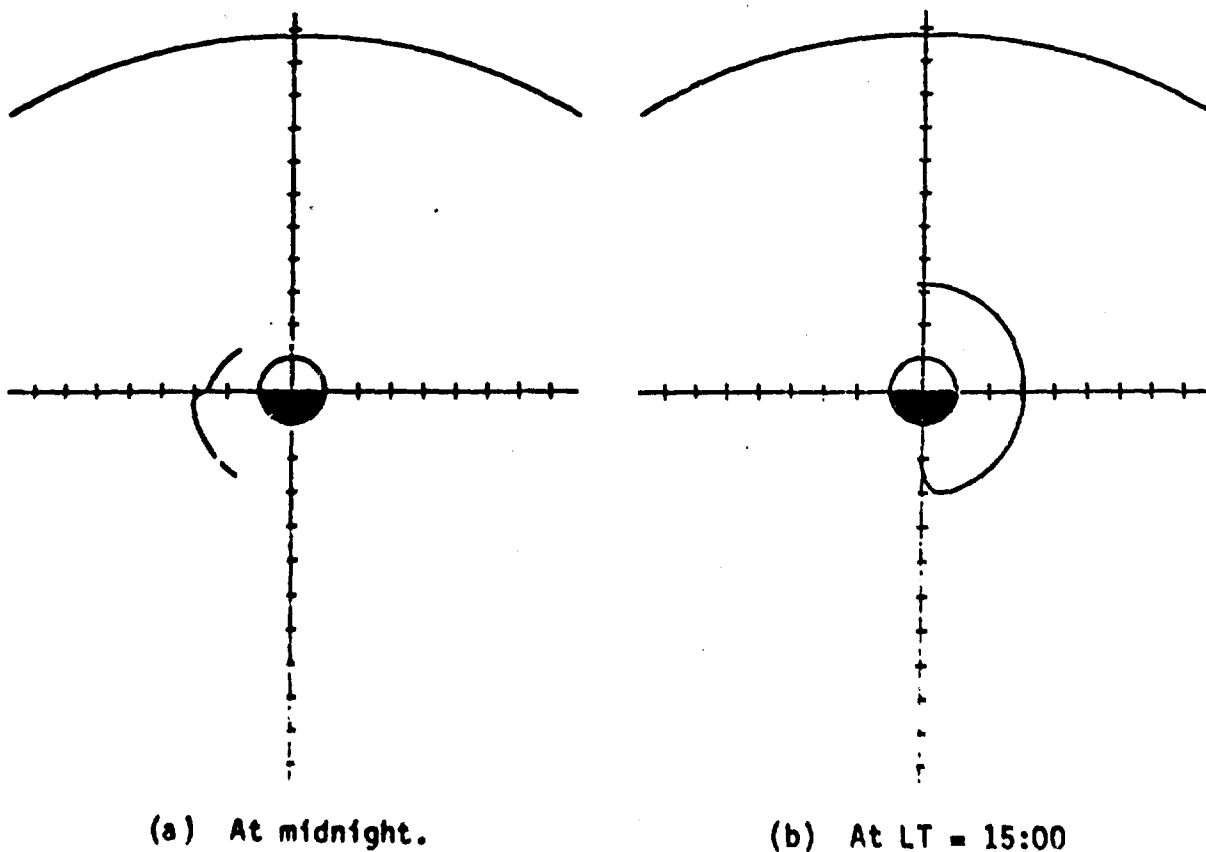

(a) At midnight.

(b) At LT = 15:00

Figure 5. - Initial convection path of argon flux tube for beam injection at L = 2. View is of equatorial plane from above north pole with magnetopause set at r = 10.8 R_e. Σp assumed to be 10 mhos on dayside and 1 mho on nightside. Ticks are in Earth radii.
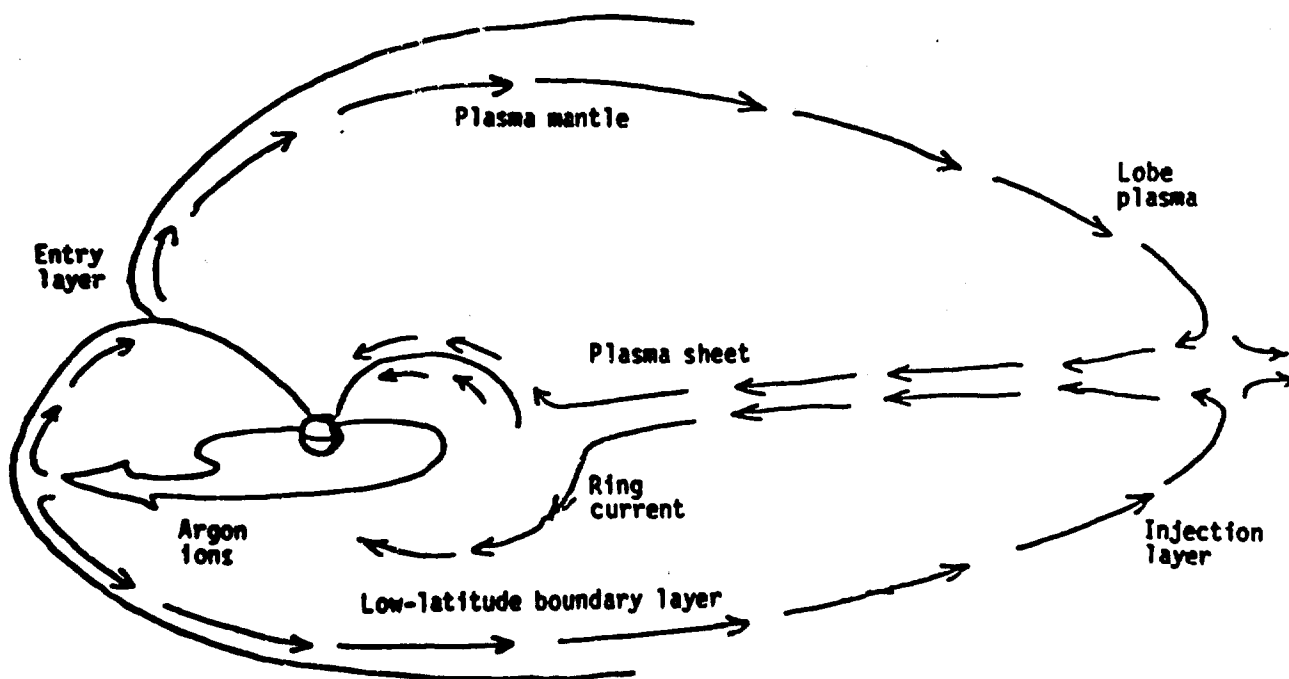
691

Figure 6. – Magnetospheric convection of argon. (Adapted from Freeman et al. (ref. 33).)